**Editors:**

**Haibo Li, Jianchun Li, Qianbing Zhang & Jian Zhao**

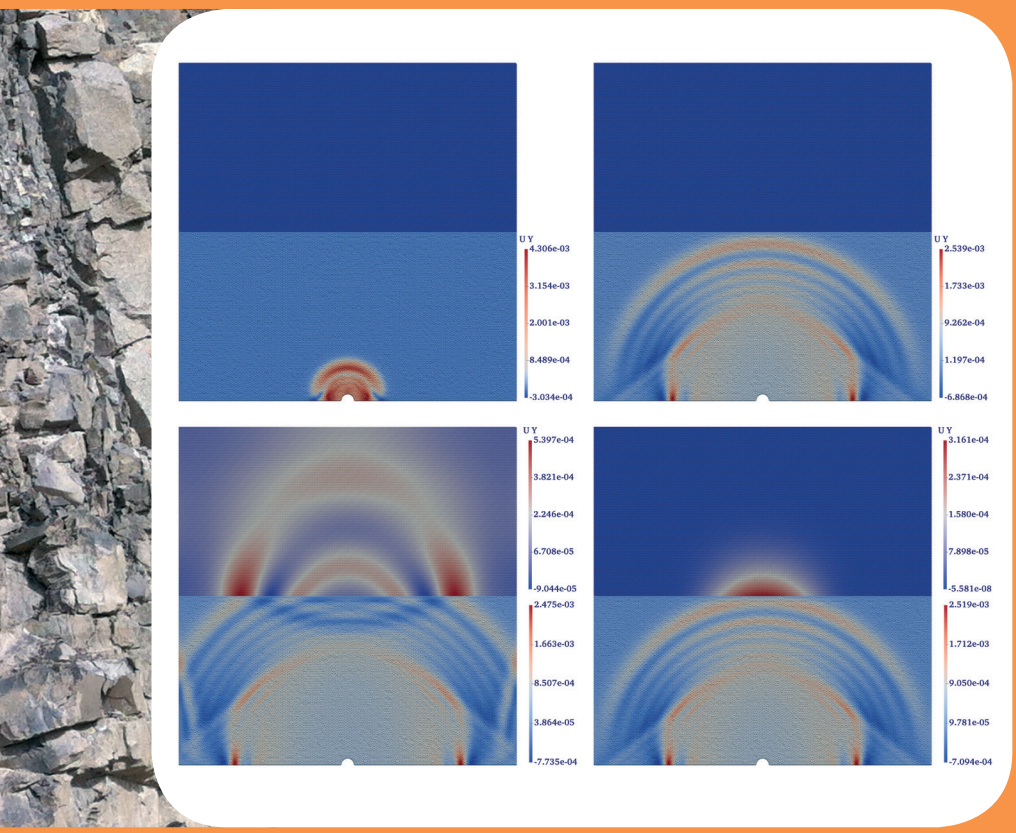


# ROCK DYNAMICS

## FROM RESEARCH TO ENGINEERING

CRC Press
Taylor & Francis Group
A BALKEMA BOOK

ROCK DYNAMICS: FROM RESEARCH TO ENGINEERING

This page intentionally left blank

PROCEEDINGS OF THE 2ND INTERNATIONAL CONFERENCE ON ROCK DYNAMICS AND APPLICATIONS (ROCDYN-2), 18–19 MAY 2016, SUZHOU, CHINA

# Rock Dynamics

## From Research to Engineering

*Editors*

Haibo Li & Jianchun Li

*Institute of Rock and Soil Mechanics, Chinese Academy of Sciences, Wuhan, China*

Qianbing Zhang & Jian Zhao

*Department of Civil Engineering, Monash University, Clayton, VIC, Australia*

CRC Press
Taylor & Francis Group
Boca Raton London New York Leiden

CRC Press is an imprint of the
Taylor & Francis Group, an **informa** business

A BALKEMA BOOK

**Cover photos:**
*Front cover photo*:
Propagation of a cylindrical transient stress wave across an interface by numerical simulation. Clockwise from top left, 5 microseconds, 24 microseconds, 25 microseconds, and 30 microseconds, after the application of the incident wave.

*Background photo*:
Rock discontinuities and contact interface observed in a quarry.

*CRC Press/Balkema is an imprint of the Taylor & Francis Group, an informa business*

© 2016 Taylor & Francis Group, London, UK

Typeset by V Publishing Solutions Pvt Ltd., Chennai, India
Printed and bound in Great Britain by CPI Group (UK) Ltd, Croydon, CR0 4YY

All rights reserved. No part of this publication or the information contained herein may be reproduced, stored in a retrieval system, or transmitted in any form or by any means, electronic, mechanical, by photocopying, recording or otherwise, without written prior permission from the publisher.

Although all care is taken to ensure integrity and the quality of this publication and the information herein, no responsibility is assumed by the publishers nor the author for any damage to the property or persons as a result of operation or use of this publication and/or the information contained herein.

Published by: CRC Press/Balkema
P.O. Box 11320, 2301 EH Leiden, The Netherlands
e-mail: Pub.NL@taylorandfrancis.com
www.crcpress.com – www.taylorandfrancis.com

ISBN: 978-1-138-02953-8 (Hbk)
ISBN: 978-1-315-47081-8 (eBook PDF)

*Rock Dynamics: From Research to Engineering – Li et al. (Eds)*
*© 2016 Taylor & Francis Group, London, ISBN 978-1-138-02953-8*

# Table of contents

Preface xi

Committees xiii

*Keynotes*

Modelling of deep mining induced seismicity for hazard estimation 3
*D.A. Beck*

Induced seismicity in the development of EGS—benefits and drawbacks 13
*D. Elsworth, Y. Fang, Q. Gan, K.J. Im, T. Ishibashi & Y. Guglielmi*

Dynamic behavior of NPR bolt and its application to rock burst control 25
*M.C. He, C. Li, W.L. Gong & D.Q. Liu*

Dynamics of impact cratering 37
*T. Kenkmann*

Analysis of nonlinear spherical wave propagation for concretes 49
*H.W. Lai, Z.J. Wang, L.M. Yang & L.L. Wang*

Determination of dynamic property of rock joints based on SHPB tests 57
*J.C. Li, H.B. Li, X. Chen & Y. Zou*

Fracture specific stiffness as the critical link among fracture properties 69
*L.J. Pyrak-Nolte*

The effect of true-triaxial stress path on induced fracturing in anisotropic gneiss 79
*R.P. Young & M.H.B. Nasseri*

*Experimental techniques and laboratory testing*

High strain rate response of Himalayan quartzitic gneiss by using split Hopkinson pressure bar device 93
*Anuradha, S. Mishra, T. Chakraborty, V. Matsagar, P. Chandel & M. Singh*

Overview of geological materials research at the Cavendish Laboratory 99
*C.H. Braithwaite, S.S. Kirk, A.P. Jardine & J.E. Field*

Study of rock inhomogeneity with ultrasonic tomography using concrete block and limestone block at laboratory scale 105
*Herman, N.P. Widodo & I. Arif*

A laboratory crushing apparatus for understanding dynamic rock fragmentation 111
*S. Huang & B. Mohanty*

Laboratory observation on the seismic response of the filled joint under high amplitude stress waves 117
*X.L. Huang, S.W. Qi & K.W. Xia*

A trial of 3D printing on rock dynamics 123
*C. Jiang, G.F. Zhao, M.Z. Gao & Y.X. Zhao*

Experimental study on dynamic response of rock masses with different joint matching coefficients 129
*N.N. Li, J.C. Li, H.B. Li & S.B. Chai*

Research on mechanical properties of gneissic granite under real-time temperature 135
*X.F. Li, D.W. Wu, X.F. Zhang & H. Deng*

Research on the static and dynamic properties of the granite in Xinjiang Province Tianhu Area for the geological disposal of the high level radioactive waste 143
*K. Man, H.S. Ma, X.L. Liu, F.Q. Gong & Z.M. Chen*

Determination of the dynamic shear strength of granite under confined pressure 151
*G.J. Min, S.W. Oh, M.S. Kim, J.J. Yoon, S.H. Cho & L.J. Park*

Strain localization in rocks under uniaxial compression and direct tension 157
*I.A. Panteleev, O.A. Plekhov & O.B. Naimark*

Behaviour of underground structures in soft rocks under different strain rate and litho-static pressure 163
*K.S. Rao, S. Mishra & N.K. Gupta*

Petrophysical and engineering behavior of oil shale from Assam, India 171
*K.S. Rao & A. Kumar*

Experimental study on stress wave propagation across joints with different joint matching coefficients 179
*L.F. Rong, J.C. Li, H.B. Li & S.B. Chai*

Effect of loading rate on mechanical properties of anisotropic sandstone under compressive loading 185
*A. Taheri*

Mechanical behavior of artificial rock contained single plane of weakness under impact loads 191
*T.T. Wang, H.H. Li, T.R. Tzeng & Z.Y. Yang*

An experimental study of dynamic tensile failure of rocks subjected to hydrostatic confinement 197
*B. Wu & K. Xia*

Dynamically induced gouge degradation and implications for fault instability 203
*W. Wu*

Measurement of dynamic surface sliding of cement joint by Hopkinson bundle bars 209
*S.L. Xu, C.Y. Shi, L. Zhang & L.J. Zhou*

Dependence of dynamic tensile strength and fracture toughness of Longyou sandstone on heat-treatment temperature and loading rate 215
*W. Yao & K. Xia*

Experimental research on rockburst tendency and acoustic emission characteristics of coal under different gas pressures 221
*Z.Q. Yin, Z.X. Hu, C.Q. Zhuo & A.Y. Yuan*

Shear strength and Hugoniot Elastic Limit (HEL) of rock materials under shock loading 227
*Q.B. Zhang*

Anti-seismic research for cracked lining structure 233
*H.C. Zhou, W.P. Xu, W.G. Qiu & K.G. Sun*

Full field strain statistics and failure mechanism of granite under dynamic and quasi-static compression 239
*L.J. Zhou, S.L. Xu & C.Y. Shi*

Application of 3D printing and micro-CT scan to rock dynamics 247
*T. Zhou & J.B. Zhu*

The effect of strain rate on compressive strength of water saturated sandstone 253
*Z.L. Zhou, X. Cai, Y. Zhao, L. Chen & C. Xiong*

*Dynamic theories and numerical modelling*

Numerical simulation for cylindrical wave transmission across jointed rock masses 263
*S.B. Chai, J.C. Li & H.B. Li*

Adaptive coupling of smooth particle hydrodynamics and finite-element method for rock blasting simulations 269
*D. Deb & A. Khan*

A parameter-variable creep damage model considering the effects of loading frequency for rock salt and its engineering application in deep storage cavern 275
*G.X. Ding, L.J. Ma, M.Y. Wang, Y. Wang & L. Dong*

Indentation fragmentation mechanism of anisotropy shale under dynamic and static loads 283
*G.J. Dong, P. Chen & T.S. Ma*

Relationships between interface stress element method and applied element method 289
*B. Feng, H. Chen & R.Q. Lan*

Numerical investigation on the effect of fracture filling material on P-wave propagation 295
*Y.L. Gui & Z.Y. Zhao*

3D seismic imaging for monitoring rock-mass degradation and excavation damage 301
*J.W. Huang, J.W. Flynn, S. Mustonen & R.P. Young*

Numerical modeling investigation on blasting of rock under different earth stresses 309
*C. Jiang & Y.J. Ning*

Classification of mechanisms of induced earthquakes: From a view of rock mechanics 315
*J.Q. Kang & J.B. Zhu*

From earthquake to aseismic creep: What governs fault slip modes? 321
*G.G. Kocharyan*

Calculation of the irreversible deformation region under a large-scale underground explosion based on block hierarchical structure 327
*J. Li, M.Y. Wang & Q.H. Qian*

Validation study of the Particle-based Numerical Manifold Method (PNMM) on stress wave propagation 335
*X. Li, Q.B. Zhang, L. He & J. Zhao*

Crack initiation and propagation simulation for polycrystalline-based brittle rock utilizing three dimensional distinct element method 341
*X.F. Li, H.B. Li, J.C. Li & X. Xia*

Study of the failure process in large-sized coal-rock mass under static and dynamic loading by three-dimensional numerical simulation 349
*X.L. Li & C.L. Li*

A FEM-based numerical study of responses of underground openings subject to plane, cylindrical, compressive and tensile waves 355
*Z.Y. Liao, N.M. Lam & J.B. Zhu*

Numerical simulation of sand production in oil well considering particle size effect 361
*X.S. Liu, M. Xu & L. Zhang*

Study on determining REV of fractured rock masses considering hydro-mechanical effect 369
*X.S. Liu, L. Zhang & Z.H. Zhou*

Dynamic stability analysis of rock slope based on permanent displacement ratio theory 375
*W.D. Ni, G.B. Zhao & M.J. Sun*

Numerical modeling of fracture behaviour of sandy mudstone under impact loading 381
*L.X. Xie, W.B. Lu, Q.H. Jiang, Q.B. Zhang & L. He*

The numerical simulation study on explosive shock response of ship large cabin 389
*X. Xiong, X.Y. Wu & J. Jin*

*Engineering applications and case studies*

The dynamic simulation of ground motion of Lushan earthquake by finite element method 397
*Y.Z. Bai, X.W. Xu & Q. Zhou*

Numerical simulation of blasting vibration on high cutting slope 403
*X.L. Cao, W.X. Gao, N. Wu, H. Zhao & D.H. Liu*

Seismic dynamic reliability analysis of bedding rock slopes based on Newmark-β method 409
*X.L. Chen, W.H. Gong, Y. Li, J.W. Qiu & X.H. Zhong*

Microseismic characteristics analysis of fault activation induced by excavation unloading at the left bank underground powerhouse of the Baihetan hydropower station, China 417
*F. Dai, A. Li, N.W. Xu & Y.L. Fan*

The cavity detection method of highway subgrade and the grouting effects contrast 423
*H.L. Deng, Y. Guo & G. Chen*

The design and implementation of automatic warning system of tunnel monitoring 429
*H.L. Deng, G. Chen & Y. Guo*

Dynamic loads and design of tunnel supports using rock mass quality 435
*R.K. Goel*

A numerical model to determine the best time to start infill drilling in a mature reservoir 443
*I. Khurshid*

Seismic monitoring of nuclear power plants in Russia 451
*S.B. Kishkina, E.G. Bugaev & I.A. Sanina*

Integrating structural and numerical solutions for road cut slope stability analysis—A case study, India 457
*J. Kundu, K. Sarkar & A.K. Singh*

In-situ monitored seismic response of a rock tunnel 463
*C.L. Kung, Y.C. Chiu, T.T. Wang & T.H. Huang*

Numerical simulation of blasting excavation in reconstruction and expansion tunnel 469
*D. Liu, W.X. Gao, B.P. Sun & D.H. Liu*

Rockburst prevention schemes of coal mines in China 475
*Z.H. Ouyang, S.K. Zhao & Q.X. Qi*

Application of microseismic monitoring technology in deep mining 483
*Z.Y. Song & H.G. Ji*

New brittleness indices to describe rock failure under compressive load 489
*A. Taheri & H. Munoz*

The effect of pre-stress on wave velocity and waveform 495
*M. Tao, H.T. Zhao, K. Du, T.B. Yin & X.B. Li*

Low transient strength of hard rocks at spontaneous failure 503
*B.G. Tarasov*

Numerical simulation and analysis of rock heap formation under seismic motion 509
*J.X. Wang & Y. Yin*

Nondestructive detection and intelligent diagnosis technology of anchorage system 517
*M. Xu, X.S. Liu & Z.X. Yan*

Multi-scale characteristics of rockburst under the multi-level stress control 523
*S.K. Zhao, Q.X. Qi, Z.H. Ouyang & Z.G. Deng*

Time history analysis method for dynamic fuzzy reliability of bedding rock slope 529
*X.H. Zhong, W.H. Gong, X.L. Chen, J.W. Qiu & Y. Li*

Pseudo-dynamic analysis of stability of layered rock slope subjected to seismic loads 541
*W. Zhou, H.B. Li, Y.Q. Liu & S.B. Chai*

Microseismic energy evolution of high rock slop during excavation
and after reinforcement 547
*D.Y. Zhuang, Z.Z. Liang, C.A. Tang & K. Ma*

This page intentionally left blank

*Rock Dynamics: From Research to Engineering – Li et al. (Eds)*
*© 2016 Taylor & Francis Group, London, ISBN 978-1-138-02953-8*

# Preface

This book is the Proceedings for the Second International Conference on Rock Dynamics and Applications (RocDyn-2)—a collection of 77 papers submitted to the RocDyn-2 conference.

The first part of the proceedings includes 8 keynote papers, covering a wide range of dynamic issues related to rock mechanics and rock engineering, from rock failure mechanism, stress wave propagation, to seismic behaviour and impact. The main body of the technical papers are divided into 3 sections: (i) experimental techniques and laboratory testing, (ii) dynamic theories and numerical modelling, and (iii) engineering applications and case studies. The division of topics follows the same fashion as the presentation program of the conference. However, there are some papers spanning 2 or even 3 sections and they are judged by the editors to be placed in the most appropriate sections.

The RocDyn-2 conference is organised by the Institute of Rock and Soil Mechanics of the Chinese Academy of Sciences and Monash University through the Southeast University—Monash University Joint Research Institute, supported by Nanyang Technological University, Tianjin University, and Southeast University. The conference is a specialised symposium of the International Society for Rock Mechanics, sponsored by the Chinese Society for Rock Mechanics and Engineering. The Organising Committee and the Advisory Committee are listed on the next page.

We are pleased to see that the rock mechanics community feels the importance and need of understanding rock dynamics. They have planned to continue International Conference on Rock Dynamics and Applications as a conference series. We hope that the proceedings will serve as a good archive to document the development of rock dynamics knowledge and the experience of engineering applications of rock dynamics. The proceedings is prepared by the editors with editorial support of Haiying Bian (editorial office of Geomechanics and Geoengineering – An International Journal, published by of Taylor & Francis), and CRC Press / Balkema staff: including Léon Bijnsdorp, Lukas Goosen and Vicky Gressie.

ZHAO Jian and QIAN Qihu
RocDyn-2 Advisory Committee Chairs
*May* 2016

This page intentionally left blank

*Rock Dynamics: From Research to Engineering – Li et al. (Eds)*
*© 2016 Taylor & Francis Group, London, ISBN 978-1-138-02953-8*

# Committees

## ORGANISING COMMITTEE

### Chairs

Haibo LI, *CAS Institute of Rock and Soil Mechanics, Hubei, China*
Jianchun LI, *CAS Institute of Rock and Soil Mechanics, Hubei, China*

### Members

Lei HE, *Southeast University, Jiangsu, China*
Lixing HUANG, *CAS Institute of Rock and Soil Mechanics, Hubei, China*
Xuhai TANG, *Monash University, Victoria, Australia*
Wei WU, *Stanford University, California, USA*
Kaiwen XIA, *University of Toronto, Ontario, Canada*
Songlin XU, *University of Science and Technology of China, Anhui, China*
Qi ZHANG, *Southeast University, Jiangsu, China*
Qianbing ZHANG, *Monash University, Victoria, Australia*
Gaofeng ZHAO, *Tianjin University, Tianjin, China*
Xiaobao ZHAO, *Nanjing University, Jiangsu, China*
Zhiye ZHAO, *Nanyang Technological University, Jurong, Singapore*
Jianbo ZHU, *Hong Kong Polytechnic University, Hung Hom, Hong Kong*

## ADVISORY COMMITTEE

### Chairs

Qihu QIAN, *China*
Jian ZHAO, *Australia*

### Members

Ömer AYDAN, *Japan*
David BECK, *Australia*
Charles DOWDING, *USA*
John FIELD, *UK*
Gérard GARY, *France*
Yossef HATZOR, *Israel*
Shisheng HU, *China*
Charlie LI, *Norway*
Yuzo OHNISHI, *Japan*
Yuri PETROV, *Russia*
Alex SPATHIS, *Australia*
Lili WANG, *China*
Fengjun ZHOU, *China*
Giovanni BARLA, *Italy*
Ezio CADONI, *Switzerland*
Conrad FELICE, *USA*
William FOURNEY, *USA*
R.K. GOEL, *India*
Stefan HIERMAIER, *Germany*
Heinz KONIETZKY, *Germany*
Xibing LI, *China*
Frederic PELLET, *France*
Genhua SHI, *USA*
Dick STACEY, *South Africa*
Paul YOUNG, *Canada*
Yingxin ZHOU, *Singapore*

This page intentionally left blank

*Keynotes*

This page intentionally left blank

*Rock Dynamics: From Research to Engineering – Li et al. (Eds)*
*© 2016 Taylor & Francis Group, London, ISBN 978-1-138-02953-8*

# Modelling of deep mining induced seismicity for hazard estimation

D.A. Beck
*Beck Engineering Pty Ltd., Sydney, Australia*

ABSTRACT: Mining engineers must certify that the capacity of excavations in their mine exceeds the expected demand. This requires the engineer to satisfactorily estimate the expected future loads that an excavation will be subjected to, as well as the capacity of the rock mass—ground support system. In seismically active mines, this essential task is more difficult as high rates of deformation and dynamic loading are still comparatively infrequent events and the simulation of support and reinforcement for dynamic loading is more complex. Empirical methods of estimating excavation capacity for dynamic rock related hazards are also very poorly evolved, and have limited efficacy. In this paper, computational forecasting of potential for dynamic deformation in rock masses surrounding mines as well as the simulation of potential large events themselves is discussed.

## 1 INTRODUCTION

When a hard working pillar, or rock bridge in the mine fails, or a highly stressed fault slips, load is redistributed from that yielded 'structural element' of the rock mass. Other parts of the mine must do that 'work'. Whether other components elsewhere in the mine subsequently fail is a function of their capacity and the load path and ultimate loading which evolves as the system converges to a new equilibrium. Subsequent failures are rarely due to impulsive loads or vibrations from the seismic wave emanating from the original failure. Though seismic waves do damage excavations in mines, the magnitude and occurrence of the hazard is less than the exposure of personnel to increasing rock mass damage and deformation due simply to load redistribution caused by mining and under-supporting of excavations.

Most often, the 'dynamic' damage seen in working areas of a mine which is hazardous to personnel, is the rapid dilation of rock in the walls of the excavation or dilation adjacent to and associated with dislocation of discontinuities. The dynamic damage occurred as an essential consequence of additional stress, which came on to that part of the mine following an episode of excavation or failure elsewhere.

The most common example is in tunnels adjacent to work areas, which experience a very rapid increase in the depth of damage in the walls when stress becomes more adverse following some other change in the mine. If that additional damage were to occur slowly, the installed ground support would only need to accommodate the strains and retain the loose material, subject to the loads that evolve in the loose material due to gravity. In this case, the engineer would have considerable opportunity to intervene before the situation become dangerous.

When the new damage occurs quickly enough and in a large enough increment so that there are additional accelerations imparted to the newly loosened material, the loads that ground support must sustain may transiently be higher than that due to gravity alone, and there is no opportunity to intervene part way through the damage process.

An example of a grossly distorted tunnel, which failed in a dynamic way is shown in Figure 1. In this case, the stress in the tunnel wall increased during a several hour period, after a nearby pillar failed. Several hours after the nearby pillar failure which did generate a large seismic wave, the failure in the photograph occurred violently, ejecting a significant volume of rock into the drive. The ejection was not caused by a stress wave emanating from elsewhere—it occurred because of the rate of dilation of the rock in the tunnel wall, as it failed.

Figure 1. An example of dynamic failure of the rock mass around a tunnel not caused by a remote seismic source.

From an engineering perspective, the mining engineer designing ground support and excavations in a mine must undertake 2 broad tasks:

- Estimation of the potential for dynamic deformation and seismic events, including appreciating the mechanisms by which damage may occur to an excavation, including both rapidly (dynamically) increasing dilation of the rock mass due to increasing stress as well as the effects of seismic waves.
- Simulation of the response of installed support and the discontinuous rock mass around the excavation.

## 2 FORECASTING POTENTIAL FOR DYNAMIC DEFORMATION

Stress, or components of stress are the most common parameters used to estimate seismic hazard levels in mines, but stress is a poor predictor because stress is stored energy. If the energy is not released there are no seismic events.

Measures seeking to quantify the potential for energy release at particular excavation steps are more reliable. Local Energy Release Density (LERD, after Wiles 1998), Modelled Ground Work (MGW, after Beck et al. 2001), Energy Release Rate (after Ryder 1987) and nuanced interpretations of the magnitude of induced stress-change all seek to quantify the work that a rock 'element' is done within the load 'system'. That 'work' can correlate with the energy that would be released should that rock be mined or fail.

Board (1996) used the ESS method and a discontinuum model together, to estimate seismic source parameters on fractures around a mining front in a longwall mine, calibrated using measured seismicity. The analysis estimated the likeliest locations and magnitudes for a given mine geometry. Yield (the trigger for energy release) was emergent in the analysis.

Beck & Brady (2001) undertook a conceptually similar approach, but attempted to estimate event probability by comparison of the modelled results with field data from the Deep Copper Mine, Australia. A cell evaluation technique was used to compare MGW, yield potential and measured events to compute a probabilistic function and measure its predictive efficacy. That analysis showed that if the potential for failure is estimated well enough (for example using ESS, or MGW), combining that with one of the simple 'energy' measures did allow a useable differentiation of high and low risk zones.

The main limitations of these approaches, limited by the computational power of the day, are that the MGW and ESS quantify a potential magnitude of changes in the system over an increment of time or due to an increment of excavation. Rate of Energy Release, or RER on the other hand is instantaneous, peak rate of energy release from a volume of rock. As it measures the rate of change, it more directly correlates with potential for surplus energy to be emitted into the surrounding rock in the form of seismic waves, or for violent yield.

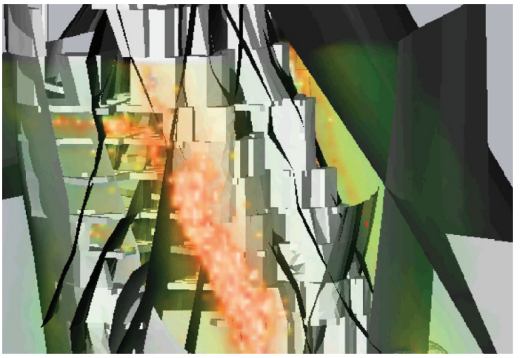

Figure 2. An example model showing the typical structural resolution for computation of RER for stoping mines.

RER can be computed on faults and in the rock mass and can be directly compared to the measure which it seeks to forecast—event occurrence and magnitude. A valid rock mechanics model for this purpose is one that satisfactorily forecasts both the extent and magnitude of rock mass and discontinuity damage using an explicit time integration scheme. On this basis, only 3d, dynamic, strain softening, dilatant discontinuum models, able to replicate observed damage and deformation at a sufficient resolution will be applicable for estimating RER. Most important is the requirement to represent discontinuities at a sufficient scale in the model. Beck et al. (2013) proposed guidelines for sufficient incorporation of discontinuities, depending on the target resolution of the analysis. In essence, for this application, much smaller length scales must be explicitly incorporated than is common in most mining simulation. An example model showing the typical structural resolution for computation of RER for stoping mines, is shown in Figure 2, though higher resolution is desirable.

Few models are built to this specification as they require considerable effort and computing power. So far, all models for RER have employed the Levkovitch Reusch 2 (LR2) discontinuum framework (Reusch et al. 2010). To establish a quantitative relation between modelled RER and expected or measured seismic potential, the 'Cell Evaluation Method' or CEM (Beck & Brady, 2001) is employed, but making use of RER instead of MGW.

Using RER in this way, the entire model is discretised into regular, volumetric 'cells' or 'test blocks'. RER is calculated in every single test block within the model, for every single excavation step. Next, the number of real, measured seismic events in each test block is counted for each and every model step. When the data is assembled, the probabilistic correlation between real event and modelled RER can be computed. The relation between RER and the event probability, (x) of a mine tremor of a certain magnitude, X, occurring in a test block, is denoted:

$$p(X) = x \approx \frac{n_{RERi}}{e_{RERi_j}} \tag{1}$$

where, $e_{RERi_j}$ is the total number of test blocks having values within any range of RER release rate, $j$ is the fixed interval of RER being evaluated and the sum of blocks containing events within that magnitude range as $n_{RERi}$, $i$ is the event magnitude range (eg. 0ML to 1ML) being considered.

There are a number of conditions that have to be satisfied for $p(X)$ to be a true probability, and these are outlined in Beck & Brady (2001).

An example correlation between RER and measured event occurrence is shown in Figure 3. The correlation is based on over 30000 events measured over 4 years at a deep block caving mine. It shows a very clear, the exponential relationship between the RER and event occurrence. The relationship and how this can be used to calibrate a model can be understood by considering the relation between damage and acoustic emissions, after Beck et al. (2009).

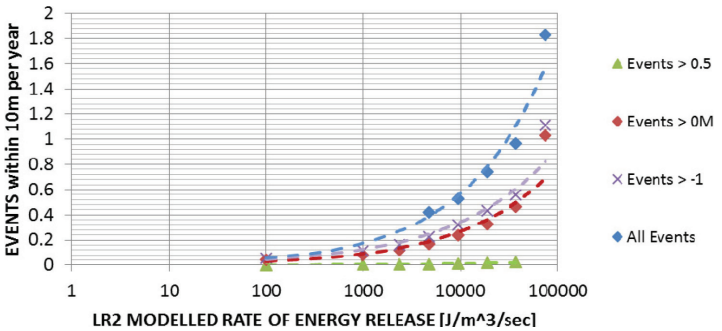


Figure 3. Correlation between modelled RER and Event occurrence, by Magnitude at an example mine. The correlation is based on over 30000 events measured over 4 years.

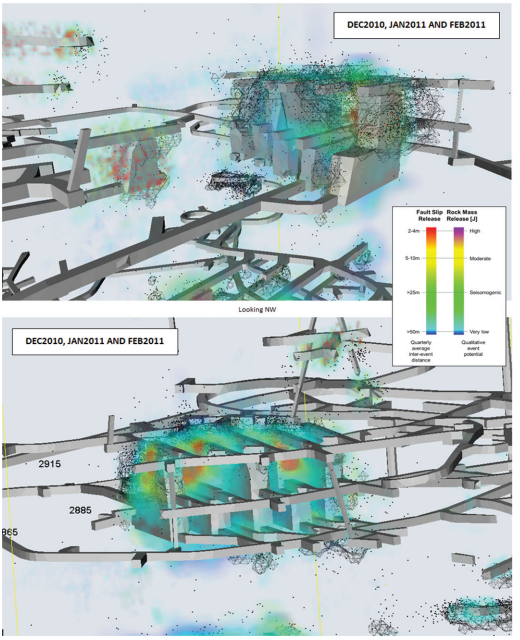


Figure 4. Modelled Rate of Energy Release versus Seismicity for an example period from NRS mine (after Beck et al. 2012). The wireframes show measured seismic clusters and points show measured seismic events, while colours show modelled seismic potential.

Having established a probabilistic relation, hazard can be quantified throughout the mine as outlined in Beck, Levkovitch & Simser (2012) for the Nickel Rim South Mine in Canada. The model incorporated stope by stope extraction, a very detailed structural model and a high resolution geological model. LR2 was implemented as described above, and examples of the close correlation between modelled RER and seismicity are reproduced in Figure 4. The Figure shows measured event clusters as wireframes, and various measures of modelled energy release as volume rendered clouds.

The measured event clusters in the Figure are Inter-Event (IE) distance isosurfaces of approximately 5–10 m. For this study, high intensity seismic activity was defined as a cluster with an IE distance of <5 m. Moderate intensity corresponded to an IE distance of <10, seismogenic zones i.e. continuous and bounded regions of increased activity above random, or background microseismicity was assessed by volumes with an IE distance of <25 m. Areas with an IE distance of >25 m were considered to experience low level or background noise only.

The effect of the process is to express potential or measured exposure of each area of the mine to seismicity as a function of events of a certain magnitude, within a certain distance, during an explicit period, as required, so that problem areas can be investigated further:

- The mechanism of potential dynamic instability damage is investigated, typically by evaluating the increments of displacement associated with periods of high RER in the model. An example image from such an evaluation is shown in Figure 5.
- Options to change the mine plan to reduce the likelihood or severity of dynamic stability are considered, typically using the model.
- Ground support and other control measures to manage residual hazard are proposed, and evaluated to confirm that they have sufficient capacity, as described below.
- During mining, all control measures are implemented and audited to confirm they are sufficient. If they are not, or the rock mass response is not as expected, the causes are investigated and necessary adjustments to the plan are made.

## 3 SIMULATING LARGE MINING INDUCED SEISMIC EVENTS

Having established a potential mechanism for dynamic instability and areas of interest using RER and increments of displacement, the sufficiency of the proposed excavation-ground support system must be evaluated. Simulating these classes of events must involve:

- Applying the dynamic movements from an area of interest in the donor model to a very detailed, discontinuum sub model of the support and rock mass in the area of interest.
- Increasing or decreasing the size and strength of the 'test event' by scaling the movements to establish the limits and identify the weaknesses of the support system.

The resolution of the sub model is limited by the resolution of the discontinuity model. Typically, the explicit incorporation of sub tunnel scale discontinuities is usually essential.

### 3.1 *Establishing the representative test events*

An example area of interest from a deep, high stress mine was shown in Figure 5. That area had very high RER, and the model indicated that during that period, there was a 'budget' for very significant movements in a fashion known to correlate with high potential for dynamic

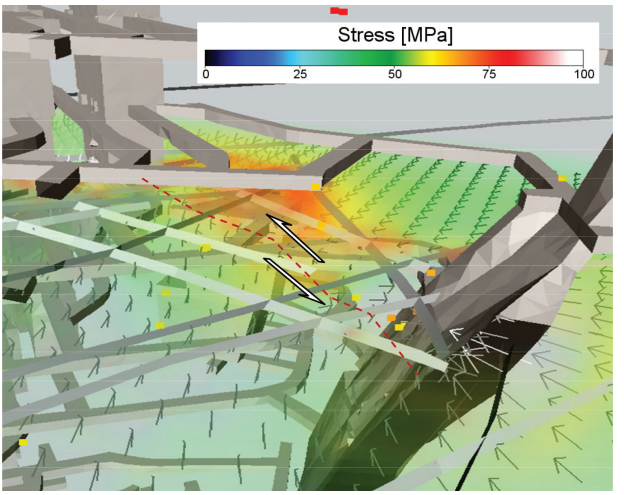


Figure 5. Simulated major principal stress (cloud) and displacements (vectors) at a location with high modelled RER, indicating significant potential for shear rupture of a major pillar.

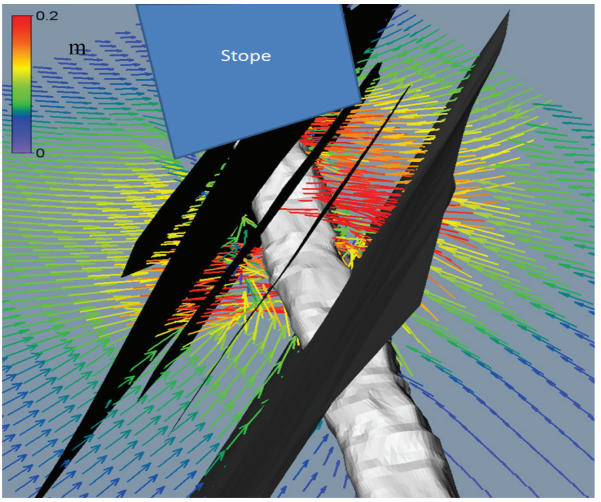


Figure 6. Oblique view showing displacement vectors for the example test event, indicated by the global model.

hazards. Another example is shown from a global model in Figure 6 of another mine. In this area of the example mine, the peak fault-slip dislocation indicated by the global model was approximately 300 mm at the worst affected section of drive for a multi-ring firing, with the centroid of fault slip occurring just into the hangingwall from the drive. This event occurs in the model because the relevant faults traversing the test site had been 'locked' or 'stuck' for successive blasts (advances of the stope front in the model) and then slipped in a single event due to stoping induced sill pillar yield around the locked fault.

The sub modelling to evaluate the proposed ground support system for this site occurs in two stages: (i) the quasi static pre-loading and deforming phase and (ii) the dynamic test phase.

3.1.1 *Quasi-static pre-loading phase (pre-event stage)*

The dynamic events must be applied to the tunnel in its current estimated damage state, which includes an envelope of damaged rock around the excavation. We need to accumulate this damage in the sub model, because it has a strong effect on the dynamic response of the excavation and ground support system. In mines where high stress conditions prevail, rock-mass damage can extend deeply into the tunnel walls with the most intense damage near the surface, with decreasing damage further from the tunnel. To arrive at this condition, the history of mining before the event is replicated in the test model by:

- Extracting the quasi-static deformation history for each element node on the boundaries of the test model from the same locations in the calibrated mine-scale model, up to the start of the test event.
- Applying these 3D deformation histories to each boundary node of the test model.

The key point is that it is displacements at equally spaced time increments from the mine-scale model, not stresses which are transferred from the mine-scale model to the test model boundaries. This replicates the deformation and distortion and stress. Transferring stress alone to each node would not replicate the deformation and damage.

The DFN, as-built tunnel wall geometry, major faults and ground support for the test model are shown in oblique cut-away views in Figure 7. The images show the discontinuities and the detailed construction of the tunnel to match the 3D surveys, and the exact matching of the support installation to the tunnel topology.

We note that the indicated resolution of discontinuities in the model is at the lower limit of that required for sufficient dynamic analysis or a tunnel scale problem, as outlined in Beck et al. (2013).

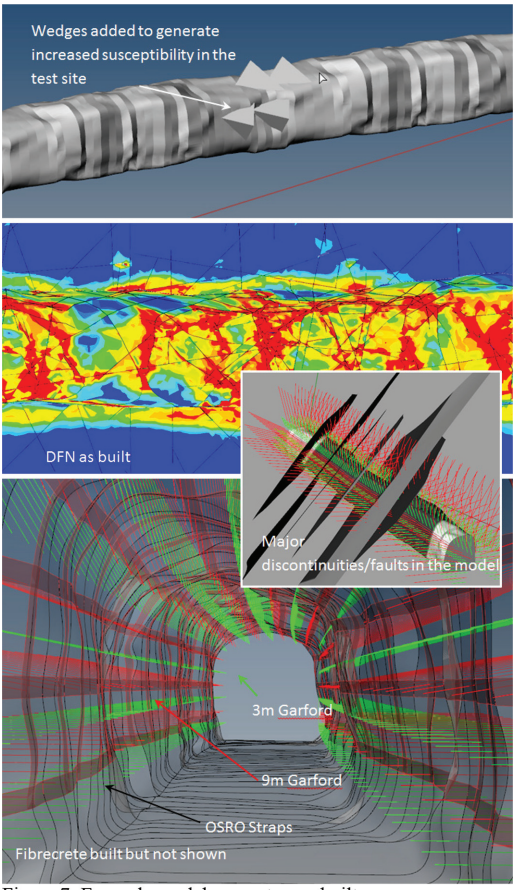


Figure 7. Example model geometry, as built.

### 3.1.2 *Dynamic loading phase*

For the dynamic phase of the test model, we apply the history of displacement for each sub model boundary node taken from the mine-scale model as follows:

- We divide the displacements versus time for each boundary node into much smaller increments by interpolation.
- We apply these very small, incremental boundary displacements with a velocity history, based on our calibrated expectations for an event of the target size. The velocity starts at zero, ramps up to a maximum and is ramped back down again. This process 'converts' increments of displacement from the coarser mine-scale model for the period we have identified as matching the target event size, into a more realistic dynamic event in the sub model.
- We can use the mine-scale models solution and energy versus time plots from seismograms of the period surrounding measured events as a guide as to how to ramp the velocity of the event up and down. The process of achieving a realistic outcome at the test site does require some testing and adjusting, with the ultimate measure the nature of the waveform generated at the test site. At Ernest Henry Mine (Campbell et al. 2011), the spectra and duration of the simulated events was compared to similar measured data to confirm sufficient calibration.
- For the example shown, we used other measured large events with magnitudes similar to that of interest for this study from the mine to estimate a total ramp-up and ramp down time. This period is not the same as the total event duration seen in a seismogram, which

is only the recorded seismic event. The cumulative energy versus time plots for individual large events at the mine showed that the 90–95% of the seismic energy for a large event occurs in a very characteristic pulse of 0.5–0.7 seconds. The 'tail' that occurs after the main displacement phase represents a very small proportion of the total energy dissipated during an event and we presume corresponds to a small amount of the permanent deformation arising from the event.

- After the initial period of enforced boundary displacements, we let the model continue until it reaches a stable static equilibrium (comes to rest).
- The reflections and continuing vibrations take several seconds to diminish as they do in the real mine. Blocks or wedges that are moving also continue to move, for example, they may continue to fall. Truly free blocks—those liberated and disconnected from the rock mass can be removed from the model during this phase to save computation time.
- At the end of the test, the performance of the system is evaluated. If the system has failed, he event size is reduced and the system re-tested to find the safe working limits of the support system.
- If the support is intact, the magnitudes of the applied boundary displacements are ramped up. Over several iterations the peak capacity and response of the rock-ground support system to a range of deformation events is established.

A seismogram and displacement time history for a node in the wall of the tunnel in the sub model is shown in Figure 8, taken from one of the test models. The graph shows the particular node displaces over 150 mm during the event, and this movement is matched on the opposite wall, so the closure during the event at that location is in the order of 250–300 mm as indicated by measured deformation observed for the largest damaging events at the mine and the global model.

The seismogram should look different to common seismograms as seen in the mine site micro seismic system, as those sensors are not placed on the walls of tunnels in areas where very significant seismic damage is expected (they are placed further away to achieve better coverage). They are placed outside, not inside the seismic source, and are also displacement corrected.

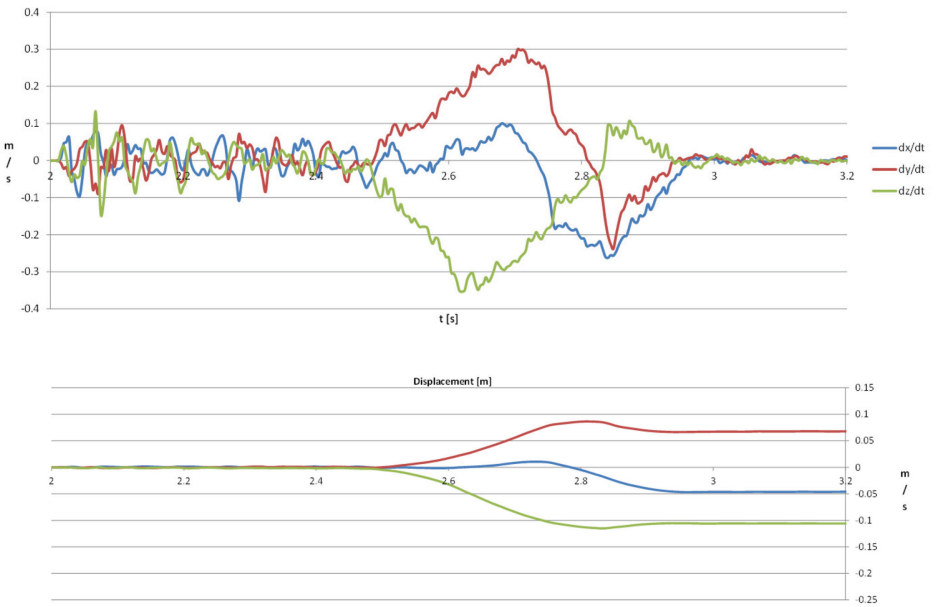


Figure 8. Simulated seismogram and displacement time history for a node at the boundary of the tunnel in the sub model.

### 3.1.3 *Example simulation results*

An image from the test simulation is shown in Figure 9. For the test event (peak velocity at tunnel = 0.44 m/s, maximum tunnel closure = 300 mm) the modeling indicated that the support performs satisfactorily in most of the affected area, but the OSRO straps yielded excessively, reaching 100% of their strength between the brow and the fault, where approximately >250 mm of inwards movement is indicated on the affected wall and there is significant movement in the backs.

A number of brow cables were also indicated to exceed a nominal pull-out of 250 mm, but did not technically fail. Generally, the particular cablebolts simulated can theoretically withstand 300 mm of pull-out. Considering the various sources of uncertainty, we would not rely on a bolt which has displaced so far in a brow.

As a result of these issues with the design, the model was re-run with a series of smaller test events, to ultimately establish a capacity. The support system eventually was found to withstand displacements correlated with a smaller 2.3 ML event (Peak velocity at tunnel = 0.32 m/sec, maximum tunnel closure = 0.25 m). Example results for the smaller event are shown in Figure 10.

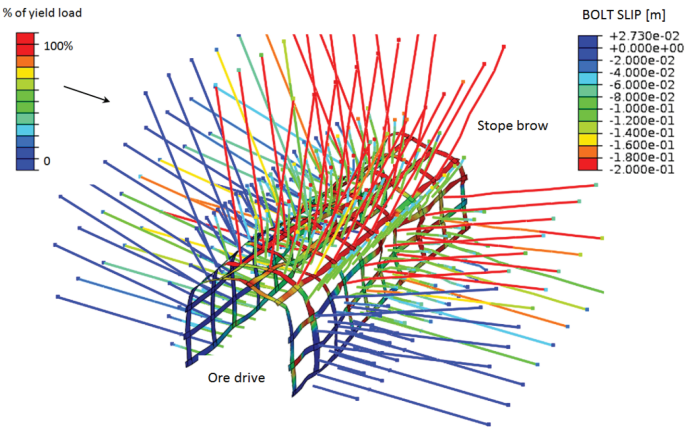


Figure 9. Loads and damage after a 2.8 ML test event. Red on support elements equates to 100% of the slip load for bolts, and the yield strength for straps. Failed straps are deleted from the images i.e. bolts and straps can yield without failing. The nodes at the end of the bolts indicate slip in metres.

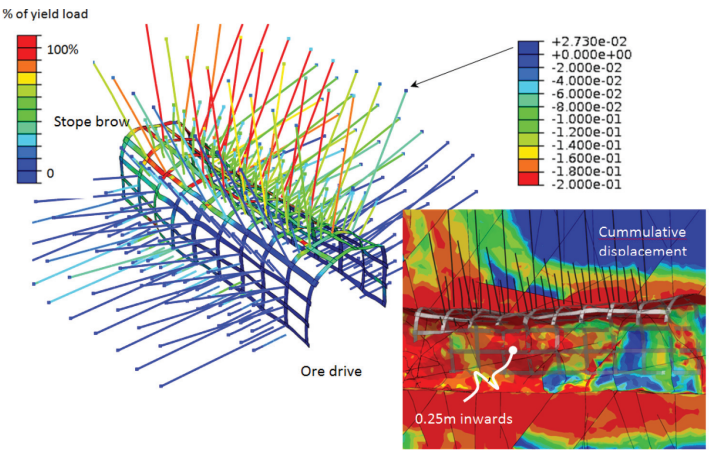


Figure 10. Loads in Osro Straps and bolts after a 2.3 ML event. Red equates to 100% of the slip load for bolts (i.e. red indicates slip), and the yield strength for straps. Failed straps are deleted from the image. The colour of the points at the end of the bolts indicate bolt slip in m.

## 4 CONCLUSIONS

In too many highly stressed mines, the effects of seismic waves are the only dynamic hazard that is considered, even though the risk from such events is typically lower than risk arising from direct exposure to dynamic failures of excavations. The mines consider only the proximity of workers to seismic events, rather than properly considering excavation stability. This leads to an underestimation of risk and a misappropriation of resources: ground support budgets are spent across large areas that are at low risk, and real problem areas, which are much more localized, are not properly catered for.

We have proposed a scheme for estimating support capacity and sufficiency in areas at risk from high dynamic demand and presented an example work flow for evaluating the sufficiency of support designs subjected to that demand.

The example simulations show that realistic, detailed forecasting of hazards, and dynamic simulation of large seismic events is possible. Each part of the procedure is relatively standard and results can be verified at each stage by comparing modelled results to field measurements.

The workflow and technology explained here may prove useful for specifying ground support designs for complex shaped excavations or excavations subjected to dynamic loads in a mining environment, which at the moment is an area of geotechnical engineering of some importance. Empirical guidelines exist but they cannot account well for the geometry of the excavation, effects of structure or repeated loading and are not easily verified using field data.

In the mining context, at present there are no significant technical hurdles preventing adoption of similar analysis practice for analogous problems, with all tools required for the simulation available off-the-shelf and at a cost comparable to traditional analysis. In future, similar simulation should become more commonplace.

## REFERENCES


Beck, D., Lilley, C., Reusch, F., Levkovitch, V., Putzar, G. & Flatten, A. 2013. A preliminary, calibrated scheme for estimating rock mass properties for non-linear, discontinuum models. In *Sinorock. Rock Characterisation, Modelling and Engineering Design Methods*.

Beck, D.A. & Brady, B.H.G. 2001. Evaluation and application of controlling parameters for seismic events in hard-rock mines. *International Journal of Rock Mechanics and Mining Sciences*. Editorial reference: 2002/002093.

Beck, D.A., Levkovitch, V. & Simser, B. 2012. Explicit discontinuum simulation for probabilistic forecasting of fault slip and rockmass seismic potential. In *Deep and High Stress Mining*. The Australian Centre for Geomechanics.

Board, M. 1996. Numerical examination of mining-induced seismicity. In Barla G. (ed.), *Special Lectures: ISRM International Symposium on Prediction and Performance in Rock Mechanics and Rock Engineering*. Torino, Italy. pp. 89–113.

Campbell, A, Henley, K. & Lilley, C.R. 2011. Prevention of blast induced damage to underground mine infrastructure from open pit operations—A case study. *Explo 2011*, AusIMM, Melbourne.

Levkovitch, V. & Beck, D. 2013. Numerical simulation of the released energy in strain softening rock materials and its application in estimating seismic hazards in mines. In *Rockbursts and Seismicity in Mines 8*. Russia.

Reusch, F., Levkovitch, V. & Beck, D. 2010. Multi-scale, non-linear numerical analysis of mining induced deformation in complex environments, 697. In Jian Zhao, Vincent Labiouse, Jean-Paul Dudt and Jean-François Mathier (eds.), *Rock Mechanics in Civil and Environmental Engineering*, CRC Press.

Ryder, J.A. 1987. Excess shear stress (ESS). An engineering criteria for assessing unstable slip and associated rockburst hazards. In *Proceedings of the 6th ISRM conference Montreal*. pp. 1211–1215.

Wiles, T.D. 1998. *Correlation between local Energy Release Density and observed bursting conditions at Creighton Mine*. Report under contract for INCO Ltd. Mines Research. Sudbury, Canada.

*Rock Dynamics: From Research to Engineering – Li et al. (Eds)*
*© 2016 Taylor & Francis Group, London, ISBN 978-1-138-02953-8*

# Induced seismicity in the development of EGS—benefits and drawbacks

D. Elsworth & Y. Fang
*Pennsylvania State University, Pennsylvania, USA*

Q. Gan
*University of Aberdeen, Aberdeen, UK*

K.J. Im
*Pennsylvania State University, Pennsylvania, USA*

T. Ishibashi
*Fukushima Renewable Energy Institute, AIST, Japan*

Y. Guglielmi
*Lawrence Berkeley National Laboratory, Berkeley, USA*

ABSTRACT: The development of a successful Enhanced/Engineered Geothermal System (EGS) reservoir at commercial scale has proved an elusive goal—despite the prospects of an immense resource and a near-limitless supply of sustainable baseload power. Key challenges relate to both creating and sustaining a high-throughput reservoir from an initially very low permeability deep reservoir and in achieving this with minimal induced seismicity. In the following we (i) explore the nature of early- and late-time induced seismicity anticipated in such projects, (ii) observed at contemporary and historic sites, and explore how this may be linked to permeability evolution through (iii) permeability-seismicity scaling and in (iv) coupling with the evolving rate and state properties of the reservoir.

## 1 INTRODUCTION

The success of unconventional (EGS) geothermal reservoirs requires that high-fluid-throughput and thermally-long-lived geothermal reservoirs may be universally engineered and developed, at will. High-fluid-throughput in traditional basement rocks requires that reservoir permeabilities at depth (~5 km) must be elevated from the microDarcy to the milliDarcy range—this avoids untenable pumping costs and avoids inadvertently fracturing the reservoir by extreme fluid overpressures. Although fracturing would appear desirable in developing conduits with high-fluid-throughput, it typically violates the second tenet of a desired long thermal life. A long-thermal life requires that high heat-transfer area is maintained concurrent with high flow rates. This is only feasible if fluid circulation in the reservoir has a broad and even sweep through media with a short thermal diffusion length (small fracture spacing) thus avoiding short-circuiting and damaging feedbacks of thermal permeability enhancement. We explore progress towards these elusive outcomes in the following—the ability to develop high fluid throughput reservoirs with high thermal efficiency while simultaneously limiting negative environmental impacts of induced seismicity. Implicit in this view is the feasibility to use passive seismicity to map the reservoir and to constrain the evolution of mechanical and transport response in the reservoir.

## 2 RESERVOIR EVOLUTION

Key needs in the successful development of unconventional (EGS) geothermal reservoirs are to (i) stimulate sufficient permeability to enable high mass flow rates while (ii) simultaneously retaining high heat transfer area *via* broad fluid sweep through the reservoir. This is straightforward in conventional geothermal reservoirs where initial permeabilities are both high (yielding high flow rates), broadly distributed, largely uniform and with low sensitivity to changes in fluid pressure and hence effective stresses (allowing broad thermal sweep through the reservoir and muted feedback towards flow localization). The converse is true in EGS reservoirs—they begin with very low permeabilities, must be stimulated to develop sufficient flow rates, and are then sensitive to flow-localization through the combined influence of fluid pressures and especially thermal-drawdown-induced stresses.

### 2.1 *Thermal response*

A simple scaling analysis may be used to illustrate that there are two end-member behaviors for thermal drawdown in EGS reservoirs (see Figure 1). The ratio of the heat rate transferred across the reservoir by the cold fluid ($\dot{H}_f$) to that supplied to the cold fluid from the hot rock ($\dot{H}_s$) defines a dimensionless heat transfer rate, $Q_D$. This heat transfer rate scales with fluid circulation rate, $Q_f$, fracture spacing, $s$, and reservoir volume, $V$, as $Q_D \propto Q_f s^2 / V$ and defines the heat transfer capabilities of the reservoir in two end-member behaviours. One, at low flow rates, where a cooling front propagates through the reservoir and the reservoir is thermally spent when that front reaches the downstream well (Fig. 1, mid-height right, and bottom, red lines). And a second, at high flow rates, where heat is only removed slowly from the rock and the outlet temperature begins low and stay low for the full duration of thermal drawdown unless flow rate is reduced (Fig. 1, mid-height left, and bottom, blue lines). These end-member conditions are:

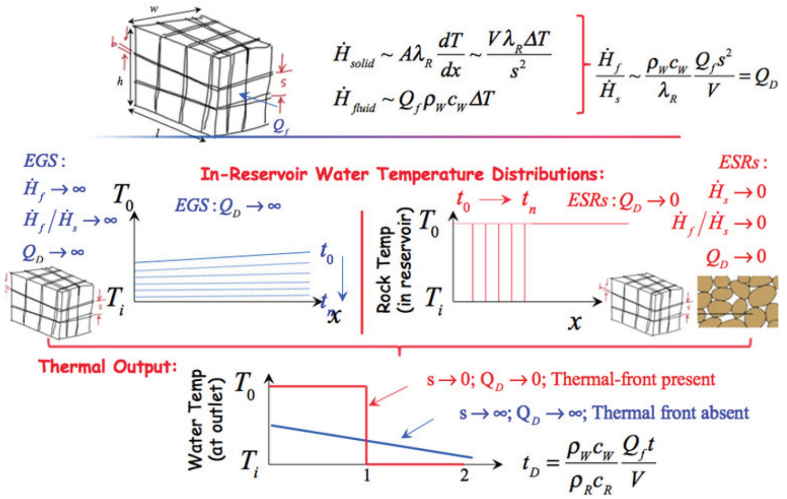


Figure 1. Simple scaling analysis illustrating that at low dimensionless circulation rates ($Q_D \to 0$) indicative of large fracture spacing in EGS reservoirs the rock temperature cooling front propagates through the reservoir as a discrete front (mid-height right) and at high dimensionless circulation rates ($Q_D \to \infty$, mid-height left, blue) for engineered sedimentary reservoirs with small fracture spacing (centre left) the temperature distribution is uniform. These two end-member drawdown modes result in different breakthrough characteristics of the cold water front (bottom).

### 2.2 *Thermal front present*

For small $Q_D$ (small flow rate, small fracture spacing or large reservoir volume) the water is able to completely drain the heat from the reservoir rock as it enters at the injection well. At the location of this front the water temperature is immediately raised to the initial temperature of the rock in the reservoir. However, behind the front the reservoir rock temperature is uniformly the temperature of the cold injected fluid (Figure 1, mid-height right, red lines). This is a desirable situation for a geothermal reservoir as a maximum thermal sweep of the reservoir occurs. But if fracture spacing is large then the small enabled flow rate (to satisfy small $Q_D$) may be too small to give a sufficient volume/mass of that hot fluid to be viable.

### 2.3 *Thermal front absent*

Conversely, for large $Q_D$ (high flow rate, large fracture spacing, or small reservoir) the cold injectate traverses the reservoir with little heat uptake (Fig. 1, centre left, blue lines) and leaves the reservoir cool at outlet (Fig. 1, bottom, blue line). The temperature drawdown of the rock within the reservoir is near uniform (not shown but similar to Fig. 1, mid-height left).

## 3 RESERVOIR SEISMICITY

Massive water injection has the potential to elevate pore pressures within porous and fractured formations and to reactivate faults, either seismically or aseismically. Possible mechanisms of fault reactivation are not limited to hydromechanical effects. In geothermal systems where the reservoir is chilled with the forced-circulation of cold fluid, the induced thermal shrinkage stress will also control changes in effective stress and may cause fault activation and induced seismicity. Thermal drawdown in the fractured porous medium may be determined by accommodating the essential components of the reservoir—heat transfer from the reservoir matrix to the fluid by conduction and then advection across the reservoir. Consequently, prediction of the modes of heat transfer will be essential in predicting the timing and magnitude of induced fault reactivation. The following explores the role of late stage fault re-activation by thermal drawdown. Then, the impact of fluid circulation rates on the heterogeneity of thermal drawdown that may develop within the reservoir and its potential impact on the timing and magnitude of induced seismicity are investigated.

### 3.1 *Method*

We use a coupled Thermal-Hydrological-Mechanical (THM) model (Taron & Elsworth 2009, 2010) to explore the different factors governing fault reactivation of a critically stressed strike-slip fault. In order to investigate the influence of fluid pressures and thermal stresses on the reactivation of critically stressed faults, we analyze anticipated stress changes using a simple model for a fault acted upon by far-field stresses (Gan & Elsworth 2014a).

The reservoir geometry includes a 2-D rectangular (1500 m $\times$ 600 m $\times$ 15 m) reservoir containing three sets of orthogonal fractures (see Figure 2 (a)). A strike-slip fault is located in the center of reservoir flanked by equidistant injection and withdrawal wells. The initial distribution of reservoir temperature is uniform with an initial rock and fluid temperature of 250°C, initial reservoir pressure of 18.8 *MPa*, and with cold water injected under constant mass flow rate with a constant enthalpy of $2.0 \times 10^5$ *J/kg* (equivalent to 43°C ) and with the production well operated under a constant pressure of 13.8 *MPa*. A minimum in-situ stress of 28.8 *MPa is* imposed in the W-E direction and the maximum horizontal stress of 45 *MPa* is applied in the N-S direction. The model boundaries are set as no-flow boundaries with applied constant stresses.

### 3.2 *Results discussion*

Figure 2 (b) confirms that indeed late time seismic events may occur within the 30-year injection history when fluid is injected at 50°C into a host of 250°C, where the fracture host

permeability is kept as $10^{-14}$ $m^2$, and the fault permeability is $10^{-17}$ $m^2$ comprising a low permeability fault core. The first seismic slip event occurs due to hydro-mechanical effects at $1.4 \times 10^4$ $s$ (3.9 hours), and the second slip occurs at $1.4 \times 10^8$ $s$ (4.4 years) when the thermal front arrives at the fault and causes significant temperature drawdown. The magnitude of the second slip event that is induced by the thermal shrinkage stress is weaker than the first event induced by hydro-mechanical effects. The first event has a relative slip distance of 36 cm and a magnitude of 3.1 with the second event displacing only 6 cm with a magnitude of 2.6.

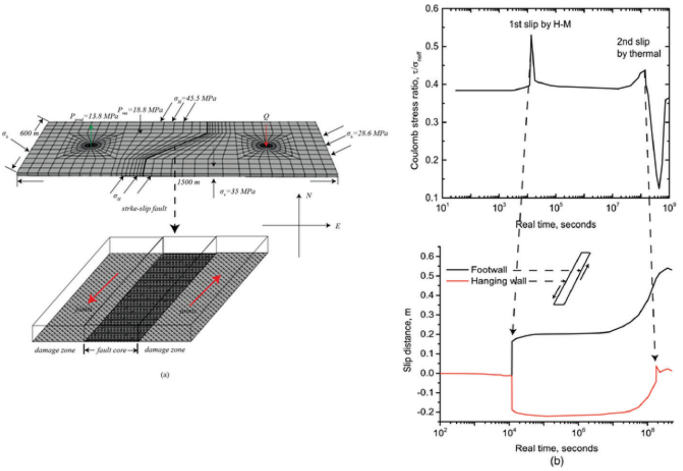


Figure 2. (a) Model geometry and applied stress boundary condition, initial condition, (b) the evolution of fault Coulomb stress ratio (right top), slip distance evolution of both footwall (green line) and hanging wall (blue line).

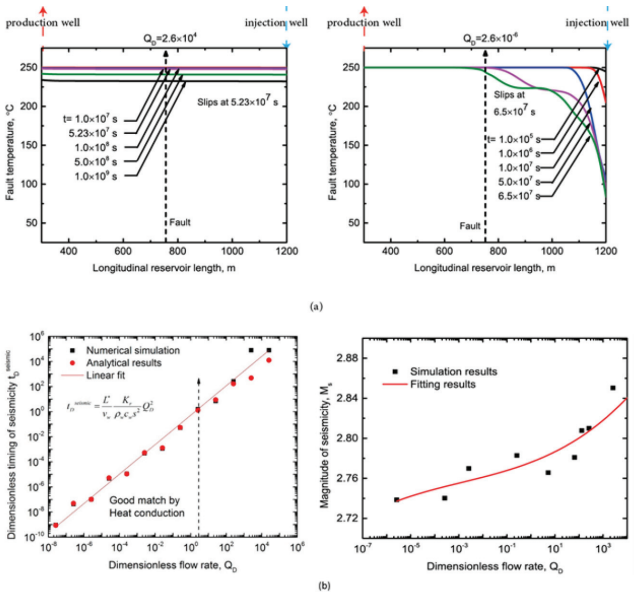


Figure 3. (a) Thermal front propagation from the injection well (right axis) towards the production well (left axis) under different $Q_D$ values, (b) validation of the dimensionless timing equation for the onset of seismicity between numerical simulation results and the analytical results under various $Q_D$ values ($Q_D = 2.6 \times 10^{-8} \sim 2.6 \times 10^2$) and corresponding maximum magnitude of seismicity based on the slip distance results under different flow rate $Q_D$.

Figure 3 shows the displacement of the thermal front within the rock as non-dimensional flow rates $Q_D$ are varied (Gan & Elsworth 2014b). The injection well is to the left ($x = 0\ m$) with the production well to the right ($x = 900\ m$). The fault is intermediate (dashed arrow) between the injection and production wells. The flat and uniform drawdown curve corresponds to the larger magnitudes of $Q_D$ (Figure 3a top left). Uniform longitudinal thermal drawdown of the rock results in the early breakthrough of cold water. Conversely, when the $Q_D$ values are smaller than $2.6 \times 10^{-2}$, the thermal front propagates as a thermal shock. Figure 2a top right with the smallest $Q_D$ value of $2.6 \times 10^{-6}$ shows the slowest rate of propagation of the thermal front which identifies the case for the most delayed breakthrough. This represents the case that is most desired in retaining outlet temperatures the highest although flow rates may not be sufficiently high to be economically viable as a geothermal reservoir.

The dimensionless form of timing of the onset of seismicity is linked to the arrival of this front at the location of the fault. Figure 3 shows that this timing relation is correct for $Q_D <$ 5.2 where the injected fluid is able to completely deplete the heat from the reservoir adjacent to the injection well. When the value of $Q_D$ is gradually increased above 5.2, then heat transfer by rapid advection dominates over conduction. In this condition there is no distinct thermal front to change the stress state of the fault and the error in the prediction of timing from this simple relationship $t_D \sim Q_D$ becomes more significant. Moreover, the slip distance distributions for each patch along the fault reflect the magnitude of the seismic events (Fig. 3 (b)) that are associated with the different forms of the migrating thermal front. As the dimensionless injection rate $Q_D$ increases, the corresponding magnitude of seismicity event also grows.

## 4 GEODESY-SEISMICITY LINKAGES

Surface deformations of significant magnitude have been observed in a number of geothermal fields by both interferometric methods (InSAR) (Fialko & Simons 2000, Vasco et al. 2002; Foxall & Vasco 2008, Falorni et al. 2011, Eneva et al. 2012, Ali et al. 2013) and by direct measurement of surface tilt (Vasco et al. 2002). Subsurface deformations induced by cold water injection generally conform to two different modalities: (i) isotropic volume change and (ii) injection induced shear offset on finite faults. We examine the expected magnitudes of displacement, tilt and strain resulting for production from geothermal reservoirs and compare this with the instrumental resolution of common measurements. We use the Mogi volumetric model (Mogi 1958) and the Okada shear slip model (Okada 1985) within an elastic half-space to define signal magnitudes with consideration of coupling and decoupling processes between reservoir and the surrounding rock. We then compare these results with the resolution of current geodetic methods (1 mm for displacement, 1 nano-radian for tilt and 1 nano-strain for strain) (Im et al. 2015).

### 4.1 *Volume change (thermal contraction)*

Volumetric strain, $\varepsilon_v$, induced by the temperature change of unconstrained media is

$$\varepsilon_v = \alpha_v \Delta T \tag{1}$$

where, $\alpha_v$ is volumetric thermal expansion coefficient and $\Delta T$ is temperature change. Eqn. (1) only assumes strain under zero stress. The presence of the surrounding rock, however, reduces the magnitude of deformation (Eshelby 1957). Volumetric strain of a soft inclusion in an infinite medium can be represented as (Im et al. 2015),

$$\varepsilon_v = \frac{1}{1 + \frac{2(1-2\nu)}{(1+\nu)} \frac{E_{host}}{E_{res}}} \alpha_v \Delta T \tag{2}$$

where, $\nu$ is Poisson's ratio and $E_{host}$ and $E_{res}$ are the Young's modulus of the surrounding rock and inclusion, respectively.

Figure 4 is a one-dimensional model of reservoir cooling at a depth of 2500 m and resulting induced surface deformation. The model compares two end-members of thermal drawdown behavior: (i) thermal front present (Fig. 2. (a) red) and (ii) thermal front absent case (Fig. 2. (a) blue). The resulting surface deformation signals of vertical displacement tilt and strain with three different depletion states (10%, 30% and 50% depleted) are shown. Surface deformations are calculated from superposed Mogi solutions assuming $\alpha_v = 5 \times 10^{-5}$1/°C, $\Delta T = 100$°C, $E_{res} = E_{host}$ and Poisson's ratio 0.25 (Eqn. (10)). This simple model shows that the magnitude of surface deformation, and its variation (especially tilt and strain), is sufficient to identify the reservoir depletion behavior and therefore specific geodetic tools could be used for reservoir imaging of thermal depletion. (plots e, f, and g).

## 4.2 *Shear deformation*

A number of seismic events, some of significant magnitude (M > 3), occur simultaneous with fluid circulation in geothermal reservoirs (Majer et al. 2007). Monitoring the shear offset of such faulting using surface or near-surface geodetic tools could potentially allow the visualization of the evolving major flow paths within the geothermal reservoir. Although each seismic event is not significant enough to induce observable surface deformation, (i) stacking of seismic fault events within a fault zone and (ii) aseismic or slow-slip fault reactivation will allow large seismic slip in the reservoir. Figure 5 shows the relationships between fault size and maximum magnitude of surface deformations for a rectangular fault at a depth 2500 m with a 60º dip. It indicates that the magnitude of surface deformation increases with both fault size and shear offset. In fact, the fault size and slip distance are mutually dependent. Assuming constant stress drop across the fault, the larger the area of the fault, the larger the shear offset (Zoback & Gorelick 2012). Accordingly, it is expected that a sizable area of fault slip would generate a detectable surface deformation signals. The Okada slip solution indicates that for a 200 m × 200 m fault at depth 2500 m, even several millimeters of slip can be detected with tilt- and strain-meters.

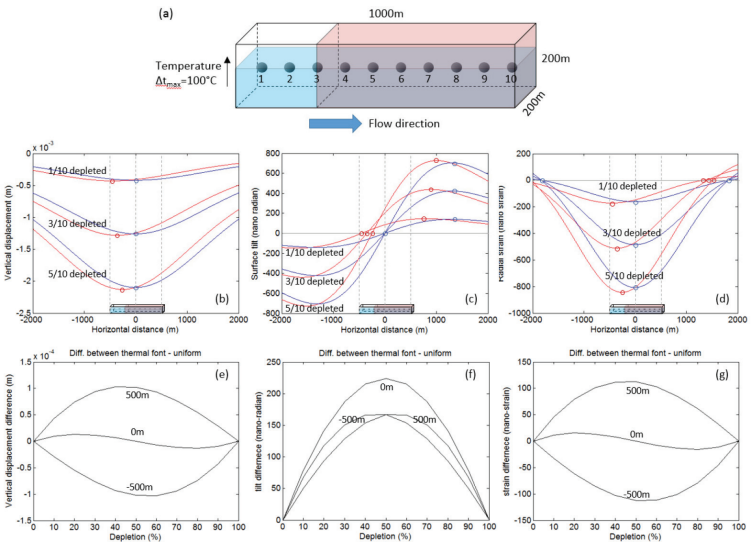


Figure 4. Surface geodetic signals of thermal front present (red) and absent (blue) case. 1000 m × 200 m × 200 m size reservoir is placed at a depth of 2500 m. Plots (b), (c) and (d) represent the geodetic signals on the surface and plots (e), (f) and (g) represent the difference of geodetic signals between thermal front present and absent cases at certain surface locations (injection point, middle of the reservoir and production point).

### 4.3 *Field data and discussion*

The magnitude of thermal contraction in geothermal fields can be estimated from the energy extraction rate. Assuming a conversion efficiency of 10% from thermal recovery to electrical conversion (including running at sub-capacity), the total heat energy extracted at 1 MW for 1 year from a geothermal field is ~$3.15 \times 10^{14}$ J. Using this conversion scenario and rock properties assumed as $\alpha_v = 5 \times 10^{-5}$, density 2700 kg/m$^3$ and specific heat of 900 J/kg·K with a deformation ratio of 0.56 ($E_{host} = E_{res}$, $\nu = 0.25$), allows us to infer that 1 MW geothermal operation for 1 year induces ~$3.63 \times 10^3$ m$^3$ of subsurface volume change. We compare the magnitudes of expected maximum surface deformation due to thermal contraction to the observed maximum vertical displacement (Brady Hot Springs, Coso and Dixie Valley) and tilt (Hijiori and Okuaizu) in Figure 6. In order to calculate the subsurface volume change, we used current (2014) capacities for the operating fields (Brady Hot Springs, Coso, Dixie Valley and Okuaizu) and total injected volume for the period of observation in the Hijiori injection test. Our results show that observations at Brady Hot Springs and Coso show similar or slightly smaller than predicted surface deformations. In contrast, surface deformations observed at Dixie Valley, Okuaizu and Hijiori are considerably larger than expected. The observed smaller surface deformations are straightforward to explain because: (i) we use current (2014) maximum operational capacity, which may be larger than the actual capacity over the same period; (ii) only a single Mogi source is modeled for each example; and (iii) decoupling of the spherical reservoir from the elastic crust is not considered. Accordingly, observed smaller surface deformation than predicted in the Brady Hot Springs and Coso geothermal fields are both easily explicable and, moreover, the similarities of their magnitudes implies that thermal contraction plays a significant role in inducing the large observed surface deformations. The results for Dixie Valley, Okuaizu and Hijiori, however, clearly show the need for another significant deformation source in addition to thermal contraction of a spherical reservoir. Considering the extensive network of faults (typically several kilometers in horizontal extent) in these reservoirs, the large deformations suggest the necessary involvement of systematic shear reactivation in inducing the large surface deformations.

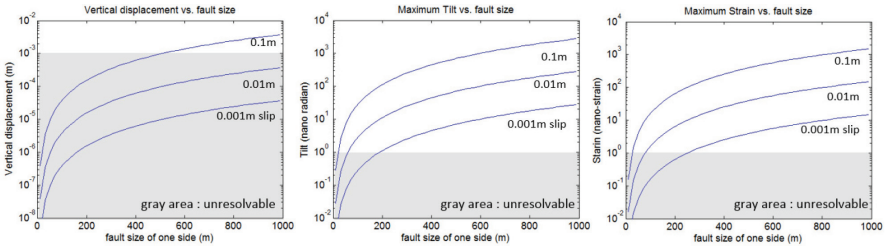


Figure 5. Maximum magnitude of surface deformation vs. fault size (length of one side of rectangular fault) with three slip distances (0.001 m, 0.01 m and 0.1 m) at depth 2500 m. The magnitude of surface deformation increase with both fault area and total slip.

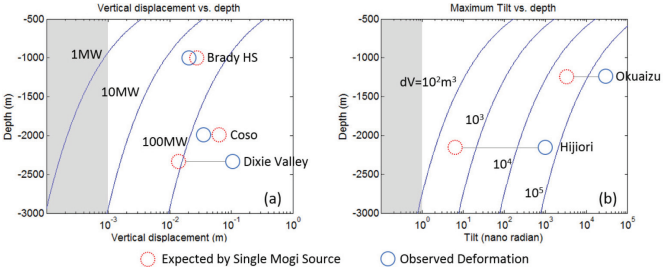


Figure 6. Comparison of expected maximum surface deformation due to thermal contraction (red dashed circles) and observed maximum deformation (blue solid circle). The large gap between predicted and observed values in Dixie Valley, Okuaizu and Hijiori implies the probable involvement of shear offset to produce the large observed surface deformation.

## 5 PERMEABILITY-SEISMICITY COUPLING

Microseismic monitoring is one effective and useful method to characterize the spatial distributions of fractures as well as fluid migration in the subsurface (Maxwell & Urbancic 2001, Canada et al. 2010, Downie et al. 2013). This feedback occurs since the injected fluid reactivates pre-existing fractures and thus triggers microearthquakes (MEQs) (Nicholson & Wesson 1990, Majer et al. 2007, Suckale 2009, Ellsworth 2013, Guglielmi et al. 2015). In this study, we propose a model to couple in situ MEQ data and in situ permeability at various reservoir scales and apply this model to analyze reservoir permeability through the observed in situ seismicity during the first two rounds of stimulation of the Newberry EGS project in 2014 that followed an earlier 2012 stimulation (Cladouhos et al. 2015, Fang et al. 2015a).

### 5.1 *Method*

This seismicity-permeability coupling model assumes that induced seismicity is controlled by the Mohr-Coulomb failure criterion and applies the moment magnitude of MEQs to recover fracture shear slip (Stein & Wysession 2009). We combine permeability estimates from both the "cubic" law (Fang et al. 2015b) and from Oda's crack tensor (Fang et al. 2015c) to map the in-situ permeability of the reservoir at two selected depths (2500 to 2600 m and 2600 to 2700 m). To analyze all seismic events, we use a total of 99 focal mechanism solutions as a statistical reference and randomly assign the strike and dip angle values to non-moment-tensor (MT) seismic fractures based on a normal distribution. The observed moment magnitudes of the MEQs are constrained between –0.28 to 2.0 with a *b* value close to unity, suggesting that the seismic fractures in the Newberry EGS reservoir vary between meters and one-hundred meters (Fig. 7).

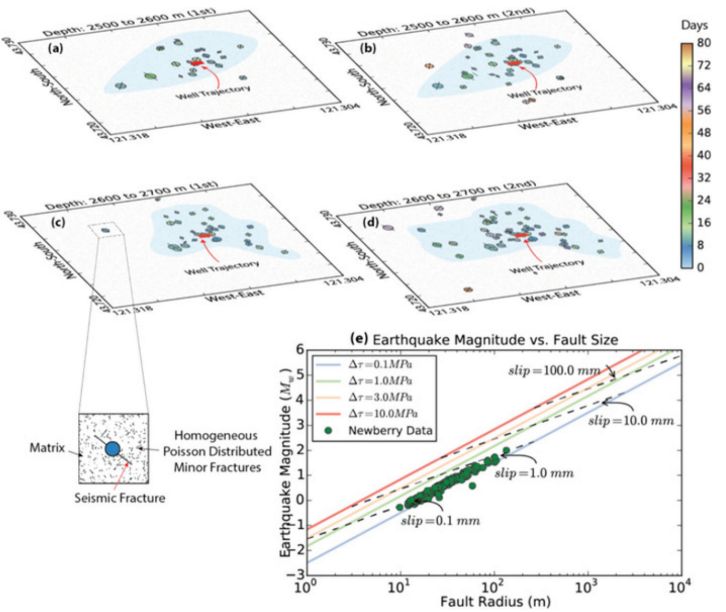


Figure 7. (a) and (b) Map view of fracture distributions derived from microseismic events (both 1st and 2nd round stimulation) at a depth of 2500 m to 2600 m. (c) and (d) Map view of fracture distributions derived from microseismic events (both 1st and 2nd round stimulation) at a depth of 2600 m to 2700 m. (e) Relationship of fracture size and moment magnitude and the corresponding slip distances. Slip distances of fractures in Newberry EGS reservoir labeled as greed dots (Modified from Zoback & Gorelick 2012).

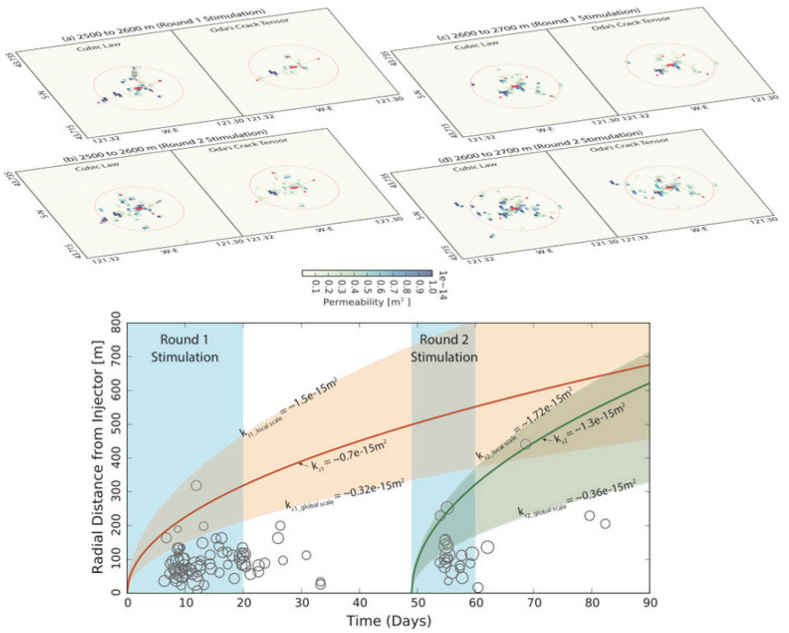


Figure 8. (a) to (d) Celluar grid of stimulated permeability created using both cubic law and Oda's crack tensor methods for both 1st and 2nd round stimulation at a depth of 2500 to 2600 m and 2600 to 2700 m respectively. The grid size is 30 m. Bottom: Spatio-temporal distribution of fluid-injection-induced seismicity during the 2014 Newberry EGS stimulation. Diffusion-length versus time curve labeled for equivalent permeabilities at reservoir scale.

### 5.2 *Results and discussion*

The relation between slip distances of seismic fractures and fracture size is presented in Figure 7(e), showing that slip increases linearly (from ~0.1 mm to ~2.1 mm) with growing fracture trace length. Figure 8 presents the stimulated permeability map of the resulting discrete fractures in Figure 7, illustrating that the most permeable zone is created adjacent to the injection well in the first round stimulation (northwestern quadrant). After the second stimulation, the permeability is enhanced around the injection well. In the depth range 2500 m to 2600 m, enhanced permeability develops preferentially towards the southwest while in the depth range 2600 to 2700 m the trend changes to the southeast. Comparing the mapped cellular permeability recovered by both the cubic law method and by Oda's crack tensor theory, it is expected that the cellular permeability evaluated by the cubic law is slightly higher than that by Oda's crack tensor theory. However, the equivalent permeabilities of both methods at reservoir scale are the same and independent of grid size. Confirmatory and independent estimates of the equivalent mean permeability may be recovered at reservoir scale using pore-pressure diffusion lengths (Shapiro et al. 1997) and the 99 MT events. The diffusion-length versus time curves are shown in Figure 8 (bottom), suggesting that the reservoir permeability evolved from ~$0.7 \times 10^{-15}$ m$^2$ to ~$1.3 \times 10^{-15}$ m$^2$ which are bounded by the estimated permeability values.

## 6 RSF-PERMEABILITY COUPLING

The evolution of fracture permeability during shearing is crucial in defining the impact of hydraulic stimulation in geothermal reservoirs and in describing earthquake mechanisms in induced seismicity. This phenomenon may be explored by using numerical models (Fang et al. 2015c, Ishibashi et al. 2016) or through field experiments (Guglielmi et al. 2015a,

b) where permeability evolution is seen to be mainly associated with shear and with a large aseismic component. Here, the concept of "self-propping shear stimulation", as a mechanism for enhancing fracture permeability, is well known. This suggests that understanding microscopic phenomena during fracture shearing is necessary to define the evolution of fracture permeability. The evolution of fracture permeability may be interpreted by concepts of dilation and wear recovered from rate-state characterization of frictional behavior (i.e., RSF).

### 6.1 *Methods*

Laboratory fluid-flow experiments may be used to evaluate fracture permeability evolution associated with transient increases in shear velocity during frictional shearing. Core plugs of Westerly granite are saw-cut to form a smooth axial fracture that is subsequently roughened to simulate a natural fracture with controlled surface topography (Fig. 9 (a)). Fluid-flow experiments are conducted in a triaxial pressure vessel to independently apply confining pressure, pore pressure, and shear velocity, and to concurrently monitor the evolution of fracture permeability, $k$, during experiments (Fig. 9 (b)). We conduct velocity stepping experiments, where shear-induced dilation is expected to occur in response to shearing velocity increase (Samuelson et al. 2009), under a range of conditions: background shearing rate of ~1 μm/s with steps to ~10 and ~15 μm/s at confining stresses of 1, 3, and 6 MPa. Subsequently, we employ a lumped parameter model, where rate-state characterization of frictional behavior is introduced, to interpret permeability evolution during fracture shearing.

### 6.2 *Results and discussions*

Results of frictional shearing at a confining stress of 6 MPa are shown in Figure 10 (a). Permeability is seen to reduce due to the removal of fracture surface asperities and the

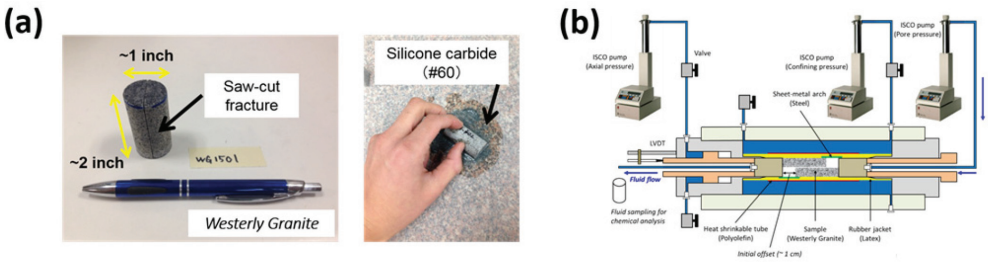


Figure 9. (a) Core plug of Westerly granite containing single fracture roughned with silicone carbide and (b) experimental system for fracture permeability measurement during frictional shearing.

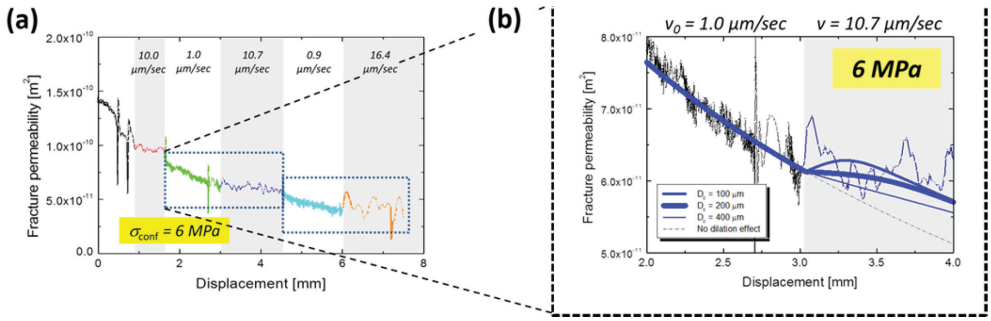


Figure 10. (a) Fracture permeability evolution associated with transient increases in shear velocity during frictional shearing at confining stress of 6 MPa and (b) comparison of fracture permeability evolution either measured experimentally or recovered from lumped-parameter modeling for various values of critical slip distance.

production of gouge. Fracture surface measurements with white light interfelometry (Zygo NexView), confirms the reduction in surface topography (Vertical interval and RMS). The trend of permeability-versus-displacement clearly varies in response to an increase in shearing velocity. The $k$ values following a velocity increase are larger than would be expected by extrapolating the permeability-displacement trend at lower velocity (see insets in Figure 10 (a)). We interpret this discrepancy in $k$ as being caused by shear-induced dilation.

This concept is probed by linking permeability evolution to concepts of dilation and wear recovered from rate-state characterization of frictional behavior (Marone 1998). Figure 10 (b) shows one example of the evolution of fracture permeability between experiment (black line) and model (blue line). By introducing RSF behavior into the model, we successfully explain the enhancement in fracture permeability that follows an increase in shear velocity. Moreover, considering that the a-b value of Westerly granite is generally negative (< 0) (Kilgore et al. 1993), we suggest that velocity-weakening (i.e., seismic slip) rock fracture is characterized by permeability enhancement due to shear-induced dilation. Such a link between fracture permeability evolution and frictional evolution during shearing should be further explored to describe earthquake mechanisms in induced seismicity.

## 7 CONCLUSIONS

Significant challenges exist in the successful development of EGS—these include challenges of creating and engineering a reservoir, at-will, and in varied geographical locations without hindrance of the specifics of the geology. Important tools in achieving this goal are in the understanding of key processes influencing the success and longevity of the geological heat exchanger, applying repeatable methods in its creation and in using robust methods to monitor and control the reservoir and its productivity.

## REFERENCES


Ali, S.T., Davatzes, N.C., Mellors, R J., Foxall, W., Drakos, P.S., Zemach, E., Kreemer, C., Wang, H.F., & Feigl, K.L. 2013. InSAR measurements and numerical models of deformation at Brady Hot Springs geothermal field (Nevada), 1995–2012, in *AGU Fall Meeting Abstracts* 1:5.

Canada, S.C.M.S. et al. 2010. Fault Activation During Hydraulic Fracturing, *EAGE*, (June 2010): 14–17, doi:10.1190/1.3255145.

Cladouhos, T.T., Petty, S., Swyer, M.W., Uddenberg, M.E., Grasso, K., & Nordin, Y. 2015. Results from Newberry Volcano EGS demonstration, 2010–2014. *Geothermics*, doi:10.1016/j.geothermics.2015.08.009.

Downie, R., Xu, J., Grant, D., Malpani, R., & Viswanathan, A. 2013. Microseismic parameters help to calibrate complex hydraulic fracture models. *World Oil*, (SPEC. SUPPL. MARC): 13–16.

Ellsworth, W.L. 2013. Injection-induced earthquakes. *Science* (*80-.*). 341(6142): 142–149, doi:10.1126/science.1225942.

Eneva, M., Adams, D., Falorni, G., & Morgan J. 2012. Surface deformation in Imperial Valley, CA, from satellite radar interferometry. *Geoth. Resour. Counc. -Trans* 36: 1339–1344.

Eshelby, J.D. 1957. The Determination of the Elastic Field of an Ellipsoidal Inclusion, and Related Problems. *Proc. R. Soc. A Math. Phys. Eng. Sci.* 241(1226): 376–396, doi:10.1098/rspa.1957.0133.

Falorni, G., Morgan, J., & Eneva M., 2011. Advanced InSAR Techniques for Geothermal Exploration and Production, *GRC Trans.* 35: 1661–1666.

Fang, Y., den Hartog, S.A.M., Elsworth, D., Marone, C., & Cladouhos, T. 2015a. Anomalous distribution of microearthquakes in the Newberry Geothermal Reservoir: Mechanisms and implications. *Geothermics*, doi:10.1016/j.geothermics.2015.04.005.

Fang, Y., Elsworth, D., & Cladouhos, T.T. 2015b. Estimating in-situ permeability of stimulated EGS reservoirs using MEQ moment magnitude: an analysis of Newberry MEQ data. In *40th Stanford Geothermal Proceedings*.

Fang, Y., Elsworth, D., & Cladouhos, T.T. 2015c. Mapping permeability tensors in fractured geothermal reservoirs using MEQ data. In *49th US Rock Mechanics/Geomechanics Symposium*.

Fialko, Y. & Simons, M. 2000. Deformation and seismicity in the Coso geothermal area, Inyo County, California: Observations and modeling using satellite radar interferometry. *J.* Geophys. Res. 105(B9), 21781, doi:10.1029/2000 JB900169.

Foxall, B., & Vasco, D.W. 2008. Inversion of synthetic aperture radar interferograms for sources of production-related subsidence at the Dixie Valley geothermal field. *Lawrence Berkeley Natl. Lab.*

Gan, Q., & Elsworth, D. 2014a. Analysis of fluid injection-induced fault reactivation and seismic slip in geothermal reservoirs. *J. Geophys. Res. Solid Earth* 119(4): 2013 JB010679, doi: 10.1002/2013 JB010679.

Gan, Q., & Elsworth, D. 2014b. Thermal drawdown and late-stage seismic-slip fault reactivation in enhanced geothermal reservoirs. *J. Geophys. Res. Solid Earth* 119(12): 8936–8949.

Guglielmi, Y., Cappa, F., Avouac, J.-P., Henry, P., & Elsworth, D. 2015a. Seismicity triggered by fluid injection–induced aseismic slip. *Sci.* 348 (6240): 1224–1226, doi:10.1126/science.aab0476.

Guglielmi, Y., Elsworth, D., Cappa, F., Henry, P., Gout, C., Dick, P., Durand, J. 2015b. In situ observations on the coupling between hydraulic diffusivity and displacements during fault reactivation in shales. *J. Geophys. Res. Solid Earth* Vol. 120. doi:10.1002/2015 JB012158.

Im, K., Elsworth, D., Guglielmi, Y.G., & Mattioli, G.S. 2015. Use of geodesy to discriminate deformation mechanics in geothermal reservoirs. In *49th US Rock Mechanics/Geomechanics Symposium*, American Rock Mechanics Association.

Im, K.J., Elsworth, D., Guglielmi, Y., & Mattioli, G. 2015. Geodetic imaging of production, thermal depletion and fault reactivation in geothermal reservoirs. Submitted for publication.

Ishibashi, T., Watanabe, N., Asanuma, H., & Tsuchiya, N. 2016. Linking microearthquakes to fracture permeability evolution. *Geofluids Special Thermatic Issues "Crustal Permeability"* (Book Chapter), in press.

Kilgore, B.D., Blanpied, M.L., & Dieterich J.H. 1993. Velocity dependent friction of granite over a wide range of conditions. *Geophys. Res. Lett.* 20(10): 903, doi:10.1029/93GL00368.

Majer E.L., Baria, R., Stark, M., Oates, S., Bommer, J., Smith, B., & Asanuma, H. 2007. Induced seismicity associated with Enhanced Geothermal Systems. *Geothermics* 36(3): 185–222, doi:http://dx.doi.org/10.1016/j.geothermics.2007.03.003.

Marone, C. 1998. Laboratory-derived friction laws and their application to seismic faulting. *Annu. Rev. Earth Planet. Sci.* 26: 643–696, doi:10.1146/Annurev.Earth.26.1.643.

Maxwell, S.C., & Urbancic, T.I. 2001. The role of passive microseismic monitoring in the instrumented oil field. *Lead. Edge* 20(6): 636, doi:10.1190/1.1439012.

Mogi, K. 1958. Relations between the eruptions of various volcanoes and the deformations of the ground surfaces around them. *Bull. Earthq. Res. Inst.* 36: 99–134, doi:10.1016/j.epsl.2004.04.016.

Nicholson, C. & Wesson R.L. 1990. Earthquake hazard associated with deep well injection: A report to the U.S. Environmental Protection Agency. *US Geol. Surv. Bull. 1951,* 74pp.

Okada, Y. 1985. Surface deformation due to shear and tensile faults in a half-space Okada, Y Bull Seismol Soc AmV75, N4, Aug 1985, P1135–1154, *Int. J. Rock Mech. Min. Sci. Geomech. Abstr.*, *75*, 1135–1154, doi:10.1016/0148-9062(86)90674-1.

Samuelson, J., Elsworth, D., & Marone C. (2009), Shear-induced dilatancy of fluid-saturated faults: Experiment and theory, *J. Geophys. Res. Solid Earth* 114(12): 1–15, doi:10.1029/2008 JB006273.

Shapiro, S.A., Huenges, E., & Borm G. 1997. Estimating the crust permeability from fluid-injection-induced seismic emission at the KTB site. *Geophys. J. Int.* 131(2): F15-F18, doi:10.1111/J.1365-246x.1997.Tb01215.X.

Stein, S. & Wysession, M. 2009. *An Introduction to Seismology, Earthquakes, and Earth Structure*, Wiley.

Suckale, J. 2009. Induced seismicity in hydrocarbon fields. *Adv. Geophys.* 51(09): 1976–1984, doi:10.1016/S0065-2687(09)05107-3.

Vasco, D.W., Karasaki, K., & Nakagome, O. 2002. Monitoring production using surface deformation: The Hijiori test site and the Okuaizu geothermal field, Japan. *Geothermics* 31(3): 303–342, doi:10.1016/S0375-6505(01)00036-0.

Zoback, M.D., & Gorelick S.M. 2012. Earthquake triggering and large-scale geologic storage of carbon dioxide. *Proc. Natl. Acad. Sci. U.S.A.* 109(26): 10164–10168, doi:10.1073/Pnas.1202473109.

*Rock Dynamics: From Research to Engineering – Li et al. (Eds)*
*© 2016 Taylor & Francis Group, London, ISBN 978-1-138-02953-8*

# Dynamic behavior of NPR bolt and its application to rock burst control

M.C. He, C. Li, W.L. Gong & D.Q. Liu
*State Key Laboratory for Geomechanics and Deep Underground Engineering, China University of Mining and Technology (Beijing), Beijing, China*
*School of Mechanics and Civil Engineering, China University of Mining and Technology (Beijing), Beijing, China*

ABSTRACT: This paper presents an innovative bolt which has the Negative Poisson's Ratio effect (NPR bolt). The NPR bolt can absorb energy and sustain high constant resistance and large deformation. The working principle of this new type of bolt is introduced and a series of dynamic laboratory tests have been conducted to verify its large deformation resistance and high dynamic bearing capacity. The results of the dynamic tests show that the NPR bolt can withstand repeated impact, and maintain the stability of the constant value under impact load. Finally, the NPR bolt is applied for rock burst control.

## 1 INTRODUCTION

Bolt/Cable-supporting technology is one of effective quasi-supporting means in tunnel, which can reinforce the surrounding rock structure effectively, strengthen the roadway structural strength and improve the stability of surrounding rock significantly, and has gradually become the main measure for tunnel support all over the world (Corbett 1996). As an effective quasi-supporting way in tunnel, bolt-supporting technology, which will change the structure and strength of the surrounding rock, can significantly improve the stability of the rock mass surrounding a tunnel. In addition, with the characteristics of low cost, fast installation, low labour intensity, more utilization of tunnel section, better and safer working conditions, bolt-supporting technology will gradually become a major support way for tunnel support worldwide. It has also represented the main direction of tunnel support technology (Jiang et al. 2014). Because of the superiority of bolting technology, it has more than 50 years development history since the first use in ore, coal system in China in the 1950s. This advanced supporting technology has been widely used in mining, construction, hydropower and other engineering fields, which has become the main supporting method on geotechnical engineering.

With the reduction on shallow resources, underground mining becomes deeper. At present, a large number of mines in China have reached kilometres underground. At greater depth, the geological environment becomes more complicated (He et al. 2014, He 2011). Obviously, there are more engineering disasters and malignant accidents caused by high geo-stress, high temperature, high-pressure gas and hydraulic pressure, as well as the deteriorated working conditions and increasing cost; it becomes more difficult to sustainable exploitation of deep resources. In the next 20 years, mining depth will reach 1000–1500 m in many coal mines, which will cause engineering disasters such as the percussive ground pressure, gas explosion, mine pressure intensified, appeared large deformation of surrounding. Because the allowable deformation of surrounding rock for traditional bolt is below 200 mm generally, the support technology based on traditional bolt can not withstand the nonlinear large deformation of deep tunnel (He et al. 2014). Moreover, the traditional bolts belong to Poisson's ratio

materials (namely plastic hardening material), which have lower plasticity and toughness after the formation process due to the influence of cold-hardening effect. These bolts always lead to support failure when the instantaneous high impact loads of surrounding rock exceed the yield strength of the bolt material.

The Poisson's ratio, also known as the lateral deformation coefficient, defined as the negative ratio of the lateral strain (radial strain) and vertical strain (axial strain) when the material is subjected to vertical compression or tension. It means that the Negative Poisson's Ratio (NPR) can be defined as the positive ratio of the lateral strain and vertical strain, the formula is defined as: ($\nu_{npr} = \varepsilon_x / \varepsilon_y$) ($\nu_{npr}$ means NPR, $\varepsilon_x$ means the lateral strain, $\varepsilon_y$ means the vertical strain) (Hu et al., 2011). Compared with traditional materials, the NPR material has better physical and mechanical properties, such as higher shear modulus, rebounding toughness and enhanced resistance against gap and fracture. When an external impact is exerted, the lateral expansion of the NPR material can offset the influence of the impact, so as to improve the resistance ability. The outward expansion of the NPR material can absorb more energy during the material bending process (the traditional material is SAG damaged), and it can be used as the cushioning material if the Poisson's ratio is small enough. Therefore, the NPR material can be identified as a structural material and function material which has broad application prospects in the medicine, machinery and even military fields (Salit & Weller 2009, Zhang et al. 2015, Shi et al. 2003).

Rock burst is a kind of dynamic phenomenon in coal mines, because of the sudden release of energy in the surrounding rock and coal of tunnels and at the working face. With increasing depth of coal mining, the situation of impact prevention is severe with more and more occurrence of coal burst, tools sticking and other dynamic failure phenomena during excavation which seriously affect the safe production in deep coal mining (Li 2014). The existing measures, such as drilling pressure, discharge pressure blasting and deep hole blasting can alleviate or inhibit the effect of rock bursts. The basic reason for rock burst during tunnel excavation or service is that deep mining under high temperature, high geo-stresses, high osmotic pressure and strong mining disturbance conditions, thus causing a great deal of rock burst occurrence. The main prevention measures at present are the u-shape contractible supporting, circular frames, the anchor net supporting, u-shaped combined support, steel tube concrete, full length anchorage support and cribbing, etc. However, the existing prevention measures during tunnel construction or serve time is not ideal, with increasing supporting difficulty and higher cost.

Because the allowable deformation of surrounding rock for traditional bolt is below 200 mm generally, the support technology based on traditional bolt can't withstand the nonlinear large deformation of deep tunnel. Moreover, the traditional bolts belong to Poisson's ratio materials (namely plastic harden material), which have lower plasticity and toughness after the formation process due to the influence of cold-hardened effect. These bolts always lead to support failure when the instantaneous high impact loads of surrounding rock exceed the yield strength of the bolt material.

For the existing situation of supporting materials and rock burst control, by the thought of conquering the unyielding with the yielding, He et al. put forward the basic concept based on large deformation control in 2007 and established the framework of large deformation and constant resistance bolt (namely NPR bolt in this paper) design (He et al. 2012, 2014). In 2009, with the efforts of our research team, finally succeeded in developing a 130 kN NPR bolt. This paper focus on both field and laboratory experiment processes, performing detailed study on the mechanism properties and anti-drawing performance of this130 KN bolt.

## 2 NPR BOLT

### 2.1 *Development of NPR bolt*

With the growing demands for energy resources, mining depths for both metal ore and coal mines across the world have went beyond 1000 m. Some metal and nonferrous metal mines in

China have entered into 800–1200 m such as Ling Long gold mine (beyond 800 m) and Lion Mountain copper mine (1100 m) located in Shandong Province. Many coal mines in China will be entering into mining depths as deep as 1500 m in the coming 20 years (He et al. 2014). At the same time, for reinforcing the large-scale rock burst, bolt should have the capability of exporting elongation more than 1 m at high resistance. In order to adapt to the increasing demands for the support system and bolt devices in deep underground engineering control projects, a novel energy-absorbing bolt having ultra-high energy-absorbing capacity by deforming with an extraordinarily large elongation at high constant resistance were developed by He (known as the NPR bolt) (He et al. 2014).

### 2.2 *Structure of HE bolt*

Figure 1 shows schematically the structure of the NPR bolt which is a compound device consisting of the following components, i.e., a piston-like cone body installed on a bolt shank (a rebar), a sleeve pipe with its inner diameter slightly smaller than the large-end diameter of the cone body, a face pallet and tightening nut functioned as the retention device. The fixed length of the shank bar is bonded by means of grout. When the axial external load (pull/tensile force) is applied on the far end (the face pallet end) of NPR bolt in the direction opposite to the anchored end, the sleeve pipe will displace in the same direction relative the cone which is actually the elongation of the NPR bolt. The motion of the sleeve is equivalent to the displacement of the cone relative to the internal surface of the sleeve pipe. The large-end diameter of the cone is slightly larger than the inner diameter of the sleeve pipe in order to generate the frictional resistance (i.e. the working resistance of the NPR bolt) during the relative sliding between the cone and sleeve pipe. The elastic limit of the shank bar is larger than the frictional resistance. Thus the shank only deforms elastically when NPR bolt is subjected to the external load. HE cable has a similar structure with the NPR bolt. In principle, replacing the shank bar with strand rope makes the HE cable (He 2009, 2010).

### 2.3 *Working principle of NPR bolt*

Figure 2 shows the working principle of the NPR bolt in stabilizing the surrounding rock mass. Figure 2a shows the installation of the NPR bolt when the full free length of the shank bar is contained in the sleeve pipe the fixed length of the shank is encapsulated in the borehole. The anchored end of the shank is bonded by means of grouts located in the stable interior region beyond the volume of material undergoing deformation and displacements. The sleeve pipe is also encapsulated in the borehole and pallet and nut necessary surface retaining support. Figure 2b shows the working state for the NPR bolt at which the bolt is loaded by deformation of the rock surrounding a borehole and displacements associated with the

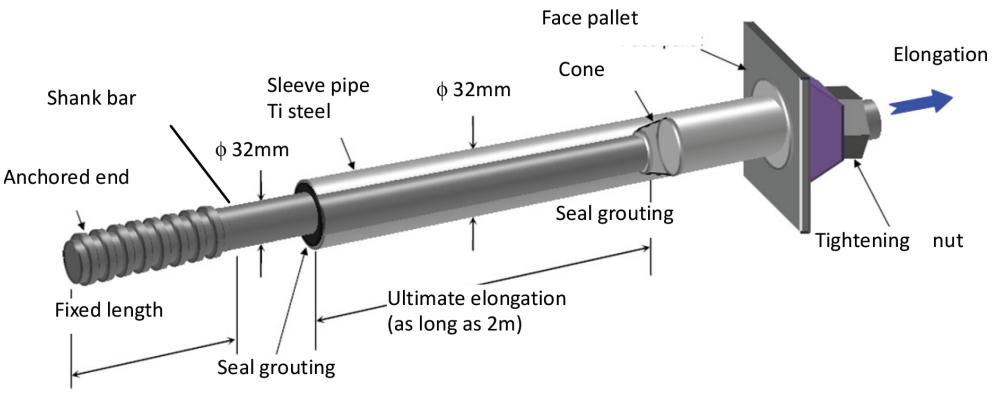


Figure 1. Schematic of the three-dimensional view of the NPR bolt (after He et al. 2014).

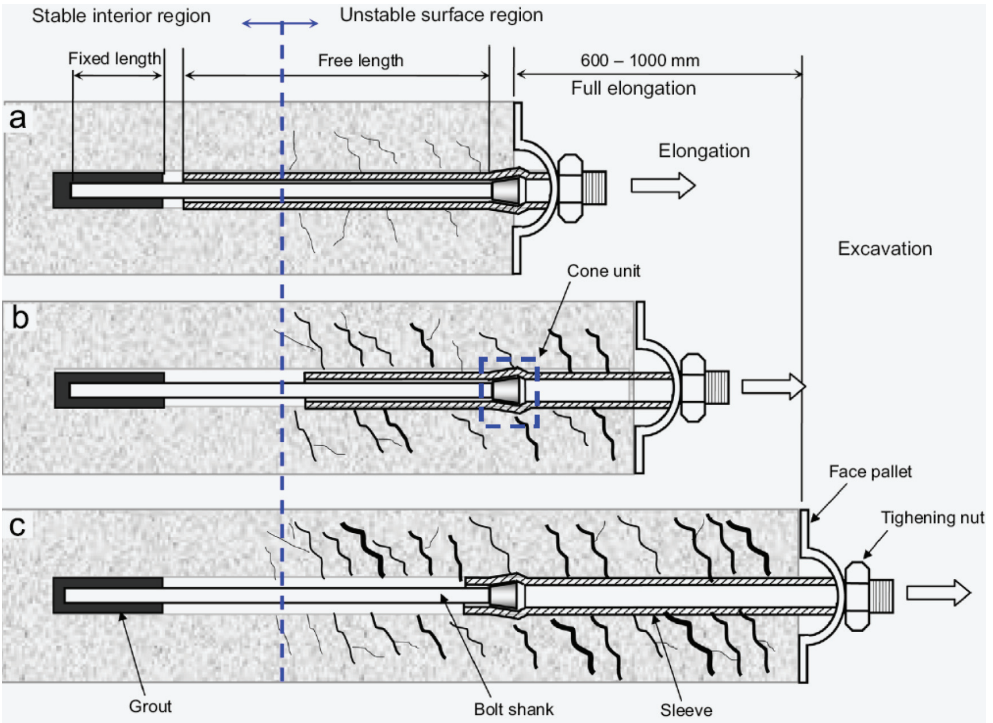


Figure 2. Working principle of the NPR bolt in stabilizing the surrounding rock mass (after He et al., 2014): (a) installation of the NPR bolt; (b) working state when rock mass undergoes deformation, and (c) retaining rock mass deformation at full elongation.

extension of the virginal discontinuities. During deformation of the surrounding rock, the bolt system will restrain the dilation so that a tensile force (pull force) is induced at the face pallet exerting on the sleeve pipe. When the pull force exceeds the threshold resistance force, $P_0$ (the frictional force when the cone slides inside the sleeve), the sleeve pipe will displace in the direction opposite to the anchored end of the bar, exporting elongations.

The threshold resistance force, $P_0$, is dependent on the elastic property of the sleeve pipe, structure of the cone body and frictional properties of the interface between the cone and internal surface of the sleeve, and independent of the external load under the static loading conditions (He et al., 2014). The element sliding (or structural deformation) mechanism at a constant force, $P_0$ (known as "constant resistance"), employed by the NPR bolt is the so-called "apparent yield" (Thompson et al. 2012), i.e. the bolt will be at rest unless the external load reaches its threshold magnitude $P_0$. The external load generated by rock deformation is consumed by the relative frictional displacement across the interface between cone the sleeve. Unlike the else currently used energy-absorbing bolts such as the Cone bolt whose load transfer is realized by the cone ploughing through the high strength grouts in the boreholes (Player et al. 2008), the load transfer of the NPR bolt is realized within the made elements, i.e. the cone-sleeve relative slippage. Figure 2c shows the working state for the NPR bolt at full elongation in retaining the rock mass deformation.

## 3 ELONGATION AND IMPACTING EXPERIMENT

### 3.1 *Elongation and impacting experiment system*

Currently SHPB research material impact test device is the most classic one of indoor experiment devices for study the dynamic performance of rock specimens. The device can measure

the relationship of stress and strain of material under dynamic impact. Because the device has many advantages such as simple measuring method and involving a wide range of strain, it can be used for diversified dynamic performance experiments such as tensile, compression and bending tests. In order to study the tensile and deformation performance of NPR bolt under dynamic impact, He et al. developed the Elongation and Impacting Experiment System for NPR bolt. Figure 3 shows schematically the basic composition of the system.

This system consists of a SHPB dynamic loading system, an Elongation and Impacting System (Fig. 4) and data acquisition system. According to different research objects, the Elongation and Impacting System is composed of a Single Bolt System (Fig. 4a) and a Bolts Group System (Fig. 4b) which can analyse and compare the dynamic mechanical properties between traditional bolt and NPR bolt under the situation of single bolt, double bolts and bolts group.

In Figure 4, the Elongation and Impacting System consists of an impacting bar (A), a specimen fixed base (B), a bolt specimen (C), a pallet (D) and a guiding frame (E). The impacting bar is guided by the guiding frame to make sure coaxial with the SHPB dynamic loading system. The bolt specimen is fixed by the specimen fixed base which is made of high strength steel in order to make sure coaxial with the impacting bar. The specimen fixed base is fixed by nut to keep the stability. The sensor (F) is placed in the pallet to measure the instantaneous impacting force.

A complete experimental process is as follows:

1. Set up gas pressure strength and release the gas,
2. Gas pressure pushes the bullet (cylindrical high strength steel),

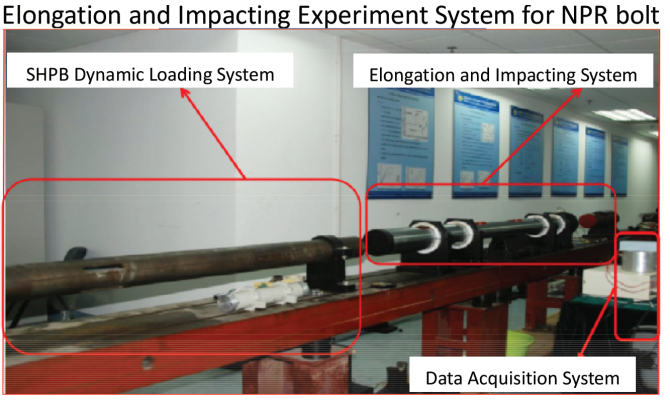


Figure 3. Schematic of Elongation and Impacting Experiment System for NPR bolt.

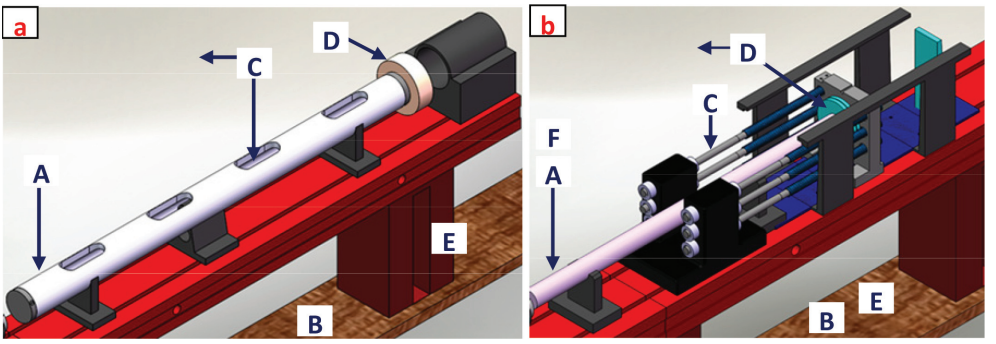


Figure 4. 3D model of Elongation and Impacting System: (a) Single Bolt system; (b) Bolts Group system.

3. Bullet impacts the impacting bar,
4. Impacting bar impacts the pallet (bolt specimen is attached with the pallet),
5. Recording tensile performance of the bolt.

### 3.2 *Experiment parameters and result*

Figure 5 shows the basic physical parameters and measurement points of one NPR bolt sample, i.e. MG-15-7(300) obtained in the dynamic experiment before and after experiment. Before the experiment, the axial dimensions (per 5 rings) and radial dimensions (measuring a-a and b-b by crossing method) were measured and calibrated. It is seen that the elongation of constant resistance device is 450 mm and the rate of elongation of sleeve pipe is about 35.57%.

Figure 6 shows the expansion curves of the bolt samples. From the figures, the average dimension of the concave of the sleeve pipe is about 29.5 mm before experiment and 31.0 mm after experiment, the average expansion dimension is about 1.5 mm. The average dimension of the convex of the sleeve pipe is about 32.5 mm before experiment and 33.1 mm after experiment, the average expansion dimension is about 1.6 mm.

From the data, it can be seen that the sleeve pipe becomes longer and thicker during the experiment process, which shows significant Negative Poisson's Ratio effect. In this experiment, the lateral strain ($\varepsilon_x = \Delta d / d_0$) is defined as the ratio of the diameter deformation ($\Delta d$) of sleeve pipe and its initial diameter ($d_0$), the vertical strain ($\varepsilon_y = \Delta l / l_0$) is defined as the ratio of the diameter deformation ($\Delta l$) of sleeve pipe and its initial diameter ($l_0$). The ratio

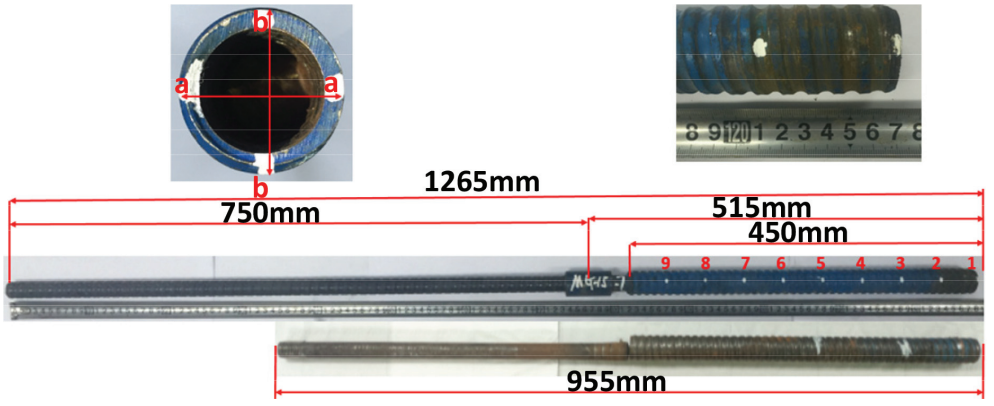


Figure 5. The basic physical parameters and measurement points of NPR bolt.

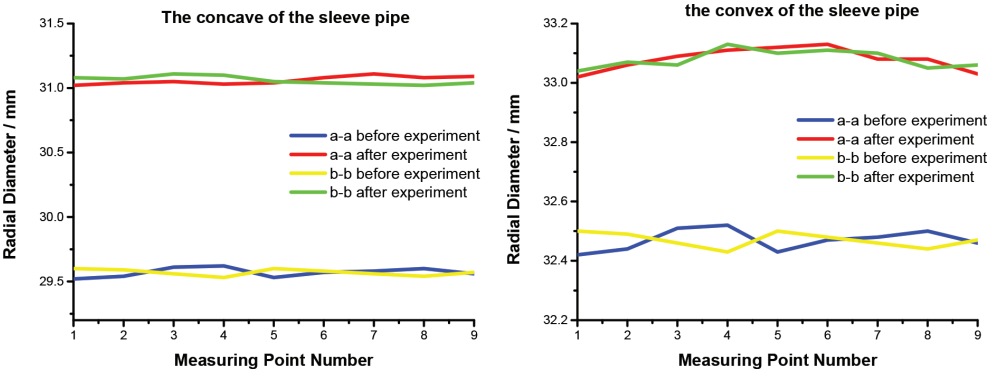


Figure 6. Schematic of change of expansion of NPR bolts.

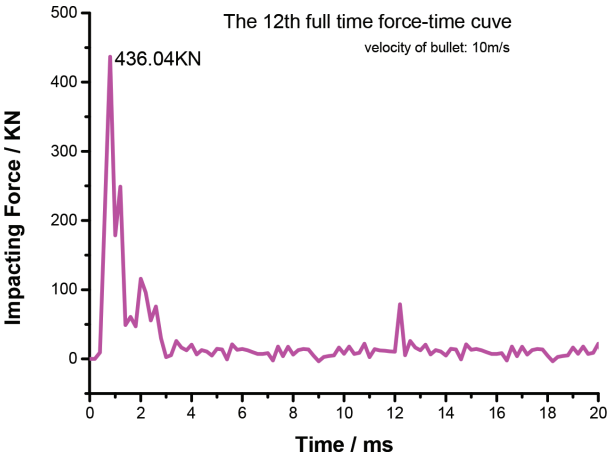


Figure 7. Force-time curve of single impacting.

($\nu_{npr} = \varepsilon_x / \varepsilon_y$) of the lateral strain and the vertical strain is the equivalent Negative Poisson's Ratio of the material of NPR bolt. After calculation, the equivalent Negative Poisson's Ratio of the concave of sleeve pipe is –0.143 and the convex is –0.052.

After the physical parameter analysis, the relevant data are calculated and the force-time curve is plotted to study the anti-impact mechanical property of NPR blot. Figure 7 is the 12th full time force-time curve of the bolt specimen under dynamic impacting (the velocity of bullet is 10 m/s). It can be seen that the peak force can reach 436.04 kN in 1 ms and the force falls back to 0 kN in 4 ms which means the NPR bolt can absorb the impacting energy rapidly and have the a good ability to adapt to dynamic impacting.

## 4 WEIGHT-FALLING EXPERIMENT

### 4.1 *Weight-falling experiment system*

The weight-falling impact tests on the NPR bolt were carried out using the Dynamic Testing System for NPR bolt developed in China University of Mining and Technology, Beijing (Fig. 8). The testing machine can be used to evaluate the performances of resistance and absorbing impacting energy for the NPR bolt by measuring the extension length of the NPR bolt's rod body itself and the radial deformation of the rod body. The testing machine consists of a main stand and measuring and controlling systems with the following technical specifications:

– Maximum impact energy: 15000 J;
– Effective range of the impacting height: 0–1500 mm;
– Elevation velocity: 0–3 m/min;
– Continuous-speed shifting;
– The falling height with five level: 840, 880, 920, 960, and 1000 kg;
– Allowed diameter of testing bolt: 34 and 22 mm; length: 1500–2500 mm.

### 4.2 *Testing procedure and parameters*

The goal for the weight-falling test is to evaluate the energy absorbing capacity and uniformity under the dynamic impact. For minimizing the influences of the machining errors on the testing results, we also used one NPR bolts selected in the same manufacture batch with a nominal length of 2400 mm, diameter of the bolt rod 22 mm, and outer diameter of the sleeve tube 32 mm (see Table 1).

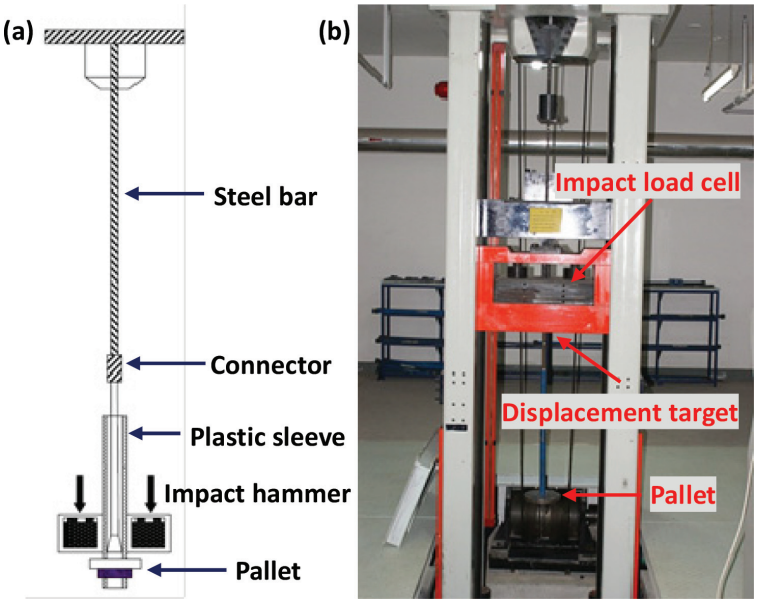


Figure 8. Test procedure and test setup for the dynamic impact experiment: (a) alignment of the test and (b) test setup.

Table 1. NPR BOLT samples for the weight-falling tests.

| NPR BOLT No. | Shape | Outer diameter for sleeve (mm) | Diameter for the rod (mm) | Length for NPR BOLT (mm) | Ultimate elongation (mm) | Falling height (mm) |
|---|---|---|---|---|---|---|
| MG-12-02 | Round | 32 | 22 | 2400 | 702.16 | 700 |

As shown in Figure 8, the testing NPR bolt was cramped tightly in the testing machine and then installing the pallet and setting up the initial position, after that setting the maximum dropping height, confirming all the procedures are getting ready, and finally conducting the test with the pre-designed cyclic-loading scheme till the completion of all the cycles. The elongation (the structural deformation) of the NPR bolt can be measured by the measuring system of the test set up. To be exact, the elongation of the bolt was measured by the auto-controlled displacement gauge, and the impacting force was measured by YFF-force transducer with an accuracy of 0.025 N and maximum measuring capacity of 250 kN, which was designed according to the principle of piezo-electricity in the quartz crystals, converting the force into the electric charges.

### 4.3 *Experiment results and discussions*

Figure 9a shows the plot of the impacting force vs. elapsed-time under 700 mm falling height for No. MG-12-2 NPR bolt and Figure 9b shows the major peaks and valleys for the plot in Figure 9a. The test results have some similarities to No. MG-12-2 NPR bolt and are summarized as follows:

A. Yielding deformation or elongation phase: the impact force fluctuates around a mean value 67.1 kN (the averaged tensile force for NPR bolt), which is lower than that of the MG-12-1 NPR bolt; phase A is the working phase with effective deformation for the NPR bolt; the maximum impact of 318.76 kN occurred in the initial stage of this phase higher than the MG-12-1; more peaks afterwards are at a comparable magnitude.

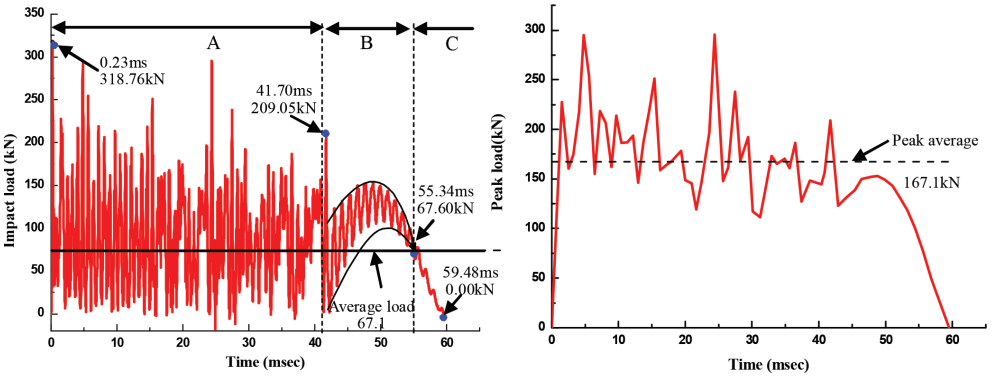


Figure 9. Relationship between the impact force and the elapsed time for No. MG-12-2 NPR bolt under 700 mm falling height. (a) plot of impact force vs. time, and (b) major peaks and valleys of the plot in Figure 9a. (A: working phase with large deformation; B: critical phase with elastic deformation due to the material elasticity, and C: the out-dated phase for the NPR bolt).

B. Elastic deformation phase: the duration of this phase is small and the deformation is due to the rod material's elasticity. This is a critical phase indicating that the NPR bolt is close to failure. Note that under higher falling height, the NPR bolt has longer elastic deformation range.
C. Residual deformation phase: the rod body is deteriorated and loses its load-bearing capacity. This phase can not be counted into the effective deformation range. The phase is shorter than that in the former NPR bolt.

## 5 PRACTICAL APPLICATIONS

### 5.1 *Project overview*

The purpose of the development of NPR bolt and rock burst research is aimed to guide to practical project and continue to optimize and improve in the practice process. In this paper, the practical application example is an abandoned working face which is a mining area in the Seam 7# North, No.1213 tunnel of Hongyang Three mine, located in Shenyang City, Liaoning Province. The mining depth of Hongyang mine is more than 1000 m. In recent years, the tunnel had experienced several nonlinear dynamic phenomena, such as large deformation of surrounding rocks and rock burst, which affected mining production and caused safety risks of staff and machinery seriously.

Based on the above reasons and in order to verify the actual anti-impacting performance of NPR bolt when rock burst happens, the support effect of NPR bolts is compared with the ordinary ones under the same geology condition and supporting strength. According to the design requirements, the test section is arranged in the No.1213 tunnel with length of 40 m under −850 m level which is divided into 4 average parts from I to IV. Figure 10 shows the layout of the test section. Sections I and IV are the traditional support measure with ordinary strand anchor cable (Φ21.7 mm × 6500 mm), Sections II and III are the NPR support with NPR cable (constant resistance 350 kN, 6500 mm and preload force 30 t).

### 5.2 *Results*

After the support strengthening process, the test sections were constructed blasting caverns within 3# emulsion explosives. There are 3 test programs and the results are shown in Figure 11:

1. Comparing the different support effects in Sections I and II with same 10 kg explosives,

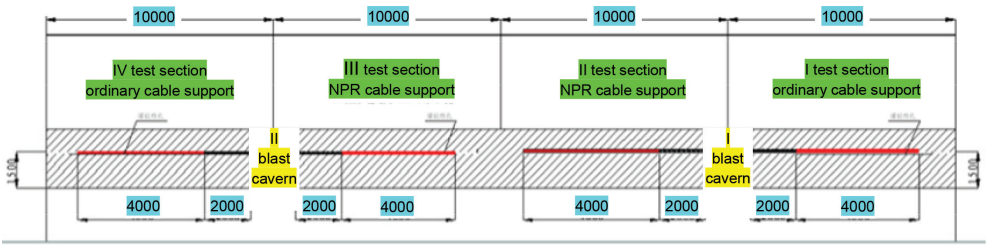


Figure 10. Layout of test section.

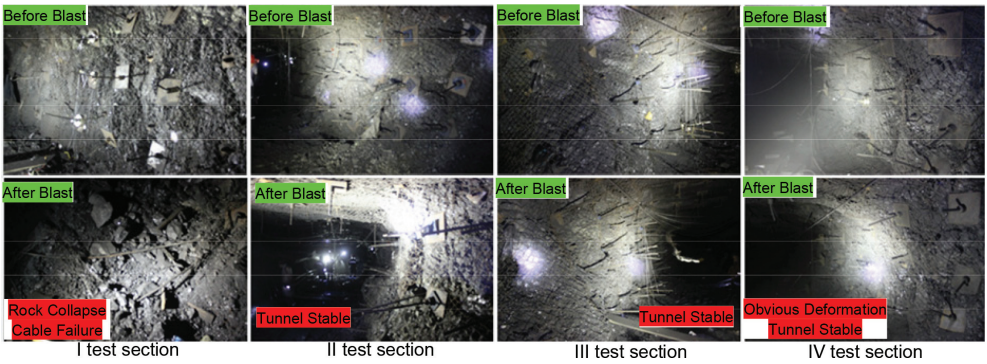


Figure 11. Comparison of each test section before and after blasting.

2. Analyzing the anti-impacting strength of NPR support in Section III with in-situ repeated blasts (11.4 kg and 19 kg explosives),
3. Analyzing the anti-impacting strength of ordinary support in Section IV with lower blast (5 kg explosives).

The test results show that:

1. Comparing Sections I and II, the ordinary support section appear destructive phenomenon such as surrounding rock collapse and cable outstretch failure and the NPR section keep tunnel stable and controllable deformation under the same blasting impacting energy, which means that the NPR cable has better anti-impacting ability than the ordinary one.
2. Analysing the tunnel deformation phenomenon of Section III with in-situ repeated blasts, the tunnel keep stable with acceptable deformation, which means that the NPR cable can absorb the mutative impacting energy to release the surrounding rock energy controllably and keep tunnel and support safe.
3. Comparing the tunnel damage phenomenon of Sections II and IV, although the ordinary cable can keep the tunnel stable, larger deformation occurs in parts of the ordinary cable with less explosives blasting than the NPR cable, which means the NPR cable can endure more impacting energy than the traditional one.

## 6 CONCLUSION

For the existing situation of supporting materials and rock burst control, by the thought of controlling the deep large deformation problem, He et al. developed the NPR bolt with

high-level working resistance, extraordinarily large elongation and unique Negative Poisson's Ratio effect. The elongation is as long as 300–100 mm in the current products. The resistance depends on the elastic properties of the sleeve pipe and geometrical parameters of the cone, and independent of the external loads.

The dynamic behaviours of NPR bolt are obtained in the two different classic experiment, including elongation and impacting experiment and weight-falling experiment. The first experiment verify the sleeve pipe of NPR bolt become longer and thicker during the experiment process which shows significant Negative Poisson's Ratio effect, meanwhile, the NPR bolt can absorb the impacting energy rapidly and have the a good ability to adapt to dynamic impacting. The weight-falling experiment described the mechanics character and deformation mechanism of NPR bolt in three different working phase under dynamic impacting comprehensively which authenticate mutually the design working principle of NPR bolt.

In order to verify the actual anti-impacting performance of new NPR support form, detect the engineering hazard timely, ensure the security and stability when rock burst happens, the paper compared the support effect of NPR bolts with the ordinary ones under the same geology condition and supporting strength in Seam 7# North, No.1213 tunnel of Hongyang Three mine. The test results show that the deformation of NPR sections are less obvious and more controllable than the traditional ones which means NPR bolt support have favourable protective and therapeutic effects in deep rock burst disasters.

## REFERENCES


Corbett, G.R. 1996. The Development of Coal Mine Portable Micro seismic Monitoring System for the Study of Rock Gas Outbursts in the Sydney Coal Field, *Nova Scotia*. PhD thesis. McGill, Canada.

He, M.C. (Patented in 2011, No. ZL 2010 1 0196197.2, Certificate No. 852069).

He, M.C., Gong, W.L., Wang, J., Qi, P., Tao, Z.G., Du, S., & Peng, Y.Y. 2014. Development of a novel energy–absorbing bolt with extraordinarily large elongation and constant resistance. *International Journal of Rock Mechanics & Mining Science* 67: 29–42.

He, M.C., & Guo, Z.B. 2014. Mechanical property and engineering application of anchor bolt with constant resistance and large deformation. *Chinese Journal of Rock Mechanics and Engineering* 33(7): 1297–1308.

He, M.C., Wang, J., Sun, X.M., & Yang, X.J. 2014. Mechanics characteristics and applications of prevention and control rock bursts of the negative passion's ratio effect anchor. *Journal of China Coal Society* 39(2): 214–221.

He, M.C., Xia, H.M., Jia, X.N., Gong, W.L., Zhao, F., & Liang, K.Y. 2012. Studies on classification, criteria, and control of rock bursts. *Journal of Rock Mechanics and Geotechnical Engineering* 4(2): 97–114.

Hu, H, Wang, Z.Y., & Liu, S. 2011. Development of auxetic fabrics using flat knitting technology. *Textile Research Journal* 81(14): 1493–1502.

Jiang, Y.D., Pan, Y.S., Jiang, F.X., Dou, L.M., & Ju, Y. 2014. State of the art review on mechanism and prevention of coal bumps in China. *Journal of China Coal Society* 39(2): 205–213.

Li, C.L.C. 2010. A new energy absorbing bolt for rock support in high stress rock masses. *International Journal of Rock Mechanics& Mining Sciences* 47:396–404.

Salit, V., Weller, T. 2009. On the feasibility of introducing auxetic behavior into thin-walled structures. *Acta Materialia* 57(1): 125–135.

Shi, W., Yang, W., & Li, Z.M. 2003. Advances in negative Poisson's ratio materials. *Polymer Bulletin* 12: 48–57.

Zhang, W., Hou, W.B., & Hu, P. 2015. Mechanical properties of new negative Poisson's ratio crush box with cellular structure in plateau stage. *Acta Materiae Compositae Sinica* 32(2): 534–540.

This page intentionally left blank

*Rock Dynamics: From Research to Engineering – Li et al. (Eds)*
*© 2016 Taylor & Francis Group, London, ISBN 978-1-138-02953-8*

# Dynamics of impact cratering

T. Kenkmann
*Institute of Earth and Environmental Sciences–Geology, Albert-Ludwigs-Universität Freiburg, Freiburg, Germany*

ABSTRACT: Impact cratering is a fundamental geological process in the solar system. The formation of impact craters is a highly dynamic and complex process that subjects the impacted target rocks to numerous types of deformation. The impact process can be subdivided into three subsequent stages, the contact and compression stage, the excavation stage, and the modification stage. In the first stage extremely high pressures and temperatures occur when the initial shock wave passes through the target rock and projectile and causes widespread shock metamorphism. Rocks are set in motion and the resulting flow field in the target excavates and ejects rock materials (2nd stage). Gravitationally induced mass movements modify the transient crater cavity and lead to simple or complex crater morphologies (3rd stage).

## 1 INTRODUCTION

Planetary bodies with solid surfaces are mostly covered by impact craters (e.g. Melosh 1989). This testifies that impact cratering is among the most important geological processes in the solar system. For instance, Mars has more than 300.000 craters larger than 1 km. In contrast, only 188 impact craters have been confirmed on Earth so far (Hergarten & Kenkmann 2015). The permanently changing face of our planet is the obvious reason for this sparse crater record. Understanding the dynamics of impact cratering is essential for unraveling the history of the solar system; though it has also applied aspects: Hypervelocity impacts still pose a threat to human civilization. The 15-m meteorite impact crater, formed 2007 at Carancas, Peru, (Kenkmann et al. 2009) or the encounter of a 19 m bolide that exploded in the atmosphere near Cheljabinsk, Russia on Feb. 15, 2013 (Popova et al. 2013) indicates the continued threat we face from impact events.

Our understanding of impact phenomena has significantly improved over the last decades. A strong contribution came from numerical simulations in combination with advancements in computational power. The hydrocodes in use today are capable of accounting for 3D-geometries, multi-material targets, strength, strain localization, fragmentation and particle-atmosphere interactions (e.g., Wünnemann et al. 2003, Collins et al. 2004, Pierazzo et al. 2008, Senft & Stuart 2009, Artemieva & Pierazzo 2011). Likewise, achievements in experimental techniques (e.g., Hugoniot data, equations of state, and constitutive properties) are important for numerical modeling of impact phenomena (e.g., Holsapple 1993, Kenkmann et al. 2011). Structural field analysis of terrestrial craters record the complexity of impact cratering (e.g. Grieve 1991, Osinski & Spray 2005, Kenkmann et al. 2014). Complementary to the study of terrestrial craters are new spacecraft missions, that continue to deliver high-resolution remote-sensing images of impact craters. These data provide new constraints on crater formation for a variety of target materials and boundary conditions such as gravity.

Deformation features observed in impact craters are formed under very different and rapidly changing boundary conditions (Fig. 1). Maximum stresses and strain rates are reached at the very beginning of an impact process when a shock wave passes through the target rocks. During the collision of a kilometer-sized asteroid, pressures may vary over eight orders of magnitude, from several hundreds of gigapascals to a few kilopascals during late stage

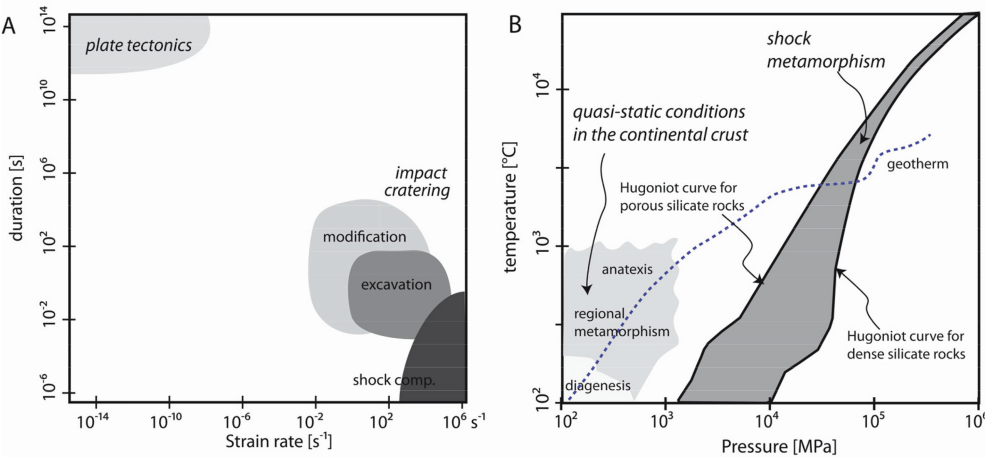


Figure 1. A) Strain rate and range of duration of the three cratering stages. B) Pressure-temperature diagram comparing regional metamorphism and shock metamorphism (modified after Kenkmann et al., 2014).

movements (Collins et al., 2005; Kenkmann et al. 2014). Temperatures range over five to six orders, from more than ten-thousand degrees near the point of impact to room temperature, within a short period of time (Collins et al. 2005). Excluding long-term relaxations of impact craters, strain rates may vary from over $10^{+6}s^{-1}$ during shock loading to $10^{-1}s^{-1}$. The duration of deformation ranges from microseconds during shock loading to minutes when gravity-driven mass movements take place (Fig. 1). The impact process is subdivided into different stages, (i) the contact and compression stage, (ii) the excavation stage, and (iii) the modification stage (Gault et al. 1968, Melosh 1989).

## 2 THE CONTACT AND COMPRESSION STAGE

### 2.1 *Physical processes*

The contact and compression stage comprises the period from the initial contact of an impacting body ("projectile") with the ground ("target") until the compression ends. During the contact and compression phase, the kinetic energy of the impacting projectile splits into internal energies of projectile and target and remaining kinetic energies of both projectile and target. This conversion results in the generation of shock waves that develop at the interface of projectile and target. Shock waves are characterized by an abrupt, nearly discontinuous change in pressure, temperature and density. They travel through media at a higher speed than an elastic wave, induce a flow of the media they have traversed, cause irreversible deformation within the media that is known as shock metamorphism, and heat the material. Mass, momentum, and energy are conserved during the transition from an unshocked to a shocked state (Hugoniot-Rankine equations), but not entropy. An equation of state relates pressure, specific volume, and the internal energy for each material (Kenkmann et al. 2014).

The amplitude of the shock decays with distance travelled by the shock wave due to geometric spreading and consumption of energy. The degree of attenuation is material dependent, e.g. in porous rocks shock wave magnitude decays faster than in low-porosity rocks. Behind the shock wave, a rarefaction wave generated by reflection of the shock wave at the free releases the compressed material from its high-pressure state and finishes the first phase of impact cratering. Shock wave compression is irreversible, whereas decompression is reversible; hence, the passage of the shock wave results in a net increase in temperature (internal energy and entropy) and a residual particle velocity in the rocks (Melosh 1989). The duration

of the contact and compression stage phase depends on the diameter of the projectile and the shock wave velocity. Even for mega-impacts such as the Chicxulub event 65 Ma ago, this period may last only for several tenths of a second (Fig. 1).

### 2.2 *Shock metamorphism*

The Hugoniot Elastic Limit (HEL) represents the maximum stress a rock can withstand under shock compression without plastic deformation and internal rearrangement. Above this limit rocks undergo a shock metamorphic overprint; below this limit brittle deformation dominates (Fig. 2a). Shock-deformation effects in minerals and rocks allow the unambiguous identification of impact craters even if the craters are morphologically degraded by erosion, as there is no other natural process capable of producing certain types of shock features. Strongly shocked minerals and rocks (>25 GPa) are affected by the subsequent excavation flow in such a way that they are displaced and found either as a part of the ejecta blanket outside the crater, as crater fill material, or as injected material in the crater floor. The highest shock levels recorded beneath the crater floor usually do not exceed 25 GPa and occur in the central parts of the crater.

Except for shatter cones (Sagy et al. 2004) (Fig. 2b), all other unambiguous indicators for shock metamorphic are visible only at the microscopic scale. Shock effects in major rock-forming minerals quartz (e.g., Langenhorst & Deutsch 1994, Stöffler & Langenhorst 1994), feldspar (Ostertag 1983), and olivine (Reimold and Stöffler, 1978; Stöffler et al., 1991) have been systematically shock-calibrated by means of planar shock recovery experiments and can be used as piezometers to reconstruct shock pressure isobars if rocks are devoid of pore space (Table 1 in Kenkmann et al., 2014). Low shock pressures are indicated by shatter cones (~1–10 GPa, Fig 2b), planar fractures (PFs, Fig. 2c) in quartz (~5–10 GPa), and feather features (FFs, Fig. 2c) (Poelchau & Kenkmann 2011), which all form through dynamic fragmentation processes.

Planar deformation features (PDFs, Fig. 2d-e) are probably the most important shock criteria. They are narrow-spaced parallel sets of amorphous lamellae oriented along specific crystallographic directions. In quartz they develop at a shock pressure interval ranging from 5–10 GPa to 35 GPa (Stöffler & Langenhorst 1994). The width of the lamellae increases with the shock magnitude so that above 35 GPa the entire grains are transformed into diaplectic glass. Diaplectic glasses are the result of solid-state amorphization. They have slightly higher refractivity indices than standard glass. Diaplectic quartz glass develops in a shock interval of 35–60 GPa, while diaplectic feldspar glass, named maskelynite, occurs in the shock pressure interval 35–45 GPa (Table 1 in Kenkmann et al., 2014).

Phase transformations in $SiO_2$ are linked with the formation of diaplectic glasses. Stishovite nuclei grow within amorphous PDF lamellae above ~13 GPa and coesite forms globular clusters within diaplectic quartz glass at 35 GPa. At even higher shock pressures true melting occurs (lechatelierite) upon pressure release (Fig. 2f). Vaporization of rock forming minerals occurs roughly above ~100 GPa. For comprehensive reviews of the progressive stages of shock metamorphism we refer to Stöffler & Langenhorst (1994), French (1998), and French & Koeberl (2010). The shock pressure calibration applies for dense materials but not for porous rocks. Porosity leads to pore space crushing and localized shock pressure excursions with magnitudes as high as four times as the average shock pressure (Güldemeister et al. 2013).

### 2.3 *Fragmentation*

The geometry of fractures formed in the very early stage of cratering is affected by the propagation speed of the fracture tip. The theoretical speed limit for tensile fracture propagation is the Raleigh wave speed. Fractures that propagate at high speed, reaching a considerable fraction of the Raleigh wave velocity, tend to bifurcate. Shatter cones representing conical fracture pattern whose surfaces are sculptured by diverging sub-cone ridges and grooves, are believed to be the result of multiple symmetric crack branching (Fig. 2b).

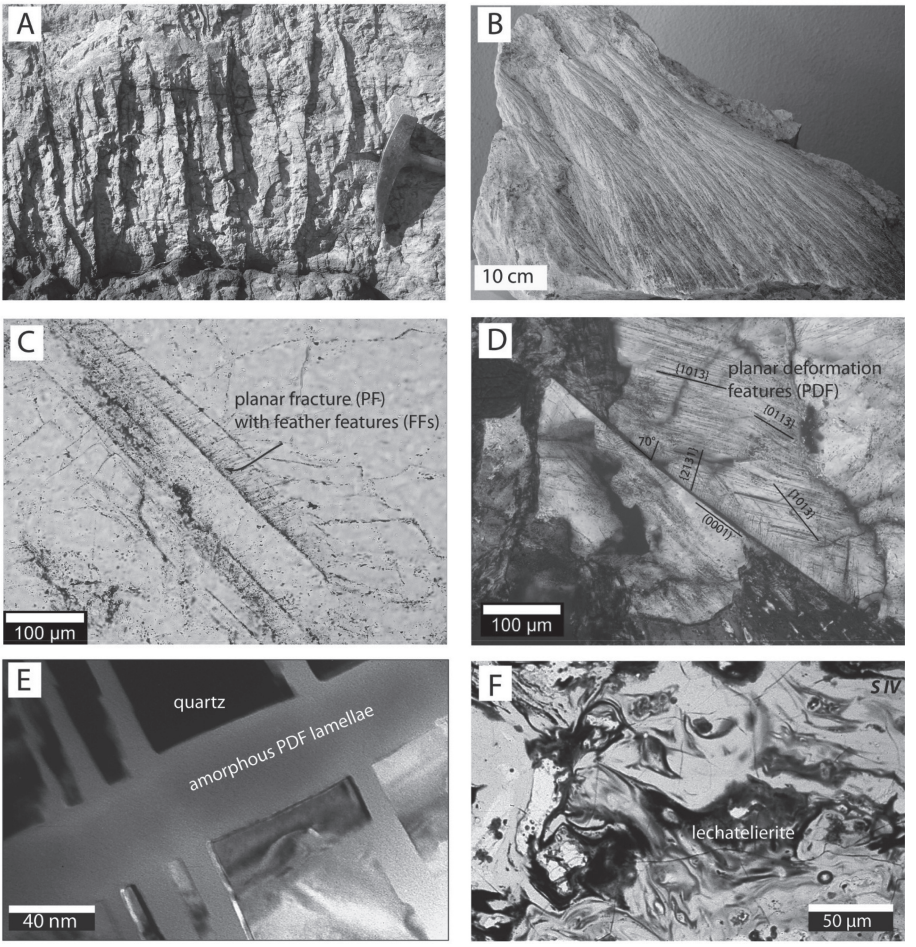


Figure 2. A) Closed-spaced fracture network in quartzite, Matt Wilson crater, Australia. B) Shatter cone from the Steinheim crater, Germany. C) Micrograph of quartz from a sandstone (Matt Wilson structure, Australia), exhibiting a set of planar fractures and feather features. D) Micrograph of shocked quartz in a granitic clast from suevite of the Nördlinger Ries crater, Germany. Multiple sets of planar deformation features (PDFs) along with a planar fracture and feather features are visible. E) TEM image of shocked quartz from a shock recovery experiment into quartzite. The quartz grain shows amorphous PDF lamellae. F) Melted quartz (lechatelierite) with schlieren textures and vesicles. Suevite sample from Seelbronn, Ries.

The response of minerals and rocks to high loading rates and loads well beyond the point of failure is critical for the understanding of fracturing and fragmentation during the early phase of an impact event. A material-specific rate dependency exists for high strain rates that control the fragmentation process. The fracture stress and fragment size depend on the loading strain rate (e.g., Grady & Kipp 1993) in such a way that the fragment size decreases and the fracture stress increases with increasing strain rate. Material tests over a large range of strain rates show that for both uniaxial compressive strength and tensile strength, after a certain "transition strain rate" (~$10^1$-$10^3$ $s^{-1}$) the material's strength begins to rapidly increase. As a cause for this behavior, it has been suggested that at high strain rates, material inertia begins to affect the nucleation and propagation of cracks (e.g., Kipp et al. 1980). Relative to their quasi-static strengths, brittle materials show an up to four-fold increase in compressive strength and an eight-fold increase in tensile strength, within the range of experimentally generated strain rates (e.g., Kimberley et al. 2013, Zhang & Zhou 2013).

Brittle failure of rock is related to a reduction of particle size. It has been shown that resulting particle sizes are properly described by a fractal size distribution (e.g., Marone & Scholz 1989, Sammis & Biegel 1989) and can be quantified by a resulting power-law, in which the exponent is referred to as the "fractal dimension" or D-value. Recent experimental analysis of the particle size distribution in impact cratering experiments also suggests a fractal particle-size distribution for impact-loaded rocks (Buhl et al. 2013). In these experiments, D-values decrease with increasing distance from the point of impact, reflecting a decrease in damage. Pulverization of rock characterizes the inner zone of the craters.

## 3 THE EXCAVATION STAGE

### 3.1 *Physical processes*

The excavation stage includes both the expansion and dissipation of the shock wave and the opening of the crater cavity. As the shock wave propagates hemispherically from the initial contact area, the engulfed material is compressed and accelerated (Fig. 3). Upon unloading the material is not completely decelerated and a residual velocity remains (Melosh, 1989). The value of this final particle velocity component typically corresponds to between one-third to one-fifth of the peak particle velocity during shock wave compression (Melosh 1989). Finally the shock wave decays to a stress wave that travels with the bulk sound speed in the rock.

A kinematic model of the excavation flow, the so-called Z-model was proposed by Maxwell (1977). The streamlines of the excavation flow near the point of impact are directed downward and outward, away from the point of impact (Fig. 3). Streamlines radiating outward gradually bend upward and outward due to the reduced pressure gradient towards the

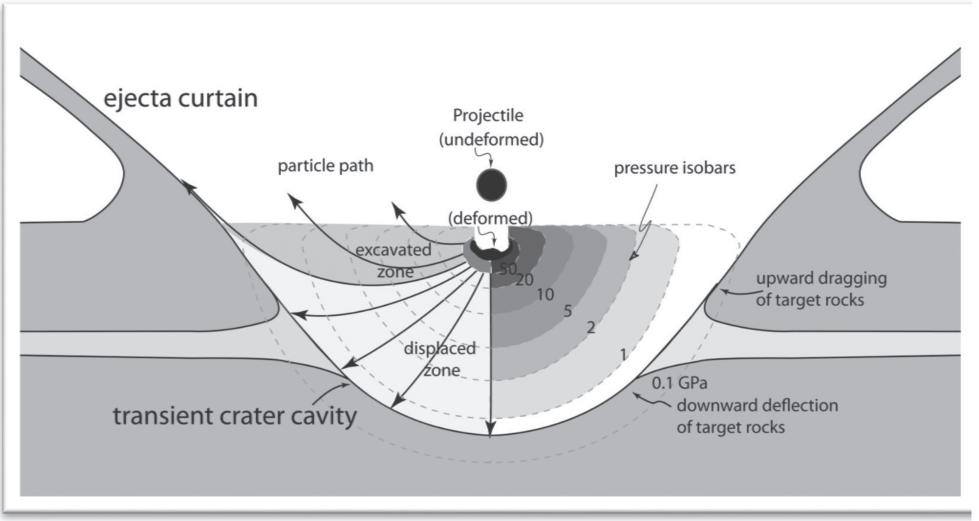


Figure 3. Schematic diagram of the initial impact, and subsequent formation of the transient crater cavity during the excavation stage. Upon impact, a hemispherical shock wave passes through the target rocks. Close to the point of impact, rocks are melted or turned to vapor. With increasing distance, the pressure of the shock wave decays and deforms the rock to different stages of shock metamorphism. The passage of the shock wave sets the target material in motion, following specific particle paths that either lead to the excavation and ejection of the material in the top third of the transient crater, or to the displacement and downward deflection of target rocks in the bottom two thirds of the transient crater. (modified after French 1998 and Kenkmann et al. 2014).

surface, caused by the reflection of the shock wave off the free surface. The flow field leads to the opening of a cavity that has a parabolic shape in cross-section (Fig. 3). It is only the material from the upper one-third to half that is entrained in the excavation process and is deposited as ejecta (Fig. 3). Target material from the deeper parts is displaced downward into the ground and does not leave the cavity. On airless planetary bodies the debris ejected from the growing crater follow ballistic trajectories. The innermost ejecta are launched first, become ejected to high altitudes, and travel fastest. Ejecta originating farther from the center are launched later, move more slowly, and become deposited in the ejecta blanket nearer to the crater rim (Melosh 1989). This combination leads to the formation of an ejecta curtain that has the shape of an inverted cone. The cone expands outwards and the ejecta debris of this cone is deposited on the target surface at increasing distances from the crater. The excavation flow is halted and the cavity stops growing when the remaining kinetic energy is insufficient to displace the target against its own weight (gravity-dominated cratering) or to overcome the cohesive strength of the target material (strength-dominated cratering). The resulting unstable cavity at the end of the excavation stage is called the transient cavity. Experimental observation of transient craters in particulate targets yields depth-diameter ratios of roughly 1/3 (Kenkmann et al. 2014).

### 3.2 *Fracturing during the excavation stage*

The products of the excavation stage are different types of fragmented rocks, so called breccias. They are subdivided into rocks, consisting of only one rock type (monomict breccias) or a mixture of different lithologies (polymict breccias). They devoid of a melt component (lithic breccia) or they either contain melt lumbs in a particulate matrix (suevite or suevitic breccia) or contain melt as a matrix phase (impact melt rock breccia). The debris of the ejecta curtain forms a blanket around the transient crater cavity. These ejecta blankets are continuous to approximately 2–3 crater radii, but become discontinuous with increasing radial range. Beside the deposits of the ejecta blanket, the crater cavity itself is filled with various, often melt-bearing types of breccias deposited from a presumably very hot ejecta plume above the cavity. The formation of these various types of breccias requires the fragmentation of rock masses involved in the excavation flow, which occurs through several subsequent processes: (i) tensile or mixed mode failure during shock pressure release, (ii) shear and tensile failure plus abrasion during the dense material stream flow within the transient cavity, in particular near the cavity floor, (iii) tensile break-up during ballistic flight by aerodynamic drag and particle collision and by the release of stored elastic strain, (iv) fragmentation during the initial deposition of the ejecta blanket, and (v) fragment size reduction by the entrainment in the radially outward moving ejecta blanket debris flow.

During the excavation flow a considerable amount of rock becomes injected into the walls of the crater subsurface. The total elevation of transient crater rims is the sum of uplift induced by the injection of material into the crater walls and the deposition of ejecta at the edge of the transient crater. Another important process associated with the excavation process is spallation. It occurs when the expanding shock wave or pressure wave approaches free surfaces and interferes with tensile stress waves reflected from these surfaces. Spallation dominantly occurs near the target surface when the local tensile strength of the target rock is exceeded (Melosh 1984). The zone of spallation may have a wider lateral extent than the transient crater cavity and is thus also recognizable in the periphery of the crater cavity. In layered targets, spallation effects can be observed in the periphery of craters up to 1.8 crater radii (Kenkmann & Ivanov 2006).

Fractures, which develop early in the cratering process, when strain rates are very high, tend to be short and closely spaced. Often irregular to parallel fracture networks develop (Fig. 2a) that are pervasive and trans-granular. During the excavation flow fractures coalesce and become longer. Faults of hundreds of meters to even kilometers length with single-slip off-sets of up to several kilometers (Spray 1997) are always formed during the final stage of cratering, the modification stage.

## 4 THE MODIFICATION STAGE

### 4.1 *Physical processes*

In the modification stage, the direction of flow is effectively reversed with respect to the excavation flow, and acts to modify and collapse the transient cavity. The modification stage begins when the excavation flow comes to a halt. Gravity is the principal force that drives the collapse of the transient cavity. The transient cavity is negatively buoyant and creates an upward force on the crust due to the displaced mass in the crater. This gravitational force attempting to close the crater is counteracted by the strength of the target. If the buoyancy force is too small, strength prohibits the target material from moving upwards and inwards to modify the cavity and a simple crater is formed (Collins et al. 2004, Kenkmann et al. 2014). If the size of the transient cavity exceeds a certain threshold, buoyancy forces exceed the target's strength and the entire cavity can completely or partly collapse. This starts at the deepest point of the cavity in the very center, where the upward-directed buoyancy force is strongest and a complex crater is formed. The relative balance between both mechanisms, the buoyancy acting to close the crater, and material strength acting to stabilize the cavity, determines whether a simple or complex crater is formed.

Depending on the degree of modification, the final crater is classified into either a simple or complex morphology (Dence 1965). Simple and complex impact craters have fundamental differences in morphology and structure, both being a function of size. Simple craters generally have a bowl-shaped morphology and a raised rim (Fig. 4a) and their depth-to-diameter ratio is roughly 0.2. Complex impact craters are generally larger than simple craters and have a depth-to-diameter ratio in the order of 1/10. They have terraced rims and an uplifted central portion of the crater floor (Fig. 4b).

The crater diameter at which the simple-to-complex transition occurs varies between planetary bodies and is inversely proportional to the surface gravity (Pike, 1988) indicating that

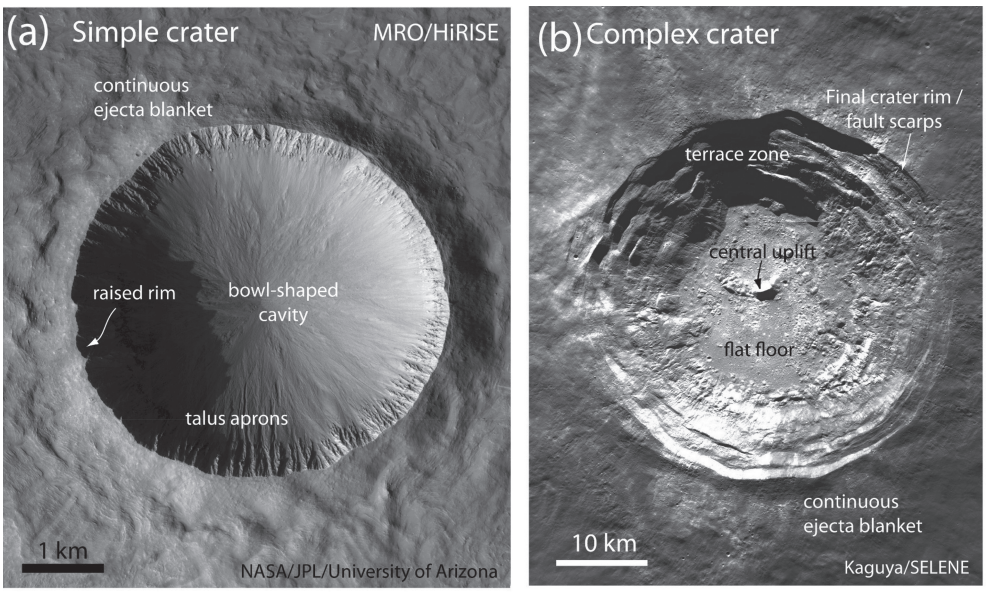


Figure 4. Comparison of simple and complex crater morphologies. A) Unnamed simple crater on Mars (38.7°N/ 316.1°E) displaying an elevated crater rim and steeply dipping upper cavity walls. The mid and lower part of the wall is covered by talus deposits (HiRISE image). B) The complex impact crater Aristarchus on the Moon, showing a central peak, a flat crater floor and an extensive slump terrace zone (Kaguya/SELENE image). Note the different scale bars in the two images (Kenkmann et al. 2014).

gravity is the main driving force for crater modification. On the Moon (surface gravity: 1.62 $ms^{-2}$) the largest impact craters with simple geometries have diameters of 16 km, on Mars (3.69 $ms^{-2}$), simple craters reach maximum diameters of ~8 km on average, and on Earth (9.81 $ms^{-2}$), the largest simple craters were formed in crystalline targets and have diameters of up to 4 km (Brent, Canada). The size-morphology progression is also controlled by the strength as the mechanical property of the target material working against the modification of the transient crater. For instance, in sedimentary targets the size limit for simple craters on Earth is about 2 km diameter. On icy bodies (i.e., Europa, Ganymede, Callisto) the transition lies at 2–3 km diameter and is nearly an order of magnitude smaller than the transition diameter of the Moon, despite similar gravitational fields (Schenk 2002, Barnouin et al. 2012).

With increasing diameter, the gravitationally-driven central uplift of complex craters can grow fast and high enough that inertial flow leads to an overshooting of the equilibrium height of the central uplift. The central uplift itself becomes gravitationally unstable and collapses under its own weight. In this case, a downward and outward directed collapse flow occurs. This flow interacts with and superposes the material that is simultaneously moving from the cavity rim towards the crater center. Craters showing this type of extensive modification are called peak-ring craters. The 65 Ma Chicxulub impact crater in Mexico is the most prominent example of a peak ring crater on earth.

The largest impact craters are multi-ring structures that develop when the depth of the transient cavity is comparable to the thickness of the lithosphere. Multi-ring basins are known from Mercury (Caloris basin, 1300 km in diameter), the Moon (e.g. Orientale, 900 km in diameter), Mars (e.g., Argyre, 1800 km in diameter) (Ivanov et al., 2010) and Callisto (Valhalla, 3800 km in diameter). McKinnon (1981) showed that for a given impact energy the number of rings primarily depends on the thickness and strength of the lithosphere and the viscosity of the underlying asthenosphere. For a very thin, weak lithosphere and underlying asthenosphere of sufficiently low viscosity (almost a liquid), the basin formation is followed by multiple oscillations of the cavity and outward propagation of gravity waves which disrupt the entire lithosphere (ripple ring basins). Thicker lithospheres restrict the number of rings that can form. Each ring represents scarps that result from conjugate systems of normal faults (graben) with circumferential strike on average. Ring formation is suppressed if the lithosphere is too thick.

The end of the modification stage is reached when all significant motion of the target comes to rest. The duration of crater modification depends on impact energy, gravity, and strength properties of the target material; the duration of collapse is proportional to $(D/g)^{1/2}$, which is approximately the period of a gravity wave of a wavelength equal to the crater diameter D at a surface gravity g (Melosh 1989). Long-term lithostatic crustal relaxations that are triggered by mass deficits of very large impact craters can persist over millions of years and are accommodated by plastic flow at mid to lower crustal levels or even in the underlying mantle, as was observed in the case of the 180 km Chicxulub crater (Morgan et al. 2000).

### 4.2 *Structures related to the modification stage*

The deformation inventory formed during the modification stage is in some respect comparable to that of landslides and also to certain tectonic environments. Major differences between gravity-driven collapse of large impact craters and upper crustal tectonics occur in the slip behavior and the particle trajectory field. As a first approximation, particle paths have a radial symmetry during inward flow with respect to the impact center (Kenkmann 2002). Shear displacements occur as single-slip events, with displacements ranging from centimeters to probably kilometers in very large craters as can be derived e.g. from the vertical off-set of terraces of lunar or martian craters.

Geological observations show that the target underneath the crater floor is disintegrated into blocks, in particular in the central uplift. These blocks are commonly internally deformed (bent or folded) at the millimeter to decameter scale, and bounded on all sides by faults. Block size increases as a function of distance from the crater center (Grady & Kipp 1993). The intensity of impact deformation increases from the rim to the center. Pervasive cataclasis and granular flow down to the grain scale is present between the blocks (Kenkmann 2003).

Melt is a common characteristic of impact structures, in particular of large impact craters. A long-lasting controversial debate exists on the discrimination of shock-related melt formation and frictional melting and their significance for the mechanics of the cratering process. In small craters, the shock-related melt volume is a tiny fraction of the transient crater volume that forms a thin sheet lining the final crater floor. In contrast, large impact craters such as the 180 km Chicxulub crater, Mexico, or the 200 km Sudbury crater, Canada, contain kilometer thick sheets of impact melt rock forming a pool in the crater center. Frictional melting of rocks is a result of high rates of deformation and a nearly complete transformation of kinetic energy to heat. This leads to black amorphous vein networks called pseudotachylites. Thin pseudotachylite veins can form during shock compression underneath the crater floor of the transient crater. They are also known from meteorites (Stöffler et al. 1991) and can contain high-pressure polymorphs. Larger scale pseudotachylites are believed to form during the modification stage (Reimold & Gibson 2005).

### 4.3 *Strength degradation*

The extensive target deformation that occurs during the collapse of the transient crater cavity and the formation of the central uplift is inconsistent with standard strength properties of rocks. Static analysis of cavity slumping has shown that, for substantial rim collapse or floor uplift to occur, the actual effective strength must be less than ~3 MPa with little or no internal friction (Melosh 1977, McKinnon 1978). Moreover, the same low strength and friction are required by dynamic models of crater formation (e.g., O'Keefe & Ahrens 1999, Wünnemann & Ivanov 2003). Consequently the effective strength and friction coefficient of the target rocks underneath the crater floor must somehow be temporarily reduced. Providing a physical explanation for the apparent transitory low strength of the target is an enduring problem in impact cratering mechanics (Melosh 1989, Melosh & Ivanov 1999, Senft & Stewart 2009).

An obvious weakening mechanism is fracturing and fragmentation induced by the passage of the shock wave. A well-developed theory for temporarily reducing friction both within a rock mass and along fault zones is acoustic fluidization (Melosh 1979, 1996). The shock wave that passes through the target rocks generates scattered seismic vibrations within the fractured rock mass beneath and surrounding the crater and along the narrow fault zones. These vibrations result in pressure fluctuations of the ambient overburden pressure. During periods of low pressure, frictional resistance decreases, leading to slip events in low-pressure zones. The time—and space-averaged effect of this process is that the rock mass behaves rheologically as a viscous fluid with a certain yield strength. Hence, this mechanism elegantly explains the distributed brittle deformation and formation of discrete blocks that are orders of magnitude smaller than the size of the transient cavity. It also explains the apparent crater-scale continuous deformation, as observed in many terrestrial craters. Slip movements may generate additional seismic vibrations that provide a positive feedback for the weakening mechanism, and thus enable large displacements along localized fault zones (Melosh,1996). Parameterizations of the macro-scale effect of acoustic fluidization have been used in numerical impact models for many years (e.g., Melosh & Ivanov 1999, Collins et al. 2004), producing dynamic crater formation models that are in good agreement with observational constraints on cavity collapse, and reproducing the general size-morphology progression of craters on crystalline planetary surfaces (e.g., Wünnemann & Ivanov 2003).

Melting during various stages of impact cratering might provide sufficient lubrication to lower the strength of block contacts during the later stages of movement (Spray 2010). Indeed, aligned melt networks of presumably frictional origin (Spray & Thompson 1995, Spray 1997) were identified at several large craters. In other cases, however, particularly in small to mid-sized complex craters, pseudotachylitic veins are not found. Moreover, although the total displacements and slip rates necessary to generate melt along a fault are easily achieved during crater formation, the volume of friction melt expected is very small (less than a few volume percent) compared to the volume of collapsing material (Melosh 2005). Hence, whether or not sufficient friction melt can be formed to lubricate crater collapse remains uncertain.

Dynamic friction shows a state—and rate-dependency. Slip weakening and strain-rate weakening has been well documented experimentally for different lithologies (Spray 1988, Di Toro et al. 2004). Strain-rate weakening dominantly occurs at relatively low temperature and pressure under abrasive wear conditions. During crater collapse very rapid, long-distance, high strain motions occur under relatively low normal load, thus these weakening mechanisms might play a relevant role. Senft & Stewart (2009) implemented a parametric strain-rate weakening model in a numerical hydrocode of crater formation that reduces the friction in damaged cells that exceed specified minimum total strain and strain-rate criteria. Despite a dependence of the detail of the results on resolution, the model's success in matching observed features in large craters suggests that the temporary strain-rate weakening of fault zones is sufficient to explain complex crater collapse.

## ACKNOWLEDGEMENTS

I would like to thank the organizers for inviting me to the RockDyn-2 conference and for giving me the opportunity to link impact cratering with the rock mechanics and engineering community. The author would like to thank the German Research Foundation DFG for ongoing support.

## REFERENCES

Artemieva, N.A. & Pierazzo, E. 2011. The Canyon Diablo impact event: 2. Projectile fate and target melting upon impact. *Meteoritics and Planetary Science* 46: 805–829.

Barnouin, O.S., Zuber, M.T., Smith, D.E., Neumann, G.A., Herrick, R.R., Chappelow, J.E., Murchie, S.L. & Prockter, L.M. 2012. The morphology of craters on Mercury: Results from MESSENGER flybys. *Icarus* 219: 414–427.

Buhl, E., Kowitz, A., Elbeshausen, D., Sommer, S., Dresen, G., Poelchau, M.H., Reimold, W.U., Schmitt, R.T. & Kenkmann, T. 2013. Particle size distribution and strain rate attenuation in hypervelocity impact and shock recovery experiments. *Journal of Structural Geology* 56: 20–33.

Collins, G.S., Melosh, H.J. & Ivanov, B.A. 2004. Modeling damage and deformation in impact simulations. *Meteoritics and Planetary Science* 35: 217–231.

Collins, G.S., Melosh, H.J. & Marcus, R.A. 2005. Earth Impact Effects Program: A Web-based computer program for calculating the regional environmental consequences of a meteoroid impact on Earth. *Meteoritics and Planetary Science* 40: 817–840.

Dence, M.R., 1965. The extraterrestrial origin of Canadian craters. *Annals of the New York Academy of Sciences* 123: 941–969.

French, B.M. 1998. *Traces of catastrophe: a handbook of shock-metamorphic effects in terrestrial meteorite impact craters.* Lunar and Planetary Institute, Houston, TX, Contribution CB-954.

French, B.M. & Koeberl, C. 2010. The convincing identification of terrestrial meteorite impact structures: What works, what doesn't, and why. *Earth-Science Reviews* 98: 123–170.

Gault, D.E., Quaide, W.L.& Oberbeck, V.R. 1968. Impact cratering mechanics and structures. In: French, B.M, Short, N.M., (Eds.) *Shock metamorphism in natural materials*. Baltimore, Mono Book Corp., p. 87–99.

Grady, D.E. & Kipp, M.E. 1993. Dynamic fracture and fragmentation. In: Asay, J.R., Shahinpoor, M. (Eds.), *High-Pressure Shock Compression of Solids*. Springer, New York.

Grieve, R.A.F. 1991. Terrestrial impact: The record in the rocks. *Meteoritics* 26: 175–194.

Güldemeister, N., Durr, N., Wünnemann, K. & Hiermaier, S. 2013. Propagation of impact-induced shock waves in porous sandstone using mesoscale modeling. *Meteoritics and Planetary Science* 48: 115–133.

Holsapple, K.A. 1993. The scaling of impact processes in planetary sciences. *Annual Reviews in Earth and Planetary Science* 21: 333–373.

Ivanov, B.A., Melosh, H.J. & Pierazzo, E. 2010. Basin-forming impacts: Reconnaissance modeling. In: Gibson, R.L., Reimold, W.U. (Eds.), *Large Meteorite Impacts and Planetary Evolution IV*. Geological Society of America Special Papers 465: 29–49.

Kenkmann, T. 2002. Folding within seconds. *Geology* 30: 231–234.

Kenkmann, T. 2003. Dike formation, cataclastic flow, and rock fluidization during impact cratering: an example from the Upheaval Dome structure, Utah. E*arth and Planetary Science Letters* 214: 43–58.
Kenkmann, T. & Ivanov, B.A. 2006. Target delamination by spallation and ejecta dragging: An example from the Ries Crater's periphery. *Earth and Planetary Science Letters* 252: 15–29.
Kenkmann, T., Artemieva, N.A., Wünnemann, K., Poelchau, M.H., Elbeshausen, D., & Núñez del Prado, H. 2009. The Carancas meteorite impact crater, Peru: Geologic surveying and modeling of crater formation and atmospheric passage. *Meteoritics and Planetary Science* 44: 985–1000.
Kenkmann, T., Wünnemann, K., Deutsch, A., Poelchau, M.H., Schäfer, F. & Thoma, K. 2011. Impact cratering in sandstone: The MEMIN pilot study on the effect of pore water. *Meteoritics and Planetary Science* 46: 890–902.
Kenkmann, T., Poelchau, M.H. & Wulf, G. 2014. Structural Geology of impact craters. *Journal of Structural Geology* 62: 156–182.
Kimberley, J. & Ramesh, K.T. 2011. The dynamic strength of an ordinary chondrite. *Meteoritics and Planetary Science* 46: 1653–1669.
Kimberley, J., Ramesh, K.T. & Daphalapurkar, N.P. 2013. A scaling law for the dynamic strength of brittle solids. *Acta Materialia* 61: 3509–3521.
Kipp, M.E., Grady, D.E. & Chen, E.P. 1980. Strain-rate dependent fracture initiation. *International Journal of Fracture* 16: 471–478.
Langenhorst, F. & Deutsch, A. 1994. Shock experiments on pre-heated α- and β-quartz: 1. Optical and density data. *Earth and Planetary Science Letters* 125: 407–420.
Maxwell D.E. 1977. Simple Z model of cratering, ejection, and the overturned flap. In: Roddy, J., Pepin, R.O., Merill, R.B. (Eds.), *Impact and explosion cratering.* Pergamon Press, New York, 1003–1008.
McKinnon, W.B. 1978. An investigation into the role of plastic failure in crater modification: Proceedings *Lunar Planetary Science Conference* 9: 3965–3973.
McKinnon, W.B. 1981. Application of ring tectonic theory to Mercury and other solar system bodies. In: Schultz, P.H., Merrill, R.B. (Eds.). *Multi-ring basins: Formation and Evolution.* Proceedings of the Lunar and Planetary Science Conference, Houston, TX, New York and Oxford, Pergamon Press, p. 259–273.
Melosh, H.J. 1977. Crater modification by gravity: a mechanical analysis of slumping. In Roddy, J., Pepin, R.O., Merill, R.B. (Eds.) *Impact and explosion cratering*. Pergamon Press, New York, p. 1245–1260.
Melosh, H.J. 1979. Acoustic fluidization: A new geologic process? *Journal of Geophysical Research* 84: 7513–7520.
Melosh, H.J. 1984. Impact ejection, spallation and the origin of meteorites. *Icarus* 59: 234–260.
Melosh, H.J. 1989. Impact cratering: A geological process. New York, Oxford University Press.
Melosh, H.J. 1996. Dynamical weakening of faults by acoustic fluidization. Nature 379: 601–606.
Melosh, H.J. 2005. The mechanics of pseudotachylite formation in impact events. In: Henkel, H., Koeberl, C. (Eds.), *Impact Tectonics*. Springer, Berlin, p. 55–80.
Melosh, H.J. & Ivanov, B.A. 1999. Impact crater collapse. *Annual Review of Earth and Planetary Sciences* 27: 385–415.
Morgan, J., Warner, M., Collins, G.S., Melosh, H.J. & Christeson, G.L. 2000. Peak-ring formation in large impact craters: Geophysical constraints from Chicxulub. *Earth and Planetary Science Letters* 183: 347–354.
O'Keefe, J.D. & Ahrens, T.J., 1999. Complex craters: Relationship of stratigraphy and rings to impact conditions. *Journal of Geophysical Research* 104: 27091–27104.
Osinski, G.R. & Spray, J.G. 2005. Tectonics of complex crater formation as revealed by the Haughton impact structure, Devon Island, Canadian High Arctic. *Meteoritics and Planetary Science* 40: 1813–1834.
Ostertag, R. 1983. Shock experiments on feldspar crystals. *Journal of Geophysical Research: Solid Earth* 88: B364-B376.
Pierazzo, E., Artemieva, N.A., Asphaug, E., Baldwin, E.C., Cazamias, J., Coker, R., Collins, G.S., Crawford, D.A., Davison, T., Elbeshausen, D., Holsapple, K.A., Housen, K.R., Korycansky, D.G. & Wünnemann, K. 2008. Validation of numerical codes for impact and explosion cratering: Impacts on strengthless and metal targets. *Meteoritics and Planetary Science* 43: 1917–1938.
Pike, R.J. 1988. Geomorphology of impact craters on Mercury, In: *Mercury*. Tucson, AZ, University of Arizona Press, p. 165–273.
Poelchau, M.H. & Kenkmann, T. 2011. Feather features: A low shock pressure indicator in quartz. *Journal of Geophysical Research* 116: B02201, doi:10.1029/2010JB007803.

Popova, O.P., Jenniskens, P., Emel'yanenko, V., Kartashova, A., Biryukov, E., Khaibrakhmanov, S., Shuvalov, V., & 53 further authors 2013. Chelyabinsk Airburst, Damage Assessment, Meteorite Recovery, and Characterization. *Science:* doi: 10.1126/science.1242642.

Reimold, W.U. & Stöffler, D. 1978. Experimental shock metamorphism of dunite. *Lunar and Planetary Science Conference Proceedings* 9: 2805–2824.

Reimold, W.U. & Gibson, R.L. 2005. "Pseudotachylites" in Large Impact Structures. In: Koeberl, C., Henkel, H. (Eds.) *Impact tectonics*. Springer Berlin Heidelberg. p.1–53.

Sagy, A., Fineberg, J. & Reches, Z.E. 2004. Shatter cones: Branched, rapid fractures formed by shock impact. *Journal of Geophysical Research: Solid Earth* 109: B10209, doi:10.1029/2004JB003016.

Sammis, C.G. & Biegel, R.L. 1989. Fractals, fault-gouge, and friction. *Pure and Applied Geophysics* 131: 255–271.

Schenk, P.M. 2002. Thickness constraints on the icy shells of the Galilean satellites from a compariso of crater shapes. *Nature* 417: 419–421.

Senft, L.E., & Stewart, S.T. 2009. Dynamic fault weakening and the formation of large impact craters. *Earth and Planetary Science Letters* 287: 471–482.

Spray J.G. 1988. Generation and crystallization of an amphibolite shear melt: an investigation using radial friction welding apparatus. *Contrib. Mineral. Petrol*. 99: 464–475.

Spray, J.G. 1997. Superfaults. *Geology* 25: 579–582.

Spray, J.G. 1998. Localised shock—and friction-induced melting in response to hypervelocity impact. In: Grady, M.M., Hutchinson, R., McGall, G.J.H. & Rothery, D.A. (Eds.) *Meteorites: Flux with time and Impact Effects*: Geological Society London, Special Publication 140, 171–180.

Spray, J.G. 2010. Frictional melting processes in planetary materials: From hypervelocity impact to earthquakes. *Annual Review of Earth and Planetary Sciences* 38: 221–254.

Spray, J.G. & Thompson, L.M. 1995. Friction melt distribution in a multi-ring impact basin. *Nature* 373: 130–132.

Stöffler, D. & Langenhorst, F. 1994. Shock metamorphism of quartz in nature and experiment: I. Basic observation and theory. *Meteoritics* 29: 155–181.

Stöffler, D., Keil, K. & Scott, E.R.D. 1991. Shock metamorphism of ordinary chondrites. *Geochimica et Cosmochimica Acta* 55: 3845–3867.

Wünnemann, K. & Ivanov, B.A. 2003. Numerical modelling of impact crater depth-diameter dependence in an acoustically fluidized target. *Planetary and Space Science* 51: 831–845.

Zhang, Q.B. & Zhao, J. 2014. A Review of Dynamic Experimental Techniques and Mechanical Behaviour of Rock Materials. *Rock Mechanics and Rock Engineering* 47 (4): 1411–1478.

*Rock Dynamics: From Research to Engineering – Li et al. (Eds)*
*© 2016 Taylor & Francis Group, London, ISBN 978-1-138-02953-8*

# Analysis of nonlinear spherical wave propagation for concretes

H.W. Lai
*Mechanics and Materials Science Research Center, Faculty of Mechanical Engineering and Mechanics, Ningbo University, Ningbo, China*
*Department of Municipal Engineering, Zhejiang University of Water Resources and Electric Power, Hangzhou, China*

Z.J. Wang
*Northwest Institute of Nuclear Technology, Xi'an, China*

L.M. Yang & L.L. Wang
*Mechanics and Materials Science Research Center, Faculty of Mechanical Engineering and Mechanics, Ningbo University, Ningbo, China*

ABSTRACT: Both the positive and inverse problem of spherical waves propagating in concrete are studied. Using characteristics method, the nonlinear spherical waves in concrete, including the radial stress $\sigma_r(r, t)$, circumferential stress $\sigma_t(r, t)$, radial strain $\varepsilon_r(r, t)$ and the circumferential strain $\varepsilon_t(r, t)$ are calculated based on the ZWT constitutive relation. Numerical results illustrate that the viscosity effects and nonlinear effects in concrete cannot be ignored. Based on universal spherical wave conservation equations and combined with the rate-independent law of elastic volume deformation, the inverse analysis method for spherical waves (called 'nv + T0/SW') are developed to determine constitutive behavior of concrete when n particle velocity profiles are measured. The satisfactory agreement between the 'characteristics solutions' and the 'nv + T0/SW' inverse solutions confirms the validity of the proposed new method, which may be more suitable for studying the dynamic behavior of heterogeneous materials with large aggregates such as concretes and rocks et al.

## 1 INTRODUCTION

In practical engineering problems, such as underground explosions and engineering blasts, there are often problems of point explosion, point impact and spherical cavity-walls subjected to explosion loading, where the spherical wave propagation should be dealt with (Wang 2005, Zukas et al. 1982). The dynamic response of concrete structures under explosive/impact loading is intrinsically dependent on the dynamic behavior of concrete materials involved in the structures. Thus the importance of research on the dynamic behavior of concrete materials under high strain rates (called strain rate effect for short) cannot be overemphasized.

Unlike the cases under quasi-static experiments, the experiments of dynamic behavior of materials under explosive/impact loading involve stress wave propagation (called stress wave effect for short). The main difficulty lies in that the strain rate effect and the stress wave effect are usually inter-coupled. In fact, on the one hand, no wave propagation can be analyzed without knowing the dynamic constitutive relation of the material; consequently the basic characteristics of wave propagation inevitably depend on the strain-rate dependence of mechanical behavior of materials (Wang 2005, Wegner 1993). On the other hand, in the study of dynamic constitutive relations at high strain rates, wave propagation effects should not be neglected.

To solve the mentioned problem, the methods named as Wave Propagation Technique (WPT) in studies on dynamic behavior of materials under explosive/impact loading have been developed. Among various types of WPT, the Lagrange analysis attracts most researchers'

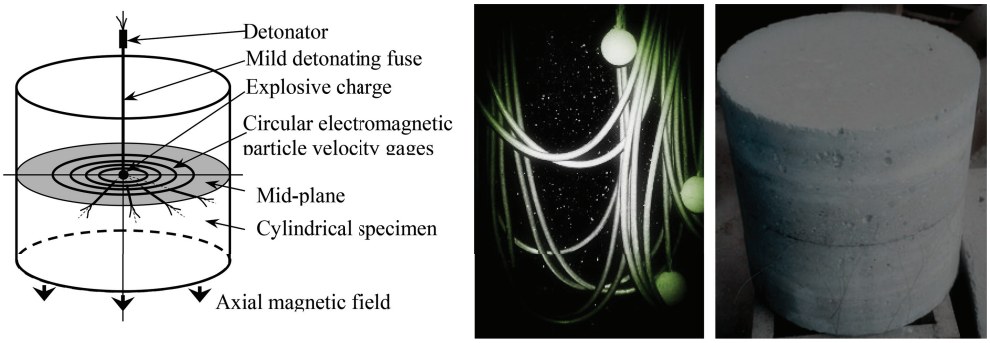


Figure 1. Scheme for Lagrange analysis of spherical waves in concrete with mini-explosion technique.

attention (e.g., Fowles & Williams 1970, Cowperthwaite & Williams 1971, Grady 1973, Wang et al. 2010, Lai & Wang 2011, Lai et al. 2013), because no pre-assumption for the constitutive relation of test material is required. In this work, the characteristics analyses of nonlinear visco-elastic spherical waves (as the so-called positive problem) and the Lagrange analysis of spherical wave based on particle velocity wave measurements (as the so-called inverse problem) in concrete is presented.

## 2 EXPERIMENTAL METHOD

Spherical wave experiments are more suitable for studying the dynamic behavior of heterogeneous materials with large aggregates such as concretes and rocks et al in 3-D stress state, since the characteristic size of specimens in spherical wave experiments could be in the order of meters, at least an order of magnitude larger than the aggregate size of concrete-like materials.

The spherical wave test apparatus is schematically shown in Figure 1 (Wang et al. 2000, Lin et al. 2007). By use of a set of magneto-electric velocimeter, a series of particle velocity wave profiles $v(r_i,t)$ at different radii $r_i$ are measured.

## 3 CHARACTERISTICS ANALYSIS OF SPHERICAL WAVES

### 3.1 *Governing equations for nonlinear visco-elastic spherical waves*

Although the fracture strain of concrete material under high strain rates is as low as in the order of $10^{-3}$, the rate-dependent character is remarkable (Wang et al. 2003). So, it could be regarded as a kind of nonlinear visco-elastic materials, rather than an elastic brittle material.

In the spherical coordinates (Fig. 2), the governing equations of nonlinear visco-elastic spherical waves consist of three parts: the continuity equation (1) representing the mass conservation, the motion equation (2) representing the momentum conservation,

$$\frac{\partial \varepsilon_r}{\partial t} = \frac{\partial v}{\partial r}, \tag{1a}$$

$$\frac{\partial \varepsilon_\theta}{\partial t} = \frac{v}{r}, \tag{1b}$$

$$\frac{\partial \sigma_r}{\partial r} + \frac{2(\sigma_r - \sigma_\theta)}{r} = \rho_0 \frac{\partial v}{\partial t}, \tag{2}$$

and the nonlinear visco-elastic constitutive equation, which plays a key role in the study here.

The nonlinear dynamic constitutive response in one dimensional stress form for a variety of plastics and even concretes can be well described by the so-called ZWT nonlinear thermo-viscoelastic constitutive equation (Eq. 3) (Wang 2003), and the corresponding rheological model is shown in Figure 3, consisting of a nonlinear (non-Hookean) spring and two Maxwell elements in parallel connection.

$$\sigma = \sigma_e(\varepsilon) + E_1\int_0^t \dot{\varepsilon}(\tau)\exp(-\frac{t-\tau}{\theta_1})d\tau + E_2\int_0^t \dot{\varepsilon}(\tau)\exp(-\frac{t-\tau}{\theta_2})d\tau, \qquad \sigma_e(\varepsilon) = E_0\varepsilon + \alpha\varepsilon^2 + \beta\varepsilon^3 \tag{3}$$

where $\sigma$ denotes the stress, $\varepsilon$ the strain, $\dot{\varepsilon}$ the strain rate, $t$ the time, and the first term $\sigma_e(\varepsilon)$ describes the nonlinear elastic equilibrium response, $E_0$ denotes the initial elastic modulus and $\alpha$, $\beta$ are nonlinear elastic constants; the next integral term describes the linear viscoelastic response at low strain rates, in which $E_1$ and $\theta_1$ are the elastic constant and relaxation time, respectively; and the last integral term describes the linear viscoelastic response at high strain rates, in which $E_2$ and $\theta_2$ are the elastic constant and relaxation time, respectively.

In the case of spherically symmetric, the generalized ZWT equation for nonlinear viscoelastic spherical waves consists of two parts: the volumetric part and the distortional part (Wang et al., 2013a). Neglecting the volumetric viscosity as usual, the former is expressed as

$$\frac{\partial\sigma_r}{\partial t} + 2\frac{\partial\sigma_\theta}{\partial t} - 3K_{eff}(\Delta)\left(\frac{\partial\varepsilon_r}{\partial t} + 2\frac{\partial\varepsilon_\theta}{\partial t}\right) = 0 \tag{4a}$$

and the latter is expressed as

$$\frac{\partial\varepsilon_r}{\partial t} - \frac{\partial\varepsilon_\theta}{\partial t} = \frac{1}{2G_{eff}(\varepsilon_r)}\left(\frac{\partial\sigma_r}{\partial t} - \frac{\sigma_{eff}(\varepsilon_r)}{\theta_2} + \frac{\sigma_r}{\theta_2}\right) - \frac{1}{2G_{eff}(\varepsilon_\theta)}\left(\frac{\partial\sigma_\theta}{\partial t} - \frac{\sigma_{eff}(\varepsilon_\theta)}{\theta_2} + \frac{\sigma_\theta}{\theta_2}\right) \tag{4b}$$

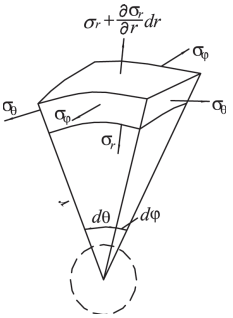


Figure 2. Infinitesimal element in spherical coordinates.

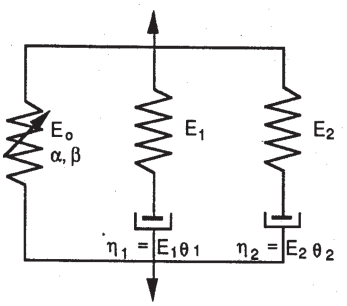


Figure 3. Constitutive model of ZWT equation.

where $\sigma_{eff}(\varepsilon) = E_0\varepsilon + \alpha\varepsilon^2 + \beta\varepsilon^3 + E_1\varepsilon$ is the nonlinear elastic response, $\Delta = \varepsilon_r + 2\varepsilon_\theta$ is the volumetric deformation, $K_{eff}(\Delta) = E_{eff}(\Delta/3)/3(1-2\nu)$ is the nonlinear volumetric module, $E_{eff} = \frac{d\sigma_e}{d\varepsilon} + E_1 + E_2$ is the nonlinear Young's module and $G_{eff}(\varepsilon) = E_{eff}(\varepsilon)/2(1+\nu)$ is the nonlinear shear module, respectively. The Poisson ratio $\nu$ is assumed independent on strain-rate and strain as usual.

Based on the ZWT nonlinear visco-elastic constitutive relation, the governing equations which reflect high-strain-rate effects, are established for nonlinear visco-elastic spherical waves, including 5 partial differential equations (Eqs. 1a, 1b, 2, 4a, 4b), solving 5 unknown variables, the radial particle velocity $v$, radial stress $\sigma_r$, circumferential stress $\sigma_\theta$, radial strain $\varepsilon_r$ and the circumferential strain $\varepsilon_\theta$.

### 3.2 *Numerical examples by characteristics method*

A numerical example of nonlinear visco-elastic spherical waves by characteristics method is shown below for concrete. According to our previous experimental studies on concretes in one dimensional stress state, the ZWT constitutive parameters in Table 1 are used for calculation.

The initial condition used is taken as $v(r,0) = \sigma_r(r,0) = \sigma_\theta(r,0) = \varepsilon_r(r,0) = \varepsilon_\theta(r,0) = 0$ for $r_0 < r \le \infty$ and an experimentally measured particle velocity $v$ at $r_0$ = 100 mm, as shown in Figure 4a, is taken as the boundary condition. The wave profiles are calculated at different radii, $r_i$ = 120, 140, 160 and 180 mm. The numerical results for $v(r_i, t)$, $\sigma_r(r_i, t)$, $\sigma_\theta(r_i, t)$, $\varepsilon_r(r_i, t)$ and $\varepsilon_\theta(r_i, t)$ are given in Figure 4a, 4b, 4c, 4d and 4e, respectively.

As can be seen from those figures, a common feature exists, namely, the peak of wave profiles attenuates markedly with wave propagation regardless what concerned is $\sigma_r(r, t)$ or other variables. Another feature should be noticed is that even under a compressible boundary condition the circumferential stress $\sigma_\theta$ quickly changes from a compressible state into a tensile state (Fig. 4c), and the circumferential strain $\varepsilon_\theta$ is correspondingly in a tensile state (Fig. 4e). The tensile magnitude of $\sigma_\theta$ and $\varepsilon_\theta$ is of significance in failure analysis, particularly for brittle materials, since once the maximum tensile value of $\sigma_\theta$ or $\varepsilon_\theta$ exceeds the critical tensile strength of material, the failure happens. This is the reason why spherical waves could result in a tensile failure even the boundary condition is a compressible loading.

Table 1. Visco-elastic constitutive parameter for concrete.

| ρ | $E_0$ | α | β | $E_1$ | $E_2$ | $\theta_2$ | ν |
|---|---|---|---|---|---|---|---|
| kg/m$^3$ | GPa | GPa | GPa | GPa | GPa | μs | 1 |
| 2246 | 11.8 | 593.8 | –1.320e6 | 11.8 | 14.37 | 0.44 | 0.23 |

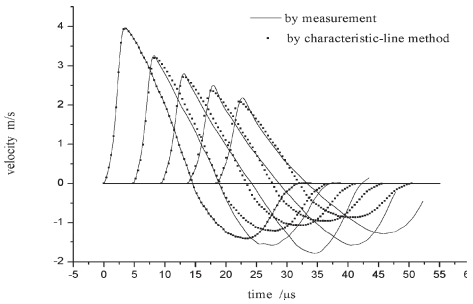


Figure 4a. Velocity $v$ profiles by the characteristics solution in concrete.

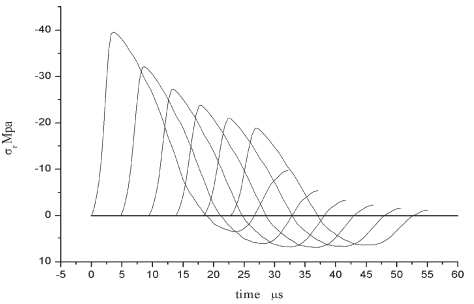


Figure 4b. Radial stress $\sigma_r$ profiles by the characteristics solution in concrete.

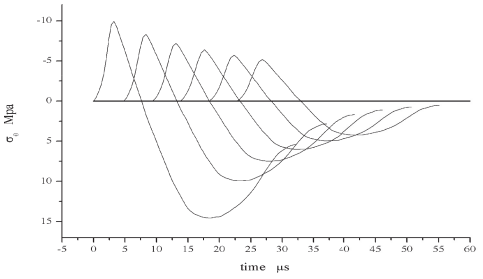


Figure 4c. Circumferential stress $\sigma_\theta$ profiles by the characteristics solution in concrete.

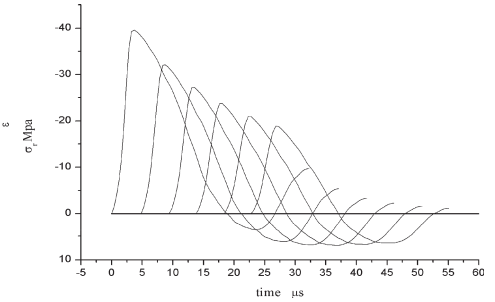


Figure 4d. Radial strain $\varepsilon_r$ profiles by the characteristics solution in concrete.

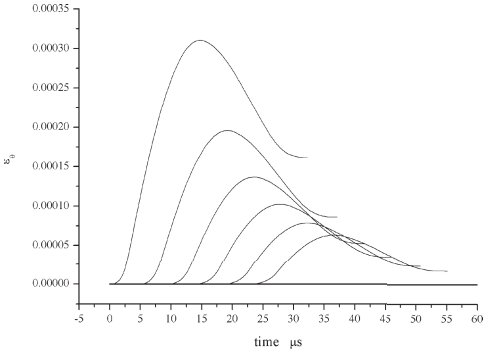


Figure 4e. Circumferential strain $\sigma_\theta$ profiles by the characteristics solution in concrete.

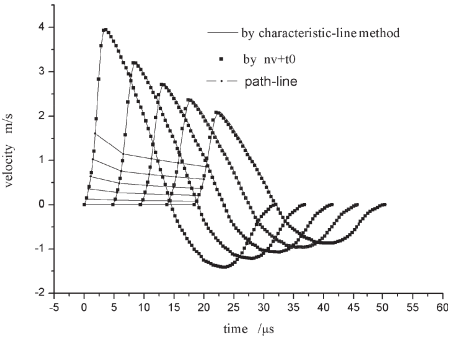


Figure 5. Velocity profiles experimentally measured in concrete sample.

## 4 LAGRANGE ANALYSIS OF SPHERICAL WAVE 'NV+T0/SW'

The traditional Lagrange analysis of wave propagation is based on the conservation equations without any pre-assumption of material constitutive relation. Mathematically, this is to solve the so-called "second class inverse problem" under the known initial boundary conditions for determining the dynamic constitutive relation. However, in the case of spherical waves, when the radial particle velocity profiles being measured by n velocity gauges at the n Lagrangian coordinates $r_i$ ($i$ = 1,2,…,n), it is no longer easy to solve the other four unknowns from the three conservation equations (Eqs. 1a, 1b and 2). A new method of Lagrange analysis of spherical waves named "nv+T0/SW", which is a generalization of the method named "nv+T0" in one dimensional (Wang et al., 2013b), is developed to overcome this difficulty as shown below.

### 4.1 *Principle of Lagrange analysis of spherical wave "nv+T0/SW"*

#### 4.1.1 *Solving of $\varepsilon_r$ and $\varepsilon_\theta$*

The radial strain $\varepsilon_r$ and the circumferential strain $\varepsilon_\theta$ an be easily determined from the continuity equation representing the mass conservation (1a and 1b) by integrating with the regard to time. Usually, it is known that $v(r_i, t) = 0$ at $t = 0$. Thus, by utilizing this zero-initial condition, $\varepsilon_\theta(r_i,t)$ at $r_i$ ($i$ = 1,2,…,n) can be determined by numerical integral operation firstly. Then, the corresponding first-order derivatives $\partial v(r_i,t)/\partial r_i$ can be obtained by numerical differential operation. Moreover, from continuity equation (1a), the radial strain $\varepsilon_r(r_i,t)$ can be determined.

#### 4.1.2 *Solving of $\sigma_r$ and $\sigma_\theta$*

However, the radial stress $\sigma_r(r_i,t)$ and circumferential stress $\sigma_\theta(r_i,t)$ could not be obtained from the momentum conservation equation (2) so easily. The system consisting of three conservation

equations is incomplete to solve the five unknowns $v$, $\sigma_r$, $\sigma_\theta$, $\varepsilon_r$ and $\varepsilon_\theta$ and requires an additional equation to complete the system when the particle velocities $v(r_i, t)$ are measured. Since the law of nonlinear elastic volume deformation (Eq. 4a) is rate-independent and can be predetermined under quasi-static condition, it can be used as the additional equation required.

Since the radial strain $\varepsilon_r$ and the circumferential strain $\varepsilon_\theta$ can be well calculated as shown previously, the Eq. 4a provides a relation between the partial derivative $\partial\sigma_\theta/\partial t$and the partial derivative $\partial\sigma_r/\partial t$, or can be expressed as the following form:

$$\frac{\partial\sigma_\theta}{\partial t}=\frac{1}{2}\left(3K_{eff}\left(\varepsilon_r\right)\left(\frac{\partial\varepsilon_r}{\partial t}+2\frac{\partial\varepsilon_\theta}{\partial t}\right)-\frac{\partial\sigma_r}{\partial t}\right)\frac{K_{eff}\left(\varepsilon_\theta\right)}{K_{eff}\left(\varepsilon_r\right)} \tag{4a'}$$

On the other hand, according to the definition of total derivative along the path-line (Grady, 1973) as shown below

$$\left.\frac{d\sigma_r}{dr}\right|_p=\left.\frac{\partial\sigma_r}{\partial r}\right|_t+\left.\frac{\partial\sigma_r}{\partial t}\right|_r\frac{dt}{dr}=\left.\frac{\partial\sigma_r}{\partial r}\right|_t+\left.\frac{\partial\sigma_r}{\partial t}\right|_r\left.\frac{1}{r'}\right|_p \tag{5}$$

and substituting Eq. (2) into Eq. (5), the partial derivative $\partial\sigma_r/\partial t$ can be expressed as

$$\frac{\partial\sigma_r}{\partial t}=r'\left(\left.\frac{d\sigma_r}{dr}\right|_p-\rho_0\frac{\partial v}{\partial t}+\frac{2\left(\sigma_r-\sigma_\theta\right)}{r}\right) \tag{6}$$

Once the particle velocity waves $v(r_i,t)$ at n Lagrangian positions $r = r_i$ are measured by the n particle velocity gauges, their first-order partial derivatives $\partial v\left(r_i,t\right)/\partial t_i$ with regard to time $t$ can be easily determined.

By utilizing the zero-initial condition ($\sigma_r=\sigma_\theta=v=\frac{d\sigma_r}{dr}=\frac{dv}{dr}=0$, at $t = 0$), the radial stress at the n Lagrangian positions $r = r_i$ on path line $P_1$, $\sigma_r(r_i,t)|_{p=1}$, can be easily obtained by integrating $\partial\sigma_r\left(r_i,t\right)/\partial t_i$ with regard to time $t$. Then $\partial\sigma_\theta(r_i,t)/\partial t_i$is known from (4a'), and the circumferential stress $\sigma_\theta(r_i,t)\big|_{p=1}$ at the n Lagrangian positions $r = r_i$ on path-line $P_1$ can be easily obtained by integrating $\partial\sigma_\theta\left(r_i,t\right)/\partial t_i$ with regard to time $t$. Followed by analogy, the radial stress $\sigma_r(r_i,t)\big|_{p=2}$ and the circumferential stress $\sigma_\theta(r_i,t)\big|_{p=2}$ at the next path-line position can be determined, and so on.

Note that this method can be used not only for the loading stage but also for the unloading stage. Such a new method for spherical waves is shortened as " nv+T0/SW".

### 4.1.3 *The solving of $\theta_2$ for ZWT materials*

What the most attractive in the "nv+T0/SW" inverse method is that no pre-assumption for the distortional constitutive relation of test material is required.

However, if the dynamic behavior of tested material can be described by the ZWT model (called ZWT material for shorter), then the relaxation time in high strain rates, $\theta_2$, can be immediately determined from Eq. (4b), which can be re-written as the following form

$$\theta_2=\frac{\frac{1}{2G_{eff}\left(\varepsilon_r\right)}\left(\sigma_r-\sigma_{eff}\left(\varepsilon_r\right)\right)-\frac{1}{2G_{eff}\left(\varepsilon_\theta\right)}\left(\sigma_\theta-\sigma_{eff}\left(\varepsilon_\theta\right)\right)}{\left(\frac{\partial\varepsilon_r}{\partial t}-\frac{\partial\varepsilon_\theta}{\partial t}\right)-\left(\frac{1}{2G_{eff}\left(\varepsilon_r\right)}\frac{\partial\sigma_r}{\partial t}-\frac{1}{2G_{eff}\left(\varepsilon_\theta\right)}\frac{\partial\sigma_\theta}{\partial t}\right)} \tag{7}$$

It has been pointed that the dynamic behavior of a ZWT material is mainly dependent on the parameters $E_2$ and $\theta_2$ (Wang et al., 2013). Once the $E_2$ has been determined by the "nv+T0/SW" method, $\theta_2$ is the only key parameter to be determined and it can be now determined by Eq. (7).

## 4.2 *Numerical examples in concrete by "nv+T0/SW" inversion*

Firstly, the spherical wave experimental records of $v(r_i, t)$, $i = 0, 1, 2, 3, 4$, are measured at different $r_i$, as shown in Figure 5. Note that the so-called path-lines are also partly shown in the

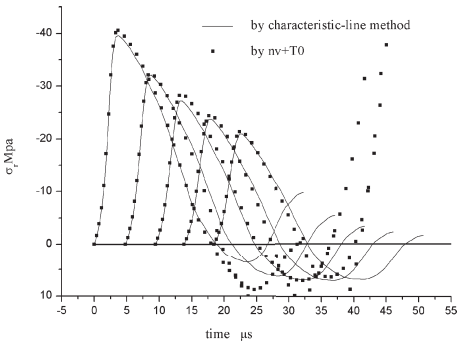


Figure 6a. The 'nV+$T_0$/SW' solution of $\sigma_r(r_i, t)$ in concrete and its comparison with the characteristics solution.

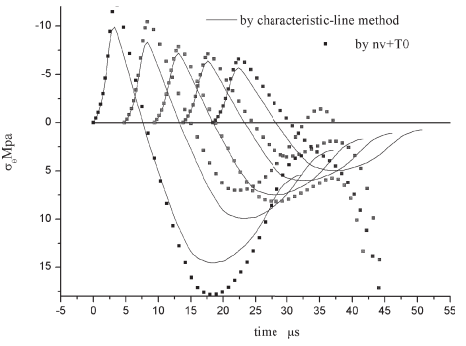


Figure 6b. The 'nV+$T_0$/SW' solution of $\sigma_\theta(r_i, t)$ in concrete and its comparison with the characteristics solution.

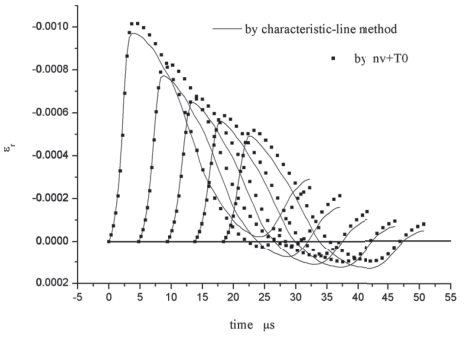


Figure 6c. The 'nV+$T_0$/SW' solution of $\varepsilon_r(r_i, t)$ in concrete and its comparison with the characteristics solution.

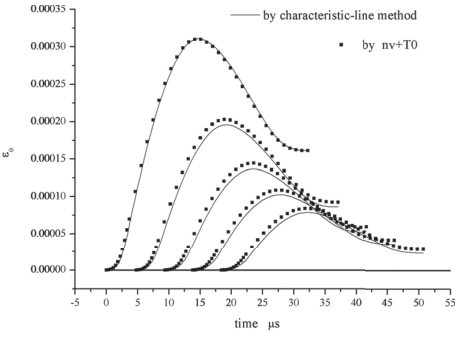


Figure 6d. The 'nV+$T_0$/SW' solution of $\varepsilon_\theta(r_i, t)$ in concrete and its comparison with the characteristics solution.

same figure. Then by using the "nv+T0/SW" method, the radial stress $\sigma_r(r_i, t)$, circumferential stress $\sigma_\theta(r_i, t)$, radial strain $\varepsilon_r(r_i, t)$ and circumferential strain $\varepsilon_\theta(r_i, t)$ at the different Lagrangian positions $r_i$ in concrete specimen are inversely solved, as shown in Figure 6a, Figure 6b, Figure 6c and Figure 6d, respectively.

Note that the same spherical wave experimental record of $v(r_i, t)$ at $r_i = r_0 = 100$ mm was used as the boundary condition for characteristics calculation in "3.2 *Numerical Examples by characteristics method*", the corresponding results calculated (referring to Fig. 4) are now given in the Figure 6 for comparison. It is interesting to find that no marked difference in profile shape exists between the "nv+T0/SW" solutions and the "characteristics solutions". Such satisfactory agreement between those two solutions confirms the following two points, namely (i) the validity of the proposed new method "nv+T0/SW", and (ii) the dynamic behavior of the concrete tested could be described by the ZWT model in high strain rates.

## 5 CONCLUSIONS

From the above results, the following main conclusions can be drawn:

1. A series of particle velocity profiles of spherical waves in concrete specimen are measured by the magneto-electric velocity-meter at the different Lagrangian positions, which not only discover the characters of particle velocity wave in concrete, but also provide a basis for characteristics analyses of spherical wave propagation in concrete (positive problem

solution) and for experimentally study on dynamic behavior of concrete in 3-D stress state and high strain rates (inverse problem solution).

2. Taking one particle velocity profile measured as the boundary condition, and by use of the ZWT nonlinear visco-elastic constitutive model, the different forms of spherical waves in concrete, including the radial stress $\sigma_r(r_i, t)$, circumferential stress $\sigma_\theta(r_i, t)$, radial strain $\varepsilon_r(r_i, t)$ and the circumferential strain $\varepsilon_\theta(r_i, t)$ profiles, are simulated by the characteristics method, showing that the constitutive viscosity effects and nonlinear effects in concrete should not be ignored.
3. Starting from a series of particle velocity profiles measured, a new method of Lagrange inverse analysis of spherical wave named "nv+T0/SW" is proposed. The satisfactory agreement between the "nv+T0/SW solutions" and the "characteristics solutions" confirms the validity of the proposed new "nv+T0/SW" method. This new method may be more suitable for studying the dynamic behavior of heterogeneous materials with large aggregates such as concretes and rocks et al in 3-D stress state, since the characteristic size of specimens in spherical wave experiments could be in the order of meters, at least an order of magnitude larger than the aggregate size of concrete-like materials.

## ACKNOWLEDGEMENTS

The authors acknowledge the financial supports from the National Natural Science Foundation of China (NSFC 11390361, 11172244), and by K.C. Wong Magna Fund in Ningbo University.

## REFERENCES

Cowperthwaite, M., & Williams, R.F. 1971. Determination of constitutive relationships with multiple gauges in non-divergent waves. *Journal of Applied Physics* 42: 456.

Fowles, R., & Williams, R.F. 1970. Plane stress wave propagation in solids. *Journal of Applied Physics.* 41: 360.

Grady, D.E. 1973. Experimental analysis of spherical wave propagation. *J. Geo. Res*. 78: 1299.

Lai, H.W., & Wang, L.L. 2011. Studies on dynamic behavior of Nylon through modified Lagrangian analysis based on particle velocity profiles measurements. *Journal of Experimental Mechanics* 26 (2): 221–226.

Lai, H.W. Wang, Z.J. Yang L.M., & Wang, L.L. 2013. Characteristics analyses of linear visco-elastic spherical waves. *Explosion and Shock Waves* 33(1): 1–10.

Lin, Y.R., Wang, Z.J., Li, Y.L. et al. 2007. Constitutive relation using particle velocity data of spherical waves. *J PLA Univ Sci Tech. 8*: 606–610.

Wang, Zhan-Jiang. Li, Xiao-Lan. Zhang, & Ruo-Qi. et al. 2000. An experimental apparatus for spherical wave propagation in solid. *Explosion and Shock Waves* 20: 103–109.

Wang, L.L., Shi, S.Q., Chen, J.Y., Huang, D.J., Shen, L.J. 2003. Influence of strain-rate and stress-state on dynamic response of cement mortar, *International Journal of Structural Stability and Dynamic* 3(3): 419–433.

Wang, L.L. 2003. Stress wave propagation for nonlinear viscoelastic polymeric materials at high strain rates. *Chinese Journal of Mechanics, Series A* 19 (1): 177–183.

Wang, L.L. 2005. *Foundations of stress waves*, Beijing: National Defense Industry Press.

Wang, L.L., Zhu, J., & Lai, H.W. 2010. Understanding and Interpreting of the Measured Wave Signals in Impact Dynamics Studies. *Chinese Journal of High Pressure Physics* 24 (4): 279–285.

Wang, L.L, Lai, H.W. Wang, Z.J., & Yang L.M. 2013a. Studies on nonlinear visco-elastic spherical waves by characteristics analyses and its application. *International Journal of Impact Engineering* 55: 1–10.

Wang, L.L. Ding, Y.Y., & Yang, L.M. 2013b. Experimental investigation on dynamic constitutive behavior of aluminum foams by new inverse methods from wave propagation measurements. *International Journal of Impact Engineering* 62: 48–59.

Wegner, J.L. 1993. Propagation of waves from a spherical cavity in an unbounded linear viscoelastic solid. *International Journal of Engineering Science* 31: 493–508.

Zukas, J., Nicholas, T., & Swif, H. et al. 1982. *Impact Dynamics*. New York: Wiley-Interscience.

*Rock Dynamics: From Research to Engineering – Li et al. (Eds)*
*© 2016 Taylor & Francis Group, London, ISBN 978-1-138-02953-8*

# Determination of dynamic property of rock joints based on SHPB tests

J.C. Li & H.B. Li
*State Key Laboratory of Geomechanics and Geotechnical Engineering, Institute of Rock and Soil Mechanics, Chinese Academy of Sciences, Wuhan, China*

X. Chen
*School of Civil and Environment Engineering, University of Science and Technology Beijing, Beijing, China*

Y. Zou
*Laboratory of Soil Mechanics, School of Architecture, Civil and Environmental Engineering, École Polytechnique Fédérale de Lausanne (EPFL), Lausanne, Switzerland*

ABSTRACT: The paper gives a briefly introduce about the recently experimental studies for the dynamic property of rock joints based on SHPB tests. The joints include artificial joints filled with sand and clay and artificial non-filled joints cut on granite and aluminum alloy blocks. The experimental method for wave separation is explained for the modified SHPB test with short rock bars. The influence factors on the dynamic property of rock joints are investigated, such as the water content, the thickness of filling layer, the pulse loading intensity, the loading rate, the joint matching coefficient and the spatial geometry of joint surface.

## 1 INTRODUCTION

The mechanical behavior of rock mass is significantly affected by the vastly existing discontinuities, primarily joints. One of the main tasks in the fields of rock mechanics and engineering is to well understand the mechanical properties of the discontinuities and their effects on rock mass behavior. The discontinuities are generally called as joints of rock masses. In nature, there are many kinds of rock joints. As for the filling material, the rock joints are divided into filled joints with filling material or non-filled joint. The physical properties of rock joints affect the normal and shear strength, deformability, permeability, etc. The test results of Pyrak-Nolte et al. (1990) showed that the dynamic stiffness of rock joints was always higher than the quasi-static stiffness, and the dynamic stiffness was related to the stress and saturated conditions.

Among various experimental methods, the Split Hopkinson Pressure Bar (SHPB) tests have been used widely in recent years for its easy operation and practicability. Originally developed by Kolsky (1949), it has become a standard experimental technique nowadays for testing dynamic properties of a variety of engineering materials (Chen et al. 1999). It has also been adopted successfully in rock engineering for rocks (Li et al. 2000, Xia et al. 2007, Zhang & Zhao 2013, 2014a, b) and joints (Li & Ma 2009, Wu et al. 2012, Chen et al. 2015a, b).

Rock joints can be filled with materials, such as sand, silt, breccia, gouge, mylonite and other geomaterials. The static or quasi-static physical properties of some filling materials have been experimentally investigated and it has been found that they affect the stiffness and strength of the filled rock joints (Infanti & Kanji 1978, Singh & Goel 1999, Sinha & Singh 2000). Joints have much lower stiffness and strength when they are filled with soft materials. Li & Ma (2009) carried out the experimental study of stress wave propagation across artificial filled rock joints using modified Split Hopkinson Pressure Bar (SHPB) apparatus,

comprising granite bars, and got the stress-strain relation of the filled joint. The stress-strain relation was then regressed as an exponential form (Li et al. 2010) in which the curve-fitting coefficients reflect the effect of water content and thickness of the filled joint. The dynamic property of filled joints was then described as a three-phase medium model, which showed the interaction among three phases (e.g. air, water and rock solid) under the dynamic condition (Ma et al. 2011). Later, Wu et al. (2012) adopted Split Hopkinson Rock Bars (SHRB) made of norite to study the rate-dependent characteristics of the smooth-contact nonfilled and filled joints.

A commonly accepted joint model in rock mechanics and engineering (Cook 1992) is the Bandis-Barton (B-B) joint model (Bandis et al. 1983), which was originally developed from quasi-static deformation tests for natural non-filled rock joints. The effective contact area, joint roughness, and properties of the asperities and filling materials have been found to influence the normal stiffness of joints (Bandis et al. 1983). Many researchers focused on the roughness of rock joints that affects the mechanical properties of rock masses and wave propagation. It is understood that there are interrelationships between the seismic response of a fracture to the hydraulic and mechanical behavior of the fracture (Pyrak-Nolte 1996). And the fracture specific stiffness is implicitly related to the geometry of the void space and contact area which comprise the fracture (Pyrak-Nolte & Morris 2000). The modeling results of Hopkins (2000) indicated that with small contact areas uniformly distributed across the surfaces, joints could have nearly the same stiffness of a perfectly mated interface. Zhao et al. (2008) studied the quasi-static and dynamic property of artificial joints cast by cement mortar using a static/dynamic uniaxial compression machine (Model RDT-10000) when loading rate changed from $10^{-1}$ MPa/s to $10^{3}$ MPa/s. The test results showed that the nonlinearity of joint deformation arises from the increase of joint contact area incurred due to the closure and damage of the asperities. Recently, Chen et al. (2015) adopted the modified SHPB apparatus including rock bars and specimens to study wave propagation across artificial rock joint and the effect of contact situation of the joint surface. Li et al. (2015) carried out experimental study on the influence of Joint Matching Coefficient (JMC) on the dynamic property of rock joint and wave propagation using conventional SHPB apparatus, where the specimen was composed of a cut rock block and an uncut block.

The aim of the paper is to briefly introduce the recently experimental results for the dynamic property of rock joints based on SHPB tests. The experimental studies were conducted by our research group, including those carried out by Li et al. (2009, 2015), Chen et al. (2015) for filled joints and non-filled joints. The influence factors for the dynamic behaviour of joints are also introduced in the paper.

## 2 FILLED ROCK JOINTS

### 2.1 *Modified test setup*

Two series of SHPB tests using the granitic pressure bars shown in Figures 1(a) to 1(c) were carried out for sand and clay filled layers, respectively, which were the test specimen. The filled layers represent artificial rock joints with a filling material. Each series of test includes 27 groups of tests, that is, the sand and clay layers with thickness of 3 mm, 4 mm and 5 mm were used as the filling of the joint, three different water contents, dry, 5% and 10% were tested for the joint filling layers, and three pulse loadings of different intensities were applied by the swing-angles of 20°, 30° and 40°, which were generated by a pendulum hammer. The sand particle size ranged from 0.25 mm to 0.5 mm and the clay particle size was about 0.0015 mm in average.

The two granite bars having the same diameters of 50 mm, and lengths of 970 mm and 1005 mm were cored from the same rock site, and in the tests, they were used as the incident and transmitter bars. It was closely examined that there were no apparent fractures on the core surface of the two granitic bars. The Young's modulus of the granitic bars was 60 GPa, the density was 2650 kg/m3. The reason to use the granitic pressure bars was to exactly simu-

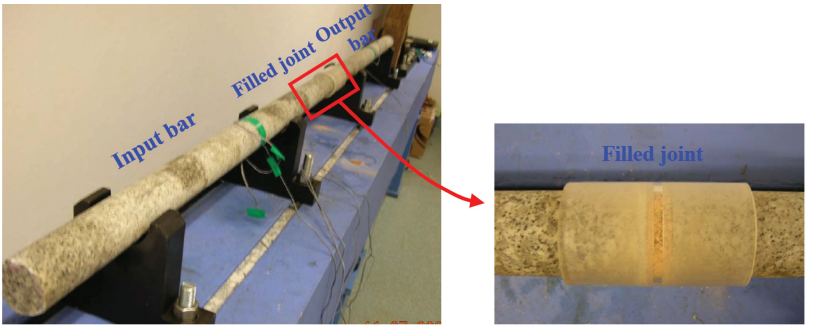


(a) Granite pressure bars (b) A filling layer sandwiched between two bars

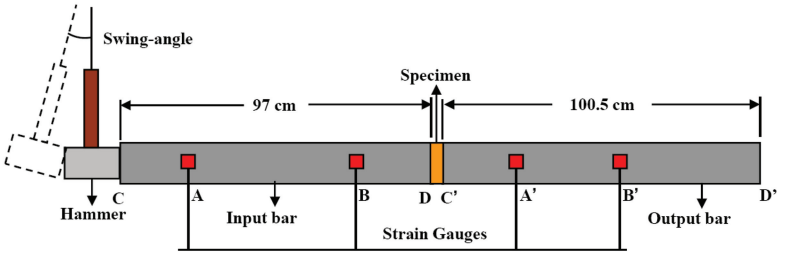


(c) Test setup

Figure 1. Modified SHPB test set-up.

late longitudinal wave propagation in rock media with a filled joint. The sand or clay layer was contained in a plastic tube and sandwiched between the two granitic pressure bars. During the tests, the incident and the transmitter bars had respectively been glued with two strain gauges. The two granitic-bar/sand-layer interfaces were smooth and contacted firmly.

When the swing-angle was 40°, the four strain gauge readings from the tests are illustrated in Figure 2 for the clay layer with 3 mm thickness and 0% water content, respectively. It can be observed from the test data that the incident and reflected waves measured on the incident pressure bar overlapped because of the short length of the granitic bars. Wave separation should be carried out by analyzing the two strain gauges readings on each pressure bar. The reason to cause the wave overlapping is the short of granite bars in the modified SHPB test.

### 2.2 *Data processing method*

During the SHPB tests, the measuring technique using pressure bars are based on the two elementary waves propagating in opposite directions. The conventional SHPB technique uses long steel bars and a short loading pulse so that the incident wave and the reflected wave in the incident bar can be separated. Since the rock bars are short, the strain gauge readings on the incident and transmitter bars are the overlap of two elementary waves propagation in two opposite directions. Zhao & Gary (1997) and Benatar et al. (2003) studied the materials behavior of the PMMA bars under dynamic loads using two-point strain-gauge wave separation method. Based on this wave separation method, the incident, reflected and transmitted waves were separated and obtained to analyze wave propagation across an artificial rock joint (Li & Ma 2009).

If we define the wave propagation time intervals from the beginning point C of input bar to the gauge A, from the gauge A to the gauge B, and from the gauge B to the end point D of input bar are denoted as $t_A$, $t_0$ and $t_B$, respectively, the two opposite strain waves can be separated and expressed as

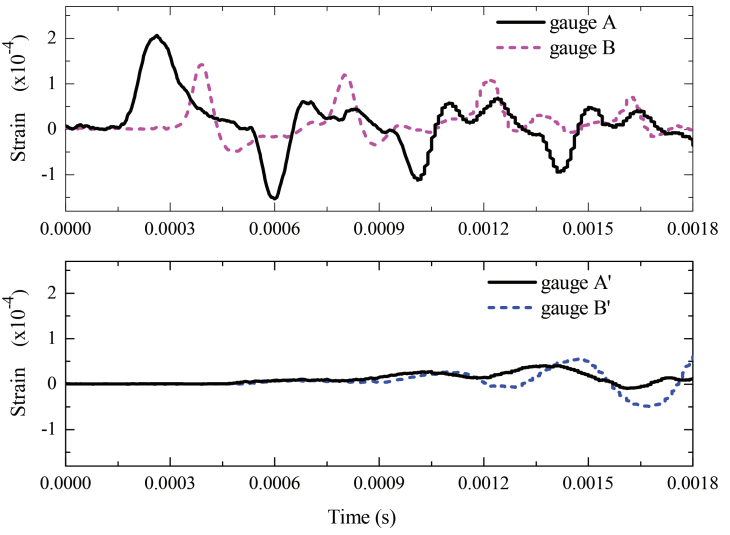


Figure 2. Strain gauge readings on the incident and transmitter bars for clay filled joint (3 mm-width, dry joint, swing-angle = 40°).

$$\begin{cases} \varepsilon_{AP}(x_A,t) = [\varepsilon_A(t) - \varepsilon_{BN}(x_B,t-t_0)] \cdot H_1(t-t_1) \\ \varepsilon_{BP}(x_B,t) = \varepsilon_{AP}(x_A,t-t_0)] \cdot H_2(t-t_2) \\ \varepsilon_{BN}(x_B,t) = [\varepsilon_B(x_B,t) - \varepsilon_{BP}(x_B,t)] \cdot H_3(t-t_3) \\ \varepsilon_{BN}(x_A,t) = \varepsilon_{BN}(x_B,t-t_0)] \cdot H_4(t-t_4) \end{cases} \tag{1}$$

where $H_i(t)$ is the Heaviside function; $\varepsilon_A$ and $\varepsilon_B$ are the test recordings on the strain gauges A and B, respectively; $\varepsilon_{AP}$ and $\varepsilon_{AN}$ are the positive and negative strain waves across the gauge A, respectively; $\varepsilon_{BP}$ and $\varepsilon_{BN}$ are the positive and negative strain waves across the gauge B, respectively; and $t_1 = t_A$, $t_2 = t_A + t_0$, $t_3 = t_A + t_0 + 2t_B$, $t_4 = t_A + 2t_0 + 2t_B$, $\varepsilon_{RN}(x_B, t - t_0) = 0$ when $t < t_4$.

For an arbitrary point on the bar, the two opposite strain waves can be obtained by time shifting the positive and negative waves at gauge A or B, that is

$$\varepsilon_p(x,t) = \varepsilon_{Ap}(x_A, t - \frac{x - x_A}{c}),\ \varepsilon_N(x,t) = \varepsilon_{AN}(x_A, t - \frac{x_A - x}{c}) \tag{2}$$

Hence, the strain is the sum of these two opposite waves and the particle velocity of this point is proportional to the difference of the two opposite waves. According to the fundamental theory of SHPB test, the pressure $\sigma$, strain rate $\dot{\varepsilon}$ and strain $\varepsilon$ of the joint layer can be expressed as

$$\sigma = \frac{E}{2}\left[(\varepsilon_{IP} + \varepsilon_{IN}) + (\varepsilon_{TP} + \varepsilon_{TN})\right] \tag{3}$$

$$\dot{\varepsilon} = \frac{c}{L}\left[(\varepsilon_{IP} - \varepsilon_{IN}) - (\varepsilon_{TP} - \varepsilon_{TN})\right] \tag{4}$$

$$\varepsilon = \frac{c}{L}\int_0^t \left[(\varepsilon_{IP} - \varepsilon_{IN}) - (\varepsilon_{TP} - \varepsilon_{TN})\right] dt \tag{5}$$

where $\varepsilon_{IP}$ and $\varepsilon_{IN}$, $\varepsilon_{TP}$ and $\varepsilon_{TN}$ are the two opposite strain waves at the down-stream end D of the incident bar and the up-stream end C' of the transmitter bar in Figure 2 which are also the incident-bar/joint and transmitter-bar/joint interfaces; $E$ and $L$ are the Young's modulus

of the rock bar; $c$ is the wave propagation velocity in the rock bars; and $L$ is the thickness of the filled layer, or the filled joint. The dynamic behavior of a filled joint can then be obtained from Equations (3) and (5).

### 2.3 *Test results and discussions*

When the readings of the four strain gauges were recorded during the modified SHPB tests, such as Figures 2 for some particular cases, Equation (1) was used to do wave separation for the four strain wave readings. The positive and negative waves along the incident and transmitter bars could be obtained. For an arbitrary point at the pressure bars, the two opposite strain waves could be calculated from the time shifting Equation (2). The sum of the two opposite strain waves which presented the strain of the point could thus be determined. Then the incident, reflected and transmitted strain waves were obtained.

For the 27 groups (i.e. three thick joints with three water contents applied by three pulse loads) of modified SHPB tests for clay fillings, the incident, reflected and transmitted strain waves were obtained from the test-setup and wave separation method. Similarly, other 27 groups of modified SHPB tests were also conducted for clay filings to get the incident, reflected and transmitted waves.

Considering the displacement of the joint, or $\Delta L = \varepsilon L$, the pressure on the filling material and closure of the filled layer can be derived from Equations (3) to (5). The strain rates of such drop hammer tests were in a medium range from $10^0$ to $10^2$. The relations between the pressure and closure are illustrated in Figures 3 and 4 for sand and clay filled layers with thickness of 3 and 4 mm and water content 0 and 5%, where the filling material with water content 0% means the dry filling material. Comparison between Figures 3 and 4 shows that the kind of filling material influences the dynamic behavior of joints. For example, when the filled joint is dry and 3 mm thick, a normal stress of 2 MPa will produce the closure of 0.15 mm for the sand filled joint while 0.38 mm for the clay filled joint. It indicates that the clay filling layer deform more easily than the sand filling layer when the layer thickness, water content and applied normal stress are the same for two kinds of layers. From Figure 3 or 4, we also find that the filling layer thickness and water content affect its dynamic response. When the layer thickness becomes greater, e.g., from 3 mm to 4 mm, the corresponding closure of the layer turns to more obvious for a given stress on the joint. The filled joint with

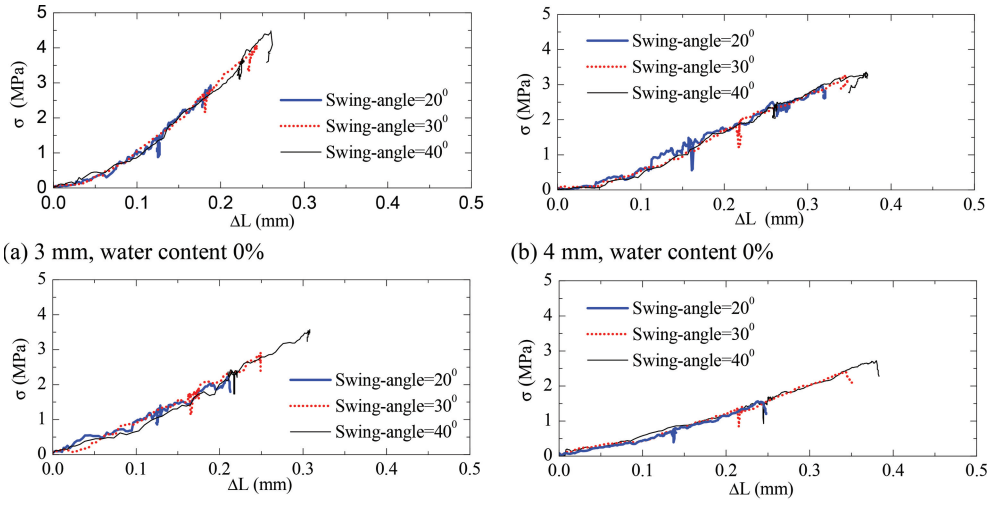


Figure 3. Closure-pressure relations for the sand filled layers.

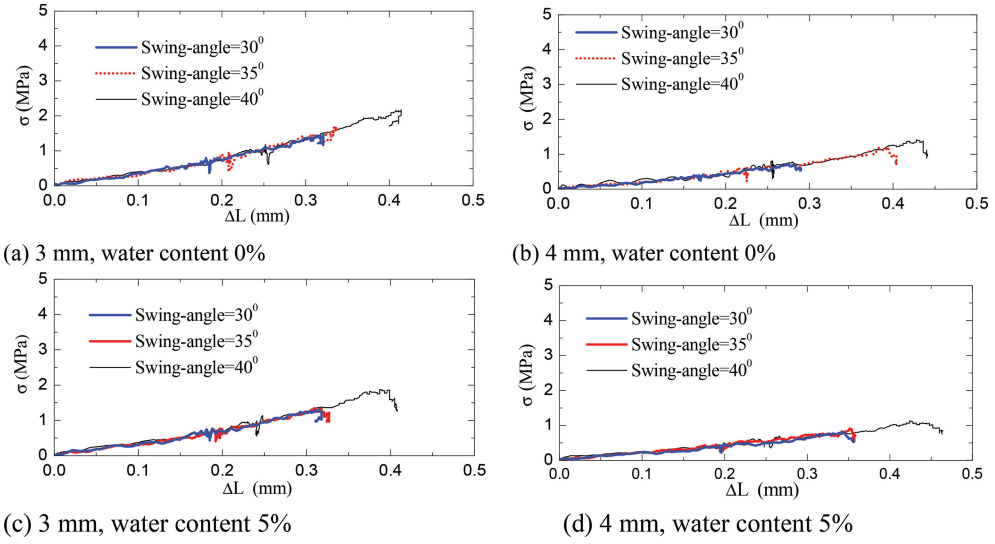


Figure 4. Closure-pressure relations for the clay filled layers.

3 mm in thickness and 0% in water content appears stiffer than the other three filled joints when the layer thickness changes from 3 to 4 mm and the water content varies from 0% to 5%. In addition, it can be observed from the figure that the closure-pressure relation is nonlinear, and closure increases with the increase of the pressure for both filling materials. In the tests, the loading intensity produced by the hammer was controlled by the swing-angle. It is noted that a larger closure can be obtained when the load intensity generated by the hammer is higher. The stress-closure relations for different swing-angle have the similar tendency for a filling layer the same water content and layer thickness. This indicates that the dynamic stress-closure relation is less sensitive to the input intensity.

For filled rock joints, a three-phase medium model (Ma et al. 2010) was proposed, where the parameters of the model were determined from the modified SHPB test results. The closure-pressure relation for filled layers described the loading path of the three-phase medium model, which shows highly nonlinear.

The rate-dependency characteristics of filled joints was studied by Wu et al. (2012) by carrying out modified SHPB tests on non-filled smooth-contact and filled rock joints at three low loading rates of approximately 30, 60 and 80 GPa/s. The incident and transmitted bars of the modified SHPB apparatus adopted by Wu et al. (2012) were made of rocks with length of 1,500 m and square cross section of $40 \times 40$ mm. the filling material was dry quartz sands with particle size of 1 to 2 mm. The test results show that the non-filled smooth-contact joint displays stress equilibrium, while the filled joint exhibits stress discontinuity. The stiffness of both non-filled and filled joints increase with the higher loading rate, and decreases with the increase of filled joint thickness for a given loading rate. Filled joints show lower strength and larger deformation than the non-filled smooth-contact joint.

## 3 NON-FILLED ROCK JOINTS WITH ROUGH SURFACE

### 3.1 *Test setup*

Here, we first carried out the traditional SHPB test to study the dynamic stress-closure of rock joint with rough surface, as shown in Figure 5. The SHPB apparatus is made up of a striking system, input and output steel bars, a momentum trap bar and a data acquisition system. The input and output bars have the same geometry, that is, the diameter and length

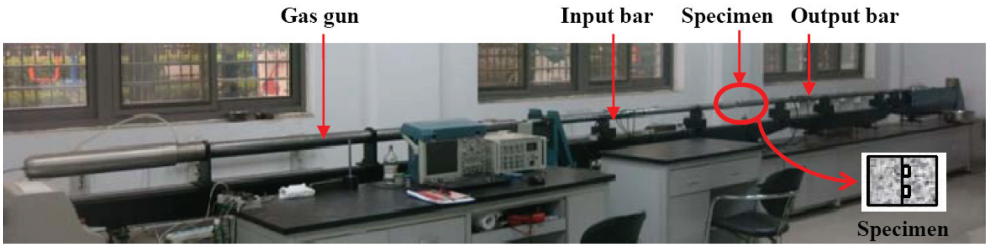


Figure 5. Test setup for non-filled joints with rough surface.

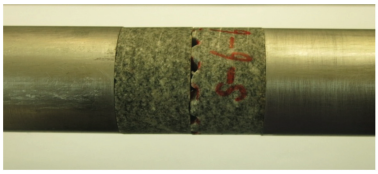

(a) Specimen during the test

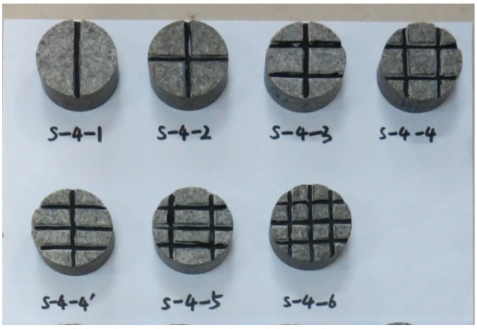


(b) Cut blocks with notch width of 4 mm

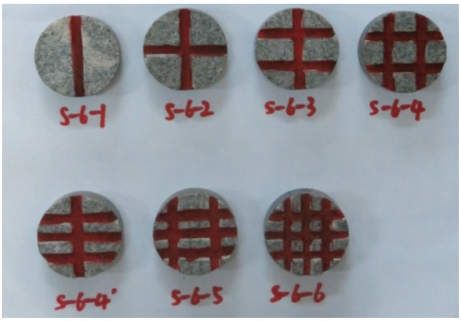


(c) Cut blocks with notch width of 6 mm

Figure 6. Specimens for the SHPB test of non-filled joints.

are 50 mm and 2500 mm, respectively. The gas gun was adopted to produce a high speed steel striker impinging on the input bar. The mechanical parameters of the bars and striker were: Young's modulus $E$ is 210 GPa, the density $\rho$ is 7800 kg/m$^3$ and wave propagation velocity $c$ is 5124 m/s.

The specimen was made of granite with density 2630 kg/m$^3$, the Young's modulus 30 GPa and Poisson ratio 0.30. Each test specimen was composed of two granite cylindrical blocks with diameter of 50 mm and thickness of 25 mm, as shown in Figure 6(a). One block had two smooth-flat end surfaces and was called un-cut block, while the other block had one smooth-flat and one rough surfaces, as shown in Figure 6(b) and was called cut block. The rough surface of the cut block was generated with a number of notches. The notches were 3 mm dept and 4 and 6 mm wide, respectively. The rough contact of the two blocks gave rise to the artificial joint, as shown in Figure 6(a). The total length of each specimen is 50 mm.

The contact area of two blocks equals to the minus of the cross section area of un-cut blocks and the notch area of the cut blocks. We define the ratio of contact area to the cross section of un-cut blocks as the contact area ratio, which can be denoted as the Joint Matching Coefficient (JMC) according to the definition by Zhao (1997). The JMC of each cut blocks shown in Figure 6(b) is shown in Table 1.

Table 1. The matching coefficient of an artificial joint (JMCs).

| Cut blocks | S-4-1 | S-4-2 | S-4-3 | S-4-4' | S-4-4 | S-4-5 | S-4-6 |
|---|---|---|---|---|---|---|---|
| JMC | 0.90 | 0.80 | 0.70 | 0.66 | 0.64 | 0.60 | 0.52 |
| Cut blocks | S-6-1 | S-6-2 | S-6-3 | S-6-4' | S-6-4 | S-6-5 | S-6-6 |
| JMC | 0.85 | 0.71 | 0.60 | 0.51 | 0.48 | 0.42 | 0.32 |

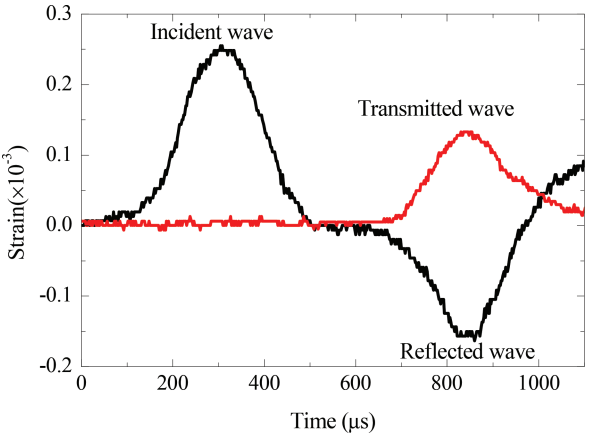


Figure 7. A typical record for a specimen with JMC 0.52 and notch width of 4 mm.

### 3.2 *Data processing method*

From the test recordings of two strain gauges on the input and output bars, such as one typical recordings shown in Figure 7, the normal stress and strain of the specimen can be calculated from Equations. (3) to (5), that is,

$$\sigma = \frac{E}{2}(\varepsilon_{IP} + \varepsilon_{IN} + \varepsilon_{TP}) \tag{6}$$

$$\varepsilon = \frac{c}{L}\int_0^t (\varepsilon_{IP} - \varepsilon_{IN} - \varepsilon_{TP})dt \tag{7}$$

where $\varepsilon_{\mathrm{IP}}$ is the incident strain wave, $\varepsilon_{IN}$ is the reflected strain wave, $\varepsilon_{TP}$ is the transmitted wave, and there is no $\varepsilon_{TN}$.

The SHPB test is regarded as one-dimensional wave propagation problem. The deformation of each specimen is the sum of the deformations of the artificial joint and the adjacent blocks. Therefore, from Hook's law, the closure of the joint is expressed as

$$\Delta \mathrm{L} = \varepsilon L - \sigma(\mathrm{L} - l)/E_{\mathrm{r}} \tag{8}$$

where $l$ denotes the joint thickness and equals to 3 mm and $E_{\mathrm{r}}$ denotes the Young's modulus of intact rock and equals to 30 GPa. The length of the specimen L equals to 5 cm.

### 3.3 *Test results and discussions*

In the traditional SHPB test, the two elementary waves propagating in two opposite directions did not overlap, as shown in Figure 7. Hence, the incident and reflected strain waves in the input bar and the transmitted strain wave in the output bar are the records of strain

gauges mounting on the two bars. From Equations (6) and (7), the time history of stress on one specimen composed of two contacted blocks and the strain of the specimen can be obtained, so to get the relation between stress and strain of the specimen.

When Equation (8) is considered, the relation between the normal stress and closure of artificial joints can be analyzed. Figures 8(a) and 8(b) show the stress-closure relation of the artificial joint with different JMCs or contact area ratios when the notch widths are 4 and 6 mm, respectively. We can see from Figure 8 that the loading path of joint with greater value of JMC is almost linear, while the loading path of joint with lower value of JMC appears nonlinear property. Meanwhile, Figure 8 shows that a higher normal stress on the joint generally causes a bigger joint closure during loading path. Generally, the non-filled joint with a higher JMC has a greater deformation than the joint with a lower JMC when the noth width and the stress on the joint are given. For example, when the stress on the joint with notch width of 4 mm is 20 MPa, the closure for the joint with JMC 0.5 is around 0.04 mm but the closure for the joint with JMC 0.66 is around 0.85 mm. Although the joint with higher JMC shows stiffer than the joint with lower JMC, the maximum value of closure of the former is smaller than the latter.

We define the specific normal stiffness is the ratio of pressure at the half value of normal stress to the closure. Figure 9 shows the specific normal stiffness of joints when JMC varies from 0.52 to 0.90 for 4 mm notch width and from 0.32 to 0.71 for 5 mm notch width. The fitting curves are also drawn in the figure. The fitting curves indicate that the joint specific

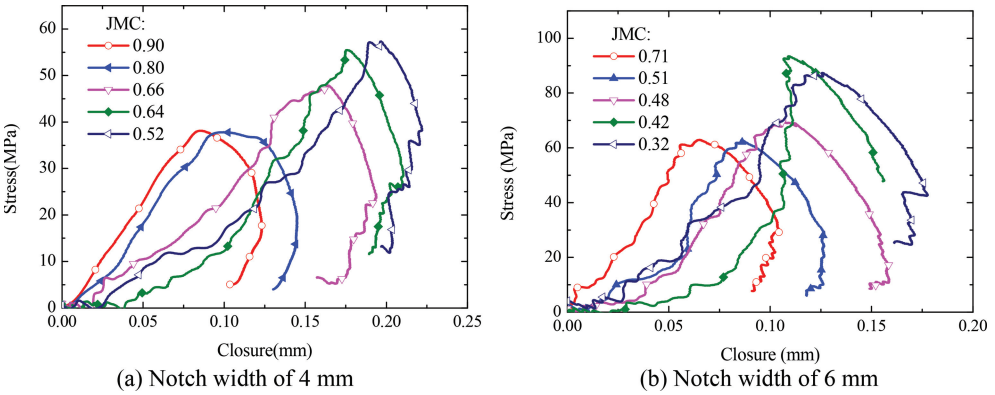


Figure 8. Stress-closure relation of artificial joints with different JMCs.

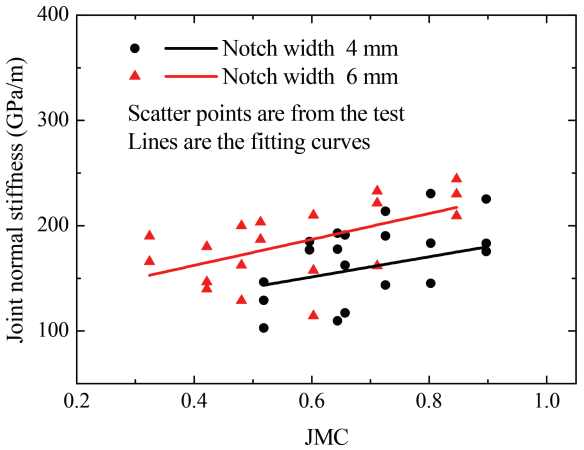


Figure 9. The specific stiffness of joints with different JMCs.

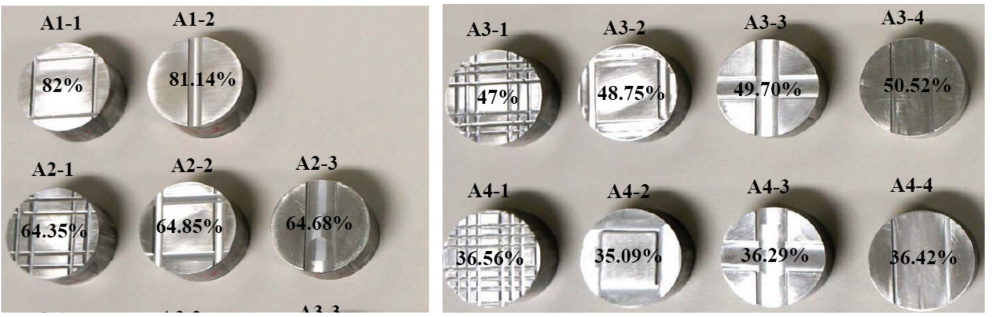


Figure 10. Aluminum specimen with cut end surface.

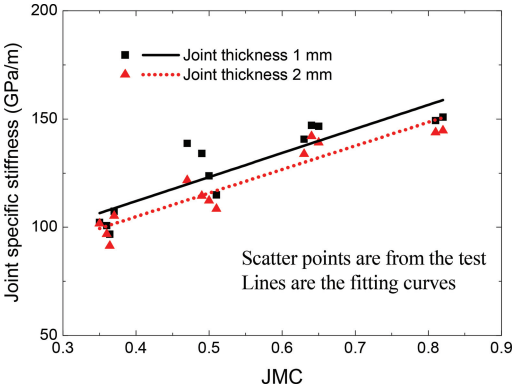


Figure 11. Joint specific stiffness for joint width 1 and 2 mm.

stiffness generally increases with the increase of JMC when the notch width of joint rough surface is given. By comparison, we find that for a given JMC the joint with notch width of 6 mm become stiffer than the joint with notch width of 4 mm. This indicates that the spatial geometry of the contact surface of joints influences the joint stiffness. We then carried out the further study to analyze the effect of spatial geometry on the dynamic property of joints.

### 3.4 *Effect of spatial geometry*

In order to study the effect of spatial geometry of contact area on rock joint specific stiffness, a series of modified SHPB test were carried out by Chen et al. (2015) based on her previous research (Chen et al. 2015). In the modified SHPB test, the SHPB apparatus included a striker, input and out bars and specimen. The striker, input and out bars and specimen were cylindrical and had the same cross section with diameter of 40 mm, but different lengths, i.e. 50, 1200, 1200 and 20 mm, respectively. All the bars and specimen were made of the same kind of aluminum alloy. The metal was chose for specimen is for easy cutting on the surface to generate rough contact. The density of the aluminum alloy is 2700 kg/m$^3$, and the Young's modulus is 70 GPa.

Each specimen include two end surfaces: one is smooth and flat and another is cut with a number of crossed distributed notches sawn to form an artificial joint, as shown in Figure 10. The joint width is denoted as the notch depth and the contact area ratio or JMC is calculated from the notch width.

According to the basic theory of SHPB test and Hook's law, the normal stress and the closure of the artificial joint was obtained from test recording. Figure 11 shows the relation between the joint specific stiffness and the joint contact ratio when the notch depths or joint thicknesses are 1 and 2 mm. By comparison, the joint specific stiffness for joint thickness

1 mm is stiffer than the joint with thickness of 2 mm. In general, the joint specific stiffness becomes greater with increasing joint contact area ratio or JMC. Meanwhile, the joint specific stiffness are different for the specimens having nearly same contact area ratio (e.g. A3–1, A3–2, A3–3 and A3–4 with contact area ratio of 47%, 18.75%, 49.7% and 50.52%, respectively). The similarly phenomena can also be found for the joint stiffness of specimens A4–1, A4–2, A4–3 and A4–4. This indicates from another way that the spatial geometry of the joint surface (e.g. the distributions of notches) affects the dynamic property of rock joints.

## 4 CONCLUDING REMARKS

The above review briefly introduces the recent experimental studies for dynamic property of joints based on SHPB test. From modified SHPB test using granite input and output bars, the dynamic property of filled joints is affected by the type of filling materials, the water content and joint thickness. Additionally, the pulse loading intensity is not sensitive to the tendency of the stress-closure relation of filled joints, while the stiffness of filled joints increases with the higher loading rate. A series of SHPB tests show that the JMC (equals to the contact area ratio) and the thickness of joints as well as the spatial geometry of joints are the influence factors of the dynamic property of non-filled joints. The nonlinear behaviour of a non-filled joint is related to the more contact area or more deformation of asperities during loading.

It should be noticed that the present SHPB tests are only for artificial rock joints. When the test method is improved with some advanced techniques, our further study will be conducted for natural joints and the Joint Roughness Coefficient (JRC) will be considered.

In addition to the SHPB tests to determine the dynamic properties of rock joints, tests using plate test platform (Wu, 2015) are also being conducted in collaboration with the research groups at Australian Monash University and Swiss Federal Institute of Technology in Lausanne. In the plate tests, rock joints are represented by a variety if typical profiles to represent different roughness and matching. Plane wave or cylindrical wave is applied to the tests to study the transmission and reflection of wave at the joint. The length of joint can be up to 1 m and will provide good representation of real joint scale.

## ACKNOWLEDGEMENTS

This work is supported by the Chinese National Science Research Fund (Grant Nos. 41272348, 41525009). We also thank the research groups of Professor Jian Zhao (Monash, EPFL and NTU) and of Professor Guowei Ma (NTU) for the support and collaboration on this research topic.

## REFERENCES

Bandis, S.C., Lumsden, A.C. & Barton, N.R. 1983. Fundamentals of rock fracture deformation. *Int. J. Rock Mech. Min. Sci. Geomech. Abstr.* 20(6): 249–268.

Benatar, A., Rittel, D. & Yarin, A.L., 2003. Theoretical and experimental analysis of longitudinal wave propagation in cylindrical viscoelastic rods. *J. Mech. Phys. Solids.* 51: 1413–1431.

Chen, X., Li, J.C., Cai, M.F., Wu, W., Zou, Y. & Zhao, J. 2015. Experimental study on wave propagation across a rock joint with rough surface. *Rock Mech. Rock Eng.* 48: 2225–2234.

Chen, X., Li, J.C., Cai, M.F., Zou, Y., Zhao, J. 2015. A further study on wave propagation across a single joint with different roughness. *Rock Mech. Rock Eng.* (Accepted).

Chen, W., Zhang, B. & Forrestal, M.J. 1999. A split Hopkinson bar technique for low-impedance materials. *Exp. Mech. 3*9(2): 81–85.

Cook, N.G.W. 1992. Natural joint in rock: mechanical, hydraulic and seismic behaviour and properties under normal stress, Jaeger Memorial Dedication Lecture. *Int. J. Rock Mech. Min. Sci. Geomech. Abstr.* 29(3): 198–223.

Infanti, N. & Kanji, M.A. 1978. In situ shear strength, normal and shear stiffness dfetermainations at Agua Vermelha Project. In *Proceedings of the 3rd International Congress of IAEG*, Madrid, 2, 175–183.

Kolsky, H. 1949. An investigation of the mechanical properties of materials at very high rates of loading. *Proc. Phys. Soc. B.* 62: 676–700.

Li, J.C. & Ma, G.W. 2009. Experimental study of stress wave propagation across a filled rock joint. *Int. J. Rock Mech. Min. Sci.* 46(3): 471–478.

Li, J.C., Ma, G.W. & Huang, X., 2010. Analysis of Wave Propagation through Filled Rock Joint. *Rock Mech. Rock Eng.* 43(6): 789–798.

Li, J.C., Li, N.N., Chai, S.B., Li, H.B. & Zhao, X.B. 2015. SHPB test study on wave propagation across rock masses with different joint matching coefficients. (Submitted).

Li, X.B., Lok, T.S. & Zhao, J. 2000. Oscillation elimination in the Hopkinson bar apparatus and resutant complete dynamic stress strain curves for rocks. *Int. J. Rock Mech. Min. Sci.* 37(7): 1055–1060.

Ma, G.W., Li, J.C. & Zhao, J. 2011. Three-phase medium model for filled rock joint and interaction with stress waves. *Int. J. Numer. Anal. Methods Geomech. 3*5(1): 97–110.

Pyrak-Nolte, L.J., Myer, L.R. & Cook, N.G.W. 1990. Transmission of seismic waves across single natural fractures. *J Geophys Res*. 95(B6): 8617–38.

Pyrak-Nolte, L.J. & Morris, J.P. 2000. Single fractures under normal stress: the relation between fracture specific stiffness and fluid flow. *Int. J. Rock Mech. Min. Sci.* 37(18): 245–262.

Pyrak-Nolte, L.J., 1996. The seismic response of fractures and the interrelations among fracture properties. *Int. J. Rock Mech. Min. Sci. Geomech. Abstr.* 33(8): 787–802.

Singh, B. & Goel, R.K. 1999. *Rock Mass Classification: a Practical Approach in Civil Engineering.* Elsevier: Oxford, 1999.

Sinha, U.N. & Singh, B. 2000. Testing of rock joints filled with gouge using a triaxial apparatus. *Int. J. Rock Mech. Min. Sci.* 37: 963–981.

Wu, W., Li, J.C. & Zhao, J. 2012. Loading Rate Dependency of Dynamic Responses of Rock Joints at Low Loading Rate. *Rock Mech. Rock Eng.* 45(3): 421–426.

Wu, W. 2015. Slip initiation of granular gouge friction in a rock discontinuity induced by static and dynamic loads. *Int. J. Rock Mech. Min. Sci.* 80: 196–201.

Xia K., Nasseri M.H.B. & Mohanty B. 2008. Effects of microstructures on dynamic compression of Barre granite. *Int. J. Rock Mech. Min. Sci.* 45(6): 879–887.

Zhang Q.B. & Zhao, J. 2013. A review of dynamic experimental techniques and mechanical behaviour of rock materials. *Rock Mech. Rock Eng.* 47(4): 1411–1478.

Zhang, Q.B. & Zhao, J. 2014a. Quasi-static and dynamic fracture behaviour of rock materials: phenomena and mechanisms. *International Journal of Fracture* 189(1): 1–32.

Zhang Q.B. & Zhao, J. 2014b. Determination of mechanical properties and full-field strain measurements of rock material under dynamic loads. *Int. J. Rock Mech. Min. Sci.* 60: 423–439.

Zhao, J., Cai, J.G., Zhao, X.B. & Li, H.B. 2008. Dynamic model of fracture normal behavior and application to prediction of stress wave attenuation across fractures. *Rock Mech. Rock Eng.* 41(5): 671–93.

Zhao, J. 1997. Joint surface matching and shear strength part A: joint matching coefficient (JMC). *Int. J. Rock Mech. Min. Sci.* 34(2): 173–178.

Zhao, H. & Gary, G. 1997. A new method for the separation of waves: application to the SHPB technique for an unlimited duration of measurement. *J. Mech. Phys. Solids* 45(8): 1185–1202.

*Rock Dynamics: From Research to Engineering – Li et al. (Eds)*
*© 2016 Taylor & Francis Group, London, ISBN 978-1-138-02953-8*

# Fracture specific stiffness as the critical link among fracture properties

L.J. Pyrak-Nolte
*Purdue University, Indiana, USA*

ABSTRACT: Fractures with weakly and strongly correlated aperture distributions were used to explore a fundamental scaling relationship between fracture stiffness and fluid flow in a fracture. Computational models were used to analyze fluid flow through a fracture undergoing deformation and chemical alteration. Fracture stiffness captures the deformation of the fracture void geometry and enables collapse of the numerical flow-stiffness data, from multiple length scales, to a single scaling function. Simulations of wave propagation across fractures with varying contact area but with fixed asperity spacing show that elastic wave transmission is also sensitive to the fracture geometry. The hydro-mechanical scaling relationship provides a path forward for the remote characterization of fluid flow through fractured rock.

## 1 INTRODUCTION

Long term safety and optimization of subsurface engineering activities require geophysical monitoring methods that can delineate and characterize evolving fractures and fracture systems. Fractures and other discontinuities pose serious challenges for seismic detection because such mechanical discontinuities span many orders of magnitude in size, are structurally complex and are subjected to complicated mechanical, hydraulic and geochemical processes that alter fractures over time. Thus, both the interrelationship among fracture properties (Fig. 1) and the scaling behavior of these relationships are needed for the optimal design of geophysical monitoring systems and for simulations used to interpret geophysical data to predict subsurface performance.

The interrelationship among the hydraulic, mechanical and seismic properties of fractures requires a basic understanding of fractures from a hydrologic, geomechanics and geophysics

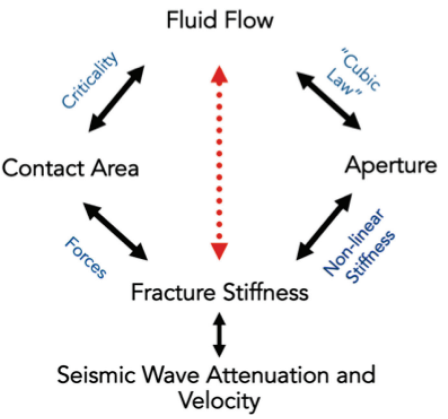


Figure 1. Interrelationships among fracture properties.

viewpoint. Fluid flow through fractures and fracture systems depend on length scales associated with the size and spatial distribution of the connected apertures (that depend on stress) within a fracture (Fig. 1). The size of the apertures controls the volumetric flow rate while the spatial distribution of apertures affects the connectivity of the flow paths. Fracture deformation is controlled by length scales associated with the size and spatial distribution of contacts between the two surfaces of a fracture and depends on the loading condition. Contact area supports the stresses imposed on the fracture and the aperture distribution affects the nonlinearity of the deformation-stress relationship (Hopkins 1990). Thus fluid flow and fracture deformation are implicitly related through the geometry of the fracture.

Fracture specific stiffness, also known as unit joint stiffness, was introduced by Goodman et al. (1968) to describe the behavior of a fracture because it could be measured in the laboratory without detailed analysis of the fracture geometry. For a single macroscopic fracture, fracture specific stiffness or fracture compliance captures the complexity of aperture and contact area distributions. Kendall & Tabor (1971) showed experimentally and Hopkins et al. (1987, 1990) have shown numerically that interfaces with the same amount of contact area but different spatial distributions of the contact area have different stiffnesses. Greater separation between points of contacts results in a more compliant fracture, i.e. details of the micro-mechanical heterogeneity control the deformation properties of a fracture.

Recently, Petrovitch et al. (2013, 2014) demonstrated numerically that fracture specific stiffness is an effective parameter that captures the deformed topology of a fracture and can be used as the basis of a scaling relationship for fluid flow through fractures. While this relationship holds for random distributions of weakly correlated apertures, it remained an open question whether this relationship would apply to spatially correlated aperture distributions or to fractures with preferential erosion that results in channelized flow. This paper presents a review of recent work (Pyrak-Nolte & Nolte 2016) that developed an extended scaling relationship that accounts for spatial correlations in fracture aperture distributions and also captures the behavior of channelized flow within a fracture. In addition, the sensitivity of seismic wave propagation to the fracture geometry for several idealized cases is demonstrated. Fracture specific stiffness is the link among the seismic, hydraulic and mechanical properties of a fracture. The scaling relationships of Pyrak-Nolte & Nolte (2016) provide a guide for incorporating the appropriate fracture behavior into continuum models of the subsurface where stresses vary with depth. The link between stiffness and seismic wave attenuation/velocity provides a fundamental basis for achieving the ultimate goal of remotely monitoring fluid flow or relative fluid flow among fractures in the subsurface.

## 2 FLUID FLOW—FRACTURE SPECIFIC RELATIONSHIP

### 2.1 *Numerical approach*

Recently, Pyrak-Nolte & Nolte (2016) demonstrated a scaling relationship between fluid flow and fracture specific stiffness for fractures with apertures with different spatial correlations and for fractures with highly channelized flow paths. The investigation of the scaling properties of the flow-stiffness relationship for single fractures required models to simulate fracture geometry, fracture deformation and fluid flow through a fracture. Multiple realizations of fracture void geometry with distinctly different spatial distributions of fracture apertures and contact area were used to determine the relationship between flow and stiffness as a function of scale. A stratified continuum percolation method (Nolte & Pyrak-Nolte 1991) was used to generate the void geometry of a fracture (i.e. the contact area and variable-apertures voids) without the need to generate two independent rough surfaces. The stratified continuum percolation method constructs a two-dimensional hierarchical aperture distribution with a tunable spatial correlation. Figure 2 shows examples of a subset of the fracture geometries used in the analysis by Pyrak-Nolte & Nolte (2016). A random aperture distribution (1T) and a spatially correlated aperture distribution (5T) are shown in Figures 2a and 2b. The aperture distributions shown in Figures 2c & 2d are based on a 5T pattern that was subjected to

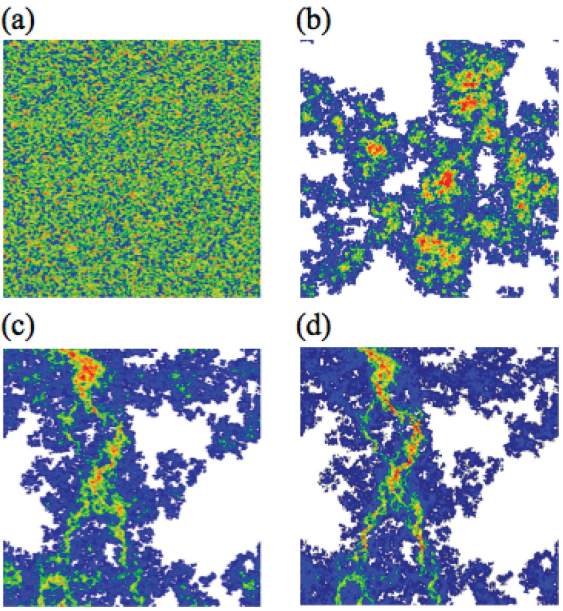


Figure 2. Examples of fracture aperture distributions for conditions of (a) 1T spatially uncorrelated, (b) 5T spatially correlated, (c) 5TX25 chemically-eroded spatially correlated, and (d) 5TX100 chemically-eroded spatially correlated. White regions represent contact area. Aperture increases from dark blue to green to yellow to red.

chemical erosion. Chemical erosion was assumed to be transport dominated such that the amount of erosion was taken to be proportional to the flux through a given aperture. As the proportionality factor increased, the flow paths through the fracture became channelized (Fig. 2d).

For each fracture type, 100 realizations were generated at the $512 \times 512$ fracture array scale. Fluid flow through, and deformation of, a fracture were studied on five lengths scales; i.e. from the entire $512 \times 512$ fracture array down to $32 \times 32$ subsection arrays of the fracture (or scales from 1, ½, ¼, 1/8, 1/16). For the scales of 1, ½, ¼, 1/8, and 1/16, the number of patterns studied were 100, 200, 400, 800 and 1600, respectively. More patterns were studied at the small scales because of the local fluctuations in fracture geometry.

Fracture stiffness was calculated by modeling the deformation of asperities and a deformable half space. Fractures were deformed numerically under a normal load using a method similar to Hopkins (1990). Prior to Hopkins, most approaches for deforming a fracture assumed a uniform deformation for the solid matrix material or allowed interpenetration of the asperities. Unlike those approaches, Hopkins' model includes short and long-range interactions among the asperities and the related deformation of the solid matrix. The model used by Petrovitch et al. (2013, 2014) was used to compute the displacement-stress curves for a given fracture, from which the stiffness was extracted.

Finally, fluid flow through the deformed fractures was simulated using a network model similar to that of Cheng et al. (2004) in which the aperture distribution is replaced by a network of elliptical pipes that are connected from the inlet to the outlet. The elliptical pipe approach for fluid flow through a fracture was also shown to model 2D micro-model experimental data more accurately (Cheng et al. 2004) than a lattice grid approach, which over estimated the flow data by 30–50%. The output from the code for each fracture array contains the flow as a function of stress. For additional information on the numerical codes used in this study, the reader is referred to Petrovitch (2013), Petrovitch et al. (2013, 2014) and Pyrak-Nolte & Nolte (2016).

## 2.2 *Extended scaling relationship*

Figure 3 (*left*) shows the average flow as a function of average fracture specific stiffness based on multiple realizations of the aperture distributions 1T, 5T, 5TX25 and 5TX100 (Fig. 2) with fracture lengths ranging from 0.0625 to 1 meter. The simulation data illustrate that the hydraulic and mechanical response of a fracture depends on fracture length, aperture distribution, void volume, and contact area. For all aperture simulations, a strong scale dependence is observed in the flow-stiffness relationship with large fractures supporting the least amount of flow (Fig. 3 *left*) for given type of aperture distribution. Also, flow depends strongly on the spatial correlation in the fracture aperture. The 1T and 5T aperture distributions (Fig. 2 a & b) have similar void volumes but the spatial correlations affect the amount of contact area (and in turn the connectivity of flow paths), the mean aperture and the critical neck (smallest aperture on the dominant flow path or path of largest apertures). The average mean aperture for the 5T distributions was 36% larger than that for the 1T realizations. However, the average critical neck of the 5T patterns was smaller by 28% compared to that for 1T fractures.

Preferential erosion of the flow paths resulted in enhanced flow rates (Fig. 3 *left*) because of strong channelization along the critical path (Figs. 2c & d). In addition, the increase in void volume caused by channelization produced more compliant fractures even though the contact area remained the same. Very high stress was required to close a channelized path, which was very rarely achieved for the 5TX100 fractures. The dependence of fluid flow on the length of the fracture was reduced for the strongly channelized patterns (5TX100) because channelized flow becomes quasi-one dimensional.

Based on the data in Figure 3 (*left*), it would appear that all fractures behave differently because of the variation in fracture void topology. However, it is this topology that links the mechanical and hydraulic properties of a fracture as first demonstrate by Petrovitch et al. (2013) for weakly correlated aperture distributions (Fig. 2a). Petrovitch showed that fracture specific stiffness captured the deformed topology of a fracture under stress; the same deformed topology that controls fluid flow through a fracture. The flow-stiffness relationship developed by Petrovitch is

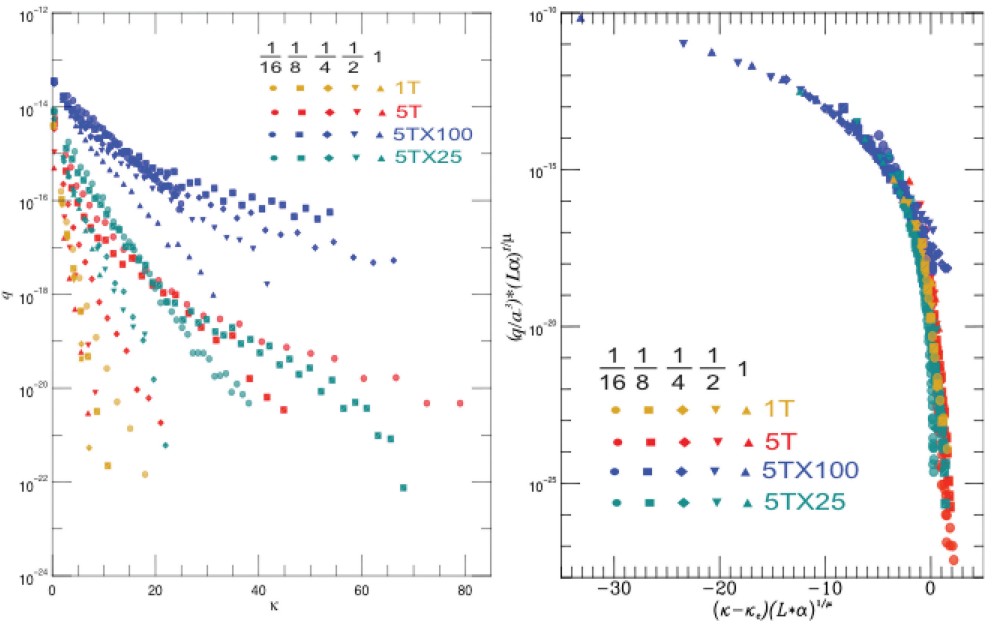


Figure 3. (*left*) Flow ($m^3/s$) as function of fracture specific stiffness (TPa/m) for 1T, 5T, 5TX25 and 5TX100 for length scales from 0.0625 to 1 meters. (*right*) Scaled flow ($m^3/s$) as a function of scaled stiffness (TPa/m) for the data shown on (*left*).

$$q\frac{L}{a_o^3} = L^{-t/\mu}F\left[\left(\kappa-\kappa_c\right)L^{1/\mu}\right] \tag{1}$$

where $q$ is the volumetric flow rate, $L$ is the scaled length of the fracture ($L = L_n/L_o$ where $L_n$ is a particular scale and $L_o$ is the largest scale), $\kappa$ is the fracture specific stiffness, $\kappa_c$ is the critical fracture specific stiffness, $a_o$ is the mean aperture at the largest scale, $\mu$ is the geometric correlation exponent ($\mu = 4/3$) and $t/\mu$ is the flow exponent. Equation (1) is a critical scaling relationship based on finite-size scaling theory and percolation theory.

Pyrak-Nolte & Nolte (2016) extended this scaling relationship to account for fractures with different spatial correlations and to account for highly channelized flow paths. The extended scaling relationship is

$$q\frac{L}{a_o^3} = \left(L\alpha\right)^{-t/\mu}F\left[\left(\kappa-\kappa_c\right)\left(L\alpha\right)^{1/\mu}\right] \tag{2}$$

where $a_o$ has been redefined as the ratio of the average aperture at the largest scale to the average aperture of the critical neck, $\alpha$ is the ratio of the correlation exponent at a stress $\sigma$ to the correlation exponent at the lowest stress at the largest scale. The relationship was applied to the data shown in Figure 3 (*left*) and resulted in the data collapse that is shown in Figure 3 (*right*). This collapse contains the simulation data from all five scales for the 1T, 5T, 5TX25 and 5TX100 fracture realizations.

As described by Pyrak-Nolte & Nolte (2016), the data collapse exhibits two regimes: $(\kappa–\kappa_c)(\alpha L)^{1/\mu} < -1$ and $(\kappa–\kappa_c)(\alpha L)^{1/\mu} \sim 0$. A fracture falls into the effective medium regime when $(\kappa–\kappa_c)(\alpha L)^{1/\mu} < -1$ and the velocity field is fairly uniform across the fracture. In this regime, the flow is dominated by the porosity of the fracture such as for the highly channelized case of 5TX100 and for large-scale fractures (Fig. 3 *right*). As spatial correlations are introduced or stress is applied to a fracture, fewer connected flow paths exist and the fracture behavior falls into the second regime $(\kappa–\kappa_c)(\alpha L)^{1/\mu} \sim 0$. This regime is dominated by the connectivity of the flow paths, where small changes in stress may close the critical neck thus breaking connectivity. The transition between these two regimes occurs at the knee in the curve (Fig. 3 *right*) when fracture porosity and connectivity both play a role in controlling fluid flow through the fracture.

Equation (2) is an important step forward in incorporating the effects of fracture topology on mechanical deformation and on control of fluid flow through fracture. This relationship is possible because fracture specific stiffness is a surrogate for the deformed fracture topology, both the apertures and contact area. Pyrak-Nolte & Nolte (2016) also noted that fractures in different rock types could be compared by multiplying the quantity $(k–k_c)$ by the ratio of the moduli, for example $E_{\text{rock1}}/E_{\text{rock2}}$, where $E_{\text{rock1}}$ is the reference rock type. As shown in Figure 1, the relationship between fluid and fracture stiffness provides the foundations for the ultimate goal of using seismic wave measurements to characterize and monitor relative fluid flow through fractures. In the next section, the effect of fracture geometry on the interpretation of fracture stiffness from elastic wave transmission is discussed.

## 3 INTERPRETING FRACTURE STIFFNESS FROM SEISMIC WAVE TRANSMISSION

### 3.1 *Analytical approach*

Theoretical models for wave propagation across a fracture capture the complexity of fracture topology with fracture specific stiffness. Often, a fracture is represented as a displacement discontinuity, also referred to as a non-welded contact or linear slip interface (Mindlin 1960, Kendall & Tabor 1972, Schoenberg 1980, 1983, Kitsunezaki 1983, Pyrak-Nolte & Cook 1987, Pyrak-Nolte et al. 1990a, b), where the complicated fracture topology is represented

by normal and shear fracture specific stiffnesses. Based on the displacement discontinuity theory, when the material is the same for the media on either side of a fracture (i.e., $Z_1 = Z_2 = Z$ = phase velocity * density) and the fracture is represented by $k$, the transmission coefficient for a compressional wave is

$$\left|T(\omega)\right| = \frac{1}{\sqrt{1+\left(\frac{\omega}{\omega_c}\right)^2}}, \tag{3}$$

where $w_c$ is the characteristic frequency and is equal to $w_c = 2\ k/Z$. For this purely elastic model, the amount of energy transmitted or reflected from a fracture depends on the frequency of the signal, specific stiffness of the fracture and the seismic impedance of the half-spaces (rock matrix). The fracture behaves as a low pass filter with a cutoff frequency of $w_c$ (Fig. 4). Though the solution is frequency-dependent, the energy is conserved at a displacement discontinuity interface, as demonstrated $|R(w)|^2 + |T(w)|^2 = 1$. For additional details, the reader is referred to Pyrak-Nolte et al. (1990a, b, 2016) and Cook (1992).

If fracture specific stiffness increases ($w/w_c$ decreases) because of an increase in stress, the transmission across a fracture increases because the contact area increases as apertures are reduced in size and close. A key question is how sensitive is fracture specific stiffness interpreted from elastic wave transmission/reflection to the details of the void geometry.

### 3.2 *Numerical approach*

Compressional wave propagation across a single fracture was simulated in 2D for a range of contact lengths and void widths (Fig. 5) to determine the sensitivity of elastic waves to the details of the fracture topology. A Discontinuous Galerkin (DG) approach was used to generate compressional waves from a point source that were propagated across a fracture. The DG method provides highly accurate solutions that enable waves to travel over multiple wavelengths with minimal dispersion (Dumbser & Kaser 2006). For more information on the DG

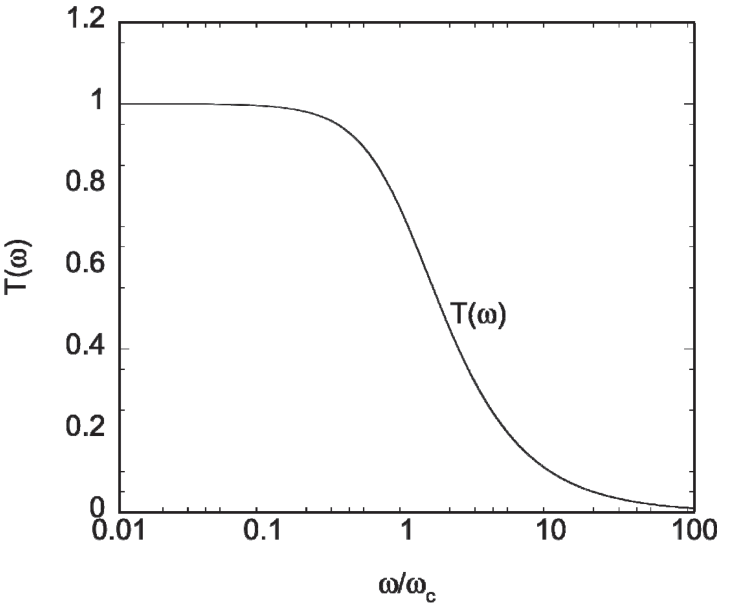


Figure 4. Transmission coefficient as function of normalized frequency where $w_c = 2\ k/Z$ based on displacement discontinuity theory.

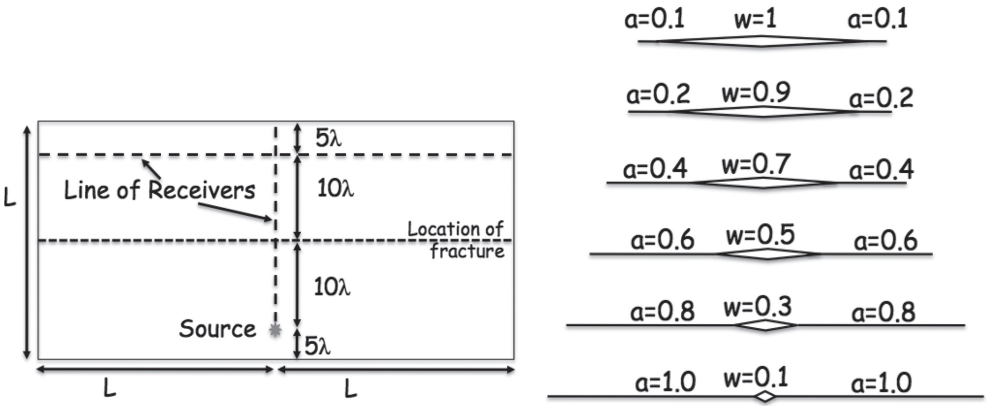


Figure 5. (*left*) Sketch of simulation geometry for a single fracture. (*right*) Contact length, a, and void width, w, (in millimeters) for simulated fractures.

method used in this study, the reader is referred to Petrovitch (2013) and Shao et al. (2015). In this study, the fracture resides in an isotropic medium with a compressional wave velocity of 3600 m/s, a shear wave velocity of 1900 m/s and density of 2080 Kg/m$^3$. Simulations were performed using the computational domain shown in Figure 5 (*left*) where L = 0.108 m and the wavelength, λ, is 3.6 mm at 1 MHz. The fracture geometry was uniformed and composed of contacts with length *a* and voids with widths *w* (Fig. 5 *right*). The height of the void was held constant at 0.1 mm. In this study, the asperity spacing (*a*+*w*) was maintained at 1.1 but *a* and *w* were allowed to vary. The number of voids varied as the width of void and contact length changed. A computational domain with the same dimensions but with no fracture was used to obtain an "intact" signal to use as a reference signal.

### 3.3 *Effect of geometry on compressional wave transmission*

Angel & Achenbach (1985) examined wave transmission across a fracture represented by an array of co-linear cracks and found, for the far field, frequency dependent transmission and reflection coefficients that also depended on crack length and crack spacing. Myer (2000) showed that the displacement discontinuity captured scattering from a synthetic fracture based on Angel & Achenbach (1985) derivation but noted that deviations can occur when the wavelength is less than four times the crack spacing and also when the wavelength is on the same order as crack size (void width). In this study, both the void width and the asperity spacing were less than a wavelength for all cases.

Figure 6 (*left*) provides a comparison of waves propagated across the various fracture geometries shown in Figure 5 (*right*). As the contact area increased, the transmitted wave exhibited an increase in amplitude, a decrease in arrival time and an increase in frequency as indicated by the decrease in the period of the wave. To interpret fracture specific stiffness for each fracture, a Fast Fourier Transform (FFT) of the intact signal was convolved with the complex conjugate of the transform function from the displacement discontinuity theory (Pyrak-Nolte et al. 1990a, b). An inverse FFT of this product was taken to produce a "theoretical" or "predicted" signal to compare to the signals from the fracture simulations. The stiffness that produced the lowest Chi-squared value between the theoretical signal and a fracture signal was selected as the stiffness of the fracture.

Fracture specific stiffness is observed to increase as the contact area ($a/(a+w)$) of the fracture increases (Fig. 6 *right*). Though the asperity spacing is maintained, scattering from the voids leads to a loss of energy recorded at the receiver. Based on the void geometry used in this simulation, fluid flow through these simulated fractures is greater for fractures with lower contact area. These simple examples demonstrate that elastic waves are sensitive to the void topology. However, significantly more research is needed to develop a scaling relation-

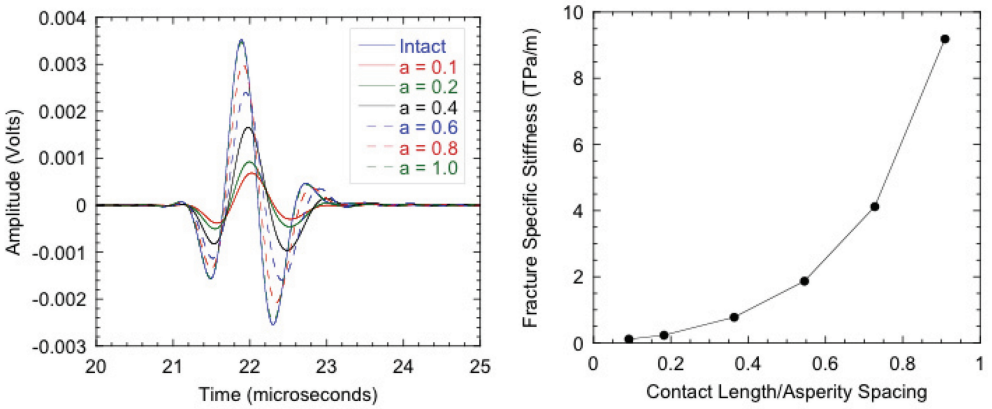


Figure 6. (*right*) Simulated compressional waves transmitted across an intact sample and fracture samples with the same asperity spacing but different contact length (Fig. 5). (*left*) Fracture specific stiffness as a function of contact area.

ship to link the dynamic fracture specific stiffness interpreted from elastic wave propagation to the scaling relationship for fluid flow—fracture specific stiffness given by Equation (2).

## 4 CONCLUSIONS

A scaling relationship between fluid flow and fracture specific stiffness for a fracture exists that accounts for spatial correlations in the aperture distribution as well as highly channelized flow paths that can occur during chemical erosion. This is an important relationship because fracture specific stiffness can be estimated from seismic wave attenuation and velocity. A simple analysis demonstrated that fracture specific stiffness determined from transmitted compressional waves is also sensitive to the fracture void geometry. Fracture specific stiffness captures the complex geometry of a fracture and on how this geometry deforms under stress. The ability to link fracture specific stiffness to fluid flow provides a method for delineating potential pathways through fractured rock using geophysical techniques that are sensitive to fracture stiffness.

## REFERENCES

Angel, Y.C. & Achenbach, J.D. 1985. Reflection and transmission of elasitic waves by a periodic array of cracks: oblique incidence. *Wave Motion* 7(4): 375–397.

Cheng, J.T., Morris, J.P., Tran, J., Lumsdaine, A., Giordano, N.J., Nolte, D.D. & Pyrak-Nolte, L.J. 2004. Single-phase flow in a rock fracture: micro-model experiments and network flow simulation. *International Journal of Rock Mechanics and Mining Sciences* 41(4): 687–693.

Cook, N.G.W. 1992. Jaeger Memorial Dedication Lecture. Natural Joints in Rock: Mechanical, Hydraulic and Seismic Behaviour and Properties under Normal Stress. *International Journal of Rock Mechanics and Mining Sciences and Geomechanics Abstracts* 29(3): 198–223.

Dumbser, M. & Käser, M. 2006. "An arbitrary high-order Discontinuous Galerkin method for elastic waves on unstructured meshes—II. The three-dimensional isotropic case." *Geophysical Journal International* 167(1): 319–336.

Goodman, R.E., Taylor, R.L. & Brekke, T.L. 1968. A model for the mechanics of jointed rock. *Journal of Soil Mechanics & Foundations Division of the American Society of Civil Engineers* 94: 637–659.

Hopkins, D.L. 1990. *The Effect of Surface Roughness on Joint Stiffness, Aperture and Acoustic Wave Propagation*. Ph.D. Thesis, University of California, Berkeley.

Hopkins, D.L., Cook, N.G.W. & Myer, L.R. 1987. Fracture stiffness and aperture as a function of applied stress and contact geometry. *Rock Mechanics: Proceedings of the 28th US Symposium*. Tucson, Arizona. Rotterdam: Balkema. 673–680.

Hopkins, D.L., Cook, N.G.W. & Myer, L.R. 1990. Normal joint stiffness as a function of spatial geometry and surface roughness. *Proceedings of the International Symposium on Rock Joints*. Loen, Norway. 203–210.

Kendall, K. & Tabor, D. 1971. An ultrasonic study of the area of contact between stationary and sliding surfaces. *Proceedings of the Royal Society of London*, Series A 323: 321–340.

Kitsunezaki, C. 1983. Behavior of plane waves across a plane crack. *J. Mining Coll. Akita Univ, series A* 3(6): 173–187.

Mindlin, R.D. 1960. Waves and vibrations in isotropic planes. *Structural Mechanics*. eds. J.W. Goodier & W.J. Hoff, Pergammon.

Myer, L.R. 2000. Factures as collectins of cracks. *International Journal of Rock Mechanics and Mining Sciences* 37: 231–243.

Nolte, D.D. & Pyrak-Nolte, L.J. 1991. Stratified Continuum Percolation—Scaling Geometry of Hierarchical Cascades. *Physical Review* A 44: 6320–6333.

Petrovitch, C.L. 2013. *Universal Scaling of Flow-Stiffness Relationship in Weakly Correalted Fractures*. PhD. Thesis, Purdue University, West Lafayette, Indiana.

Petrovitch, C.L., Nolte, D.D. & Pyrak-Nolte, L.J. 2013. Scaling of fluid flow versus fracture stiffness. *Geophysical Research Letters* 40: 2076–2080.

Petrovitch, C.L., Pyrak-Nolte, L.J. & Nolte, D.D. 2014. Combined scaling of fluid flow and seismic stiffness in single fractures. *Rock Mechanics and Rock Engineering* 47: 1613–1623.

Pyrak-Nolte, L.J. & Cook, N.G.W. 1987. Elastic interface waves along a fracture. *Geophys. Res. Lett*. 11(14): 1107–1110.

Pyrak-Nolte, L.J., Myer L.R. & Cook, N.G.W. 1990a. Transmission of Seismic-Waves across Single Natural Fractures. *Journal of Geophysical Research-Solid Earth and Planets* 95(B6): 8617–8638.

Pyrak-Nolte, L.J., Myer, L.R. & Cook, N.G.W. 1990b. Anisotropy in seismic velocities and amplitudes from multiple parallel fractures. J. Geophys. Res. 95(B7): 11345–11358.

Pyrak-Nolte, L.J. & Nolte, D.D. 2016. Approaching a universal scaling relationship between fracture stiffness and fluid flow. *Nature Communications*. 7:10663 doi: 10.1038/ncomms10663.

Pyrak-Nolte, L.J., Shao, S. & Abell, B.C. 2016. Elastic waves in fractured isotropic and anisotropic media. To appear in CRC Volume *Rock Mechanics and Engineering*, edited Xia-Ting Feng.

Shao, S., Petrovitch, C.L. & Pyrak-Nolte, L.J. 2015. Wave guiding in fractured layered media. In *Fundamental Controls on Fluid Flow in Carbonates, Geological Society, London, Special Publications*. 406, pp. 375–400.

Schoenberg, M. 1980. Elastic wave behavior across linear slip interfaces. *J. Acoust. Soc. Am*. 5, 68: 1516–1521.

Schoenberg, M. 1983. Reflection of elastic waves from periodically stratified media with interfacial slip. *Geophysical Prospecting* 31: 265–292.

This page intentionally left blank

*Rock Dynamics: From Research to Engineering – Li et al. (Eds)*
*© 2016 Taylor & Francis Group, London, ISBN 978-1-138-02953-8*

# The effect of true-triaxial stress path on induced fracturing in anisotropic gneiss

R.P. Young & M.H.B. Nasseri
*University of Toronto, Toronto, Canada*

ABSTRACT: Samples of anisotropic gneiss oriented at 0, 30, 60 and 90 degrees to the maximum loading stress were tested in a true-triaxial deformation cell. The loading path was designed to simulate the in situ stresses that rock would be exposed to during the excavation, heating and cooling of canister holes created for the proposed containment of radioactive waste. The results show that the deformation response would not be replicated with a traditional triaxial test were the intermediate and minimum stress are assumed to be equal. In two situations the loading history induced failure when the intermediate stress was reduced. Acoustic emission and velocity data are used to characterize the damage and the sensitivity of the velocity data provide a future method to link laboratory to in situ observations.

## 1 INTRODUCTION

Understanding damage around boreholes and tunnels in rock is significant to numerous engineering applications. Borehole breakout and spalling, where the preferential orientation of stresses can induce failure, is a classic manifestation of this damage. Ever since the early work of Kirsch over a century ago we have endeavored to understand the complex interactions of stress and geometry on failure. More recently rock mechanics experimental testing and discrete particle numerical models have been used to deconvolve the complex fracture processes that lead to crack coalescence and the various modes of failure in rock materials (Hoek & Martin 2014). One application, which requires an understanding of failure around underground openings, is the concept of deep geological disposal of radioactive waste. Several countries have proposed schemes that involve the placement of spent fuel in canisters that will be placed in large diameter boreholes in tunnel complexes that are between 300 m and 500 m below the surface. Three such countries include Canada, Sweden and Finland where extensive investigations have been undertaken in crystalline rock to create a design that will be safe for the long term management, storage and disposal of radioactive waste.

As part of national radioactive waste management research, underground facilities have been built to carry out full scale in situ tests that simulate the process of placing artificial canisters that are heated within the same geometries of boreholes and tunnels that would be required for a final repository. Such notable examples of these experiments have been carried out at the Underground Research Laboratory in Canada, the Aspo Hard Rock Laboratory in Sweden and the Onkalo Facility in Finland. What is critical to the success of such experiments is to be able to predict the behavior of the rock host as it is subjected to the loading path exerted on it by the various processes of creating the tunnel and boreholes and subsequently being heated and cooled over thousands of years by the spent fuel canisters (Martin 1997).

This paper aims to contribute to this understanding by looking at the effect of true-triaxial loading history on the strength, deformation and induced fracturing that occurs at the various stages of creating the large diameter boreholes used in repository design. The underground facilities mentioned above have all carried out full-scale simulated canister emplacement experiments in situ, monitored them with extensive instrumentation including geophysical measurements for induced seismicity and velocity tomography (Young & Collins

2001). Advanced numerical models have also been used to simulate the complex loading path experienced by the rock in the vicinity of these canister holes. As part of this process classic rock mechanics tests are carried out to determine the material properties of the rock so that the models can be calibrated and used to understand the in situ results. Traditionally triaxial testing is part of this program and the vast majority of these triaxial tests are carried out with the minimum and intermediate principal stress being equal. Research has shown that this simplification gives an approximation for the strength and behavior of rock under confined conditions. However, in situ this is not always the case and situations can arise, through induced stresses and anisotropy in the rock, where the difference in the intermediate and minimum stress can play a more significant role in the subsequent failure processes (Kwasniewski et al. 2013, Young et al. 2013, Nasseri et al. 2014).

## 2 EXPERIMENTAL PROCEDURE: TRUE-TRIAXIAL TESTING

This paper builds on an initial set of experiments that were carried out in 2015 at the University of Toronto Rock Fracture Dynamics Facility (RFDF). The tests were to determine the nature of failure in anisotropic crystalline gneissic rock subjected to a state of true-triaxial stress that simulated in situ stress conditions around canister holes. The initial 4 laboratory tests are described in Nasseri et al. (2016) and are enhanced here with an additional suite of 4 tests that were conducted to extend understanding and determine properties of the rock once the sample had reached a damage threshold. In situ stress measurements and numerical modeling was used to determine the state of true-triaxial stress around the in situ canister holes during the various stages of excavation, heating and cooling during the Posiva Onkalo Spalling Experiment (POSE). Details of the experiment and site are described in Vali et al. (2015), Johansson et al. (2015), Posiva (2013) and Ohman et al. (2009). 80 mm cubic samples of anisotropic gneiss, from the Onkalo site, were used for the testing program. Two samples were tested for each orientation of foliation (0, 30, 60 and 90 degrees) with respect to the maximum principal stress direction used during testing.

Table 1 shows the stresses for the loading steps used, for the true-triaxial testing, to simulate the loading history experienced in situ. The loading steps for all samples were the same with the exception that for the second suite of samples unloading was carried out as soon as the damage threshold was reached.

Young et al. (2013) describe the RFDF facility used here and the experimental procedure for testing anisotropic gneiss is the same as that described in Nasseri et al. (2016).

Table 1. Shows the stress path, determined by Posiva, for performing true-triaxial experiments for both series of gneiss specimens.

| Step | $\sigma_3$ (MPa) | $\sigma_2$ (MPa) | $\sigma_1$ (MPa) | Simulated in situ condition |
|---|---|---|---|---|
| 0 | 5 | 5 | 5 | loading |
| 1 | 10 | 10 | 10 | build s3 |
| 2 | 10 | 18 | 18 | build s2 |
| 3 | 10 | 18 | 27 | build s1 = *in situ* |
| 4 | 3 | 18 | 55 | excavation_1 |
| 5 | 1 | 5 | 55 | excavation_2 |
| 6 | 1 | 10 | 85 | heating |
| 7 | 1 | 30 | 110 | heating EH3 max |
| 8 | 1 | 20 | 140 | heating HE1 max |
| 9 | 10 | 18 | 27 | cooled to *in situ* |
| 10 | 5 | 5 | 5 | unloading |

"*Step 0:* Stresses were increased along the three axes ($\sigma_1$, $\sigma_2$ and $\sigma_3$) using constant force control mode in the polyaxial machine up to 5 MPa. Using translational control mode it is possible to have the same load distribution on opposites faces of the cube for each axis during loading. Compressional and two shear wave velocities were measured at the target stresses. Continuous streaming of AE data were stored as soon as wavelets started to appear on the visualisation screen for all stages. Stress-strain responses were recorded along three axes once 5 MPa of hydrostatic stress has been achieved.

*Step 1:* Stresses were increased up to 10 MPa, simultaneously, on all three axes at a constant loading rate of 0.1 kN/s. Wave velocities were measured at the end of loading step 1.

*Step 2:* While keeping the stress at 10 MPa along $\sigma_3$, stresses were increased simultaneously up to 18 MPa along $\sigma_1$ and $\sigma_2$ directions under a constant force control mode at a same rate of 0.1 kN/s. Velocities were measured at the end of step 2.

*Step 3:* While keeping stresses constant at 10 MPa and 18 MPa along $\sigma_2$ and $\sigma_3$ directions using force control mode, $\sigma_1$ was raised up to 27 MPa using constant displacement control mode at a rate of 0.0002 mm/s. Velocity measurements were carried out during loading step 3.

*Step 4:* Keeping $\sigma_2$ constant at 18 MPa, $\sigma_3$ was unloaded to 3 MPa using constant force control mode, $\sigma_1$ was raised to 55 MPa using constant displacement control mode of 0.0002 mm/s. Velocities were measured during and at the end of step 4.

*Step 5:* Keeping $\sigma_1$ constant at 55 MPa, $\sigma_2$ and $\sigma_3$ were unloaded to 5 MPa and 1 MPa, respectively, using a constant force control mode of 0.1 kN/s. Velocities were measured at the end of step 5.

*Step 6:* Leaving $\sigma_3$ constant at 1 MPa, $\sigma_2$ and $\sigma_1$ were raised up to 10 MPa and 85 MPa, respectively. Velocity measurements were carried out during loading step 6.

*Step 7:* While keeping $\sigma_3$ constant at 1 MPa, $\sigma_2$ and $\sigma_1$ were raised up to 30 MPa and 110 MPa, respectively. Velocity measurements were carried out during loading step 7. If samples failed at this step, step 8 was abandoned and samples were unloaded to the step 1stress level.

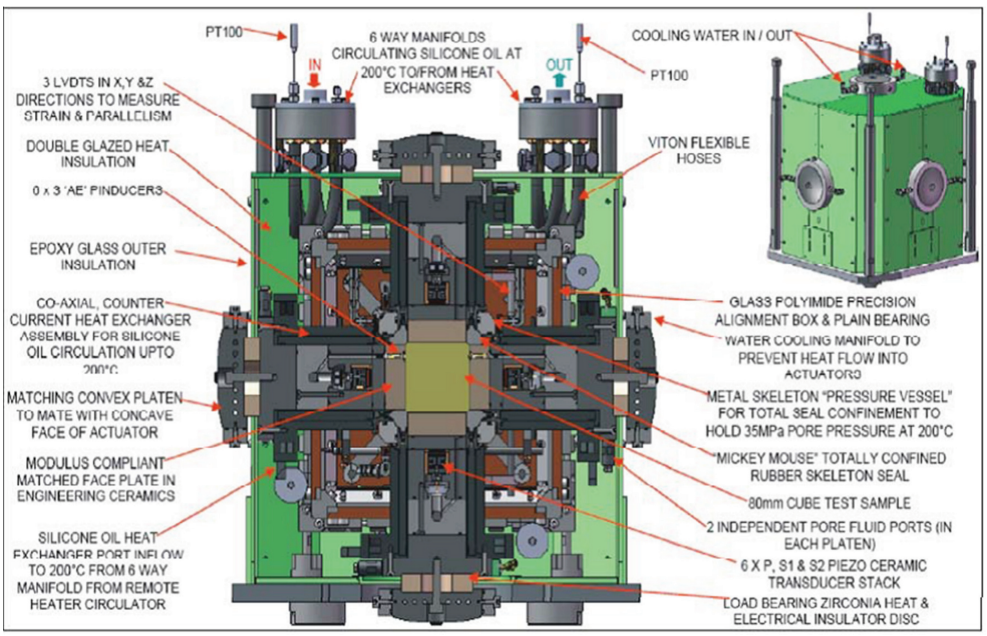


Figure 1. Details of the components of the True-Triaxial Geophysical Imaging Cell designed and manufactured by Ergotech.

*Step 8:* While keeping $\sigma_3$ still constant at 1 MPa, $\sigma_2$ was unloaded to 20 MPa and $\sigma_1$ was raised up to 140 MPa, respectively. Velocity measurements were carried out during loading step 8. If samples failed at the end of this step, then step 9 was followed and stresses were unloaded in the same order as it was implemented along each axis back to step 1. Velocity measurements were carried out during the unloading procedure and back to step zero stresses.

*Step 9:* For samples that did not fail up to step 8, step 9 was then performed."

Figure 1 shows the geophysical imaging cell used for this study, which was positioned in a MTS polyaxial loading frame controlled by six independent servo actuators. Using this innovative system, it is possible to carry out multi-axis (independent control of all three principal deformation stresses) thermo-mechanical, geophysical and hydrological measurements essentially simultaneously on rock specimens well into the post-failure regime. The deformation system simulates temperature, pressure and fluid environments in the upper crust with maximum loads able to induce fracture and failure in rocks, while continuously monitoring changes to the physical properties of the samples including three axes permeability, induced Acoustic Emission (AE) and seismic velocity. Six sets of dedicated P, Sv and Sh transducers provide regular velocity measurements along the three stress axes and 18 AE detectors record induced seismicity continuously. This allows the growth of fractures to be controlled and monitored over a range of simulated earth-like and engineered conditions.

## 3 RESULTS: TRUE TRIAXIAL TESTING AND STRESS PATH

The results are presented systematically for the four orientations of anisotropy. The first figures for each orientation show the stress strain behavior, the second set of figures the velocity data that was obtained for the loading steps and the third set of figures show the AE response from the onset of activity to the end of testing.

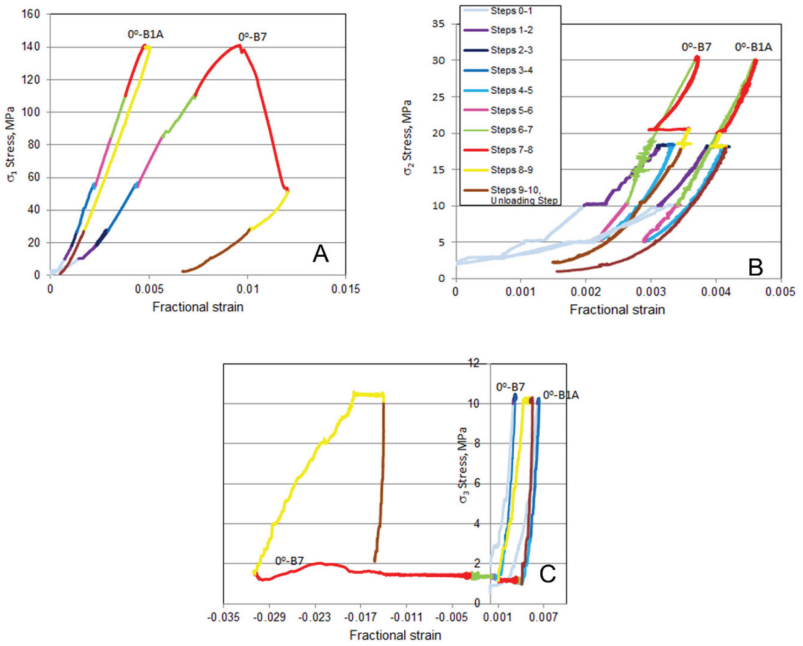


Figure 2. Stress-strain curves for nine steps of loading A) for the $\sigma_1$ direction for specimens B7 and B1 A, B) for $\sigma_2$ and C) for $\sigma_3$ for the two 0 degree oriented gneiss specimens.

Figure 2 shows the stress strain curves for the samples with anisotropy oriented at 0 degrees to the maximum stress direction. Specimen B7 failed at a peak strength of 140 MPa at the end of loading step 8 and reached a residual strength of 51 MPa. Specimen B1 A, displayed a similar strength at the end of loading step 8 and this was associated with the onset of acoustic emission activity. The sample was then unloaded. Deformational responses along $\sigma_3$ and $\sigma_2$ for specimen B7 shows a larger dilatational value than that of B1 A. Dilatational strain along the $\sigma_3$ axis for the B7 specimen (loading step 8) shows the highest strain value of 3%. B1 A shows a small amount of permanent axial strain confirming the fact that this specimen reached the damage threshold. This strain is much smaller than shown by specimen B7 reaching a maximum permanent axial strain of 1.2%.

Figure 3 shows the velocity data for the samples with anisotropy oriented at 0 degrees to the maximum stress direction. $V_{PZ}$, $V_{PY}$ and $V_{S1Z,}$ for both specimens, show much higher values than $V_{PX}$ and $V_{S1X}$ as the former propagate parallel to the plane of symmetry and the latter propagate normal to it (YZ plane). $V_{PY}$ and $V_{S1Y}$ fluctuate as a function of loading step especially during loading steps 4 to 5 when $\sigma_2$ changes from 18 MPa to 5 MPa and $\sigma_3$ changes from 3 MPa to 1 MPa. This is detecting the reduction in compressive forces parallel to the $\sigma_2$ and $\sigma_3$ axes. Post failure velocities are slower in all cases. Figure 4 shows the located acoustic emission events for the samples with anisotropy oriented at 0 degrees to the maximum stress direction.

Failure of the B7 specimen is accompanied with a significant number of AE events prior to peak strength and AE activity starts at the beginning of loading step 6. In specimen B1 A, AE activity starts at the end of loading step 7 and continued to the end of loading step 8 when the specimen was unloaded prior to failure.

Temporal and spatial analysis of AE events clearly shows that the fracture nucleation and fracture propagation took place along sub-vertically oriented weak planes with respect to the $\sigma_1$ direction and along the YZ plane of symmetry in both specimens.

Figure 5 shows the stress strain curves for the samples with anisotropy oriented at 30 degrees to the maximum stress direction. Specimen B12 was tested up to failure and post peak. Axial strain is 1.2% when $\sigma_1$ reaches a maximum peak value of 110 MPa at the end of loading step 7. The specimen reached a residual strength of 38 MPa with an ultimate axial deformation of 1.3%. Continuous loading along $\sigma_1$ and reduction of the two horizontal stresses of $\sigma_3$ and $\sigma_2$ to 1 MPa and 5 MPa respectively, during loading step 5, causes nucleation and fracture propagation along the weakest plane and continued until ultimate failure of the B12 specimen. For specimen B12, $\sigma_2$ reached a value of 27 MPa with a lateral deformation of 0.55% during failure. The variation of $\sigma_3$ with diametral strain reaches a maximum of 3% along the least principal stress direction and accommodates the largest dilatation strain for fractures to grow at the end of loading step 7. Specimen B11 was unloaded prior to peak strength and

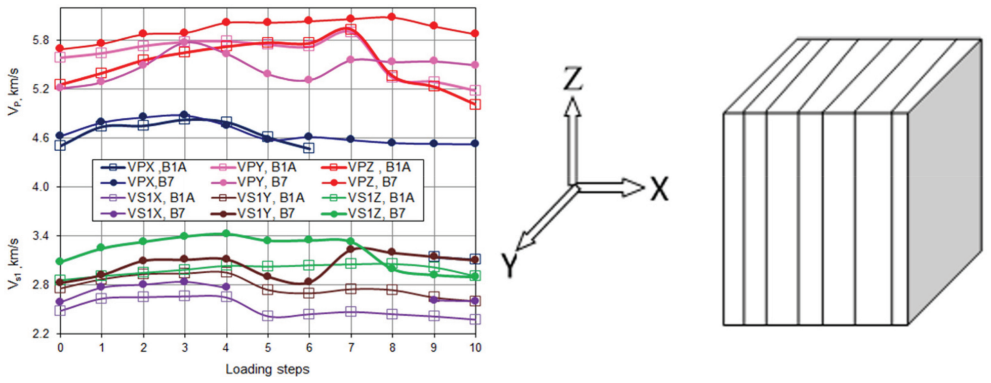


Figure 3. Variation of $V_P$ and $V_{S1}$ measured along three orthogonal axes as a function of loading steps for two specimens B1 A and B7. The sketch shows the alignment of foliation plane orientation with respect to the seismic wave velocity measurements.

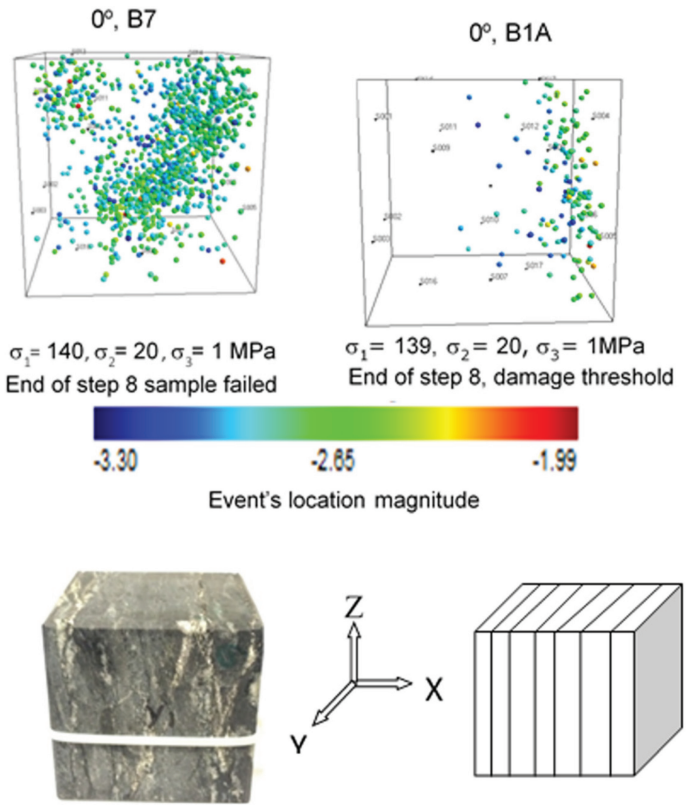


Figure 4. Acoustic emission activity recorded for specimens B7 and B1 A. The scale shows relative location magnitude (the same scale is used for AE events on Figs. 7,10 and 13). The tested B1 A specimen is shown and the sketch shows the direction of foliation planes with respect to the applied principal stress directions.

$\sigma_1$ reached a maximum peak strength of 93 MPa. For specimen B11, $\sigma_2$ reaches a value of 18 MPa with lateral deformation strain of 0.5% at peak strength. Variation of $\sigma_3$ with diametral strain reaches a maximum of 1% along the least principal stress direction accommodating smaller dilatation strain and thus arrests fractures at the end of loading step 7.

Figure 6 shows the velocity data for the samples with anisotropy oriented at 30 degrees to the maximum stress direction. $V_{PY}$ and $V_{S1Y}$ measured along the strike of the foliation planes show a larger value in comparison to $V_{PZ,}$ $V_{PX}$ and $V_{S1Z}$ and $V_{S1X}$ that are measured at an angle of 30° and 60° with respect to the strike of foliation planes. $V_{PY}$ and $V_{S1Y}$ fluctuate as a function of loading steps especially during loading step 3 to 6 and continue to decline at loading steps 6 to 7 due to activation of weak planes causing more damage along the dip direction of the foliation planes. Post failure velocities are slower in all cases.

Figure 7 shows the located acoustic emission events for the samples with anisotropy oriented at 30 degrees to the maximum stress direction. Nucleation and fracture propagation along the weakest plane (30° to $\sigma_1$) is highlighted by AE locations parallel to dip direction of the foliation planes making a 30° angle with respect to the $\sigma_1$ direction in both specimens.

Activation of slip along the dip direction for specimen B11 happens much earlier than that of specimen B12. Specimen B12 is characterized with a larger number of AE events in comparison with specimen B11 since the former specimen was loaded to failure. Close observation of the failure pattern on the B12 specimen clearly indicates that failure takes place along the preferably oriented weak plane (30°) with respect to the $\sigma_1$ axis. Temporal and spatial analysis of AE events clearly shows that the fracture nucleation and fracture propagation

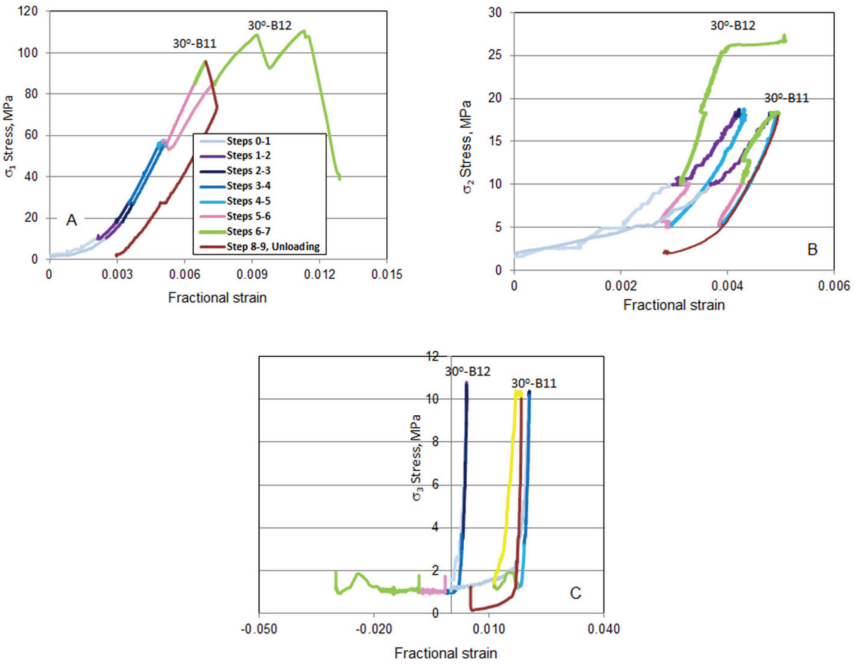


Figure 5. Stress-strain curves for nine steps of loading A) for the $\sigma_1$ direction for two specimens B11 and B12, B) for $\sigma_2$ and C) for $\sigma_3$ for the two 30° gneiss specimens.

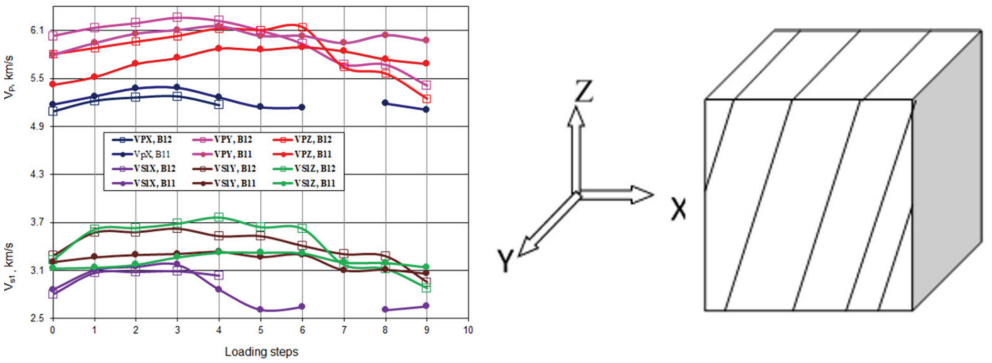


Figure 6. Variation of $V_P$ and $V_{SI}$ measured along three orthogonal axes as a function of loading steps for two specimens B12 and B11. The sketch shows the alignment of foliation plane orientation with respect to the seismic wave velocity measurements.

took place along 30° oriented weak planes with respect to the $\sigma_1$ direction and the failure pattern matches well with AE locations.

Figure 8 shows the stress strain curves for the samples with anisotropy oriented at 60 degrees to maximum stress direction. Both specimens B9 and B6 show similar stress-strain curves prior to failure. Specimen B9 shows the variation of $\sigma_1$ with axial strain registering a value of 0.7% when $\sigma_1$ reaches a maximum peak value of 125 MPa at the middle of loading step 8. The specimen reached a residual strength of 45 MPa showing an ultimate axial deformation of 0.93%. Whereas specimen B6 reaches a maximum $\sigma_1$ of 131 MPa with an axial strain of 0.5% prior to unloading steps 8 to 10. Variation of stress-strain curves along the $\sigma_2$ axis is almost identical for both specimens of B9 and B6 confirming the reproducibility in

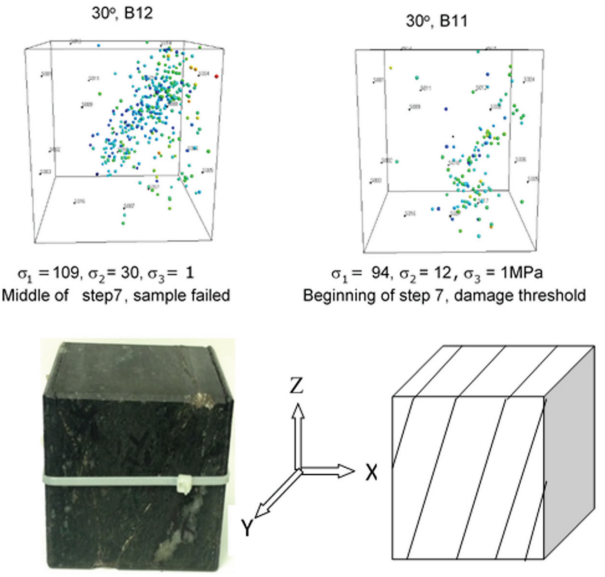


Figure 7. Acoustic emission activity for the specimens B12 and B11. The tested B12 specimen is shown and the sketch shows the direction of foliation planes with respect to applied principal stress directions.

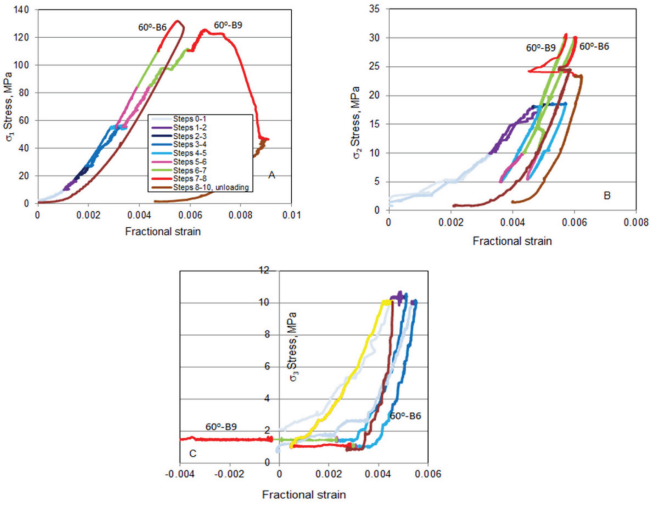


Figure 8. Stress-strain curves for nine steps of loading A) for the $\sigma_1$ direction for two specimens B6 and B9, B) for $\sigma_2$ and C) for $\sigma_3$ for the two 60° gneiss specimens.

results along that axis. Specimen B9 shows more dilatational strain during failure (beginning of loading step 8) up to 3% when residual stress reached a value of 45 MPa, while $\sigma_3$ was kept at 1 MPa of constant stress. Failure of specimen B9 and increased AE activity for specimen B6 happened at the time of decreasing intermediate principal stress from 30 MPa to 20 MPa in the middle of loading steps 7 to 8 which appears to have triggered failure. The lateral strain along the $\sigma_3$ axis for specimen B6 during peak strength is 0.25%, since the specimen was unloaded immediately after the onset of accelerated AE activity.

Figure 9 shows the velocity data for the samples with anisotropy oriented at 60 degrees to the maximum stress direction. $V_{PY}$ and $V_{S1Y}$ measured along the strike of the foliation

planes for both specimens B9 and B6 show a larger value in comparison to the wave velocities measured along Z and X axes. $V_{PY}$ and $V_{S1Y}$ fluctuate as a function of loading step especially during loading steps 4 to 6 due to the elastic response along the Y axis on removal of stress from 18 MPa to 5 MPa. Post failure velocities are slower in all cases.

Figure 10 shows the located acoustic emission events for the samples with anisotropy oriented at 60 degrees to the maximum stress direction. Temporal and spatial analysis of AE events for both specimens B9 and B6 show that the propagation of fracture at the final stages of failure started from the left lower side of the sample, diagonally propagating towards the right upper side of the specimen. A reduced number of AE events for specimen B6 is due to the unloading once the damage threshold was reached. A close observation of the failure pattern on the B9 specimen clearly indicates that failure takes place along the preferably oriented weak plane (60°) with respect to $\sigma_1$ axis.

Figure 11 shows the stress strain curves for the samples with anisotropy oriented at 90 degrees to the maximum stress direction. Both specimens B4 and B2 A survived all prescribed loading steps with only a few AE events at the end of loading step 8. Both specimens

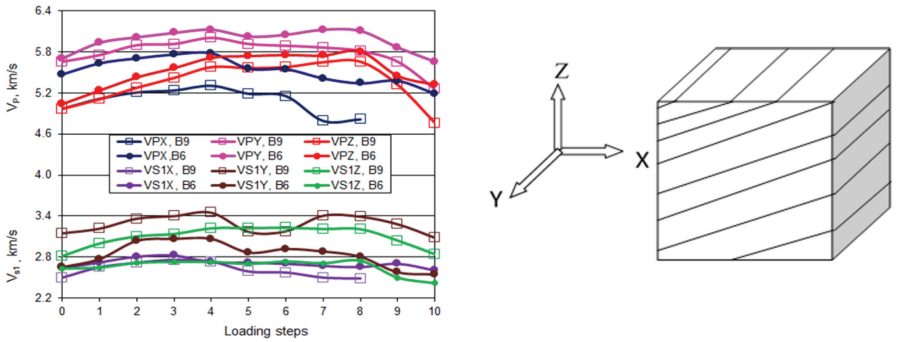


Figure 9. Variation of $V_P$, $V_{S1}$ and $V_{S2}$ measured along three orthogonal axes as a function of loading steps for two specimens B9 and B6. The sketch shows the alignment of foliation plane orientation with respect to the seismic wave velocity measurements.

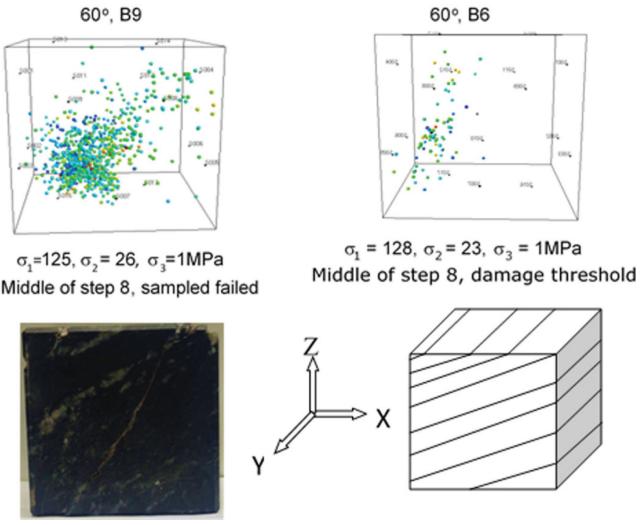


Figure 10. Acoustic emission activity for specimens B9 and B6. The tested B9 specimen is shown and the sketch shows the direction of foliation planes with respect to applied principal stress directions.

show almost identical stress-strain behaviour for the $\sigma_1$ principal stress direction. Whereas specimen B2 A shows 10 times the dilatational strain (0.5% against 0.05%) during loading steps 5 to 8.

Figure 12 shows the velocity data for the samples with anisotropy oriented at 90 degrees to the maximum stress direction. Similar to all other orientations, specimens B4 and B2 A show the effect of 3D seismic wave propagation direction with respect to anisotropic foliation at the initial loading step (5 MPa of hydrostatic stress). $V_{PX}$ and $V_{S1X}$ are the fastest seismic wave velocities measured along the XY plane for the B4 specimen whereas $V_{PY}$ and $V_{S1Y}$ are the fastest for the B2 A specimen. Axial loading along the Z axis does affect all seismic wave velocities up to loading step 4, after which, seismic wave velocities measured along $\sigma_2$ and $\sigma_3$ are both affected by unloading step 4 to 5 and later on loading steps 6 to 8. The compressional and shear wave velocities measured along the X, Y and Z axes at the initial loading step (5 MPa of hydrostatic stress) for both specimens are lower than their respective velocities measured at loading step 10 after unloading to 5 MPa of hydrostatic stress. This phenomenon is due to the viscoelastic nature of the micro-fractures oriented along the XY plane, which remained closed after unloading step 10.

Figure 13 shows the located acoustic emission events for the samples with anisotropy oriented at 90 degrees to the maximum stress direction. Specimen B4 shows sparse AE

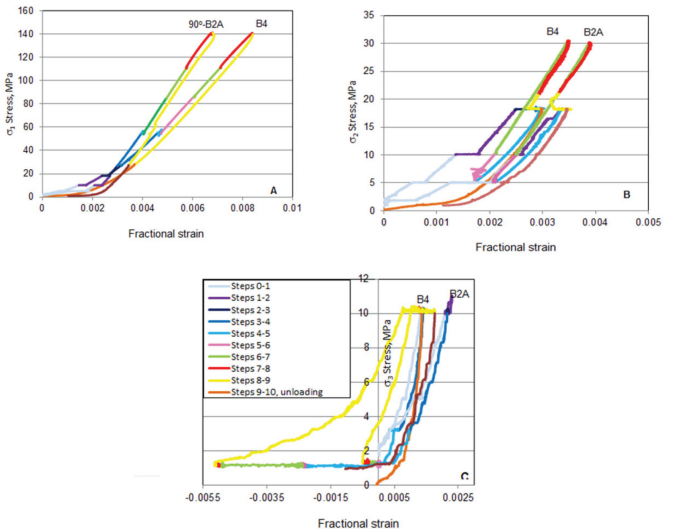


Figure 11. Stress-strain curves for nine steps of loading A) for the $\sigma_1$ direction for two specimens B4 and B2 A, B) for $\sigma_2$ and C) for $\sigma_3$ for the two 90° gneiss specimens.

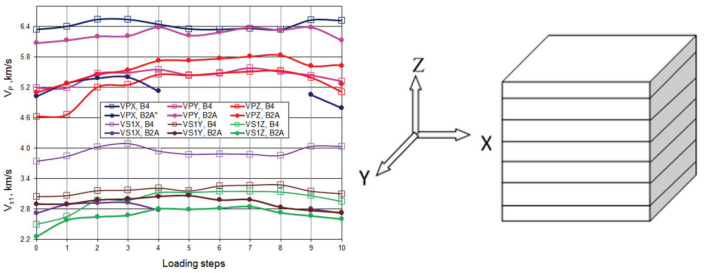


Figure 12. Variation of $V_P$, $V_{S1}$ and $V_{S2}$ measured along three orthogonal axes as a function of loading steps for two specimens B4 and B2 A. The sketch shows the alignment of foliation plane orientation with respect to the seismic wave velocity measurements.

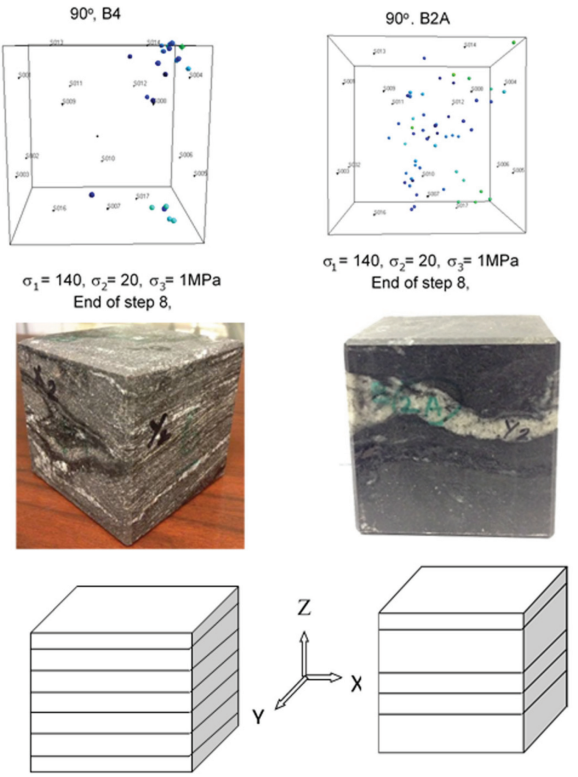


Figure 13. Acoustic emission activity recorded for specimens B4 and B2 A. The tested B4 and B2 A specimens are shown and the sketch shows the direction of foliation planes with respect to applied principal stress directions.

Table 2. Summarizes the effect of the foliation planes on strength, seismic wave velocity and AE activity for the gneiss specimens tested under true-triaxial conditions following a stress path outlined in Table 1.

| Specimen's name | Max. $\sigma_1$, (MPa) | Max & Min $V_{PX}$, km/s | Max & Min $V_{PY}$ km/s | Max & Min $V_{PZ}$ km/s | Max & Min $V_{S1X}$, km/s | Max & Min $V_{S1Y}$, km/s | Max & Min $V_{S1Z}$, km/s | Remarks |
|---|---|---|---|---|---|---|---|---|
| 0° Mica gneiss B7 | 140 | 4.83<br>3.02 | 5.81<br>5.18 | 5.93<br>5.01 | 2.84<br>2.59 | 2.81<br>2.59 | 3.12<br>2.83 | AE highlighting failure plane, failed end of step 8 |
| B1A | 139 | 4.88<br>4.52 | 5.77<br>5.21 | 6.08<br>5.69 | 2.66<br>2.38 | 2.95<br>2.6 | 3.06<br>2.86 | |
| 30° Mica gneiss B12 | 110 | 5.28<br>5.09 | 6.26<br>5.41 | 6.14<br>5.25 | 3.08<br>2.80 | 3.62<br>2.96 | 3.64<br>2.88 | AE highlighting failure plane, failed end of step 6 and 7 |
| B11 | 93 | 5.38<br>5.11 | 6.11<br>5.97 | 5.89<br>5.42 | 3.17<br>2.61 | 3.33<br>3.06 | 3.32<br>3.13 | |
| 60° Mica gneiss B9 | 125 | 5.31<br>4.79 | 6.01<br>5.26 | 5.58<br>4.76 | 2.76<br>2.49 | 3.45<br>3.08 | 3.23<br>2.81 | AE highlighting failure plane, failed middle of step 8 |
| B6 | 131 | 5.78<br>5.19 | 6.13<br>5.66 | 5.81<br>5.04 | 2.82<br>2.60 | 3.07<br>2.54 | 2.73<br>2.42 | |
| 90° Mica gneiss B4 | 140 | 6.54<br>6.34 | 5.55<br>5.19 | 5.48<br>4.62 | 4.02<br>3.74 | 3.28<br>3.04 | 3.15<br>2.50 | Fewer AE, not failed |
| B2A | 140 | 5.40<br>4.79 | 6.38<br>5.93 | 5.83<br>5.10 | 2.92<br>2.72 | 3.07<br>2.79 | 2.80<br>2.26 | |

activity happening at the end of loading step 8, which showed some local damage on the corner of the specimen. Specimen B2 A was characterized with a different type of foliation (thicker quartz veins) and shows more AE activity located at the middle of the specimen.

## 4 CONCLUSIONS

Table 2 summarizes the key findings of this study and highlights the strength anisotropy, velocity measurements and AE activity for the two series of experiments. The results show that anisotropic gneiss subjected to the simulated loading path for canister placement in the POSE experiment exhibit failure in specimens with foliation oriented at 0, 30 and 60 degrees with respect to the major principle stress direction and the samples at 30 degrees are the weakest. For two of the specimens tested at 0 and 60 degrees, with respect to the maximum principal stress, failure happened when the intermediate principal stress was being unloaded. Higher $V_{PX}$ and $V_{PY}$ than $V_{PZ}$ for 90 degree specimens highlight the transversely isotropic nature of the gneissic samples. Similar phenomena were observed for $V_{PY}$ and $V_{PZ}$ for the 0 degree specimens. Temporal and spatial analysis of AE events show that fracture initiation and propagation are sensitive to foliation plane orientation and that failure planes coincide with foliation planes in failed specimens. The simulated true-triaxial POSE experimental loading and unloading path is complex and results in strength and behavioural characteristics which would not be replicated with conventional triaxial testing when $\sigma 2 = \sigma 3$.

## ACKNOWLEDGEMENTS

We thank Posiva Oy, Finland and Dr. T. Siren and J. Suikkanen for their support of this research and for providing the numerical simulations for the loading steps. We would also like to thank current and former members of the research group including Dr. Mehdi Ghofrani Tabari, Mahdi Sehizadeh and William Ye, Maria Tibbo and Dr Toivo Wanne for their contributions to this research. We are also grateful for the innovative ideas provided by Laszlo Lombos and Applied Seismology Consultants/Itasca for their software support. Young also thanks the Natural Sciences and Engineering Research Council of Canada for supporting the research program and students at the Rock Fracture Dynamics Facility with a discovery grant.

## REFERENCES

Hoek, E. & Martin, C.D. 2014. Fracture Initiation and Propagation in Intact Rock. *J. Rock Mechanics and Geotechnical Engineering* 6(4): 287–300.

Johansson, E., Siren, T. & Kemppainen, K. 2015. ONKALO – Underground Rock Characterization Facility for In-situ Testing for Nuclear Waste Disposal. *13th ISRM Congress 2015 on Rock Mechanics*, Montreal, Canada, May 10–13, 2015. ISBN 978–1-926872-25-4.

Kwasniewski, M., Li, M. & Takahashi, M. (Eds) 2013. *True Triaxial Testing of Rock*. Taylor and Francisco Group, Balkema.

Martin, C.D. 1997. The effect of Cohesion Loss and Stress Path on Brittle Rock Strength. *Can. Geotech. J.*, 34(5): 698–725.

Nasseri, M.H.B., Goodfelow, S.D., Lombos, L., and Young, R.P. 2014. 3-D Transport and Acoustic Properties of Fontainebleau Sandstone during True-triaxial Deformation Experiments. *Int. J. Rock Mech. Min. Sci.* 69: 1–8.

Nasseri, M.H.B. Sehizadeh, M, Ye, S.H. Young, R.P., Flynn, J.W., Suikkanen, J. & Siren, T. 2016 in Press. Strength, Deformation and Seismic Response of Olkiluoto Migmatitic Gneiss under Laboratory True-Triaxial Stress. *Proceedings ISRM Rock Stress Conference*.

Öhman, I., Heikkinen, E., Säävuori, H., Vuoriainen, S., Paulamäki, S., & Aaltonen, I. 2009. *Summary of Petrophysical Analysis of Olkiluoto Core Samples 1990–2008*. Posiva Oy.

Posiva Oy., 2013. *Olkiluoto Site Description 2011*. Report POSIVA 2011–02: Posiva Oy.

Valli, J., Hakala, M., Wanne, T., Siren, T. & Suikkanen, J. 2015. *Onkalo POSE Experiment – POSE Back Analyses Plan.* Posiva Working Report 2015–22. Posiva Oy, Finland.

Young, R.P. & Collins., D.C. 2001. Seismic Studies of Rock Fracture at the Underground Research Laboratory, Canada. *Int. J. Rock Mech. Min. Sci.* 38: 787–799.

Young, R.P., Nasseri, M.H.B. & Lombos, L. 2013. Imaging the Effect of Intermediate Principal Stress on Strength, Deformation and Transport Properties of Rocks Using Seismic Methods. In Kwasniewski, M., Li, M., and Takahashi, M. (Eds): *True Triaxial Testing Of Rocks.* Taylor and Francisco Group/ Balkema, 167–179.

*Experimental techniques and laboratory testing*

This page intentionally left blank

*Rock Dynamics: From Research to Engineering – Li et al. (Eds)*
*© 2016 Taylor & Francis Group, London, ISBN 978-1-138-02953-8*

# High strain rate response of Himalayan quartzitic gneiss by using split Hopkinson pressure bar device

Anuradha, S. Mishra, T. Chakraborty & V. Matsagar
*Department of Civil Engineering, Indian Institute of Technology (IIT) Delhi, New Delhi, India*

P. Chandel & M. Singh
*Terminal Ballastic Research Laboratory (TBRL), Defense Research and Development Organisation (DRDO), Chandigarh, India*

ABSTRACT: Mountainous rocks have been beneficial in developing the pathway for water flow in hydropower projects which aids in attainment of renewable source of energy. With the increase in the development of hydropower projects in mountains, the concern towards its design optimality increases to various hazards e.g. earthquake, bomb blast or missile attacks. Rocks when subjected to dynamic loading experiences a very high strain rate of $10^2$–$10^4$/sec. Therefore, it is required to study the response of rock under high strain rate loading. In the present work, the dynamic stress-strain response of a metamorphic rock, Quartzitic Gneiss having its origin from Himalayas is studied by using Split Hopkinson Pressure Bar (SHPB) device. The physical, petrological and static properties of the quartzitic gneiss are also studied. The increase of peak stress and elastic modulus with respect to increased strain rate is observed to study the dynamic behavior of the rock. The dynamic increase in strength of the rock with respect to the static strength of the rock is observed for different strain rates and a correlation for dynamic increase factor with respect to strain rate is given herein.

## 1 INTRODUCTION

Hydropower projects have a crucial role in the socio economic development of a nation. Right from electricity generation to irrigation hydel projects have felt their presence in every field. Now days numerous such projects have cropped up in mountainous terrain due to inherent gradient available for electricity generation. Any natural like near fault earthquake or manmade hazard like bomb blast, projectile attack damaging the structure will have a drastic impact on the life and property around it. Therefore the design of the structure is of paramount importance for the nation so that it can resist any unanticipated load in addition to the usual structural load and also the load from the surrounding rock mass. The unanticipated loads in the infrastructure may lead to high rate of loading in the surrounding rock with a strain rate in the range of $10^2 \sim 10^4$/sec. Both the strength and the stiffness of rocks are affected when subjected to such high rate of loading. Hence, it is necessary to characterize the response of rocks at such high strain rate for adequate design of the infrastructure through experimental and numerical investigations.

The numerical simulation of in situ stress conditions at various loading rates require use of experimental results at variuos strain rates and confinements as obseverd during any impact. Split Hopkinson Pressure Bar (SHPB) device is used to measure dynamic response of materials at a strain rate regime of $10^2 \sim 10^4$/sec (Field et al. 2004). The SHPB device was invented in 1949 by Kolsky (1949) and subsequently modified in 1953 by Kolsky (1953) for testing the dynamic properties of metals. In Civil Engineering practice, the SHPB tests were performed on various brittle materials such as concrete and ceramics (Ross et al. 1989 and 1995, Chen & Ravichandran 1996 and 2000, Sarva & Nemmat-Nasser 2001), rock (Perkins & Green 1970, Xia et al. 2008, Dai

et al. 2010) and others. Zhang et al. (2014) reviewed the mechanical behaviour of rock materials under different loading conditions. It was observed that under uniaxial loading the cracks initiation was axially parallel to the loading direction and degree of fragmentation increases with increasing loading rate. The critical cracks popagate in a much shorter time therefore rock fails before the real failure rate. The energy absorbing capacity of rock increases with inreasing strain rate but in case of smaller specimen the friction plays a predominant role thereby reducing the energy abosrbing capacity of rock. It was noted that it was not possible to measure the initial tangent modulus of rock at high strain as the stress equilibrium condition is not achieved in initial stage. Since no significant microcracks develop in the initial condition therefore it can be assumed that the elastic modulus remain unaffected by strain rate. Dynamic modulus is very sensitive to the fractures and fluctuates more easily. Non-uniformity and micro cracks in rock leads to abnormal behaviour in static and dynamic properties. The time of fracture in the SHPB device ranges from 1–100 μs. Doan & Gary (2009) stated that the failure pattern depends on the strain rate and the transition of faliure pattern from single fragment to intense fracturing can be observed at strain rate of 100/sec to 150/sec. It was also observed that the uniaxial compressive strength of rock increases linearly upto strain rate of $10^1$/sec. After that it increases dramatically. Zhang et al. (2014) performed the numercial simulation at different strain rates using the data from Mohr-Coulomb criteria and found out that the results are consistent at low confining pressure. However, Hoek Brown criteria represents the true dynamic triaxial condition at both low and high confining pressures as the m value remains unaffected at different loading conditions. Its was also observed that the with increase in temperature, the dynamic compressive strength decreases. The fracture toughness or resistance to crack propagation of the material is sensitive to the strain rate. For the dynamic study two effects, inertia effect and strain rate effect must be considered as described by Zhang et al. (2014). The use of samples of diameter 50 mm or 10 times the grain size with slenderness ratio of 0.5–1.0 and use of pulse shaping techniques can be used to minimise the interia effect.

However, high strain rate characterization of quartzitic gneiss has never been cited in the literature. The present study critically assesses the static and dynamic response of quartzitic gneiss. This rock was collected from lower Himalayas range located in Uttarakhand, India. The static tests have been carried out at Rock Engineering Laboratory, Indian Institute of Technology (IIT) Delhi, India. The dynamic tests have been carried out at Terminal Ballistics Research Laboratory (TBRL), Chandigarh, India.

## 2 EXPERIMENTAL SETUP

Split Hopkinson Pressure Bar (SHPB) or Kolsky apparatus is one of the most commonly used technique to determine material properties under extreme loading conditions in the strain rate regime of $10^2 \sim 10^4$/sec. Figure 1 shows the schematic diagram of the split Hopkinson pressure bar device which consists of three long cylindrical bars of the same diameter e.g., striker bar, incident bar and transmitter bar. In a compression test, the sample is fixed between the incident bar and transmitter bar. The bars in SHPB device is made up of maraging steel having yield strength equal to 1750 MPa. The diameter of striker, incident and transmission bars is 20 mm while length of the incident and transmission bars is 2000 mm each. The striker bar is accelerated using a gas gun and this produces a compressive stress wave in the input bar. The compressive stress wave travels through the incident bar and upon reaching the bar-specimen interface, a part of the stress wave is reflected back into the incident bar as reflected wave and a part gets transmitted through the interface into the specimen and then to the transmission bar. The incident stress pulse and transmitted stress pulse are measured in real time using strain gauges on the input and output bars (120 Ω, 900 tee rosette precision strain gages designated as EA-06–125TM-120) mounted at the mid-point positions along the length of two bars. Stress, strain and strain rate generated in the specimen is calculated using one dimensional wave propagation theory. In the present tests, pulse shapers of 0.2 mm were used to extend the initial rise time and the duration of the incident pulse to achieve constant strain rate loading within the specimen.

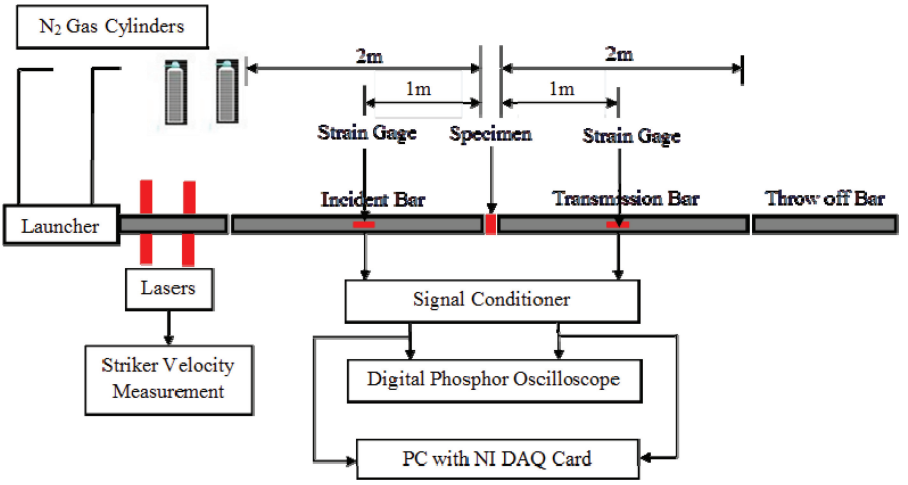


Figure 1. Schematic diagram of split Hopkinson pressure bar (Mishra. et al. (2015)).

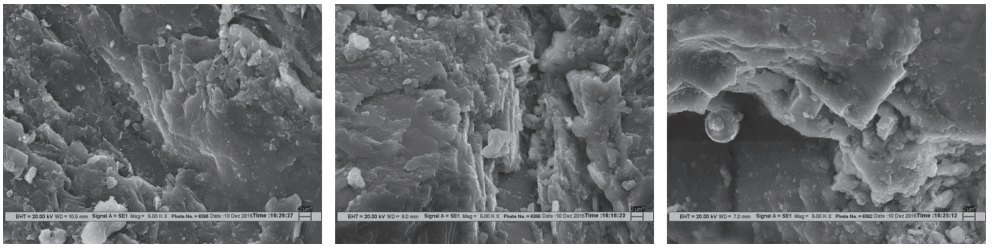

Figure 2. SEM test of the quartzitic gneiss at magnifications of 500x, 2500x and 5000x.

A conventional analysis in SHPB renders strain $\varepsilon_s(t)$, strain rate $\dot{\varepsilon}_s(t)$ and stress $\sigma_s(t)$ histories in the specimen given by the equations below.

$$\varepsilon_s(t) = -\frac{C}{L}\int_0^t \varepsilon_r dt, \varepsilon_s(t) = -\frac{C}{L}\varepsilon_r, \sigma_s(t) = \frac{A}{A_0}E\varepsilon_t \tag{1}$$

where $C$ is the elastic wave speed in the bar, $L$ is the length of the specimen, $A$ is the cross-sectional area of the specimen, $A_0$ is the cross-sectional area of the incident bar and the transmission bar, $\varepsilon_r$ and $\varepsilon_t$ are the strains developed in the reflected bar and the transmission bar, respectively.

## 3 EXPERIMENTAL DETAILS

### 3.1 *Petrological test*

The mineralogy and structure of the rock is identified by performing Scanning Electron Microscope (SEM), X-Ray Diffraction (XRD) and thin section tests. Scanning electron microscope test is conducted to understand the basic structure of the rock as shown in Figure 2.

X-ray diffraction test is conducted to analyse the minerology of the rock. The XRD graph is shown in Figure 3. It is observed that the rock contains a very high percentage of feldspar with mica and quartz. Some carbonate and kaolinite minerals are also present in the rock. Thin section concludes and confirms the mineral composition of rock found through XRD

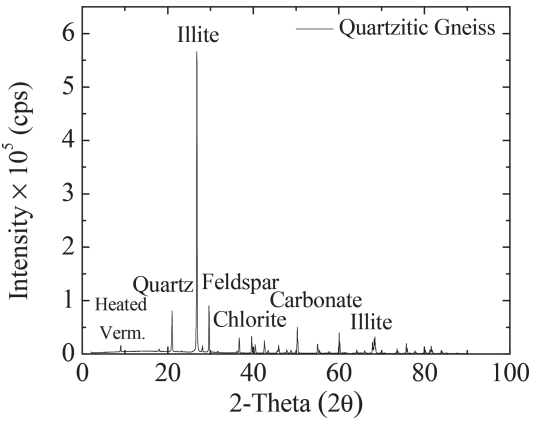


Figure 3. X-ray diffraction graph of quartzitic gneiss.

that it mainly consists of a very high percentage of quartz with biotite, orthoclase feldspar, muscovite which is lusterous in its appearance. It also has traces of amphibole. The test also shows that the rock is very opaque and has alternate bands of foliated and non-foliated structures.

### 3.2 *Static test*

The static tests are conducted in Rock Engineering Laboratory, IIT Delhi. The physical property tests e.g. dry density, specific gravity and slake durability, and static tests e.g. uniaxial compressive strength test and Brazilian test, are conducted. The dry density, specific gravity and slake durability of the rock are found to be 2615 kg/m$^3$, 2.667, and 99.56%, respectively. The uniaxial compressive strength and tensile strength of the rock are tested to be 81.72 MPa and 12.52 MPa, respectively. The Elastic modulus and Poisson's ratio of the rock are calculated to be 51.07 GPa and 0.16 respectively.

### 3.3 *Dynamic test*

The rock samples are prepared with diameter 18 mm and slenderness ratio 0.5 for dynamic test using SHPB device. The samples are made with perfectly parallel ends which is of paramount importance as slight undulation in the sample would lead to great variation in result. The rock samples of quartzitic gneiss are tested for dynamic compressive strength at high strain rates from 323/sec to 985/sec in SHPB device. The stress-strain curves have been plotted for different strain rate values and the peak stress is noted for each strain rate. Figures 4 (a), (b) and (c) shows the stress-strain response, peak stress and modulus of elasticity with increasing strain rate for quartzitic gneiss. Figure 4(a) shows the stress-strain response of Quartzitic gneiss for strain rates varying from 323/sec to 985/sec. The peak stresses obtained are 115.47 MPa at 323/sec, 104.05 MPa at 370/sec, 166.65 MPa at 550/sec, 189.15 MPa at 710/sec, 269.64 MPa at 877/sec and 221.56 MPa at 985/sec. It can be seen from Figure 4(b) that the peak stress increases with increase in strain rate. It can be seen that there is an increase in strength of rock by approximately 22% for strain rate till 877/sec. The elastic modulus remains approximately constant for all the strain rates tested. It can be explained by the plastic flow of the rock beyond the elastic limit under higher rate of loading. The elastic modulus is insensitive to increase in strain rate. The increase in elastic modulus and decrease in peak strength for strain rate of 985/sec may be due to experimental error.

The strength of the rocks increases rapidly with increase in the loading rate from quasi-static to dynamic. The dynamic compressive stress 269.64 MPa at 877/sec is more than thrice as that of static compressive stress dynamic increase factor (*DIF*) is calculated for the strain

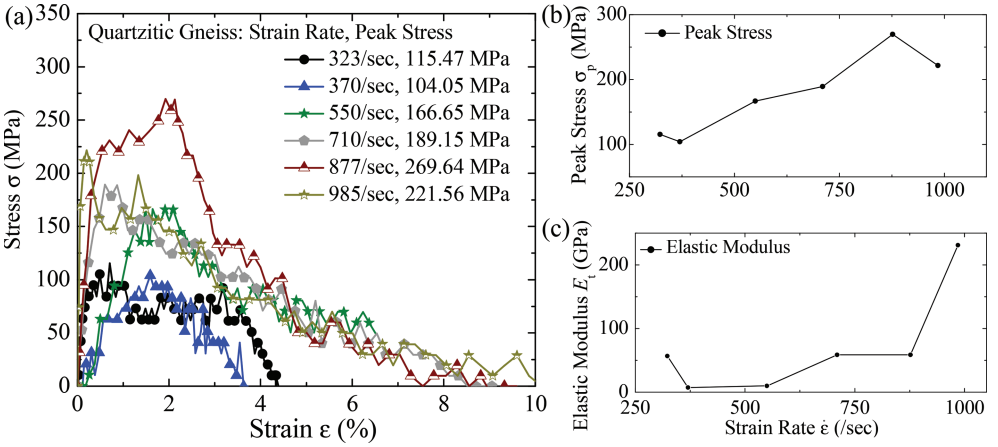


Figure 4. (a) Stress vs strain response of quartzitic gneiss (b) Peak stress vs strain rate (c) Elastic modulus vs strain rate.

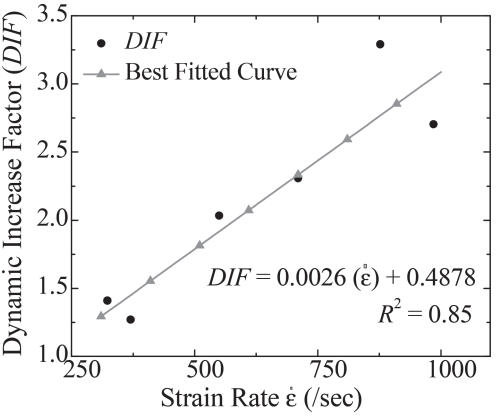


Figure 5. Dynamic increase factor vs strain rate.

rate tested by comparing the dynamic strength with the static strength. From Figure 5, it is seen that the dynamic strength of quartzitic gneiss varies from 1.2 to 3.2 times the static strength for a strain rate range of 323 to 985/sec.

A correlation equation has been developed for the calculated dynamic increase factors with strain rate by setting a best fitted curve through the obtained results with coefficient of determination ($R^2$) = 0.85 which satisfies the 95% confidence interval. The correlation for quartzitic gneiss is given by

$$DIF = 0.0026(\dot{\varepsilon}) + 0.4878 \quad \text{for 323/sec to 985/sec} \tag{2}$$

It may be noted that the *DIF* equation will be applicable for the strain rate range considered in the current work.

## 4 CONCLUSIONS

High strain rate characterization of quartzitic gneiss have been carried in the present work for a strain rate range varying from 323/sec to 985/sec through compressive SHPB test. The physical properties and static stress-strain behavior of the rocks have also been studied. The

following conclusions are drawn from the tests. The peak stress increases by 22% for strain rate till 877/sec. The modulus of elasticity of the rock is insensitive to strain rate. An equation for the Dynamic Increase Factor (*DIF*) has been proposed for quartzitic gneiss given by

$$DIF = 0.0026(\dot{\varepsilon}) + 0.4878 \quad \text{for 323/sec to 985/sec}$$

## REFERENCES


Blanton, T.L. 1981. Effect of strain rates from $10^{-2}$ to 10 $sec^{-1}$ in triaxial compression tests on three rocks. *International Journal of Rock Mechanics and Mining Sciences and Geomechanics Abstracts* 18(1): 47–62.

Chen, W. & Ravichandran, G. 1996. Anexperimental technique for imposing dynamic multiaxial compression with mechanical confinement. *Experimental Mechanics* 36: 155–158.

Dai, F., Xia, K.W. & Tang, L.Z. 2010. Rate of dependence of the flexural tensile strength of Laurentian Granite. *International Journal of Rock Mechanics and Mining Sciences* 47: 469–475.

Doan, M. -L., Gary, G. 2009. Rock pulverization at high strain rate near the San Andreas fault. *Nat. Geosci.* 2(10): 709–712.

Field, J.E., Walley, S.M., Proud, W.G., Goldrein, H.T. & Siviour, C.R. 2004. Review of experimental techniques for high rate deformation and shock studies. *International Journal of Impact Engineering* 30(7): 725–775.

Fuenkajorn, K. & Kenkhunthod. N. 2010. Influence of loading rate on deformability and compressive strength of three Thai sandstones. *Geotechnical and Geological Engineering* 28: 707–715.

Fukui, K., Okubo, S., Ogawa, A. 2004. Some aspects of loading-rate dependency of Sanjome andesite strengths. *International Journal of Rock Mechanics and Mining Sciences* 41(7): 1215–1219.

Gray, G. 2000. Classic split-Hopkinson pressure bar testing. In: *American Society of Metals handbook, Mechanical Testing and Evaluation*, Kuhn, H. & Medlin, D. (Eds.), Ohio, USA, ASM International, American Society for Metals, 8, 1027–1094.

Lu, Y.B., Li, Q.M., Ma, G.W. 2010. Numerical investigation of the dynamic compressive strength of rocks based on split Hopkinson pressure bar tests. *International Journal of Rock Mechanics and Mining Sciences* 47(5): 829–838.

Lundberg, B. 1976. A split Hopkinson bar study of energy absorption in dynamic rock fragmentation. *International Journal of Rock Mechanics, Mining Sciences and Geomechanics Abstracts* 13: 187–197.

Ming, L., Xian-biao, M., Li-li, C., Rong-rong, M., Guang-hui, Z. 2014. High strain rate effects on mechanical behavior of coal-serial sandstone. *Electronics Journal of Geotechnical Engineering* 19: 6035–6046.

Mishra, S., Parashar, V., Chakraborty, T., Matsagar, V., Chandel, P., Mangla, V., Singh, M. 2015. High strain rate response of sedimentary rocks under dynamic loading using split Hopkinson pressure bar. *Protect 2015—Fifth International Workshop on Performance, Protection & Strengthening of Structures under Extreme Loading,* Michigan State University in East Lansing.

Olsson, W.A. 1991. The compressive strength of tuff as a function of strain rate from $10^{-6}$ to $10^{3}$/sec. *International Journal of Rock Mechanics, Mining Sciences and Geomechanics Abstracts* 28(1): 115–118.

Qi, C.Z., Wang, M.Y., Qihu, Q. 2009. Strain-rate effects on the strength and fragmentation size of rocks. *International Journal of Impact Engineering* 36: 1355–1364.

Ross, C.A., Thompson, P.Y. & Tedesco J.W. 1989. Split Hopkinson pressure-bar tests on concrete and mortar in tension and compression. *ACI Materials Journal* 86: 475–481.

Sarva, S., Nemat-Nasser, S. 2001. Dynamic compressive strength of silicon carbide under uniaxial compression. *Materials Science and Engineering A* 317 (1–2): 140–144.

Xia, K., Nasseri, M.H.B., Mohanty, B., Lu, F., Chen, R. & Luo, S.N. 2008. Effects of microstructures on dynamic compression of Barre granite. *International Journal of Rock Mechanics and Mining Sciences* 45: 879–887.

Zhang, Q.B., Zhao, J. 2014. A review of dynamic experimental techniques and mechanical behaviour of rock materials. *Rock Mechanics and Rock Engineering* 47: 1411–1478.

Zhao, J., Li, H.B., Wu, M.B., Li, T.J. 1999. Dynamic uniaxial compression tests on a granite. *International Journal of Rock Mechanics and Mining Sciences* 36: 273–277.

*Rock Dynamics: From Research to Engineering – Li et al. (Eds)*
*© 2016 Taylor & Francis Group, London, ISBN 978-1-138-02953-8*

# Overview of geological materials research at the Cavendish Laboratory

C.H. Braithwaite, S.S. Kirk, A.P. Jardine & J.E. Field
*SMF Group, Cavendish Laboratory University of Cambridge, UK*

ABSTRACT: Over a number of years, the Fracture and Shock physics group has engaged with the blast mining industry to investigate the physics of geological materials. This has encompassed a wide variety of materials including a number of sandstones, gneiss, schist, granite and iron ore. Efforts have mainly focused on loading the materials using a gas gun in a one dimensional strain configuration to measure high strain rate properties in compression, tension and shear. Progress has been made towards generalizing these results to provide predictive methodologies for other materials. In addition, a methodology has been developed to examine, using a variety of time resolved and post experimental diagnostics, the fragmentation of small geological samples under explosive loading. Results from a variety of experiments will be presented, along with a discussion of future directions and challenges in the field.

## 1 INTRODUCTION

Geological materials are the source of a significant amount of the resources that are relied on to ensure that the modern world continues to function. The vast majority of these materials are obtained through the process of blast mining, which subjects the materials to a high rate, high amplitude loading regime. As more material is mined, yields tend to fall, and this has meant that optimizing the process of blast mining has become increasingly important to mining companies. Much of the effort has focused on developing computational modelling tools (Onederra 2013), however there is a requirement for these models to be underpinned by experimental data, and a thorough understanding of the underlying scientific processes that govern the material behavior.

The Fracture and Shock Physics Group at the University of Cambridge has a long standing interest in the high rate properties of materials including geological materials. Facilities have been developed to enable information to be gathered across a range of strain rates, from quasi-static, to shock loading. Additionally, many of these techniques are able to be applied to different loading geometries, probing material response in compression, tension and shear. Recently the group has been developing laboratory methods to study fragmentation with a geometry and loading profile that is more representative of the situation found in a borehole, to help to bridge the gap to larger scale studies that have been conducted elsewhere.

This paper mainly focusses on the obtaining of material data in the shock regime and discusses some of the main challenges found when investigating geological materials. It has a focus on materials that are intact, meaning that research on sands, for example, has been excluded. Additionally, while some comments are made about the properties of porous geological materials, the majority of the research has been conducted on fully dense, polycrystalline materials. It has not been possible within the confines of this publication to do justice to all of the data obtained, so where relevant further details can be found in the referenced publications.

## 2 MATERIALS

Owing to the huge variety of geological materials it is not possible to conduct full experimental investigations of all possible materials one will encounter in a mining situation. In order to

Table 1. Densities and sound speeds for a variety of geological materials investigated at the Cavendish.

| Material | Density (kg m$^{-3}$) | Longitudinal sound speed (m s$^{-1}$) | Shear sound speed (m s$^{-1}$) |
|---|---|---|---|
| Lake Quarry Granite (Kirk 2014) | 2666 ± 3 | 5430 ± 20 | 3500 ± 20 |
| Gosford Sandstone (Kirk 2014) | 2096 ± 15 | 2330 ± 30 | 1460 ± 30 |
| Siltstone (Braithwaite 2009) | 6860 ± 110 | 3790 ± 80 | 2838 ± 7 |
| Kimberlite (Braithwaite 2009) | 5530 ± 80 | 2890 ± 40 | 2760 ± 20 |
| Amphibolitic Gneiss (Braithwaite 2009) | 6380 ± 80 | 3880 ± 100 | 2664 ± 10 |
| Amphibolite (Braithwaite 2009) | 6610 ± 50 | 3890 ± 40 | 3001 ± 5 |
| Quartz/Feldspathic Gneiss (Braithwaite 2009) | 5720 ± 190 | 3500 ± 90 | 2650 ± 2 |
| Sandstone (Braithwaite 2009) | 1970 ± 50 | 1360 ± 20 | 1926 ± 5 |
| Biotite Schist (Braithwaite 2009) | 5970 ± 160 | 3530 ± 70 | 2893 ± 8 |
| Basalt (Braithwaite 2009) | 5020 ± 50 | 2290 ± 20 | 2675 ± 9 |
| Iron Ore (Braithwaite 2009) | 6030 ± 200 | 3430 ± 80 | 4460 ± 160 |
| Gabbro (Millett 2000) | 6210 ± 10 | 3510 ± 20 | 2880 ± 20 |
| Dolerite (Tsembelis 2001) | 5890 ± 70 | 3340 ± 110 | 2890 ± 30 |
| TKB (Willmott 2004) | 3560 ± 40 | 1850 ± 10 | 2490 ± 40 |

generalize the results therefore to other materials it is necessary to conduct simple, well controlled characterization investigations to elucidate some of the fundamental material properties that can then be compared against unknown materials. The simplest of these are density and sound speed measurements, both in longitudinal and shear directions. This allows for derived quantities such as various moduli and the poisons ratio to be determined. These are tabulated for a variety of geological materials examined at the Cavendish in Table 1.

While these simple techniques have a lot to offer in terms of material characterization, there are a number of other techniques which have been employed in order to give increased levels of information, specifically at the grain level. Modern electron microscopy can be combined with a backscatter electron and x-ray detectors to give information about mineralogical contents. While this is only a slice through a sample, a number of samples can be processed to build up picture of the average. Furthermore, the identification of grain types leads to the possibility of using advanced techniques such as hydrocodes with the ability to import microstructure, assuming that suitable material models can be found for the mineral types concerned. Once constituent mineral types have been identified, and assuming that suitable contrast can be found between them, then x-ray tomography allows for a fully three dimensional picture to be constructed. This gives a significantly enhanced appreciation of the interactions between the grains and how this might affect the material response.

## 3 EXPERIMENTAL TECHNIQUES

The majority of the experiments were conducted using the Cavendish plate impact facility (Bourne 1995), a single stage light gas gun capable of accelerating projectiles to a velocity of around 1100 m/s. This generates stresses in the majority of geological materials up to around 20 GPa, which is appropriate to the blast mining regime. The gun has a 2 inch bore which means that geological samples can reasonably be expected to be representative of the bulk, at least over relatively modest length scales.

The gas gun experiments have been used to probe compressional behavior, both in a forward (standard material flier plate, rock target) and reverse (rock flier in to a well characterized witness plate) ballistic configuration, shear strength (through the measurement of lateral stresses) and dynamic tensional strength using a spall geometry. The compressional behavior also includes information about the unloading of the sample upon the release of the high pressure state.

Care has to be taken with the diagnostics for experiments with geological materials owing to the inhomogeneity of the materials and also potential piezoelectric effects. For this reason, in some materials the use of in-material stress gauges is inappropriate, and laser based

interferometric diagnostics have been used as an alternative. In all cases there is a risk that the portion of the sample measured will not be representative. Without the ability to spatially resolve diagnostics, such an effect is unavoidable, however any effect should be shown up in the results as a scatter about the mean value that shows the "bulk" response.

The fragmentation experiments have been adapted from a system developed for metal rings (Braithwaite 2012). While the data is currently not available to be published, fragmentation experiments have been conducted, with time resolved velocimetry, high speed photography and soft capture of fragments. This allows for investigations into particle size distributions on a small scale, that can be directly related back to the original microstructure of the material.

## 4 RESULTS AND DISCUSSION

### 4.1 *Compression*

In compression the main output of the experiments is a Hugoniot relationship. This shows the locus of states that can be achieved in a single shock loading, from an initial state. This is expressed in terms of a number of variables, and while a pressure-volume space would be logical from a thermodynamics point of view, it doesn't correspond to the measurements that are made, and so pressure-particle velocity is more commonly used instead. In such a space, an elastic material will have a linear relationship between the two variables. This is what we find for the majority of non-porous polycrystalline geological materials, as shown in the example in Figure 1a. However, it can be shown from looking at the lateral stress in the materials that the elastic limit is far below the maximum stress that the material appears to behave elastically. This seeming discrepancy can be explained by considering the fact that the non-elastic processes that occur in rocks are generally related to fracture, which might be expected to have a greater influence on the shear behavior than the compressional. Considering the material is inertially confined in the experiments the compression of a material which has "fractured" but has not been allowed to move apart would not be expected to be significantly different from the intact material. A difference can be seen however when looking at the unloading curve, although this is still relatively elastic in nature when compared for example to materials that undergo compaction. An example of the Hugoniot and release in sandstone is shown in Figure 1b, and contrasts significantly with the non-porous material. Firstly, there is no measurable elastic behavior, as the material begins to crush up under almost any level of loading and the release is significantly different to the loading line (which is a straight line from the origin to the Hugoniot point, it does not follow the Hugoniot). This is of importance, as the difference between the two gives an insight into the amount of energy that is lost during a loading-unloading cycle, i.e. significantly more in the porous material.

Prediction of these Hugoniot properties is important. Any prediction methodology needs to be simple to apply and involve relatively little experiment. For porous materials it is possible

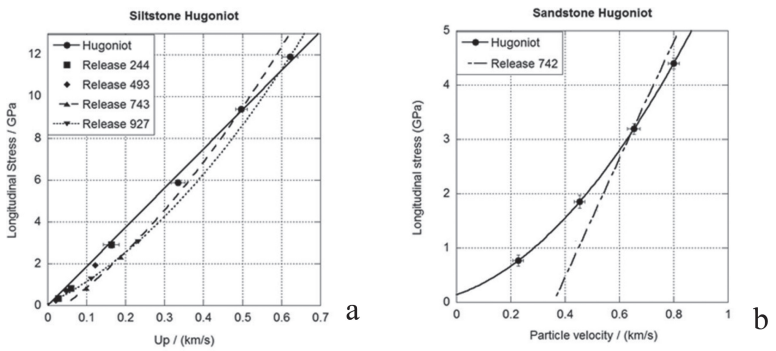


Figure 1. Hugoniots for siltstone (a) and sandstone (b) the linear behavior in siltstone contrasts with compaction in sandstone. The release paths are also different implying greater energy absorption in sandstone.

to apply compaction models such as the p-alpha and p-lambda model to the data, but these, like with most compaction models are mostly empirical fits, and currently a good predictive methodology has not been found. A better attempt can be made in the non-porous case. As the material is behaving as though it were elastic, a comparison with the elastic modulus (found from the product of the longitudinal sound speed and the density) shows a reasonable correlation, as can be seen in Figure 2. It is possible that with additional information about how sound propagates through the structure combined with characterizing the properties of the individual minerals that this could be improved still further.

### 4.2 *Shear loading*

Using stress gauges in two different orientations and taking the difference in the stress recorded gives a measure of the shear strength, and doing this at different impact velocities allows a trend of shear strength with increasing pressure to be determined. An example of this is shown in Figure 3. The point of departure from elastic loading is known as the Hugoniot elastic limit. Ideally it would be possible to predict this point from a simple measurement, but so far this has not been possible. One suggestion is that as the non-elastic behavior is mostly fracture based, that an approach based on a Griffiths type flaw criteria might be suitable. Unfortunately, it is not simple in geological materials to determine what the intrinsic flaw size is. Certainly the grain size is one potentially important length scale, and empirically it can be seen that in the materials examined most of the materials with a higher HEL have a smaller grain size. However, there is no obvious trend beyond this with the current data. A table of measured elastic limits is given in Table 2.

### 4.3 *Dynamic tension*

Measurement of dynamic tension in geological materials is difficult, particularly when compared with more homogeneous materials. However, the failure of material in tension, due to wave reflection, is very important in the blast mining process (Field 1971). While it has been possible to make some measurements, as shown in Table 3, the scatter on the measurements is large, and in many cases the experimental techniques used do not produce adequate data. The reason for this is possibly that the spall geometry relies on a material failing along a plane that is oriented in a particular direction. In a geological material however it is likely that failure will initiate along weak grain boundaries and then progress in the direction of the grain boundary. This may well not be in the direction of the plane that is expected, thus meaning that the measurements to not capture the spall behavior correctly. In addition, compared with many materials, the tensile strength is relatively low, which again makes measurements more complicated.

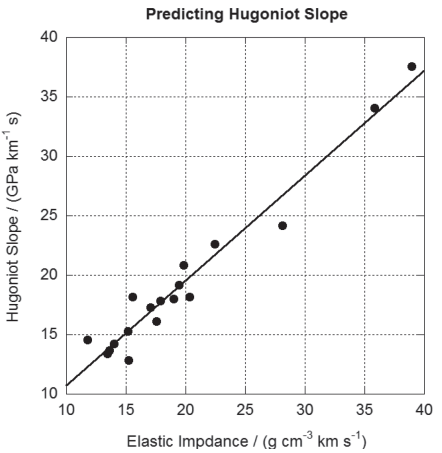


Figure 2. Plot showing correlation of elastic impedance and slope of Hugoniot for the materials in this paper and various values from literature (Marsh 1980).

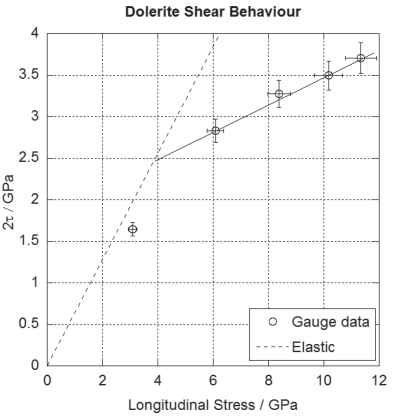


Figure 3. Shear behavior in dolerite, showing an elastic response and deviation from that above ~4 GPa.

Table 2. Measured elastic limits for geological materials.

| Material | HEL (GPa) |
|---|---|
| Siltstone (Braithwaite 2009) | 4.8 |
| Kimberlite (Braithwaite 2009) | 1.6 |
| Quartz/Feldspathic Gneiss (Braithwaite 2009) | 1.3 |
| Basalt (Braithwaite 2009) | 4.2 |
| Iron Ore (Braithwaite 2009) | 3 |
| Gabbro (Millett 2000) | 3.9 |
| Dolerite (Tsembelis 2001) | 3.8 |
| TKB (Willmott 2004) | 0.6–0.9 |

Table 3. Measured dynamic tensile strengths for geological materials, note the biotite schist value is based on only one measurement.

| Material | Tensile strength (GPa) |
|---|---|
| Siltstone (Braithwaite, 2009) | 55 ± 6 |
| Kimberlite (Braithwaite, 2009) | 21 ± 4 |
| Biotite schist (Braithwaite, 2009) | ~26 |

## 5 FUTURE DIRECTIONS

While this paper presents a fairly wide ranging series of experimental investigations into geological materials, it is clear that there are still significant knowledge gaps Future research should address these with an aim to refine and improve predictive capability of computation models.

Grain level diagnostics can potentially provide an insight into the effect that microstructure has on the material response. Geological materials have often, as in the case of this paper, been treated as a continuum, which is clearly an approximation given that they are generally heterogeneous. Fracture and fragmentation properties in particular are likely to be microstructure influenced, and improved measurements in this area would be a great benefit to industry. Porous geological materials currently lack a coherent understanding of the compaction behavior, again something which could be probed with improved diagnostic capability. The above challenges can also be further complicated by the addition of environmental considerations. All of the experiments presented in this paper were conducted at room temperature, under no compressive load and in a rough vacuum. This is not representative of the conditions that these materials are encountered in certain mining situations, and research needs to be conducted in this area.

Computational modelling is also an area where significant improvements have been made in recent years. A trend towards multi-scale modelling, where the effects at a small scale are used to inform material behavior at a larger scale would appear to be ideally suited to some of the challenges of working with geological materials at high rates. However, some of the advances in this area are dependent on the development of suitable material models for individual minerals.

## 6 CONCLUSIONS

Over a number of years, a wide range of geological materials have been investigated in the Cavendish Laboratory in a plate impact geometry, examining materials in compression, tension and shear. However, emphasis has been placed on characterization of materials prior to dynamic experimentation to make generalization and prediction of the properties of unknown materials more straightforward. This has involved simple measurements of density and sound speed, as well as more complex apparatus such as electron microscopes and x-ray tomographs.

In compression a predictive methodology has been found, comparing the slope of the Hugoniot to the measured elastic impedance of the material. However, a greater understanding of the minerology would allow for this method to be improved. Porous materials are more problematic, and currently compaction behavior is not well modelled or predicted from a first principals basis.

Shear measurements have managed to elucidate the elastic limits of some materials, but at the current stage, not enough materials have been investigated to allow for generalizations to be made about behavior. In addition, further efforts are required in the characterization of the materials in the static state to allow for predictions to be made of shear strength for a given unknown material.

Tensile measurements have similar problems to shear measurements. More research needs to be conducted to understand the mechanisms of tensile failure in geological materials. However, with access to more diagnostic measurement points, and combined with data taken from alternative loading geometries such as explosively loaded rings, it is likely that progress can be made.

## ACKNOWLEDGEMENTS

The authors acknowledge the support of a number of companies including, De Beers, Rio Tinto and Orica. Technicians in both the Cavendish Laboratory and the University of Cambridge Earth Sciences department were invaluable in preparing specimens and experimental apparatus.

## REFERENCES

Bourne, N.K. et al. 1995. Design and construction of the UK plate impact facility. *Meas. Sci. Technol,* 6: 1462–1470.

Braithwaite, C.H. 2009. *High Strain Rate Properties of Geological Materials*. PhD, Cambridge.

Braithwaite, C.H., et al. 2012. Comparing CTH simulations and experiments on explosively loaded rings. *Shock Compression of Condensed Matter* 1426(1): 1049–1052.

Field, J.E. & Ladegaard-Pedersen, A., 1971. The importance of the reflected stress wave in rock blasting. *Int. J. Rock Mech. and Min. Sci.* 8: 213–226.

Kirk, S.S.et al. 2014, Shock compression of geological materials. *Journal of Physics: Conference Series 500, 062005.*

Marsh, S.P. 1980. *LASL Shock Hugoniot Data*. University of California Press, Berkeley, California.

Millett, J.C.F., Tsembelis, K. & Bourne, N.K. 2000. Longitudinal and lateral stress measurements in shock-loaded gabbro and granite. *J. Appl. Phys.* 87: 3678–3682.

Onederra, I.A. et al. 2013. Modelling blast induced damage from a fully coupled explosive charge. *International Journal of Rock Mechanics and Mining Sciences* 58: 73–84.

Tsembelis, K. et a, 2001. The principal Hugoniot and dynamic strength of dolerite under shock compression. In *Shock Compression of Condensed Matter — 2001*, Furnish M., Thadhani N. & Horie, Y. (Eds.), AIP, Melville, NY, 1385–1388.

Willmott, G.R. 2004. *Shock Studies of Kimberlite, Diamond and Brittle Embedded Particles*. PhD, Cambridge.

*Rock Dynamics: From Research to Engineering – Li et al. (Eds)*
*© 2016 Taylor & Francis Group, London, ISBN 978-1-138-02953-8*

# Study of rock inhomogeneity with ultrasonic tomography using concrete block and limestone block at laboratory scale

Herman, N.P. Widodo & I. Arif
*Institut Teknologi Bandung, Bandung, Indonesia*

ABSTRACT: Ultrasonic wave propagation test is a non-destructive test that can be used to detect inhomogeneity of rock. Time of Flight (ToF) of ultrasonic wave was measured by direct method through the interior of block, using PUNDIT device (Portable Digital Indicating Non-destructive tester) with transducer of stress wave in ranges of frequency 80 kHz. Two reconstruction algorithms have been used, namely, the tomographic ART algebraic reconstruction technique and the SIRT simultaneous iterative reconstructive technique, in order to represent a contour map of ultrasonic velocity distribution within the block observed. All the tests were conducted at laboratory scale on several blocks, such as concrete block with artificial void, concrete block with artificial discontinuity, and limestone block with two artificial holes, furthermore the ultrasonic method were applied to detect these conditions. The results show that the tomographic algorithm is proven as a tool to detect the inhomogeneity of the block.

## 1 INTRODUCTION

Ultrasonic wave propagation test is a non-destructive test that can be used to detect the condition of structure or to detect the inhomogeneity of rock, such as the damage of the rock, fracture, and void that can be recognize as a weak travel time of ultrasonic wave compared to one that travel through the solid rock. The principle of ultrasonic test is a measurement of traveling time from certain point (transmitter) to another point (receiver), and this written as a Time of Flight (ToF). The ultrasonic velocity is the length of those two points divided by the ToF. The measurement method is conducted by measure ultrasonic velocity at several point around the object, then by combining that ultrasonic ToF measurement results, we may know the imaging of material interior, and this technique is known as Ultrasonic Tomography.

Tomography refers to the cross-sectional imaging of an object from either transmission or reflection data collected by measurement of the object from many different direction (Kak and Slaney 1987). The early application of tomography is in medical purpose, in order to detect internal organs. And now tomography is widely use to other disciplines, such as biology, geophysics, oceanography, plasma physics, material science, etc (Grangeat 2009).

One of the tomographic technique that widely use is the iterative method (Kaczmarz algorithm) that was developed by Kaczmarz in 1928, then by Gordon in 1970 develop that method into an Algebraic Reconstruction Technique (ART). The ART technique has been used by Haach and Juliani (2014), who researched about ultrasonic tomography to detect damages in concrete. The research was tried to reconstruct image from concrete prism, before and after uniaxial loading. From the ultrasonic measurement, the reconstruction map of velocity was successfully recognized the discontinuities and the damage (Haach and Juliani 2014).

In this present research, several sample are prepared, limestone block and concrete block are built and test. The reconstruction algorithm applied into this sample for mapping an

ultrasonic velocity. Algorithm, calculation and interpretation was applied into computer programs, by using MS Excel (Microsoft 2010) and Matlab (MathWorks). Neural network for imaging was also carried out based on the result of the reconstruction data.

## 2 TOMOGRAPHIC IMAGING

Ultrasonic tomography obtained by combining an ultrasonic wave velocity measurement test taken from various sides that intersect. Tomographic is a technique about study of the problem on an object base on measurement of transmitted or emitted radiation, in this case radiation energy is from ultrasonic wave. The Algebraic Reconstruction Technique is used in this study to solve linear equation, where the mesh or pixel must be defined before the calculation starts. $f_j$ is the mesh value, $i$ is the iteration number, ToF ($p_i$) value is taken directly from the measurement, $q_i$ is computed ToF based on weighted length and intensity of mesh, the $w_{ij}$ is the length of the path in the element of certain mesh, and $w^2_{ik}$ is the normalizing factor for this equation, where the value is measured from each mesh that contact with wave from measurement. According to Kak and Slaney (1987) the algebraic reconstruction can be mathematically described by

$$f_j^{(i)} = f_j^{(i-1)} + \frac{(p_i - q_i)}{\sum_{k=1}^{N} w_{ik}^2} w_{ij} \tag{1}$$

where, $q_i$ is

$$q_i = f_j^{(i-1)} . \overrightarrow{w_i} = \sum_{k=1}^{N} f_j^{(i-1)} w_{ik} \tag{2}$$

Algebraic reconstruction is an algorithm to produce a linear equation using an iterative method to solve the equation. There is two algorithm used to solve the equation, that are ART (algebraic reconstruction technique) and SIRT (simultaneous iterative reconstructive technique). The ART is an algorithm where the first initial value for each pixel is projected to the first equation of linear system. The value of the first equation is then projected on the second equation and so on, repeated in an iterative process. Whereas SIRT is an iterative algebraic algorithm where a first initial value is projected on first equation for all measurement point, then the mean value is calculated and the procedure is repeated in an iterative process.

## 3 EXPERIMENTAL METHODOLOGY

Several blocks were prepared in this study, which are limestone block with two holes given in the top side, the dimension 20 cm × 20 cm × 7 cm, concrete block with cement and sand ratio 1:3 with dimension 21 cm × 21 cm × 21 cm with two baseball inserted in the block, the other block was a laminated block also prepared to test, and concrete block with dimension 45 cm × 45 cm × 30 cm with hole in the middle and discontinuous plane. The ultrasonic velocity was measured with ultrasonic tools PUNDIT, and the coupling between the transducer face and the sample was greased to avoid a small rough surface. Figure 1 is the measuring point and meshing for small block.

All measurement done to all sample, limestone and concrete block, where total measurement for small block 20 cm and 21 cm is 144 times, and for big block 45 cm, total measurement is 676 times. There are two different sizes of the pixel or mesh, 36 total meshes for small block, and 169 meshes for big block. All the blocks that have been prepared can be seen in Figure 2.

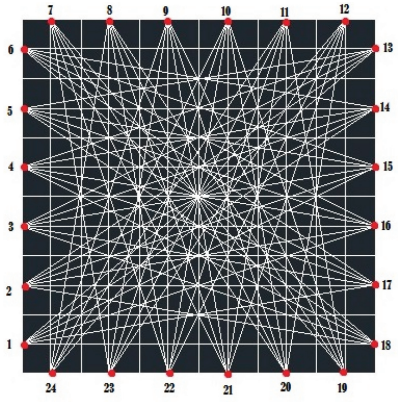


Figure 1. Measurement point and meshing for tomographic imaging.

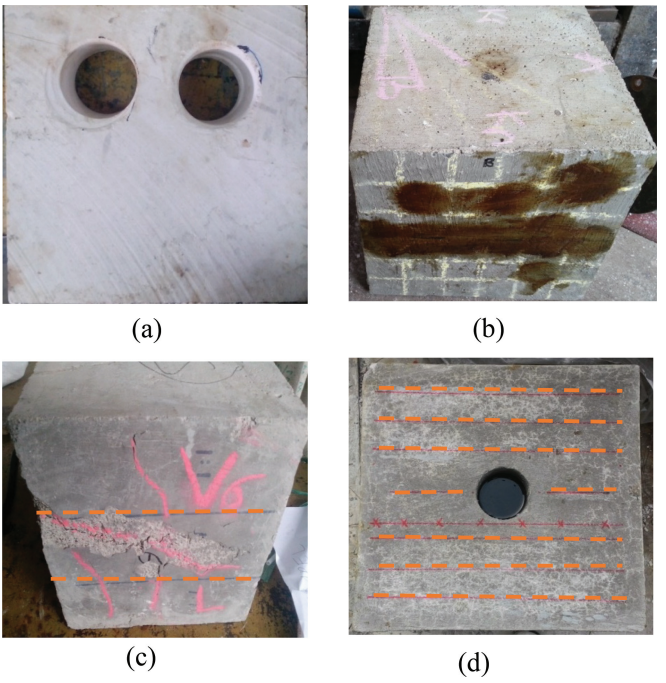


Figure 2. (a) Limestone block with two discontinuous, (b) Concrete block with baseball inserted, (c) Damaged laminated block, (d) Concrete block with center hole and discontinuity.

## 4 RESULT AND ANALYSIS

Measurement points must be defined to get the map of ultrasonic wave velocity, the measurement points and mesh were set according to Figure 1. Result from reconstruction for each mesh is show in the map of velocity, the color ranges is default by Matlab program. To get the smooth result from reconstruction, the result was interpolated with 2D interpolation using Matlab code (interp2), from 36 meshes to 25921 meshes. In this research Artificial Neural Network ANN also done to study the data from reconstruction using Matlab, Figure 3 present a contour map using ART and SIRT algorithm for limestone block.

Data from the Figure 3 show the Time of Flight versus distance of the ultrasonic measurement, where the ToF increases with the increase of the distance. This figure is for limestone

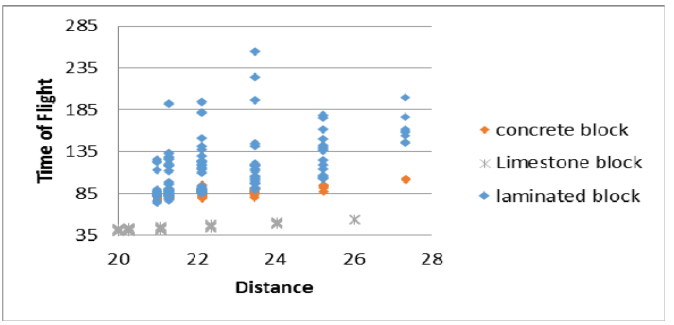


Figure 3. Distance versus Time of Flight of ultrasonic measurement.

block, concrete block with baseball inserted, and concrete that has been damaged and cast by different composition of concrete (laminated). A total of 144 measurements were performed for each block, limestone and concrete block show a good result with slow increasing of time when the distance getting further. For laminated block, show a higher dispersion of the data.

Figure 4 shows that the SIRT algorithm give a better result than ART algorithm, discontinuity can be recognized clearly from SIRT, where the map of ultrasonic velocity show blue color in the top side, that mean there is some discontinuity there, or the velocity of ultrasonic wave is get slower than other side of contour map. And for ART, there is more dispersion of blue area, however it is hard to identify the condition of block (in this case, limestone with holes).

For the concrete block with baseball inserted (Fig. 5), the region of baseball can be clearly identified, the higher value shows in the map with red color. SIRT (Fig. 5a) shows a close position of baseball according to block, while for ART algorithm, the position of baseball likely move to the top with high dispersion value show in the map velocity (Fig. 5b). The comparison of two algorithms shows that the SIRT algorithm gives better value and close to actual measurement ultrasonic velocity value (the value of reconstruction is 4200 m/s to 5600 m/s for limestone block, and for concrete block is 2400 m/s to 2900 m/s). However, the ART algorithm shows a higher range of value (4600 m/s to 6600 m/s for limestone block and 2400 m/s to 3400 m/s for concrete block).

Furthermore, Laminate block and big concrete block were also prepared for ultrasonic tests. All the measurement of this block has been applied to the algorithm reconstruction SIRT, and the result is shown in Figure 6(a), where the discontinuity is hard to detect and the technique cannot be used to clearly identify the major discontinuity. The block damage and the lamination make the high range value of ultrasonic velocity.

Figure 6(b) is a reconstruction by SIRT algorithm of concrete block with center hole as shown in Figure 2(d). The result shows a detection of center hole by recognizing of velocity map, which the minimum velocity is marking by blue color. Discontinuity plane gives effect to the measurement result, that the ultrasonic velocity slower when passing through the plane. Therefore, when it reconstructed, the mesh value gives same effect as mesh with the hole. Compare with the velocity in the same direction with the discontinuity plane the mesh value gives higher velocity (red color).

In addition to the reconstruction algorithm SIRT and ART, Artificial Neural Network is use to learn the map of velocity from reconstruction, toolbox from Matlab is use to perform ANN. The two layer feed-forward neural net fitting, with ten hidden layer, where the hidden layer neuron is use to detect relationship between networks, training using 90% of total data, learning using Levenberg-Marquardt algorithm. In comparing with the SIRT reconstruction (Fig. 5(a)), result from ANN (Fig. 7(a)) is close to SIRT result. Value of coefficient of determination is 0.9562 from Figure 7(b), and ANN can be considered as a tool to evaluate the condition of the blocks.

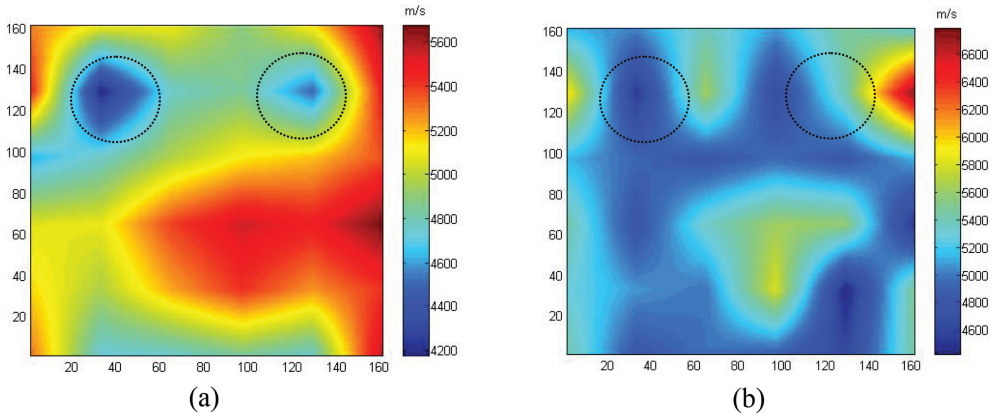


Figure 4. Reconstruction for limestone block (a) SIRT algorithm, (b) ART algorithm.

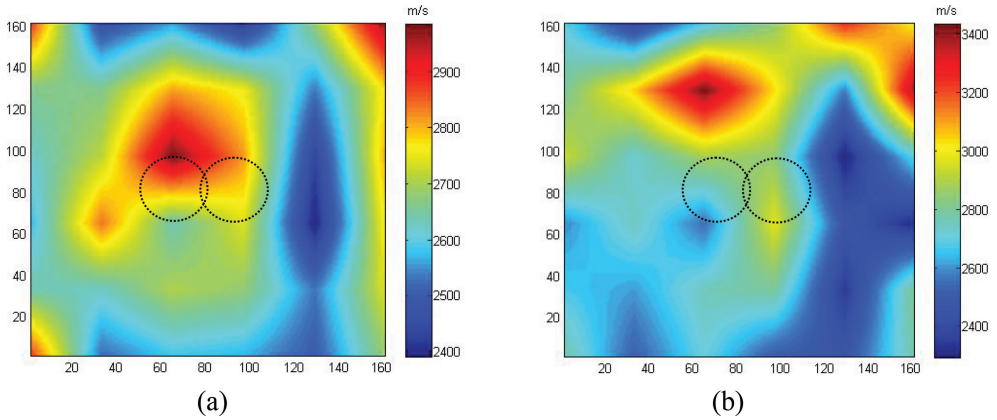


Figure 5. Reconstruction for concrete block with ball inserted (a) SIRT algorithm, (b) ART Algorithm.

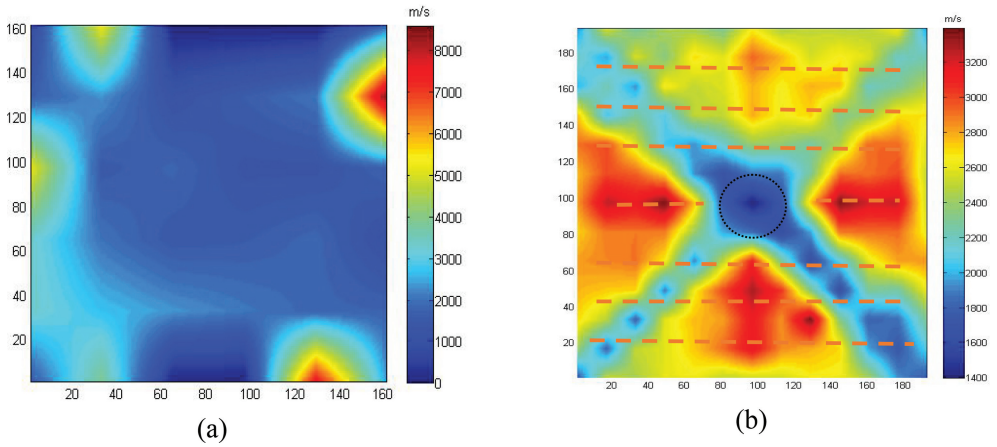


Figure 6. (a) Reconstruction for concrete with different cast laminated block, (b) Reconstruction for block with discontinuity and center hole using SIRT based on Figure 2(d).

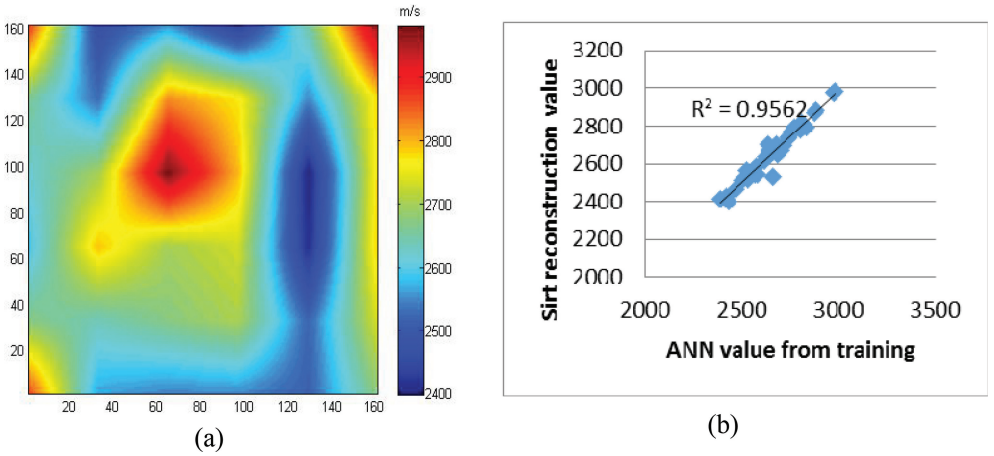


Figure 7. (a) Image reconstruction from ANN, (b) Correlation between ANN and SIRT.

## 5 CONCLUSION

The present research shows that the algorithms can be as useful tools for tomographic imaging of blocks interior. Reconstruction algorithms that use SIRT and ART were evaluated to identify the inhomogeneity of rock with the map of ultrasonic velocity. The ultrasonic velocity reduces when the measurement faces a discontinuity, and affects the reconstruction. The SIRT algorithm presented a better result than ART, when showing the map of ultrasonic velocity. The ANN technique used to learn SIRT value, showed a good correlation between the two methods by the coefficient of determination. Further research is strongly recommended especially using smaller interval and mesh to get smoother tomographic imaging.

## ACKNOWLEDGEMENTS

Great appreciation present to Mr. Sudibyo, Mr. Gito, Mr. Kurnia, Mr. Purwanto, Mr. Nurman, Mrs. Sari, Mr. Iwan, and my classmates Wigas, Aqla, and Kartini at Laboratory for their assistance in this research. Authors are also grateful to the Magister program of Mining Engineering, Faculty of Mining and Petroleum Engineering, Institut Teknologi Bandung, Indonesia.

## REFERENCES

ASTM C597-02, *Standard Test Method for Pulse Velocity through Concrete*. ASTM International.

Bungey, J.H., Millard, S.G. & Grantham, M.G. 2006. *Testing of Concrete in Structures*. Taylor and Francis Group. New York.

Gordon, R., Bender, R. & Herman, G.T. 1970. Algebraic Reconstruction Technique (ART) for Three-dimensional Electron Microscopy and X-Ray Photography, *J. Theor. Biol.* 29: 471–481.

Grangeat, P. 2009. *Tomography*. John Wiley and Sons, Inc. London.

Haach, V.G. & Juliani, L.M. 2014. Application of ultrasonic tomography to detection of damages in concrete. *Proceedings of the 9th international Conference on Structural Dynamics*, Porto: Portugal.

Kak, A.C. & Slaney, M. 1987. *Principles of Computerized Tomographic Imaging*. IEEE Press. New York.

Onur, A.H. & Bakrac, S. 2009. Determination of discontinuities in marble block via a nondestructive ultrasonic technique. *International Journal of Mineral, Metallurgy and Materials* 16(5): 487.

Singh, V.P. & Kotiyal, Y.C. 2013. Prediction of compressive strength using artificial neural network. *International Journal of Civil, Structural, Construction and Architectural Engineering* 7(12): 640.

*Rock Dynamics: From Research to Engineering – Li et al. (Eds)*
*© 2016 Taylor & Francis Group, London, ISBN 978-1-138-02953-8*

# A laboratory crushing apparatus for understanding dynamic rock fragmentation

S. Huang & B. Mohanty
*Department of Civil Engineering, University of Toronto, Toronto, Canada*

ABSTRACT: In rock crushing process, a key goal is understanding of fragmentation behaviour, which could be used to improve productivity and efficiency in mining operations. In this study, the input parameters, such as feed size, output particle size, and the energy expended in the process are carefully monitored. The test was based on a modified Hopkinson pressure bar system and a Piston-holder system. The energy consumed by the sample during fragmentation was determined by considering the energy carried by the incident wave and the reflected wave. A granite with the feed size ranging from 9.5 to 12.7 mm was employed in this study. The samples were impacted sequentially from one to ten times, with fragment size reduction determined after each set of impacts by sieve analysis. The link between fragment size distribution and the energy absorbed by the samples was examined.

## 1 INTRODUCTION

Various size distribution analyses are in current use for assessing fragment size distribution in blasting and crushing operation. However, measuring size distribution in an actual blast or in a crusher is a daunting task, especially through standard photogrammetric techniques. Thus, it is necessary to design a laboratory test to simulate the rock fragmentation process in the field. A considerable amount of experimental studies have been carried out to characterize the behaviour of rock crushers involving specific rock types. However, these studies are mainly site specific, and the results are largely empirical. Most studies have attempted to link the input parameters, such as feed size and crusher parameters, with output particle size, and global energy expended in the process. However, the physical mechanism of crushing process is still not well understood, as the energy consumed by the rock sample is hard to calculate during standard crushing or grinding tests; furthermore, multi-particle tests are hard to perform in laboratory due to irregular shape of the subject rock sample. Attention has been focused till now on the investigation of the gross input energy and the resulting particle size (Moshgbar et al. 1995, Parkin & Bearman 1994, Parkin &Calkin 1994). In laboratory, the breakage of single particle samples is performed to simplify the complex problem of rock crushing (Tavares 2007). From single particle breakage data, several important factors can be determined for crusher design, such as particle strength(Bergstrom 1985, Unland & Szczelina 2004, Dowding & Lytwynyshyn 1982), and energy-size reduction correlations (Yashima et al. 1987).

The rock fragments in the crusher are not only fractured by the jaws/cones, but also by the surrounding fragments. Also, for irregular shaped particle crushing test, the shape of sample has a significant influence on the test results (Tavares 2007). Normally, multi-layered samples are placed in a container and impacted a certain number of times by drop weight, and the fragment size reduction and input energy are calculated in order to acquire average performance for the rock types studied, as shown in Figure 1. Asim (1984) utilized a drop weight apparatus to investigate progressive (accumulative) crushing of particles in beds of cement clinkers. He reported that the empirical selection functions can be a practical means of mill performance evaluation. But fragmentation involving multi-particle impact tests is

much more complex than that in single particle impact, due to the interaction between particles, and the difficulty in controlling the input energy.

In this paper, we employed the Hopkinson Pressure Bar system with a piston-holder device to perform the bed particle fragmentation test. The Hopkinson pressure bar system is a dynamic test apparatus introduced by Hopkinson in 1872. Nowadays, this system and its various modified forms are widely used as a calibrated loading system for studying dynamic behavior of materials (Jiang & Vecchio 2009).

## 2 EXPERIMENTAL INVESTIGATION

### 2.1 *Dynamic fragmentation apparatus*

A 38 mm diameter Hopkinson bar system with a piston-holder system is employed. As a standard facility for dynamic testing, Hopkinson bar system is comprised of a 300 mm striker bar and a 1,500 mm incident bar, that are made of high strength steel as shown in Figure 2. A pair of strain gauges is mounted 680 mm away from the interface of the incident bar and the piston. In addition, a piston and holder system is designed to load the bedded samples as shown in Figure 3. The inner diameter of the holder is 127 mm.

Based on one dimensional wave propagation theory, the energy $W$ carried by the two waves are (Kolsky, 1953):

$$W = \int_0^t E\, \varepsilon^2 A\, C\, d\tau \tag{1}$$

where, $E = 200$ GPa is Young's modulus of the bar, $A = 0.0381$ m is the diameter of the bar, $C = 5000$ m/s is the P-wave velocity of the bar. The energy used to break sample $\Delta W$ after each impact then is:

$$\Delta W = W_i - W_r \tag{2}$$

where $W_i$ and $W_r$ are energy carried by the incident wave and reflected wave, respectively.

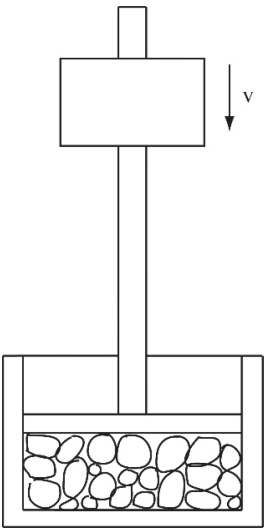


Figure 1. Schematics of a bed impact test (loading by a drop weight) (after Yarali & Soyer, 2011).

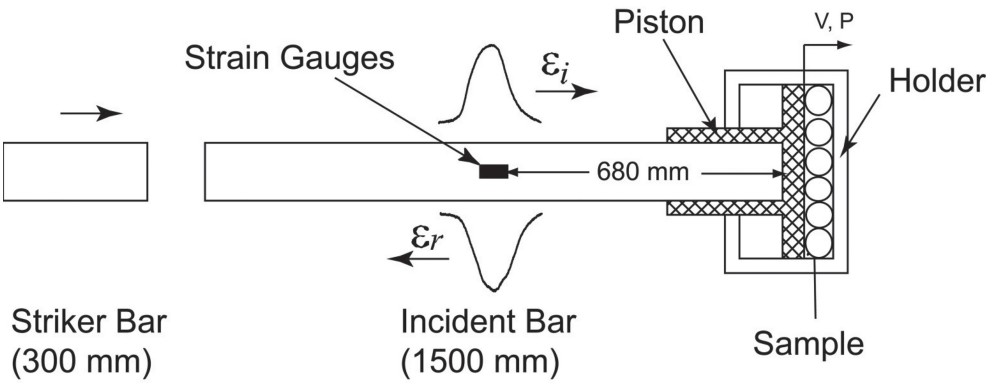


Figure 2. Schematics of the dynamic fragmentation system consisting of a Hopkinson bar system and a piston-holder system.

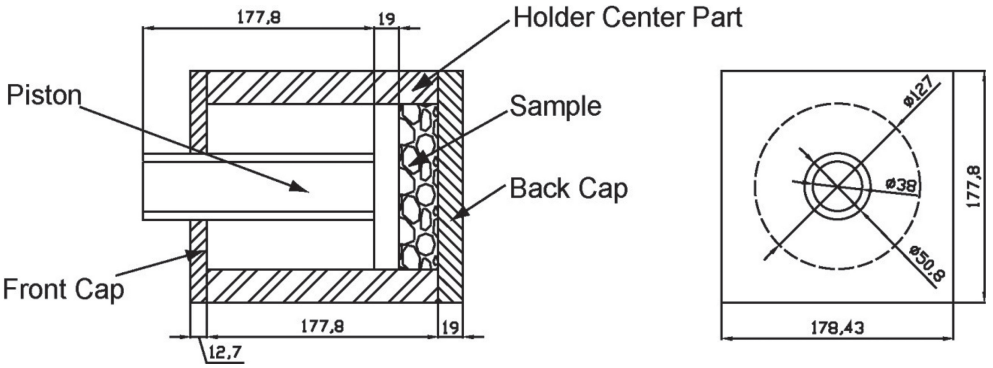


Figure 3. Schematics of the piston-holder system.

## 2.2 *Selection of target rocks*

In this work, Barre Granite (BG) is adopted to investigate the crushing behaviour of rocks, because this rock has been well researched by our research group and have sufficient mechanical and physical data (Nasseri et al. 2005, 2006). The samples were collected from the south-west region of Burlington in the state of Vermont, USA. The measured physical and mechanical properties of BG are listed in Table 1.

The samples were sieved before the test, and the particle sizes ranging from 9.5–12.7 mm are adopted, as shown in Figure 4. The range of the particle size is determined by the size of the piston-holder system and opening of sieves. These samples are irregular in shape as shown in Figure 4.

## 2.3 *Particle crushing test*

The impact velocity of the striker on the incident bar was monitored by a laser gauge. For each test, the sample was weighed and the packed volume in the holder measured to make sure of the consistence of the test. For each impact velocity, 10 tests were performed in sequence. After each impact, the rock sample was retrieved and a sieve analysis was carried out. Then a new batch of samples was put in the holder, while maintaining the same 'bulk' density (measured by the height of the bedded particles) and the assembly was subjected to two impacts (with the same impact velocity). The procedure was repeated for the next test with three consecutive impacts, and so on, until tests had been completed with ten impacts. The test results with sieve analysis are designated by the following nomenclature: $BAL_1I_3V_2$, where;

Table 1. The physical and mechanical properties of limestone (FL).

| Rock type | Young's Modulus (GPa) | Density (kg/m$^3$) | P-wave Velocity (m/s) | Compressive strength (UCS) (MPa) | Tensile strength (MPa) |
|---|---|---|---|---|---|
| Barre granite | 45 | 2646 | 3940 | 212 | 12.7 |

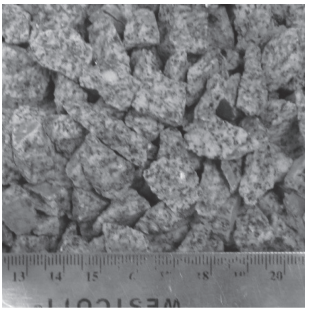

Figure 4. BG samples with size type A (9.5 mm to 12.7 mm) for the multi-particle crushing test.

B: the type of rock: granite (BG);
A: size range of rocks (9.5 ~ 12.7 mm);
L: stack layer and sub-number is the total number of layers;
I: impact and sub-number is the number of impacts (for multiple impacts, samples are retained in the holder during multi-impacts till end of test);
V: impact velocity of the striker: $V_1$ = 14 m/s.

## 3 RESULTS

### 3.1 *Particle size reduction*

Figure 5 shows the particle size distribution for the granite (BG) after the tests. As stated earlier, the sample was crushed from one to ten times, and after each test (for single as well as multiple impacts) the particle size distribution was determined by sieve analysis. The figures show that particle size diminishes after each impact, as expected. However, after about the seventh impact the reduction tends to be minimal. This is attributed to the 'cushioning effect' of the finer particles, which prevent further transmission of the impact energy into the remaining coarser samples.

### 3.2 *Crushing energy*

Based on the Equation 1 and 2, the input energy of a multi-impact test ($W_{input}$) was calculated by accumulating the $\Delta W$ of each impact as shown in Figure 6. The slope of the fitting line (38.9 J) is the average energy absorbed by the sample in each impact. The very high correlation coefficient value indicates the high repeatability of our tests.

### 3.3 *Rock crushing behaviour*

In order to consider the particle reduction under different number of impacts, a crushing index $t_{10}$ was introduced, which is widely used in research to characterize comminution of rock (Tavares 2007). This parameter expresses the weight percentage of crushing product, of which the size is less than 1/10 of the average feed size (Genc et al. 2004). For the average feed size of 10 mm as in this investigation, $t_{10}$ would represent the weight percentage of crushed

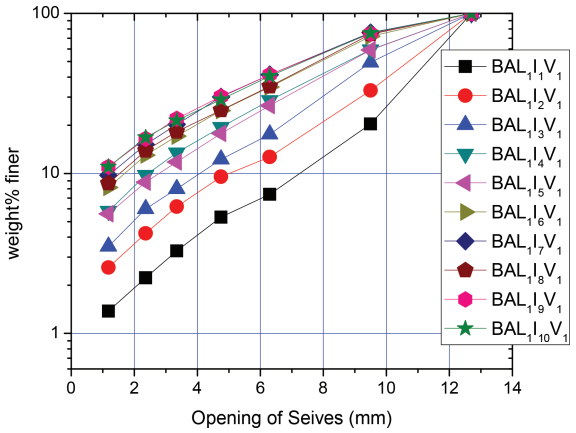


Figure 5. Particle size distribution of BG for a set of tests. (Single-bed layer, and impact velocity of sticker: 14 m/s; subscript $I_5$ denotes analysis after five consecutive impacts).

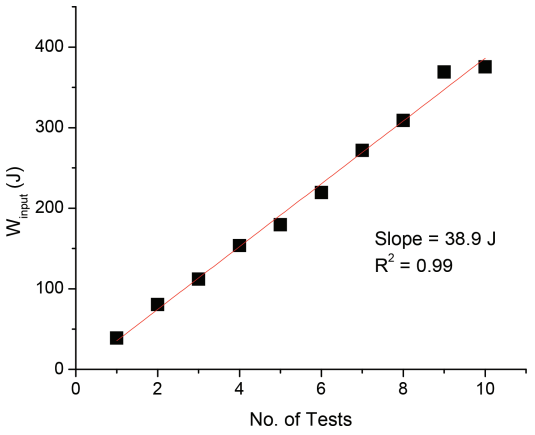


Figure 6. The cross-plot of the number of test and the input energy of a multi-particle crushing test ($W_{input}$).

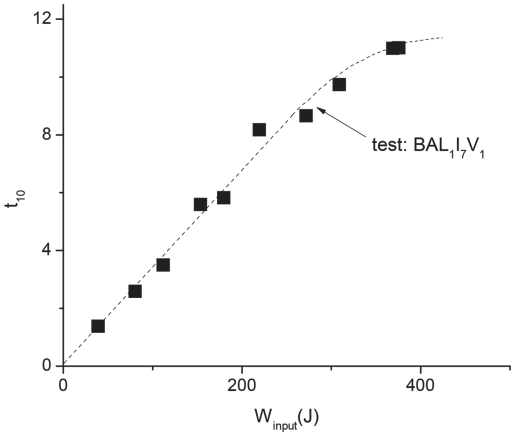


Figure 7. The cross-plot of the crushing index ($t_{10}$) and the input energy ($W_{input}$) for the multi-particle crushing test.

fragments, of which the size is less than 1 mm. Figure 7 clearly shows the linear relation between $t_{10}$ and $W_{input}$, which indicates the crushing behaviour of rock fragments is highly correlated with the energy absorbed by the samples under dynamic loading.

## 4 CONCLUSION

A calibrated apparatus, based on Hopkinson Pressure bar principles, was designed to simulate rock fragmentation action, to shed insight into the mechanical size reduction process in rocks. Fragmentation and size reduction of the multi-particle feed samples were achieved through calibrated impacts, where the impact velocity of the striker was strictly controlled. The resulting fragment size reduction was correlated with the number of impacts the samples were subjected to. Barre granite was adopted as the target rock in this work. The BG samples was investigated under the feed sizes ranging 9.5–12.7 mm. Single-layer samples were considered in this work and the impact velocity of the striker was kept at 14 m/s. The resulting fragments after each set of impacts were sieved to determine the various size fractions. In the tests, particle size diminishes after each impact. In addition, the energy absorbed by the samples was monitored for each impacts and the input energy of multi-impact tests was found that has a linear relation with the number of impact. The investigation shows that the input energy in crushing is directly proportional to the size reduction as defined by $t_{10}$, which is the weight percentage of crushed fragments (<1 mm). However, this linear relation ends after seven impact tests, which can be explained as the cushioning effect. In conclusion, the new crushing apparatus shows its advantages to capture the energy consumption of crushed samples and to examine the crushing behaviour of rocks.

## REFERENCES


Asim, M.E. 1984. Investigations of cement Clinker Grindability Using Drop-weight Tests and its Relation to Tube Mill Performance. *Zement-Kalk-Gips* 11: 577–584.

Bergstrom, B.H. 1985. Crushability and Grindability. IN Weiss, N. L. (Ed.) *SME Mineral Processing Handbook.* Littleton, SME.

Dowding, C.H. & Lytwynyshyn, G. 1982. Point Load-Deformation Relationships and Design of Jaw Crusher Plates. *Powder Technology* 31: 277–286.

Genc, O., Ergun, L. & Benzer, H. 2004. Single particle impact breakage characterization of materials by drop weight testing. *Physicochemical Problems of Mineral Processing* 38: 241–255.

Jiang, F. & Vecchio, K. S. 2009. Hopkinson bar loaded fracture experimental technique: a critical review of dynamic fracture toughness tests. *Applied Mechanics Reviews* 62.

Kolsky, H. 1953. *Stress Waves in Solid.,* Oxford: Clarendon Press.

Moshgbar, M., Parkin, R. & Bearman, R.A. 1995.The impact of system tribology on automatic-control of cone crushers. *Transactions of the Institute of Measurement and Control* 17: 2–9.

Nasseri, M.H.B., Mohanty, B. & Robin, P.Y.F. 2005. Characterization of microstructures and fracture toughness in five granitic rocks. *International Journal of Rock Mechanics and Mining Sciences* 42: 450–460.

Nasseri, M.H.B., Mohanty, B. & Young, R.P. 2006. Fracture toughness measurements and acoustic emission activity in brittle rocks. *Pure and Applied Geophysics* 163: 917–945.

Parkin, R.M. & Bearman, R.A. 1994. Energy-conservation via optimal-control of cone crushers. *Proceedings of the Institution of Mechanical Engineers Part E-Journal of Process Mechanical Engineering* 208: 165–170.

Parkin, R.M. & Calkin, D.W. 1994. Roadstone Aggregate - an Intelligent Route to Computer-Integrated Manufacturing. *Robotics and Computer-Integrated Manufacturing* 11: 345–350.

Tavares, L.M. 2007. Breakage of single particles: Quasi-Static. IN Salman, A.D., Ghadiri, M. & Hounslow, M. (Eds.) *Handbook of Powder Technoloy.* Elsevier.

Unland, G. & Szczelina, P. 2004. Coarse crushing of brittle rocks by compression. *International Journal of Mineral Processing* 74: S209-S217.

Yashima, S., Kanda, Y. & Sano, S. 1987. Relationships between particle-size and fracture energy or impact velocity required to fracture as estimated from single-particle crushing. *Powder Technology* 51: 277–282.

*Rock Dynamics: From Research to Engineering – Li et al. (Eds)*
*© 2016 Taylor & Francis Group, London, ISBN 978-1-138-02953-8*

# Laboratory observation on the seismic response of the filled joint under high amplitude stress waves

X.L. Huang & S.W. Qi
*Key Laboratory of Shale Gas and Geoengineering, Institute of Geology and Geophysics, Chinese Academy of Sciences, Beijing, China*

K.W. Xia
*Department of Civil Engineering, University of Toronto, Toronto, Ontario, Canada*

ABSTRACT: Propagation of high amplitude stress waves through an artificial filled joint was experimentally investigated using a modified steel Split Hopkinson Pressure Bar (SHPB) system. Quartz sand was used to simulate the joint fillings and its particle size distributions after each test are analyzed. Three deformation stages were discovered as the amplitude of the incident wave increases, i.e., initial compaction, crushing and crushing and compaction. In the initial compaction stage and the crushing and compaction stage, the fillings are mainly compacted, and thus the transmission coefficient increases with the amplitude of the incident wave. However, in the crushing stage, the transmission coefficient decreases with the increase of the amplitude of the incident wave. The observed dependence of the transmission coefficient on the wave amplitude is consistent with the particle size distribution of recovered fillings.

## 1 INTRODUCTION

The filled joint commonly exists in the natural rock mass and it is often filled with granular materials such as clay, quartz sand and weathered rock as shown in Figure 1. Field investigation show that the thickness of the fillings is up to several centimeters, and fillings have a noticeable effect on the mechanical behavior of the filled joint (Barton 1974, Sinha & Singh 2000). When blasting stress waves imping on the filled joint, for one thing only part of

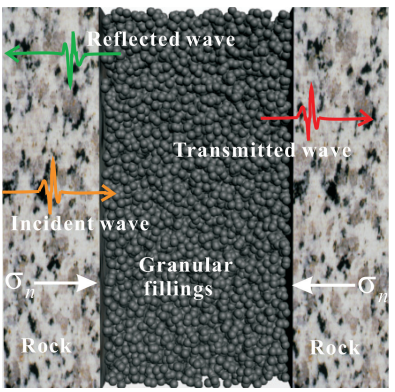


Figure 1. A filled joint under stress waves.

stress waves can propagate through the filled joint while the other part is reflected back. For another thing, the fill material is compacted under the compressive stress $\sigma_n$ which influences the propagation of the stress wave instead. The research on the seismic response of the filled joint under high amplitude stress wave is one of fundamental tasks in the rock dynamics.

In the previous studies, analytical models were propose to study the seismic response of the filled joint by treating a filled joint as a continuous elastic or viscous-elastic thin layer medium with a finite thickness welded between the background rocks (Fehler 1982, Rokhlin & Wang 1991, Zhu et al. 2012, Li et al. 2013, 2014, 2015). The Thin Layer Medium (TLM) model is actually a direct extension of the layer medium model in seismological theory (Brekhovskikh 1960; Bedford & Drumheller, 1994). Nevertheless, researchers found that the filled joint has nonlinear stress-closure relation under low amplitude stress waves and hysteresis effect obviously appears when unloaded using modified rock Split Hopkinson Pressure Bar (SHPB) (Li & Ma 2009, Wu et al. 2012). It is thus proved that TLM model over-idealizes the deformation behavior of the filed joint. Laboratory tests should be conducted to further investigate the seismic response of the filled joint.

Many tests have been carried out using modified rock SHPB (Li & Ma 2009, Wu et al. 2012, 2013, 2014). In these experimental studies, the amplitudes of stress waves in the rock SHPB was limited to 8 MPa (Wu et al. 2012) for protecting the rock bars. It is however observed that practical blasting stress waves often have much higher amplitude according to the field test data (Singh 2002, Khandelwal & Singh 2007). Therefore, high amplitude stress waves should be induced and subjected to the filled joint. The purpose of the current paper is to report our laboratory observation data on the seismic response of the filled joints under high amplitude stress waves.

## 2 EXPERIMENTAL METHODS

Figure 2 shows the experimental setup that is mainly composed of a gas gun, a striker bar, an incident bar and a transmitted bar. The incident and transmitted bars have a same diameter of 25.4 mm but different lengths of 2000 mm for the incident bar and of 1500 mm for the transmitted bar. A short striker bar with a length of 200 mm is launched to impact the end of the incident bar by the gas gun to induce high amplitude stress waves. All bars are made of high-strength steel with density of 7980 kg/m$^3$ and P-wave velocity of 5058 m/s. The filled joint is simulated by placing a thin layer of coarse quartz sand between the incident and transmitted bars. The coarse sand has the bulk density of 1600 kg/m$^3$ and its initial grain size ranges from 0.25 to 2 mm. A steel holder with an inner and outer diameter of 25.5 mm and 37.5 mm, respectively (see Fig. 2) is used to prevent the outflow of fillings when loaded. By setting different striking velocities, we can get stress waves with different amplitudes, which can be real-

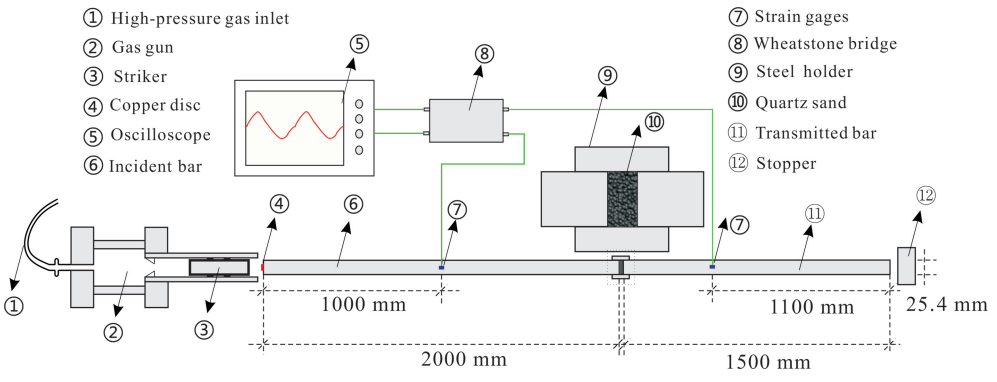


Figure 2. Schematics of the experimental setup.

ized through adjusting the gas pressure. Pulse-shaper techniques (Xia et al. 2008) are applied to achieve half-sinusoidal stress waves. The pulse shaper is made up of soft copper and has same dimension, which can produce stress waves with approximately identical duration. By detailed experimental design, strain gages are installed in the reasonable places to get incident and transmitted waves without interference by reflected waves. We measured the incident and reflected waves in the incident bar, and transmitted waves in the transmitted bar.

## 3 TESTING RESULTS

### 3.1 *Incident and transmitted waveforms*

In the tests, 8 g of sand fillings were adopted and average thicknesses was calculated as 9.87 mm. For the filled joint with given thickness, we increased the pressure of the gas gun from a low value, i.e., 6.5 psi. Stress waves are calculated according to $\sigma_n = E\varepsilon$, where $\sigma_n$ is the compressive stress in the bars, $E$ the Young's modulus of the bars, and $\varepsilon$ the monitored strain.

Figure 3 shows the incident waves corresponding to the gas pressures of 6.5 psi, 10.0 psi and 24.0 psi and the corresponding transmitted waveforms through the filled joint with mean thickness of 9.87 mm. It can be observed that when the gas pressure is 6.5 psi, the transmitted wave is an approximately half-sinusoidal wave. However, when the gas pressure is 10.0 psi, the transmitted wave becomes a little flatter and there appears a sudden decrease of the slope in the waveform. We denote this transition point as $\xi$ in the waveform. When the gas pressure reaches 24.0 psi, there exists another transition point $\psi$ besides $\xi$. After $\psi$, the slope of the waveform abruptly increases.

### 3.2 *Transmission coefficient*

Figure 4 shows the variation of the transmission coefficient versus the amplitudes of the incident stress waves. The transmission coefficient is defined as the ratio of the transmitted wave peak value to the incident wave peak. From Figure 4, it can be observed that the transmission coefficient varies nonlinearly with the amplitude of the incident wave. This variation can be divided into three stages. With the increase of the amplitude, the transmission coefficient first increases to a peak; then it decreases instead; after achieving a minimum it increases again.

### 3.3 *Grain size curves*

Figure 5 shows grain size distribution curves of the recovered fillings under different wave amplitudes. From Figure 5, it can be seen that the grain size distribution curves basically coincide when the wave amplitude increases from 94.5 MPa to 115.8 MPa. However, the distribution curves obviously change when the wave amplitude varies from 143.9 MPa and 203.1 MPa. The number of the smaller particles gradually increases. Finally, the distribution curves change slightly when the wave amplitude varies from 238.8 MPa to 290.3 MPa.

## 4 INTERPRETATION AND DISCUSSION

When the normal stress is small, the fillings were only compacted and particles cannot be crushed. Thus the recovered fillings basically have identical distribution curves (see curves in case of 94.5 MPa and 115.8 MPa). We call this process as *initial compaction* stage. In this stage, the density of the fillings and the specific stiffness of the filled joint increase with the normal stress. It has been found that the increase of both the density of the fillings and stiffness of the filled joint can allow more waves to propagate through the filled joint (Zhu et al., 2011). Hence, the transmission coefficient increases with the wave amplitude in the *initial compaction* stage as shown in Figure 4. When the normal stress is high enough, particles of fillings were crushed. As

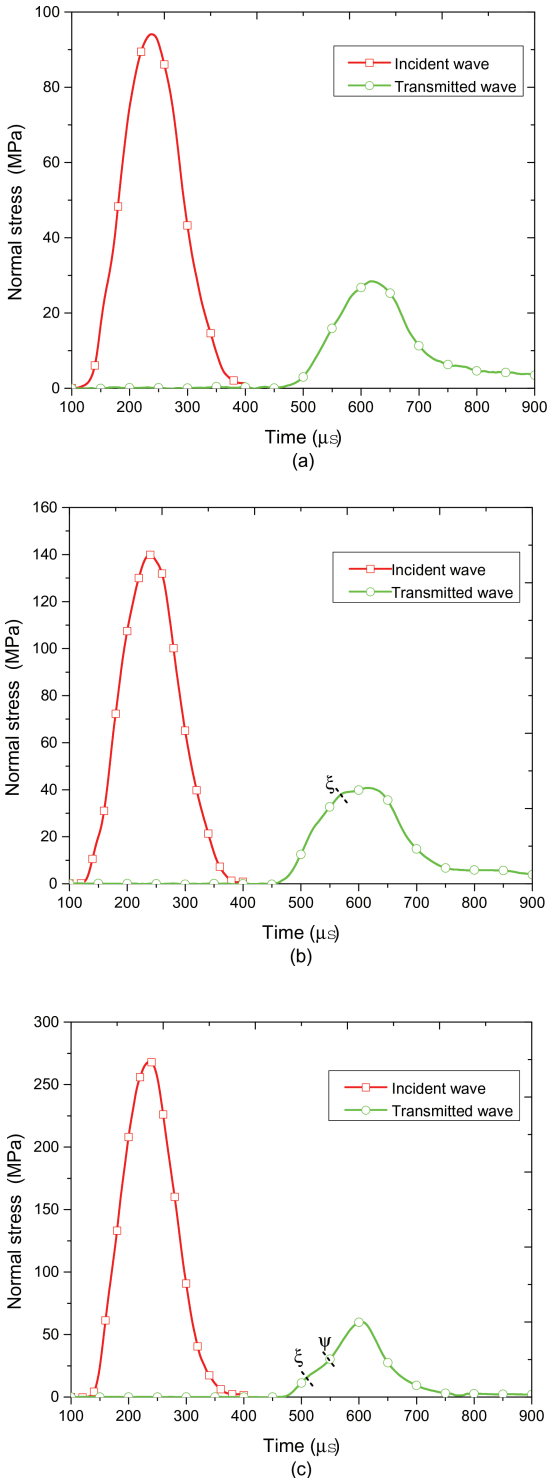


Figure 3. The incident waves and the corresponding transmitted waveforms through the fillings when the gas pressure is set as (a) 6.5 psi; (b) 10.0 psi and (c) 24.0 psi respectively.

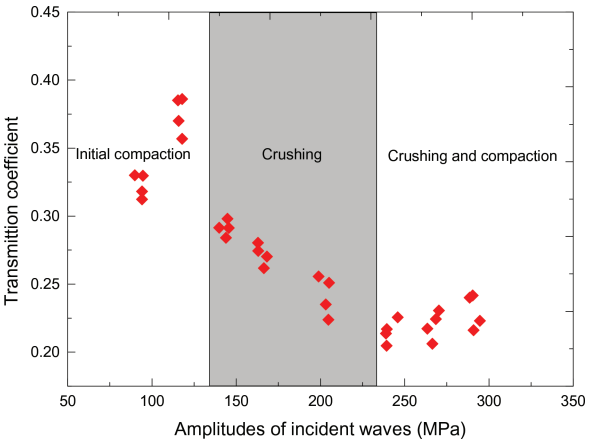


Figure 4. Variation of transmission coefficient with the amplitude of the incident wave.

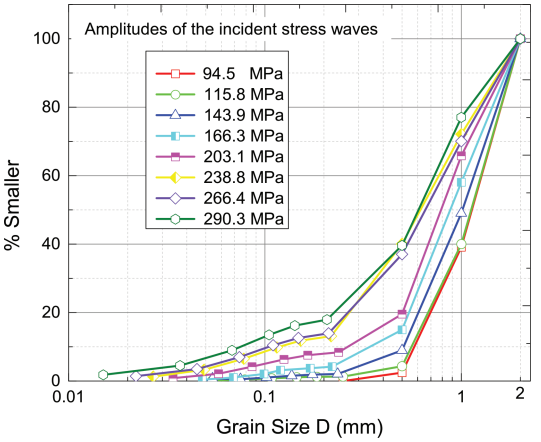


Figure 5. Grain size distributions of the fillings after loaded by stress waves with different amplitudes.

a result, the grain size distribution curves changes abruptly (see curves in case that the amplitude ranges from 143.9 MPa to 203.1 MPa). We name this process as *crushing* stage. In the *crushing* stage, the stiffness of the filled joint gradually decreases with the normal stress. Meanwhile, the crushing process of the particles consumes part of wave energy. Consequently, the slope of the waveform decreases suddenly (see Fig. 3b) and the transmission coefficient decreases with the increase of the wave amplitudes in the *crushing* stage as shown in Figure 4. When the normal stress is very high, crushing and compaction occurs simultaneously and the compaction plays the domain role. In this process, the grain size distribution curves change little (see curves in case that the amplitude ranges from 238.8 MPa to 290.3 MPa). We call this process as *crushing and compaction* stage. Similar to the *initial compaction* stage, the transmission coefficient increase again with the increment of the wave amplitude in this stage (see Fig. 4). The slope of the waveform abruptly increases again with the increment of the amplitude (see Fig. 3c).

## 5 CONCLUSIONS

The deformation of the fillings under the high amplitude stress waves can be divided into three stages, i.e. the *initial compaction* stage, the *crushing* stage and the *crushing and compac-*

*tion* stage. In the *initial compaction* stage and the *crushing and compaction* stage, the fillings were mainly compacted and few particles were crushed. Consequently, the transmission coefficient increases with the increment of the amplitude of the stress waves. However, the particles of the fillings were crushed in the *crushing* stage, which consumes part of wave energy and reduces the stiffness of the filled joint. As a result, the transmission coefficient decreases with increasing the wave amplitude in this stage.

## ACKNOWLEDGEMENTS

This research is supported by funds from National Natural Science Foundation of China under Grants Nos. 41322020, 51479131 and 41172272, Chinese Academy of Science under Knowledge Innovation Project Grant Nos. KZZD-EW-05-02, KZCX2-EW-QN10 and the China Scholarship Council (CSC).

## REFERENCES

Barton, N. 1974. A review of the shear strength of filled discontinuities in rock. *Norwegian Geotechnical Institute Publication* 105: 1–38.

Bedford, A. & Drumheller, D. 1994. *Elastic Wave Propagation*. Wiley.

Brekhovskikh, L. 1960. *Waves in Layered Media.* New York: Academic.

Fehler, M. 1982. Interaction of seismic waves with a viscous liquid layer. *Bulletin of the Seismological Society of America* 72: 55–72.

Khandelwal, M. & Singh, T. 2007. Evaluation of blast-induced ground vibration predictors. *Soil Dynamics and Earthquake Engineering* 27: 116–125.

Li, J. & Ma, G. 2009. Experimental study of stress wave propagation across a filled rock joint. *International Journal of Rock Mechanics and Mining Sciences* 46: 471–478.

Li, J.C., Li, H.B., Jiao, Y.Y., Liu, Y.Q., Xia, X. & Yu, C. 2014. Analysis for oblique wave propagation across filled joints based on thin-layer interface model. *Journal of Applied Geophysics* 102: 39–46.

Li, J.C., Liu, T.T., Li, H.B., Liu, Y.Q., Liu, B. & Xia, X. 2015. Shear wave propagation across filled joints with the effect of interfacial shear strength. *Rock Mechanics and Rock Engineering*. 48(4):1547–1557.

Li, J.C., Wu, W., Li, H., Zhu, J. & Zhao, J. 2013. A thin-layer interface model for wave propagation through filled rock joints. *Journal of Applied Geophysics* 91: 31–38.

Rokhlin, S. & Wang, Y. 1991. Analysis of boundary conditions for elastic wave interaction with an interface between two solids. *The Journal of the Acoustical Society of America* 89: 503–515.

Singh, P. 2002. Blast vibration damage to underground coal mines from adjacent open-pit blasting. *International Journal of Rock Mechanics and Mining Sciences* 39: 959–973.

Sinha, U. & Singh, B. 2000. Testing of rock joints filled with gouge using a triaxial apparatus. *International Journal of Rock Mechanics and Mining Sciences* 37: 963–981.

Wu, W., Li, J. & Zhao, J. 2012. Loading rate dependency of dynamic responses of rock joints at low loading rate. *Rock mechanics and rock engineering* 45: 421–426.

Wu, W., Li, J.C. & Zhao, J. 2014. Role of filling materials in a P-wave interaction with a rock fracture. *Engineering Geology* 172: 77–84.

Wu, W., Zhu, J.B. & Zhao, J. 2013. Dynamic response of a rock fracture filled with viscoelastic materials. *Engineering Geology* 160: 1–7.

Xia, K., Nasseri, M.H.B., Mohanty, B., Lu, F., Chen, R. & Luo, S.N. 2008. Effects of microstructures on dynamic compression of Barre granite. *International Journal of Rock Mechanics and Mining Sciences* 45: 879–887.

Zhu, J., Perino, A., Zhao, G., Barla, G., Li, J., Ma, G. & Zhao, J. 2011. Seismic response of a single and a set of filled joints of viscoelastic deformational behaviour. *Geophysical Journal International* 186: 1315–1330.

Zhu, J., Zhao, X., Wu, W. & Zhao, J. 2012. Wave propagation across rock joints filled with viscoelastic medium using modified recursive method. *Journal of Applied Geophysics* 86: 82–87.

*Rock Dynamics: From Research to Engineering – Li et al. (Eds)*
*© 2016 Taylor & Francis Group, London, ISBN 978-1-138-02953-8*

# A trial of 3D printing on rock dynamics

C. Jiang
*School of Civil and Environmental Engineering, The University of New South Wales, Sydney, NSW, Australia*

G.F. Zhao
*State Key Laboratory of Hydraulic Engineering Simulation and Safety, School of Civil Engineering, Tianjin University, Tianjin, China*

M.Z. Gao
*State Key Laboratory of Hydraulics and Mountain River Engineering, Sichuan University, Chengdu, Sichuan, China*

Y.X. Zhao
*State Key Laboratory of Coal Resource and Safe Mining, China University of Mining and Technology, Beijing, China*

ABSTRACT: Rock dynamics attracts great attention in rock mechanics. However, specimen preparation in experimental study is not easy. 3D printing started to be involved to improve this process, Including Polylactic Acid (PLA) and resin. However, their plastic behavior is much unlike brittle rock. In this work, a gypsum-like power material using inkjet 3D printing (3DP) technique was applied to produce pre-cracked specimens for dynamic Split Hopkinson Pressure Bar (SHPB) test. High speed camera observed that the failure pattern of this material is similar to brittle rock-like material such as Portland Cement Concrete (PCC).Our results indicate that sample preparation by 3D printing will make far more contributions to rock dynamics because it is highly competitive due to its quickness in prototyping, precision and flexibility on the geometry, and high material homogeneity.

## 1 INTRODUCTION

Dynamic fracturing of rock is a typical problem in rock mechanics and rock engineering. Comprehensive understanding of dynamic cracking in rock is essential to provide more scientific guidance for safe and economic consideration in underground excavation, hydraulic fracturing, blasting, rock disintegration, etc. The research on rock dynamics can be simply grouped into three categories—analytical analysis, numerical analysis and experimental analysis. Theoretical studies mainly focus on wave propagation, and the models are usually applied to simple geometries of crack problems, and they become extremely complicated when there are random discontinuities or involved material heterogeneity. Numerical methods including continuum (e.g. Finite Element Method (FEM), Finite Difference Method (FDM), Boundary Element Method (BEM) or discontinuum based methods (discrete element method (DEM), Distinct Lattice Spring Model (DLSM)) have limitations as well (Zhao 2011, Jing 2003). Experiment studies of rock dynamics have used some test apparatus such as drop-weight machine (Whittles et al. 2006, Banthia et al. 1989) and Hopkinson pressure bar (Dai et al. 2010), and the dynamic process can be monitored in micro second step by high speed camera. However, the specimen preparation is not easy on natural rocks such as sandstone, limestone, marble and granite. In addition to the effect of anisotropy or heterogeneity from the production, to make preset cracks into the specimen is challenging. Traditional method uses disc cutter and saw wire to produce the preset crack, which is not an

easy process. Although more advanced methods, water-jet system (Wong and Einstein, 2009) and engraving machine (Dong et al. 2015), were adopted, these techniques have limitations with result of small cutting depth and presence of rounded crack tips (Dong et al. 2015; Lee and Jeon 2011). Instead, artificial rock materials are used in rock experiment because they can produce more homogenous specimens. The preset cracks of these artificial rock are usually produced by inserting a metal slim (copper or steel) into the desired position in the mould (Haeri et al. 2014, Wong et al. 2001).

3D printing, as a new developed technique, has advantages on specimen preparation in many aspects. Firstly, it is a fast prototyping technique so the preparation time is short. Secondly, it is precise and flexible to control the geometry of the specimen which is especially useful in producing the preset cracks. Thirdly, the specimens from 3D printing have high degree of homogeneity which is hardly achieved by traditional preparation methods. Up to now, there are only a few preliminary studies using 3D printing material (resin or plastic material (PLA)) in rock mechanics (e.g. Ju et al. 2014, Jiang and Zhao 2015). The mechanical behavior of these printing material are ductile and plastic, which is not suitable to be used in study of dynamic crack coalescence. Fereshtenejad and Song (2016) conducted Uniaxial Compressive Strength (UCS) test on powder-based gypsum-like 3D printing material, where the effects of the printing direction, printing layer thickness, binder saturation level, and heating process are investigated. They claimed an optimized printing method could produce Uniaxial Compressive Strength (UCS) specimens similar to rock.

In this work, the gypsum-like material was further investigated. A number of specimens with different preset cracks arrangements were produced and tested under SHPB system with high-speed camera. The consistencies of the crack paths in 3D printing material, Portland Pozzolana cement and numerical models will be examined and suitability of the application of 3D printing on rock dynamics will be tested.

## 2 3D PRINTING PROCESS

The 3D printer is model ProJet 660 from 3D system Inc, and the raw printing material is in powder state which is mainly Calcium Sulphate Hemihydrate $CaSO_4 \cdot 0.5H_2O$ (3D Systems Inc 2013). The powder is transformed to stiff substance by a liquid binding agent. The printing process is briefly outlined in Figure 1. Firstly, the raw model is built in a Computer Aided Design (CAD) software. Secondly, a STL file is required which contains the surface information of the model. Thirdly, the 3D printing software called *3D print* can edit the printing setting (e.g. binder saturation, model position). Lastly, the printer can finish the job in a short time. During the printing, a layer in 0.1 mm thickness will be spread and the inkjet head will spray the binder in the specified position. Then next layer in 0.1 mm thickness will cover over. This process repeats and layers are stacked vertically until the job finishes. After that, the unused powder is recycled by a vacuum, and the trapped and unbound powder on the specimens is carefully removed by the air wand. Two groups of specimens were designed, multi-cracked specimen and special crack specimen (Figs 3 and 4) in disc shape with 40 mm in diameter and 20 mm in thickness.

## 3 SHPB TEST SETUP

The overall set-up of the SHPB system is shown in Figure 2. This is a traditional SHPB set up with a 0.6 m strike bar, a 2 m incident bar, a 2 m transmitted bar, a gas gun, a pressure control

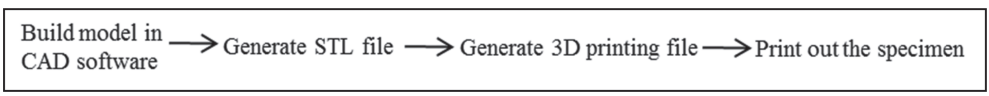


Figure 1. Process of 3D printing.

station and an absorption bar. The material of the all the bars is rigid steel with density of 7800 kg/m$^3$, Young's modulus of 200 GPa and Poisson's ratio of 0.285. Two strain gauges are stuck to the middle of incident bar and transmitted bar to obtain the strain. The pulse shapers used in this experiment are rubber discs.

In addition, a high speed camera, Photron Fastcam 1.1A, makes it possible to analysis the crack development in an interval of a few micro seconds. This camera can capture the images up to 675,000 frames per second (fps). There is a limit for the shutter speed duo to two reasons. Firstly, there has to be enough lighting in high shutter speed mode. Secondly, the development of crack requires more captured images in higher shutter mode but the camera has only 8 GB memory which limits the total number of saved images. To avoid missing the fracture moment, end-trigger mode was selected. In this mode, the camera is continuously recording until the user presses the trigger button, with images captured before the trigger being retained in the memory. In this paper, the frame rate was chosen up to 100,000 fps and the pixels were 192 × 192.

## 4 RESULTS

The first group of disc is named multi-cracked specimens. There are parallel preset cracks, and the alignment is illustrated in Figure 3a. the SHPB results indicate the crack coalescence is not always at the tips of the adjacent preset cracks. One of the influences is from the spacing or called bridge area between the preset cracks (Haeri et al. 2014). The experiments of (Haeri et al. 2014) using Portland Pozzolana Cement (PPC) are picked out as comparison. Although there are slight differences of the crack path between the two experiments (i.e. the occurrence of the wing crack), the general crack mode is similar, which proves the 3D printing material is suitable to mimic brittle rock-like specimen in the tension-induced crack experiment. In addition, the 3D printing material is more homogenous than the PPC and can produce more consistent results. Furthermore, the 0.2 mm-thickness crack in 3D printed specimen is much more precise than the 1 mm-thickness crack in PPC, thus reducing the influence from the width of the crack.

The second group of disc is named special-cracked specimens. They are 40 mm in diameter and 20 mm in thickness. The only difference among the three models is the length of the vertical crack, namely short (S), medium (M) and long (L). Similar to the previous group, there is no wing crack appears on the vertical preset crack. However, it is observed that the crack path is not identical among the three types. In the S type specimen (Fig. 4a), the cracks skirted around the vertical crack. In the M type specimen (Fig. 4b), the crack from the

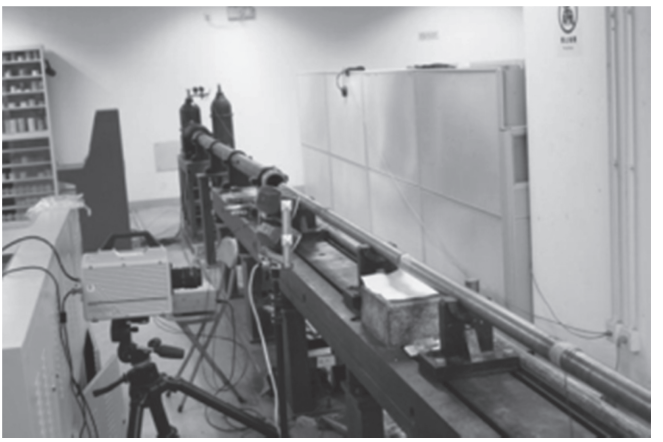

Figure 2. Setup of SHPB system.

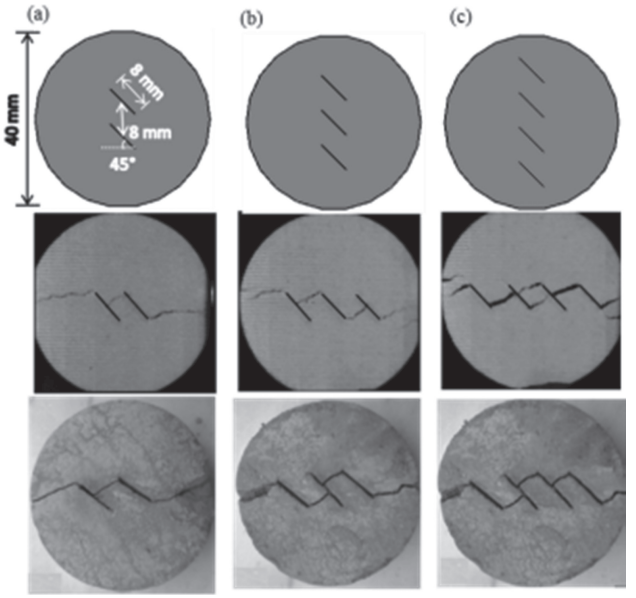


Figure 3. Coalescence path in 3D printed specimens and cemented specimen (from Haeri et al. 2014) with multiple pre-existing cracks.

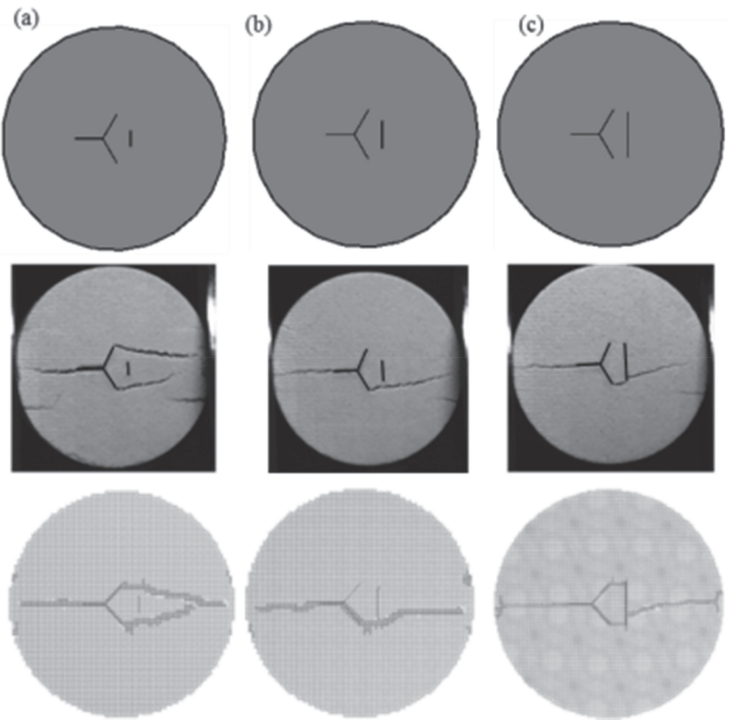


Figure 4. Coalescence path in 3D printed specimens with special pre-existing cracks.

downward preset crack shifted towards the tip of that preset crack. It needs to be mentioned that, in both S and M types specimen, there is no crack coalescence to the vertical crack. Therefore, the difference of the crack paths is from the indirect influence of the vertical crack. Similarly in engineering projects, the crack trajectory (e.g. propagation direction, curvature) is influenced by the adjacent joints or faults. When the length of the vertical crack increases further (L type model in Fig. 4c), the crack coalesced to the tip of vertical crack and the continuing crack started above the lower tip of the vertical crack. The numerical simulation from Distinct Lattice Spring Model (DLSM) produced similar crack pattern. As the model in the numerical simulation is perfectly homogenous, it proves that 3D printed specimens have high degree of homogeneity.

A more detailed example of an S type specimen has been illustrated in Figure 5. The shutter speed is 100,000 fps so that the time interval between the adjacent frames is 10 μs. The frame number is marked in each image. In the first five frames, there is no primary crack observed. However, the lateral deformation of the specimen can be noticed. In the 6th frame, the cracks initiated at the tips of the horizontal crack, the upward crack and the downward crack. After that, the initiated crack in the horizontal crack and upward crack propagated extremely fast and went through the specimen in the 8th frame. Meanwhile, the initiated crack from the downward crack propagate relatively more slowly. The secondary crack can be observed from the 3rd frame near the left end of the specimen. In the 10th frame, a secondary crack appears at the right end. The cracks become clear and wider in the later frames, resulting the specimens failing with several fragments. As this material is highly homogeneous, it can provide precious calibration and validation data for numerical models during a whole failure process.

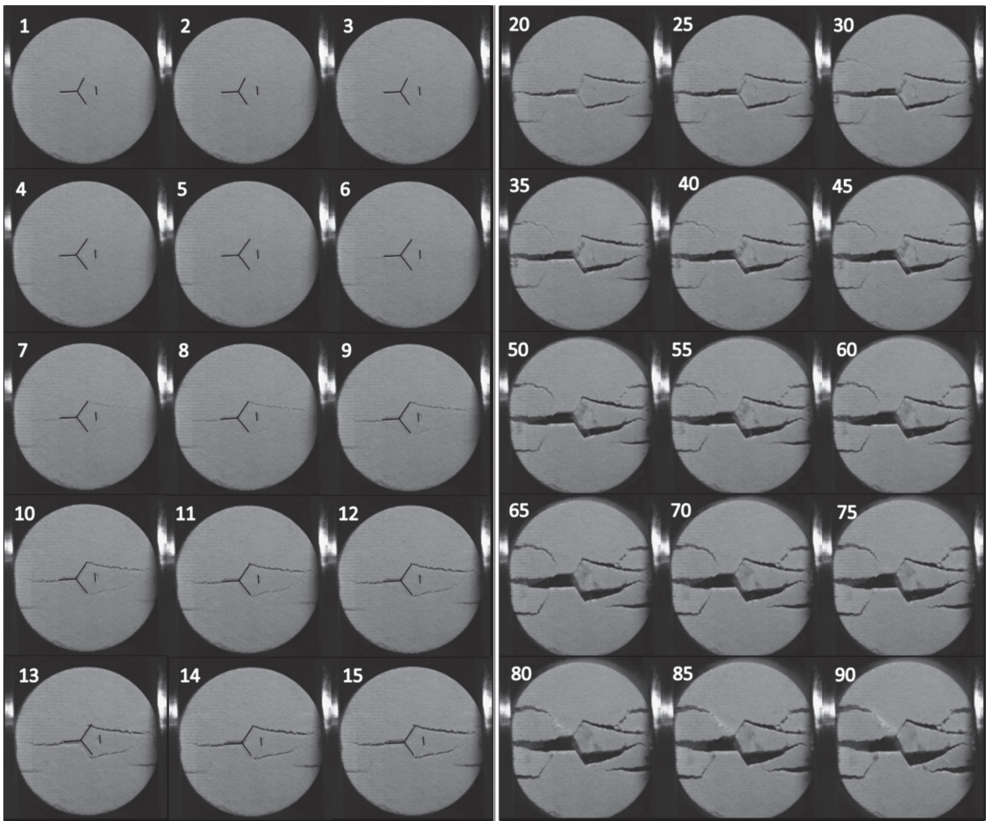


Figure 5. Development of crack path in an S type specimen (with 100,000 fps; Time interval = 10 μs).

## 5 CONCLUSION

This paper describes a trial of the 3d printing material on SHPB experiment. The 3DP technique using power based material successfully produced the disc specimens with super narrow preset cracks. Traditional SHPB system, together with high-speed camera, fractured the specimens in a desired mode. The results indicated that this gypsum-like material is suitable in mimicking the brittle rock-like materials in rock dynamics study. In addition to that, the advantages of this material in terms of the quickness, homogeneity and precision and flexibility have been demonstrated through the process.

## REFERENCES


3D Systems Inc. 2013. Safety data sheet: VisiJet PXL Core Retrieved 14 Jan, 2016, from http://www.3dsystems.com/sites/www.3dsystems.com/files/22-83100-s12-01-asds_ghsenglish-australiavisijet_pxl_core.pdf

Banthia, N., Mindess, S., Bentur, A. & Pigeon, M. 1989. Impact testing of concrete using a drop-weight impact machine. *Experimental Mechanics* 29: 63–69.

Dai, F., Chen, R., Iqbal, M. J. & Xia, K. 2010. Dynamic cracked chevron notched Brazilian disc method for measuring rock fracture parameters. *International Journal of Rock Mechanics and Mining Sciences* 47: 606–613.

Dong, Q., Ma, G., Wang, Q., Xia, M., Zhen, H. & Li, Q. 2015. Experimental comparative analysis of wing crack extension failure behavior: two types of fissures under uniaxial compression. *Rock Mechanics and Rock Engineering (in press)*.

Fereshtenejad, S. & Song, J.J. 2016. Fundamental Study on Applicability of Powder-Based 3D Printer for Physical Modeling in Rock Mechanics. *Rock Mechanics and Rock Engineering* 1–10.

Haeri, H., Khaloo, A. & Marji, M. 2014. Experimental and numerical analysis of Brazilian discs with multiple parallel cracks. *Arabian Journal of Geosciences* 1–12.

Jiang, C. & ZHao, G. F. 2015. A Preliminary Study of 3D Printing on Rock Mechanics. *Rock Mechanics and Rock Engineering* 48:1041–1050.

Jing, L. 2003. A review of techniques, advances and outstanding issues in numerical modelling for rock mechanics and rock engineering. *International Journal of Rock Mechanics and Mining Sciences* 40: 283–353.

Ju, Y., Xie, H., Zheng, Z., Lu, J., Mao, L., Gao, F. & Peng, R. 2014. Visualization of the complex structure and stress field inside rock by means of 3D printing technology. *Chinese Science Bulletin* 59: 5354–5365.

Lee, H. & JeonN, S. 2011. An experimental and numerical study of fracture coalescence in pre-cracked specimens under uniaxial compression. *International Journal of Solids and Structures* 48: 979–999.

Whittles, D.N., Kingman, S., Lowndes, I. & Jackson, K. 2006.Laboratory and numerical investigation into the characteristics of rock fragmentation. *Minerals Engineering* 19: 1418–1429.

Wong, L.N.Y. & Einstein, H.H. 2009. Crack Coalescence in Molded Gypsum and Carrara Marble: Part 1. Macroscopic Observations and Interpretation. *Rock Mechanics and Rock Engineering* 42: 475–511.

Wong, R.H.C., Chau, K.T., Tang, C.A. & Lin, P. 2001. Analysis of crack coalescence in rock-like materials containing three flaws—Part I: experimental approach. *International Journal of Rock Mechanics and Mining Sciences* 38: 909–924.

Zhao, J. 2011. An overview of some recent progress in rock dynamics research. *Advances in Rock Dynamics and Applications.* CRC Press.

*Rock Dynamics: From Research to Engineering – Li et al. (Eds)*
*© 2016 Taylor & Francis Group, London, ISBN 978-1-138-02953-8*

# Experimental study on dynamic response of rock masses with different joint matching coefficients

N.N. Li, J.C. Li, H.B. Li & S.B. Chai
*State Key Laboratory of Geomechanics and Geotechnical Engineering, Institute of Rock and Soil Mechanics, Chinese Academy of Sciences, Wuhan, Hubei, China*

ABSTRACT: The paper investigates the effect of contact area of joint surface on stress wave propagation and the dynamic property of joints by using Split Hopkinson Pressure Bar (SHPB) apparatus. Artificial joints were made with two blocks, one surface of one block was sawn to shape a number of notches while the surface of the other one was flat and smooth. Each sample has the same depth but different width of notches. Based on the fundamental theory of SHPB test, the transmission coefficients, the deformation of rock specimens and the closure volume of joints were obtained. The experimental results show that the deformation of rockmass is mainly caused by the joint deformation and the closure volume of joints increase when contact area declines. The transmission coefficients increase almost linearly with contact area ratio for a given notch width.

## 1 INTRODUCTION

Joints have significant effects on the mechanical behavior of rock masses. Furthermore, wave propagation in jointed rock masses has distinctly different behavior compared to that in a continuous medium. Study on the dynamic property of joints and its effect on wave propagation has been a research focus both in the field of theory and experiments. Bandis et al. (1983) presented B-B model to describe the stress-closure behavior of joints. And, the joint closure property depended both on the surface topography and the elastic property of the material (Brown & Scholz 1985, 1986). Then Zhao & Cai (2001) extended the displacement discontinuity method for wave propagation across joints with nonlinearly deformational behavior (B-B model) to theoretically study the P-wave transmission across single dry fractures. Pyrak-Nolte et al. (1990a, b) studied the effect of linearly elastic joint on seismic wave propagation. Later, a time domain recursive method was proposed and applied to study wave propagation across nonlinear joints with an arbitrary incident angle (Li et al. 2012, Li 2013). The mechanical properties of rock masses and the influence of joints on wave propagation are determined by the physical and geometrical characteristics of joints (e.g. JRC, JMC, thickness, filing material property and other factors). The Joint Roughness Coefficient (JRC) was firstly proposed to describe the joint surface configuration (Barton & Choubey 1977). In subsequent study, Bandis et al. (1983) found the effective contact area, JRC, properties of the asperities and filling materials influence the normal stiffness of joints. Misra & Marangos (2010) studied the effect of roughness on joint closure and wave propagation. In addition, Joint Matching Coefficient (JMC) was then proposed as an important factor governing the normal closure, stiffness, shear strength and hydromechanical properties of the joints (Zhao 1987, 1997). Li et al. (2009) studied the effect of joint width and water content on the dynamic stress-strain relation of the filled joints. The modeling results of Hopkins (2000) indicated that contact area influenced the joint stiffness significantly. From test results, Chen et al. (2015) found that the contact area ratio and thickness of joints affect the dynamic pressure-closure relation.

Although it is clear that the joint characteristics have significant influence on wave propagation and the dynamic property of rock masses, there are relatively few researches to study the effect of joint contact area (Hopkins 2000, Chen et al. 2015). A series of dynamic tests were carried out using the Split Hopkinson Pressure Bar (SHPB) apparatus developed by Kolsky (1949) in the present study. According to the experimental results, the effect of contact area ratio and spatial geometry of contact surface on wave propagation across jointed rock mass and dynamic property of joint are analyzed and discussed.

## 2 EXPERIMENTAL STUDY

### 2.1 *Experimental setup*

The dynamic tests were performed in compression mode using SHPB apparatus at room temperature, as shown in Figure 1. The SHPB apparatus is made up of a striker, a input bar, an output bar, a momentum trap bar and a data acquisition system. Both the diameters and the lengths of input and output bars are the same, which are 50 mm and 2500 mm, respectively. The length of striker bar is 400 mm and the diameter is 50 mm. The Young's modulus $E$ of the bars is 210 GPa, the density $\rho$ is 7800 kg/m$^3$ and the longitudinal wave velocity $c_0$ is 5124 m/s.

### 2.2 *Specimen preparation*

Natural joint surface is complex and random which leads to the difficulty in sample preparation. Hence, the artificial granite joints were used in the present study. The density of the specimen is 2630 kg/m$^3$, Young's modulus is 30 GPa and Poisson ratio is 0.30, respectively.

Each test specimen was composed of two granite blocks, as shown in Figure 2(b). The blocks were cylinders with diameter and thickness being 50 mm and 25 mm, respectively. Both surfaces of the block ends were polished strictly to ensure flatness. Then the cutting machine was used to groove on the surface of the blocks, as shown in Figure 2(a). The depth of the notches was 3 mm, i.e. the joint thickness is 3 mm. The blocks were divided into three groups according to the width of notches, i.e. 4 mm, 5 mm and 6 mm, respectively. Each group includes seven blocks with notch number ranging from 1 to 6, where the blocks s-4-4 and s-4-4' (or blocks s-5-4 and s-5-4', blocks s-6-4 and s-6-4') shown in Figure 2(a) have the same notch line number and notch width but different notch distribution pattern. For the blocks with same notch number but different notch width, such as s-4-2, s-5-2 and s-6-2, the center line of the notches were arranged at the same position on the block surfaces. An artificial joint was generated from the two contact surfaces of the notched blocks and another block without notches. Here, the contact area ratio which denotes the Joint Matching Coefficient (JMC) is defined as the ratio of the sum area of convex surface on notched blocks to the surface area of un-cutting blocks. As shown in Table 1, different notch number and width of blocks lead to different JMC values.

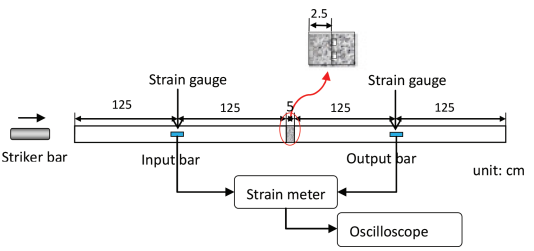


Figure 1. Schematic view of SHPB test equipment.

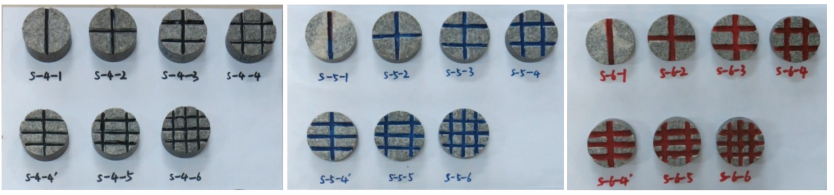

notch width of 4 mm notch width of 5 mm notch width of 6 mm

(a) Granite blocks with notches

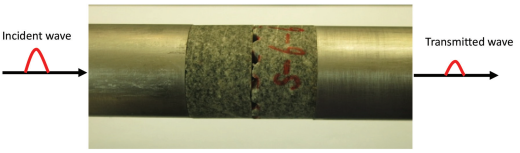


(b) Specimen during the test

Figure 2. Specimens for the SHPB test.

Table 1. The matching coefficient of an artificial joint (JMCs).

| Number of notch | 1 | 2 | 3 | 4 | 4 | 5 | 6 |
|---|---|---|---|---|---|---|---|
| Notch width | JMC | | | | | | |
| 4 mm | 0.897 | 0.803 | 0.726 | 0.657 (for s-4-4') | 0.644 | 0.597 | 0.519 |
| 5 mm | 0.872 | 0.756 | 0.663 | 0.583 (for s-5-4') | 0.561 | 0.507 | 0.417 |
| 6 mm | 0.847 | 0.712 | 0.603 | 0.513 (for s-6-4') | 0.481 | 0.422 | 0.324 |

## 3 SHPB TESTS RESULTS AND ANALYSIS

### 3.1 *Experimental waveforms*

22 groups of tests were conducted to investigate the effect of contact area on stress wave propagation and the dynamic mechanical property of rock joints. Each group of tests includes three repeated ones to guarantee the efficiency of the experimental study. During the tests, a small piece of rubber was selected as the pulse shaper whose diameter and thickness were 2.5 mm and 1 mm, respectively. And petroleum jelly was used to reduce the friction between the specimen and the bars. To avoid the damage in the specimen, the impact velocity of striker bar was controlled to be about 1.0 m/s in the study.

As the impact velocity of striker was almost the same, similar waveforms of incident wave were generated for different specimens. For brevity, Figure 3 shows the typical records of strain gauges when the notch width was 6 mm and the JMC was 0.712. The incident and reflected waves in the input bar and the transmitted wave in the output bar can be seen clearly from the records. The amplitude of the incident wave is about 255 με, the amplitude of the transmitted wave is 174 με. The attenuation occurs when stress wave propagates across the joint. The incident, reflected and transmitted waves for other specimens were similar to the waveforms shown in Figure 3.

### 3.2 *Analysis of stress-strain relation*

According to the fundamental theory of SHPB test, the stress $\sigma$, strain rate $\dot{\varepsilon}$, and strain $\varepsilon$ of the specimen can be calculated by the following expressions:

$$\sigma = \frac{EA}{2A_S}\left(\varepsilon_i + \varepsilon_r + \varepsilon_t\right) \tag{1}$$

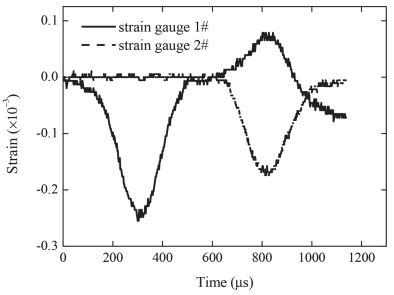


Figure 3. Records for typical specimen.

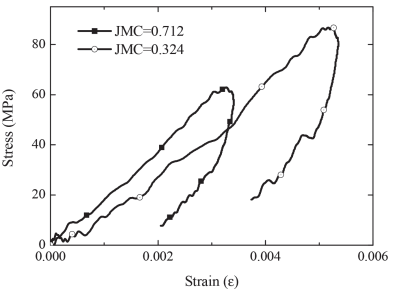


Figure 4. Stress-strain relation of specimens.

$$\dot{\varepsilon} = \frac{c_0}{l_0}\left(\varepsilon_i + \varepsilon_r + \varepsilon_t\right) \tag{2}$$

$$\varepsilon = \frac{c_0}{l_0}\int_0^t \left(\varepsilon_i - \varepsilon_t - \varepsilon_r\right)dt \tag{3}$$

where $E$ = Young's modulus of input and output bars; $A$ = the area of the interface between the bars and specimen; $c_0$ = wave spreading velocity in the input and output bars; $l_0$ = the length of specimen; $\varepsilon_i$, $\varepsilon_t$, $\varepsilon_r$ = incident, transmitted and reflected waves recorded by the strain gauges, respectively; and $t$ = time.

From Equations 1–3, we can obtain stress and strain values of the specimen when incident, transmitted and reflected strain waves were obtained. From the variation of stress and strain with time history, the relation between the stress and strain of the specimen can be obtained. Figures 4 shows the curves of stress versus strain for the specimen with notch width of 5 mm but JMC being 0.712 and 0.324, respectively. It is observed from Figure 4 that during loading process all of the deformation of specimens increase with pressure acting on the specimen until arriving at the peak value. From Figure 4, the maximum deformation of specimen becomes larger when JMC becomes lower. In addition, the relation between stress and strain of specimen is influenced by JMCs. It is almost linear when the JMC is 0.712 and it becomes nonlinear when JMC is 0.324.

### 3.3 *Joint closure analysis*

As the total deformation of each joint block is caused by the artificial joint and the adjacent rocks, that is,

$$\Delta u = \Delta u_r + \Delta u_j \tag{4}$$

here, $\Delta u$ = displacement of specimen, $\Delta u_r$ = deformation of adjacent rock and $\Delta u_j$ = deformation of joint, respectively. From Hooke's law, there is

$$\varepsilon = \frac{\sigma\left(l_0 - l_j\right)}{E_r l_0} + \frac{\varepsilon_j l_j}{l_0} = \frac{\sigma\left(l_0 - l_j\right)}{E_r l_0} + \frac{\Delta u_j}{l_0} \tag{5}$$

where $\varepsilon$ = total strain of specimen, i.e. the value calculated from Equation 4, $E_r$ = Young's modulus of intact rock, which equals to 30 GPa, $\varepsilon_j$ = strain of joint and $l_j$ = joint thickness which is 3 mm in the study. Equation 5 can be rewritten as

$$\Delta u_j = \varepsilon l_0 - \frac{\sigma\left(l_0 - l_j\right)}{E_r} \tag{6}$$

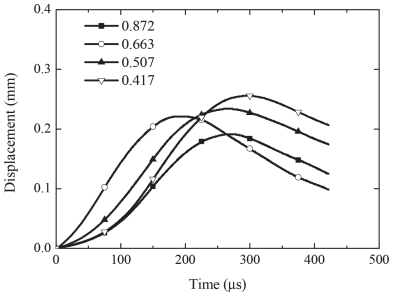


Figure 5. Displacement values of specimens with different JMCs (notch width 5 mm).

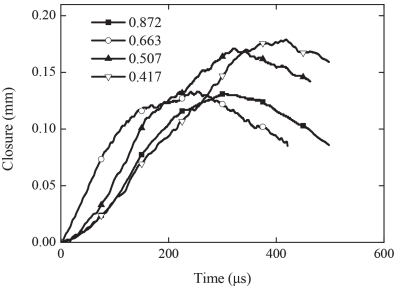


Figure 6. Closure values of joints with different JMCs (notch width 5 mm).

Table 2. The specific stiffness of an artificial joint.

| JMC | Stiffness (GPa/m) | JMC | Stiffness (GPa/m) | JMC | Stiffness (GPa/m) |
|---|---|---|---|---|---|
| Notch width 4 mm | | Notch width 5 mm | | Notch width 6 mm | |
| 0.897 | 194.6 | 0.872 | 201.1 | 0.847 | 230 |
| 0.803 | 186.4 | 0.756 | 185.1 | 0.712 | 221.4 |
| 0.726 | 182.5 | 0.663 | 184.95 | 0.603 | 210 |
| 0.657 | 156.9 | 0.583 | 175.5 | 0.513 | 195.2 |
| 0.644 | 160.1 | 0.561 | 161.2 | 0.481 | 193.5 |
| 0.597 | 177 | 0.507 | 148.8 | 0.422 | 180 |
| 0.519 | 126.1 | 0.417 | 135.8 | 0.324 | 165.9 |

Figure 5 show specimen displacement values versus time when the width of notch is 5 mm and JMCs are 0.872, 0.663, 0.507 and 0.417, respectively. We can see from the figure that the displacement values of specimens during the test increase with the decrease of JMC.

Similar to the tendency of curves shown in Figure 5, Figure 6 shows that the peak value of joint closure is higher when the value of JMC declines. From Figures 5–6, the peak values of deformation of specimen and joint are about 0.191 and 0.131 mm, respectively, for JMC being 0.872, about 0.234 and 0.171 mm, respectively, for JMC being 0.507 and about 0.256 and 0.18 mm, respectively, for JMC being 0.417. The percentages of the deformation of joint in whole deformation of the specimen are 68.6%, 73.1% and 70.3%, although the ratio of the joint thickness to the specimen length is only 6%. It indicates that the deformation of the specimen is mainly caused by the deformation of the joint. Figure 6 indicates nonlinear deformation occurs when JMC is relatively small.

The closure of joints is closely related to the joint stiffness. To investigate the influence of JMC on initial normal stiffness, the specific normal stiffness $k_n$ is defined as

$$k_n = \frac{\sigma}{\Delta u_j} \tag{7}$$

where $\Delta u_j$ = closure over the entire range of compressive stress and $\sigma = \sigma_{\Delta u_j/2}$, i.e. the compressive stress corresponding to the half value of joint closure (Malama & Kulatilake 2003).

We can observe from Table 2 that the joint specific stiffness generally increases with the increase of JMC when the notch width of specimen is given. For example, for joints with notch width of 6 mm, the joint specific stiffness varies from about 165.9 GPa/m for JMC of 0.324 to 230 GPa/m for JMC of 0.847. By comparison, it is found that for a given JMC the specific stiffness for joint with notch width of 4 mm is the lowest while the specific stiffness for joints with notch width of 6 mm is the highest. For example, for the specimens named s-4–6, s-5–5 and s-6–4 with JMC being around 0.51, the stiffness is 126.1, 148.8 and 195.2 GPa/m, respectively. It indicates that joints having compact contact area are harder and more difficult to deform, and vice versa.

## 4 CONCLUSIONS

The test results demonstrate that wave propagation and dynamic property of joints are obviously influenced by the joint contact area ratio (e.g. JMC). From the test experimental study, the following findings can be summarized as:

1. When stress wave propagates across joints, wave attenuation occurs.
2. The dynamic normal property of rock joints is related to the JMC. The deformation of joint block increases with the decreasing of JMC. What's more, the stress-strain relation of rockmass behaves nonlinear when JMC is smaller enough.
3. The deformation of joint block is mainly caused by the artificial joint though the ratio of the joint thickness to the specimen length is only 6%.
4. Spatial geometry of joints influences the stiffness of joints. For a given JMC, the specific stiffness for joint surface with wide notches is larger than that for joint surface with narrow notches.

## ACKNOWLEDGEMENTS

The study was supported by the National Science Foundation of China (No. 41525009, 41272348) and the Scientific Research Foundation for Returned Chinese Scholars (No. 2012-940).

## REFERENCES

Bandis, S.C., Lumsden, A.C. & Barton, N.R. 1983. Fundamentals of rock joint deformation. *International Journal of Rock Mechanics and Mining Sciences & Geomechanics Abstracts* 20(6): 249–268.

Barton, N. & Choubey, V. 1977. The shear strength of rock joints in theory and practice. *Rock mechanics* 10(1–2): 1–54.

Brown, S.R. & Scholz, C.H. 1985. Closure of random elastic surfaces in contact. *Journal of Geophysical Research: Solid Earth* (1978–2012) 90(B7): 5531–5545.

Brown, S.R. & Scholz, C.H. 1986. Closure of rock joints. *Journal of Geophysical Research: Solid Earth* (1978–2012) 91(B5): 4939–4948.

Chen, X., Li, J.C., Cai, M.F., Zou, Y. & Zhao, J. 2015. Experimental study on wave propagation across a rock joint with rough surface. *Rock Mechanics and Rock Engineering* 48(6): 2225–2234.

Hopkins, D.L. 2000. The implications of joint deformation in analyzing the properties and behavior of fractured rock masses, underground excavations, and faults. *International Journal of Rock Mechanics and Mining Sciences* 37(1): 175–202.

Kolsky, H. 1949. An investigation of the mechanical properties of materials at very high rates of loading. *Proceedings of the Physical Society*. Section B 62(11): 676.

Li, J.C. & Ma, G.W. 2009. Experimental study of stress wave propagation across a filled rock joint. *International Journal of Rock Mechanics and Mining Sciences* 46(3): 471–478.

Li, J.C., Li, H.B., Ma, G.W. & Zhao, J. 2012. A time-domain recursive method to analyse transient wave propagation across rock joints. *Geophysical Journal International* 188(2): 631–644.

Li, J.C. 2013. Wave propagation across non-linear rock joints based on time-domain recursive method. *Geophysical Journal International* 193(2): 970–985.

Malama, B. & Kulatilake, P. 2003. Models for normal fracture deformation under compressive loading. *International Journal of Rock Mechanics and Mining Sciences* 40(6): 893–901.

Misra, A. & Marangos, O. 2010. Rock-joint micromechanics: relationship of roughness to closure and wave propagation. *International Journal of Geomechanics* 11(6): 431–439.

Pyrak-Nolte, L.J., Myer, L.R. & Cook, N.G. 1990a. Transmission of seismic waves across single natural fractures. *Journal of Geophysical Research: Solid Earth* (1978–2012) 95(B6): 8617–8638.

Pyrak-Nolte, L.J., Myer, L.R. & Cook, N.G. 1990b. Anisotropy in seismic velocities and amplitudes from multiple parallel fractures. *Journal of Geophysical Research: Solid Earth* (1978–2012) 95(B7): 11345–11358.

Zhao, J. 1987. *Experimental Studies of the Hydro-thermo-mechanical Behaviour of Joints in Granite*. Diss. Imperial College London.

Zhao, J. 1997. Joint surface matching and shear strength part A: joint matching coefficient (JMC). *International Journal of Rock Mechanics and Mining Sciences* 34(2): 173–178.

Zhao, J. & Cai, J.G. 2001. Transmission of elastic P-waves across single fractures with a nonlinear norm-al deformational behavior. *Rock Mechanics and Rock Engineering* 34(1): 3–22.

*Rock Dynamics: From Research to Engineering – Li et al. (Eds)*
*© 2016 Taylor & Francis Group, London, ISBN 978-1-138-02953-8*

# Research on mechanical properties of gneissic granite under real-time temperature

X.F. Li
*91552 Force Construction Management Office, Sanya, China*

D.W. Wu
*School of Urban Design, Wuhan University, Wuhan, China*

X.F. Zhang & H. Deng
*Zhongjiao Wuhan Harbour Engineering Design Research Institute Co. Ltd., Wuhan, China*

ABSTRACT: The adaptive automatic triaxial testing machine test study on mechanical properties at different temperatures of the role of gneissic granite conduct, failure mechanism analysis gneissic granite peak stress, peak strain, elastic modulus variation with temperature. The results showed that: the temperature of the mechanical characteristics of gneissic granite greater impact, as the temperature rises, the mechanical properties of gneissic granite obvious damage, peak stress and elastic modulus decreased peak strain increases. In gneissic granite elastic modulus variation with temperature start, assuming that rock infinitesimal strength to obey two Weibull distribution parameters derived considering thermal effect of damage evolution equation and damage constitutive equation.

## 1 INTRODUCTION

Rock is a different cement and mineral particles and contains a lot of micro-cracks and micro-holes and other defects in natural materials, their physical and mechanical properties by severe temperature. Processing railways, highways, utilities, inter-basin water transfer, and other mineral resources in the field of underground rock engineering, rock mechanics often need to consider the effect of temperature characteristics. Thus, fully aware of the influence of temperature on mechanical properties of rock, for ensuring the long-term temperature influence of rock engineering stability and security of the key.

Over the years, scholars have conducted research on the mechanical properties of rock temperature effects. Alm et al. (1985) The mechanical properties and failure mechanisms of granite are subject to different temperatures after heat treatment. Oda (1993) studied the basic mechanical properties and failure mechanism of rock under the effect of temperature. Lau & Jackson (1995) studied the elastic modulus of the lower confining pressure granite, Poisson's ratio, compressive strength and failure criterion variation with temperature. Zhang et al. (1987), Xu & Liu 2000, Wang et al. 2002 and Du et al. 2004 studied the elastic modulus, Poisson's ratio, compressive strength and other mechanical parameters change with temperature. Zhu et al. (2006) studied the sintering temperature after different tuff, granite and mechanical properties rhyolitic tuff breccia shape. Su et al. (2008) studied the changes of the mechanical parameters of rough sandstone after high temperature. Zhang et al. (2009) using the test methods were investigated through room temperature to 800°C high temperature, the marble, limestone and sandstone peak intensity, peak strain and elastic modulus variation with temperature. Wang et al. (2013) analyzed the physical and mechanical properties of marble at different temperatures and temperature cycling effects. From the current research

situation, the more rock mechanical properties after high temperature relates to energy storage, nuclear waste disposal, etc., on a real-time temperature of underground rock engineering little research. In fact, at a certain temperature rock engineering environment, the rock due to thermal expansion (Kang 2008) is irreversible, and the components constituting the rock at different temperatures show a different morphology, so the temperature of the cooling or at room temperature test, the results of the rock under the temperature conditions are very different.

Paper chooses gneissic granite material, the use of automatic triaxial testing machine under conventional triaxial compression test temperature effects, discuss the role of different temperatures gneissic granite mechanical characteristics of the impact of the establishment of damage constitutive equation considering the effect of temperature, in order for the relevant rock engineering practice to provide theoretical and experimental basis.

## 2 EXPERIMENTS

### 2.1 *Sample material*

Gneissic granite sample selected Xinjiang Tashikuergan homogeneous heat Khattar Hydropower Project Water Tunnel Tunnel Section within the range, based on rock mechanics test standard, processed into diameter and height ratio of 1:2 cylinder, the size of φ50 mm × 100 mm, the average density was 2.66 g/cm$^3$. In order to ensure uniform rock-like properties selected to reduce discrete test results, before the test, the use of non-metallic NM-4 A-type ultrasonic analyzer and ZC4 Hammer specimens were acoustic wave detector and rebound test, select a similar nature gneiss specimens were tested.

### 2.2 *Test equipment and processes*

The test equipment Lille University of Science and automated triaxial testing machine TOP INDUSTRIE cooperation with R & D, testing equipment panorama shown in Figure 1, the maximum operating temperature is 90°C.

The test temperature is divided into normal temperature (20°C), 30°C, 40°C, 50°C, 60°C, 70°C temperature grade five, to carry out triaxial confining pressure 10 MPa. To reduce the difference to a rock sample analysis results and difficulties caused by the error, at each temperature condition for each selected three rock samples tested rock samples of dried specimens.

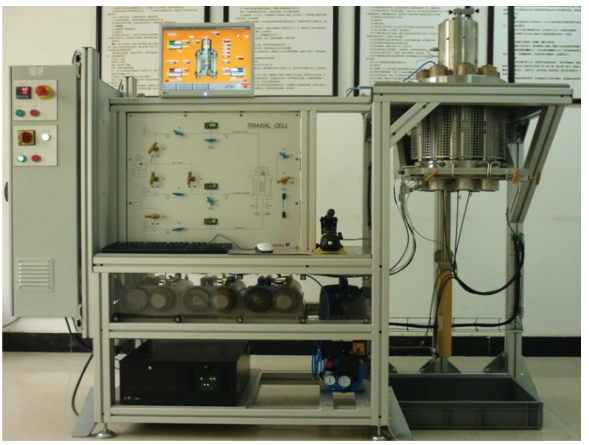


Figure 1. Triaxial test equipment.

The test was divided into two phases: the first phase of heating process (heating and insulation), the temperature of the pressure chamber from room temperature to rise to a certain heating rate desired test temperature, in order to ensure uniform heating of the sample the temperature rises to the set point thermostat 6 h; the second stage was loading, load pressure control were used with a loading rate of 1 MPa/min, the hydraulic pump on the rock samples by confining pressure was applied to the set value after applying an axial partial stress, triaxial test routine. After the test, rock samples were removed, and the test results were analyzed.

## 3 TEST RESULTS AND ANALYSIS

Under these test conditions, gneissic granites at different temperatures role triaxial compression results in Table 1. Figure 2 shows the failure modes and fracture morphology gneissic After the temperature 30°C, at 50°C, 70°C temperature conditions for testing three samples of granite. After comparative analysis of three temperature conditions showings failure modes and fracture morphology of hemp granite can be found: the temperature changes, the difference between failure modes gneissic granite little shear fracture surface are a penetrating, fracture surface and the maximum principal stress direction was about 30° angle, the destruction of the fracture relatively flat. As the temperature increases, in addition to the main fracture surface, a plurality of parallel sample surface cracks appear in the main direction of the fracture surface. Note When triaxial compression gneissic granite at a temperature of 20°C ~ 70°C impact shear failure is still the main form of the deformation, the failure mechanism has not been changed.

### 3.1 *Peak stress variation with temperature*

Figure 3 is a curve gneissic granite peak stress and temperature. As can be seen from the figure: from room temperature to 40°C, the temperature effect gneissic granite peak stress decreased with increasing temperature, but at 40°C~50°C under peak stress increased slightly with temperature, an increase of about 5.71%, 70°C gneissic granite peak stress drop, peak stress from 165.99 MPa down to 137.29 MPa, a drop of 17.29% can be considered constant confining pressure gneissic granite peak stress decreases with increasing temperature, variation is obvious.

Table 1. Testing results under temperature.

| NO. | Tem. (°C) | (MPa) | (%) | (GPa) |
|---|---|---|---|---|
| #14 | 20 | 164.83 | 0.4405 | 38.616 |
| #15 | 20 | 169.31 | 0.4525 | 38.886 |
| #16 | 20 | 163.83 | 0.4378 | 38.001 |
| #17 | 30 | 150.11 | 0.4379 | 38.118 |
| #18 | 30 | 157.29 | 0.4427 | 38.536 |
| #19 | 30 | 150.72 | 0.4318 | 37.585 |
| #20 | 40 | 141.49 | 0.4134 | 38.099 |
| #21 | 40 | 146.76 | 0.4331 | 38.749 |
| #22 | 40 | 139.21 | 0.4151 | 37.679 |
| #23 | 50 | 147.31 | 0.4296 | 37.723 |
| #24 | 50 | 155.89 | 0.4547 | 38.749 |
| #25 | 50 | 148.66 | 0.4335 | 37.495 |
| #26 | 60 | 148.34 | 0.4432 | 37.374 |
| #27 | 60 | 152.38 | 0.4552 | 38.389 |
| #28 | 60 | 147.45 | 0.4405 | 37.147 |
| #29 | 70 | 133.58 | 0.4905 | 35.873 |
| #30 | 70 | 142.78 | 0.5243 | 37.217 |
| #31 | 70 | 135.51 | 0.4975 | 35.837 |

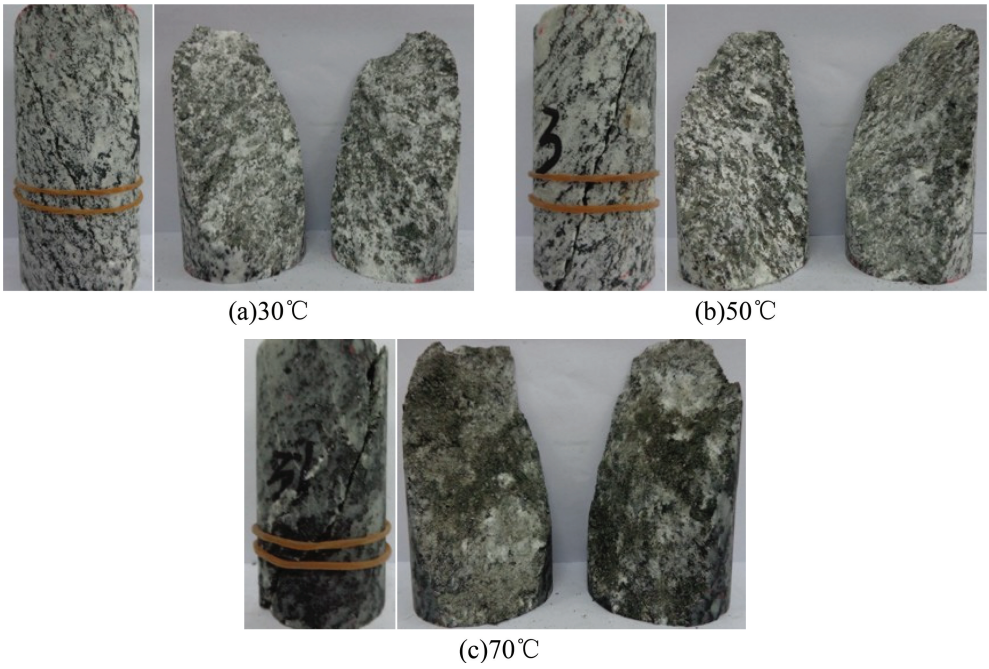


Figure 2. Shapes under different temperature.

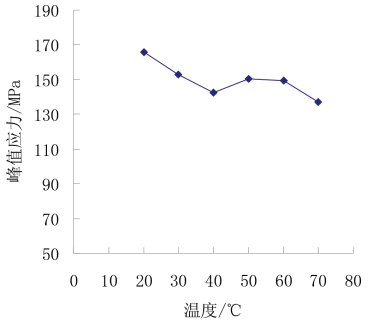


Figure 3. Granite peak stress versus temperature curve.

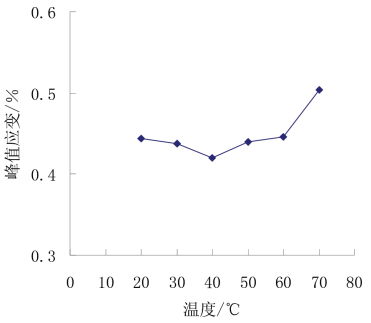


Figure 4. Ma granite peak strain and temperature.

### 3.2 *Peak strain variation with temperature*

Figure 4 is a curve gneissic granite peak strain and temperature. As can be seen from Figure: from room temperature to 40°C, gneissic granite peak strain decreased slightly with temperature, a decline of about 5.21%, peak strain at 40°C ~ 70°C effects were $4.205 \times 10^{-3}$, $4.393 \times 10^{-3}$, $4.463 \times 10^{-3}$, $5.041 \times 10^{-3}$, respectively, an increase of 4.47%, 6.14%, 19.88%, 70°C peak strain increase of 13.64% relative to room temperature, the analysis from the overall trend, indicating that the temperature effect on the influence of sample peak strain more significant, gneissic granite peak strain increases with temperature increases.

### 3.3 *Elastic modulus variation with temperature*

Figure 5 is a gneissic granite elastic modulus versus temperature curve. As can be seen from the figure: from room temperature to 30°C, gneissic granite elastic modulus decreased with increasing temperature, but at 30°C~40°C elastic modulus increased slightly with temperature,

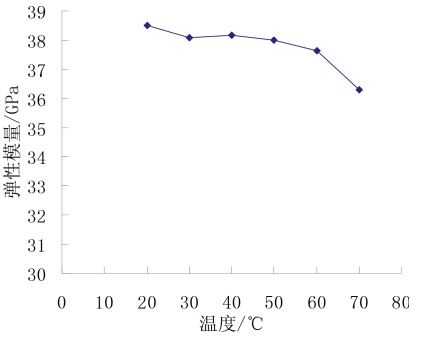


Figure 5. Ma granite relationship between elastic modulus versus temperature curve.

an increase of about 0.25% in 40°C~70°C under the elastic modulus of rock specimen with increasing temperature declining, 70°C showings Ma granite specimen elastic modulus relative to the normal temperature drop of 5.69%, indicating that the temperature inside the specimen thermal stress, resulting in gneissic granite injury, the peak stress is reduced at the same time, the elastic modulus is also reduced.

## 4 TEMPERATURE EFFECTS GNEISSIC GRANITE INJURY

### 4.1 *Ma granite heat damage*

So that the internal temperature of gneissic granite produce large amounts of microscopic cracks, peak stress, elastic modulus with increasing temperature decreased presented, indicating the temperature of inflicting damage. As can be seen from Figure 5, the elastic modulus is a function of temperature, the elastic modulus of paper damage variables to describe the mechanical properties of granite sheet hemp affected by temperature, thermal damage definitions:

$$D_T = 1 - \frac{E_T}{E_0} \tag{1}$$

where $E_T$, $E_0$ the temperature, the elastic modulus at room temperature of 20°C, respectively, thermal damage value gneissic granite passes calculated at different temperatures (Table 2).

### 4.2 *Effect of temperature damage evolution equation*

Ma granite sheet damage evolution by continually Micro Cell damage caused, the damage variable is defined as the number of destroyed and the total number of infinitesimal infinitesimal ratio:

$$D = \frac{N_P}{N_{总}} \tag{2}$$

assuming that the rocks inside Micro Cell obey two parameters Weibull distribution, namely

$$f(k) = \frac{m}{F}\left(\frac{k}{F}\right)^{m-1} \exp\left[-\left(\frac{k}{F}\right)^{m}\right] \tag{3}$$

Table 2. Different temperatures backsheet hemp granite heat damage.

| T/°C | 20 | 30 | 40 | 50 | 60 | 70 |
|---|---|---|---|---|---|---|
| $E_T$/GPa | 38.501 | 38.08 | 38.176 | 37.989 | 37.637 | 36.309 |
| $D_T$ | 0.0000 | 0.0109 | 0.0084 | 0.0133 | 0.0224 | 0.0569 |

where $m$, $F$ reflect the uniformity characteristics of rock, the average strength characteristics, respectively. Gneissic granite uniformity, the peak strength, elastic modulus variation with temperature is similar, it is:

$$\begin{aligned} m(T) &= m_0(1-D_T) \\ F(T) &= F_0(1-D_T) \end{aligned} \tag{4}$$

Formula (4), $m_0$, $F_0$ representing the normal condition showings Weibull parameters hemp granite, the number of micro unit has a certain level of stress is destroyed

$$N_P = \int_0^k N_{总} f(t)dt \tag{5}$$

Substitution of Equations (3), (4) and (5) into Equation (2) gives the injury variables are:

$$D = 1 - \exp\left[ -\left( \frac{k}{F_0(1-D_T)} \right)^{m_0(1-D_T)} \right] \tag{6}$$

Based on Drucker-Prager failure criterion of rock strength is infinitesimal:

$$f(\sigma) = \alpha I_1 + \sqrt{J_2} = \frac{\sin\varphi}{\sqrt{9+3\sin^2\varphi}} I_1 + \sqrt{J_2} = k \tag{7}$$

(7) $\varphi$ In the formula for the internal friction angle of the rock; $I_1$ the first invariant of the stress tensor; $J_2$ the second invariant of the stress tensor. Expressed as:

$$\begin{aligned} I_1 &= \sigma_1 + 2\sigma_3 \\ J_2 &= \frac{1}{3}(\sigma_1 - \sigma_3)^2 \end{aligned} \tag{8}$$

Substitution of Equation (7) into Equation (6) gives gneissic granites at different temperatures under the action of damage evolution equation expression:

$$D = 1 - \exp\left[ -\left( \frac{\alpha I_1 + \sqrt{J_2}}{F_0(1-D_T)} \right)^{m_0(1-D_T)} \right] \tag{9}$$

### 4.3 *Consider the damage constitutive equation temperature effect*

According to the test plan and test conditions assume different temperatures gneissic granite effective axial stress $\sigma_1'$, confining pressure and effective stress $\sigma_2'(\sigma_2' = \sigma_3')$, the corresponding strain respectively $\varepsilon_1$ and $\varepsilon_2$ $(\varepsilon_2 = \varepsilon_3)$

Can be obtained by the generalized Hooke's law

$$\varepsilon_1 = \frac{(\sigma_1' - 2\mu\sigma_3')}{E} \tag{10}$$

According to the principle of equivalence has strain

$$\sigma_1^{'}=\frac{\sigma_1}{1-D}$$
$$\sigma_3^{'}=\frac{\sigma_3}{1-D} \tag{11}$$

Substitution of Equation (11) into Equation (10) gives

$$\sigma_1 = 2\mu\sigma_3 + (1-D)E\varepsilon_1 \tag{12}$$

Equation (1) is substituted into Equation (12) to give gneissic granite considering thermal effect of the damage constitutive equation:

$$\sigma_1 = 2\mu\sigma_3 + E_0(1-D_T)(1-D)\varepsilon_1 \tag{13}$$

## 5 CONCLUSION

1. At room temperature (20°C) to 70°C role when gneissic granite triaxial compression form, failure mechanism has not been changed, still the main shear failure.
2. At room temperature (20°C) to 70°C role gneissic granite internal thermal stress, damage, peak stress with decreasing temperature, while also a corresponding reduction in the elastic modulus, peak strain but with temperature increases.
3. By introducing thermal damage, assuming infinitesimal rock strength to obey two parameters Weibull distribution, damage evolution equation was established to consider the temperature effect, can accurately reflect the temperature of gneissic granite mechanical properties.
4. The use of equivalent strain theory and the generalized Hooke's law, the establishment of a gneissic granite damage constitutive equation considering temperature effects: $\sigma_1 = 2\mu\sigma_3 + E_0(1-D_T)(1-D)\varepsilon_1$.

## REFERENCES


Alm, O. et al. 1985. The influence of micro crack density on the elastic and fracture mechanical properties of stropa granite. *Physics of the Earth and Planetary Interiors* 40: 161–179.

Du, S.J., Liu, H., Zhi, H.T. et al. 2004. Testing study on mechanical properties of post-high-temperature granite. *Chinese Journal of Rock Mechanics and Engineering* 23(14): 2359–2364. (in Chinese).

Kang, J. 2008. *Research and Application of Therm Cracking of Rock*. Dalian: Dalian University of Technology Press: 147–149. (in Chinese).

Lau, J.S.O. & Jackson R. 1995. The effects of temperature and water-saturational on mechanical properties of Lac du Bonnet pink granite. *8th Int. Con. on Rock Mech.*, Tokyo, Japan.

Oda, M. 1993. Modern developments in rock structure characterization. *Comprehensive Rock Engineering* 1: 185–200.

Su, C.D., Guo, W.B., Li, X.S. 2008. Experimental research on mechanical properties of coarse sandstone after high temperatures. *Chinese Journal of Rock Mechanics and Engineering* 27(6): 1162–1170. (in chinese).

Wang, R., Zhu, D.Y. et al. 2013. Influence of temperature on the mechanical performance of marble. *Metal Mine* 04: 49–53. (in Chinese).

Wang, Y.Y., Zhang, H.J., Huang, X.C. et al. 2002. Experimental study on whole stress-strain course of marble under the action of high temperature. *Chinese Journal of Rock Mechanics and Engineering* 21(Supp. 2): 2345–2349. (in Chinese).

Xu, X.C & Liu, Q.S. 2000. A preliminary study of basic mechanical properties for granite at high temperature. *Chinese Journal of Geotechnical Engineering* 22(3): 332–335. (in Chinese).
Zhang, J.H., Wang, J.T., Zhao, A.G. 1987. Fracture properties of granite at high temperature. *Rock and Soil Mechanics* 8(4): 11–16. (in Chinese).
Zhang, L.Y., Mao, X.B., Lu, A.H. 2009. Experimental study on the mechanical properties of rocks at high temperature. *Science in China (Series E)* 52(3): 641–647.
Zhu, H.H., Yan, Z.G., Deng, T. et al. 2006. Testing study on mechanical properties of tuff, granite and breccia after high temperatures. *Chinese Journal of Rock Mechanics and Engineering* 25(10): 945–1950. (in Chinese).

*Rock Dynamics: From Research to Engineering – Li et al. (Eds)*
*© 2016 Taylor & Francis Group, London, ISBN 978-1-138-02953-8*

# Research on the static and dynamic properties of the granite in Xinjiang Province Tianhu Area for the geological disposal of the high level radioactive waste

K. Man & H.S. Ma
*Division of Environment Engineering, Beijing Research Institute of Uranium Geology, Beijing, China*
*Key Laboratory of China National Nuclear Corporation on High Level Radioactive Waste Geological Disposal, Beijing, China*

X.L. Liu
*State Key Laboratory of Hydroscience and Hydraulic Engineering, Tsinghua University, Beijing, China*

F.Q. Gong
*School of Resources and Safety Engineering, Central South University, Hunan, China*

Z.M. Chen
*University of Science and Technology Beijing, China*

ABSTRACT: Based on the MTS815 Flex Test GT for the rock testing and SHPB (Split Hopkinson Pressure Bar), the static and dynamic properties of the granite in Xinjiang province Tianhu area have been studied deeply, which is a preselected area for the HLW (High Level radioactive Waste) geological disposal. For the granite in the borehole, the tension testing, uniaxial compression testing, dynamic tension testing, dynamic compression testing and the one dimension coupled static and dynamic loading testing have been carried out separately. Specifically, all the rock tested is from the same borehole under one same depth, i.e. 360 m, therefore, the testing results could be considered much more representative of the granite. The tension strength is about 11.75 MPa, and the uniaxial compression strength is 175 MPa or so, which is about 14 times than the tension strength. With the dynamic conditions, the dynamic tension strength is about 25 MPa~35 MPa under the stress rate is $0.34\sim0.51 \times 10^6$ MPa/s. And the dynamic compression strength located in 138 MPa~208 MPa under the strain rate is 80~160/s. With the loading rate increases, the strength is also increase, whatever the tension strength or the compression strength, which shows the loading rate effect of the rock. Furthermore, the one dimension coupled static and dynamic tension loading testing has been carried out. It is found that with the precompression stress increase, the impact dynamic strength increases. It could reach maximum when the precompression stress is about 50% of the static tension strength. Meanwhile, with the precompression stress increase, the coupled static and dynamic strength increases obviously, especially it could reach about three times of the static precompression stress, and about one and half times of the dynamic strength. The testing results show that the failure model of the coupled static and dynamic loading is also tension failure, which is the same as the static tension and conventional dynamic loading test. Through a series of the testing above, rock in this area maybe considered stable and this area could be a selected area for the HLW geo-disposal. However, the testing result is inadequate, and the other testing, for example, the seepage testing, the in site stress testing and other should be moved forward, not only in one borehole, but also in different kinds of borehole in diverse depth. Then, the rock in this area could be researched in detail, and the result and the theoretical knowledge could be applied to the blasting and excavation of the deep geo-engineering and the HLW geo-disposal.

## 1 INTRODUCTION

High-level radioactive waste has its own features of long half-life and great toxicity, its safe disposal is a common challenge faced by all nuclear power states around the world. At present, the deep geological disposal is generally considered feasible for high level radioactive waste disposal which is buried at a distance of geological body underground 500~1000 m, to ensure it effectively isolated with biosphere in tens of thousands of years or even longer. Granite for its good stability, high strength and low permeability is considered as an ideal project surrounding rock of high-level radioactive waste disposal, it is also the main candidate surrounding rock for high-level radioactive waste disposal in our country (Pan & Qian 2009, Wang et al. 2004).

The static behavior of rock, such as strength parameters, deformation modulus plays a guiding role in the design, construction, support and monitoring of rock mass engineering. Static parameters include compressive strength, tensile strength, elastic modulus, Poisson's ratio, friction coefficient, and cohesion and so on. However, the rock dynamic behavior is of great significance to engineering (Zhou & Xie 2005, Paterson & Wong 2005, Singh 1989, Nemat-Nasser & Horii 1984). In engineering excavation, Rock has been surrounding in a certain state of in-situ stress before it under dynamic load, which is many kinds of rock materials have been in a state of static stress before loading. Rock mass is not only influenced by a certain high in-situ stress, but also the superimposed effect of the dynamic load, such as the mining disturbance and even earthquake. The rock dynamic parameters also include physical quantities which corresponding to the static parameters, such as dynamic compressive strength, dynamic tensile strength, dynamic elastic modulus, and dynamic Poisson ratio and so on. Researching on these rock engineering problem, in some case it's not enough by considering dynamic load or static load simply though sometimes meet the requirements of engineering (Li XB et al. 2008, Golshani 2006, Li HB et al. 2000). Especially high-level radioactive waste disposal project is constructed in deep geological body, which is often in high dimensional and three-dimensional static stress state. It can be simulated approximately by the two-dimensional and three-dimensional static load of rocks under the effect of dynamic load. Currently, for coupled static and dynamic loads problem, it is relatively insufficient on the experimental methods of combined loading and the experimental testing of rock failure, still need to carry out further research (Zhang 2002, Dai Xia 2010).

Tianhu area of Xinjiang province as one of the preselected area of high-level radioactive waste disposal, are being gradually carried on the study of the various mechanical properties of granite. Therefore, the static and dynamic loading tests are carried out on the granite core in this paper, which performed basic research on the mechanical properties of the rock in this area.

## 2 TEST PREPARATION

### 2.1 *Multifunction static test equipment of rock*

Rock static test equipment used MTS815 multi-function rock mechanics test system in Sichuan University, which is produced by the MTS Company in US. It's mainly used for conventional mechanical test of rock, concrete and other materials, and it can achieve full digital control with automatic triaxial pressure and measuring systems.

This device is one of the most complete functions, the highest technical level of rock mechanics test equipment for its multiple functions (e.g. ordinary temperature and pressure and high temperature and pressure, static and dynamics, uniaxial compression and triaxial compression, pore water pressure and seepage pressure, indirect tension and direct tension, longitudinal wave velocity and shear wave velocity, and acoustic emission testing positioning, three-point bending test). The vibration frequency of dynamic test is above 5 Hz, the vibration waveform can be set to sine wave, triangle wave, square wave, oblique wave and random wave, and vibration phase between $0 \sim 2\pi$. MTS can be carried out with single axis and three axis test on the special test requirements, as well as can achieve no impact switch on the axial load, axial displacement, large range of axial route, circumferential displacement.

### 2.2 *Dynamic impact equipment of rock*

The SHPB setup is used for dynamic impact equipment. The date acquisition system is similar to the general SHPB. It can achieve rock axial static pressure of 0~200 MPa, confining pressure of 0~200 MPa, impact of dynamic load of 0~500 MPa, the strain rate of specimen $10^0$~$10^3$ $s^{-1}$. Both of the diameter of input bar and output bar is 50 mm.

The "spindle-shaped" bullet is placed in emission cavity that can eliminate P-C oscillation, achieve stable half-sine (rise section of loaded wave stabilized at about 100 μs), the maximum diameters of the material and the elastomer are correspondent to that of incident bar and transmission bar, the constant strain rate can be achieved using the half-sine stress wave.

### 2.3 *Preparation of the rock specimen*

The material selected the granite with well-integrity and well-proportioned. The complete core was carried out in the depth of 360 m. Test specimens are processed according to the routine test of rock mechanics performance. The diameter of drilling core is 63 mm. It need fine processing by using rock coring machine, cutting machine and polished machines equipments for meeting the test standards. It's recommended in "Standard Test Method of Engineering Rock" GB/T 50266-99 and "Water Resources and Hydropower Engineering rock testing procedures" SL264-2001 for rock basic physics experiments, uniaxial and triaxial compression tests that the diameter of rock cylinder should be 48~54 mm; the length to diameter ratios is 2.0~2.5, the tolerance of length and diameter should be ±0.3 mm; the unevenness of the surface of the specimen ends allow deviation of ±0.05 mm; section should be perpendicular to the axis of the specimen with the tolerance of ±0.25.

In this experiment, size and accuracy are recommended in "rock engineering test method standards" GB/T50266-99 for better comparing static load test results with dynamic load test results. All static test specimens were processed into the cylinder with the size of Φ50 mm × H100 mm and dynamic test specimens were processed into with the size of Φ25 mm × H50 mm. Two end faces of all specimens were carefully polished. And the nonparallelism and nonperpendicularity were less than 0.02 mm. Geometry size, density and longitudinal wave are performed on the processed specimens.

## 3 STATIC MECHANICAL PROPERTIES TEST

Static mechanical properties tests of the rock include static tensile strength tests and static compressive strength tests. The basic rock mechanical parameters of uniaxial tensile strength, uniaxial compressive strength and modulus of elastic deformation have important reference value for the design, construction and post-construction monitoring of rock mass engineering. The static tensile test and static uniaxial compression test were performed in this paper.

In order to analysis the rock mechanics parameters which compared between static loading and dynamics loading, and to make a reference for the axial compression default of static-dynamic coupling loading test, this paper measured static tensile strength of rock specimens before static-dynamic coupling loading test so that we can form early stage cognizance to the rock specimens mechanical properties. Brazil disc splitting method was used for uniaxial tensile test which is an indirect tensile strength test method. During the test, the specimens were loaded in a special fixture. Test loaded by the way of controlling displacement, and the displacement loading rate of 3 mm/min, loading the specimen, record the pressure value until it is destructed. Then the tensile strength of rock is obtained by using the calculation formula. Rock specimen upper and lower loading end surface are complete, i.e. the damage effect of the loading end is not obvious by the local stress concentration, which indicates that the test results are good, and the test data is reliable. Through this experiment, the average tensile strength of the rock specimen is 11.75 MPa, this value as the static tensile strength of all the specimens.

## 4 DYNAMIC MECHANICAL PROPERTIES TEST

The research on the dynamic mechanical properties of rock is becoming more and more important. It should be noted that the mechanical response of rock under dynamic loading is very different from that of static loading, which is caused by the inertial effects inside rock mass, and then bring the dynamic rate effect. The internal force of the rock is quickly destroyed under the dynamic impact or dynamic blasting effect. Due to the inertia effect, destruction of particles present different mechanical properties and failure states, exhibits pulled off, or shear failure modes. That is, as the different action rate, the failure form of the rock is also different.

According to the requirement of engineering development, the applied load of rock is typical of the combination of static and dynamic loads. The mechanical response of rock under static and dynamic loading is more practical. The rock mass is not only influenced by the static external force caused by geological conditions of ground stress, but also by the dynamic damage caused by excavation disturbance. Under dynamic load, the stability of rock mass should be considered. In addition, under static load, the stability of dynamic loading rock mass should be also considered the effect of dynamic and static combined loading. Therefore, this paper not only carries on the conventional dynamic compression test, the dynamic tensile test, but also carries on the static and dynamic combined load test. The dynamic characteristics of the drilling core are analyzed comprehensively by the above rock dynamic test.

Dynamic compression tests are used to obtain the dynamic compressive strength and the relationship with the strain rate. The strain rate of 80~160/s, the dynamic compressive strength of the sample is 138 MPa~208 MPa. Dynamic tensile impact test was carried out to obtain the dynamic tensile strength of rock, and the change of the strength with the loading strain rate. The test is also one of the basic test methods for the dynamic characteristics of rock.

For dynamic compression impact test, the circular end face of specimen is placed in parallel to the incident bar and transmission bar, contact with two bars by surface—surface; but for dynamic tensile impact test, the specimen is vertically placed on the incident bar and transmission bar, chamfered edge connect discs of two bars by line-surface. In the process of dynamic impact test, it is required to clamp rock samples closely, a block which the size is smaller than that of specimen can be placed in the bottom of rock specimen for stable placement and normal load of the impact test. By a series of dynamic tensile impact tests, it is found that the dynamic tensile strength of the sample is about 25 MPa~35 MPa when the loading rate is $0.34\sim0.51 \times 10^6$ MPa/s. It was found that the dynamic tensile strength increased with the increase of the loading rate. And it verified the dynamic rate effect of the brittle material of rock.

Through the one-dimensional coupled static and dynamic impact test to understand rock impact loading better. It should be noted that the impact pressure and impact velocity of punch of this kind of impact test is similar to that of first kind of axial pressure, so that compares and analyses the impact data under different axial tensile strength. Experiment of different impact dynamic pressure and different axial static load were carried out by referring the static splitting strength and dynamic tensile strength of granite and controlling seven impact loading of 0.3 MPa, 0.32 MPa, 0.35 MPa, 0.38 MPa, 0.40 MPa, 0.42 MPa, 0.45 MPa which axial static load changes of 3.53 MPa, 5.88 MPa, 8.23 MPa, 10.58 MPa (about 30%, 50%, 70%, 90% of the static tensile peak strength of specimen).

When the axial static pressure is small, part of specimen internal micro cracks has been compressed to close before it is impacted which resulting in increased modulus, but because there is no closed completely, the impact specimen is still showing a approximate elastic change trend. When the axial static pressure is large, specimen internal micro cracks not only has been compressed to close, and has been increased. Presumably, the stress-strain curve is directly entered into the nonlinear stage with no initial approximate elastic phase at this time.

It can be concluded that the impact tensile strength in dynamic-static coupling loading is 80%~280% higher than that in static loading which in the same dynamic load and different

static load. For the same axial compressive loading, with the increase of the loading rate, the impact strength of rock is also improved. It is generally believed that the mechanical properties of rock will change greatly under the dynamic load, and the dynamic strength of the rock is much larger than that of the static strength, and the deformation modulus increases obviously. Rock mechanical strength is an important characteristic parameter for studying the static properties and dynamic properties. Therefore, this paper analyzes the mechanical strength of the rock and expands the difference and relationship between the various strength parameters. Then preliminary engineering cognition on the rock mass in this area was formed.

For rock specimen, the tensile strength has important significance for its engineering properties. The failure modes of rock specimens are more tensile failure in the view of micro mechanics. With static tensile test and conventional SHPB impact test. The relationship of impact tensile strength and loading rate of rock specimens under different static loads and impact coupled static and dynamic loads as follows:

In summary, the rock dynamic tensile strength increases with the increase of impact load, and the maximum can reach 3 times than the tensile strength. This reflects the rate-dependent effect of rock. The load level is different, while the specimen strain rate is also different. When the axial static pressure is smaller, the specimen is still in elastic stage under the axial static load, at this time, the capacity of the specimen to bear the coupled static and dynamic load increases with the increase of static load. It can be considered the rock material is intensified by coupled load. The expansion of micro crack is restrained by the axial static load, especially the crack plane perpendicular to the axial static load. When no axial static load effect, dynamic load stress wave will be reflected as tensile wave in its surface, derived the expansion of crack. However, when the axial static load is existent, the crack gap is closed, the stress wave can be transmitted without reflection, and the degradation of the material is greatly suppressed.

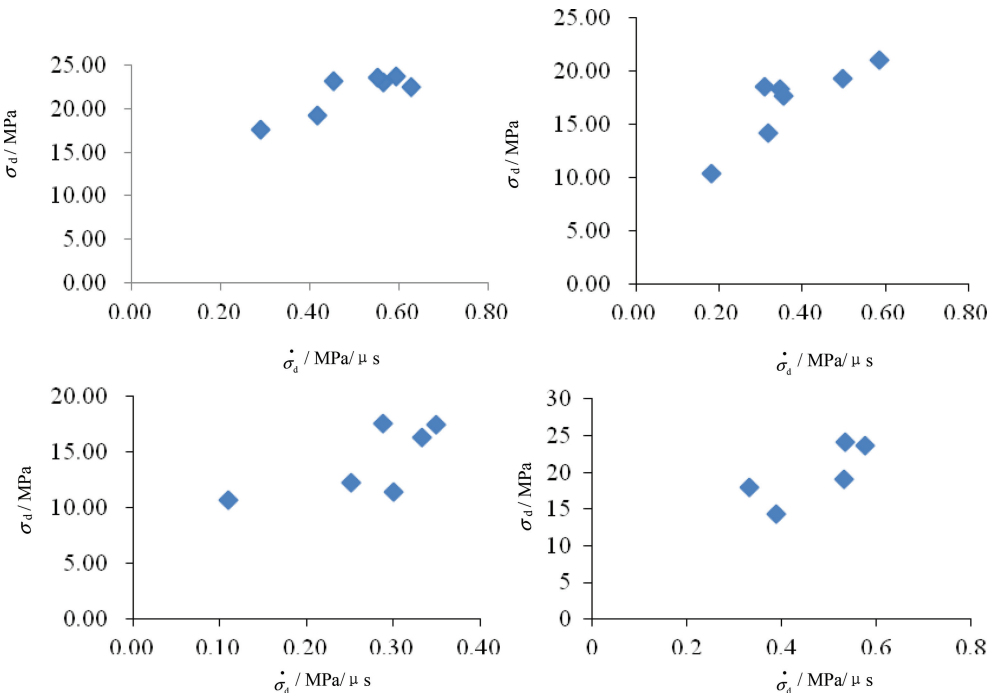


Figure 1. Relationship between dynamic tension and loading rate under static pressure (3.53 MPa, 5.88 MPa, 8.23 MPa, 10.58 MPa).

When the axial static pressure is biggish, the internal micro cracks of rock specimen not only completely closed under static compression, but also began to grow internal injury, produce new micro cracks. When the stress wave is loaded, the incident wave from the crack surface is reflected as a tensile one cracking along the crack. That is, the specimen has been partially damaged by the impact of the dynamic load. If continue to bear the dynamic impact, it will be more easy to crack damage, and accelerate the degradation of the specimen.

When the axial pressure is small, less impact energy can cause the crack to expand and the specimen to destroy; when the axial pressure is too high, the particles inside the rock specimen have already produced a certain crack, and does not require too high impact energy can cause damage to the specimen. Therefore, the impact strength and the axial pressure of the specimen has a process of first increases and then tends to smooth.

From the change trend of the coupled static and dynamic tensile strength, the static-dynamic coupling strength is the minimum value of 21.23 MPa when the axial pressure is 3.53 MPa. The static-dynamic coupling strength is the maximum value of 28.6 MPa when the axial pressure is 3.53 MPa. From the curve of overall showed a trend of increase. Using the coupled static and dynamic loads strength to characterize the influence of the axial static pressure on the impact strength is not completely consistent with using directly impact strength to characterize the influence between the impact strength and the axial static pressure. This is because the roles of different axial pressure on rock specimens are not consistent, when the axial pressure is bigger or smaller, the force produced in internal cracks is not same, and the impact strength has a critical value. In the case of a certain axial static pressure, the impact strength can reach the maximum value. As it is performed in the project, more disturbances are needed to make the rock mass reach the failure state under the role of a large static pressure. But if the static pressure becomes bigger, the rock mass has the pre rupture, at this time, the rock mass can be destroyed by a small disturbance. Before the phenomenon of rock burst, although sometimes the disturbance is not strong, but it has caused a huge rock burst phenomenon, from this point of view we can reveal the occurrence mechanism of a specific type of rock burst.

But for coupled dynamic and static load strength, it performed the rock mechanical response under all external forces, which reflects the greater confining pressure, the more elastic energy released by the excavation, the more serious damage in underground rock mass excavation. Elastic energy released by two parts, that is not only the energy generated by the external disturbance, but also the elastic energy of surrounding rock surrounding rock mass.

At the same time, it is found that the coupled dynamic and static load strength increases with the growth of static load and the impact strength, the maximum value can reach 3 times of the static load, and the anti impact load is 1.5 times. This reflects not only the rate dependent effect of rock material, but also the special mechanical properties of materials under dynamic and static loads. The greater static load supported by the rock, the bigger coupled static and dynamic tensile strength, the trend which the static load has the enhancement effect on the tensile strength is more obvious. However, the change law of static load on dynamic impact strength is enhanced at first and then weakened.

## 5 CONCLUSION

1. Based on the MTS815 Flex Test GT for the rock testing and SHPB, for the granite core from the same borehole under one same depth, i.e. 360 m, which is a preselected area for the HLW (High Level radioactive Waste) geological disposal, the tension testing, uniaxial compression testing, dynamic tension testing, dynamic compression testing and the one dimension coupled static and dynamic loading testing have been carried out separately. Through static test measured the tension strength is about 11.75 MPa, and the uniaxial compression strength is 175 MPa or so, which is about 14 times than the tension strength.
2. With the dynamic conditions, the dynamic tension strength is about 25 MPa~35 MPa under the stress rate is $0.34\sim0.51 \times 10^6$ MPa/s. And the dynamic compression strength

located in 138 MPa~208 MPa under the strain rate is 80~160/s. With the loading rate increases, the strength is also increase, whatever the tension strength or the compression strength, which shows the loading rate effect of the rock.

3. Furthermore, the one dimension coupled static and dynamic tension loading testing has been carried out. It is found that with the precompression stress increase, the impact dynamic strength increases. It could reach maximum when the precompression stress is about 50% of the static tension strength. Meanwhile, with the precompression stress increase, the coupled static and dynamic strength increases obviously, especially it could reach about three times of the static precompression stress, and about one and half times of the dynamic strength. The testing results show that the failure model of the coupled static and dynamic loading is also tension failure, which is the same as the static tension and conventional dynamic loading test.

## REFERENCES


Dai, F., Xia, K.W., Tang, L.Z. 2010. Rate dependence of the flexural tensile strength of Laurentian granite. *Int. J. Rock Mech. Min. Sci.* 47(3): 469–475.

Golshanir 2006. A micromechanical model for brittle failure of rock and its relation to crack growth observed in triaxial compression tests of granite. *Mechanics of Materials* 38: 287–303.

Li, H.B., Zhao, J., Li, T.J. 2000. Micromechanical modeling of the mechanical properties of a granite under dynamic uniaxial compressive loads. *International Journal of Rock Mechanics and Mining Sciences* 37: 923–935.

Li, X.B., Zhou, Z.L., Lok, T.S. et al. 2008. Innovative testing technique of rock subjected to coupled static and dynamic loads. Int. J. Rock Mech. Min. Sci. 45(5): 739–748.

Nemat-Nasser S. & Horii H. 1984. Rock failure in compression. *Int. J. Engng. Sci.* 22: 999–1011.

Pan, Z.Q. & Qian, Q.H. 2009. Strategic research for deep geological disposal of high level radioactive waste. Beijing: Atomic Energy Press.

Paterson, M.S. & Wong, T.F. 2005. *Experimental Rock Deformation: The Brittle Field*. 2nd ed. New York: Springer Verlag.

Singh, J. 1989. Strength of rocks at depth. In Maury, V. & Fourmaintrax, D. (eds.) *Rock at Great Depth*. Rotterdam: Balkema.

Wang, J., Fan, X.H. et al. 2004. Geological disposal of high-level radioactive waste in China: progress in last decade. Beijing: Atomic Energy Press.

Zhang, Z.X. 2002. An empirical relation between mode I fracture toughness and the tensile strength of rock. *International Journal of Rock Mechanics and Mining Sciences* 39: 401–406.

This page intentionally left blank

*Rock Dynamics: From Research to Engineering – Li et al. (Eds)*
*© 2016 Taylor & Francis Group, London, ISBN 978-1-138-02953-8*

# Determination of the dynamic shear strength of granite under confined pressure

G.J. Min, S.W. Oh, M.S. Kim, J.J. Yoon & S.H. Cho
*Department of Mineral Resources and Energy Engineering, Chonbuk National University, Jeonju, Republic of Korea*

L.J. Park
*Agency for Defense Development, Daejeon, Republic of Korea*

ABSTRACT: The shear strength of rocks is crucial when designing geo-structures, such as rock slope, tunnels, and underground space. Many researchers have suggested methods for determining the shear strength of rocks and concrete using a direct shear-box test, punch shear test, etc. In order to use the shear strength as an input parameter for simulating dynamic fracture problems that adopt a frictional failure criterion, it is necessary to obtain the dynamic shear strength with increasing normal stress.

In this study, a modified Hoek tri-axial cell, which is applicable to the Split Hopkinson Pressure Bar (SHPB), was suggested to obtain confining pressure dependent dynamic shear strength. The dynamic shear strengths were determined in increments of constant confining pressure and loading rates. Our findings show that dynamic shear strength increases with increasing confining pressure and significantly increases with loading rate increments. The value of cohesion also increased with increasing loading rate, while the internal friction angle remained constant. Validation of the suggested loading rate dependent frictional dynamic failure criteria of a granite rock is discussed.

## 1 INTRODUCTION

At impact velocities of a few hundred m/s, the rock penetration of a steel bar becomes more dependent on shear strength, which is dependent on confined pressure, than tensile strength and compressibility. The internal friction angle of the rock as a target is more important than its cohesion in predicting the penetration depth (Heuze 1990). However, it is conceivable that penetrator/rock friction rate dependency under various impact velocities may be described using rate dependent cohesion and friction angles. Many researchers have suggested methods for measuring the shear strength of rocks and concrete, such as direct shear-box test and block punch index test, under static loading conditions (Schrier van der 1988, Sulukcu & Ulusay 2001). A dynamic punch test method utilizing a Split Hopkinson Pressure Bar (SHPB) system was suggested to estimate the dynamic shear strength of rocks (Huang et al. 2011). However, the methods were limited in terms of obtaining the friction angle.

This paper introduces a tri-axial punch test method for determining a cohesion and friction angle under various loading rates. The Split Hopkinson Pressure Bar (SHPB) system, which utilizes a modified Hoek cell, was used to dynamically punch a disk shape granite sample under static confined pressure. The shear strength of granite samples as a function of given confined pressure under various punching velocities were examined to suggest a loading rate dependent frictional failure criterion.

## 2 EXPERIMENT

### 2.1 *Description of the experimental approaches*

A SHPB system, which consists of an impact bar, an incident bar, a transmitted bar, an impact bar launching system, and a data acquisition device, was adopted to perform the shear punch test of a granite disc sample.

The sample inside a modified Hoek pressure cell is sandwiched between a 20 mm diameter incident bar and a 50 mm diameter transmitted bar. Semi-conduct strain gauges are glued on the bars to monitor strain signals over time: incident strain ($\varepsilon_I$), reflect strain ($\varepsilon_R$), and transmitted strain ($\varepsilon_T$). Figure 1 shows the modified SHPB system that utilizes the Hoek pressure cell to obtain dynamic shear strength under different normal stresses (i.e., confined pressure) at various impact velocities.

In order to achieve the dynamic force balance that acts on the sample, the pulse-shaper technique using thin copper disc is applied (Chen & Song 2010, Cho et al. 2014).

The Hoek cell was designed to maintain contact between bars and rock disc under confining pressure. Figure 2 shows the details of the modified Hoek cell. The constant confining pressure was applied to the rock sample through the flexible membrane. The inner diameter of the transmitted bar supporter is slightly larger than the diameter of the incident bar. The incident bar is directly used as the punch hammer.

Using the elastic strain signals ($\varepsilon_I$,$\varepsilon_R$,$\varepsilon_T$) measured by the strain gauges on the bars, the applied forces $P_1$ and $P_2$ on both sides of a sample can be computed as:

$$P_1 = EA_I(\varepsilon_I + \varepsilon_R) \tag{1}$$

$$P_2 = EA_T(\varepsilon_T) \tag{2}$$

where $E$ = Young's modulus of bars $A_I$ = cross-sectional area of the incident bar; and $A_T$ = the transmitted bar.

To achieve a dynamic stress equilibrium state through the sample before failure, it is necessary to ensure the dynamic force balance ($P_1 \approx P_2$). If the forces at the both ends of specimen are identical, the dynamic shear stress can be estimated as:

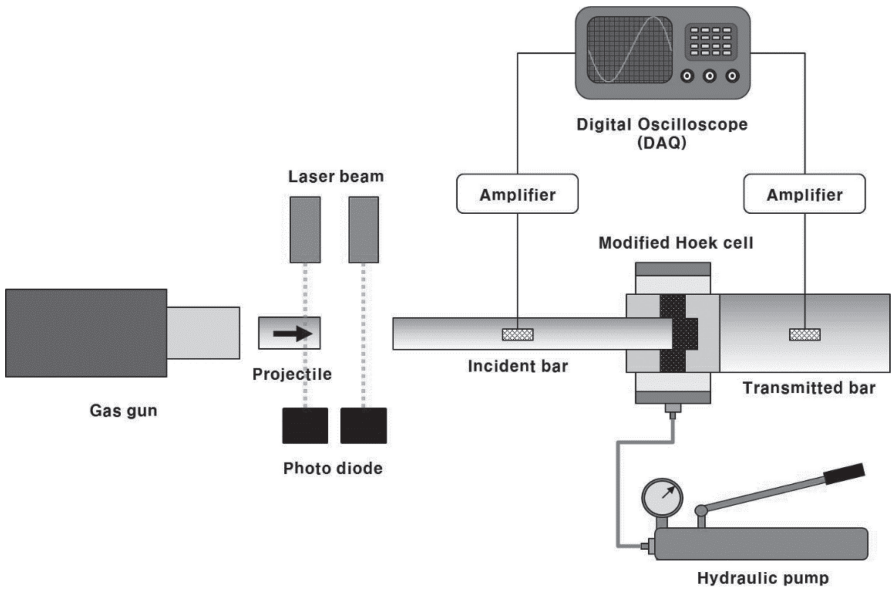


Figure 1. Schematics of a modified SHPB system for a dynamic tri-axial shear test.

$$\tau = \frac{P}{\pi DB} \tag{3}$$

where $\tau$ = dynamic shear stress; $P$ = dynamic stress measured on the transmitted bar; $D$ = the diameter of the incident bar; and $B$ = the thickness of the sample.

### 2.2 *Sample preparation*

Table 1 lists the physical and mechanical properties of a granitic rock. In order to place it inside the Hoek pressure cell, disc shaped samples were prepared as shown in Fig. 3(a). The diameter and thickness of the samples are 50 mm and 20 mm, respectively.

### 2.3 *Test conditions and results*

The launching velocity of the impact bar was controlled to achieve a wide range of loading rate $\dot{\tau}$, and the confining pressure was increased manually up to a constant value of 1, 5, and 10 *MPa* for each sample. Figure 3 (b) show the granite disc specimen after the dynamic punch test. Table 2 summarizes the test conditions and dynamic tri-axial punch test results.

Peak dynamic shear stress indicates the maximum value among the dynamic shear stresses calculated by using Eq. (3). The peak dynamic shear stress increases with increasing confining pressure and significantly increases with loading rate $\dot{\tau}$. Figure 4 plots the peak dynamic shear stress as a function of confining pressure for different loading rates.

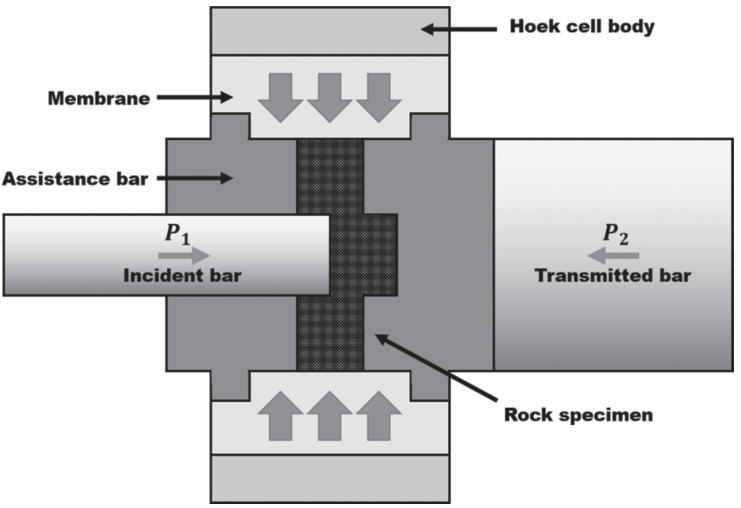


Figure 2. Schematics of the modified Hock tri-axial pressure cell.

Table 1. Mechanical properties of the granitic rock.

| Property | Value |
|---|---|
| Density ($kg/m^3$) | 2604 |
| Porosity (%) | 0.23 |
| P-wave velocity ($m/s$) | 3731 |
| S-wave velocity ($m/s$) | 2239 |
| Young's modulus ($GPa$) | 46 |
| Poisson's ratio (v) | 0.21 |
| Uniaxial compressive strength ($MPa$) | 202 |
| Tensile strength ($MPa$) | 10 |

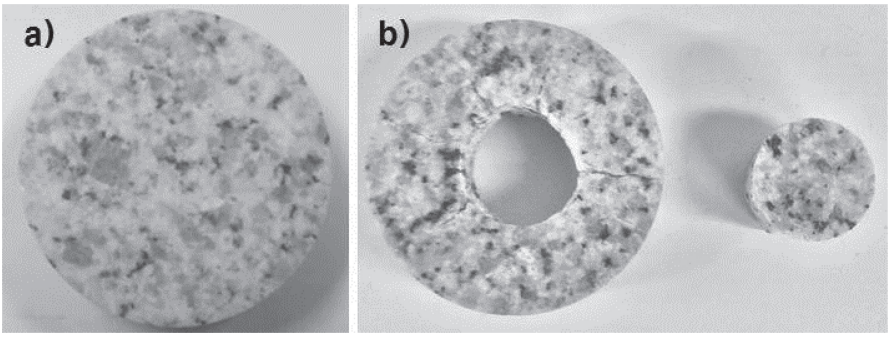


Figure 3. A granite disc sample before (a) and after (b) the dynamic punch test.

Table 2. Test conditions and dynamic tri-axial punch test results.

| $\dot{\tau} = 1701\,GPa/s$ | | $\dot{\tau} = 2217\,GPa/s$ | | $\dot{\tau} = 3001\,GPa/s$ | |
|---|---|---|---|---|---|
| Confining pressure ($MPa$) | Peak dynamic shear stress ($MPa$) | Confining pressure ($MPa$) | Peak dynamic shear stress ($MPa$) | Confining pressure ($MPa$) | Peak dynamic shear stress ($MPa$) |
| 0 | 48.91 | 0 | 96.79 | 0 | 107.29 |
| 0 | 66.19 | 0 | 100.06 | 0 | 113.02 |
| 0 | 71.78 | 0 | 85.59 | 0 | 98.14 |
| 1 | 72.93 | 1 | 50.51 | 1 | 94.51 |
| 1 | 67.24 | 1 | 98.26 | 1 | 113.21 |
| 1 | 69.528 | 1 | 101.1 | 1 | 111.45 |
| 5 | 68.44 | 5 | 91.76 | 5 | 108.15 |
| 5 | 74.97 | 5 | 85.76 | 5 | 95.16 |
| 5 | 84.25 | 5 | 100.57 | 5 | 120.14 |
| 10 | 64.42 | 10 | 109.41 | 10 | 116.15 |
| 10 | 69.5 | 10 | 98.73 | 10 | 108.76 |
| 10 | 87.14 | 10 | 98.35 | 10 | 120.14 |

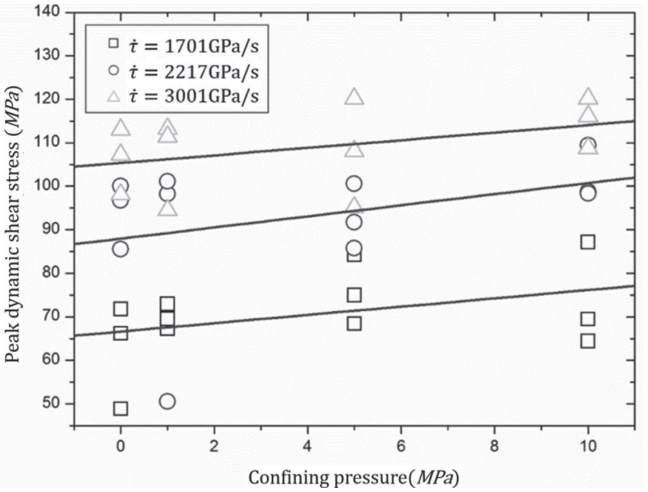


Figure 4. Peak dynamic shear stress as a function of confining pressure under different loading rates.

## 3 DISCUSSION

The linear Mohr-Coulomb criteria can be expressed in terms of the confining pressure instead of normal stress $\sigma_n$ as follows:

$$\tau = c + \sigma_n \tan\phi \tag{4}$$

where $\tau$ = peak dynamic shear stress, $c$ = cohesion (confining pressure), and $\phi$ = internal friction angle. As shown in Figure 4, the value of cohesion increases with increasing loading rate, while the internal friction angle remains constant. Therefore, it can be believed that the Mohr-Coulomb criterion, Eq. (4), should be modified to:

$$\tau_d + \tau_s + A\log(\dot{\tau}_d / \dot{\tau}_s) + \sigma_n \tan\phi \tag{5}$$

where $\tau_d$ = dynamic tri-axial shear strength, $\tau_s$ = tri-axial shear strength under quasi-static state, $\dot{\tau}_d$ = dynamic loading rate, $\dot{\tau}_s$ = loading rate under quasi-static state, and $A$ = material constant. The value of $A$ calculated, according to Eq. (5) and Table 2, was 22.40.

## 4 CONCLUSION

The dynamic tri-axial punch tests using the SHPB system and the modified Hoek cell were conducted to obtain the confining pressure dependency of dynamic shear strength under different loading rates.

As a result, the peak dynamic shear stress increased with a rise in confining pressure and significantly increased with loading rate $\dot{\tau}$. In accordance with the linear Mohr-Coulomb criteria, the value of cohesion increased with a loading rate increase, while the internal friction angle remained constant. The loading rate–dependent Mohr-Coulomb criteria based on the dynamic tri-axial punch test results were suggested.

## ACKNOWLEDGEMENTS

The authors gratefully acknowledge the financial support provided by the Defense Acquisition Program Administration and Agency for Defense Development.

## REFERENCES

Chen, W.W. 2011. Split Hopkinson (Kolsky) bar: Design, testing and applications. *Mechanical Engineering Series*.

Cho, S.H. 2014. Determination of dynamic fracture toughness of rock using straight notched disk bending (SNDB) Specimen. *International Symposium 8th Asian Rock Mechanics Symposium*.

Heuze, F.E. 1990. An overview of projectile penetration into geological materials, with emphasis on rocks. *International Journal of Rock Mechanics and Mining Sciences & Geomechanics Abstract* 27:1–14.

Huang, S. 2011. A dynamic punch method to quantify the dynamic shear strength of brittle solids. *Dynamic Behavior of Materials* 1:157–163.

Kolsky, H. 1953. *Stress Waves in Solids*. Oxford: Clarendon Press.

Labuz, J.F. 2012. Mohr–Coulomb failure criterion. *Rock Mechanics and Rock Engineering* 45:975–979.

Muralha, J. 2013. ISRM suggested method for laboratory determination of the shear strength of rock joints. Revised version. *Rock Mechanics and Rock Engineering* 47:291–302.

Schrier, van der. 1988. The block punch index test. *Bulletin of the International Association of Engineering Geology* 38:121–126.

Sulukcu, S. 2001. Evaluation of the block punch index test with particular reference to the size effect, failure mechanism and its effectiveness in predicting rock strength. *International Journal of Rock Mechanics & Mining Sciences* 38:1091–1111.

Zhao, J. 2000. Applicability of Mohr-Coulomb and Hoek–Brown strength criteria to the dynamic strength of brittle rock. *International Journal of Rock Mechanics & Mining Sciences* 37:1115–1121.

This page intentionally left blank

*Rock Dynamics: From Research to Engineering – Li et al. (Eds)*
*© 2016 Taylor & Francis Group, London, ISBN 978-1-138-02953-8*

# Strain localization in rocks under uniaxial compression and direct tension

I.A. Panteleev, O.A. Plekhov & O.B. Naimark
*Institute of Continuous Media Mechanics UB RAS, Perm, Russia*

ABSTRACT: This work is devoted to the investigation of spatio-temporal strain localizations under uniaxial quasistatic compression and tension of rocks with the use of the digital image correlation method. Conducted experiments allow us to establish specific forms of strain localization under uniaxial tension of sylvinite and uniaxial compression of granite. Tensile experiment showed the existence of equidistant zones of strain localization and deformation activation of one of zones at the stage of macrofracture initiation. For uniaxial compression tests of granite, it has been found that process of strain localization was realized only in the form of slow deformation waves with different directions of displacement inside: the longitudinal and transverse waves. The velocity of such waves decreased up to $10^{-4}$ m/s with increasing of applied load. At the prefracture stage localized strain waves of different types concentrated near the exit area of main crack on the specimen surface.

## 1 INTRODUCTION

At the present time, there are two different types of strain localization in rocks. The first one is the strain localization on existent discontinuities of geomedia, such as cracks, faults, blocks borders et al. The second one is inelastic strain localization in the form of some spatial-temporal structures: spiral lines of slip and shear in loose media, dilatation and compaction bands in porous media. Another form of strain localization is "slow deformation waves". Earlier, in (Zuev et al. 2012), it has been shown that the plastic flow in some rocks under quasistatic compression remains localized over the whole period of the deformation process up to the sample fracture. The forms of macrolocalization are governed by the strain hardening laws operating at the corresponding stages of the process. The acquired information on the forms of strain macrolocalization in rocks under uniaxial compression does not differ from the previously obtained data for alkali-halide crystals (Barannikova et al. 2009). The experiments with sylvinite specimens revealed only a single zone of localized strain field, which moved over the specimen surface at the velocity of $10^{-5}$ m/s (at strain rate $6 \times 10^{-5}$ $s^{-1}$). This single deformation wave corresponds to a linear stage of strain hardening. For other stages of the strain flow in sylvinite under compression load the forms of localization cannot be registered because of cracking and spalling occurring at the lateral rock faces. According to preliminary experiments of authors of this work, such forms of strain localization are also typical for brittle rocks under uniaxial compression. In case of tension tests, the similar investigation of this phenomenon has never been done before.

This work is devoted to the investigation of spatial-temporal type of localized deformation on the surface of brittle and quasi-plastic rock specimens under quasistatic uniaxial compression and direct tension. Mechanical tests were performed on granite and sylvinite specimens. Digital Image Correlation method (DIC) was used to reconstruct the displacement and strain fields on the specimen surface. This empirical information can form the basis for reconsideration of existing approaches to the construction of constitutive models, which describe the behavior of quasi-plastic and quasi-brittle rocks under quasi-static loading and are used for simulation of geotechnical constructions in mining.

## 2 EXPERIMENTAL METHODS AND MATERIALS

### 2.1 *Materials and loading condition*

Mechanical tests were performed on prismatic specimens of sylvinite with lateral size of $30 \times 30$ mm and height of 90 mm (uniaxial direct tension tests) and on prismatic specimens of granite with lateral size of $50 \times 50$ mm and height of 100 mm (uniaxial compression tests). The specimens were tested in the electro-mechanical testing machine having a capacity of 250 kN. The direct tension mode was realized via a special reversing device, which converted a compressive force into tensile force. The device and the prepared specimen are shown in Figure 1. The experiments were performed at room temperature. To eliminate the error associated with the specimen bending in the reversing device, the measurements of longitudinal (axial) strains were made on the specimen surface with two cantilever sensors, which were placed symmetrically with respect to the specimen center. The displacement rate in uniaxial tensile tests was $1.6 \times 10^{-6}$ m/s. In uniaxial compression tests loading velocity was controlled and assigned of 0.5 kN/min.

### 2.2 *Used nondestructive testing techniques*

Digital optical system LaVision Strain Master was used to track surface displacements caused by specimen deformation. The algorithm for processing the video data stream is based on the digital image correlation method. This method allows us to recover with a high degree of precision the evolution of the surface displacements and strains in the specimen made of different materials under different types of loading. The mathematical algorithm of the DIC method is presented for example in (Sutton et al. 1983, Sutton et al. 2009). The Strain Master System consists of a digital camera, LED backlight, a synchronization system and a personal computer with special software. The elements of this system are shown in Figure 1. The digital camera has a resolution of $1600 \times 1200$ pixels and it is set at a distance of approximately 30 cm from the specimen. Images are acquired with the frequency of ten frames per second.

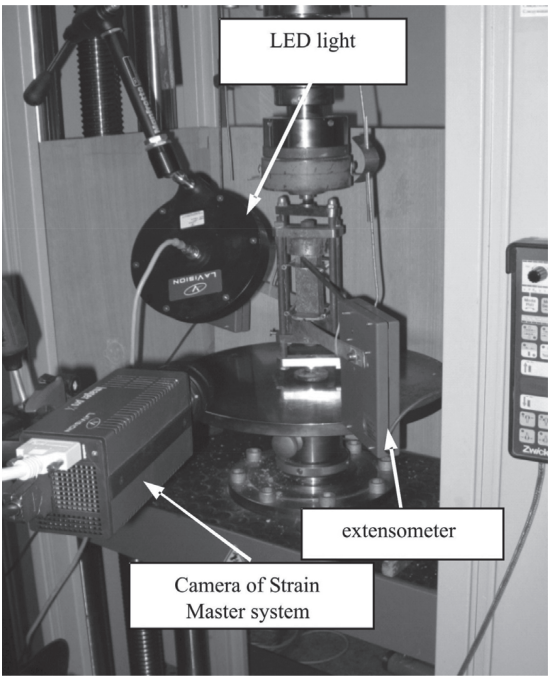


Figure 1. Experimental equipment.

The displacement and strain fields were calculated for the surface area of the specimen measuring 54.5 mm by 29 mm (in uniaxial direct tension tests) and 46 mm by 98 mm in uniaxial compression tests.

## 3 RESULTS AND DISCUSSION

### 3.1 *Uniaxial direct tension of sylvinite specimens*

The analysis of evolution of the strain tensor component distribution over the lateral surface of the sylvinite specimen during deformation shows that right from the beginning of loading the deformation process proceeds non-uniformly. Figure 2 shows the distribution of the longitudinal strain over the specimen surface at different time points. The deformation heterogeneity manifests itself as a system of equidistant zones of localized strain field oriented towards the loading axis at an angle of $\pm\pi/4$. The localized strain field zones are formed already at the first steps of tension and remain stationary over the whole period of loading. As is seen from the diagram of longitudinal deformation distribution, the areas outside the localization zones are in the unstrained state. Inside the localization area the strain reaches the value of 0.5% under total deformation of the specimen of 0.36%. The distribution of the lateral deformation over the sylvinite surface under tension is also inhomogeneous, though the system of equidistant zones is not clearly viewed.

The spatial periodicity of the localized bands (deformation bands) is seen more clearly on the plot of the longitudinal strain versus time for the central line of the specimen, which is shown in Figure 3. As is evident from the figure, in the localized areas, the deformation may develop both as a tensile mode and a compression mode. This observation is nontrivial in view of the

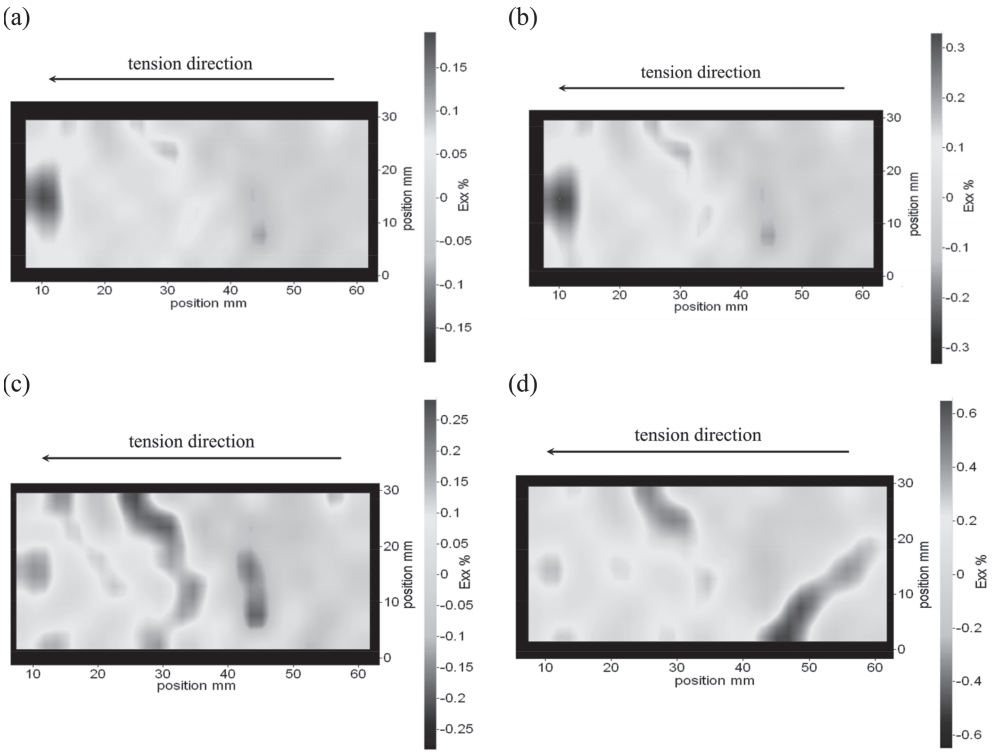


Figure 2. Maps of longitudinal strain on the specimen surface at different value of total deformation (a – 0.06%, b – 0.12%, c – 0.21%, d – 0.36%).

fact that on the macroscopic scale the specimen is under tensile load. The spatial period of the localized strain field zones is 13.6 mm. The analysis of the maximum strain locations demonstrates that the strain in localized zones grows continuously and the strain maximum moves from one area to another. The deformation process in the form of equidistant localized zones proceeds until the stress in the specimen reaches its maximum. At this point the macrolocalization changes its form: the deformation process continues only in one of the localization zones and ends in fracture, whereas in the other areas the deformation is completed (see Fig. 3.).

Thus, following the terminology introduced in (Zuev et al. 2009) the process of deformation in sylvinite specimens under quasi-static tension, proceeds as a sequence of two forms of spatial-temporal localization: a system of equidistant stationary areas of localized strain field and a single stationary dissipative localized structure, in which the deformation grows in an avalanche-like manner and ends in macro-fracture. Realization of one of the shapes of localized strain fields in the sylvinite specimen under tension depends on the level of the applied stress, which correlates with the previous results obtained for a number of rocks, metals and alloys (Zuev et al. 2009, 2012).

### 3.2 *Uniaxial compression of granite specimens*

Experiments on quasistatic compression of granite allow us to obtain data on evolution of displacement and strain on the lateral surface of the sample. It was established that deformation process runs homogeneously only at the first stage of deformation (prior to strain of 0.02–0.03%). Further deformation process is implemented as a series of successively waves of localized strain propagated on the specimen surface. It is observed localized longitudinal waves as well as transverse waves. As a result, it can be concluded that waves of localized transverse strain occurred from the level of applied stress of 60–65% from rupture. On average, deformation inside waves of localized strain differs from the value of background deformation (outside the wave) from 2 up to 5 times greater depending on the applied stress. Figure 4 shows distribution of longitudinal and transverse strains and two components of displacement vector for different time moments of deformation of granite specimen.

Conducted experiments allowed us to distinguish special features of strain localization process in the form of deformation waves. Firstly, strain localization wave is a front of a sharp displacement jump of a deformed surface (Fig. 4a). Secondly, longitudinal and transverse waves of localized strain are separated in the space. Waves of localized strain with a

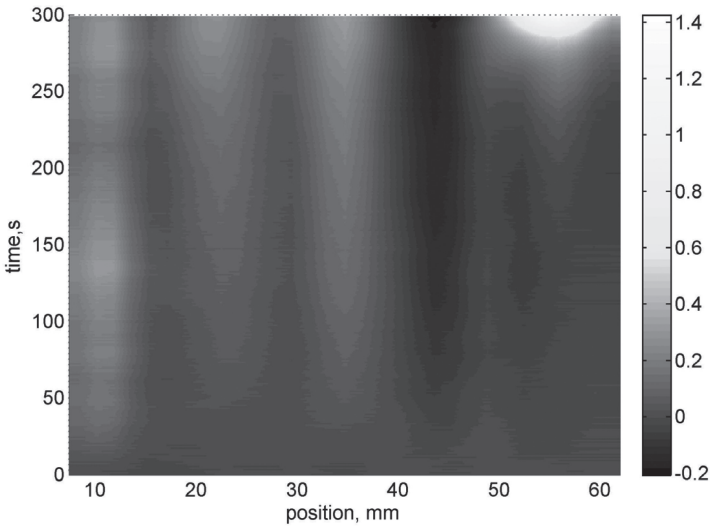


Figure 3. Evolution of longitudinal strain for middle line of sample.

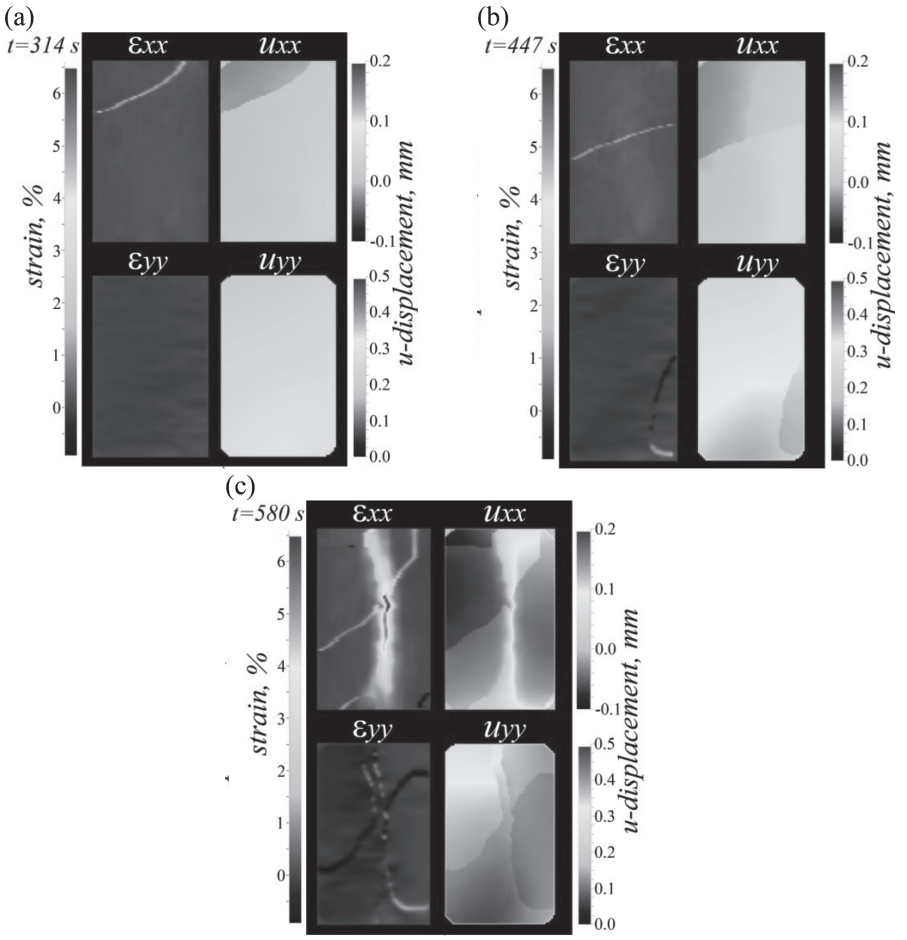


Figure 4. Evolution of distribution of diagonal strain tensor components and displacement vector components on the granite surface for different time moments (a – 314 s. (0.5 $\sigma_{cr}$), b – 447 s. (0.71 $\sigma_{cr}$), c – 580 s. (0.92 $\sigma_{cr}$)); $\sigma_{cr}$ – critical stress.

strong transverse component don't have longitudinal and waves with a strong longitudinal component have a weak transverse component (Fig. 4). Thirdly, when the main crack comes to the surface of specimen, localized waves start to "shrink" to the place of its emergence on the surface (Fig. 4c).

The obtained data has let us to the conclusion that velocity of localized waves recorded during uniaxial compression of granites and marbles is 6–7 orders of magnitude less than characteristic velocities of elastic waves propagation in this materials. The velocity of propagation of localized waves depends on the applied stress value. Velocity of waves of localized transverse strain is three times bigger on the average during the deformation process; the individual waves can either accelerate or decelerate. Velocity of waves of longitudinal strain is one order of magnitude less than velocity of localized transverse strain.

## 4 CONCLUSIONS

This work is devoted to the studying of the spatial-temporal form of deformation localization in sylvinite under uniaxial tension and in granite under uniaxial compression by modern methods of non-destructive control: digital image correlation. The use of digital optical

system LaVision, based on the digital image correlation method, allowed us to reconstruct the strain filed on the lateral surface of the specimen during loading.

For uniaxial tension tests of sylvinite it has been found that the process of deformation is localized in space during the whole loading period. At the stage of active deformation up to a maximum stress, the deformation process in the specimen proceeds in the form of a system of equidistant localized strain field zones oriented towards the loading axis at an angle of $\pm\pi/4$. The localized strain field zones are formed from the very beginning of tension and remain stationary with a passage of time. Such a form of localization takes place both for longitudinal strain and for transverse strain. It has been shown, that in the localized areas the deformation can be of two types—tension and compression. The areas outside of the localization zones are in the unstrained state. Around the highest possible stress, a change of the shape of localized strain fields occurs and the deformation process goes on only in one of zones. It proceeds in the avalanche-like manner and ends in fracture.

For uniaxial compression tests of granite, it has been found that process of strain localization was realized only in the form of slow deformation waves with different directions of displacement inside: the longitudinal and transverse waves. The velocity of such waves decreased up to $10^{-4}$ m/s with increasing of applied load. At the prefracture stage localized deformation waves of different types concentrated near the exit area of main crack on the specimen surface.

Obtained data could be used for verification of modern physical models of deformation and fracture of quasi-plastic and quasi-brittle rocks used in the development of mineral deposits.

## ACKNOWLEDGEMENTS

This work was supported by the Russian Science Foundation, Project No. 14-19-01173.

## REFERENCES

Barannikova, S.A., Nadezhkin, M.V., Zuevm L.B. 2009. On the Localization of Plastic Flow under Compression of NaCl and KCl Crystals. *Physics of the Solid State* 51(6): 1142–1148.

Sutton, M.A., Wolters, W.J., Peters, W.H., Ranson, W.F., McNeil, S.R. 1983. Determination of displacements using an improved digital correlation method. *Image and Vision Computing* 1(3): 133–139.

Sutton, M.A., Orteu, J.J., Schreier, H.W. 2009. *Image Correlation for Shape, Motion and Deformation Measurements: Basic Concepts, Theory and Applications*. New York: Springer.

Zuev, L.B., Barannikova, S.A., Zhigalkin, V.M., Nadezhkin, M.V. 2012. Laboratory observation of slow movements in rocks. *Journal of Applied Mechanics and Technical Physics* 53(3): 467–470.

Zuev, L.B., Danilov, V.I., Barannikova, S.A., Gorbatenko, V.V. 2009. Autowave model of localized plastic flow of solids. *Physics of Wave Phenomena* 17(1): 66–75.

*Rock Dynamics: From Research to Engineering – Li et al. (Eds)*
*© 2016 Taylor & Francis Group, London, ISBN 978-1-138-02953-8*

# Behaviour of underground structures in soft rocks under different strain rate and litho-static pressure

K.S. Rao & S. Mishra
*Department of Civil Engineering, Indian Institute of Technology Delhi, New Delhi, India*

N.K. Gupta
*Department of Applied Mechanics, Indian Institute of Technology Delhi, New Delhi, India*

ABSTRACT: The underground facilities are used for a wide range of civil and military applications (railways, highways and material storage). These structures are constructed in different possible ground conditions ranging from soft ground to massive jointed rock. Generally, the loads on tunnels consist of both static (overburden) and dynamic (blast, earthquake and traffic) loads. Therefore, the support system is usually designed to resist all transient loads developed during construction activities as well as the short-term ground loads.

Therefore, in the present work an attempt is made to simulate the in-situ condition through the physical modeling, to understand the tunnel deformation behavior by varying overburden thickness in soft rocks. The model material is selected on the basis of engineering properties of the different mix proportions of PoP, sand and clay (UCS, elastic modulus and Poisson's ratio), and the Plaster of Paris (PoP) mixed with sand and some percent of clay (50% PoP, 40% Badarpur sand, and 10% Kaolinite) is selected for physical modeling, as the PoP alone shows brittle behavior. It is interpreted that the height of overburden and thickness of lining are critical factors in correlating degree of fracture and damage to the tunnel—lining. Further, the deformation and degree of damage is determined for lined and unlined material and hence controlling the fracture in the existing conditions.

## 1 INTRODUCTION

Civil engineering tunnels are constructed in the full spectrum of possible ground conditions ranging from soft ground to massive unjointed rock, coupled with various states of in situ stress and hydrogeology. Dams and hydroelectric power plants look for a better geological condition; tunnels and highways look for a better alignment escaping from weak zones, whenever possible. Even though the shape of the opening mainly depends on the purpose for which it is to be used, the safe design and construction of an underground opening requires the knowledge of the stress distribution and the displacements that occurs in and around the openings. When an opening is excavated in a medium, the in situ stress field is disturbed and new set of stresses are induced around the surrounding of the opening. Before the tunnel is excavated, the in situ stresses $\sigma_v$, $\sigma_{h1}$, and $\sigma_{h2}$ are uniformly distributed in the slice of rock under consideration. After removal of the rock from within the tunnel, the stresses in the immediate vicinity of the tunnel are changed and new stresses are induced. Three principal stresses $\sigma_1$, $\sigma_2$ and $\sigma_3$ acting on a typical element of rock are shown and explained well in Figure 1.

Most of the theories, existed compute the vertical stress at a point as the stress due to the lithostatic pressure, and the horizontal stress as that stress required to completely restrain lateral deformation of an elastic body acted upon by the vertical stress. The theory predicts that the horizontal stress will be some fraction of the vertical or overburden stress dependent upon the value of Poisson's ratio for the rock. The stability of underground excavations is affected

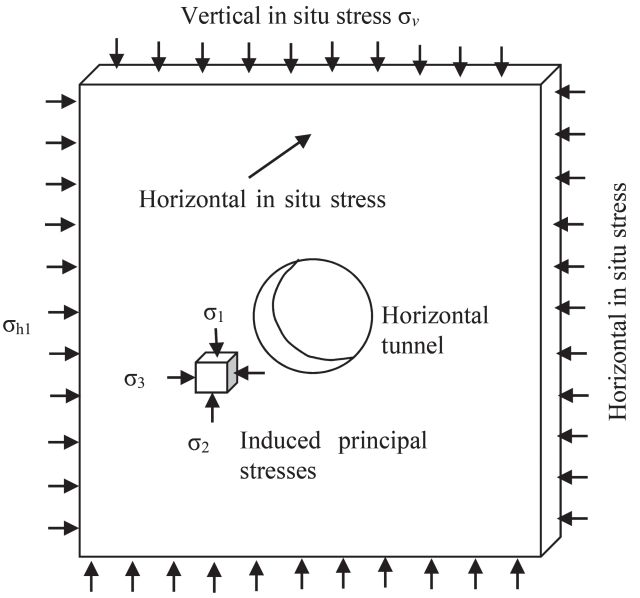


Figure 1. Illustration of principal stresses induced in an element of rock close to a horizontal tunnel subjected to a vertical in situ stress $\sigma_v$, and horizontal in situ stress $\sigma_{h1}$ in a plane normal to the tunnel axis and a horizontal in situ stress $\sigma_{h2}$ parallel to the tunnel axis (Hook 2007).

by its shape, size of opening, in situ stress, soil/rock conditions etc. Knowledge of the magnitudes and directions of these in situ and induced stresses is an essential component of underground excavation (Goodman 1989). The horizontal stresses acting on an element of rock at a depth 'z' below the surface is much more difficult to estimate than the vertical stresses.

$$\sigma_h = k.\ \sigma_v \tag{1}$$

Terzaghi & Richart (1952) suggested that, for a gravitationally loaded rock mass in which no lateral strain was permitted during formation of the overlying strata, the value of k is independent of depth and is given by $k = \nu/(1 - \nu)$, where ν is the Poisson's ratio of the rock mass. Measurements of horizontal stresses at civil and mining sites around the world show that the ratio k tends to be high at shallow depth and that it decreases at depth (Brown & Hoek 1978, Herget 1988). Therefore it is very important to investigate the behavior of tunnels openings under litho-static pressure. The behavior of tunnels under different overburden depths is very important for the safe and economical designs.

### 1.1 *Problems associated with soft rocks*

Soft rocks are classified as very weak rocks. The geological material having UCS varying from 0.1 MPa to 5 MPa are rocks, exposed to atmosphere with low depths and different grades of weathering. Many researchers have proposed definition for soft rocks (Fan 1995, Guo 1996, Lin 1999). It is well established that the soft rocks such as sandstone and mudstone (Nickmann et al. 2006, Yoshinaka et al. 1997), have the main characteristics of large deformability, strong dependence on degree of saturation or temperature, and susceptibility to alteration. Therefore these soft rocks have been classified into two sets (Clerici 1992, Russo 1994): geological soft rock and engineering soft rock. The geological soft rock has the intrinsic properties of weakness while the engineering soft rock generates significant plastic strain and creep strain.

However, in the field of rock mechanics the upper limit of the strength of soft rocks is about 25 MPa as Unconfined Compressive Strength (UCS) (Table 1). On the other hand, the lower limit of the strength of soft rock is more difficult to establish, so as to maintain the

difference between soil and rock. Terzaghi and Peck (1967) established that the material with SPT above 50 and UCS greater than 0.4 MPa, behavious more like rock than soil. Dobereiner (1984) used an UCS value of 0.5 MPa. Many researchers distinguished rock by the crumbling phenomenon. Baud & Gambin (2011) utilized another criterion, based on the limit pressure in pressure meter testing, indicating values of 2–10 MPa, and depending on the elastic modulus to the limit pressure ratio.

It is very difficult to predict the actual behavior and degree of damage of such rocks. Problems associated with these rocks are due to its unfavorable behavior that prevents their utilization for important engineering works. These rocks present undesirable behaviors, such as low strength, disaggregation, crumbling, high plasticity, slaking, fast weathering, and many other characteristics. Soft rocks have intermediate strength between soils and hard rocks. In some cases, they are too soft to be tested in rock mechanics equipment and too hard for soil mechanics equipment. Therefore, in the present work an attempt is made to simulate the in-situ condition through the physical modeling, to understand the tunnel deformation behavior under different loading conditions in soft rocks. Further, the analysis is also performed using finite element method and compared with the experimental results.

### 1.2 *Strain rate effect*

All underground facilities are always subjected to different loading conditions and insitu stresses some of them are listed below (Table 2). It is well established in literature that the fracturing of rock mass and strain rates are interrelated. When the strain rate is low the size

Table 1. Classification of geomaterial on the basis of UCS value and ground type.

| Classification | UCS (MPa) | Ground types |
|---|---|---|
| Soft ground | | (a) Recent alluvium and glacial drift deposits including water-bearing sands, gravels, silts, and clays, and boulder clay.<br>(b) Eocene, Cretaceous and Jurassic stiff fissured clays |
| Very weak to moderately strong rock | up to 50 | Low strength rocks including shales, Cretaceous Chalk, Triassic (Keuper) Marl and Jurassic rock formations. |
| Strong rock | 50–100 | Many Triassic and Permian rock formations, sandstones and medium strength Carboniferous Coal Measures. |
| Very strong and extremely strong rock | above 100 | The hard Carboniferous and older rocks, the limestones and harder rocks. |

Table 2. Effect of strain rate on degree of fracture (Rao et al. 2015).

| Loadings | Strain Rate | Type | Degree of fracture |
|---|---|---|---|
| STATIC | 0 to 0.1 | a. Construction or Demolition of heavy/multi storey structures (Overburden pressure)<br>b. Continuous vehicular movements/ High traffic volume<br>c. Cyclic loading | a. Size and quantity of fragments are more<br>b. Spalling, Perforation, Compressive failure, Line cracks, progressive failure |
| QUASI—STATIC/ DYNAMIC | 0.1 to 10,000 | a. Missile attacks/Bomb penetration (Under terrorist activities)<br>b. Excavation and Construction by Blasting<br>c. Seismic load/Heavy machine foundation | a. Size and quantity of fragments are less<br>b. Pulverisation, Compressive failure followed by tensile failure, Completely crushes zones |

and quantity of fragments are more and for high strain rate the fragments are less. The strain rate of loading can be roughly estimated by the size and quantity of fragments, but this will give the range of strain rate. Therefore in the present study, low strain rate (static) is used to understand the exact behavior of unlined and lined tunnel and surrounding rock mass.

## 2 EXPERIMENTATION

### 2.1 *Material characterization and geometry*

The material used for the preparation of model is a mixture of Plaster of Paris (PoP), Sand and Clay, to simulate soft rock. Numbers of test are performed on different mix proportions of these materials, as shown in Table 3. The material is selected on the bases of its stress—strain behavior. The material should have Unconfined Compressive Strength (UCS) more than 1 MPa and should show strain softening behavior. The material should not show brittle type of failure (PoP and PoP mixed with Clay). Therefore the composition selected for the experimentation consists of 50% PoP, 35% Sand and 15% Clay by weight and the water—powder ratio considered is 0.6. The material properties of the cylindrical samples of (38 mm diameter) PoP and selected material are shown in Table 4 and Figure 2. The lining material selected for the experimentation is PVC and its properties are also shown in Table 3.

The geometry of the model is based on the testing area and the stress distribution around the circular opening in rock mass (Terzaghi & Richart 1952). The diameter of the circular opening is defined by the workability and feasibility. If the diameter is too small then the placement of strain measurement system is very difficult and if it is too big then it will make whole model very heavy (difficult in handling). Therefore the diameter of the opening is set as 50 mm and the scaled lining thickness is 1.5 mm. According to the radius of the opening the dimension of the model are 300 mm × 200 mm × 200 mm, as shown in Figure 3a.

Table 3. Material properties of different mix proportions.

| Material | | | | | |
|---|---|---|---|---|---|
| % PoP | % Sand | % Clay | UCS (MPa) | Modulus $E_{t50}$ (MPa) | Poisson's Ratio ν |
| 100 | – | – | 6.78 | 4476.32 | 0.22 |
| 90 | – | 10 | 4.86 | 4216.47 | 0.27 |
| 80 | – | 20 | 3.74 | 2757.28 | 0.11 |
| 90 | 10 | – | 5.26 | 4650.86 | 0.23 |
| 80 | 20 | – | 6.44 | 5002.35 | 0.24 |
| 50 | 30 | 20 | 1.38 | 2045.57 | 0.11 |
| 50 | 20 | 30 | 1.21 | 1220.00 | 0.31 |
| 50 | 40 | 10 | 5.65 | 4001.90 | 0.23 |
| 50 | 10 | 40 | 0.97 | 1051.67 | 0.21 |
| 50 | 35 | 15 | 4.48 | 3271.80 | 0.16 |

Table 4. Material properties of PoP, model material and PVC pipe.

| Property | PoP | Selected Material | Lining (PVC) |
|---|---|---|---|
| Dry Density (g/cc) | 1.17 | 1.41 | 1.4 |
| Sonic Wave Velocity (m/s) | 1947.2 | 1724.5 | – |
| UCS (MPa) | 6.78 | 4.48 | – |
| Modulus $E_{t50}$ (MPa) | 4476.32 | 3153.8 | 3800 |
| Poisson's Ratio ν | 0.22 | 0.16 | 0.35 |
| Cohesion, c (MPa) | 0.78 | 1.81 | – |
| Friction Angle φ (°) | 51 | 42 | – |
| Deere-Miller's chart, 1966 | EH | EH | – |

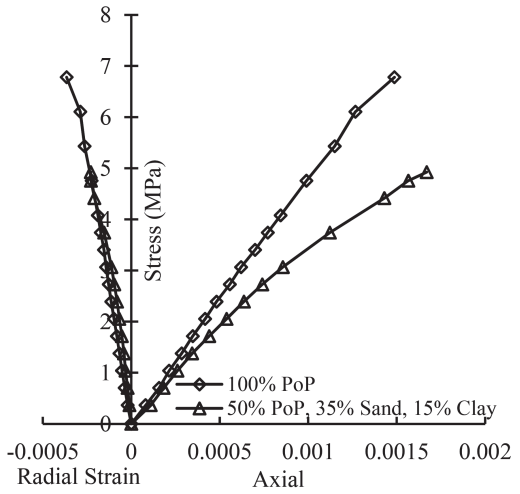


Figure 2. Stress—Strain curve for PoP and Model material.

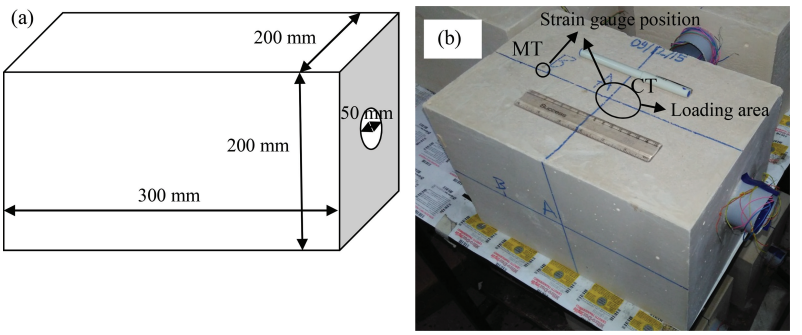


Figure 3. Key sketch for the model test and final model for the testing with strain gauges.

### 2.2 *Testing procedure*

The samples are prepared by mixing the required amount of PoP, sand and clay with water and poured in a mould having holes in two opposite faces. The prepared samples are dried at room temperature for 30 days before testing under servo controlled loading frame of 100-ton capacity. Now to measure the strains at different location while loading, the strain gauges are fixed inside the tunnel at top and the bottom on two locations, one at the center of the model and other is in between center and face of the model (Fig. 3b). Further the loading is applied at the center on the circular area of diameter 50 mm, to maintain the ratio of loading area diameter with tunnel diameter equal to 1.

The testing is performed under displacement controlled mode and the loading rate is kept as 0.01 mm/sec. The confinement is applied on two faces of the model with the help of platens of dimension 300 mm × 200 mm × 20 mm. The force applied by these platens just before the testing is maintained as 1 KN, to simulate the confinement condition. The testing assembly is shown in the Figure 4.

## 3 RESULTS AND DISCUSSIONS

The load—deformation behavior, vertical deformation at the loading area, fractured zone length and the effect of lining are examined for each test in order to analysis the fracture threshold. Further the numerical validation is performed for the model.

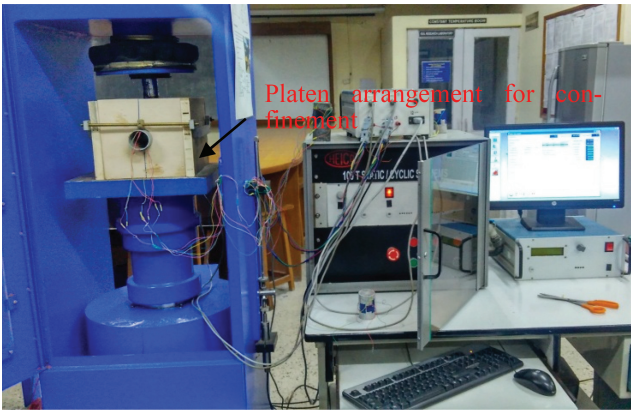


Figure 4. Loading frame and data acquisition system.

### 3.1 *Load—deformation behavior*

The typical load vs deformation curves are plotted for the lined and unlined physical model, for different locations. The punching of the loading area can be clearly seen form the Figures 5 and 7. It is observed that the peak load for the lined tunnel (16.6 KN) is higher than the unlined tunnel (13.7 KN) for the overburden of thickness of 75 mm. It is also interpreted that the displacement of the loaded area in the case of lined tunnel as lower than that of the unlined case. In both cases the pattern of load-displacement curve is same, which shows that the surrounding material is homogeneous. It is also observed that the peak load for overburden of 25 mm is lower and it increases as the overburden increases due to the resistance offered by the surrounding material in the form of stress distribution.

Further the load vs strain curves are obtained for the different positions of strain gauge in lined and unlined tunnel. The variation of strains at different location can be observed from Figures 6 and 7. It is observed that the strain on the top surface of tunnel at the time of failure in lined tunnel is more than that of the unlined tunnel. It is also observed that the strain at the Center—Top (CT) position is more than the strain at Middle—Top (MT) position (Figures 3, 6). It is also observed that the strains on the crown of the tunnel are more than the bottom of the tunnel. Further, the strains experienced by the bottom surface of the tunnel are low. The total length of the cracked portion observed experimentally in unlined tunnel is 124 mm along the tunnel axis and 45 mm transverse to tunnel axis.

It can be concluded from the experimentation that the length and shape of fractured zone in tunnels depends on the type of loading and the depth of the tunnel from the surface. It is also concluded that the stresses in rock mass decreases as the position of measurement moves away from the loading position and becomes negligible at the distance of 1.5d (d is diameter of tunnel) from the loading position (Fig. 7), when load is applied directly above the tunnel.

Similarly the tests are also performed for the different overburden pressure at the same loading rate and results are compared in Table 5. It is observed that the dimensions of the crack is increased with increase in over burden but the peak load capacity is also increased with the overburden depth.

## 4 CONCLUSION

The underground facilities are used for a wide range of civil and military applications. These underground structures are constructed in different possible ground conditions ranging from soft ground to massive jointed rock. Generally, the loads on tunnels consist of both static (overburden) and dynamic (Blast, earthquake and traffic) loads. Therefore, in the present work an attempt is made to simulate the in-situ condition through the physical and numerical

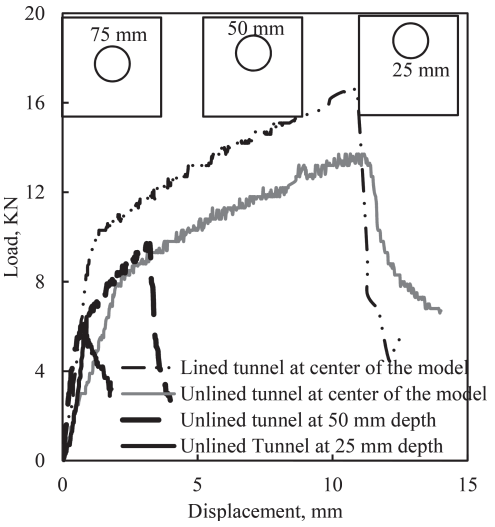


Figure 5. Load—Displacement curve of loading area for lined and unlined tunnel.

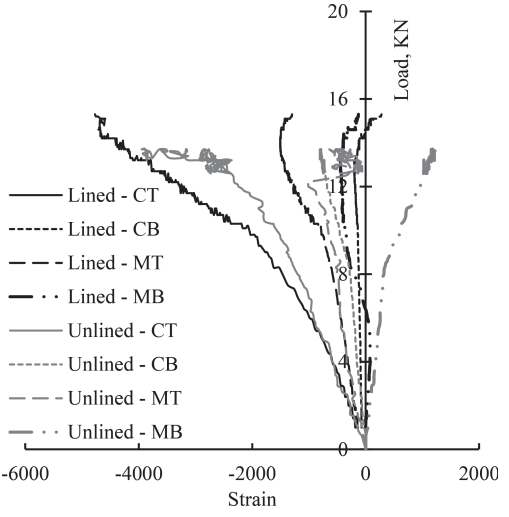


Figure 6. Load—Strain curves at different locations in tunnel.

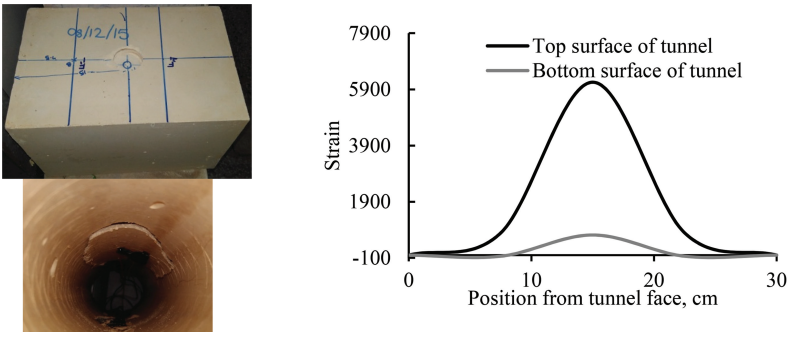


Figure 7. Deformed shape after testing and distribution of strain along the tunnel length.

Table 5. Quantification of fracture on the basis of over burden.

| Depth of over burden from loading surface (mm) | 25 | 50 | 75 |
|---|---|---|---|
| Peak load (KN) | 6.6 | 9.9 | 13.7 |
| Punching at loading area (mm) | 1 | 4 | 14 |
| Crack length along tunnel axis (mm) | 9.2 | 9.7 | 12.4 |
| Crack length transverse to the tunnel axis (mm) | 3.7 | 4.1 | 4.5 |

modeling, to understand the tunnel deformation behavior under different loading conditions in soft rocks.

In the present work, both vertical and horizontal lodes are applied on the model by using the platens arrangement on the side faces. Due to this confinement effect the horizontal force, which is dependent on the vertical force is applied on the model.

It is concluded that the depth of overburden is a very critical parameter in quantification of fracture threshold and degree of damage. It is observed that the punching under the loading area occurred, which shows rock type of punching shear failure. The deformations of lined and unlined tunnels are investigated and it is observed that the tunnel follows the Gaussian distribution along the length. Further, the deformation and degree of damage is determined for lined and unlined conditions. It is observed that the surrounding material is failing in shear and the failed surface has taken elliptical shape at the top of tunnel.

## REFERENCES


Baud, J. P. & Gambin, M. 2011. Classification of soils and rocks based on pressuremeter tests under high pressure. In *Proceedings of the 15th European Conference on Soil Mechanics and Geotechnical Engineering*, *pp. 32*.

Brown, E.T. & Hoek, E. 1978. Trends in relationships between measured in-situ stresses and depth. *Int. J. Rock Mech. Min. Sciences* 15(4): 211–215.

Clerici, A. 1993. Indirect determination of the modulus of deformation of rock masses-case histories. In *ISRM International Symposium-EUROCK 93*.

Deere, D.U. & Miller, R.P. 1966. Engineering Classification and Index Properties for Intact Rock. U.S. Air Force Weapons Lab., Techn. Rep., AFNL-TR-65–116.

Dobereiner, L. 1984. *Engineering Geology of Weak Sandstones*. PhD Thesis, Imperial College, London.

Fan, Q.Y. 1995. Discussions about determination of soft rock and critical depth of tunnels. *Ground Pressure and Strata Control* (Suppl. 1): 115–7.

Goodman, R.E. 1989. *Introduction to Rock Mechanics*.

Guo, Z. 1996. A study on the mechanical properties of the incompetent rocks. *Journal of Engineering Geology* 4(3): 79–84.

Herget, G. 1988. *Stresses in Rock*. Rotterdam: Balkema.

Hook, E. 2007. *Practical Rock Engineering*. Canada: Rocscience.

Lin, Y.L. 1999. The research on several theoretical problems about engineering mechanics of soft rock. *Chinese Journal of Rock Mechanics and Engineering* 18(6): 690–693.

Nickmann, M., Spaun, G. & Thuro, K. 2006. Engineering geological classification of weak rocks. *International Association for Engineering Geology and the Environment:* 492–499.

Rao, K. S., Mishra, S. & Gupta, N. K. 2015. Fracture propagation of rocks under dynamic regime, *EGNM-15: 345–358.*

Rao, K.S., Sarmah, R. & Mishra, S. 2015. Effect of projectile penetration on shallow tunnels. *IGC-2015,* Pune, India.

Russo, G. 1994. Some considerations on the applicability of major geomechanical classifications to weak and complex rocks in tunnelling. *GEAM XXXI,* Torino, pp. 63–70.

Terzaghi, K. & Peck, R.B. 1967. *Soil Mechanics in Engineering Practice*. New York: Wiley.

Terzaghi, K. & Richart, F.E. 1952. Stresses in rock about cavities. *Geotechnique* 3(2): 57–90.

Yoshinaka, R., Tran, T. V. & Osada, M. 1997. Pore pressure changes and strength mobilization of soft rocks in consolidated-undrained cyclic loading triaxial tests. *Int. J. Rock Mech. Min. Sciences* 34(5): 715–726.

*Rock Dynamics: From Research to Engineering – Li et al. (Eds)*
*© 2016 Taylor & Francis Group, London, ISBN 978-1-138-02953-8*

# Petrophysical and engineering behavior of oil shale from Assam, India

K.S. Rao & A. Kumar
*Department of Civil Engineering, Indian Institute of Technology Delhi, New Delhi, India*

ABSTRACT: Oil shale is a compact laminated rock of sedimentary origin containing organic matter known as kerogen. The steps involved for in-situ extraction process are hydrofracturing, injection to achieve communication, and fluid migration at the underground location. Therefore, it is very important to understand the physico-mechanical behaviour of such anisotropic rocks. The favourable characteristics of Assam coal for conversion to liquid fuels have been known for a long time. Studies have indicated that these coals and carbonaceous shale constitute the principal source rocks that have generated the hydrocarbons produced from the region. In the present work an attempt is made to understand the engineering behavior of Indian oil shales experimentally. The in situ coring is performed to get the samples for testing purposes, as coring in laboratory is very difficult due to its highly anisotropic nature. Different tests are performed to understand the petrology of these samples, further the chemical analyses are also done to exactly quantify the organic and inorganic contents in these rocks. The physical and mechanical properties of these rocks are investigated by considering different anisotropic angles. Further, the petrophysical test results are correlated with the mechanical properties. These properties and correlations will further help in increasing the yield of these rocks.

## 1 INTRODUCTION

The search for alternative energy sources to petroleum has increased these days because of increase in need and depletion of petroleum reserves. Due to this the importance of oil shales as an economically viable substitute has increased many folds in last 20 years. Oil shale is defined as a compact laminated rock of sedimentary origin and contains organic matter that yields oil when distilled (Yen & Chilingarian 1976, Shanks et al. 1976, Robinson 1976). Oil shales are formed from the contemporaneous deposition of fine grained mineral debris and organic degradation products derived from the breakdown of biota. Conditions required for the formation of oil shales include abundant organic productivity, early development of anaerobic conditions, and a lack of destructive organisms.

These oil shales come under unconventional oil in unconventional rocks. Depth of these rocks varies from few meters to few thousand meters. Oil extraction from these rocks can be done by retorting process, which involves drastically breaking the bond between the organic and inorganic matter. The two approaches for retorting are surface retorting and in-situ processing. In surface retorting, the mined and crushed oil shales are subjected to temperature ranging from 400–600°C. Due to high temperature conditions the chemical bonds between the organic and inorganic compound are broken. In the case of In-situ process, mining of shale is not required. This process involves, fracturing, injection to achieve communication, and fluid migration at the underground location. Upon heating (retorting) oil shale at temperatures in the range of 300 to 400°C, the kerogen decomposes into oil, gas and residual carbon (Nowacki 1981). Therefore, many researchers have investigated the mineralogy of these rocks and found dolomite, calcite, quartz, ilite, soda feldspar, potash feldspar, pyrite, and analcite as common composition (Wen et al. 1976, Burnham et al. 1980, Jaganathan

et al. 1986, Rao & Kumar 2015). Further, the presence of organic content in oil shales is also established by petrology (Augustyn et al.1976, Lin 1990, David & White 1986). Apart from petrology, the researchers have also studied the mechanical behaviour under high temperature and pressure conditions (Chong et al. 1979, 1982, 1984, William & Andreas 1993, Zeuch 1983, Zhao et al. 2012). Large number of experiments has been performed on Green River Formation Oil Shale from the Mahogany Zone and the elastic constants are expressed as a function of organic content and stress levels. Chong et al. (1979, 1980) and Zeuch 1983, proposed the empirical relations between uniaxial compressive strength, organic content and temperature. Kumar and Rao (2015) compared the mechanical and physical properties of oil shales with different rocks and investigated the applicability of the existing failure criterions and calculated different parameters.

In the present study, an attempt is made to understand the geological depositional environment, petrography and mechanical properties of oil shales. The presence of organic matter, inorganic composition, lamination direction, burial depth and temperature affects the engineering properties of such materials. The favourable characteristics of Assam coal for conversion to liquid fuels have been known for a long time. Studies have indicated that these coals and carbonaceous shale constitute the principal source rocks that have generated the hydrocarbons produced from the region. A number of Indian sedimentary basins possess large volumes of source rock sediments, with wide spectrum of geological age ranging from proterozoic to tertiary period. Therefore, the sampling process and petrology of some Indian origin oil shale are also discussed in detail.

## 2 GEOLOGY OF INDIAN OIL SHALE

North-East India is endowed with rich deposits of coal. The coal is found in the Barail Formation of Tertiary age. Carbonaceous shale occurs interbedded with the coal. These formations outcrop on the surface towards the south of the oil fields in a region called the Belt of Schuppen. Studies have indicated that these shales constitute the principal source rocks that have generated the hydrocarbons produced from the region. The yield from these deposits ranges from 80–280 kg hydrocarbon per ton of rock. The rocks which can be characterised as oil shales are part of the Barail and Disang geological formations of North East India. This belt is delineated on the east by Halflong–Disang thrust and on the west by Naga thrust. Makum coal basin is an isolated tectonic block of this belt where the coal bearing Barail Group of rocks were sandwiched between two thrusts namely Margherita thrust on the north and Halflong–Disang thrust on the south. The coal bearing Barail Group is furter divided into Naogaon, Baragolai and Tikak Parbat Formation in ascending order. They are present over the area covered by the Naga and Patkai Hill ranges, i.e. over an area about 300 by 50 kms. It lies between latitudes 27°03′ to 27°20′ and longitudes 95°10’ to 95°30′. Assuming a mineable depth of about 500 metres this total rock volume works out to around 7500 cubic kms, equivalent to a rock weight of 150 billion tonnes. This results in an in-place shale oil reserve of greater than 15 billion tonnes (Sarmah 2013, Baruah et al. 2003). The sourse of organic matter in indian oil shale are algae, plants remains and animal remains. The presence of fossilized bamboo and leaf imprint shows the coalification condition and tranquil condition during the deposition period.

## 3 PETROLOGY

For mineralogy XRD analysis, EDX technique, thinsection and SEM techniques are used. Whereas XRD analysis on these indian oil shales shows both crystalline and amorphous phase in all the samples. Based on the XRD and EDX results, the crystalline components were identified as quartz along with kaolinite, Illite and pyrite (Fig. 1 and Table 1). It is observed from the SEM analysis that the mineral matter consist of partical size less than 20 μ,

therefore these oil shales mostly consist of clay and silt. All the images of SEM shows that the oil shale are very porous in nature. The laminated structure in these rocks are observed from these SEM images. The grain boundaries are loosely bonded having loose clay particles. The quartz mineral can be identified at 5000X magnification, showing the fracture plane of quartz. Presence of chlorite and illite dust is also observed. The porosity and the organic matter is clearly visible in these images. The circular void space shows the presence of organic matter in these rocks (Fig. 2). Optical microscopic images of oil shale shows the richness of these rocks. It is observed that these rocks contain organic matter. The opaque brown and black matrix shows the presence of structure less groundmass which are scattered throughout the matrix in no fixed manner except that their long axis oriented towards the bedding plane (Fig. 3).

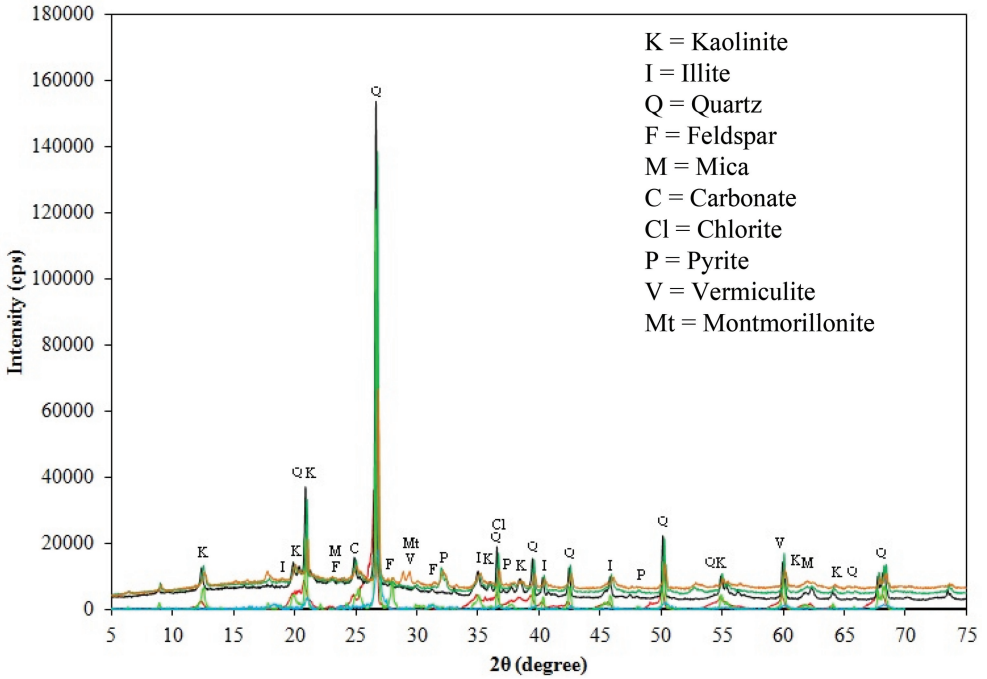


Figure 1. Representative XRD pattern of Indian origin oil shale sample.

Table 1. Mineral content by X-Ray diffraction results and EDX spectroscopy.

| XRD | | EDX | | | |
|---|---|---|---|---|---|
| Mineral | % Content | Element | Atomic no. | Normalized wt. % | Atomic % |
| Carbonate | 47.22 | O | 8 | 50.84 | 52.7 |
| Chlorite | 3.41 | C | 6 | 24.49 | 33.82 |
| Feldspar | 1.96 | Si | 14 | 8.88 | 5.25 |
| Kaolinite | 14.67 | Al | 13 | 6.04 | 3.71 |
| Illite | 10.61 | S | 16 | 3 | 1.55 |
| Pyrite | 1.19 | Fe | 26 | 2.96 | 0.88 |
| Quartz | 11.51 | Na | 11 | 1.01 | 0.73 |
| Vermiculite | 6.55 | Mg | 12 | 0.99 | 0.68 |
| Mica | 0.45 | Ti | 22 | 0.92 | 0.32 |
| Montmorillonite | 1.99 | K | 19 | 0.87 | 0.37 |

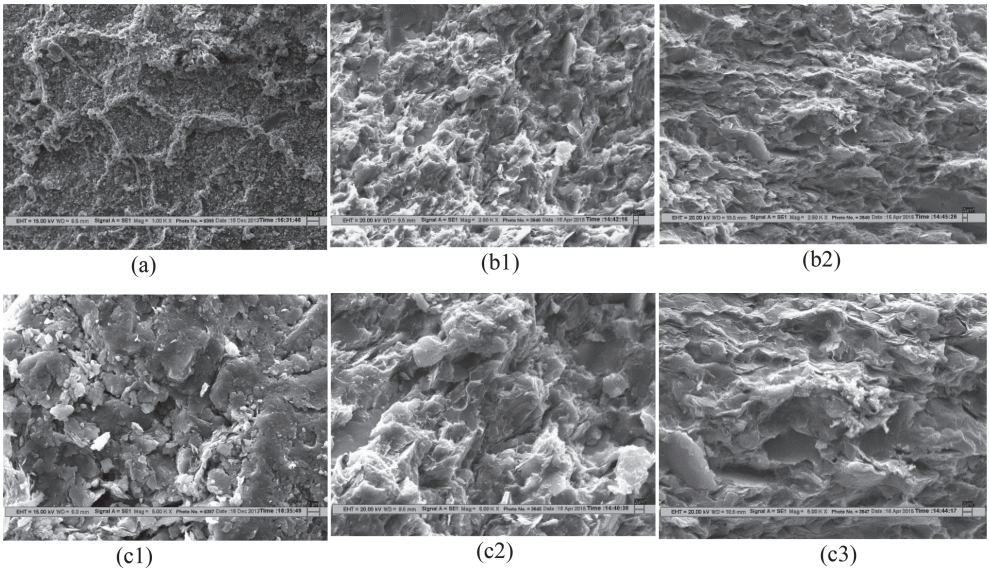


Figure 2. SEM images of oil shale at magnification of (a) 1000 X, (b) 2500 X and (c) 5000 X.

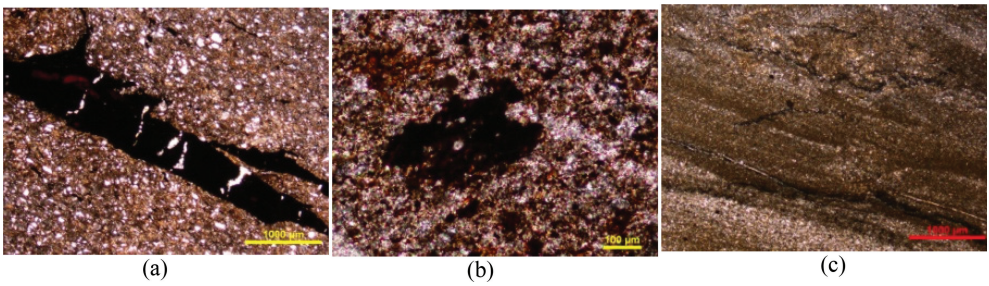


Figure 3. Optical microscopic images of oil shale samples indicating the organic content and laminated structure.

## 4 MECHANICAL PROPERTIES

Many researchers proved that the mechanical properties of oil shale depend on the oil shale grade (organic matter content). It is well established that the tensile and compressive strength as well as modulus of elasticity show negative correlations with organic matter content (Kumar & Rao 2015). Therefore, it is very important to determine and understand the organic content effect on mechanical properties. In the present study an attempt is made to understand the effect of anisotropy on the tensile and unconfined compressive strength of rocks. For the testing purpose the cores are drilled out from the large blocks by using portable drill machine. The drilling is performed on the site, to protect the samples from weathering while transportation. Further the cored samples are finished to the required dimensions in the Rock mechanics laboratory of Indian Institute of Technology Delhi and the testing is performed using the existing equipments for Brazilian testing and Point load testing.

### 4.1 *Experimentation program*

For the experimentation approximately 90 samples are prepared (L/D ratio of 1 and 0.5). According to the IS-8764, 1:1 ratio of samples are used for point load strength index determination. Which is further correlated to the unconfined compressive strength of rocks.

$$I_{s50} = P/(D^{1.5} \times \sqrt{50}) \text{ MPa} \quad (1)$$

where $I_{s50}$ is Corresponding point load strength index for the standard core size of 50 mm, P is braking load in N, D is distance of platens in mm.

Further the point load strength index is correlated to UCS value by

$$\sigma_c = 22\ I_{s50} \text{ MPa} \quad (2)$$

where $\sigma_c$ is unconfined compressive strength in MPa.

While experimentation the loading is done at different angles from the lineation plane. The angle of loading (β) with the lineation axis is shown in Figures 4 a and b. The angle of loading and anisotropic angle considered in the present study are 0, 45 and 90°. The prepared sample for testing is shown in Figure 5 (a). It is observed from the Figure 6, that the Unconfined Compressive Strength (UCS) at the angles 0 and 90 degree are maximum whereas the minimum UCS value will occur in between 30 and 45 degrees. The UCS value for 45 degree loading angle is minimum in all the cases because of the thin and laminated structure. The failure is happening along the predefined plane of weakness and the shearing of the organic material is taking place, as the foliations are filled with kerogen.

The testing is also performed for the sonic wave velocity determination. The compression wave velocity ($V_p$) at different anisotropic angles is measured. It is observed that the velocity is minimum at 90 and maximum at 0 degree anisotropic angle. It can be seen from Figure 7, that the $V_p$ decreases with increase in anisotropy angle and the trend is almost linear. This behaviour is due to the presence of voids and the laminated structure of rocks. The resistant to wave velocity is minimum along the lineation and maximum for transverse direction.

Similarly the experimentation for determining the tensile strength of the oil shales is performed at different loading angles, as per IS-10082. Figure 5 (b), shows the prepared samples for the Brazilian test apparatus. It is observed from the Figure 8, that the tensile strength is

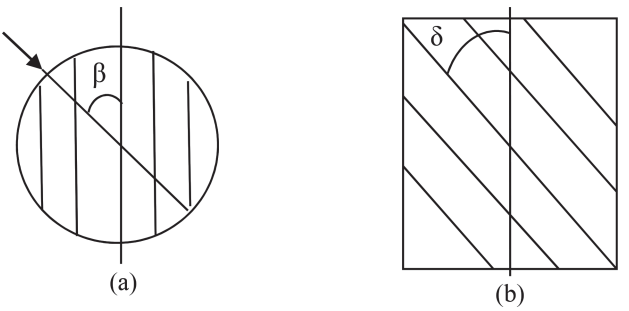


Figure 4. Key diagram for (a) loading angle (b) anisotropic angles.

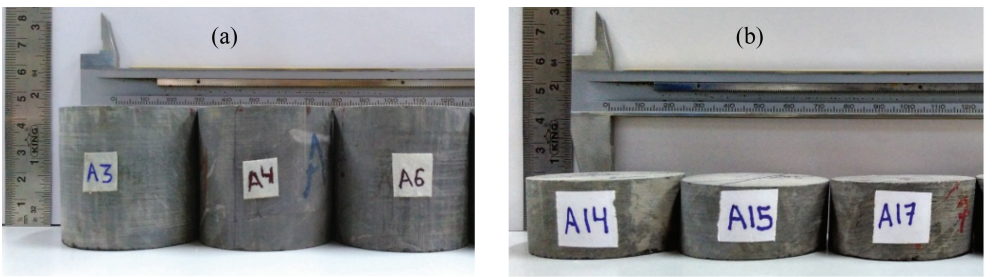


Figure 5. Samples for (a) Point load testing (L/D = 1) and (b) Tensile strength testing (L/D = 0.5 ratio).

minimum at angle between 30 and 45 degree and maximum at angle 90 degree for each loading condition. Tensile strength decreases with increase in loading angle, up to 45 degree and then starts increasing. The minimum tensile strength is obtained for 45 degree anisotropic angle at 45 degree loading angle (Fig. 9). Further, Different properties of the Indian oil shale are tabulated in Table 2 and compared with shale rock. It is concluded that these oil shales are soft rocks having strength less than 28 MPa. The difference in the strength of these rocks is mainly due to the presence of kerogen in oil shales. Further more extensive testing is under process for the better correlations for the future use.

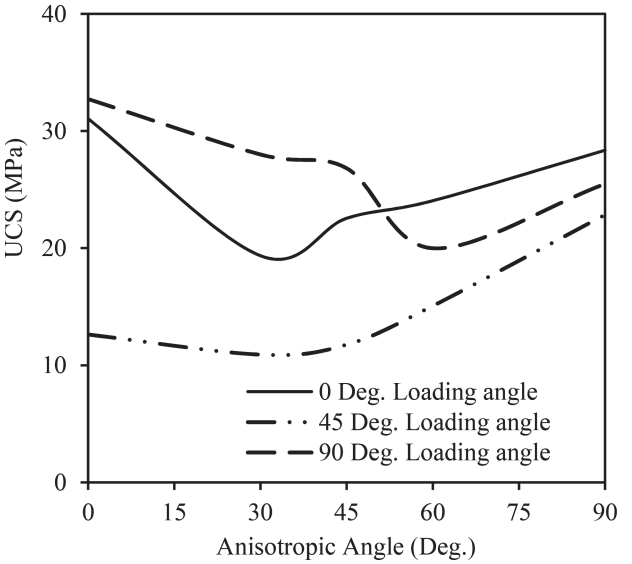


Figure 6. Variation of UCS with anisotropic angle for different loading angles.

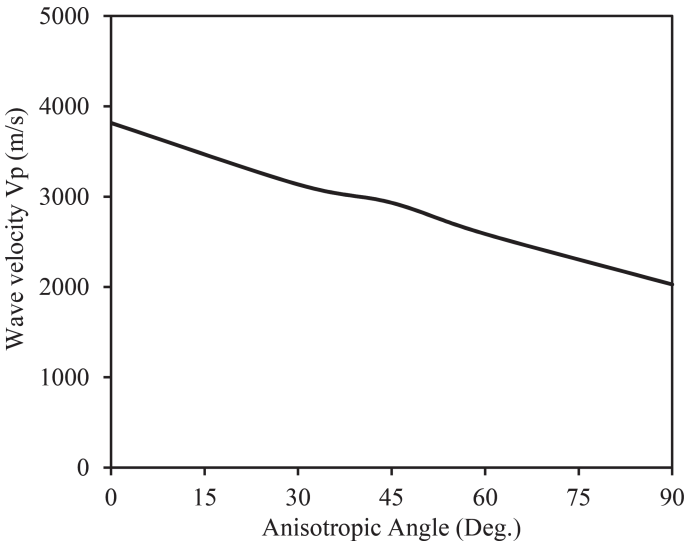


Figure 7. Variation of compression wave velocity ($V_p$) with anisotropic angle.

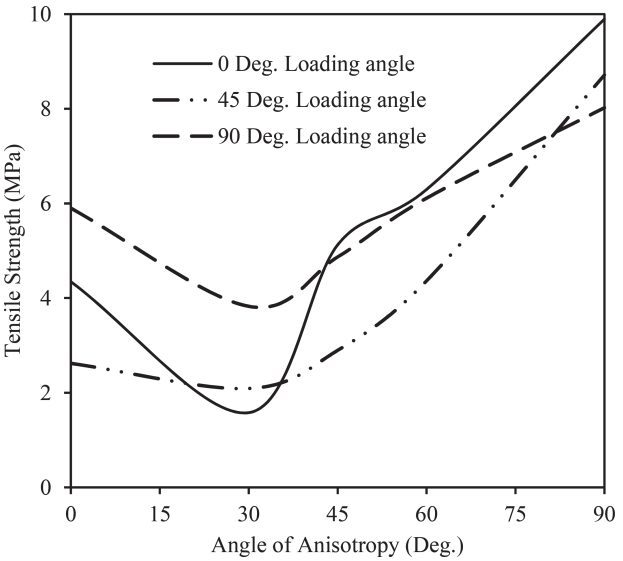


Figure 8. Variation of tensile strength with anisotropy angle.

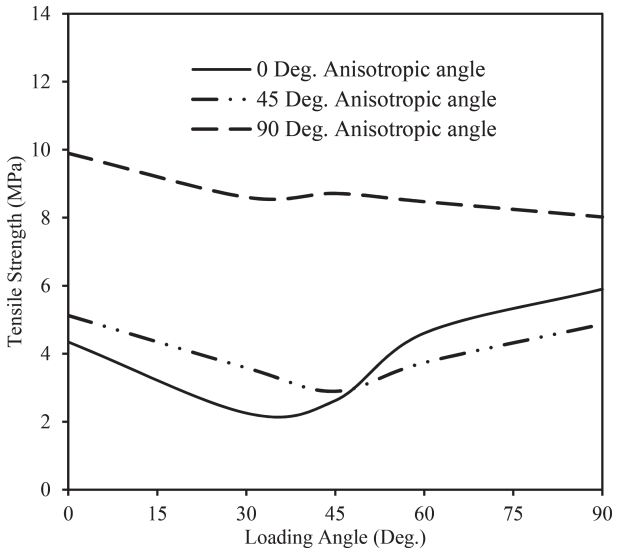


Figure 9. Variation of tensile strength with loading angle.

Table 2. Different properties of Indian oil shale.

| Property | Oil shale | Shale |
|---|---|---|
| Density (g/cc) | 2.59 | 2.4–2.6 |
| Specific gravity | 2.6 | 2.6 |
| Wave velocity, $V_p$ (m/s) at 0° | 3815.76 | |
| Wave velocity, $V_p$ (m/s) at 90° | 2017.65 | |
| UCS (MPa) | 19 | 50–150 |
| Tensile strength (MPa) | 4.927 | 10–20 |

## 5 CONCLUSIONS

Oil shale is a natural, impermeable, fine-grained, laminated black or brown combustible material, and it consists of organic material of high molecular weight called kerogen which is finely distributed in an inorganic matrix. The main difference between shale and oil shale is the kerogen content in the oil shale. It is observed that the physical and mechanical properties of oil shale are dependent on the organic content. The porosity of oil shale is close to zero and its bulk density is inversely proportional to the organic content. The exact mineral composition of oil shales is quantified by using XRD and EDX techniques of chemical analysis. The circular voids in SEM images show the presence of organic matter and the clear laminated structures are also observed. It is interpreted that the drilling length drastically increases with drilling angles and tensile strength at that angle. It is observed that the UCS, tensile strength and compression wave velocity are strongly dependent on the anisotropy. It is concluded that the Indian oil shale have very low strength property due to the presence of organic matter and relatively younger in age. It is also observed that the 45–45 degree angle combination is most critical for engineering applications. The present work will help the engineers and researchers to estimate the mechanical properties of oil shale for the stability of bore holes and the slopes at mining sites.

## REFERENCES


Augustyn, D., Iley, M. & Marsh, H. 1976. Optical and scanning electron microscope study of brown coals. *Fuel* 55(1): 25–38.

Baruah, M. 2003. Distribution and nature of organic/mineral bound elements in Assam coals, India. *Fuel* 82(14): 1783–1791.

Burnham, A.K., Stubblefield, C.T. & Campbell, J.H. 1980. Effects of gas environment on mineral reactions in Colorado oil shale. *Fuel* 59(12): 871–877.

Chong, K.P., Ward, J. & Chang, B. 1979. Oil shale properties by split cylinder method. *J. Geotech. Engn. Div. ASCE* 105(5): 595–611.

Chong, K.P., Uenishi, K. & Smith, J.W. 1980. Non–Linear three dimensional mechanical characterization of Colorado oil shale. *Int. J. Rock Mech. Min Sci*. 17(6): 339–347.

Chong, K.P., Smith, J.W. & Borgman, E.S. 1982. Tensile strengths of Colorado and Utah oil shales. *Journal of Energy (USA)* 6(2): 81–85.

Chong, K.P., Chen, J.L., Dana, G. & Sailor, S. 1984. Triaxial testing of Devonian oil shale. *Journal of Geotechnical Engineering* 110(10): 1491–1497.

David, M.R. & White, A. 1986. Scanning macerals electron microscopy of coal. *Fuel* 65: 277–280.

Jaganathan, J., Mohan, M.S. & Zingaro, R.A. 1986. Identification of arsenic–bearing minerals in a sample of Green River oil shale. *Fuel* 65(2): 266–269.

Lin, C.L. 1990. Characterization of coals and macerals by X–ray diffraction. *Fuel* 69(7): 821–825.

Kumar, A. & Rao, K. S. 2015. Engineering behavior of oil shale at elevated temperature and confining pressure. *5th Young Indian Geotechnical Engineers Conference,* Vadodra.

Nowacki, P. 1981. *Oil Shale Technical Data Handbook*. Noyes Data Corporation, Park Ridge, New Jersey.

Rao, K.,S. & Kumar., A. 2015. Geological and engineering behavior of oil shales. *EGNM – 15*, India.

Robinson, W. E. 1976. Origin and characteristics of Green River oil shale. *In: Oil Shale (T. F. Yen and G.V. Chilingarian, eds.),* Elsevier Scientific Publishing Co., Amsterdam, pp. 61–80.

Shanks, W. C., Seyfried, W. E., Meyer, W. C. & O'Neil, T. J. 1976. Mineralogy of oil shale. *In: Oil Shale (T. F. Yen and G. V. Chilingarian, eds.),* Elsevier Scientific Publishing Co., pp.81–102, Amsterdam.

Sarmah, R.K. 2013. Study of the maceral composition and coal facies of the Oligocene coals in Makum coalfield, Upper Assam, India. *Geology* 3(6): 281–285.

Wen, C.S., Kwan, J. & Yen, T.F. 1976. Exploratory experiments on pyrite removal from oil shale by an electrolytic process. *Fuel* 55(1): 75–78.

William, D.I. & Andreas, K.K. 1993. Experimental deformation of shale: Mechanical properties and microstructure indicators of mechanism. *International Journal of Rock Mechanics & Mining Sciences* 30(7): 723–734.

Yen, T.F. & Chilingarian, G.V. 1976. *Oil Shale. Elsevier Publishing Co., Ams*terdam, Ch.1.

Zhao, Y., Wan, Z., Feng, Z., Yang, D., Zhang, Y. & Qu, F. 2012. Triaxial compression system for rock testing under high temperature and high pressure. *Int. J. Rock Mech. Min. Sci*. 52:132–138.

Zeuch, D.H. 1983. The mechanical behavior of Anvil Points oil shale at elevated temperatures and confining pressures. *Canadian Geotechnical Journal* 20(2): 344–352.

*Rock Dynamics: From Research to Engineering – Li et al. (Eds)*
*© 2016 Taylor & Francis Group, London, ISBN 978-1-138-02953-8*

# Experimental study on stress wave propagation across joints with different joint matching coefficients

L.F. Rong, J.C. Li, H.B. Li & S.B. Chai
*State Key Laboratory of Geomechanics and Geotechnical Engineering, Institute of Rock and Soil Mechanics, Chinese Academy of Sciences, Wuhan, China*

ABSTRACT: The joints have a certain effect on stress wave propagation across rock masses. This paper presents an experimental study on stress wave propagation across joints with different joint matching coefficients by carrying out ultrasonic wave tests. The steel cylinders with different contact areas were adopted to simulate the joint rough surfaces and simplify the specimen preparation. Through the tests, the initial pulse of the transmitted wave across the joints is obtained. By comparing the measured results, the attenuation effect of single joint and two parallel joints with different joint matching coefficients on wave propagation is investigated. The experiment results show that the transmission coefficients for the jointed specimens are influenced by various parameters of joint, such as Joint Matching Coefficient (JMC), distribution type of contact area of joint surface, the number of joints and joint spacing.

## 1 INTRODUCTION

Rock joints are common type of the structural planes existing in natural rock masses. When a wave propagates across the joints, it is often attenuated and slowed, so the presence of the joints has great effect on stress wave propagation (Pyrak-Nolte 1996). A lot of researches have been carried out to study stress wave propagation across one joint or joint set. The Equivalent Medium Method (EMM) (e.g. Schoenberg & Muir 1989, Cook 1992) is one of the theoretical methods in common use, which describes the macroscopical property of the jointed masses based on principles of continuum mechanics. The other theoretical method used widely is the Displacement Discontinuity Method (DDM) (e.g. Schoenberg, 1980, Pyrak-Nolte et al. 1990), which considers that the stress across the joint are continuous, but displacements across the joint are not.

The mechanical property of the joints (e.g. stiffness) is important to analyze stress wave propagation across a jointed mass by using the displacement discontinuity method, which is significantly influenced by the characteristic of the joint surface. An empirical equation is proposed to describe the relationship between the Joint Roughness Coefficient (JRC) and the initial stiffness of the natural joints by Bandis et al. (1983). Zhao (1997) considered the Joint Matching Coefficient (JMC) based on the percentage of joint surfaces in contact is one of the important influence factors on stiffness. The effect of the distribution types of contact area of joint surface on joint stiffness was studied numerically by Hopkins (2000).

The effects of interface in partial contact on attenuation of stress wave were studied experimentally by using ultrasonic wave device (Myer et al. 1985, Myer et al. 1986, Cai et al. 2000, Zhao et al. 2006), while the effects of contact area ratio of joint on stress wave propagation were studied experimentally by using Split Hopkinson Pressure Bar (SHPB) (Li et al. 2015, Liu et al. 2014, Chen et al. 2015). Ju et al. (2006, 2007) and Li et al. (2009) discussed the relationship between the fractal dimensions of joint surface and dissipation of the energy of stress wave. Li et al. (2014) studied wave propagation across a single rough fracture by the modified thin-layer interface model.

In the present study, ultrasonic wave tests of the jointed specimens were conducted to study wave propagation across joints with different joint matching coefficients. The specimen is made of steel so as to simplify the specimen preparation whilst keeping the problem in

elastic state. The transmission coefficients for stress wave across the jointed specimens were obtained from test data. The experiment result shows that the parameters of joint such as JMC, distribution type of contact area of joint surface, the number of joints and joint spacing have obvious influence on transmission coefficients.

## 2 EXPERIMENTAL STUDY

### 2.1 *Test setup*

The ultrasonic experimental setup mainly comprises a static uniaxial compressive machine, a pair of ultrasonic transducers, and RSM-SY5 intelligent sound wave apparatus. Ultrasonic wave was generated by applying spike pulses of 500 V from the sound wave apparatus to an ultrasonic transducer containing a P-type piezoelectric crystal. The central frequency of the generated P-wave was 130 kHz. After passing through the specimen, the ultrasonic wave was received by another transducer and converted to an electrical signal which was digitized by the sound wave apparatus and stored in the personal computer. The experimental setup was shown in Figure 1.

### 2.2 *Specimen preparation*

The specimens were made of 45~# steel that is of high seismic quality factor to eliminate intrinsic attenuation as much as possible. The Young's modulus ($E$) and density ($\rho$) of 45~# steel is 195 GPa and 7850 Kg/m$^3$, respectively. There were two kinds of specimens containing single joint and two parallel joints, respectively. As shown in Figure 2a, the specimen with a single joint was composed of two intact steel cylinders with both length and diameter being 50 mm. The total length of the specimens is 100 mm. A joint perpendicular to the longitudinal axis of the specimen was sandwiched between the two cylinders. The joint has two surfaces, one is flat and the other is rough. The rough surface was grooved symmetrically to form notches with depth of 2 mm as mismatch area. In addition, there were two types of the distribution of notches, one was aggregated where a notch was along the edge of the joint surface, as shown in Figure 3a, the other was discrete where the notches were uniformly, as shown in Figure 3b. When the width and number of the notches vary, the joints with different contact area or the joints with different JMCs were obtained. As shown in Figure 2b, the specimen with two parallel joints was composed of three separate intact cylinders. The whole length of the specimen was still 100 mm. The contacts of the three cylinders are two joints perpendicular to the longitudinal axis of the specimens. The lengths of the middle cylinders were 10 and 25 mm, which represent the Joint Spacing (JS).

The intact cylinders were divided into three series, i.e. A, B and C. Series A had flat surfaces and five different lengths and denoted as A1-A5. Series B had aggregated contact surfaces and denoted as B1-B19, and series C had discrete surfaces with uniformly distributed notches and denoted as C1-C19. The diameters of all intact cylinders were 50 mm, while the lengths and joint matching coefficients are shown in Table 1. For the sake of clearness to record, the specimens

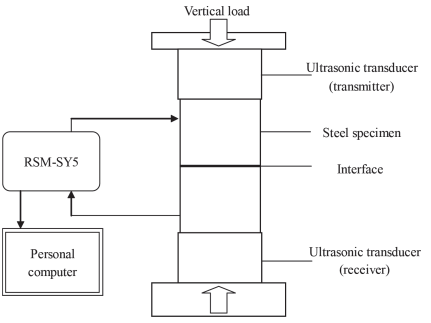


Figure 1. Schematic view for ultrasonic wave test setup.

containing single joint with aggregated contact area were denoted as single-joint-B, while the specimens containing two joints with aggregated contact aera were denoted as two-joint-B. Similarly, the specimens containing joints with discreted contact area were denoted as single-joint-C and two-joint-C, respectively. To distinguish the two-joint specimens with different joint spacings, the suffix like "-joint spacing" was added to the name of specimens, for example, the two-joint-B specimens with joint spacing of 10 mm were denoted as two-joint-B-10.

### 2.3 *Experiment procedure*

Ultrasonic tests were carried out under normal stress of 20 MPa so as to ensure intimate contact between joint surfaces, besides, a certain amount of silicone grease was painted on the surfaces of ultrasonic transducers to reinforce acoustic coupling. Firstly, an intact steel speci-

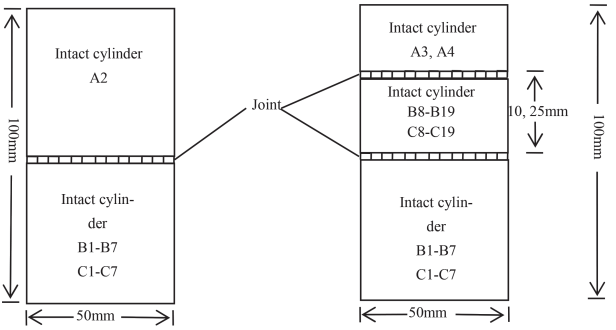


(a) with one joint (b) with two parallel joints

Figure 2. Specimens prepared for ultrasonic tests.

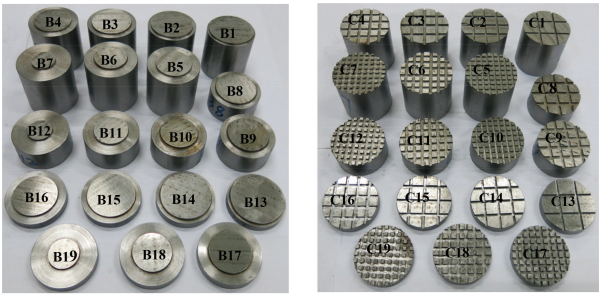


(a) Aggregated surfaces of joints (b) Discreted surfaces of joints

Figure 3. Intact steel cylinders.

Table 1. The lengths and joint matching coefficients of the intact cylinders.

| | Joint Matching Coefficients (JMC) | | | | | | | |
|---|---|---|---|---|---|---|---|---|
| | 1 | 0.82 | 0.74 | 0.62 | 0.53 | 0.43 | 0.36 | 0.21 |
| Length | Number | | | | | | | |
| 100 mm | A1 | | | | \ | | | |
| 50 mm | A2 | B1,C1 | B2,C2 | B3,C3 | B4,C4 | B5,C5 | B6,C6 | B7,C7 |
| 40 mm | A3 | | | | \ | | | |
| 25 mm | A4 | | \ | B8,C8 | B9,C9 | B10,C10 | B11,C11 | B12,C12 |
| 10 mm | A5 | B13,C13 | B14,C14 | B15,C15 | B16,C16 | B17,C17 | B18,C18 | B19,C19 |

men (A1) was tested to obtain reference wave form of ultrasonic pulses transmitting through an intact specimen. It was used as reference to compare with the wave forms of ultrasonic pulses across jointed specimens. Secondly, ultrasonic tests of single-joint specimens were carried out to measure ultrasonic pulses transmitting across single joint with different JMCs and distribution types of contact area. By comparing the waveforms from single-joint specimens with reference waveform, the attenuating effects of single joint with various JMCs and different distribution types of contact area were examined. Finally, ultrasonic tests of two-joint specimens were carried out to obtain ultrasonic pulses transmitting across two parallel joints separated with the spacing of 10 mm and 25 mm, respectively. By comparing the measured results from two-joint specimens with reference wave form, the attenuating effect of two parallel joints with different spacings was examined.

## 3 EXPERIMENT RESULTS AND DISCUSSION

A total of 42 ultrasonic tests were conducted on intact, single joint and two joint specimens under the same normal stress (20 MPa). The single-joint-B and two-joint-B specimens were tested by one pair of ultrasonic transducers which are different with those were used to test the single-joint-C and two-joint-C specimens, for the reason that one pair of ultrasonic transducers had been broken accidently in experiment. Both of the pairs of ultrasonic transducers were used to test the intact specimen (A1) to obtain reference wave form respectively.

The received wave forms consist of an initial transmitted pulse, followed by later reflections from various interfaces (e.g. the interfaces between transducer and specimen), however, the initial pulses is very important in the analysis of wave attenuation across joints. For saving space, some of initial pulses are given in the text as shown in Figures 4 and 5.

Figure 4 shows the initial transmitted pulses measured from the intact, single-joint-B, two-joint-B-10 and two-joint-B-25 specimens with joint matching coefficient being 0.43, while Figure 5 shows the initial transmitted pulses measured from the intact, single-joint-C, two-joint-C-10 and two-joint-C-25 specimens with joint matching coefficient being 0.43 by another pair of transducers. Both Figure 4 and Figure 5 show the amplitudes of the initial pulses are relative to the number of joints and joint spacing. The amplitude of the initial pulses decreases with increasing either the number of joints or joint spacing when the joint coefficients are the same. In addition, the whole initial pulse is slowed because of the existence of joint, when the number of joints or the joint spacing increases, the initial pulse is slowed more.

In the ultrasonic wave propagation process, the main attenuation factors are material, geometry and the presence of joints. For the material of the specimens are 45~# steel that if of high seismic factor, intrinsic attenuation can be ignored. Furthermore, the geometry of the jointed specimens are identical with that of intact specimen, the effect of geometry of the specimens is equal. Based on the above points, the initial pulse of reference wave obtained

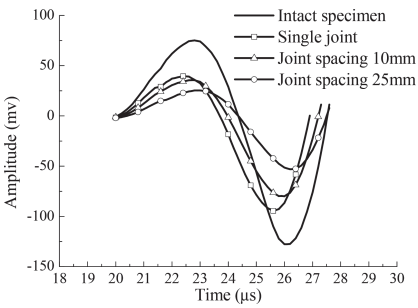


Figure 4. Initial pulses of intact, single-joint-B and two-joint-B specimens (JMC = 0.43).

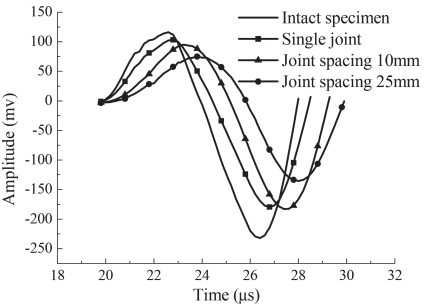


Figure 5. Initial pulses of intact, single- joint-C and two-joint-C specimens (JMC = 0.43).

from the ultrasonic tests of intact specimen can be considered as incident wave before transmitting across joints, while the initial pulse of wave measured from the ultrasonic tests of the jointed specimens can be considered as transmission wave. The first half part of initial pulses is influenced less than latter half by followed ultrasonic waves reflected from various interfaces, so the first peak of initial pulses is considered as the peak value of the incident wave or transmission wave. The transmission coefficients T, is defined as

$$T = \frac{T_p}{I_p} \tag{1}$$

where $T_p$ = amplitude of transmission wave, $I_p$ = ampliude of incident wave.

Figure 6 demonstrates that the transmission coefficient $T$ for the joints with aggregated contact area clearly decreases with the decrease of joint matching coefficient (JMC) when number of joints and joint spacing are invariant, while increases with the decreasing the number of joints and joint spacing when joint matching coefficient (JMC) is invariant. The relationship between the transmission coefficient T and JMC is quasi-linear function. The linear fits of the three groups (single-joint-B, two-joint-B-10 and two-joint-B-25) are obtained in Figure 6, and they could be expressed as $T = 0.8124 \times JMC + 0.177$ for single-joint-B, $T = 0.7522 \times JMC + 0.1484$ for two-joint-10, and $T = 0.7222 \times JMC + 0.0458$ for two-joint-25, respectively.

The transmission coefficient $T$ for single joint with matched surface (JMC = 1) is approximately one, but for two-joint with matched surface is less than one. The reason may be that the surfaces of joint are slightly uneven in spite of that surface finish is good. However, the trends of test results are clear enough to ignore the effect of the slightly uneven surfaces.

Figure 7 reveals that the transmission coefficient $T$ for joints with discrete contact area with uniform distribution, having the same trend with that for the joints with aggregated contact area, decreases with the increase of the number of joints or joint spacing and the decrease of JMC. The relationship between the transmission coefficient $T$ and JMC is natural logarithm function. The natural logarithm fits of the three groups (single-joint-C, two-joint-C-10 and two-joint-C-25) are obtained in Figure 7, and they could be expressed as $T = 0.215 \times \ln(JMC) + 0.995$ for single-joint-C, $T = 0.244 \times \ln(JMC) + 0.926$ for two-joint-C-10 and $T = 0.279 \times \ln(JMC) + 0.894$ for two-joint-C-25, respectively.

Comparison between Figures 6 and 7 shows that the transmission coefficient for joints with aggregated contact area is less than that for joints with discrete contact area with uniform distribution, when the JMC, the number of joints and joint spacing are the same. And it can be explained by Displacement Discontinuity Method (DDM), the joints with discrete contact area with uniform distribution are stiffer than the joints with aggregated contact area, which is consistent with the study results of Hopkins (2000).

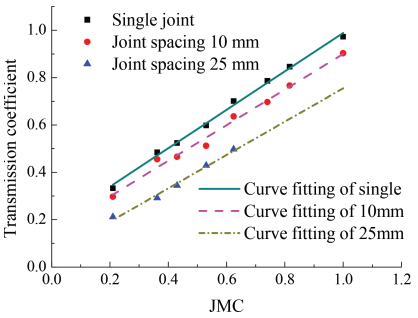


Figure 6. Transmission coefficients and fitting curves of the single- joint-B, two-joint-B-10 and two-joint-B-25 specimen.

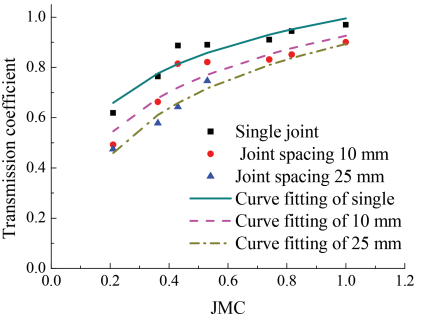


Figure 7. Transmission coefficients and fitting curves of the single- joint-C, two-joint-C-10 and two-joint-C-25 specimen.

## 4 CONCLUSIONS

The attenuation of stress wave across joints with different parameters (i.e. JMC, distribution type of contact area, number of joints, joint spacing) is investigated by carrying out ultrasonic wave tests. Through comparing the peak values of initial pulses transmitting from the jointed specimens and an intact specimen, the transmission coefficients for jointed specimens are obtained. For each of distribution types of contact area of joint surface, the transmission coefficient decreases with the increase of joint spacing or the number of joints, and with the decrease of JMC. The relationship between the transmission coefficient $T$ and JMC is quasi-linear function for joints with aggregated contact area, while the relationship between the transmission coefficient $T$ and JMC is natural logarithm function for joints with discrete contact area with uniform distribution. In addition, the joints with discrete contact area with uniform distribution are stiffer than the joints with aggregated contact area.

## ACKNOWLEDGEMENTS

The study is supported by the National Science Foundation of China (No. 41525009, 41272348) and the Scientific Research Foundation for Returned Chinese Scholars (No. 2012-940).

## REFERENCES

Bandis, S.C., Lumsden A.C. & Barton N.R. 1983. Fundamentals of rock joint deformation. *Int J Rock Mech Min Sci & Geomech Abstr* 20(6): 249–268.

Cai, J.G. 2001. *Effects of Parallel Fractures on Wave Attenuation in Rock Masses*. Ph. D. Thesis, Nanyang Technological University, Singapore.

Chen, X., Li, J.C. et al. 2015. Experimental study on wave propagation across a rock joint with rough surface. *Rock Mech Rock Eng* 48(6): 2225–2234.

Cook, N.G.W. 1992. Natural joint in rock: mechanical, hydrau-lic and seismic behavior and properties under normal stress. *Int J Rock Mech Min Sci Geomech Abstr* 29(3): 198–223.

Hopkins, D.L. 2000. The implications of joint deformation in analyzing the properties and behavior of fractured rock masses, underground excavations, and faults. *Int J Rock Mech Min Sci* 37(1): 175–202.

Ju, Y., Li, Y.X., et al. 2006. Stress wave propagation and energy dissipation in jointed rocks. *Chinese Journal of Rock Mechanics & Engineering* 25(12): 2426–2434. (In Chinese).

Ju, Y., Sudak, L. & Xie, H. 2007. Study on stress wave propagation in fractured rocks with fractal joint surfaces. *International Journal of Solids and Structures* 44(13): 4256–4271.

Li. J.C., Li, H.B. & Zhao, J. 2014. Study on wave propagation across a single rough fracture by the modified thin-layer interface model. *Journal of Applied Geophysics* 110: 106–114.

Li, Y.X., Xie, H. et al. 2009. Study on rules of transmission and reflection of stress wave across fractal joint. *Chinese Journal of Rock Mechanics & Engineering* 28(1):120–129. (In Chinese).

Li, N.N., Li, J.C., et al. 2015. SHPB experiment on influence of contact area of joints on propagation of stress wave. *Chinese Journal of Rock Mechanics & Engineering* 34(10): 1994–2000. (In Chinese).

Liu, T., Li, J.C., et al. 2014. Effects of contact area on stress wave propagation and joint mechanical properties. *Chinese Journal of Rock Mechanics & Engineering* 33(9): 1749–1755. (In Chinese).

Pyrak, N., L.J., Myer, L.R. & Cook, N.G.W. 1990. Transmission of seismic-waves across single natural fractures. *J Geophys Res* 95(B6):8617–8638.

Pyrak-Nolte, L.J. 1996. Seismic response of fractures and the interrelations among fractures. *Int J Rock Mech Min Sci* 33(8):787–802.

Myer, L.R., Hopkins, D. & Cook, N.G.W. 1985. Effects of contact area of an interface on acoustic wave transmission characteristics. *American Rock Mechanics Association*.

Myer, L.R., Hopkins, D.L. & Cook, N.G.W. 1989. Effects of an interface in partial contact on attenuation of acoustic waves. *Geophysics* 151–1521.

Schoenberg, M. 1980. Elastic wave behavior across linear slip interfaces. *J Acoust Soc Am* 68(5): 1516–1521.

Schoenberg, M. & Muir, F. 1989. A calculus for finely layered anisotropic media. *Geophysics* 54(5): 581–589.

Zhao, J. 1997. Joint surface matching and shear strength part A: joint matching coefficient (JMC). *Int J Rock Mech Min Sci* 34(2): 173–178.

Zhao, J., Cai, J.G. et al. 2006. Experimental study of ultrasonic wave attenuation across parallel fractures. *Geomechanics and Geoengineering* 1(2): 87–103.

*Rock Dynamics: From Research to Engineering – Li et al. (Eds)*
*© 2016 Taylor & Francis Group, London, ISBN 978-1-138-02953-8*

# Effect of loading rate on mechanical properties of anisotropic sandstone under compressive loading

A. Taheri
*The University of Adelaide, Adelaide, Australia*

ABSTRACT: An experimental investigation was carried out on the Hawkesbury sandstone to study effects of loading rate on the peak strength and deformability during uniaxial monotonic compressive testing. Axial load and axial and lateral deformations were measured precisely from start of loading until post-peak state. To predict properties of anisotropic Hawkesbury sandstone samples, a methodology to conduct monotonic testing was devised including the development of an innovative peak strength prediction method. The strength of the sandstone was increased with an increase in loading rate. The Tangent Young's modulus was found to increase slightly with increase of loading rate. Poisson's ratio of samples were also affected by loading rate, however, no conclusive trend was observed. A preliminary model was developed to predict variations of the Hawkesbury sandstone peak strength under different loading rates.

## 1 INTRODUCTION

Mechanical behaviour of rocks under monotonic loading is critical in understanding the stability of surface and underground excavation in civil engineering and mining development projects. To date, the behaviour of rocks under monotonic loadings has been studied by many researchers. Zhao et al. (2014) carried out uniaxial compression tests on coal with strain rates from $10^{-3}$/s to $10^{-2}$/s. They concluded that compressive strength increases with the increase in strain rate. Kodama et al. (2013) conducted monotonic uniaxial compression tests with strain rates from $4.2 \times 10^{-7}$/s to $4.2 \times 10^{-3}$/s on tuff. Test results under dry conditions showed an insignificant relation between strain rate and peak strength. It was also found that peak axial strain is not affected by strain rate. Contrary to this, Ma & Daemen (2006) investigate the effect of loading rate on welded tuff and found that both peak strength and peak axial strain increase with an increase in strain rate. Li et al. (2014) performed a study on coarse crystal marble samples with strain rates from $10^{-5}$/s to $10^{-1}$/s. They found that both Young's modulus and peak strength show an increasing trend with an increase in strain rate. However, no strain rate dependency was found for peak strain and Poisson's ratio values. The authors claimed that strain rate of $5 \times 10^{-3}$/s is the threshold point where single-plane shear and conjugate X-shaped shear are the main failure modes prior to the threshold, and extensile and splitting failures are dominant modes after this threshold. Similar to this, in the monotonic uniaxial tests with strain rates from $10^{-6}$/s to $10^{3}$/s on non-welded tuff by Olsson (1991), it was found that strain rate has a limited influence on peak strength for strain rate from $10^{-6}$/s to $10^{-2}$/s. However, a clear increasing trend of peak strength was observed with the increase in loading rate above $10^{-2}$/s. Fuenkajorn et al. (2012) carried out a series of uniaxial monotonic loading tests on Maha Sarakham salt with loading rates from 0.001 MPa/s to 10 MPa/s. They concluded that both peak strength and stiffness increase with loading rate. Okubo et al. (1990), however, didn't find any relationship between loading rate and stiffness during triaxial compression tests on andesite, granite and tuff. This finding is supported by Jeong et al. (2007) who observed in their study that both Young's modulus and Poisson's ratio are not affected by strain rate in the uniaxial compression tests on Kumamoto andesite.

In addition, Lajtai et al. (1991) showed that different rocks may behave differently when loading rate changes. They found that strain rate has a negligible effect on peak strength of a brittle rock and a significant effect on peak strength of a ductile rock.

The above discussion clearly shows that, so far, several studies have been undertaken to investigate the effect of loading rate on mechanical properties of rocks. However, loading rate dependency of rock material heavily depends on material properties, testing condition and the adopted loading rate. The scatter between outcomes of previous studies in different rocks is even more significant when it comes to rock deformability properties.

Porous sandstones formed underneath the sea beds or lands contain a large amount of intergranular pore spaces. Due to this granular property, sandstones create subsurface energy basins by trapping hydrocarbons in the form of petroleum and natural gas. In order to make use of these resources, sandstones will need to be drilled to allow for resource extraction. However, the on-site process of energy or fluid extraction including any drilling depends on the mechanical properties of these sandstones and their response to loading conditions during drilling. Therefore, it is important to understand the change in properties of this type of rock subjected to different loading rates. However, there are very limited studies on effect of loading rate on mechanical properties of porous rocks such as sandstone. For this study the Hawkesbury sandstone which is a medium-strong sedimentary rock is selected. It is aimed to investigate the effect of loading rate on peak strength, Young's modulus and Poisson's ratio under uniaxial monotonic loading.

## 2 EXPERIMENTAL METHOD

### 2.1 *Rock samples and testing set-up*

For this study the Hawkesbury sandstone which is a medium-strong sedimentary rock was selected. Hawkesbury sandstone is an early Middle Triassic (Anisian) formation widely exposed in the Sydney Basin in Australia. The rock has an average UCS of 44 MPa and average density of 2.3 gr/cm$^3$. Cylindrical specimens were prepared by coring the rock blocks. The diameter of the specimens was 42 mm. The end faces and sides of the specimen were prepared smooth and straight according to the ISRM standard (Fairhurst & Hudson 1999). The aspect ratio (i.e. length to diameter ratio) of the samples was maintained at 2.4 for all the samples.

Tests were conducted by using a closed-loop servo-controlled testing machine with a loading capacity of 250 kN. The loading rate can be adjusted from 0.0001 to 600 mm/min. The triaxial cell is equipped with a Linear Variable Differential Transformer (LVDT) to measure axial displacement and control axial loading. Axial load (by a load cell), axial strain (by two extensometers and external LVDTs) and lateral strain (by a ring extensometer) were acquired continuously by a data acquisition system at a rate of 4 data points per second.

### 2.2 *Loading set-up*

Base on a study performed by Bastian et al. (2014), Hawkesbury sandstone is not completely a homogenous rock. To investigate the effect of cyclic loading on mechanical properties, it was essential to have identical samples. To remove variations among samples they cored all the samples in a same direction using a rock block. However, the uniaxial compressive strength of the samples were varied up to 25%. In order to analyze the effect of loading rate on rock mechanical properties, it is essential to eliminate the effect of sample variation. To solve this problem, a method to predict rock peak strength, $q_{f1}$, without failing the specimen is required to allow results to be confidently attributed to loading rate change, rather than estimating rock strength from previous tested specimens under monotonic loading assuming that all the samples are completely identical. This method is briefly explained below as it is discussed in detail by Taheri et al. (2015).

Analysing the results of monotonic tests on the Hawkesbury sandstone, it was found that during monotonic loading the secant Young's modulus, $E_{sec}$, evaluated by the external LVDT, keeps increasing until the axial stress come to a point closer to the failure point, after which

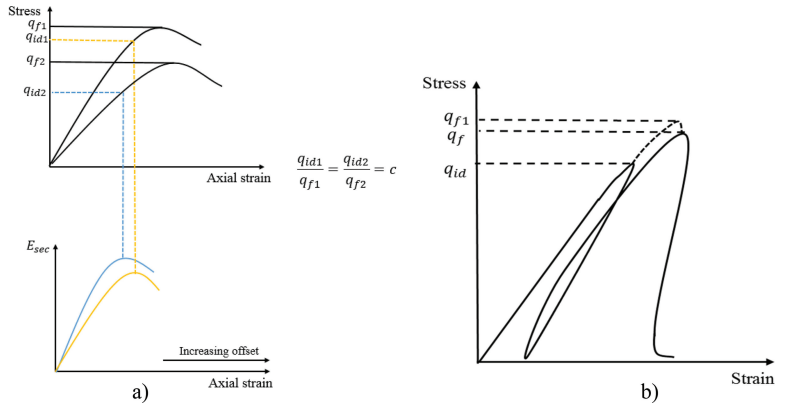


Figure 1. Loading method adopted in this study; a) Use of $E_{sec}$ = max as an indicator point to predict peak strength, b) Applying a pre-monotonic loading to predict peak strength.

the $E_{sec}$ starts decreasing. The results showed that this point is a reliable indicative point to predict peak strength without damaging the sample. As schematically shown in Figure 1(a), the deviator stress value at this indicator point, $q_{id}$, always provides a constant value for the ratio of $q_{id}/q_f$. Taheri et al. (2015) investigated the possibility of applying an offset to the secant Young's modulus in order to reduce the variability of $q_{id}/q_f$. The purpose of the offset also is to smooth out small scale fluctuations in the data as shown in the following equation:

$$E_{sec}\ with\ offset = \frac{Deviator\ stress}{strain + offset} \tag{1}$$

Therefore, in this study, pre-monotonic test was conducted in each monotonic loading test which was used to obtain the stress ($q_{id}$) at maximum $E_{sec}$, without failing the sample. The peak strength ($q_{f1}$) was estimated by using $q_{id}$ divided by the constant, $c$. In this study offset value of 0.1% and $c$ value of 0.94 were selected to estimate the peak strength of each sample under constant loading rate of 0.05 mm/min. When $E_{sec}$ maximum point is reached, sample fully unloaded and then reloaded at a selected loading rate (i.e. slower or faster than 0.05 mm/min). In each test, after the sample is failed at its peak strength, $q_f$, the normalization of $q_f/q_{f1}$ was carried out to exclude the variations among samples in terms of peak strength values and investigate the effect of loading rate on peak strength of the Hawkesbury sandstone. As shown by Bastian et al. (2014) variations among the Hawkesbury sandstone specimens in terms of deformability parameters is negligible, therefore, normalization of deformability parameters wasn't required. Figure 1(b) shows the testing method adopted for this study.

## 3 TEST RESULTS

After performing several monotonic tests at basic loading rate of 0.05 mm/min to determine a suitable values for offset and $c$ constant (explained in Section 2), in total 7 monotonic tests in different loading rates were carried out. Table 1 demonstrates the loading rate adopted for each test and the normalized peak strength values. These results are used to evaluate effect of loading rate on peak strength. Figure 2 shows examples of the axial stress—axial, lateral and volumetric strains obtained at different loading rates. All the strains are calculated accurately using local extensometers. As can be seen in Figure 2, axial and lateral strains increase from beginning of loading until post-peak state. Volumetric strain, however, increases up to a point known as crack damage point (Bieniawski 1967) and then reverses and moves into negative values (i.e. sample volume increase) near the peak strength point.

Table 1. Peak strength normalized values obtained by monotonic loading.

| Sample | Loading rate (mm/min) | $q_f\,(MPa)$ | $q_{f1}(\,MPa)$ | $q_f/q_{f1}$ |
|---|---|---|---|---|
| HS 5 | 0.0005 | 33.496 | 35.506 | 0.943 |
| HS 19 | 0.002 | 37.894 | 38.791 | 0.977 |
| HS 7 | 0.01 | 33.759 | 34.785 | 0.970 |
| HS 8 | 0.1 | 38.560 | 38.018 | 1.014 |
| HS 17 | 1 | 41.775 | 40.150 | 1.040 |
| HS 18 | 10 | 44.335 | 39.694 | 1.117 |
| HS 29 | 30 | 40.836 | 36.725 | 1.112 |

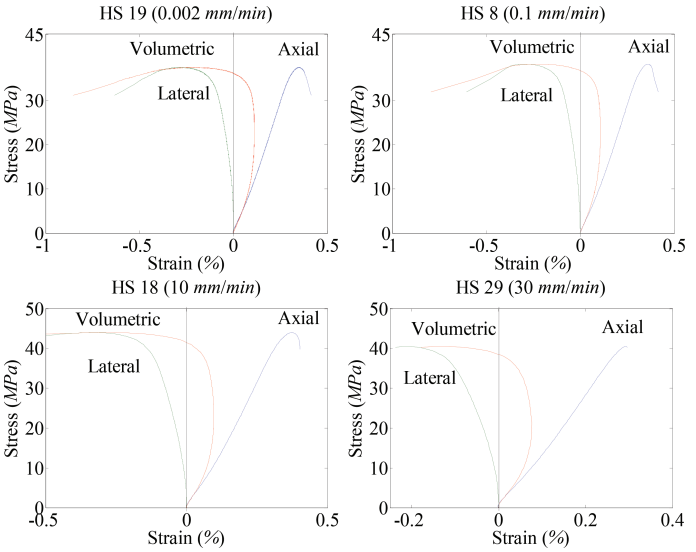


Figure 2. Stress-strain-stress relations for monotonic loadings.

## 4 EFFECT OF LOADING RATE ON ROCK PROPERTIES

### 4.1 *Peak strength*

Figure 3(a) shows normalized peak strength ($q_f/q_{f1}$) values versus loading rates. As it may be seen in this figure, peak strength generally increases with an increase in loading rate. This demonstrated that the Hawkesbury sandstone can sustain more axial stress when subjected to higher loading rates. This results are in agreement with previous studies by Li et al. (2014), Fuenkajorn et al. (2012) and Zhao et al. (2014). This outcome clearly shows how the closure of pores before dilatancy is critical to the strength of this porous rock. The sudden stress created by higher loading rate increase the rate of pores closure which allows the rock to sustain more stress before the development of critical lateral cracks dominating the failure. The relation between peak strength and loading rate can be presented by the following equation:

$$\frac{q_f}{q_{f1}} = 0.0158 \times \ln(\dot{d}) + 1.0558,\ R^2 = 0.9504 \tag{2}$$

where $\dot{d}$ is loading rate (mm/min). Hashiba et al. (2006) developed a model that describe the effect of loading rate dependency to strength for various rocks:

$$\frac{\sigma_a}{\sigma_b} = \left(\frac{\dot{\varepsilon}_a}{\dot{\varepsilon}_b}\right)^{\frac{1}{n+1}} \tag{3}$$

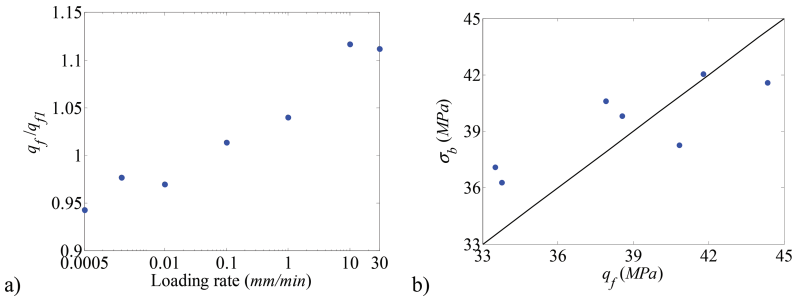


Figure 3. Effect of loading rate on the peak strength; a) Loading rate versus peak strength; b) Comparison between experimental results and the results predicted by Hashiba et al. (2006) model.

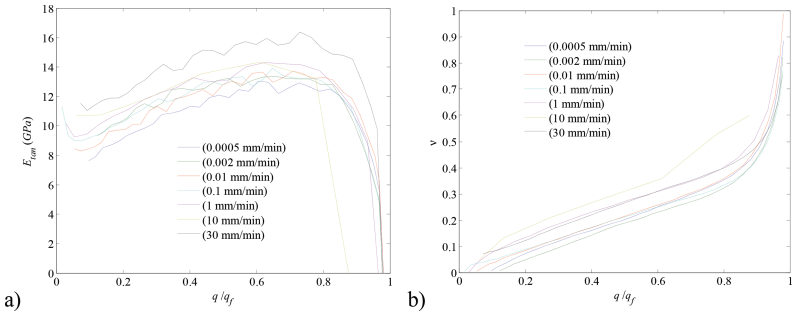


Figure 4. Change of deformability properties against $q/q_f$; a) Tangent Young's modulus; b) Poisson's ratio.

where $\sigma_a$ and $\sigma_b$ are stresses corresponding to strain rates $\dot{\varepsilon}_a$ and $\dot{\varepsilon}_b$ at some arbitrary strain and $n$ is the parameter of loading rate dependency which is different for different rocks.

To examine the application of this model on the Hawkesbury sandstone, $\dot{\varepsilon}_a$ was assumed to be as the basic loading rate in the pre-monotonic loadings which was 0.05 mm/min and $\dot{\varepsilon}_b$ as the loading rate in the main loading ranging between 0.0005 mm/min to 30 mm/min. The value of $n$ for sandstone is suggested to be 42 (Hashiba et al. 2006). Figure 3(b) shows $\sigma_b$, peak strength values predicted by the Hashiba et al. (2006) model plotted against $q_f$, peak strength values measured at each loading rate. This Comparison shows that the model can predict peak strength increase with an increase in loading rate with enough accuracy.

## 4.2 *Deformability properties*

The effects of loading rate on the stress-strain properties of the Hawkesbury sandstone were studied. The tangent Young's modulus, $E_{\tan}$, and the Poisson's ratio, $v$, during shearing were evaluated from the stress-strain relations in the monotonic loadings with different loading rates. The relationships between $E_{\tan}$ and $v$ and the shear stress ratio, $q/q_{\max}$, at different loading rates are plotted in Figures 4(a) and (b).

As can be seen in Figure 4(a), $E_{\tan}$ generally increases until 60% of the peak strength. A continuous degradation in stiffness can be clearly see after this point. This point represents the onset of crack initiation point where stable random axial cracking creates in rock sample (Bieniawski 1967). In addition, Figure 4(a) clearly shows that rock stiffness increases with an increase in loading rate. This is mainly because, when the porous rock is under stress, the stiffness increases mainly due to the closure of existing voids and the collapse of weak elements. Higher loading rate exerts the stress on the rock with higher velocity which intensifies the crack closure, where under lower loading rate, more new micro-cracks have time to evolve along with the crack closure. Therefore the rock is less compacted at lower loading rate which results in having lower stiffness.

The results presented in Figure 4(b) shows that samples loaded in loading rate of 10 mm/min and then 1mm/min and 30 mm/min exhibit the higher Poisson's ratio values, whereas

those loaded at 0.002 mm/min and then 0.0005 min/min have lower values. Therefore, it can be said that there is a slight increase in Poisson's ratio with an increase in loading rate, however, the results cannot lead to a strong conclusion. More studies on change of the lateral and the axial strain of sandstone in different loading rates is required to obtain a solid conclusion.

## 5 CONCLUSIONS

An experimental investigation was carried out on the Hawkesbury sandstone to study the effect of loading rate on the peak strength and the deformability during uniaxial monotonic compressive testing. To predict properties of anisotropic Hawkesbury sandstone samples, a methodology for successful loading rate testing was devised including the implementation of an innovative peak strength prediction method. In monotonic uniaxial compressive loading, the peak strength of the Hawkesbury sandstone increased with an increase in loading rate. A fitting model has been generated to describe the change of peak strength with loading rate. The tangent Young's modulus were found to increase slightly with increase of loading rate. Poisson's ratio of samples were also affected by loading rate, however, the results didn't lead to any promising conclusion.

## REFERENCES


Bastian, T.J., Connelly, B.J., Lazo Olivares, C.S., Yfantidis, N. & Taheri, A. 2014. Progressive damage of Hawkesbury sandstone subjected to systematic cyclic loading. *Research Journal Review*, AusIMM 3: 15–22.

Bieniawski, Z.T. 1967. Mechanism of brittle fracture of rock. *International Journal of Rock Mechanics and Mining Sciences & Geomechanics Abstracts* 4: 395–406.

Fairhurst, C.E. & Hudson, J.A. 1999. Draf ISRM suggested method for the complete stress-strain curve for intact rock in uniaxial compression. *International Journal of Rock Mechanics and Mining Science*s 36: 279–89.

Fuenkajorn, K. Sriapai, T. & Samsri, P. 2012. Effect of loading rate on strength and deformability of Maha Sarakham salt. *Engineering Geology* 135–136: 10–23.

Hashiba, K., Okubo, S. & Fukui, K. 2006. A new testing method for investigating the loading rate dependency of peak and residual rock strength. *International Journal of Rock Mechanics and Mining Sciences* 43: 894–904.

Jeong, H.S., Kang, S.S. & Obara, Y. 2007. Influence of surrounding environments and strain rates on the strength of rocks subjected to uniaxial compression. *International Journal of Rock Mechanics and Mining Science* 44: 321–331.

Kodama, J. Goto, T. Fuji, Y. & Hagan, P. 2013. The effect of water content, temperature and loading rate on strength and failure process of frozen rocks. *International Journal of Rock Mechanics and Mining Science* 62:1–13.

Lajtai, E.Z., Duncan, E.J.S. & Charter, B.J. 1991. The effect of strain rate on rock strength. *Rock Mechanics and Rock Engineering* 24: 99–109.

Li, Y.R, Huang, D. & Li, X.A. 2014. Strain rate dependency of coarse crystal marble under uniaxial compression: strength, deformation and strain energy. *Rock Mechanics and Rock Engineering* 47: 1153–1164.

Ma, L. & Daemen, J.J.K. 2006. Strain rate dependent strength and stress-strain characteristics of a welded tuff. *Bull Eng Geol Env* 63(3): 221–230.

Okubo, S. Nishimatsu, Y. & He, C. 1990. Loading rate dependence of Class II rock behaviour in uniaxial and triaxial compression test-an application of a proposed new control method. *International Journal of Rock Mechanics and Mining Science and Geomechical Abstracts* 27(6): 559–562.

Olsson, W.A. 1991. The compressive strength of tuff as a function of strain rate from $10^{-6}$ to $10^{3}$/sec. *International Journal of Rock Mechanics and Mining Science and Geomechical Abstracts* 28: 115–118.

Taheri, A., Royle, A., Yang, Z. & Zhao, Y. 2015. Study on variations of peak strength of a sandstone during cyclic loading. *Geomechanics and Geophysics for Geo-energy and Geo-Resources*, DOI 10.1007/s40948-015-0017-8.

Zhao, Y.X., Liu, S.M., Zhao, G.F., Elworth, D., Jiang, Y.D. & Han, J.L. 2014. Failure mechanics in coal: Dependence on strain rate and microstructure. *Journal of Geophysical Research: Solid Eart*h, 10.1002/2014JB 011198, 6924–6935.

*Rock Dynamics: From Research to Engineering – Li et al. (Eds)*
*© 2016 Taylor & Francis Group, London, ISBN 978-1-138-02953-8*

# Mechanical behavior of artificial rock contained single plane of weakness under impact loads

T.T. Wang
*Institute of Mineral Resources Engineering, National Taipei University of Technology, Taipei, Taiwan*

H.H. Li
*Department of Environmental Information and Engineering, Chung Cheng Institute of Technology, National Defense University, Taiwan*

T.R. Tzeng
*Chung Hsing Surveying Co., Ltd., Taiwan*

Z.Y. Yang
*Department of Civil Engineering, Tamkang University, Taiwan*

ABSTRACT: This study aims to explore the effects of impact loads on the failure types and the peak dynamic strength of artificial rocks contained a single plane of weakness with orientation angles of 45°, 60°, 75° and 90°. A series of uniaxial compression tests by Split Hopkinson Pressure Bar (SHPB) is conducted under the loading rate ranges of $10^2$–$10^3$ GPa/s, and the specimens after the SHPB tests are collected and analyzed by the sieve analysis to classify the failure modes.

## 1 INTRODUCTION

### 1.1 *Theory of single plane of weakness*

The mechanical response of nature rock such as slate, shale or foliated metamorphic rock are varied with the orientation of the plane of weakness or the foliation-planar fabric. Although the directionally dependent behavior is complex, it can be simply revealed by the Jaeger's single plane of weakness theory (Jaeger 1960). Namely, the peak strength and failure mode of intact rock containing a single plane of weakness are different with the orientation of the plane, and the failure modes include slip on the plane and shear fracture of the intact rock material. However, how the impact load effects the mechanical response of intact rock containing a single plane of weakness is still unknown, and it is investigated by Split Hopkinson-Pressure Bar (SHPB) in this study.

### 1.2 *Development and applications of SHPB*

The development of SHPB can be retraced to Hopkinson (1914) who used the induced-wave propagation to measure the pressures produced during dynamic events. Afterward two long elastic pressure bars in series, with the sample sandwiched in between, were adopted to measure the dynamic stress-strain response of materials under the strain rate $10^2$–$10^4$ $s^{-1}$ (Davies 1948, Kolsky 1949,1953). In the early application, SHPB was used to explore the dynamic mechanical properties of metal (Hauser et al. 1961). Subsequently, SHPB was used widely on the dynamic uniaxial compressive test of concrete (Ross et al. 1989, 1995) and rock (Kumar 1968; Perkins & Green 1970, Olsson 1999, Zhao et al. 1999, Zhao et al. 2000, Cai et al. 2007, Li et al. 2000, Wang et al. 2006). Alternate Hopkinson bar schemes were designed for loading samples in uniaxial tension (Harding et al. 1960, Kawata 1979, Nicholas 1972, Bailly et al. 2011), torsion (Duffy 1971) and lateral confinement conditions (Christensen 1972).

## 2 METHODOLOGIES

### 2.1 *One-dimension wave propagation theory*

The SHPB test is based on two fundamental assumptions (Kolsky 1953): (1) one-dimensional stress wave propagation in the elastic bar; (2) homogenous deformation of the specimen. Based on the theory of one-dimensional stress wave propagation, the strain, strain rate and stress of the specimen can be analysis according to the recorded strain history in the elastic bar. The homogeneity of sample deformation is concerned with the inertial effects and the interfacial friction effect. From the elementary wave theory, it is known that the solution to the wave equation (1) can be expressed as d'Alembert's solutions (2)(3):

$$\frac{\partial^2 u}{\partial x^2} - \frac{1}{C^2}\frac{\partial^2 u}{\partial t^2} = 0 \tag{1}$$

$$u_1 = f_1(x - Ct) + f_2(x + Ct) = u_i + u_r \tag{2}$$

$$u_2 = f_3(x - Ct) = u_t \tag{3}$$

$$C = \sqrt{\frac{E}{\rho}} \tag{4}$$

where the $u_1$ and $u_2$ are the particle displacements in the input and output interfaces of the specimen, the wave velocity $C$ can be obtained from the elastic modulus $E$ and the density ρ of the elastic bar. The displacement $u_1$, $u_2$, and the average strain $\varepsilon_{avg}$ and strain rate $\dot{\varepsilon}$ can be expressed as the function of the incident wave $\varepsilon_i$, the reflected wave $\varepsilon_r$ and the transmitted wave $\varepsilon_t$. The sketch map of the input and output bar and the position of specimen in the SHPB test is show in Figure 1(a).

$$u_1 = C\int_0^t (\varepsilon_i - \varepsilon_r)dt \tag{5}$$

$$u_2 = C\int_0^t \varepsilon_t dt \tag{6}$$

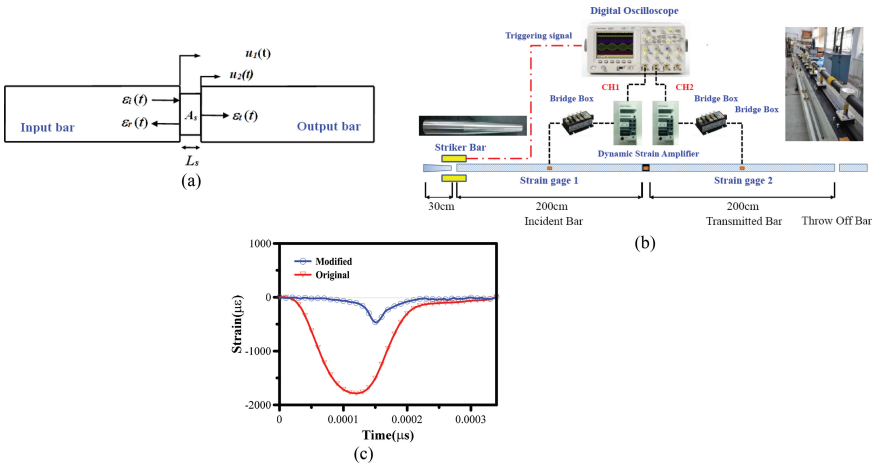


Figure 1. (a) Direction of incident, reflected and transmitted strain waves in the elastic bars; (b) setup of SHPB test; (c) the original and modified incident wave forms.

$$\varepsilon_{avg} = \frac{u_2 - u_1}{L_s} = \frac{C}{L_s}\int_0^t (\varepsilon_i - \varepsilon_r - \varepsilon_t)\mathrm{d}t \tag{7}$$

$$\dot{\varepsilon} = \frac{C(\varepsilon_i - \varepsilon_r - \varepsilon_t)}{L_s} \tag{8}$$

According to the equations (7), (8) and (11), the average stain and strain rate of specimen can be obtained, and the process analysis is so call three wave method. The dynamic stresses acted on the input and output sides of the specimen are $\sigma_{in}$ and $\sigma_{out}$ respectively, as shown in Equations (9)(10), where the $P_1$ and $P_2$ are the forces transmitted by these two bars, the $A$ and $A_s$ are the cross section area of elastic bar and specimen separately.

$$\sigma_{in} = \frac{P_1}{A_s} = \frac{AE(\varepsilon_i + \varepsilon_r)}{A_s} \tag{9}$$

$$\sigma_{out} = \frac{P_2}{A_s} = \frac{AE\varepsilon_t}{A_s} \tag{10}$$

The tangent slope corresponding to the half of peak value of $\sigma_{in}$ was defined as the loading rate, and the peak value of $\sigma_{out}$ was defined as the peak strength of the intact rock containing single plane of weakness.

### 2.2 *Setup of SHPB test*

The SHPB apparatus adopted in this study consisted of the following: compressed gas launcher, two long elastic bars, bearing and alignment fixtures, strain gages mounted on both bars, and associated instrumentation including data acquisition system and control unit, as shown in Figure 1(b). The diameter and length of the elastic bar were 4 cm and 200 cm, which was composed of bearing steel and the Young's modulus is 208 GPa, density was 7.85 g/cm$^3$ and the theoretical wave velocity was 5131 m/s. The conical striker was adopted to avoid a sharp rising edge of incident wave.

The strain gages with gage length 10 mm are mounted on the middle elastic bars and the specimen in the axial and radial directions. The wires of strain gages are jointed to the strain gauge bridge boxes which are connected to the signal amplifiers. The signal recorder is the Agilent DSO5054A oscilloscope with 500 MHz bandwidths, 4 GSa/s and 4 channels.

The chamber pressure adopted in this study is ranged from 0.6–1.0 kg/cm$^2$, and the generated impact loads are still too large for the artificial rock sample. In order to reduce the impact energy and observe various failure types, especially slip failure, an energy absorption pad made of silicone was placed between the striker and incident bars. The original and modified incident wave forms are shown in Figure 1(c), and the range of the corresponding loading rates after wave modification is ranged from $10^2$–$10^3$ GPa/s.

### 2.3 *Mechanical properties of artificial rock*

The artificial rock was a mix of gypsum, sand and water with the weight ratio 1:0.4:0.4. The mix was filled in a mold. When the specimen was hardened, it was stored in a temperature 25°C and humidity 50% cabinet. The specimen was ready to use after 6–7 days when its density became a constant of 1.76 g/cm$^3$. According to the results of uniaxial compression tests on cylindrical specimens with 50 mm in diameter and 125 mm in height, the unconfined compressive $\sigma_s$ and the tensile strength $\sigma_t$ of the artificial rock were 18.11 MPa and 2.13 MPa, the Young's modulus $E_s$ was 16.87 GPa, and the Poisson's ratio ν was 0.21. The ratio of compressive to tensile strength $\sigma_s/\sigma_t$ was 8.5, the ratio $E_s/\sigma_s$ was 559. According to the classification method suggested by Deere (1973), the artificial rock was in the category of low strength brittle rock.

## 2.4 *Preparation of artificial rock containing a single plane of weakness*

The mixture was poured in molds to make a half of artificial rock sample, as shown in Figure 2(a), and two half-parts with same inclination were combined to a intact rock containing a single plane of weakness. Figure 2(b) illustrates the direction of the impact load and the orientation angle $\beta$ of single plane of weakness. The orientation angles considered were 45°, 60°, 75° and 90° respectively, and there were four artificial rock samples for each testing condition.

## 2.5 *Classification of failure type*

Rock fragments were collected after the SHPB tests and the distribution of fragment sizes was analysis by the traditional sieve analysis adopted in soil mechanics, as shown in Figure 3. The weight of the fragments retaining on each sieve was recorded and converted into a percentage of weight. Subsequently, the failure types were classified into slip failure, slip along with fracture failure, rupture failure and crush failure according to the values of uniformity coefficient $C_c$ and $D_{30}$:

$$C_c = \frac{D_{30}^2}{D_{10} \times D_{60}} \tag{10}$$

where $C_c$ is uniformity coefficient, $D_{10}$, $D_{30}$ and $D_{60}$ are the diameter corresponding to 10%, 30% and 60% finer in the particle-size distribution.

Failure type I implies slip failure and the mechanical responses are controlled by the properties of the interface; failure types III and IV imply rupture and crush failures which reply the dynamic responses of intact material under impact load; failure type II is the transition of the mechanical responses which are controlled by interface or material.

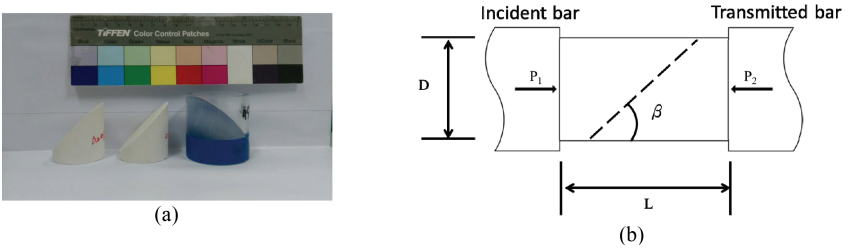


Figure 2. Artificial rock containing a single plane of weakness: (a) the half of artificial rock sample and (b) the orientation angle $\beta$ of the weakness to the impact load.

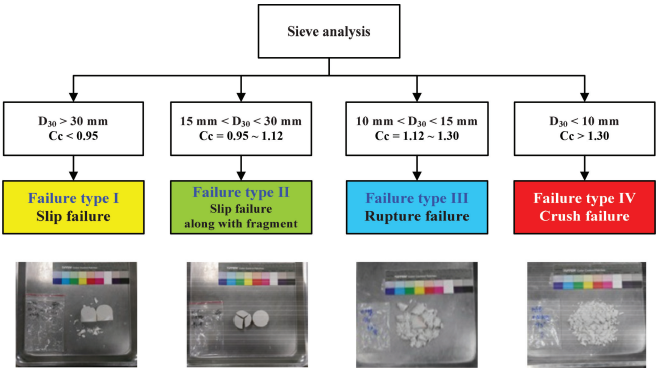


Figure 3. Processing of the classification of failure type by sieve analysis, and four failure types were categorized.

## 3 EXPERIMANTAL RESULTS

### 3.1 *Failure types*

The failure types of artificial rock contained a single plane of weakness with various orientation angles and under different loading rates are demonstrated in Table 1, and it can be concluded as follows:

1. In the case of orientation angle 45°, a series of failure types (type I to type IV ) was observed with loading rates increasing from 100 ± 10 GPa/s to 3233 ± 130 GPa/s. Slip and slip alone with fragment failures occurred under lower loading rate conditions (100 ± 10 ~ 303 ± 21 GPa/s); rupture and crush failures occurred when the loading rate higher than 303 GPa/s.
2. In the cases of orientation angle 60°, 75° and 90°, only three failure types (types I, II and IV) were observed and the failure type III (rupture failure) was not found.
3. If the loading rate greater or equal than 1818 ± 222 GPa/s, the main failure types were Types III and IV, and it implied that the failure patterns of the artificial rock samples were controlled by the artificial rock material even though the orientation angle was 45°.

Table 1. Failure types of artificial rock contained a single plane of weakness with various orientation angles and under different loading rates.

| | β | | | |
|---|---|---|---|---|
| Loading rate (GPa/s) | 45° | 60° | 75° | 90° |
| 100 ± 10 | Type I | Type I | Type I | Type 0* |
| 120 ± 8 | Type I | Type I | Type I | Type II |
| 242 ± 61 | Type I | Type II | Type II | Type II |
| 303 ± 21 | Type II | Type II | Type II | Type II |
| 1818 ± 222 | Type III | Type IV | Type IV | Type IV |
| 2061 ± 101 | Type III | Type IV | Type IV | Type IV |
| 2424 ± 254 | Type III | Type IV | Type IV | Type IV |
| 3233 ± 130 | Type IV | Type IV | Type IV | Type IV |

* No slip and no fragment failures occurred.

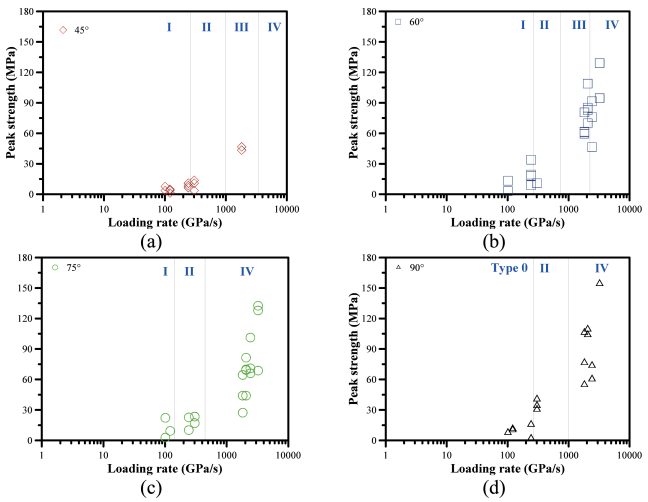


Figure 4. The variations of peak stress under loading rates $10^2$–$10^3$ GPa/s: $\beta$ = (a) 45°, (b) 60°, (c) 75°, (d) 90°.

### 3.2 *Peak strength*

The variations of peak strength of the artificial rock samples with different orientation angles of single plane of weakness are illustrated in Figure 4. For the cases of orientation angles 45°, 60° and 75°, as illustrated in Figures 4(a)(b)(c), the variation tendencies of the peak strength were not significant when the loading rate was less than 400 GPa/s, and the low values of peak strength (≦ 15 MPa) were observed especially in the case of orientation $\beta = 45°$. However, when the loading rate was greater than $10^3$ GPa/s, the peak strength rose obviously with increasing loading rate especially in the cases of orientation angles 60°, 75° and 90°, as illustrated in Figures 4 (b)(c)(d), where the main failure types were types III and IV, and the peak strength values were greater than the uniaxial compressive strength of the intact artificial rock ($\sigma_s = 18.11$ MPa).

## 4 CONCLUSIONS

This study performed SHPB tests on artificial rock contained single plane of weakness with orientation angles 45°, 60°, 75° and 95° at loading rates ranging from $10^2$–$10^3$ GPa/s. The experimental results reveal that the failure types are mainly affected by the orientation angle $\beta$ and the loading rate. Compared to quasi-static loading condition and the corresponding failure modes proposed by Jaeger, the failure types of the artificial rock contained single plane of weakness are deeply influenced by the loading rates and can be categorized into slip, slip and fracture, rupture and crush failures. In addition, the peak strength of the artificial rock contained a discontinuity are contributed mainly by the interface when the loading rates are less than $10^3$ GPa/s, especially in the cases of orientation angles 45°, 60° and 75°. However, the peak strength is provided by the intact material when the loading rates are less than $10^3$ GPa/s.

## REFERENCES


Christensen, R.J., Swanson, S.R. & Brown, W.S. 1972. Split-Hopkinson bar tests on rock under confining pressure. *Experimental Mechanics* 12(11): 508–513.

Davies, E.D.H. & Hunter, S.C. 1963. The dynamic compression testing of solids by the method of the split Hopkinson bar. *Journal of the Mechanics and Physics of Solids* 11: 155–179.

Deere, D.U. & Merritt, A.H. & Coon, R. 1973. Engineering classification of in-situ rock. *International Journal of Rock Mechanics and Mining Sciences* 4(5):177.

Hopkinson, B. 1914. A method of measuring the pressure produced in the detonation of high explosives or by the impact of bullets. *Philosophical Transactions of the Royal Society* A213: 437–452.

Jaeger, J.C. 1960. Shear fracture of anisotropic rocks. *Geological Magazine* 97(1):65–72.

Kolsky, H. 1949. An investigation of the mechanical properties of materials at very high rates of loading. *Proceedings of the Physical Society*, Section B, London: 676–700.

Kummer, A. 1968. The effect of stress rate and temperature of the strength of basalt and granite. *Geophysis* 33(3): 501–510.

Li, H.B. & Zhao. J. 2000. Micromechanical modeling of the mechanical properties of granite under dynamic uniaxial compressive loads. *International Journal of Rock Mechanics and Mining Sciences* 37: 923–935.

Perkins, R.D. & Green, S.J. 1970. Uniaxial stress behavior of porphyritic tonalite at strain rates to 103/second. *International Journal of Rock Mechanics and Mining Sciences* 7: 527–535.

Ross, C.A. & Thompson, P.Y. & Tedesco, J.W. 1989. Split-Hopkinson pressure-bar tests on concrete and mortar in tension and compression. *ACI Materials Journal* 86: 475–481.

Ross, C.A., Tedesco, J.W. & Kuennen, S.T. 1995. Effects of strain rate on concrete strength. *ACI Materials Journal* 92(1): 37–47.

Zhao, J., Li, H.B., Wu, M.B. & Li, T.J. 1999. Dynamic uniaxial compression tests of a granite. *International Journal of Rock Mechanics and Mining Sciences* 36: 273–277.

Zhao, J. & Li, H.B. 2000: Experimental determination of dynamic tensile properties of a granite. *International Journal of Rock Mechanics and Mining Sciences* 37: 861–866.

Zhou, Z., Li, X., Ye, Z. & Liu, K. 2010. Obtaining Constitutive Relationship for Rate-Dependent Rock in SHPB Tests. *Rock Mechanics and Rock Engineering* 43: 697–706.

*Rock Dynamics: From Research to Engineering – Li et al. (Eds)*
*© 2016 Taylor & Francis Group, London, ISBN 978-1-138-02953-8*

# An experimental study of dynamic tensile failure of rocks subjected to hydrostatic confinement

B. Wu & K. Xia
*Department of Civil Engineering and Lassonde Institute, University of Toronto, Ontario, Canada*
*State Key Laboratory of Hydraulic Engineering Simulation and Safety, School of Civil Engineering, Tianjin University, China*

ABSTRACT: To simulate the in situ stress state of underground rocks, a modified Split Hopkinson Pressure Bar (SHPB) system is utilized to load Brazilian Disc (BD) samples hydrostatically, and then exert dynamic load to the sample by impacting the striker on the incident bar. Five groups of Laurentian granite BD samples (with static BD tensile strength of 12.8 MPa) under the hydrostatic confinement of 0 MPa, 5 MPa, 10 MPa, 15 MPa, and 20 MPa were tested under different loading rates. The result shows that the dynamic tensile strength increases with the hydrostatic confinement stress. It is also observed that under the same hydrostatic pre-stress, the dynamic tensile strength increases with the loading rate, revealing the so called material rate dependency. Furthermore, the increment of the tensile strength decreases with the hydrostatic confinement stress, which resembles the behavior of rock static tensile strength under confining pressure as reported in the literature.

## 1 INTRODUCTION

Tensile failure is a main failure mode of rocks in underground rock engineering projects, in which rocks are subjected to dynamic disturbances while under in situ stresses. As well known, pores and microcracks are potential sources of failure for rock materials because of stress concentration (Aadnoy & Angellolsen 1995, Bordia 1971, Zhang et al. 2014). When disturbed by dynamic loads from blasting, seismicity, or rockbursts, the underground rocks would be vulnerable to tensile failure. The discontinuities in the rock result in tensile stress locally around the opening, so the dynamic tensile failure of rocks under pre-tension has been investigated by researchers (Wu et al. 2015, Zhou et al. 2014). However, the far field rocks under hydrostatic pressure can also fail in tension under dynamic loads. Therefore, it is the purpose of this paper to investigate the dynamic tensile failure of rock materials under hydrostatic pressure state.

Over the past few years, significant progress has been made in the characterization of rock failure under high loading rates (Chen et al. 2009, Dai et al. 2010, Dai et al. 2013, Huang et al. 2010, Wu et al. 2014, Xia et al. 2008). Under superposed dynamic loads with the static tectonic stress, the rock behaves differently as compared to the material subjected solely to either static stress or impact loading. Christen et al. (1972) and Lindholm et al. (1974) conducted dynamic compressive tests on rock material under confining pressures, the result shows that all test rock samples exhibited an increase in compressive strength with the increase of the confining pressure and the loading rate. Zhou et al. (2014) and Wu et al. (2015) conducted impact tests on rock materials under static pre-tension. They concluded that the dynamic tensile strength of rock materials decreases with the increase of the static pre-tension. Jaeger & Hoskins (1966) studied static tensile failure of confined rocks, which also presents an increase in strength with the confining pressure. However, comprehensive study is needed to examine the dynamic tensile failure of hydrostatically confined rocks, which is objective of the current work.

In this paper, the Brazilian Disc (BD) sample is adopted for the measurement of dynamic tensile strength of rock materials under hydrostatic confinement, which is applied through a hydraulic press. The dynamic loading is exerted using a low speed gas gun, as in a conventional

SHPB system. After the experiments, the samples are recovered to visualize the failure patterns and distribution of cracks.

## 2 SAMPLE PREPARATION AND TESTING METHODOLOGY

### 2.1 *Specimen preparation*

The rock samples are made from Laurentian Granite (LG) taken from the Laurentian region of Grenville province of the Precambrian Canadian Shield, north of St. Lawrence and northwest of Quebec City, Canada. The mineral grain size of LG varies from 0.2 to 2 mm with the average quartz grain size of 0.5 mm, and the average feldspar grain size of 0.4 mm, with feldspar being the dominant mineral followed by quartz and biotite. The physical and mechanical properties of LG are summarized in Table 1 (Iqbal & Mohanty 2006).

Rock cores with a nominal diameter of 40 mm were drilled from the same block. Special care was taken to prepare the Brazilian disc specimens with a thickness of 16 mm. All specimens were polished to have a surface roughness of less than 0.5% of the sample thickness, as required in the ISRM suggested method.

### 2.2 *Experimental apparatus*

The experimental apparatus is the modified Split Hopkinson Pressure Bar (SHPB) system, which includes three bars (a striker bar, an incident bar, and a transmitted bar) (Zhou et al, 2012) and a hydraulic system (Fig. 1). The elastic bars are made of high strength maraging steel with density of 8100 kg/m$^3$, Young's modulus of 200 GPa and P-wave velocity of 5107 m/s. The length of the incident bar, the transmitted bar and the striker is about 1800 mm long, 1500 mm, and 200 mm, respectively. The hydraulic system is mainly composed of a cylinder that applies lateral confinement to the rock samples (Cylinder 1), and a pressure chamber that provides axial preload (Cylinder 2) to the bars and sample. The hydraulic system is similar to that innovated by Frew et al. (2010), who developed a modified SHPB system for dynamic tests under confinement. However, in the current design, the bars are connected near the other end of the incident bar through a flange (Fig. 1).

As shown in Figure 1, the two cylinders are connected to the same hydraulic press by separate valves. When the two valves are open at the same time, both the lateral confining stress on the sample and the stress on the transmitted bar are equal to the oil pressure $\sigma_0$. Since the transmitted bar is force balanced, the force on the transmitted bar at the sample end equals that at the pump end. Hence the sample is in hydrostatic stress state when the two valves are both open at the same time. It can be shown in the similar way that for a sample with arbitrary shape, as long as it is symmetric with respect to the loading axis, the sample is under hydrostatic confinement if the pressure in both cylinders is identical.

Table 1. Summary of physical and mechanical properties of Laurentian Granite.

| Density g/cm$^3$ | Porosity % | Young's modulus GPa | Poisson's ratio | Brazilian tensile strength MPa | UCS MPa |
|---|---|---|---|---|---|
| 2.63 | 0.64 | 92 | 0.21 | 12.8 | 259 |

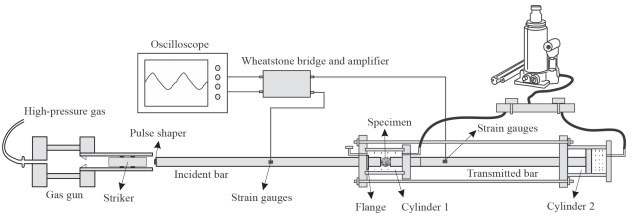


Figure 1. Schematics of the modified SHPB system with the Brazilian disc specimen.

## 3 TESTING RESULTS

### 3.1 *Data reduction*

When the desired hydrostatic stress is achieved, dynamic loading is applied from the impact of the striker bar on the free end of the incident bar. The incident pulse propagates along the incident bar before it hits the sample, leading to a reflected stress wave and a transmitted stress wave that are recorded by the strain gauges attached on the incident and transmitted bar surfaces. The motion induced by the incident wave is to the right and thus the flange has no effect on the wave propagation. The strains of incident wave, reflected wave and transmitted wave are denoted by $\varepsilon_i$, $\varepsilon_r$ and $\varepsilon_t$, respectively.

Based on the one dimensional stress wave theory, and assuming stress equilibrium during loading (Zhou et al., 2012) (i.e. $\varepsilon_i + \varepsilon_r = \varepsilon_t$), the history of the force on the two ends of the sample is:

$$P_1(t) = P_2(t) \tag{1}$$

where $P_1(t)$ = dynamic force at the incident bar end, and $P_2(t)$ = dynamic force on the transmitted bar after the impact. The tensile stress history at the center of the disc sample can be determined as:

$$\sigma(t) = \frac{2A_bE_b\varepsilon_t(t)}{\pi BD} \tag{2}$$

where $E_b$ = Young's Modulus of the bars, $A_b$ = cross-sectional area of the bars; $B$ = thickness of the sample, and $D$ = diameter of the sample. The tensile strength is the maximum value of the tensile stress when the confined rock sample is damaged. There is an approximately linear region in $\sigma(t)$, and its slope is taken as the loading rate.

### 3.2 *Effects of loading rate and hydrostatic confinement*

The pulse shaper technique is applied to facilitate the force balance in the specimen during the experiments, which has been discussed by Frew et al. (2002) in details for SHPB tests on brittle materials. We use the combined shaper method by putting a rubber disc in front of the copper or aluminum disc, to shape the incident wave from the rectangular shape to a sinusoidal wave, and to reduce the rising slope of the incident pulse.

Existing studies (Dai et al. 2010, Zhou et al. 2012) have demonstrated that BD tests are valid when the stress equilibrium condition is satisfied. In this paper, five groups of samples are tested under the hydrostatic confinements of 0 MPa, 5 MPa, 10 MPa, 15 MPa, and 20 MPa. Figure 2a illustrates the correlation between tensile strength and the loading rate when the rock samples are under 10 MPa hydrostatic stress. It can be observed that the tensile strength increases with the loading rate almost linearly, revealing the phenomenon of rate dependency that is common for engineering materials, such as rock (Zhang & Zhao 2013) and concrete (Cusatis 2011, Fujikake et al. 2006).

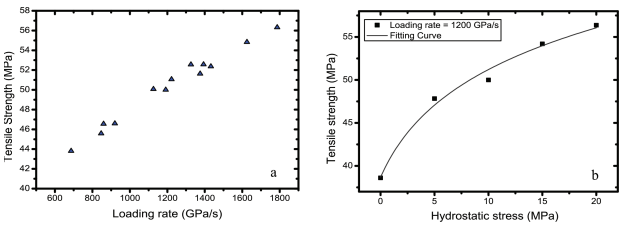


Figure 2. a) Dynamic tensile strength versus loading rate under 10 MPa hydrostatic confinement; b) Dynamic tensile strength versus hydrostatic confinement under 1200 GPa/s loading rate.

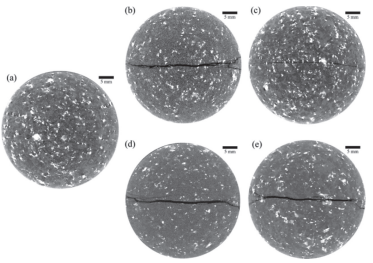


Figure 3. Recovered samples under different loading rates and hydrostatic confinement: a) intact rock sample, b) hydrostatic confinement 10 MPa, loading rate 700 GPa/s, c) hydrostatic confinement 20 MPa, loading rate 700 GPa/s, d) hydrostatic confinement 10 MPa, loading rate 1400 GPa/s, and e) hydrostatic confinement 20 MPa, loading rate 1400 GPa/s.

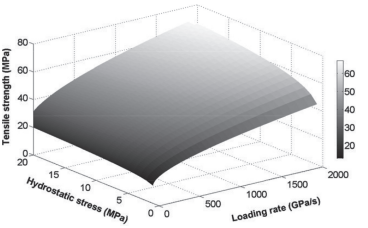


Figure 4. The 3D plot of dynamic tensile strength with loading rate and hydrostatic confinement.

Besides the rate dependency mentioned above in Figure 2a, the correlation between dynamic tensile strength and hydrostatic confinement is illustrated in Figure 2b, which shows the testing results under the same loading rate of 1200 GPa/s. What can be seen from Figure 2b is that the dynamic tensile strength of the rock increases with the increasing hydrostatic confinement; however, the strength increment decreases with the confinement, which means it is harder to further increase the dynamic tensile strength. For example, when the confinement is 0 MPa, the dynamic tensile strength of the sample is 38.60 MPa; when the hydrostatic stress is 10 MPa, the dynamic tensile strength increases to 50 MPa, which is 11.4 MPa higher than the one without confinement. However, the dynamic tensile strength of the one under 20 MPa hydrostatic confinement is 56.37 MPa, which is only 6.37 MPa higher than the former. This decrease of the increment is also observed for rocks tested statically and dynamically under confinement in the literature (Jaeger & Hoskins 1966, Lindholm et al., 1974).

According to the testing results, we propose that the stress of the tested rock samples at failure is logarithmic related to the hydrostatic confinement. Using this algorithm, the testing results are fitted by the curve as shown in red, and the fitted equation is:

$$S = 29.4 + 8.5 \ln\left(\frac{P}{P_0} + 2.98\right) \tag{3}$$

where $S$ = dynamic tensile strength, $P$ = hydrostatic pressure, $P_0$ (1 MPa) = reference hydrostatic confinement. It is obvious that the fitted curve can represent the correlation between the dynamic tensile strength and hydrostatic confinement well.

Figure 3 shows some recovered samples with different hydrostatic confinement and loading rate to study the failure pattern of the BD samples under such loading conditions. Sample BD15-10 in Figure 3a is an intact sample for comparison, Figure 3b and c are the samples under the loading rate of 700 GPa/s, while Figure 3d and e are the samples under the loading rate of 1400 GPa/s. Figure 3b and d are subjected to the same hydrostatic confinement of 10 MPa, while Figure 3c and e are subjected to the sample hydrostatic confinement of 20 MPa. The dynamic tensile strength of the samples shown in Figure 3b, c, d and e are 43.81 MPa, 48.22 MPa, 51.63 MPa and 59.74 MPa, respectively. From the comparison among the recov-

ered samples, it is obvious that the fracture is always tensile in the loaded diametral plane, regardless of the levels of the confinement and the loading rate. The fracture is more obvious when the rocks are under 10 MPa confinement (Figs. 3b, d) than the samples under 20 MPa confinement (Figs. 3c, e). The reason is that the higher confinement restrains the opening of the cracks more effectively, leading to the narrower fracture in samples. In addition, the samples subjected to 1400 GPa/s (Figs. 3d, e) seem damaged more severely than those subjected to 700 GPa/s (Figs. 3b, c), revealing the rate dependence because higher loading rate means less time for the propagation and coalescence of microcracks before failure, thus more microcracks are involved in the failure process, leading to higher apparent strength of the rock samples.

## 4 INTERPRETATION AND DISCUSSION

Based on the correlation between the tensile strength and the loading rate and hydrostatic confinement as shown in Figure 2, an empirical equation is proposed to fit the testing results and explain the dynamic tensile behaviour of rocks under hydrostatic confinement:

$$S = S_0\left(1+\alpha\ln\left(1+\frac{P}{P_0}\right)\right)\left(1+\beta\left(\frac{\dot{\sigma}}{\dot{\sigma}_0}\right)^n\right) \tag{4}$$

where $S$ = dynamic tensile strength of the test rock materials, $S_0$ (12.8 MPa) = static BD strength of the rock material. $P$ = hydrostatic confinement, $P_0$(1 MPa) = reference hydrostatic confinement; $\dot{\sigma}$ = loading rate of each impact test, $\dot{\sigma}_0$ (1 GPa/s) = reference loading rate. $\alpha$, $\beta$ and $n$ are fitting parameters.

The physical meaning of the equation is that, when the loading rate is 0 and there is no confinement, the strength of the rock is the static tensile strength S; the dynamic tensile strength of the rock logarithmically increases with the hydrostatic confinement. The data fitting based on Equation (4) and the experimental result leads to the values of the parameters as: $\alpha = 0.1804$, $\beta = 0.0436$, and $n = 0.5257$.

Based on the fitted function, a 3D plot is obtained to show the dynamic tensile strength of rocks with loading rate and hydrostatic confinement, as in Figure 4. It is obvious that the dynamic tensile strength increases with both the hydrostatic stress and the loading rate. It can be also seen from the 3D plot that the increment of the dynamic tensile strength decreases with the loading rate and the hydrostatic stress. This is indicated in Equation (4) since the first derivative of tensile strength with respect to loading rate and hydrostatic stress are both positive, while the second derivative of the tensile strength with respect to loading rate and hydrostatic stress are both negative. When the confining pressure reaches a certain value, or at a certain underground depth, the dynamic tensile strength of rock materials would mainly depend on the loading rate, it does not change much as the confinement increases further under the same loading rate.

## 5 CONCLUSIONS

In this work, we propose a modified SHPB testing technique with a Brazilian disc specimen to measure the dynamic tensile strength under different hydrostatic confinement. Five groups of Laurentian granite sample were impacted with different loading rates under the hydrostatic stress of 0 MPa, 5 MPa, 10 MPa, 15 MPa and 20 MPa.

The results show that there is a significant enhancement in tensile strength with the increase of the loading rate, which is the rate dependency for many engineering materials. The dynamic tensile strength increases with the hydrostatic confinement due to the restrain of opening and propagation of microcracks by confinement. Another important finding is that the increment of the tensile strength decreases as the hydrostatic confinement becomes higher, which is the same as the static strength under confining pressure. When the confining pressure reaches a certain value, or at a certain underground depth, the dynamic tensile

strength of rock materials would mainly depend on the loading rate, it does not change much as the confinement increases further under the same loading rate.

## ACKNOWLEDGEMENTS

This work has been supported by the Innovative Research Groups of Natural Science Foundation of China (NSFC) under Grant No. 51321065 and NSFC Grant No. 51479131. K. Xia's research was partially supported by the Natural Sciences and Engineering Research Council of Canada (NSERC) through the Discovery Grant No. 72031326.

## REFERENCES

Aadnoy, B.S. & Angellolsen, F. 1995. Some effects of ellipticity on the fracturing and collapse behavior of a borehole. *International Journal of Rock Mechanics and Mining Sciences & Geomechanics Abstracts* 32(6): 621–627.

Bordia, S.K. 1971. Effects of size and stress concentration on dilatancy and fracture of rock. *International Journal of Rock Mechanics and Mining Sciences* 8(6): 629–640.

Chen, R. Xia, K. Dai, F. Lu, F. & Luo, S.N. 2009. Determination of dynamic fracture parameters using a semi-circular bend technique in split Hopkinson pressure bar testing. *Engineering Fracture Mechanics* 76(9): 1268–1276.

Christen, R.J. Swanson, S.R. & Brown, W.S. 1972. Split-Hopkinson-bar tests on rock under confining pressure. *Experimental Mechanics* 12(11): 508–513.

Cusatis, G. 2011. Strain-rate effects on concrete behavior. *International Journal of Impact Engineering* 38(4): 162–170.

Dai, F. Huang, S. Xia, K. & Tan, Z. 2010. Some fundamental issues in dynamic compression and tension tests of rocks using split Hopkinson pressure bar. *Rock Mechanics and Rock Engineering* 43(6): 657–666.

Dai, F. Xia, K. Zuo, J.P. Zhang, R. & Xu, N.W. 2013. Static and dynamic flexural strength anisotropy of Barre granite. *Rock Mechanics and Rock Engineering* 46(6): 1589–1602.

Frew, D.J. Akers, S.A. Chen, W. & Green, M.L. 2010. Development of a dynamic triaxial Kolsky bar. *Measurement Science & Technology* 21(10): 105704(10).

Fujikake, K. Senga, T. Ueda, N. Ohno, T. & Katagiri, M. 2006. Effects of strain rate on tensile behavior of reactive powder concrete. *Journal of Advanced Concrete Technology* 4(1): 79–84.

Huang, S. Chen, R. & Xia, K. 2010. Quantification of dynamic tensile parameters of rocks using a modified Kolsky tension bar apparatus. *Journal of Rock Mechanics and Geotechnical Engineering* 2(2): 162–168.

Iqbal, N. & Mohanty, B. 2006. Experimental calibration of stress intensity factors of the ISRM suggested cracked chevron-notched Brazilian disc specimen used for determination of mode-I fracture toughness. *International Journal of Rock Mechanics and Mining Sciences* 43(8): 1270–1276.

Jaeger, J.C. & Hoskins, E.R. 1966. Rock failure under confined Brazilian test. *Journal of Geophysical Research* 71(10): 2651–2659.

Lindholm, U.S. Yeakley, L.M. & Nagy, A. 1974. Dynamic strength and fracture properties of Dresser basalt. *International Journal of Rock Mechanics and Mining Sciences* 11(5): 181–191.

Wu, B. Chen, R. & Xia, K. 2015. Dynamic tensile failure of rocks under static pre-tension. *International Journal of Rock Mechanics and Mining Sciences* 80: 12–18.

Wu, B. Kanopoulos, P. Luo, X. & Xia, K. 2014. An experimental method to quantify the impact fatigue behavior of rocks. *Measurement Science & Technology* 25(7).

Xia, K. Nasseri, M.H.B. Mohanty, B. Lu, F. Chen, R. & Luo, S.N. 2008. Effects of microstructures on dynamic compression of Barre granite. *International Journal of Rock Mechanics and Mining Sciences* 45(6): 879–887.

Zhang, M.W. Shimada, H. Sasaoka, T. Matsui, K. & Dou, L.M. 2014. Evolution and effect of the stress concentration and rock failure in the deep multi-seam coal mining. *Environmental Earth Sciences* 72(3): 629–643.

Zhang, Q.B. & Zhao, J. 2013. A review of dynamic experimental techniques and mechanical behavior of rock materials. *Rock Mechanics and Rock Engineering* 47(4): 1411–1478.

Zhou, Y.X. Xia, K. Li, X.B. Li, H.B. Ma, G.W. Zhao, J. Zhou, Z.L. & Dai, F. 2012. Suggested methods for determining the dynamic strength parameters and mode-I fracture toughness of rock materials. *International Journal of Rock Mechanics and Mining Sciences* 49(2012): 105–112.

Zhou, Z. Li, X. Zou, Y. Jiang, Y. & Li, G. 2014. Dynamic Brazilian tests of granite under coupled static and dynamic loads. *Rock Mechanics and Rock Engineering* 47(2): 495–505.

*Rock Dynamics: From Research to Engineering – Li et al. (Eds)*
*© 2016 Taylor & Francis Group, London, ISBN 978-1-138-02953-8*

# Dynamically induced gouge degradation and implications for fault instability

W. Wu
*Institute of Rock and Soil Mechanics, Chinese Academy of Science, Wuhan, China*
*Stanford University, Stanford, USA*

ABSTRACT: When a gouge-filled rock discontinuity is subjected to dynamic perturbations, the intrinsic and extrinsic factors, such as gouge properties and loading environments, make its dynamic response extremely complex. Under various loading/unloading conditions, such as stress wave incidence and normal stress unloading, stress drop is a common phenomenon that can be observed with other features in experimental, numerical, and field works. When gouge contacts are approaching to a critical stress state for the shear failure, gouge damage and contact detachment occur accompanied by stress drop and energy relaxation. The stress drop associated with gouge degradation could be a reliable feature to make induced geological hazards interpretable and predictable. It also shows that the reduction of normal and shear stresses is a reasonable explanation of fault instability induced by nearby tunnel excavation.

## 1 INTRODUCTION

Gouge materials, formed through geological processes in the earth's crust, may exist in all scales of rock discontinuities. The heterogeneous materials strongly affect the mechanical response of rock discontinuities. For instance, the dynamic response of such discontinuities depends on gouge thickness (Wu et al. 2013a, c, Li et al. 2013), gouge composition (Wu et al. 2014a, 2015), water content (Wu & Zhao 2015, Ikari et al. 2007), rock mass structure (Zhu et al. 2012, Wu et al. 2013a, b), as well as external perturbations (Wu et al. 2012, Marone 1998). These factors, including gouge properties and loading conditions, make the dynamic response extremely complex. In recent years, the dynamically-induced frictional slip on gouge-filled discontinuities has received considerable interest, because it is associated with the mechanism of induced earthquakes. For example, the nonlinear response of gouge materials is responsible for triggered slow slip on earthquake faults (Johnson et al. 2012). However, our understanding on the dynamic case remains considerably inadequate. It is important to access reliable features in the slip process to make induced geological hazards interpretable and predictable.

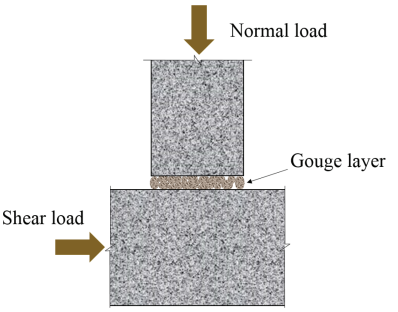


Figure 1. Schematic diagram of a rock discontinuity filled with a layer of granular gouges subjected to external normal and shear loads.

In previous studies, a direct-shear model was developed to simulate a rock discontinuity filled with a layer of granular gouges subjected to a normal load and a shear load (Fig. 1). A dynamic loading system was applied to generate an incident P-wave as a shear load to dynamically induce the frictional slip on the gouge layer (Wu & Zhao 2014). An unloading system was used to reduce a normal load applied on the gouge layer to simulate the slip process during nearby underground excavation (Wu et al. 2014b). This study reexamined the experimental results and discussed stress drop associated with gouge degradation as a common feature to interpret induced geological hazards. The common feature was reliable to reflect the dynamic response of rock discontinuities under various intrinsic and extrinsic conditions. An example of fault instability induced by nearby tunnel excavation was interpreted by considering stress drop and gouge degradation.

## 2 WAVE-INDUCED GOUGE DEGRADATION

When an incident wave acted as a shear load to induce the frictional slip on a rock discontinuity filled with granular gouges, the discontinuity exhibited continuous motion. The incident wave accelerated the slip process along the loading direction, whereas the reflected wave from boundaries decelerated this process. The granular gouges in the complex process were subjected to late-arriving waves along the loading direction and reflected waves along the opposite direction. In order to understand the wave-induced gouge degradation, this study used the dynamic-induced direct-shear model to isolate the slip process induced by the first cycle of an incident wave and to rule out late-arriving and reflected waves for simplifying this process (Wu 2015).

Figure 2(a) shows the P-wave during the first incidence, which is divided into three stages, an incident stage (Stage I), a slip stage (Stage II), and a reflected stage (Stage III). The duration of each stage was 150 μs. The incident wave had a velocity of 5000 m/s, a frequency of 3.3 kHz, and a half-wavelength of 0.75 m. In the incident stage, an impact event between rock plates generated an incident P-wave traveling down to the gouge layer. The loading system restricted a second impact to avoid late-arriving waves. The slip stage was designed to observe the slip process solely induced by the incident wave, because no wave propagated along the gouge layer in this stage. In the reflected stage, the P-wave that was reflected back from the plate end reached the gouge layer after the slip process.

The relation between shear stress and slip displacement during the incident and slip stages is shown in Figure 2(b). The incident wave initially induced a sheared granular network consisting of force chains to support increasing shear stress (Majmudar & Behringer 2005). And then, the shear stress started to steadily increase with strong oscillation (gouge rearrangement), and reached the maximum value near the end of this stage. The slip process occurred when the shear stress was the maximum value, and was accompanied by the reduction of shear stress in the slip stage. A forward slip path and a backward slip path can be observed in this stage, which indicated the separation of gouge contacts along the discontinuity and

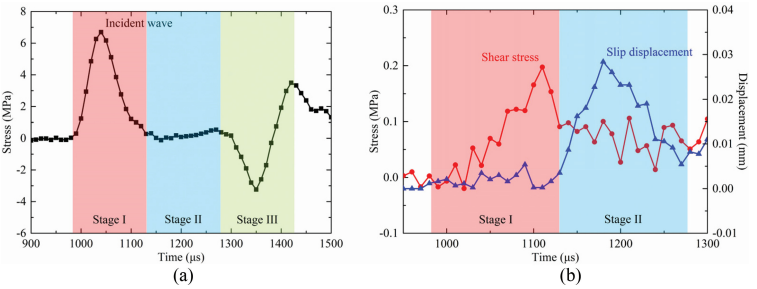


Figure 2. Wave-induced frictional slip on a gouge layer, (a) an incident P-wave in three stages: the incident stage (Stage I), the slip stage (Slip II), and the reflected stage (Stage III), (b) shear stress drops when the slip displacement increases.

the formation of new contacts after the maximum slip displacement, respectively. A net balance between two slip paths was the real slip displacement. As expected, the maximum slip displacement appeared before the reflected stage, so the slip process was solely induced by the incident wave. It can be observed that the periods of shear stress increase and slip process were related to the loading duration of an incident wave.

The gouge degradation was associated with the reduction of shear stress. According to the dynamic fracture mechanics (Freund 1990), when the strain energy being released in the gouge layer exceeded the fracture energy of gouge materials, gouge contacts were damaged accompanied by stress reduction and slip process. Broken gouges can form new contacts to arrest the slip, when the released strain energy decreased below the fracture energy.

## 3 EXCAVATION-INDUCED GOUGE DEGRADATION

Underground excavation can reduce tectonic stresses applied to adjacent rock masses and perturb the stress equilibrium of rock discontinuities, which may lead to rock collapse and induced seismicity. The shear failure of a rock discontinuity was commonly considered through the increase of shear stress. However, the decrease of normal stress induced by nearby underground excavation may also cause the shear failure. For a rock discontinuity filled with granular gouges, the response of gouge materials to external stresses was one of the major factors in controlling the shear resistance of the discontinuity. To investigate the excavation-induced gouge degradation, this study used the unload-induced direct-shear model to evaluate the slip process of a gouge layer subjected to a constant shear stress and a decreasing normal stress (Wu et al. 2014).

Figure 3(a) shows that a normal stress of 4 MPa and a shear stress of 0.75 MPa are first applied to simulate the frictional equilibrium of the gouge layer. During the test, it was proposed that the shear stress kept constant, and the normal stress decreased at a constant unloading rate of 0.46 MPa/s until the slip process occurred. This study simplified the reduction of tectonic stress in adjacent rock masses and considered the decrease of normal stress to induce the slip processes.

The measured normal and shear stresses drop when the slip process occurs, as shown in Figure 3(b). First, the shear stress started to slightly decrease a few seconds before the slip process. The unloading rate of the normal stress in the pre-slip period also slightly exceeded the proposed unloading rate. The reduction of both stresses in this period indicated that gouge contacts were approaching to a critical stress state for the shear failure. And then, both normal and shear stresses sharply dropped about 50% in the first slip period, when the shear failure occurred. The shear stress drop was equal to the normal stress drop multiplied by the coefficient of maximum static friction. The coefficient of friction was less than 1, so the shear stress drop was always smaller than the normal stress drop. This figure also shows that the slip displacement dramatically increases with the stress drop. The larger amount of stress drop in

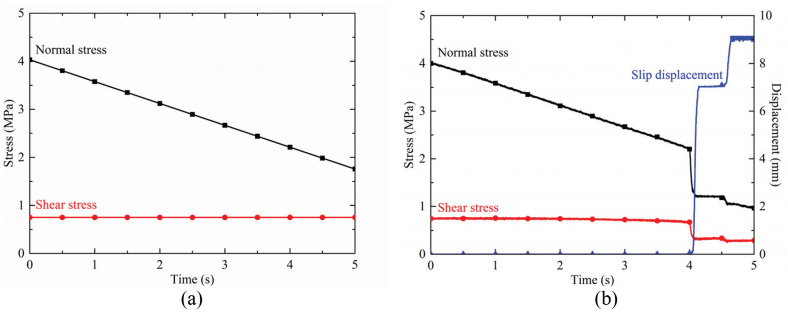


Figure 3. Excavation-induced frictional slip on a gouge layer, (a) proposed decreasing normal stress and constant shear stress applied on the gouge layer, (b) both normal and shear stresses drop when the slip process occurs.

the first slip event was accompanied by a greater increase of slip displacement, indicating that the slip process mainly consumed the strain energy released from the gouge layer.

The stress drops in the normal and shear directions were due to the damage of gouge contacts. According to the energy budget, the fracture energy reduced with decreasing normal stress. When the fracture energy decreased below the strain energy being released in the gouge layer, the slip process occurred accompanied by the damage of gouge contacts. Hence, the stress drop in this process also indicated the degradation of gouge materials.

## 4 DISCUSSION AND IMPLICATIONS

Owing to the limitation of testing techniques, most of experimental studies indirectly investigate gouge degradation based on observable factors, such as, particle size reduction, energy consumption, stress drop, as well as shear modulus decrease. The slip-induced comminution reduces the size of large gouge particles, and the particle size distribution becomes narrower (Gu & Wong 1994). The dynamic stress drives the shear modulus reduction of a gouge layer, but the modulus can recover because of frictional healing (Johnson & Jia 2013). Among these factors for evaluating gouge degradation in a slip process, stress drop is a macroscopic phenomenon that can be commonly observed with other factors and easily monitored by conventional testing techniques. This phenomenon is attributed to energy consumption, which creates new surface area through particle breakage (Wilson et al. 2004, Fulton & Rathbun 2011). Hence, the stress drop induced by stress wave incidence and normal stress unloading, as shown in above, can be related to gouge degradation.

Although there is lack of direct evidence on gouge degradation in a slip process, many numerical works have interpreted gouge degradation in a slip process. The gouge particles in this process behave rolling with surface erosion along rock wall under a low normal stress and severe breakage into pieces under a high normal stress (Zhao 2013). The number of weak contacts reduces with decreasing elastic modulus, indicating the frictional weakening of a gouge layer and the breakage of gouge particles at weak points (Ferdowsi et al. 2015). The numerical results are consistent with experimental observations, and reveal the underlying process of gouge degradation from microscopic to macroscopic scales.

During underground excavation, stress drop can be observed prior to the instability of rock discontinuities. A UDEC model examined the wave-induced stress drop along a rock discontinuity next to an excavated tunnel during the construction of the Gottard Base Tunnel, Switzerland (Hagedorn & Stadelmann 2009). As shown in Figure 4, a rock discontinuity between intact rock and jointed rock was located close to the tunnel EON. When a P-wave from the right side was approaching the discontinuity, a stress drop of 17 MPa was obtained near the tunnel. The stress drop may be attributed to the failure of fracture asperities and the degradation of gouge materials. Afterwards, the shear stress recovered to 14.5 MPa. The residual shear stress was due to the reformation of gouge and asperity contacts along the discontinuity. The recovery process can be strengthened depending on gouge mineralogy, tectonic stress, and interseismic duration (Marone 1998).

The stress drop associated with gouge degradation can be also used to interpret fault activation during tunnel excavation. During the excavation of the multi-function section Faido, which is the southernmost access point of the Gotthard Base Tunnel, more than 100 earthquakes were recorded and caused severe damage in the tunnel. A seismological study suggested that the same fault segment was ruptured repeatedly owing to the excavation work (Husen et al. 2013), as shown in Figure 5. This study also proposed that the horizontal stress applied on the fault decreased due to the shrinking of rock masses after the excavation, and the vertical stress increased due to stress transfer by the excavation work. The vertical stress may be increased by storing the seismic energy from drill and blast in the fault zone. Nevertheless, the stress drop associated with gouge degradation could be a more reasonable explanation. When the fault was approaching to a critical slip state during the excavation, the failure of gouge materials lost the ability to support external stresses and released stored strain energy. Both normal and shear stresses applied on the fault were thus dramatically

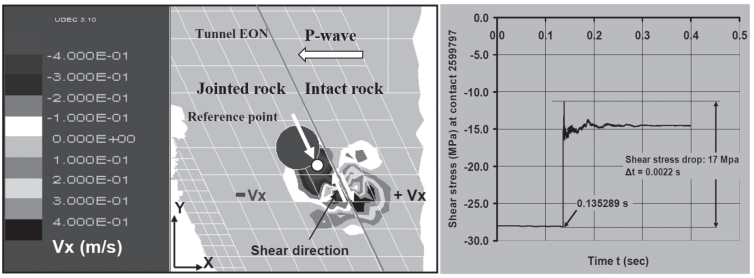


(a) (b)

Figure 4. Numerical simulation of wave-induced stress drop along a rock discontinuity between intact rock and jointed rock (after Hagedorn & Stadelmann 2009), (a) the particle velocity along the x direction near the discontinuity close to an excavated tunnel, (b) the time history of shear stress at a certain contact along the discontinuity.

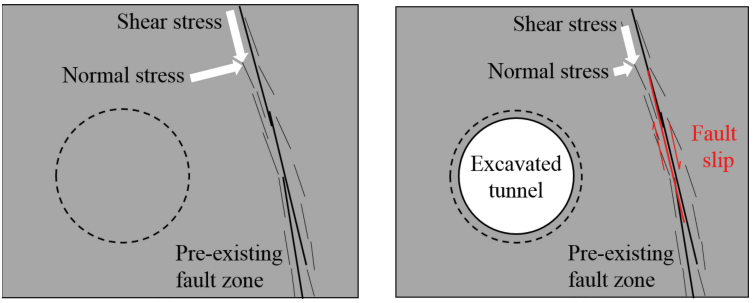


(a) (b)

Figure 5. Fault slip induced by the excavation of the Gotthard Base Tunnel, Switzerland (modified from Husen et al. 2013), (a) the frictional equilibrium of a pre-existing fault zone subjected to normal and shear stresses before the excavation, (b) the frictional slip of the fault zone during the excavation and the reduced normal and shear stresses applied on the fault.

reduced during this process, and the normal stress reduction was larger than the shear stress reduction. The released strain energy could be the primary reason for driving the fault slip.

## 5 CONCLUSIONS

The response of gouge materials is a major factor in controlling the shear resistance of gouge-filled rock discontinuities subjected to various external loads, such as stress wave incidence and normal stress unloading. Many measurable features can reflect the response, and stress drop is a phenomenon that can be commonly observed with other factors and easily monitored by conventional techniques. When gouge contacts are approaching to a critical stress state for the shear failure, gouge damage and contact detachment occur accompanied by stress drop and energy relaxation. The stress drop associated with gouge degradation could be a reliable feature to make induced geological hazards interpretable and predictable. An example of fault instability can be reasonably interpreted based on the reduction of normal and shear stresses.

## ACKNOWLEDGEMENT

This work was sponsored by the Open Research Fund of State Key Laboratory of Geomechanics and Geotechnical Engineering, Institute of Rock and Soil Mechanics, Chinese Academy of Sciences (Grant No. Z013001) and by the Swiss National Science Foundation (Grant No. P2ELP2_151931).

## REFERENCES


Ferdowsi, B., Griffa, M., Guyer, R.A., Johnson, P.A., Marone, C. & Carmeliet, J. 2015. Acoustically induced slip in sheared granular layers: application to dynamic earthquake triggering. *Geophys. Res. Lett.* 42:9750–9757.

Freund, L.B. 1990. *Dynamic fracture mechanics*. Cambridge: Cambridge University Press.

Fulton, P.M. & Rathbun, A.P. 2011. Experimental constraints on energy partitioning during stick-slip and stable sliding within analog fault gouge. *Earth Plan. Sci. Lett.* 308:185–192.

Gu, Y. & Wong, T.F. 1994. Development of shear localization in simulated quartz gouge: effect of cumulative slip and gouge particle size. *Pure Appl. Geophys.* 143:387–423.

Hagedorn, H. & Stadelmann, R. 2009. Gotthard Base Tunnel: UDEC simulations of micro tremors encountered during construction. *Prof. 9th Int. Conf. Analysis of Discontinuous Deformation* 1:373–380.

Husen, S., Kissling, E. & Deschwanden, A.V. 2013. Induced seismicity during the construction of the Gotthard Base Tunnel, Switzerland: hypocenter locations and source dimensions. *J. Seismol.* 17:63–81.

Ikari, M.J., Saffer, D.M. & Marone, C. The effect of hydration state on the frictional properties of montmorilloite-based fault gouge. *J. Geophys. Res.* 112:B06423.

Johnson, P.A. & Jia, X. 2005. Nonlinear dynamics, granular media and dynamic earthquake triggering. *Nature* 437:871–874.

Johnson, P.A., Carpenter, B., Knuth, M., Kaproth, B.M., Le Bas, P.Y., Daub, E.G. & Marone, C. 2012. Nonlinear dynamical triggering of slow slip on simulated earthquake faults with implications to Earth. *J. Geophys. Res.* 117:B04310.

Li, J.C., Wu, W., Li, H.B., Zhu, J.B. & Zhao, J. 2013. A thin-layer interface model for wave propagation through filled rock joints. *J. Appl. Geophys*. 91:31–38.

Majmudar, T.S. & Behringer, R.P. 2005. Contact force measurements and stress-induced anisotropy in granular materials. *Nature* 435:1079–1082.

Marone, C. 1998. The effect of loading rate on static friction and the rate of fault healing during the earthquake cycles. *Nature* 391:69–72.

Wilson, B., Dewers, T., Reches, Z. & Brune, J. 2005. Particle size and energetics of gouge from earthquake rupture zones. *Nature* 434:749–752.

Wu, W., Li, J.C. & Zhao, J. 2012. Loading rate dependency of dynamic responses of rock joints at low loading rate. *Rock Mech. Rock Eng.* 45:421–426.

Wu, W., Li, J.C. & Zhao, J. 2013a. Seismic response of adjacent parallel rock filled fractures with dissimilar properties. *J. Appl. Geophys.* 96:33–37.

Wu, W., Zhu, J.B. & Zhao, J. 2013b. A further study on seismic response of a set of parallel rock fractures filled with viscoelastic materials. *Geophys. J. Int.* 192:671–675.

Wu, W., Zhu, J.B. & Zhao, J. 2013c. Dynamic response of a rock fracture filled with viscoelastic materials. *Eng. Geol.* 160:1–7.

Wu, W. & Zhao, J. 2014. A dynamic-induced direct-shear model for dynamic triggering of frictional slip on simulated granular gouges. *Exper. Mech.* 54:605–613.

Wu, W., Li, J.C. & Zhao, J. 2014a. Role of filling materials in a P-wave interaction with a rock fracture. *Eng. Geol.* 172:77–84.

Wu, W., Zou, Y., Li, X. & Zhao, J. 2014b. An unload-induced direct-shear model for granular gouge friction in rock discontinuities. *Rev. Sci. Instrum.* 85:093902.

Wu, W. 2015. Slip initiation of granular gouge friction in a rock discontinuity induced by static and dynamic loads. *Int. J. Rock Mech. Min. Sci.* 80:196–201.

Wu, W., Li H.B. & Zhao, J. 2015. Dynamic responses of non-welded and welded rock fractures and implication to wave attenuation across rock masses. *Int. J. Rock Mech. Min. Sci.* 77:174–181.

Wu, W. & Zhao, J. 2015. Effect of water content on P-wave attenuation in a rock fracture filled with granular materials. *Rock Mech. Rock Eng.* 48:867–871.

Zhao, Z.H. 2013. Gouge particle evolution in a rock fracture under shear: a microscopic DEM study. *Rock Mech. Rock Eng.* 46:1461–1479.

Zhu, J.B., Zhao, X.B., Wu, W. & Zhao, J. 2012. Wave propagation across rock joints filled with viscoelastic medium using modified recursive method. *J. Appl. Geophys.* 86:82–87.

*Rock Dynamics: From Research to Engineering – Li et al. (Eds)*
*© 2016 Taylor & Francis Group, London, ISBN 978-1-138-02953-8*

# Measurement of dynamic surface sliding of cement joint by Hopkinson bundle bars

S.L. Xu, C.Y. Shi, L. Zhang & L.J. Zhou
*CAS Key Laboratory of Mechanical Behavior and Design of Materials, University of Science and Technology of China, Hefei, China*

ABSTRACT: Hopkinson bundle bars device is developed on the Split Hopkinson Pressure Bar (SHPB) system to investigate the dynamic slip characteristics of cement joint under compression-shear combined loading. The experimental configuration of one-bar/three-bar incidence and three-bar transmission is employed to measure signals of different locations in specimen, which used to determine the slipping state of joint surfaces. And the overall slipping states of joint surfaces are then obtained. The study is helpful to reveal local slipping and whole slipping state of joint surface.

## 1 INTRODUCTION

Rock is one of the most widely used materials in geotechnical engineering, civil engineering, hydraulic engineering, etc. Natural rocks are complex medium with such defects as cracks and pores at the meso and micro scale, and joints at the macro scale. Quasi-static and dynamic strength properties of rock mass in geotechnical engineering are mainly determined by these complicated meso and macro geometry structures. Rock materials are both load-path dependent and strain-rate dependent. Specific efforts had been made on the improvement of experimental techniques to investigate the compression properties of rock joints.

Previous works focused on the deformation properties, i.e. normal stiffness and tangent stiffness, of rock joint under quasi-static loading. Only a few works presented the dynamic responses of jointed rocks due to complexity of interaction of waves with joint surfaces. The rules of interaction of stress waves with joint surfaces were preliminarily discussed. Wu et al. (2012) had used a granite-bar system to investigate compression properties of granite joint filled with sand. Wu et al. (2014) had further used rock plates under lateral pressure to study the dynamic shear behavior. These experimental results provide a basis understanding of the dynamic compression and shear properties of joint surfaces. But local slip and local unevenly distributed deformation of joint cannot be reflected. Xu et al. (2013) had investigated the dynamic sliding of granite-pair with light gas gun.

Based on the work of Albertini et al. (1997), two experimental configurations i.e. one-bar incidence and three-bar transmission, three-bar incidence and three-bar transmission, are employed in the present paper to explore the dynamic compression and shear responses of joint surface, and rule of wave propagation in the process of impact is discussed.

## 2 EXPERIMENTS

### 2.1 *Sample preparation*

Cement mortar was made up as the weight proportioning: water/cement/standard sand = 220 g/500 g/1250 g. The density of cement specimen is 2.14 g/cm$^3$, and material parameters are illustrated in Table 1. Specimens are firstly processed to be cylinders of 37 mm in diameter and 30–40 mm in length, and then sawed into two parts with designed oblique

Table 1. Mechanical parameter of cement.

| | Uniaxial compression | | | | Passive lateral confining | | |
|---|---|---|---|---|---|---|---|
| Strain rate /$s^{-1}$ | 0.001 | 54 | 117 | 157 | 305 | 552 | 1099 |
| Elastic modulus E /GPa | – | 9.8 | 9.8 | 9.8 | 20.5 | 21.5 | 22 |
| Strength Y /MPa | 35 | 61 | 75 | 81 | 57.9 | 63 | 71.4 |

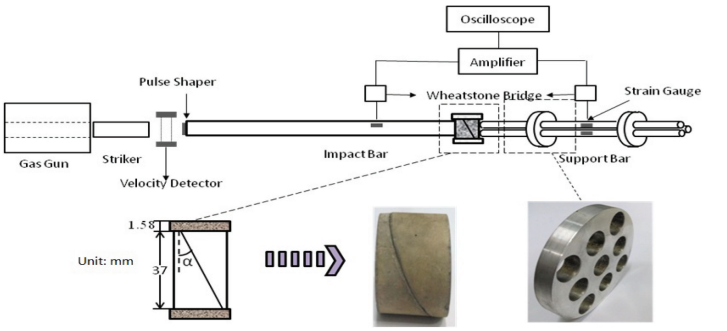


(a) one-bar incidence and three-bar transmission.

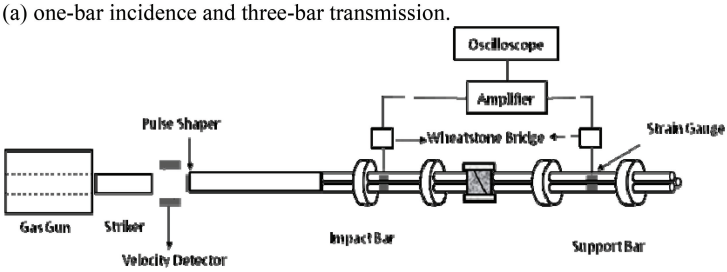


(b) three-bar incidence and three-bar transmission

Figure 1. Experimental setup of SHPB bundle bars testing system.

angles, i.e. 20, 30, and 45 degrees, which illustrates the angle from the impact direction to the normal direction of joint surface. During experiments, these two cutting surfaces are polished by 5# sandpaper, and they are affixed together with Vaseline.

### 2.2 *SHPB bundle bars setup*

SHPB technique had been widely used in the investigation of the strain rate effect of materials. Albertini et al. (1997) had proposed the bundle bars system to eliminate the transversal inertial effects. We develop this bundle bars to measure local deformation of specimens, and it is shown in Figure 1.

Experimental equipment of one-bar incidence and three-bar transmission is shown in Figure 1 (a). In which, an incident aluminum bar with length 1500 mm and diameter 37 mm and three small transmission aluminum bars with length 900 mm and diameter 14.5 mm are employed. These three small bars are positioned by special designed plate with nine holes, which provides nine positions for small bars. The outer sleeve of the specimen with joint surfaces is sheathed with an aluminum sleeve with thickness 1.58 mm and inner diameter 37 mm. Impact speed of striker is 13 m/s.

Experimental equipment of three-bar incidence and three-bar transmission is shown in Figure 1 (b). In which, both three incident aluminum bars and three transmission aluminum bars are with length 900 mm and diameter 14.5 mm, and they are positioned by nine-hole plate. All of the small bars are pasted with strain gauge to record the waveforms. The outer

sleeve of the specimen is with thickness 1.58 mm and inner diameter 37 mm. In order to study the characteristics of joint surfaces, the deformation of the specimen is controlled in the elastic range. Therefore, impact speed is controlled within 4 m/s. It merits attention that waves propagating in the incident bars and the transmission bars are in 1-D stress state, but waves propagating in specimens are in 1-D strain state.

### 2.3 *Experiments*

During experiments, the specimen is sandwiched between the incident bar and the transmission bar. The impact of the striker on the incident bar through the pulse shaper generates an elastic incident wave propagating through the incident bar/three small bars. When the incident wave travels to the interface of the incident bar and the specimen, part of the incident wave is reflected as a reflected wave in the incident bar due to the impedance mismatch of the incident bar and the specimen, and the rest is transmitted as a transmission wave in the transmission bar. The specimen is compressed by the transmitted loads. When the stress equilibrium state in the specimen is achieved, the reflection and transmission of stress waves on these inner surfaces could be ignored. Validation of experimental results should be done with the three-wave method.

The principle of dynamic slip of joint surface is shown in Figure 2. When there is no sliding of joint surface, amplitude of incident signal will be fully applied on the joint surface, and amplitudes of both the incident signal and the transmitted signal are the same, which shown in Figure 2 (a) and corresponds to Point A in Figure 2 (c). When the joint surface slides, the incident signal applied on the joint surface should be decomposed along two directions, i.e. along the joint surface and vertical to the joint surface. The joint surface slides due to bearing capacity of shear stress ($\tau_s$) along the direction of joint surface. Therefore, when the incident wave interacts with cement joint, only part of the incident signal is transmitted. As shown in Figure 2 (b), the interaction of the incident wave with the joint surface will generate the normal ($\sigma_n^T$) and tangential ($\sigma_\tau^T$) transmission signals and the normal ($\sigma_n^R$) and tangential ($\sigma_\tau^R$) reflection signals. Since there is no wave impedance changes in normal direction, the reflection signal $\sigma_n^R \to 0$. But the shear component will be partially transmitted and partially reflected, which corresponds to the state analysis, i.e. points A and C, shown in Figure 2 (c). The velocity of right part of joint will increase from zero to $V^T$ (point B), and that of left part of joint will decrease from $V_0$ to $V^R$ (Point C). Therefore, there is the relative slip velocity difference ($V^R$ - $V^T$) between the joint surfaces. The principle is the same as Xu et al. (2013).

In the experiments of light gas gun, processes of wave propagation are recorded. However, the results of SHPB tests reveal multiple reflections of stress waves. The process of gradual equilibrium of the dynamic compression is always developed with that of the tangential shear deformation. The analysis of dynamic compression and shear behavior should be conducted at the same time.

The experiments are carried out on the Φ37 SHPB devices in the Impact dynamic lab of USTC. The incident and reflection waves are measured by strain gauges on the incident bar,

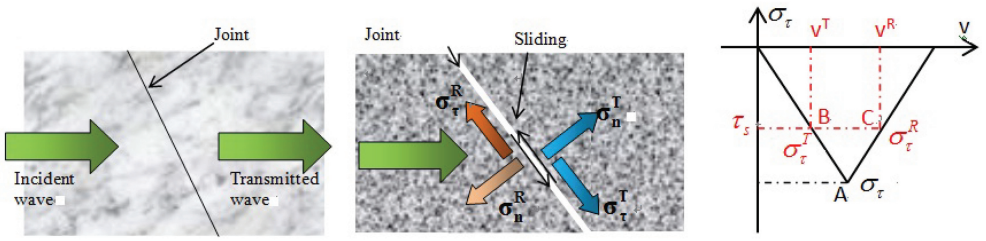


(a)No slipping (b) slipping of joint surface (c) the slipping state

Figure 2. Wave propagating in the slipping state of joint surface.

and the transmitted wave is measured by strain gauges on the transmission bar. These signals are recorded by a high-speed digital oscilloscope, i.e. Tektronix TDS640 A. A systematic error of 5% is preliminarily estimated for the whole measurement system.

## 3 EXPERIMENTAL RESULTS

### 3.1 *One-bar incidence and three-bar transmission*

Figure 3 illustrates recorded waveforms of cement joint with an oblique angle of 45 degrees and under an impact speed of 13 m/s. There are three transmission waves for every experiment, which obtained by three small transmission bars. Their positions are different and their waveforms are measured. In experiments, the right part of joint is destroyed, but the left part of joint remains intact. Therefore, local failure strengths of sample could be evaluated by the right part of joint, and wave structure of compression wave and shear wave could be analyzed by the left part of joint.

In Figures 3 (a) and (b), the incident and reflected waves of two specimens almost the same. Compared with the incident waves, there is obvious unloading process, which marked by a yellow star, before the unloading wave arrives. The calculation duration of S wave reflection is 75us when taking the wave velocities of P wave and S wave as 4 km/s and 2.8 km/s, respectively. And in the measured waveforms, the unloading process arrives 69us later than the loading P wave. According to analyses of Section 2.3, the unloading process should be generated by the reflected shear wave.

There are 12 possible positions of transmission bars when adjusting the nine-hole plate, and they are marked with numbers 1–7 and 2'-6', as shown in Figure 3. In Figure 3 (a), for example, three small transmission bars are located at positions marked "3", "3'" and "6", respectively. Recorded transmission waves of these points could be used to evaluate local strength of specimen. During the process of loading, there is a slot point in all three waves, which might result from material damage at local. At position 1, there is a great gap in waveform, and it might result from material failure at local. Therefore, local dynamic strength of cement could be calculated.

The calculation stresses of slot points are shown in Table 2. The results showed that the dynamic compressive strength varies with positions, and it is higher than the quasi-static strength, 35 MPa, but lower than dynamic strength, 54.67 MPa, when the strain rate is 54 $s^{-1}$. However, since the stress on the left side of joint surface is relatively low, about 26 MPa, it remains intact, and it could be used to observe the propagating of S-wave.

### 3.2 *Three-bar incidence and three-bar transmission*

Figure 4 demonstrates recorded waveforms of cement joint with an oblique angle of 45 degrees and under an impact speed of 4 m/s. There are three groups of incident waves and transmitted waves. The specimens keep intact, and it is different from that of Section 3.1. Since

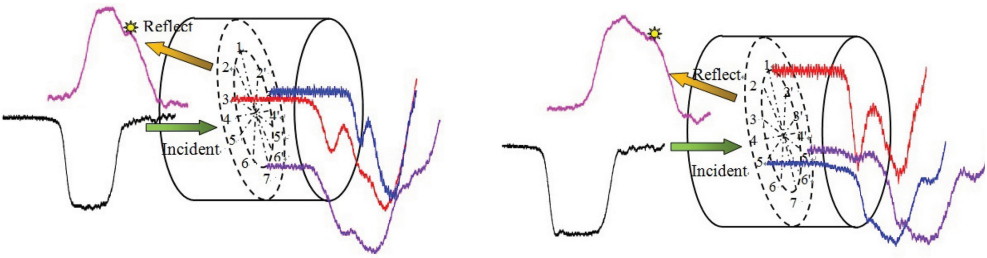


(a) Cement No.2 (b) Cement No.3

Figure 3. Recorded waveforms at different positions.

Table 2. Failure stresses at different positions of cement joint with oblique angle 45 deg.

| Positions | 1 | 2 | 3(3') | 4 | 5(5') | 6 | 7 |
|---|---|---|---|---|---|---|---|
| Failure stress /MPa | 46 | 54 | 32 | 43 | 44 | 51 | 54 |

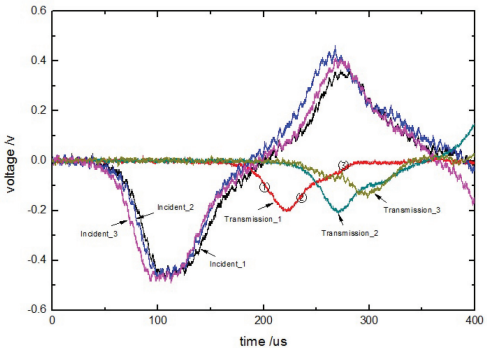


Figure 4. Recorded waveforms of three-bar incidence and three-bar transmission.

the process of gradual equilibrium of the dynamic compression of oblique cement joints is always developed with that of the tangential shear deformation, the analysis of dynamic compression and shear behavior should be conducted at the same time, and there are no separated shear wave and compression wave. The reflected wave and the transmitted wave are combined with shear wave and compression wave. It is verified by wave profiles propagating in one small bar, which shows almost the same wave structures. The transmitted wave could be divided into three stages, i.e. the loading stage, the sliding stage, and the unloading stage, which marked by ①, ②, and ③, respectively. It merits attention that all three stages are combined with shear wave and compression wave, and surface sliding should take place during loading process due to shear stress larger than instant shear strength of joint surface.

## 4 DYNAMIC COMPRESSION AND SHEAR PROPERTIES OF JOINT SURFACES

If the specimen is thin enough and the dynamic load is relatively small, the recorded signals denote the deformation characteristics of joint. The calculation involves in two parts, i.e. the normal compression and the tangential deformation properties. According to the analysis of Section 2.3, stresses and strain in the normal and tangential directions of cement joint are calculated by three-wave-method. Figure 5 demonstrates normal stress-strain relationships at three positions. It shows great differences of normal compression at three positions on joint surface. The compression differences of three small bars result from material and local contact differences between bars and the specimen. Local failure occurs at position of Bar_3.

The tangential deformation behavior of joint is relatively complicated, and there involves in two stages, i.e. the shear deformation stage and the shear slip stage. The first stage could be treated by the three-wave method. As for the shear slip stage, when the shear stress reaches a certain value, surface sliding occurs and friction coefficient of joint surface starts to decrease. With normal stress increasing, friction coefficient gradually decreases and shear stress increase slowly. And then, when the normal stress reaches to the peak, both friction coefficient and shear stress decrease rapidly. Figure 6 (a) illustrates the whole shear stress-time profiles of three bars. They are similar with those of normal stress. According to previous discussions, the loading process of shear stress could be divided into two stages. Figure 6 (b) illustrates the shear stress-time profiles of the first stage, and Figure 6 (c) illustrates those of the second stage. More details will be presented in future. In addition, the impact velocity of this experiment is controlled within 4 m/s, and the maximum slip displacement is 3~3.5 um.

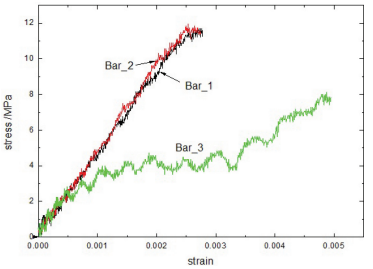


Figure 5. Stress-strain curve of longitudinal compression.

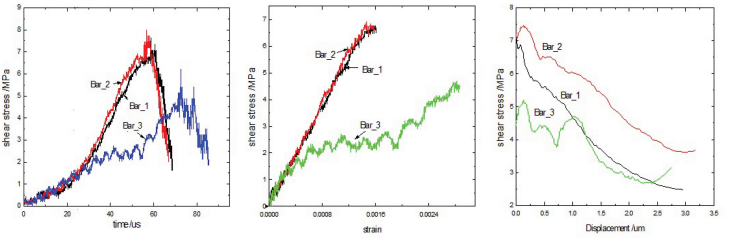


(a) Shear stress-time curve (b) The first stage with no slipping (c) The second stage with slipping

Figure 6. Curves of shear compression.

## 5 CONCLUSIONS

Hopkinson bar bundles system is proposed in the present paper to measure the dynamic slip characteristics of joint surfaces based on SHPB devices. By employing such two configurations as one-bar/three-bar incidence and three-bar transmission, the dynamic compression and shear properties of cement joint are investigated. It is interesting that surface sliding could be measured and evaluated by this technique, and it is great development of the experimental technique proposed by Xu et al. (2015). It also shows that the dynamic slip analysis could be carried out by using three small bars to receive the failure signals at different locations. It merits attention that the specimens should be thin enough and the loads should be in the elastic range, thereafter the specimen deformation could be taken as deformation of joint surface. However, interaction of bars is not discussed in the present paper, and it should be investigated by numerical analyses and theoretical method in future.

## ACKNOWLEDGEMENT

This work was supported by National Natural Sciences Fund of China (Grant Nos. 11272304, 11472264).

## REFERENCES

Albertini, C., Cadoni, E., Labibes, K. 1997. Impact fracture process and mechanical properties of plain concrete by means of an Hopkinson bar bundle. *Journal de Physique* IV, 07 (C3): 915–920.

Wu, W, Li, J.C., Zhao, J. 2012. Loading rate dependency of dynamic responses of rock joints at low loading rate. Rock Mechanics and Rock Engineering, 45: 421–426.

Wu, W. &Zhao, J. 2014. A dynamic-induced direct-shear model for dynamic triggering of frictional slip on simulated granular gouges. *Experimental Mechanics* 54: 605–613.

Xu S.L., Liu Y.G., Huang J.Y., Xi D.Y. 2013. Dynamic responses of rock-pair subjected to impact loading, In Jian zhao & Jianchun Li (eds), *Rock Dynamics and Applications--State of the art*: 193–198.

Xu S.L., Huang J.Y., Wang P.F., et al. 2015. Investigation of rock material under combined compression and shear loading: an experimental technique. *International Journal of Impact Engineering* 86: 206–222.

*Rock Dynamics: From Research to Engineering – Li et al. (Eds)*
*© 2016 Taylor & Francis Group, London, ISBN 978-1-138-02953-8*

# Dependence of dynamic tensile strength and fracture toughness of Longyou sandstone on heat-treatment temperature and loading rate

W. Yao & K. Xia
*Department of Civil Engineering, University of Toronto, Toronto, Ontario, Canada*

ABSTRACT: The mechanical properties of Longyou Sandstone (LS) (a material for Longyou rock caverns) under the combination of high loading rate and high temperature are important parameters for the protection of the caverns. Thus, the LS sample were first heat treated by various temperatures (150°C, 250°C, 350°C, 450°C, 600°C and 850°C) and the thermal damage was then characterized by the 3D X-ray Micro-Computed Tomography (CT) method. Meanwhile, the density and P-wave velocity of heat-treated sample and reference sample were measured. The values of CT value, density, and P-wave velocity decrease with the elevated heat-treatment temperature except for 450°C. Thereafter, according to the suggested method for determining dynamic tensile strength and dynamic fracture toughness of rock by International Society of Rock Mechanics (ISRM), Brazilian Disc (BD) and Notch Semi-Circular Bend (NSCB) samples were employed in the Split Hopkinson Pressure Bar (SHPB) system to measure the dynamic tensile strengths and the Mode-I fracture toughness of these LS samples under different dynamic loading rates. The dynamic tensile strength and fracture toughness of LS increase with the loading rate at a given heat-treatment temperature, and both the tensile strength and fracture toughness at the same loading rate decreases with the heat-treatment temperature except for 450°C. This phenomenon can be explained by the variation of the numbers of micro-cracking in LS sample for the different heat-treatment temperatures. With the thermal damage variable derived from the average CT value, empirical formulas were established to relate the dynamic tensile strength and fracture toughness of LS to the loading rate and the heat-treatment temperature. The results demonstrate that the dynamic tensile strength and Mode-I fracture toughness of LS are significantly influenced by the heat-treatment, especially under higher loading rate.

## 1 INTRODUCTION

As the Ninth Wonder of the World, Longyou rock caverns in Longyou County, Zhejiang Province of China attract a number of tourists as well as archaeologists, historians, specialists in engineering geology and rock mechanics. Many publications are available on various aspects of Longyou caverns, including engineering geological conditions (Li et al. 2009, Yang et al. 2000), siltstone properties and weathering characteristics (Yue et al. 2010, Zhang et al. 2015).

Due to their long-term integrity with large span and little support, the collapses of roof are one of vital issues for the protection of Longyou rock caverns. In addition, one of significant factors resulted in the roof collapse of Longyou rock caverns is dynamic loading, which is caused by the walking of a large number of visitors and earthquakes (Zhang et al. 2015). Thus, the mechanical properties of Longyou Sandstone (LS) (a material for Longyou rock caverns) under dynamic loading are important parameters for the protection of the caverns. Yue et al. (2010) studied the tensile strength of LS under static loading. Huang et al. (2010) measured the static and dynamic tensile strength of dry and fully saturated LS. Shao et al. (2010) studied the elastic wave velocity and mechanical properties of LS under different water contents. Huang et al. (2012) reported the static and dynamic compressive and shear strength of LS. Huang & Xia (2015) investigated the effect of heat-treatment on the dynamic compressive strength of LS. Furthermore, the installation of beam-pillar supporting systems involves rock drilling and cutting and thus induces the thermal damage on LS during the dynamic loading.

However, despite of the existing research efforts on LS, there is no attempt to systematically investigate the thermal damage on the tensile strength and fracture toughness of LS under dynamic loading. It is therefore the objective of this work to investigate the thermal damage in LS under elevated heat-treatment temperatures by 3D X-ray CT method and the effect of thermal damage on the static and dynamic tensile strength and fracture toughness of LS, which can provide the important parameters for protecting the Longyou rock caverns.

Following the introduction, Section 2 describes the LS sample characterization and damage variable. Experimental techniques are presented in Section 3. Section 4 discusses the experimental results and empirical models. Section 5 summarizes the results and concludes the work.

## 2 SAMPLE PREPARATION AND CHARACTERIZATION

### 2.1 *Sample preparation*

According to the suggested methods for determining the dynamic properties of rock material by International Society for Rock Mechanics (ISRM) (Zhou et al., 2012), Brazilian Disc (BD) sample and Notch Semi-Circular Bend (NSCB) sample were applied to measure the dynamic tensile strength and fracture toughness of LS in this study, respectively. The diameter and thickness of BD sample are 40 mm and 20 mm, respectively. In addition, NSCB specimen is a semi-circular disc with 40 mm diameter and 20 mm thickness. A sharp notch with around 1 mm thickness was perpendicularly machined to the diametrical cut in the center of disc (Dai et al. 2010).

Seven groups of LS samples for two types of specimen were prepared: samples without heat-treatment and samples thermally treated in a servo-controlled electrical furnace for 2 hours with 2°C/min heating/cooling speed under six different temperatures (150°C, 250°C, 350°C, 450°C, 600°C, and 850°C).

### 2.2 *Sample characterization*

Since the thermal damage after heat-treatment in the rock sample is usually present as 3D, the 3D X-ray CT was used to obtain the thermal damage in LS in this study (Huang & Xia 2015). The CT values, which describe the variation of the micro-cracks and chemical changes in the LS

Table 1. Density and P-wave velocity of LS sample with various heat-treatment temperatures.

| Temperature (°C) | Density (g/cm$^3$) | P-wave velocity (km/s) | CT value (*Hu*) | Damage variable (%) |
|---|---|---|---|---|
| 25 | 2.190 | 1.723 | 2885 | 0 |
| 150 | 2.188 | 1.700 | 2878 | 1.47 |
| 250 | 2.170 | 1.583 | 2843 | 8.83 |
| 350 | 2.160 | 1.549 | 2830 | 11.56 |
| 450 | 2.180 | 1.693 | 2857 | 5.88 |
| 600 | 2.140 | 1.441 | 2813 | 15.13 |
| 850 | 2.050 | 1.140 | 2790 | 19.96 |

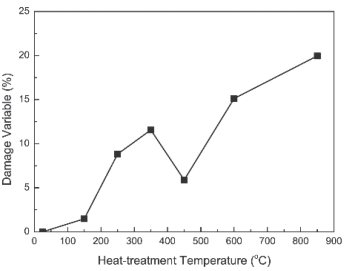


Figure 1. Variation of damage variable with the heat-treatment temperature.

material, were derived from the calibrated 3D CT images and the damage induced by the heat-treatment is characterized by the CT values (Feng et al., 2004;, Yao et al., 2015). In addition, since both the density and P-wave velocity of rock-like material are affected by thermal damage due to heat-treatment (Yin et al. 2012, Sengun 2014), the bulk density and P-wave velocity of LS sample were also measured under different heating temperatures. For each heat-treatment temperature, the average CT values, densities and P-wave velocities $v_p$ of LS are shown in Table 1. The CT value, the densities and $v_p$ for LS decrease with the heat-treatment temperature except for 450°C.

Since the average CT value represents the real 3D damage induced by the heat-treatment, damage variable $D$ is introduced to describe the thermally induced damage in LS (Feng et al. 2004):

$$D = \left(H_0 - H\right) / \left[\left(1000 + H_0\right) m^2\right] \tag{1}$$

where $D$ = the damage thermally introduced by a certain heat-treatment temperature, $H_0$ = the average CT value of LS sample without heat-treatment and $H$ = the average CT value of LS heat-treated sample, the space resolution of CT machine $m = 0.35$. The damage variable $D$ for each heat-treatment temperature is shown in Table 1 and Figure 1.

## 3 EXPERIMENTS

### 3.1 *Dynamic tension and fracture toughness test*

Following the ISRM suggested methods (Zhou et al. 2012), Split Hopkinson Pressure Bar (SHPB) system was employed to carry out dynamic tensile strength and fracture toughness test for LS. As shown in Figure 2a, the SHPB system consists of a striker bar, an incident bar, a transmitted bar and a testing system (including strain gauge, dynamic strain meter and oscilloscope). With the impact between the striker and the incident bar, the incident compressive pulse $\varepsilon_i$ is produced. When the incident pulse arrives the specimen-bar interface, part of the incident wave is reflected as reflected wave $\varepsilon_r$ in the incident bar and the remainder propagates through the specimen to the transmitted bar as the transmitted wave $\varepsilon_t$. These three waves were obtained by using the strain gauge system (Figure 2a). According to the strains obtained from these three waves, the forces $P_1$ and $P_2$ on both ends of the specimen can be calculated (Kolsky 1953):

$$P_1 = AE(\varepsilon_i + \varepsilon_r),\ P_2 = AE\varepsilon_t \tag{2}$$

where $A$ = the cross-sectional area of bars and $E$ = Young's modulus of bars.

Following the suggested method by ISRM (Zhou et al. 2012), the BD sample and NSCB sample were used to measure dynamic tensile strength and fracture toughness of LS and shown in Figures 2b and 2c, respectively. The tensile stress in the center of BD sample can be obtained by using the following formula:

$$\sigma_t(t) = 2P(t) / \left(\pi B D_B\right) \tag{3}$$

where $P(t)$ = the loading force, $B$ = the thickness of the BD specimen and $D_B$ = the diameter of the BD specimen. Dynamic tensile strength $T_d$ is determined as the maximum value of $\sigma_t$.

In addition, the Stress Intensity Factor (SIF) for mode-I fracture in NSCB sample is calculated by the following equation (Dai et al. 2010):

$$K_I(t) = \left[P(t) S / \left(B R^{3/2}\right)\right] \cdot Y(a/R) \tag{4}$$

where $K_I(t)$ = the time-varying Mode-I SIF, $a$ = the crack length, $B$ = the thickness of the disc, $R$ = the radius of disc, $S$ = distance between the two supporting pins, and $P(t)$ = the time-varying loading force. The dimensionless geometric function $Y(a/R)$ depends on the crack geometry and can be calculated with a standard finite element software package (e.g., ANSYS). Dynamic fracture toughness $K_{IC}^{D}$ of the sample is obtained at the maximum value of $K_I$.

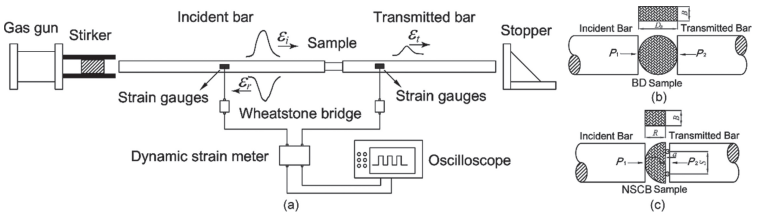


Figure 2. (a) Schematic of SHPB system; (b) BD sample; (c) NSCB sample.

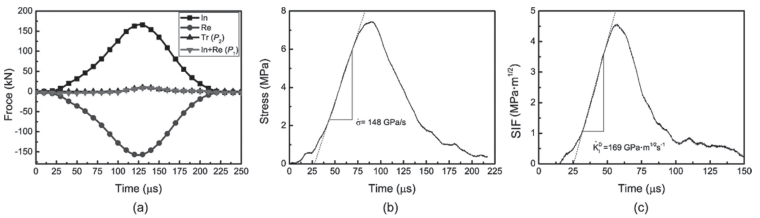


Figure 3. (a) Dynamic force balance and loading rate determination for a typical (b) BD test and (c) NSCB test.

### 3.2 *Dynamic force balance and loading rate*

The validation of using Eq. (3) and Eq. (4) for dynamic data reduction is that the dynamic force balance across the BD and NSCB specimen is reached during the whole dynamic loading (Zhou et al. 2012). Thus, for all dynamic BD and NSCB tests, the pulse shaping technique was adopted to achieve the dynamic force balance. According to Eq. (2), the dynamic force $P_1$ and $P_2$ on both sides of the BD and NSCB specimen can be calculated. As shown in Figure 3a, the dynamic stress equilibrium on both ends of sample is reached for a typical test. Moreover, the loading rate can be determined from the slope of linear region of the time-tensile stress in BD sample and the time-SIF in NSCB sample, respectively. The dash lines shown in Figure 3b and 3c are the loading rate for the typical dynamic tensile strength and fracture toughness test.

## 4 RESULTS AND DISCUSSIONS

As shown in Figure 4, BD and NSCB samples were generally split into two halves along the loading axis after dynamic tests. In addition, in Figure 5, both the tensile strength and fracture toughness of LS increase with the loading rate for all heat-treatment temperatures. Moreover, for the same loading rate, the tensile strength and fracture toughness decrease with the increase of heat-treatment temperature except for 450°C. This trend is consistent with that in the physical properties (i.e. the CT value, density and P-wave velocity) of LS.

The reason for the variation of the strength and fracture toughness of rock-like material due to the heat-treatment is the thermally induced damage by micro-cracking and chemical reaction (Huang & Xia 2015, Yin et al. 2012). Thus, this trend of the tensile strength, fracture toughness and physical properties of LS sample with heat-treated can be explained by thermal damage. The decrease of the tensile strength, fracture toughness and physical properties at 150°C, 250°C and 350°C can be explained as the decomposition (e.g. dehydration and dehydrogenation) of minerals in clay and micro-cracking at given heat-treatment temperature, whereas the increase of these properties of LS sample at 450°C attributes to the baking effect of clay minerals, which leads to the closure of original cracks/voids (Huang & Xia 2015, Tian et al. 2014). Furthermore, the decrease of CT values at 600°C and 850°C is caused by the combination of the increase of thermally induced micro-cracks (Heap et al. 2013, Huang & Xia 2015, Yin et al. 2012) and the formation of voids due to phase transition from $\alpha$ to $\beta$ quartz at temperature of 573°C, as well as the decomposition of calcite above 700°C (Peng & Redfern 2013).

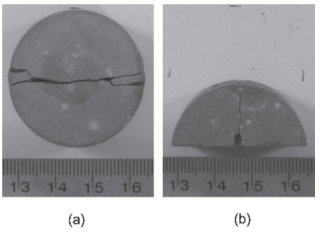


Figure 4. Typical recovered samples from dynamic (a) BD and (b) NSCB test (the scale is 10 mm).

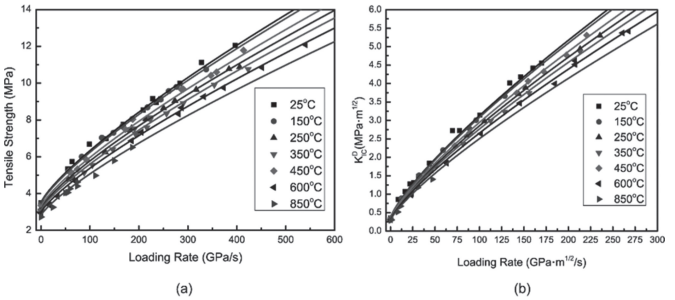


Figure 5. Dynamic (a) tensile strength and (b) fracture toughness of LS with fitting curves under different heat-treatment temperatures.

The effective dynamic tensile strength $T_d$ and fracture toughness $K_{IC}^D$ under a specific heat-treatment temperature can be related to the static tensile strength and fracture toughness without heat-treatment through the damage variable. In order to fully describe the dependence of the dynamic tensile strength and fracture toughness of LS on both loading rate and thermal effect, the following formulas are proposed:

$$T_d = (1-D)T_0\left[1+a\left(\dot{\sigma}/\dot{\sigma}_0\right)^b\right],\ K_{IC}^D = (1-D)K_{IC}^S\left[1+c\left(\dot{K}_I^D/\dot{K}_I^0\right)^d\right] \tag{5}$$

where $T_0$ = the static tensile strength and $K_{IC}^S$ = the fracture toughness under room temperature, $\dot{\sigma}$ and $\dot{K}_I^D$ = loading rate, $\dot{\sigma}_0 = 0.001$ GPa/s and $\dot{K}_I^0 = 0.001\text{GPa}\cdot\text{m}^{1/2}/\text{s}$ are the reference loading rate, $a$, $b$, $c$ and $d$ = fitting constants. The first term in the product on the right side of Eq. (5) describes the thermal damage and the third term is the loading rate. The Genetic Algorithm was applied to get the best fitting curves (in Fig. 5, where $a = 8.502\times10^{-5}$, $b = 0.796$, $c = 7.97\times10^{-4}$ and $d = 0.797$). The formula represents the trend of the data well.

It is noteworthy that both the data and the fitting curve illustrate that the effect of thermal damage on the tensile strength and fracture toughness of LS is more significant at higher loading rates than that at static and lower loading rates. This phenomenon may be attributed to the fact that the effect of the amount of micro-cracks induced by heat-treatment on the tensile strength of LS is more profound at higher loading rate (Yin et al. 2012, Yao et al. 2015).

## 5 CONCLUSIONS

In this work, the LS samples were heat treated under various temperatures (150°C, 250°C, 350°C, 450°C, 600°C and 850°C). The CT value, density and P-wave velocity of heat-treated and reference sample were measured. The CT value, density and P-wave velocity decrease with the elevated heat-treatment temperature except for 450°C. In addition, the damage variable derived from the average CT value for LS specimen was used to quantify the thermal damage. Thereafter, BD and NSCB samples were employed in the SHPB system to measure the dynamic tensile strength and fracture toughness of LS samples under different dynamic loading rates. The dynamic tensile

strength and fracture toughness of LS increase with the loading rate at a given heat-treatment temperature, and both the tensile strength and fracture toughness at the same loading rate decrease with the heat-treatment temperature except for 450°C. This phenomenon can be explained by the variation of the numbers of micro-cracking in LS sample for the different heat-treatment temperatures. Moreover, empirical equations were established to relate the dynamic tensile strength and fracture toughness of LS to the loading rate and the heat-treatment temperature.

## ACKNOWLEDGMENTS

Funding was provided by the Innovative Research Groups of Natural Science Foundation of China (NSFC) under Grant #51321065 and NSFC Grant #51479131, and the National Basic Research Program of China (973 Program) under Grant # 2013CB035904.

## REFERENCES

Dai, F., Chen, R. & Xia, K. 2010. A semi-circular bend technique for determining dynamic fracture toughness. *Experimental Mechanics* 50(6): 783–791.

Feng, X.T., Chen, S.L. & Zhou, H. 2004. Real-time computerized tomography (CT) experiments on sandstone damage evolution during triaxial compression with chemical corrosion. *International Journal of Rock Mechanics and Mining Sciences* 41(2): 181–192.

Heap, M.J., Lavallée, Y. Laumann, A. Hess, K.U. Meredith, P.G. Dingwell, D.B. Huismann, S. & Weise, F. 2013. The influence of thermal-stressing (up to 1000°C) on the physical, mechanical, and chemical properties of siliceous-aggregate, high-strength concrete. *Construction and Building Materials* 42: 248–265.

Huang, S. & Xia, K. 2015. Effect of heat-treatment on the dynamic compressive strength of Longyou sandstone. *Engineering Geology* 191: 1–7.

Huang, S., Xia, K. & Dai, F. 2012. Establishment of a dynamic Mohr–Coulomb failure criterion for rocks. *Internatonal Journal Nonline Science Numerical Simulation* 13(1): 55–60.

Huang, S., Xia, K. Yan, F. & Feng, X.T. 2010. An experimental study of the rate dependence of tensile strength softening of Longyou sandstone. *Rock Mechanics and Rock Engineering* 43(6): 677–683.

Kolsky, H. 1953. *Stress waves in solids.* UK:Oxford.

Li, L.H., Yang, Z.F. Yue, Z.Q. & Zhang, L.Q. 2009. Engineering geological characteristics, failure modes and protective measures of Longyou rock caverns of 2000 years old. *Tunnelling and Underground Space Technology* 24(2): 190–207.

Peng, Z. & Redfern, S.a.T. 2013. Mechanical properties of quartz at the α-β phase transition: Implications for tectonic and seismic anomalies. *Geochemistry, Geophysics, Geosystems* 14(1): 18–28.

Sengun, N. 2014. Influence of thermal damage on the physical and mechanical properties of carbonate rocks. *Arabian Journal of Geosciences* 7(12): 5543–5551.

Shao, M., Li, L. & Li, Z. 2010. Elastic wave velocity and mechanical properties of sandstone under different water contents at longyou grottoes. *Chinese Journal of Rock Mechanics and Engineering* 29(A02): 3514–3518.

Tian, H., Ziegler, M. & Kempka, T. 2014. Physical and mechanical behavior of claystone exposed to temperatures up to 1000°C. *International Journal of Rock Mechanics and Mining Sciences* 70: 144–153.

Yang, Z., Wang, S. & Xu, B. 2000. Analysis of the engineering geological conditions of Longyou stone caverns and primary study on the protection strategies. *Journal of Engineering Geology* 8(3): 292–295.

Yao, W., Xu, Y. Wang, W. & Kanopolous, P. 2015. Dependence of dynamic tensile strength of Longyou sandstone on heat-treatment temperature and loading rate. *Rock Mechanics and Rock Engineering*: 1–17.

Yin, T., Li, X. Xia, K. & Huang, S. 2012. Effect of Thermal Treatment on the Dynamic Fracture Toughness of Laurentian Granite. *Rock Mechanics and Rock Engineering* 45(6): 1087–1094.

Yue, Z., Fan, S. Yang, Z. Li, L. Zhang, L. & Zhang, Z. 2010. A hypothesis for crack free interior surfaces of Longyou caverns caved in argillaceous siltstone 2000 years ago. *Frontiers of Architecture and Civil Engineering in China* 4(2): 165–177.

Zhang, Z. Li, L. Xu, W. Fu, Y. & Feng, J. 2015. Flat-plate roof collapse of shallow caverns and protective measures: a case study of Longyou ancient siltstone caverns. *Natural Hazards* 76(1): 191–213.

Zhou, Y.X., Xia, K. Li, X.B. Li, H.B. Ma, G.W. Zhao, J. Zhou, Z.L. & Dai, F. 2012. Suggested methods for determining the dynamic strength parameters and mode-I fracture toughness of rock materials. *International Journal of Rock Mechanics and Mining Sciences* 49: 105–112.

*Rock Dynamics: From Research to Engineering – Li et al. (Eds)*
*© 2016 Taylor & Francis Group, London, ISBN 978-1-138-02953-8*

# Experimental research on rockburst tendency and acoustic emission characteristics of coal under different gas pressures

Z.Q. Yin
*Key Laboratory of Deep Coal Mine Excavation Response and Disaster Prevention and Control, Anhui University of Science and Technology, Huainan, Anhui, China*

Z.X. Hu & C.Q. Zhuo
*School of Mining and Safety, Anhui University of Science and Technology, Huainan, Anhui, China*

A.Y. Yuan
*Faculty of Resources and Safety Engineering, China University of Mining and Technology (Beijing), Beijing, China*

ABSTRACT: The specimens under the conditions of uniaxial compression, different gas-pressure conditions (0.0, 0.5, 1.0, and 1.5 MPa), sample strengths, deformation, energy, count of acoustic-emission signals, and laws influenced by gas pressure were investigated by self-developed equipment for coal containing gas. The results show that with the increase of gas pressure, the elastic strain energy stored and dissipated energy decrease, no evident influence on the evaluation of rockburst tendency by elastic strain energy indices, but dissipated energy for unit volume strain decreases rapidly before the destruction of the specimen. However, AE signal of high ring count value occurs at a higher percentage of peak strength for samples in atmospheric condition when compared to gas-containing coal samples. Therefore, gas should be considered when the evaluation of rockburst tendency in high gassy coal mines.

## 1 INTRODUCTION

As a typical coal and rock dynamic disaster, the rockburst is destructive, with strong, sudden energy release that seriously threatens safe production in coal mines (Cai 2008, Xue et al. 2015). Not only the stress distribution laws of coal seam, but also the rockburst tendency of the coal rock material was the main causes of the dynamic disasters in the progress of coal mining. Various indexes of rockburst have been established to describe the rockburst tendency of the coal rock material, to develop the rockburst forecast and provide basis for effective control (Feng et al. 2000, Qi et al. 2011, Zhang et al. 2008).

However, the mechanism of rockburst in coal mine is complex, especially in deep mining. The gas content in coal rock has an increasing with the increase of mining depth (Xie et al. 2014). By means of a great deal of investigation in site, the scientific evidences of relativity between rockburst and content in coal rock were found, gas in high pressure mostly took part in the generation of rockburst (Li et al. 2005). Some previous studies have been devoted over the past years to characterize behaviour on coal containing gas, the static compressive strength and elastic modulus of coal materials decreases as gas pressure increases (Liag et al. 1995, Xie et al. 2014). The capacity of coal movement increase with the energy of gas expansion in the coal seam, so, the risk of rock burst has increased dramatically (Qi et al. 2014). In the condition of higher coal mining stress and gas pressure, the occurrence of rockburst is interaction of the elastic deformation energy of coal rock and the expansion energy of gas release.

Although the tendency of the rockburst of coal seam have been obtained by in-situ monitoring, experimental observations and theory analysis, there have been very few studies on characterizing energy dissipation in loading process of gas-containing coal. Research on

energy dissipation is fundamental to have a deep insight of rockburst tendency. In this paper, using self-made gas sealing equipment, the characterization of the energy dissipation of coal rock in a gas-occurring was investigated, and identification of the precursor information rockburst tendency was conducted by the use of acoustic emission monitoring.

## 2 EXPERIMENTAL METHODS

### 2.1 *Sample preparation*

All coal specimens used in the experiment were obtained from the 11426 working face of the Xieqiao Mine in Huainan area in China. All selected specimens were free from visible uneven structures or defects. Furthermore, both ends and side faces of the specimens were ground carefully as required to measure the physical and mechanical characteristics of the coal. Then, the size of the coal specimens was set to 25 mm × 25 mm × 50 mm, and both the non-parallelism and non-perpendicularity of the specimens were less than 0.02 mm.

### 2.2 *Experimental equipment*

As shown in Figure 1, the gas-containing coal experimental system consisted of three devices: the gas seal device, the uniaxial experiment, and the data collection device. The gas seal device was connected to the gas supply device through an air pipeline. At room temperature, four levels of the simultaneous gas-containing coal uniaxial full strain compression and acoustic emission experiments have been conducted with gas pressures of 0, 0.5, 1.0, and 1.5 MPa. Five samples were tested in each level. Before testing, the pre-set gas pressure in the gas seal device was maintained for 24 h. For the test, RMT-150 rock press machine was used to apply axial loads to the gas-containing coal samples. The axial loading was assisted by displacement control, and the loading rate was 0.1 mm/min.

Two testing holes were prepared in the gas seal device, the static strain indicator and strain gauges were connected by these holes. Two strain gauges (BX120-2 AA) were used for the strain measurement are shown in Figure 2.

The gauges were installed in the circumferential and axial directions on all coal specimens to measure the lateral strain ($\varepsilon_l$) and axial strain ($\varepsilon_a$) of the specimens during the loading process. The strain history of strain gauges that were connected to the high-speed static strain indicator (YE2539) was recorded, thereby enabling the identification of the stress thresholds for crack closure, stable propagation, and unstable propagation. Strain data collection was conducted twice per second. Deformation and acoustic emission signals are monitored through the strain plates and the acoustic emission equipment.

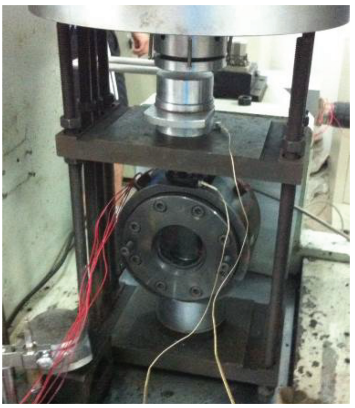

Figure 1. Testing system of coal absorbed gas.

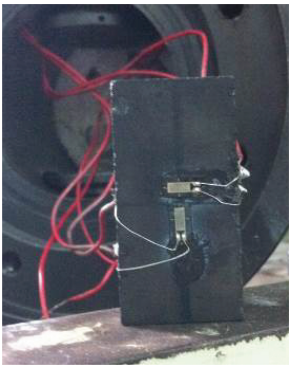

Figure 2. Coal specimens with installed strain gauges.

## 3 EXPERIMENTAL DISCUSSION

### 3.1 *Stress-strain behaviour*

The typical uniaxial stress-strain curves of the coal specimens under different gas pressures (0, 0.5, 1.0, and 1.5 MPa) is presented in Figure 3. Figure 3 shows that the static compressive strength decreased gradually from 23.8 MPa to 11.9 MPa and the axial strain decreased gradually from 0.73% to 0.44% when gas pressure from 0 MPa to 1.5 MPa, but the lateral strain increased from –0.41% to –0.61%. The elastic modulus of coal specimens decreased gradually from 3.66 GPa to 3.05 GPa with gas pressure. Coal specimens exhibited changing trend of low stress-induced large lateral strain under the influence of the gas pressure, these lateral strain were –0.05%, –0.05%, –0.08%, and –0.31 MPa when the axial stress were 10 MPa under different gas pressures (0, 0.5, 1.0, and 1.5 MPa), respectively. As observed on the coal specimens, the mechanical parameters were obvious influence by gas pressure.

### 3.2 *Energy characteristics in fracture process*

According to the first law of thermodynamics, the absorption energy ($U$) in the coal specimen is defined as (Bogusz et al. 2015):

$$U = U_d + U_e \tag{1}$$

where $U_d$ is the dissipated energy in the creation of deformation of coal specimen, $U_e$ is elastic energy in the coal specimen. The relationship of energy release and energy dissipation in coal specimen unit is presented in Figure 4.

The energy absorption ($U$) of coal specimen in the uniaxial compression tests is given by:

$$U = \int_0^{\varepsilon_1} \sigma_1 d\varepsilon_1 = \sum_{i=1}^{n} \frac{1}{2}(\sigma_i + \sigma_{i-1})(\varepsilon_i - \varepsilon_{i-1}) \tag{2}$$

where $\sigma_i$, $\varepsilon_i$ are axial stress and strain respectively.

The elastic energy stored, as follows:

$$U_e = \frac{1}{2E_u}\sigma_i^2 \tag{3}$$

where $E_u$ is the unloading modulus, as shown in Figure 4.

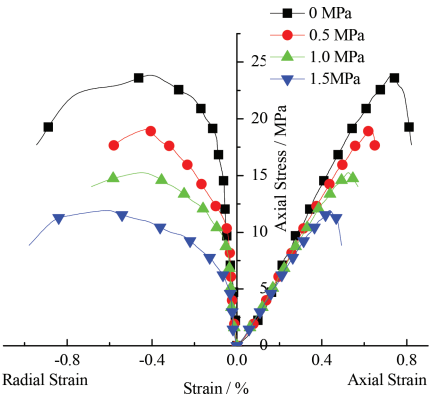


Figure 3. Stress–strain curves for tested specimens.

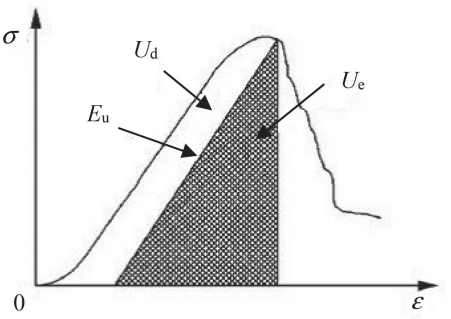


Figure 4. Relationship between elastic strain energy and dissipated energy in rock unit.

Through the loading and unloading tests, it is found that the error between the elastic modulus $E$ and the unloading modulus $E_u$ is very small (Liang et al. 2015). So, in the energy calculation, unloading elastic modulus is replaced by elastic modulus.

From Eq. (1) to Eq. (3), the dissipated energy in the uniaxial compression tests, as follows:

$$U_d = U - U_e = \int_0^{\varepsilon_1} \sigma_1 d\varepsilon_1 - \frac{1}{2E}\sigma_1^2 \tag{4}$$

Figure 5 shows the energy dissipation properties of samples under different gas pressure. It is clear that the energy of absorption, elastic and dissipated per unit volume decrease linearly with increasing gas pressure. Since the dissipated energy of the samples is used to form irreversible deformation, a low dissipated energy indicates that small deformation is created in the same sample.

However, as shown in Figures 3 and 5, the dissipated energy per unit volume decreases with the gas pressure, but the lateral strain increase. Thus, the low energy dissipated corresponds to the large deformation of gas-containing coal sample under high gas pressure.

In order to quantitatively describe the dissipated energy per unit volume strain of coal samples under different gas pressures. The dissipation energy rate $W$ defined as follows:

$$W = \frac{U_d}{\Delta\varepsilon_v} = \frac{U_d}{\Delta(\varepsilon_a + 2\varepsilon_l)} \tag{5}$$

where $\varepsilon_v$ is volumetric strain, $\varepsilon_a$ is axial strain, $\varepsilon_l$ is lateral strain.

Figure 6 shows the variation tendency of the dissipation energy rate $W$ and the gas pressure. From Figure 6, it is evident that the dissipation energy rate nonlinearly decreases with the gas pressure. The failure degree of the rockburst is reflected by the elastic energy and the dissipation energy rate. Before destruction of the coal specimen, the decrease of the elastic energy indicates the decrease of the outburst-proneness, but the decrease of the dissipation energy rate indicates the specimen is more prone to suffer damage. So, the mechanical parameters, gas pressure and mining stress should be comprehensive consideration when the evaluation of rockburst proneness in high gassy coal mines.

### 3.3 *Characteristics of AE counts*

Figure 7 shows the AE counts versus strain for typical specimen under different gas pressures.

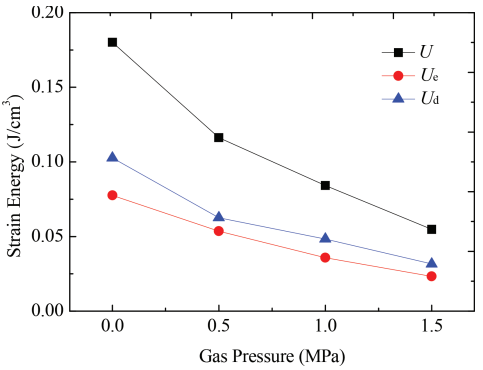


Figure 5. Energy changing with gas pressure.

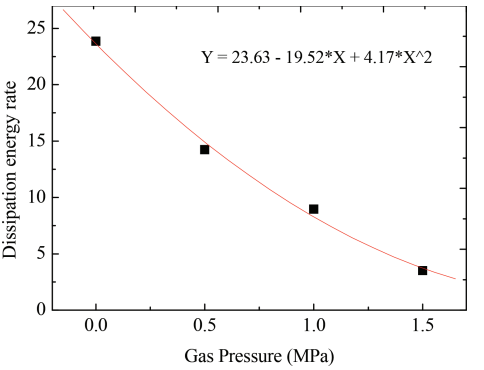


Figure 6. Relation of dissipation energy rate and gas pressure.

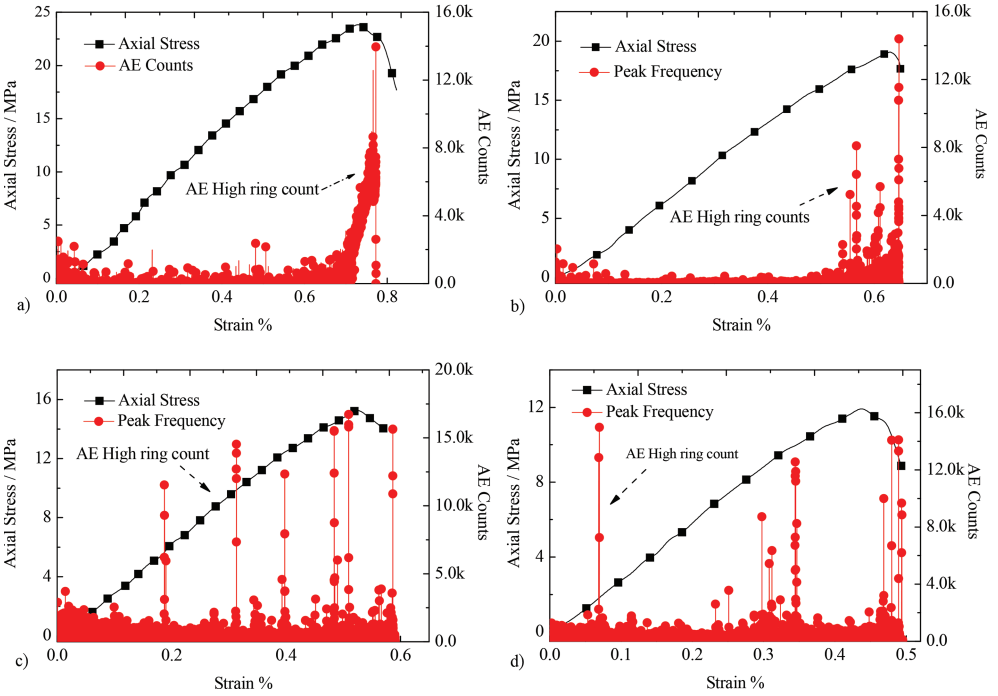


Figure 7. The AE ring count value of specimens under different gas pressure a) 0 MPa, b) 1.0 MPa, c) 1.5 MPa, d) 2.0 MPa.

From Figure 7, it is evident that the initial AE counts are lesser with increasing strain for non-gas saturated specimen. With the stress is increased to the peak stress, the AE counts increases gradually, and the maximum value is occurred at the specimen failure. With the increase in gas pressure, the times of generating AE signal of high ring count increases at lower stress, and the stress decreases gradually. Therefore, the possibility of gas-containing coal samples being damage increases under low stress. That when gas pressure increases, the damage of gas-containing coal more rapidly, AE signal of counts releases rapidly, time coverage period of AE signal of high ring count value becomes longer, and that the AE signal of high ring count can reflect gas-coal instability timely. So, the time of coal failure can be predicted by the AE counts in advance.

## 4 CONCLUSIONS

In this paper, an experimental study was conducted for a range of gas pressure levels (0, 0.5, 1.0 and1.5 MPa) using a series of uniaxial compression tests. This study investigates the gas pressure dependence of stress–strain, dissipation energy and AE counts characteristics. The main conclusions are as follows: The presence of gas in coal pore causes the coal rock strength and elastic energy to be reduced. The testing results that the gas-containing coal samples belongs to low impact tendency. The dissipated energy per unit volume strain and the strain of the first time AE signal high ring count value decrease with the gas pressure, coal seams could be more prone to failure under gas adsorption.

## ACKNOWLEDGMENTS

This work was supported by the National Natural Science Foundation of China (NO. 51304007), the State Key Program of National Natural Science Foundation of China

(U1361208), National Key Basic Research Program of China (2014CB260403), Anhui Provincial Natural Science Foundation (1408085MKL42) and China Postdoctoral Science Foundation (NO. 2013M531495).

## REFERENCES

Bogusz, A. & Bukowska, M. 2015. Stress-strain characteristics as a source of information on the destruction of rocks under the influence of load. *Journal of Sustainable Mining* 14(1): 46–54.

Cai, M. 2008. Influence of intermediate principal stress on rock fracturing and strength near excavation boundaries-Insight from numerical modeling. *International Journal of Rock Mechanics and Mining Science* 45(5): 763–772.

Feng, T., Xie X., Xie, X. & Pan, C. 2000. Brittleness of rocks and brittleness indices for describing rockburst proneness. *Mining and Metallurgical Engineering* 20(4): 18–19.

Li, T., Cai, M., Wang, J., Li, D. & Liu, J. 2005. Discussion on relativity between rockburst and gas in deep exploitation. *Journal of China Coal Society* 30(5): 20–25.

Liang, B., Zhang, M., Pan, Y. & Wang, L. 1995. The experimental research on the effect of gas on mechanical properties and mechanical response of coal. *Chinese Journal of Geotechnical Engineering* 17(5): 12–18.

Liang, C., Wu, S., Li, X. & Xin, P. 2015. Effects of strain rate on fracture characteristics and mesoscopic failure mechanisms of granite. *International Journal of Rock Mechanics and Mining Science* 76:146–154.

Qi, L., Cheng, X., Cheng G. & Cheng, Y. 2014. Research on the burst triggering mechanism under the coupling action of higher stress and gas pressure. *Journal of North China Institute of Science and Technology* 11(2): 18–21.

Qi, Q., Peng, Y., Li, H., Li, J., Wang, Y. & Li C. 2011. Study of bursting liability of coal and rock. *Chinese Journal of Rock Mechanics and Engineering* 30(S1): 2736–2742.

Xie, G. X., Hu, Z. X. & Wang, L. 2014 Coal mining dilatancy characteristics of high gas working face in the deep mine. *Journal of China Coal Society* 39(1): 91–96.

Xue, S., Yuan, L., Wang, J., Wang, Y. & Xie, J. 2015. A coupled DEM and LBM model for simulation of outbursts of coal and gas. *International Journal of Coal Science and Technology* 2(1): 22–29.

Zhang, J. & Fu, B. 2008 Rockburst and its criteria and control. *Chinese Journal of Rock Mechanics and Engineering* 27(10): 2034–2042.

*Rock Dynamics: From Research to Engineering – Li et al. (Eds)*
*© 2016 Taylor & Francis Group, London,* *ISBN 978-1-138-02953-8*

# Shear strength and Hugoniot Elastic Limit (HEL) of rock materials under shock loading

Q.B. Zhang
*State Key Laboratory of Geomechanics and Geotechnical Engineering, Institute of Rock and Soil Mechanics, Chinese Academy of Sciences, Wuhan, China*
*Department of Civil Engineering, Monash University, Clayton, VIC, Australia*

ABSTRACT: Plate impact experiments have been conducted on one fine-grained metamorphic rock, Carrara marble and one coarse-grained igneous rock, South Africa Gabbro. Embedded manganin stress gauges (i.e. longitudinal and lateral gauges) are used for the measurements of shock stresses. Shear strength are obtained by the difference of the longitudinal stress and lateral stress. Results suggest that rock materials are deforming in the inelastic manner and Hugoniot Elastic Limit (HEL) is deduced. Experimental results are compared and contrasted to the existing data for other geological materials. The detailed expWerimental procedures used to make measurements are to great extent standard methods when determining mechanical properties and deformation fields at high pressure.

## 1 INTRODUCTION

Rock dynamics studies the mechanical behaviour of rock materials and rock masses under dynamic loading conditions, where an increased rate of loading induces a change in mechanical properties and fracture behaviour (Zhang & Zhao 2014, Zhou & Zhao 2011). Dynamic loadings are in the form of time histories of pressure, velocity, particle velocity and acceleration. The shock properties of geological materials have long been a source of interest. Traditionally, the main driving forces have been planetary impact and geological research. Recently, there has been a growing interest in the shock properties of geological materials. The shock behaviour of rocks has a wide range of applications, such as rock engineering structures subjected to explosive and blasting loadings (Grady & Kipp 1979, Kanel et al. 2000, Rossmanith et al. 1997, Zhao et al. 1999). A shock wave is a sharp discontinuity in pressure, temperature, energy and density (more specifically, a shock wave is a traveling wave front across which a discontinuous adiabatic jump in state variables occurs). It comprise an integral part of the study of dynamic behaviour of materials under high pressure (Zukas 1990, Field et al. 2004, Bourne 2013, Meyers 1994). Rock materials are routinely shattered using blasting charges and the strain rates of over $10^4$ $s^{-1}$ are common (Zhao et al. 1999, Willmott & Proud 2007, Braithwaite 2009, Kirk et al. 2014, Zhang 2014, Zhang & Zhao 2015).

Shear strength has also been observed to increase with strain rate (Zhang & Zhao 2014). Laboratory tests have demonstrated that rocks exhibit brittle fracture at low temperatures and stresses if the strain rate is slow enough; this is attributed to 'subcritical' (at levels below the failure strength) crack growth (Ko & Kemeny 2011). Additionally, material failing in the ductile regime should also show strain-rate dependence since the mechanisms of plastic deformation generally depend upon strain rate. The shear strength is usually determined by the relationship between longitudinal and lateral stresses at high pressures (Millett et al. 2000a). It should be noted that the strain state of the material is in uniaxial strain only for a finite time in the plate impact experiments. Once release waves from the boundary of the plate arrive at the point of interest, the strain state is no longer in uniaxial strain. It is also commented that the method of using longitudinal and lateral stress gauges to calculate shear

stress is superior to previous methods, which requires to calculate the hydrostatic of material (Tsembelis et al. 2002).

The Hugoniot Elastic Limit (HEL) is the threshold on the shock Hugoniot at which a material transitions from an elastic state to an elastic-plastic state in the state of uniaxial strain (Bourne 2013). As the deformation is visco-plastic, this HEL is not actually a fixed value for a given material in every situation. Numerous studies have reflected on features of these precursor waves in brittle materials, and their relationships to the underlying deformation mechanisms (Grady 1998). One common way to determine a HEL value is to decide the amplitudes of elastic precursor waves in diagnostic records. However, the two-wave structures are not observed by many researchers in the diagnostics (Braithwaite 2009). A change in slope for example might not be seen due to the similar values of the shock and elastic impedances (Millett et al. 2000a, Millett et al. 2000b, Tsembelis et al. 2002). Therefore, it has been attempted to measure the shear strength and to determine deviation from elastic behaviour and infer an HEL. It is also demonstrated that the HEL can be determined through examining lateral gauge histories and determining the shear strength of the material (Tsembelis et al. 2002). HEL values of polycrystalline ceramics was summarized by (Kanel et al. 2000). The HEL data for Minerals are given by (Ahrens & Gregson, 1964): 1.5–2.5 GPa for calcite, 4–5 GPa for plagioclase rocks, and 4–9 GPa for quartzite and novaculite, by (Takazawa et al. 1998): 5.8–7.2 GPa for jadeite, and by (Murri et al. 1975): feldspar 4 GPa. Shock metamorphism experiments on quartz and plagioclase (Ahrens & Rosenberg, 1968). The data of shear strength and HEL of rock materials under shock loading were seldom reported in the literature. One of the key points is that there is often significant scatter on the measurements.

## 2 EXPERIMENTAL PROCEDURES

### 2.1 *Material characteristics*

In order to compare with the previous studies, two types of rock material that were well studied in dynamic tests were chosen for experiments, namely one igneous rock (South Africa gabbro), and one metamorphic rock (Carrara marble). Figure 1 shows the prepared square plates with the length of 60 mm. The longitudinal, $C_L$, and shear, $C_S$, wave speeds were obtained by measuring transit time of the pulses to travel twice a specimen thickness using 5 MHz ultrasonic transducers. The mechanical properties were determined by ISRM suggested methods, i.e., uniaxial compressive strength $\sigma_{uc}$, elastic modulus $E$ and Poisson's ratio $v$, and tensile strength $\sigma_t$. Physical and mechanical properties of two rocks are given in Table 1.

### 2.2 *The plate impact facility*

The Ultra-High Strain Rate (UHSR) experiments were performed using the plate impact facility at the Cavendish Laboratory, Cambridge University (Bourne et al. 1995). The facility

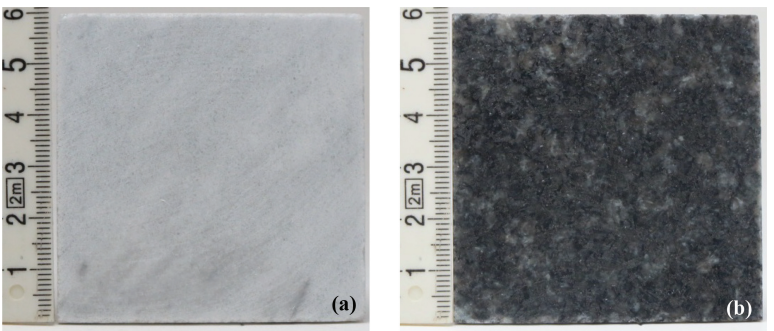


Figure 1. Photographs of the prepared specimens of: (a) Carrara marble, (b) South Africa gabbro.

Table 1. Physical and mechanical properties of rock materials under quasi-static loads.

| Rock Type | $\rho$ g/cm$^3$ | $C_L$ km/s | $C_S$ km/s | $E$ GPa | $\nu$ | $\sigma_{uc}$ MPa | $\sigma_{uc}$ MPa |
|---|---|---|---|---|---|---|---|
| Marble | 2.68 | 5.340 | 2.800 | 40 | 0.20 | 86.3 | 7.2 |
| Gabbro | 2.90 | 6.500 | 3.020 | 61 | 0.13 | 227.2 | 11.55 |

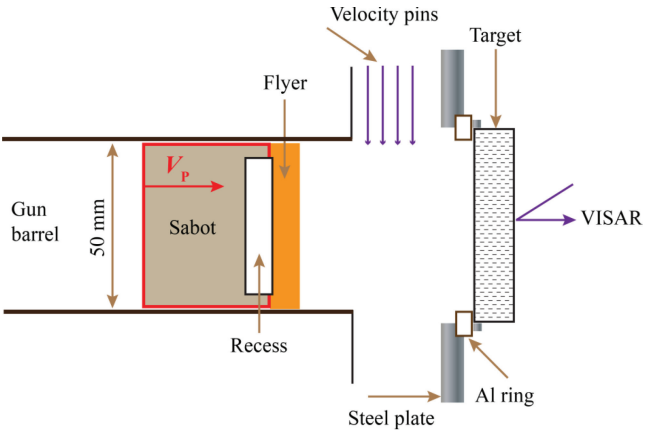


Figure 2. Schematic of an experiment in a plate impact facility (No to scale).

consists of a projectile body (primarily including a single-stage light gas gun, a projectile and a barrel) and a target assembly (including a target chamber and an expansion chamber). The barrel has a bore of 50 mm and a length of 5 m, and a projectile is launched by the gas gun at velocities up to 1,100 m/s. Figure 2 shows the mechanism and procedure for launching a polycarbonate sabot. The sabot is inserted into the breech plug placed at the end of the barrel and a vacuum of below 0.1 Mbar is drawn behind the sabot to prevent it from moving down the barrel. After keeping the sabot in place, the gas reservoirs are charged for launching.

### 2.3 *Testing methods*

In any uniaxial strain state, the basic definitions of terms and behaviour must start with the variables of pressure, strain, and principal stresses. The lateral stress is measured by embedding gauges in a lateral orientation. The lateral stress $\sigma_y$ can be reduced using the analysis of (Rosenberg & Partom 1985). The difference between the longitudinal stress ($\sigma_x$) and lateral stress ($\sigma_y$) can be considered to be a shear stress in an isotropic material (assuming von Mises isotropy) (Bourne 2013),

$$\tau = \frac{1}{2}(\sigma_x - \sigma_y) \tag{1}$$

In turn, both lateral and shear stresses can be related to the longitudinal stress (assuming that the stress is elastic) by the Poisson's ratio,

$$\sigma_y = \frac{\nu}{1-\nu}\sigma_x,\ \tau = \frac{1-2\nu}{2(1-\nu)}\sigma_x \tag{2}$$

The flyers made of Copper C101 are 48 mm in diameter and 10 mm in thickness. Two gauges are often used in order to give an indication whether any significant attenuation is taking place over the distance of travel in the target. Figure 3 shows a typical plate impact target where two

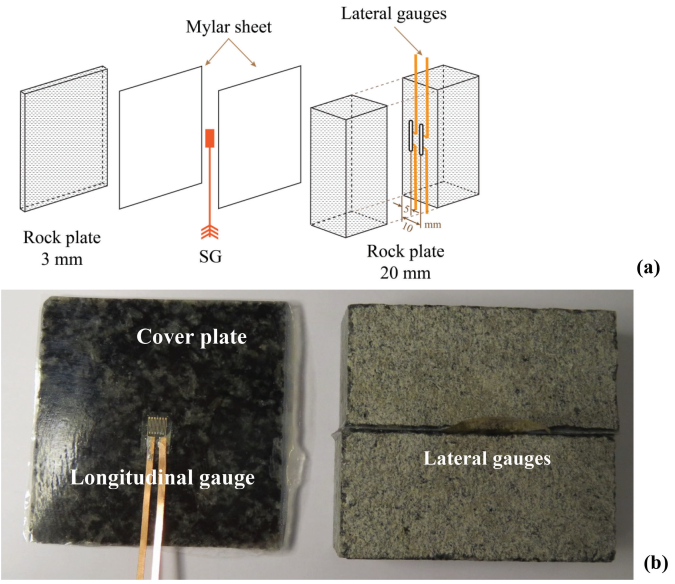


Figure 3. (a) Schematic illustration (exploded), and (b) a photo of a rock target containing one longitudinal gauge and two embedded lateral gauges.

lateral gauges were embedded (type J2M-SS-580SF-025). To insulate and protect the gauges, a 25 μm thick Mylar sheet was fixed to the specimen plates using a slow cure epoxy (Loctite® 0151™ Hysol® Epoxy Adhesive). The plate and Mylar sheet were clamped using a specially machined clamp apparatus for a minimum of 24 hours until the slow cure epoxy set. Since there is a layer of epoxy paralleling to the direction of travel of the projectile, it is possible for epoxy compressed preferentially down this layer, termed jetting. This would lead to erroneous results. A 3 mm thick cover plate is thus used on the front of the sample to prevent this from happening. A longitudinal gauge is placed behind the cover plate to obtain additional information. The interpretation of lateral gauge is based on the impedance matching technique (Rosenberg & Partom 1985), and this method assumed that the strain in a thin (foil) laterally embedded gauge was equivalent to that of the surrounding material. The approach employed in converting measured changes in voltage across the manganin gauge to lateral stresses also considered both the elastic-plastic response of manganin gauge (Rosenberg & Brar 1995) used and the pressure dependence of its response at stresses below its HEL (Millett et al. 1996).

## 3 EXPERIMENTAL RESULTS AND DISCUSSION

Figure 4 shows typical lateral stress histories of marble and gabbro measured by the two embedded gauges. This demonstrates not only that there is no significant attenuation in the material over the distance concerned, but also that the one dimensional strain condition has not been released from the sides in the time frame of this experiment.

The difference between the longitudinal stress and lateral stress are used to calculate shear strength. The shear strength is calculated using equation (1), and then plot the variation of shear strength with the longitudinal stress. The longitudinal stress can either be determined from the embedded longitudinal gauge on the back of cover plate for examining lateral stress, or by using a previously determined Hugoniot. For the comparison with the locations of longitudinal gauge (15 mm from the impact face) in the compression tests, only the data of 10 mm gauges have been used. The theoretical elastic response can be plotted using equation (2). It can be seen from Figure 5 that the data of 5 and 10 mm gauges in marble have no systematic difference; whereas in gabbro the 5 mm gauges record higher values of lateral

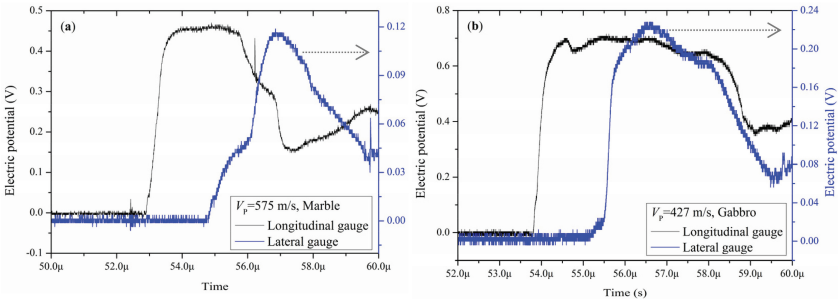


Figure 4. Figure 7:21 Lateral gauge traces of: (a) Carrara marble at impact velocity of 575 m/s, (b) South Africa gabbro at impact velocity of 427 m/s.

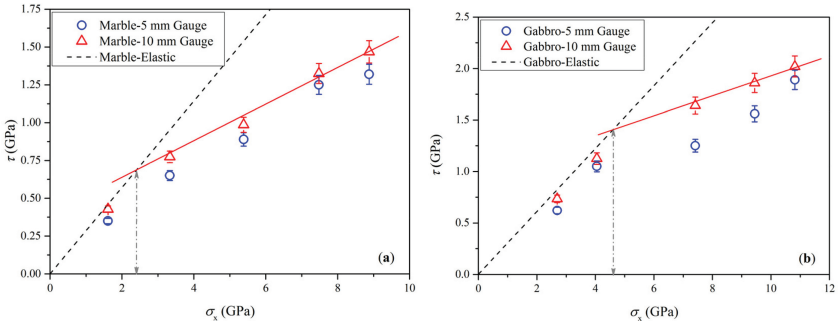


Figure 5. Dynamic shear stress measurements and elastic response showing the HEL of: (a) Carrara marble, (b) South Africa gabbro.

stress than the 10 mm gauges, probably due to the shock wave attenuation or lateral releases in the coarse-grained materials. Dynamic shear strength is inelastic over somewhat the stress range of the experiments, because the data all lie below the theoretical value. It is possible to find where the shear behaviour departs from the elastic, namely the HEL as reported by (Tsembelis et al. 2002). Therefore, a line was fitted to the data points above the HEL and the intercept of this line with the line of elastic behaviour was taken as the HEL. The HEL values are approximately 2.4 and 4.6 GPa for marble and gabbro, respectively, and the data show that above this value there is little increase in shear strength with axial impact stress.

## 4 CONCLUSIONS

Plate impact experiments are conducted to determine Hugoniot curves, spall tensile strength, shear strength and Hugoniot Elastic Limit (HEL) of the fine-grained marble and coarse-grained gabbro. Manganin stress gauges are used for the measurement of stress velocity. Lateral stresses were measured using embedded lateral gauges. The shear strength has been calculated during plate impact in the axial stress range 3–12 GPa, and is shown to increase significantly with shock stress. Both rocks were found to have an obvious HEL and the HEL values are estimated to be 2.4 GPa for marble and 4.6 GPa for gabbro.

## ACKNOWLEDGEMENTS

This work is supported by the Swiss National Science Foundation (No. 200020_129757) and Open Research Fund of State Key Laboratory of Geomechanics and Geotechnical Engineering, Institute of Rock and Soil Mechanics, Chinese Academy of Sciences (No. Z014005).

## REFERENCES


Ahrens, T.J. & Gregsow, V.G. 1964. Shock compression of custal rocks: Data for quartz, calcite, and plagioclase rocks. *J. Geophys. Res.,* 69, 4839–4874.

Ahrens, T.J. & Rosenberg, J.T. 1968. Shock metamorphism: Experiments on quartz and plagioclase. *Shock metamorphism of natural materials*, 59–81.

Bourne, N.K. 2013. *Materials in mechanical extremes: Fundamentals and applications*, Cambridge, Cambridge University Press.

Bourne, N.K., Rosenberg, Z., Johnson D.J., Field, J.E., Timbs, A.E. & Flaxman, R.P. 1995. Design and construction of the UK plate impact facility. *Meas Sci Technol,* 6, 1462.

Braithwaite, C. 2009. *High strain rate properties of geological materials.* PhD, University of Cambridge.

Field, J.E., Walley, S.M., Proud, W.G., Goldrein, H.T. & Siviour, C.R. 2004. Review of experimental techniques for high rate deformation and shock studies. *Int J Impact Eng,* 30, 725–775.

Grady, D.E. 1998. Shock-wave compression of brittle solids. *Mech Mater,* 29, 181–203.

Grady, D.E. & Kipp, M.E. 1979. The micromechanics of impact fracture of rock. *Int J Rock Mech Min Sci Geomech Abstr,* 16, 293–302.

Kanel, G.I., Bless, S.J. & Rajendran, A.M. 2000. Behavior of brittle materials under dynamic loading. *Texas University at Austin Inst For Advanced Technology Report.*

Kirk, S., Braithwaite, C., Williamson, D. & Jardine, A. 2014. Shock compression of geological materials. *Journal of Physics: Conference Series,* 500, 062005.

Ko, T.Y. & Kemeny, J. 2011. Subcritical crack growth in rocks under shear loading. *J. Geophys. Res.,* 116, B01407.

Meyers, M.A. 1994. *Dynamic behavior of materials*, John Wiley & Sons, Inc.

Millett, J.C.F., Bourne, N.K. & Rosenberg, Z. 1996. On the analysis of transverse stress gauge data from shock loading experiments. *J Phys D Appl Phys,* 29, 2466.

Millett, J.C.F., Tsembelis, K. & Bourne, N.K. 2000a. Longitudinal and lateral stress measurements in shock-loaded gabbro and granite. *J Appl Phys,* 87, 3678–3682.

Millett, J.C.F., Tsembelis, K., Bourne, N.K. & Field, J.E. 2000b. The shock Hugoniot of two igneous rocks. *AIP Conference Proceedings,* 505, 1247–1250.

Murri, W.J., Grady, D.E. & Mahrer, K.D. 1975. Equation of state of rocks. Stanford Research Institute. Final report, 31 March 1973–1 Sep 1974.

Rosenberg, Z. & Brar, N.S. 1995. The influence of the elasto-plastic properties of piezoresistance gauges on their loading-unloading characteristics as lateral shock stress transducers. *J Appl Phys,* 77, 1443–1448.

Rosenberg, Z. & Partom, Y. 1985. Lateral stress measurement in shock-loaded targets with transverse piezoresistance gauges. *J Appl Phys,* 58, 3072–3076.

Rossmanith, H.P., Daehnke, A., Nasmillner, R.E.K., Kouzniak, N., Ohstu, M. & Uenishi, K. 1997. Fracture mechanics applications to drilling and blasting. *Fatig Fract Eng Mater Struct,* 20, 1617–1636.

Takazawa, E., Sekine, T., Kobayshi, T. & Zhu, Y. 1998. Hugoniot equation of state and high-pressure transformation of jadeite. *J Geophys Res,* 103, 12261–12268.

Tsembelis, K., Proud, W.G. & Field, J.E. 2002. The principal Hugoniot and dynamic strength of Dolerite under shock compression. *AIP Conference Proceedings,* 620, 1385–1388.

Willmott, G.R. & Proud, W.G. 2007. The shock Hugoniot of Tuffisitic Kimberlite Breccia. *Int J Rock Mech Min,* 44, 228–237.

Zhang, Q.B. 2014. *Mechanical Behaviour of Rock Materials under Dynamic Loading.* PhD thesis, École Polytechnique Fédérale de Lausanne.

Zhang, Q.B. & Zhao, J. 2014. A review of dynamic experimental techniques and mechanical behaviour of rock materials. *Rock Mech Rock Eng,* 47, 1411–1478.

Zhang, Q.B. & Zhao, J. The Response of Rock Materials to One-dimensional Shock Loading. *11th International Symposium on Rock Fragmentation by Blasting*, 2015. The Australasian Institute of Mining and Metallurgy: Melbourne, 665–672.

Zhao, J., Zhou, Y.X., Hefny, A.M., Cai, J.G., Chen, S.G., Li, H.B., Liu, J.F., Jain, M., Foo, S.T. & Seah, C.C. 1999. Rock dynamics research related to cavern development for ammunition storage. *Tunn Undergr Sp Tech,* 14, 513–526.

Zhou, Y.X. & Zhao, J. (eds.) 2011. *Advances in rock dynamics and applications*: CRC Press.

Zukas, J.A. (ed.) 1990. *High velocity impact dynamics,* New York: John Wiley & Sons, Inc.

*Rock Dynamics: From Research to Engineering – Li et al. (Eds)*
*© 2016 Taylor & Francis Group, London, ISBN 978-1-138-02953-8*

# Anti-seismic research for cracked lining structure

H.C. Zhou, W.P. Xu, W.G. Qiu & K.G. Sun
*Key Laboratory of Transportation Tunnel Engineering, Ministry of Education, Civil Engineering, Southwest Jiaotong University, Chengdu, China*

ABSTRACT: Earthquakes occurred frequently this century. The earthquake created an inestimable damage to tunnels and underground structures. Also, cracked lining widely exist in practical projects. Based on model test, the preliminary study to the seismic response rule of cracked lining tunnel had been conducted. The following conclusions can be obtained. Under the same rock pressure, the additional moment of hard rock is larger than for soft rock. The bigger the rock pressure is, the larger additional moment of structures will be. The additional moment of intact lining and cracked lining are relatively large in the direction of 45 degrees to the horizontal direction. When there is only one crack, the moment of the lining is reduced near the crack. When there are more cracks in the lining, the bending moment has stress concentration near the crack. The conclusion of these experiments can provide a reference for the designer.

## 1 INTRODUCTION

Many tunnels have been damaged noticeably in earthquakes in last two decades including 1999 Chi-Chi, Taiwan earthquake (Wang 2001) and 2008 Wenchuan earthquake (Wang 2013). The response of tunnel lining was studied by shaking table (Yakovlevich 1987). Experiments were carried out on the underwater tunnel by means of the mechanical vibration (Shunzo 1984). The seismic response of two parallel shield tunnels were tested, and the influence of the parallel distance on the seismic response of the structures was studied (Goto 1988). Based on the investigation of earth-quake damage and seismic analysis, the characteristics of dynamic response of underground structure were summarized (Kuesel 1969). The basic rules of seismic damage of underground structures were summarized (Hashash 2001). In 1980s the flexibility ratio concept was introduced into the seismic research (St. John 1980). An analytical method for the interaction between structure and ground was proposed by scholars (Yousser 2001). However, study on seismic response of cracked lining is rare. In this paper, we analyze the seismic response of cracked lining by model experiment.

## 2 MODEL TEST

### 2.1 *Test instrument*

In order to simulate seismic problems of a tunnel structure, a shear box developed. To monitor the data in real time, dynamic and static strain analysis system was used to monitor the internal force of the tunnel model. The displacement meter was arranged on one side of the shear box, and the dynamic change of the lateral displacement of the shear box in the test process was measured. The loading system was a chain block, and the chain block can be adjusted to cause the shear box to generate a lateral offset. The strain test system and displacement test system have been shown in Figure 1.

## 2.2 *Test material and model preparation*

The surrounding rock materials were stone and sunflower seed. The material of the lining was reinforced plaster. Model's size was 450 mm (length) × 200 mm (diameter) × 12 mm (thickness). Cracks of the lining model were made by saw blade. And the types of lining and positon of cracks were shown in Figure 2. Figure 3 shows the positon of strain gauges.

## 2.3 *Test condition*

In this experiment, 2 kinds of surrounding rock materials and 4 types of lining have been chosen separately. Also, two forms of rock pressure have been performed which are free and fully watered bottles on the surface. The rock materials are shown in Figure 4. The types of soil and test cases have been shown in Table 1 and Table 2.

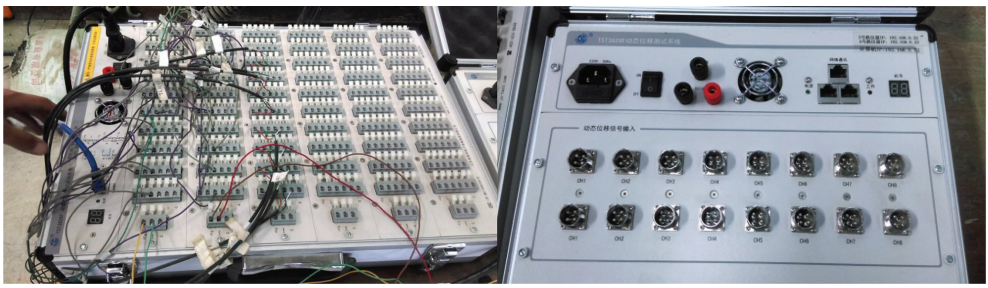

Figure 1. Strain test system and displacement test system.

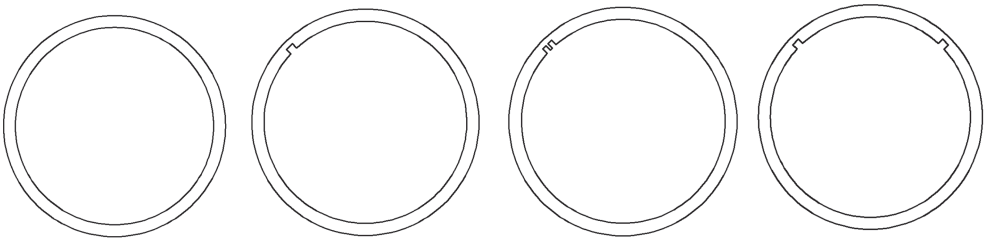

(a) No.1 intact lining (b) No.2 cracked lining (c) No.3 cracked lining (d) No.4 crack lining

Figure 2. Types of lining.

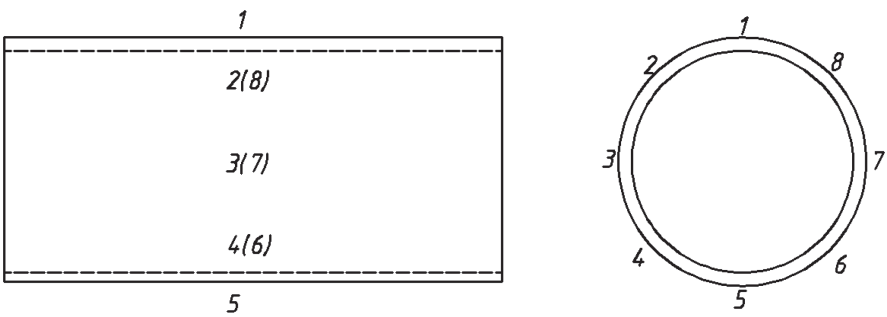


(a)Side view (b)Front view

Figure 3. Depicts position of strain gauges.

(a)sunflower seed (b)stone

Figure 4. Rock materials.

Table 1. Types of soil.

| | Rock materials | Rock pressure |
|---|---|---|
| Soil 1 | sunflower seeds | water bottles |
| Soil 2 | sunflower seeds | without bottles |
| Soil 3 | stone | water bottles |
| Soil 4 | stone | without bottles |

Table 2. Test cases for this experiment.

| | Soil 1 | Soil 2 | Soil 3 | Soil 4 |
|---|---|---|---|---|
| Lining 1 | Case 11 | Case 12 | Case 13 | Case 14 |
| Lining 2 | Case 21 | Case 22 | Case 23 | Case 24 |
| Lining 3 | Case 31 | Case 32 | Case 33 | Case 34 |
| Lining 4 | Case 41 | Case 42 | Case 43 | Case 44 |

## 3 TEST RESULTS

### 3.1 *No.1 intact lining*

The moment of lining measured by different sensors are shown in Table 3. Figure 5 shows the maximum bending moment for the No.1 intact lining.

The additional moment is relatively large in the direction of 45 degrees to the horizontal direction. The maximum value appears at point 4 and point 6. Under the same rock pressure, the additional moment for the surrounding rock of is larger than that of seeds. When the rock pressure increases, the additional moment of structures also enlarge.

### 3.2 *No. 2 cracked lining*

The moment of lining measured by different sensors are shown in Table 4. Figure 6 shows the maximum bending moment for the No. 2 cracked lining.

The law of moment is the same as the No.1 intact lining. The moment for point 2 is the smallest. The moment of the No. 2 cracked lining at the measuring point 6, 8 is greater than that at point 2, 4. The moment of the lining is reduced near the crack.

### 3.3 *No. 3 cracked lining*

The moment of lining measured by different sensors are shown in Table 5. Figure 7 shows the maximum bending moment of No. 3 cracked lining.

Table 3. The moment of No.1 intact lining unit:$10^{-2}$ N·m.

| | 1 | 2 | 3 | 4 | 5 | 6 | 7 | 8 |
|---|---|---|---|---|---|---|---|---|
| Case 11 | –31.2 | –173.4 | –20.3 | –193.2 | –1.4 | –201.7 | 23.3 | 156.0 |
| Case 12 | –15.3 | –121.9 | –12.3 | 99.1 | –9.5 | –114.7 | –19.0 | 80.6 |
| Case 13 | –103.1 | –742.2 | –180.1 | 790.3 | 71.2 | –881.8 | –21.9 | 658.2 |
| Case 14 | –65.4 | –381.6 | –123.5 | 461.0 | 62.5 | –569.0 | 21.1 | 378.1 |

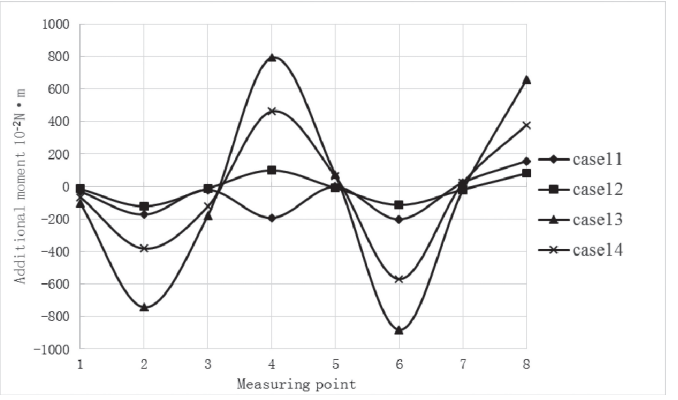


Figure 5. The maximum bending moment of the No.1 intact lining.

Table 4. The moment of No. 2 cracked lining unit:$10^{-2}$ N·m

| | 1 | 2 | 3 | 4 | 5 | 6 | 7 | 8 |
|---|---|---|---|---|---|---|---|---|
| Case 21 | –31.2 | –160.4 | 26.9 | 189.6 | –87.2 | –179.3 | 33.5 | 195.2 |
| Case 22 | –10.2 | –75.5 | –8.7 | 100.6 | –58.8 | –83.5 | 23.3 | 90.0 |
| Case 23 | 271.7 | –244.7 | –81.5 | 602.8 | –436.6 | –683.6 | –51.7 | 955.6 |
| Case 24 | 2.2 | –339.0 | –8.7 | 418.3 | –126.4 | –399.2 | 42.3 | 397.0 |

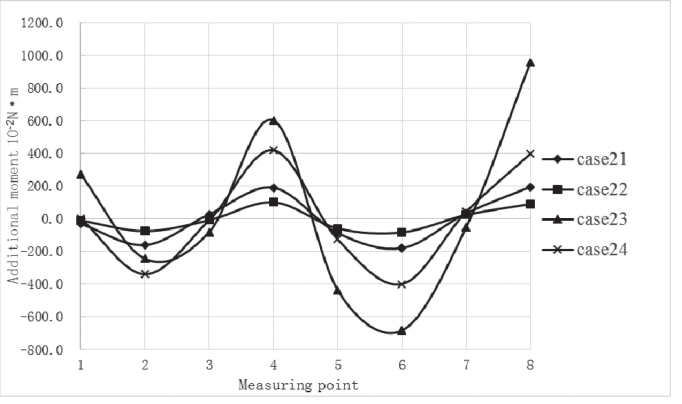


Figure 6. The maximum bending moment of the No. 2 cracked lining.

The discipline of moment for this lining is the same as the No. 2 cracked lining. The bending moment at point 2, 4, 6, 8 is smaller than that of the No. 1 intact lining. Under earthquake loading, the more serious the crack of lining is, the bigger the bending moment is.

Table 5. The moment of No. 3 cracked lining unit: $10^{-2}$ N·m.

| | 1 | 2 | 3 | 4 | 5 | 6 | 7 | 8 |
|---|---|---|---|---|---|---|---|---|
| Case 31 | 90.0 | –175.7 | 40.3 | 175.9 | 100.3 | –214.8 | 53.2 | 269.3 |
| Case 32 | –18.1 | 85.6 | –38.2 | –88.3 | –23.6 | 99.4 | –54.6 | –141.5 |
| Case 33 | 632.5 | –351.5 | 120.4 | 850.7 | 440.3 | –2026.6 | 142.7 | 1358.4 |
| Case 34 | 262.9 | –481.3 | 154.4 | 487.9 | 242.4 | –670.6 | 187.9 | 823.7 |

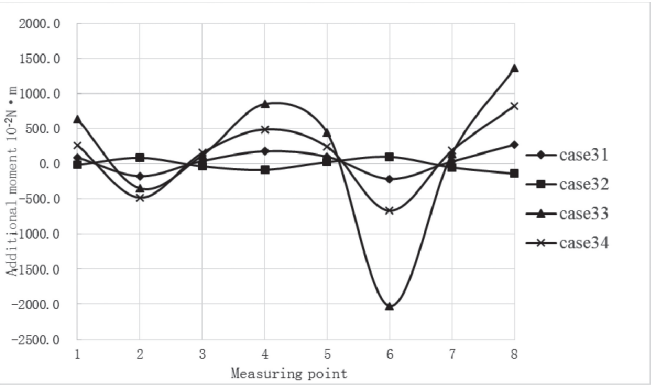


Figure 7. The maximum bending moment of the No. 3 cracked lining.

Table 6. The moment of No. 4 cracked lining unit: $10^{-2}$ N·m.

| | 1 | 2 | 3 | 4 | 5 | 6 | 7 | 8 |
|---|---|---|---|---|---|---|---|---|
| Case 41 | –45.1 | –132.1 | 17.5 | 159.2 | –41.4 | –148.0 | 46.6 | 140.8 |
| Case 42 | –4.3 | 53.7 | 33.4 | –68.0 | –5.1 | 66.0 | 10.2 | –71.8 |
| Case 43 | 235.3 | –1937.7 | 5.9 | 466.1 | 39.9 | –534.1 | –157.3 | 588.6 |
| Case 44 | 27.5 | –327.9 | –137.3 | 344.5 | 75.5 | –356.3 | –65.5 | 412.9 |

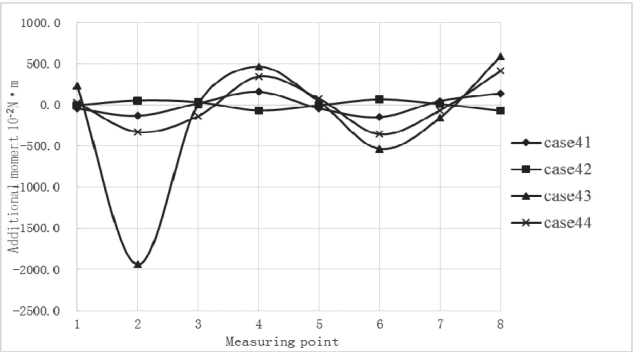


Figure 8. The maximum bending moment of the No. 4 cracked lining.

### 3.4 *No. 4 cracked lining*

The moment of lining measured by different sensors are shown in Table 6. Figure 8 shows the maximum bending moment of No. 4 cracked lining.

The increase of cracks at different locations will reduce the moment, this may be due to the decrease in the stiffness. But the bending moment has stress concentration near the cracks.

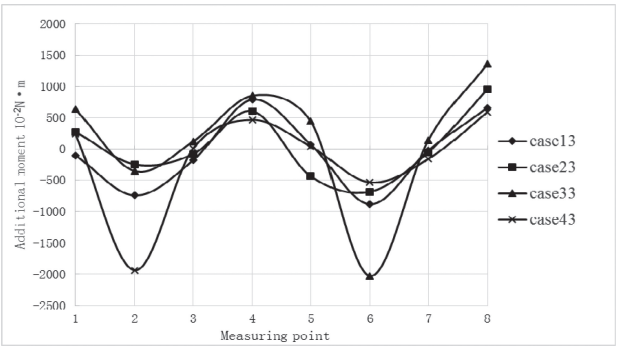


Figure 9. The maximum bending moment for the soil 3.

### 3.5 *Comparison of different lining*

For the same surrounding rock and rock pressure, when there is only one crack, the moment of the lining is reduced near the crack. When there are more cracks, the bending moment has behaved stress concentration near the crack, as shown in Figure 9.

## 4 CONCLUSIONS

The following conclusions can be obtained through analyzing the seismic response of cracked lining. Under the same rock pressure, the additional moment of stone surrounding rock is larger than seeds surrounding rock. An additional moment of structures is larger in the large confining pressure situation. The Additional moment is relatively large in axis position of 45 degrees. When there is only one crack, the moment of the lining is reduced near the crack. When there are many cracks in the lining, the bending moment has stress concentration near the crack.

## ACKNOWLEDGEMENTS

This work is funded by the National Natural Science Foundation of China (Grant No. 51578463) and the Fundamental Research Funds for the Central Universities (No. 2682015CX086 and No. 2682015CX089).

## REFERENCES

Goto, Y, Matsuda, Y, Ejiri, J., et al. 1988. Influence of Distance between Juxtaposed Shield Tunnels on their Seismic Response. *Proc.9th world Conf. on Earthquake Eng.,* Tokyo-Kyoto, Japan.

Hashash, Y.M.A., Hook, J.J. 2001. Seismic design and analysis of underground structures. *Tunnelling and Underground Space Technology* 16: 247–293.

Kuesel, T.R. 1969 Earthquake design criteria for subways. *Journal of the Structural Division, ASCE* 95(ST6): 1213–1231.

Shunzo, O. 1984. *Introduction to Earthquake Engineering.* 2nd Edition. Tokyo: University of Tokyo Press.

St. John, C.M. 1987. A seismic design of underground structures. *Tunnelling and Underground Space Technology* 2: 165–197.

Wang, W.L., Wang, T.T., Su, J.J. et al. 2001. Assessment of damage in mountain tunnels due to the Taiwan Chi-Chi earthquake. *Tunneling and Underground Space Technology* 16(3):133–50.

Wang, Z.Z. & Zhang, Z. 2013. Seismic damage classification and risk assessment of mountain tunnels with a validation for the 2008 Wenchuan earthquake. *Soil Dynamics and Earthquake Engineering* 45: 45–55.

Yakovlevich, D.I. & Borisovna, M.J. 1978. Behavior of tunnel liner model on seismic platform. *Symposium on earthquake engineering*. University of Roorkee. Oct. 5–7, 1:379–382.

Yousser, M.A. Hashash et al. 2001. Seismic design and analysis of underground structures. *Tunnelling and Underground Space Technology* 16: 247–293.

*Rock Dynamics: From Research to Engineering – Li et al. (Eds)*
*© 2016 Taylor & Francis Group, London, ISBN 978-1-138-02953-8*

# Full field strain statistics and failure mechanism of granite under dynamic and quasi-static compression

L.J. Zhou, S.L. Xu & C.Y. Shi
*CAS key Laboratory for Mechanical Behavior and Design of Materials, University of Science and Technology of China, Hefei, Anhui, China*

ABSTRACT: Experiments of granite under dynamic compression at strain rate 42/s, 65/s and 84/s with a Split Hopkinson Pressure Bar (SHPB) system are conducted in the present paper. Quasi-static test at strain rate $3 \times 10^{-5}$/s is performed with Material Testing System (MTS) for reference of specimen at low strain rate. A high speed camera and a Charge Coupled Device (CCD) are employed in dynamic and quasi-static tests respectively for images acquirement of specimen surfaces. Digital Image Correlation (DIC) method is applied to the images shot in the compression process for the quantitative full-field transverse normal strain measurement on surface of specimen. Color maps of strain field show the strain localized on regions where cracks concentrate. Statistics on strain filed exhibit a typical Weibull distribution. According to different features in strain distribution, the compression process is divided into three stages which coincide with the stages of cracks nucleation, interaction and breaking through specimen leading to failure, respectively. Evolution of Weibull parameters for strain field indicates the strain rate effects on the crack propagation and failure mechanism of granite.

## 1 INTRODUCTION

Brittle rocks such as granite, marble and sandstone consist of mineral grains with multiple species and sizes, and contain microscopic pores and cracks. Therefore, great heterogeneity of internal structure exists in brittle rocks, and the deformation is heterogeneous for brittle rocks. Tensile microscopic cracks nucleation, interaction and coalesce to macroscopic cracks is the main failure mechanism for brittle rocks subjected to compression (Tapponier & Brace 1976). The mechanical behaviors of brittle rocks have been substantially investigated at different strain rates (Frew et al. 2001, Zhang et al. 2000), varying from quasi-static to dynamic conditions. Significant strain rate effects are shown in brittle rocks. However, deformation of specimen is acquired indirectly from traditional methods such as strain gauges and mechanical extensometers. These measurements are not sufficiently accurate for the slight strain of brittle rocks. Moreover, the mesoscopic local strain is impossible to observe since only global deformation can be measured by traditional methods. Thus, investigations on strain rate effects and failure mechanism of brittle rocks are far from plenty.

As a non-contact strain measurement technique, Digital Image Correlation (DIC) method is of great concerns in recent years (Zhang & Zhao 2013, Chen et al. 2014). Compared with traditional method, DIC can measure the full-field strain with simple devices and operations. The heterogeneity in microscopic distribution of cracks (Bai et al. 1992, Wong et al. 2006) and force (Lan et al. 2010) inside brittle materials have been appreciably investigated. Nonetheless, heterogeneous strain distribution of strain field has not been studied quantitatively.

In the present study, dynamic compression tests on granite materials of various strain rates are conducted by SHPB with high speed camera, and quasi-static compression test is con-

ducted by MTS with Charge Coupled Device (CCD). All the specimens are sprayed to make speckle patterns. Through DIC method, transverse normal strain field on surface of granite specimen is calculated, and mapped by colors. Statistics on strain field are conducted, and fitted by Weibull distribution. Strain rate effects on cracks growth and failure mechanism of granite are also interpreted by evolution of Weibull parameters.

## 2 EXPERIMENTAL SETUP

### 2.1 *Granite specimen*

The fine-grained granite from Shandong province, China is adopted as the test material. The granite mainly consists of quartz, feldspar and mica. The specimens are manufactured into cuboid bulk for observation. Draw ratio of the specimen must fall in the range of 0.5~1.0 to guarantee the stress equilibrium in specimen subjected to stress pulse propagation (Olsson 2001). Size of the specimen is chosen to be 25 mm × 25 × mm × 20 mm. Surfaces of the specimens are all polished for smoothness, and sprayed with manual speckles.

### 2.2 *Dynamic test*

Dynamic compression loading tests at strain rate 42/s, 65/s and 84/s are conducted with the SHPB setup in conjunction with a high speed camera, and the schematic diagram of the system is shown in Figure 1.

Loading direction is along the $x$ axis. The striker, the incident bar and the transmission bar are all made of aluminum with the diameter of 37 mm, and lengths of 300 mm, 2000 mm and 2000 mm, respectively. High speed camera (Phantom V12.1) is employed to take snapshots of specimen surface during compression. Shooting direction is along the $z$ axis. In the present study, pixels array size of the view field is set at 256 × 256, and frame interval is set at 14 μs. Region for the specimen surface is inside the view field, and should be cut out from the snapshot. Images of the specimen surfaces, which have the common resolution of 240 × 208 pixels, will be calculated by the algorithm of DIC method written by MATLAB to obtain the strain field on surface of granite specimen.

### 2.3 *Quasi-static test*

Quasi-static compression test at strain rate of $3 \times 10^{-5}$/s is performed with the Material Test System (MTS), and the test system is shown in Figure 2. Images are perceived by the Charge Coupled Device (CCD). Resolution of the view field is 1280 × 960 pixels, and the region for surface of specimen is cut out which owns the resolution of 646 × 520 pixels. The frame interval is 1 s. Data processing method of quasi-static compression test was the same with dynamic condition.

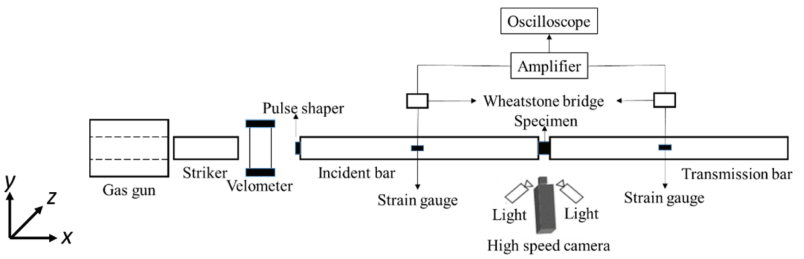


Figure 1. Schematic diagram of the dynamic compression loading setup.

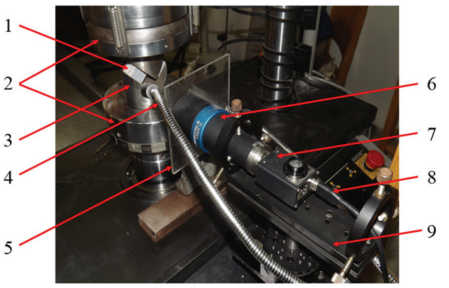


Figure 2. Quasi-static loading tests system. (1) Specimen. (2) Compression bulk on MTS. (3) Cushions. (4) Cold light. (5) Lucite plate. (6) Telecentric lens. (7) Charge coupled device (CCD). (8) Data line. (9) Base of the image acquisition setups.

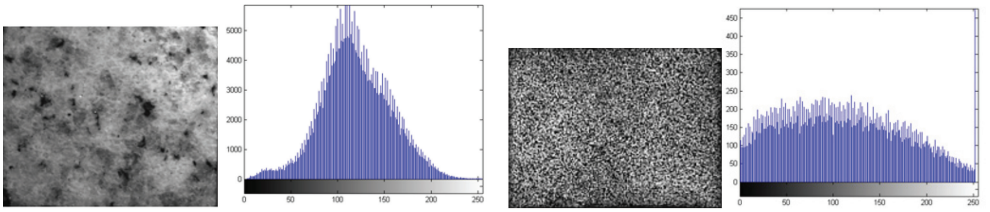


Figure 3. Comparison of natural and manual speckle patterns. (a) Natural speckle patterns. (b) Histogram of natural speckle patterns. (c) Manual speckle patterns. (d) Histogram of manual speckle patterns.

## 3 MANUAL SPECKLES

Quality of speckle patterns is judged by the mean gray level intensity (Pan et al. 2010), which is expressed as:

$$\delta_f = \frac{\sum_{i=1}^{W}\sum_{j=1}^{H}\sqrt{f_x(x_i,y_j)^2 + f_y(x_i,y_j)^2}}{W \times H} \tag{1}$$

where $W$ and $H$ are the width and height of the speckle patterns field respectively, $f_x(x_i, y_i)$ and $f_y(x_i, y_i)$ are the gray level intensity derivative of $x$ and $y$ at point $(x_i, y_i)$ respectively. Natural rock materials have natural speckle patterns fields on surfaces, as shown in Figure 3 (a). Figure 3 (b) is the histogram of gray level intensity distribution, and $\delta_f$ is calculated to be a small value at 7.7. In the present study, speckle patterns are set manually by spray paint on granite specimen surface, as shown in Figure 3 (c). The histogram shown in Figure 3 (d) indicate that the gray level intensity of manual speckle patterns is widely distributed, and $\delta_f$ is calculated to be 57.7 which is remarkably lager than the value of natural speckle patterns. With respect to natural speckle patterns, speckle patterns sprayed manually is of obvious advantages.

## 4 QUANTITATIVE CHARACTERIZATION OF STRAIN FIELD ON GRANITE

### 4.1 *Strain distribution under dynamic and quasi-static compression*

Figure 4(a) shows the stress-time curve of granite specimen under dynamic compression at strain rate 42/s. Red points on the curve indicate instants of snapshots taken by high speed camera every 14 μs, which are partly shown in Figure 4(c). DIC analyses are carried out

between adjacent images to obtain the incremental strain fields. And strain field at a specific red point is derived by accumulation of incremental strain fields prior to this point.

In the present study, only transverse normal strain ($\varepsilon_{yy}$) field are taken into account. Since that the microstructure of rocks is primarily influenced by propagation of extensile cracks (Myer et al. 1992), and specimens tested under dynamic and quasi-static compression in our experiments all failed with cracks approximatively parallel to the axis of loading ($x$ axis). Color maps of transverse normal strain ($\varepsilon_{yy}$) field at several loading instants (red points circled out: 70 μs, 140 μs and 154 μs) are shown in Figure 4(d). It can be noted that the large amplitude eventually concentrated on local regions, especially on left and right sides of the strain field. Subsequently, several microscopic cracks located on these regions breaking through the specimen can be seen on the snapshot shown in Figure 4(b). And in the end the specimen catastrophically shattered into tiny fragments. The strain localization, which leads to failure of the granite specimen, may be primarily attributed to the microscopic heterogeneity of brittle rock (Bai et al. 1992, Wong et al. 2006, Lan et al. 2010).

To verify this hypothesis, transverse normal strain ($\varepsilon_{yy}$) at all calculation points were equally grouped into 20 intervals, and the proportion of each interval was obtained (each interval was represented by the mean value). The proportion distributions of strain intervals at every loading instant all exhibit a typical Weibull distribution feature (Weibull 1951). This characteristic has been observed from the fracture probability related to the crack size distribution of marble (Wong et al. 2006), and from the distribution of number density of micro-cracks in aluminum under impact loading (Bai et al. 1992).

The entire strain values are fitted by Weibull probability density function using MATLAB. To derive the Weibull distribution of strain interval proportion, the Weibull probability density function was multiplied by the length of interval (($\varepsilon_{yy\,max} - \varepsilon_{yy\,min}$)/20). Then the distribution can be expressed as

$$p(\varepsilon) = \frac{\varepsilon_{yy_\max} - \varepsilon_{yy_\min}}{20} \frac{k}{\lambda}\left(\frac{\varepsilon_{yy}}{\lambda}\right)^{k-1} \exp\left(-\left(\frac{\varepsilon_{yy} - \varepsilon_{yy_\min}}{\lambda}\right)^{k}\right) \tag{2}$$

where $\lambda$ and $k$ are Weibull parameters. Strain interval proportion and the corresponding Weibull distribution curves are presented in Figure 4(b). The parameter $k$, which is referred to as Weibull modulus, implies the homogeneity of strain distribution.

On the basis of the strain distribution, dynamic loading process of the granite specimen can be divided into three stages as sited on the stress-time curve in Figure 4(a), which corresponds to the four periods during compression process of granite (Xu et al. 2015). The first stage is composed of compaction and quasi-linear compression, while the strain field is of great homogeneity as shown in loading instant 70 μs of Figure 4(e). Nucleation of micro cracks (Bai et al. 1992) is proved in this stage. The second stage is non-linear stage, while the strain distribution proves bimodal feature as shown in loading instant 140 μs of Figure 4(e). This feature is observed by Lan et al. (2010) in distribution of normal contact stress between grains set in a granite model. In this stage, strain localization can be noted apparently, which may be caused by the interaction and coalescence of micro cracks. The third stage is failure stage, while macro cracks form and break through the entire specimen. The strain distribution transforms into Weibull distribution of low Weibull modulus with high heterogeneity as shown in loading instant 154 μs of Figure 4(e).

Strain field for quasi-static test at strain rate $3 \times 10^{-5}$ was calculated with a snapshot interval 50 s for comparison to dynamic conditions. Localized strain also propagates and evolves on upper left of the observing surface. However, strain localization concentrates on a single region in quasi-static condition as shown in Figure 5(d). Hence only one macroscopic crack breaks through the specimen and leads to failure, which can be seen in Figure 5(b). The specimen finally spalls into columnar fragments along the direction parallel to the axis of loading ($x$ axis). Figure 5(e) indicates that there is no bimodal feature exhibited in stage 2 of the quasi-static compression process. And the Weibull distribution shows higher heterogeneity in stage 3 compared to dynamic condition.

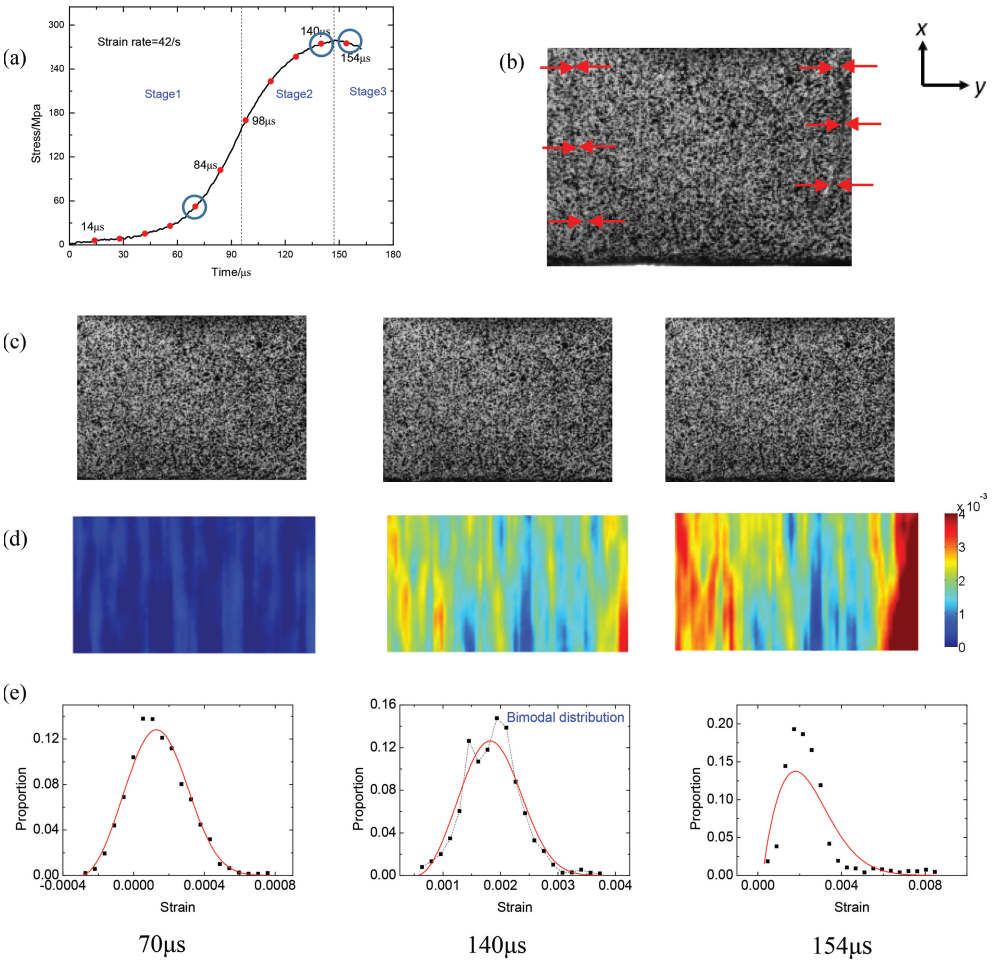


Figure 4. Dynamic compression process of granite specimen at strain rate 42/s. (a) Stress-time curve. (b) Fail specimen with macroscopic cracks. (c) Snapshots of the specimen at several loading instants: 70 μs, 140 μs and 154 μs. (d) Color maps of transverse normal strain ($\varepsilon_{yy}$) field. (e) Strain distribution at several loading instants.

The distinction between size of fragments of the granite specimens, as well as strain distribution features in the stages for micro cracks propagating and macro cracks forming (corresponding to stage 2 and 3 sited on stress-time curves) subjected to dynamic and quasi-static compression, both reveal that the strain rate effect exists in failure mechanism of granite.

### 4.2 *Effects of strain rate on failure mechanism*

Evolution of the distribution parameters can directly reflect the evolution of cracks which leads to failure of the specimen. The Weibull modulus $k$, which refers to the homogeneity of strain field, is summarized in Figure 6. The initial Weibull modulus, and falls in the range of 2.88 to 4.00. The range is close to that of micro crack statistics for marbles without loading, which is 2.03 to 3.29 (Wong et al. 2006). This correspondence indicates that the distribution on strain field is controlled by micro structure inside the rock materials once again. Evolution of Weibull modulus on strain fields subjected to dynamic compression is approximately horizontal, while that for quasi-static compression is significantly going down. Decrease of the Weibull modulus over compression stress means a more heterogeneous strain distribution on

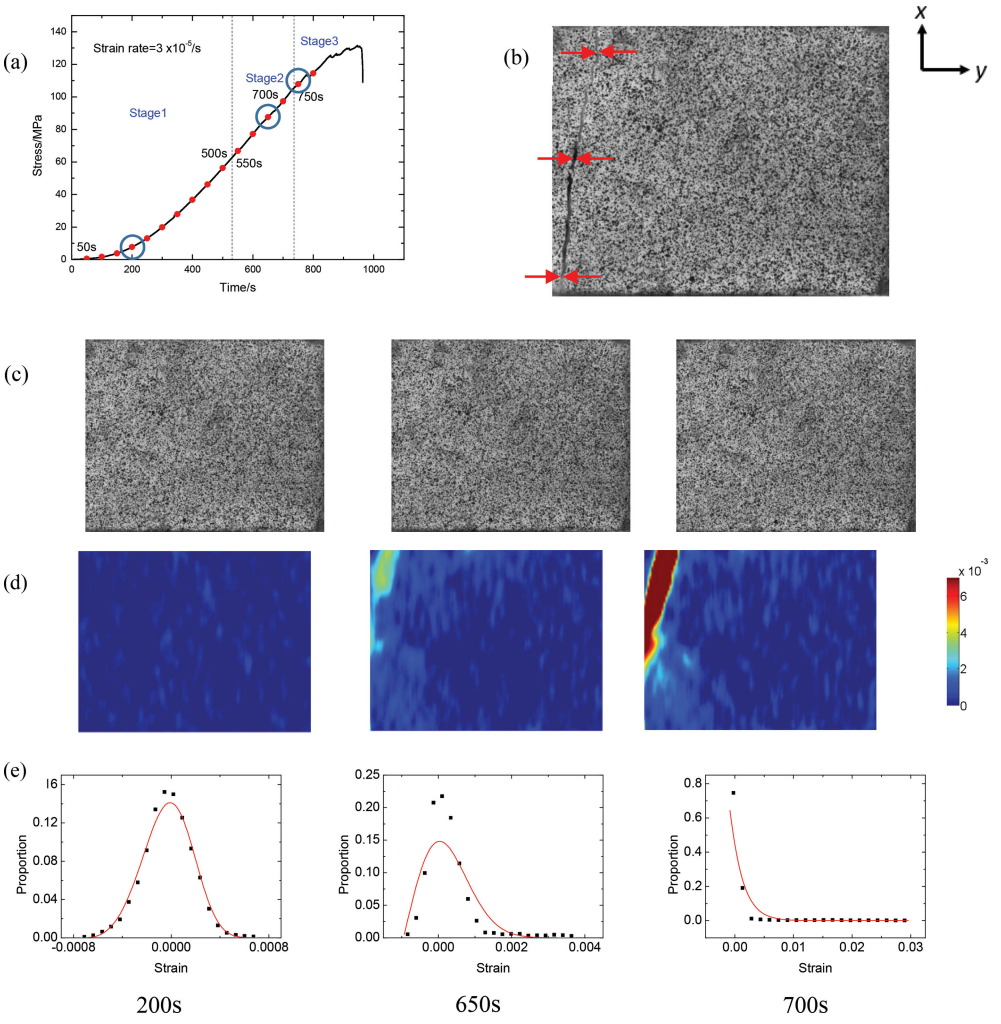


Figure 5. Quasi-static compression process of granite specimen at strain rate $3 \times 10^{-5}$/s. (a) Stress-time curve. (b) Fail specimen with macroscopic cracks. (c) Snapshots of the specimen at several loading instants: 200 s, 650 s and 750 s. (d) Color maps of transverse normal strain ($\varepsilon_{yy}$) field. (e) Strain distribution at several loading instants.

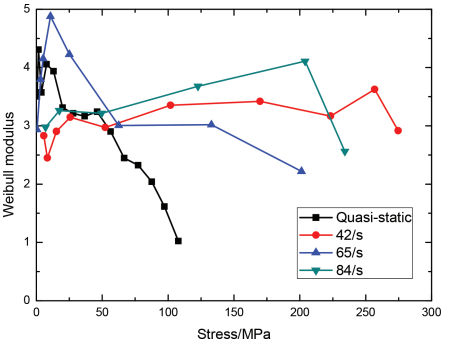


Figure 6. Evolution of Weibull modulus.

strain field subjected to quasi-static compression, comparing to the dynamic compression. That is, a significantly higher proportion of the larger strain is achieved in dynamic strain field at stage 2 of compression process than the quasi-static condition. As to the inherent structure reflecting by strain field on surface of specimen, the quantity of cracks forming by coalescence of micro cracks subjected to dynamic compression is significantly greater. Failure of this specimen may be induced by a small amount of predominant cracks form during the compression subjected to quasi-static compression. This distinction in quantity of cracks may interpret the phenomenon that the crushing extent of specimen under dynamic compression is significantly higher than the specimen under compression.

## 5 CONCLUSIONS

In the present study, cuboid granite specimens are tested under dynamic compression at three various strain rate of 42/s, 65/s and 84/s. And a quasi-static test at strain rate of $3 \times 10^{-5}$/s is conducted for comparison. Images of surface sprayed with manual speckle patterns on the specimens are shot, and strain field of surface is computed by the DIC method. The strain field is mapped by colors, and strain localization is clearly shown on the color map. Strain distribution of the strain field is counted. The strain distribution exhibits typical Weibull features, and a four-parameter Weibull distribution function is employed for strain field statistics. Evolution of the Weibull distribution parameters over compression process reveals the strain rate effects on failure mechanism of granite. Cracks forming in granite are more widely distributed under dynamic compression. This strain rate effects verified the different patterns of fragments of failure granite specimens subjected to dynamic and quasi-static compression.

## ACKNOWLEDGEMENTS

This work is supported by the National Natural Science foundation of China (Grant Nos: 11272304, 11472264).

## REFERENCES

Bai, Y., Ling, Z., Luo, L. et al. 1992. Initial development of microdamage under impact loading. *Journal of Applied Mechanics* 59(3): 622–627.

Chen, J., Guo, B., Liu, H. et al. 2014. Dynamic brazilian test of brittle materials using the split Hopkinson pressure bar and digital image correlation. *Strain* 50(6): 563–570.

Frew, D., Forrestal, M., Chen, W. 2001. A split Hopkinson pressure bar technique to determine compressive stress-strain data for rock materials. *Experimental Mechanics* 41(1): 40–46.

Huang, J., Lu, L., Fan, D. et al. 2016. Heterogeneity in deformation of granular ceramics under dynamic loading. *Scripta Materialia* 111: 114–118.

Lan, H., Martin, C.D., Hu, B. 2010. Effect of heterogeneity of brittle rock on micromechanical extensile behavior during compression loading. *Journal of Geophysical Research: Solid Earth* (1978–2012), 115(B1).

Lecompte, D., Smits, A., Bossuyt, S. et al. 2006. Quality assessment of speckle patterns for digital image correlation. *Optics and lasers in Engineering* 44(11): 1132–1145.

Myer, L.R., Kemeny, J.M., Zheng, Z. et al. 1992. Extensile cracking in porous rock under differential compressive stress. *Applied Mechanics Reviews* 45(8): 263–280.

Olsson, W. 2001. Quasistatic propagation of compaction fronts in porous rock. *Mechanics of Materials* 33: 659–668.

Pan, B., Wu, D., Xia, Y. 2010. Study of speckle pattern quality assessment used in digital image correlation. *Chinese Journal of Experimental Mechanics* 2: 120–129 (in Chinese).

Tapponnier, P., Brace, W.F. 1976. Development of stress-induced microcracks in Westerly granite. *International Journal of Rock Mechanics and Mining Sciences & Geomechanics Abstracts* 13(4): 103–112.

Wong, T., Wong, R., Chau, K. et al. 2006. Microcrack statistics, Weibull distribution and micromechanical modeling of compressive failure in rock. *Mechanics of Materials* 38(7): 664–681.
Weibull, W. 1951. A statistical distribution function of wide applicability. *J. Appl. Mech. 1*8: 293–297.
Xu, S., Huang, J., Wang, P. et al. 2015. Investigation of rock material under combined compression and shear dynamic loading: An experimental technique. *International Journal of Impact Engineering* 86: 206–222.
Zhang, C. 2014. *Application of Digital Image Correlation in Dynamic Testing*. Hefei: University of Science and Technology of China (in Chinese).
Zhang, Q.B., Zhao, J. 2013. Determination of mechanical properties and full-field strain measurements of rock material under dynamic loads. *International Journal of Rock Mechanics and Mining Sciences* 60: 423–439.
Zhang, Q.B., Zhao, J. 2014. A review of dynamic experimental techniques and mechanical behaviour of rock materials. *Rock Mechanics and Rock Engineering* 47(4): 1411–1478.
Zhang, Z.X., Kou, S.Q., Yu, J. et al. 1999. Effects of loading rate on rock fracture. *International Journal of Rock Mechanics and Mining Sciences* 36(5): 597–611.

*Rock Dynamics: From Research to Engineering – Li et al. (Eds)*
*© 2016 Taylor & Francis Group, London, ISBN 978-1-138-02953-8*

# Application of 3D printing and micro-CT scan to rock dynamics

T. Zhou
*Department of Civil and Environmental Engineering, The Hong Kong Polytechnic University, Hong Kong SAR*

J.B. Zhu
*Department of Civil and Environmental Engineering, The Hong Kong Polytechnic University, Hong Kong SAR*
*State Key Laboratory of Hydraulic Engineering Simulation and Safety, School of Civil Engineering, Tianjin University, Tianjin, China*

ABSTRACT: In this work, a translucent resin material produced by three-dimensional printing (3DP) technology was used to mimic volcanic rock. 3DP, micro-CT scan and 3D reconstruction technologies were employed to transform the digital rock cores into physical rock models. Dynamic compressive and Brazilian disc tests were performed on the Split Hopkinson Pressure Bar (SHPB) system to study its dynamic behaviours. The experimental results indicate that the strength properties and pre-peak stress-time curve of the 3DP models agree well with those of the rock samples. Fracturing process and failure pattern of the 3DP Brazilian disc are also similar to the rock sample. The innovative approach of incorporating micro-CT scanning and 3DP technology provides insight into studying dynamic behaviours of rock materials.

*Keywords*: 3DP; Micro-CT scan; 3D reconstruction; Rock dynamics; SHPB

## 1 INTRODUCTION

Rock is a heterogeneous material, containing numerous weak planes and internal flaws such as voids, inclusions, joints and weak surfaces, etc. Under external loading, micro-cracks often nucleate and propagate along these pre-existing defects, and ultimately leading to unstable failure of rock. Therefore, precise investigation of the defects and accurate characterization of failure mechanism of rock materials are of crucial importance in rock mechanics and rock engineering.

Up to now, numerous experimental investigations have been performed to study failure mechanisms of brittle rock materials. However, most of them were based on rock-like materials such as curing gypsum and cementing plaster (Wong & Einstein 2009, Wong & Chau 1998) or PMMA (Dyskin et al. 2003, Germanovich et al. 1994). Specimens fabricated by these materials are generally considered to be homogeneous which is obviously differing from the natural rock materials. Moreover, the rock-like materials can neither produce internal defects identical to those of the natural rock nor assist to visualize the internal cracks growth. It is, therefore, of great significance to develop new technologies and materials, which could solve the aforementioned drawbacks, to study failure mechanisms of rock materials.

Three-dimensional printing (3DP), also termed as Rapid Prototyping (RP), is defined as the process of joining materials, usually layer upon layer, to fabricate objects from three-dimensional graphical data. It is a computer-aided design and manufacturing process and almost has no restrictions on geometrical shapes (Yan & Gu 1996). It has advantages over traditional means in precise fabrication, fast and flexible preparation, high repeatability, and visibility and some specific applications such as preparation of internal defects. Due to these benefits, 3DP has, recently, been widely applied in biomedicine (Wu et al. 2011), aerospace (Rochus et al. 2007), construction (Buswell et al. 2007) and soil science (Otten et al. 2012), etc.

However, studies of applying 3DP in rock mechanics are extremely limited. Recently, Jiang & Zhao (2015) explored the potential application of 3DP for rock mechanics. They printed samples with polylactic acid (PLA) on a "3D Touch" printer which applied Fused Deposition Modeling (FDM) technology. However, it is difficult for PLA to well mimic rock due to its elastoplastic deformational behavior (Jiang & Zhao 2015). Fereshtenejad & Song (2016) studied the applicability of powder-based 3DP for physical modeling in rock mechanics. They found that increasing binder saturation and heating samples at 150ºC for about an hour could significantly enhance the strength of the powder-based 3DP samples. Jiang et al. (2015) also conducted tentative experiments on powder-based 3DP specimens to investigate the serviceability of printed specimens as substitutes for natural rock specimens in experimental deformation and failure studies. Nevertheless, the 3DP materials in these studies are opaque, and hence, it is impossible to visualize and study the internal defects.

In this study, translucent resin (Accura® 60) produced via Stereolithography (SLA) technology was selected to mimic volcanic rock after trying many different 3DP materials. Micro-CT scan, 3D reconstruction and SLA 3DP technologies were together used to transform the 3D digital rock core into 3DP samples whose complex inner structure is almost identical to that of the natural volcanic rock specimen. Dynamic compressive and Brazilian disc tests were, subsequently, performed with the Split Hopkinson Pressure Bar (SHPB) system to apply 3DP to rock dynamics.

## 2 3DP OF SAMPLE

### 2.1 *Micro-CT scanner*

An X-ray Micro-CT XRM 500 scanner was used to accurately extract the internal structure of the rock sample. The voltage of X-ray light source is 160 kV and its exposure time is 18 s. The maximum scanning range is 50 × 50 mm, and the corresponding pixel of its charge coupled device is 2000 × 2000. During scanning, the sample was positioned perpendicular to the scanning direction. In order to match the printing resolution of the 3D printer (50 um), the spatial resolution of the X-ray micro-CT scanner was also set to 50 um. As an example, Figure 2b shows four pieces of micro-CT images of the volcanic rock, in which the black colour represents cracks and voids, while the white and grey colours represent mineral grains.

### 2.2 *3D printer*

In this study, the SLA Viper si$^2$ was employed to produce the 3DP resin samples (as shown in Figure 2e and f). The printer has a maximum build envelope in standard mode of 250 × 250 × 250 mm (XYZ), and its theoretical resolution in vertical can be up to 2.5 um. However, in order to balance the printing resolution and time, vertical resolution (layer thickness) was set to 50 um in the present work. The wavelength of the laser is 354.7 nm. During printing, the laser beam traces a cross-section of the part pattern on the surface of the photopolymer resin. As photopolymer is photosensitive to laser beam, the resin is solidified and a single layer of the desired project is created. The advantages of the SLA Viper si$^2$ include smooth surface finishing, excellent optical clarity, high accuracy and excellent fine feature detail that require minimal finishing (3D Systems 2003).

### 2.3 *3DP material*

Accura® 60, a photopolymer resin, was selected as the printing material. It is a translucent material with a solid density of 1.21 g/cm$^3$. Although the pure solidified resin material exhibits elastoplastic mechanical property, we found that after some targeted treatments, the 3DP resin material became brittle. For example, after freezing to –73.5°C (dry ice treatment) or printing with an internal square crack, the 3DP resin sample becomes brittle, deforms without barrelling and splits into banded fragments at the peak stress. Figure 1 shows the fragments of 3DP

samples with targeted treatments. Therefore, it is believed that the translucent resin material printed by SLA technology can well mimic rocks with relatively large porosity or defects.

In this study, Hainan volcanic rock was used to construct 3D digital rock cores for the following 3DP. The basic mechanical properties of the volcanic rock are listed in Table 1, in which the mechanical parameters $\sigma_c$ and $\sigma_t$ are static uniaxial compressive strength and tensile strength, respectively.

Figure 2 shows the workflow of producing 3DP rock model. First, the natural volcanic rock samples were well prepared according to the ISRM recommended standard (Zhou et al. 2012).

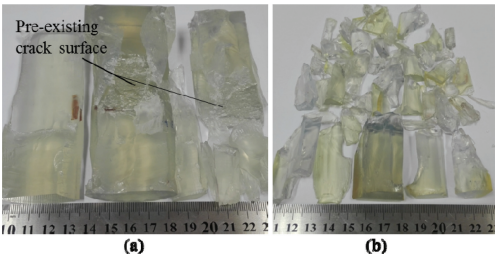


Figure 1. Fragments of 3DP resin samples with special treatments. (a) 3DP resin sample with single pre-existing square crack; (b) intact 3DP resin sample froze by dry ice (–73.5°C).

Table 1. Mechanical properties of the volcanic rock.

| $\sigma_c$ (MPa) | $\sigma_t$ (MPa) | $E$ (GPa) | $v$ | Density (g/cm$^3$) | Porosity |
|---|---|---|---|---|---|
| 81.3 | 7.1 | 40.1 | 0.24 | 2.6 | 7.2% |

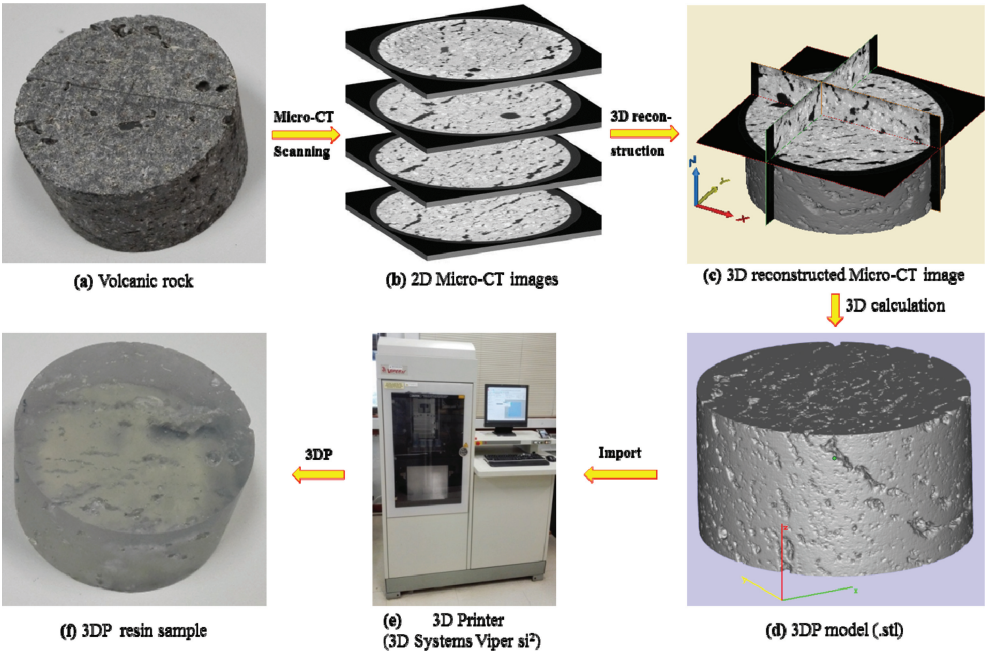


Figure 2. Workflow of printing resin sample. (a) Step 1: prepare rock sample; (b) Step 2: Micro-CT scanning the rock sample; (c) Step 3: reconstruct 3D Micro-CT image from 2D Micro-CT images; (d) Step 4: generate 3DP model (.stl) with MIMICS software; (e) Step 5: print the volcanic rock model layer by layer with Viper si$^2$; (f) Step 6: 3DP resin sample.

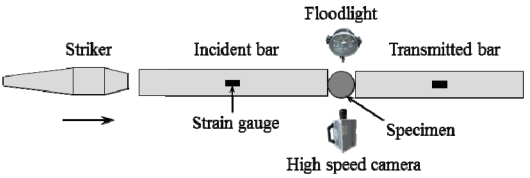


Figure 3. The schematic of SHPB system.

Then, the X-ray Micro-CT XRM 500 scanner was used to scan the sample layer by layer. After scanning, the commercial MIMICS software was used to reconstruct the 3D digital rock core from 2D micro-CT images. It should be noted that the segmentation of the voids (cracks) from the 2D micro-CT images should be carefully operated, because it significantly affects the accuracy of inner structure of the reconstructed 3D digital rock core. Finally, the data of 3D digital rock core was imported into the Viper si$^2$ 3D printer, which produced the 3DP resin sample according to the printing parameters such as printing path, layer thickness, and laser irradiation time.

## 3 SHPB TESTS

Dynamic tests were performed with the Split Hopkinson Pressure Bar (SHPB) system. It consists of a cone-shaped striker (0.36 m in length), an incident bar (2 m in length) and a transmitted bar (1.5 m in length) as shown in Figure 3. The diameter and elastic modulus of the elastic bars are 50 mm and 240 GPa, respectively. During the test, the rock and 3DP specimens were sandwiched between the incident and transmitted bars.

For dynamic Brazilian disc tests, the dynamic tensile strength $\sigma_{dt}$ can be expressed as:

$$\sigma_{dt} = \frac{2P}{\pi DT} \tag{1}$$

where $P$ is the maximum force of the transmitted pulse, $D$ and $T$ are the diameter and thickness of the sample, respectively.

In this study, a High-Speed (HS) camera (FASTCAM SA1.1) was used to monitor the dynamic fracturing process of the samples. In order to balance the image resolution and the frame rate, a frame rate of 100,000 frames per second was chosen.

## 4 RESULTS

Figure 4 illustrates the dynamic stress-time curves of the volcanic rocks and the corresponding 3DP resin samples. Although the post-peak dynamic stress evolution of the 3DP samples are different from that of real rocks, the dynamic compressive and tensile strengths as well as the pre-peak stress-time behavior agree well with those of the volcanic rocks. It indicates that the 3DP resin can well mimic the mechanical properties of the present rock.

Figure 5 presents the dynamic fracturing process of the volcanic rock samples and the 3DP resin samples. In general, the fracturing process and failure pattern of 3DP samples are similar with those of natural volcanic rocks. The crack development in 3DP resin samples was much slower than that of volcanic samples. It is mainly due to the large elastic deformation at the beginning of the loading stage. Therefore, the fracturing process of the 3DP resin samples was delayed significantly and the whole failure process was also prolonged. This also explains why the post-peak dynamic stress of the 3DP samples dropped slowly. It can be seen from Figure 5(b) and (d) that new cracks nucleated and propagated within the 3DP resin samples, and ultimately leading to the sample failure. It indicates that the approach of incorporating micro-CT scanning and 3DP technology can provide insight into studying dynamic fracture and failure behaviours of rock materials.

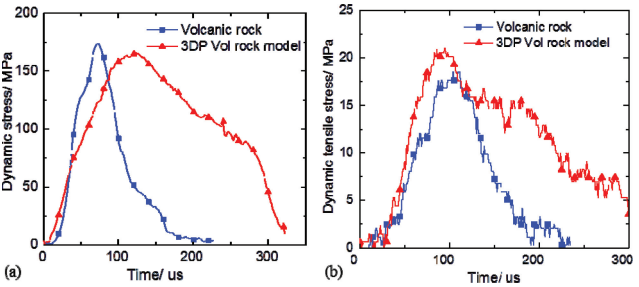


Figure 4. Results of dynamic stress-time curves. (a) dynamic compressive stress-time curves, (b) dynamic tensile stress-time curves.

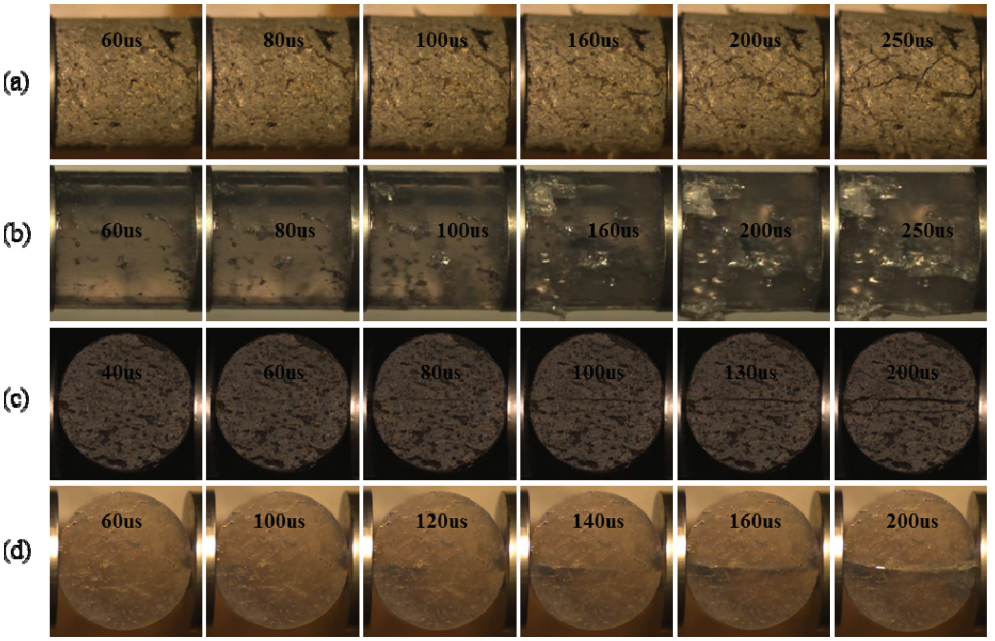


Figure 5. Dynamic fracturing process of rock and 3DP samples. (a) fracturing process of volcanic rock under compression, (b) fracturing process of 3DP resin sample under compression, (c) fracturing process of Brazilian disc of volcanic rock, (d) fracturing process of Brazilian disc of 3DP resin sample.

## 5 DISCUSSION AND CONCLUSIONS

In this study, dynamic tests have been carried out to apply 3DP and micro-CT scan to rock dynamics. Based on the experimental results, the following conclusions can be drawn:

1. Combining with high resolution micro-CT scanning and 3D reconstruction technologies, SLA 3D printers can produce rock models whose internal structures are almost identical to those of the natural rock specimens.
2. The dynamic compressive and tensile strengths as well as the pre-peak stress-time curve of the 3DP resin samples agree well with those of the volcanic rocks, which confirm the feasibility and validity of using 3DP and micro-CT scan to study rock dynamics.
3. With the aid of micro-CT scan, the SLA 3DP provides insight into studying dynamic fracture and failure behaviours of rock.

However, it should be pointed out that the observation of internal fracturing process under compression was not excellent in the present test. This may be attributed to several factors, among which the curved and imperfect polishing surface as well as inappropriate lighting condition might be dominant. Therefore, prismatic 3DP samples with relative small dimension are recommended in future tests, because the flat surface can not only improve the grinding and polishing accuracy but also enhance the quality of the high speed camera images. In addition, other than one, two high speed cameras are recommended to monitor the internal cracks growth from two orthogonal directions (the adjacent two surfaces) in order to observe and understand internal fracturing more clearly.

## REFERENCES


3D Systems 2003. Viper si2 manual.

Buswell, R.A., Soar, R., Gibb, A.G. & Thorpe, A. 2007. Freeform construction: mega-scale rapid manufacturing for construction. *Automation in Construction*, 16, 224–231.

Dyskin, A., Sahouryeh, E., Jewell, R., Joer, H. & Ustinov, K. 2003. Influence of shape and locations of initial 3-D cracks on their growth in uniaxial compression. *Engineering Fracture Mechanics*, 70, 2115–2136.

Fereshtenejad, S. & Song, J.-J. 2016. Fundamental study on applicability of powder-based 3D printer for physical modeling in rock mechanics. *Rock Mechanics and Rock Engineering*, 1–10.

Germanovich, L., Salganik, R., Dyskin, A. & Lee, K. 1994. Mechanisms of brittle fracture of rock with pre-existing cracks in compression. *Pure and Applied Geophysics*, 143, 117–149.

Jiang, C. & Zhao, G.-F. 2015. A preliminary study of 3D printing on rock mechanics. *Rock Mechanics and Rock Engineering*, 48, 1041–1050.

Jiang, Q., Feng, X., Song, L., Gong, Y., Zheng, H. & Cui, J. 2015. Modeling rock specimens through 3D printing-tentative experiments and prospects. *Acta Mechanica Sinica*, 1–11.

Otten, W., Pajor, R., Schmidt, S., Baveye, P.C., Hague, R. & Falconer, R.E. 2012. Combining X-ray CT and 3D printing technology to produce microcosms with replicable, complex pore geometries. *Soil Biology and Biochemistry*, 51, 53–55.

Rochus, P., Plesseria, J.-Y., Van Elsen, M., Kruth, J.-P., Carrus, R. & Dormal, T. 2007. New applications of rapid prototyping and rapid manufacturing (RP/RM) technologies for space instrumentation. *Acta Astronautica*, 61, 352–359.

Wong, L. & Einstein, H. 2009. Systematic evaluation of cracking behavior in specimens containing single flaws under uniaxial compression. *International Journal of Rock Mechanics and Mining Sciences*, 46, 239–249.

Wong, R.H. & Chau, K. 1998. Crack coalescence in a rock-like material containing two cracks. *International Journal of Rock Mechanics and Mining Sciences*, 35, 147–164.

Wu, C., Luo, Y., Cuniberti, G., Xiao, Y. & Gelinsky, M. 2011. Three-dimensional printing of hierarchical and tough mesoporous bioactive glass scaffolds with a controllable pore architecture, excellent mechanical strength and mineralization ability. *Acta biomaterialia*, 7, 2644–2650.

Yan, X. & Gu, P. 1996. A review of rapid prototyping technologies and systems. *Computer-Aided Design*, 28, 307–318.

Zhou, Y.X., Xia, K., Li, X.B., Li, H.B., Ma, G.W., Zhao, J., Zhou, Z.L. & Dai, F. 2012. Suggested methods for determining the dynamic strength parameters and mode-I fracture toughness of rock materials. *International Journal of Rock Mechanics and Mining Sciences*, 49, 105–112.

*Rock Dynamics: From Research to Engineering – Li et al. (Eds)*
*© 2016 Taylor & Francis Group, London, ISBN 978-1-138-02953-8*

# The effect of strain rate on compressive strength of water saturated sandstone

Z.L. Zhou, X. Cai, Y. Zhao, L. Chen & C. Xiong
*School of Resources and Safety Engineering, Central South University, Changsha, Hunan, P.R. China*

ABSTRACT: The strength of rock materials is largely affected by water, and the static properties have been widely studied before, while there is virtually no data for dynamic compressive strength of saturated rock at different strain rates. In order to comprehensively investigate the effect of water on the dynamic compressive strength of rock, the Split Hopkinson Pressure Bar technique was applied to conduct dynamic compressive tests on both dry and saturated sandstone specimens at a wide range of strain rates. The test results showed that the compressive strength of both dry and saturated sandstone specimens was rate dependent, and the compressive strength of saturated specimens had stronger rate dependence than that of dry specimens. The Water Affecting Factor (WAF), as the ratio of the strength under dry state over that under saturated state, was introduced to describe the effect of water on the compressive strength at different strain rates, the WAF under static condition was close to 1.38, and the WAF decreased with the increase of strain rate. When the strain rate reached 190/s, the WAF reduced to 0.98, i.e., the compressive strength of saturated specimens was higher than that of dry ones at that time.

## 1 INTRODUCTION

In rock engineering applications, the rock and rock mass are usually broken and failed induced by impact, explosion, rock burst and seismic events, where the strain rate involved is in the range of 10 to 103/s (Huang et al. 2011), so the dynamic mechanical properties of rock materials should be paid much attention. Meanwhile, many rock engineering applications are in humidity condition for a long time, the mechanical properties of rock are largely affected by water. It is accepted that the effect of water on compressive strength of rock is absolutely negative, which are responsible for landslides that occur after heavy rains and degradation of pillars in mining engineering. However, water injection was found to be effective in rockburst relief and prevention recently, which means that water may have some positive effects on the compressive strength of rock. Therefore, the investigation on the dynamic compressive strength affected by water under different strain rates is greatly meaningful to assess the stability of rock structure and control the hazard of rock engineering.

The static compressive strength of saturated rock materials has been widely studied, which is probably due to their direct practical relevance to rock engineering applications. Colback & Wild (1965) showed that the uniaxial compressive strength of well-saturated quartzitic sandstone could reduce up to 50%. Broch (1974) reported Unconfined Compressive Strength (UCS) reductions of 33–53% for phaneritic igneous and metamorphic rocks of low porosity (0.3–1.2%) from dry to saturation. Hawkins & Mcconnell (1992) investigated the influence of water content on the strength and deformability of 35 different British sandstone rocks and proposed an empirical relationship between water content and uniaxial compressive strength. Vasarhelyi (2005) also conducted a lot of experiments to investigate the effect of water saturation on the static properties of rocks and obtained the relationship between different perto-physical parameters. Li et al. (2012) accomplished a large amount of tests on two kinds of meta-sedimentary rock specimens (meta-siltstone and meta-sandstone) to investigate the

influence of water content on mechanical properties under triaxial compression, and found that when the state of rock specimen was changed to wet from dry, the peak cohesion increase about 3% while the friction angle decreased 26% for meta-siltstone; and the peak cohesion increased about 14% while the friction angle decreased 10% for meta-sandstone. From the above, it is commonly understood that the static compressive strength of fully saturated rock materials is usually smaller than that of dry ones.

However, all the results mentioned above are based on static tests, limited studies can be found on the dynamic properties of saturated rocks. In fact, the rock and rock mass are usually broken and failed dynamically in rock engineering applications, such as impact, explosion, rock burst and seismic events, thus the investigation on the dynamic compressive strength weakened by water is greatly meaningful to assess the stability of rock structure and control the hazard of rock engineering. To examine the effect of water on dynamic tensile strength, Ogata et al. (2004) conducted a series of SHPB experiments at high porosity sandstone in both dry and saturated state and claimed that water decreased dynamic tensile strength compared to what they were in the dry state. Huang et al. (2010) investigated the water-weakening effect on the tensile strength of Longyou sandstone with a wide range of loading rates, their experimental results demonstrated that the tensile strength of sandstone is water softening and the softening factor decreases with the increase of loading rate. Nevertheless, the dynamic compressive properties of saturated rock have hardly studied before, and the water-weakening mechanisms of rock under dynamic compression are not acceptable universally. Thus, more information about the effect of water on the dynamic properties of rocks at different strain rates should be investigated.

In this study, impact tests have been conducted on both dry and saturated sandstone specimens at a wide range of strain rates by means of the Split Hopkinson Pressure Bar (SHPB) setup, the strength with the same strain rate but different saturation states was compared, and the strain rate sensitivity of the compressive strength was also examined.

## 2 EXPERIMENTAL PROCEDURES

### 2.1 *Specimen preparation*

In this paper, all specimens were extracted from one sandstone block from Yunnan Province of China with high geometrical integrity and petro-graphic uniformity. They were manufactured in accordance with the standards in the ISRM suggested specification (Zhou et al. 2012). All specimens were cut into cylindrical shape with diameter of 50 mm and a length to diameter ratio of 1:1. The ends of specimens were polished to ensure the surface roughness less than 0.02 mm and the end surface was perpendicular to its axis less than 0.001 radians. After the measurement of the dimensions of all specimens, the P-wave velocities of all specimens were also measured to pick out specimens with similar velocity for the tests. Some physical properties of the sandstone were listed in Table 1.

### 2.2 *SHPB technique and its principle*

SHPB is a very popular and promising experimental technique for the study of dynamic behaviors of materials for its easy operation and relatively accurate results. Recently, it is improved and suggested as an ISRM method for dynamic tests of rock materials (Zhou et al. 2012).

As shown in Figure 1, the SHPB system, modified by Li et al. (2011), consists of a cone-shaped striker bar, an input bar, an output bar and an absorption bar, which are made of

Table 1. Summary of physical properties of the sandstone.

| Density kg·m$^{-3}$ | Porosity % | Saturated water content % | P-wave velocity m/s |
|---|---|---|---|
| 2337.5 | 6.2 | 3.5 | 2640.9 |

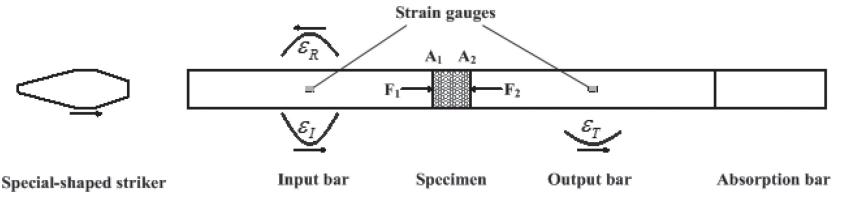


Figure 1. Configuration of the SHPB system.

high strength 40 Cr steel with a density of 7800 kg·m$^{-3}$, an elastic modulus of 250 GPa and a nominal yield strength of 800 MPa. The specimen is sandwiched between the input and output bars. To overcome the premature failure and provide more reliable guarantee for the stress equilibrium assumption, the striker with cone shape was used to produce half-sine waves in this study (Zhou et al. 2011).

During a test, the cone-shaped striker bar is shot out from the gas gun at high velocity and impacts the front end of the input bar. Then a half-sine wave (input wave) is generated and propagates along the input bar towards the specimen. Once the wave reaches the bar/specimen interface, a part of it is reflected, whilst the remaining part goes through the specimen and transmits into the output bar. By collecting signals on the input and output bars, the dynamic parameters of the specimen can be obtained.

In Figure 1, $A_1$ denotes the input bar/specimen interface and $A_2$ represents the specimen/output bar interface. $\varepsilon$ represents the measured signals on the bars, where the subscripts $I$, $R$ and $T$ represent incident, reflected and transmitted pulses respectively. The arrowheads show the direction of wave propagation. According to incident, reflected and transmitted waves signals, the relationship of the stress, strain and strain rate of the specimen can be derived as follows:

$$\sigma(t) = \frac{A_e E_e}{2A_s}[\varepsilon_I(t) + \varepsilon_R(t) + \varepsilon_T(t)] \tag{1}$$

$$\varepsilon(t) = \frac{C_e}{L_s}\int_0^t [\varepsilon_I(t) - \varepsilon_R(t) - \varepsilon_T(t)]dt \tag{2}$$

$$\dot{\varepsilon}(t) = \frac{C_e}{L_s}[\varepsilon_I(t) - \varepsilon_R(t) - \varepsilon_T(t)] \tag{3}$$

and the dynamic forces on the input bar/specimen interface ($F_1$) and the output bar/specimen interface ($F_2$) can be calculated:

$$F_1 = E_e A_e[\varepsilon_I(t) + \varepsilon_R(t)] \tag{4}$$

$$F_2 = E_e A_e \varepsilon_T(t) \tag{5}$$

where $A_e$ = cross-sectional area of elastic bars; $C_e$ = wave velocity of elastic bars; $E_e$ = Young's modulus of elastic bars; $A_s$ = cross-sectional area of specimen; and $L_s$ = length of the specimen.

### 2.3 *Experimental program*

A total of 60 specimens were prepared in dynamic compressive tests and separated into two groups: the specimens were in dry and saturated conditions. All specimens were placed in a 105°C oven long enough to reach the completely dry state, then the dry mass of the specimens were measured after they had cooled down to room temperature. After that, 30 specimens were selected and immersed into purified water within a airtight container

maintained in a vacuum environment for 48 hours, at this time, these specimens were thought to be completely saturated. After that, all prepared specimens were put into airtight plastic bags and stored in a room with constant temperature and relative humidity to avoid moisture loss.

As known, in SHPB dynamic test, the strain rates of specimen were mainly controlled by adjusting the gas pressure. To obtain the dynamic compressive strength of sandstone specimens with a wide range of strain rates, the two groups of specimens should be impacted under different gas pressures. Before formal tests, preliminary tests were conducted to determine the range of gas pressures. During the preliminary tests, we found that no obvious break damage occurred in the sandstone specimens until the gas pressure increased to 0.4 MPa, at that time, the specimen fractured into a number of large size fragments or only macro-cracks were generated, whereas the sandstone specimen was crushed into powder when the gas pressure was adjusted to 0.7 MPa. Considering the preliminary tests results and the research objective, the range of gas pressures were designed from 0.4 to 0.8 MPa for the dynamic compressive tests in this paper.

The dynamic compressive tests were conducted on all specimens. The test procedures were in accordance with the ISRM suggested methods (Zhou et al. 2012).

## 3 TEST RESULTS

### 3.1 *Dynamic stress equilibrium*

For a valid dynamic compressive test, the basic requirement is that the specimen could reach stress equilibrium before failure (Zhou et al., 2010). This can be checked by comparing the stresses at the two sides of specimen during the whole dynamic loading.

Figure 2 shows the stresses history for a typical dynamic compressive test, it can be seen that the curve of the sum of the incident and reflected waves almost overlaps with that of the transmitted wave. This indicates that $F_1$ and $F_2$ are nearly identical during the dynamic compressive test period. With this condition, the axial inertial effects are eliminated because there is no global force difference in the specimen to induce inertial force (Dai et al. 2010). In this study, the dynamic stress equilibrium on the both ends of all specimens is critically assessed.

### 3.2 *Determination of strain rate*

In dynamic tests, the strain rate was found to play an important role in control the strength of rock materials, i.e. the dynamic compressive strength of rock would markedly increase with the increase of strain rate (Zhang & Zhao 2013, Xia & Yao 2015). Hence, the dynamic compressive strength of rocks is comparable with similar strain rate. According to the method for determining the dynamic compressive strength of rock materials suggested by ISRM, the strain rate of specimen can be determined from the time evolution of strain rate (Zhou et al. 2012). Figure 3 illustrates a typical strain rate history calculated by formula (3) for a dynamic compressive test. It can be seen that there exists an approximately plat region of the curve with time from 54 to 68 μs before the failure point, the average value of the plat region can be defined as the strain rate of the specimen. In this study, the strain rates of all specimens in dynamic compressive tests were determined by this method.

### 3.3 *Compressive strength under different strain rates*

Figure 4 shows the compressive strength of dry and saturated specimens under different strain rates. The static tests have been conducted in our previous work. When the strain rate is higher than 70/s, the relationships between the dynamic compressive strength of dry and saturated specimens and the strain rates, which are plotted as two fitting curves in Figure 4, can be described by two polynomial formulas:

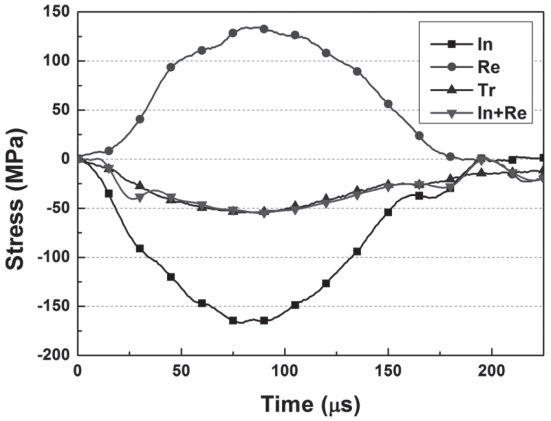


Figure 2. Dynamic stress equilibrium check for a typical dynamic compressive test (In: Incident wave, Re: Reflected wave, Tr: Transmitted wave).

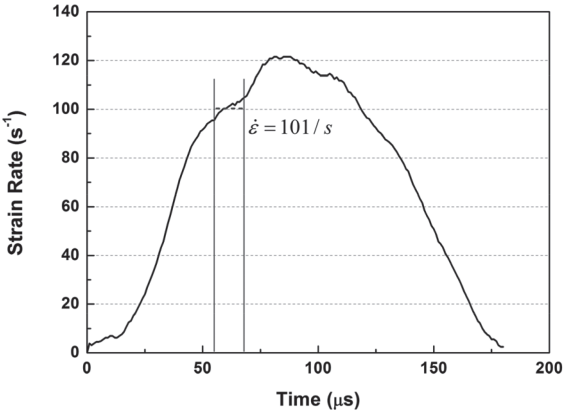


Figure 3. Determination of the strain rate for the dynamic compressive test.

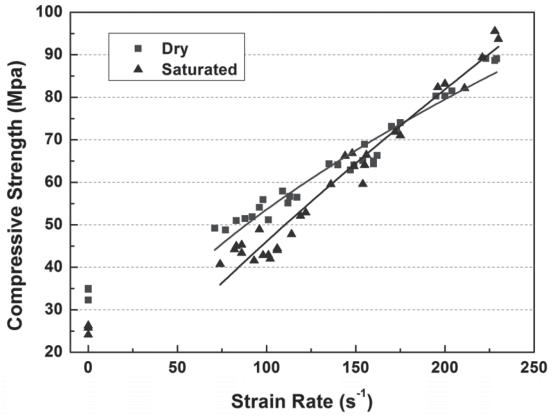


Figure 4. Variation of compressive strength versus strain rate.

$$\sigma_d(\dot{\varepsilon}) = 3.896\dot{\varepsilon}^{0.569}, R^2 = 0.946 \quad (6)$$

$$\sigma_w(\dot{\varepsilon}) = 1.013\dot{\varepsilon}^{0.829}, R^2 = 0.960 \quad (7)$$

where $\sigma_d$ = compressive strength of dry specimens; $\sigma_w$ = compressive strength of saturated specimens; $\dot{\varepsilon}$ = strain rate; and $R^2$ = variance.

It can be seen that the compressive strength of saturated specimen is obviously lower than that of dry specimen under static compressive test, and the difference value decreases with the increase of strain rate. When the strain rate reaches about 175/s, the compressive strength of dry and saturated specimen are close to equal. After that, the compressive strength of saturated specimen is higher than that of dry specimen.

### 3.4 *Dynamic increasing factor*

It also can be seen that the compressive strength of both the dry and saturated specimens are rate dependent from Figure 4 and Formulas (6)–(7), i.e. the compressive strength increases with the increase of strain rate. Thus, to quantify the rate dependence, the Dynamic Increasing Factor (DIF) under different strain rates is introduced to represent the effect of strain rate on the compressive strength of rock specimen. The DIF is defined as (Zhang & Zhao 2014):

$$S_d = \frac{\sigma_d^{\sim}}{\sigma_s} \quad (8)$$

where $S_d$ = DIF; $\sigma_d^{\sim}$ = dynamic compressive strength; and $\sigma_s$ = static compressive strength.

According to formulas (6)–(7), we pick both the dynamic compressive strength of dry and saturated specimens on the fitting curves at strain rates of 70, 90, 110, 130, 150, 170, 190, 210 and 230/s. Then, the DIFs under different strain rates are shown in Figure 5. It can be seen that the compressive strength of saturated specimen has higher rate dependence than that of dry one, and their difference is observed to increase with the increase of strain rate. For example, at strain rate of 90/s, the DIFs of dry and saturated sandstone specimens and the difference are 1.46, 1.68 and 0.22, respectively. While at the strain rate of 110/s, each of them increases to 1.63, 1.98 and 0.35.

### 3.5 *Water affecting factor*

According to Figure 4, at the same strain rate, the compressive strength of saturated specimen is obviously different from that of dry specimen because of water affecting. To quantify the water affecting effect, the Water Affecting Factor (WAF) is introduced to describe the

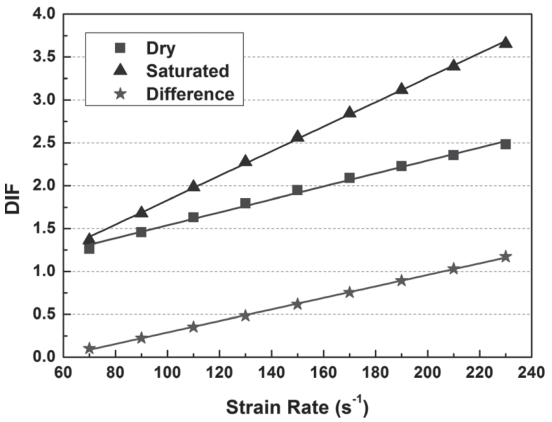


Figure 5. Variation of DIF versus strain rate.

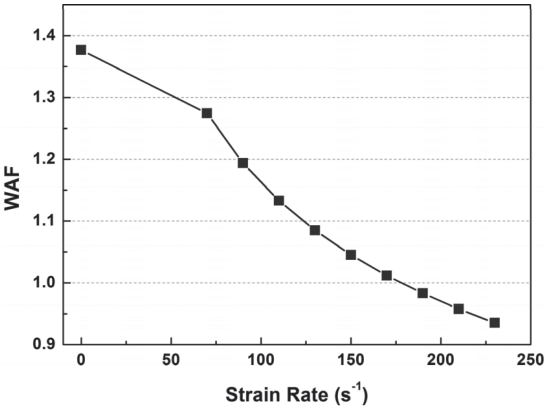


Figure 6. Variation of WAF versus strain rate.

water effects on the compressive strength of rocks under the same strain rate. The WAF is expressed by (Huang et al. 2010):

$$S_w = \frac{\sigma_d}{\sigma_w} \tag{9}$$

where $S_w$ = WAF; $\sigma_d$ = compressive strength of dry specimen; and $\sigma_w$ = compressive strength of saturated specimen.

As the same method presented in DIF, the compressive strength of dry and saturated specimens at strain rates of 70, 90, 110, 130, 150, 170, 190, 210 and 230/s were determined by formulas (6)–(7), then the WAFs at different strain rates were obtained (Fig. 6). It can be seen that the WAF obviously decreases with the increase of strain rate, which means that the water may make positive effect on dynamic compressive strength under relatively higher strain rate. Particularly, when the strain rate reaches 190/s, the WAF is approximately 0.98, i.e. the compressive strength of saturated specimens is higher than that of dry ones at that time.

## 4 CONCLUSIONS

This work has investigated the water effect on the compressive strength of sandstone. The dynamic compressive tests were conducted on dry and saturated sandstone specimens by SHPB technique, the relationship between the compressive strength and strain rate was obtained.

The test results show that both of the compressive strength of dry and saturated sandstone specimen is rate dependent, and the compressive strength of saturated specimen has higher rate dependence than that of dry one. It also reveals the fact that the static compressive strength obviously reduces when the dry specimen was saturated, however, when the strain rate exceeds 190/s, the dynamic compressive strength of saturated specimen begins to be higher than that of dry specimen. These may indicate that, the effect of water on the strength of rock specimen is related to the strain rate.

The results offer direct scientific evidence for the investigation of the effect of water on rock materials. Further study is needed to reveal the mechanism of water-rock interaction with different strain rates.

## ACKNOWLEDGEMENTS

The work reported here was supported by financial grants from the National Natural Science Foundation of China (51322403, 51274254), and the National Basic Research Program of

China (2015CB060200). The authors are very grateful to the financial contribution and convey their appreciation of the organization for supporting this basic research.

## REFERENCES

Broch, E. 1974. The influence of water on some rock properties, *Proc. Of 3rd Congress of the International Society for Rock Mechanics*: 33–38.

Colback, P. & Wild, B. 1965. The influence of moisture content on the compressive strength of rocks. *Proc. Of the 3rd Canadian Symposium on Rock Mechanics*: 55–83.

Dai, F., Huang, S., Xia, K. & Tan, Z. 2010. Some fundamental issues in dynamic compression and tension tests of rocks using split Hopkinson pressure bar. *Rock Mechanics & Rock Engineering* 43(6): 657–666.

Dyke, C.G. & Dobereiner, L. 1991. Evaluating the strength and deformability of sandstones. *Quarterly Journal of Engineering Geology* 24(1): 123–134.

Grgic, D., Giot, R., Homand, F. & Giraud, A. 2005. Effect of suction on the mechanical behaviour of iron ore rock. *International Journal for Numerical & Analytical Methods in Geomechanics* 29(8): 789–827.

Hadizadeh, J. & Law, R.D. 1991. Water-weakening of sandstone and quartzite deformed at various stress and strain rates. *International Journal of Rock Mechanics & Mining Sciences & Geomechanics Abstracts* 28(5): 431–439.

Han, G. 2003. Rock stability under different fluid flow conditions. *University of Waterloo*.

Hawkins, A.B. & Mcconnell, B.J. 1992. Sensitivity of sandstone strength and deformability to changes in moisture content. *Engineering Geology* 25(2): 115–130.

Huang, S., Xia, K. & Lan, Q. 2011. Dynamic tests of cemented paste backfill: effects of strain rate, curing time, and cement content on compressive strength. *Journal of Materials Science* 46(15): 5165–5170.

Huang, S., Xia, K., Yan, F. & Feng, X. 2010. An experimental study of the rate dependence of tensile strength softening of longyou sandstone. *Rock Mechanics & Rock Engineering* 43(6): 677–683.

Li, D., Wong, L.N.Y., Liu, G. & Zhang, X. 2012. Influence of water content and anisotropy on the strength and deformability of low porosity meta-sedimentary rocks under triaxial compression. *Engineering Geology* 126(7): 46–66.

Li, X., Zhou, Z., Liu, D. 2011. Wave shaping by special shaped striker in SHPB tests. *Advances in Rock Dynamics and Applications, CRC Taylor & Francis Group, Boca Raton*: 105–124.

Ogata, Y., Jung, W.J., Kubota, S., Wada, Y., Ogata, Y. & Jung, W.J. et al. 2004. Effect of the strain rate and water saturation for the dynamic tensile strength of rocks. *Materials Science Forum*: 465–466, 361–366.

Vásárhelyi, B. 2005. Statistical analysis of the influence of water content on the strength of the Miocene limestone. *Rock Eechanics and Rock Engineering* 38(1): 69–76.

Wang, H., Jin, W., Li, Q., Wang, H. & Jin, W. 2009. Saturation effect on dynamic tensile and compressive strength of concrete. *Advances in Structural Engineering* 12(2): 279–286.

Xia, K., & Yao, W. 2015. Dynamic rock tests using split Hopkinson (kolsky) bar system-a review. *Journal of Rock Mechanics & Geotechnical Engineering* 7(01): 27–59.

Zhang, Q.B. & Zhao, J. 2014. A review of dynamic experimental techniques and mechanical behaviour of rock materials. *Rock Mechanics & Rock Engineering* 47(4): 1411–1478.

Zhou, Y.X., Xia, K., Li, X. B., Li, H. B., Ma, G.W., Zhao, J. & Dai, F. 2012. Suggested methods for determining the dynamic strength parameters and mode-I fracture toughness of rock materials. *International Journal of Rock Mechanics and Mining Sciences* 49: 105–112.

Zhou, Z., Li, X., Liu, A. & Zou, Y. 2011. Stress uniformity of split Hopkinson pressure bar under half-sine wave loads. *International Journal of Rock Mechanics and Mining Sciences* 48(4): 697–701.

*Dynamic theories and numerical modelling*

This page intentionally left blank

*Rock Dynamics: From Research to Engineering – Li et al. (Eds)*
*© 2016 Taylor & Francis Group, London, ISBN 978-1-138-02953-8*

# Numerical simulation for cylindrical wave transmission across jointed rock masses

S.B. Chai, J.C. Li & H.B. Li
*State Key Laboratory of Geomechanics and Geotechnical Engineering, Institute of Rock and Soil Mechanics, Chinese Academy of Sciences, Wuhan, China*

ABSTRACT: The stress wave caused by underground explosion is usually assumed to propagate across rock masses in cylindrical form. The cylindrical wave propagation is a great concern of underground structure safety. This paper presents a study on cylindrical P-wave propagation across a single joint with linear elastic behavior using UDEC software. A semicircular cylindrical cavity is established at the bottom of the model to simulate the cylindrical wave loading. By calculation, UDEC is proved to be efficient to simulate cylindrical wave propagation. For the simplified UDEC models, the corresponding transmission and reflection coefficients are obtained. Parametric studies are carried out to investigate the influence of joint stiffness, the frequency of incident waveandthe position of monitoring point on the transmission and reflection coefficients.

## 1 INTRODUCTION

Discontinuities, especially rock joints widely exist in many natural rock masses, which have significant effects on the mechanics behavior of the rock mass and greatly affect stress wave propagation (Pyrak-Nolte 1996). Many investigation have been carried out to study stress wave propagation across a rock joint. Among various theoretical methods, the Equivalent Medium Method (EMM) (e.g. Schoenberg & Muir 1989, Cook 1992) and the Displacement Discontinuity Method (DDM) (e.g. Schoenberg 1980, Pyrak-Nolte et al. 1990) have been used widely. The two methods have been developed and widely applied to analyze stress wave propagation in more complex jointed rock mass. For example, combined with EMM, the Virtual Wave Source Method (VWSM) (Li et al. 2010, Zhu et al. 2011) was adopted to study wave propagation across multiple joints considering the multiple wave reflections among joints. Zhao & Cai (2001) combined the method of characteristics with the DDM to study P- and S-wave propagation normally across a single or a set of parallel unfilled joints. Based on DDM, the interaction between blast waves and a single rock joint with arbitrary incident angle was analyzed by Li & Ma (2010). Besides theoretical methods, numerical simulation is an alternative way to study wave propagation in jointed rock masses. Based on the displacement discontinuity theory, the DEM (e.g. Cundall 1971) is more widely and efficiently applied in the analysis of stress wave propagation. The Universal Discrete Element Code (UDEC) has been proved to be effective to simulate wave propagation across joints. For example, Chen & Zhao (1998) simulated the wave propagation and dynamic responses of a rock mass with joints under explosive loading with UDEC. Zhao et al. (2008) modeled the stress wave vertically propagating among linear and nonlinear joints and obtained the relationship for interaction between stress waves and joints. After validating the capability of UDEC in studying wave propagation across rock joints, Zhu et al. (2013) carried out a numerical study on wave transmission across multiple intersecting joint sets.

When an explosion with cylindrical charge or a tunneling explosion occurs, the first generated detonation wave compress the surrounding air and cause the air shock wave which will load on chamber wall (Henrych 1979). The stress wave in elastic media caused by the cylindrical charge explosion is taken as cylindrical wave (Yang 1991). Compared with plane wave propagation across a single joint, investigation for cylindrical stress wave interaction with rock joint have been

less reported. When cylindrical wave propagate in media, the wavefront is in a form of cylindrical surface, the radial velocity of each particle on a wavefront is constant. In addition, apparent attenuation of cylindrical waves is caused by geometrical spreading which is obviously different with plane wave (Dowding 1996). When impinging on a rock joint, the velocity and incident angle for each wave beam arriving at the joint are not the same which make the analysis for cylindrical wave propagation cross rock joints very complex. Therefore, numerical modeling is turned to be an acceptable and meaningful method which can provide some reference for physical tests and theoretical analyses on cylindrical wave propagation to some extent.

The aim of the present study is to numerically simulate cylindrical wave propagation across a single rock joint by UDEC. A semicircular cylindrical cavity is established atthe UDEC model to simulate the cylindrical wave loading, by investigating wave propagation in a rock with no discontinuity, UDEC is proved to be efficient to simulate cylindrical wave propagation. And then, the transmission and reflection coefficients for cylindrical wave propagation cross a joint are obtained. The parametric studies show that both the normalized stiffness of the joint and the frequency of the incident wave affect the components of transmission and reflection coefficients. Besides, the effects of the position of monitoring points are also investigated.

## 2 NUMERICAL SIMULAITON FOR CYLINDRICAL WAVE PROPAGATION

### 2.1 *UDEC model*

As shown in Figure 1, the model dimension is taken as 100 × 60 m. To better simulate the cylindrical wave loading, a semicircular cylindrical cavity is established at the bottom of the block, with the radius of 5 m. The mesh size is 1 m, which is much smaller than 1/8~1/12 of the wavelength, to ensure the calculation accuracy. The rocks are assumed to be elastic and homogeneous. The mechanical parameters of rock material are shown in Table 1. These properties are similar to those in Zhao's study (Zhao 1996). In order to analyze the characteristics of wave propagation more clearly, the material damping effect is ignored.

In this present dynamic analysis of UDEC, the lower boundary is adopted as symmetrical boundary while the top, left and right boundaries are the viscous boundary. The semicircular cylindrical cavity shown in Figure 1 is assumed as the initial wavefront, the cylindrical wave at this time is adopted as a half-cycle sinusoidal stress wave with frequency 50 Hz, amplitude 1 m/s and duration 0.01 s. The incident wave is loaded in the form of velocity. An elastic joint exists in the rock mass, as shown in Figure 1, it is supposed to be fictitious joint, parallel to the x-axis with a normal distance of 30 m from the center of the cavity. The normal stiffness of the joint is considered as 3.5 GPa/m while the shear stiffness is 1.0 GPa/m.

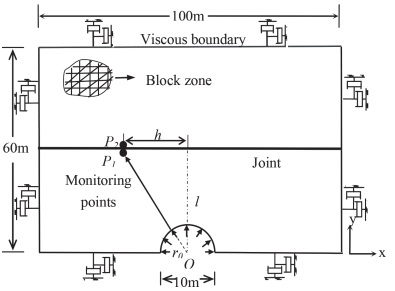


Figure 1. UDEC model for cylindrical wave propagation across a single rock joint.

Table 1. Properties of rock material in UDEC modeling.

| Properties | Density ($\rho$, kg/m$^3$) | Bulk modulus ($K$, GPa) | Shear modulus ($G$, GPa) | P wave velocity ($c_p$, m/s) | S wave velocity ($c_s$, m/s) |
|---|---|---|---|---|---|
| Value | 2650 | 59.5 | 23 | 5830 | 2940 |

## 2.2 *Verification of UDEC simulation on the cylindrical wave propagation*

A lot of the existing research results show that the UDEC is convenient, accurate and feasible to simulate one-dimensional or plane stress wave propagation in the jointed rock mass, while the numerical study in cylindrical wave simulation is relatively less. In this section, an investigationis carried out to verify the feasibility of UDEC simulation in cylindrical wave propagation.

A half symmetrical model without any joint with a dimension of $100 \times 50$ m is used to fully make use of the memory of the computer and to reduce the computational time, as shown in Figure 2. Other condition of the model is same as those in Figure 1.Three groups of monitoring points with certain radius ($r$) are set in the model, as shown in Figure 2. The $A$ series points are distributed along y-axis while $B$ and $C$ series points are along the direction in 60 degrees with x-axis, respectively, distribute on left and right sides of the y-axis.

History of the velocity components is monitored at every point along the x- and y-axis shown in Figure 2. According to the composition of the recorded velocities, the history of radial velocity for every monitoring point can be derived as

$$v_r = \sqrt{v_x^2 + v_y^2} \tag{1}$$

where $v_r$ is the radial velocity for every monitoring point, $v_x$ and $v_y$ are the components of $x$- and $y$-direction, respectively. The amplitude of radial stress wave for every point is obtained and plotted in Figure 3. It is noticed that the radial velocity of the different points with same radius are very close. Moreover, in Figure 3, the fitting curve for the radial velocity with the radius is obtained with the expression as $v_r = 1.80r^{-0.5}$ and the coefficient of determination $R^2 = 0.986$. It means that the radial velocity amplitude of cylindrical wave with the increase of the radius decays in inverse proportion to $r^{-0.5}$ which is in line with the existing conclusions (Wang 2007). Therefore, the loading method described above for cylindrical wave is feasible.

## 2.3 *Cylindrical wave propagation across a joint*

As is shown in Figure 1, there are two monitoring points along the two sides of the joint. History of the velocity components at either point along the x- and y-axis are monitored, noted as $v_{nx}$ and $v_{ny}$ (n = 1,2, represents Point P1 or P2). For point P1, the velocity records contains the incident wave and reflected wave history, while for point P2, the velocity history represents the transmitted wave. To make it clear, the velocity history of P1 in the case that there is no joint in the rock mass is recorded, noted as $v_{0x}$ and $v_{0y}$. Thus, the incident wave impinging on the joint can be obtained as

$$v_I(t) = \sqrt{v_{0x}^2(t) + v_{0y}^2(t)} \tag{2}$$

When an elastic wave impinges on the interface of two media, both reflection and transmission take place (Kolsky 1953). Therefore, when the cylindrical P wave impinges the joint,

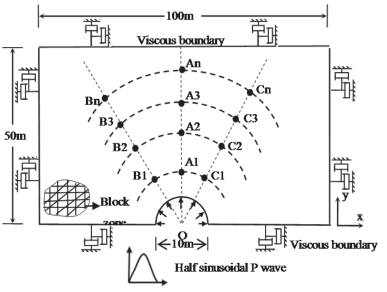


Figure 2. Schematic view of the cylindrical wave propagation.

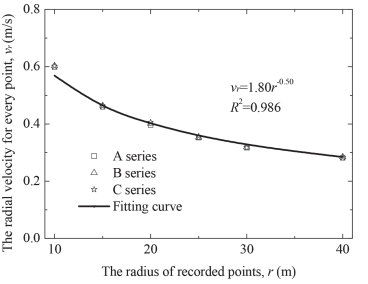


Figure 3. The relation of the radial velocity amplitude for different series points with the radius.

the transmitted P- and S-waves and reflected P- and S-waves will be generated. Thus, the recorded transmitted wave velocity is the combination of the transmitted P- and S-waves, so does the reflected wave velocity. Hence, the velocity components along the x- and y-direction are adopted to reflect the transmission and reflection effect of the joint. Accordingly, the transmitted wavecomponents can be expressed as

$$v_{Tx}(t) = v_{2x}(t),\ v_{Ty}(t) = v_{2y}(t) \tag{3}$$

and the reflected wave components can be expressed as can be derived as

$$v_{Rx}(t) = v_{0x}(t) - v_{1x}(t),\ v_{Ry}(t) = v_{0y}(t) - v_{1y}(t) \tag{4}$$

From Eqs. (2) to (4), the incident, transmitted and reflected waves for every point on the joint when a cylindrical P-wave propagation impinging on can be obtained. To better understand the propagation characteristic, the components of transmission coefficients, $T_x$ and $T_y$, for x- and y-direction and the components of reflection coefficients, $R_x$ and $R_y$, are defined and expressed as

$$T_m = \frac{\max|v_{Tm}|}{\max|v_I|},\ R_m = \frac{\max|v_{Rm}|}{\max|v_I|} (m = x \text{ and } y) \tag{5}$$

## 3 PARAMETRIC STUDY

As Figure 1 shows, for different monitoring point, the incident angle is different which leads to the different influence on the transmission and reflection coefficients. Additionally, the joint properties and wave frequency will affect the coefficients. Therefore, it is necessary to carry out parametrical study to analyze effect of the position of the monitoring point, joint stiffness and the incident wave frequency on the transmission and reflection coefficients. Besides the parameters shown in Section 2.1, the normalized vertical and horizontal distance between the monitoring point with the original point are defined as $L = l/r_0$ and $H = h/r_0$, respectively. The symbols $K_n$ denote the normalized normal stiffness of the joint, and the normal and tangential stiffness of the joint are $k_n = K_n(z_p\omega)$ and $k_s = K_n(z_s\omega)$, where $\omega = 2\pi f$.

### 3.1 *Effect of the position of monitor point*

In order to study the effect of position of monitoring joint point on the transmission and reflection coefficients, the Equation (5) is used to eliminate the attenuation by geometrical spreading of the cylindrical wave. When investigate the horizontal distance, the normalized vertical distance $L = 6$, i.e. $l = 30$ m; on the contrary, we define $H = 6$ when study the vertical distance. Besides, we define $K_n = 1$. Figure 4(a) shows the transmission and reflection coefficients versus the normalized horizontal distance. It can be seen that the x-direction transmission coefficient $T_x$ and the x-direction reflection coefficient $R_x$ monotonously increase with the increasing horizontal distance; the coefficients in y-direction, $T_y$ and $R_y$, reduce and the decreasing rate is relatively high for $H$ less than 6. As mentioned in Section 2, the velocity components along the x- and y-direction are the combination of the components of transmitted or reflected P- and S-waves in each direction. When the horizontal distance increases, the incident angle of the wave impinging on the joint is increasing, meanwhile, the emergent angles of reflected and transmitted waves are increasing which leads to the reduce in y-direction and the increase in x-direction.

The relation of the transmission and reflection coefficients with the normalized vertical distance between the monitoring point and the original point is shown in Figure 4(b). It can be observed that the curve for each coefficient except $R_y$ is non-monotonous. With the increasing of the vertical distance, the reflection coefficient $R_y$ increases gradually while the other three coefficients increase for a while and then reduce slowly. When $L$ is near 4, $T_x$ and $R_x$ reach maximum value.

### 3.2 *Effect of joint stiffness on wave propagation*

Figure 5 shows the transmission and reflection coefficients with the normalized joint stiffness at the point with $L = 6$ and $H = 5$. It is found that the transmission coefficients, $T_x$ and $T_y$, both increase with the increase of the joint normal stiffness, and the rising rate is relatively high for $K_n$ less than 1. At the monitoring point, $T_y$ is greater than $T_x$ when the joint normal stiffness is given. Meanwhile, Figure 5 shows that the variations of the transmission coefficients with the joint stiffness become stable when the normalized joint stiffness $K_{\mathrm{n}}$ is greater than 1. In addition, the rising rate of the vertical component is becoming lower when the normal stiffness is greater. On the contrary, the reflection coefficients, $R_x$ and $R_y$, reduce with the increasing of the joint stiffness. There, $R_y$ decreases rapidly when $K_n$ is less than 1 and then tends to be stable when the normal stiffness is greater while $R_x$ gradually reduce with the increasing of $K_n$. When $K_{\mathrm{n}}$ near to zero, the transmission coefficients are zero and the reflection coefficients is the maximum which means all the waves are reflected from the joint.

### 3.3 *Effect of the Frequency of the incident Wave*

For a certain monitoring joint point, Figure 6 illustrates the relation between the reflection and transmission coefficients with the frequency of the incident wave. The normal and tangential stiffness of the joint are adopted as $k_n = 3.5$ GPa/m and $k_s = 1.0$ GPa/m, respectively. It can be observed that the x-direction transmission coefficient, $T_x$, increases gradually when the frequency is less than 50 Hz and then decreases smoothly with increasing frequency of the incident wave, while $T_y$ keeps decrease with the increase of the incident wave frequency. Both of the reflection coefficients, $R_x$ and $R_y$, almost monotonously increase with increasing frequency of the incident wave except that a little fluctuation exists in the two curves. It reflects that it is more difficult for the wave with higher frequency to transmit across the joint. In another words, the transmission coefficients have low value while reflection coefficients have high value when the frequency is relatively high which reflects the joint filtering effect to high frequency.

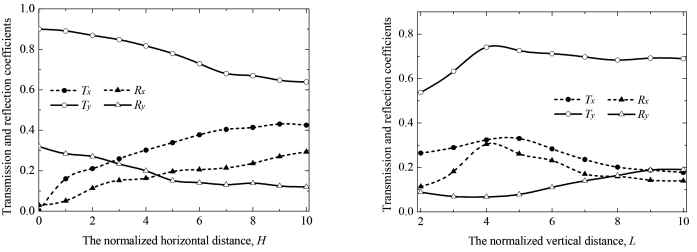


(a) Effect of horizontal distance (b) Effect of vertical distance

Figure 4. Transmission and reflection coefficients of different monitoring points.

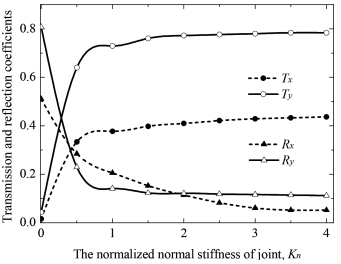


Figure 5. The relation between transmission and reflection coefficients with normalized stiffness $K_n$.

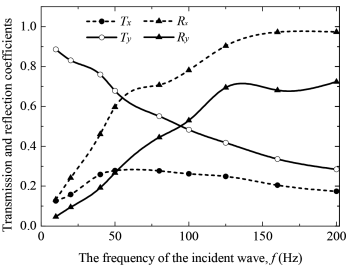


Figure 6. Relation between transmission and reflection coefficients and the frequency of incident wave.

## 4 CONCLUSIONS

The transmission of a cylindrical P-wave across a single joint with linear elastic behavior is investigated numerically using UDEC. By verification, UDEC is effective to simulate cylindrical wave propagation in the rock mass. When cylindrical wave propagation across a single joint is investigated, the components of transmitted and reflected waves along x- and y-axis at any monitoring point are recorded and the corresponding transmission and reflection coefficients are obtained. The parametric studies show that both normal and tangential stiffness of either joint obviously affects the wave propagation process; the frequency of the incident wave has less influence on the transmission and reflection coefficients. Besides, the transmission and reflection coefficients at any monitoring point are different. Although the numerical modeling for cylindrical wave transmission across a joint in the present study is simplified to some extent, the results might still provide a reference for revealing cylindrical wave propagation in jointed rock masses.

## ACKNOWLEDGEMENTS

The study is supported by the National Science Foundation of China (No. 41525009, 41272348) and the Scientific Research Foundation for Returned Chinese Scholars (No. 2012-940).

## REFERENCES

Chen, S.G. & Zhao, J. 1998. A study of UDEC modelling for blast wave propagation in jointed rock masses. *Int J Rock Mech Min Sci* 35(1): 93–99.

Cook, N.G.W. 1992. Natural joint in rock: mechanical, hydraulic and seismic behavior and properties under normal stress. *Int J Rock Mech Min SciGeomechAbstr* 29(3): 198–223.

Cundall, P.A. 1971. A computer model for simulating progressive large scale movements in blocky rock systems. *Pros Symp Int Soc Rock Mechanics*, Nancy, Frence 1(*n*-8): 129–136.

Dowding, C.H. 1996. *Construction Vibration*. Prentice-Hall, Engle-wood Cliffs.

Henrych, J. 1979. *The Dynamics of Explosion and Its Use*. New York: Elsevier Scientific.

Kolsky, H. 1953.*Stress waves in solids*. Clarendon, Oxford.

Li, J.C. & Ma, G.W. 2010. Analysis of blast wave interaction with a rock joint. *Rock Mech Rock Eng* 43(6): 777–787.

Li, J.C., Ma, G.W. & Zhao J. 2010. An equivalent viscoelastic model for rock mass with parallel joints. *J Geophys Res: Solid Earth* (1978–2012): 115(B3).

Pyrak-Nolte L.J. 1996. Seismic response of fractures and the interrelations among fractures. *Int J Rock Mech Min Sci* 33(8): 787–802.

Pyrak-Nolte, L.J., Myer, L.R. & Cook, N.G.W. 1990. Transmission of seismic-waves across single natural fractures. *J Geophys Res* 95(B6): 8617–8638.

Schoenberg, M. 1980. Elastic wave behavior across linear slip interfaces. *J AcoustSoc Am* 68(5): 1516–1521.

Schoenberg, M. & Muir, F. 1989. A calculus for finely layered anisotropic media. *Geophysics* 54(5):581–589.

Wang, L.L. 2007. *Foundations of Stress Waves*. Elsevier.

Yang S.Y. 1991. *Dynamics Base of Rock Blasting*. Beijing: China Coal Industry Publishing House. (in Chinese).

Zhao, J. 1996. Construction and utilization of rock caverns in Singapore, Part A: Bedrock resource of the Bukit Timah granite. *TunnUndergrSp Tech* 11(1): 65–72.

Zhao, J. & Cai, J.G. 2001. Transmission of elastic P-waves across single fractures with a nonlinear normal deformational be-havior. *Rock Mech Rock Eng* 34(1): 3–22.

Zhao, X.B., Zhao, J., Cai, J.G. & Hefny, A.M. 2008. UDEC modeling on wave propagation across fractured rock masses. *Comput Geotech* 35(1): 97–104.

Zhu, J.B., Deng, X.F., Zhao, X.B. & Zhao, J. 2013. A numerical study on wave transmission across multiple intersecting joint sets in rock masses with UDEC. *Rock Mech Rock Eng* 46(6): 1429–1442.

Zhu, J.B., Zhao, X.B., Li, J.C., Zhao, G.F. & Zhao J. 2011. Normally incident wave propagation across a joint set with the virtual wave source method. *J Appl Geophys* 73: 283–288.

*Rock Dynamics: From Research to Engineering – Li et al. (Eds)*
*© 2016 Taylor & Francis Group, London,* *ISBN 978-1-138-02953-8*

# Adaptive coupling of smooth particle hydrodynamics and finite-element method for rock blasting simulations

D. Deb & A. Khan
*Department of Mining Engineering, Indian Institute of Technology, Kharagpur, West Bengal, India*

ABSTRACT: This work presents a new approach in simulation of rock blasting process by coupling the Finite Element Method (FEM) and the Smooth Particle Hydrodynamics (SPH) method. The rock is initially modelled with FEM whereas the explosive is modeled with SPH. Interaction is achieved by including the elements near the rock-gas interface in the neighbor list of SPH system and applying the calculated traction to element sides. Further, highly distorted rock elements are automatically converted to particles and linked to the FEM system on the fly. A patch test is demonstrated to check the validity of the proposed technology.

## 1 INTRODUCTION

Simulating the phenomenon of blasting of rocks, which involve high strain rates using the Finite Element Method (FEM), becomes difficult as FEM suffers from mesh tangling. Corrections such as mesh rezoning, element erosion etc. to do away with badly distorted elements must be employed. This increases the computational time. Mesh-less methods such as the Smooth Particle Hydrodynamics (SPH) method by Lucy (1977) and Monaghan & Glingold (1983) can handle large distortions inherently but it is more computationally expensive than FEM. It also suffers from certain potent instabilities when applied to problems of deforming solids. Moreover, applications of boundary conditions in SPH is tedious. Coupling the FEM and the SPH method could be more efficient in such problems, where regions of high strain rates and large deformations are modelled with SPH particles to capture deformations and the remaining regions are modelled with FEM to save computational time and seamlessly apply boundary conditions. This work adopts with suitable modifications the algorithm proposed by Xiao et al. (2011) that treat elements near the coupling interface as imaginary particles to calculate forces on particles from adjacent elements and impose equivalent tractions on element edges on the coupling interface in accordance with the particle stress associated with that element. In this work, since rock basting is a fluid-solid interaction problem the expanding gas of the decomposing explosive is exclusively modeled with SPH particles. The rock is modelled with FEM under suitable boundary conditions and the severely distorted rock elements are changed to SPH particle during the course of computation.

## 2 THE SMOOTH PARTICLE HYDRODYNAMICS METHOD

The basic equations of SPH method are derived from the conservation laws of mass, momentum and energy and they take the following SPH discretized form:

$$\frac{\partial \rho_i}{\partial t} = \sum_{j=1}^{N} m_j \left( v_i^\beta - v_j^\beta \right) \frac{\partial W_{ij}}{\partial x_i^\beta} \tag{1a}$$

$$\frac{\partial v_i^\alpha}{\partial t} = \sum_{j=1}^{N} m_j \left( \frac{\sigma_i^{\alpha\beta}}{\rho_i^2} + \frac{\sigma_j^{\alpha\beta}}{\rho_j^2} + \Pi_{ij}\delta^{\alpha\beta} + R_{ij}^{\alpha\beta} f^n \right) \frac{\partial W_{ij}}{\partial x_i^\beta} \tag{1b}$$

$$\frac{\partial E_i}{\partial t} = 0.5 \times \sum_{j=1}^{N} m_j \left( \frac{\sigma_i^{\alpha\beta}}{\rho_i^2} + \frac{\sigma_j^{\alpha\beta}}{\rho_j^2} + \Pi_{ij}\delta^{\alpha\beta} \right) \left( v_j^\alpha - v_i^\alpha \right) \frac{\partial W_{ij}}{\partial x_i^\beta} \tag{1c}$$

$$\frac{\partial r_i^\alpha}{\partial t} = v_i^\alpha \tag{1d}$$

where $\rho$ is the density, $m$ is the mass, $v$ is the velocity, $\sigma$ is the stress, $E$ is the specific internal energy per unit mass, $x$ is the coordinate direction, $r$ is the position, $i$ and $j$ are particle indices, $\alpha$, $\beta$ are the Cartesian coordinate indices and $\delta$ is the Kronecker delta function. $W$ is the kernel function, and $\Pi$ is the artificial viscosity. The summation is taken over the total number of neighbors $N$ of particle $i$, (Liu & Liu 2003). The Kernel function, $W$ used in this work is the Cubic-Spline function of the form given in Pramanik & Deb (2014). Initial smoothing length given by, $h_0 = \alpha_h \Delta$ in which $\alpha_h$ is a constant known as dilation factor and $\Delta$ is the particle spacing. The smoothing length varies both in time and space and is updated using the method proposed by Benz (1989) and Liu et al. (2002). The artificial viscosity term $\Pi_{ij}\delta^{\alpha\beta}$ in equation 1b and 1c is required as a shock resolving mechanism given by Monaghan (1992). The "Tensile Instability" which make particles clump together is treated by introducing the "Artificial Stress" term $R_{ij}^{\alpha\beta} f^n$ in the momentum equation and is given by Gray et al. (2001). The stress term in Equations 1b and 1c reduce to pressure $p$ for fluids. A linear elastic stress-strain constitutive equation for the rock is used, $\dot{\tau} = \mathbf{D}\dot{\gamma}$ where $\dot{\gamma}$ is the total strain rate tensor, $\mathbf{D}$ is the constitutive matrix and $\dot{\tau}$ is the work conjugate stress rate tensor. The SPH approximation of the strain rate tensor is given by:

$$\dot{\gamma}_i^{\alpha\beta} = \frac{1}{2} \sum_{j=1}^{N} \frac{m_j}{\rho_j} \left( v_{ji}^\alpha \frac{\partial W_{ij}}{\partial x_i^\beta} + v_{ji}^\beta \frac{\partial W_{ij}}{\partial x_i^\alpha} \right) \tag{2}$$

where the velocity difference $v_{ji} = v_j - v_i$ and summation over repeated index is implied. For the decomposing explosive gas, the Jones–Wilkins–Lee (JWL) equation of state is used to relate the state variables $\rho$, $E$ and $p$:

$$p = A\left(1 - \frac{\omega\theta}{R_1}\right) e^{-R_1/\theta} + B\left(1 - \frac{\omega\theta}{R_2}\right) e^{-R_2/\theta} + \omega\theta\rho_0 E \tag{3}$$

The JWL parameters and their units of measurement of explosives used in this paper are given in Table 1 Pramanik & Deb (2014).

Initial density $\rho$ is in $kg/m^3$, initial internal energy $E_0$ in $J/kg$, the C-J speed $D_{CJ}$ in $m/s$, A and B are pressure terms in $GPa$, $R_1$, $R_2$ and $\omega$ are real constants.

For the integration in time of the rate Equations 1(a-c) and 2 the second order accurate leapfrog scheme was used in this work along with XSPH formulation by Monaghan (1989).

## 3 LARGANGIAN FORMULATION OF FINITE ELEMENT METHOD

The Lagrangian formulation uses the Green-Lagrange strain tensor, $\gamma = 0.5 \times (\mathbf{C} - \mathbf{I})$ the Cauchy-Green deformation tensor, $\mathbf{C} = \mathbf{F}^T\mathbf{F}$ and the deformation gradient tensor, $\mathbf{F} = \partial \mathbf{x} / \partial \zeta$

Table 1. Reaction product parameters for high explosives in JWL form.

| Explosive | ρ | $E_0$ | $D_{CJ}$ | A | B | $R_1$ | $R_2$ | ω |
|---|---|---|---|---|---|---|---|---|
| TNT | 1,630 | $4.29 \times 10^6$ | 930 | 371.2 | 3.210 | 4.15 | 0.95 | 0.30 |

where $\mathbf{x}$ is the position of an elementary particle in the deformed configuration called the "spatial coordinates" and $\boldsymbol{\zeta}$ is the position in the reference configuration (usually the undeformed configuration) called the "material coordinates". The auxiliary stress measure used is the 2nd Piola-Kirchhoff stress tensor $\boldsymbol{\tau}$ which is related to the Cauchy stress tensor $\sigma = \mathbf{F}.\tau.\mathbf{F}^{\mathrm{T}} / \det \mathbf{F}$ where the determinant of the deformation gradient tensor det$\mathbf{F}$ is related to the instantaneous density as $\rho = \rho_0 / \det\mathbf{F}$ and this is used for density update. Using $\boldsymbol{\tau}$ and $\boldsymbol{\gamma}$ in the virtual work equation and integrating with respect to a reference leads to two contribution of the tangential stiffness matrix $\mathbf{K}$. The first one is from the linear part of the strain increment $\mathbf{K}_L$ called the material part and the second contribution is from the nonlinear strain increment $\mathbf{K}_{NL}$ called the geometric part expressed as:

$$\mathbf{K}_L = \int_{V_0} \mathbf{B}_L^T \mathbf{D} \mathbf{B}_L dV, \quad \mathbf{K}_{NL}^t = \int_{V_0} \mathbf{B}_{NL}^T {}^t\mathbf{B}_{NL} dV \tag{4}$$

The expressions for the linear strain-displacement matrix $\mathbf{B}_L$, the 2nd Piola-Kirchhoff stress-matrix $\boldsymbol{\Gamma}^t$ and the non-linear strain-displacement matrix $\mathbf{B}_{NL}$ can be found in de Borst, Crisfield, Remmers, & Verhoosel (2012). As such the dynamic equilibrium equation reads:

$$\mathbf{M}\frac{\partial^2 \mathbf{U}}{dt^2} + \mathbf{C}\frac{\partial \mathbf{U}}{dt} + \left(\mathbf{K}_L + \mathbf{K}_{NL}\right)\mathbf{U} = \mathbf{f}_{ext} \tag{5}$$

where $\mathbf{M}$ is the mass matrix, $\mathbf{C}$ the damping matrix, $\mathbf{U}$ the vector of nodal displacements and $\mathbf{f}_{ext}$ is the vector of external forces. For the time integration of equation (5) the generalized-$\alpha$ method by Chung & Hulbert (1993) and outlined in Kuhl & Ramm (1999) is used. The equation of motion is applied to a general mid-point instead of the end-points in each time-step:

$$\mathbf{M}\ddot{\mathbf{u}}_{t+1-\alpha_m} + \mathbf{C}\dot{\mathbf{u}}_{t+1-\alpha_f} + \mathbf{N}_{t+1-\alpha_f} = \mathbf{f}_{t+1-\alpha_f} \tag{6}$$

where $\alpha_m$ and $\alpha_f$ are the generalized mid points ($0 < \alpha_m < \alpha_f < 1$) and the subscripts denote the time discrete combinations on acceleration velocity, displacements and internal and external force vectors represented by the general variable $\mathbf{H}$ is of the form, $\mathbf{H}_{t+1-\alpha} = (1-\alpha)\mathbf{H}_{t+1} + \alpha\mathbf{H}_t$.

Using the Newmark's approximations in time (Newmark 1959) for the velocities and accelerations at the mid-points of time steps (Khul & Crisfield 1999) in Equation 6 leads to the following effective structural equation:

$$\begin{aligned}\mathbf{G}\left(\mathbf{u}_{t+1}\right) \equiv\ & \mathbf{N}_{t+1-\alpha_f} - \mathbf{f}_{t+1-\alpha_f} \\ & + \mathbf{M}\left[\frac{1-\alpha_m}{\beta\Delta t^2}\left(\mathbf{u}_{t+1} - \mathbf{u}_t\right) + \frac{1-\alpha_m}{\beta\Delta t}\left(\dot{\mathbf{u}}_t\right) + \frac{1-\alpha_m-2\beta}{2\beta}\left(\ddot{\mathbf{u}}_t\right)\right] \\ & + \mathbf{C}\left[\frac{\left(1-\alpha_f\right)\gamma}{\beta\Delta t}\left(\mathbf{u}_{t+1} - \mathbf{u}_t\right) + \frac{\left(1-\alpha_f\right)\gamma-\beta}{\beta}\left(\dot{\mathbf{u}}_t\right) + \frac{\left(1-\alpha_f\right)\left(\gamma-2\beta\right)}{2\beta}\right] = 0\end{aligned} \tag{7}$$

Applying the Newton-Raphson strategy and using the two term Taylor expansion of Equation 7 leads to the effective iterative structural equation, $\bar{\mathbf{K}}\left(\mathbf{u}_{t+1}^k\right)\Delta\mathbf{u} = -\mathbf{G}\left(\mathbf{u}_{t+1}^k\right)$ as:

$$\bar{\mathbf{K}}\left(\mathbf{u}_{t+1}^k\right) = \mathbf{K}_{t+1-\alpha}^t\left(\mathbf{u}_{t+1}^k\right) + \frac{1-\alpha_m}{\beta\Delta t^2}\mathbf{M} + \frac{1-\alpha_f}{\beta\Delta t}\mathbf{C} \tag{8}$$

The tangential stiffness matrix $\mathbf{K}_{t+1-\alpha_f}^t\left(\mathbf{u}_{t+1}^k\right) = (1-\alpha_f)\left(\mathbf{K}_L + \mathbf{K}_{NL}\right)$ and internal force vector $\mathbf{N}$ is given as. $\mathbf{N}^t = \int_{v0} \mathbf{B}_{\mathrm{L}}{}^{\mathrm{T}} \boldsymbol{\tau}^t \, dV$.

The effective iterative structural equation is solved for $\Delta\mathbf{u}$ until convergence up to a set limit and the displacement in each iteration is obtained as $\mathbf{u}_{t+1}^{k+1} = \mathbf{u}_{t+1}^k + \Delta\mathbf{u}$. End time velocities and accelerations are updated using standard Newmark's scheme. The Newmark's parameters $\beta = 0.273006$ and $\gamma = 0.545$ and the mid-points $\alpha_m = 0.01$, $\alpha_f = 0.055$ is used in this work. The

time-step size $dt$ is calculated based on the Courant–Friedrichs–Lewy condition [Liu & Liu (2003)] for both the FEM and SPH domains and the least of the two is taken.

## 4 THE COUPLING ALGORITHM

The essential idea is to model the force exchanges that occur between particles and elements. This is achieved by treating the elements near the coupling interface as imaginary particles there-by completing the boundary deficiency in the SPH calculations, as shown in Figure 1. The stresses derived from the particles are imposed on the element edges on the interface as equivalent tractions.

### 4.1 *Determination of elements treated as imaginary particles*

At the start of computation for any arbitrary element, the condition $d_{gi} < \eta R_i$ is checked for all particles where $d_{gi}$ is the distance from the gravity center of any element to the center of particle $i$, $R_i = 2h_i$ is the radius of the influence domain of particle $i$, and $\eta > 1$ is an inclusion factor. If there is an element $j$ satisfying this condition for the any particle $i$, then that element is identified as one needed to be treated as imaginary particle. In our work $\eta = 2$ was used to include enough imaginary particles.

Once the imaginary particles are identified from elements, their properties are set according to the element properties. The position and velocity are taken to be the average nodal values of that element. The stress of the imaginary particle is taken to be average of the gauss stress. The initial smoothing length is $\alpha_h$ times the square root of the original area of element and radius of the particle is half of this smoothing length. Mass of each imaginary particle is taken to be the mass of the element. This update is done in each computational cycle.

### 4.2 *Calculation of forces on particles from adjacent elements*

The forces on particles from elements are determined based on neighboring particles including both the imaginary particles and real particles applied as $N = N_{Imaginary} + N_{Real}$ in Equation 1 and 2.

### 4.3 *Calculation of forces on element nodes from adjacent particles*

The particles stresses are averaged over all particles associated with the element side and the traction is calculated using the current normal of the edge. Assuming the traction to act uniformly on the element nodes of that edge, the nodal force is calculated by interpolation

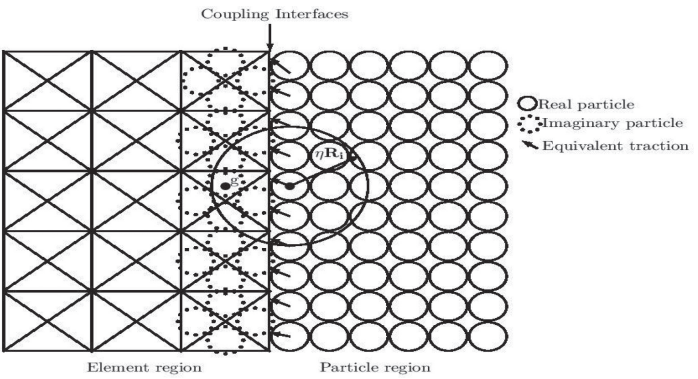


Figure 1. Schematic diagram showing the coupling interface along with the search radius for determination of imaginary particles.

and integration over the edge along the same line as application of traction boundary conditions in standard FEM.

### 4.4 *Determination of particles associated to element sides*

The procedure of calculating and applying tractions on FEM counterpart require the determination of the interface edges and particle association. The details can be found in Xiao, Han, & Hu (2011) where they have calculated the penetration distance $\delta$ and accordingly associated the particles to the edge whose penetration distance is less than a set limit.

## 5 ADAPTIVE COUPLING TECHNIQUE

The simulation starts with the rock modelled wholly by FEM and the explosive modelled with SPH. As time progresses and decomposed explosive begin to expand and push against the rock (by the process of coupling as mentioned in section 4.4), deformations tend to increase until the FEM mesh is distorted. At this point, of time some of the extremely distorted elements are removed from the FEM computation, converted to real SPH particles, and linked to the remaining FEM model by the same coupling procedure and simulation continues. In each time-step, the quality $Q$ of any triangular element is checked by twice the ratio of the radius of in-circle and radius of the circumscribed circle. An equilateral triangle achieves the maximum possible quality of one. If $Q$ is less than a critical value $Q_c = 0.5$, the element is considered to be distorted and recorded as one converted to a particle. The Group Base Conversion (GBC) as described in Xiao et al. (2011) is followed where elements in FEM model are divided into groups at the beginning of the computation. During the computational process, if one or more elements in a group satisfy the conversion criterion, then all elements in that group are converted to particles. At this time, the coupling interface is also updated.

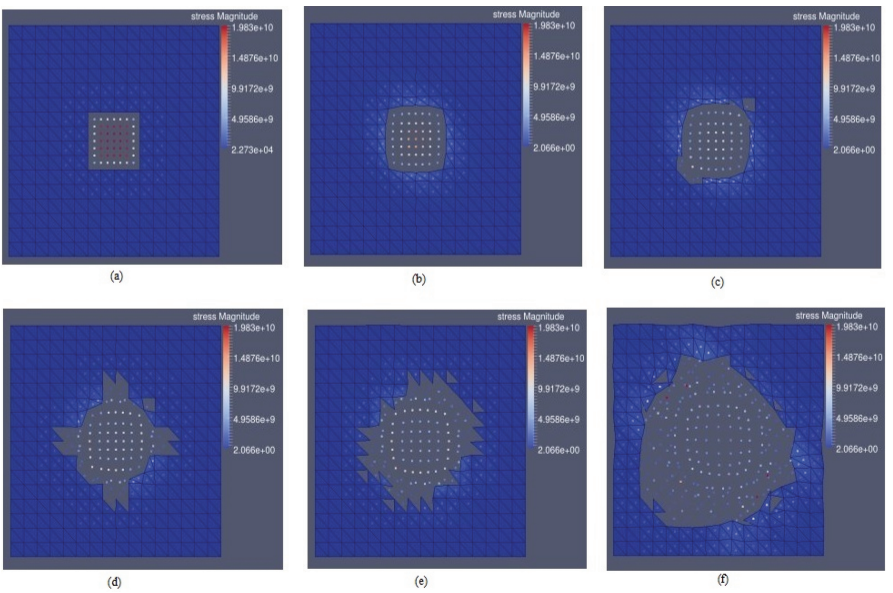


Figure 2. Mesh deformation and particle displacements at different times t (a) at t = 0.00 secs. (b) at t = $1.68 \times 10^{-8}$ secs. (c) at t = $2.57 \times 10^{-8}$ secs. (d) at t = $2.7 \times 10^{-8}$ secs. (e) at t = $3.65 \times 10^{-8}$ secs. (f) at t = $6.67 \times 10^{-8}$ secs.

## 6 NUMERICAL TEST

To demonstrate the validity of the developed algorithm a patch test is presented. The 2-D model consists of a square rock sample of dimension 1 sq. units with a centrally placed square hole of dimension 0.25 sq. units that is filled with TNT under plain strain condition. Young's modulus of rock is $5.0 \times 10^9$ *Pa*, Poison's ratio is 0.3 and has density 2500 $kg/m^3$. The properties of TNT are given in Table 1. The structured FEM mesh initially consist of 478 CST elements and the explosive is discretized using 49 particles in a regular grid and the model is restrained at the bottom surface along both directions. The procedure is implemented in a C++ code with an integrated FEM and SPH solver. Figure 2 shows the evolution of coupling interface, generated rock particles and the stress distribution in the model. The simulation is stopped when the coupling interface reaches a free surface.

## 7 CONCLUSION

This work presents a new approach to blast simulation in rocks by coupling the FEM and SPH method as well as an adaptive technique based algorithm. Although a simple patch test problem is presented, it shows that the developed technique works correctly. The pressure generated initially is close to the *CJ*-Pressure of TNT ($\approx 2.1 \times 10^{10}$) and remains for some time due to confinement by the rock. Then as the distorted elements are replaced by particles and simulated by SPH method, the pressure drops. This is quite intuitive since as the rock particles move farther it creates space for the expanding gas and the pressure decreases. Further, the evolution of the coupling interface and application of force on it is observed to be justly simulated. Moreover, the gas particles encroach the space created by displaced rock. Application and validity to real problems is underway.

## REFERENCES


Benz, W. 1989. Smooth Particle Hydrodynamics: a review. *NATO Workshop.* Les; Arcs, France.

Chung, J., & Hulbert, G.M. 1993. A time integration algorithm with improved numerical dissipation: the generalized-α method. *Jrnl of Appl. Mech. 60*: 371–375.

de Borst, R., Crisfield, M.A., Remmers, J.J. & Verhoosel, C.V. 2012. *Non-Linear Finite Element Method of Solids and Structures* (Second ed.). John Wiley & Sons Ltd.

Gray, J.P., Monaghan, J.J., & Swift, R.P. 2001. SPH Elastic Dynamics. *Compt. Method Appl. Mech. in Engrg.* 190: 6641–6662.

Khul, D. & Crisfield, M.A. 1999. Energy-conserving and decaying algorithms in non-linear structural dynamics. *Int. J. Numer. Meth. Engng.* 45: 569–599.

Kuhl, D. & Ramm, E. 1999. Generalized Energy-Momentum Method for non-linear adaptive shell dynamics. *Comput. Methods Appl. Mech. Engrg.* 178: 343–366.

Liu, G.R. & Liu, M.B. 2003. *Smoothed Particle Hydrodynamics A Meshfree Particle Method.* Singapore: World Scientific Publishing Co. Pte. Ltd.

Liu, G.R., Dai, K.Y., Lim, K.M. & Gu, Y.T. 2002. A point interpolation mesh free method for static and frequency analysis of two-dimansional piezoelectric structures. *Smart Materials and Structures* 171–180.

Lucy, L.B. 1977. Numerical approach to testing the fission hypothesis. *Astronomical Journal* 82: 1013–1024.

Monaghan, J.J. & Glingold, R.A. 1983. Shock Simulation by the particle method SPH. *J. Compu. Phys.* 52: 374–389.

Monaghan, J.J. 1989. On the problem of particle penetration in particle methods. *Journal of computational physics* 82: 1–15.

Monaghan, J.J. 1992. Smoothed particle hydrodynamics. *Annu. Rev. Astron. Astrophys.* 30: 543–74.

Newmark, N.N. 1959. A method of computation for structural dynamics. *J. Engrg. Mech. Div.* 136: 293–315.

Pramanik, R. & Deb, D. 2014. Implementation of Smoothed Particle Hydrodynamics for Detonation of Explosive with Application to Rock Fragmentation. *Rock Mech. Rock Eng.* 48(4): 1683–1698.

Xiao, Y., Han, X. & Hu, D. 2011. A Coupling Algorithm of Finite Element Method and Smoothed Particle Hydrodynamics for Impact Computations. *CMC* 23(1): 9–34.

*Rock Dynamics: From Research to Engineering – Li et al. (Eds)*
*© 2016 Taylor & Francis Group, London, ISBN 978-1-138-02953-8*

# A parameter-variable creep damage model considering the effects of loading frequency for rock salt and its engineering application in deep storage cavern

G.X. Ding
*State Key Laboratory of Disaster Prevention and Mitigation of Explosion and Impact, PLA University of Science and Technology, Nanjing, China*

L.J. Ma & M.Y. Wang
*School of Mechanical Engineering, Nanjing University of Science and Technology, Nanjing, China*
*State Key Laboratory of Disaster Prevention and Mitigation of Explosion and Impact, PLA University of Science and Technology, Nanjing, China*

Y. Wang & L. Dong
*State Key Laboratory of Disaster Prevention and Mitigation of Explosion and Impact, PLA University of Science and Technology, Nanjing, China*

ABSTRACT: Laboratory tests were conducted to assess the effects of loading frequency on the time-dependent behaviour and damage properties of rock salt under confining stress states. An axial two-stage irreversible deformation complied from the loci of minimum load of each cycle was observed, which is similar to that of conventional creep tests under static loads. The unloading modulus was found to decrease negative-exponentially with respect to duration time. The damage variable was represented in terms of the decay of material stiffness. To take into account the effects of loading frequency on time-dependent degradation for rock salt, a unified damage evolution equation was formulated based on the experimental results. A creep damage model for rock salt was proposed by introducing the non-stationary modular components into the Burgers viscoelastic model. Numerical simulation was further performed utilizing the newly developed model to evaluate the stability and serviceability of storage cavern in bedded salt formation under various loading scenarios. The simulated results indicate that a longer injection-withdrawal cycle results in a greater volume convergence rate of storage cavern. The dilatancy region surrounding the storage cavern extends progressively along the radial direction with increasing loading cycle.

## 1 INTRODUCTION

Due to the representative favorable creep, low permeability, and damage-healing characteristics, rock salt is considered an ideal geologic host rock for underground resource storage and waste disposal. As one of the prime alternatives for energy reserve, underground cavern in rock salt has found extensive applications around the world since its first use in 1940s. The first solution-mined gas storage in Jintan salt deposit, China, started for normal operation in 2007. It has long been recognized that the rheological property and relevant constitutive relationship of rock salt is of vital importance to the long-term stability and serviceability of storage cavern. Continuum Damage Mechanics (CDM) was initially introduced by Chan et al. (1992) to study the inelastic flow caused by damage evolution from creep to the creep rupture stage.

Normally, the mechanical parameters of the constitutive models for representing inelastic flow induced by coupled creep, damage, and damage healing are assumed to be constant

or stationary in most cases. In fact, the Young's modulus, strength, and viscosity of rock mass subjected to multi-field stress and weathering tend to decrease with respect to time (Sun 2007). The reduction of mechanical parameters objectively reveals the degradation of mechanical properties. Therefore, the damage evolution process could be represented by introducing variable parameters into the creep constitutive model, which provides a new approach to investigate the creep damage property of rock material (Zhang et al. 2009, Zhu et al. 2010, Yang & Cheng 2011, Wang et al. 2013).

In practical engineering, the rock mass around deep salt storage cavity is not only under a actual in-situ stress state but also subjected to repeated cycles of loading induced by the fluctuation of internal pressures during product injection-withdrawal periods. The mechanical behaviour of rock salt under different loading paths is dramatically diverse (Guo et al. 2012). It is well established that the deformation, strength and damage properties of rock salt under cyclic loading is highly dependent on the maximum applied stress, stress amplitude, loading frequency, temperature, and waveform (Ma et al. 2013, Ren et al. 2013, Fuenkajorn & Phueakphum 2010). The operated injection–ejection frequency could vary from daily to annual depending on the types of resource stored and the market demand. The loading frequency variation reaches a value of two orders of magnitude. Rare efforts, however, have been made to identify the effects of loading frequency on the mechanical properties of rock salt.

This paper aims to experimentally and theoretically assess the time-dependent deformation behaviour and damage properties of rock salt under different cyclic loading frequencies. Based on the tests results, a parameter-variable creep damage model taking into account the effects of loading frequency for rock salt is proposed. Numerical simulation analysis is then performed to evaluate the impacts of cyclic loading frequency on the stability and serviceability of the Jintan bedded salt cavern using the new developed constitutive model.

## 2 CYCLIC LOADING-UNLOADING TEST

### 2.1 *Sample preparation*

The rock cores were drilled form the Qianjiang salt deposit located at the depth of 1990–2080 m underground in Hubei Province, China. The Qianjiang rock salt mainly consists of ~85% NaCl, ~0.72% $Na_2SO_4$, 1.2% $CaSO_4$ and 7–10% other insoluble contents (e.g., glauberite, argillaceous, anhydrite). To avoid the damage induced by water, the salt cores were prepared by dry sawing and grinding with a diameter-to-length ratio of 1:2. The depth of parallelism of the upper and lower end faces of the cylinder was kept within ±0.03 mm. All the triaxial cyclic tests with different loading frequencies were conducted out using a TAW-2000 mechanical frame with electrical-hydraulic servo-control systems.

### 2.2 *Loading scheme*

The triaxial cyclic loading tests adopted load control. The confining pressure was first applied to a given value at a constant stress rate of 0.05 MPa/s. Then, the axial load was specified to the mean stress of cyclic load at a constant loading rate of 1 kN/s while fixing the confining pressure. Finally, a sine wave axial load taking the mean cyclic load as the initial value was applied with three different loading frequencies, i.e., 0.025 Hz, 0.05 Hz and 0.1 Hz, respectively. As shown in Table 1, $\sigma_{max}$ and $\sigma_{min}$ are the maximum stress and the minimum stress,

Table 1. Experiment scheme of triaxial cyclic loading.

| Specimen | Size($L \times D$) | Density/g/cm$^3$ | $\sigma_{max}$/MPa | $\sigma_{min}$/MPa | $\sigma_m$/MPa | $\sigma_a$/MPa | $\Sigma_3$/MPa | $f$/Hz |
|---|---|---|---|---|---|---|---|---|
| #1 | $104.28 \times 51.61$ | 2.064 | 38.7 | 20.17 | 29.44 | 9.26 | 14 | 0.025 |
| #2 | $103.22 \times 50.64$ | 2.145 | 38.7 | 20.17 | 29.44 | 9.26 | 14 | 0.05 |
| #3 | $101.07 \times 50.91$ | 2.163 | 38.7 | 20.17 | 29.44 | 9.26 | 14 | 0.1 |

$\sigma_m = (\sigma_{max}+\sigma_{min})/2$ is the mean stress of cyclic load, $\sigma_a = (\sigma_{max}-\sigma_{min})/2$ is the stress amplitude, $\sigma_3$ is the confining pressure, and $f$ is the loading frequency.

### 2.3 *Cyclic stress-strain curve*

Cyclic strain-stress curve exhibits typical sparse-dense-sparse three phases. Only the former sparse and dense phases were observed in this study, corresponding to the transient and steady states of axial deformation of rock salt, as shown in Figure 1. In the first two phases, the irreversible deformation (plastic and creep deformation) within each cycle gradually decreases with the cycling time and tends to be constant. The axial strain rate also tends to be stable, that is, the capability of rock salt resisting irreversible deformation increases with loading cycle. For each cycle, the unloading curve and reloading curve form a hysteresis loop with a certain width. The area of hysteresis loop represents the energy consumed in each loading cycle. The energy absorbed by the specimen is mainly consumed for the friction loss between mineral particles as well as the expansion of primary microcracks and the initiation of new fractures. The hysteresis loop area decreases gradually with the increasing of loading cycle, indicating that the energy consumption of rock salt reduces. That is, the damage induced by cyclic loading in terms of internal crack extension and new crack generation also decrease and drive to be stable accordingly.

## 3 A PARAMETER-VARIABLE CREEP DAMAGE MODEL FOR ROCK SALT

### 3.1 *Unified damage evolution equation considering the effect of loading frequency*

As the reduction of Young's modulus indicates the damage evolution and material degradation, the damage variable can be expressed as the decay of stiffness.

$$D = 1 - \frac{E_t}{E_0} \tag{1}$$

where $E_t$ is the measured unloading modulus at time $t$, and $E_0$ is the initial modulus.

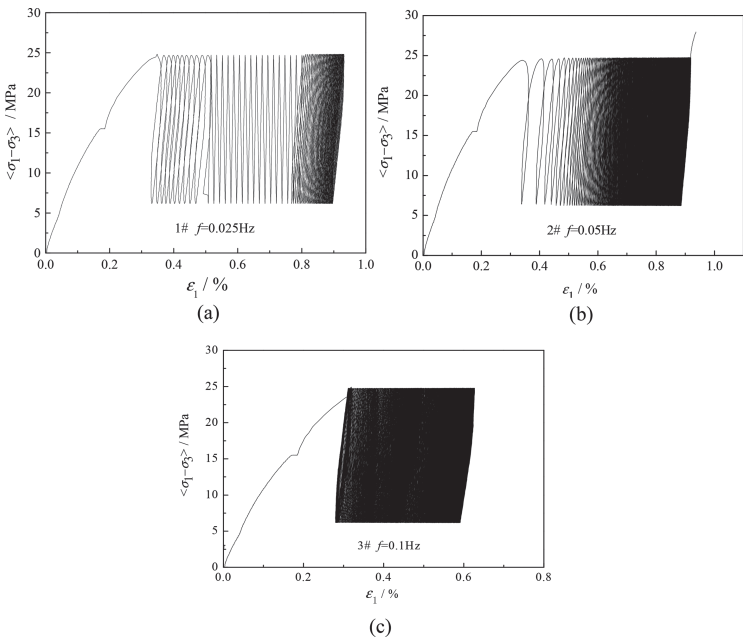


Figure 1. Axial stress-strain curves of rock salt under different loading frequencies.

The Young's modulus of rock salt subjected to triaxial cyclic loading exponentially decreases from initial modulus $E_0$ to long-term modulus $E_\infty$, which is similar to that of creep tests under static load. Likewise, the damage evolution equation can be given as follows:

$$D = \frac{E_0 - E_\infty}{E_0}(1 - e^{-\alpha t}) \tag{2}$$

where $\alpha$ is a constant related to damage degree.

The influence of loading frequency on the long-term damage degree $(E_0–E_\infty)/E_0$ and coefficient $\alpha$ could be represented with empirical equations:

$$\frac{E_0 - E_\infty}{E_0} = m\mathrm{e}^{nf},\ \alpha = rf^s \tag{3}$$

where $l$, $m$, $r$ and $s$ are the fitting parameters.

By substituting Equation 3 into Equation 2, the damage variable considering the effect of loading frequency has the form:

$$D = m\exp(nf)\left[1 - \exp\left(-rf^s t\right)\right] \tag{4}$$

Figure 2 presents the comparison of measured damage variable and the best-fitting results using damage evolution equation (Eq. 4). As seen in Figure 2, the damage variable complied from loci of unloading curve of each cycle increases nonlinearly with time or loading cycle in the initial stage, then drives to a constant after a certain time. Generally, the predicted damage variable agrees well with the observed value for three different loading frequencies. The proposed damage evolution equation can reasonably capture the trend of damage development for rock salt under cyclic loading. The relevant best fitted parameters are as follows: $m = 0.659$, $n = –7.33$, $r = 7.538$, $s = –0.694$.

### 3.2 *Creep damage model with variable parameters and its verification*

Based on the tests of rock salt under triaxial cyclic loading, the development of axial creep deformation consists of primary and steady stain, which coincides with the creep behavior described by the Burgers viscoelastic model. The Burgers creep model is composed of a Maxwell model and a Kelvin model connected in series. The volumetric behavior of rock salt is assumed elastic and the tensor form of Burgers creep model can be written as:

$$2(H_K\ddot{e}_{ij} + G_K\dot{e}_{ij}) = \frac{H_k}{G_m}\ddot{S}_{ij} + \frac{G_k}{H_m}S_{ij} + \left(\frac{G_k}{G_m} + \frac{H_k}{H_m} + 1\right)\dot{S}_{ij} \tag{5}$$

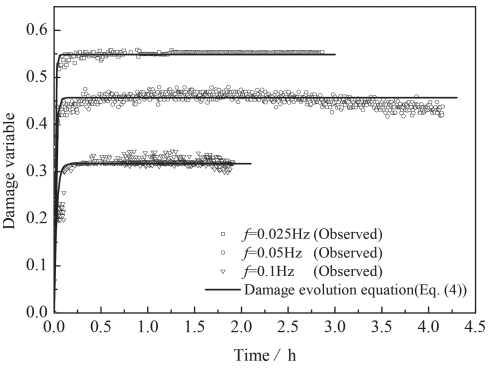


Figure 2. Comparison of the best fitting curves and the experimental data of damage variable for rock salt under different loading frequencies.

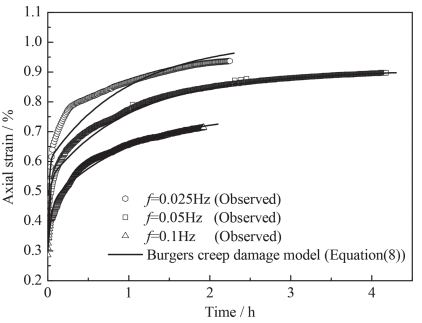


Figure 3. Comparison of Burgers creep damage model and the experimental data of axial strain for rock salt under different loading frequencies.

where $G_M$ and $G_K$ denote the shear modulus of the spring in the Maxwell body and Kelvin body respectively, $H_M$ and $H_K$ denote the viscosity coefficient of the dash pot in the Maxwell body and Kelvin body respectively, $e_{ij}$ is the deviator strain, $S_{ij}$ is the deviatoric stress.

Variable parameters are included in the Burgers model to reflect material degradation. The reduction of viscosity coefficients are mainly due to the sliding and dislocation in the crystal structure of rock salt accompanied with the newly created micro-cracks. Each parameter is assumed to change in the same way as Young's modulus. We have:

$$G_K^t = G_K^0(1-D),\ G_M^t = G_M^0(1-D),\ H_K^t = H_K^0(1-D),\ H_M^t = H_M^0(1-D) \tag{6}$$

where $G^0_M$, $G^0_K$, $H^0_M$, and $H^0_K$ are initial value of each parameter.

The Burgers creep damage model can finally be formulated by replacing the original parameters in Equation 5 with time dependent ones in Equation 6.

$$2(1-D)(H_K^0\ddot{e}_{ij} + G_K^0\dot{e}_{ij}) = \frac{H_K^0}{G_M^0}\ddot{s}_{ij} + \frac{G_K^0}{H_M^0}s_{ij} + \left(\frac{G_K^0}{G_M^0} + \frac{H_K^0}{H_M^0} + 1\right)\dot{s}_{ij} \tag{7}$$

For the triaxial cyclic creep test ($\sigma_2 = \sigma_3$), the axial creep equation of non-stationary Burgers model can be deduced:

$$\varepsilon_1(t) = \frac{1}{9K}\left[(\sigma_1 + 2\sigma_3) + 3K\frac{\sigma_1 - \sigma_3}{1-D}\left(\frac{1}{G_m^0} + \frac{1}{G_k^0} + \frac{t}{H_m^0} - \frac{1}{G_k^0}\exp\left(-\frac{G_k^0}{H_k^0}t\right)\right)\right] \tag{8}$$

where $\sigma_1$ is the maximum principal stress, $\sigma_3$ is the minimum principal stress.

The parameters obtained by fitting Equation (8) to the axial stain-time curves compiled from loci of the minimum load of each cycle are as follows: $G^0_m = 5.148$ GPa, $H^0_m = 179.71$ Gpa·h, $G^0_k = 3.216$ GPa, $H^0_k = 3.06$ Gpa·h, $K = 3.56$ Gpa. Figure 3 shows that the proposed Burgers creep damage model can better reflect the two-phase axial strain of rock salt specimens under different loading frequencies.

## 4 NUMERICAL SIMULATION OF SALT CAVERN STABILITY

### 4.1 *Geometric model*

The simplified shape of the constructed gas storage cavern is composed of two half ellipsoids located at the top and the bottom and a cylinder located in the middle connecting the two half ellipsoids. The heights of the top half ellipsoid and the bottom half ellipsoid are 45 m and 15 m, respectively, the radius of the cavern is 30 m, and the height of cylinder is 50 m. The dimensions of the simulation cube (including two mudstone layers, one salt layer, and four mudstone interlayers) is $950 \times 300 \times 300$ m$^3$ as demonstrated in Figure 4.

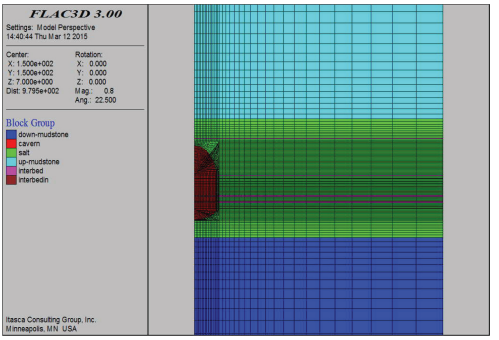


Figure 4. Geometric model mesh of calculation cube.

The thickness of the salt strata is 150 m. The thicknesses of the upper and lower mudstone layers are both 400 m. The surface stratum is converted to an equivalent uniform load of 8.23 MPa applied on the upper surface of the calculation model. Only one-fourth of the axisymmetric cube is taken for numerical simulation because of the symmetry of the structure and load. The four side faces are applied with lateral displacement constraints and the bottom surface is the applied with vertical displacement constraint. The magnitude of the vertical principal stress is assumed to be equal to the overburden weight, that is, the lateral pressure coefficient is set to 1.

### 4.2 *Constitutive model and property parameters*

The proposed Burgers creep damage model is applied to describe the viscoelastic response of rock salt. The two-component Notorn power law is adopted to model the creep behaviour of mudstone with the parameter set $A = 3 \times 10^{-8}$ MPa/d and $n = 2.4$ (Ma et al. 2013). The numerical modeling takes into account the effects of loading frequency on the stability of rock salt cavern due to the injection-withdrawal durations (e.g., 0.5d, 1d, 7d, 30d, 180d, 365d). The applied maximum and minimum operation pressures are 15 MPa and 6 MPa, respectively.

### 4.3 *Results analysis*

#### 4.3.1 *Deformation of rock mass around salt cavern*

Figure 5 presents the displacement field of the rock salt cavern under cyclic internal pressure. In Figure 5, the displacement direction of surrounding rock is toward the cavern center. The cavern roof settles, the cavern waist shrinks and the bottom heaves, which indicates that the storage cavern is in an overall rheological shrinkage state. The volume convergence of salt cavern for different injection-production cycles was calculated and plotted in Figure 6.

From Figure 6 we can see that the volume shrinkage of salt cavern increases approximately linearly over time. The shorter the operation cycle, the lower is the rate of volume reduction. According to the experimental results, the rock salt damage is loading-frequency dependent under cyclic loading-unloading conditions. The cyclic creep damage is more obvious at a low frequency (long cycle) than at a high frequency (short cycle). The corresponding cavern deformation behaves the same way in the low-frequency range, which is consistent with the laboratory tests.

Specifically, the effect of the injection-production period or frequency on the volume convergence is not evident in the first 5 years, however getting accumulated in the 30 years operation. The volume shrinkage ratio of the cycle of 365d is 8% greater than that of 0.5d. In addition, for several short periods, the overall difference in volume shrinkage is not obvious, especially for the periods of 1d, 7d and 30d, which is only 0.2%.

It is worth noting that the volume shrinkage rate of salt cavern is larger at the initial phase than the subsequent phases. For example, the average volume shrinkage rate of the operation cycle of 0.5d is 1.913 $m^3$/d for the first 5 years, 1.236 $m^3$/d for the phase from the 6th year to the 10th year, and 0.919 $m^3$/d for the phase from the 11th year to the 20th year.

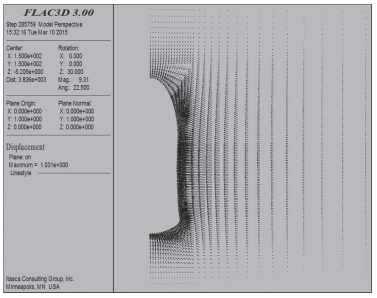


Figure 5. Displacement field of salt cavern subjected to cyclic internal pressure.

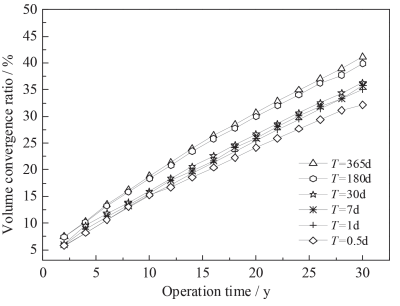


Figure 6. Volume convergence of salt cavern for different injection-withdrawal periods.

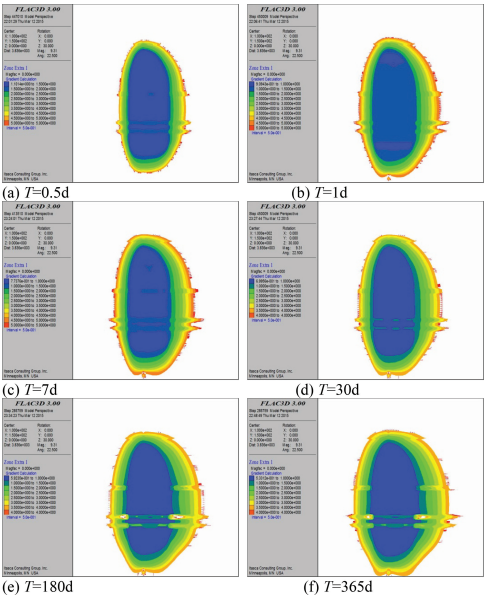


Figure 7. Contour of safety factor of rock salt around storage cavern after 30 years operation for different injection-withdrawal cycles.

### 4.3.2 *Factor Of Safety (FOS)*

Rock salt exhibits different physical and mechanical behaviours below and above the dilatancy boundary. Rock salt dilatancy is closely related to the occurrence of the microfracture, creep damage, permeability increase, and microacoustic emissions. The Factor Of Safety (*FOS*) is adopted to quantify the propensity for salt to dilate, which is defined as the ratio of $\sqrt{J_2}$ stress that will produce dilatancy according to dilatancy boundary function to the calculated $\sqrt{J_2}$ stress at $I_1$stress state (Ratigan et al. 1991):

$$FOS = 0.27I_1 / \sqrt{J_2} \tag{9}$$

where $I_1$is the first invariant stress, $J_2$ is the second invariant of deviatoric stress. A factor of safety of 1.0 is the critical stress state for dilatancy to occur. Dilatancy is expected to decrease with increasing *FOS* value. The predicted results of safety factor surrounding rock salt storage cavern under different loading cycles are shown in Figure 7.

In Figure 7, salt dilatancy is more likely to happen near the middle portion than other region of the underground cavern. Noted that all the *FOS* values around salt cavern remain in the safe range (*FOS* >1.0) for the loading cycle of 0.5d. The contour plot of *FOS* indicates that the

dilatancy region surrounding the storage cavern expands progressively along the radial direction with a increase in the cyclic injection-production cycle. The extension in the mudstone interbeds is even deeper, which could possibly lead to the oil and gas leakage between adjacent caverns. The predicted *FOS* results are similar for the loading cycles of 180d and 365d, corresponding to the minimum safety factors of 0.592 and 0.533, respectively. Similar results could also be found for the loading cycles of 7d and 30d. The relevant minimum safety factors are 0.733 and 0.699, respectively.

## 5 CONCLUSIONS

The axial strain of rock salt complied from cyclic stress-strain curve can be divided into transient stage and steady stage, which is similar to that of creep tests under static loads. The axial strain rate and the degradation rate of salt samples tend to decrease gradually with increasing loading frequency within the range tested. The formulated parameter-variable based creep damage model accurately describes the time-dependent behaviour of rock slat under triaxial cyclic loading with different loading frequencies.

The volume convergence of storage cavern increases roughly linearly with respect to operating time. Besides, the longer the injection-withdrawal cycle, the greater is the rate of volume convergence. The corresponding dilatancy of rock mass surrounding extends much deeper in the mudstone interbeds than that in other regions. The dilatancy region around the storage cavern propagates progressively in the radial direction with an increase in the loading cycle.

The constitutive model for rock salt developed in this study can provide operations with improved geotechnical design for rock salt storage caverns.

## ACKNOWLEDGEMENTS

This research has been financed and fully supported by the National Basic Research Program of China (973 Program, No.2013CB036005), the National Natural Science Foundation of China (Grant Nos. 51527810, 51309234, 51304219 and 51021001), which are greatly appreciated by the authors. The authors also thank the financial support of the Natural Science Foundation of Jiangsu Province (BK20130065) and the China Postdoctoral Science Foundation (2015M570451).

## REFERENCES

Chan, K.S., Bodner, S.R., Fossum, A.F. & Munson, D.E. 1992. A constitutive model for in elastic flow and damage evolution in solids under triaxial compression. *Mech Math* 14:1–14.

Fuenkajorn, K. & Phueakphum, D. 2010. Effects of cyclic loading on mechanical properties of Maha Sarakham Salt. *Engineering Geology* 112: 43–52.

Guo, Y.T., Yang, C.H. & Mao, H.J. 2012. Mechanical properties of Jintan Mine rock salt under complex stress paths. *Int J Rock Mech Min Sci* 56:54–61.

Ma, L.J., Liu, X.Y. & Wang, M.Y. et al. 2013. Experimental investigation on mechanical properties of rock salt under triaxial cyclic loading. *Int J Rock Mech Min Sci* 62: 34–41.

Ratigan, J.L., Sambeek, L.L., DeVries, K.L. & Nieland, J.D. 1991. *The Influence of Seal Design on the Development of the Disturbed Rock Zone in the WIPP Alcove Seal Tests, RSI-0400*, prepared by RE/SPEC Inc., Rapid City, SD, for Sandia National Laboratories, Albuquerque, NM.

Ren, S., Bai, Y.M. & Zhang, J.P. et al. 2013. Experimental investigation of the fatigue properties of salt rock. *Int J Rock Mech Min Sci* 64:68–72.

Sun, J. 2007. Rock rheological mechanics and its advance in engineering applications. *Chinese Journal of Rock Mechanics and Engineering* 26(6): 1081–1106.

Wang, J.B., Liu, X.R., Huang, M. & Liu, X.J. 2013. A non-stationary viscoelasto-plastic creep model for salt rock. *Disaster Advances* 6(4):93–101.

Yang, S.Q. & Cheng, L. 2011. Non-stationary and nonlinear visco-elastic shear creep model for shale. *Int J Rock Mech Min Sci* 48:1011–1020.

Zhang, Q.Y., Yang, W.D & Zhang, J.G. et al. 2009. Variable parameters-based creep damage constitutive model and its engineering application. *Chinese Journal of Rock Mechanics and Engineering* 28(4): 732–739.

Zhu, J.B., Wang, B. & Wu A.Q. 2010. Study of unloading triaxial rheological tests and its nonlinear damage constitutive model of Jinping Hydropower Station green sandstone. *Chinese Journal of Rock Mechanics and Engineering* 29(3): 528–534.

*Rock Dynamics: From Research to Engineering – Li et al. (Eds)*
*© 2016 Taylor & Francis Group, London, ISBN 978-1-138-02953-8*

# Indentation fragmentation mechanism of anisotropy shale under dynamic and static loads

G.J. Dong, P. Chen & T.S. Ma
*College of Oil and Gas Engineering, Southwest Petroleum University, Chengdu, China*
*State Key Laboratory of Oil and Gas Reservoir Geology and Exploitation, Southwest Petroleum University, Chengdu, Sichuan, China*

ABSTRACT: Low Rate Of Penetration (ROP) is one of the key technical difficulties in the anisotropic shales reservoir. Rock fragmentation efficiency is improved under coupled dynamic-static load. A new model for estimating the indentation fragmentation process of shale is developed. The damage and failure behaviors of rocks are simulated by using the explicit contact finite element method. According to the macro indentation experiment, a simulation model of rock fragmentation is verified. Rock fragmentation process is studied under three types of load conditions, including static load, dynamic load and coupled dynamic-static load. The results show that rock failure occurs along with the direction of maximum principal stress, mainly depending on tensile and shear stress, followed by the compressive stress. With the increase of static load, indentation depth increases, and the volume of fractured rock is enlarged as well, but there is a non-linear relationship between the static pressure and fragmentation volume. With the increase of dynamic load velocity, the transverse transmission range of stress wave get smaller, the longitudinal transmission depth of stress wave increases, and the transmission depth of the impact energy is improved. When the peak value of load is the same, energy density under dynamic-static combination load is higher than that under static load condition, and rock fragmentation efficiency is also improved significantly, which further explains the indentation fragmentation mechanism of shale. The mechanical behaviors of indentation fragmentation under complex dynamic-static loads conditions should be considered in the design of ROP optimization and drilling tools.

## 1 INTRODUCTION

Low Rate Of Penetration (ROP) is one of the key technical difficulties in shale gas reservoir, which increases the drilling time and cost. Percussive-Rotary Drilling (PRD) plays an increasingly important role in improving the ROP.PRD is developed from rotary drilling and percussive drilling. One of the earliest reports of percussion drilling technique occurred in 1940s (Harpst 1949). Since then different terms have been used, such as downhole hammer, percussion hammer, Down-The-Hole hammer, percussive drill, percussive-rotary drill. (Whiteley & England 1986). Significant gains in understanding the percussive mechanism have also been achieved in the laboratory (Kahraman & Bilgin 2003, Green & Judzis 2005, Niu 2008). The dynamic and static load experiments of rock broken is carried out (Li & Tao 2004.), PRD is one of the best ways to improve the drilling efficiency of hard formation. The fragment test of granite is studied by the use of the dynamic and static rock-breaking test bench (Zhao et al. 2005), reasonable load of single cutter cutting rock under the impact-static action was proposed. Simulation model of PRD is established based on FLAC3D, rock fragmentation mechanism of bit cutter is studied (Bruno and Han, 2005). Simulation model of PRD system is established (Lin et al. 2005), which can predict ROP, impact energy and piston impact force. Rock fragmentation process of PRD was studied by plastic strain failure model and this process is divided into four stages, PRD mainly depends on impact load, but rotatory load (Huang et al. 2010). With the use of lower Weight On Bit (WOB),

PRD has been shown to improve ROP in some hard formations, such as siliceous granite, sandstone, etc.

There are lots of research results about indentation breaking mechanism of rock for single cutter, however the bit cutter breaks rock under static load and dynamics load in percussive-rotary drilling. Rock fragmentation mechanism is complex under coupled static load and dynamic load. The preliminary results have been obtained from some indoor experiments, but in order to understand the rock breaking process under dynamic and static load, numerical simulation method can be used for studying the detailed development process of rock breaking. Because the bit-rock crushing process is a strongly nonlinear contact problem, it is necessary to analyze the single cutter indentation fragmentation by the contact nonlinear finite element method.

## 2 SIMULATION MODEL DESCRIPTION

### 2.1 *Boundary conditions and meshing analysis*

Factors affecting drilling efficiency include formation lithology, mechanical parameters, the flow field and the bit type. In order to analysis the numerical simulation model, need some assumptions: (1) The model doesn't consider the existence of original crack in rock, and doesn't consider the effect of internal pore pressure of rock; (2) The effect of temperature and the flow field is neglected; (3)The numerical model is established based on the indoor macro physical experiment. According to the assumptions and indoor experiment, the numerical simulation model of rock indentation mechanism is built by using ABAQUS software. For this numerical study of PRD, it is assumed that the rock mass will yield according to the Drucker–Prager yield criterion (Bearman et al. 1997). The numerical model consists of indenter and the rock. The model is the axisymmetric structure, in order to improve calculate the speed, a quarter part of the model is taken as the research object, the indenter and rock surface contact.

Model size determinate whether the entire model can represent for research question, the size of the rock indenter breaking experiment model consists of the rock size the indenter size (Fig. 1). Rock size consist of L1, L2 and L3, the stress boundary can't be influenced by three dimensions, try to reduce the size, this paper identified L1 = 80 mm, L2 = 80 mm, L3 = 100 mm. According to actual indenter size, indenter radius R = 1 mm, indenter length L = 30 mm.

Loads applied to the model include three forms, static concentrated force, impact load, the coupled action of static and impact load. The load was applied to the top of the drill bit, the value of different load mainly depends on the research problem. Indenter-rock interaction analysis focuses on the stress distribution of the rock fragmentation process. 1/4 part of the model include element 17718, node 15758.

## 3 ANALYSIS AND VERIFICATION OF THE NUMERICAL MODEL

### 3.1 *Mechanical properties*

The study area is located in Sichuan Basin, which is one of most important shale gas reservoirs in China. Longmaxi shale formation is one of gas reservoirs within the Weiyuan block

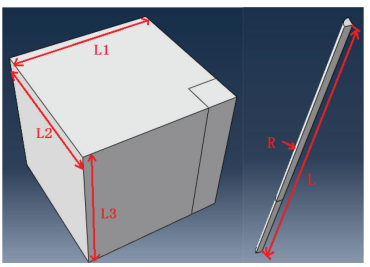


Figure 1. The model size.

in the Sichuan area, which located in southwestern china. The Longmaxi shale formation extends vertically from the depth of 3248 m to the depth of 3780 m. The storage reservoir has a thickness of 8 m. Rock mechanical parameters used in the model are based on LWD date of a horizontal well as well as laboratory experiments. There is complex contact between drill bit and rock, friction coefficient was identified as 0.2 (Table 1).

### 3.2 *Analysis and verification of the model*

The validation of numerical model by the comparative analysis of the macroscopic experimental and simulation results.

Three numerical broken condition and the corresponding experimental condition as show in the Figure 2. t = 0s is initial state of rock broken, rock didn't produce stress. With the increase of indentation depth, when t = 2s, plastic deformation of rock element occurs, and other rock elements are being squished, macro characterization of rocks has slightly convex. When indentation depth increases to 0.3 mm (t = 3 s), rock fragmentation occurs surrounding the indenter, the shape and size was close to the experimental results, which can verify the credibility of the model.

## 4 INDENTATION FRAGMENTATION MECHANISM ANALYSIS

### 4.1 *Rock broken analysis under different static loads*

According to the results of numerical simulation as show in Figures 3–5. rock fragmentation mainly along the direction of maximum principal stress under three kinds of static load,

Table 1. Rock and indenter mechanical parameters used in the model.

| | Values | |
|---|---|---|
| Parameters | Rock | Indenter |
| Density (g/cm$^3$) | 2.46 | 7.85 |
| Elasticity modulus (GPa) | 20.7 | 210 |
| Poisson's ratio | 0.22 | 0.3 |
| Frictional angle (°) | 33 | |
| Cohesion (MPa) | 16.6 | |
| Impact load (N) | | 1000 |
| Static load (N) | | 2000 |

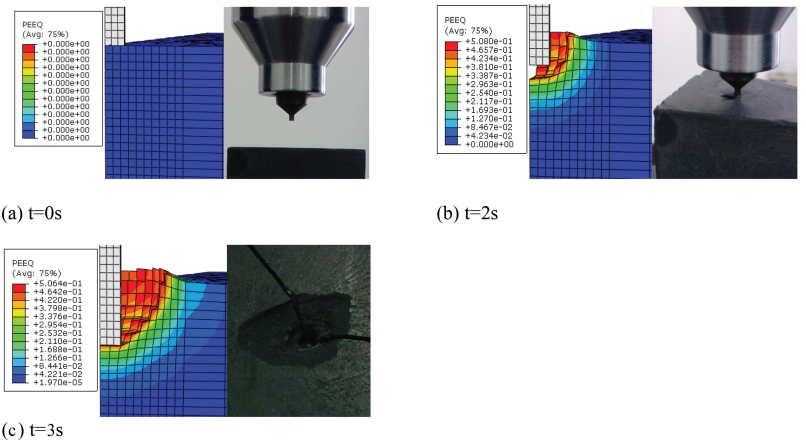


(a) t=0s (b) t=2s

(c) t=3s

Figure 2. The equivalent plastic strain compared with the experimental results.

which mainly depend on the tensile shear damage and tension damage; With the increase of static load, indentation depth increase, as well as the volume of rock broken increased, with the increase of indentation time, the peak value of different static load is different. The greater the peak power of the static load, the greater the rock crushing resistance. The static load and broken volume is not a simple linear relationship, which agree with the experimental results, static load reach to a certain value, the Rate Of Penetration (ROP) will reach the maximum, which is close to the actual statistics date.

### 4.2 *Rock broken analysis under different impact loads*

When the impact velocity V = 0.5 m/s and V = 5 m/s, stress occurred between the indenter and rock (Figs. 6–8). However, due to contact load is small, the impact velocity is slow, rock broken doesn't occur. When the impact velocity V = 50 m/s, the maximum principal stress of rock exceeds the limit value of tensile failure of the rock, eventually rock is invaded a certain depth. With the increase of impact velocity, indentation depth increase. The greater impact velocity of rock, the larger reaction force fluctuation. Every peak force of rock broken will fluctuating increase, which has a similar trend with the measured curve and experimental results.

The impact velocity is different, and the transmission range of stress is also different. When V = 0.5 m/s and V = 50 m/s, with the increase of impact velocity, lateral transmission range of stress get smaller, vertical transmission depth increases. Crushing pit shapes in different speed are similar to the range of maximum principal stress.

### 4.3 *Rock broken analysis under different loads forms*

When t = 2.5 s, Rock fragmentation doesn't occur under static and coupled loads (Fig. 9–11), but the strain value of the rock has nearly reached the broken state; When t = 5 s, rock fragmentation occurred under static load and coupled load. The range of stress under coupled

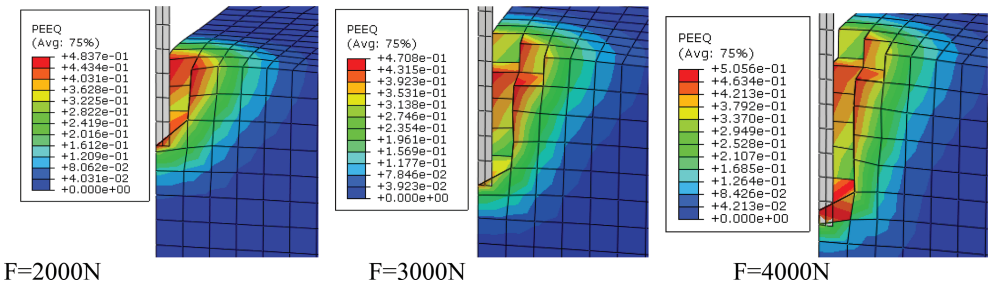


Figure 3. The equivalent plastic strain contour of rock fragmentation under different static loads.

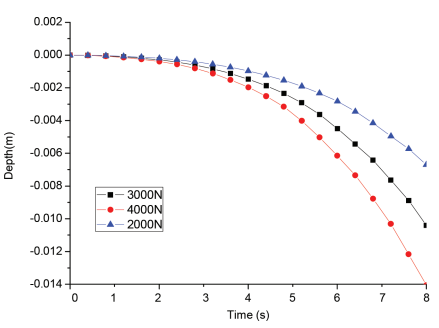


Figure 4. Indentation depth and time under different static loads.

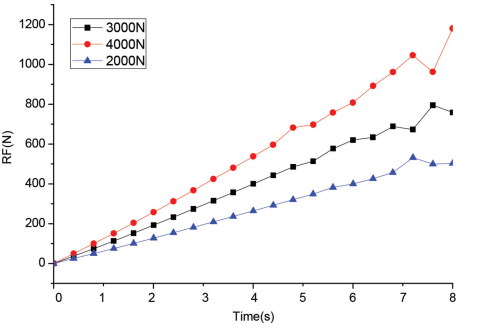


Figure 5. Reaction force and time under different static loads.

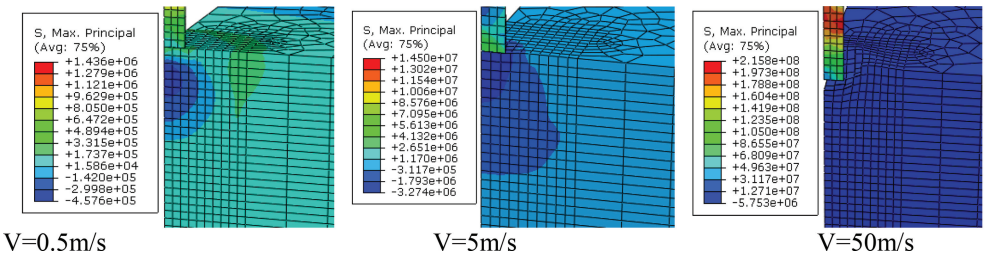


Figure 6. The maximum principal stress of rock fragmentation under different impact velocity.

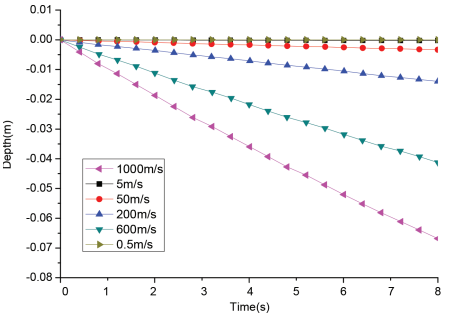


Figure 7. Indentation depth and time under different impact velocity.

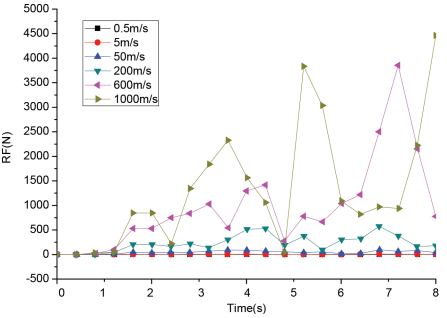


Figure 8. Reaction force and time under different impact velocity.

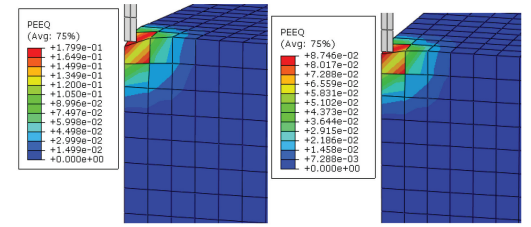


(a) t=2.5s 2000N ( static ) 1000N ( impact ) 3000N ( static )

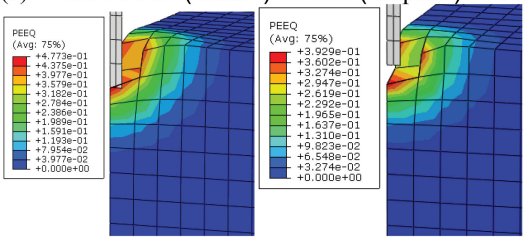


(b) t=5s 2000N（static）1000N（impact）3000N（static）

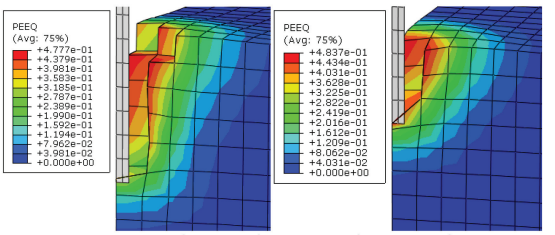


(c) t=10s 2000N ( static ) 1000N ( impact ) 3000N ( static )

Figure 9. The equivalent plastic strain contour of rock fragmentation under different loads forms.

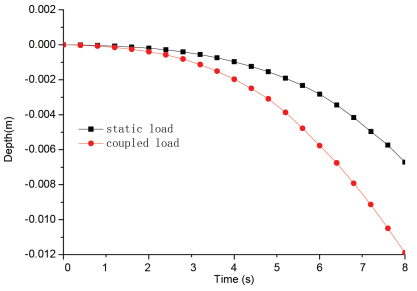


Figure 10. Indentation depth and time under different load forms.

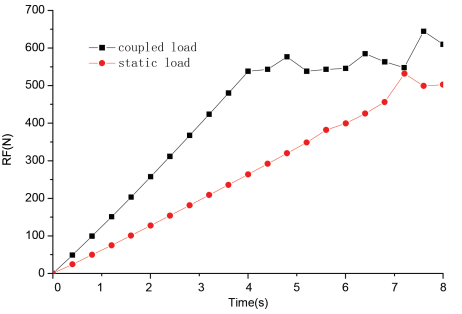


Figure 11. Reaction force and time under different load forms.

loads is larger than under static load, but the volume of rock broken is close; When t = 10 s, indentation depth and volume under coupled load is higher than under static load. Wave number of reaction force under coupled load is more than under static load. Rock will produce more cracks and higher fragmentation efficiency. Energy density under coupled load is higher than under static load. The rock is more easily broken. Which further explained the high efficiency problem of rock fragmentation under coupled static and dynamic load.

## 5 CONCLUSION

According to the macro experiments demonstrate the validity of rock broken numerical model. The stress field of rock fragmentation process is calculated. Rock fragmentation mainly along the direction of maximum principal stress under three kinds of static load, which mainly depend on the tensile shear damage and tension damage; he greater the peak power of the static load, the greater the rock crushing resistance. The static load and broken volume isn't a simple linear relationship. The impact velocity is different, and the transmission range of stress is also different. When V = 0.5 m/s and V = 50 m/s, with the increase of impact velocity, lateral transmission range of stress get smaller, vertical transmission depth increases. Energy density under coupled load is higher than under static load. The rock is more easily broken.

## REFERENCES

Harpst, W.E & Davis, E.E. 1949. Rotary percussion drilling. *Oil and Gas Journal* 182–187.

Whiteley, M.C. & England W.P. 1986. Air drilling operations improved by percussion-bit/hammer-tool tandem. *SPE Drilling Engineering* 1(5): 377–382.

Li, GH & Tao, X.H. 2004. Testing study on crushing work ratio of rock under dynamic and static load. *Chinese Journal of Rock Mechanics and Engineering* 14: 032.

Niu, D. 2008. Rigid Impact-the Mechanism of Percussive Rock Drilling. *The 42nd US Rock Mechanics Symposium (USRMS)*, American Rock Mechanics Association.

Green, S., Judzis, A. et al. 2005. Single cutter impact tests investigate deep-well hammer-drilling performance. *SPE* 97173.

Kahraman, S. & Bilgin, N. et al. 2003. Dominant rock properties affecting the penetration rate of percussive drills. *International Journal of Rock Mechanics and Mining Sciences* 40(5): 711–723.

Han, G. & Bruno, M.S. et al. 2006. 3D simulation of rock breakage with air hammers in gas-well drilling. *Proceedings of the 2006 SPE Gas Symposium*. Calgary, Oklahoma, May: 15–17.

Zhao, F. & Li, X. et al. 2005. Theoretical analysis and experiments of rock fragmentation under coupling dynamic and static loads. *Chin. J. Rock Mech. Eng.* 24(8): 1315–1320.

Lin, Y.H. & Shi, T.H. et al. 2005. Simulation of impact force and penetration rate of air hammer bit drilling. *Chinese Journal of Rock Mechanics and Engineering* 18: 023.

Huang, Z. & Fan, Y. et al. 2010. Simulation study on rock-breaking mechanism of percussion-rotary bit. *Journal of Southwest Petroleum University (Science & Technology Edition)* 1: 029.

Bearman, R.A. & Briggs, C.A. et al. 1997. The applications of rock mechanics parameters to the prediction of comminution behaviour. *Minerals Engineering* 10(3): 255–264.

*Rock Dynamics: From Research to Engineering – Li et al. (Eds)*
*© 2016 Taylor & Francis Group, London, ISBN 978-1-138-02953-8*

# Relationships between interface stress element method and applied element method

B. Feng & H. Chen
*Key Laboratory of Earthquake Engineering and Engineering Vibration, Institute of Engineering Mechanics, China Earthquake Administration, Harbin, China*

R.Q. Lan
*Institute of Geophysics, China Earthquake Administration, Beijing, China*

ABSTRACT: This work addresses the relationships between Interface Stress Element Method (ISEM) and Applied Element Method (AEM). We investigated the similarities and discrepancies between the two methods in theory by comparing their model compositions and stiffness matrixes. The results indicate that Applied Element Method is a special case of Interface Stress Element Method. Numerical examples also verify this finding.

## 1 INTRODUCTION

### 1.1 *Rigid body spring model*

There are mainly two kinds of numerical methods. One is based on continuum material equations, like Finite Element Method (FEM) and Boundary Element Method (BEM). The other is based on discontinuous material model, like Discrete Element Method (DEM) and Discontinuous Deformation Analysis (DDA). However, for structural analysis, we usually need to follow the behavior of structures from small deformation to crack initiation and propagation, fracture of structural members, even till total collapse. It is a typical continuum-discontinuum problem.

To solve this problem, Rigid Body Spring Model (RBSM) was proposed at first (Kawai & Kondou 1976). It regards the material in continuum status as rigid discrete elements connected by springs, and simulates the damage of material as fracture of springs. This method can follow most behavior of structures from zero loading up to complete collapse. However, the accuracy of RBSM in small deformation range is usually less than that of FEM. The accuracy of analysis results in other ranges is also affected due to this reason.

### 1.2 *Interface stress element method and applied element method*

Based on RBSM, several enhanced techniques, like Modified Distinct Element Method (MDEM), Extend Distinct Element Method (EDEM), Interface Stress Element Method (ISEM) and Applied Element Method (AEM), were proposed one after another. Among them, ISEM and AEM are both well studied and applied.

Surprisingly, ISEM and AEM seem to have no intersections, although they are similar to each other. ISEM was originally used in geotechnical engineering (Zhuo & Zhao 1993). Then AEM was firstly applied for structural analysis (Meguro & Hatem 1997). From then on, they have developed in parallel for many years. Their models and formulas are also fairly different, at least in the form. Is it true that ISEM and AEM are really parallel numerical methods? Or one is a special case of the other? To answer these questions, relationships between them have to be identified clearly.

In this paper, we investigated the similarities and discrepancies between these two methods in theory, by comparing their model compositions and stiffness matrixes. Numerical examples were also employed to confirm our finding.

## 2 COMPARISON ON MODEL COMPOSITIONS

### 2.1 *Model compositions of AEM*

As shown in Figure 1, AEM also models the structure as an assembly of rigid elements connected by springs. This is same to RBSM. The only difference is that in AEM, there are many pairs of normal and shear springs between one element and its neighbor. Each pair of springs merely represents stresses and deformations of a small area (hatched area in Fig. 1). Failure process of material can be simulated by fractures of these springs gradually.

This is an important improvement. It is the key point why AEM is more applicable than RBSM in analysis of structural failure behavior.

### 2.2 *Model compositions of ISEM*

As shown in Figure 2, rigid elements are also used in ISEM model. In each rigid element, there are one centroid node and several corner nodes. The centroid node represents the rigid motion of an element, and the corner nodes are used to follow the positions of corner points on each element.

Unlike RBSM, there are no springs between elements in ISEM model. They are replaced by a new type of connectors, namely interfaces, which distribute around the rigid elements and fuse together on the bordering area one element connects with another. An interface represents the stresses occurred on the boundary of an element and the deformations accumulated inside a real deformable element.

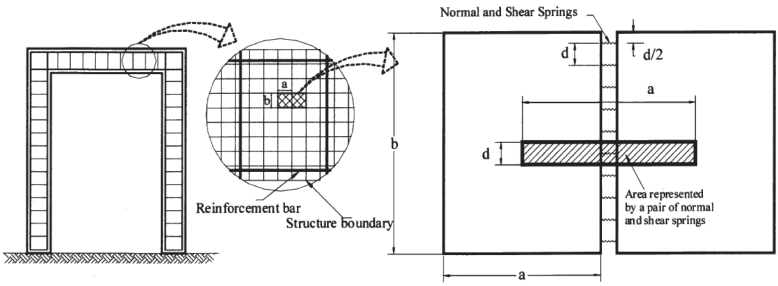


Figure 1. Modelling of structure to AEM (Meguro & Hatem 2000).

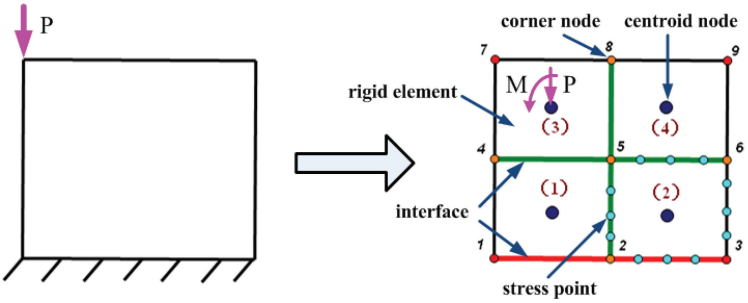


Figure 2. Model compositions of ISEM (Feng 2012).

For each interface, it can be divided into many sub-interfaces, on each of which there is a stress point. According to the status of stresses and deformations on stress points, we can also follow the progressive failure behavior of material gradually.

### 2.3 *Similarities and discrepancies*

From the compositions of the models, we can find several similarities between ISEM and AEM. 1) They both divide the studied region into rigid elements connected by connectors (spring or interface). 2) They both use rigid displacement mode, as same as RBSM, to describe the rigid motion of an element. 3) They both divide the connector into pieces, to simulate progressive failure behavior of material more accurately.

There are also some discrepancies between them. 1) The mechanical properties of the spring in AEM are quite different from those of the interface in ISEM. This is the start point for other differences. 2) The interface is more capable of describing complex material properties than the spring. For this reason, ISEM keep its model compositions unchanged no matter how complex the material is. For AEM, which is originally designed for identical material, its model compositions have to be modified when it meets multi-material problems (Mayorca & Meguro 2003). 3) In ISEM, the stiffness matrix for an interface or a sub-interface can be calculated exactly by integration. AEM compute them in a simple way, while the accuracy is drastically affected by number of springs between two elements (Hatem 1998).

From the facts discussed above, we can find that there are many high correlations between AEM and ISEM. They not only are similar to each other, but also coincide basically in the mechanics nature. It is reasonable to infer that one is a special case of the other. To verify it, comparison on stiffness matrixes is performed next.

## 3 COMPARISON ON STIFFNESS MATRIXES

AEM follows a standard procedure, as same as that in FEM, to calculate its global stiffness matrix. So does ISEM. Due to this, if the local stiffness matrix for a spring pair in AEM is different from that for its corresponding sub-interface in ISEM, then their global matrixes are definitely different.

For simplicity, we just compare the local stiffness matrix for one pair of spring with that for its corresponding sub-interface, to find out what components are different.

### 3.1 *Local stiffness matrix for a spring pair*

In AEM, the stiffness matrix in the local coordinate system for a spring pair (such as the pair of springs located within the hatched area in Fig. 1) is a $6 \times 6$ symmetric square matrix (Mayorca 2003):

$$k = \begin{bmatrix} K_n & 0 & -K_nA_y & -K_n & 0 & K_nB_y \\ 0 & K_s & K_sA_x & 0 & -K_s & -K_sB_x \\ -K_nA_y & K_sA_x & K_nA_y^2 + K_sA_x^2 & K_nA_y & -K_sA_x & -K_nA_yB_y - K_sA_xB_x \\ -K_n & 0 & K_nA_y & K_n & 0 & -K_nB_y \\ 0 & -K_s & -K_sA_x & 0 & K_s & K_sB_x \\ K_nB_y & -K_sB_x & -K_nA_yB_y - K_sA_xB_x & -K_nB_y & K_sB_x & K_nB_y^2 + K_sB_x^2 \end{bmatrix} \quad (1)$$

In this equation, $A_x = x_c - x_m$; $A_y = y_c - y_m$; $B_x = x_c - x_n$; $B_y = y_c - y_n$, where $(x_c, y_c)$, $(x_m, y_m)$ and $(x_n, y_n)$ are local coordinates of the spring pair, element A' s centroid and element B' s centroid, respectively.

$K_n = E \cdot d \cdot t / a$; $K_s = G \cdot d \cdot t / a$, for single material, where E = Young modulus; G = shear modulus; d = the distance between springs; t = thickness of the element; and a = the length of the representative area (Hatem 1998).

### 3.2 *Local stiffness matrix for a sub-interface*

In ISEM, the local stiffness matrix for a sub-interface is also a $6 \times 6$ symmetric square matrix, which is obtained by Equation 2 (see Feng 2012 for further details).

$$k' = \iint_{S_e} C_e^T N^T D N C_e ds \tag{2}$$

If we discretize an identical material domain by ISEM, using the same scheme employed in AEM, then the local stiffness matrix for a sub-interface is described as follows:

$$k' = \begin{bmatrix}
d_n S & 0 & -d_n S A_y & -d_n S & 0 & d_n S B_y \\
0 & d_s S & d_s S A_x & 0 & -d_s S & -d_s S B_x \\
-d_n S A_y & d_s S A_x & d_n S A_y^2 + d_s S A_x^2 + d_n S \frac{d^2}{12} & d_n S A_y & -d_s S A_x & -d_n S A_y B_y - d_s S A_x B_x - d_n S \frac{d^2}{12} \\
-d_n S & 0 & d_n S A_y & d_n S & 0 & -d_n S B_y \\
0 & -d_s S & -d_s S A_x & 0 & d_s S & d_s S B_x \\
d_n S B_y & -d_s S B_x & -d_n S A_y B_y - d_s S A_x B_x - d_n S \frac{d^2}{12} & -d_n S B_y & d_s S B_x & d_n S B_y^2 + d_s S B_x^2 + d_n S \frac{d^2}{12}
\end{bmatrix} \tag{3}$$

where, dn = E / a; ds = G / a; S = d · T; the meanings of other parameters are as same as those in Equation 1.

### 3.3 *Comparison*

By comparing each element in k with that at the same position in k′, we can find out that only four pairs of components are inconsistent. Coincidently, they all locate at the 3rd row and the 3rd column of each sub-matrix. More coincidently, their absolute differences are all $d_n S d^2 / 12$.

These results are caused by that AEM computes its local stiffness matrix in a simple way, which cannot calculate the rotational stiffness items in k accurately. On the other hand, ISEM calculates its local stiffness matrix in the way of numerical integration, by which all items in k′ can be obtained exactly.

Obviously, k is an approximation of k′. The formulas for stiffness matrix (local or global) in AEM are also simplified forms of those in ISEM. This also indicates that AEM is a special type of ISEM.

## 4 NUMRICAL EXAMPLES

We use two simple examples (linear static analyses on a laterally loaded cantilever, as shown in Figure 3, in which l = 12 m; h = 2 m; b = 1 m; P = 60 KN; $E = 1.0 \times 10^{11}$ Pa, v = 0.33.) to verify the results yielded from theory analysis. Example 1 focuses on the influence of d in AEM; Example 2 compares the precision of AEM with that of ISEM, when d is very small.

### 4.1 *Example 1*

In example 1, we meshed the cantilever with a $1 \times 6$ grid, in which each element is a square. To determine the influence of d in AEM, a series of simulations were performed, in which the

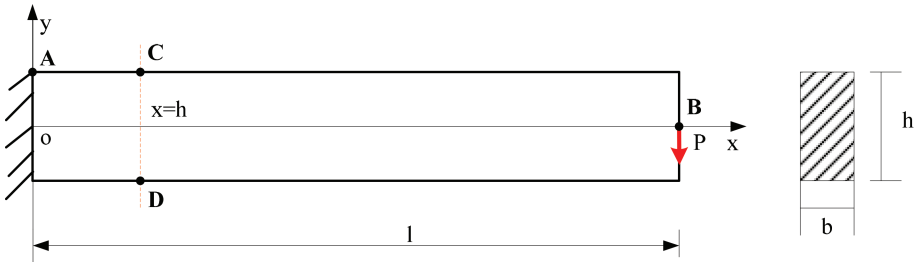


Figure 3. Laterally loaded homogeneous cantilever with rectangular cross section.

Table 1. Results from ISEM and AEM, when n = 1.

| | $y_{max(B)}$ | $\sigma_{x(C)}$ |
|---|---|---|
| Result | mm | MPa |
| Analytical solution | 0.5184 | 0.9000 |
| ISEM | 0.5340 | 0.9000 |
| AEM | * | * |

*Program ceased, no results.

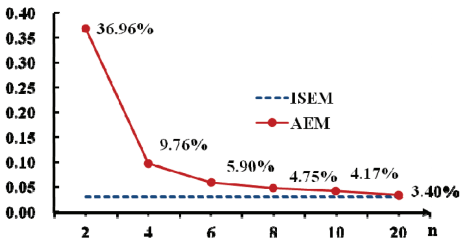


Figure 4. Ratios of error for $y_{max(B)}$ in Example1 ( n > = 2).

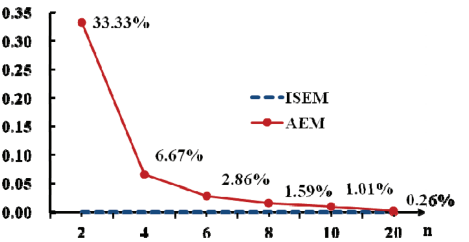


Figure 5. Ratios of error for $\sigma_{x(C)}$ in Example1 (n > = 2).

number of spring pairs between two adjacent elements (denoted by n) increased gradually. For comparison, corresponding simulations were also carried out by ISEM.

Surprisingly, when n = 1, the AEM program ceased with a message of "Error in GK". This means that the global stiffness matrix here is no longer a positive definite matrix, which is caused by the errors in the local stiffness matrixes. In contrast, the corresponding calculation in ISEM was performed normally with high accuracy (see Table 1). This indicates that there are inaccurate items in the stiffness matrixes of AEM definitely. Moreover, in an extreme case, their influence can be badly dominant.

As shown in Figures 4–5, the ratios of error reduce as n increases in AEM, while they keep constant in ISEM. This shows that when d becomes smaller, its influence in AEM also becomes smaller.

### 4.2 *Example 2*

In Example 2, we meshed the cantilever with a refined grid (5 × 30), in which the size of each element is much smaller (a = 0.2 m). The same simulations as those in example 1 were also performed one by one.

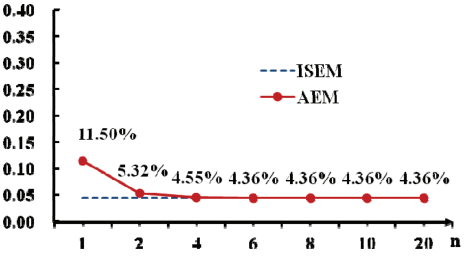


Figure 6. Ratios of error for $y_{max(B)}$ in Example 2.

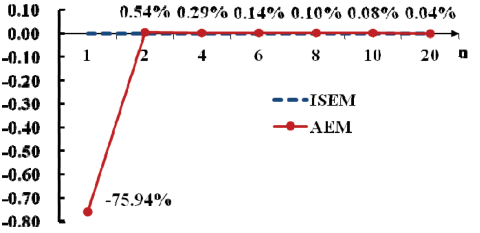


Figure 7. Ratios of error for $\sigma_{x(C)}$ in Example 2.

As shown in Figures 6–7, as d decreases, the precision of AEM increases. When n = 1, the simulation in AEM can be performed normally, although its ratios of error are still very high. When n > = 2, the precision of AEM is much better than that in Example 1. However, its accuracy is still worse than ISEM. On the other hand, the results obtained from ISEM are nearly same with those in example 1. Number of sub-interfaces has no effect on its accuracy.

This indicates that for AEM, even d is very small, its precision is still affected by the number of spring pairs. Fortunately, this effect vanishes very fast as n increases, which makes AEM applicable if we can set the number of spring pairs appropriately.

## 5 CONLUSIONS

The relationships between ISEM and AEM were identified clearly in this paper. Although there are some differences between their model compositions, formulas and stiffness matrixes, they are essentially the same numerical method in the mechanics nature. Actually, AEM is a special case of ISEM.

## REFERENCES

Feng, B. 2012. *Object-oriented Interface Stress Element Method and its coupling with FEM in time domain analysis*. Harbin: Institute of Engineering Mechanics, China Earthquake Administration.

Hatem, T. 1998. *A New Efficient Method for Nonlinear, Large Deformation and Collapse Analysis of Structures*. Tokyo: the University of Tokyo.

Kawai, T. & Kondou, K. 1976. New beam and plate elements in finite element analysis. *Journal of the Seisan Kenkyu* 28(9): 409–413.

Mayorca, P. 2003. *Strengthening of Unreinforced Masonry Structures in Earthquake Prone Regions*. Tokyo: the University of Tokyo.

Mayorca, P. & Meguro, K. 2003. Modeling masonry structures using the Applied Element Method. *Journal of the Seisan-Kenkyu* 56(6): 581–584.

Meguro, K. & Hatem, T. 1997. A new efficient technique for fracture analysis of structures. Bulletin of *Earthquake Resistant Structure Research Center, Institute of Industrial Science, the University of Tokyo* 30:103–116.

Meguro, K. & Hatem T. 2000. Applied element method for structural analysis: theory and application for linear materials. *Structural Eng./Earthquake Eng., International Journal of the Japan Society of Civil Engineers (JSCE)* 17(1): 21 s–35 s.

Zhuo, J.S. & Zhao, N. 1993. Piecewise rigid body-interface spring method for problems of discontinuous medium. *Journal of Hohai University* 21(5): 34–43.

*Rock Dynamics: From Research to Engineering – Li et al. (Eds)*
*© 2016 Taylor & Francis Group, London, ISBN 978-1-138-02953-8*

# Numerical investigation on the effect of fracture filling material on P-wave propagation

Y.L. Gui & Z.Y. Zhao
*Nanyang Centre for Underground Space, School of Civil and Environmental Engineering, Nanyang Technological University, Singapore*

ABSTRACT: The P-wave propagation through fractured rock mass is simulated using UDEC with a cohesive fracture model. A series of laboratory tests from literature on P-wave propagation through rock mass containing single fracture and two parallel fractures are introduced and the numerical model used to simulate these laboratory tests are described. The simulation results show that the proposed model, particularly the cohesive fracture model can capture very well the wave propagation characteristics in rock mass with un-welded and welded fractures with and without filling materials. In the meantime, in order to identify the significance of fracture on wave propagation, filling material with different particle sizes and the fracture thickness are discussed, and both factors are found to be crucial for wave attenuation.

## 1 INTRODUCTION

Natural rock mass contains continuous intact rocks and discontinuities, such as faults, joints, fissures and beddings. These discontinuous geological structures are most likely filled with weathered residuals, for example sands, clays and organic materials from plants. A better understanding of the wave propagation mechanism of the filled discontinuities in rock mass is theoretically and practically meaningful.

Laboratory testing methods study the phenomenon through direct physical measurements (Wu et al. 2015). These laboratory tests provide intuitive understanding towards wave propagation across a rock mass with welded or un-welded single or multi-parallel fractures either with or without filling materials. Nevertheless, the preparation and implementation of the tests are expensive and time-consuming (Zhao et al. 2014). Moreover, these laboratory tests have some challenges in measurement accuracy and it is always not easy to separate the interaction among the incident, transmission and reflection waves, therefore it is difficult to understand the attenuation mechanism of the fractures. To tackle the problem a wave separation technique proposed by Zhao & Gary (1997) needs to be iteratively used based on the measurement location on the rock bar. However, due to the limited number of data points recorded, the error from the wave separation can be considerable. In addition, the size of the physical model is always limited for an experimental testing, which limits its application to the engineering practice. In order to provide an overall view of in-situ wave propagation law, various numerical methods have been widely used, including Finite Element Method (FEM) (Wang et al. 2008), Finite Difference Method (FDM) (Reeshidev & Minnal 2008), Boundary Element Method (BEM) (Bazyar & Song 2006), Discrete Element Method (DEM) (Resende et al. 2010, Li et al. 2014), Discontinuous Deformation Analysis (DDA) (Gu & Zhao 2009), Numerical Manifold Method (NMM) (Zhao et al. 2014), and Distinct Lattice Spring Model (DLSM) (Zhu et al. 2011, Zhao 2014) and so on. These available numerical methods are able to predict the wave propagation in relatively simple scenarios, for example, very limited number of fractures, and linear-elastic fracture behaviour.

This paper focuses on a comprehensive numerical investigation into the wave propagation in rock mass with embedded un-welded or welded fractures with or without filling materials using UDEC. The rock mass has either single fracture or twin-fracture. The welded fractures are modelled using a mix-mode cohesive fracture model (Gui et al. 2015) which takes into

elastic, plastic, and damage mechanical behaviour into consideration to capture the wave attenuation, while the un-welded fracture are simulated by the conventional Mohr-Coulomb model. The numerical simulation results, especially the attenuation factors, are compared with the laboratory results, and good agreements are obtained.

## 2 SHRB TESTS AND NUMERICAL MODELS

The numerical experiments in this paper are based on the one-dimensional Split Hopkins Rock Bar (SHRB) tests conducted by Wu et al. (2015). Figure 1 presents the general setup of the tests. The dimension of the rock bars was 1500 mm in length and $40 \times 40$ mm$^2$ for cross section. The incident and transmission rock bars used were Dark Impala norite. There were various tests with single fracture (Figure 1a) and twin-fracture (Figure 1b) conducted. Four scenarios are considered for the single fracture: a non-welded fracture without filling materials (NF-NW), a non-welded fracture with filling materials (F-NW), a welded fracture without filling materials (NF-W) and a welded fracture with filling materials (F-W). As for the twin-fracture cases, three groups of adjacent parallel fractures are considered, namely, Group 1: an F-NW (Fracture 1) and an F-W (Fracture 2), Group 2: a NF-W (Fracture 1) and an F-W (Fracture 2), and Group 3: a NF-W (Fracture 1) and a NF-W (Fracture 2). For the filled fracture, dry quartz sand with particles ranging from 1 to 2 mm was filled in a 2 mm thickness fracture. In real experiments, a half cycle 2 kHz sinusoidal P-wave with amplitude of 8 Pa was applied to the incident bar by a rock striker. A, B, and C in Figure 2 are the measuring points in simulations. During the simulation, the horizontal stress and strain were measured.

In the numerical simulations, to avoid the interaction between the incident and reflected waves, a non-reflection boundary condition was applied at the ends of the incident and transmission bars and also a longer length of incident bar, i.e., 4500 mm was adopted. The transmission bar is set as 1500 mm. For the twin-fracture cases, a longer incident and center bar with length of 4500 mm and 3000 mm was applied, while the transmission bar is set as 1500 mm. Therefore, a complete half wave form can be measured before the arrival of reflected wave in all the bars. The sand size used for the simulations was 1 mm. Figures 1(c) and (d) present the zoom-in view of the non-filled fracture and filled fracture in numerical modeling, respectively. For the non-filled fracture, a single crack with zero thickness is utilized. However, the fracture zone in the filled fracture is discretized using Voronoi tessellation blocks with average size of 1 mm. In terms of the contact law of the blocks, the cohesive fracture model described in Gui et al. 2015 and a conventional Mohr-Coulomb model (Itasca,

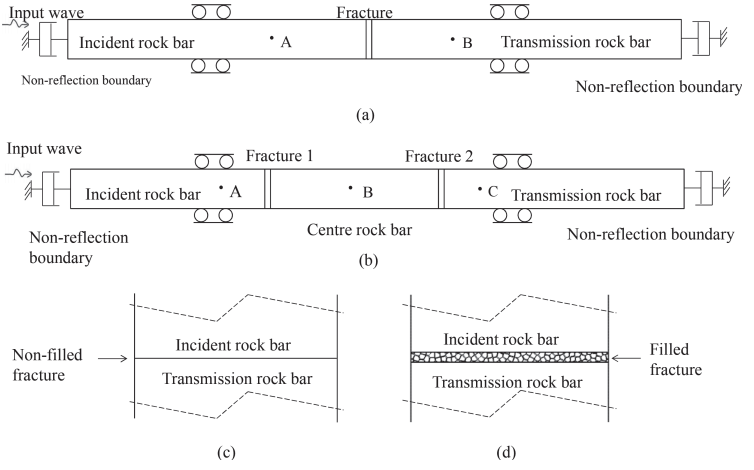


Figure 1. Sketch of the numerical models and boundary conditions: (a) single fracture, (b) parallel twin-fracture and enlarged view for (c) non-filled fracture and (d) filled fracture.

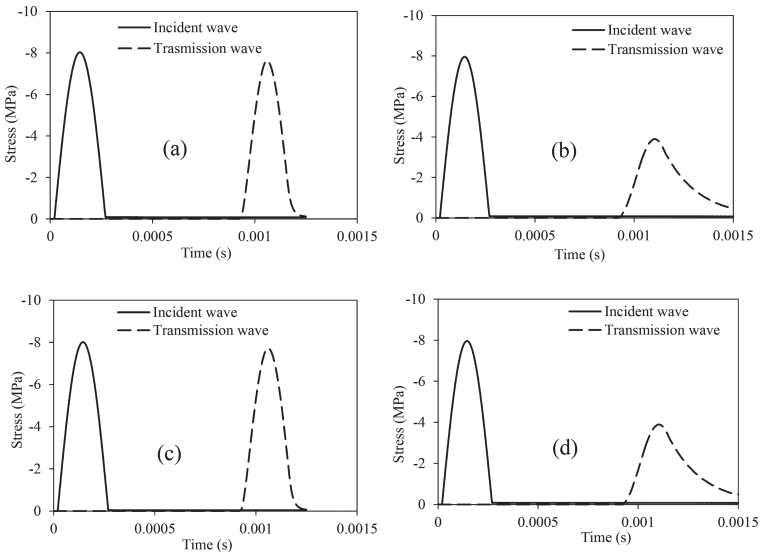


Figure 2. Modeled incident wave and transmission wave in single fracture cases for (a) NF-NW, (b) F-W, (c) NF-W, and (d) F-NW.

Table 1. The filling material and rock parameters used in the simulation.

| | Young's modulus, $E$ (GPa) | Poisson's ratio, υ | Density, ρ (kg/m$^3$) |
|---|---|---|---|
| Rock bar | 63.6 | 0.355 | 2900 |
| Filling material | 1.0 | 0.25 | 1572 |

2008) are used for the welded and non-welded fracture, respectively. Based on the geometry of the laboratory tests, the plane-stress condition is applied for the one-dimensional wave propagation simulations. The parameters of the filling materials (dry quartz sand + epoxy) and the Dark Impala norite bar are listed in Table 1.

## 3 RESULTS AND DISCUSSION

### 3.1 *Singl fracture*

In the single fracture experimental tests, the striking velocity was normally applied on the incident bar through a rock striker released from a compressed spring with stiffness of 9.52 N/mm, creating a half cycle sinusoidal normal pressure with amplitude of 8 MPa.

Figure 2(a) shows the simulated waves in the incident and transmission bars with the unwelded fracture without the filling materials. It can be seen that a good shaped half circle sinusoidal wave with stress amplitude of 8 MPa has been reproduced in the incident bar. The amplitude of the transmission wave is slightly smaller than that of incident wave. Due to the elongated length of the incident bar, the measured wave is the incident positive wave according to wave frequency and the P-wave velocity in the norite, which is calculated as

$$C_p = \sqrt{\frac{K + 4G/3}{\rho}} \tag{1}$$

where $C_p$ is the P-wave velocity of the rock. $K$, $G$ and $\rho$ are the rock bulk modulus, shear modulus and density, respectively. Taking the parameters from Table 1 into Eq. (1), the cal-

culated wave propagation velocity in the norite rock bars is 6000 m/s. However, due to the existence of the fracture, there is attenuation when the wave propagates across the fracture. The wave attenuation when propagating across a fracture is evaluated using attenuation factor. The definition of the attenuation factor is defined as (Wu et al. 2015)

$$\frac{1}{Q} = \frac{1-(\varepsilon_p^T / \varepsilon_p^I)}{\pi} \tag{2}$$

where $1/Q$ is the attenuation factor, $\varepsilon_p^T$ and $\varepsilon_p^I$ are the strain of the positive wave in the transmission bar and incident bar, respectively. Therefore, the wave attenuation factor obtained from the simulation is 0.054, which is close to the experimental value from Wu et al (2015), in which the wave attenuation factor ranges from 0.061 to 0.069.

Figure 2(b) shows the simulation results of the P-wave propagating across a welded fracture with the filling materials. The thickness of the fracture is 2 mm. The filling material is represented using Voronoi tessellation blocks with average size of 1 mm. Due to the existence of the filling material in the fracture, the incident wave is attenuated significantly more than that in the fracture without filling materials (i.e., zero thickness fracture). The attenuation factor is 0.16 for the fracture with the filling materials, as compared with the attenuation factor of 0.054 for the fracture without the filling materials. This is due to the interaction of the sand particles/blocks under the dynamic loading, which consumes a large amount of the energy. Comparing the transmission wave and the incident wave, apart from the decrease of the amplitude, the wave length of the transmission wave is apparently increased, demonstrating the frequency of the transmission wave is smaller than the incident wave since the wave propagation velocity in the transmission bar is the same as the wave propagation velocity in the incident bar. The result agrees with theoretical models that higher frequency P-wave has lower transmission coefficient (Zhu et al. 2011) when it passes through a rock fracture. This also implies that the rock fracture is able to filter out the higher frequency component of incident wave and this phenomenon is particularly apparent in the fracture with filling materials.

The simulation result of the welded fracture without the filling materials is presented in Figure 2(c). It can be seen that the attenuation of the incident wave is similar to the un-welded fracture without filling materials and the attenuation factor is 0.01146. Figure 2(d) presents the simulation results of the un-welded fracture with the filling materials, which gives an attenuation factor of 0.1624.

### 3.2 *Twin-racture*

In this study, three different fracture combinations are considered: Group 1, a non-welded fracture with filling materials (Fracture 1) and a welded fracture without filling materials (Fracture 2); Group 2, a welded fracture without filling materials (Fracture 1) and welded fracture with filling materials (Fracture 2); Group 3, a welded fracture without filling materials (Fracture 1) and a welded fracture without filling materials (Fracture 2). Same incident wave as the single fracture case is used.

Figures 3 present the simulation result of Group 1, Group 2 and Group 3. Take Group 1 as an example (Figure 3a), when the striker impinges the incident bar, a half cycle sinusoidal compressive wave was created in the incident bar. As the wave propagates from the left to the right along the incident bar (refer to Figure 1b), it is called positive wave. When the wave propagates across Fracture 1 (i.e., non-welded fracture with filling materials), it is partially reflected and partially transmitted. The positive part (tensile wave) of the incident wave in Figure 3(a) is the reflected wave with an opposite sign to the positive wave. The transmitted wave of Fracture 1 becomes the incident wave for Fracture 2 (welded fracture with filling materials). When the incident wave of Fracture 2 passes through Fracture 2, a much lower reflection is occurred. And the measured incident wave for Fracture 2 has almost same wave form as the measured transmission wave for Fracture 2. The other two groups' simulation can be analyzed similarly.

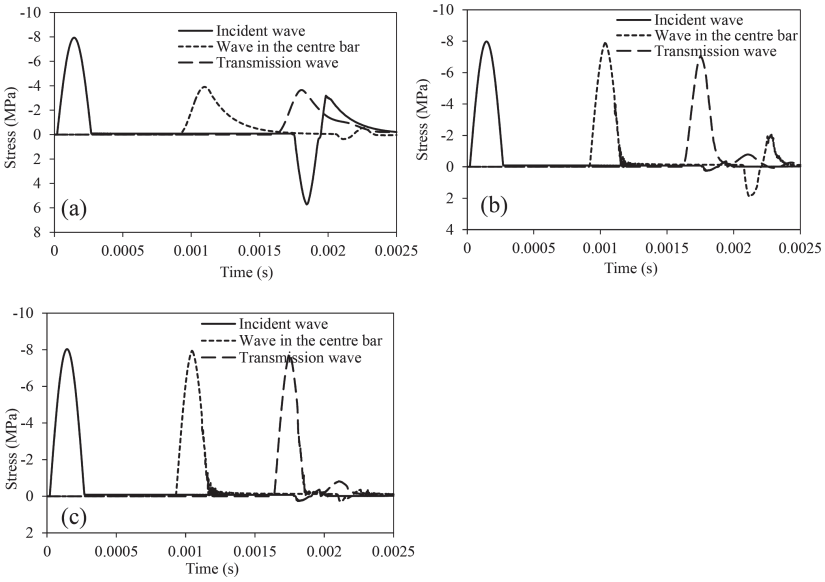


Figure 3. Modeled incident wave, wave in the center bar and transmission wave in twin-fracture cases for (a) Group 1, (b) Group 2, and (c) Group 3.

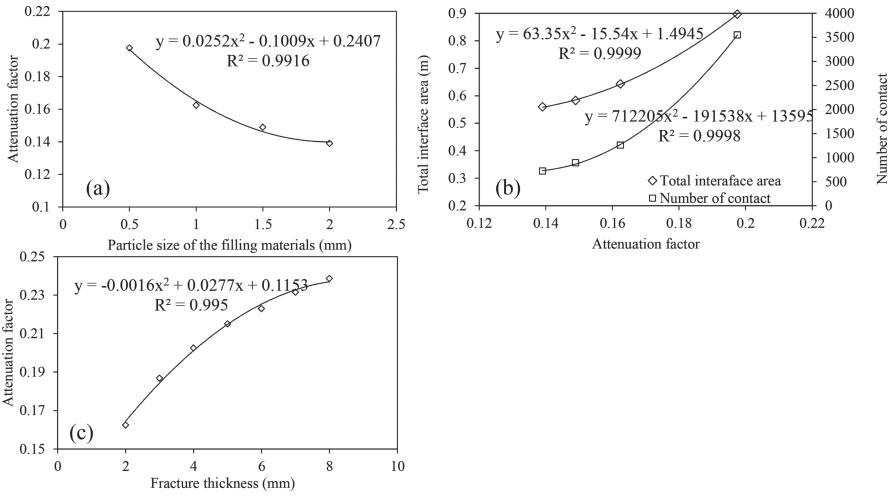


Figure 4. The effect of filling material in a single fracture scenario, (a) particle size effect, (b) area of particle interface effect and (c) fracture thickness effect.

### 3.3 *Effec of filling materials*

The numerical simulations in the previous sections were conducted based on constant sand size and fracture thickness. In this section, various sand particle sizes (i.e., 0.5, 1, 1.5, and 2 mm) are applied to investigate the influence of filling sand size on the P-wave propagation across a non-welded fracture with filling materials. Figure 4(a) shows the obtained attenuation factor using Eq. (1) for a wave propagating through the un-welded fracture with the filling materials with different particle sizes. It can be seen that the attenuation factor decreases with increasing particle sizes. Specifically, the attenuation factor is around 0.2 when the particle size is 0.5 mm;

however, it deceases to a value close to 0.14 when the particle size increases to 2 mm. This is due to the significant increase of interface in terms of total interface area as well as the number of contacts if the particle size decreases. Figure 4(b) plots the relationship between the attenuation factor and the total contact interface area and the number of contacts. Every interface between two neighboring particles plays a role of attenuator. Nature rock joints are filled with finer filling materials if they are more weathered. The mechanical behavior of the joints also can crush the filling material into finer components. Therefore, from this study, it is known that freshly formed rock joints attenuate less wave energy compared to more weathered rock joints.

Then, seven different fracture thicknesses on the wave attenuation factor are investigated and the simulated attenuation factors are shown in Figure 4(c). The un-welded fracture with 1 mm particle size filling materials is adopted for all the simulations. It is obvious that the increase of thickness can increase the attenuation factor. This can also be explained through the number of contacts and the total interface area. Thus, in numerical simulation, both filling material particle sizes and fracture thickness have to be well considered in order to present a reasonably modeling of wave propagation in rock mass.

## 4 CONCLUSIONS

Wave propagation in rock mass with single fracture and twin-fracture are investigated. A mix-mode cohesive fracture model is applied to the welded fracture while conventional Mohr-Coulomb friction model is used to represent the non-welded model. The simulation results reveal that the un-welded fracture with filling materials provide highest attenuation factor while the welded fracture without filling materials can attenuate the least energy. To investigate the effect of the particle size and the fracture thickness of the filling material on the wave propagation across a fracture, four particle sizes and seven fracture thickness are modeled in the study. The simulation results show that a finer particle size and a larger fracture thickness can increase the stress wave attenuation.

## REFERENCES


Bazyar, M.H. & Song, C. 2006. Transient analysis of wave propagation in non-homogeneous elastic unbounded domains by using the scaled boundary finite-element method. *Earthq Eng Struct D* 35(14):1787–1806.

Gu, J. & Zhao, Z.Y. 2009. Considerations of the discontinuous deformation analysis on wave propagation problems. *Int J Numer Anal Meth Geomech* 33:1449–1465.

Gui, Y., Ha, H.H. & Kodikara, J. 2015. An application of a cohesive fracture model combining compression, tension and shear in soft rocks. *Comput Geotech* 66:142–157.

Itasca Consulting Group, Inc. 2008. UDEC manual, USA.

Reeshidev, B. & Mrinal, K.S. 2008. Finite-difference modelling of S-wave splitting in anisotropic media. *Geophys Prospect* 56(3):293–312.

Resende, R., Lamas, L.N., Lemos, J.V. & Calçada, R. 2010. Micromechanical modelling of stress waves in rock and rock fractures. *Rock Mech Rock Eng* 43(6):741–761.

Wang, Z.L., Li, Y.C. & Wang, J.G. 2008. Numerical analysis of blast-induced wave propagation and spalling damage in a rock plate. *Int J Rock Mech Min Sci* 45:600–608.

Wu, W., Li, H.B. & Zhao, J. 2015. Dynamic responses of non-welded and welded rock fractures and implications for P-wave attenuation in a rock mass. *Int J Rock Mech Min Sci* 77:174–181.

Zhao, H. & Gary, G. 1997. A new method for the separation of waves. Application to the SHPB technique for an unlimited duration of measurement. *J Mech Phys Solids* 45(7):1185–202.

Zhao, X.B., Zhao, J., Cai, J.G. & Hefny, A.M. 2008. UDEC modelling on wave propagation across fractured rock masses. *Comput Geotech* 35:97–104.

Zhao, G.F. 2014. Modeling stress wave propagation in rocks by distinct lattice spring model. *J Rock Mech Geotech Eng* 6:348–355.

Zhao, G.F., Zhao, X.B. & Zhu, J.B. 2014. Application of the numerical manifold method for stress wave propagation across rock masses. *Int J Numer Anal Meth Geomech* 38:92–110.

Zhu, J.B., Zhao, G.F., Zhao, X.B. & Zhao, J. 2011. Validation study of the distinct lattice spring model (DLSM) on P-wave propagation across multiple parallel joints. *Comput Geotech* 38: 298–304.

*Rock Dynamics: From Research to Engineering – Li et al. (Eds)*
*© 2016 Taylor & Francis Group, London, ISBN 978-1-138-02953-8*

# 3D seismic imaging for monitoring rock-mass degradation and excavation damage

J.W. Huang & J.W. Flynn
*Itasca Microseismic and Geomechanical Evaluation (IMaGE), UK*

S. Mustonen
*POSIVA OY, Finland*

R.P. Young
*University of Toronto, Toronto, Canada*

ABSTRACT: Mine development and rock mass excavation impose stress changes in the surrounding rock that typically introduce mechanical failure, causing seismicity or acoustic emission and rock degradation, and consequently altering velocity inside the rock mass. Methods of detecting these changes include both passive and active monitoring techniques. Passive microseismic monitoring utilising the acoustic emission energy and provides insight into the rock failure. Ultrasonic velocity tomography, on the other hand, is a velocity imaging technique to characterise the rock deformation in the damage zones and thus provides better evaluation of the integrity. Based on these two monitoring methods, we introduce a seismic imaging technique that is able to detect the velocity variation of the rock mass using both passive seismic and active ultrasonic sources. In this paper, we first demonstrate the performance and advantages of this imaging technique in locating microseismic events and recovering velocity variations using synthetic data. We then apply the technique in two different scenarios: (1) induced seismicity monitoring during the caving development of Lift 2 of Northparkes mine and (2) active ultrasonic survey in an Excavation Damage Zone (EDZ) in the underground nuclear facility Onkalo. We show that the fracture evolution and dynamic velocity variations inside the rock mass is well detected by the tomographic velocity images. Time-lapse images could be produced to reveal the stress evolution at different development and production phases. With the passive sources covering the seismogenic zone and active survey illuminating the aseismic zone, this technique can fully utilize all the ray paths available and provide enhanced images of the rock damage and degradation.

## 1 INTRODUCTION

Human activities such as mine site development, reservoir stimulation, and geothermal energy extraction would cause rock degradation and generate micro-seismicity or acoustic emission. The monitoring of seismicity is generally used to give critical feedback to the on-going operations. Passive microseismic tomography similar to earthquake tomography (e.g. Thurber 1983) honors the coupling between the velocity and the location and jointly locate induced events and update rock velocity model traveled by the ray paths. Recent application of passive microseismic tomography in petroleum field (e.g. Zhang et al. 2009, Tselentis et al. 2011) replies on conventional ray tracing to calculate travel times, as the reservoir velocity model in those cases are usually well represented by a layered (1D) or a smoothed (3D) model. In mining and geothermal field, however, complex velocity structures and arbitrary discontinuities are commonly observed. Therefore, we propose to use a more robust method (fast sweeping method) to calculate the travel times (Zhao 2004) in complex 3D heterogeneous velocity model. In addition, the conventional linearized travel-time inversion becomes unstable as regions with poor ray

coverage are included in the model. Damped least square method can stabilize the inversion but scarifies the model resolution. The adjoint method-based tomography (Huang & Bellefleur 2012) formulates an inverse problem as a forward problem and only updates the region with adequate coverage. If passive sources are used such as microseismicity or acoustic emissions, the events can be re-located after each velocity update iteration.

In the following section, after brief introduction of the fast sweeping and the adjoint method, we will use a synthetic data set to demonstrate the performance of the fast sweeping and adjoint based travel-time tomography in locating MS events and recovering velocity variations. We then apply this imaging technique to passive monitoring arrays at Northparkes mine and show that the fracture evolution is associated with the dynamic velocity variations in the seismogenic zones. Similar observation has also been reported by Mercier et al. (2015). In the second example, we perform cross borehole ultrasonic velocity tomography in the Excavation Damage Zone (EDZ) of the ONK-TKU-3620 niche using controlled active source to image a 7 $m^3$ rock volume beneath the tunnel floor. The results showed that the excavation damage was confined to the top 0.5 m associated with a higher degree of fracturing or damage.

## 2 METHODOLOGY

### 2.1 *The fast sweeping and the adjoint method*

Fast Sweeping Method (FSM) is a finite difference method directly solving the following Partial Differential Equation (PDE):

$$|\nabla T(x)|^2 = 1/c^2(x), x \in R^3 \setminus x_s \tag{1a}$$

with boundary condition

$$T(\boldsymbol{x}_s) = \tau_0, \tag{1b}$$

where $T(\boldsymbol{x})$ is the travel-time and $c(\boldsymbol{x})$ the propagation velocity at location $\boldsymbol{x}$, respectively. The operator $|.|$ is the vector norm and $\nabla$ the gradient. The point source is located at $\boldsymbol{x}_s$ with initial time $\tau_0$ with respect to a reference time.

This method possesses numerous advantages over conventional ray tracing (see details in Huang & Bellefleur 2012, Huang et al. 2013). One example from a mining case is shown in Figure 1. The velocity of the model ranges from 0 to 4 km/s with the low velocity region representing air gap and mobility zone. The zero velocity is treated as barriers in which the travel time is undefined. The model contains ~$10^4$ grid points and the total computation time is less than 5 seconds on a single CPU core. Seismic rays can still be traced following the gradient of the travel time field and provide the ray polarization as well as travelling distance for both P- and S-wave to any geophone locations (Figs. 1b and 1c).

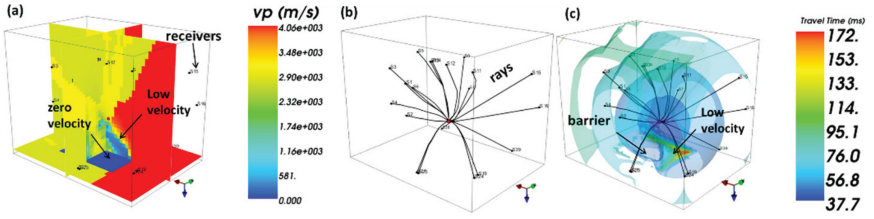


Figure 1. (a) The velocity model constructed from yield zone modelling of a developing underground caving mine, (b) the seismic rays traced based on the gradient of travel time and (c) the contour of the travel time rendered as isosurfaces. The full computation time is less than 5 seconds using a single CPU.

The adjoint method formulates the inverse problem as the minimization of the misfit function under the constraint of the PDE, and an adjoint PDE is obtained to avoid intensive computation of the Fréchet derivative. In our case, we obtain the following adjoint PDE:

$$\nabla \cdot (-\lambda \nabla T) = 0, x \in R^3 \setminus \Gamma \tag{2a}$$

with the boundary condition

$$(n \cdot \nabla T)\lambda = T^* - T, x \in \Gamma \tag{2b}$$

where **n** is the normal vector to the surface $\boldsymbol{\Gamma}$ where the sensors are deployed, $\lambda$ is the adjoint solution, which can be solved using the fast sweeping method as well.

The velocity can then be iteratively updated using:

$$c_n + 1 = c_n + \alpha \delta c, \text{and } \delta c = -\lambda / c^3 \tag{3}$$

where $\alpha$ is the step size.

Figure 2 shows a velocity perturbation example calculated using equation 3 for a point source surrounded by 6 geophones in a homogeneous velocity model (3 km/s). Using 2 km/s as the initial velocity, the spatial pattern of $\delta c$ shows the ray coverage and indicates that the value along the ray paths shall be increased whereas the area outside remains unchanged. This example demonstrates that the adjoint method is able to update the model adaptive to the ray coverage.

## 2.2 *Seismic imaging with passive/active sources*

Our seismic imaging technique uses first arrival time of P- or S-wave and is composed of 5 steps:

a. Select *a priori* model for the P- or S-wave velocity structure appropriate for the area being investigated;
b. Make an initial estimate of the passive source location and initial time (hypocentral parameters) and fix the active source locations.
c. Calculate theoretical P- or S-wave travel times from the sources to the stations, and compute the corresponding arrival-time residuals;
d. Evaluate derivatives of the arrival time residuals with respect to variations of the hypocentral parameters and with respect to variations in the velocity;
e. For a set of events, find adjustments to both the hypocentral and velocity parameters which will minimize the arrival time residuals, and obtain a new estimate of the passive source locations and the velocity structure.

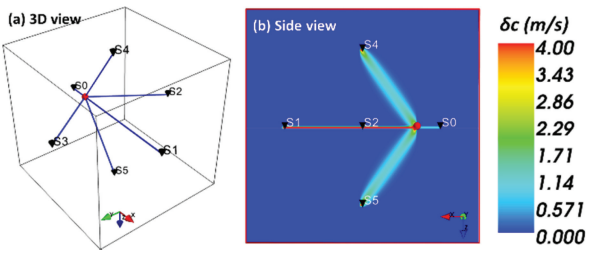


Figure 2. (a) A 3D view of the source (red dot) and geophone stations (black cones). The source and stations are connected by straight lines. (b) The side view of the velocity perturbation. The spatial pattern of $\delta c$ is consistent with the ray path between the source and stations. The velocity along the ray path shall be increased whereas the region not covered by ray paths is not updated.

Steps of c) to e) are performed iteratively until the travel-time residuals are minimized to a target level. The workflow is shown in Figure 3. At the end of the iteration, if the residual reduction is less than a target threshold, the inversion is considered converged and the final hypocenter parameters and velocity images are output. Comparing with active source imaging, the passive source imaging includes one extra step of hypocenter parameter inversion, i.e., loop 1 in Figure 3. Using a synthetic data set from 21 tri-axial borehole geophones, we demonstrate the performance of this workflow.

The true model is layered with dimensions of 200 m by 200 m by 256 m model and 2 m grid interval (see Figure 4a). The dots at the center represent 200 microseismic events. The source mechanism for all events is a mixture of tensile and shear crack with primary frequency of ~150 Hz.

We first locate all 200 microseismic events following the conventional microseismic processing workflow (e.g., Pettitt & Young, 2007). The homogeneous velocity and the initial hypocenter positions are then input into the seismic imaging workflow (Figure 3). The discrepancy between the calculated travel-time and the picked travel-time is used to update both velocity and hypocentral parameters. Comparing with the true velocity well logs (Figure 4b), the tomographic velocity recovers multiple velocity layers as well as the high-velocity region where the microseismic events occur.

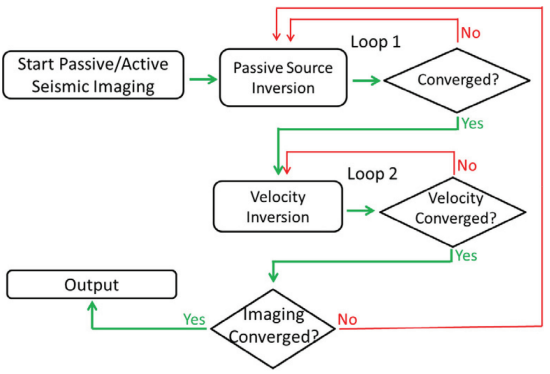


Figure 3. The workflow of our passive/active seismic imaging consists of two loops of inversion, one for passive source hypocenter parameter and the other for velocity. At the end of iteration, if the decrease of residual is larger than the target threshold, the two loops are repeated till the convergence criterion is satisfied.

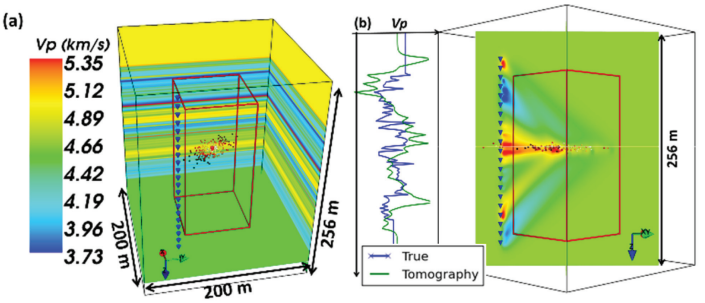


Figure 4. (a) The true velocity model and the monitoring array geometry using a string of borehole geophones (blue cones). The red box marks the monitoring volume and the dots inside show the true location of the modeled 200 microseismic events. (b) The tomographic velocity after passive seismic imaging. It recovers multiple velocity layers penetrated by the borehole.

## 3 APPLICATIONS

### 3.1 *Rock damage imaging in northparkes cave mine*

The microseismic events used in this study were recorded during the monitoring of the early stages development and caving of Lift 2 the E26 orebody at Northparkes Mine. The undercut level at Lift 2 of Northparkes Mine locates at a depth of 830 m and covers a footprint of approximately 200 m in diameter. With 27 monitoring stations deployed around the projected cave volume, we have located 1525 events in a period of 10 days at early stages of cave development using a homogeneous velocity model (3.9 km/s). Considering that events within the volume surrounded by the monitoring stations are usually located with the lowest uncertainty, we only use the 869 events for passive seismic imaging (see Figure 5) corresponding to early stages of caving, with most of the events occurred close to the east side of the dioritic body.

The iso surface visualization (Figure 5) reveals a low velocity region (~3 km/s) developed close to the dioritic body around which most early activity concentrates induced by the caving operation within the selected period. The high velocity region (~4.2 km/s) inside the dioritic body suggests a different geomechanical behavior of this body. Increases in transmission velocity can be associated with local stress concentrations during the caving process, an observation that will require a time-lapse processing of seismic data (Mercier *et al*. 2015).

### 3.2 *Ultrasonic tomography of the excavation damage zone*

Ultrasonic velocity surveys in the frequency range of 20 kHz to 120 kHz were carried out in the Excavation Damage Zone (EDZ) of the ONK-TKU-3620 niche, excavated through drill and blast, to obtain a P-wave tomographic image of the top 0.8 m of the tunnel floor

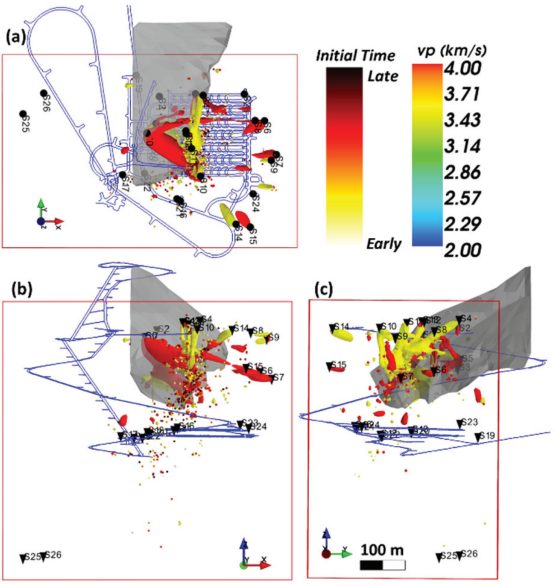


Figure 5. Three different views of Lift 2 of Northparkes Mine showing the geophone locations (black cones), and the mine infrastructure (blue lines). (a) is viewing from the top, (b) towards North and (c) towards West. The axis *x*, *y*, and *z* are pointing in East, North and Upward direction, respectively. Only 869 MS events surrounded by the 27 stations are used for passive seismic imaging. The low velocity region (in yellow) around the dioritic body is induced by the caving operation whereas the high velocity region (in red) partially overlapped within the dioritic body indicates it may have higher velocity than the surrounding rock and a different geomechanical behavior.

as part of the geophysical characterisation of the EDZ. The P-wave tomography covered a three-dimensional volume of the EDZ field sampled by multiple two-dimensional planes defined by drill-holes, providing 30 2-D sections along the North-South, East-West, North West-South East and North East-South West directions (Figure 6).

A total of 24 sensors were deployed in the field with a spacing of 0.05 m, performing four surveys at different positions for each tomographic section in order to provide a homogeneous spacing of 0.05 m. The sensors were able to switch between pulsing and receiving mode and provide up to 552 ray-paths for each tomographic plane. Only high-quality cross-hole P-wave first arrivals were used to produce the tomographic velocity images. The results showed that the P-wave velocity varies between 4.8 km/s and 6.5 km/s, with higher velocities at the northern end of the EDZ field (Figure 7).

A more robust and general interpretation can be drawn from stacking the results from tomograms in blocked depth levels, as presented in Figure 8. Figure 8a shows the stack of all tomographic measurements stacked at intervals of 0.1 m. The vertical profile shows almost constant P-wave velocities around 6 km/s below a depth of 0.5 ± 0.1 m. This result can be interpreted as a boundary for the EDZ. Figure 8b, c and d show the same profile split for the different areas in the EDZ field, showing in general higher velocities for the top 0.6 m for the

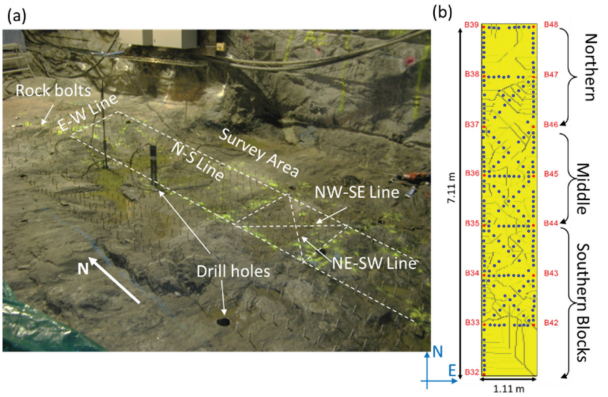


Figure 6. (a) A photo of the surveyed area in the EDZ field at ONKALO's ONK-TKU-3620 niche. The survey area is outlined by white dashed lines. Multiple holes were drilled to deploy borehole sensors. (b) Plan view of the surveyed area. Red dots and fonts mark the location of drill-holes. The three blocks: northern, middle and southern, were analysed in the following section.

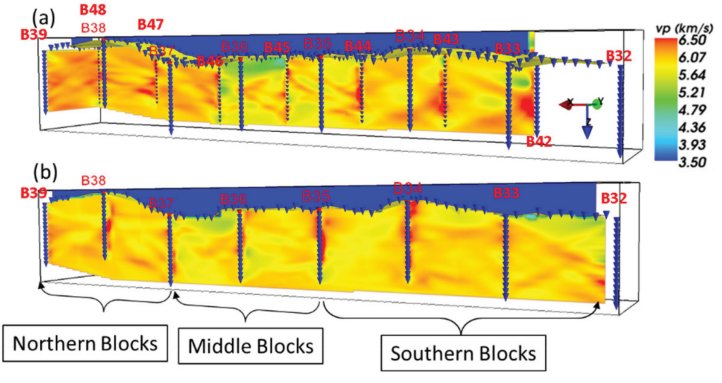


Figure 7. All planes in 3D using only cross borehole rays. Viewing the east side N-S planes (a). Viewing the west side N-S planes (b).

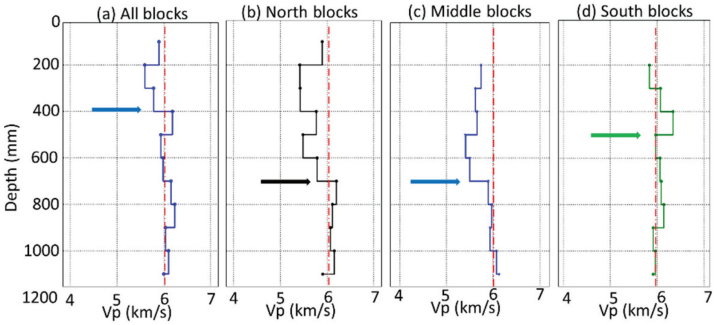


Figure 8. (a) Stack of all tomographic velocity measurements per depth level. The profile shows values remain constant around 6 km/s below 0.4–0.5 m below the surface. (b, c, d) show the stack of tomographic velocity profile for the northern, middle, and southern blocks, respectively. The dashed red line is used to mark the reference velocity value of 6 km/s.

south blocks of the study area. Below this depth, all blocks show the same measured P-wave velocities, indicating the rock is not affected below this depth for all areas.

## 4 CONCLUSIONS

In this paper, we introduced a seismic imaging technique that utilize microseismicity/acoustic emission and ultrasonic surveys to image the velocity of rock mass and detect the damage inside rock volume. We applied this technique on two field data sets, one from cave mining monitoring project and one from tunnel excavation ultrasonic survey. We showed that the fracture evolution and dynamic velocity variations inside the rock mass is well detected by the tomographic velocity images using passive and active seismic source imaging. Time-lapse images could be produced to reveal the stress evolution at different development and production phases. With the passive sources covering the seismogenic zone and active survey illuminating the aseismic zone, the combination of both types of sources can provide enhanced images of the rock damage and degradation.

## REFERENCES

Huang, J.W. & Bellefleur, G. 2012. *Joint transmission and reflection travel-time tomography using the fast sweeping method and the adjoint-state technique*, Geophys. J. Int. 188: 570–582 doi: 10.1111/j.1365–246X.2011.05273.x

Huang, J.W., Reyes-Mountes, J. & Young, P. 2013. *Passive three-dimensional microseismic imaging for mining-induced rock-mass degradation*. In Marek Kwasniewski & Dariusz Lydzba (Eds) *Rock Mechanics for Resources, Energy and Environment*, September 11, 2013 CRC Press, p1000

Mercier, J.P., de Beer, W., Mercier, J.P. & Morris, S. 2015. Evolution of a block cave from time-lapse passive source body-wave traveltime tomography. *Geophysics* 80: WA85-WA97, doi:10.1190/geo2014–0155.1

Pettitt, W.S. & Young, R.P. 2007. *InSite Seismic Processor: User Operations Manual Version 2.14*. Applied Seismology Consultants Ltd.

Thurber, C.H. 1983. Earthquake locations and three-dimensional crustal structure in the Coyote Lake area, central California. *J. Geophys. Res.* 88: 8226–8236, doi: 10.1029/JB088iB10p08226.

Tselentis, G.A., Martakis, N., Paraskevopoulos, P. & Lois, A. 2011. High-resolution passive seismic tomography for 3D velocity, Poisson's ratio ν, and P-wave quality QP in the Delvina hydrocarbon field, southern Albania. *Geo-physics* 76: B89; http://dx.doi.org/10.1190/1.3560016 (24 pages)

Zhang, H., Sarkar, S., Toksöz, M.N., Kuleli, H.S. & Al-Kindy, F. 2009. Passive seismic tomography using in-duced seismicity at a petroleum field in Oman. *Geophysics* 74(6): WCB57–WCB69, doi: 10.1190/1.3253059

Zhao, H.K. 2004. A fast sweeping method for Eikonal equations. *Math. Comput.* 74: 603–627.

This page intentionally left blank

*Rock Dynamics: From Research to Engineering – Li et al. (Eds)*
*© 2016 Taylor & Francis Group, London, ISBN 978-1-138-02953-8*

# Numerical modeling investigation on blasting of rock under different earth stresses

C. Jiang & Y.J. Ning
*School of Manufacturing Science and Engineering, Southwest University of Science and Technology, Mianyang, Sichuan, China*

ABSTRACT: Considering the influence of earth stresses, one-hole blasting of rock under the effect of explosion-induced stress waves is numerically modeled by the Discontinuous Deformation Analysis (DDA) method. It is found that, when the side pressure coefficient of the earth stresses is one, the maximum crack radius and the cracking area decrease with the increase of the initial earth stress level in the model; When the side pressure coefficient is different from one, the major direction of the crack propagations coincides with the maximum compressive principal direction of the earth stresses. The capability restraining and direction guiding effects of the initial earth stresses on the blasting-induced cracks are obviously captured. The numerical simulations reproduce some of the well-known findings observed in rock blasting. This numerical study helps to understand the role of earth stresses in rock blasting and thus have an instructive meaning for practical rock blasting design.

## 1 INTRODUCTION

Earth stress is the natural stresses in the rock mass, which are not only the basis of the evaluation of geological environment and the crustal stability, but also the important information for design and construction of the geological engineering. The blasting of rock, as an efficient and economical method of breaking rock, has been widely applied to the excavation of rock for a long time in the fields of mining engineering, slope engineering and underground engineering et al. The research on technology of drilling and blasting have been carried out extensively by many scholars through physical experiments, theoretical analysis and numerical simulation, etc. (e.g., Dally et al. 1975, Grady et al. 1980, Stecher & Fourney 1981, Huang et al. 2006), but the influence of the initial earth stress conditions on drilling and blasting was not specially considered for most of existing achievements. Compared with experimental research methods, numerical simulation methods have the characteristics without several limiting factors, e.g. space and time et al. At present, more and more researchers have begun to study rock blasting through numerical simulations. To numerically simulate blasting of rock, discontinuous numerical methods, such as the Distinct Element Method (DEM) and the Discontinuous Deformation Analysis (DDA) method, can be used.

The DDA, as one representative discontinuum-based numerical method (Shi 1988), has been widely used in the modeling of the mechanical behaviors of jointed rock masses under static and/or dynamic loadings. In the DDA method, the sub-block cracking modeling methods, which have been investigated in detail by Lin et al. (1996), Ning et al. (2010) and Jiao et al. (2011), have been used to model the fracturing failure of rock. Meanwhile, the simulations of the propagation of stress waves in rock masses are the foundation for the modeling of rock blasting under the effect of explosion-induced stress waves, and several problems regarding the simulation of stress wave propagations in rock masses with the DDA method have been discussed by Gu et al. (2009), Ning et al. (2012), and Zhang et al. (2013). In the aspect of simulation of rock blasting, Mortazavi & Katsabanis (2001), Ning et al. (2010) and Ning et al. (2011) used the DDA method to model and reproduce the process of the rock burst and throwing

under the effect of explosion gas pressure. Considering the effect of explosion-induced stress waves, the process of the one-hole blasting of rock was simulated and analyzed by Ning et al. (2015) in which an improved DDA sub-block cracking modeling method was used (Ni & Ning 2014) and the characteristics and mechanism of rock cracking and damage are revealed. The effect of rock mechanical parameters on the results of tunnel rock blasting was also modeled and discussed by Zhao et al. (2011). However, the influences of the initial earth stress conditions on the result of rock blasting were not considered in all the above work. The purpose of this paper is to investigate this problem through DDA numerical modeling, and in the current work, only the explosion-induced stress wave is taken into account as the blasting loading.

## 2 THE SUB-BLOCK CRACKING MODELING METHODS

In the DDA with first-order displacement functions, the stress/strain in each block is a constant. The basic idea of the sub-block cracking methods in the DDA is to use artificial joints to divide a continuous physical domain into sub-block elements. The artificial joints are endowed larger joint strength to simulate the distributions of deformations and stresses in the physical domain, and cracks are assumed to generate or propagate along the artificial joint surfaces based on certain failure criteria, e.g., the maximum tensile strength criterion for tensile fracturing failure and the Mohr-Coulomb criterion for shear fracturing failure, respectively. When the fracturing failure is based on the contact stresses on the interfaces of artificial joints (Ning et al. 2010), as the contact stresses change with the directions of the artificial joints, the preset of the artificial joints has an obvious influence on the cracking modeling results. So, an improved sub-block cracking method based on the sub-block element stress situations was coupled into the DDA method (Ni & Ning 2014).

In the improved sub-block cracking method of the DDA, the maximum principal stress and maximum shear stress of each single sub-block element are obtained in each time step of the DDA simulation, then the tensile or shear fracturing failures are considered by using the maximum tensile strength criterion or the Mohr-Coulomb criterion, respectively. Because this method determines fracturing failures along artificial joint surfaces by the stress situations of adjacent sub-block elements, the distribution of the preset sub-block elements (or artificial joints) has no obvious influence on the cracking strength judgment. The failure strengths can be obtained accurately in aspects of the simulations of pure tension or shear, and the simulation results of the fracturing routes are affected by the distributions of the preset artificial joints slightly (Ni & Ning 2014).

## 3 SIMULATION OF ROCK BLASTING WITH SINGLE BOREHOLE

### 3.1 *The model*

As shown in Figure 1, the blasting model has dimensions of 8.0 m × 8.0 m. The initial borehole with a diameter of $d = 0.1$ m is located in the center of the model. The Viscous Boundary Condition (VBC) is used for the model boundaries and the rock mass is divided into triangular sub-block elements. The linear elastic constitutive model is adopted as the material model of the rock and the density, Young's modulus, and Poisson's ratio are chosen to be $\rho = 2500$ kg/m$^3$, $E = 30$ GPa, and $\mu = 0.25$, respectively. The rock mechanical parameters, namely the parameters of artificial joints, including friction angle, cohesion, and tensile strength, are assumed to be $\theta = 45°$, $c = 15$ MPa, and $\sigma_t = 10$ MPa, respectively. The step maximum displacement ratio, time step and contact spring stiffness in the DDA simulation are chosen to be $5 \times 10^{-4}$, $1 \times 10^{-7}$ s, and $20E$, where $E$ is Young's modulus, respectively.

The initial earth stress condition is modeled by imposing initial stresses on each element in the rock mass. The blasting of rock under two different groups of earth stress conditions is numerically simulated. Group 1: the initial earth stresses in the vertical direction are chosen to be $\sigma_y = 0$ MPa, 4.5 MPa, 7.5 MPa, and 15 MPa, respectively, with the side pressure coefficient

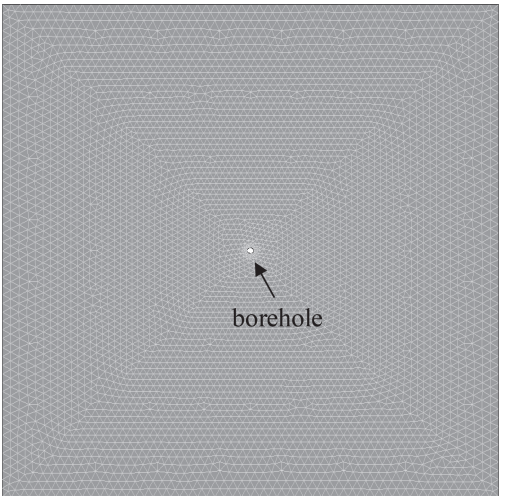


Figure 1. Geometrical model for one-hole blasting of rock (dimensions: 8.0 m × 8.0 m).

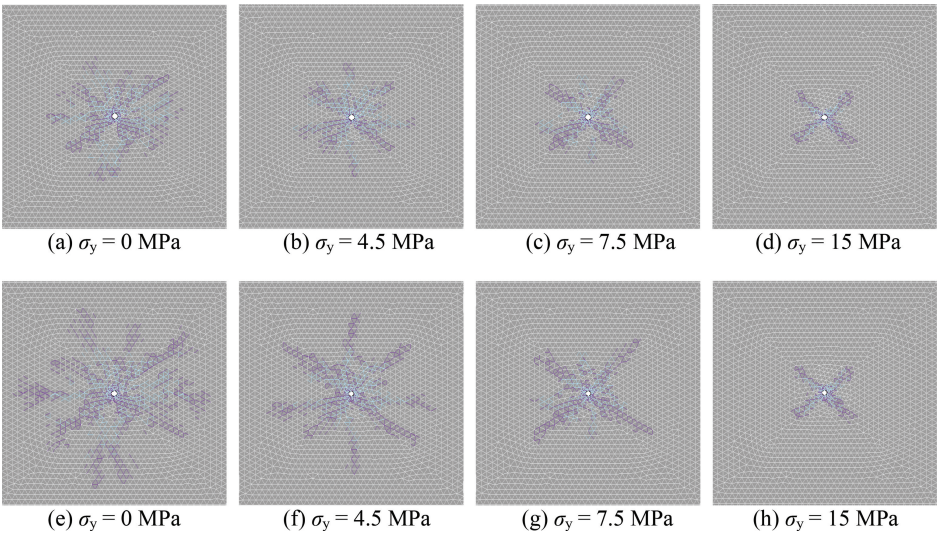


Figure 2. Simulation results under earth stress condition Group 1 (dimensions: 4 m × 4 m): (a) to (d), $t$ = 1.5 ms; (e) to (h), $t$ = 1.8 ms.

of $\lambda = 1.0$. Group 2: the initial stresses are chosen to be $\sigma_y = 15$ MPa, whereas the side pressure coefficients are chosen to be 0.2, 0.5, 2, and 2.5, respectively. The loading of explosion-induced stress waves is numerically simulated by applying a uniform triangular compressive pressure on the wall of the initial blast chamber with a peak value of $P_{max} = 200$ MPa, a rise time of $t_1 = 0.1$ ms, and a decay time of $t_2 = 0.4$ ms, respectively. Considering the redistribution of the initial earth stresses in the rock mass, especially around the borehole, the blasting loading is delayed 1.0 ms after the application of the initial earth stresses.

### 3.2 *Simulation results under earth stress condition Group 1*

Figure 2 gives several scenarios of the simulated blasting process under earth stress condition Group 1. To show the cracking area more clearly, in each scenario only a zone of

4.0 m × 4.0 m in the center of the model is displayed. Figure 2a gives the simulation result under zero initial earth stress. Cracks appear around the borehole under the effect of the explosion-induced stress waves first and extend along the radial direction. The number of shear cracks (in blue) is equal to the number of tensile cracks (in purple) approximately. Then, with the propagation of the explosion-induced stress waves in the rock, the crack zone expands gradually and several major radial crack bands are formed, as shown in Figure 2e. Meanwhile, dispersive cracks appear far away from the borehole. Thereafter, new cracks appear more and more slowly because of the attenuation of the stress waves due to energy consumption.

Generally, Figures 2a, b, c and d indicate that the generation and propagation of cracks are restrained by the increasing initial earth stresses. With larger initial earth stresses, the cracks develop more slowly with a decrease fraction of shear cracks. The blasting crush zone area around the borehole and the number of the major radial crack bands decreases obviously with the increase of the initial earth stresses.

### 3.3 *Simulation results under earth stress condition Group 2*

Figure 3 gives several scenarios of the simulated blasting process under earth stress condition Group 2. Also only a zone of 4.0 m × 4.0 m in the center of the model is displayed. Combined with the simulation results in Figure 2d and h under a vertical earth stress of 15 MPa and a side pressure coefficient of 1.0, there are several conclusions can be obtained. On the one hand, when the side pressure coefficient is smaller than one, the cracks mainly propagate in the form of the major crack bands in the vertical direction accompanied with some disperse cracks in the relatively far region. On the other hand, when the side pressure coefficient is larger than one, the cracks mainly propagate in the form the major crack bands in the horizontal direction. Generally, with the same initial earth stress in the vertical direction and the increase of the side pressure coefficient from 0.2 to 2.5, namely the increase of the initial earth stress in the horizontal direction from 3 MPa to 37.5 MPa, the major crack bands originating from the initial borehole wall change from vertical to horizontal with a lower developing velocity and a decreasing band length due to an increasing level of the initial earth

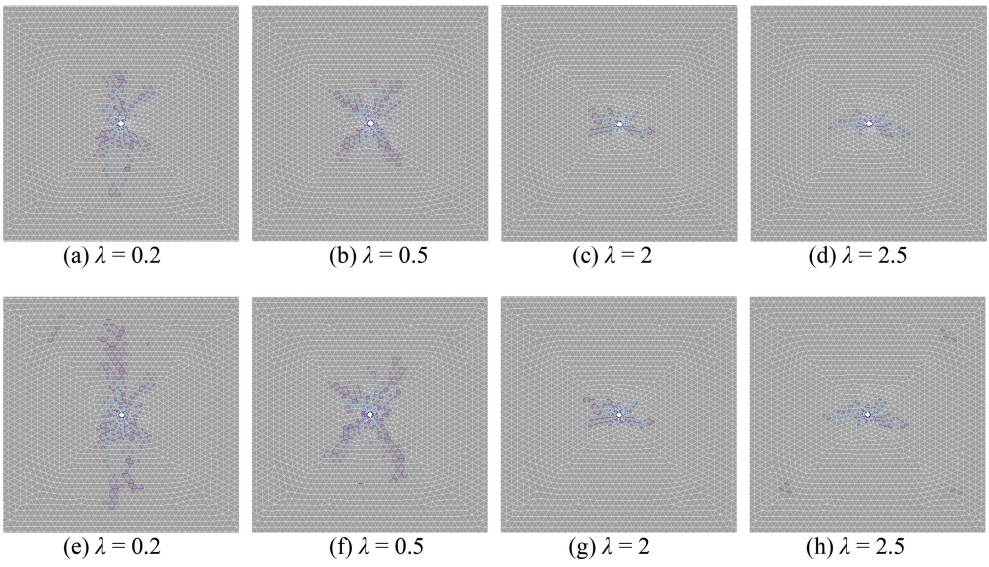


Figure 3. Simulation results under earth stress condition Group 2 (dimensions: 4 m × 4 m): (a) to (d), $t$ = 1.5 ms; (e) to (h), $t$ = 1.8 ms.

stresses. When the side pressure coefficient is 1.0, the cracks in the vertical and the horizontal directions are almost equal, as shown in Figure 2.

## 4 CONCLUSIONS

One-hole blasting in rock with different conditions of the initial earth stresses under the effect of explosion-induced stress waves is numerically modeled by the DDA method. It is found that, when the side pressure coefficient of the earth stresses is 1.0, the crack radius and the cracking area decrease with the increase of the initial earth stress level in the model, which indicates that the initial earth stresses have a significant influence on the growth capability of cracks. When the side pressure coefficient is different from 1.0, the major direction of the crack propagations coincides with the maximum compressive principal direction of the earth stresses, which indicates that the initial earth stresses have a direction guiding effect on the crack propagations. The numerical results are beneficial for the understanding of the role of earth stresses in rock blasting, and have an instructive meaning for practical rock blasting design, especially under conditions with high levels and large side pressure coefficient of the earth stresses in the rock.

## ACKNOWLEDGEMENT

This work is financially supported by the National Natural Science Foundation of China under Grant No. 51204137.

## REFERENCES

Dally, J.W. & Fourney, W.L. et al. 1975. Influence of containment of the bore hole pressures on explosive induced fracture. *International Journal of Rock Mechanics and Mining Sciences & Geomechanics Abstracts* 12(1): 5–12.

Grady, D.E. & Kipp, M.E. et al. 1980. Continuum modelling of explosive fracture in oil shale. *International Journal of Rock Mechanics and Mining Sciences & Geomechanics Abstracts* 7(3): 147–157.

Gu J. & Zhao, Z.Y. et al. 2009. Considerations of the discontinuous deformation analysis on wave propagation problems. *International Journal for Numerical and Analytical Methods in Geomechanics* 33(12): 1449–1465.

Huang T. & Chen, P.W. et al. 2006. Numerical simulation of two-hole blasting using numerical manifold method. *Explosion and Shock Waves* 5:434–440. (in Chinese).

Jiao, Y.Y. & Zhang, X.L. et al. 2011. Two-dimensional DDA contact constitutive model for simulating rock fragmentation. *Journal of Engineering Mechanics* 138(2): 199–209.

Lin, C.T. & Amadei, B. et al. 1991. Extensions of discontinuous deformation analysis for jointed rock masses. *International Journal of Rock Mechanics and Mining Sciences & Geomechanis* 33(7): 671–694.

Mortazavi, A. & Katsabanis, P.D. 2011. Modelling burden size and strata dip effects on the surface blasting process. *International Journal of Rock Mechanics and Mining Sciences* 38(4): 481–498.

Ni, K.S. & Ning, Y.J. 2014. The optimization and validation of sub-block method for modelling rock fracturing within Discontinuous Deformation Analysis framework. *Chinese Journal of Underground Space and Engineering* 10(5): 1017–1022. (in Chinese).

Ning, Y.J. & Yang, J. et al. 2010. Modelling rock fracturing and blast-induced rock mass failure via advanced discretisation within the discontinuous deformation analysis framework. *Computers and Geotechnics* 38(1): 40–49.

Ning, Y.J. & Yang, J. et al. 2011. Modeling rock blasting considering explosion gas penetration using discontinuous deformation analysis. *Rock Mechanics and Rock Engineering* 44(4): 483–490.

Ning, Y.J. & Zhao, Z.Y. et al. 2012. Using the discontinuous deformation analysis to model wave propagations in jointed rock masses. *CMES: Computer Modeling in Engineering & Sciences* 89(3): 221–262.

Ning, Y.J. & Jiang, C. et al. 2015. Numerical modeling of rock failure in drilling blasting under the effect of explosion-induced stress waves. *Journal of Beijing Institute of Technology*, accepted. (in Chinese).
Shi, G.H. 1988. Discontinuous Deformation Analysis—A New Numerical Model for the Static and Dynamics of Block Systems. Berkeley: University of California, Berkeley.
Stecher, F.P. & Fourney, W.L. 1981. Prediction of crack motion from detonation in brittle materials. *International Journal of Rock Mechanics and Mining Sciences & Geomechanics Abstracts* 18(1): 23–33.
Zhang, Y.H. & Fu, X.D. et al. 2013. Study on elastic P-wave propagation law in unfavorable geologic structures with discontinuous deformation analysis method. *Arabian Journal of Geosciences* 6(11): 4557–4564.
Zhao, Z.Y. & Zhang, Y. et al. 2012. Tunnel blasting simulations by the discontinuous deformation analysis. *International Journal of Computational Methods* 8(2): 277–292.

*Rock Dynamics: From Research to Engineering – Li et al. (Eds)*
*© 2016 Taylor & Francis Group, London, ISBN 978-1-138-02953-8*

# Classification of mechanisms of induced earthquakes: From a view of rock mechanics

J.Q. Kang
*State Key Laboratory of Hydraulic Engineering Simulation and Safety, School of Civil Engineering, Tianjin University, Tianjin, China*

J.B. Zhu
*State Key Laboratory of Hydraulic Engineering Simulation and Safety, School of Civil Engineering, Tianjin University, Tianjin, China*
*Department of Civil and Environmental Engineering, The Hong Kong Polytechnic University, Hong Kong SAR*

ABSTRACT: The induced earthquake has attracted a lot of attentions in the world recently. The earthquakes induced by fluid injection and extraction, reservoir impoundment and mining/rock removal have been reported, studied and reviewed in a number of literatures. In this paper, from a view of rock mechanics, three fundamental mechanisms are summarized, i.e., the increase of pore pressure, the change of stress, and the change of frictional coefficient. The stimulation of reservoir-related earthquakes and earthquakes induced by fluid injection are sufficiently interpreted by a Coulomb-Mohr failure criterion and effective stress law in the saturated rock. The mining induced earthquakes mainly result from the change of stress. More remarkably, additional physical or chemical effects of fluids may lead to weakening of materials in fault zones owing to stress corrosion.

## 1 INTRODUCTION

Numerous earthquakes occur each year around the world. Among them, a number of low-magnitude seismic events have been in connection with human activities and are called 'induced seismic events' or 'induced earthquakes'. Induced earthquakes with relation to human activities have been noticed since as early as 1920s. Recently, more and more scientists have paid attention to induced earthquakes in the world. Activities with a potential to induce earthquakes include the impoundment of water reservoir (Simpson 1986), fluid injection (Raleigh et al. 1972; Seeber et al. 2004), fluid extraction in the oil and gas industry (Segall 1989, Grasso 1992, Segall et al. 1994), mining/rock removal (McGarr 1976, Richardson & Jordan 2002), and underground nuclear explosions (Boucher et al. 1969).

The mechanism of fluid pressure increase was firstly applied to interpret fluid injection induced earthquakes near Denver, which laid the foundation for understanding the phenomenon of induced earthquakes (Hubbert & Rubey 1959). Gough (1970a, b) firstly conducted the definite quantitative analysis at Lake Kariba at the Zambia–Zimbabwe border. With consideration to the role of reservoir load in induced earthquakes, Bell & Nur (1978) and Roeloffs (1988) stated that reservoir load induced stresses at seismogenic depths are so small that they can only affect the ambient stress field. Gupta et al. (1972a, b) identified the effect of increasing rate of the reservoir water level, duration of loading, maximum levels achieved and duration of retention of high levels on the frequency and magnitude of earthquakes near the reservoir. The relatively simple models of reservoir with finite depth, but infinite width (1D case), was introduced for investigating the influence of pore fluid pressure on induced

earthquakes (Snow 1972). Based on Biot's consolidation theory, Withers & Nyland (1976) and Bell and Nur (1978) proposed more sophisticated analytical models.

In this paper, from a view of rock mechanics, the source mechanisms of induced earthquakes are classified into three categories, i.e., change of stress, change of frictional coefficient ($\mu$) and increase in pore pressure ($p$). In accordance with the above three mechanisms, the mechanism of earthquakes induced by fluid injection and extraction, the impoundment of water reservoir and mining/rock removal are also introduced separately in this paper.

## 2 INCREASE IN PORE PRESSURE

### 2.1 *Hydraulic Fracturing*

Hydraulic Fracturing (HF) is widely applied in the reservoir stimulation for geothermal reservoirs, gas and oil secondary recovery where low-permeability sedimentary rocks exist (e.g. 'tight' sandstones and shale), and in-situ stress measurement. Hence, a large number of fault or fracture reactivation events caused by hydraulic fracturing have been reported (e.g. Wolhart et al. 2005, Maxwell et al. 2008, Cipolla et al. 2012). However, the magnitude of earthquakes stimulated by hydraulic fracturing is generally very low.

The increase of surface area of rock around the wellbore is achieved by pumping water, proppant and chemicals into the rock. During or soon after hydraulic fracturing, the fluid pressure along a fault plane may increase. If critically stressed, the fault can be reactivated and slip unstably.

### 2.2 *Mohr-coulomb failure criterion*

According to the Mohr-Coulomb failure criterion, a slip will happen along the weak plane when the shear stress ($\tau$) resolved across the fault goes beyond the inherent shear strength ($c$) and the frictional strength on the plane of slip. Quantitatively, this condition is expressed by the following equation:

$$\tau_{crit} = c + \mu\sigma_n \tag{1}$$

where $\tau_{crit}$ = the critical shear stress causing slip on a plane; $\mu$ = the friction coefficient; and $\sigma_n$ = the normal stress loading on the plane.

Compared with the frictional strength on the plane of slip, $c$ is nearly zero in the weak fault zones. As the theory of the effective stress describes, the effective ($\sigma_n$) decreases by an amount equivalent to the pore pressure ($P$). Therefore, the critical shear stress is redefined:

$$\tau_{crit} = \mu(\sigma_n - P) \tag{2}$$

The Mohr-Coulomb failure criterion with the consideration of the effective stress may provide a rough interpretation of induced earthquakes. Owing to the fluid pressure increase, the effective strength of crustal faults can decrease below the critical threshold. As a result, the faults may suddenly slip and induced earthquakes occur.

## 3 CHANGE OF STRESS

### 3.1 *Fluid extraction*

Production of underground resources may lead to deformation of reservoir rock. These volume deformation alters local stress conditions. When the stress condition reaches the failure state, the seismic slip occurs within or around the reservoir.

Segall (1989) suggested that poroelastic stresses related to reservoir contraction resulted in extraction-induced earthquakes. The slight contraction of reservoir rocks is created with

decreasing pore pressure. Meanwhile, this contraction also disturbs the adjacent crust. As a result, subsidence and horizontal contraction occur around the reservoir. More seriously, earthquakes may be induced. As shown in Figure 1, the minimum horizontal stress linearly increases with pore pressure. Therefore, decreasing pore pressure results in the reduction of the minimum horizontal stress.

Faulting related to fluid extraction is illustrated schematically in Figure 2. Two kinds of faulting occur in the reservoir, which depend on the ambient stress state. Because of the extensional effect, normal faulting may occur at boundaries of the reservoir. On the contrary, the compressional effect lead to reverse faulting above or below the reservoir.

### 3.2 *Temperature change*

Because water is circulated from geothermal reservoirs, the temperature decreases in the geothermal reservoirs (Ernest 2007). Based on the thermoelastic strain theory, the contraction of fracture surfaces results from the interaction between cool water and hot rock. The slight opening of the fracture results in the decrease of static friction. A fracture slip may be followed, when the weak plane was close to failure in a regional stress field.

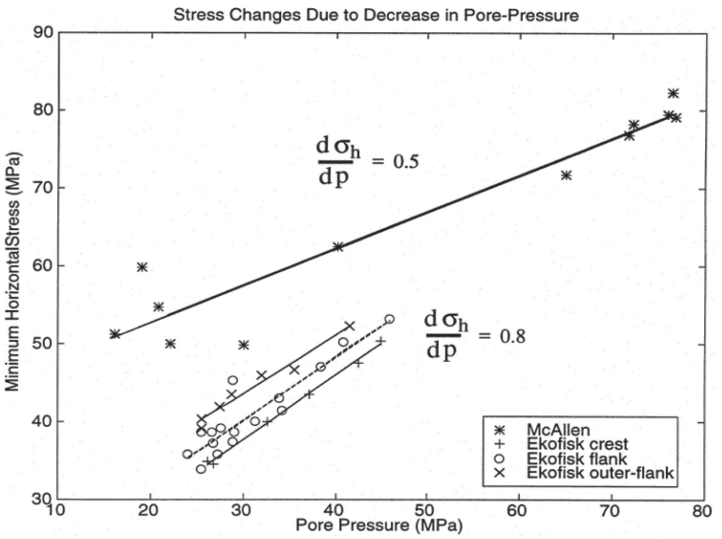


Figure 1. Stress changes due to decrease in reservoir pore pressure. (Segall 1989).

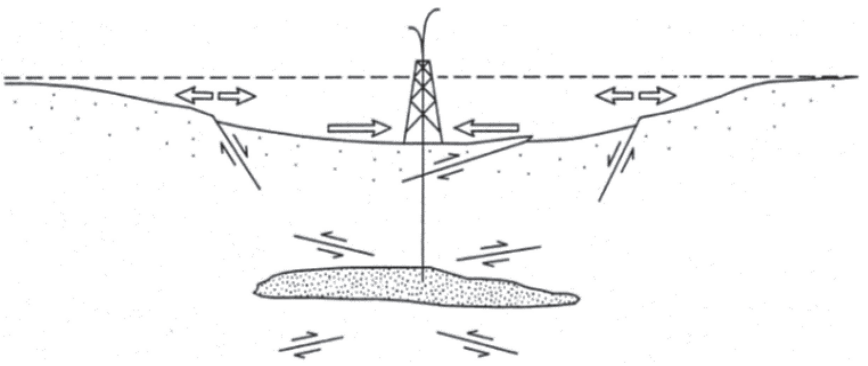

Figure 2. Summary of observed faulting associated with fluid withdrawal. (Segall 1989).

### 3.3 *Reservoir loading and quarry unloading*

As illustrated in Figure 3, the radius and center of the Mohr circle change with the load and pore pressure. Moreover, the tectonic environment plays a significant role on induced earthquakes. Because of the increase of the radius of Mohr circle, failure envelope may be touched and the reservoir loading will induce earthquakes in the region of normal faults. Similarly, the quarry unloading may generate earthquakes in a thrust faulting environment.

## 4 CHANGE OF FRICTIONAL COEFFICIENT

### 4.1 *Chemical corrosion*

In addition to pore pressure, fluid injection also enhances chemical process, e.g., stress-aided corrosion, on weak planes. The phenomenon that pore water or pore pressure diffusion occurs along pre-existing fractures has been reported in many literatures (e.g., Witherspoon & Gale 1977). Generation of new cracks is attributed to stress corrosion effect of fluids (Anderson & Grew 1977). For example, the geochemical alteration of fracture surfaces resulting from injecting non-native fluids into the formation may change the frictional coefficient of those surfaces. And small earthquakes would be more likely to occur (Ernest 2007).

### 4.2 *Temperature change*

The temperature can also alter the frictional coefficient. In the enhanced geothermal system, for example, the high-pressure cool water is pumped into the hot rock and the water temperature rises sharply. And the temperature balance system will be disrupted due to the change of the ambient temperature. In waste water disposal and hydropower reservoirs, the depth of injected water can reach hundreds of meters. The high pressure in deep rock will also increase the temperature. Dependence of frictional coefficient on temperature could be explained from a view of molecular motion. The increase of the temperature can not only enhance the thermal motion but also enlarge the motion space. Owing to thermal expansion, the distance between the molecules increases. And with the polymer unwinding, thermodynamic properties, viscoelasticity and other physical properties of rock change dramatically. Moreover, rock experiences heat exchange. Therefore, the friction coefficient on the surface is highly dependent on the ambient temperature.

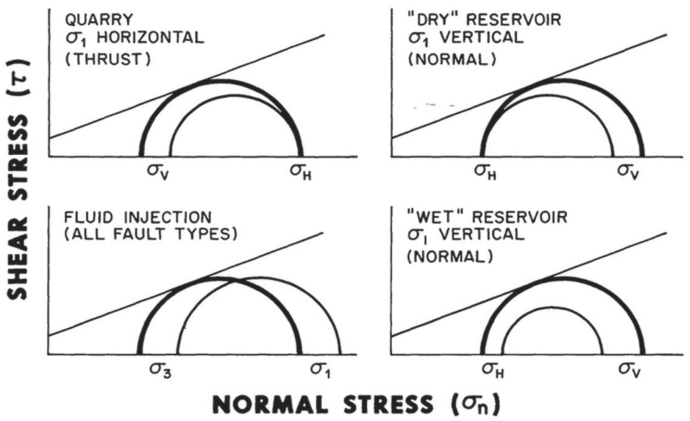


Figure 3. Mohr circle representation of several direct effects of reservoir loading and quarry unloading. (Christopher 2002).

## 5 CONCLUSION

Based on previous reports and studied of induced earthquakes associated with engineering activities, it is concluded that induced earthquakes occur when the mechanically steady state of seismogenic rocks is adequately perturbed. From a view of rock mechanics, three fundamental source mechanisms are summarized, i.e., the increase of pore pressure, the change of stress, and the change of frictional coefficient.

Earthquakes may occur when the stress loading on the weak plane increases or its strength decreases. The reduction of the strength is attributed to the decrease of normal stress, the change of frictional coefficient, or the increase of the pore pressure.

Induced seismicity in Surface quarries and deep mines is mainly due to the change of the ambient stress state. Increased pore pressure is the dominant factor of liquid injection induced earthquakes. Reservoir induced earthquakes may involve all the three aforementioned mechanisms.

Although individual induced earthquake has been thought to be dominated by a single mechanism by many researchers, our view is that causes of induced earthquakes may not be single but more likely to be coupled among stress, temperature and pore pressure.

## REFERENCES


Anderson, O.L. & Grew, P.C. 1977. Stress Corrosion Theory of Crack Propagation with Application to Geophysics. *Rev. Geophysics. Space Phys*. 15: 77–104.

Bell, M.L. & Nur, A. 1978. Strength changes due to reservoir-induced pore pressure and stresses and application to Lake Oroville. *Geophys. Res*. 83: 4469–4483.

Boucher, G., Ryall, A., & Jones, A.E.1969. Earthquakes associated with underground nuclear explosions. *Geophys. Res*. 74: 3808–3818.

Cipolla, C., Maxwell, S. & Mack, M. 2012. Engineering Guide to the Application of Microseismic Interpretations. *SPE* 152165.

Christopher H.S. 2002. *The Mechanics of Earthquakes and Faulting*: Cambridge University Press.

Ernest L. & Majer 2007. Induced seismicity associated with Enhanced Geothermal Systems. *Geothermics* 36: 185–222.

Gough, D.I. & Gough, W.I. 1970a. Stress and deflection in the lithosphere near Lake Kariba, 1. *Geophys* 21: 65–78.

Gough, D.I. & Gough, W.I. 1970b. Load induced earthquakes at Kariba, 2. *Geophys. J.R. Astron. Soc*. 21: 79–101.

Grasso, J.1992. Mechanics of seismic instabilities induced by the recovery of hydrocarbons. *Pure Appl. Geophys*.139: 507.

Gupta, H.K., Rastogi, B.K., & Narain, H. 1972a. Common features of the reservoir associated seismic activities. *Bull. Seismol. Soc. Am*. 62: 481–492.

Gupta, H.K., Rastogi, B.K. & Narain, H. 1972b. Some discriminatory characteristics of earthquakes near the Kariba, Kremasta and Koyna artificial lakes. *Bull. Seismol. Soc. Am*. 62: 493–507.

Hubbert MK & Rubey WW 1959. Mechanics of fluid-filled porous solids and its application to overthrust faulting. *Geol.Soc. Am. Bull* 70: 115–66.

Maxwell, S.C., Shemeta, J., Campbell, E. & Quirk, D. 2008. Microseismic Deformation Rate Monitoring. *SPE* 116596.

McGarr, A.1976. Seismic moment and volume change. *Geophys. Res*. 81: 1487–1494.

Raleigh, C.B., Healy, J.H. & Bredehoeft, J.D. 1972. Faulting and crustal stress at Rangely, Colorado. *AGU Geophys. Monogr*. 16: 275–284.

Richardson, E. & Jordan, T. 2002. Seismicity in deep gold mines of South Africa: implications for tectonic earthquakes. *Bull. Seismol. Soc. Am*. 92: 1766–1782.

Roeloffs, E.A. 1988. Fault stability changes induced beneath a reservoir with cyclic changes in water level. *J. Geophys. Res*. 93: 2107–2124.

Seeber, L., Armbruster, J.G. & Kim, W.Y. 2004. A fluid-injection-triggered earthquake sequence in Ashtabula, Ohio: implications for seismogenesis in stable continental regions. *Bull. Seismol. Soc. Am*. 94: 76–87.

Segall, P. 1989. Earthquakes triggered by fluid extraction. *Geology* 17: 942–946.

Segall, P., Grasso, J.R. & Mossop, A. 1994. Poroelastic stressing and induced seismicity near the lacq gas field, Southwestern France. *J. Geophys. Res*. 99: 15423–15438.
Simpson 1986. Triggered earthquakes. *Annual Reviews of Earth and Planetary Science* 14: 21–42.
Snow, D.T. 1972. Geodynamics of seismic reservoirs. *Proc. Symp. Percolation through Fissured Rock, Ges*. *Erd-und Grundbau*. Stuttgart, Germany T2 J: 1–19.
Withers, R.J. & Nyland, E. 1976. Theory for the rapid solution of ground subsidence near reservoirs on layered and porous media. *Eng. Geol*. 10: 169–185.
Wolhart, S.L., Harting, T.A., Dahlem, J.E., Young, T.J., Mayerhofer, M.J. & Lolon, E.P. 2005. Hydraulic Fracture Diagnostics Used to Optimize Development in the Jonah Field. *SPE* 102528.
Witherspoon, P.A. & Gale, J.E. 1977. Mechanical and Hydraulic Properties of Rocks Related to Induced Seismicity. *Eng. Geol*. I1:23–5.

*Rock Dynamics: From Research to Engineering – Li et al. (Eds)*
*© 2016 Taylor & Francis Group, London, ISBN 978-1-138-02953-8*

# From earthquake to aseismic creep: What governs fault slip modes?

G.G. Kocharyan
*Institute of Geospheres Dynamics Russian Academy of Sciences, Moscow, Russia*

ABSTRACT: The gradual transition from stick-slip to stable sliding is studied in lab experiments. The results allow concluding, that the sliding mode and the part of deformation energy spent to the seismic radiation are determined by a ratio of two parameters—the fault stiffness and the stiffness of surrounding rock massif. This conclusion gives new explanation for huge scatter of the values of radiated energy of earthquakes with close seismic moments. Presence of some minerals and water in the fault principal slip zone can essentially reduce the shear stiffness of a fault and the radiation efficiency of a fault slip.

## 1 INTRODUCTION

The 2008 workshop on a Long Range Science Plan for Seismology (Lay 2009) considered promising research directions for the next decades and identified 10 Seismological Grand Challenge research questions. The First Grand Challenge was formulated as "How the faults slip?" In the frames of this problem several key questions and issues were formulated. Among these questions was the following: "What physical properties control diverse types of fault sliding?" and "What governs transitions from stick-slip behavior to steady sliding?"

A drastic increase of resolution capability of the seismic and geodetic observations during the recent years allowed to determine reliably the existence of various modes of displacements on the interfaces of structural blocks of the Earth's crust (Peng & Gomberg 2010). The sliding motion of faults exhibits a wide range of complex behaviors. Recorded deformation events are differentiated to several classes by the speed of rupture propagation and the process duration in the earthquake source. When faults slip at sufficiently fast velocities seismic waves are radiated, which results in large displacements and 'normal' earthquakes. In some cases, the slip may not reach dynamic velocities, but low-amplitude, low-frequency seismic waves are still radiated. Such events are indentified as Low Frequency Earthquakes (LFE) and Very Low Frequency Earthquakes (VLFE). When a fault slips so slowly that seismic radiation can be neglected they say about Slow Slip Events (SSE).

An analysis of observed data reveals significant differences in the portions of deformation energy spent for seismic radiation even within the class of "normal" earthquakes. Energies radiated by earthquake sources with close seismic moments may differ by several orders of magnitude. The scaled value $e = E_s/M_0$, which is the ratio of radiated energy $E_s$ to the seismic moment $M_0$, varies in the range of $10^{-6}$ to $10^{-3}$ at the average value of about $2 \cdot 10^{-5}$ (Choy & Boatwright 1995). For LFEs the typical value of $E_s/M_0$ is in the range of $5 \cdot 10^{-8}$ to $5 \cdot 10^{-7}$. In the case of VLFE the ratio $E_s/M_0$ gets into the range of $10^{-9}$ to $10^{-7}$. Durations of recorded large-scale SSEs vary in a wide range from days to several years.

There are several models explaining the occurrence of different slip modes. They may be divided into two categories. In the first group variations of friction properties of the sliding surface are assumed after exceeding a certain threshold of the velocity of relative displacement of fault edges (Ikari et al. 2013). The second group of models supposes that parameters defining the shear resistance force vary with space, i.e. in different areas either velocity

strengthening or velocity weakening takes place. Such transition usually takes place in transient areas beneath locked fault zones at the depth of about 15 km or more. Such models can't explain huge scattering of scaled radiated energy over more than 2 or 3 orders of magnitude in other setting, for example in mining, when alterations of stress conditions are relatively small.

The present paper describes the results of laboratory experiments which demonstrate the existence of another mechanism of occurrence of various slip modes not described before. We found that small variations of fault gouge composition, which weakly affects the ultimate fault strength, may result in significant variations of the shear stiffness of discontinuity, sufficient for alteration of the slip mode.

## 2 FAULT STIFFNESS AND SEISMIC ENERGY OF EARTHQUAKES

Experimental laboratory studies have allowed development of the empirical "rate-and-state" friction law where the frictional resistance force depends on the velocity of relative displacement of surfaces and the duration of stationary contact (Dieterich 1979). According to Dieterich's law the effect of contact dynamical weakening is a necessary condition of the stable stick-slip mode. Additional condition for the beginning of stick-slip is that the shear stiffness of the fault $k_s$ must be high enough to exceed the stiffness $K$ of surrounding rock massif:

$$k_s \approx \bar{\sigma}_n \left| \frac{d\mu}{du} \right| > K \tag{1}$$

where $\mu(u)$ = dependence of friction coefficient on relative displacement of fault edges $u$, and $\bar{\sigma}_n$ = average effective stress normal to the fault plane.

The energy $E_s$ radiated during slip in a homogeneous infinite space is the difference between the variation of elastic energy $\Delta E_e$ and the energy dissipated during faulting $\Delta E_d$. So the earthquake energy balance can be written as:

$$E_s = \Delta E_e - \Delta E_d \tag{2}$$

The total dissipated energy $\Delta E_d$ is formed from the fracture energy of the earthquake $\Delta E_G$ and the work $\Delta E_f$ performed on the fault plane of area S against friction forces during the slip:

$$\Delta E_d = \Delta E_f + \Delta E_G = S \cdot \int_0^{D_{tot}} \sigma_f(u) du \tag{3}$$

The fracture energy is written as: $\Delta E_G = S \cdot \int_0^{D_c} [\sigma_f(u) - \sigma_d]\, du$ and the portion of dissipated energy converted into heat is $\Delta E_f = \sigma_d \cdot D_{tot} \cdot S$.

If $\Delta E_G$ is interpreted as the energy spent to origination of a new surface near the fracture tip, then this component will be small for most earthquakes. However, in faulting the energy dissipation occurs both during destruction of asperities on the edge surfaces, and during formation of micro- and macro-cracks in the neighborhood of fault core and in the fault damage zone, so that all these energy expenditures can be included into $\Delta E_G$.

The part of energy spent to destruction depends not only on the material properties, but also on the velocity of fracture propagation, as well as on the form of the dependence of $\sigma_f(u)$. It is convenient to characterize the latter by the fault shear stiffness (1). As one can see in Equation (4), the slower the resistance to shear decreases with displacement, the higher the fracture energy of earthquake $\Delta E_G$ is, and the less portion of energy turns into seismic radiation.

## 3 LABORATORY EXPERIMENTS

The process of transition of the cumulated potential energy into the kinetic energy of block sliding was studied in laboratory experiments, which were performed on the "slider model"): a spring-loaded sliding block on a frictional surface. A thin layer of gauge about 2 mm thick was placed between a concrete block and a concrete base. A principal scheme of experiments is shown in Figure 1. The spring end was loaded at a constant velocity $v_0$ by electrical drive during the whole experiment. The mass of movable block was 130 kg, and the contact area was $S$ = 254 cm$^2$. The average normal stress at the contact was $\sigma_n$ = 50 kPa. During every test the shear force and the block displacement were recorded. The spring stiffness K plays the role of the stiffness of massif, while the stiffness of gouge filled contact imitates the one of tectonic fault. In the described test series, the gouge material composition was altered by adding powdered talc to quartz sand. Grain size of the latter was less than 200 μm. The tests were carried out using different springs that loaded the movable block at different stiffness. The velocity of spring end connected to the electric drive was $v_0$ = 1 μm/s.

In laboratory experiments the following quantity can be considered as the analogue of seismic moment: $M_{lab} = K \cdot D \cdot L$. Indeed, in nature the seismic moment is the product of shear force $F_s$ acting at the fault plane by the fault length L:

$$M_0 = G \cdot D \cdot L^2 = G \cdot \frac{D}{L} \cdot L^3 = \Delta\sigma_s \cdot S \cdot L = \Delta F_s \cdot L \tag{4}$$

In this relation $G$ = shear modulus of massif in the vicinity of the fault, $D$ = displacement produced by the earthquake, $S \approx L^2$ = area of rupture, $\Delta\sigma_s$ = tangential stress drop at the fault due to slip. For the lab experiment with slider one can write: $\Delta F_s = K \cdot D$, where D = maximum displacement during dynamic slip, L = block length. Thus, in laboratory the relation $e_{lab} = E_k/(K \cdot D \cdot L)$ is the analogue of energy/moment ratio $e = E_s/M_0$, which in seismology is used to characterize the seismic efficiency of an earthquake. Here $E_k$ = block kinetic energy.

Depending on talc content in the sand/talc mixture the slip mode drastically changed. As talc content increased in the gouge, the block movement behavior transformed from the stick-slip mode to stable sliding. Typical plots of the block slip velocity and displacement are given in Figure 1. When the gouge consists of pure quartz sand or sand/talc mixture with low talc content the dynamic slip occurs within hundreds of milliseconds with the resulting drop of applied shear force and partial transformation of energy stored in the spring into the kinetic energy of the block movement (Fig. 1a). As the talc content increases the magnitudes of shear force drop decrease, so do the block maximal velocity and displacement. At the same time the slip duration increases (Fig. 1b) and reaches several tens of seconds.

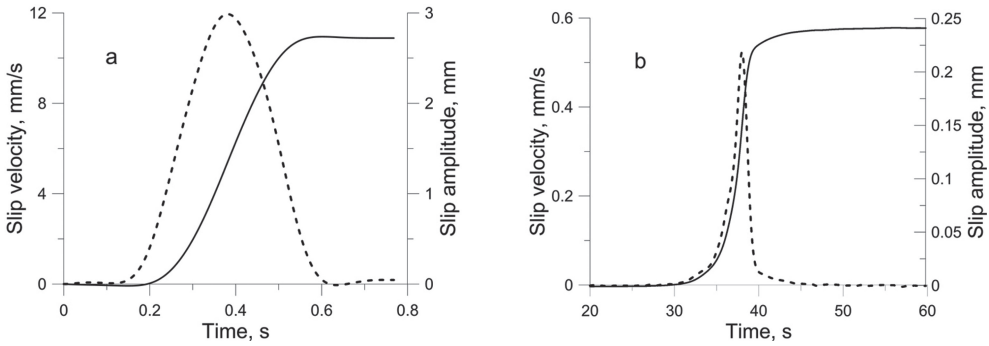


Figure 1. Time dependences of the movable block displacement and displacement velocity (dotted line) relative to the fixed block. a, b–gouge of quartz sand mixture with 5% and 30% talc content, respectively. Spring stiffness is K = 10.8 N/mm.

In experiments with the spring as stiff as $K$ = 10.8 N/mm, the drop of maximal slip velocity by more than an order of magnitude (from ~5 mm/s to ~0.25 mm/s) and a drastic rise of slip duration (from ~1 s to ~15 s) occur when talc content increase from 20% to 25% of mass. For mixtures with talc content over 35–40% the block sliding becomes quasi-stable and variations of shear resistance are weakly expressed. Typical plots of shear force $F$ versus displacement $D$ on the interface for episodes of stick-slip are shown in Figure 2. Kinetic energy $E_k$ of the block, the fracture energy $\Delta E_G$, and the energy converted to heat $\Delta E_f$ are shown by different shading. It can be seen that as talc content increases the ratio $E_k/\Delta E_G$ decreases.

An analysis of $F(D)$ functions indicates that maximal shear stiffness of the interface defined by expression (1) decreases as the talc content increases. In the case when the gouge consists of pure quartz sand the maximal stiffness is $|k_s|_{max} \approx 2.5\ 10^4$ Pa/mm. An addition of 5% talc decreases this value approximately twice $|k_s|_{max} \approx 1.2\ 10^4$ Pa/mm, and for talc content of 20% the maximal stiffness falls nearly by an order of magnitude $|k_s|_{max} \approx 0.15\ 10^4$ Pa/mm. An increase of talc content to 35–40% results in that $|k_s|_{max}$ will be less then the specific stiffness of spring $\hat{K} = K/S \cong 425\,\mathrm{Pa/mm}$ and the fracture transits to the mode of stable sliding. When talc content in the gouge increases to 35%, the contact strength (maximal applied shear force) decreases by 17% in comparison with the pure quartz sand. The talc content affects considerably stronger the shear force drop during the sliding process. The force drop amplitude falls from $\Delta Fs$ = 22.5 ± 1 N for pure quartz sand to $\Delta Fs$ = 0.5 ± 0.1 N for sand/talc mixture with the talc content of 35% (Fig. 3). The kinematic parameters of the sliding process (displacement, maximal velocity, slip episode duration) change relatively slowly in the

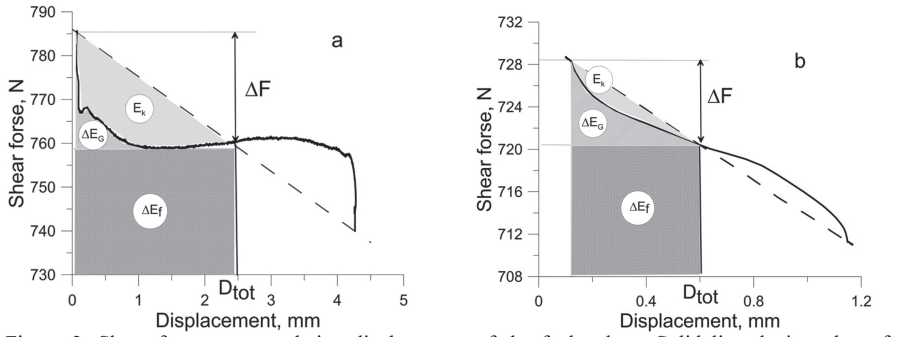


Figure 2. Shear force versus relative displacement of the fault edges. Solid line depicts shear force resistance in fracture; dotted line depicts elastic force of spring with stiffness $K$ = 10.8 N/mm. a–pure quartz sand; b–talc content 20%.

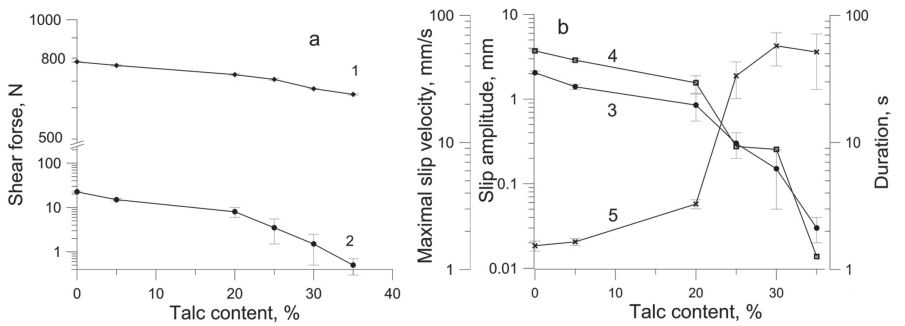


Figure 3. Variation of contact strength (1), force drop (2), displacement (3), maximal slip velocity (4), and the slip episode duration (3) vs talc content in the gauge. Vertical lines are standard deviations. Spring stiffness is $K$ = 10.8 N/mm. Axis of ordinates on the left panel is "disrupted" in a range of 200 to 500 N.

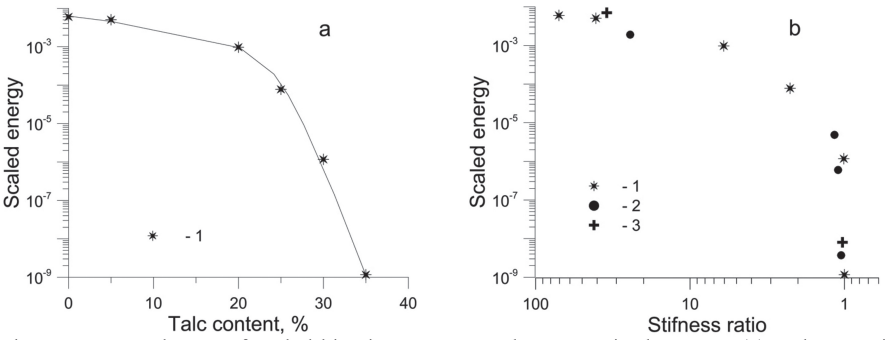


Figure 4. Dependences of scaled kinetic energy on talc content in the gouge (a) and on a stiffness ratio (b) 1–spring stiffness is $K = 10.8$ N/mm; 2–$K = 16.9$ N/mm; 3–$K = 30.9$ N/mm.

range of talc content of $\nu = 0 - 20\%$ (Fig. 3b). Further increase of the talc content results in a drastic drop of maximal velocity of the block displacement accompanied by a corresponding rise of the slip duration. Dependence of $e_{lab}$ on talc content in the gouge is shown in Figure 4a. In the area of pronounced stick-slip mode ($0 \le \nu \le 20\%$) an increase of talc content results in the drop of radiation efficiency approximately by an order of magnitude. In the area of transient processes ($20\% < \nu \le 35\%$) the value of $e_{lab}$ abruptly drops by a several orders of magnitude, so that at $\nu \sim 35\%$ the reduced kinetic energy diminishes to a vanishingly small value. Figure 4b shows the dependence of $e_{lab}$ on the ratio of the maximal fault shear stiffness $|k_s|_{max}$ to the spring specific stiffness $K/S$. As the fault stiffness decreases and approaches the spring stiffness, the scaled kinetic energy drastically drops.

Thus, the performed tests indicate that one of the main parameters that defines the efficiency of transition of cumulated elastic energy into the kinetic energy of the block movement, and respectively, into the radiated seismic energy, is the ratio of the maximal fault shear stiffness to the rock massif stiffness. The stiffer spring (or rock massif) results in a rapid scaled kinetic energy $e_{lab}$ reduction, more rapid for the lower fault stiffness. As stiffness ratio $S \cdot |k_s|_{\max} / K \to 1$ the stick-slip mode becomes impossible, i.e. the condition (1) ceases to be true and all potential energy is converted into the frictional heating.

## 4 DISCUSSION AND CONCLUSION

The experiments allowed to perform a detailed study of the transition from the stick-slip mode with the dynamic release of a portion of cumulated energy to the stable sliding on block interface. The first of the above modes corresponds to normal earthquakes in nature, and the other one–to aseismic creep. The tests clearly identified transient deformation events with low displacement amplitudes and very low slip velocities. Those events lasted tens and hundreds times longer, and amplitudes of stress drops were 1–2 orders of magnitude less than in dynamical events during the stick-slip. However, those slow movements formally had all the stages typical for the stick-slip mode including block acceleration, slip, deceleration, stop, and quiescent state of shear stress accumulation. The intermediate deformation modes are the analogues of such natural phenomena as LFEs, VLFEs, and SSEs.

A gradual change of the sliding mode in experiments occurred either at the expense of variating material composition of fracture gouge by adding talc to quartz sand, or by changing the spring stiffness. Averaged components of energy for separate slip events calculated at the results of several test series are given in Table 1. The averaged values of the contact strength $F_p$ and the force drop $\Delta F$ are also shown in the table.

As one can see in Table 1, the portion of deformation energy converted into the block kinetic energy (the analog of seismic energy of earthquake) drops by three orders of magnitude with the increase of talc content to 30%, while the fracture energy decreases insignificantly, staying

Table 1. Average parameters for individual slip events (Spring stiffness K = 10.8 N/mm).

| Talc content (%) | $F_p$, N | ΔF, N | $E_k/\Delta E_e$ (%) | $\Delta E_G/\Delta E_e$ (%) | $V_r/C_s$ |
|---|---|---|---|---|---|
| 0 | 783 ± 2 | 22.5 ± 1 | 1.32 | 0.2 | 0.97 |
| 5 | 767 ± 5 | 15 ± 0.1 | 1.0 | 0.17 | 0.95 |
| 20 | 727 ± 5 | 8.0 ± 0.2 | 0.27 | 0.28 | 0.58 |
| 25 | 707 ± 4 | 3.5 ± 0.2 | 0.021 | 0.21 | 0.09 |
| 30 | 670 ± 2 | 1.5 ± 0.1 | $3 \times 10^{-4}$ | 0.29 | 0.003 |

approximately the same. It is important to note that in comparison with kinetic energy the contact strength changes quite slowly; as talc content increases from 20 to 30%, $E_k$ decreases 4500 times, while contact strength $F_p$ decreases only by 8%. The force drop decreases 5.3 times faster than the strength drop, but three orders of magnitude slower than the kinetic energy does. The drastic drop of kinetic energy in experiments occurs as a result of decreasing maximum contact stiffness by adding talc to quartz sand and so that $|k_s|_{max}$ approaches the stiffness of elastic element. The ratio of the fracture energy $\Delta E_G$ to the radiated energy $Es$ is an integral parameter, which in the theory of disruption is linked to fracture propagation velocity $Vr$. We use the well-known relation to estimate this parameter: $\frac{\Delta E_G}{\Delta E_G + E_{ss}} = \sqrt{\frac{1-V_r/C_s}{1+V_r/C_s}}$ where $C_s$ = S-wave velocity. It can be seen that as the talc content increases the velocity of fracture propagation $V_r$ decreases from the value close to $Cs$ to the one, which is two orders of magnitude less. Accurate calculation of $\Delta EG$ and $Es$ for the case when talc content corresponds to slow slip events (~35–40% at the spring stiffness of 10.8 N/mm) is difficult; however, approximate evaluations display further decrease of fracture propagation velocity.

So, performed experiments give the possibility to suggest a new explanation of the huge scattering of the values of radiated energy of earthquakes with close seismic moments. In experiments, presented in this study, we have reproduced the modes of inter-block sliding with scaled kinetic energy values varied in a wide range of several orders in magnitude. At the same time the differences in the contact strengths and stress drops were relatively small. The obtained results allow conclude that the sliding mode and, particularly, the portion of deformation energy spent to seismic radiation is defined by the ratio of two parameters—the fault stiffness to the stiffness of surrounding rock massif. A particular consequence of this statement is the well-known condition of stick-slip occurrence.

## ACKNOWLEDGMENTS

This study was funded by Russian Scientific Foundation (Grant 14-17-00719).

## REFERENCES

Choy, G.L. & Boatwright, J.L. 1995. Global patterns of radiated seismic energy and apparent stress. *Journal of Geophysical Research* 100: 18205–18228.

Dieterich, J. 1979. Modeling of rock friction: 1. Experimental results and constitutive equations. *J. Geoph. Res.* 84(B5): 2161–2168.

Ikari, M.J., Marone, C., Saffer, D.M. & Kopf, A.J. 2013. Slip weakening as a mechanism for slow earthquakes. *Nature Geosciences.* 6 (6): 468–472.

Lay, T. (eds) 2009. *Seismological Grand Challenges in Understanding Earth's Dynamic Systems.* Report to the National Science Foundation, IRIS Consortium, 76 pp.

Peng, Z. & Gomberg, J. 2010. An integrated perspective of the continuum between earthquakes and slow-slip phenomena. *Nature geosciences* 3: 599–607.

*Rock Dynamics: From Research to Engineering – Li et al. (Eds)*
*© 2016 Taylor & Francis Group, London, ISBN 978-1-138-02953-8*

# Calculation of the irreversible deformation region under a large-scale underground explosion based on block hierarchical structure

J. Li, M.Y. Wang & Q.H. Qian
*State Key Laboratory of Disaster Prevention and Mitigation of Explosion and Impact, PLA University of Science and Technology, Nanjing, China*

ABSTRACT: Based on the block hierarchical structure of practical rock masses, this paper presents a systematic study of the mechanical process that structural blocks at different hierarchical levels undergo a confined motion (rotation and translation) under the explosion seismic wave, thus actuating strain concentrations at the surfaces of weakening. Then some neglected conditions of Kocharyan's work in calculating scales of activated blocks is given, the equivalent strain $\varepsilon_*$ is redefined, and the calculation formula of irreversible deformation region radius under large-scale underground explosion is re-derived. The existing test data confirms its accuracy.

*Keywords*: block hierarchical structure; geoblocks; irreversible deformation; large-scale underground explosion; equivalent strain

## 1 INTRODUCTION

Thousands of underground nuclear tests have been carried out around the world, and the accumulated data (Hamilton et al. 1969, Glasstone & Dolan 1977, Kocharyan & Spivak 2001, Qian 2007, Hong et al. 2008) has shown the unsuitability of continuum mechanics for describing the mechanical behaviour of practical rock masses.

1. According to the tests data of American & Russian contained underground explosions (Bucknam 1969, Mckeown & Dickey 1969, Hamilton et al. 1969, Dickey et al. 1972, Glasstone & Dolan 1977, Kocharyan et al. 2001), Scientists have noticed the long-range effects of large-scale underground explosions, i.e., the irreversible deformation region radius ($R_d \approx 800 \sim 1100Q^{1/3}$ m) were nearly an order of magnitude greater than the crack regions (approximately 80~120 $Q^{1/3}$m). These can't be explained by traditional continuum mechanics.
2. According to the continuous model, the deformation caused by an underground explosion should decrease continuously with the distance. However, in Russian underground explosion test data (Kocharyan & Spivak 2001), the strains localized in discontinuities exceed the corresponding values measured in the rock blocks by 2~3 orders of magnitude. These results indicate that significant deformation localization phenomena occur near the faults.
3. The discovery of the alternating-sign response of rock mass (Adushkin & Oparin 2012, 2014) to blast impacts proves that rock blocks segmented by cracks, joints or faults have undergone relative (or even opposite) rotations and motions, which cannot be expressed by continuum mechanics.

The above phenomena indicate that, in order to estimate the irreversible deformation region radius of a large-scale underground explosion, the rock mass cannot be treated as a continuum. Actually, under long-term tectonic movement, a rock mass is intersected by magnitudes of discontinuities of different scales that divide the rock mass into structural constituents-rock blocks different in size. The scale of the structural inhomogeneity has a

highly wide range of size: from $10^{-8}$m (crystal lattice defects of rock mineralogical composition) to $10^{6}$m (extent of large tectonic faults). According to Sadovsky(1979), Adushkin & Spivak (1990), Kozyrev & Lukichev (1995), Oparin et al. (1998), Kurlenya & Oparin (1999, 2000), Oparin & Simonov (2010), Adushkin & Oparin (2012, 2014) and others, the nonlinear mechanical behaviour of geomaterials and rock masses is mainly caused by their structural inhomogeneity (or block-hierarchical structure).

According their concepts, the rock mass is divided into a large number of blocks of different ranks and sizes, the boundaries of which are the faults or cracks, which are filled with materials that are of inferior strength to the blocks. Under external forces, if the stress acting on the rock mass is smaller than the strength of the filling material, then the rock mass remains whole and can be seen as a continuum. On the other hand, as the stress increases, one or several weak structural planes in a certain region may reach their limits and divide the original continuum into smaller structure units, so that in this case, the material can no longer be seen as a continuum. With the further stress increase, the rock blocks can also be damaged, but the stress required will far exceed the previous value.

Obviously, in zones far away from the explosion centre, the dynamic stresses caused by the explosion are not large enough to destroy the high-strength rock blocks, considering that the rigidity of the blocks is far greater than that of the filling materials. Thus, the deformation of the blocks themselves can be negligible, so the irreversible deformation of the rock mass is mainly the result of the space-limited motion (rotation and translation) of the blocks which will cause the destruction of the filling materials between blocks. The main characteristic of the deformation in this case is the relative motion along the geological structural surface.

Hence, the calculation of the irreversible deformation regions under a large-scale underground explosion must be based on the block-hierarchical structure of the rock mass. Just based on this consideration, Kocharyan et al. (2001) presented calculation methods for the irreversible deformation region radius under a large-scale underground explosion.

In this paper, by assuming that the structure of the rock mass follows Sadovsky's concept of the block hierarchy, Kocharyan's work is re-deduced and improved, some neglected conditions of Kocharyan's work in calculating scales of activated blocks are given, and the calculation formula of irreversible deformation region radius under large-scale underground explosion is re-derived.

## 2 CONCEPT OF BLOCK HIERARCHY

According to Sadovsky's concept of the block hierarchy, from the giant continent plate to fine sands or even smaller crystal structures, the rock mass is the composition of blocks in different scales, and the blocks are separated by faults or cracks, which are filled with materials of inferior strength to the rock mass (Sadovsky 1979, Kurlenya & Oparin 1999). Just consider the structure of rock masses as a complex hierarchical system seen in Figure 1, the blocks of rank $i = 0$ are embedded by the blocks of rank $i = 1$, and the blocks of rank $i = 1$ are embedded by the blocks of rank $i = 2$ … i.e., the large blocks are embedded by the small blocks, and the small blocks are embedded by the smaller blocks.

Based on analysis of extensive filed data on the structure of geoblocks at the regional and planetary levels, and available information on the block-hierarchical structure of ore

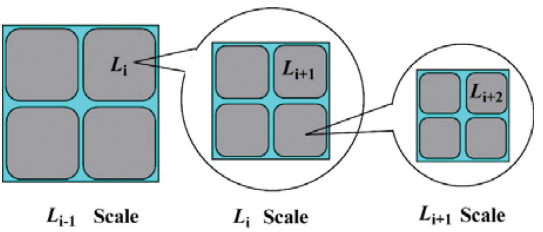


Figure 1. Block hierarchical structure of the rock mass.

and rock masses of mines, two key characteristics of "self-organizing" systems have been found (Kurlenya & Oparin 1999). The first is the linear coefficient of structural embedment, i.e., $\lambda = L_i / L_{i+1} = (2 \sim 5)$, where $L_i$ is the size of the blocks of rank $i$; the other is the geomechanical "invariant" $\mu_\Delta = a_i / L_i = (1/2 \sim 2) \cdot 10^{-2}$, i.e., there is a stable relationship between the values of cracks opening $\delta_i$ and the diameters of the blocks $L_i$ that are separated by them.

The deformation of the rock mass consists of the deformation of the blocks and the filling materials. In the case that the effects caused by the explosion are not sufficient to destroy the filling materials, the rock mass can be regarded as a continuum, and its deformation and motion can be described by the elasticity. As the effects increase, when the dynamic stress caused by the explosion is enough to destroy the filling material but lower than the block strength, the blocks will undergo space-limited motion under the effects of a high geostress and dynamic stress (Adushkin & Spivak 1990, Adushkin & Oparin 2012). During the space-limited motion, the shape of the blocks can be regarded as unchanged. Thus, the case that the rock mass is divided into a large number of blocks can be regarded as the result of that some of the filling materials around it have reached this ultimate strength, and the sizes of the newly formed blocks are directly related to the effects caused by the explosion.

## 3 DERIVATION OF THE FORMULA OF THE IRREVERSIBLE DEFORMATION REGION

Assume that at a distance of $r$ from the explosion centre, the size of the activated blocks under the given explosion equivalent $Q$ is $L_*$ (the linear sizes of the activated blocks are supposed to correspond to the size of the natural rock blocks $L_i$), and then we can establish the motion equations of the blocks by employing the following idealized model, as shown in Figure 2.

To simplify the analysis, the following assumptions are adopted:

1. The rigidity of the blocks is far greater than that of the filling materials;
2. The dynamic stresses caused by the weak disturbances are not large enough to destroy the rigid blocks of high strength, so the occurrence of the local irreversible deformation is due to the failure of the filling materials;
3. The activated blocks are standard blocks of uniform size, and their movements are independent;
4. The relation between the neighbouring blocks satisfies

$$L_i / L_{i+1} = k_2, (k_2 > 1) \tag{1}$$

5. The relation between the block size and the thickness of the filling materials satisfies

$$a_i / L_i = k_1 \tag{2}$$

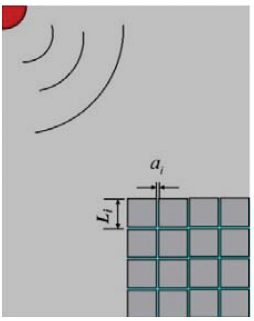


Figure 2. Space-limited motion of the blocks under the explosion seismic wave.

where $k_1$, $k_2$ are invariant (Adushkin & Spivak 1990, Kurlenya et al. 1993)

$$k_2 = \lambda = 2 \sim 5, k_1 = \mu_\Delta = (1/2 \sim 2) \cdot 10^{-2} \tag{3}$$

The test results show that the rock blocks will undergo a space-limited rotation or translation under the explosion as seen in Figure 3, and thus cause a shear strain of the filling materials which can be expressed as

$$\varepsilon = U_i / a_i \tag{4}$$

The rigidity of the blocks is assumed to be large enough so that the neighbouring blocks cannot penetrate into each other. Based on this, the rotation or translation of the blocks in order $i$ is determined by the width of fault $a_i$ and its ultimate strain $\varepsilon_{\max}$, i.e.,

$$U_{i*} = \varsigma a_i \tag{5}$$

Where $\varsigma$ is the ultimate compression ratio of the filling material.

$$\varsigma = \varepsilon_{\max} < 1 \tag{6}$$

The hierarchical structure of the blocks and their motion are simplified as the model shown in Figures 1 and 4. Suppose that the blocks with ranks larger than that of the activated block $L_* = L_i$ will all undergo a translation or rotation under the explosion (Adushkin & Spivak 1990, Adushkin & Oparin 2012).

For space-limited translation model as shown in Figure 4a, the blocks of sizes $L_i$, $L_{i+1}$, $L_{i+1}$ ……have a common point, $x_j$, so the macro-displacement of the point consists of the displacements of blocks in different ranks, which can be expressed as

$$U = U_i + U_{i+1} + U_{i+2} + \cdots \tag{7}$$

If each block reaches its ultimate rotation, then the macro-displacement of the activated block is

$$U_* = U_{i*} + U_{i+1*} + U_{i+2*} + \cdots = \varsigma(a_i + a_{i+1} + a_{i+2} + \cdots) \tag{8}$$

For space-limited rotation model, consider that during the rotation of the blocks, the displacement $U$ and rotation $\omega$ have the following relation

$$|\mathbf{U}_i| = \frac{L_i}{2} \cdot |\omega_i| \tag{9}$$

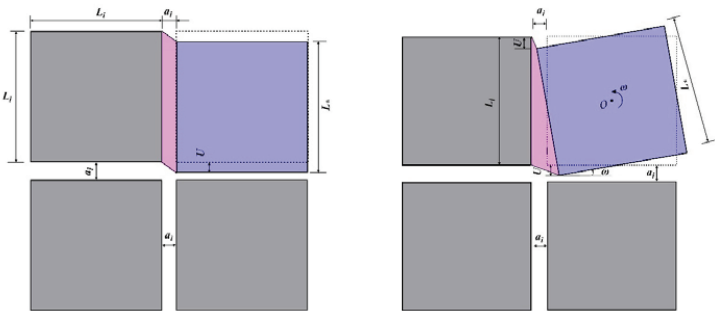

a. Space-limited translation b. Space-limited rotation

Figure 3. Local deformation of filling material caused by a space-limited motion of blocks.

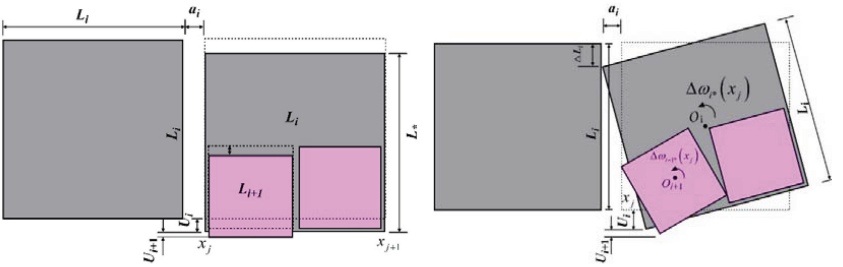


Figure 4. Composition of the macro-displacement caused by space-limited motions of blocks.

Thus, the ultimate rotation can be defined as

$$\Delta\omega_{i*} = U_{i*} \big/ \left(L_i/2\right) = 2\varsigma a_i / L_i \tag{10}$$

Similarly, in the case that the blocks of sizes $L_i$ and $L_{i+1}$, $L_{i+1}$ and $L_{i+2}$ … all reach their ultimate rotations, then the macro-displacement of their common point, $x_j$, has the following form

$$U = U_i + U_{i+1} + U_{i+2} + \cdots \tag{11}$$

When all of the blocks have reached their maximum rotations, then the macro-displacement of the activated block can be expressed as

$$U_* = \frac{\Delta\omega_{i*}\left(x_j\right)}{2} L_i + \frac{\Delta\omega_{i+1*}\left(x_j\right)}{2} L_{i+1} + \frac{\Delta\omega_{i+2*}\left(x_j\right)}{2} L_{i+2} + \cdots = \varsigma\left(a_i + a_{i+1} + a_{i+2} + \cdots\right) \tag{12}$$

where $\Delta\omega_{i*}\left(x_j\right)$ and $\Delta\omega_{i+1*}\left(x_j\right)$ …… are the rotations of the common point caused by the blocks of size $L_i$ and $L_{i+1}$ ……, respectively.

Equations (8) and (12) show that the macro-displacement expressions corresponding to the translation and rotation are the same. Considering the hierarchical structure of the blocks, upon substituting Equations (1) and (2) into Equation (12), the following equation is obtained:

$$U_* = \varsigma\left(a_i + a_{i+1} + a_{i+2} + \cdots\right) = \varsigma\left(k_1 L_i + k_1 L_{i+1} + k_1 L_{i+2}\right) + \cdots = \varsigma\left(k_1 L_* + k_1 \frac{L_*}{k_2} + k_1 \frac{L_*}{k_2{}^2} + \cdots\right) \tag{13}$$

According to Equation (13), the blocks of size $L_*$ make the largest contribution to the macro-displacement and the deformation of the rock mass, while the effects of the blocks of higher rank to the displacement are small and can be ignored (Adushkin & Spivak 1990, Adushkin & Oparin 2012). Thus, Equation (13) can be rewritten as

$$U_* \approx \varsigma\left(k_1 L_* + k_1 \frac{L_*}{k_2}\right) \tag{14}$$

According to Equation (14), the size of the activated blocks is

$$L_* \approx k_2 U_* \big/ \varsigma\left(1 + k_2\right) k_1 \tag{15}$$

In the following sections, we will estimate the scale of the activated blocks and the deformation of the rock masses under a given explosion wave. The effects of the concentrated explosion can be simplified as spherical symmetric compression waves, and according to (Adushkin & Spivak 1993, Qian &Wang 2010), the radial velocity is given by

$$v(r,t) = v_0(r)\sin(\pi t/\tau), \quad 0 \le t \le \tau \tag{16}$$

where $v_0(r) = A\left(r/Q^{1/3}\right)^{-n}$ represents the maximum velocity of the particles at a distance of $r$ from the explosion centre, $\tau = BQ^{1/3}\left(r/Q^{1/3}\right)^{m} / C_p$ is the corresponding explosion wave duration, $C_p$ is the longitudinal wave velocity, and $A$, $B$, $m$, $n$ are constants that can be determined by tests (Adushkin & Spivak 1993).

According to Equation (16), the displacement of the particles is

$$U = \int_0^{\tau} v(r,t)\,\mathrm{d}\,\tau = \int_0^{\tau} v_0 \sin\left(\frac{\pi t}{\tau}\right)\mathrm{d}\,\tau = \frac{v_0\tau}{\pi}\left(1-\cos\frac{\pi t}{\tau}\right) \tag{17}$$

At time $t = \tau$, the displacement in Equation (17) reaches its maximum and can be expressed as

$$U_{\max} = 2v_0\tau/\pi \tag{18}$$

Let $U_* = U_{\max}$, and substituting Equation (18) into Equation (15), the sizes of the activated blocks can be expressed as

$$L_* = \frac{2ABk_2}{\pi C_p \varsigma k_1(1+k_2)} r^{m-n} Q^{(n-m+1)/3} \tag{19}$$

Equation (19) can also be expressed as

$$\frac{L_*}{\sqrt[3]{Q}} = A'\left(\frac{r}{\sqrt[3]{Q}}\right)^{m-n} \tag{20}$$

where $A' = \frac{2ABk_2}{\pi C_p \varsigma k_1(1+k_2)}$ is constant.

Equations (19) and (20) show that the scale of the activated blocks is determined by the explosion equivalent and the distance to the explosion centre.

The irreversible deformation region radius obtained from Equation (19) is

$$r^{n-m} = \frac{2ABk_2}{\pi C_p \varsigma k_1(1+k_2)L_*} Q^{(n-m+1)/3} \text{ or } \frac{r}{Q^{1/3}} = \left(\frac{2ABk_2}{\pi C_p \varsigma L_* k_1(1+k_2)}\right)^{\frac{1}{n-m}} Q^{\frac{1}{3(n-m)}} \tag{21}$$

To give the accurate radius of the irreversible deformation region, we need to know the value of $\varsigma$, but it is a pity that at present, $\varsigma$ is unknown. Adushkin and Spivak (1993) adopted the equivalent strain $\varepsilon_* = U_{\max}/L_* = U_*/L_*$ to evaluate the irreversible deformation, and based on the study of the tidal movement, the value of $\varepsilon_*$ is taken $(1\sim 2)\times 10^{-5}$.

According to Equation (14), the relation between $\varepsilon_*$ and $\varsigma$ is

$$\varepsilon_* = \frac{U^*}{L_*} \approx k_1\varsigma\left(1+\frac{1}{k_2}\right) \tag{22}$$

Substituting Equation (22) into Equation (21), the estimated irreversible deformation region radius is

$$\frac{r}{Q^{1/3}} = \left(\frac{2AB}{\pi\varepsilon_* C_p L_*}\right)^{\frac{1}{n-m}} Q^{\frac{1}{3(n-m)}} \tag{23}$$

Table 1. Irreversible deformation region radius calculated by Eq. (23).

| | *Rock Parameters* | | | | *Calculated results* | |
|---|---|---|---|---|---|---|
| | A | n | B | m | $R_d$ | $\upsilon_*$ |
| Granite | $1.0\times10^4$ | 1.65 | $1.14\times10^{-5}$ | 2.3 | 1128 m | 0.09 m/s |
| | $1.3\times10^4$ | 1.65 | $1.14\times10^{-5}$ | 2.3 | 753 m | 0.2 m/s |
| | $1.3\times10^4$ | 1.7 | $1.14\times10^{-5}$ | 2.3 | 1308 m | 0.07 m/s |

## 4 ESTIMATION OF THE IRREVERSIBLE DEFORMATION REGION RADIUS

To estimate the irreversible deformation region using Eqs. (23), we have to determine the value of $A$, $B$, $n$ and $m$.

By analyzing huge numbers of underground explosions, Kocharyan & Spivak (2001) gave the value of $A$ and $n$ from a perspective of experimental statistics. Take granite for example: $A=(1\sim1.3)\times10^4, n=1.6\sim1.75$

$B$ and $m$ can be estimated indirectly. According to the literature (Qian and Wang 2010 ): when $r=R_{cavity}\approx(7-12)Q^{1/3}$, $\tau\approx10^{-3}Q^{1/3}$ , and when $r=R_{crush}\approx(30-40)Q^{1/3}$ $\tau\approx20\cdot10^{-3}Q^{1/3}$ , where $R_{cavity}$ and $R_{crush}$ are the radii of the cavity and crushing zone.

Since $R_{crush}\approx(3\sim5)R_{cavity}$, then $m\approx1.86\sim2.72$ . If set $m\approx2.3, R_{cavity}\approx7Q^{1/3}$ , then we get $B\approx1.14\cdot10^{-5}$.

Set $C_p$ = 5000 *m*/*s*, thus for a given explosion ($Q$ = 1$kt$), we can gain the calculated results of irreversible deformation region radius as summarized in Table 1, where $R_d$ is the estimated irreversible deformation region, and $\upsilon_*$ is the estimated maximum velocity of the particles at a distance of $r=R_d$.

This result coincides well with the test results reported by Kocharyan et al. (2001), i.e., $R_d/Q^{1/3}\approx(650\sim1400)m/kt^{1/3}$, $\upsilon_*\approx0.05\sim0.15\,m/s$. Besides, it is quite different from the calculation results using classical theory of continuum mechanics, which is only about $R_d\approx(80\sim120)Q^{1/3}m$.

However, this result also shows that Eq. (23) seems to be too sensitive with coefficients $(m-n)$ , when $n$ increased from 1.65 to 1.7, the calculated irreversible deformation region radii added almost 500 m (from 753 m to 1308 m ). In our next paper, we will introduce a new formula gained by analysis of the oscillation energy of geoblocks activated in the process of explosion wave propagation, this formula will consist fewer coefficients and will be proven to be more suitable for calculating the irreversible deformation region under a large-scale underground explosion.

## CONCLUSIONS

Based on the block hierarchical structure of practical rock masses, Kocharyan's work is re-deduced and improved to calculate the irreversible deformation region radius under a large-scale underground explosion. The conclusions are drawn as follows:

1. At the point far away from the explosion centre, the effects of the blast wave are not large enough to destroy the high-strength blocks, so the irreversible deformation is mainly due to the destruction of the filling material. Based on the hierarchical structure of the blocks, the confined rotation and translation of geoblocks under the explosion is analyzed, and then the formula of the activated blocks sizes and the corresponding irreversible deformation region radius under the given explosion is obtained.
2. Compared with Kocharyan's work, the major improvements of this paper are that: both rotation and translation of structural blocks under the explosion seismic waves were analysed in this paper. Besides, by introducing the ultimate compression ratio of the filling material $\varsigma$, the physical implication of equivalent strain $\varepsilon_*$ is redefined.
3. Through the redefined equation of $\varepsilon_*$ (Eqs. (22)), we can get that, the invariant $\mu_\Delta$ (or $k_1$) made positive contributions to the local irreversible deformation of rock mass, because

it presented a quantitive estimation of the " possibe motion freedom" of the structural blocks in a practical rock mass.

4. Although the calculated result coincides well with the test results, Eq. (23) was proven to be sensitive to coefficients $A$, $B$, $m$ and $n$, especially for the value of $(m-n)$. In fact, due to the limitations of few existing tests data and their measurement error, it is still difficult for us to capture the accurate value of those coefficients. So how to optimize the formula, and reduce unnecessary parameters is still a topic worth studying.

## ACKNOWLEDGMENTS

The authors would like to acknowledge the financial support from the National Natural Science Foundation of China (Grant No. 51527810, No. 51309233) and the National Basic Research Program of China (973 Program, No. 2013CB036005), which is greatly appreciated by the authors.

## REFERENCES

Adushkin, V.V. & Spivak, A.A. 1990. Characteristic features of the deformation of a block medium during blasting. *Journal of Mining Science* 26(2): 142–147.

Adushkin, V.V. & Spivak, A.A. 1993. *Geomechanics of large-scale explosion*. Mosocow: Nedra.

Adushkin, V.V. & Oparin, V.N. 2012. From the alternating-sign explosion response of rocks to the pendulum waves in stressed geomedia. part I. *Journal of Mining Science* 48(2): 203–222.

Adushkin, V.V. & Oparin, V.N. 2014. From the alternating-sign explosion response of rocks to the pendulum waves in stressed geomedia. part III. *Journal of Mining Science* 50(4): 623–645.

Bucknam 1969. Geologic effects of the Benham underground nuclear explosion, Nevada Test Site. *Bulletin of Seismological Society America* 59: 2209–2219.

Dickey, D.D. & Mckeown, F.A. & Bucknam, R.C. 1972. Preliminary results of ground deformation measurements near the Cannikin explosion. *Bulletin of the Seismological Society of America* 62(6): 1505–1518.

Glasstone, S. & Dolan, P.J. 1977. *The effects of nuclear weapons, 3rd edition*. United States Department of Defense and the Energy Research and Development Administration. US Government, pp 231–275.

Hamilton, R.M. & Mckeown, F.A. & Healy, J.H. 1969. Seismic activity and faulting associated with a large underground nuclear explosion. *Science* 166(3905): 601–604.

Hong, T.K. & Baag, C.E. & Choi, H. & Sheen, D.H. 2008. Regional seismic observations of the 9 October 2006 underground nuclear explosion in North Korea and the influence of crustal structure on regional phases. *Journal of Geophysical Research Atmospheres* 113(B3): 1711–1730.

Kozyrev, S.A. & Lukichev, S.V. 1995. Characteristic features of the seismic effect of massive blasting in highly stressed block masses. *Journal of Mining Science* 31(1): 43–50.

Kocharyan, G.G. & Spivak, A.A. 2001. Movement of Rock Blocks during Large-Scale Underground Explosions. Part I: Experimental Data. *Journal of Mining Science* 37(1): 64–76.

Kocharyan, G.G. & Spivak, A.A. & Budkov. 2001. Movement of rock blocks during large-scale underground explosion. Part II: Estimates by analytical models, numerical calculations, and comparative analysis of theoretical and experimental data. *Journal of mining science* 37(2): 149–168.

Kurlenya, M.V. & Oparin, V.N. 1999. Problems of nonlinear geomechanics. part I. *Journal of Mining Science* 35(3): 216–230.

Kurlenya, M.V. & Oparin, V.N. 2000. Problems of nonlinear geomechanics. part II. *Journal of Mining Science* 36(4): 305–326.

Kurlenya, M.V. & Oparin, V.N. & Eremenko, A.A. 1993. Relation of linear block dimensions of rock to crack opening in the structural hierarchy of masses. *Journal of Mining Science* 29(3): 197–203.

Mckeown, F.A. & Dickey, D.D.1969. Fault displacements and motion related to nuclear explosions. *Bulletin of Seismological Society America* 59(6): 2253–2269.

Oparin, V.N. & Yushkin, V.F. & Akinin, A.A. & Balmashnova, E.G. 1998. A new scale of hierarchically structured representations as a characteristic for ranking entities in a geomedium. *Journal of Mining Science* 34(5): 387–401.

Oparin, V.N. & Simonov, B.F. 2010. Nonlinear deformation-wave processes in the vibrational oil geotechnologies. *Journal of Mining Science* 46(2): 95–112.

Qian, Q.H. 2007. *Selections from Academician Qian Qihu's theses*. Beijing: Science Press.

Qian, Q.H. & Wang, M.Y. 2010. *Impact and explosion effect in rock and soil*. Beijing: National defense industry Press.

Sadovsky, M.A. 1979. Natural lumpiness of rocks. *Doklady AN SSSR* 247(4): 829–832.

*Rock Dynamics: From Research to Engineering – Li et al. (Eds)*
*© 2016 Taylor & Francis Group, London, ISBN 978-1-138-02953-8*

# Validation study of the Particle-based Numerical Manifold Method (PNMM) on stress wave propagation

X. Li, Q.B. Zhang, L. He & J. Zhao
*Department of Civil Engineering, Monash University, Clayton, VIC, Australia*

ABSTRACT: A validation study of the Particle-based Numerical Manifold Method (PNMM) for wave propagation problems is performed. PNMM is proposed by introducing the concept of particle into the Numerical Manifold Method (NMM). PNMM has potential to simulate the microstructure and heterogeneity of rock materials. The stress wave propagation induced by explosion in a continuum is simulated first. Numerical results of the commercial code ABAQUS is selected as the reference. PNMM provides consistent results for the velocity history of selected points. Then, the stress wave propagation across a material interface is conducted. Simulation results are in good agreement with analytical wave velocities. Therefore, the capability of PNMM to simulate wave propagation is verified.

## 1 INTRODUCTION

The prediction of wave attenuation across fractured rock masses is significant in geophysics, seismic wave investigation and rock protective engineering. Theoretical models are generally able to analyze the wave propagation across a single fracture (Zhao & Cai 2001) or a set of parallel fractures (Zhao et al. 2006). However, the distribution of rock joints can be quite complex in practice, and analytical methods will be difficult to be applied. Under such a circumstance, numerical methods could provide promising solutions for stress wave propagation in rock masses.

Existing numerical methods for rock mechanics are usually categorized into three groups, i.e. continuous methods, discrete methods and coupled methods (Jing 2003). The Finite Difference or Volume Method (FDM/FVM) (Zhao et al. 2015), and Finite Element Method (FEM) (Ma & An 2008) are representative continuous methods, while Distinct Element Method (DEM) (Cundall & Strack 1979) and Discontinuous Deformation Analysis (DDA) (Shi & Goodman 1985) are two mainstream discrete methods in rock mechanics. The Numerical Manifold Method (NMM) (Shi 1992), as a coupled FEM and DDA method, provides a numerical framework that solves the problems involving continuous and discontinuous deformation in a unified way. A comprehensive review on recent development of NMM can be found in (Ma et al. 2010).

In the present study, a newly developed numerical code, the Particle-based Numerical Manifold Method (PNMM), was proposed and used to simulate the stress wave propagation across a material interface. PNMM simulates microstructures of rock materials and simplifies the geometrical and contact operation in NMM, by introducing the particle concept into NMM (Sun et al. 2013, Sun et al. 2014). Compared with existing numerical models, distinct features of PNMM in wave propagation simulation include: (1) Simulations of the microstructure of rock materials and the macroscopic mechanical behavior of rock masses are implemented in a unified framework; (2) The Degree of Freedom (DOF) of the model is independent from the simulation accuracy for the rock materials microstructure, i.e. the mineral grains can be simulated accurately (at microscopic scale) without rapidly increasing the degrees of freedom of the rock masses (at macroscopic scale); (3) PNMM has potential to simulate continuum-discontinuum wave propagation problems; (4) The easy-to-detect

particle-particle contacts at microscopic scale can be accumulated to perform the rock joint behavior at macroscopic scale.

## 2 THE PARTICLE-BASED NUMERICAL MANIFOLD METHOD (PNMM)

The basic idea of PNMM is to represent the microstructure of rock materials with a group of particles and to simulate the macroscopic behavior of rock masses through polygonal elements. This characteristic is carried out by a dual-layer-cover system and a dual-level discretization. The dual-layer-cover system refers to the covers in NMM, details can be found in the literature of NMM. As for the dual-level discretization, the first one discretizes a piece of continuum into polygonal elements, while the second one discretizes each element into a group of particles.

Based on the dual-layer-cover system, manifold elements are generated by intersecting mathematical covers and the modeling domain, in a similar way to NMM. On manifold elements, the cover function and the weight function are defined to constitute the local approximation. For each manifold element, an inner mesh is further generated. Then, one particle is generated in each inner element. The center of the particle is the centroid of the inner element. The area of the particle is equal to the area of the inner element. In such a way, the sum of particle areas remains equal to the area of the polygonal element.

The DOF of the model is defined on manifold elements, while material properties, body forces, and applied boundary conditions are defined on particles. Therefore, in the calculation of elemental matrices, the integration has to be conducted on particles. PNMM takes the centroids and areas of particles as the integration points and weights respectively. In PNMM, the mechanical field on each particle is assumed to be constant, therefore a particle integration scheme is proposed for PNMM as follow

$$\int_A f(\mathbf{x})dA = \sum_{i=1}^{p}\left[f\left(\mathbf{x}_i^c\right)\cdot A_i\right] = \pi\sum_{i=1}^{p} r_i^2\cdot f\left(\mathbf{x}_i^c\right) \tag{1}$$

where $p$ is the number of particles, $\mathbf{x}_i^c$ the coordinates of the centroid of the $i$th particle, $A_i$ the area of the $i$th particle, and $r_i$ the radius of the $i$th particle. An attractive advantage of the particle integration scheme is that the quadrature domain can be either convex or concave polygons. It is theoretically suitable for any integrand, including polynomial, exponential, and trigonometric functions. The construction framework of PNMM is schematically shown in Figure 1.

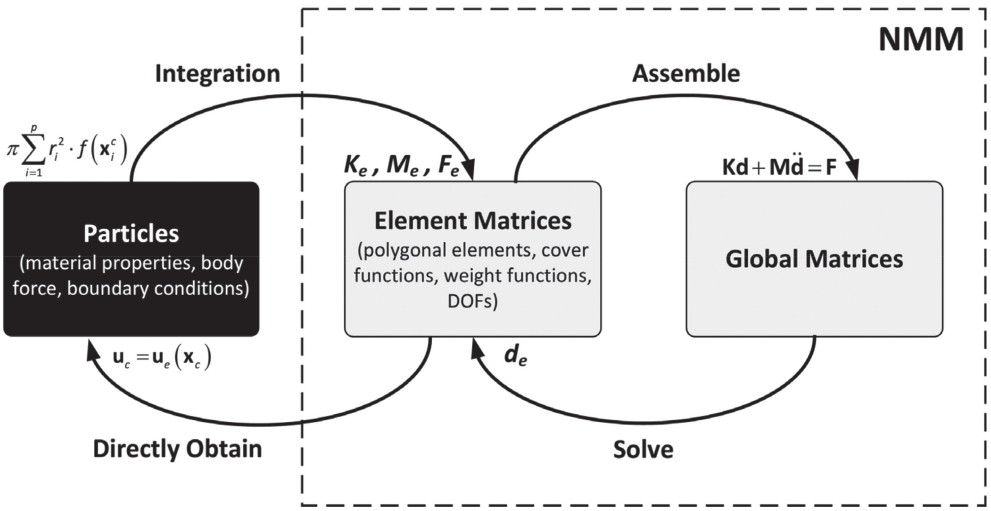


Figure 1. The construction framework of PNMM.

In calculation, mechanical responses of polygonal elements are solved prior to particles, by solving global equations in matrix form. Then, the behavior of each internal particle is simply derived from the mechanical fields of its governing element, as

$$\mathbf{u}_c = \mathbf{u}_e(\mathbf{x}_c), \quad \boldsymbol{\varepsilon}_c = \boldsymbol{\varepsilon}_e(\mathbf{x}_c), \quad \boldsymbol{\sigma}_c = \boldsymbol{\sigma}_e(\mathbf{x}_c) \tag{2}$$

## 3 VALIDATION OF PNMM

### 3.1 *Stress wave propagation in continuum*

The first example is the wave propagation in a rock cavern with dimension of *100m X 50m* as shown in Figure 2. The radius of the rock cavern is 2 m. The Young's modulus, Poisson's ratio, and density of the rock cavern is 63.6GPa, 0.2, and 2610 kg/m$^3$ respectively. The theoretical wave velocity of P-wave can be calculated as 5200 m/s. The propagated wave is induced by an explosion load $P$ applied on the rock cavern. The maximum pressure $P_{max}$ is 30 MPa. The durations of the rising stage $t_1$ and the descending stage ($t_2$-$t_1$) are 0.1 ms and 0.4 ms respectively. The adopted PNMM model consists of 41,145 particles.

Simulation results of PNMM indicate that the blasting wave arrives at the upper bound of the model at the time of 9.4 ms, which agrees well with the theoretical wave velocity. The velocity time-history results of two monitoring points predicted by PNMM are in good agreement with those simulated by ABAQUS in Figure 3. Therefore, the ability of PNMM in modelling wave propagation in homogeneous elastic materials is verified.

### 3.2 *Stress wave propagation across material interface*

The second example is the wave propagation across a material interface. The model configuration and material properties are illustrated in Figure 4. The propagated wave is induced by an explosion load applied on a rock plate and transmitted to a steel plate. The applied explosion load $P$ is the same as the previous example. Four monitoring points are set to examine the incident wave, transmitted wave, and reflected wave.

The adopted PNMM model consists of 89,726 particles. Figure 5 shows the process of wave propagation in the rock cavern predicted by PNMM. The incident wave arrives the material interface before 25 ms (Fig. 5b). This result agrees well with the theoretical wave velocity, which is calculated to be 2063.3 m/s. Then, the transmitted wave and reflected wave are generated (Fig. 5c). The transmitted wave arrives at the upper bound of the steel plate at

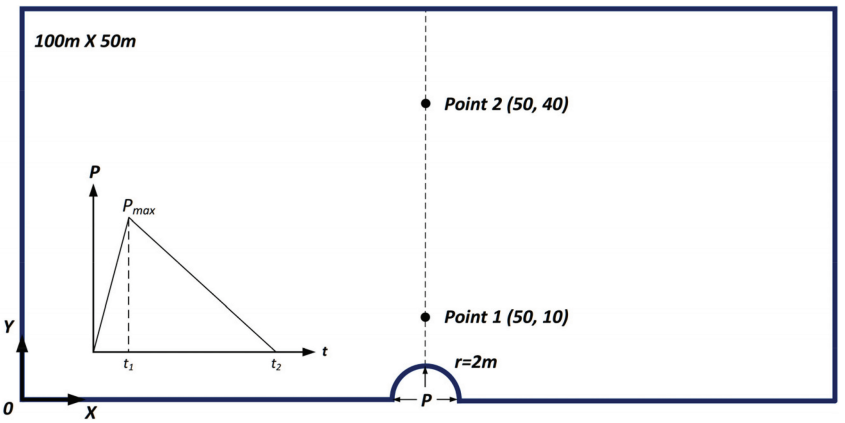


Figure 2. Cavern stress wave propagation: model configuration.

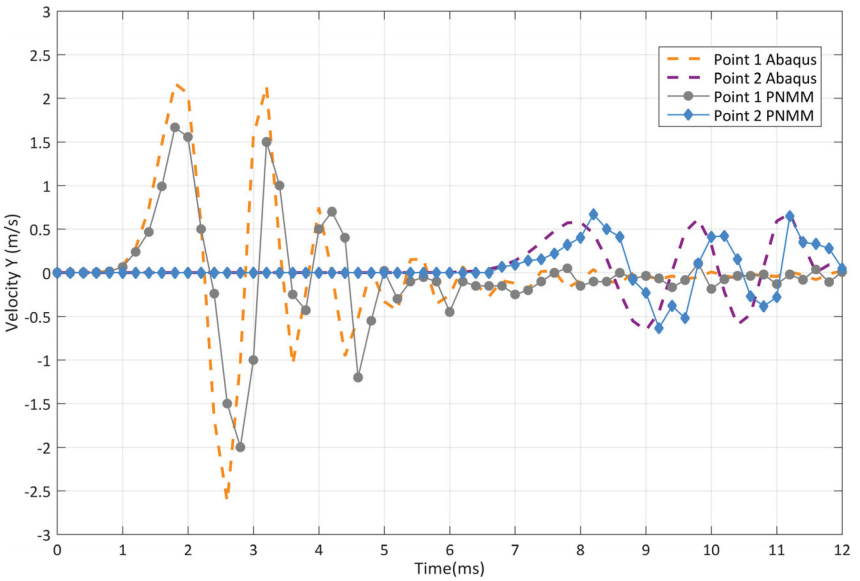


Figure 3. Cavern stress wave propagation: time-history results.

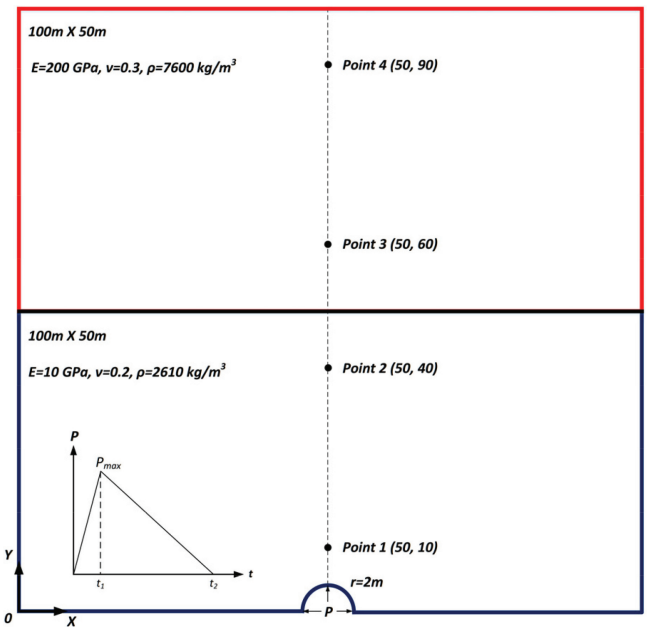


Figure 4. Stress wave propagation across rock-steel interface: model configuration.

about 30 ms. The velocity time-history results of monitoring points predicted by PNMM are shown in Figure 6. From the result of Point 2, one can conclude that the reflected wave passes through at about 30 ms, as the velocity downwards in this period has a greater maximum value than the last period.

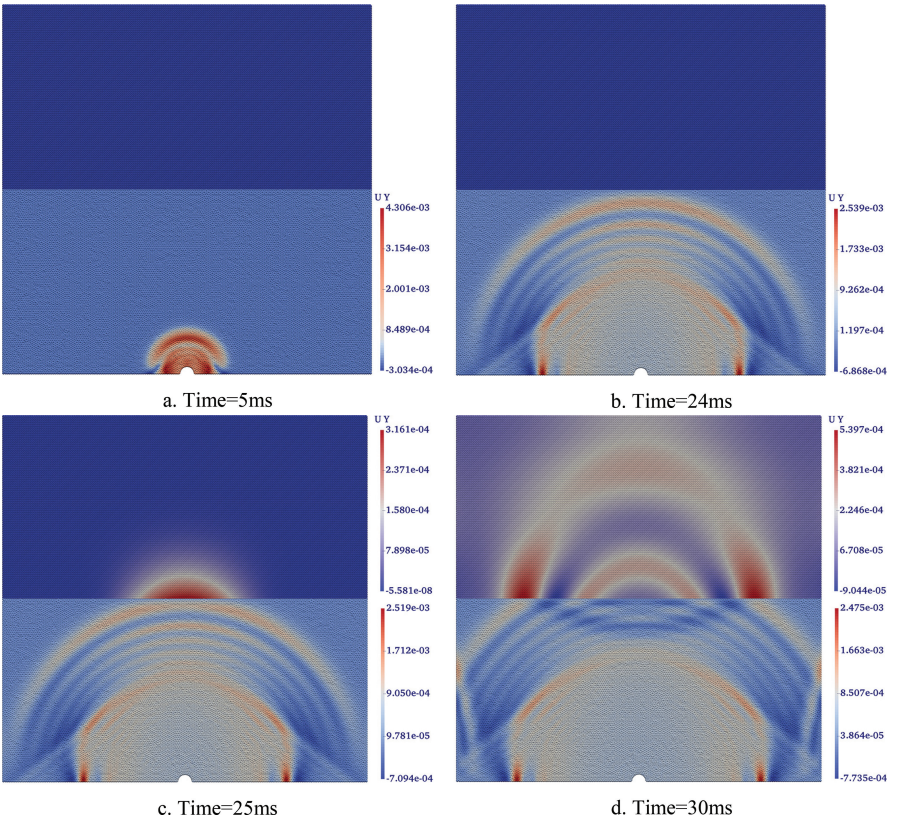


Figure 5. Stress wave propagation across rock-steel interface: process.

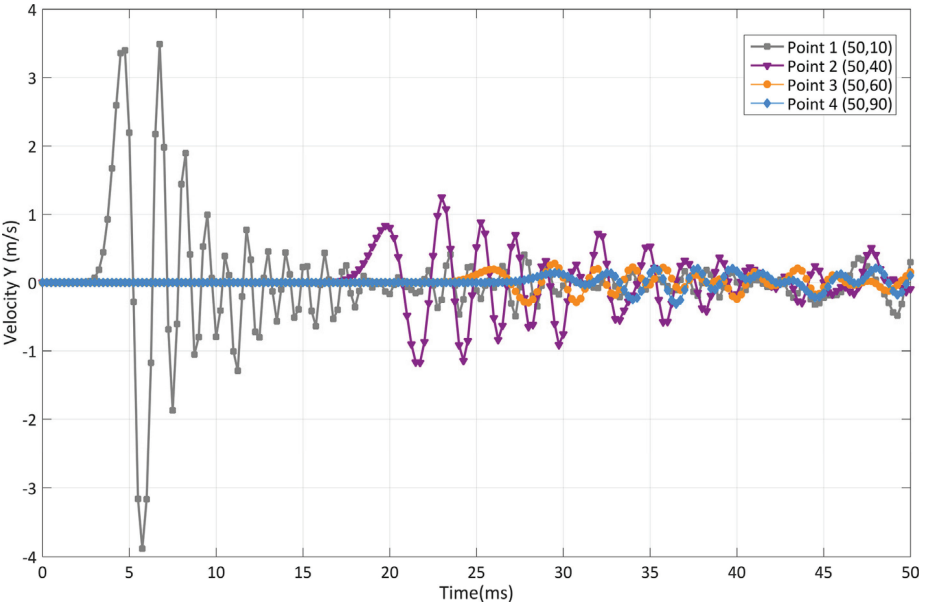


Figure 6. Stress wave propagation across rock-steel interface: time-history results.

## 4 CONCLUSION

The capability of PNMM to model stress wave propagation is verified in this paper. To calibrate the numerical result of PNMM, two examples are provided. The first example is the wave propagation in the continuum. Numerical results of ABAQUS are taken as the reference. Simulation results show that PNMM is able to provide reasonable velocity time-history prediction. The second example it the wave propagation across a material interface. The incident wave, transmitted wave and reflected wave are well simulated by PNMM. The contours of displacements are plotted at different time steps. Therefore, PNMM is proven to be applicable in the simulation of stress wave propagation. Further application of PNMM in more complex conditions, e.g., heterogeneous materials and the failure induced by stress wave propagation, can be carried out in the future.

## ACKNOWLEDGEMENTS

This work is financially supported by the China Scholarship Council (CSC) and the Laboratory of Rock Mechanics (LMR) at École Polytechnique Fédérale de Lausanne (EPFL). The authors also appreciate the help provided by Prof. Chun'an Tang at Dalian University of Technology on the post-process of PNMM.

## REFERENCES

Cundall, P.A. & Strack, O.D.L. 1979. A discrete numerical model for granular assemblies. *Géotechnique* 29: 47–65.

Jing, L. 2003. A review of techniques, advances and outstanding issues in numerical modelling for rock mechanics and rock engineering. *International Journal of Rock Mechanics and Mining Sciences* 40: 283–353.

Ma, G., An, X. & He, L. 2010. The numerical manifold method: A review. *International Journal of Computational Methods* 7: 1–32.

Ma, G.W. & An, X.M. 2008. Numerical simulation of blasting-induced rock fractures. *International Journal of Rock Mechanics and Mining Sciences* 45: 966–975.

Shi, G.-H. & Goodman, R.E. 1985. Two dimensional discontinuous deformation analysis. *International Journal for Numerical and Analytical Methods in Geomechanics* 9: 541–556.

Shi, G.-H. 1992. Modeling rock joints and blocks by manifold method. Rock Mechanics: *Proceedings of the 33th US Symposium*, New Mexico. American Rock Mechanics Association: 639–648.

Sun, L., Zhao, G.F. & Zhao, J. 2013. Particle manifold method (PMM): A new continuum-discontinuum numerical model for geomechanics. *International Journal for Numerical and Analytical Methods in Geomechanics* 37: 1711–1736.

Sun, L., Zhao, G.F. & Zhao, J. 2014. A multiscale manifold method using particle representations of the physical domain. *Geomechanics and Geoengineering* 9: 124–132.

Zhao, J. & Cai, J.G. 2001. Transmission of elastic P-waves across single fractures with a nonlinear normal deformational behavior. *Rock Mechanics and Rock Engineering* 34: 3–22.

Zhao, J., Zhao X.B. & Cai, J.G. 2006. A further study of P-wave attenuation across parallel fractures with linear deformational behaviour. *International Journal of Rock Mechanics and Mining Sciences* 43: 776–788.

Zhao, K., Bonini, M., Debernardi, D., Janutolo, M., Barla, G. & Chen, G. 2015. Computational modelling of the mechanised excavation of deep tunnels in weak rock. *Computers and Geotechnics* 66: 158–171.

*Rock Dynamics: From Research to Engineering – Li et al. (Eds)*
*© 2016 Taylor & Francis Group, London, ISBN 978-1-138-02953-8*

# Crack initiation and propagation simulation for polycrystalline-based brittle rock utilizing three dimensional distinct element method

X.F. Li, H.B. Li, J.C. Li & X. Xia
*State Key Laboratory of Geomechanics and Geotechnical Engineering, Institute of Rock and Soil Mechanics, Chinese Academy of Sciences, Wuhan, China*

ABSTRACT: A three dimensional (3D) Voronoi tessellations based on Distinct Element Method (DEM) is proposed for simulation of crack initiation and propagation in polycrystalline-based brittle rocks. Damage evolution equations for brittle rocks have been extensively studied in the past. However, the damage model with respect to Mesoscopic Method has not been widely developed due to difficulty of direct observation for microcracks in laboratory tests. The Voronoi tessellation approach which can measure the invisible cracks was firstly utilized to simulate the Uniaxial Tension Test (UTT) in this study. A series of simulated Uniaxial Tension Tests were conducted to investigate the relationships between micro-parameters and macro-response and validation study with laboratory test was also carried out. Moreover, a novel damage model relying on crack initiation and propagation was defined and comparisons of evolution equation between existed models were also conducted to validate the accuracy and robust of the model. A good agreement was found between the simulated results and laboratory observations (e.g. failure modes, peak strength and cracks location). Different methods are proposed to detect the damage thresholds such as crack initiation value (CI) and crack interaction value (CD). Comparisons are also discussed to accurately measure the thresholds values.

## 1 INTRODUCTION

Comparing with theoretical analysis and experimental tests, numerical simulation is more efficient for investigating macro behaviors and crack damage progression for brittle rocks. Generally, reasonable softening constitutive relation for materials is a curial issue in rock engineering and geotechnical applications. Conventional numerical approaches such as FEM, BEM and meshfree method are limited to continuum hypothesis which eliminates the material softening during the analysis of failure process. However, for brittle material, the failure is a sudden incident without enough time to control. Before the ultimate failure, material prosperities such as stiffness, failure strength are deteriorated to some extent based on the micro level. Therefore, softening of rock is important in the estimation of structure safety due to the fact that well designed structures show considerable crack growth before attaining failure strength (Vonk 1993).

Softening of material is induced by cracks initiation and damage evolution during the process of external loading. Cracks simulation is the key point to reveal the deterioration of material. In DEM, the rock-like material can be simulated as random distributed assemblies with pre-existing discontinuities (Gao 2013). The discrete elements which called as "contacts" can detach and overlap (Itasca 2013a). Potyondy & Cundall (2014), Cho et al. (2007) and Yoon et al. (2008) have used Particle Flow Code (PFC) to perform the compression mechanical behaviors of rock. The results show that spherical balls will contribute to lower peak strength envelope compared with the strength envelope obtained in laboratory (Potyondy & Cundall 2004). Potyondy (2012) describes the most recent solution to this problem using a new flat joint logic whereby joints form the contacts between PFC particles and the models bear some resemblance to Voronoi logic. The similar problem was solved by Kazerani & Zhao (2010) utilizing UDEC with Voronoi tessellations. Christianson et al. (2006) applied the UDEC Voronoi method to investigate the

triaxial testing for lithophysal tuff and found that the numerical results agreed well with data from laboratory tests. Subsequently, Gao (2013) extended this problem to 3-dimensional model with Trigon logic. In practical, most rock-like materials are grain-based with crystallites. Random polygonal blocks which called Voronoi are generated to perform the poly-crystal structure of grain-based rock such as granite in 3DEC. The blocks within Voronoi can be rigid or deformable and the contacts between Voronoi represent the grain boundaries allowing for crack damage development (Ghazvinian 2014). This logic was introduced by Ghazvinian (2014) to investigate uniaxial compression behaviors. To date, there is no publication for direct tension test simulation using this approach.

This paper aims to simulate behaviors of tension test for grain-based rock with Voronoi approach. The effect of Voronoi tessellations size and micro-parameters are studied for calibrating the macro-response of laboratory tests. Additionally, cracks damage development is performed and failure modes are presented to validate laboratory observations. Different methods to measure the damage thresholds are discussed.

## 2 DEM SIMULATION

### 2.1 *Voronoi tessellations*

It is well understood that grain-based in polycrystalline materials can be simulated by Voronoi tessellations (Espinosa & Zavattieri 2002). Mathematically, Voronoi tessellation of a 3-D space is a collection of 3-D entities that fills the space with no overlaps and gaps. The entities are polyhedral and are defined as zones of influence of a particular set of points as shown in Figure 1.

In such a case, the tessellations are referred as "Poisson-Voronoi tessellations" and the polyhedral is convex. The intersection of two polyhedrons is a plane which called "tessellation face" and that of three polyhedrons is a straight line called "tessellation edge". The tessellation vertex is the intersection point of four polyhedrons. In DEM, the tessellation face is taken as contacts allowing the cracks occur along the boundaries. To some extent, if the tessellations are small enough comparing with the sample size, the accuracy of this method can be guaranteed. The Voronoi polyhedron is taken as deformable and each face is divided to small zones by free meshing referring to Figure 1c.

### 2.2 *Polycrystalline microstructures distribution*

Proper microstructures distribution is related to the accuracy of simulation results. A set of cylindrical specimens were curved from three cubes filled with 20,000, 40,000 and 60,000 Voronoi grains by Ghazvinian (2014). The results show that the peak strength is independent of the grain size but the damage is related to the pre-existed microstructures. On the other aspect, regularized tessellations influence the free meshing. If the quantity of "small edges" reaches a certain level, the calculation efficiency and meshing velocity will be largely slowed. In order to solve this problem, a reasonable distribution for Voronoi tessellations is discussed in this section.

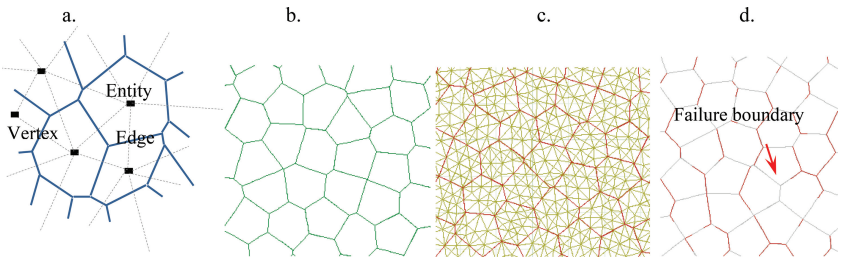


Figure 1. Schematic of the Voronoi tessellations. a. physical model of Voronoi, b. Voronoi tessellation generated by 3DEC, c. finite element meshing, d. contacts failure along the boundaries.

Two parameters, namely edge length and face diameter decided the regularization of the specimen. As a rule of thumb, the tessellation faces always obey uniform or normal distribution. The former one is used to investigate regular artificial material and the latter is for natural material. Figure 2 shows the grains generated by MATLAB randomly (a) and shaped by regularization technique (b). Blocks with small edges are unavoidable due to random tessellations as shown in Figure 2a. The regularization technique removes the small edge and re-cut the blocks to obtain a reasonable edge length or diameter distribution. The regularization technique decreases the frequency of polyhedrons with large ratio of edges and contributes a more smooth distribution for specimens.

### 2.3 *AE activity simulation and damage evolution*

Block and contact consist of fundamental elements for discrete element. The block herein is taken as linear elastic without ultimate strength and the contact is controlled by the contact constitutive law. Figure 3 schematically illustrates the contact normal and shear behaviors. Acoustic Emissions (AE) are generated spontaneously during rock failure process due to microcracking initiation. In 3DEC, the rupture of every contact is assumed to be the source of an acoustic event since the failed contact results in a release of elastic energy stored in the elements. AE activities always accompany with energy transmission and cracks initiation. In order to track the cracks propagation, the AE activities are recorded by the following equation

$$N = \sum_{i=1}^{m} n_i \tag{1}$$

where $m$ is the number of calculation steps and $n_i$ is the failed contacts in the $i$th step. It is believed that there is a link between damage evolution and acoustic emissions. Ma et al. (2011) assumed the damage variable $D$ is calculated as

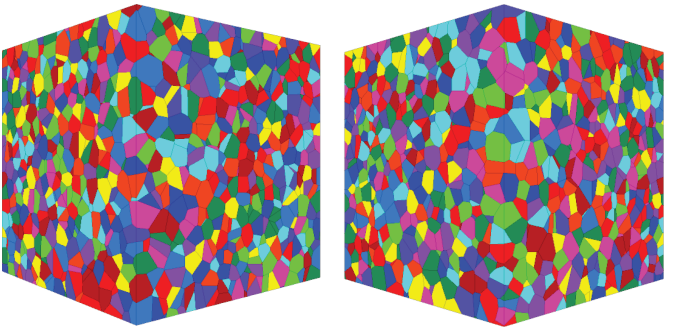

Figure 2. A 10000-grain Voronoi tessellations of cube. a. randomly generated, b. regularized model.

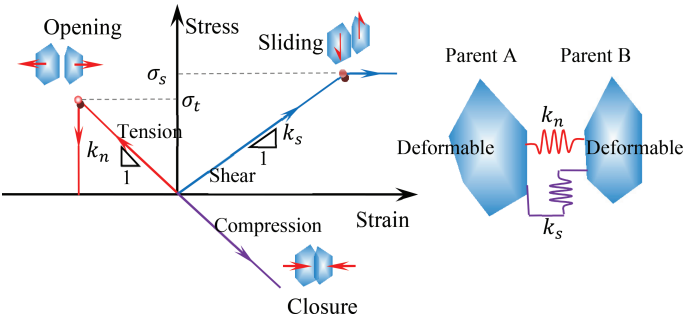


Figure 3. Constitutive law for micro-contacts.

$$D = \frac{\sum_{i=1}^{m} n_i}{\sum_{i=1}^{M} n_i} \tag{2}$$

$M$ is the total step and $\sum_{i=1}^{M} n_i$ is the total acoustic emissions. The reasonability of this assumption has been validated by Tang et al. (1997).

### 2.4 *Model generation and calibration*

Simulation model is generated at the same size of laboratory sample with diameter 5 cm and height 12.5 cm. For direct tension test, the top and bottom ends are applied a constant velocity. In order to eliminate the inertia effect at the beginning of static loading, the target velocity loading is divided to ten stages to keep the specimen in a dynamic equilibrium. For discrete element method based on the explicit difference method, the judgement for the accuracy of calculation is dependent on the state of each block. In other words, the unbalance force is the response for judging if the block is under a static loading state. Therefore, a servo-controlled system is proposed here to keep the maximum unbalance force within a specified range. The specific approach is to adjust the loading velocity to get a stable unbalance force as Eq. 3, where $\dot{u}_i^{(t+\Delta t/2)}$ is the velocity of gridpoint $i$ at time $t+\Delta t$, $\sum F_i^{(t)}$ is the sum force of all blocks and $\alpha$ is the local damping efficient. $\Delta t$ is the time-step for the model and $m_n$ is the mass of the gridpoints.

$$\dot{u}_i^{(t+\Delta t/2)} - \dot{u}_i^{(t-\Delta t/2)} = \left\{ \sum F_i^{(t)} - \alpha \left| \sum F_i^{(t)} \right| \mathrm{sgn}(\dot{u}_i^{(t-\Delta t/2)}) \right\} \frac{\Delta t}{m_n} \tag{3}$$

Additionally, measurement system is another part we should take care of. Strain and stress are directly measured by setting appropriate history points and measurement ball. Six points with a space of 10 mm are fixed on the two sides of central plane to calculate the lateral strain of the specimen. The two ends are fixed as tension zones which are applied with a certain velocity along the z direction. The axial strain is measured by averaging strain of two ends with five grid points. The stress is measured by the average stress whose centroid falls within the measurement ball.

The macro-behaviors of Voronoi tessellations are influenced by the micro-properties of deformable blocks and contacts. Some scholars utilized rigid bodies to simulate the compression failure for rock mass. To some extent, the grains in Voronoi tessellations are lager enough to be taken as deformable comparing with the polycrystalline which are modelled as rigid bodies on the micro level. Moreover, a calibration process is needed to obtain the reasonable parameters. The process can be summarized in the following steps.

a. Grain size is dependent on the calculation velocity of the software and cracks failure modes for the model. As mentioned in the previous section, the elastic modulus and peak failure strength are not sensitive to grain size. The proper range of the grain size is only a geometrical problem, not a mechanical problem. In this study, the grain size is adjusted by the quantity of the grains.
b. Modulus is a key parameter for material which is controlled by normal stiffness $k_n$ and shear stiffness $k_s$ of contacts. It is clear that $k_n$ and $k_s$ equal to $K/t$ and $G/t$, where $K$, $G$ and $t$ are bulk modulus, shear modulus and thickness of the contact, respectively. The Young's modulus can be denoted as $9GK/(3K+G)$. Poisson's ratio is proportional to $k_n/k_s$ ratio. Actually, in 3DEC, when the ratio is 5~8, the Poisson's ratio can reach 0.2~0.25.c.
c. Failure condition is determined by cohesion and tension strengths of the contacts. According to the contact constitutive law, tension crack occurs when the strength of the contact exceeds the ultimate tension strength, similarly, the shear failure obey the same principle.

The sensitivity analysis for micro-parameters of contacts has been depicted in details by (Ghazvinian 2014). The concluded relationships are all empirical laws which are fitted by trails and errors. The detail process for calibration is not addressed here.

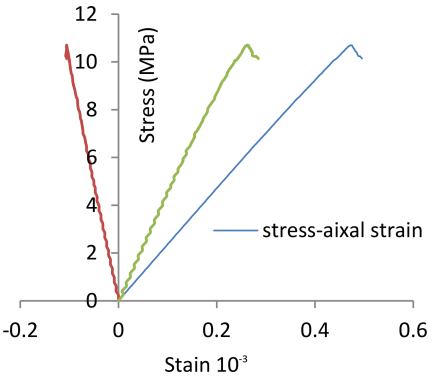


Figure 4. Stress-strain curves for UTS model.

Table 1. Micro-properties for blocks and contacts.

| Properties | Values |
|---|---|
| Block density (kg/m$^3$) | 2900 |
| Young's modulus $E_c$ (GPa) | 450 |
| Poisson's ratio υ | 0.22 |
| Bulk modulus $k_n$ (GPa/m) | 40000 |
| Stiffness ratio $k_n/k_s$ | 8 |
| Normal strength σ (MPa | 45 |
| Shear strength τ (MPa | 45 |
| Friction angle θ | 25 |
| Grain size (mm) | 0.18 |

Table 2. Model calibration for real rock (macro-properties).

| | Experimental | Numerical (mean ± std. dev.) | MD (%) | CV (%) |
|---|---|---|---|---|
| UTS $\sigma_t$ (MPa) | 11.46 | 10.99 ± 1.08 | 4.1 | 9.4 |
| Elastic | 23.5 | 22.7 ± 2.3 | 3.4 | 9.8 |
| Poisson's ratio $v$ | 0.22 | 0.212 ± 0.023 | 3.6 | 10 |

MD = (Mean Num.-Exp.)/Exp.*100%; CV = Std.dev Num/Exp.*100%.

Figure 4 shows the stress-strain curves for UTS model when the micro-properties are calibrated as in Table 1. It is clear that no dilation phenomenon occurs for tension test of rock. The Young's modulus and Poisson's ratio are calculated and validation for experimental tests is conducted in Table 2. Meanwhile, MD is the mean deviation error and CV is the standard deviation error. It can be concluded that the numerical results calibrate well with experiments with error being less than 5%.

## 3 RESULTS AND DISCUSSION

### 3.1 *Damage evolution for micro-cracks*

Damage evolution is progressive corresponding to loading process. For brittle material, material deterioration is an obvious phenomenon resulting from crack propagation. In order to depict the evolution equation for various failure modes, damage variable is introduced herein. Figure 5 shows the stress and damage curves with respect to strain. Six stages are

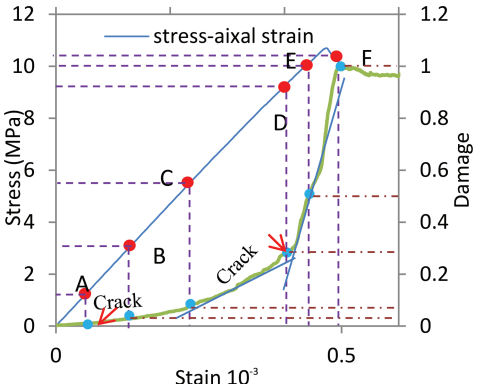


Figure 5. Relationship between loading process and damage evolution for UTS model.

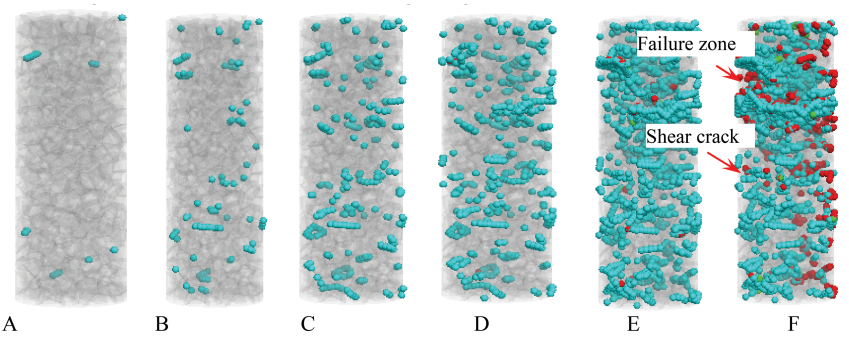


Figure 6. Distributed micro cracks at different stages corresponding to Figure 6 during axial tension test.

captured to analyse the distribution of micro cracks in Figure 6. It can be seen that at beginning of loading, the material keeps in an undamaged state. When the stain/stress reaches a certain value which we called stage A, cracks are initiated within the specimen, and this point is always taken as the crack initiation threshold. After stage A, the increment for cracks is a constant which results in a linear increasing trend for damage evolution equation between stage A and stage D. From Figure 6, it shows that micro cracks generated in specimen are randomly distributed. But after stage D, an exponential relationship is obtained by the simulated results. The following increasing of cracks is dramatic before the stress reaches the peak strength. However, when the stress exceeds the peak, macro fracture occurs and the material failed. The later cracks are not geometric randomly distributed any more; the space distribution obeys the stress concentration degree of the specimen and results in a assembling around the macro fracture referring to Figures 6E and F.

Additionally, tensile cracks dominate the failure mode. During the later period of loading, especially after the peak strength, shear cracks are generated but the quantity is small, only 13% of total cracks. Generally, cracks initiate during elastic part and rapidly develop before the failure strength. Several turning points which we define as damage thresholds are existed. In order to perform the softening behaviors of materials, damage model is attempted to be built in following section.

### 3.2 *Damage thresholds detection*

The tension failure process can be divided to four states for rock-like material as shown in Figure 7. At the beginning of loading, the stress of contact does not exceed the failure strength and no cracks are generated at this stage. When the loading is continued, micro cracks are ini-

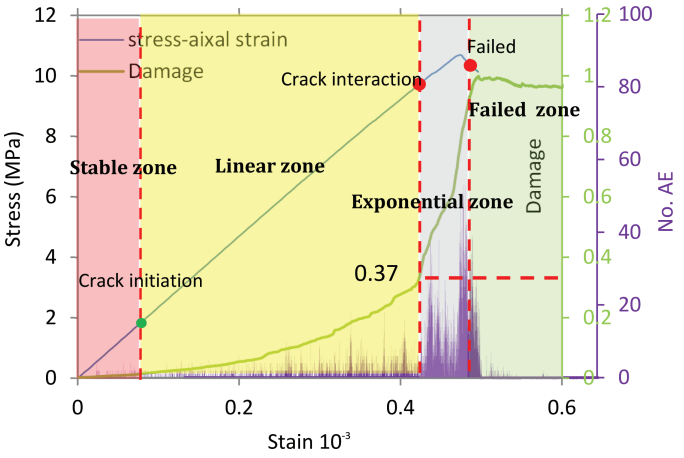


Figure 7. Variation of stress, damage and Acoustic emissions vs. strain of tension test simulation.

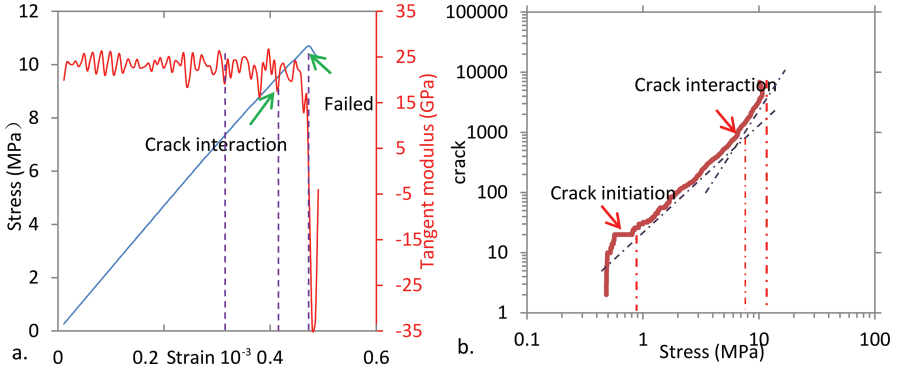


Figure 8. Different methods for obtaining damage thresholds. a. tangent modulus; b. cracks increasing.

tiated and the trend is a linear relationship. The turning point is taken as Crack Initiation (CI) which represents the crack begins to occur. The frequency of AE is an approximately constant which results in a stable damaging process. If the stress exceeds another critical value which we called cracks interaction (CD), the increasing trend turns to be exponential and the AE is dramatic. After the exponential zone, macro fracture occurs and the material failed. It can be seen that the corresponding stress of CI is about 1.8 MPa and the CD is 9.7 MPa in this case. The positions on the stress-strain curve are 17% and 90% of the peak value, respectively.

In order to accurately measure the thresholds, several methods are proposed in this study. Figure 7 illustrates the AE to present the increment of micro failure. This method has an advantage of detecting CI value. But for CD value, there is no clear line to judge where the crack interaction point is. Figure 8a is a macro parameter for damage definition using effective modulus of material according to Lemaitre & Dufailly (1977). It is believed that macro stiffness deterioration is induced by accumulative micro damage. Macro response is more sensitive to CD value and this method can be well used to detect the cracks interaction threshold. Figure 8b uses cracks to investigate the slope change trend of damage. Two linear parts are taken to divide the CI and CD. To sum up, the CD measured by AE is 0.37 and by effective modulus is 0.42, and the value by cracks increasing is 0.21. By comparison, method by macro parameter is the maximum and the cracks increasing method is most fuzzy. Appropriate method is chosen according to the material class and subjected stress conditions. Example, for creep and fatigue problems, effective modulus will present damage process more clearly, but for dynamic loading, AE method or crack increasing is more applicable.

## 4 CONCLUSIONS

In order to reveal the crack propagation and damage evolution for grain-based rock under direct tension test, a 3D Voronoi tessellations model of DEM is developed and verified. In this study, the theories for the tessellations model are presented and micro-parameters are calibrated with experimental tests. The conclusions are summarized as follows:

- The Voronoi tessellations model has the ability of simulating damage evolution for rock mass. And the contact failure mechanism can well explain the crack propagation process.
- Tension cracks are the dominating failure mode for tension test with a percentage of 87% of all cracks. Two obvious parts, namely linear zone and exponential zone, are existed during the loading process. When the tension cracks exceed a certain value, the damage evolution propagates dramatically. Tangent modulus method, cracks increasing method and Acoustic emission method are introduced to detect the damage thresholds, respectively. The CI and CD are calculated as 17% and 90% of the peak strength for brittle rock under tension test by AE emission method.
- The detected thresholds by three methods are discussed and the macro parameter by tangent modulus is larger than micro parameter such as AE emission or cracks. For dynamic loading or fracture problem, the micro parameter method is more accurate and for creep or fatigue, macro parameter method has more advantages.

## REFERENCES


Cho, N., Martin, C.D., Sego, D.C. 2007. A clumped particle model for rock. *International Journal of Rock Mechanics and Mining Sciences* 44(7): 997–1010.

Christianson, M., Board, M., Rigby, D. 2006. UDEC simulation of triaxial testing of lithophysal tuff. In *Proceedings of the 41st US Symposium on Rock Mechanics*, Golden, CO, p. 8.

Espinosa, H.D. & Zavattieri, P.D. 2003. A grain level model for the study of failure initiation and evolution in polycrystalline brittle materials. Part I: Theory and numerical implementation. *Mechanics of Materials* 35(3): 333–364.

Gao, F. 2013. *Simulation of Failure Mechanisms around Underground Coal Mine Openings Using Discrete Element Modelling*. PhD Thesis, Department of Earth Sciences. Simon Fraser University.

Ghazvinian, E., Diederichs, M.S., Quey, R. 2014. 3D random Voronoi grain-based models for simulation of brittle rock damage and fabric-guided micro-fracturing. *Journal of Rock Mechanics and Geotechnical Engineering* 6(6): 506–521.

Itasca 2013. *3DEC (3 Dimensional Distinct Element Code) Version 5.0*. Minneapolis, MN, USA: Itasca Consulting Group Inc.

Kazerani, T. & Zhao, J. 2010. Micromechanical parameters in bonded particle method for modelling of brittle material failure[J]. *International Journal for Numerical and Analytical Methods in Geomechanics* 34(18): 1877–1895.

Lemaitre, J. & Dufailly, J. 1977. Modelization and identification of endommagement plasticity of material. *Proceedings of the 3 rd French Congress of Mechanics*, Grenoble, France. 17–21.

Ma, H., Yin, L., Ji, H. 2011. Numerical study of the effect of confining stress on rock fragmentation by TBM cutters. *International Journal of Rock Mechanics and Mining Sciences* 48(6): 1021–1033.

Potyondy, D.O. & Cundall, P.A. 2004. A bonded-particle model for rock. *International Journal of Rock Mechanics and Mining Sciences* 41(8): 1329–1364.

Potyondy, D.O. 2012. A flat-jointed bonded-particle material for hard rock[C]//Proceedings of 46th US rock mechanics geomechanics symposium (ARMA), Chicago. 2012: 12–501.

Tang, C. 1997. Numerical simulation of progressive rock failure and associated seismicity. *International Journal of Rock Mechanics and Mining Sciences* 34(2): 249–261.

Vonk R.A.A. 1993. *Micromechanical Investigation of Softening of Concrete Loaded in Compression*. Stevin-Laboratory of the Faculty of Civil Engineering, University of Technology.

Yoon, J., Jeon, S., Stephansson, O., Zang, A. Dresen, G. 2008. A new method of microparameter determination for PFC2D synthetic rock model generation. *Proc. of the 1st International FLAC/DEM Symposium on Numerical Modeling*, Minneapolis, USA, Aug., 443–450.

*Rock Dynamics: From Research to Engineering – Li et al. (Eds)*
*© 2016 Taylor & Francis Group, London, ISBN 978-1-138-02953-8*

# Study of the failure process in large-sized coal-rock mass under static and dynamic loading by three-dimensional numerical simulation

X.L. Li
*Mine Safety Technology Branch of China Coal Research Institute, Beijing, China*
*State Key Laboratory of Coal Mining and Clean Utilization (China Coal Research Institute), Beijing, China*

C.L. Li
*China Institute of Water Resource and Hydropower Research, Beijing, China*

ABSTRACT: A large-size experiment of unloading coal-rock mass is used to study the failure process resulted from deformation when subjected to static load, impact dynamic load and superposition of static-dynamic load by means of numerical simulation. Firstly, the mechanical model of dynamical excavation in circular tunnel with nonuniform geostress is explored, the distribution law of initial stress and the processing method for unloading are studied, and burst failure mechanisms in coal and rock is investigated. The three-dimensional numerical simulation of unloading coal-rock mass is built, then the burst failure in unloading coal-rock mass under static and dynamic loading is investigated and analyzed. The numerical simulation results showed that the important effect of impact dynamic load on the unloading coal-rock mass is shock wave repeating actions, which cause both tunnel sides shear failure to rib spalling and top strata tensile failure at large range to roof splitting. The influence of loading rate on the impact characteristics of the tunnel is notable, which is mainly embodies in the peak of failure load, the destruction regions, and the destruction types. In unloading coal-rock mass, the influence degree about superposition of static and dynamic load is larger than that of single one.

## 1 INTRODUCTION

In the procession of colliery exploitation, coal and rock in unloading condition due to excavation and dynamic loading disturbance due to blasting vibration and roof caving etc. the early stage specimen stress equilibrium is broken. Until ultimate strength of mechanical system is reached, coal and rock will show impact breakage characteristics to release elasticity violently, and lead to rock or coal dynamical disasters such as rock burst and so on. Their results can be disastrous and can result in tremendous numbers of casualties and socioeconomic loss.

Better understanding of the dynamic fracture processes of unloading coal and rock promises benefit in many areas from rock mechanics to mining engineering and rock burst prediction. It is essential to understand how fractures initiate and propagate under different loading conditions. During the past several decades, researchers have carried out many dynamic tests of rock using the apparatus such as the Split Hopkinson ar (SHPB), experimental system, and different numerical simulation software.

The effect of dynamic disturbance on tunnel surrounding rock were analyzed in the above researches by means of different test or software and with loading path, loading rate, in-situ stress, tunnel depth and so on. These push unloading coal-rock mass researches forward. However the research object almost were Φ50 mm coal or rock cylindrical samples or 50–100 m coal-rock model, 1000 mm unloading coal-rock mass was not. The large-size model that experiment scale lays between small specimen and large model can fill in the scale blank and find trans-scale correlation.

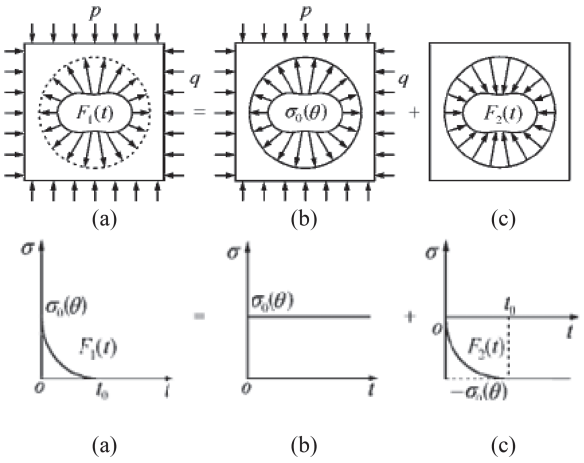


Figure 1. Mechanical model of circular tunnel.

## 2 THE UNLOADING COAL-ROCK MASS MECHANISMING STARTED

Commonly, circular tunnel that excavated at certain depth in infinite underground is considered a plane strain condition. When the vertical crustal stress(p) and the horizontal crustal stress(q) are unequal, the process of excavation unloading can be considered as an action of a series of exterior load applied at excavation boundary, and these load values are gradually decreasing from initial stress to zero.

First, the initial stress in coal and rock are determined. Then a unit body is taken from excavation boundary, the stress are calculated by Equation (1).

$$\left.\begin{aligned}\sigma_0 &= \frac{p+q}{2} + \frac{q-p}{2}\cos(2\theta)\\ \tau_0 &= \frac{p-q}{2}\sin(2\theta)\end{aligned}\right\} \tag{1}$$

where $\sigma_0$, $\tau_0$ are initial radial stress and tangential stress on the excavation boundary.

Hence the initial stress distribution on excavation boundary before unloading is approximately shown as Figure 1. The radial stress is always positive stress (A normal stress is positive if it is compressive.) and its value is different. While the tangential stress is both positive and negative (if it in clockwise, it is positive stress.) and its value is different at different position.

Essentially, the process of excavation unloading is a gradually decreasing process of initial stress at excavation boundary. The drilling-blasting method is different from TBM method for excavation mainly in unloading path and time. Generally, Figure 1 (a) can be decomposed into Figure 1 (b) and Figure 1 (c). They are calculated respectively, then are superposed two calculation results. The tangential tress of unloading is calculated in the same way.

## 3 THREE-DIMENSIONAL NUMERICAL SIMULATION OF UNLOADING COAL-ROCK MASS

### 3.1 *Numerical unloading coal-rock mass*

According to the unloading coal-rock mass mechanism above paragraphs, three dimensional numerical model of unloading coal-rock mass will be build. In order to reflect the characteristics of unloading coal-rock mass and ensure the reasonability of static-dynamic loading applied, a large-sized unloading coal-rock mass model of $450 \times 450 \times 260$ mm is built.

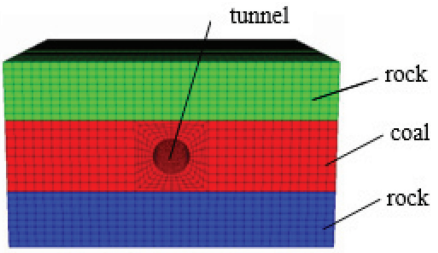


Figure 2. Three-dimensional numerical simulation of unloading coal-rock mass.

Table 1. The parameters of model.

| | Density | Bulk modulus | Shear modulus | Cohesion | Friction | Tensile |
|---|---|---|---|---|---|---|
| Strata | kg/m$^3$ | GPa | MPa | MPa | ° | MPa |
| Roof | 2707 | 12.8 | 10 | 13.8 | 29.5 | 4.6 |
| Coal | 2170 | 0.85 | 0.75 | 4.5 | 20 | 0.4 |
| Floor | 2707 | 62 | 11.7 | 20.25 | 43.5 | 3.9 |

The layered structure of coal-rock mass is a major factor resulted in the occurrence of rock burst. Because of the large difference of material properties between coal and rock, the discontinuous of stress and deformation can be resulted in the role of high stress, which will induce impact failure of the coal or rock. so the large scale model of unloading coal-rock mass is designed as the "rock-coal-rock" rectangular model, which the thickness of rock 80 mm and coal 100 mm, and a Φ50 mm circular at center as shown in Figure 2.

The coal-rock mass from a certain rock burst mine are taken as prototype, the physical and mechanical parameters are obtained by the physical mechanics experiment, as listed in Table 1. The sides of the model are horizontal restraint, with bottom fixed constraint and upper surface free.

According to the burst failure mechanism above in coal and rock, mohr-coulomb is taken as the constitutive model, and tensile stress and shear stress as the failure criterion.

### 3.2 *Load design*

The loading rate is the main factors that influence the impacting characteristics within unloading coal-rock mass. Static load, dynamic load and dynamic-static load are applied separately, the impact characteristics of surrounding coal or rock are analyzed by means of stress distribution and deformation.

1. Static load. Based on compressive strength of coal-rock mass, the value of critical load is obtained by trial calculation repeatedly. It is applied on the top of the unloading coal-rock model as static load until the model failure.
2. Impact dynamic load. Taking the typical triangular impact load for example, the duration is 0.07 MS and the load reaches the peak value of 30 MPa at 0.35 ms. It is applied impact dynamic load in one cycle on the tunnel, and the time-stress curve is shown in Figure 3.
3. Superposition of static-dynamic load. The certain static load is applied around the model first, then impact dynamic load is applied on the tunnel as soon as it stability, until the model is failure.

## 4 RESULTS AND ANALYSIS

### 4.1 *Stress of unloading coal-rock mass under dynamic load Text and indenting*

Under dynamic load, the variation of the stress at the top, bottom and side of the tunnel in surrounding unloading coal-rock mass is given in Figure 4.

Figure 3. Time-history curve of impact dynamic load.

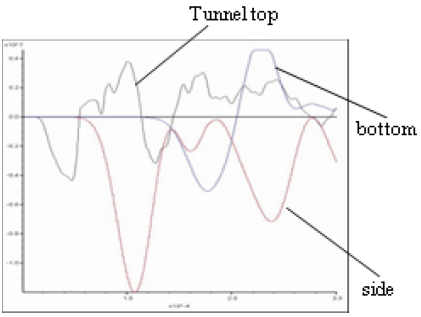


Figure 4. The stress-strain curve of unloading coal-rock mass.

In Figure 4, although the impact dynamic loading time is only one cycle, shock waves of which energy reduces gradually are formed in coal-rock mass. The coal and rock at tunnel top, bottom and two sides surrounding unloading area are failure finally under the repeating actions of shock wave.

At first, impact dynamic load reach at tunnel top, the coal and rock have influence on the compressive and tensile stress act alternatively, until tensile failure. When the impact dynamic load goes from the tunnel top to the roadside coal, the coal in unloading state at the sides of tunnel is compressed and sheared to fail under intense impact from dynamic load. Finally, when the dynamic load pass down the tunnel bottom, the load energy and the circulation function abates, while partly stress transfer from top and sides to bottom, so the compressive stress and tensile stress at the bottom are slightly higher than the top. But they did not exceed their strength limit to unbroken.

### 4.2 *Stress and deformation failure under different load*

The maximum stress and plastic zone distribution in unloading coal-rock mass under static and impact dynamic load are shown in Figure 5 and Figure 6 respectively.

The influence of loading rate on the impact characteristics of the tunnel is notable. The following conclusions we can gain:

1. The peak of failure load is different. Failure occurs within unloading coal-rock mass when the static load is 20 MPa when the impact dynamic load is 9.26 MPa that is far less than the static load.
2. The destruction regions are different. In the "rock-coal-rock" unloading coal-rock mass structure, the unloading coal areas are the weakest in load bearing, which are the destroyed areas under static and dynamic load. However, because of the different load rates, the destruction regions mainly in coal seam under static load and partly in unloading coal (that is much less than the static load) and the top strata under impact dynamic load.
3. The destruction types are different. The coal seam in unloading coal-rock mass is shear failure to rib spalling caused by static load. Under impact dynamic load, although it is also rib spalling in small range, but mainly is tensile failure in top strata at large range to roof splitting.

The main reason is that the static loading rate is slow, leaving the stress enough time to fully transfer and redistribute, which make the highly stress on the top transfer to the coal seam. So the stress distribution in unloading coal-rock mass can become more homogeneous. However, the loading time of impact dynamic load is short leading to the stress increased rapidly in some regions. As soon as the ultimate bearing capacity of unloading coal-rock mass is exceeded, impact damage will occur (as shown in Fig. 5).

### 4.3 *Stress and deformation failure under superposition of static and dynamic load*

More generally, the tunnel in coal mine is under superposition of static (in-situ rock stress) and dynamic load (blasting, roof broken, etc), which the stress and plastic section distribution as indicated on Figure 7 and Figure 8.

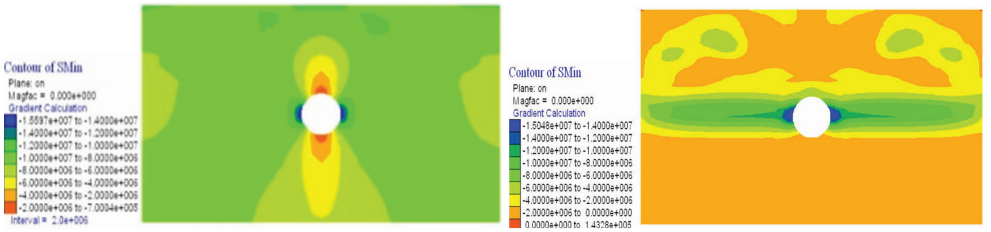


(a) Static load (b) Impact dynamic load

Figure 5. The maximum stress of unloading coal-rock mass.

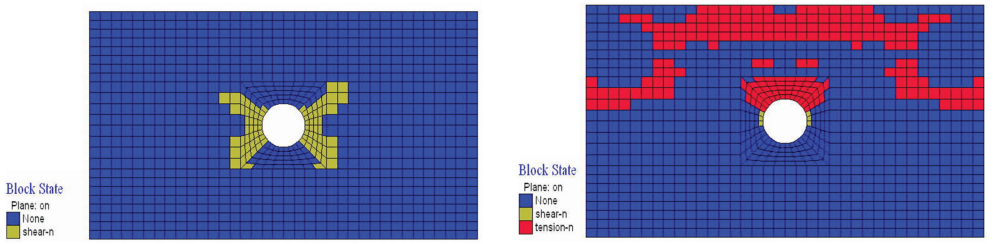


(a) Static load (b) Impact dynamic load

Figure 6. The plastic-section of unloading coal-rock mass.

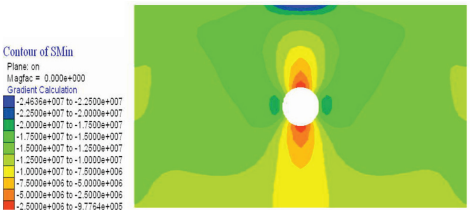


Figure 7. The maximum stress.

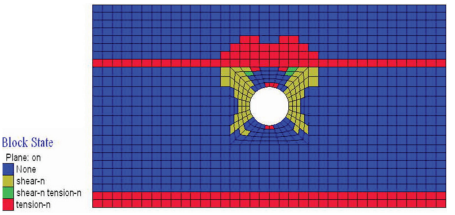


Figure 8. The plastic-section.

The influence degree of the superposition of static and dynamic load is larger than that single static load or dynamic load in unloading coal-rock mass.

Firstly, the strength of unloading coal-rock mass can be raised by static load, the damage regions of unloading rock-coal mass keeps invariant at the early stage until the energy accumulation reaches its limit, by impact dynamic load is increased slightly, large range of instantaneous damage in the unloading coal-rock mass will be induced. Its failure region and failure extent are increase obviously, broken area mainly lies in upper corners and sides of tunnel, and the forming transfixion damage extending from the upper corner damage to the top.

## 5 RESULTS AND ANALYSIS

A large-size experiment was used to investigate the burst failure in unloading coal-rock mass subjected to static load, impact dynamic load and superposition of static-dynamic load, by numerical simulation the following conclusions are drawn from our numerical simulations:

1. The important effect of impact dynamic load on the unloading coal-rock mass is shock wave repeating actions.
2. Because the sufficient degree in the stress redistribution caused by loading rate is different, the influence on impacting characteristics of unloading coal-rock mass is obviously.

The damaged peak under impact dynamic load is far less than the static load. The destroyed areas are all around unloading coal seam, however the destruction regions mainly are surrounding unloading coal seam under static load while are both top strata and partly unloading coal, which much less than the static load under impact dynamic load. The burst failure is shear failure in coal caused by static load, while is mainly tensile failure in top strata caused by impact dynamic load.

3. In unloading coal-rock mass, the influence degree about superposition of static and dynamic load is larger than that single one. So a little impact dynamic load will induce rock burst when the unloading coal-rock mass reaches its critical state under static load.

## ACKNOWLEDGMENTS

This work was supported and financed by the National Natural Science Foundation of China (No.51404140, 51304117), which is gratefully acknowledged.

## REFERENCES

Cai, M., Tasaka, P.K. & Maejima, Y. et al. 2004. Generalized crack initiation and crack damage stress thresholds of brittle rock masses near underground excavations. *International Journal of Rock Mechanics and Mining Sciences*: 833–847.

Chong, K.P. & Boresi, A.P. 1990. Strain rate dependent mechanical properties of New Albany reference shale. *Int J Rock Mech Min Sci Geomech Abstr*: 199–205.

Frew, D.J., Forrestal, M.J. & Chen, W. 2001. A split Hopkinson pressure bar technique to determine compressive stress-strain data for rock materials. *Exp Mech*: 4–6.

Gao, F.Q., Gao, X.F. & Kang, H.P. 2009. FLAC analysis of mechanical response of surrounding rock mass in deep tunnel. *Chinese Journal of Underground Space and Engineering*: 680–685.

Grady, D.E. & Kipp, M.E. 1979. The micromechanics of impact fracture of rock. *Int J Rock Mech Min Sci Geomech Abstr*: 293–302.

He, M.C., Miao, J.L. & Li, D.J. et al. 2007. Experimental study on rockburst processes of granite specimen at great depth. *Chinese Journal of Rock Mechanics and Engineering*: 865–876.

He, M.C., Wang, X.Y. & Liu, W.T. et al. 2008. Numerical simulation on asymmetric deformation of deep soft rock roadway in Kongzhuang Coal Mine. *Chinese Journal of Rock Mechanics and Engineering*: 673–678.

Huang, B.X. & Liu, J.W. 2013. The effect of loading rate on the behavior of samples composed of coal and rock. *International Journal of Rock Mechanics & Mining Sciences*: 23–30.

Li, X.B., Li, D.Y. & Guo, L. et al. 2007. Study on mechanical response of highly-stressed pillars in deep mining under dynamic disturbance. *Chinese Journal of Rock Mechanics and Engineering*: 922–928.

Li, Z.L., Dou, L.M, & Cai, W. et al. 2014. Investigation and analysis of the rock burst mechanism induced within fault–pillars. *International Journal of Rock Mechanics & Mining Science*: 192–200.

Lu, A.H., Yu, S.L. & Qin, H. et al. 2008. Stability of layered crack structure in roadway surrounding rock under stress wave. *Journal of China University of Mining & Technology*: 768–774.

Qian, Q.H. & Qi, C.Z. 2008. Dynamic strength and dynamic fracture criteria of rock and rock mass. *Journal of Tongji University (Natural Science)*: 1599–1605.

Shan, R.L., Xue, Y.S. & Zhang, Q. 2003. Time dependent damage model of rock under dynamic loading. *Chinese Journal of Rock Mechanics and Engineering*: 1771–1776.

Taylor, L.M., Chen, E.P. & Kuszmaul, J.S. 1986. Microcrack induced damage accumulation in brittle rock under dynamic loading. *Comput Method Appl Mech Eng*: 301–310.

Zhang, Z.X., Kou, S.Q. & Yu J et al. 1999. Effects of loading rate on rock fracture. *Int J Rock Mech Min Sci Geomech Abstr*: 597–611.

Zhao, J. 2000. Application of Mohr-Coulomb and Hoek-Brown strength criteria to the dynamic strength of brittle rock. *Int J Rock Mech Min Sci Geomech Abstr*: 105–112.

Zhu, W.C., Zuo, Y.J. & Shang, S.M. et al. 2007. Numerical simulation of instable failure of deep rock tunnel triggered by dynamic disturbance. *Chinese Journal of Rock Mechanics and Engineering*: 915–921.

Zuo, Y.J., Tang, C.N., Zhu, W.C. & Tan, Z.H. 2006. Mechanism analysis on failure of deep rock laneway under dynamic disturbance. *Journal of China Coal Society*: 742–746.

*Rock Dynamics: From Research to Engineering – Li et al. (Eds)*
*© 2016 Taylor & Francis Group, London, ISBN 978-1-138-02953-8*

# A FEM-based numerical study of responses of underground openings subject to plane, cylindrical, compressive and tensile waves

Z.Y. Liao & N.M. Lam
*Department of Civil and Environmental Engineering, The Hong Kong Polytechnic University, Hong Kong SAR*

J.B. Zhu
*Department of Civil and Environmental Engineering, The Hong Kong Polytechnic University, Hong Kong SAR*
*State Key Laboratory of Hydraulic Engineering Simulation and Safety, School of Civil Engineering, Tianjin University, Tianjin, China*

ABSTRACT: A FEM-based numerical study is carried out to investigate the dynamic responses of underground openings in jointed rock masses. The heterogeneity and damage process of rocks are taken consideration in the numerical study. Effects of joint normal stiffness, joint spacing, joint orientation, amplitude of applied stress wave, cylindrical wave and tensile wave on the measured Peak Particle Velocity (PPV) around the tunnel are addressed. The simulation results show that the existence of joints has great influence on the stability of the underground tunnel. In addition, the cylindrical wave decays quickly due to both geometrical attenuation and joint reflection. The PPVs around the tunnel are highly dependent on the source location of the cylindrical wave and the wave amplitude. Furthermore, the large-amplitude tensile wave is difficult to transmit across the joints, because of the caused opening of joints. However, for the shallow buried tunnel, the reflected tensile waves from the ground surface may still lead to the instability of tunnel.

*Keywords*: Underground opening; Rock Joint; Peak particle velocity; FEM

## 1 INTRODUCTION

The stability of underground tunnel is of great significance for reducing huge losses of economy and casualties. It has received lots of attention, particular for the condition of dynamic disturbance. The existence of joints complicates the dynamic responses of underground openings. When a wave transmits across jointed rock masses, multiple reflection and transmission will occur. Therefore, it is of great interests and significance to study the dynamic responses of the underground tunnel in jointed rock masses.

As a criterion to determine the stability of the underground tunnel, Peak Particle Velocity (PPV) is commonly utilized in rock engineering (Dowding, 1984). Great efforts have been made on studying dynamic responses of the underground tunnel. In addition, the effects of joints on the stability of the underground tunnel are also investigated (Deng et al., 2015, Deng et al., 2014).

However, previous studies were mainly focused on effects of joints, and the rock was usually considered as a homogeneous and rigid material. Plane compressional wave was adopted as the dynamic source. In addition, the heterogeneity and damage process of rocks were not taken into consideration. In this paper, the FEM based numerical code Rock Failure Process Analysis (RFPA) is adopted to simulate the responses of the underground tunnel in jointed rock masses under the dynamic disturbances. The rock heterogeneity and damage are well characterized in the numerical model. And Goodman element is selected to describe the behaviors of joints. In addition to plane compressional waves, cylindrical wave and tensile wave are also included.

Parametrical studies of joint normal stiffness, joint orientation, amplitude of applied stress wave, location of applied cylindrical wave and tensile wave are carried out to investigate the tunnel dynamic responses. The objective of this study is to provide a better understanding of the damage processes of the underground tunnel when subject to dynamic loadings.

## 2 PARAMETRICAL STUDY ON TUNNEL RESPONSES SUBJECT TO DYNAMIC LOADING

### 2.1 *Model setup*

The schematic diagram of the numerical model is shown in Figure 1a. The size of analytical jointed rock masses is 50 m wide and 60 m deep with 250 × 300 elements. The heterogeneity of rocks is included in the numerical model through assuming that the properties of elements satisfy a statistical distribution (Tang, 1997). In addition, the Goodman element method is utilized to describe the behaviors of joints (Goodman et al., 1968). Parametrical studies on joint normal stiffness, joint spacing, joint orientation, dynamic loading magnitude, location of applied cylindrical stress wave and tensile wave are conducted in this paper. In the following parametrical studies, all parameters will not change except for the addressed one. And for the general model, a circular shaped tunnel with a diameter of 10 m is located at a depth of 45 m. A joint set is horizontally established from the top to the bottom of the model. The dynamic disturbance is applied on the top boundary of the model, and the simplified triangular wave with amplitude of 80 MPa and duration of 0.002 s is used. In addition, the viscoelastic artificial boundary is adopted on the free boundaries of model to eliminate the effects of the reflected stress waves. The materials' properties for the general model are listed in Table 1.

In order to investigate the dynamic responses of the underground tunnel, four measuring points, which are located at the top, bottom, left side and right side of the underground tunnel, are selected to record the particle velocity histories during the numerical tests.

### 2.2 *Simulation results*

#### 2.2.1 *Effects of joint normal stiffness*

The effects of joint normal stiffness ($k_n$) are investigated in this section. Figure 2 illustrates the failure conditions of the underground tunnel for different joint normal stiffness. As

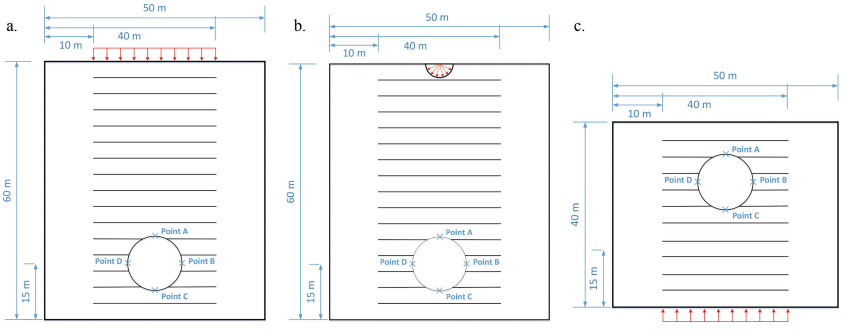


Figure 1. Schematic diagram of numerical models.

Table 1. Materials' properties.

| | Elastic modulus (GPa) | Uniaxial compressive strength (MPa) | Density (Kg/m$^3$) | Poisson's ratio | Normal stiffness (GPa/m) | Shear stiffness (GPa/m) |
|---|---|---|---|---|---|---|
| Rock | 65 | 200 | 2120 | 0.25 | / | / |
| Joint | / | / | / | / | 50 | 25 |

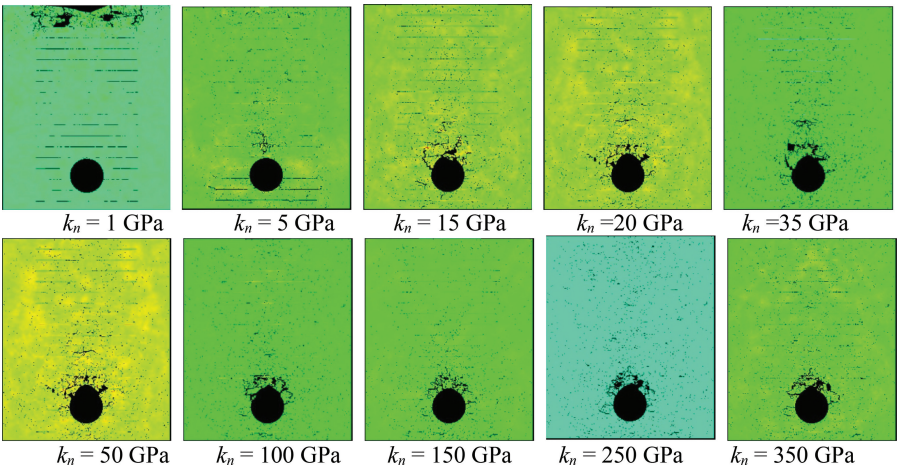


Figure 2. Numerically simulated failure patterns of underground tunnel with different joint normal stiffness.

shown in Figure 2, for the condition of $k_n$ = 1 GPa, the stresses are concentrated on the top of the model. There is almost no damage around the tunnel. This is because of the low wave transmission capacity when joint normal stiffness is small. However, with increasing $k_n$, more wave energy can be transmitted across the joints, and hence, the damage of tunnel increases. Figure 6a shows the measured PPVs around the tunnel with different joint normal stiffness. It is found that the PPV of each location increases before keeping constant.

2.2.2 *Effects of joint spacing*

Figure 3 shows the corresponding numerically simulated failure patterns for different joint spacing. It can be found that the damage degree first decreases before gradually increases. The PPV results around the underground tunnel are shown in Figure 6b. The PPV at the top of the underground tunnel first decreases to the minimum value before it increases. This is because the multiple wave reflections among the joints and the number of joints included in the numerical model. However, no strict rule can be found among other three measuring points (i.e. the left, right and bottom of the underground tunnel).

2.2.3 *Effects of joint orientation*

Figure 4 illustrates the numerically simulated failure patterns with different joint orientations (dip angles). It is found that the failure zones mainly occur at the top of the tunnel. However, the damage degree first decreases before increases with increasing joint orientation. In addition, the failure zones are distributed on the left side of the model when the joint dip angle ranges from 30° to 75. Figure 6c summaries the PPVs around the tunnel with different joint orientations. The highest PPV occurs at the top of the tunnel, while the lowest one is located at the bottom. The PPVs first decrease to the minimum value before it increase for the measured points at the top, left and right sides of the tunnel. However, the PPV at the bottom of the tunnel is roughly kept constant after decreasing.

2.2.4 *Effects of amplitude of applied stress wave*

The effects of amplitude of applied stress wave are investigated in this section, while other parameters are kept the same. The failure patterns are shown in Figure 5. The extent of the failure zones increases as the amplitude of applied stress wave increases. The PPV results in Figure 7a demonstrate that the wave amplitude has great influence on the top, left and right sides of tunnel. However, the PPV at the bottom of tunnel roughly keeps constant with different loading magnitudes.

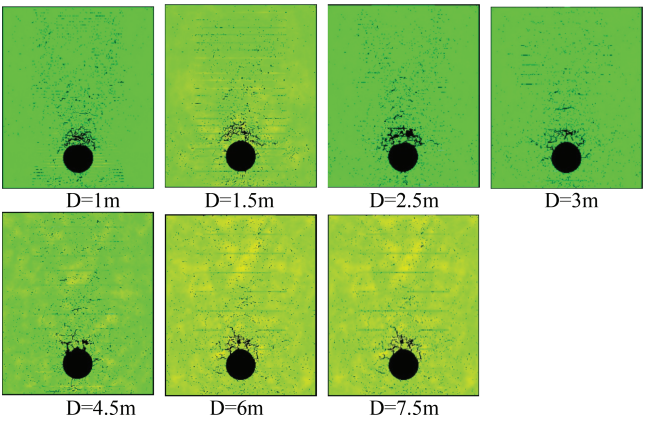


Figure 3. Numerically simulated failure patterns of the underground tunnel with different joint spacing.

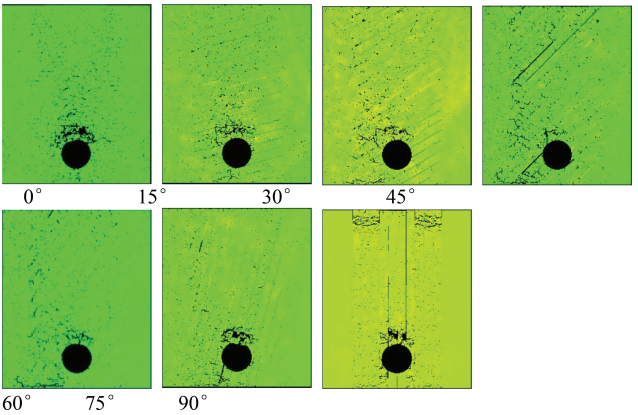


Figure 4. Numerically simulated failure patterns of the underground tunnel with different joint orientations.

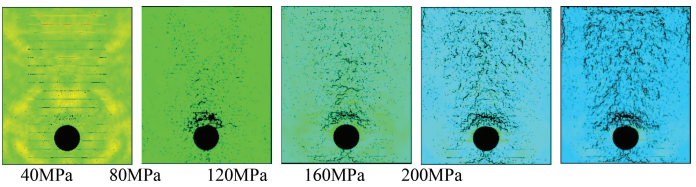


Figure 5. Numerically simulated failure patterns of the underground tunnel with different loading amplitude.

### 2.2.5 *Effects of the location of applied cylindrical stress wave*

The plane wave is applied as the dynamic disturbance in above parametrical studies. Plane wave is only far-field approximation. In most cases, the generated wave from, for example, earthquakes and blasting, are in the form of cylindrical waves in a two-dimensional space. Therefore, it is also necessary to study cylindrical waves and their effects on underground openings, as shown in Figure 1b.

It is known that the magnitude of the cylindrical wave decays as $R^{-1/2}$, where the parameter $R$ refers to the principal radius of curvature at the wavefront. Therefore, in order to find out the wave attenuation caused by joints, the PPVs in the jointed rock masses are to be compared with those in intact rock. Figure 7b shows the PPV vs propagation distance under

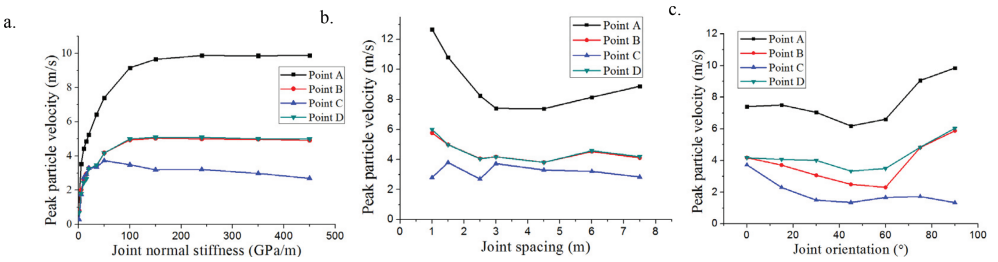


Figure 6. Numerically simulated PPV results (a. PPV vs joint normal stiffness; b. PPV vs joint spacing; c. PPV vs joint orientation).

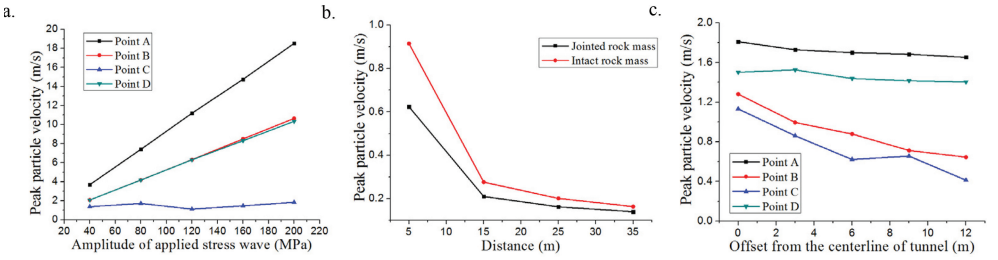


Figure 7. Numerically simulated PPV results (a. PPV vs amplitude of applied stress wave; b. PPV vs propagation distance of the cylindrical wave; c. PPV vs distance from center of top surface).

conditions of jointed rock masses and intact rock. The attenuation of PPV with distance for intact rock is dominated by geometrical attenuation. The wave attenuation in jointed rock masses is caused by both the geometrical attenuation and attenuation at joints. Therefore, the difference between them are in fact the wave attenuation at joints.

Different locations of the applied cylindrical wave are also investigated. The cylindrical stress wave is applied on the top left of the numerical model with different distance from the center of tope surface. Figure 7c presents the PPV vs the distance. It can be found that the PPVs around the tunnel all decrease with increasing distance from the center of top surface, although the decrease is more significant at the bottom and right side of tunnel.

### 2.2.6 *Effects of tensile wave*

The underground tunnels are occasionally suffered from dynamic tensile disturbances. There are two types of sources of tensile waves. One is the directly applied dynamic tension, while the other one is the tensile wave after reflection of compressional wave at free surfaces, e.g., the ground and tunnel surfaces. Therefore, two types of numerical models with different loading conditions are established to simulate the dynamic responses of the underground tunnel in this section. For the case of direct dynamic tension, the numerical model is the same as that shown in Figure 1a, except the loading direction. For the latter condition, the numerical model is shown in Figure 1c. The shallow tunnel with a diameter of 10 m is included in the model. The dynamic compressive wave is applied at the bottom of the numerical model. And the expected tensile wave will be generated when the compressive one reflected from the ground surface.

Figure 8 illustrates the simulation results under the direct dynamic tension. It can be found that the capacity of jointed rock masses in transmitting tensile wave is very low. The stresses are mainly concentrated on the first layer of jointed rock masses and can barely transmit through the joint. This is because the joint is opened after arrival of tensile wave. And it is difficult for wave to transmit through open joints. For the second condition, the simulation results with different tunnel depths (Z) are presented in Figure 9. The compressive wave propagates from the bottom to the top of the model. It is found that tensile failures are observed at the top of the jointed rock masses due to the effect of the reflected tensile waves. In addi-

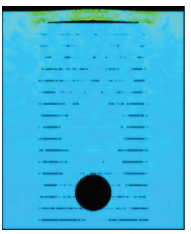

Figure 8. Numerically simulated failure pattern of the underground tunnel under dynamic direct tensile wave.

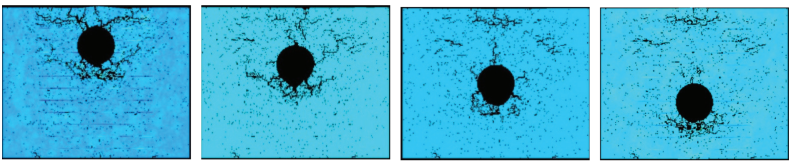


Figure 9. Numerically simulated failure patterns of the underground tunnel with different tunnel depths.

tion, this effect weakens the stability of the tunnel if it is shallow ($Z$ = 10 m in Figure 9). However, with increasing $Z$, the damage degree at the top of tunnel decreases.

## 3 CONCLUSIONS

This paper investigates the behaviors of the underground openings in jointed rock masses when subject to dynamic loadings. A series of numerical modellings are carried out to analyze the effects of joint properties, types of dynamic disturbance and location of loading source on the stability of the underground tunnel. The simulation results demonstrate that the joint properties have great influence on the PPV. In addition, with increasing loading amplitude, the PPV around the tunnel also increases. The magnitude of cylindrical wave decays with increasing propagation radius, especially in jointed rock masses. In addition, the location of applied cylindrical wave also affects the dynamic responses of underground openings. Furthermore, the capacity of jointed rock masses in propagating dynamic tensile wave is very low, because of resulting open joints. For shallow tunnels, the reflected tensile wave from the ground surface significantly endanger the tunnel stability.

## REFERENCES

Deng, X.F., Chen, S.G., Zhu, J.B., Zhou, Y.X., Zhao, Z.Y. & Zhao, J. 2015. UDEC–AUTODYN Hybrid Modeling of a Large-Scale Underground Explosion Test. *Rock Mechanics and Rock Engineering* 48(2): 737–747.

Deng, X.F., Zhu, J.B., Chen, S.G., Zhao, Z.Y., Zhou, Y.X. & Zhao, J. 2014. Numerical study on tunnel damage subject to blast-induced shock wave in jointed rock masses. *Tunnelling and Underground Space Technology* 43: 88–100.

Dowding, C. 1984. Estimating earthquake damage from explosion testing of full-scale tunnels. *Advances in tunnelling technology and subsurface use* 4(3): 113–117.

Goodman, R.E., Taylor, R.L. & Brekke, T.L. 1968. A model for the mechanics of jointed rock. *Journal of Soil Mechanics & Foundations Div*.

Tang, C.A. 1997. Numerical simulation of progressive rock failure and associated seismicity. *International Journal of Rock Mechanics & Mining Sciences* 34(2): 249–261.

*Rock Dynamics: From Research to Engineering – Li et al. (Eds)*
*© 2016 Taylor & Francis Group, London, ISBN 978-1-138-02953-8*

# Numerical simulation of sand production in oil well considering particle size effect

X.S. Liu & M. Xu
*School of Civil Engineering, Chongqing University, Chongqing, China*
*Key Laboratory of New Technology for Construction of Cities in Mountain Area, Chongqing University, Chongqing, China*

L. Zhang
*Chongqing Grid Company Limited, Chongqing, China*

ABSTRACT: Considering particle size distribution curve of practical reservoir sandstone, a numerical model based on PFC3D under Cylindrical Coordinate System has been proposed to simulate sand production considering the fluid pressure gradient force and drag force based on similarity principle. Macro stress distribution indicated that introduction of fluid flow disturbed the mechanical condition of the reservoir sandstone, and larger flow rate increased the stress value more greatly; the mean stress and deviatoric stress reflected the development of the plastic zone when flow rate increasing, and this increased the probability of the sand yielding with the maximum plastic zone 16.5 mm, which indicated the localized effect. And the stress on parallel bonds indicated broken bonds near the inner hole, and when the flow rate was more than 2 m/s, stronger arch effect in radial direction could prevent the particles separating from the sandstone. The above results have showed the similar variation as the macro stress distribution, and also indicate that the forward numerical model considering particle size effect can reflect the practical mechanism of sand production.

## 1 INTRODUCTION

Sand production is one of the bottlenecks for the oil sustainable development in recent years, and the sanding mechanism is becoming the key to improve the reservoir productivity and reduce the oil extraction cost. According to recent researches, many researchers has achieved investigations based on theoretical analysis, experiments and numerical methods. For example, Willson et al. (2002), Wan et al. (2004) and Papamichos et al. (2004) have put forward the yielding and sanding model of the perforation holes to predict the sanding rate and sanding production. Ispas et al. (2006) and Vaziri et al. (2003) have combined many TWC tests and CT apparatus to monitoring the particles deformation during the sandstone broken process under different confining pressure and flowing conditions. And Detournay et al. (2009) has used the elasto-plastic FEM model to describe the sand production of the oil wellbore and corresponding well propagation mode. The above researches have played an important role on the understanding sanding mechanism, however, the limitation of the laboratory cores and simplicity of the analysis, the sanding mechanism should be deeply investigated under complex surrounding environment.

With the improvement of the computer performance and the numerical modeling technique, many researchers have involved in the micromechanics to investigate the perforation tests to reveal the mechanism of the sand production. Dorfmann et al. (1997) and Preece et al. (1999) has used a micro sanding model to simulate the particles movement and sand production. Li et al. (2002) has researched on the motion characteristics of the particles considering 2-Dimensional Darcy's flowing. The above results have mainly described the

particles motion considering 2-Dimensional Darcy's flowing under the cartesian coordinate system. However, due to the complexity of the oil formation stress, denudation, migration and boundary conditions, the physical process of the sand production is also very complex. In order to correctly reappear the sanding occurring and developing process, a 3-D micro numerical model (Liu Xianshan et al. 2013, Li et al. 2006) simulating the sanding mechanism is significant to solve this problem.

The practical sandstone particles diameter is so small that the sanding numerical model will include a large number of particles based on the 3-Dimensional particle flow code, many degree solutions require much more computer memory resulting in the low efficiency and non-convergence. If the generating sandstone particles using random method cannot represent the practical sandstone particles, the particle size effect will result in the difference between the numerical simulation and practical perforation sanding. In order to improve the precision and correction, according to the particle distribution curve to amplify the sandstone particle size, and the sanding numerical model under the Cylindrical Coordinate System based on PFC3D. For numerical simulation, the parallel bonds has been introduced to model the boning status of the practical sandstone (Liu Xianshan et al. 2013, Jiang et al. 2006), and the fluid-solid coupling effect has been simulated based on the similarity principle considering the pressure gradient force and drag force, this will more correctly simulate the mechanism of the sand production.

According to the practical physical property of the sandstone reservoir and the perforation test during the oil extraction, the PFC3D model considering the particle size effect has been forward to research on the macro and micro mechanical characteristics under different fluid flowing conditions. The research should be a new thought and technique for sand production prediction and sanding control optimization, which is benefit for ensuring the oil production and sustainable development.

## 2 THE THEORY OF SAND PRODUCTION OF THE OIL WELLBORE

### 2.1 *3-D fluid-solid coupling theory based on the cylindrical coordinate system*

In order to more correctly the fluid-solid coupling effect in the perforation test (Alassi et al. 2006), the gradient force of the fluid pressure and the drag force due to different speed between the fluid and particles. The expressions are as follows.

According to the Ergun's equation, the gradient force of the fluid pressure $\nabla p_j (j = r, \theta, z)$ is given by

$$\nabla p_j = \frac{dp}{dx_j} = -\left( 150 \frac{(1-n)^2}{n^3 \bar{d}_p^2} \nu_f \rho_f u_{j,0} + 1.75 \frac{(1-n)}{n^3 \bar{d}_p} \rho_f u_{j,0}^2 \right) \tag{1}$$

where $\nu_f$ = kinematics viscosity ($m^2/s$); $\rho_f$ = density of the fluid ($kg/m^3$); $u_{j,0} (j = r, \theta, z)$ = apparent relative velocity ($m/s$); and $\bar{d}_p$ = the average particle diameter ($m$); $n$ = the porosity.

As for the drag force generated by the difference between the fluid and the particle, the drag force $f_{\text{int}_j} (j = r, \theta, z)$ ($N/m^3$) based on 3-D Navier-Stokes equations can be calculated by

$$f_{\text{int}_j} = \beta_{\text{int}_j} \left( \bar{v}_j - u_j \right) \tag{2}$$

where $\beta_{\text{int}_j} (j = r, \theta, z)$ = the drag force coefficient, also is the fluid-particle friction coefficient (Pa.s/m$^2$). Considering the variation of the practical porosity $n$, $\beta_{\text{int}_j} (j = r, \theta, z)$ can be expressed by

$$\beta_{\text{int}_j} = 150 \frac{(1-n)^2}{n \bar{d}_p^2} \mu_f + 1.75 \frac{(1-n) \rho_f}{\bar{d}_p} \left| \bar{v}_j - u_j \right| \tag{3}$$

where $\overline{d}_p$ = the average particle diameter ($m$); $n$ = the porosity; $\overline{v}_j$ = the average particles velocity (m/s) and $u_j$ = the practical fluid velocity (m/s).

According to the above theory, the force $f_{d_{ij}}(i)\,(i=1,\cdots,n_p, j=r,\theta,z)$ on the particle can be given by

$$f_{d_{ij}} = -\left(\frac{\beta_{\text{int}_j}}{1-n}\left(\overline{v}_j - u_j\right) + \nabla p_j\right)\frac{\pi}{6}d_{pi}^3 \tag{4}$$

where $n_p$ = the number of all the particles; and $d_{pi}$ = the particle diameter.

Therefore, for 3-D numerical model under the Cylindrical Coordinate System, the coupling force $f_{d_{ij}}$ considering different fluid flowing conditions can be calculated to deeply reveal the macro and micro mechanical characteristics, and consequently the fluid-solid coupling effect during the sanding considering different environment can be obtained.

### 2.2 *Similarity technique considering the particle size effect*

Rock is a nonlinear deformed material whose property will be influenced by stress. When rock structures are processed physical simulation, the stress of the model should be equal to that of the prototype so that the model can represent the prototype as close as possible. Centrifugal model is the best model with high similarity among all types of the physical models, and the centrifugal test is reported to analyze water flowing in soil. When using the centrifugal test, there are two assumptions: (1) Equivalent gravity field $N_g$ ($N$ is constant, $g$ is the acceleration of gravity (m/s$^2$) can be generated accurately by the centrifugal apparatus. (2) Mechanical characteristics of the model and prototype is similar under the acceleration $Ng$. As for the most of static problems, the centrifugal apparatus can generate the equivalent gravity field with acceleration $Ng$, but for some dynamic problems, this assumption is not necessarily the truth. When relative movement between the rock particle and the water is appearing, and the Reynolds number is less than 1, the mechanical characteristics of gravity field with acceleration NG is similar to that of 1.0 g.

In practice, the rock particle is small. In order to balance the calculation efficiency and the simulation results within rational time, particle size is amplified $M_r$ (>1) times in the numerical model. Therefore, considering the same size of the perforation hole, particles should be generated enough to eliminate the size effect for the numerical model. When the particle diameter has been amplified $M_r$ times, Reynolds number related to the particle size changes even in the same flowing conditions. And due to the variation of the Reynolds number, the turbulence will appear in the research field, however, the Darcy's flow is dominated in the practical perforation testing. Similar to the centrifugal test, the similarity principle should be considered when the particle size has been changed.

There is the same size between the numerical model and the practical perforation test, but the particle radius cannot represent the real particle radius. According to the similarity principle, the ratio of the volume is a cube of the particle diameter. As for the fluid flow, the similarity principle is related to the flowing mode resulting in different motion of the particles located in different positions, and thus the similarity principle of the centrifugal test cannot be applied in this DEM perforation test. Since the PFC3D numerical model and the practical perforation hole have the same size, pressure gradient of the fluid flow is remains the same considering the same flowing velocity. The loss of the fluid pressure can be determined. According to the Equation(2) in section 2.1, the pressure loss is related to the fluid-solid coupling force $f_{\text{int}}$. In order to ensure $\beta_{\text{int},PFC3D} = \beta_{\text{int},Original}$ for the numerical model, considering same porosity $n$ of the numerical model and the prototype model and the same relative velocity $\left(\overline{v}-u\right)_{PFC3D} = \left(\overline{v}-u\right)_{Original}$ between the fluid and the particle for both models, when the particle radius is expressed by $r_{PFC3D} = M_r r_{Original}$, the density and viscosity coefficient of the fluid may be written as $\rho_{f,PFC3D} = M_r \rho_{f,Original}$ and $\mu_{f,PFC3D} = \left(M_r\right)^2 \mu_{f,Original}$. Finally, $r_{PFC3D}$, $\rho_{f,PFC3D}$ and $\mu_{f,PFC3D}$ are introduced into the equations in Section 2.1 to fulfill the numerical simulation considering the change of particle size.

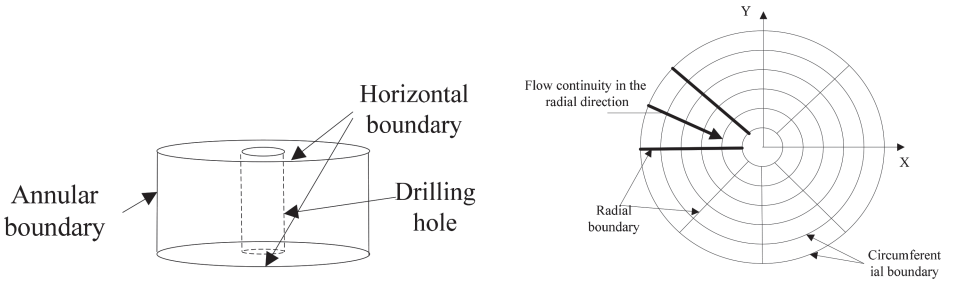


Figure 1. Physical model of the oil well and fluid cells in a cylindrical coordinate system x-y view.

Table 1. Parameters of the coupled fluid-solid simulation model.

| Parameter of the numerical model | | Parameter of the particle | | Parameter of the parallel bond | | Parameter of the fluid | |
|---|---|---|---|---|---|---|---|
| Inner radius $R_i$ (mm) | 6 | Total number | 40152 | Normal strength $S_{pb}^{N}$ (kPa) | 1.25e6 | Density $\rho_f$ (kg/m$^3$) | 785 |
| Outer radius $R_o$ (mm) | 75 | Radius (mm) | 0.55~1.5 | shear strength $S_{pb}^{S}$ (kPa) | 1.5e6 | Viscosity $\mu_f$ (Pa.s) | 1.40e-3 |
| Height $h$ (mm) | 12 | Density (kg/m$^3$) | 2600 | | | | |
| | | Friction coefficient | 0.5 | | | | |

## 3 NUMERICAL MODELING

Considering the bonding condition of the reservoir sand particles and the fluid-solid coupling effect, a 3-D numerical model based on the PFC3D under the Cylindrical Coordinate System is established to reveal the mechanism of the sand production. The boundary conditions in Figure 1 is set as horizontal boundary at the top and bottom platen and annular boundary along the inner and outer radius. And the model is divided by 288 fluid elements with $12 \times 12 \times 2$ in the radial direction, tangential direction and vertical direction as shown in Figure 1. The geometric parameters and mechanical parameters are listed in Table 1. The outer radius, inner radius and the height of the model are 75 mm, 6 mm and 12 mm, respectively; $M_r = 15$ is chosen according to the practical sand particle size for further numeric simulation.

As for the numerical simulation, he parallel bonds are introduced based on Fish language of the PFC3D to model the real bonding conditions. Considering the fluid flowing from the outer annular boundary to the inner boundary along the radial direction to form the radial perforation condition, the fluid-solid coupling calculation is carried out. And then, the inner annular boundary is deleted due to the self-support of the inner wellbore. The changed boundary conditions result in real-time variation of the interaction between the sand particles and the fluid. Therefore, both the particles' positions and porosity have been changed, and finally the model turns to be stable gradually in the process of fluid-solid coupling calculation. As for the numerical simulation, the porosity variation in each fluid cell changes slightly in any given small time step due to the explicit solution of the PFC3D and the nonlinearity of the fluid-solid coupling calculation.

## 4 RESULTS ANALYSIS

### 4.1 *Macro mechanical characteristics of sand production*

Based on the sanding model by PFC3D, the curves of tangential stress $\sigma_\theta$ and radial stress $\sigma_r$ varying with $r/R_i$ have been obtained as shown in Figure 2, the results reveal the stress

evolution of the sandstone reservoir during the sand production (Liu Xianshan et al. 2013). Smaller stress occurs when fluid flow is not considered, and change of the stress becomes more obvious once the flow velocity increases to 2 m/s. Figure 2 shows that the tangential curve becomes steeper and the peak value becomes as the increase of flow velocity, which indicates that the increasing fluid velocity results in larger stress on the model. Figure 2 indicates that radial stress increases more greatly around the inner hole, especially when the flowing velocity increases to 5 m/s or larger velocity, the variation becomes more obvious. The main reason is that the increasing flow velocity results in particle with broken bonds dislodging and moving around the inner hole by the fluid flowing, and consequently the stuck particles around the inner hole causes the stress increasing. Therefore, Figure 2 indicates that the stress becomes strong with the increasing of fluid flow velocity, and the more the fluid flow velocity is, the greater the stress will be. At the same time, the stress curve also indicates that the fluid flowing disturbs the mechanical condition of the reservoir sandstone and weakens the particle strength resulting in enlarging the plastic zone. Then, the bonds between the particles are destroyed more seriously, and the numbers of sandstone particles without constraint increase, leading to more serious sand production. Therefore, fluid-solid coupling effect due to different fluid flowing dominates the mechanical characteristics, and is the important factor for the sand production.

Additionally, the numerical analysis has revealed the relation of the deviatoric stress varying with $r/R_i$. Figure 3. shows curves of the deviatoric stress ($\sigma_\theta - \sigma_r$ and $\sigma_\theta - \sigma_z$). Results indicate that the stress increase with increasing fluid flowing velocity, which implies the shearing condition in the process of the sand production. The deviatoric stress in Figure 3 shows that the stress changes more obviously when the fluid flowing velocity is larger than 2 m/s, and the variation is explained by the divisions of the whole wellbore model.

The model is divided by 23 areas with the width of 3 mm as shown in Figure 4. Figure 4 also describes the relation of the deviatoric stress $\sigma_\theta - \sigma_r$ and average stress $p$, and the curves are compared with the yielding curve and peak curve in the test. The comparison indicates that the yielding radius is 16.5 mm away from the inner hole, and that the material in this area is not shearing broken before reaching the peak strength, and thus the rapid broken of the parallel bonds does not appear. The above analysis also shows that the local failure of the model is largely due to the deficiency of fluid flow velocity. Under this condition, sand production is the result of high flow speed and confining pressure.

### 4.2 *Micro mechanical characteristics of the sand production*

The numerical simulation exhibits the variation of the average tensile stress and shear stress on different positions in Figure 5. Figure 5 indicates the larger stress around the oil wellbore, and when the tensile stress becomes larger, increasing fluid flowing velocity results in great shear stress of the model. Considering the fluid flowing velocity reaching 6 m/s, only 0.379% (152/40112)

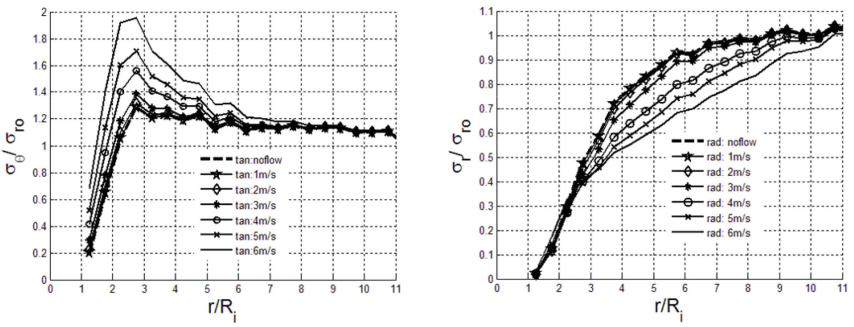


Figure 2. Tangential stress and radial stress distribution of the model.

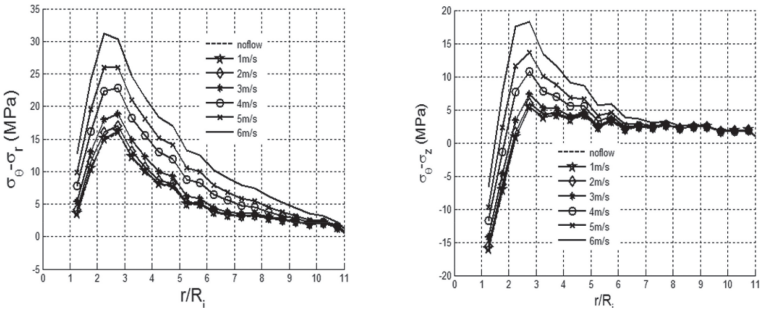


Figure 3. Deviatoric stress $\sigma_\theta - \sigma_r$ and $\sigma_\theta - \sigma_z$ distribution for different position.

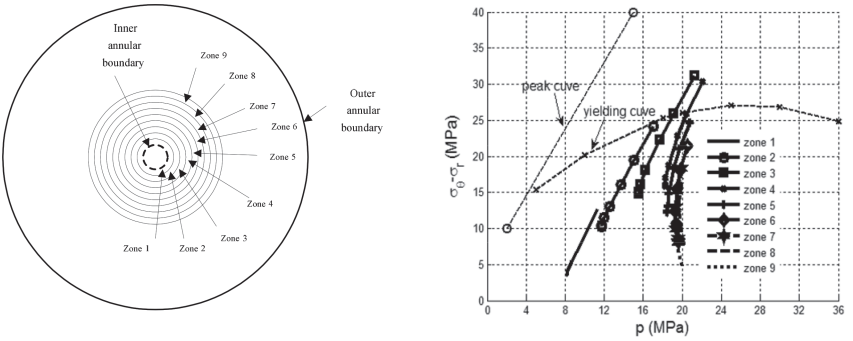


Figure 4. Division plot of the model and the mean stress in the different vs the deviatoric stress $\sigma_\theta - \sigma_r$.

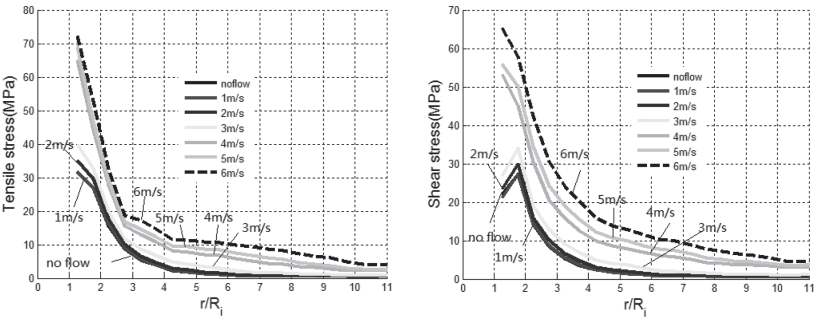


Figure 5. Tensile stress and shear stress distribution for different position.

parallel bonds are broken, and these broken bonds are mainly located in the inner hole. And addition, Figure 5 indicates that the variation of the contact density is minor when the fluid flow velocity is larger than 2 m/s, but the radial stress increases. It means higher pressure along the radial direction and the stronger arch effect in radial direction. The development of tensile stress and shear stress and the arch effect prevent the particles dislodging and moving.

## 5 CONCLUSIONS

The PFC3D numerical model under the Cylindrical Coordinate System has been proposed to study the sand production mechanism. In this paper, the parallel bonding model has been introduced to represent the real bonds of the sandstone particles and, the fluid-solid coupling

effect including the gradient force and drag force of the fluid has been considered. Main results are as follows.

1. As for the above model, the computer performance, numerical calculation efficiency and the limitation of PFC3D will cause long-time calculation and non-convergence due to excessive particles, so the numerical model will consider the particle size effect to deal with fluid-solid coupling effect based on similarity principle, so the model can better simulate the macro-micro characteristics of the sand production.
2. Macro stress indicates that fluid flow increases the stress of the sandstone model, but cannot generate larger shear force to exceed the peak strength of the rock material. Increasing fluid flow velocity largely disturbs the rock structure to make the more particles dislodge.
3. Stress variation on parallel bonds indicates that increasing radial stress helps to form a stable arch in the wellbore, and the parallel bonds may prevent the particles dislodging, thus the rate of sand production is much small. Te fluid-solid coupling force is so small that the fluid flow mainly drags the particles into the wellbore to show local influence on the mechanical characteristics.

## ACKNOWLEDGEMENTS

The research is financially supported by 973 Program of China under Grant No. 2014CB046903, No. 106112014CDJZR200014 & 106112014CDJZR200015 by Fundamental Research Funds for the Central Universities, and the Project No. 51478065 by National Natural Science Foundation.

## REFERENCES

Alassi, H., L. Li, R. Holt. 2006. Discrete element modeling of stress and strain evolution within and outside a depleting reservoir[J]. *Pure Applied Geophysics*, (163): 1131–1151.

Detournay, C. 2009. Numerical modeling of the slit mode of cavity evolution associated with sand production. *SPE Journal,* 14(4): 797–804.

Dorfmann, A. 1997. Micromechanical modeling of sand production and arching effects around a cavity. International Journal of Rock Mechanics and Mining Sciences, 34(3–4): 1–14.

Ispas et al. 2006.Interim report on perforation testing for improved sand management. *Technical report, BP and ASRC Energy Services and TerraTek*.

Jiang, M., YU H., Harris D. 2006. Bond rolling resistance and its effect on yielding of bonded granulates by DEM analysis. *International Journal for Numerical and Analytical Methods in Geomechanics*, (30): 723–761.

Li, L., Holt R. 2002. Particle scale reservoir mechanics. *Oil and Gas Science and Technology*, 57(5): 525–538

Li, L., Papamichos E., Cerasi P. 2006. Investigation of sand production mechanics using DEM with fluid flow. *EUROCK Multiphysics Coupling and Long Term Behavior in Rock Mechanics*, 241–247.

Liu Xian-shan, Xu Ming. 2013. Micromechanism of sand production in oil well based on 3-Dimensional coupled fluid-solid model. *Rock and Soil Mechanics*, 34 (8): 2363–2370.(in Chinese).

Papamichos. 2004. Wellbore stability analysis: from linear elasticity to post bifurcation modeling. *International Journal of Geomechanics*. 4(1): 2–12.

Preece, D., Jensen R. 1999. Sand production modeling using superquadric discrete elements and coupling of fluid flow and particle motion. *Rock Mechanics for Industry Proceedings — Symposium on Rock Mechanics,* (37).

Vaziri H.H., Y. Xiaob, Islamb R., Lemoine E. 2003. Physical modeling study of the influence of shale interbeds and perforation sequence on sand production. *Journal of Petroleum Science and Engineering*, (37) 11–23.

Wan R.G., Wang J. 2004. Analysis of sand production in unconsolidated oil sand using a coupled Erosion-stress-deformation model. *Journal of Canadian Petroleum Technology*, 43(2): 47–53.

WillsonI, S.M, Moschovidis, et al. 2002. New model for predicting the rate of sand production. *SPE/ISRM 78168, Proceedings of the SPE/ISRM Rock Mechanics Conference, Irving, Texas*, 20–23.

This page intentionally left blank

*Rock Dynamics: From Research to Engineering – Li et al. (Eds)*
*© 2016 Taylor & Francis Group, London, ISBN 978-1-138-02953-8*

# Study on determining REV of fractured rock masses considering hydro-mechanical effect

X.S. Liu
*School of Civil Engineering, Chongqing University, Chongqing, China*
*Key Laboratory of New Technology for Construction of Cities in Mountain Area, Chongqing University, Chongqing, China*

L. Zhang
*Chongqing Grid Company Limited, Chongqing, China*

Z.H. Zhou
*State Grid Chongqing Transmission and Transformation Co. Ltd., Chongqing Grid Company Limited, Chongqing, China*

ABSTRACT: The Representative Elementary Volume (REV) of fractured rock masses plays an important role on determining the rock mechanical characteristics. Firstly studying the general methodology of rock REV are summarized, and the modelling of Discrete Fracture Networks (DFN) is proposed as the investigation foundation of the REV of fractured rock masses, and then the numerical method to determine the REV is analysed and used in the case study. Combined modelling technique of random fractured network with discrete numerical method, the size effect of rock parameters has been analysed under single fluid flow condition and hydro-mechanical coupling condition. The calculation results of examples mentioned above indicate that the permeability tensor will decrease with the increasing stress and gradually tend to smooth while the studying scale increasing. The above achievements show that the proposed numerical method is an efficient approach to determine the rock mechanical parameters and REV, and also should be extended to complex three-dimensional problem in the geotechnical field in future.

## 1 INTRODUCTION

The natural rock masses has experienced a long period of complex and unbalanced geological process, the rock masses has been cut by the fractures, and the randomness of the fractures distribution has induced the rock masses to present obvious discontinuous, heterogeneous and anisotropic characteristics (Harrison et al. 2000, Jing 2003). And the geological investigation has stated that fractures in disorder are obeying some probability distribution, and the geometric characteristics of above factures such as fracture width, dip, length and density determine the formation of the fractured network, so the mechanical property of rock masses implies some uncertainties. According to current research investigations, the value of rock mechanical parameters obtained by the field tests or laboratory tests appear obviously different due to different rock sample size, so the rock size effect is widely used to research on the rock strength, deformation, permeability and stress measure.

From the 1990s, the Representative Elementary Volume (REV) (Zhou et al. 1999, Xia et al. 2003) describing the parameter of the rock size effect has been paid more attention by many researchers. Generally speaking, the mechanical parameters such as deformation modulus, permeability coefficient will decrease with lager sample size, and the rock size increases to some critical size, the above parameter cannot change, and the critical size may be named REV of the above parameter. However, the field testing results may correctly describe the

rock property when the sample size equal to the REV, and also the physical model and corresponding mechanical parameters related to REV for numerical analysis should be determined ahead of time. Therefore, REV of the fractured rock masses is a significant topic to be deeply researched in the field of the rock mechanics, a reliable and rational determination method is important to correctly select calculation model and parameters to research on the rock mechanics, seepage and corresponding coupling analysis.

The numerical method (Min et al. 2003, Wang et al. 2002, Kulatilake et al. 2000) proposed in this paper to research on the REV based on the fractured network technique can describe the geometric characteristics in detail, complex constitutive relationship of the fractures and fractures interaction, and the mechanical characteristics of the rock cut by the fractures can be considered. Therefore, REV of the rock masses can be analyzed by the above numerical analysis method.

## 2 NUMERICAL MODELLING THEORY TO DETERMINE REV

The permeability of the rock masses has been researched based on the numerical method (Bai et al. 1999) combined the discrete element method and the fracture network technique. The calculation process to simulate the equivalent permeability tensor, mechanical parameters and REV is described as following Figure 1. Firstly, investigate the geological conditions and grasp the fractures distribution, then generate fracture network using Monte–Carlo method and build the numerical model. And then, for a certain sample size of rock masses, the permeability tensor and corresponding mechanical parameters can be determined by imposing hydro-mechanical boundary to simulate the hydro-mechanical characteristics on the numerical model. Especially for REV, the research sample size should be changed and repeat the simulating tests, the parameters variation can be obtained considering different research size. When the material parameters cannot change with varying sample size, the sample size may be determined as REV.

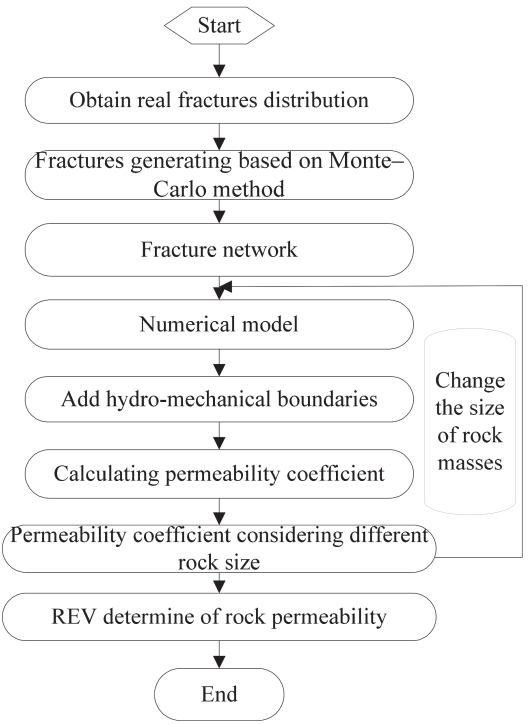


Figure 1. REV determination by numerical simulation.

## 3 CASE ANALYSIS

### 3.1 *Calibration of the numerical model*

Suppose the seepage field as the square 10 m × 10 m with two groups of orthotropic fractures is shown in the Figure 2. And the parameters of the numerical model include that the hydraulic aperture of both groups of fractures with 0.5 mm, the coefficient of viscosity υ with $0.927 \times 10^{-6}$ m$^2$/s, one fracture spacing with 0.4 m, and the other with 0.8 m. The seepage boundary is firstly supposed as the given water head 10 m and 0 m on the left and right boundary, and linear water head from left 10 m to right 0 m on the top and bottom boundary. And then change the seepage boundary, suppose the given water head as 10 m and 0 m, and linear water head from top 10 m to bottom 0 m on the left and right boundary. According to the DEM theory, the permeability tensor has been determined in Table 1. The results indicated that the maximum calculation error between the numerical simulation value and theoretical value, and the results proved the accuracy and feasibility of the proposed DEM to calculate the permeability tensor of the fractured rock masses.

### 3.2 *REV determination of rock permeability*

The determination of seepage REV is based on the above DEM. Suppose 4 groups of random fractures listed in Table 2, the center coordination is uniform distribution, and the length and dip obey the normal distribution, and the hydraulic width of the four group fractures is 0.5 mm. The fractures network generated by Monte–Carlo method in the field of size 15 m × 15 m is shown in Figure 3. And change the research size of the rock model to research on the size effect of the permeability tensor, and the equivalent permeability coefficient curve is shown in Figure 4.

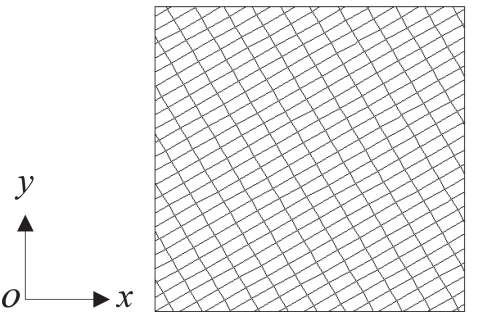


Figure 2. Fractured network with two groups of orthotropic fractures (10 m × 10 m).

Table 1. Comparison between the theoretical value and numerical simulation value.

| Theoretical value ($10^{-4}$ m/s) | | | | | Numerical simulation value ($10^{-4}$ m/s) | | | |
|---|---|---|---|---|---|---|---|---|
| $\alpha$(°) | 0 | 15 | 30 | 45 | 0 | 15 | 30 | 45 |
| $K_{xx}$ | 2.81 | 2.72 | 2.46 | 2.11 | 2.70 | 2.75 | 2.48 | 2.14 |
| $K_{yy}$ | 1.41 | 1.50 | 1.76 | 2.11 | 1.35 | 1.51 | 1.72 | 2.14 |
| $K_{xy}$ | 0 | 0.352 | 0.609 | 0.703 | 0 | 0.400 | 0.577 | 0.715 |
| $K_{max}$ | 2.81 | 2.81 | 2.81 | 2.81 | 2.70 | 2.87 | 2.79 | 2.86 |
| $K_{min}$ | 1.41 | 1.41 | 1.41 | 1.41 | 1.35 | 1.39 | 1.41 | 1.43 |
| $\theta$(°) | 0 | 15 | 30 | 45 | 0 | 16.38 | 28.24 | 45.00 |
| Relative error of $K_{max}$ by numerical method and theoretical method | | | | | –3.91% | 1.78% | –0.71% | 1.78% |
| Relative error of $K_{min}$ by numerical method and theoretical method | | | | | –4.26% | –1.42% | 0 | 1.42% |

Table 2. Distribution of the fractures.

| No. of fracture groups | | Density/m$^2$ | Length m | Dip ° |
|---|---|---|---|---|
| I | Mean value | 2.5 | 2.00 | 115.0 |
| | Mean square deviation | | 0.50 | 10.0 |
| II | Mean value | 2.0 | 2.00 | 25.0 |
| | Mean square deviation | | 0.30 | 5.00 |
| III | Mean value | 0.8 | 2.00 | 75.0 |
| | Mean square deviation | | 0.10 | 7.00 |
| IV | Mean value | 0.7 | 2.00 | 0.00 |
| | Mean square deviation | | 0.10 | 1.00 |

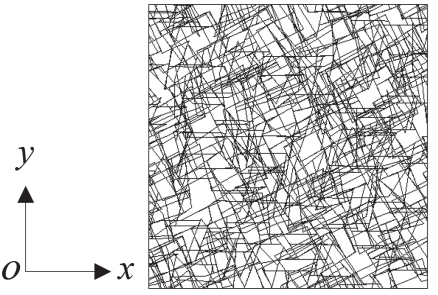


Figure 3. Permeability network of the fractured rock (15 m × 15 m).

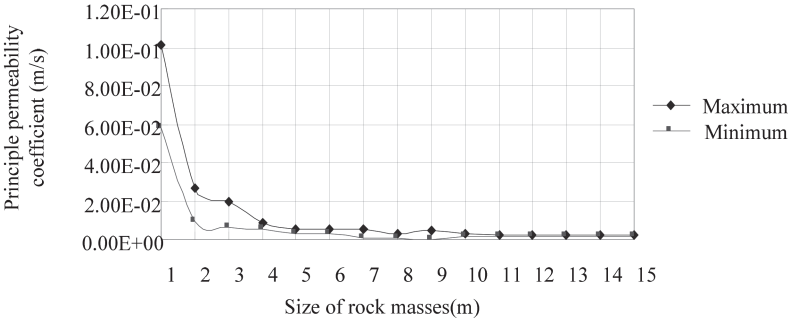


Figure 4. Principle permeability coefficient considering different rock size.

According to the curve variation in the Figure 4, the equivalent principle permeability coefficient varied with the rock size increasing, which indicated the size effect of the permeability coefficient. And the curve indicated that the permeability coefficient tended to a stable value when the rock size reached to a certain size. The numerical simulation indicated that the rock size was about 10 m × 10 m when the equivalent permeability coefficient tended to a certain value, the results illuminated seepage REV of this sample could be valued 10 m × 10 m, and corresponding maximum and minimum principal permeability coefficient were $K_{max} = 2.09 \times 10^{-3}$ m/s and $K_{min} = 1.01 \times 10^{-3}$ m/s.

### 3.3 *REV determination considering hydro-mechanical coupling process*

Also, the fractured network and geometric parameters are same to that of single seepage condition, and the mechanical parameters of the fractures and rock is listed in Table 3. In order to research on seepage REV considering hydro-mechanical coupling effect

Table 3. Mechanical parameters.

| Parameters | Density kg/m$^3$ | Elastic modulus GPa | Poisson's ratio | Stiffness ratio $k_n/k_s$ GPa/m |
|---|---|---|---|---|
| Rock | 2650 | 10 | 0.23 | |
| Fractures | | | | 150 |

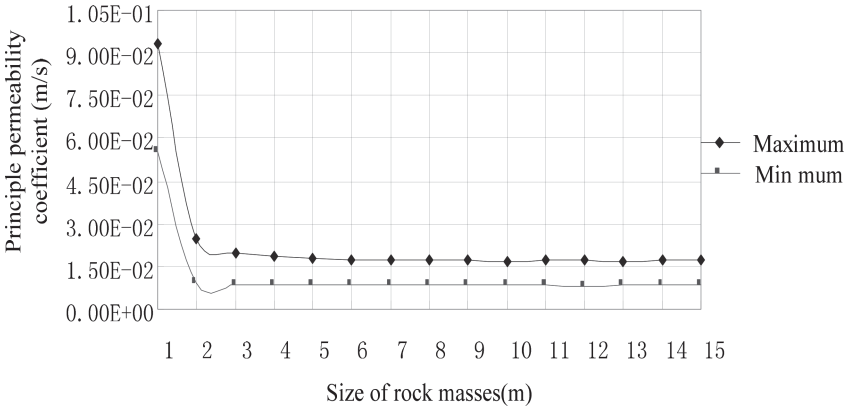


Figure 5. Principle permeability coefficient with different rock size considering hydro-mechanical coupling effect.

(Rutqvist et al. 2001, 2002, Tang et al. 2002), the hydro-mechanical boundary should be changed as follows: normal compressive stress ($\sigma_y$) valued 1 MPa ~ 15 MPa on upper and lower boundary, the water head with 1 m ~ 15 m on left boundary, with 0 m on right boundary, and linear variation of water head on upper and lower boundary from left to right. And change the seepage boundary conditions, the water head with 1 m ~ 15 m on upper boundary, with 0 m on lower boundary, and linear variation of water head on left and right boundary from the upper to the lower.

The results in Figure 5 showed that the permeability coefficient decreased with increasing stress, which indicated that elastic compressive deformation when enduring the compressive stress induced decreasing the hydraulic width so as to decrease the permeability coefficient. And the curve variation also indicated the size effect, and the seepage REV can be determined as 7 m × 7 m considering hydro-mechanical coupling effect, and corresponding maximum and minimum permeability coefficient were $K_{max} = 1.72 \times 10^{-3}$ m/s and $K_{min} = 0.841 \times 10^{-3}$ m/s.

## 4 CONCLUSIONS

From the above research, REV has been deeply investigated based on the combination of the fracture network technique and discrete element method, the results show that the proposed numerical method can really reflect the constitutive relationship and mechanical characteristics and determine seepage REV and corresponding mechanical parameters more correctly than other statistical method.

1. REV is a notional volume depending on the material property, so REV is related to the mechanical parameters of the rock masses. As a criterion to obtain correct different parameters of rock masses and describe the size effect of mechanical parameters, REV is important to be deeply investigated.

2. The fractures characteristics is important to determine the REV of rock masses, so the fractures network technique should be developed in detail. The calibration results of the proposed numerical method can better simulate the size effect and determine REV considering hydro-mechanical conditions.
3. The size effect of the permeability coefficient has been studied considering single seepage condition and hydro-mechanical coupling conditions. The results show that permeability decreases with stress increasing and the value tends to be a stable value while the sample size increasing.

The above results have indicated that REV is significant for correctly describing the property of the rock masses. Therefore, in order to better determine REV considering complex rock environment and rock structures, rational and reliable 3-dimensional fractures network technique, constitutive relationship of rock masses and analysis method should be deeply investigated in the future.

## ACKNOWLEDGEMENTS

The research is financially supported by 973 Program of China under Grant No. 2014CB046903, No. 106112014CDJZR200014 & 106112014CDJZR200015 by Fundamental Research Funds for the Central Universities, and the Project No. 51478065 by National Natural Science Foundation the authors gratefully acknowledge these supports.

## REFERENCES

Bai, M., Meng, F., Elsworth, D. 1999. Numerical modelling of coupled flow and deformation in fractured rock specimens. *Int. J. Numer. Anal. Meth. Geomech.* 23: 141–160.

Harrison, J.P. & Hudson, J.A. 2000. *Engineering Rock Mechanics. Part 2: Illustrative Workable Examples.* Sarkka, P. & Eloranta, P. (eds). Oxford: Pergamon.

Jing, L. 2003. A review of techniques, advances and outstanding issues in numerical modeling for rock mechanics and rock engineering. *Int. J. Rock Mech. Min. Sci.* 40(3): 283–353.

Kulatilake, P.H.S.W. & Panda, B.B. 2000. Effect of block size and joint geometry on jointed rock hydraulics and REV. *ASCE J. Eng. Mech. 1*26(8): 850–864.

Min, K.B. & Jing, L. 2003. Numerical determination of the equivalent elastic compliance tensor for fractured rock masses using the distinct element method. *Int. J. Rock Mech. Min. Sci.* 40: 795–816

Olsson, R. & Barton, N. 2001. An improved model for hydro-mechanical coupling during shearing of rock joints. *Int. J. Rock Mech. Min. Sci.* 38(3): 317–329.

Rutqvist, J. & Brgesson, L. 2001. Thermo-hydro-mechanics of partially saturated geological media: governing equations and formulation of four finite element models. *Int. J. Rock Mech. Min. Sci.* 38(1): 129–142.

Rutqvist, J. & Wu, Y.S. 2002. A modeling approach for analysis of coupled multiphase fluid flow, heat transfer, and deformation in fractured porous rock. *Int. J. Rock Mech. Min. Sci.* 39(4): 429–442.

Tang, C.A. & Tham, L.G. 2002. Coupled analysis of flow, stress and damage (FSD) in rock failure. *Int. J. Rock Mech. Min. Sci.* 39(4): 477–489.

Wang, M., Kulatilake, P.H.S.W. 2002. Estimation of REV size and three-dimensional hydraulic conductivity tensor for a fractured rock mass through a single well packer test and discrete fracture fluid flow modeling. *Int. J. Rock Mech. Min. Sci*. 39: 887–904.

Xia, Z.H., Zhang, Y.F., Fernand, E. 2003. A unified periodical boundary conditions for representative volume elements of composites and applications. *International journal of Solids and Structures* 40: 1907–1921

Zhou, C.B. & Yu, S.D. 1999. Discussion of representative elementary volume (REV) — a basic problem of valued mechanical parameter. *Journal of Engineering Geology* 7(4): 42–46

*Rock Dynamics: From Research to Engineering – Li et al. (Eds)*
*© 2016 Taylor & Francis Group, London, ISBN 978-1-138-02953-8*

# Dynamic stability analysis of rock slope based on permanent displacement ratio theory

W.D. Ni, G.B. Zhao & M.J. Sun
*Huadong Engineering Corporation, PowerChina, Hangzhou, Zhejiang, China*

ABSTRACT: A new method (Permanent Displacement Ratio Theory: PDRT) is proposed for analyzing dynamic stability of rock slope under seismic loading. The PDRT takes permanent displacement of rock slope as failure criterion, and provides an index which has a clear physical meaning to evaluate the dynamic stability of rock slope based on dynamic strength reduction theory. Hence, the PDRT fully combined the advantages of seismic permanent displacement method and dynamic stability factor method. An example given by E. Hoek and J. W. Bray is presented to demonstrate the computational process of PDRT, and then the dynamic stability law of the example under different scales of seismic intensity is analyzed. Finally, the PDRT is applied to study a rock slope case in Wenchuan earthquake regions of China, and a dynamic stability factor of 0.95 is obtained, the result matched the actual situation well, which testified the practicability of the PDRT.

## 1 INTRODUCTION

The dynamic stability issue of rock slope under seismic loading is a common focus of geotechnical engineering and earthquake engineering. At present, the evaluation methods of rock slope's dynamic stability mainly include two categories: Seismic Permanent Displacement Method (SPDM) and Dynamic Stability Factor Method (DSFM). The SPDM is well studied by plenty of scholars (Cai & Bathurst 1996, Wang & Lin 2010, Baziar et al. 2012), but this method has not been widely accepted in practical engineering application, because it cannot give a unified criterion of failure. Simultaneously, the DSFM mainly include: pseudo-static method (Yang et al. 2014), dynamic time history method (Liu et al. 2003) and dynamic strength reduction method (Li et al. 2007), etc. The DSFM can give a unified factor to evaluate the dynamic stability of rock slope, however it still has many defects, such as: the pseudo-static method cannot take dynamic features of slope material and fluctuation characteristics of seismic loading into account; the dynamic time history method can provide a change process of slope's dynamic stability during earthquake, but without the capability to give a synthetic index for evaluating slope's entire dynamic stability.

Therefore, this paper presents a new method for analyzing dynamic stability of rock slope, which fully combined the advantages of the SPDM and the DSFM. In this new method, three dimension distinct element software 3DEC is selected as computing platform, and dynamic strength reduction method is used to obtain the relationship function between rock slope's seismic permanent displacement and strength reduction factor. It is defined that rock slope developed in failure state when its seismic permanent displacement reaches a certain ratio of sliding surface's length, and the certain corresponding strength reduction factor is defined as dynamic stability factor. The proposed method takes permanent displacement of rock slope as failure criterion, and provides an index which has a clear physical meaning to evaluate the dynamic stability of rock slope based on dynamic strength reduction theory, consequently it has a broad application prospects.

## 2 METHODS

Related research shows that (Zheng et al. 2010): under seismic loading, rock slope's seismic permanent displacement increases with the increase of strength reduction factor, and increment of seismic permanent displacement is not obvious when the strength reduction factor is relatively smaller, however, the seismic permanent displacement increases quickly when the strength reduction factor over a certain value. As shown in Figure 1, the increment of seismic permanent displacement is inconspicuous when the strength reduction factor is relatively smaller, however, once the strength reduction factor over 1.55, the seismic permanent displacement has a significant increment. Therefore, the increase rate of seismic permanent displacement becomes faster gradually with the increase of strength reduction factor.

According to the above analysis, it can be found that the relationship between seismic permanent displacement and strength reduction factor is an obvious exponential function form. Therefore, a standard exponential function is adopted to describe this relationship, as shown in Equation 1.

$$D(k) = a \cdot e^{n \cdot k} \tag{1}$$

Where $D(k)$ = seismic permanent displacement; $k$ = strength reduction factor; $a$ and $n$ = undetermined coefficients, determined by the calculation results.

This paper combined the advantages of the SPDM and the DSFM, and based on which a new concept of Permanent Displacement Ratio Theory (PDRT) is proposed. In the PDRT, rock slope is defined into failure state when its seismic permanent displacement $D(k)$ reaches a certain ratio of sliding surface's length, and that certain corresponding strength reduction factor $k_0$ is defined as dynamic stability factor $F_{\mathrm{d}}$. As a result, Equation 2 can be obtained.

$$D(k_0) = a \cdot e^{n \cdot k_0} = \delta \cdot L \tag{2}$$

Where $\delta$ = permanent displacement ratio, $L$ = sliding surface's length, in plan sliding mode take the length of the sliding surface, in wedge sliding mode take the length of intersection line.

The solution of Equation 2 is just the value of dynamic stability factor $F_d$, as show in Equation 3.

$$F_{\mathrm{d}} = k_0 = \ln[(\delta \cdot L)/a]/n \tag{3}$$

The PDRT takes permanent displacement of rock slope as failure criterion, and provides an index $F_d$ which has a clear physical meaning to evaluate the dynamic stability of rock slope, it fully combined advantages of the SPDM and the DSFM, and the computation is very convenient in practical engineering application.

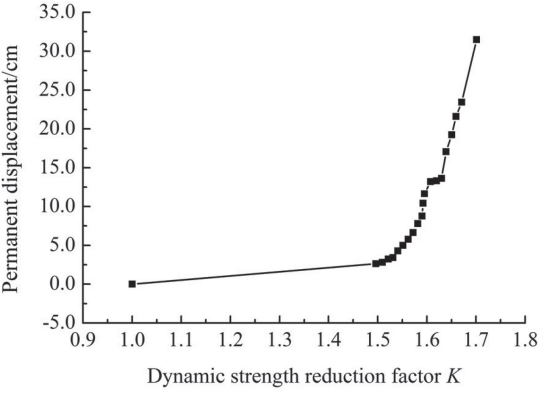


Figure 1. Relationship between seismic permanent displacement and strength reduction factor.

## 3 DYNAMIC STABILITY

A typical wedge slope example provided by Hoek & Bray (1981) is presented to demonstrate the feasibility and correctness of the PDRT. As shown in Figure 2, the difference of elevation between the vertices point and the nadir point of the line of intersection is 30.5 m, and the density of the rock mass is $2.563 \times 10^3$ kg/m$^3$. And other main geometric and mechanical parameters of the example are showed in Table 1.

Simple harmonics $a = \lambda\cos(2\pi ft)$ are used to simulate the seismic loadings with different degrees of seismic intensity. The values of the amplitude $\lambda$ are 0.31, 0.63, 1.25 and 2.50 m/s$^2$, corresponding to the acceleration amplitudes of V, VI, VII and VIII degrees of seismic intensity respectively (Hu 1998). The frequency $f = 2$ Hz and the duration of the seismic loading is 10 s.

The current research about seismic permanent displacement has not been given a unified standard of failure criterion, according to the related study (Zheng et al. 2010, Dai & Li 2007) and the relationship curve's characteristics of permanent displacement and strength reduction factor, a selection of 5% is given as the permanent displacement ratio $\delta$ in this paper. The length of the example's intersection line is 76.03 m via space geometry calculation, and then, the dynamic stability of the example in each degrees of seismic intensity is analyzed by the PDRT. Computation results are show in Table 2.

According to the computation results show in Table 2, dynamic stability factor $F_d$ of the wedge slope example is 1.25, 1.21, 1.16 and 1.09 corresponding to V, VI, VII and VIII degrees of seismic intensity respectively. Obviously, the wedge slope example's dynamic stability factor $F_d$ decrease with the increase of seismic intensity, meanwhile the decreasing amplitude of dynamic stability factor $F_d$ gradually increased with the increase of the seismic intensity, which is consistent with the actual engineering experience.

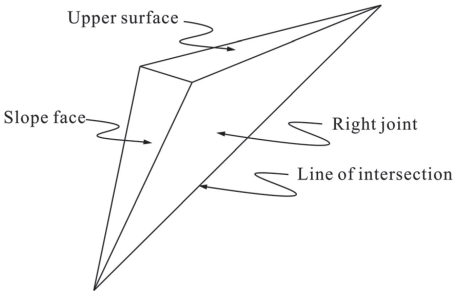


Figure 2. Sketch of wedge slope example.

Table 1. Geometric and mechanical parameters of the example.

| | Geometric parameters | | Mechanical indexes | |
|---|---|---|---|---|
| Position | Dip (°) | Dip direction (°) | Friction (°) | Cohesion (kPa) |
| Left joint | 45 | 105 | 20 | 23.9 |
| Right joint | 70 | 235 | 30 | 47.8 |
| Slope face | 65 | 185 | — | — |
| Upper surface | 12 | 195 | — | — |

Table 2. Dynamic stability computation results for each degrees of seismic intensity.

| Degrees of seismic intensity | V | VI | VII | VIII |
|---|---|---|---|---|
| Undetermined coefficient $a$ | $1.0 \times 10^{-28}$ | $2.0 \times 10^{-23}$ | $2.0 \times 10^{-16}$ | $2.0 \times 10^{-16}$ |
| Undetermined coefficient $n$ | 52.465 | 44.311 | 32.361 | 34.234 |
| Relative coefficient $R$ | 0.9840 | 0.9666 | 0.9519 | 0.9837 |
| Dynamic stability factor $F_d$ | 1.25 | 1.21 | 1.16 | 1.09 |

The computational process of PDRT is well demonstrated by this wedge slope example. In this process, the law of the example's dynamic stability factors under different degrees of seismic intensity is researched, and the results matched the actual engineering experience well, which verified the feasible and reasonable of PDRT.

## 4 CASE STUDY

Baihuadaqiao rock slope is located on the right bank of the Minjiang River, and the dip direction of the slope is 7°, the elevation of the slope's toe is 870 m and the crest is 1039 m, length of the sliding surface is 32.33 m, and the bedrock is lithic sandstone of Triassic xujiahe group. During the Wenchuan earthquake, the Baihuadaqiao rock slope collapsed along the bedding sliding surface, and the slumped rock mass completely destroyed the Baihua Bridge of China National Highway 213 below the slope.

A three-dimensional model is established according to the actual terrain by 3DEC, as shown in Figure 3. In this model, all rock blocks comply with the Mohr-Coulomb criterion and all joints are assigned the Coulomb slip criterion. And the primary parameters of rock mass and joint used in this model are show in Table 3 and Table 4 respectively.

The horizontal waveform data of the 2008 Wenchuan earthquake are selected as the seismic input, which were recorded on CD2 station in Chengdu by China Earthquake Administration. The main 50 seconds data of the waveform recorded by the BHE Channel (EW direction) and BHN Channel (NS direction) are shown in Figure 4 and Figure 5 respectively.

Dynamic stability analysis is carried out based on the dynamic module built-in 3DEC, and the Baihuadaqiao rock slope's relationship between seismic permanent displacement and strength reduction factor is shown in Figure 6.

As shown in Figure 6, under the Wenchuan earthquake seismic loading, the Baihuadaqiao rock slope's relationship between seismic permanent displacement and strength reduction factor is also match exponential function form. According to the dynamic stability computation results, the fitting function as show in Equation 4.

$$D(k_0) = 1.95 \times e^{57.88 \cdot k} \tag{4}$$

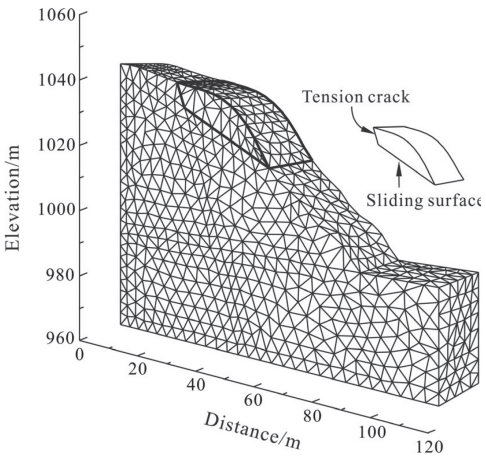


Figure 3. Sketch of wedge slope example.

Table 3. Mechanical parameters of rock mass in model.

| Density Kg·m$^{-3}$ | Bulk modulus GPa | Shear modulus GPa | Friction angle (°) | Cohesion MPa | Tensile strength MPa |
|---|---|---|---|---|---|
| 2667 | 15.1 | 10.2 | 48.5 | 11.4 | 5.6 |

Table 4. Mechanical parameters of joints in model.

| Location | Normal stiffness GPa·m$^{-1}$ | Shear stiffness GPa·m$^{-1}$ | Friction angle (°) | Cohesion MPa |
|---|---|---|---|---|
| Tension crack | 8.2 | 5.1 | 18.0 | 5.0 |
| Sliding surface | 10.2 | 6.4 | 31.5 | 15.0 |

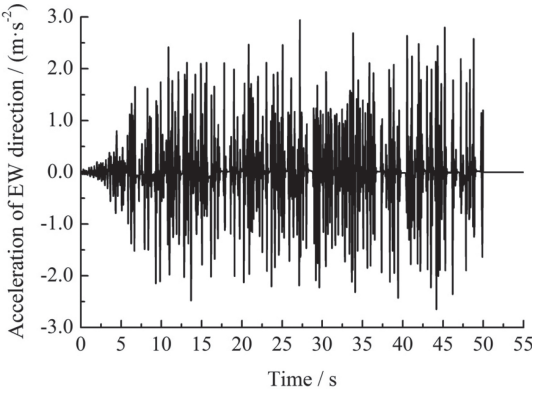


Figure 4. Acceleration time series of Wenchuan earthquake (BHE channel).

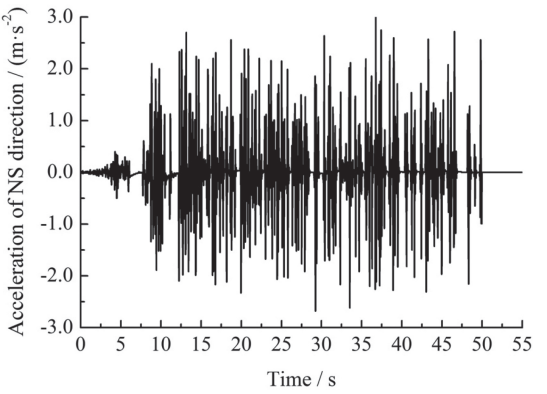


Figure 5. Acceleration time series of Wenchuan earthquake (BHN channel).

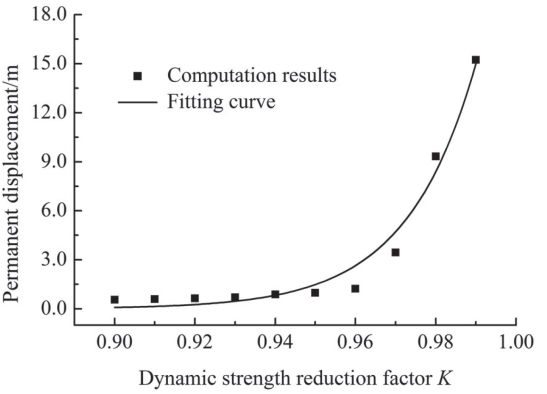


Figure 6. Dynamic stability computation results of the case study.

Therefore, the undetermined coefficients $a$ and $n$ is $1.95 \times 10^{-24}$ and 57.88 respectively. Then dynamic stability factor $F_d$ of 0.95 can be obtained by substituting these undetermined coefficients into the Equation 3. The computation result shows that the Baihuadaqiao rock slope should be instable under the Wenchuan earthquake seismic loading. Hence the computation result matched the situation of geological survey.

## 5 CONCLUSIONS

A new method: PDRT is proposed for analyzing the dynamic stability of rock slope under seismic loading based on 3DEC, The PDRT fully combined the advantages of the SPDM and the DSFM, takes permanent displacement of rock slope as failure criterion, and provides an index which has a clear physical meaning to evaluate the dynamic stability of rock slope based on dynamic strength reduction theory.

A typical wedge slope example provided by Hoek and Bray is presented to demonstrate the computational process of PDRT, by which the law of example's dynamic stability factors under different degrees of seismic intensity is researched, and the results verified the feasible and reasonable of the PDRT.

Finally, the PDRT is taken to study an actual case of Baihuadaqiao rock slope in Wenchuan earthquake region, a dynamic stability factor of 0.95 is obtained for Baihuadaqiao rock slope during Wenchuan earthquake, and the computation results matched the situation of geological survey well, which verified the engineering practicability of the PDRT.

## REFERENCES


Baziar, M.H., Rezaeipour, H. & Jafarian, Y. 2012. Decoupled solution for seismic permanent displacement of earth slopes using deformation-dependent yield acceleration. *Journal of Earthquake Engineering* 16(7): 917–936.

Cai, Z. & Bathurst, R.J. 1996. Deterministic sliding block methods for estimating seismic displacements of earth structures. *Soil Dynamics and Earthquake Engineering* 15(4): 255–268.

Dai, M.L. & Li, T.C. 2007. Analysis of dynamic stability safety evaluation for complex rock slopes by strength reduction numerical method. *Chinese Journal of Rock Mechanics and Engineering* 26 (supp. 1): 2749–2754.

Hoek, E. & Bray, J.W. 1981. *Rock Slope Engineering*. London: Institute of Mining and Metallurgy.

Hu, Y.X. 1998. *Seismic engineering*. Beijing: Earthquake Press.

Li, H.B., Xiao, K.Q. & Liu, Y.Q. 2007. Factor of safety analysis of bedding rock slope under seismic load. *Chinese Journal of Rock Mechanics and Engineering* 26(12): 2385–2394.

Liu, H.L., Fei, K. & Gao, Y.F. 2003. Time History Analysis Method of Slope Seismic Stability. *Rock and Soil Mechanics* 24(4): 553–556.

Wang, K.L. & Lin, M.L. 2010. Development of shallow seismic landslide potential map based on Newmark's displacement: the case study of Chi-Chi earthquake, Taiwan. *Environmental Earth Sciences* 60(4): 775–785.

Yang, C.W., Zhang, J.J. & Fu, X. 2014. Improvement of pseudo-static method for slope stability analysis. *Journal of Mountain Science* 11(3): 625–633.

Zheng, Y.R., Ye, H.L. & Huang, R.Q. 2010. Study on seismic stability analysis of a slope. *Journal of Earthquake and Engineering Vibration* 30(4): 173–180.

*Rock Dynamics: From Research to Engineering – Li et al. (Eds)*
*© 2016 Taylor & Francis Group, London, ISBN 978-1-138-02953-8*

# Numerical modeling of fracture behaviour of sandy mudstone under impact loading

L.X. Xie
*State Key Laboratory of Water Resources and Hydropower Engineering Science, Wuhan University, Wuhan, China*
*Department of Civil Engineering, Monash University, Clayton, VIC, Australia*

W.B. Lu & Q.H. Jiang
*State Key Laboratory of Water Resources and Hydropower Engineering Science, Wuhan University, Wuhan, China*

Q.B. Zhang & L. He
*Department of Civil Engineering, Monash University, Clayton, VIC, Australia*

ABSTRACT: In the construction of rock engineering, the soft rock tunnel is generally excavated using the drilling and blasting method, and thus the rock mass is subjected to dynamic loading. The fracture behavior of rock mass under dynamic loading is different from that under static loading. In order to investigate fracture behaviour of sandy mudstone subjected to dynamic loading, both experiments and numerical simulations are performed at different impact velocities, respectively. Experiments are carried out with the Split Hopkinson Pressure Bar (SHPB), and numerical simulation is conducted using Holomquist-Johnson-Cook (HJC) model incorporated in the software LS-DYNA. Numerical results are in good agreement with experimental data. According to the normal stress, maximum shear stress and transversal strain distribution, the fracture process is analyzed through simulation. It is found that soft rock materials have at least two failure modes instead of a single failure mode. The fracture mechanism of sandy mudstone is mainly governed by the shear and tension failure.

## 1 INTRODUCTION

Since the geological conditions of civil engineering are complex, the tunnel is inevitably within soft rock mass. Underground rock engineering is normally excavated using the drilling and blasting method, and thus the rock is subjected to dynamic loading. However, compared with the rock mass under static loading, there are different mechanical performances for rock mass under dynamic loading (Zhang & Zhao 2014). In order to investigate the influence of dynamic loading on tunnel after excavation, the performance of the soft rock mass under dynamic loading needs to be researched, which can provide the theoretical guidance to rapid tunnel support of soft rock mass, post protection as well as rock burst prevention.

At present, for investigating on the dynamic mechanical behaviour of rock-like materials, the concentration is mainly made on the experiments and numerical simulation. As for the experiments on hard rock, the substantial research achievements have been made, including the relationship between the strain rate and dynamic strength and Young's modulus (Chong 1980, Friedman 1970, Grady 1986a, Grady 1980b, Janach 1976, Lankford 1981, Li et al. 1994, Olsson 1991, Serengeti & Boozer 1961, Zhai et al. 2007), the constitutive model (Shigenori et al. 1977, Yu 1990, Shan et al. 2003, Tang 1981, Tao & Li 2011, Li et al. 2006), the fracture mode (Ju et al. 2010) and so on. In term of the soft rock, some investigations have been made on the constitutive model and the propagation of stress waves (Xie et al. 2013a, 2013b, Zhao et al. 2013). However, there is very limited research on fracture mode of soft rock.

With respect to research on the numerical simulation, it mainly involves the development of constitutive model for analyzing the dynamic failure and stress wave propagation of rock-like materials. The developed constitutive models mainly consist of HJC model (Holomquist et al. 1993), JH model (Johnson & Holmquist 1990a, Johnson & Holmquist 1990b), RHT model (Riedel 2000), K&C model (LSTC 2007), CSCM model (LSTC 2007), RDA model (Furlong et al. 1988), TCK model (Taylor et al., 1986), time dependent damage constitutive model (Shan, et al. 2003), and some of them like HJC, JH, RHT, K&C, CSCM model have been incorporated in the software-LS-DYNA. Since the software-LS-DYNA has the powerful capacity for analysis and calculation in the nonlinearity of geometry and material models, it is widely applied in the field of rock dynamics and blasting engineering. In LS-DYNA software, the HJC model takes the large deformation and damage evolution of rock-like material into account, thus it is used for simulation investigation on the Split Hopkinson Pressure Bar (SHPB).

The aforementioned studies are mainly focused on the mechanical performance of hard rock, and substantial research results have been achieved. Meanwhile, some investigations on soft rock have been made in some degree. However, there is very limited research on fracture mode of soft rock. In the paper, HJC model in the software LS-DYNA is applied to research on the failure mode of soft rock under different impact velocities. The work is arranged in five sections: after the general instructions, the finite element model size, HJC model and material property are introduced in the section 2. In section 3, the numerical simulation results are presented. In order to validate the reasonability in simulation, the comparison and discussion are presented in the section 4. Finally, section 5 outlines the failure behavior of soft rock under dynamic loading.

## 2 NUMERIOUS MODEL

### 2.1 *Model size*

In order to compare the simulation with the experiments, the numerous model has the same size as Split Hopkinson Pressure Bar (SHPB) used for experiment. The diameter of the finite model for SHPB is 14.5 mm, incident bar 500 mm, transmission bar 500 mm; the length of the sample is 6 mm, the diameter of the sample 4.5 mm. The solid 164 element with 8 node and hexahedron is applied. The nonlinear HJC model is chosen as rock material model. In order to improve the calculation accuracy, the meshes need to be refined, the bullet grid number is 3840, and the grid number of incident bar 19200, the grid number of transmission bar 11520, the grid number of the sample 11520, the model is as shown in the Figure 1. The Surface-surface contact algorithm is chosen between the sample and compression bar. The linear elastic model is chosen for the bullet, incident bar and transmission bar, the material constants are: density $P = 7850$ kg/m$^3$, Young's modulus E = 210 GPa, Poisson ratio $v = 0.3$. Rock material constants are summarized in Table 1.

### 2.2 *HJC constitutive model equation*

The HJC constitutive model allow for the dynamic mechanical response under the large strain, high strain rate and high confined pressure (Holomquist, et al. 1993), which is widely used to model rock subjected to dynamic loading, the model is mainly involved with three equations including damage evolution, yield surface equation and equation of state, as shown in Figure 2.

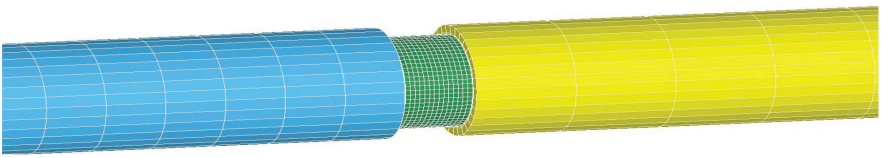

Figure 1. SHPB finite element model.

2.2.1 *Damage evolution equation*

The damage of HJC model is described by equivalent plastic strain and plastic volumetric strain, it can be expressed as

$$D = \sum \frac{\Delta\varepsilon_P + \Delta\mu_P}{\varepsilon_p^f + \mu_p^f} \tag{1}$$

where $\Delta\varepsilon_P$, $\Delta\mu_P$ denote equivalent plastic strain increment and plastic volumetric strain increment in one loop computation, respectively; $\varepsilon_P$, $\mu_P$ refer to equivalent plastic strain and plastic volumetric strain respectively; $\varepsilon_p^f + \mu_p^f$ is total plastic strain under constant pressure, P, the material will occur failure when accumulation plastic stain reaches to the value of $\varepsilon_p^f + \mu_p^f$. The specific expression is as follows;

$$\varepsilon_p^f + \mu_p^f = D_1\left(P^* + T^*\right)^{D_2} \tag{2}$$

and

$$D_1\left(P^* + T^*\right)^{D_2} \geq \varepsilon_{f_{\min}} \tag{3}$$

2.2.2 *Yield surface equation*

HJC model takes the dependent of yield surface equation on hydraulic pressure and strain rate into account, its strength is described with the normalized equivalent stress,

$$\sigma^* = \left[A(1-D) + BP^{*N}\right]\left(1 + C\ln\dot{\varepsilon}^*\right) \tag{4}$$

where $\sigma^* = \sigma / f_c'$ is normalized equivalent stress ($\sigma^* \leq \sigma_{\max}$, $\sigma_{\max}$) is maximum normalized strength the material can withstand), $\sigma$ is equivalent stress, $f_c'$ is static compression strength, D is damage variables ($0 \leq D \leq 1$); $p^* = p / f_c'$ denotes normalized static pressure, $p$ static pressure; 1 $\dot{\varepsilon} = \dot{\varepsilon} / \dot{\varepsilon}_0$ refers to dimensionless strain rate, $\dot{\varepsilon}, \dot{\varepsilon}_0$ is equivalent strain rate and reference strain rate, respectively; A is specified as normalized cohesion, which is the differ-

Table 1. Material parameters of HJC constitutive model.

| $\rho_0/kg/m^3$ | $G/Pa$ | $f_c'/pa$ | A | B | C | N | $S_{max}$ | $D_1$ | $D_2$ | $\varepsilon_{f\min}$ |
|---|---|---|---|---|---|---|---|---|---|---|
| 2.4E3 | 11.76E9 | 24.3E6 | 0.79 | 1.8 | 0.007 | 1.00 | 7.0 | 0.047 | 1.0 | 0.01 |
| $T/Pa$ | $Pc/Pa$ | $\mu_c$ | $P_1/Pa$ | $\mu_1$ | $k_1/Pa$ | $k_2/Pa$ | $K_3/Pa$ | $\dot{\varepsilon}_0$ | $f_s$ | |
| 3E6 | 8.0E6 | 6.3E-4 | 0.81E9 | 0.1 | 85E9 | –171E9 | 208E9 | 1E-6 | 0.004 | |

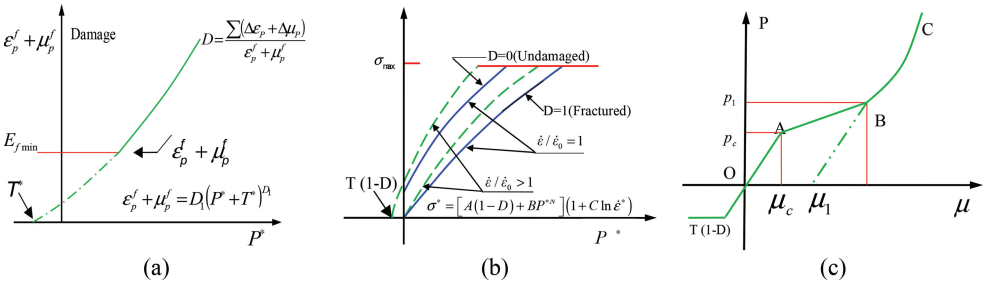


Figure 2. (a) damage model, (b) equivalent strength model and (c) relationship curve between hydrostatic pressure and volumetric strain (Holomquist et al. 1993).

ence between intact rock and completely damage rock; B refers to the normalized hardening coefficient; N is the hydraulic exponent, C strain rate coefficient.

### 2.2.3 *Equation of state*

The segmental equation of state is used to describe the relationship between the hydraulic pressure and volumetric strain.

The first region is linear elastic and occur at $p < p_c$, the expression for the relationship between $p$ and $\mu$ is as follows:

$$p = K_e \mu \tag{5}$$

and

$$K_e = p_c / \mu_c \tag{6}$$

The second region is referred to as the transition region and occur at $p_c \le p \le p_1$, in the region, the air voids are gradually compressed out of material producing plastic volumetric strain and damage, and the crack is initiated. The pressure for loading can be expressed as

$$p = p_1 + \frac{(p_1 - p_c)(\mu - \mu_1)}{\mu_1 - \mu_c} \tag{7}$$

where $p_1$ and $\mu_{p1}$ are compaction pressure and compaction volumetric strain.

Unloading in the region occurs along a modified path that is interpolated from the adjacent regions, the expression is as follows

$$p - p_{\max} = \left[ (1 - F) K_e + F K_1 \right] (\mu - \mu_{\max}) \tag{8}$$

$$F = \frac{\mu_{\max} - \mu_c}{\mu_1 - \mu_c} \tag{9}$$

In the region, the unloading pressure is expressed as

$$p - p_{\max} = K_1 (\bar{\mu} - \bar{\mu}_{\max}) \tag{10}$$

## 2.3 *Material properties*

In the simulation, the testing material constants of sandy mudstone is chosen as numerical simulation parameters, the density is given as 2400 kg/m$^3$, the compression strength 24.3 MPa, other material constants chosen from the literature (Holomquist, et al., 1993) are summarized in Table1.

# 3 NUMERICAL RESULTS

For the analysis on the fracture property of soft rock subjected to stress waves, according to the normal stress, maximum shear stress and transversal strain distribution, the fracture process is analyzed through simulation. The normal stress distribution in the direction of Z axle is showed in the Figure 3, the maximum shear stress distribution in the Figure 4, the transversal strain distribution in the direction of X axle in the Figure 5. In Figures 3–5, the representations of (a)–(f) are as follows:

(a) Stress waves propagate in the incident bar; (b) Stress waves travel to the rock elements; (c) Stress waves travel to the transmission bar; (d) Stress wave peak travel to the rock elements; (e) Stress wave peak propagate to the transmission bar; (f) Stress waves depart from rock elements.

### 3.1 *Analysis on stress change*

As seen from Figure 3(a) and Figure 4(a), the stress presents uniform distribution in the rock elements before the stress waves propagate to the rock elements, again, there is little compression and shear stress in the rock elements. Figure 3(b) and Figure 4(b) show, when stress waves propagate to the rock elements, the compression stress and shear stress increase with the increase in the stress wave intensity. As shown in the Figure 3(c) and Figure4(c), with the stress wave propagating, when they travel to the transmission bar, the compression stress and shear stress will increase as the amplitude of stress waves in sample elements increases.

When the stress wave peak travels to the soft rock element, since the reflection occurs for many times at the interface between the rock sample elements and pressure bar, leading to a trifle reduction of the compression. As stress waves reflect at the lateral surface and interface, the tensile stress will be induced in the rock elements as shown in Figure 3(d–e), here, the compression and shear stress present high level as shown in Figure 4(d–e). During the process, the tension, shear and compression stress produce the tensile and shear deformation. From Figures 4 and 5, it can be seen that the failure in the rock elements with higher tensile and shear stress is encountered.

When the stress waves depart from the rock sample elements, and propagate in the transmission bar, the compression stress is on the decline, however, since the irreversible shear deformation and tensile waves exist in the rock sample elements, the shear stress and tensile stress will remain high level, so that the failure keep on going, resulting in the intersection of crack. After the failure of rock elements, the stress will release, eventually, there is little residual stress left in the rock elements as shown in Figure 3(f) and Figure 4(f).

### 3.2 *Analysis on strain change*

From Figure 5(a–b), it can be seen that there is a little lateral deformation in the rock elements before the stress waves propagate to the transmission bar. As shown in the Figure 5(c), when stress waves travel to the transmission bar, since the stress waves reflect at the lateral surface, the transverse tensile deformation will increase, while the compression and shear stress still play an important role in the deformation of the rock elements, thus, the shear plastic deformation will also increase.

From Figure 5(d–e), it indicates that, when the stress wave peak travels to the rock elements, the tensile stress induced by reflected tensile waves at the lateral surface will produce more transverse deformation, and the failure for some of rock elements initiate at the maximum transverse deformation.

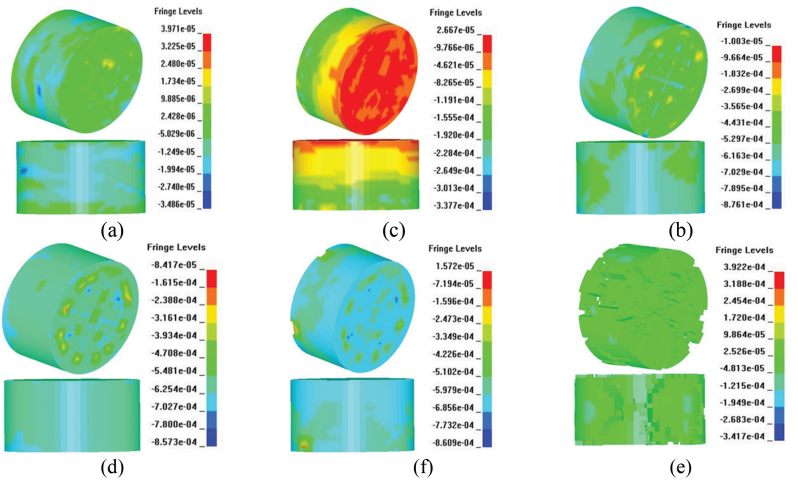


Figure 3. Stress distribution of rock element under stress wave along the Z axis (Unit: 1E10+11 Pa). *Positive denotes tension, negative denotes compression.

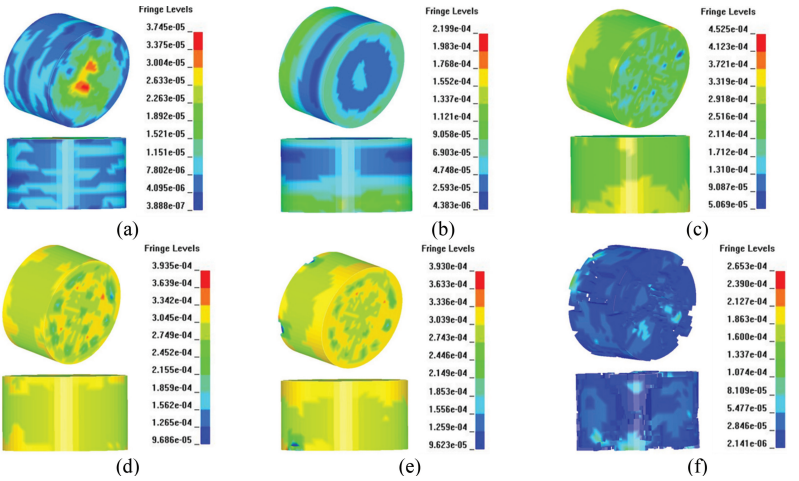


Figure 4. Max shear stress distribution of rock element under stress wave along the Z axis (Unit: 1E10+11 Pa).

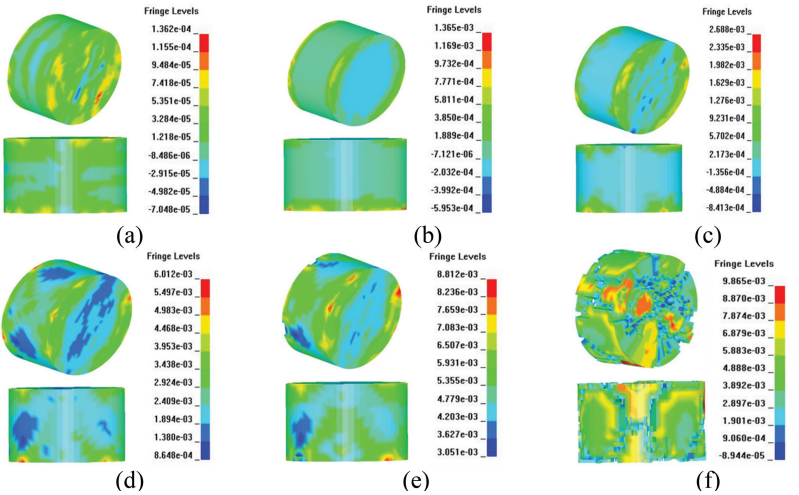


Figure 5. Strain of rock element under stress wave along the X axis.

As shown in Figure 5(f), due to the failure of the rock elements, the elastic deformation will recover after the stress releases, however, since part of the tensile deformation is not irreversible, the transverse deformation still remain large in the soft rock elements.

## 4 COMPARISON AND DISCUSSION

In order to validate the correction of the simulation results, the experiments on sandy mudstone ware made with four impact velocities, 17.54, 24.81, 27.74, 30.38 m/s. From Figure 6 (a-b), it can be seen that the dynamic strength and fracture degree increase as the strain rate increase, while the fracture size becomes smaller and smaller as strain rate increases. Under four impact velocities, the dynamic strengths corresponding to four strain rates, 373, 382, 488, 637 $s^{-1}$, are 53.4, 76.5, 90.9, 136.6 MPa, respectively. With the respect to failure mode, the axle splitting-tensile failure and shear failure present in the rock as shown in Figure 6 (b).

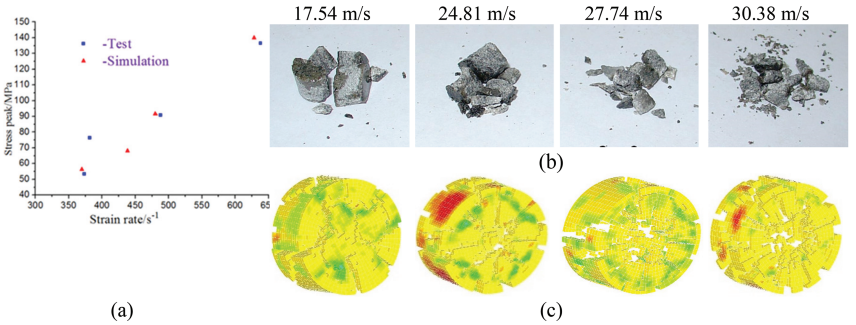


Figure 6. (a) Strength comparison, (b) experiment results, and (c) simulation results.

As seen from Figure 6, it shows that the dynamic strength and fracture property in the simulation are in good agreement with the experiment results.

## 5 CONCLUSION

In order to investigate the fracture behavior of sand mudstone under dynamic loading, mutual verification method of the experiment and simulation is applied. The experiments at four impact velocities are carried out with the SHPB, the numerical results are in good agreement with experiment results. Based on experiments and numerical simulation, the conclusion can be made as follows:

The tensile and shear stress with high level distribute in the rock sample elements as the stress waves propagate in the rock sample elements, when the tensile and shear stress exceed the strength limitation of soft rock, the failure of rock elements is encountered, and the stress peak increases with the increase in the strain rate, namely, the dynamic strength of soft rock is related to the strain rate.

The transverse deformation reaches to the maximum transverse deformation when the stress wave peak travels to the rock sample elements, here, the rock elements begin to failure, with the rock elements losing loading-bearing capacity, the stress will release, so that the elastic deformation recovers, however, since part of the tensile and shear deformations are irreversible, there is still high transverse deformation left in the rock elements.

The failure of rock elements occur at the place where the tensile and shear stress exceed the strength limitation, which implies the failure mode in the rock elements is tensile and shear failure. Therefore, the soft rock materials have at least two failure modes rather than a single failure mode, the failure mechanism of sandy mudstone is mainly governed by the shear and tension failure.

## ACKNOWLEDGEMENTS

This work is supported by Chinese National Programs for Fundamental Research and Development (973 Program) (2011CB013501), Chinese National Science Fund for Distinguished Young Scholars (51125037), the Fundamental Research Funds for the Central Universities (210274065) and the Financial Support from China Scholarship Council (the first author, CSC No. 201506270066). The authors wish to express their thanks for all the supporters.

## REFERENCES

Chong, K.P. 1980. Effects of strain rate on oil shale fracturing. *Int J Rock Mech Min Sci* 17: 35–43.
Friedman, M. et al, 1970. Observation of brittle-deformation features at the maximum stress of wetly granite and solenhofen limestone. *Int J Rock Mech Min Sci* 7: 297–306.

Furlong, J.R. et al., 1988. Numerical modeling of ceramic penetration experiments. P*roceedings of the Fourth TACOM Armor Coordinating Conference for Light Combat Vehicles*, Naval Postgraduate School.
Grady, D.E. 1980b. Continuum modeling of explosive fracture in oil shale. *Int J Rock Mech Mill Sci* 17: 147–157.
Grady, D.E. 1986a. The mechanics of fracture under high-rate stress loading. *Int. Rock Mech. Min. Sci. & Geomech. Abstr.* 23(5): 129–155.
Holomquist, T.J., Johnson, G.R. & Cook, W.H. 1993. A computational constitutive model for concrete subjective to large strains, high strain rates and high pressures. Jackson, N. & Dicker, S. (eds.) *The 14th International Symposium on Ballistics*. American Defense Prepare ness Association, 591–600.
Hu, S.S. & Wang, D.R. 2002. Dynamic constitutive relation of concrete under impact. *Explosion and Shock Waves* 22(3): 0242–0246.
Janach, W. 1976. The role of bulking in brittle failure of rock under rapid compression. *Int J Rock Mech Min Sci* 13: 177–186.
Johnson, G.R. & Holmquist, T.J. 1990a. In *Proceedings of Explomet Conference*, San Diego.
Johnson, G.R. & Holmquist, T.J., 1994b. In *High Pressure Science and Technology*, New York.
Ju, Y., Wang, H.J., Yang, Y.M., Hu, Q.A. & Peng, R.D. 2010. The simulation investigation on the deformation, fracture and energy in rock porous media for rock types under the action of stress waves. *Science in China (Technological Sciences)* 40(6): 711–726.
Lankford, J. 1981. The Role of Tensile Micro fracture in the strain rate dependence of the compressive strength of fine-grained limestone analogy with strong ceramics. *Int J Rock Mech Min Sci* 18: 173–175.
Li, X.B. & Gu, D.S. 1994. *Rock Impact Dynamics*. Changsha: Central South University of Technology Press.
Li, X.B., Zu, Y.J. & Ma, C.D. 2006. Constitutive model of rock under coupled static-dynamic loading with intermediate strain rate. *Chinese Journal of Rock Mechanics & Engineering* 25(5): 865–875.
Lindholm, U.S., Yeakley, L.M. & Nagy, A. 1974. The dynamic strength and fracture properties of dresser basalt. I*nt Rock Mech. Min.Sci. & Gemech. Abstr* 11(2): 181–191.
LSTC 2007. LS-DYNA Keyword User's Manual, Version 971. Livermore: Livermore Software Technology Corporation.
Olsson, W.A. 1991. The compressive strength of Tuff as a function of strain rate from$10^{-6}$ to $10^{3}$/sec. *Int J Rock Mech Min Sci,* 24(3): 231–250.
Riedel, W. 2000. Beton unter dynamischen lasten, Meso- undmakromechanische modelle und ihre parameter. PhD thesis, EMI-Bericht 6/00.
Serengeti, S. & Boozer, G.D. 1961. The effect of strain rate and temperature on the behavior of rocks subjected to triaxle compression. *Bulletin of the Mineral Industries Experiments-Station 4th Symposium on Rock Mechanics.*
Shan, R.L., Chen, S.L. & Li, B.Q. 2000a. Experimental study of granite constitutive properties under uniaxial impact. *Explosion and Shock Waves* 20(1): 32–38.
Shan, R.L., Xue, Y.S. & Zhang, Q. 2003b. Time dependent damage model of rock under dynamic loading. *Chinese Journal of Rock Mechanics and Engineering* 22(11): 1771–1776.
Shigenori, K. et al., 1977.On the mechanical behavior of rocks under impulsive loading. *Bulletin of the Faculty of Engineering Hokkaido University* 83: 51–62.
Tang, Z.P. 1981. *Dynamic Mechanical Properties of Epoxy Resin under High Strain Rate*. Master Thesis, University of Science & Technology of China.
Tao, J.L. & Li, K. 2011. A thermo-viscoelastic rate-dependent constitutive equation for cement mortar with damage. Explosion and Shock Waves 31(3): 269–273.
Taylor, L.M., Chen, E.P. & Kuszmaul, J.S. 1986. Microcrack induced damage accumulation in brittle rock under dynamic loading. *Computer Methods in Applied Mechanics and Engineering* 55: 301–320.
Xie, L.X., Zhao, G.M. & Meng, X.R. 2013a. Research on excess stress constitutive model of rock under impact load. *Chinese Journal of Rock Mechanics and Engineering* 32(sup1): 2772–2781.
Xie, L.X., Zhao, G.M. & Meng, X.R., 2013b. Research on damage viscoelastic dynamic constitutive model of soft rock and concrete materials. *Chinese Journal of Rock Mechanics and Engineering* 32(4): 857–864.
Yu, Y.L. 1990. Study on the dynamic behavior of magnetite and granite under high strain rates. *Explosion and Shock Waves* 10(3): 266–271.
Zhai, Y., Ma, G.W. & Zhao, J.H. 2007. Comparison of dynamic capabilities of granite and concrete under uniaxial impact compressive loading. *Chinese Journal of Rock Mechanics and Engineering* 26(4): 762–768.
Zhang, Q.B. & Zhao, J. 2014. A review of dynamic experimental techniques and mechanical behavior of rock materials. *Rock Mech Rock Eng.* 47 (4): 1411–1478.
Zhao, G.M., Xie, L.X. & Meng. X.R. 2013. A constitutive model for soft rock under impact load. *Explosion and Shock Waves* 33(2): 126–132.

*Rock Dynamics: From Research to Engineering – Li et al. (Eds)*
*© 2016 Taylor & Francis Group, London, ISBN 978-1-138-02953-8*

# The numerical simulation study on explosive shock response of ship large cabin

X. Xiong & X.Y. Wu
*Naval University of Engineering, Wuhan, Hubei, China*

J. Jin
*Navy Forces 91837, Zhoushan, Zhejiang, China*

ABSTRACT: The warship will under attack of missile in sea war and the missile will explosion in ship cabin with great probability. For improving anti-explosive shock ability of ship cabin structure and inner equipment, the FE model of cabin explosion include air was created. Then the shockwave transmission of single cabin explosion was calculated based on fluid-solid couple algorithm. The shock response of cabin was analyzed by comparing equipment base deforming and acceleration. The influence of cabin wall thickness to equipment shock response was evaluated based on calculating results and some conclusions were put forward. These conclusions has some reference value for arranging equipment reasonably in cabin and improving anti-explosion ability of cabin structure.

## 1 INTRODUCTION

In modern sea war, the ship would face battle anytime. The precision guided weapon usually form non-contact explosion in the ship cabin which could damage ship structure and equipment. Containing ship fighting capacity is very important when ship didn't sink. So it is important to analyzing ship structure shock damage. For calculating real shock response of ship equipment, it is necessary to simulate real explosion environment as much as possible. The methods of anti-explosive research are experiment, theoretical analysis and numerical calculation. The explosive experiment is most effective and directly method for test equipment anti-explosive performance. But explosive experiment cost is huge and unacceptable. In explosive condition, the cabin structure would acted by high non-linear load constitute with large aperiodicity load and plastic strain material which make precise response hardly be get by theoretical method. So the numerical calculating method is used widely for explosive shock analysis.

Ancient research of cabin explosion mainly focuses on different explosion condition response analysis of cabin structure. Hou (2007) analyzed shock wave transmission and grillage structure failure of cabin explosion. Du (2006) simulated ship side protective structure shock response and damage under attacking of semi armor piercing anti-ship missile. The simulation also considered couple acting of armor piercing, explosion piece and explosive shockwave. But the ship equipment response study on cabin explosion condition, especially analysis of cabin explosion combine with equipment response was little in ancient research.

The paper used explicit software LS_DYNA calculated cabin structure explosion shock response in air domain based on FE model of large equipment cabin structure. Then explosive shockwave transmission and equipment shock response in cabin were analyzed and some rules were summarized. The study conclusion could be provided reference to improving cabin structure and equipment anti-shock ability.

## 2 THEORY OF SOLVING METHOD

### 2.1 *Explosive shockwave transmission*

The ideal gas explosive shockwave transmission could be expresses by three dimensional Euler motion equations:

$$\frac{\partial q}{\partial t}+\frac{\partial f(q)}{\partial x}+\frac{\partial g(q)}{\partial y}+\frac{\partial h(q)}{\partial z}=0 \tag{1}$$

where q is the state vector; Equation (1) satisfy law of conservation of mass/momentum/energy; f(q), g(q) and h(q) means flow of state vector, which could be expressed:

$$q=\begin{Bmatrix}\rho\\ \rho u\\ \rho v\\ \rho w\\ E\end{Bmatrix} f(q)=\begin{Bmatrix}\rho u\\ \rho u^2+p\\ \rho uv\\ \rho uw\\ (E+p)u\end{Bmatrix} g(q)=\begin{Bmatrix}\rho u\\ \rho uv\\ \rho v^2+p\\ \rho vw\\ (E+p)v\end{Bmatrix} h(q)=\begin{Bmatrix}\rho w\\ \rho uw\\ \rho vw\\ \rho w^2+p\\ (E+p)w\end{Bmatrix} \tag{2}$$

where ρ is the material destiny, u, v and w are three velocity components at rectangle coordinate system, p is the ressure, E is gas total energy.

### 2.2 *The fluid-solid coupling algorithm*

The fluid-solid coupling algorithm could couple structure and fluid by using some constrain method and achieve mechanical parameters transmission. The coupling algorithm achieves coupling relationship by define coupling face between structure and fluid. The coupling face is force transmitter between Euler grid and Lagrange grid and is fluid domain border of Euler grid too. The algorithm steps are shown as:

1. Searching fluid elements which include structure nodes, distributing structure node parameters (mass, momentum, node force) to fluid element nodes:

$$m(M,F)_i^f=m(M,F)_i^f+h_i\cdot m(M,F)_s \tag{3}$$

2. Calculating new fluid node acceleration (velocity):

$$a(v)_i^f=\frac{F(M)_i^f}{m_i^f} \tag{4}$$

3. Constraining structure node acceleration (velocity):

$$a(v)_s=\sum_{i=1,8}h_i\cdot a(v)_i^f \tag{5}$$

where m, M, F is node mass, momentum, node force; a, v is node acceleration and velocity; h is node numbers in single fluid element; f and s is element symbol of fluid and structure. In the calculation of this paper, detonator and air were described by Euler grid and cabin structure was described by Lagrange grid.

## 3 CABIN FE MODEL CREATING

### 3.1 *Material constitutive equation and state equation*

The ship cabin structure material used double linear elastic-plastic constitutive equation and material strain rate effect was described by Cower-Symonds model. Dynamic yield strength $\sigma_d$:

$$\sigma_d = \left[\sigma_0 + E \cdot E_h \cdot \varepsilon_p / (E - E_h)\right] \cdot \left[1 + (\dot{\varepsilon} / D)^{1/n}\right] \tag{6}$$

where $\sigma_0$ is static yield strength; E is elastic modulus; $E_h$ is strain hardening modulus; $\varepsilon_p$ is effective plastic strain; $\dot{\varepsilon}$ is equivalent plastic strain rate; D, n is constant. The material failure criterion was maximum plastic strain criteria. In the FE model, material of cabin structure was steel, so the parameters of steel are $D = 40.4S^{-1}$; $n = 5$; $\sigma_0 = 2.35 \times 10^8$ Pa; $E = 2.1 \times 10^{11}$ Pa; $\gamma = 0.3$; $E_h = 2.5 \times 10^8$ Pa; $\rho = 7800$ Kg/m$^3$; failure strain $\varepsilon_f = 0.28$.

The JWL state equation of detonate is:

$$p = A\left(1 - \frac{\omega}{R_1 V}\right)e^{-R_1 V} + B\left(1 - \frac{\omega}{R_2 V}\right)e^{-R_2 V} + \frac{\omega \rho_0 e}{V} \tag{7}$$

where p is the pressure; A, B, ω, $R_1$, $R_2$ is constant; $V = \rho_0/\rho$; $\rho_0$ is initial destiny; e is mass ration internal energy. The parameters of detonate are $\rho_0 = 1630$ Kg/m$^3$; $A = 5.5748 \times 10^{11}$ Pa; $B = 7.83 \times 10^9$ Pa; $R_1 = 4.5$; $R_2 = 1.2$; $\omega = 0.34$; $e = 4.969 \times 10^6$ J/Kg; $D = 8000$ m/s.

It is supposed that air is non-viscous ideal gas and explosive shockwave expanding procedure is adiabatic. The air state equation is:

$$p = (\gamma - 1)\frac{\rho}{\rho_0}E \tag{8}$$

where p is air pressure; γ is adiabatic exponent; ρ is air density; E is air inner energy. The parameters of air are $\rho_0 = 1.29$ kg/m$^3$; $\gamma = 1.4$; $E_0 = 2.5 \times 10^5$ Pa.

### 3.2 *Creating of structure model*

For analyzing cabin explosion, the cabin which includes equipment needs to be created. The created FE model was reduction scale model which scale ration was 1:10 because of computer condition limitation. The FE model was shown as Fig. 1. The outer part is air element which size is $3.6 \times 1.2 \times 2.1$ m and element size is 0.05m. The air model was divided 72756 hex elements and 78477 nodes. The middle part is two cabins structure which size is $3.0 \times 1.5 \times 0.6$ m and initial shell thickness is 0.005 m. The cabin grillage structure could be equivalent to average shell thickness. If rectangle grillage length is L; width is B; slab thickness is D; its section area of n longitudinal skeleton is $F_i$; its section area of m transverse skeleton is $F_j$. Then the cabin equivalent slab thickness is:

$$\overline{\delta} = (LB\delta + \sum_{i=1}^{n} F_i L + \sum_{j=1}^{n} F_j B) / (LB) \tag{9}$$

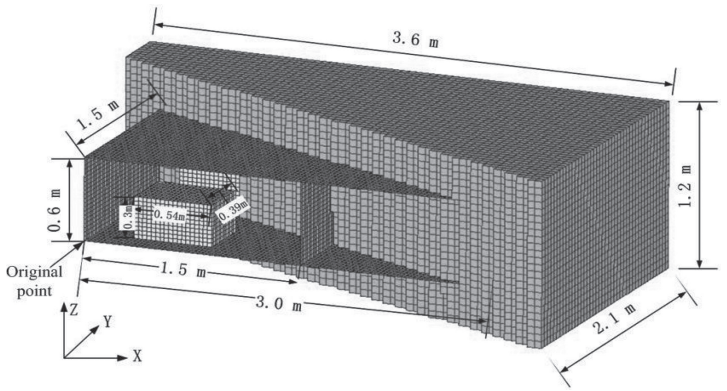


Figure 1. FE model of cabin structure.

The cabin inner is two simplify equipment model which be used to study shock response of cabin explosion. The equipment size is $0.54 \times 0.39 \times 0.3$ m; mass is 5000 Kg and divided by solid element which size is 0.03 m. Non-reflective border condition was added on six border face of air elements and cabin constrain was added on cabin bottom face. The equipment was connected by cabin and damage effect wasn't considered. The detonation is spherical TNT which size is 0.04 m. The explosive shock response was calculated by explicit software LS-DYNA.

## 4 SHOCK SIMULATING CALCULATION

### 4.1 *Explosive shockwave transmitting calculation in cabin*

For study on shockwave transmitting rule in cabin, the 0.04 s simulation of explosion in cabin which detonate is 0.04 m radius spherical TNT and detonate point coordinate is (0.1 m, 0.1 m, 0.5 m). Fig.2 is explosive shockwave transmitting isosurface figure of different time cabin XY plane. The figure could be shown that the shockwave began to spread from detonate point (a); at 0.007s, the shockwave converged at corner bypass equipment and strength was bigger than incident shockwave (b); at 0.0117 s, shockwave began transmit reversely and split two part, one part formed reflecting shockwave on equipment surface and another part go down along cabin wall (c); at 0.014 s, the shockwave converged at two corners of cabin and strength of lower right corner was big than upper left corner's (d); at 0.019 s, the shockwave transmitted narrow space between equipment and cabin wall, the shockwave strength was bigger than other space of cabin (e); at 0.025 s, the shockwave transmitting along cabin wall and equipment surface converged between two equipment and transmitted to upper right corner of cabin (f); at 0.03 s, the shockwave converged at upper right corner and strength was much lower than initial strength (g); at 0.038 s, the shockwave peak value zone transmitted to near equipment again (h). After 0.04 s, the shockwave would transmit in cabin follow above rules until shockwave energy exhausted and cabin flow field became stability.

From above analysis, the conclusion could be put forward that explosive shockwave is radial transmitting at beginning. Until form reflection on cabin wall or converge at corner. Then shockwave would transmit along cabin wall and equipment surface. In Fig. 2, it could be seen that shockwave pressure would increase at cabin structure converging place or space mutating place. So cabin structure at these places should be strengthened and equipment shouldn't be placed at these places.

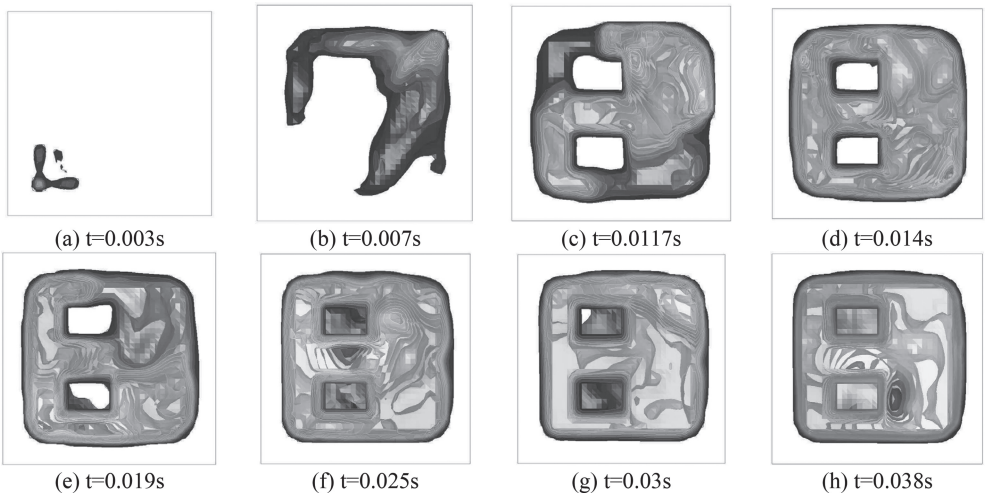


Figure 2. Shock wave pressure distributing of different time.

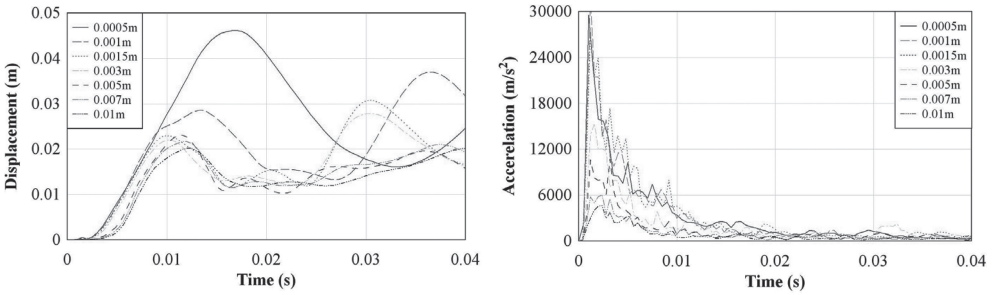


(a) Time VS Displacement curves (b) Time VS Acceleration curves

Figure 3. Explosive shock response results of different cabin thickness.

### 4.2 *Shock response calculation of cabin equipment*

The ship cabin is welded by steel sheet. The different thickness steel sheet would produce different deforming and reflect shockwave pressure for same explosion. So it is necessary to analysis steel sheet thickness influence to equipment shock response. The paper calculated 0.04 s shock response which cabin wall thickness was 0.0005 m, 0.001 m, 0.0015 m, 0.003 m, 0.005 m, 0.007 m, 0.01m and cabin equipment base displacement and acceleration time domain results were shown as Figure 3.

In Figure 3(a), the equipment base displacement is descending with cabin wall thickness increasing. The displacement descends fast when thickness is between 0.0005 m and 0.0015 m. When thickness is bigger than 0.0015 m, the base first deformation still descends but amplitude is little. The base has bigger second deformation when thickness is lower than 0.003m. When thickness is bigger than 0.005 m, the second deformation amplitude is little and base displacement curve is basically same. The cabin structure didn't cause big area plastic deformation which could be analyzed from curve's shape. After the first wave shock acting, cabin wall spring-backed. But base deformation increased with the second wave acting and the second deforming value even bigger than the first's when thickness is lower than 0.003 m. In Figure (b), all accelerating curves appear exponential decrease. The curve peak value is basically same when thickness is 0.0005 m, 0.001 m and 0.0015 m and the others curves peak value linear decrease with increasing of cabin wall thickness.

From above analysis, the conclusion could be put forward that cabin equipment shock response would be huge whenever deformation or acceleration when cabin wall thickness is little. But the values would descend quickly when thickness is bigger than 0.0015 m. So it is considered that certain thickness cabin wall could reduce shock effect of cabin equipment obviously. For decreasing base deformation, the thickness should bigger than 0.003 m. For decreasing shock acceleration, the thickness should be selected based on equipment anti-shock ability. The cabin had 0.65 m explosive crevasse when cabin wall thickness was 0.0005 m and had 0.4 m explosive crevasse when cabin wall thickness was 0.001 m. But the displacement and acceleration curves in Fig. 3 didn't reflect the change of explosive energy losing caused by explosive crevasse. So it is concluded that explosive crevasse has limited influence to equipment shock response and shouldn't consider its influence unless it is necessary.

## 5 CONCLUSIONS

Some conclusions could be draw based on above calculation and analysis:

1. The cabin FE model which includes big equipment was created and analyzed based on explosive shockwave transmitting theory and fluid-structure couple algorithm. The conclusions drew from analysis have certain reference value for improving anti-shock ability of cabin structure and equipment.

2. The shockwave transmitting is complex in cabin which includes big equipment. The shockwave peak area is focus on place where cabin wall converge and nearby equipment. The conclusion could provide reference for important equipment placing.
3. Different cabin wall thickness has important effect to equipment shock response. Generally, cabin wall thickness is bigger and the shock response of equipment is smaller. But considering mass limitation of ship weight, certain thickness value could balance anti-shock and ship weight.
4. Limited by calculating condition and experiment condition, the paper did a qualitative analysis of cabin anti-shock ability. But some valuable conclusions could be got for improving cabin anti-shock ability.

## REFERENCES


Chun, S. 2005. Nonlinear fluid-structure interaction of flexible shelters under blast loading. *Structural Dynamics & Materials Conference*. Texas.

Dai, Y.B. 2006. Ultimate bearing capacity calculation and reinforcement analysis of square cabin under explosive impact load. *Journal of vibration and shock* 25(3):124–130.

Du, Z.P. 2006. Numerical simulation of anti-ship missile attack warship broadside process. *Journal of Harbin Engineering University* 27(4):484–487.

Hou, H.L. 2007. Study on the blast load and failure mode of ship structure subject to internal explosion. *Explosion and shock waves* 23(2):151–157.

Kitamura, O. 1998. Comparative study on collision resistance of side structure. *Marine Technology* 34(2):293–308.

Livemore Software 2003. LS-DYNA Keyword User's Manual 970. California.

Mei, Z.Y. 2004. Dynamic response researches of ship's stiffened plate structure under explosive load. *Explosion and shock waves* 24(1):80–84.

Xie, W.F. 2007. Dynamic response of deformable structures subjected to shock load and cavitation reload. *Computer Mech* 40(3):667–681.

Zhu, X. 2004. Plastic dynamic response and crevasse research of ship panels subjected to air contact explosion. *Ship building of China* 45(2):43–50.

*Engineering applications and case studies*

This page intentionally left blank

*Rock Dynamics: From Research to Engineering – Li et al. (Eds)*
*© 2016 Taylor & Francis Group, London, ISBN 978-1-138-02953-8*

# The dynamic simulation of ground motion of Lushan earthquake by finite element method

Y.Z. Bai, X.W. Xu & Q. Zhou
*Key Laboratory of Active Tectonics and Volcano, Institute of Geology, China Earthquake Administration, Beijing, China*

ABSTRACT: In this paper, the finite element method with 6-node pentahedral elements will be applied to simulate the strong ground motion due to the Lushan earthquake fault dynamic rupture. In order to approximate the geophysics conditions in the region near the Lushan earthquake structure and the frictional fact along the Lushan earthquake fault plane, the layer model with different P and S wave velocities and the slip-weaken constitutive will be considered in the construction of finite element model corresponding to the Lushan earthquake fault. For validating the lastly computational result, the comparison between the calculation results and the stations records will be carried out. Basing on the above research achievements, the theoretical ground motion maps for the variation of east-west velocity component of ground motion in the earthquake process will be shown. Furthermore, for studying the correlations between the ground motion and the distribution of landslides brought by Lushan earthquake, we will simply analyze and summary the temporal and spatial distribution of ground motion caused by the Lushan earthquake. Just as the record data shown, the simulation result also shows the effect of hanging wall of fault is not so obvious, which maybe stems from the special characters of motion of blind-thrust fault during the earthquake rupture process.

## 1 INTRODUCTION

The Lushan $M_S$7.0 earthquake happened on 20 April, 2013, is another destructive earthquake which located in Sichuan Province almost exactly five years after the 2008 Wenchuan earthquake. Its epicentre is at 30.314°N, 102.934°E, in Lushan Country, along the southern segment of the Longmenshan thrust belt. But the earthquake structure of Lushan is different to that of the Wenchuan.

After the Lushan earthquake, to the present, there are a lot of research achievements on the landslide triggered by earthquake (Zhou 2014), fault slip process inversions (Wang 2013) and geology surveies (Xu et al. 2013), but there are few on the strong ground motion computation. Although there were some ground motion computation results (Zhang 2013), these computations were mainly based on the kinematic source simulation of ground motion computation (kinematic models). The computation basing on the dynamic fault rupture (dynamic models) is not reported in seismic society in China. In fact, kinematic models often assume some sort of stochastic rupture time and slip distribution on the fault. A difficulty with such models is that there is no guarantee that such rupture patterns are physically plausible. Dynamic models assure that the faulting models obey certain physical laws (elasticity and friction), but uncertainties in the dynamic models are the frictional law and fault stress persist (Oglesby 2002).

In this paper, in order to compute the ground motion due to the fault rupture dynamics in Lushan earthquake, we will build the finite element model of Lushan earthquake fault basing on present research achievements of earthquake structure. For the stress persist and fault frictional coefficients before the earthquake happened, which is not easy to get, we will assume they distribute uniformly along the fault.

## 2 TECTONIC BACKGROUND AND MODEL PARAMETERS

The epicentre of Lushan earthquake (red star) and the earthquake fault are shown in Figure 1. The fault geometry scale and the bury depth will be set according to the result of Xu (2013), which is listed in Table 1. In order to account for the layer geophysic features of Longmenshan area, we will apply the Shan's (2008) geophysical layer model whose paramteres are shown in Table 2.

## 3 FINITE ELEMENT MODEL OF LUSHAN EARTHQUAKE FAULT

Just as shown in Figure 1, we will build the finite element model of study area containing the Lushan earthquake fault. The dimensions of model in direction of normal to and along the fault strike, and depth direction are 200 km, 200 km, and 42 km respectively, as shown in Figure 2. We will use about 2,240,000 6-node pentahedral elements to fill the whole model space. The scale of the element is 1000 m × 1000 m × 750 m. The time step in the computation is set to 0.05 s. On the fault surface, the frictional relation will be applied the slip-weaken relations (Ida 1972, Palmer & Rice 1973), as shown in Eq. (1). In Eq. (1), the frictional coefficient $f$ decreases linearly as a function of slip from the static frictional coefficient $f_s$ to the dynamic frictional coefficient $f_d$ over a cricital slip-weakening distance $D_c$.

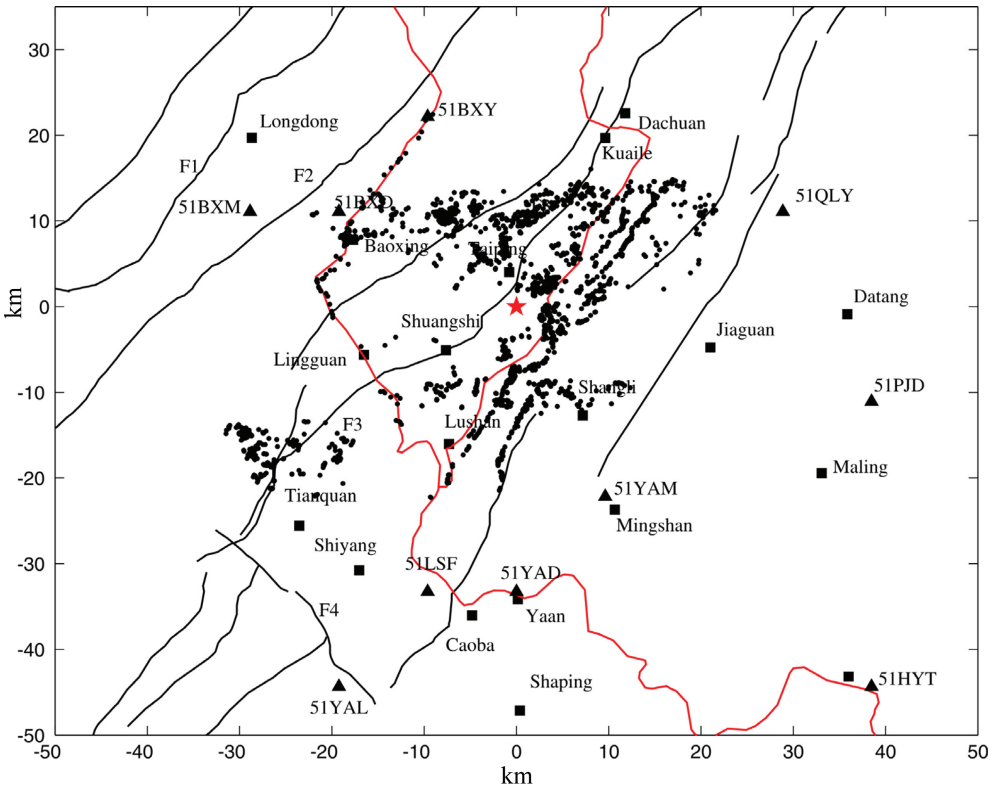


Figure 1. The epicenter and the fault of Lushan earthquake.
★ - epicenter location; ■ - city or country; ▲ - ground motion station; • - landslide location.
F1-Gengda-Longdong fault; F2-Yanjing-Wulong fault;
F3-Shuangshi-Dachuan fault;
F4-Rongjing fault. The red line is the river.

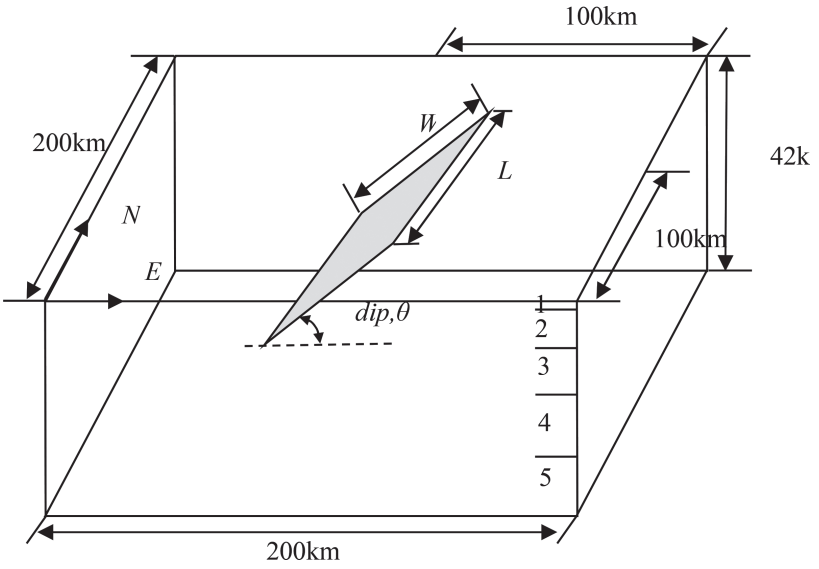


Figure 2. The geometry model of computation region.
*L*-fault strike length; *W*-fault dip width; *θ*-dip angle
The number 1–5 is the lay model whose parameters are shown in Table 2.

Table 1. The parameters of Lushan earthquake fault.

| Fault length (km) | Fault dip width (km) | Earthquake Magnitude | Earthquake moment (n·m) | Focus depth (km) | Slip angle | Dip angle | Strike |
|---|---|---|---|---|---|---|---|
| 66 | 30 | 6.7 | $1.54 \times 10^{19}$ | 16 | 88° | 38° | 205° |

Table 2. Layered crustal model in the area of the Longmenshan thrust belt (Shan et al. 2009).

| Layer number | Thickness (Km) | P wave velocity (Km*s$^{-1}$) | S wave velocity (Km*s$^{-1}$) | Density (Kg*m$^{-3}$) |
|---|---|---|---|---|
| 1 | 1.5 | 2.5 | 1.2 | 2100 |
| 2 | 6.5 | 4.5 | 2.6 | 2500 |
| 3 | 9.0 | 6.2 | 3.6 | 2800 |
| 4 | 12.0 | 6.2 | 3.6 | 2850 |
| 5 | 12.0 | 6.8 | 3.8 | 2950 |

$$f = \begin{cases} f_s & \dot{D}(t) = 0 \\ f_s - (f_s - f_d)\dfrac{D(t)}{D_c} & D(t) \le D_c \\ f_d & D(t) > D_c \end{cases} \quad (1)$$

The coefficient of dynamic friction is chose to be constand, $f_d = 0.62$ and the static friction is $f_s = 0.65$. These values are consistent with laboratory friction experiments at small slip (Andrews 2011, Wen 2012). At the same time, we will set the $D_c$ to be 0.4 m (Guatteri 2004). The failure of fault surface is applied the Coulomb criterion (Guatteri 2004) and the cohesive

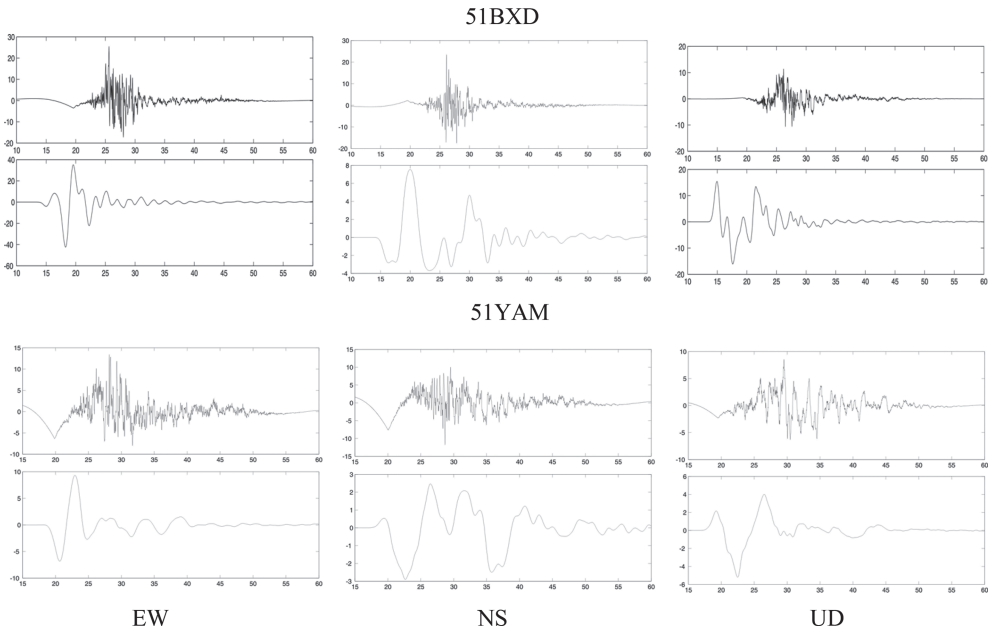


Figure 3. The comparison of ground motion velocity computed by data and FEM at station 51BXD and 51YAM.

force is set 6 MPa (Wen 2012). After setting the model parameters, we will run the computation on the IBM sever of System x3400 M3 who has 72G internal memory and two Intel(R) Xeon R-E5620 CPUs. It will take the IBM sever almost 70 hours to carry one simulation experiment.

## 4 COMPUTATIONAL RESULT AND ANALYSIS

In order to verify the computation result, we will firstly compare the velocity of ground motion computed by record data and the simulations in this paper. As shown in Figure 3, the comparison is set on the station 51BXD and 51YAM who are located in the hanging wall and footwall of the Lushan earthquake fault respectively. The unit of ground motion velocity in Figure 3 is cm/s. In Figure 3, for each station, the upper subplot is the ground motion velocity computed directly from the record data (Boore 2005) and the lower subplot is ground motion velocity gotten by finite element method. In Figure 3, from left to right, the subplot show the ground motion velocity components in East-West (EW), North-South (NS), and Up-Down (UD) directions. Through Fig. 3, we can find that the magnitude of ground velocity is approximated for two computation methods. There are more high frequency components in the ground velocity computed directly from recorded data than that result of this simulation. In addition, the position of ground velocity maximum in simulation is little earlier than that computed directly from recorded data. The above differences possibly stem from the simple geophysical layer model of simulation, assumption of uniform distribution of initial stress along the fault surface, and the shortness of finite element method on dealing with high frequency seismic waves. But the simulation result of here can be accepted, since the agreement of ground motion velocity magnitude with that of computing directly from the record data. In addition, the duration of ground motion velocity in EW, NS, and UD direction is almost the same for two stations for two computational methods.

Before this paper was prepared, we have done some research work on the analysis of ground motion record, we have found that the component of ground motion in EW and NS

direction is almost same and both of them are much stronger than that of UD direction. So in this paper, we will show the ground velocity process in EW direction during the happening of Lushan earthquake. In Figure 4, the variation of ground velocity in EW direction is shown in 60s and the black rectangle is the fault projection on the ground surface. The long side of each figure in Figure 4 stands for the direction normal to fault strike and the short one of figure for the fault strike direction. The unit in direction of along and normal to fault strike is m. The unit of ground motion velocity in Figure 4 is m/s.

In Figure 4, at the beginning of fault movement, the hanging wall effect of ground motion velocity is relatively obvious, such as the t = 10 s in the figure. When t = 10 s, from Figure 4, we can see the Peak Ground Velocity (PGV) of this time is located on the hanging wall fault and the PGV of footwall is not so large as that of hanging wall. But with the time going on, the PGV of hanging wall and footwall is almost equal. Even if the hanging wall effect is exist at the initial stage of earthquake, since the PGV of both the hanging wall and foot wall are not so large, so the hanging wall effect is not very obvious. The hanging wall effect of ground motion for Lushan earthquake is not obvious perhaps due to earthquake structure of Lushan event is blind-inverse fault.

The movement of ground motion due to the inverse fault earthquake is main squeeze and uplift motion (Bai et al. 2011). For Lushan earthquake, because of the scale in dip width is relatively small and the structure is buried, the uplift motion of ground surface is not obvious (Xu et al. 2013). From Figure 4, we can understand the squeeze movement of ground in a rough way. At the initial stage of earthquake, for an example t < = 10s, the squeeze movement in the fault projection is very complex. For the whole computational region, there is the strongest variation for EW ground motion velocity component in this area. From the Fig. 1, we can infer that the most landslide is located in this area. So from this fact, we can qualitatively conclude that there may be some positive correlation between variation of ground motion velocity and landslide distribution. And, comparing the ground motion velocity value of initial stage (t = 10s) with that of other stage, we find the PGV is mainly occurred at the initial stage of earthquake. Because the value of ground motion in other time are smaller than that in the initial stage, the main energy of Lushan earthquake is possibly radiated in the initial stage. After the initial stage of earthquake, the ground velocity will become smaller with the increasing of the time.

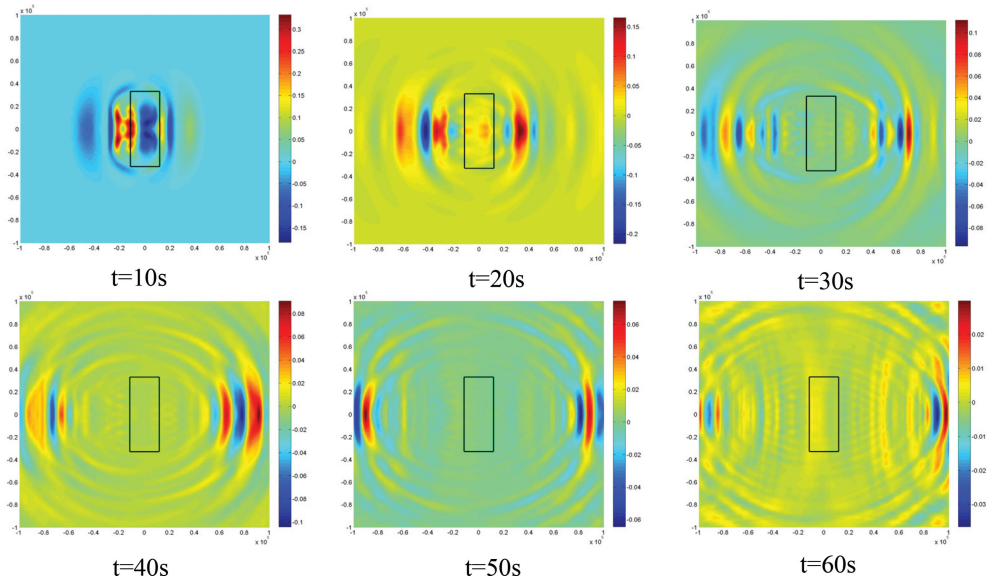


Figure 4. The snap shot of the ground velocity in EW direction.

## 5 CONCLUSION

With the geophysical research achievements of Longmenshan region, in this paper, we apply the finite element method with 6-node pentahedral elements and the slip-weaken constitutive along the fault surface to establish the numerical model of Lushan earthquake structure. Then we compute the ground motion velocity, verified by the ground motion velocity calculated from the strong motion record. Lastly, we show the snap shot of the ground velocity of EW component and analysis the correlation between the ground motion velocity and landslide. Basing on the result analysis, we find that (1) the hanging wall effect of ground motion in Lushan event is not so obvious, but at the initial stage of earthquake, hanging wall effect is relatively obvious; (2) the seismic energy is mostly radiated in the initial stage of earthquake; and (3) there is some possibly positive correlation between the variation of ground motion velocity and the landslide distribution.

## ACKNOWLEDGEMENTS

This research was supported by the Basic Research Project of Institute of Geology, China Earthquake Administration (IGCEA1503). At the same time, we are thankful to the National Strong-Motion Observation Network System (NSMONS) of China for their 372 acceleration data of 124 strong motion instruments. In addition, Professor Ralph J Archuleta of University of California, Santa Barbara, gave me much valuable advice during this paper preparing.

## REFERENCES

Anderews, D.J. & Barall, M. 2011.Specifying initial stress for dynamic heterogeneous earthquake source models. *Bulletin of the Seismological Society of America* 101: 2408–2417.

Bai, Y.Z., Xu, X.W., Xu, J. et al. 2011. A research on the distribution of deformation fields near the fault of 2008 Wenchuan earthquake. *Chinese J. Geophys*. 54: 1798–1804 (in Chinese).

Boore, D.M. 2005. On pads and filters: Processing strong-motion data. *Bulletin of the Seismological Society of America* 95: 745–750.

Guatteri, M., Mai, M. & Beroza, G. 2004. A pseudo-dynamic approximation to dynamic rupture models for strong ground motion prediction. *Bulletin of the Seismological Society of America* 94: 2051–2063.

Ida, Y. 1972. Cohesive force across the tip of a longitudinal shear crack and Griffith's specific surface energy. *J. Geophys. Res.* 77(20): 3796–3805, doi: 10.1029/JB077I00P03796.

Palmer, A.C. & Rice, J. 1973. The growth of slip surfaces in the progressive failure of over-consolidated clay. *Proc. R. Soc. London, Ser. A*, 332: 527–548, doi: 10.1098/rspa.1973.0040.

Shan, B., Xiong, X., Zheng, Y. et al. 2009. Stress changes on major faults caused by MW7.9 Wenchuan earthquake, May 12, 2008. *Sci. China Ser. D-Earth Sci.* 52(5): 593–601 (in Chinese).

Wang, W.M., Hao, J.L. & Yao, Z.X. 2013. Preliminary result for rupture process of April. 20, 2013, Lushan earthquake, Sichuan, China. *Chinese Journal of Geophysics* 56(4): 1412–1417 (in Chinese).

Wen, Y.Y., Oglesby, D.D., Duan, B.C. et al. 2012. Dynamic rupture simulation of the 2008 Mw 7.9 Wenchuan earthquake with heterogeneous initial stress. *Bulletin of the Seismological Society of America* 102: 1892–1898.

Xu, X.W., Wen, X.Z., Han, Z.J. et al. 2013. Lushan Ms 7.0 earthquake: a blind reserve-fault event. *China Sci. Bull*. 58: 3437–3443 (in Chinese).

Zhang, D.L., Huang, B., Zhang, X.B. et al. 2013. Strong ground motion distribution and simulation based on finite fault model of Lushan 7.0 earthquake on April 20, 2013. *Seismology and Geology* 35(2): 423–435 (in Chinese).

Zhou, Q., Jiang, Y.F., Wu, G. et al. 2014. Distribution of coseismic landslides in Lushan earthquake and discussion on related problems. *Seismology and Geology* 36(2): 344–357 (in Chinese).

*Rock Dynamics: From Research to Engineering – Li et al. (Eds)*
*© 2016 Taylor & Francis Group, London, ISBN 978-1-138-02953-8*

# Numerical simulation of blasting vibration on high cutting slope

X.L. Cao, W.X. Gao, N. Wu & H. Zhao
*College of Architecture and Civil Engineering, Beijing University of Technology, Beijing, China*

D.H. Liu
*Beijing Road Engineering Cost and Quota Management Station, Beijing, China*

ABSTRACT: Blasting excavation is one of the most commonly used methods in road high cutting slope construction. Under blasting vibration wave, highway excavation process and its operation is directly influenced by the stability of high cutting slope. Therefore, based on the Lutuo Road construction project, a FEM model is established by midas GTS. The stress field, displacement field and velocity distribution and transfer laws is analyzed under blasting vibration. Conclusions about the dynamic response of high cutting slope under blasting vibration are as follows: (1) As the explosion is close to the slope's corner, a stress concentration mainly effected field is formed within a certain altitude of the slope's corner. (2) The displacement and vibration velocity of the high cutting slope has obvious magnification along the vertical direction under blasting vibration, which is similar to natural earthquake effect. (3) Millisecond-delay-control blasting technology is adopted, so the vertical vibration velocity of the buildings which are 80 m away from the blasting source is controlled below 2 cm/s, which is considered to be safe according to the blasting vibration safety control standard.

## 1 INTRODUCTION

With the rapid development of economy in our country, a large number of high cutting slope appeared in highway construction which located in mountainous and hills. During the construction of high slope, seismic effect of blasting vibration, as the main external factors which affect the stability of slope, is getting more and more attention from tire researchers.

Blasting vibration and the subsequent series of chain reaction has a great influence on the stability of high cutting slope, especially when the high cutting slope is influenced by roadway excavation, stress field will redistribution, slope collapse, landslides and other disasters will likely to be induced under blasting vibration which may not only hinder the project smoothly, but also can cause property damaged badly. So further study on the influence of cutting rock high slope stability under blasting vibration, and ensure the safety of complex surroundings in the process of road construction have important practical significance.

## 2 NUMERICAL SIMULATON OF BLASTING EXCAVATION

### 2.1 *Project introduction*

Lutuo Road started at Lu Jiashan Biomass Power Plant and ended with Yang Juantou Village, buildings on both sides of Yang Juantou Village and Xi Zhuangdian Village are a little bit intensive. According to "Lutuo Road (Jing Yuan Highway~Da Huichang Road) road line selection and planning condition", provided by Beijing Academy of Urban Planning and Design, road grade is II, design speed is 60 km/h, the red line is 30 m wide, planning section of roadbed is 10 m wide and road width is 5 m.

The maximum depth of the strata exploration is 20 m. According to exploration data and indoor soil experiment results, the soil within the scope of exploration is divided into artificial accumulation layers, quarternary eluvial slope and cambrian period limestone by sedimentation time and genetic type, and further divided into three layer by the stratigraphic lithology and physical properties.

Millisecond-delay-control blasting technology is used in Lutuo Road blasting according to the design material, surrounding environment and the engineering properties.

The method of integral drill blasting is to meet the design depth at once and ensure the construction progress in good blasting area environmental condition and the excavation depth within 10 m. Stratified blasting method will be used if the excavation depth is more than 10 m. Block length should be ensured, and sandbags need to be put on the boreholes, wicker fence need to be used to control blasting slungshot when necessary. Millisecond-delay-control blasting technology is adopted to limited the biggest detonation dose, so that the influence of the surrounding building by blasting vibration can be controlled.

### 2.2 *The numerical model*

Finite element software midas GTS is used to simulate the blasting excavation and vibration effect on Lutuo Road high cutting slope, and the stress field, displacement field and velocity distribution and transfer laws of high cutting slope is analyzed under blasting load. At the same time, buildings around the blasting source are concentrate, besides, landscape Stone is 78 m away from the high cutting slope, blasting environment is complex. So numerical analysis and vibration monitoring are used to strictly control the influence of blasting vibration in the complex surrounding environment.

The soil physical parameters selection is based on the geological exploration report. At the same time, in order to simulation the influence of blasting vibration in buildings and the landscape stone more realistic, rock and soil physical and mechanical parameters selection based on the geological exploration report. At the same time, in order to more realistic simulation of blasting vibration on the surrounding scenery overhanging rock and the influence of the residents housing, simplify the buildings into masonry structure when simulating. Mainly physical and mechanical parameters are shown in Table 1.

When mesh generation, size near the blasting source goes to be smaller, and the farther the sparser, so that the computational accuracy can be ensure but also the computing speed not that slow. The number of the units is 88145 and the nodes is 53114. The size of the model is as follows: length along X-axis is 200 m, Y-axis is 300 m and Z-axis is 60 m. Blasting 3D model shows in Figure 1, and the gauge points is the position of sensors.

### 2.3 *Results analysis*

#### 2.3.1 *The results of eigenvalue analysis*

Under the condition of undamped free vibration, midas GTS program using the following formulas to calculate natural period and mode of vibration:

$$K\vec{\phi}_n = \omega_n^2 M\vec{\phi}_n \tag{1}$$

Table 1. The material parameters table.

| | Modulus of elasticity ($kN/m^2$) | Poisson' ratio | Density ($kg/m^3$) | Cohesion ($kN/m^2$) | Friction angle (°) |
|---|---|---|---|---|---|
| Rockmass | 5000 | 0.3 | 2300 | 20 | 33 |
| Landscape stone | 60000 | 0.3 | 2300 | 20 | 33 |
| Buildings | 10000000 | 0.2 | 2200 | — | — |

where $K$ is the structural stiffness matrix; $M$ is the structural mass matrix; $\omega_n^2$ is the eigenvalues of the vibration mode; $\vec{\phi}_n$ is the modal vector.

Eigenvalue is used to analysis the dynamic characteristics of structure, and also called free vibration analysis. Some important structure of the dynamic characteristics such as formation, natural vibration period (natural frequencies) and participation factors can be get through eigenvalue analysis, which are generally determined by stiffness and quality of the structure.

The period of the 1st and 2nd Vibration mode is 1.3198 s and 1.2923 s, which is obtained by eigenvalue analysis.

### 2.3.2 *The vertical displacement*

The cloud diagram of the vertical displacement under blasting load is shown in Figure 2. The analysis shows that the displacement field produced from where loads applied and spread to the whole slope deeper and farther gradually, and then buildings around will be influenced by blasting vibration.

The following results can be seen from the data in the figures. The maximum vertical displacement occurred near the blasting source, the value goes to 22.88 cm at 75 ms, and then decreased gradually. At the same time, because of the effect of blasting load, rock on the top of the slope is uplifted, the first peak value appears at 100 ms (2.89 cm), after that, the vibration wave transmission up to the slope, the second peak value appears at 200 ms (9.79 cm) because of the superimposed effect, and then the value goes to be stable.

The data shows that the vertical displacement fluctuate strenuously in the center of the blasting source. Under the blasting load, fissures in the rock developed well so that the rock near the blasting source is loosened, and the rock on the top of the slope is uplifted. Vibration will be felt but fissure cannot be produced as the safety coefficient of slope stability reduces and the rock stays integrated.

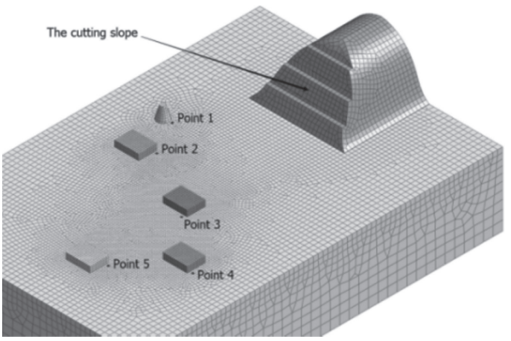


Figure 1. 3D model of numerical simulation.

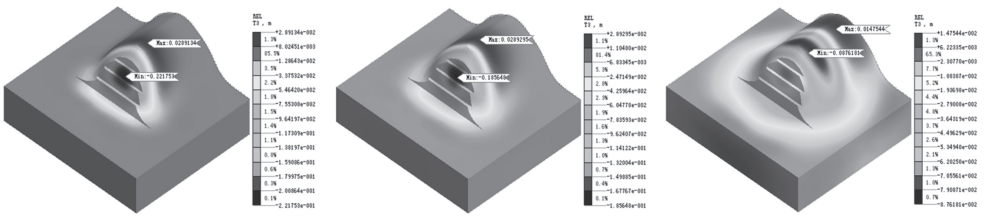

(a) t=75 ms (b) t=100 ms (c) t=200 ms

Figure 2. Cloud diagram of the vertical displacement.

2.3.3 *Vibration velocity*

Values in Figure 3 shows that the peak speed appeared at the tipping moment because of the directly shock by blasting load, the speed of the particle near the borehole reach 11.73 m/s, then dissipate rapidly with the blasting energy attenuation, speed decreases to 14.5 cm/s at 400 ms. At the same time, the speed of the particle near the top of the slope presents magnified effect, the peak speed of particle which is 5 m away from the blasting source is 64 cm/s at 75 ms, and then decreases, after 500 ms, vibration velocity of the particle goes to be stable, which is about 5 cm/s.

A number of experts and scholars at home and abroad have studied on the safety threshold of the vibration under blasting load on high cutting slope, safety threshold value standard based on the concept of damage of blasting vibration is put forward, which is according to the result of investigation and study of blasting vibration. Ollie L. Scott put forward when the velocity is less than 5.1~10.2 cm/s, the slope is safe, when the velocity is greater than 61 cm/s, the slope damaged; Court from Soviet Union believes that when the velocity is less than 20 cm/s, the slope safe, when the velocity is between 20~50 cm/s, the original fissure developed, a part of the rock fall off because of the vibration, when the velocity is between 50~100 cm/s, the original fissure developed strongly, with the block stone fall off, fissure appears in the weak structural so that the slope damage along the structural fissures.

The criterion of the rock blasting damage peak particle vibration velocity suggested by Zhang & Wang (1995) is shown in Table 2.

It can be seen from the table above that vibration velocity near the blasting source is a little bit larger; and fissure appears on the top of the slope which can reduces the stability of the slope, so safety monitoring and reinforcement measures should be strengthened in the slope protection in the future.

Vibration velocity of the particle on the slope is extracted in the simulation, besides, vibration monitoring is used at the same time. A number of monitoring points are selected in blasting around, so numerical analysis and vibration monitoring are used to strictly control the influence of blasting vibration in the complex surrounding environment. The location and the description of the monitoring points is shown in the following Table 3.

Figure 4 is the contrast curve of the vibration monitoring velocity and the numerical simulation velocity.

It can be seen from the curve that because of the relatively idealized computing environment, the result of the numerical simulation seems to be uniform, but influenced by height difference and the error of the instrument, the result of vibration monitoring seems to be higher volatility and has obvious gap with numerical calculation, even if the vibration velocity decrease with the distance from the blasting source.

At the same time, point No.1 is the nearest monitoring point where is the landscape stone located, the vibration vertical is about 1.5 cm/s which is obtained from numerical simulation and vibration monitoring, and it seems that vertical vibration can be controlled by millisecond-delay-control blasting technology according to the blasting vibration safety standard.

2.3.4 *The stress field*

The first main stress cloud diagram of buildings around is shown in Figure 5. It is shown that stress field generated from the surface of the slope, and the buildings 200 m away from

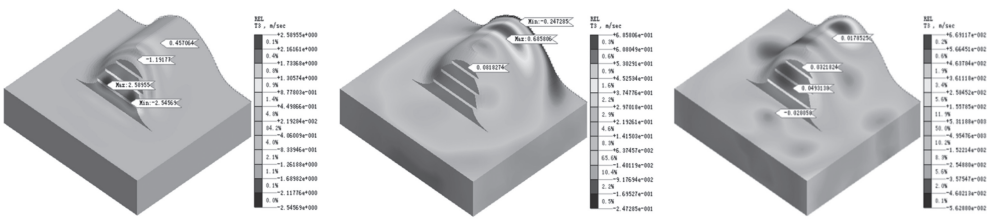

(a) t=75 ms (b) t=400 ms (c) t=800 ms

Figure 3. Cloud diagram of vibration velocity.

Table 2. The damage of rock blasting particle vibration velocity.

| The peak particle vibration velocity (cm/s) | Damage of the rock |
|---|---|
| 26 | Small open fissure on the slope |
| 56 | Small cracks on the surface |
| 75 | 3 cm wide of fissure in the granite |
| 110 | 3 cm wide of fissure in the granite; More than 10 cm wide of fissure on the surface |

Table 3. The location of the monitoring points list.

| Serial number | Distance from blasting source | Explanation |
|---|---|---|
| 1 | 78 m | Landscape Stone |
| 2 | 101 m | Staff Dormitory |
| 3 | 110 m | The Garage |
| 4 | 176 m | Duck Ranger |
| 5 | 205 m | Glass House |

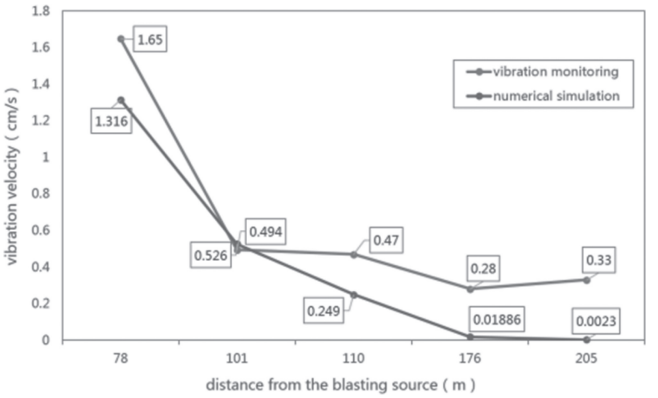


Figure 4. The contrast curve.

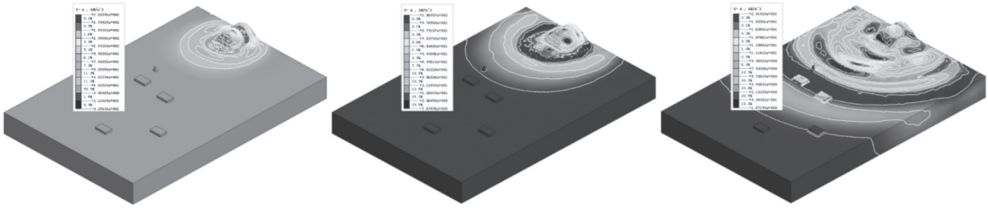

(a) t=300 ms (b) t=500 ms (c) t=1000 ms

Figure 5. Cloud diagram of the first main stress cloud diagram of buildings around.

the blasting source are influenced by the blasting waves at 1000 ms. Fissure appeared on the surface at the beginning of the blasting because of the severe vibration, but value of stress on buildings and rock hundreds meters away is only 1~10 kPa, which seems to be safe according to the blasting vibration safety control standard.

## 3 CONCLUSION

Based on the Lutuo Road construction project, numerical simulation is used to analysis the stability of the slope, and the result of dynamic response under blasting load is get to prove the scientificity and veracity of numerical simulation. Besides, an evaluation of dynamic stability of the slope is made combine with vibration monitoring, the conclusion is as follows:

1. As the explosion is close to the slope's corner, a stress concentration mainly effected field is formed within a certain altitude of the slope's corner.
2. Blasting load applied on the slope for times in millisecond-delay-control blasting technology so that multiple peak will get in the displacement and velocity, but all of the value reduce with time pass by. Besides, the displacement and vibration velocity of the high cutting slope has obvious magnification along the vertical direction under blasting vibration, which is similar to natural earthquake effect.
3. Millisecond-delay-control blasting technology is adopted, so that vertical vibration velocity of the buildings where are 80 m away from blasting source is controlled under 2 cm/s, which is considered to be safe according to the blasting vibration safety control standard.

## REFERENCES


Gao, W. & Liu, Y. 2007. Blasting theory of high and steep road cutting rock slope with multilateral boundary and its application. *Chinese Journal of Rock Mechanics & Engineering*.

Gao, W., Liu, H., Liu, H. & Shu, H. 2010. Road high cutting slope stability analysis under influence of blasting for excavation. *Chinese Journal of Rock Mechanics & Engineering*.

Huang, Y., Huang, H., Li, X., Wei, Z., Li, Z., Lu, F., Zhang, Y., Li, J., Zhu, Z., Lu, Q., Yang, Z. & Zhao, Q. 2002. Study on explosion vibration effect under buildings-application and revision of "rules of explosion safety". *Journal of Seismological Research*.

Jiao Y., He, E. & Zhang, S. 2006. Blast vibration influences on slope during transformation of surface mining to underground mining. *Mining & Metallurgical Engineering, 26*(5), 1–5.

Kuhlemeyer, R. L. & Lysmer, J. 2015. Finite element method accuracy for wave propagation problems. *Journal of Soil Mechanics & Foundations Div.* 99(5): 421–427.

Lysmer, J. 2015. Finite dynamic model for infinite media. *Journal of the Engineering Mechanics Division* 95(4): 859–878.

Ollie L. Scott., Carl E, Snyder Jr. & Lois J, Gschwender. 1995. Characterization of model perfluoropolyalkylethers by miniaturized thermal oxidative techniques - part i: modified oxidation-corrosion test. *Tribology Transactions* 38(3): 618–626.

Qi, Y., Li, X., L, C., Gu, X.,Wang, L.,Wang, H. & Ling, T. 2008. 3dec simulation of dynamic response of high-steep jointed rock slope under blast load. *Mining & Metallurgical Engineering* 28(5): 18–22.

Xiao, W., Xie, W., & Xue, D. 2013. Test and research on blasting vibration of deep-hole blasting in open pit mine. *Journal of Guiyang University*.

Zhang, S., Zhang, T. & Wu, L. 1996. An approach to slope stability due to blasting excavation. *Chinese Journal of Geological Hazard & Control*.

Zhang, Y. 1996. Study on effect of excavation blasting on dynamic stability of high rock slope at manwan hydropower station. *Engineering Blasting*.

Zhang, Z. & Wang, Z. 1995. Experimental study on stress field of explosion of linear charge. *Engineering Blasting.*

*Rock Dynamics: From Research to Engineering – Li et al. (Eds)*
*© 2016 Taylor & Francis Group, London, ISBN 978-1-138-02953-8*

# Seismic dynamic reliability analysis of bedding rock slopes based on Newmark-β method

X.L. Chen, W.H. Gong, Y. Li, J.W. Qiu & X.H. Zhong
*Institute of Geotechnical and Underground Engineering, Huazhong University of Science and Technology, Wuhan, Hubei, China*

ABSTRACT: Earthquake action is a dynamic process, and the traditional seismic reliability analysis of bedding rock slopes is usually based on the pseudo static method, which ignores the dynamic characteristics of earthquake. Furthermore, the seismic time-history analysis method considering the effects of dynamic characteristics of earthquake is time-consuming and laborious. Therefore, this paper presents an analytical method for evaluating the dynamic reliability of bedding rock slopes under earthquake action considering the seismic dynamic characteristics and randomness of strength parameters. A simplified calculation method for seismic response of bedding rock slopes is presented by using the Newmark-β method and Matlab/Simulink. Then the dynamic degree of reliability of bedding rock slopes is calculated based on the former results of seismic response by using the Monte Carlo method. A new evaluation index, overall minimum mean dynamic degree of reliability, is put forward to evaluate the overall stability of bedding rock slopes under earthquake action. Results from a numerical example indicate that this proposed simplified calculation method for seismic response is of high accuracy and efficiency. And this proposed seismic reliability analytical method can underestimate the slope stability. As a result, it will be safer for engineering evaluation.

## 1 INTRODUCTION

The stability of bedding rock slopes is influenced by many kinds of uncertainty factors, which mainly include the randomness of strength parameters (Gao et al. 2009, Sun & Zhu 2007). In recent years, the studies on seismic reliability of bedding rock slopes considering the randomness of strength parameters are relatively few. Li et al. (2011) used the quasi-static method and random response surface method to analyze the reliability of bedding rock slopes under earthquake action. Low (2008) evaluated the seismic reliability of bedding rock slopes by using the quasi-static method and Advanced First-Order Second Moment (AFOSM) method. The aforementioned studies are based on the assumption that the seismic force is taken as a kind of inertial force. However, the earthquake motion is a dynamic process. And the internal stresses of bedding rock slopes are constantly changing during the process of earthquake. Thus, the degree of reliability of bedding rock slopes should also be fluctuating with the earthquake. A slope is unstable at one moment during the process of earthquake does not mean that the slope failure must be occurred. Consequently, it is unsuitable to evaluate the anti-slide stability of the slope under earthquake action by using the minimum degree of reliability that occurs at one moment during the process of earthquake.

At present, the main analytical methods for stability of bedding rock slopes considering seismic dynamic characteristics are the Newmark's sliding block method and time history analysis method based on numerical simulation. The Newmark's sliding block method (Shukha & Rafael 2008, Pal et al. 2012), based on the rigid limit equilibrium method, calculates the seismic permanent displacements of slopes by the double integration of the seismic acceleration time history beyond the critical acceleration. However, this method lacks the reasonable failure criterion of stability. The time history analysis method based on numerical simulation (Refice & Domenico 2002) can consider the dynamic characteristics of earth-

quake, and its calculation results are relatively reasonable. However, this method has certain drawbacks, which is time-consuming and laborious, and it is highly dependent on the computing power and the software and hardware of computer. Consequently, it is necessary to improve the computational efficiency of dynamic time-history response analysis.

To solve the above problems, the main work of this paper is that: First, a simplified calculation method for seismic response of bedding rock slopes is established by using the Newmark-β method and Matlab/Simulink according to the principle of structural dynamics. Then, an analytical method for evaluating the dynamic reliability of bedding rock slopes is established based on the former results of seismic response. And a new index, overall minimum mean dynamic degree of reliability, is put forward to evaluate the overall stability of bedding rock slopes under earthquake action.

## 2 FUNDAMENTAL ASSUMPTIONS AND DYNAMIC CALCULATION MODEL

The assumptions adopted in this paper are as follows:

1. The failure mode of bedding rock slopes is the plane sliding destruction along the weak structural surface.
2. Mohr-Coulumb failure criterion is adopted.
3. The deformation of rock masses under exogenous action is negligibly small.
4. Horizontal and vertical earthquake actions are both considered.

The dynamic calculation model of bedding rock slopes is shown in Figure 1, where $\alpha$ is the slope angle. $\beta$ is the dip angle of rock stratum. ss1, ss2 are the weak structural surfaces, of which the corresponding potential sliding masses are expressed as the sliding masses 1, 2, respectively. $H_1$ and $H_2$ are heights. ① and ② are the two rock masses from the top of slope to the bottom. Unless otherwise specified, the length along the strike direction of strata used in this paper is 1 m. $\frac{\partial^2 u_{gh}}{\partial t^2}$ and $\frac{\partial^2 u_{gv}}{\partial t^2}$ are the seismic wave input from the bottom of slope model.

## 3 SIMPLIFIED CALCULATION METHOD FOR SEISMIC RESPONSE OF BEDDING ROCK SLOPES

### 3.1 *Dynamic equations of motion*

This paper adopts the viscoelastic model (Xue et al. 1990) during dynamic analysis and uses the spring (K) and damper (C) to simulate the weak structural surface. The established mass visco-elasticity model of rock masses and weak structural surfaces is shown in Figure 2, where $K_s$ and $K_n$ are the shear and normal stiffness of weak structural surfaces, respectively. $C_{s1}$ and $C_{s2}$ are the shear damping coefficients of the weak structural surfaces ss1 and ss2,

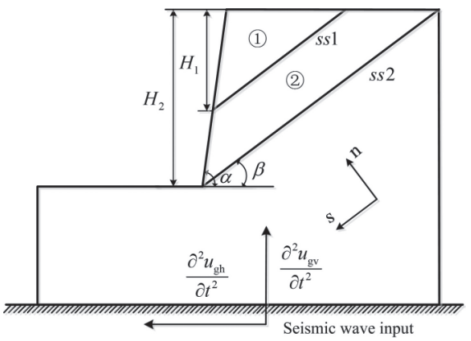


Figure 1. Dynamic calculation model of bedding rock slopes.

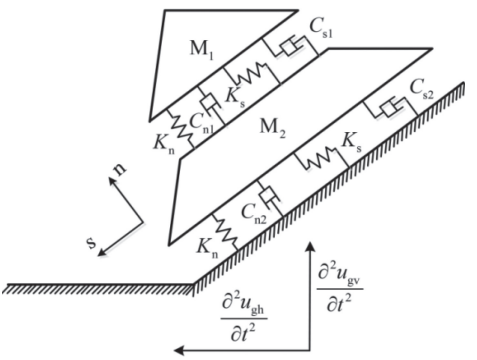


Figure 2. Mass visco-elasticity model.

respectively. $C_{n1}$ and $C_{n2}$ are the normal damping coefficients of the weak structural surfaces ss1 and ss2, respectively. Adopting the Rayleigh damping model (Bourdeau & Havenith 2008), the expression is as follows:

$$C = \frac{2\omega_1\omega_2\left(\xi_1\omega_2 - \xi_2\omega_1\right)}{\omega_2^2 - \omega_1^2} M + \frac{2\left(\xi_2\omega_2 - \xi_1\omega_1\right)}{\omega_2^2 - \omega_1^2} K \tag{1}$$

where $M$ is the mass. $K$ is the stiffness. $\omega_1$ and $\omega_2$ are the first and second natural frequencies, respectively. $\xi_1$ and $\xi_2$ are the corresponding damping ratios.

Thus, the dynamic equations of motion of the structural system in the s and n directions can be established as:

$$[M]\begin{Bmatrix} \frac{\partial^2 u_{s1}}{\partial t^2} \\ \frac{\partial^2 u_{s2}}{\partial t^2} \end{Bmatrix} + [C_s]\begin{Bmatrix} \frac{\partial u_{s1}}{\partial t} \\ \frac{\partial u_{s2}}{\partial t} \end{Bmatrix} + \{F_s\} = -[M]\{l\}\left(\frac{\partial^2 u_{gh}}{\partial t^2}\cos\beta - \frac{\partial^2 u_{gv}}{\partial t^2}\sin\beta\right) - \{W\}g\sin\beta \tag{2}$$

$$[M]\begin{Bmatrix} \frac{\partial^2 u_{n1}}{\partial t^2} \\ \frac{\partial^2 u_{n2}}{\partial t^2} \end{Bmatrix} + [C_n]\begin{Bmatrix} \frac{\partial u_{n1}}{\partial t} \\ \frac{\partial u_{n2}}{\partial t} \end{Bmatrix} + \{F_n\} = -[M]\{l\}\left(\frac{\partial^2 u_{gh}}{\partial t^2}\sin\beta + \frac{\partial^2 u_{gv}}{\partial t^2}\cos\beta\right) + \{W\}g\cos\beta \tag{3}$$

where

$$[C_s] = \begin{bmatrix} C_{s1} & -C_{s1} \\ -C_{s1} & C_{s1} + C_{s2} \end{bmatrix}, [C_n] = \begin{bmatrix} C_{n1} & -C_{n1} \\ -C_{n1} & C_{n1} + C_{n2} \end{bmatrix} \tag{4}$$

$$\{F_s\} = [K_s]\{u_{s1} \quad u_{s2}\}^T - K_s\frac{g\sin\beta}{K_s}\{M_1 \quad M_1 + M_2\}^T \tag{5}$$

$$\{F_n\} = [K_n]\{u_{n1} \quad u_{n2}\}^T + K_n\frac{g\cos\beta}{K_n}\{M_1 \quad M_1 + M_2\}^T \tag{6}$$

$$[K_s] = \begin{bmatrix} K_s & -K_s \\ -K_s & 2K_s \end{bmatrix}, [K_n] = \begin{bmatrix} K_n & -K_n \\ -K_n & 2K_n \end{bmatrix} \tag{7}$$

In which $\frac{\partial^2 u_{s1}}{\partial t^2}$ and $\frac{\partial^2 u_{s2}}{\partial t^2}$ are the seismic acceleration responses of rock masses ① and ② in the s direction, respectively. $\frac{\partial^2 u_{n1}}{\partial t^2}$ and $\frac{\partial^2 u_{n2}}{\partial t^2}$ are the acceleration responses in the n direction. $\frac{\partial u_{s1}}{\partial t}$ and $\frac{\partial u_{s2}}{\partial t}$ are the velocity responses in the s direction. $\frac{\partial u_{n1}}{\partial t}$ and $\frac{\partial u_{n2}}{\partial t}$ are the velocity responses in the n direction. $\{F_s\}$ and $\{F_n\}$ are respectively the response matrixes for the shear and normal forces of weak structural surfaces. $u_{s1}$ and $u_{s2}$ are the displacement responses in the s direction. $u_{n1}$ and $u_{n2}$ are the displacement responses in the n direction. $\{W\}$ is the mass matrix of sliding masses. $\{l\}$ is the unit transition matrix, $\{l\} = \{1 \quad 1\}^T$.

### 3.2 *Newmark-β method*

Eqs. (2) and (3) can be solved as an initial value problem. The methods to solve initial value problems are divided into the explicit method and implicit method. The equation of motion is a stiff equation, which is very sensitive to a time function. For solving the stiff equation using the explicit method, the step size should be very small. In this case, the implicit method is a commonly used remedy for this problem.

A stiff equation calculated by the implicit method is more stable and accurate than that of the explicit method, thus the step size of the calculation can be relatively bigger. The Newmark-β method is one of the representative implicit methods (Lee et al. 2005).

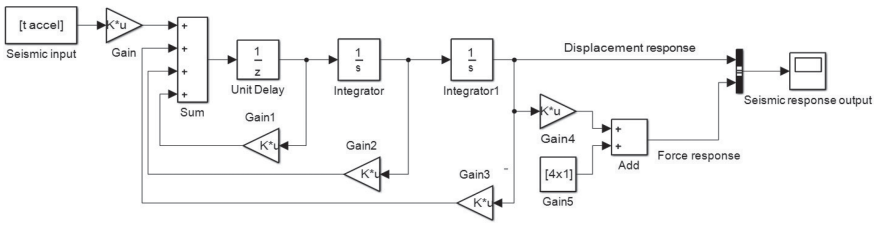


Figure 3. Simulation model of the solving process of seismic response.

And the stability researches of Newmark-β method show that it is unconditionally stable when $\beta \geq 0.5$, $\gamma \geq 0.25(0.5+\beta)^2$. Therefore, this paper selects $\beta = 0.5$, $\gamma = 0.25$.

Eqs. (2) and (3) are solved by the Newmark-β method. Thus, the seismic responses for acceleration, velocity and displacement in the overall period of time can be obtained.

### 3.3 *Implement of the solutions for seismic response*

1. Solutions for the natural vibration characteristics of structures

The natural vibration characteristics of structures refer to the natural frequency and vibration mode, for which the solutions can be transformed into the solutions for the generalized eigenvalue problem. The formula is as follows:

$$\left[K - \omega^2 M\right]V = 0 \tag{8}$$

where $\omega$ is the natural frequency of structure. $V$ is the vector quantity for vibration mode.

Using the function from Matlab called eig: $[V, P] = \mathrm{eig}(K, M)$ to calculate the natural frequencies and vibration modes. Thus, the damping matrixes of the structural system can be solved.

2. Solutions for seismic response

This paper uses the Matlab/Simulink (Taghipour et al. 2008) to implement the solutions for seismic response. Simulink toolbox provides all kinds of abundant and powerful analysis modules, which can avoid the tedious programming work, improve the efficiency of dynamic calculation and output the calculating data and figures more expediently. Thus, the related simulation model can be established and shown in Figure 3. And then the seismic responses of the rock masses can be quickly solved.

## 4 DYNAMIC RELIABILITY ANALYSIS OF BEDDING ROCK SLOPES

### 4.1 *Solution for dynamic degree of reliability*

According to the above-mentioned assumption on the plane sliding destruction, the limit state equation of sliding surface ss*i* at the moment *t* can be expressed as the following form:

$$Z_i(t) = F_{ni}(t)\tan\varphi + cL_i - F_{si}(t) = 0 \tag{9}$$

where $F_{ni}(t) and F_{si}(t)$ are the values of normal and shear forces of sliding surface ss*i* at the moment *t*. $L_i$ is the length of sliding surface ss*i*. φ and *c* are the internal friction angle and cohesion, respectively.

Making use of Monte Carlo method, the degree of reliability $P_{si}(t)$ of sliding surface ss*i* at the moment *t* can be solved as:

$$P_{si}(t) = 1 - \frac{nF}{nS} \tag{10}$$

where $nS$ is the total number of times; $nF$ is the number of times for $Z_{ei}(t) < 0$.

Thus, the dynamic degrees of reliability can be solved by Eq. (10).

### 4.2 *Overall minimum mean dynamic degree of reliability*

In the seismic response analysis, the shear strains of structural units are constantly changing during the process of earthquake. Idriss et al. (1975) and Seed et al. (1975) presented using the equivalent shear strain $\gamma_{\text{eq}}$ to substitute the change process of shear strain. And the equation is as: $\gamma_{eq} = 0.65\gamma_{\max}$, in which $\gamma_{\max}$ is the maximum value of the shear strain time history. 0.65 is the conversion coefficient, which can be determined according to the ground motion characteristics through probability analysis. Liu et al. (2003) based on the principle of equivalent shear strain put forward the concept of minimum mean safety factor, which had been verified and adopted by many other scholars (Xu et al. 2013, Tang et al. 2015). This paper presents using the minimum mean degree of reliability $\overline{P}_{si}$ to evaluate the seismic stability of sliding surface ss*i* in accordance with the calculation principle of minimum mean safety factor. The expressions are as follows:

$$\overline{P}_{si} = P_{si0} - 0.65\left[P_{si0} - \min\left(\{P_{si}\}\right)\right] \tag{11}$$

where $P_{si0}$ is the degree of reliability of sliding surface ss*i* under static loadings. $\min\left(\{P_{si}\}\right)$ is the minimum values for degree of reliability of sliding surface ss*i* during the whole process of earthquake.

Thus, the overall minimum mean dynamic degree of reliability $P_{\text{s}}$ is presented as the evaluation index to evaluate the overall stability of bedding rock slopes under earthquake action, and the expressions are as follows:

$$P_{\text{s}} = \min\left(\left\{\overline{P}_{\text{s}}\right\}\right) \tag{12}$$

where $\left\{\overline{P}_{s}\right\}$ is the matrix for the overall minimum mean degrees of reliability of sliding surfaces.

## 5 ILLUSTRATIVE EXAMPLE AND COMPARISON VALIDATION

### 5.1 *Project profile*

A bedding rock slope of the highway from Yichang to Enshi of Shanghai-Chengdu national main trunk line is illustrated. The calculation diagram is shown in Figure 4. The rocks are composed of grey weakly weathered argillaceous limestone. The density is $\rho = 2600\,\text{kg/m}^3$ . The normal and shear stiffness is $K_{\text{n}} = 3\times10^7\,\text{N/m}, K_{\text{s}} = 1\times10^7\,\text{N/r}$. Other parameters are listed as follows: $\alpha = 53°, \beta = 40°, \delta = 30°$. According to the analysis of laboratory and field tests, $c$ and $\tan\varphi$ obey normal distributions, and the values are listed in Table 1.

The safety level of this slope is one, and the site class is III. The seismic fortification intensity is 7 degrees. The input seismic wave is El-Centro wave. Adjusting the amplitude to 1.5 m/s$^2$, the acceleration time history is shown in Figure 5. The function coefficient of vertical earthquake is 2/3. The sampling period is $\Delta t = 0.02$ s, and the damping ratio is $\xi = 0.15$.

### 5.2 *Seismic response results and verification*

According to these known conditions, the first and second natural frequencies of this slope in the tangential direction can be easily solved as $\omega_{\text{s1}} = 4.6241\,\text{rad/s}$, $\omega_{\text{s2}} = 11.1746\,\text{rad/s}$ respectively. And the first and second natural frequencies in the normal direction are respectively $\omega_{\text{n1}} = 8.0091\,\text{rad/s}$ and $\omega_{\text{n2}} = 19.3550\,\text{rad/s}$. Thus, the horizontal and vertical displacement responses of rocks can be calculated. And the results are shown in Figures 6 and 7.

To verify the accuracy of this proposed simplified calculation method, a comparison with the DEM (Discrete Element Method) is presented. Figures 6 and 7 respectively give the calculation

results of horizontal and vertical displacement responses of rocks by the two methods. It can be found that the agreement between the two solutions is very close. It indicates that this proposed simplified calculation method is simple and practical, and has high computational efficiency and accuracy. Thus, the analysis of dynamic reliability can be further carried out.

### 5.3 *Dynamic fuzzy reliability analysis*

Monte Carlo method is used to solve the degree of reliability. And to guarantee the accuracy of simulation, this paper selects $nS = 10^6$. Thus, the time-history curves of dynamic degrees of reliability of sliding surfaces are obtained and shown in Figure 8.

It can be found from Figure 8 the fluctuation range of degree of reliability of sliding surface ss2 is relatively larger than that of sliding surface ss1. The interval for degree of reliability of sliding surfaces ss1 is [0.9979, 1.0000], while the interval of sliding surfaces ss2 is [0.9806, 0.9999]. It is thus clear that the reliability of sliding surface ss2 is worse, and the probability of slope failure that occurred on the weak structural surface ss2 is larger.

In view of Eq. (11), the minimum mean degrees of reliability of sliding surfaces ss1 and ss2 can be respectively calculated as $\overline{P}_{s1} = 0.9986, \overline{P}_{s2} = 0.9869$. Thus, the degree of reliability of this slope under earthquake action is obtained as $P_s = 0.9869$.

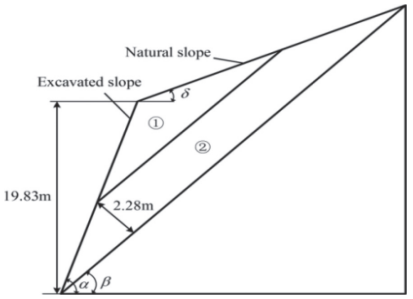


Figure 4. Calculation diagram of slope.

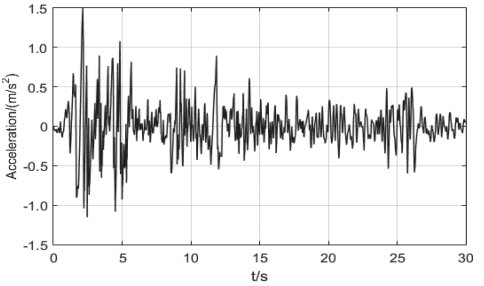


Figure 5. El Centro seismic wave.

Table 1. Statistical characteristics of strength parameters.

| Strength parameters | Sample mean $\mu$ | Standard deviation $\sigma$ | Variable coefficient $\delta$ |
|---|---|---|---|
| $c$/(MPa) | 0.02626 | 0.00355 | 0.135 |
| tan $\varphi$ | 0.6496 | 0.0741 | 0.114 |

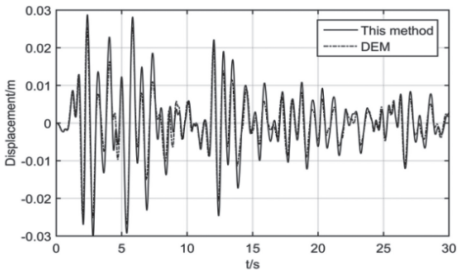


(a). Horizontal displacement response

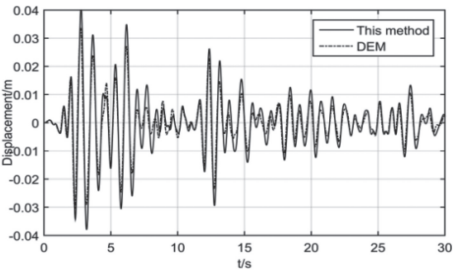


(b). Vertical displacement response

Figure 6. Seismic displacement responses of rock ①.

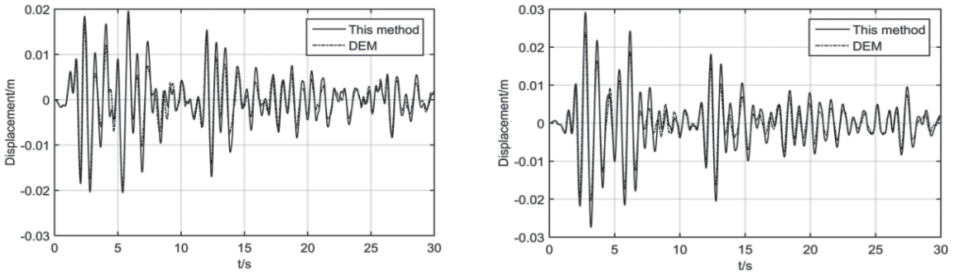


(a). Horizontal displacement response (b). Vertical displacement response

Figure 7. Seismic displacement responses of rock ②.

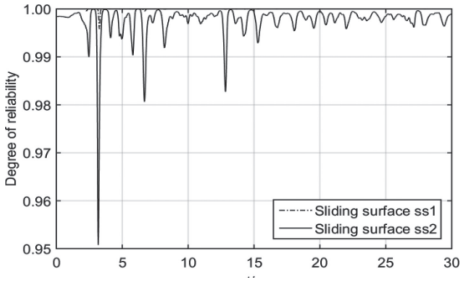


Figure 8. Time-history curves of dynamic degrees of reliability under earthquake action.

Table 2. Calculation results of degree of reliability.

| Calculation methods | Degree of reliability |
|---|---|
| This method | 0.9869 |
| Method ① | 0.9960 |
| Method ② | 0.9963 |

Table 2 shows the comparison result between the proposed analytical method and the general methods, where methods ① and ② are respectively the Monte Carlo method with quasi-static method and JC method with quasi-static method, respectively. It can be found from Table 2 that the result calculated by this method is lower. It is because that this method considers the dynamic characteristics of earthquake, and avoids the overestimating problems caused by the use of quasi-static method. Therefore, this method is more reasonable and realistic. And it will be safer for engineering evaluation.

## 6 CONCLUSIONS

The dynamic reliability of bedding rock slopes under earthquake action is studied in this paper considering the dynamic characteristics of earthquake and the randomness of strength parameters. A simplified calculation method for seismic response of bedding rock slopes is presented by using the Newmark-β method and Matlab/Simulink. Then, based on the former calculation results, an analytical method for evaluating the dynamic reliability of bedding

rock slopes under earthquake action is established. Combined with a specific example, the conclusions are as follows:

1. This proposed simplified calculation method for seismic response of bedding rock slopes is reasonable and feasible, which greatly improves the computational efficiency while maintaining high accuracy.
2. This proposed analytical method for evaluating the dynamic reliability of bedding rock slopes under earthquake action can underestimate the seismic reliability of bedding rock slopes, and it can more realistically reflect the actual situation of bedding rock slopes. Therefore, it is more reasonable and realistic, and will be safer for engineering evaluation.

## ACKNOWLEDGEMENTS

This work was supported by the Natural Science Foundation of China (Grant No. 51278217).

## REFERENCES

Bourdeau, C. & Havenith, H.B. 2008. Site effects modelling applied to the slope affected by the Suusamyr earthquake (Kyrgyzstan, 1992). *Engineering Geology* 97(3): 126–145.

Gao, R.X. Gong, W.H. & Wang Y.H. 2009. Analysis of stability and reliability of bedding rock slope by stochastic finite element method. *Rock and Soil Mechanics* 04:1165–1169. (in Chinese).

Idriss, I.M., Lysmer, J. & Hwang, R. 1975. QUAD-4: A computer program for evaluating the seismic response of soil structures by variable damping finite element procedures. *EERC Report* 73–16, University of California, Berkeley.

Lee, C.W., Lee, J.H. & Cha, B.J. 2005. Physical modeling for underwater flexible systems dynamic simulation. *Ocean engineering* 32(3): 331–347.

Li, D.Q. Chen, Y.F. & Lu, W.B. 2011. Stochastic response surface method for reliability analysis of rock slopes involving correlated non-normal variables. *Computers and Geotechnics* 38(1): 58–68.

Liu, H.L., Fei, K. & Gao, Y.F. 2003. Time history analysis method of slope seismic stability. *Rock and Soil Mechanics* 24(4): 553–556. (in Chinese).

Low, B.K. 2008. Efficient probabilistic algorithm illustrated for a rock slope. *Rock Mechanics and Rock Engineering* 41(5): 715–734.

Pal, S., Kaynia, A.M., Bhasin, R.K. & Paul, D.K. 2012. Earthquake stability analysis of rock slopes: a case study. *Rock Mechanics and Rock Engineering* 45.(2): 205–215.

Refice, A. & Domenico, C. 2002. Probabilistic modeling of uncertainties in earthquake-induced landslide hazard assessment. *Computers & Geosciences* 28(6): 735–749.

Seed, H.B., Idriss, I.M. & Lee, K.L. 1975. Dynamic analysis of the slide in the Lower San Fernando Dam during the earthquake of February 9, 1971. *Journal of Geotechnical and Geoenvironmental Engineering* 101(9): 889–911.

Shukha, R. & Rafael, B. 2008. Design implications of the vertical pseudo-static coefficient in slope analysis. *Computers and Geotechnics* 35(1): 86–96.

Sun, S.L. & Zhu, J. 2007. Reliability analysis of key block for a jointed rock slope. *Chinese Journal of Rock Mechanics and Engineering* 26(1): 131–136. (in Chinese).

Taghipour, R., Perez, T. & Moan, T. 2008. Hybrid frequency–time domain models for dynamic response analysis of marine structures. *Ocean Engineering* 35(7): 685–705.

Tang, H.M. Liu, X. & Hu, X.L. 2015. Evaluation of landslide mechanisms characterized by high-speed mass ejection and long-run-out based on events following the Wenchuan earthquake. *Engineering Geology* 12–24.

Xu, J.B., Wu, F. & Zheng, Y. 2013. Effect of elastic modulus and time interval on the seismic slope stability. *Global View of Engineering Geology and the Environment* 161.

Xue, S.Y. Wang, S.J. & Zhang, J.J. 1990. The vibrating models of block rockmass and dynamic response analysis methods. *Proceedings of the 2nd Chinese Academic Conference on Rock Dynamic Mechanics*, Yichang, China 9–20. (in Chinese).

*Rock Dynamics: From Research to Engineering – Li et al. (Eds)*
*© 2016 Taylor & Francis Group, London, ISBN 978-1-138-02953-8*

# Microseismic characteristics analysis of fault activation induced by excavation unloading at the left bank underground powerhouse of the Baihetan hydropower station, China

F. Dai, A. Li & N.W. Xu
*State Key Laboratory of Hydraulics and Mountain River Engineering, College of Water Resources and Hydropower, Chengdu, Sichuan, P.R. China*

Y.L. Fan
*China Three Gorges Corporation, Beijing, P.R. China*

ABSTRACT: To investigate microseismic characteristics of fault activation and its deformation mechanism during the excavation of the underground powerhouse, Microseismic (MS) monitoring technique and field survey was adopted. In this paper, the spatiotemporal distribution of microseismicity of fault activation is summarized and presented. In addition, deformation mechanism of fault rupture was revealed during different stages of excavation, and the results showed that fault propagation was associated with excavation and supporting of the first layer of main powerhouse, tensile fracture was main failure mode in this phase. Then, the fault got into the state of rapid unstable propagation in the initial period of stress adjustment before a steady state was realized. Excavation of the second or third layer of main powerhouse was related to fault movement and the degree of fault activation was slight in these two stages.

## 1 INTRODUCTION

With regard to fault, internal micro-fractures may often lead to macroscopic instability of fault. Therefore, there must be an intrinsic correlation between fault activation and its internal microseismicity, and it is possible to study fracture or failure processes by analyzing the evolution of internal microfracture (Ge 2005). The MS monitoring technique, as a three-dimensional, real-time monitoring technique, can detect the micro-fracturing signals of rocks and record them as seismograms (Xu et al. 2011). By analyzing the waveforms, the time, spatial locations and source parameters of MS events can be obtained. Tezuka et al. (2000) analyzed the spatial distribution of MS events which were primarily induced by fault activation. Aminzadeh et al. (2013) used tomographic inversion, fuzzy clustering, and shear wave splitting to analyse MS data to obtain reliable characteristics about fractured areas. Based on temporal and spatial distribution of MS events and deformation mechanism, Zhang et al. (2014) analysed fault activation which include the movement and propagation of the fault. Jiang et al. (2010) employed a coupled method which incorporates MS monitoring and numerical simulation to study the tectonic activation. These achievements have proven that the MS technique could be a useful tool for analyzing fracture processes. However, the problem of how to efficiently further utilize the monitored MS data to study the mechanism of evolution of fault activation still urgently needs to be solved.

In this study, the MS monitoring technique was used to determine activation processes of steep angle fault $f_{717}$ which extended through the rear parts of left bank underground powerhouse at Baihetan hydropower station. By analyzing the temporal changes in multiple MS parameters, deformation mechanism of fault rupture was revealed during different stages of excavation. These achievements can provide some references to the next phase of excavation and support design of the underground powerhouse.

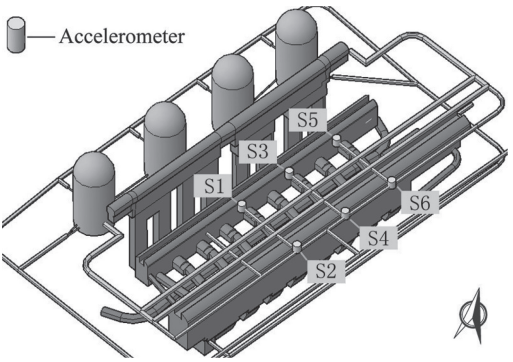


Figure 1. Sketch map of accelerometer array at main powerhouse.

## 2 ENGINEERING BACKGROUND

### 2.1 *Engineering situation*

The large-scale underground powerhouse cavern group at the Baihetan hydropower station mainly includes a main/auxiliary powerhouse, main transformer room, tail gate, and surge tank. The lengths of the left and right main/auxiliary powerhouses are 438 m and 434 m, respectively. The heights and widths of the two powerhouses are the same (86.7 m and 31 m, respectively; the width above the rock beam is 34 m). There are plenty of steep angle faults such as $f_{720}$, $f_{721}$, $f_{717}$ in this area, which are mainly hard structural planes and rock cuttings. The strike of fault $f_{717}$ intersects to the power house's stalk line with high angle and extends through the area between the 6# and 7# omnibus bar caves of the main powerhouse. The cave's initial principal stress is tectonic stress with the condition of vertical stress lower than horizontal stress. (Hydro-China Huadong Engineering Corporation 2013).

### 2.2 *MS monitoring scheme*

A high-resolution MS monitoring system manufactured by ESG (Engineering Seismology Group, Canada), was installed in the left-bank underground powerhouse at the Baihetan hydropower station. The ultimate optimal sensor array was set up through incorporating construction state, geological structure in monitoring area, and installing feasibility of sensors. The arrangement and distribution of the 6 sensors is shown in Figure 1. The 6 uniaxial accelerometers (S1-S6) were placed in anchoring branch tunnels, which are located at the upstream and downstream of the main powerhouse. Overall, the 6-channel seismic monitoring system can cover the whole crown zones of the main powerhouse during the monitoring period from October 10, 2014 to June 20, 2015.

## 3 CORRELATION BETWEEN MS ACTIVITY AND FAULT ACTIVATION

It has great significance to identify MS events induced by fault activation. In this section, MS events, which could accurately reflect the mechanism of fault activation, will be selected by studying the correlation between MS activity and fault activation.

### 3.1 *Spatial distribution of the microseismicity caused by fault activation*

Figure 2 shows the spatial distribution of MS events on monitoring region of the underground powerhouse caverns during the monitoring period. Spheres represent MS events and different sizes represent different energy scales. It can been seen that MS events with high-energy and large-magnitude were mainly located at the region of main powerhouse with

higher stake numbers, showing good agreement with the collapse condition at the sites, which indicates that the MS monitoring technique could be used to identify and delineate the potential failure regions in the underground caverns. The MS events were mainly located near Stake 0+200 m and aligned along the steep angle fault $f_{717}$, which indicates that the MS events were primarily induced by fault activation (Tezuka et al. 2000).

### 3.2 *Temporal distribution of the microseismicity caused by fault activation*

MS events occurred in particular region (N: −141.00~108.00, E: 190.00~250.00, D: 602.00~750.00) and aligned along fault $f_{717}$ will be studied in this section. Figure 3 shows the temporal distribution of MS activities, MS cumulative energy.

It can be observed that MS events frequently occurred between October and November of 2014, subjected to the excavation of first layer of main powerhouse. The number of MS events per day was nearly 20 or more. At the beginning of December, fault reached a new stable condition in the initial period of stress adjustment, corresponding with the phenomenon of decreasing of MS events rate below 5 per day. In late December, the phenomenon of increasing MS activity rate is mainly caused by a secondary instability of fault due to stress redistribution. At the end of January the stress field inside the rock mass tended toward stability and support measures enhanced the bearing capacity and restrained the development of cracking in the surrounding rock mass. Thus, fault got into a stable state and MS activity decreased.

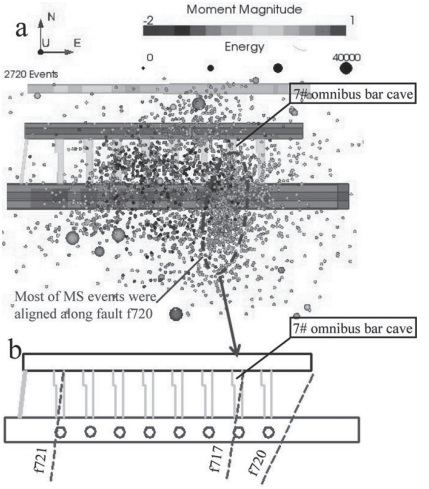


Figure 2. Relationship between spatial distribution of MS events and the location of fault. (a) Spatial distribution of MS events, (b)The planar distribution of faults.

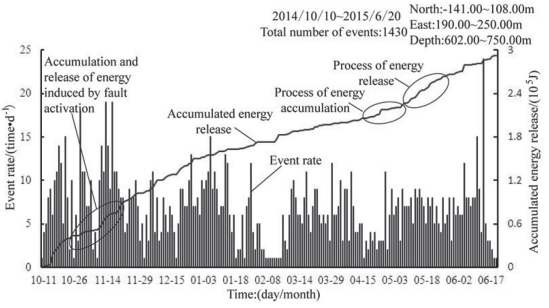


Figure 3. Relationship charts between accumulative energy loss of MS events, activity rate and time in the area controlled by fault.

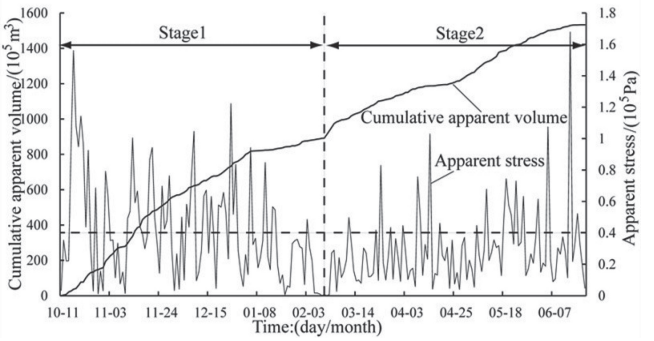


Figure 4. Changes in the cumulative apparent volume and in the apparent stress vs. time.

As mentioned above, the degree of MS activity rate could be used as an indicator to reflect the evolution process of mechanical state of fault. Therefore, it is possible to investigate the characteristics of fault activation by using MS data captured in this particular zone. In addition, fault activation can be defined as a process of energy releasing when the value of energy accumulation reaches a certain level, which is corresponding to the tendency of temporal curve of accumulative energy loss of MS events. This shows that the characteristics of MS events occurred in particular zone could accurately reflect the mechanism of fault activation.

## 4 MS CHARACTERISTICS ANALYSIS OF FAULT ACTIVATION

Two types of deformation mode of fault could be classified, which included movement and propagation of fault. The different deformation mechanism usually results in different manifestations of deformation behavior. By analyzing the temporal changes in multiple MS parameters, attempts are made to seek the deformation mechanisms responsible for fault.

### 4.1 *Deformation mechanism of fault based on apparent stress and apparent volume*

Mendecki (1997) successfully introduced quantitative seismology into the field of rock mechanics, which considered that seismic waveforms do not contain direct information regarding absolute stress and strain, reliable estimates of the apparent stress and apparent volume can be used as indicators of the local levels of stress and strain, respectively. Therefore, apparent stress and apparent volume can be applied to study the deformation mechanism of fault.

The changes in the cumulative apparent volume and apparent stress of MS events, which occurred from October 10, 2014 to June 20, 2015 and in particular region (N: –141.00~108.00, E: 190.00~250.00, D: 602.00~750.00), are shown in Figure 4. It can be seen that the stress state of the particular region can be divided into two stages based on the variation range of apparent stress. Stage 1 can be referred to as the period of excavation and supporting of the first layer of main powerhouse. And stage 2 is referred to as the period of excavation of the second or third layer of main powerhouse. Before March 2015, the apparent stress was greater than 0.04 MPa, and the increment in the cumulative apparent volume was $8.0 \times 10^7$ cm$^3$. After March 2015, the apparent stress was generally less than 0.04 MPa; however, the increment in the cumulative apparent volume was still $8.0 \times 10^7$ cm$^3$. This phenomenon, in which a higher stress did not cause a higher strain, suggests that there was a significant difference in deformation mechanism of fault rupture. Moreover, according to the studies of Zhang et al. (2014) and Mendecki (1997), fault propagation was associated with excavation and supporting of the first layer of main powerhouse and the excavation of the second or third layer of main powerhouse was related to fault movement.

### 4.2 *Deformation mechanism of fault based on Es/Ep*

It is commonly accepted that Es/Ep values associated with rock mass fracturing involving tensile failure are smaller than 3. If Es/Ep is greater than 10, the energy radiated in the P-wave is only a small proportion of that in the S-wave, and this fracturing process can be considered as involving shear failure (Gibowicz 1991, Hudyma 2008). Therefore, it is promising for judging the failure type of fault plane based on the energy ratio judging criteria.

After filtering out the disturbing signals, 1430 MS events were captured in the particular region from October 10, 2014 to June 20, 2015. Thus, 50 MS events were chosen as the calculated window and 25 MS events as the sliding window to calculate the temporal evolution of the value of Es/Ep, as shown in Figure 5.

The average ratio of MS events, which registered Es/Ep value above 10, remained consistent during the monitoring period. The average ration of MS events involving tensile failure induced by fault propagation was markedly higher than that induced by fault movement. This phenomenon mentioned above, indicates that the initiation, development and coalescence of tensile micro-fractures has significant influence on the initiation, propagation of new fault plane during fault propagation period. Meanwhile, tensile fracture was the main failure mode of surrounding rockmass affected by fault in this phase, accompanying with tiny amount of shear fracturing.

### 4.3 *Deformation mechanism of fault based on b value*

In this paper, the b value of MS events induced by fault activation was estimated using a moving window approach. For the calculated window and the sliding window, 55 events and 25 events were adopted, respectively. The magnitude of MS events in this paper was from –0.6~0.6, and we adopted $\Delta M = 0.08$ to calculate b value.

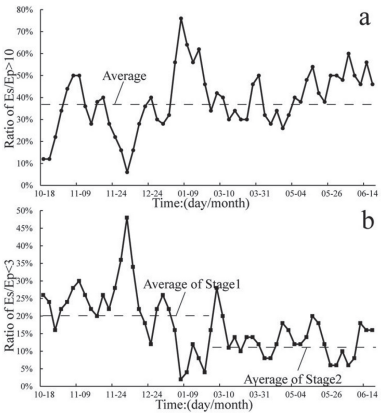


Figure 5. Variation the frequency of Es/Ep vs. time (a) Variation of the ratio of Es/Ep > 10, and (b) Variation of the ratio of Es/Ep < 3.

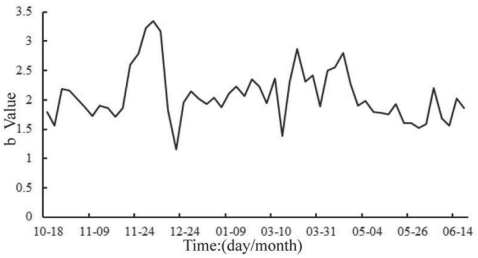


Figure 6. Variation of the b value vs. time.

Figure 6 shows the evolution law of b value with time. Before December 2014, the b value remained constant at a high level. Incorporating with MS event rate, it can be found that the proportion of small and large magnitude events remained constant. And there were much more small scale cracks during this period, which indicates the fault got into the state of progressive stable propagation on the effect of excavation of the first layer of main powerhouse. In late December, fault got into the unstable state again caused by stress redistribution. The b value decreased rapidly as a result of the proportion of large scale events induced by fault activation increasing. Incorporating with Figure 5, it can been found that large amounts of small scale cracks involving tensile failure gradually coalesced into larger scale cracks, and fault got into the state of rapid unstable propagation during this period. During fault movement, the small amplitude fluctuation of b value occurred repeatedly, which indicates that slightly frictional sliding along a pre-existing fracture resulted in lots of small-scale tensile cracks, then sharply slipping will occur when the tangential sliding force reaches the ultimate strength.

## 5 CONCLUSIONS

Most of the MS events were aligned along the steep angle fault $f_{717}$, which indicated that the MS events were primarily induced by fault activation. By analyzing MS activity rate, the evolution process of fault activation subject to excavation is further understood.

The relation between apparent stress and cumulative apparent volume is different during different stages of excavation, which indicates that deformation mechanism of fault rupture is not same. The results showed that fault propagation was associated with excavation and supporting of the first layer of main powerhouse, and excavation of the second or third layer of main powerhouse was related to fault movement.

It can be seen that the failure mode was dominated by tensile fractures in the phase of fault propagation. The *b* value decreased rapidly after late December, which revealed that the fault got into the state of rapid unstable propagation in the initial period of stress adjustment. The degree of fault activation was slight during the excavation of the second and third layer of the main powerhouse according to the fluctuation of *b* value.

## REFERENCES


Aminzadeh, F., Tafti, T.A. & Maity, D. 2013. An integrated methodology for sub-surface fracture characterization using microseismic data: a case study at the NW Geysers. *Computers Geosciences* 54: 39–49.

Gibowicz, S.J., Young, R.P., Talebi, S. et al. 1991. Source parameters of seismic events at the underground research laboratory in Manitoba, Canda: scaling relations for events with moment magnitude smaller than-2. *Bulletin of the Seismological Society of America* 81(4): 1157–1182.

Ge, M.C. 2005. Efficient mine microseismic monitoring. *International Journal of Coal Geology* 64(1/2): 44–56.

Hudyma, M.R. 2008. *Analysis and Interpretation of Clusters of Seismic Events in Mines*. Perth: University of Western Australia.

Hydro-China Huadong Engineering Corporation 2013. *Bidding Documents Reference of Civil Engineering and Installation of Metal Structures of the Left Bank Water Diversion and Power Generation System in Baihetan Hydropower Station*.

Jiang, F.X., Liu, W.J. & Ye, G.X. et al. 2010. Coupling study of microseismic monitoring and numerical simulation for tectonic activation. *Chinese Journal of Rock Mechanics and Engineering* 29(Supp2): 3590–3597.

Mendecki, A.J. 1997. *Seismic Monitoring in Mines.* London: Chapman and Hall.

Tezuka, K. & Niitsuma, H. 2000. Stress estimated using microseismic clusters and its relationship to the fracture system of the Hijiori hot dry rock reservoir. *Engineering Geology* 56: 47–62.

Xu, N.W., Tang, C.A. & Li, L.C. et al 2011. Microseismic monitoring and stability analysis of the left bank slope in Jinping I Hydropower Station in southwestern China. *International Journal of Rock Mechanics and Mining Sciences* 48(6): 950–963.

Zhang, P.H., Yang, T.H. & Yu, Q.L. et al 2013. Microseismicity induced by fault activation during the fracture process of a Crown pillar. *Rock Mechanics and Rock Engineering* 54: 39–49.

*Rock Dynamics: From Research to Engineering – Li et al. (Eds)*
*© 2016 Taylor & Francis Group, London,* *ISBN 978-1-138-02953-8*

# The cavity detection method of highway subgrade and the grouting effects contrast

H.L. Deng, Y. Guo & G. Chen
*Beijing University of Technology, Beijing, China*

ABSTRACT: Owing to exploitation of tunnel and other underground space, the structure and stress form of the original foundation soil has been changed. What's more, it also causes the damage of foundation soil structure and the destruction of the ground structures. Meanwhile, it leads to engineering accidents and serious social impact. Therefore, adopting an advanced detection technology has important engineering application value and social significance. The GPR detection technology can detect the underground unknown geological body quickly. Then, this paper conducts cavity exploration combining the K62 + 0 ~ 100 collapse section of Kun Yu highway. The detection results are used to guide the subgrade strengthening and the grouting effects have been examined which gained good application results.

## 1 INTRODUCTION

With the constant development and utilization of urban underground space, ground subsidence accidents happened very often owing to the complex engineering geological conditions and construction environment. Therefore, it is very important to improve the underground cavity detection technology continuously and improve the level of detection in order to ensure the safety of people's life and property at the most extent.

The GPR is a kind of exploration instruments to inspect and locate invisible target body underground, which is used widely in geological survey, nondestructive examination and hydrogeology survey, etc. The GPR is a kind of electromagnetic wave detection method which sends broadband pulse electromagnetic wave in a definite frequency to underground medium in order to ensure the distribution of medium. The GPR contains the host and the antenna, moreover, the antenna is composed of reception and emission. The transmitting antenna sends transmitting antenna to the tested body while the receiving antenna receive reflection wave of medium internal interface. The receiving antenna located on the ground receives the echo underground which will be transmitted to the receiver later. The signals are transferred to the radar host or the computer by cable transmission after being arranged and amplified by the receiver. What's more, the radar host or the computer will code the electromagnetic wave signals according to the amplitude of the size and display the results by grey-scale map, accumulation of waveform figure and pseudo color map in order to judge the features of the underground targets such as depth, size and location (Cai 2006, Ge 2005, He & Lun 2009, Jie 2012, Qing & Liang 2012, Ye et al. 2004, Yue & Wang 2007, Yang & Peng 2008, Zhu & Deng 2014).

## 2 THE GENERAL SITUATION

Bao Feng tunnel of Kun Yu railway passes underneath the high velocity portion which is located in the watershed area between Dian Xie basin and Yu Xi basin, and the watershed area is formed by tectonic erosion. The tunnel is in the bottom of the denudation, the terrain is undulating rolling, and horizontal gully have developed. The surface is Holocene slide rock of long four period, the thickness of the residual deposit such as silty clay and gravelly soil is

Figure 1. The cave-in mouth of the roadbed.

2~12 m. The bed rock is the slate clip sandstone, the limestone and the mudstone of Sinian period Kun Yang Qun Hei Shantou groups. The rock is completely decomposed basically, the region structure has developed, the warm water camp strike-slip fault passes through the reservoir and the tunnel under the high-speed period, the width of the surface survey fault zone is about 100 m and the engineering geological condition is poor. Bao Feng tunnel has complicated hydrogeological conditions. The reservoir of Da Chun river is located in the left of the tunnel and connected with zone formation by the water channel. The groundwater type is bedrock fissure water and karstic water, the aquifer is the slate clip sandstone and the limestone of Hei Shantou groups. And the underground water is in weak acid, the grade of erosion is H1, and the depth of underground water level is about 20 m.

Bao Feng tunnel of Kun Yu railway passes underneath the high velocity portion (the mileage is D2K11 + 400 ~ 450) and the center distance corresponds to the highway mileage K62 + 050. The tunnel vault is buried deeply 68 m and the rock class level is VI. In May 2015, when the tunnel was excavated to the section of D2K11 + 469, the upper side of the core soil in workplace appeared squeeze-out phenomenon. The extrudate is saturated weathered sandstone (silty-fine sand), the self-stability is very poor and the intermittent flow sand occurred repeatedly. In addition, on May 23, 2013, the road management department of Kun Yu railway found a pit on the right side of the cutting of Yu Xi direction in the 28 m away from the right side of DK11 + 463 of Bao Feng tunnel (corresponds to the Kun Yu highway mileage K62 + 048), and the pit is circular, the diameter is 5.3 m and the depth is 8 m. In June 2015, the outer edge of the ditches which is on the right side of the high velocity portion of Bao Feng tunnel of Kun Yu railway passing underneath appeared ground subsidence landslides, which affected the road operating safety, as shown in Figure 1. On June 23, 2015, emergency construction has been organized to manage the collapse (pouring concrete into the hole) in order to prevent and control disaster from occurrence. Since June 24, 2015, the GPR detection work and the grouting effect test has been carried on in order to ensure the position of the cavity accurately, guide the reinforcement engineering and guarantee the quality of reinforcement engineering.

## 3 THE SUBGRADE CAVITY'S MEASUREMENT RESULTS AND ENSURING THE GROUTING SCHEME

According to the on-site geological conditions and terrain conditions, 15 geological survey lines are arranged along the direction of road in order to ensure the location, size and

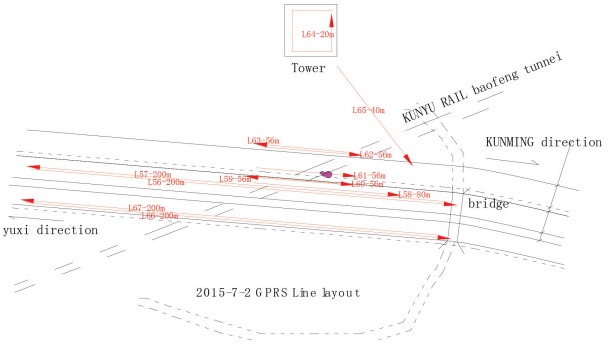


Figure 2. The detection lines' arrangement diagram of the roadbed cavity.

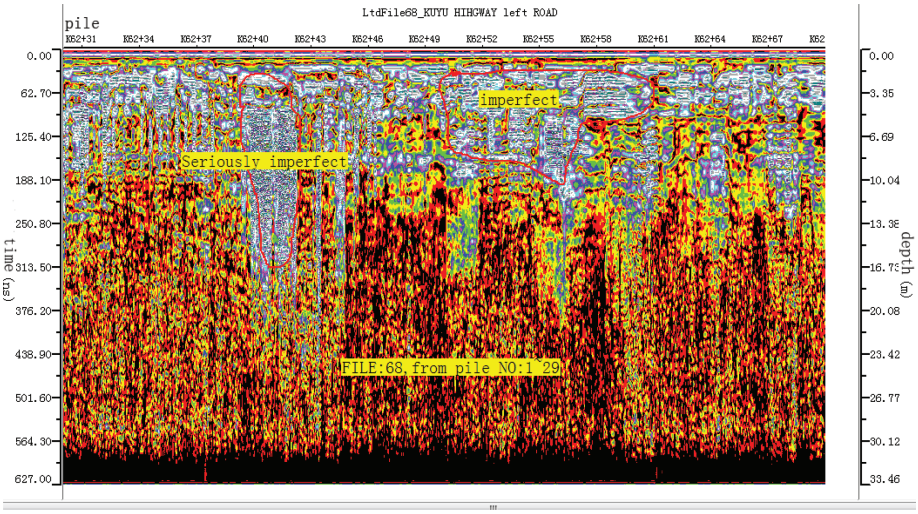


Figure 3. Geological radar pseudo color profile of the roadbed cavity.

features of the cavity under the k62+0~100 roadbed of Kun Yu highway accurately. The interval between survey lines is about 2 m and the length of survey lines is 50 meters to 200 meters. As shown in Figure 2: the sampling points are 1024, the sampling time window is 1000, the sampling rate is 64, the detection mode is Wheel control, the dielectric constant is 7, the data bits is 16, the markup extensions is 1, the trigger distance is 0.1cm, using LTD2100 geological radar host and 100 MHZ antenna to detect work.

The GPR detection results of the 5.23 collapse section in Kun Yu highway show that there is bad geological phenomenon of serious imperfect and imperfect exists respectively in K62 + 039 ~ 042, the depth of the 2 ~ 16 m range and in K62 + 50 ~ 60, the depth of the 1~10 m, which may cause the continuation of roadbed subsidence or cave-ins. As shown in Figure 3. Using the slurry to grout and reinforce the roadbed according to the result of detection. The Processing range is K62 + 020 ~ 080, the width is 4 m and the depth is 0 ~ 20 m. Using quincuncial piles to arrange grouting holes, the pitch of holes is 2 m and the water cement ratio is 1:1, the maximum grouting pressure is 2MPa. Meanwhile, segmented grouting method is adopted. Under pressure from segmentation rules, when the injection rate is not greater than 0.4 L/min, it need to grout for 10 min more, or the grouting quantity is not more than 1 L/min, it need to grout for 15 min more and the grouting time of each section should be not less than 20 min under the design pressure.

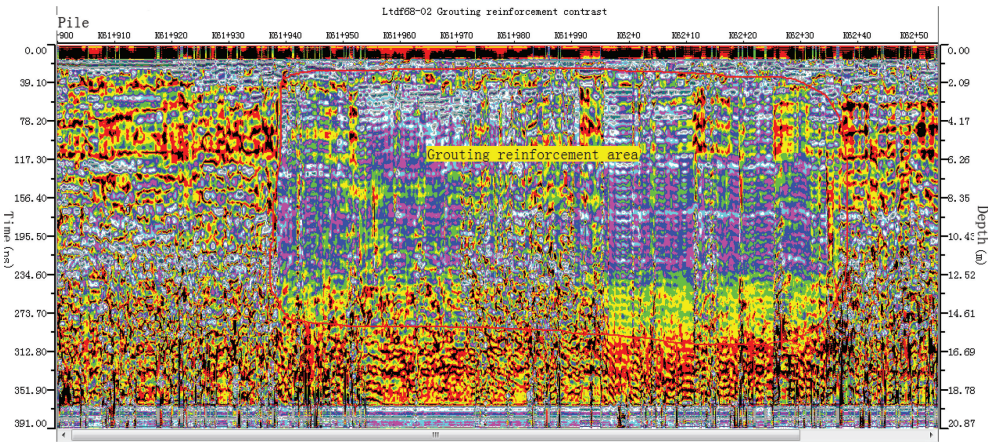


Figure 4. Geological radar pseudo color profile after the grouting.

## 4 THE GROUTING EFFECTS OF THE SUBGRADE CAVITY DETECTION AND CONTRAST

The 5.23 collapse section of Kun Yu highway was tested and contrasted the grouting effect after 24 hours at the end of the grouting. The collapse section had arranged six lines totally to test and contrast the effect of the subgrade grouting for different location respectively. Test results are shown as follows:

The grouting area boundary is obvious, the subgrade soil reinforcement is obtained after the grouting and the bearing capacity is improved obviously while the water content in roadbed is reduced.

The subgrade soil after the grouting in the grouting area is uniform and tight, which there is no empty and imperfect area.

The effective grouting depth is 16 m, and the grouting depth and scope of meet the design requirements. Geological radar pseudo color map is shown in Figure 4.

## 5 CONCLUSION AND SUGGESTION

Because of the influence of the engineering geological conditions and construction factors, it will cause the destruction of the foundation soil loss and geological structure during the development and utilization of underground space and then generate the ground collapse and landslide accident, which has seriously influenced people's life and property safety. This paper uses the geological radar detection technology to detect the cavity under Kun Yu highway roadbed, and formulates the reasonable reinforcement scheme according to the result of detection. And this paper has summarized and analyzed the subgrade cavity detection technology and cavity processing technology, which have achieved very good application results.

Using the GPR to detect the underground cavity is very professional, high technical requirements and comprehensive special technology and the selection of parameters, detection method and processing method directly affect the effect and reliability of results at the time of detection. Only under the condition of have enough professional knowledge background, strictly carrying out operation procedures can get the real detection results.

The subgrade soil cavity under the road is uncertain, irregularity and variability, so choosing reasonable reinforcement methods and design parameters during the implementation of grouting reinforcement should be based on the engineering properties and mechanical properties of subgrade soil in order to a good reinforcement effect.

## REFERENCES


Cai, H.Y. 2006. The technology study of using the ground penetrating radar to detect imperfect area of the roadbed. *Science & Technology* (7): 1–2.

Ge, R.B. 2005. An application of ground penetrating radar to detecting voids inside highway pavement-retrospect and prospect. *Geology and prospecting(S)* (45): 106–108.

He, M.K. & Lun Y.X. 2009. The GPR's application in the municipal engineering field. *Geotechnical Investigation & Surveying(S)* (2): 486–493.

Jie, H.F. 2012. The application of grouting technology in treatment of covered karst cave in tunnel. *Railway Construction Technology* (3): 43–45.

Qing, Y.H. & Liang, J. 2012. The application of grouting method in processing cave crack in ground engineering (3): 43–45.

Yang, F. & Peng, L.P. 2008. The research about interpretation method of cavity detected by the GPR. *Chinese Physical Geography* (9): 221–222.

Ye, J.W., Wu, P. & Zheng, G.L. 2004. Inspection of Pavement Structural Defects Based on the Ground Penetrating Radar. *Journal of South China University of Technology* 32(9):82–85.

Yue, C.W. & Wang, Z.W. 2007. Application of ground penetrating radar in investigation on subterranean cavitation. *Global geology* 26 (1):114–117.

Zhu, M.Y. & Deng, H.L. 2014. Application of ground penetrating radar in road defect detection. *Shanxi Architecture* 40(4): 134–136.

This page intentionally left blank

*Rock Dynamics: From Research to Engineering – Li et al. (Eds)*
*© 2016 Taylor & Francis Group, London,* *ISBN 978-1-138-02953-8*

# The design and implementation of automatic warning system of tunnel monitoring

H.L. Deng, G. Chen & Y. Guo
*Beijing University of Technology, Beijing, China*

ABSTRACT: Tunnel monitoring measurement is an important working procedure of the tunnel construction, and it is also one of the three elements of "new Austrian method". Currently, most of the data is stored and processed by EXCEL, however, due to the large amount of tunnel monitoring measurement task, the amount of data that had been collected from the scene is very huge every day, therefore, just relying on technicians manually to input, store, classified process data and generate reports which will take up a lot of manpower and material resources, and very easy to make mistakes in the meantime. Because of the lack of practical and efficient monitoring data analysis and processing technology, monitoring work is difficult to play a real role. This paper which based on Access of Microsoft has developed an automatic warning system of tunnel monitoring that has a friendly user interface. This system contains lots of functions, such as data inputting, storage, inquiring, alarm, and regression analysis, what's more, it also effectively improves the efficiency and management level.

## 1 INTRODUCTION

No matter what kind of method is used to excavate tunnel and other underground facilities in the mountain areas, it will cause internal force redistribution of the surrounding rock mass, affect its integrity and stability and change the original rock stress state. Thus, it will inevitably cause displacement deformation phenomenon such as vault sinking, clearance convergence and ground surface settlement in the construction process of tunnel. The phenomena of settlement and convergence have some certain rules. Through the study of these rules, it can able to judge if the rock mass is stability or not, the supporting structure is effective or not and the construction method of tunnel is safety or not, predict possible construction hazards and adjust the construction and supporting forms timely, thereby optimizing the construction scheme and ensuring the construction safety of the tunnel. From the present situation of the current domestic tunnel monitoring work, most of the data is stored and processed by EXCEL. Developing an automatic warning system of tunnel monitoring has an important theoretical significance and engineering application value in order to serve the information construction at the scene and manage monitoring data in a better way, process and analyze data timely and accurately. Using this system can be more convenient and accurate to find historical data in the future, and analyze and decide monitoring data quickly. Furthermore, it also meets the needs of the tunnel construction control (Chung et al. 2006, Guo et al. 2009, Deng et al. 2010, 2011, 2012, Kim et al. 2008, Wu et al. 2013a, b, Ye et al. 2009).

## 2 STRUCTURAL DESIGN OF THE SYSTEM

Tunnel monitoring data processing mainly includes data inputting, storage, querying, alarm, regression analysis, and early warning and prediction. Therefore, this system is made up of 3 subsystems, namely: Data pre-treatment and inputting system, Data analysis and querying system, and Report generation system. Data pre-treatment system can filter data which col-

lected directly by measuring instrument such as total station and remove error data because of incorrect operation in the process of data collection. What's more, it can calculate data after filtration and make the data become standard format, in order to prepare for the next inputting data. Batch processing system can calibrate the initial value of tunnel sections and edit the data format. Data inputting system can use a variety of ways to input or import the initial value and the daily data into the system and stored the data in the database uniformly. What's more, different level of the administrator has different administrative privilege. Using this system emphasizes the significance of the initial value and can avoid modifying the daily data artificially in the daily data inputting at the same time. Data querying system has been designed to inquire data in a variety of ways. This system can inquire the existing data which cannot be modified conveniently and quickly, in order to ensure the authenticity and seriousness of monitoring data. Considering all the data have to be submitted to the superior departments through the report form, report generation system has been designed for the standard format of general monitoring report. The subsystem can generate reports which are in accordance with the prescribed format. The reports include daily, weekly and monthly reports, stability analysis reports, early warning and prediction reports and other temporary reports. The overall structure of this system is shown in Figure 1.

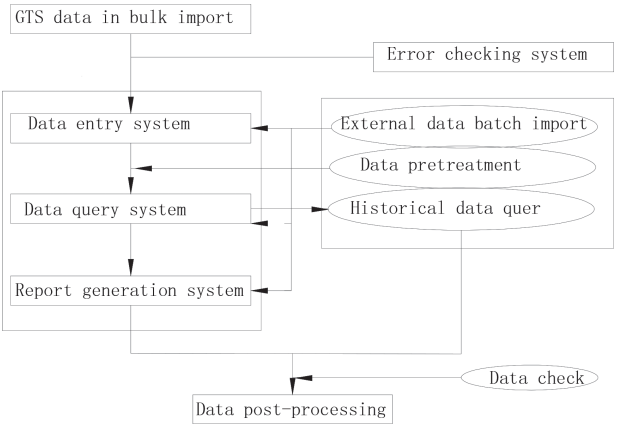


Figure 1. The overall structure of this system.

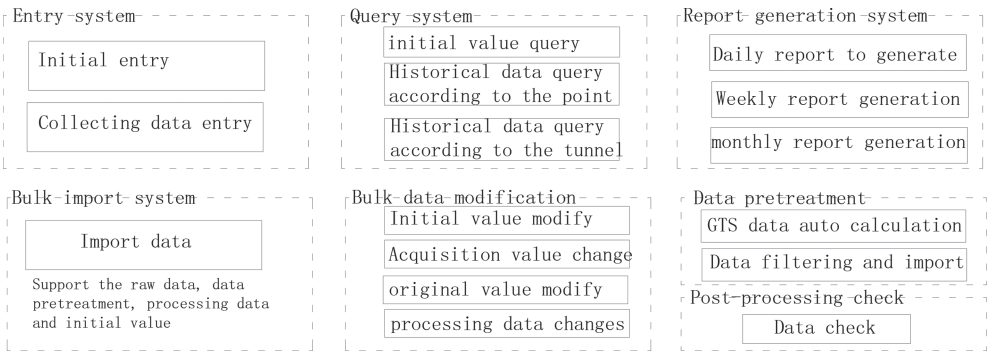


Figure 2. The main interface of this system.

This system has developed by the management platform of Microsoft Access database, which is simple to operate, and has a friendly interface. What's more, it is easy to learn how to use and master this system. The main interface is shown in Figure 2.

## 3 DATA PRE-TREATMENT AND INPUTTING SYSTEM

Data pre-processing, inputting and storage is one of the core content of this system, which includes authenticity and reliability inspection of all kinds of original monitoring information, filtering analysis, regression analysis, normalization, physical encoding, frame column saving, etc. The file types that inputted in the system include *.xls, *.csv, *.jpg and so on.

The initial value inputting workflow includes: user login (permissions validation) – creating a new record (or importing existing records) – inputting recorded data. The information needs to be inputted including tunnel name, the section mileage, the measured point, the collecting time, date, the three collection value and the distance from the surveying section to the working face. If there is a damage point, you need to input the stationing time and the modified value. The initial value inputting interface is shown in Figure 3.

The tunnel construction monitoring measurements use different measuring methods to monitor a batch of tunnel's construction safety, meanwhile, there are so many working points and measurement points, complex monitoring content and large data that using the traditional office software and working method not only wastes large manpower and material resources, large calculated amount, long computation time and even appears the calculation data overflowing, but also often appears many issues such as data error and format error, furthermore, its real-time performance is so poor that it is useless to adjust the supporting measure and the degree of informatization is low so that it can't guide the tunnel construction in time. This system can process a series of batch data, which include authenticity and reliability

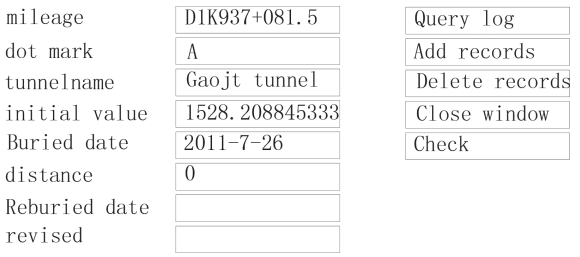


Figure 3. The initial value inputting interface.

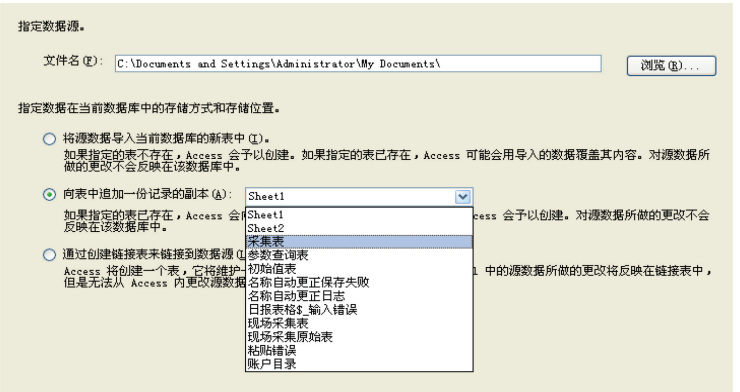


Figure 4. The batch interface.

inspection of all kinds of original monitoring information, filtering analysis, regression analysis, normalization, physical encoding, frame column saving, etc. What's more, the system can import the original data the database system in the form of collection tables, conduct batching automatically and realize calculation, calibration and storage of the collected data. The batch interface is shown in Figure 4.

## 4 DATA ANALYSIS AND QUERYING SYSTEM

Monitoring measurement is the foundation of the tunnel construction of information management. Therefore conducting monitoring data's real-time analysis, distinguishing, querying, early warning and forecasting to guide construction and avoid the risk.

This system is able to conduct the time-space analysis and the influence factor analysis according to log-linear regression model, cubic regression model, the power regression model and exponential regression model of monitoring data. The system can generate time-space analysis graph automatically, calculate regression equation and coefficient of determination R2. Meanwhile, the system also can conduct risk identification and early warning and forecasting according to the variation, the cumulative amount of change, the rate of change, the construction method and the distance from the surveying section to the working face, etc.

This system has a function of statistical analysis, which can conduct statistical analysis according to the independent or composition condition such as monitoring location, monitoring type, project name, monitoring time interval, monitoring time, burying points time, displacement value and the rate of change in order to generate statistics reports and analytical curve.

This system has designed three-level risk management system and three-level early warning mechanism. According to displacement of surrounding rock control benchmark, the tunnel

| data | T | ini.Num. | value1 | value2 | value3 | sum value | Distance |
|---|---|---|---|---|---|---|---|
| 2011-9-1 | 13 | 1380.12210 | 1380.11343 | 1380.11558 | 1380.11484 | 7.48480 | 165 |
| 2011-9-2 | 13 | 1380.12210 | 1380.11258 | 1380.11501 | 1380.11437 | 8.11648 | 175 |
| 2011-9-3 | 13 | 1380.12210 | 1380.11205 | 1380.11469 | 1380.11400 | 8.52376 | 182 |
| 2011-9-4 | 13 | 1380.12210 | 1380.11172 | 1380.11382 | 1380.11358 | 9.06267 | 188 |
| 2011-9-5 | 13 | 1380.12210 | 1380.11151 | 1380.11294 | 1380.11311 | 9.58280 | 192 |
| 2011-9-6 | 13 | 1380.12210 | 1380.11125 | 1380.11240 | 1380.11271 | 9.98337 | 196 |
| 2011-9-7 | 13 | 1380.12210 | 1380.11108 | 1380.11194 | 1380.11255 | 10.24354 | 200 |
| 2011-9-8 | 13 | 1380.12210 | 1380.11085 | 1380.11125 | 1380.11215 | 10.68534 | 205 |
| 2011-9-9 | 13 | 1380.12210 | 1380.10996 | 1380.11085 | 1380.11185 | 11.21697 | 210 |
| 2011-9-10 | 13 | 1380.12210 | 1380.10951 | 1380.11050 | 1380.11141 | 11.62876 | 212 |

Figure 5. Historical data retrieval according to the measurement point.

| mileage | sec.mileage | NO | Date | Time | ini.value | Bur.date | Vol.1 | Vol.2 | Vol.3 | Av.Vol | distance |
|---|---|---|---|---|---|---|---|---|---|---|---|
| HD1K0+190 | HD1K0+185 | A | 2011-9-1 | 8 | ########## | 2011-9-1 | 1380.99195 | 1380.99195 | 1380.99195 | 1380.99195 | 5 |
| HD1K0+190 | HD1K0+185 | A | 2011-9-1 | 13 | ########## | 2011-9-1 | 1380.99095 | 1380.99085 | 1380.99068 | 1380.99082 | 5 |
| HD1K0+190 | HD1K0+185 | AB | 2011-9-1 | 8 | ########## | 2011-9-1 | 3.78025 | 3.78010 | 3.78035 | 3.78023 | 5 |
| HD1K0+190 | HD1K0+185 | AB | 2011-9-1 | 13 | ########## | 2011-9-1 | 3.77924 | 3.77963 | 3.77968 | 3.77952 | 5 |
| HD1K0+190 | HD1K0+185 | AC | 2011-9-1 | 8 | ########## | 2011-9-1 | 5.45684 | 5.45684 | 5.45678 | 5.45682 | 5 |
| HD1K0+190 | HD1K0+185 | AC | 2011-9-1 | 13 | ########## | 2011-9-1 | 5.45587 | 5.45535 | 5.45569 | 5.45564 | 5 |
| HD1K0+190 | HD1K0+185 | BC | 2011-9-1 | 8 | ########## | 2011-9-1 | 7.77346 | 7.77325 | 7.77350 | 7.77340 | 5 |
| HD1K0+190 | HD1K0+185 | BC | 2011-9-1 | 13 | ########## | 2011-9-1 | 7.77248 | 7.77314 | 7.77284 | 7.77282 | 5 |
| HD1K0+210 | HD1K0+190 | A | 2011-8-31 | 13 | ########## | 2011-8-29 | 1380.48941 | 1380.48954 | 1380.48928 | 1380.48941 | 20 |
| HD1K0+210 | HD1K0+185 | A | 2011-9-1 | 13 | ########## | 2011-8-29 | 1380.48839 | 1380.48827 | 1380.48851 | 1380.48839 | 25 |
| HD1K0+210 | HD1K0+190 | AB | 2011-8-31 | 13 | ########## | 2011-8-29 | 3.70900 | 3.70913 | 3.70887 | 3.70900 | 20 |

Figure 6. Historical data retrieval according to the tunnel.

**Tunnel clearance measurement records**

mileage: DK977+124 instruments: GTS NO: HJD01

| name | HJD01 | | | Construction unit | China railway 22 co., LTD | | Unit engineering | HEjiadi tunnel | | meth-od | steps meth-od | part s | step s | date | 2016-01-30 |
|---|---|---|---|---|---|---|---|---|---|---|---|---|---|---|---|
| Line number | Measurement time | | | | Measurement numerals | | | | revised | Revised. | change (<d μ) cumulative | change (<d μ) | time | Change speed | note |
| | year | month | date | time | Temp. | one | two | three | Average. | | | | | | | |
| | | | | | ℃ | m | m | m | m | mm | m | mm | mm | d | mm/d | |
| A | 2016 | 02 | 15 | 7 | - | 1832.1609 | 1832.1609 | 1832.1608 | 1832.1609 | - | - | 27.19 | 27.19 | 14 | 1.9421 | Dist.20 m |

reader: reckoner: review:

Figure 7. Automatically generate reports.

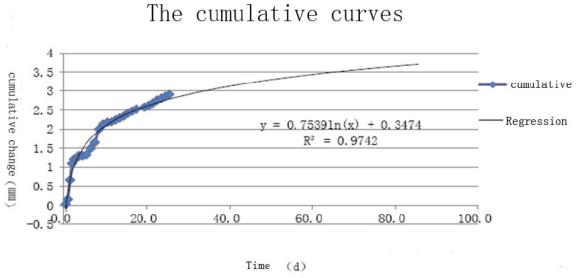


Figure 8. Monitoring data analysis curve.

construction risk has been divided into three risk management level, namely: I, II, III level. Meanwhile, the tunnel early warning and prediction has been divided into three risk level, namely: yellow, orange and red, according to the displacement of surrounding rock control benchmark and the rate of change. This system can send out early warning and prediction in the form of sound, light, electricity, text messages and micro letters. According to the tunnel surrounding rock displacement curve and the total displacement, this system also can ensure the steady state of surrounding rock, the supporting scheme and the time of constructing the secondary lining in order to come up with measures and suggestions of the construction scheme and realize the monitoring information management.

The system has designed conditional inquiry function and conditional sequence function in more than one way to realize the initial value retrieval of monitoring data, the current monitoring data retrieval, the interval of historical data retrieval, history data retrieval according to the measurement point and history data retrieval according to the project or the work area, as shown in Figure 5 and Figure 6.

## 5 REPORT GENERATION SYSTEM

Tunnel monitoring data and analysis results which are the key technical data of guiding construction must be reported, recorded and archived in various report forms in order to modify and optimize the construction scheme and ensure the reasonable time to conduct the second lining. This system has designed various standard report templates and can generate reports automatically. Meanwhile, this system also can generate a variety of forms automatically, graphics and texts which daily, weekly, monthly reports need, and all these are saved and sent in the form of PDF. Reports are shown in Figure 7 and Figure 8.

## 6 CONCLUSION AND SUGGESTION

Monitoring measurement is an important working procedure of tunnel construction and one of the three elements of "new Austrian method" because the tunnel construction environment is complex and there are a large number of uncertain factors and variability in the process of tunnel construction. The main content of monitoring measurement includes the vault sinking, the headroom change law of surrounding rock, the arch stress and the pressure of surrounding rock in order to master the steady state of surrounding rock and the stress state of primary support. Monitoring measurement provides scientific basis for ensuring reasonable construction scheme, supporting scheme and the time of constructing the secondary lining, which is an important safeguard for the tunnel construction security and the operation safety after construction.

Using advanced data management methods is the basic approach of information management because the monitoring measurement method is various, monitoring data are greatly influenced by various factors and the amount of data is very huge. This paper has introduced the design content of the automatic warning system of tunnel monitoring, developed the system software, realized the functions of monitoring data inputting, storage, analysis, querying, early warning and prediction and generating reports automatically. Meanwhile, this system also make quick query of monitoring data, early warning and prediction of risk and information management to come true in order to provide effective technical support for the safety of tunnel construction.

The automatic warning system of tunnel monitoring has the advantages of simple operation, a friendly interface and user-friendly. This system can make sure the data to be safe and reliable and the monitoring data to be complete and accurate. In conclusion, this system has improved work efficiency and has a good application prospect.

## REFERENCES


Chung, H.S., Chun, B.S., Kim, B.H. & Lee, Y.J. 2006. Measurement and analysis of Long-term behavior of seoul metro tunnels using the automatic tunnel monitoring systems. *Tunneling and underground Space Technology* 21(3): 3–4.

Deng, H.L. & Fu, X.Y. 2010. The advanced prediction and emergency management technique on construction of shallow buried large section bedding rock unsymmetrical loaded tunnel. *Proceedings of the Eleventh International Symposium on Structural Engineering*: 1755–1760.

Deng, H.L. et al. 2011. Application Research of Construction Monitoring and Early Warning System for Tunnel Construction. *Construction technology* 40(3): 54–56.

Deng, H.L. et al. 2012. The Data Management System of Tunnel Monitoring. *The 2012 International Conference on Computer-aided Material and Engineering (ICCME 2012), Advanced Materials Research 3*.

Guo, Q. & Huang, L. 2009. Software design and modules development of the expressway tunnel monitoring system. *4th IEEE Conference on Industrial Electronics and Applications*: 965–968.

Kim, J.R., Yoo, H.S., Kwon, S.W. & Cho, M.Y. 2008. Integrated tunnel monitoring system using wireless automated data collection technology. *Proceedings from the 25th International Symposium on Automation and Robotics in Construction*: 337–342.

The ministry of railways of the People's Republic of China 2007. *Railway Tunnel Monitoring Technology Procedures.* Beijing: China Railway Publishing House.

Wu, S.L., Deng, H.J. & Chen, K.J. 2013a. Automatic warning system of tunnel monitoring and application. *Document type: Conference article (CA) Conference name: 2013 International Conference on Materials, Transportation and Environmental Engineering, CMTEE* 9:457–462.

Wu, S.L., Deng, H.J. & Chen, K.J. 2013b. Visual monitoring technology of the tunnel 3D laser scanning and engineering applications. *Document type: Conference article (CA) Conference name: 2013 International Conference on Materials, Transportation and Environmental Engineering, CMTEE* 9:463–468.

Ye, Y. et al. 2009. Tunnel construction multivariate information forewarning and safety management system research. *Chinese Journal of Rock Mechanics and Engineering* 28(5): 900–907.

*Rock Dynamics: From Research to Engineering – Li et al. (Eds)*
*© 2016 Taylor & Francis Group, London, ISBN 978-1-138-02953-8*

# Dynamic loads and design of tunnel supports using rock mass quality

R.K. Goel
*CSIR-Central Institute of Mining and Fuel Research Regional Centre, Roorkee, India*

ABSTRACT: The tunnels in the rock mass are affected by the dynamic loads developed by the seismic stress waves. An approach to estimate the shear wave velocity and concept of ratio of wavelength of earthquake shear waves to tunnel span has been discussed. Various approaches for obtaining the Barton's rock mass quality Q and estimating support pressure in tunnels for dynamic conditions are available. It has been experienced in Himalayan tunnels that a tunnel through weaker rock mass suffers more damage than a good rock mass under similar dynamic conditions. Thus, an attempt has been made in the paper to suggest $Q_{dyn}$ (Q value for dynamic condition) for different ground conditions for tunnels. The proposed $Q_{dyn}$ is suggested to be used for designing the supports using the support chart of Grimstad & Barton (1993).

## 1 INTRODUCTION

In most part of the World, majority of the tunnels are built in rocks. While designing the tunnels, one of the factors to be considered is the safety of rock tunnels and caverns under dynamic loads generated mainly by seismic stress waves. Since rock masses generally contain fractures in different scales, the interaction between stress waves and rock materials and fractures affects not only stress wave attenuation, but also rock mass instability. As such the tunnels in the rock mass, though less than surface structures, are also affected by dynamic loads developed by the seismic stress waves. A major reason for the reduction in underground damage is the lower levels of shaking at depth in comparison with surface motions.

Wang & Cai (2015) have observed that the P-wave induced disturbance around the excavation is small but the S-wave induced disturbance to the wave field is large. Thus, among the seismic waves of an earthquake underground, the shear wave and interference of shear waves at the tunnel boundary is found to be more dangerous for the safety of underground structures. The earthquake waves may not notice the smaller size tunnels. But in case of large underground openings the seismic stress waves are found to be effective. Similarly, peak ground acceleration has also been correlated with the performance of underground structures (Dowding & Rozen 1978, Sharma & Judd 1991).

Sharma & Judd (1991) have studied the damage in tunnels with the depth and found that the tunnels having depth less than 50 m are likely to be affected by the earthquake. On the other hand, they observed that tunnels at a depth of more than 500 are slightly affected by the earthquakes. Sharma & Judd (1991) also observed that the earthquakes of Richter magnitude greater than 6 are found to be more damaging for the tunnels. According to Gutenberg & Richter (1954), the Richter magnitude (M) is related with modified Mercalli intensity (I) by equation, $M = 1 + (2/3)\ I$. From this equation for $M = 6$, $I = 7.5$.

In the paper two aspects have been presented. Firstly, the wavelength of shear waves and the tunnel size have been considered to know whether the tunnel is likely to be affected by the earthquake or not. Secondly, an approach for obtaining dynamic Q value ($Q_{dyn}$) has been suggested. While developing the above two concepts, it has been assumed that the shear waves are perpendicular to tunnel axis and tunnel depth is between 100 m and 500 m.

## 2 SHEAR WAVE VELOCITY AND RATIO OF WAVELENGTH TO TUNNEL SPAN

### 2.1 *Shear wave and its wavelength*

It shall be noted that the ground deformation which affects the response of the underground structure is the shear deformation due to the shear (S) waves amplification around the tunnel openings. Wang and Cai (2015) observed that the P-wave induced disturbance around the excavation is small but the S-wave induced disturbance to the wave field is large. Narayan (2016) also opined that the wave length of shear wave in the rock mass surrounding the tunnel shall be used for the stability analysis of tunnels.

Table 1 shows compressional (or P) and shear (S) waves velocities obtained from Christensen and Stanley (2003) for some commonly found rocks. These velocities are measured after applying a confining pressure of 200 MPa in igneous and metamorphic rocks (S.No. 1 to 6 in Table 1) and 10 MPa in sedimentary rocks (S.No. 7 to 10 in Table 1) (Christensen & Stanley 2003).

Wavelength of shear wave in Table 1, assuming the frequency of 50 Hz and 75 Hz, works out to be between 42.9 m and 80.6 m for igneous and metamorphic rocks and from 30.26 m to 61.2 m for sedimentary rocks (Table 1).

Barton (2002) has observed that the P-wave velocity increases with the tunnel depth and normalized Barton's rock mass quality ($Q_c$) as shown in Eqs. 1 to 3.

$$V_p = 4.4 + 0.7\log Q_c \quad \text{For tunnel depth H = 100 m} \quad (1)$$

$$V_p = 4.7 + 0.6\log Q_c \quad \text{For tunnel depth H = 250 m} \quad (2)$$

$$V_p = 5 + 0.5\log Q_c \quad \text{For tunnel depth H = 500 m} \quad (3)$$

where $V_p$ is P-wave velocity in km/sec, $Q_c = Q.\sigma_c/100$, Q is Barton's rock mass quality and $\sigma_c$ is UCS of intact rock material in MPa.

P-wave velocity at a particular depth varies with $Q_c$. From above equations (Eqs. 1 to 3) the maximum value of P-wave velocity is 6.5 km/sec for all tunnel depths and at $Q_c = 1000$. This shows that as the $Q_c$ increases the depth effect on $V_p$ reduces and ultimately converge to 6.5 km/sec.

The ratio of shear wave to P-wave velocity in Table 1 ranges from 0.53 to 0.67, i.e. shear wave velocity is 53 per cent to 67 per cent of P-wave velocity. Shear wave velocities ($V_s$) can, thus, be assumed as 60 percent of P-wave velocity. Thus, from the equation of $V_p$ (Eqs. 1 to 3) $V_s$ can be estimated using Eqs. 4 to 6 for different depths and the $Q_c$ value of surrounding rock mass.

Table 1. Compressional (P) wave and shear (S) wave velocities in different rocks.

| | | Velocity (km/sec) (Christensen & Stanley 2003) | | Wavelength (λ) of shear wave, m for frequency (f) | |
|---|---|---|---|---|---|
| S.No. | Rock types | P-Wave ($V_p$) | Shear Wave ($V_s$) | f = 75 Hz | f = 50 Hz |
| 1 | Granite | 6.25 | 3.67 | 48.9 | 73.4 |
| 2 | Basalt | 5.91 | 3.22 | 42.9 | 64.4 |
| 3 | Slate | 6.16 | 3.30 | 44.0 | 66 |
| 4 | Phyllite | 6.24 | 3.54 | 47.2 | 70.8 |
| 5 | Granitic gneiss | 6.01 | 3.50 | 46.67 | 70 |
| 6 | Quartzite | 5.96 | 4.03 | 53.7 | 80.6 |
| 7 | Sandstone | 4.55 | 2.82 | 37.6 | 56.4 |
| 8 | Limestone | 5.66 | 3.06 | 40.8 | 61.2 |
| 9 | Shale | 3.58 | 2.27 | 30.26 | 45.4 |
| 10 | Siltstone | 4.62 | 2.85 | 38 | 57 |

$$V_s = 2.64 + 0.42\log Q_c \quad \text{For tunnel depth H = 100 m} \quad (4)$$
$$V_s = 2.82 + 0.36\log Q_c \quad \text{For tunnel depth H = 250 m} \quad (5)$$
$$V_s = 3 + 0.3\log Q_c \quad \text{For tunnel depth H = 500 m} \quad (6)$$

Once the shear wave velocities are known for the rock mass surrounding the tunnel (Eqs. 4 to 6), using the frequency, the wave length of shear wave can be computed. The frequency of shear wave in the rock masses generally can be assumed between 50 Hz and 75 Hz or may be even less.

### 2.2 *Ratio of wavelength of shear waves to tunnel span*

Chen et al. (2012) found that seismically induced stresses are strongly related with the wavelength of the seismic wave. They also found that wavelength λ to tunnel span D ratio (λ/D) has a large influence on ground motion around the underground opening. According to Wang & Cai (2015) when the λ/D ratio is greater than 30, the wave amplitudes are less affected by the excavation and a seismic wave loading can be considered as 'quasi-static'. When the λ/D ratio is less than 20, significant wave interaction occurs and the wave loading needs to be considered as 'dynamic'.

Chen (2005) found that a strong impact on tunnel lining occurred when the λ/D ratio is between 1.0 and 4.5; less impact to the tunnel lining could be expected as the λ/D ratio increased. Because underground openings are not noticed by the seismic waves and no damage to the underground opening is expected. The ground motion in shallow tunnels are related to tunnel dimension and the corner frequency of an earthquake and the tunnels can become vulnerable if the λ/D ratio is small (Wang & Cai 2015).

Wang & Cai (2015) found large difference in wave field around the excavation as the direct S-waves pass through the excavation for different λ/D ratios. As the λ/D ratio decreases, dynamic wave interaction between the S-waves and the excavation increases significantly. This large dynamic wave interaction can lead to strong scattering waves and more complex wave filed around the excavation.

The above work shows that when $\lambda/D < 4.5$, strong impact of earthquake is expected on tunnel supports. Hence, $\lambda/D = 4.5$ is considered as the critical value for a tunnel to experience earthquake effects.

As an example, considering the shear wave velocity obtained from Eqs. 4–6 for tunnel depths 100, 250 and 500 m and for $Q_c$ values 0.1, 1, 4, and 10 and the frequency as 75 Hz, the critical tunnel span for $\lambda/D = 4.5$ is obtained and shown in Table 2.

Tunnel having span more than the span given in Table 2 is likely to experience the earthquake damages under the given conditions. *For example:* a tunnel having span of depth 250 m and $Q_c = 1$ has the critical span of 8.36 m (Table 2). Therefore, a tunnel having span more than 8.36 m is likely to experience damages because of earthquake. On the contrary a tunnel having span of less than 8.36 m may not experience the earthquake damage. Similarly, the approach can be used to identify the critical tunnel span for different shear wave frequencies. This highlights the effect of tunnel size while studying the effect of earthquake.

Table 2. Critical tunnel span for different $Q_c$ values and tunnel depth.

| | Critical tunnel span, m for various $Q_c$ values | | | |
|---|---|---|---|---|
| Tunnel depth (H), m | $Q_c = 0.1$ | 1 | 4 | 10 |
| 100 | 6.58 | 7.82 | 8.57 | 9.07 |
| 250 | 7.29 | 8.36 | 9.00 | 9.42 |
| 500 | 8.00 | 8.89 | 9.42 | 9.78 |

*Notation:* $Q_c = Q.\sigma_c/100$, where Q is Barton's rock mass quality and $\sigma_c$ is uniaxial compressive strength (UCS) of intact rock material.

## 3 PGA VARIATION WITH DEPTH AND STIFFNESS OF MATERIAL

It was found that at the upper surface, the reaction to earthquake waves might lead to the higher amplitudes of acceleration. But, the existence of soft and weathered rock or soil near the surface attenuates the amplitude of the propagating wave and therefore the acceleration at the earth surface might be lower than expected.

Kanai & Tanaka (1951) measured acceleration at depth up to 600 m in copper mines in Paleozoic rock. The ratio of maximum surface displacement to that at the depth of 300 m was about 6:1. Iwasaki et al. (1977) obtained acceleration records up to a depth of 150 m during a period of 5 years. The borehole accelerometers were installed at four locations around the Tokyo bay. Three of these sites were in sand and clay while the fourth was in siltstone. During the period of measurement 16 earthquakes with magnitudes ranging from 4.8 to 7.2 were recorded. The analysis showed that the maximum acceleration depended heavily upon the soil conditions. The ratio of surface/depth accelerations are about 1.5 on a rocky ground; 1.5 to 3.0 in sandy ground and 2.5 to 3.5 in clayey ground. Narayan (2016) suggested that the PGA can be assumed as half of surface PGA beyond a depth of downgoing (reflecting) and upcoming wave zone, i.e. beyond 100 m depth.

Table 3 shows a range of peak ground acceleration for different intensities of earthquakes based on California earthquake (David et al. 1999). The maximum expected peak ground acceleration from Table 3 is more than 1.24 g for earthquakes having MMI > IX.

Sharma & Judd (1991) have found surface PGA value of 0.19 g (corresponds to MMI = VI in Table 3) as the 'critical value' for underground excavations to suffer damage.

Sykora et al. (1996) carried out measurements of peak ground acceleration at different depths and found that the ratio of horizontal peak acceleration at depth to surface decreases with the depth. They also observed that the variation is different for stiffer and softer ground materials. The selected data points of Sykora et al. (1996) have been plotted for stiffer and

Table 3. Peak ground acceleration for different intensity earthquakes (David et al. 1999).

| Modified Mercalli Intensities (MMI) | Acceleration (g) |
|---|---|
| I | < 0.0017 |
| II-III | 0.0017–0.014 |
| IV | 0.014–0.039 |
| V | 0.039–0.092 |
| VI | 0.092–0.18 |
| VII | 0.18–0.34 |
| VIII | 0.34–0.65 |
| IX | 0.65–1.24 |
| X+ | > 1.24 |

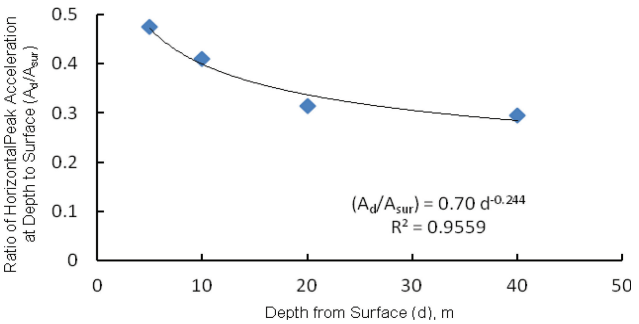


Figure 1. Variation of ratio of peak horizontal acceleration at depth to surface in a stiffer profile (Data from Sykora et al. 1996).

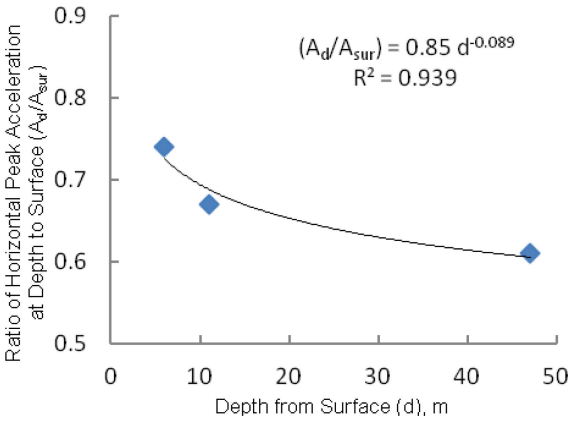


Figure 2. Variation of ratio of peak horizontal acceleration at depth to surface in a softer profile (Data from Sykora et al. 1996).

softer ground profiles as shown in Figures 1 and 2 respectively. The equation of best fit line is also given in the figures.

In rocky ground, generally, the top surface of about 5 to 8 m is weathered, representing the softer ground and then the rocks become stiffer. Considering this softer and stiffer ground/rock profile with depth and above discussion it may be safe to assume PGA as half of surface PGA for a depth range from 100 m to 500 m for which the study is carried out.

## 4 DYNAMIC ROCK MASS QUALITY

Barton (1984) recommended reduction in Q-value in seismic conditions as follows:

$$Q_{dyn} = Q/2 \tag{7}$$

where Q is Barton's rock mass quality and $Q_{dyn}$ is Barton's rock mass quality for seismic conditions.

Subsequently, Singh & Goel (2006) proposed a pseudo-static approach to get $Q_{dyn}$ using coefficient of vertical PGA ($\alpha_v$) around tunnel and Barton's rock mass quality Q as per Eq. 8.

$$Q_{dyn} = Q/(1+\alpha_v)^3 \tag{8}$$

For $\alpha_v = 0.25$, Eqs. 7 and 8 would be same. This shows that for $\alpha_v < 0.25$, the $Q_{dyn}$ value obtained from Eq. 7 would be more than the value obtained from Eq. 8.

Hajiazizi & Khatami (2013) have proposed Eq. 9 to get $Q_{dyn}$ using the Barton's rock mass quality Q and tunnel diameter D in meters. They found that the tunnel diameter or span is inversely influencing $Q_{dyn}$.

$$Q_{dyn} = 0.6\ D^{-0.3}\ Q \tag{9}$$

On re-writing Eq. 9 in the form of Eq. 8,

$$Q_{dyn} = D^{-0.3}\ Q/(1 + 0.185)^3 \tag{10}$$

By comparing Eqs. 8 and 10 it can be mentioned that in Eq. 10, in addition to tunnel span, coefficient of PGA around tunnel ($\alpha_v$) has been considered equal to 0.185. It may be noted here that the $\alpha_v$ value of 0.185 is almost matching with the critical value of coefficient of PGA suggested by Sharma & Judd (1991).

Looking into the effect of tunnel size on the ground conditions for tunnels (Singh & Goel 2011) and the effect of tunnel span in Section 2.2, the effect of tunnel size in $Q_{dyn}$ suggested by Hajiazizi and Khatami (2013) seems to be acceptable in squeezing ground conditions where rock masses are weak (generally UCS < 25 MPa). Moreover, Bhasin and Thomas (2013), from numerical modelling in elastic-perfectly-plastic medium, have also observed an increase of up to 100% in maximum axial force on tunnel lining when the tunnel diameter is increases from 5 to 20 m. Therefore, in addition to the tunnel size, in the present study it is proposed to use $Q_c$ value (normalized Barton's Q for $\sigma_c$ = 100 MPa) in place of Q. Hence, following two Eqs. 11 and 12 are proposed for estimating the $Q_{dyn}$ for non-squeezing and squeezing ground conditions. It is suggested here that these two equations shall be used cautiously and may be refined after further research and field validation.

$Q_{dyn}$ for Non-squeezing Ground Conditions ($Q_{dyn\text{-}nsq}$)

$$Q_{dyn\text{-}nsq} = Q_c/(1+\alpha_v)^3 \tag{11}$$

$Q_{dyn}$ for Squeezing Ground Conditions ($Q_{dyn\text{-}sq}$)

$$Q_{dyn\text{-}sq} = D^{-0.3}\, Q_c/(1+\alpha_v)^3 \tag{12}$$

where $Q_c = Q.\sigma_c/100$; Q is Barton's rock mass quality; $\sigma_c$ is uniaxial compressive strength (UCS) of intact rock material and $\alpha_v$ = coefficient of PGA tunnel (= half of surface PGA at tunnel depth >100 m).

The ground conditions for the tunnels may be estimated using rock mass number (N = Q with SRF as 1), the tunnel depth and the tunnel size as suggested by Singh & Goel (2011). Once the ground condition is known the rating for SRF shall be obtained from the Barton's SRF rating chart as per the ground condition to calculate Q from N. The Q-value thus obtained shall be then normalized with the UCS to get $Q_c$ for using in the above equations.

For estimating the tunnel support pressure in dynamic conditions, it is suggested that $Q_{dyn}$ shall be used in place of Q in the Barton et al. (1974) equation of tunnel support pressure estimation. Accordingly, following equations are obtained for estimating the support pressure in tunnels experiencing the non-squeezing and squeezing ground conditions.

Support Pressure for Non-squeezing Ground Conditions ($p_{dyn\text{-}nsq}$)

$$p_{dyn\text{-}nsq} = (0.2\, J_n^{0.5}/3\, J_r)\, [Q_c/(1+\alpha_v)^3]^{-1/3}\ \text{MPa} \tag{13}$$

Support Pressure for Squeezing Ground Conditions ($p_{dyn\text{-}sq}$)

$$p_{dyn\text{-}sq} = (0.2\, J_n^{0.5}/3\, J_r)\, [D^{-0.3}Q_c/(1+\alpha_v)^3]^{-1/3}\ \text{MPa} \tag{14}$$

where $J_n$ is Barton's joint set number, $J_r$ is Barton's joint roughness number and other parameters as defined above.

Using Eqs. 13 and 14, the support pressure for non-squeezing and squeezing ground conditions respectively under dynamic conditions can be estimated and the active ductile support system can be designed accordingly. Alternatively, the supports can be designed using the $Q_{dyn\text{-}nsq}$ and $Q_{dyn\text{-}sq}$ values in place of Q in Grimstad and Barton (1993) chart. It is to be cautioned here that in dynamic conditions the rock bolts shall have full-column resign grout and the reinforced concrete lining shall have perfect bond with the rock mass.

## 5 CONCLUSIONS

Following conclusions are drawn on the basis of the above study.

- The tunnels are likely to be affected by the earthquake when the ratio of wavelength of shear wave to tunnel span ( $\lambda$/D) is less than 4.5.

- Shear wave velocity is found to be about 60 per cent of P-wave velocity for some of the commonly occurring rocks. Using this, an approach to estimate the shear wave velocity of rock mass has been proposed from P-wave velocity of rock mass.
- Higher the peak ground acceleration (PGA) around the tunnel periphery, more earthquake loading on tunnel supports is expected. The PGA at a depth of more than 100 m is suggested to be half of the surface PGA.
- Rock mass quality Q value for dynamic conditions ($Q_{dyn}$) is suggested separately for non-squeezing and squeezing ground conditions to get the support pressure and to design the supports.
- It is suggested that the approach presented in this paper shall be used cautiously and may be further refined on the basis of further research in this important area of rock tunnel engineering.

## REFERENCES


Barton, N. 1984. Effects of rock mass deformation on tunnel performance in seismic regions. *Tunnel Technology and Surface Use* 4(3):89–99.

Barton, N. 2002. Some new Q-value correlations to assist in site characterization and tunnel design. *Int. J. Rock Mech. and Mining Sciences* 39: 185–216.

Barton, N., Lien, J. & Lunde, J. 1974. Engineering classification of rock masses for the design of tunnel supports. *Rock Mechanics* 6(4): 189–236.

Chen, J.R. 2005. The influence of seismic wave on long tunnel. *Proc. int. conf. World Long Tunnels,* Taiwan: 1181–1188.

Chen, Z.Y., Shi, C., Li, T.B., Yuan, Y. 2012. Damage characteristics and influence factors of mountain tunnels under strong earthquakes. *Nat. Hazard* 61(2): 387–401.

Christensen, N.I. & Stanley, D. 2003. Seismic velocities and densities of rocks. *International Handbook of Earthquake and Engineering Seismology*, W. Lee, H. Kanamori, P. Jennings, and C. Kissinger (ed.) 81B: 1587–1593 (https://www.eoas.ubc.ca/~nchriste/ chronopubs.html).

David, J.W., Quitoriano, V., Heaton, T.H. a& Kanamori H. 1999. Relationships between peak ground acceleration, peak ground velocity and modified Mercalli intensity in California. *Earthquake Spectra* 15(3): 557–564.

Dowding, C.H. & Rozen, A. 197). Damage to rock tunnels from earthquake shaking. *Journal of Geotechnical Engineering* 104 (GT2): 175–191.

Grimstad, E. & Barton, N. 1993. Updating of the Q-system for NMT. *Int. Symposium on Sprayed Concrete—Modern use of wet mix sprayed concrete for underground support*. Kompen, Opsahll and Berg (eds.) Fagernes, Norwegian Concrete Association, Oslo.

Gutenberg, B. & Richter, C.F., 1954. *Seismicity of the Earth*. Princeton Univ. Press, Princeton, N.J.

Hajiazizi, M. & Khatami, R.S. 2013. Seismic analysis of the rock mass classification in the Q-system. *Int J Rock Mech Min Sci*. 62: 123–130.

Iwasaki, T., Wakabayashi,S. & Tatsuoka, F. 1977. Characteristics of underground seismic motion at four sites around Tokyo bay. *Proc. of the Eight Joint Panel Conference of the US Japan Cooperative Program in Natural Resources*, NBS Special Bulletin: 477.

Kanai, K. & Tanaka, T. 1951. Observations of the earthquake motion at different depths of earth. *Part I, Bulletin of Earthquake Research Institute*, Tokyo, 29: 107.

Narayan, J.P. 2016. Personal discussions of author (J.P. Narayan is Associate Professor, Dept of Earthquake Engg., IIT Roorkee, Roorkee, India).

Singh, Bhawani & Goel, R.K. 2006. *Tunnelling in Weak Rocks.* Elsevier.

Singh, Bhawani & Goel, R.K. 2011. *Engineering Rock Mass Classification.* Elsevier.

Sharma, S. & Judd, W.R. 1991. Underground opening damage from earthquakes. *Eng. Geol*. 30: 263–276.

Sykora, D.W., Moriwaki, Y., Barneich, J.A. & Abrahamson, N.A. 1996. Measured variation of peak acceleration and peak particle velocity with depth at soil sites. *Eleventh World Conference on Earthquake Engineering*, 1573, Elsevier.

Wang, X. & Cai, M. 2015. Influence of wavelength-to-excavation span ratio on ground motion around deep underground excavations, *Tunnelling and Underground Space Technology* 49: 438–453.

This page intentionally left blank

*Rock Dynamics: From Research to Engineering – Li et al. (Eds)*
*© 2016 Taylor & Francis Group, London, ISBN 978-1-138-02953-8*

# A numerical model to determine the best time to start infill drilling in a mature reservoir

I. Khurshid
*University of Modern Sciences, Dubai, United Arab Emirates*

ABSTRACT: Discovered oil and gas fields after a certain production of oil and gas are regarded as mature fields. In these mature fields drilling infill wells, water-flooding and tertiary recovery methods may be used to increase production and recovery. The purpose of using one of these methods or their combination is to recover oil from the trapped or unswept zones in a reservoir. The objective of this study is to develop a numerical model to determine the best time to start infill drilling before irreversible pore collapse initiates and creates artificial traps and unswept zones. The developed model is derived by using the concept of body-centered pores in a cubic rock frame at microscopic level. On the basis of the derived model, a methodology named failure-curve method is proposed to determine the critical time of pore collapse. Thus, the best time for drilling infill wells is: before reservoir pressure/stresses touches the failure-curve. Sensitivity analysis technique is used to match the results of this study with experimental and field data, and it resulted in a good match. The model assumes that there are no constant thermal stresses and gravity forces. However, these forces might increase the creation of artificial traps and unswept zones in the reservoir.

## 1 INTRODUCTION

The oil and gas reservoirs are found deep in the earth containing oil, gas and water with impurities. These fluids are found at a certain depth, where the reservoir is at equilibrium conditions. However when oil, gas and water are produced from these reservoirs. The equilibrium is disturbed and the stress regime is changed. It is observed that with the decrease of reservoir pressure, the reservoir compacts and may lead to surface subsidence, artificial traps and unswept zones in the reservoir. The reason behind this environment and reservoir damage is: the vertical overburden (weight of rock) is constant, however the reservoir pressure decreases with oil production. Therefore, this decrease in reservoir pressure leads to severe ecological problems such as ground sagging, and ocean-floor distortion that may cause plummeting of offshore production and drilling platforms, ocean-bed pipelines collapsing, and various operational complications (Khurshid et al. 2015). This decrease in reservoir pressure can also induce fault activation and disturb cap-rock integrity. As other prospective snags, it may affect hydraulic fracturing and restricts the infill-drilling for field development and oil recovery plan.

To determine the effect of oil production and pressure depletion, Geertsma (1973) worked on different models and mentioned that the magnitude of surface subsidence depends on the amount of oil production, rock and reservoir properties (boundary conditions: faults, crest, edge or underneath water), and compressibility of fluids in the reservoir. Accordingly, this hydrocarbon production may cause reservoir rocks compaction and deforms the neighboring rock (Segall 1989). Addis (1997) performed a case study on Ekofisk oil field and stated that oil production from this field lead to decrease in reservoir pressure from 45 to 20 MPa and caused the reduction of offshore platform air-gap (round 10–15ft).

Regarding lab experiments, it is mentioned by Zhang et al. (1990) that with the increase of stresses, rock porosity reduces in the form of material deformation and it may move from elastic limit to plastic deformation leading to diminution in porosity and permeability leading

to hammering decrease in productivity. Smits et al. (1988) used uniaxial strain test to simulate the reservoir conditions in laboratory to study the behavior of rock at deep in the earth due to oil and gas production. Zoback (2007) states that Terzaghi's law shows the effects of reservoir pore pressure, its reduction and increase. Jaeger et al. (2007) mentioned that oil production may increase the effective stresses on rock due to decrease in reservoir pore pressure. Therefore, this stress increase may induce a number of unwanted consequences especially pore collapse and its failure (Hillis 2000). Therefore, to have maximum recovery it is important to start infill drilling in mature fields before permanent rock/pore failure.

As a result, a model is developed in this study to determine the best time for infill drilling. This model along with the proposed failure-curve methodology determines a best time for infill drilling and optimum oil recovery from a mature reservoir. Khurshid et al. (2015) applied the approach of optimal injection time ranges to control reservoir compaction, here the same approach is used to determine best time range for infill drilling for increasing oil recovery. To the best of our knowledge this concept is not utilized before to characterize the outcome of infill drilling. The results are also verified with field and laboratory experimental data that gave a good match. Thus, this proposed approach is very useful to determine the best time for infill drilling. Therefore, the derived model and methodology offer valuable insights to understand the geology, reservoir and effect of production during the life of a reservoir.

## 2 INFILL DRILLING TIME CALCULATION MODEL

To recover maximum oil from a reservoir, it is necessary to drill infill wells. The drilling of these new infill wells is important because due to reservoir heterogeneity, low permeability and unswept zones, and creation of artificial traps (due to oil and gas production) major amount oil cannot be produced from the reservoir. For optimal oil recovery through infill drilling, there are a number of approaches and consideration. In this context well placement optimization is given a lot of importance by different researchers. However, the objective of this study is to highlight the importance of best time ranges to drill infill wells.

It is observed that reservoir fluids such as water, oil, or gas and their pressures have important effect on the poroelastic behavior of the rock. Therefore with production, reservoir pressure and the amount of reservoir fluid decreases. As a result, it may initiate distortion in the reservoir in form of formation compaction, traps or unswept zones.

Consider a geological formation with pores, where the pores are saturated with reservoir fluids (oil, water and gas). Regarding the arrangement of these pores, it is assumed that at microscopic scale these pores are arranged in a body-centered cubic rock frame as shown in

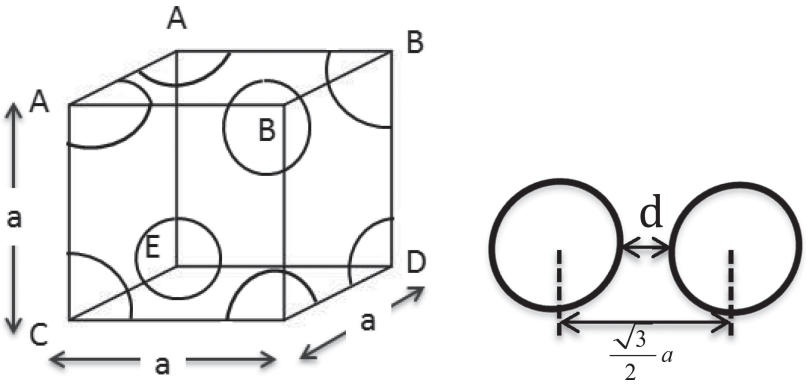


Figure 1. Arrangement of pores in a cubic frame at microscopic level (Khurshid et al. 2015).

Figure 1. Therefore, Pythagorean Theorem is used and it suggests that square of the diagonal across the body of this cube is the sum of squares of its three sides. By taking the square root, subtracting the radius gave the distance between pores,

$$d = \frac{1}{2}\left(\sqrt{3a} - 4r\right) \tag{1}$$

where $d$ is the distance between pores, $a$ is the unit frame edge length, and $r$ is the pore radius. Thus, for binary pores in a unit rock frame at microscopic level. The rock porosity can be calculated by the following equation

$$\phi = \frac{24\pi r^3}{9a^3} \tag{2}$$

From Eqs. (1) and (2), the pore radius is extracted

$$r = \left(\frac{9a^3\phi}{24\pi}\right)^{1/3} \tag{3}$$

After putting pore radius in Eq. 1, the distance between the pores can be computed as.

$$d = \frac{1}{2}\left(\sqrt{3}a - 4\left(\frac{9a^3\phi}{24\pi}\right)^{1/3}\right) \tag{4}$$

Take in account, the rock stress and their effect on rock matrix, where the stresses are dependent on square of distance between the rock pores and the length of unit rock frame.

$$\sigma \propto \left(\frac{a}{d}\right)^2 \tag{5}$$

Axial stress $\sigma_a$ is effected by the effective stress $\sigma$, thus

$$\sigma = \frac{\sigma_a}{A}\left(\frac{a}{d}\right)^2 \tag{6}$$

where A is the constant. Assuming that the collapse of pore may occur when $\sigma = \sigma_c$

$$\sigma_a = A\sigma_c/(a/d)^2 \tag{7}$$

Putting the value of the distance between pores from Eq. 4 into Eq. 7

$$\sigma_a = \frac{\beta}{2}\left\{\sqrt{3} - 4\left(\frac{9\phi}{24\pi}\right)^{1/3}\right\}^2 \tag{8}$$

where, $\beta = A\sigma_c$. Generalizing Eq. 8, (which is for the cubic system) the following equation is proposed.

$$\sigma_a = \delta + \beta(\alpha^2 - \gamma^2\phi^{2/3}) \tag{9}$$

where $\delta$ is used because actual rock has some strength at $\phi(\sigma_{min})$ shown in Figure 2, $\alpha$ is constant and it shows distance between the pores, $\gamma$ is a constant subjected to geometry and pores layout in the reservoir.

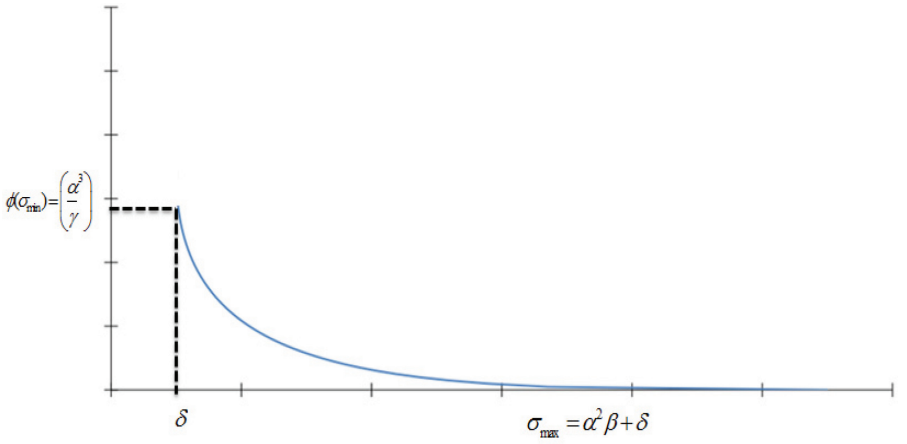


Figure 2. Porosity and pore collapse stress behaviors at different stress levels.

## 3 RESULTS, DISCUSSION, AND VALIDATION

To increase the recovery from a reservoir, operators usually drill infill wells. However, some time the wells drilled in mature fields may not give the desire results. One of the reason for such abnormal or low production is formation damage/reservoir compaction (reservoir is compacted due to pressure depletion). Therefore, it is very important to drill infill wells in a reservoir before pore collapse/failure. This pore collapse may create traps or unswept zones in the reservoir, effecting oil recovery.

To determine the values of constants in the derived model, the rock experimental data is utilized. However, after using delicate rock experiments still it is very difficult to predict rock behavior because of complexities in rock behavior (Khurshid et al. 2015). It is observed that their behavior is not only dependent on stresses, depth or temperature but also grain size, shape, strength, and orientation of pores. Therefore, experimental data at uniaxial strain conditions from Smits et al. (1988) is utilized to replicate reservoir conditions. The reason for using uniaxial strain conditions instead of uniaxial compressive stress conditions is: at uniaxial strain conditions the radial stresses in rock are kept constant (zero).

Figure 3 shows a uniaxial strain experiments data and then trial and error method is performed to define the value of parameters in the model. The point A shows a fictional porosity at the atmospheric pressure. The reservoir pressure decreases from point B somewhere on the line by production. It can be observed that the porosity of the rock remains relatively constant. However, when point C is crossed, rock porosity decreases in high numbers due to the increase of the effective stresses. The linear trend in Figure 3 shows the elastic limit (point A to C). However, when the load exceeds point C formation distortion may starts and then it increases at an exponential rate.

In this study the point C is identified as the starting point of the failure-curve. Once this point is crossed, the rock porosity decreases with stresses. Therefore, to recover maximum oil from the reservoir, it is recommend to drill infill wells between point A to C. Thus, drilling infill wells after point C will result in low oil recovery due to pore collapse/formation compaction, and creation of traps and unswept zones.

To find the parameters in Eq. 9, detailed sensitivity analysis is performed to match the results of the developed model with averaged experimental data (Smits et al. 1988). From the results in Figure 4, different matches of the developed model and their comparison with the averaged experimental data can be observed. The analysis gave an excellent match for the value at $\beta = 1980$ psi, $\alpha = 1.3$, $\gamma = 0.98$, and $\delta = 100$ psi as shown in Figure 4 (b).

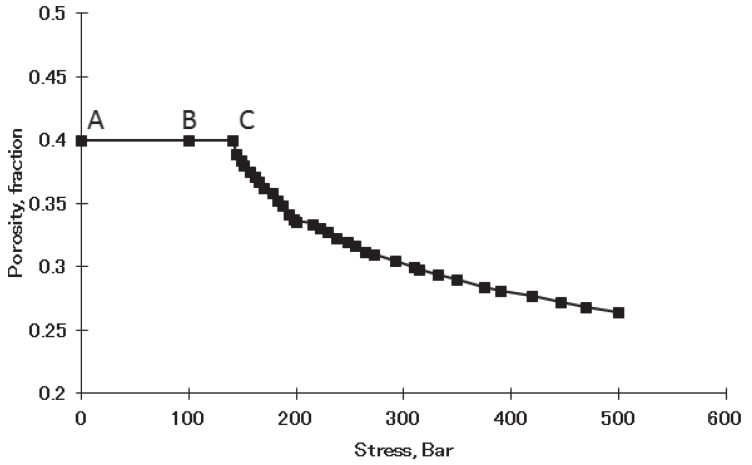


Figure 3. Rock stresses versus porosity at different initial rock porosity (Smits et al. 1988).

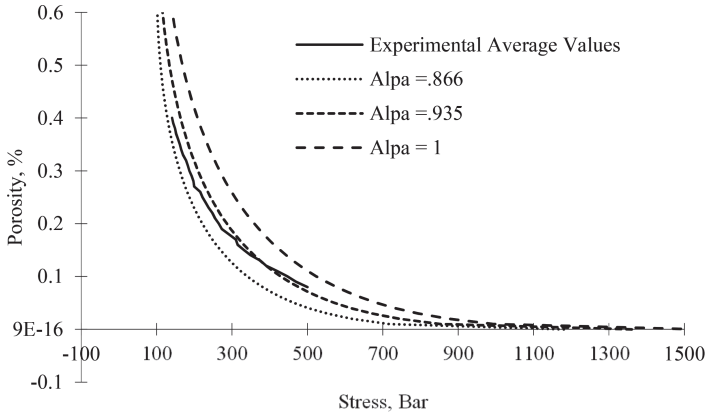


(a) Alpha Values with constant β=1440, γ=.984 and δ=50 values

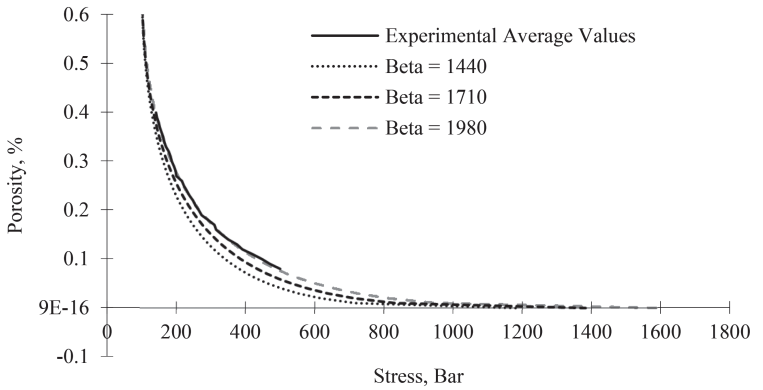


(b) Beta values with constant α=.866,γ=.984 and δ=50 values

Figure 4. (*continued*)

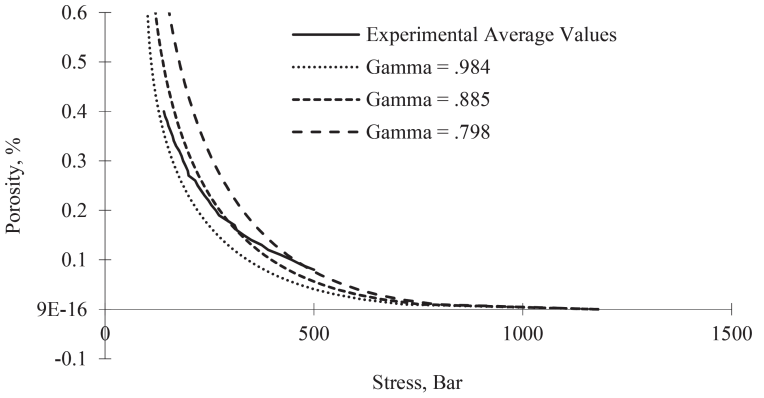


(c) Gamma values with constant α=.866,β=1440 and δ=50 values

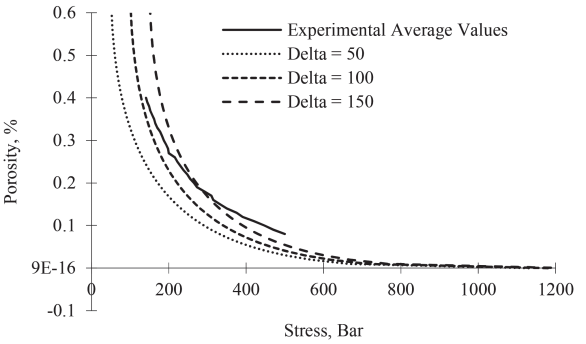


(d) Delta values with constant α=.866,β=1440, and γ=.984 values

Figure 4. Comparison of derived model parameters with experimental values.

### 3.1 *Methodology for field applications*

The technique introduced in this study can be used to determine the best time for drilling infill wells in a reservoir for maximum oil recovery. The procedure for applying the developed methodology is:

1. From a formation (by coring), perform a series of uniaxial compaction test to establish a trend at a range of initial rock porosities.
2. After these tests, determine rock porosities and plot them. A trend of porosity with pressure will be generated.
3. Match the experimental rock data with the derived model.
4. Find the values of β, γ, α, and δ.
5. Draw a horizontal line towards the curve. When the line intersects the curvy part, it shows stress at which pores will collapse.
6. Therefore, the interval before the intersection of curvy part, shows the best time for infill drilling program.

### 3.2 *Case study*

To prove the importance of the developed model, the Valhall field, North Sea is selected. Since from this field, the main drive mechanism for its production is compaction drive mech-

anism, and production has nothing to do with seismicity (Corzo et al. 2013). Also this field had high to low porosity ranges and was extremely over-pressured at reservoir pressure of 45.2 MPa. Therefore, these extreme complexities and uncertainties in the reservoir properties can perfectly identify the effectiveness of this model.

Figure 5 shows the results of the developed model. A good match can be observed between the predicted data and actual field data (Corzo et al. 2013). It can be observed that the derived model nicely matches with their data. The determined parameters for Valhall field are: (1) 32% porosity: $\beta = 8375$, $\gamma = 0.984$, $\alpha = 1.17$, and $\delta = 500$ psi and (2) 42% porosity: $\beta = 16750$, $\gamma = 1.0838$, $\alpha = 1.33$, and $\delta = 100$ psi. From Figures 5 (a) and (b) it can be observed that the pore collapse occurs when pore pressure depleted to the level of 2500 and 5000 psi with initial porosity 32% and 42%, respectively. It is evident that the both curves intersect the failure curve and prove the validity of the derived model. However, the data crosses the failure curve at different stress levels because initial reservoir porosity is different.

Therefore, whenever reservoir pressure decreases: the stresses in the reservoir may increase to a critical level leading to permanent deformation and pore collapse. Thus, the findings of this study proves that if the infill wells had drilled in Valhall field before reaching 5000 psi

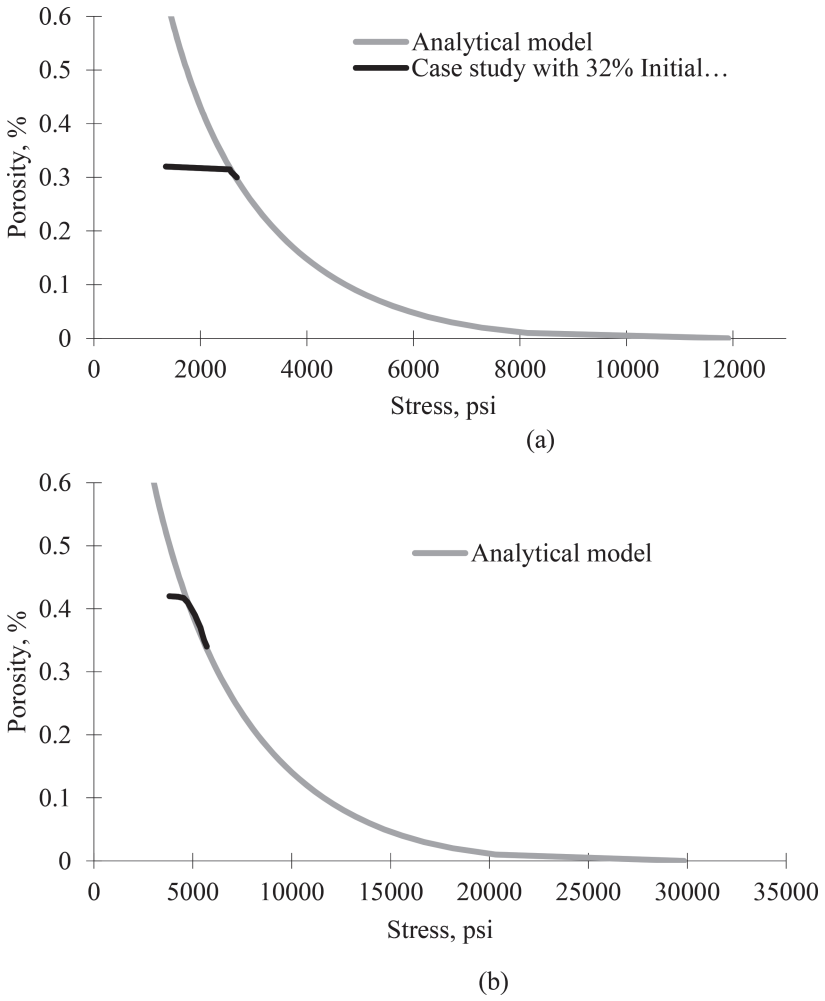


Figure 5. Validation and comparison of the derived model with field data of Valhall field, North Sea (a) 32% porosity (b) 42% porosity (data from Corzo et al. 2013).

reservoir pressure, more oil would have been recovered. As a result, the application and the results prove the applicability and benefits of the derived model.

## 4 CONCLUSIONS

- In this study a numerical model is derived to predict pore collapse by considering the arrangement of the constituent pores at microscopic level in a reservoir rock.
- The developed pore collapse prediction model and failure-curve method can determine the best time of infill drilling in mature oil and gas field. This approach can also predict the effect of depletion, compaction, and pore collapse on reservoir properties. Thus, it is suggested to start drilling infill wells in a mature field before reservoir touches the failure curve.
- The proposed model and methodology is also validated with available experimental as well as field data. The good agreement between the predicted pore collapse and the field data proves the significance of this work.

## REFERENCES


Addis, M.A. 1997. Reservoir depletion and its effect on wellbore stability evaluation. *International Journal of Rock Mechanics and Mining Sciences* 34: 401–417.

Corzo, M.M., MacBeth, C. & Barkved, O. 2013. Estimation of pore pressure change in a compacting reservoir from time-lapse seismic data. *Geophysical Prospecting* 61 (5): 1022–1034.

Geertsma, J. 1973. Land subsidence above compacting oil and gas reservoirs. *Journal of Petroleum Technology* 734–744.

Hillis, R.R. 2000. Pore pressure /Stress coupling and its implications for seismicity. *Exploration Geophysics* 31: 448–454.

Jaeger, J.C., Cook, N.G.W. & Zimmerman, R.W. 2007. *Fundamentals of Rock Mechanics*. Oxford: Blackwell Publishing.

Khurshid, I., Fujii, Y. & Choe, J. 2015. Analytical model to determine optimal fluid injection time ranges for increasing fluid storage and oil recovery: A reservoir compaction approach. *Journal of Petroleum Science and Engineering* 135: 240–245.

Segall, P. 1989. Earthquakes triggered by fluid extraction. *Geology* 17: 942–946.

Smits, R.M.M., de-Waal, J.A. & Kooten, J.F.C. 1988. Prediction of abrupt reservoir compaction and surface subsidence caused by pore collapse in carbonates. SPE 15642. *SPE Formation Evaluation* 3: 340–346.

Zhang, J., Wong, T.F. & Daniel, M.D. 1990. Micromechanics of pressure-induced grain crushing in porous rocks. *Journal of Geophysical Research* 95: 341–352.

Zoback, M.D. 2007. *Reservoir Geomechanics*. Cambridge: Cambridge University Press.

*Rock Dynamics: From Research to Engineering – Li et al. (Eds)*
*© 2016 Taylor & Francis Group, London, ISBN 978-1-138-02953-8*

# Seismic monitoring of nuclear power plants in Russia

S.B. Kishkina
*Institute of Geospheres Dynamics Russian Academy of Sciences (IDG RAS), Moscow, Russia*

E.G. Bugaev
*Scientific and Engineering Centre for Nuclear and Radiation Safety (SEC NRS), Moscow, Russia*

I.A. Sanina
*Institute of Geospheres Dynamics Russian Academy of Sciences (IDG RAS), Moscow, Russia*

ABSTRACT: Small-aperture arrays measurements taken at different nuclear plant sites showed that even under condition of thick sediments and high anthropogenic activity, usage of small-aperture arrays measurements significantly improves the quality of work small-aperture array located on thick sediments responds well to events with magnitudes Mb ≥ 1 at a distance up to 90 km; 1.5 – up to 200 km; and 1.7 (2.0) – at a distance up to 300 km. The sensitivity is improved by 0.4–0.8 Mb in case of granite massif; and in case of thick sediments it can come up to 1.5 Mb compared with separate seismic station.

## 1 INTRODUCTION

After the Fukushima nuclear disaster, a concern about safe construction and operation of NPP again is at the center of not only professional attention, but the whole world community. Safety issues should be a top priority for hazardous facilities even in cases with small probability of an accident. For example, nuclear power plant seismic safety. And in Russia nuclear power plants are located only in areas with low seismic activity. Even though possibility of an earthquake in such areas is low, the consequences of this extremely unlikely event can be catastrophic for a huge territory. Under these circumstances, organization and execution of local seismic observations to gain sufficient statistical data on the earthquakes of different magnitudes in a short period of time is a question of crucial importance. Results analysis should help with identification of earth crust zones without active faults suitable for NPP placement. Reliable statistical data should allow estimation of earthquake recurrence patterns.

These days Russia uses seismically safe nuclear power plant designs to ensure nuclear and radiation safety. Each design should take into consideration estimated maximum earthquake magnitude possibly happening in the given area once in 10000 years.

To estimate this value correctly, we need a reliable data about the design of the facility and seismic activity of the nuclear plant construction area. Below are examples of some projects of local seismic activity monitoring for the NPP areas.

## 2 SEISMIC MONITORING OF NPP AREA

Practice all over the world illustrates not just a possibility of registration and assessment of parameters of sources of weak seismic signals with magnitudes up to negative values, but also a possibility of their comparison at different range of scales (Kocharyan 2014). This significantly enriches the possibilities of using seismic data in studying parameters of seismic regime and in solving the problem of seismic hazard assessment based on probability of an earthquake occurrence within areas of low seismic activities.

The most common ways of increasing the sensitivity of seismic observations are the following: the significant seismic networks density increase (Urbancic & Young 1993, Saari 1999, Sivakumar 2008), installment of seismometers at greater depths (Oye 2005), usage of networks consisting of groups of small-aperture arrays (Wust-Bloch & Joswig 2004), or the usage of separate small-aperture arrays (Hiemer et al. 2012, Gibowicz 2008, Málek et al. 2009, Pirli et al. 2004, Braun et al. 2004). For example, in modern world local seismic monitoring is widely used at mining sites since it allows to assess the behavior of rock massif at the site and stability level of technological constructions. When installation of the monitor at greater depth is not possible, the installment of small-aperture arrays is used. Arrays, consisting of three-component stations showed significant increase of sensitivity (at least 0.4–0.8M) in comparison to existing networks of seismic observations (Pirli et al. 2004, Braun et al. 2004). This increase allowed to detect seismic events with negative magnitudes, and as a result the amount of registered events was significantly increased (Hiemer et al. 2012, Málek et al. 2009). Registration of weak seismic activity allows to create graphs which show earthquake recurrence patterns. Due to periodic seismic activity, monitoring should be performed for long periods, at least 10–20 years (Saari 1999). Analysis of recently obtained abundant database allowed to detect the presence of epicenters of weak earthquakes and their significant increase in the areas which were traditionally considered to be aseismic. The emergence of such databases is due to technogenic influence on subsoil (Ellsworth 2013) as well as due to increase of sensitivity of the seismic events registration stations.

Summarized analysis of the seismic observations results performed at the nuclear plant sites showed that the methodology employed in Russia today with the distance 15–40 km between autonomic seismic stations does not allow to reach the goal in studying seismic regime parameters and in solving the problem of seismic safety in the foreseeable future. In the first place it is not possible because of the weak seismic activity and high levels of noise which are characteristic for European part of Russia.

### 2.1 *The results of the field work of temporary small-aperture arrays in Russia*

Small-aperture arrays measurements taken at different nuclear plant sites showed that even under condition of thick sediments and high anthropogenic activity, usage of small-aperture arrays measurements significantly improves the quality of work. Every array consists of seven 3-component stations installed in pits at the depth of about 1 m. Three stations lie on each concentric circle. One more station is in the center of the array.

Based on our measurements we can say that an small-aperture array located on thick sediments responds well to events with magnitudes Mb ≥ 1 at a distance up to 90 km; 1.5 – up to 200 km; and 1.7 (2.0) – at a distance up to 300 km. The sensitivity is improved by 0.4–0.8M in case of granite massif; and in case of thick sediments it can come up to 1.5M compared with separate seismic station. Minimal registered magnitudes are: 0 at a distance ~10 km; –1 at a distance up to 4 km. We should note that these results are lower than in case of granite massif. (For example, seismic monitoring system of nuclear waste disposal site in Finland could easily register events with local magnitude up to –1 at a distance up to 5–10 km; and events with 0 magnitude at a distance up to 25–30 km (Saari 1999)). But even these modest results confirm that it is possible to perform seismic monitoring of an object and to get reliable results within a relatively short period of time of a few years.

In additional registration and determination of source parameters of signals, generated by quarry explosions, may and should be the main factor in assessment of functionality of seismic monitoring system. This is especially true for aseismic areas where the probability of strong earthquakes is low (Kishkina et al. 2010). Figure 1 shows how the magnitude of the source of the signal depends on the distance to the central point of the array. This figure shows all signals from local sources and quarry explosions. Dashed line is a function which shows the sensitivity of array under existing conditions: $Mb_{МИН} = 1.5\log10(R) – 2.0$.

Assessment of the magnitude of the project and maximum calculated earthquake (on the example of Nizhny Novgorod nuclear plant) which was obtained as a result of registration of earthquakes located at a short distance with small-aperture arrays, is one more proof that usage

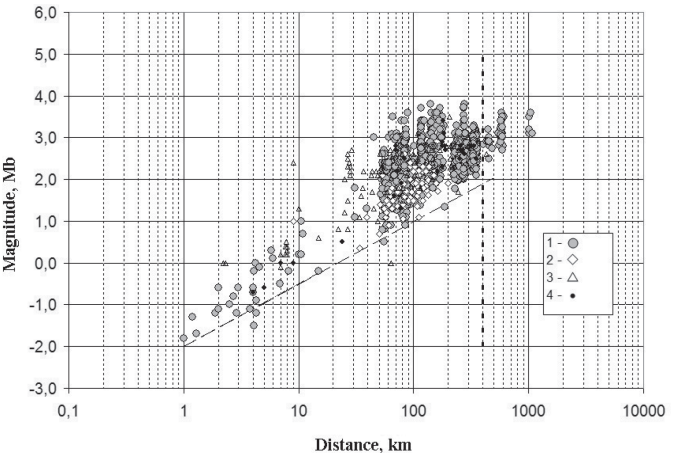


Figure 1. The dependence of magnitude signals, registered small-aperture arrays in the areas of NPP-sites in Russia, of the distance from the source. 1–4 = different NPP sites.

of small-aperture arrays to control seismic stability can be very effective. The value $M_{МПЗ} = 5,3$, which was based on registered earthquakes data is very close to the value $M_{max} = 5,0$, which was estimated based on geodynamic data. Recurrence relationship (Fig. 2) was created based on distribution of cumulative amount of seismic events during one year on the 10 km$^2$ area. Radiuses of representativeness of signal sources with different magnitudes were taken into account. It is noting that assessment of magnitudes of weak signals has some problems: probably because of the frequency limitations of the equipment the energy of weak events is underestimated. Thus, the parameters may vary depending on the refinement of the measurement results

The results confirm most small earthquakes (up to M ~ –1) locate in the lineament zones.

Space distribution sources of seismic events (Fig. 3), which were registered by groups of small-aperture arrays (Leningrad NPP-2 site, Ladoga-Baltic zone) in 2009–2010 (Kishkina et al. 2010) is shown that localization of the majority of sources of the events is controlled by the zone of dynamic effect of transversal zones of stress concentration. The points of intersection of transversal zones with marginal faults of the Ladoga-Baltic zone of lowering are the knots of highest concentration of the epicenters of weak seismic events.

Sources of local seismic events registered by array in the area of Nyzhny Novgorod NPP-site demonstrated proximity to different level structures (Fig. 4). The majority of these sources are in the area of dynamic influence of a potential hazard (M ~ 6.5) zone. Some of the sources have exogenous or even mixed genesis because they are located in the area of river Oka valley and its inflows, which is the area where active erosive and karst processes are taking place at the moment.

### 2.2 *Likelihood procedure in the case when observational data are limited*

When it is not possible to assess the seismicity of NPP area, it is advisable to assess parameters of earthquake recurrence relationship taking in consideration geodynamic and seismotectonic data. Such assessment is based on an assumption that distribution of the block sizes in the process of destruction of rigid bodies and distribution of the energy of the earthquake epicenters are following the same low (Sadovsky 1979, Rodionov 1984). In order to estimate recurrence relationship by the likelihood method, the model which describes the discrete qualities of the Earth's crust and earthquake epicenters and is characterized by similarity coefficient $k_п \sim \sqrt{10}$, was described (Bugaev et al. 2015). We are formalizing the determination of the size and the amount of the components of the model based on the conditions of deformation in fault zones, as shown in Figure 5. For NPP the size of the maximum element of the model is determined by the size of the NPP site and is defined here as three kilometers.

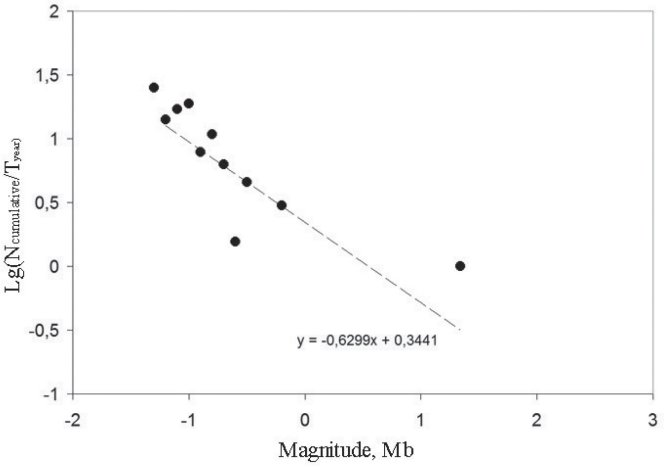


Figure 2. Recurrence relationship for Nizhny Novgorod NPP area.

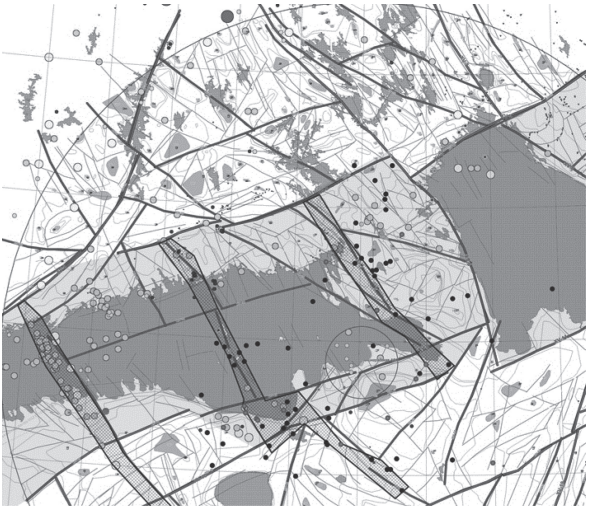

Figure 3. Spatial distribution of weak earthquake sources in the area of Leningrad NPP-2 site (Ladoga-Baltic zone). Weak earthquakes (black circles) with M ~ 0, were registered with small array, and historical earthquakes (grey circles) with 3 > M > 2.

Forecast relation per one year period presented below takes into account period of accumulation of maximum deformations T (years):

$$\lg(N_i/T) = A + D\lg L_i \quad (1)$$

where $N_i/T$ = average cumulative amount of elements with the size $L_i < L < L_{max}$, per year.

Equation (2) was obtained under an assumption that the appearance of every range of scale *n* and higher is accompanied by an earthquake with magnitude M and higher, and maximum magnitude $M_{max}$ depends on the size of range *L* (km), velocity of the crust deformation *G* (per year), and the time of expectation *t* (years) of maximum event (Bugaev et al. 2015), we will get the following:

$$M_{max} = 5.0 + 1.875\lg L + 0.625\lg G + 0.625\lg t \quad (2)$$

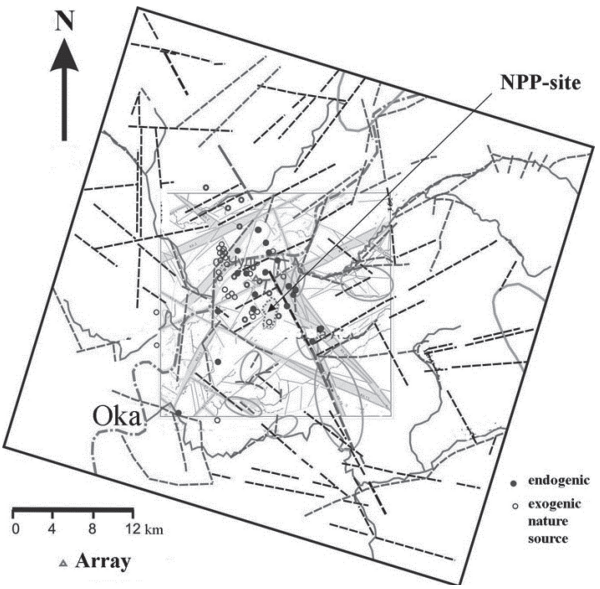


Figure 4. Spatial distribution of weak earthquake sources (M ~ 0) and exogenous sources in the area of Nyzhny Novgorod NPP-site (Oka-Volga region).

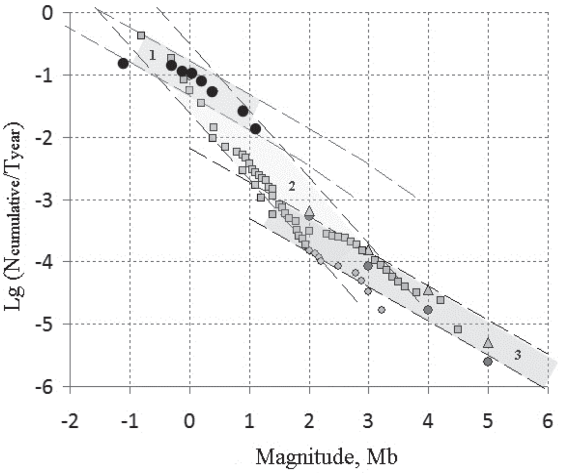


Figure 5. Measurements results and forecast relations under different conditions and the speed limit of elastic deformation for one of site in Siberia. 1 – uniaxial deformation ($t$ = 1 year; M < 0.5); 2 – volumetric deformation; 3 – uniaxial deformation (0,5 < M < 2).

Using Eqs. (1), (2) we can assess the recurrence relationship for different deformation conditions within expectation period of 10000 years.

Joint analysis of earthquake recurrence and forecast relation allows us to make assumptions about the nature of earthquakes, the conditions of their training and the nature of the destruction of the source. In particular, it can be assumed that a strong earthquake formed and manifested typically by uniaxial deformation and for them to be characterized by the excess of the elastic limit. This schedule recurrence of disastrous events is characterized by a maximum angle of inclination, which is due to the desire to limit the strain of strong earthquakes in the elastic limit as it approaches the size of the chamber to 1000 km.

## 3 CONCLUSIONS

It is especially important to register micro-earthquakes in areas of weak seismic activity, such as East-European Craton. In the areas with weak seismicity earthquakes with M > 2 can occur once in a year or once in several years. This makes local monitoring by separate stations not only non-efficient economically, but also useless. Small-aperture arrays are more effective even in regions with thick sediments and high anthropogenic activity. Estimation of probable manifestations of seismic and geodynamic processes at the areas around NPP is one of the important problems of NPP safety. Its solution cannot be unified completely. It should be solved with a reliable scientific reasoning for each specific object.

Work experience of temporary small-aperture arrays measurements by IDG RAS proved the existence of weak tectonic events with magnitudes around or below zero in Russia even when collecting data for short periods of time. The results confirm most small earthquakes (up to M ~ –1) locate in the lineament zones.

## ACKNOWLEDGEMENTS

This study was funded by Russian Scientific Foundation (Grant 16-17-00095).

## REFERENCES

Braun, T., Schweitzer, J., Azzara, R.M., Piccinini, D., Cocco, M., Boschi, E. 2004. Results from the temporary installation of a small aperture seismic array in the Central Apennines and its merits for local event detection and location capabilities. *Annals of Geophysics* 47(5): 1557–1568.

Bugaev, E., Kishkina, S., Seleev, I. 2015. Formalization of the estimation of the NPP area seismic regime parameters on geological data. *Seismic Instruments.*

Ellsworth, W.L. 2013. Injection-induced earthquakes. *Science* 341: 1225942.

Hardy, H.R. Jr., Belesky, R.M., Mrugala, M., Kimble, E.J., Hager, M.E. 1986. *A Study to Monitor Microseismic Activity to Detect Sinkholes*. Pennsylvania State Univ., Dept. of Mineral Engineering. Final Report. 202 p.

Hiemer, S., Rössler, D., Scherbaum, F. 2012. Monitoring the west Bohemian earthquake swarm in 2008/2009 by a temporary small-aperture seismic array. *Journal of Seismology* 16(2): 169–182.

Kishkina, S., Kocharyan, G., Loctev, D., Sanina, I. 2010. *Seismic Monitoring Leningrad-NPP-2 with Small-Aperture Array/ Dynamic Processes in Geospheres*. Moscow: GEOS, 2010. (in Russian).

Kocharyan, G.G. 2014. Scale effect in seismotectonics. *Geodynamics & Tectonophysics* 5(2): 353–385.

Kocharyan, G.G., Kishkina, S.B., Ostapchuk, A.A. 2010. Seismic picture of a fault zone. What can be gained from the analysis of fine patterns of spatial distribution of weak earthquake centers? *Geodynamics & Tectonophysics* 1(4): 419–440.

Málek, J., Brož, M., Stejskal, V., Štrunc, J. 2009. Small-aperture seismic arrays: instruments and detectability. *Advanced Industrial Microseismic Monitoring AIM*, Prague.

Oncel, A.O., Wilson, T.Y., Nishizawa, O. 2001. Size scaling relationships in the active fault networks of Japan and their correlation with Gutenberg-Richter b values. *Journal of Geophysical Research* 106(B10): 21827–21841.

Oye, V., Bungum, H., Roth, M. 2005. Source Parameters and Scaling Relations for Mining-Related Seismicity within the Pyha¨almi Ore Mine, Finland. *Bulletin of the Seismological Society of America*, 95(3): 1011–1026.

Pirli, M., Voulgaris, N., Alexopoulos, J., Makropoulos, K. 2004. Installation and preliminary results from a small aperture seismic array in Tripoli. *Greece. Bul. Geol. Soc. Greece* 36(3): 1499–1508.

Rodionov, V.N. 1984. Maximal earthquake as seismic regime characteristic. *Earthquakes of Middle Asia and Kazakhstan*. Dushanbe. p.96–108 (in Russian).

Rubin, A.M., Gillard, D., Got, J.L. 1999. Streaks of microearthquakes along creeping faults. *Nature* 400: 635–641.

Saari, J. 1999. An overview of possible applications of microearthquake monitoring at the repository site of spent nuclear fuel in Finland. Helsinki, Finland. December 1999.

Sadovsky, M.A. 1979. About natural lumpiness of rocks. *Doclady of Academy of Science USSR* 247(4) 829–831 (in Russian).

*Rock Dynamics: From Research to Engineering – Li et al. (Eds)*
*© 2016 Taylor & Francis Group, London, ISBN 978-1-138-02953-8*

# Integrating structural and numerical solutions for road cut slope stability analysis—A case study, India

J. Kundu, K. Sarkar & A.K. Singh
*Department of Applied Geology, Indian School of Mines, Dhanbad, Jharkhand, India*

ABSTRACT: The present work demonstrates the stability analysis of a cut slope in Jhakri area, Himachal Pradesh, India. The recent developments along the left bank of Sutlej valley have witnessed various activities such as widening of road, human settlement and hydropower projects. These actions have left the National Highway 22 very unfavorable from rock slope instability problem. In this paper, an attempt has been made through kinematic analysis and finite element simulation to understand the failure mechanism of vulnerable slope with highly jointed rock mass. The study provides an illustration that the slope is unstable because of intersecting joints with unfavorable attitude and stress accumulation at the toe region.

## 1 INTRODUCTION

Himalayan region comprises one of the largest active mountain chain on the earth with young, immature and undulating topography with diverse monsoonal season. The fragile and highly deformed nature of rocks has turned this region to be most vulnerable towards different types of slope failures (Sarkar et al. 1995, Chauhan et al. 2010, Pal et al. 2012, Singh et al. 2014). The current advances along the left bank of Sutlej valley around Jhakri area, Shimla in Himachal Pradesh, India has led to various activities such as widening of road, human settlement and expansion of hydropower projects. Lack of geological and geotechnical investigation prior to engineering constructions has created stability problem along the road. Due to these unscientific design methods, stress disequilibrium has set up resulting in slope failure in study area. The collapse of slope puts human life in grave danger as well as spawns huge economic loss. The failed rock masses possess serious disruption in communication in the Rampur-Jhakri region especially in the monsoonal season (Sarkar & Singh, 2008a, b, Singh et al. 2013). The present study deals with a road cut slope in Jhakri area, Himachal Pradesh, India, along Tibet Border Road, National Highway (NH) 22. An integrated approach of structural analysis and numerical simulation through Finite Element Method (FEM) has been implemented to identify potentially vulnerable slopes and to get an insight about deformational mechanism of the area.

### 1.1 *Regional geology of the area*

The rocks of the studied area come under Juthogh group of rocks in higher Himalaya which falls in the Main Central Thrust Zone (MCTZ). The rock types in the area are augen migmatite, biotite gneiss, quartz mica schist, garnet bearing quartz mica schist, muscovite biotite schist, and amphibolite, which are truncated by faults and other discontinuities (Singh 1979). The geological map of the area has been given in Figure 1. Regional strike of lithogical units is ENE-WSW with local variations in the trend. The rocks of juthogh group are of higher grade which tectonically overly low grade Rampur group of rocks. So the area shows an inverted metamorphism. Jutogh thrust separates Rampur group from Jutogh group of rocks. Tectonically detachment of Jutogh group has been occurred through a ductile shearing (Mukhopadhaya et al. 1997) which is named as Jeori dislocation (Singh 1979).

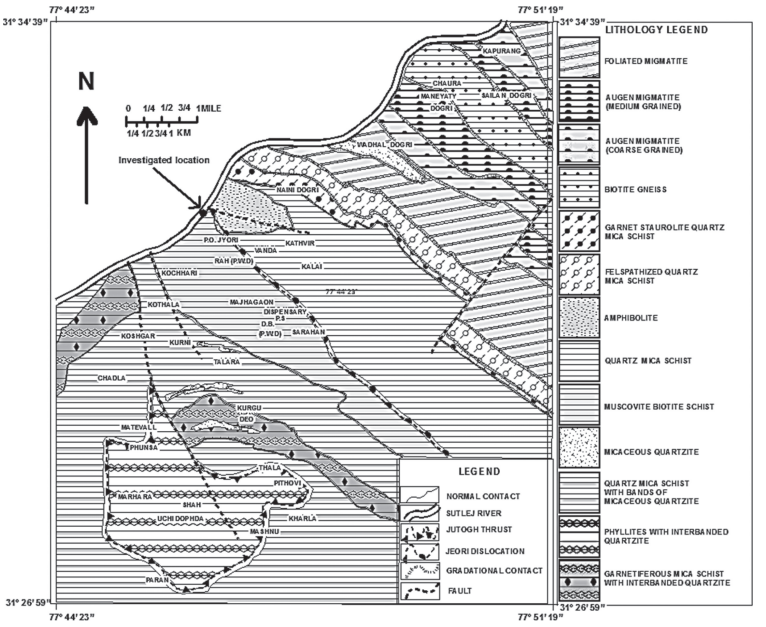


Figure 1. Geological map of Sarahan Bushair area, district Shimla, Himachal Pradesh, India. (After Singh 1979).

### 1.2 *Geotechnical details*

The studied location in this paper is near to Jeori dislocation and consists of fine grained gneissic rocks with evidences of migmatisation. The rock mass in this location is blocky in nature, intersected by three sets of joints and intruded by thin quartz veins. Out of these joint sets, two are steeply dipping and daylight on slope face while the other dips inward. The cliff has a height of about 55 meters and an angle 80°–85°. Vegetation is negligible up to 20 meters from the base but noticeable in the higher region. The geotechnical properties for rock material are determined in saturated condition as per ISRM (1981) specifications.

## 2 STRUCTURAL AND NUMERICAL ANALYSIS

### 2.1 *Kinematic analysis*

Stereographic projection has always been a major tool for solving complex problems. Determination of kinematically admissible failure modes for jointed rock slopes using stereonet is an easy practice and extremely useful technique which remains unreplaceable by modern techniques till date (Goodman 1976, Hoek & Bray 1981, Matherson 1988). The method is purely geometric which takes angular relationships between discontinuities and slope face(s) as input parameters for the analysis of possible planner, wedge and topple failure with potential failure direction (Kliche 1999). Another factor, angle of friction of joint planes has been introduced to satisfy both frictional and kinematic conditions for all type of slides. A computer program DIPS 6.0 (2015) of Rocscience has been used to perform the analysis. The input parameters for joint and slope orientations are given in Table 1, which are obtained from field investigation.

### 2.2 *Finite element-shear strength reduction (FE-SSR) analysis*

Characterizing complex rock mass especially fractured rock slope deformation and failure using numerical codes has become a major challenge in the field of engineering geology and

rock mechanics in present day. Various approaches in continuum methods such as Finite Difference Method (FDM), Finite Element Method (FEM) and Boundary Element Method (BEM), in discontinum methods visibly Discrete Element Method (DEM) and Discrete Fracture Network (DFN), finally several hybrid methods for instance hybrid FEM/BEM, hybrid FEM/DEM have been evolved which serve in rock engineering field (Jing 2003). Though many hybrid models for example hybrid FEM/DEM best define the problem for fractured rockmass, FEM has gained its maximum popularity in engineering geology because of its flexibility in handling material complexity, user-friendliness with the availability of many well developed and verified commercial codes (Jing 2003). The technique addresses complexities regarding geometry, non-linear deformability, material heterogeneity, complex boundary conditions, in situ stresses and gravity in addition to several coupled processes such as pore pressure, seismic loading. The FEM as a part of continuum analysis program, is based on the principle of dividing whole domain into finite elements, where each element shares its nodes with neighbor elements. This technique allows only small displacements forbidding large dislocation and complete detachment of elements. One more advantage is that joints can be incorporated into the model by the implementation of fracture elements (Jing & Hudson 2002). In case of blocky rock masses the displacement is very small until its failure. Due to this reason, FE-SSR method works effectively for jointed rock mass even proves equivalent to discrete modelling tools such as DEM (Hammah et al. 2007). Finite element method in conjunction with SSR technique, calculates equivalent factor of safety for the rock slopes (Matsui & San 1992, Singh et al. 2013). This approach is best explained for slope materials characterized by Mohr-Coulomb strength parameters (Hammah et al. 2007). SSR technique involves reducing strength of Mohr-Coulomb material, by a Strength Reduction Factor (SRF) until non-convergence occurs within a specified number of iterations and tolerance (Griffiths & Lane 1999). Shear strength reduction parameters are given by the equation,

$$\mathrm{Cr} = \frac{C}{F} \tag{1}$$

$$\tan(\Phi r) = \frac{\tan \Phi}{F} \tag{2}$$

where C is the cohesion, Φ is the angle of internal friction, Cr and Φr are the reduced shear strength parameters and F is the shear strength reduction factor.

Table 1. Orientation data of the cut slope used for kinematic analysis.

| Discontinuity | Dip (°) | Dip Direction (°) |
|---|---|---|
| Joint Set (J1) | 62 | 293 |
| Joint Set (J2) | 60 | 079 |
| Joint Set (J3) | 70 | 021 |
| Slope Face (SL) | 85 | 080 |

Table 2. Material parameters used in FE model obtained for saturated condition.

| Rock Parameters | Value | Joint Parameters | Value |
|---|---|---|---|
| Unit Weight | 0.028 MN/m$^3$ | Peak cohesion | 0.25 MPa |
| Peak cohesion | 3.2 MPa | Peak friction angle | 23° |
| Peak friction angle | 28° | | |
| Residual cohesion | 2.85 MPa | | |
| Residual friction angle | 24° | | |
| Dilation angle (Degree) | 0° | | |
| Young's modulus (GPa) | 39 GPa | | |
| Poisson's ratio | 0.27 | | |

In this paper, a cut slope of jointed rock mass has been analyzed using a geotechnical software RS$^2$ (2015) of Rocscience, which uses finite element code for the solution of rock and soil problems. The geometry for the model was prepared in a close approximation to field inspection with overall slope angle 83° and height of 55 m from the road level. A total of 3000 Uniform triangular mesh with 6 nodded elements are employed to make the geometry suitable in respect of complexity and computation time. Mohr-coulomb criterion with gravity loading has been assigned for the material strength as well as fracture element. Both field stress and body force was applied as initial element loading. Two daylighting joint sets are incorporated into the model while the third set installed dipping opposite to the slope face. The input parameters obtained in saturated condition for material and joint sets are given in Table 2.

## 3 RESULTS AND DISCUSSION

### 3.1 *Kinematic analysis*

The analysis has been carried out for all type of kinematically determinable failure and it is found that the cut slope is vulnerable to planner, wedge as well as toppling failure. It has a potential for wedge failure in two directions towards 070° and 006° respectively (Fig. 2a). Also the slope shows possibility of direct toppling failure and planner failure, both towards 079° (Figs. 2b, c). In Figure 2d, a field photo illustrates joints with both the wedges.

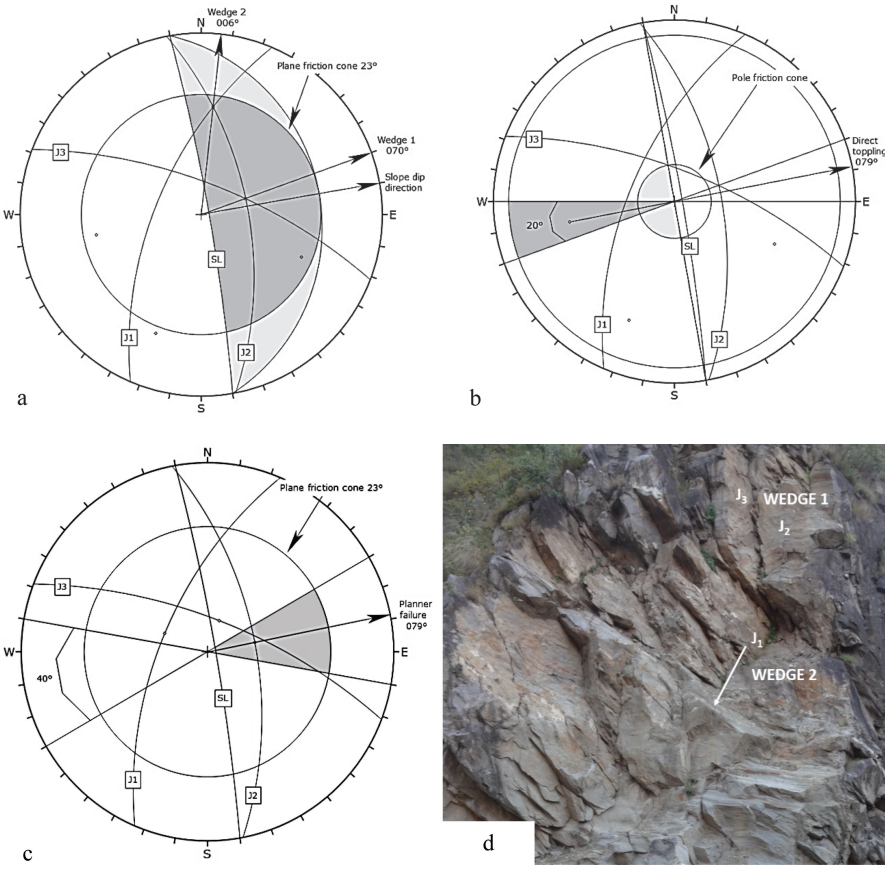


Figure 2. Kinematic analysis (a) showing wedge failure in two directions. One towards 70 and another towards 6. (b) Direct toppling towards 79. (c) Planner failure towards 79. (d) Represents joint alignment and two wedges, wedge 1 at higher inclination and wedge 2 at lower inclination.

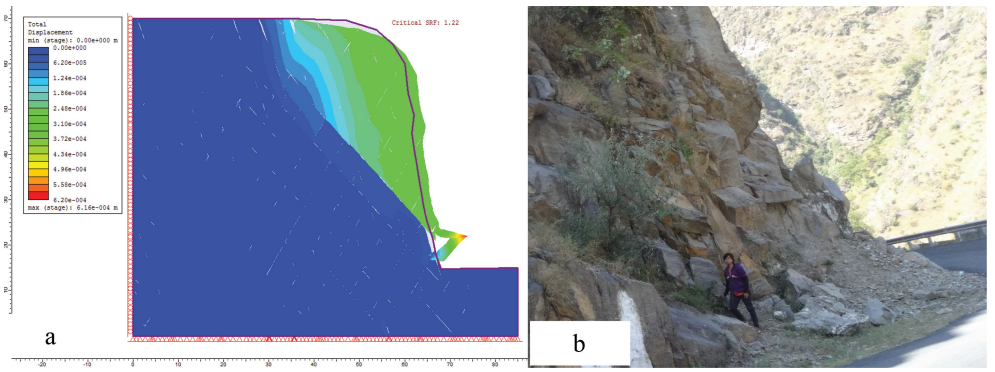


Figure 3. (a) Deformation contour from Finite Element Analysis with maximum total displacement of 6.20e$^{-4}$ m at toe region. (b) Field photo showing deformation at toe region of the slope.

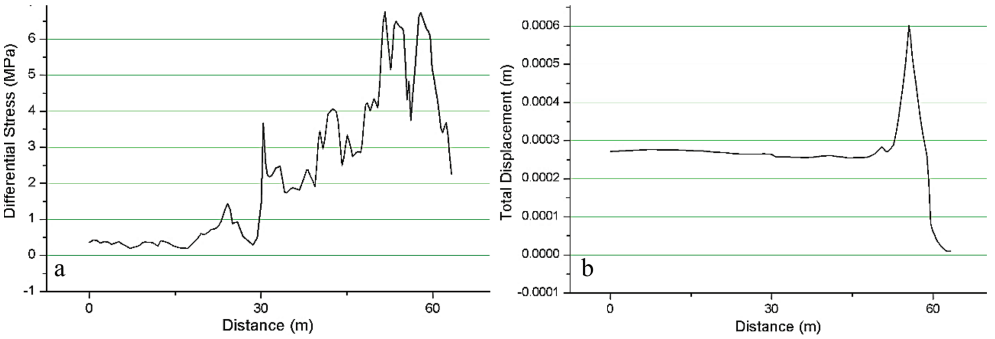


Figure 4. (a) Distance from top to toe along the slope surface vs. Differential Stress graph, representing an increasing trend of Differential Stress towards the toe of the slope. (b) Distance from top to toe along the slope surface vs. Total Displacement, showing maximum displacement at the toe portion where deformation contour is protruding (Fig. 3a).

### 3.2 *Finite element-shear strength reduction (FE-SSR) analysis*

The results for maximum total displacement are 6.20e$^{-4}$ m while it shows a minimum strength factor of −1. Figure-3a illustrates deformation contours where it displays maximum distortion at the foot region. Here displacement exaggeration in the picture has been made for visual purpose. The disturbances in that region of the slope have been well documented in the field (Fig. 3b). The analysis resulted for a maximum joint shear stress of 0.607 MPa at the maximum deformed section of the slope. Also the graphs in (Figs. 4a, b) represent maximum differential stress, maximum total displacement in the vulnerable foot region. It also shows minimum strength factor −1 in the region. A factor of safety of 1.22 attained through FE-SSR analysis which convince the slope as unstable. Again visual observation of failed rock mass deposits at the base of slope confirms the result.

## 4 CONCLUSIONS

In the present study, road-cut slope along National Highway (NH) 22 in Jhakri region has been investigated for stability analysis using kinematic method and numerical FEM techniques. The rockmass shows high concentration of stress providing some signal for yielding, if present pace of excavation is continued. The factor of safety obtained using FEM method is 1.22, which indicates that the road cut slope is unstable. It is also observed that the failure

surface and location estimated by the numerical method match with the kinematic analysis, field observation and records. In the study area, the rock mass of the existing slope is highly jointed, so fully grouted rock bolting with wire mesh may be necessary to prevent failure.

## REFERENCES


Chauhan, S., Sharma, M., Arora, M.K. & Gupta, N.K. 2010. Landslide Susceptibility Zonation through ratings derived from Artificial Neural Network. *International Journal of Applied Earth Observation and Geoinformation* 12: 340–350.

DIPS 6.0. 2015. *Rocscience Tutorial: Stability Analyses in Dips Based on Kinematic Considerations and Frictional Properties of Joint Planes*.

Goodman, R.E. 1976. *Methods of Geological Engineering in Discontinuous Rocks*. San Francisco: West Publishing.

Griffiths, D.V. & Lane, P.A. 1999. Slope stability analysis by finite elements. *Geotechnique* 49(3): 387–403

Hammah, R.E., Yacoub, T.E., Corkum, B., Wibowo, F. & Curran, J.H. 2007. Analysis of blocky rock slopes with finite element shear strength reduction analysis. *Proceedings of the 1st Canada-U.S. Rock Mechanics Symposium*, Vancouver, Canada: 329–334.

Hoek, E. & Bray, J.W. 1981. *Rock Slope Engineering*, London: Institution of Mining and Metallurgy.

ISRM 1981. Rock characterization testing & monitoring. *ISRM Suggested Methods*.

Jing, L. 2003. A review of techniques, advances and outstanding issues in numerical modelling for rock mechanics and rock engineering. *International Journal of Rock Mechanics & Mining Sciences* 40: 283–353.

Jing, L. & Hudson, J.A. 2002. Numerical methods in rock mechanics. *International Journal of Rock Mechanics & Mining Sciences* 39: 409–427.

Kliche, C.A.1999. *Rock Slope Stability*. SME. Littleton, *CO*.

Matherson, G.D. 1988. The collection and use of field discontinuity data in rock slope design. *The Quarterly Journal of Engineering Geology* 22: 19–30.

Matsui, T. & San, K. 1992. Finite element slope stability analysis by shear strength reduction technique. *Soils and Foundations* 32(1): 59–70.

Mukhopadhaya, D.K., Ghosh, T.K., Bhadra, B.K. & Srivastava, D.C. 1997. Structural and metamorphic evolution of the rocks of the Jutogh Group, Chur half-klippe, Himachal Himalayas: A summary and comparison with the Simla area. *Proc. Indian Acad. Sci., Earth Planet. Sci.* 106: 197–207.

Pal, S., Kaynia, A.M., Bhasin, R.K. & Paul, D.K. 2012. Earthquake stability analysis of rock slopes: a case study. *Rock Mechanics and Rock Engineering* 45: 205–215.

RS 2. 2015. *Rocscience Tutorial: Shear Strength Reduction*.

Sarkar, S., Kanungo, D.P. & Mehrotra, G.S. 1995. Landslide Hazard Zonation: A Case Study in Garhwal Himalaya, India. *Mountain Research and Development* 15(4): 301–309.

Sarkar, K. & Singh, T.N. 2008a. Slope stability study of Himalayan rock-A numerical approach. *International Journal of Earth Science and Engineering* 1(1): 7–16.

Sarkar, K. & Singh, T.N. 2008b. Slope failure analysis in road cut slope by numerical method. *ISRM International Symposium*. Tehran: 635–642.

Singh, P.K., Wasnik, A.B., Kainthola, A., Sazid, M. & Singh T.N. 2013. The stability of road cut cliff face along SH-121: a case Study. *Natural Hazards* 68(2): 497–507.

Singh, R., Umrao, R.K. & Singh, T.N. 2014. Stability evaluation of road-cut slopes in the Lesser Himalaya of Uttarakhand, India: conventional and numerical approaches. *Bulletin of Engineering Geology and the Environment* 73: 845–857.

Singh, K.P. 1979. Deformation history of the rocks around Sarahan Bushair, Himachal Pradesh. *Structural geology of the Himalaya*, Saklani, P.S. (Ed.): 163–182.

*Rock Dynamics: From Research to Engineering – Li et al. (Eds)*
*© 2016 Taylor & Francis Group, London, ISBN 978-1-138-02953-8*

# In-situ monitored seismic response of a rock tunnel

C.L. Kung
*Department of Civil Engineering, National Taiwan University, Taipei, Taiwan*
*United Geotech, Inc., Taipei, Taiwan*

Y.C. Chiu
*Institute of Mineral Resources Engineering, National Taipei University of Technology, Taipei, Taiwan*

T.T. Wang
*Department of Materials and Mineral Resources Engineering, National Taipei University of Technology, Taipei, Taiwan*

T.H. Huang
*Department of Civil Engineering, National Taiwan University, Taipei, Taiwan*

ABSTRACT: As the operation time of tunnels grows, the potential damages due to earthquake have become an issue that cannot be neglected. This research implemented accelerators in a highway tunnel passing through a slope in southeast Taiwan. After a seismic event with 5.0 Richter magnitude from 12.7 km beneath, 12.8 km to the case tunnel, the coseismic acceleration at five different locations in the tunnel returns satisfactory outcome. The Fourier spectra after Discrete Fast Fourier Transform reveal a 4–6 Hz predominant frequency of the tunnel lining. The maximum coseismic acceleration is 37.38 gal. All five accelerators on vault and two sidewalls show similar predominant frequencies in three dimension, proving that the predominant frequency of a site governs the predominant frequency of a tunnel. However, the secondary frequencies of accelerators on hill side sidewall of 11.4 and 11.7 Hz in vertical direction are apparently higher than the other two accelerators on creek-side sidewall of 8.6 and 6.4 Hz. The results describe the influences of both site characteristics and topography on the seismic response of a tunnel. The rare in-situ monitored data sets a starting post to quantify and verify contemporary methodologies on seismic-related problems of tunnels.

## 1 INTRODUCTION

With over 1,000 tunnels, the total length of tunnels in Taiwan has exceeded 1,000 km, not including military tunnels. Located in plate suture zone, the operational tunnels in Taiwan are always under the threat of strong earthquakes. Seismic damages of lining can significantly influence tunnel function, and would take a lot of money to recover. Reports on seismic damaged tunnels came worldwide, for example, Dowding & Rozen (1978) collected 71 cases from the United States and Japan, Sharma & Judd (1991) assembled 192 reports from 85 earthquakes throughout the world, Wang et al. (2001) assessed the damages of 57 tunnels during Chi-Chi earthquake in Taiwan, Asakura et al. (2008) gathered rock tunnels damaged in 17 earthquakes during 1923–1995 in Japan, Wang et al. (2009) and Shen et al. (2014) aggregated 18 mountain tunnels damaged after Wenchuan earthquake in China.

Most related studies investigate the mechanism of tunnel seismic damages due to earthquakes by numerical simulation and physical model experiments (Bazier et al. 2014, Chen 2011, Chen et al. 2012, Sun et al. 2011, Wang et al. 2014). However, limited by inevitable

simplifications, assumptions and boundary problems, the above methods deviate more or less from the real situation. Chiu et al. (2015) monitored a rock tunnel that passed through a deforming slope with optic fiber. The results suggest that the two sides of an existing crack may displace relatively during an earthquake, cracks are likely to elongate and widen in severe earthquakes with large magnitudes, reducing the entire stability of the tunnel. Besides, large displacements caused by severe earthquakes or resonance between the earthquake and tunnel structure also damage tunnel lining and affect its life time. Therefore, this research acquires the seismic response of a tunnel through in-situ monitoring. The acceleration at different locations in a tunnel during an earthquake is recorded. Predominant frequencies were estimated after Discrete Fast Fourier Transform. In comparison with free field acceleration from nearby seismic station, the effects of site and structural properties on seismic response of a tunnel were investigated.

## 2 IN-SITU MONITORING AND SIGNAL PROCESSING

A highway tunnel in southeast Taiwan is chosen as the case in this research. The following include a brief introduction on geographic and geologic condition around the tunnel, the monitoring instrument setup and data processing procedure.

### 2.1 *Site and monitoring instrument*

The case tunnel is a two-lane highway tunnel that passes through a ridge (Fig. 1). The tunnel is horseshoe shaped, 310 m long, 6.5 m high and 9 m in width (Fig. 2b). The monitored location is about 5.5 m from ground surface. Quartz mica schist is the major rock type, investigation shows no adjacent large scale geologic structure. Micro tremor measured and analyzed by Lo (2013) indicate that the predominant frequency of this site is within 0.5–5.0 Hz. There are two nearby surface seismic stations established by the Central Weather Bureau, Taiwan. First, TTN051 (No.51, at 121.0251°E, 23.1870°N) at Wulu Elementary School, Lidao, which is 6.8 km northwest from the tunnel with height 1040 m. The other is TTN041 (No.41, at 121.1252°E, 23.1323°N) at Chulai Elementary School, Sinwu, 10 km southeast from the tunnel, at 443 m elevation.

The main consideration in arranging monitoring instruments is the seismic response of different locations on the identical tunnel section. Four three-dimensional accelerators were installed at section A-A' (Fig. 2a), one three-dimensional accelerators were mounted at section B-B'. The defined coordinate system is shown on Figure 3a. Accelerator A4 is located at the hillside spring line, where the arch transits to the vertical sidewall (Fig. 3b). A2 and A3 are installed on the arch vault, about 30 degrees and 45 degrees from the zenith to creek side and hill side, accordingly. A1 is placed on the creek side wall, about 1 m from the pavement. A5 is installed at about the same height as A4, but on section B-B' (Figs. 2–3).

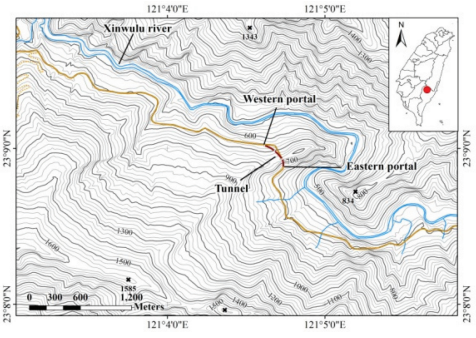


Figure 1. Topographic map of the case tunnel.

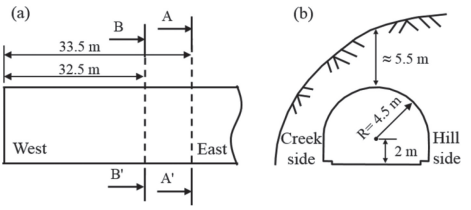


Figure 2. The (a) longitudinal map and (b) cross (Wang 2010). section A-A' of the monitoring location in the case tunnel.

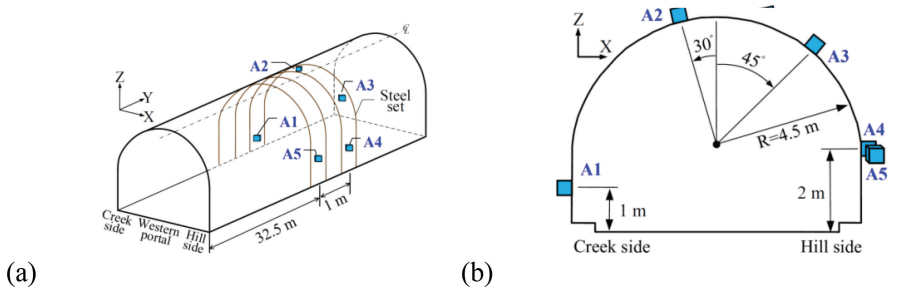


Figure 3. The arrangement of accelerators installed in the tunnel in (a) perspective view and (b) cross section.

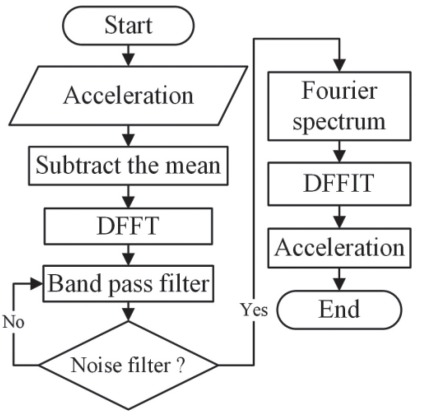


Figure 4. Flow chart of signal processing.

### 2.2 *Signal processing*

The accelerator was Type 2460-002 Micro Electro Mechanical Systems (MEMS) triaxial accelerator made by the Silicon Designs, Inc. The sampling frequency of three-dimensional accelerators were set to be 100 Hz. Using Matlab as the platform, this research follows the procedure in Figure 4 to process the monitored acceleration. First, the mean value of acceleration is calculated and subtracted, the acceleration then shifted to a baseline of mean. Second, Discrete Fast Fourier Transform (DFFT) is performed to transfer acceleration from time domain to frequency domain, determine predominant frequencies in three directions (X, Y and Z). Third, since the noise of the instrument itself falls on 20 Hz, and the background noise is generally 0–0.8 Hz, a band pass filter 0.5–15 Hz is determined (Kung 2014). Eventually, the frequency spectra were transformed back to the time domain by inverse Discrete Fast Fourier Transform (DFFIT).

## 3 RESULT

The results of this research is based on an earthquake in May 25, 2014 (UTC+8), No.75 earthquake numbered after the Central Weather Bureau, Taiwan. The earthquake occurred at 121.16°E, 23.06°N, 12.8 km from the case tunnel with a Richer magnitude 5.0. Data of seismic stations came from the Geophysical Database Management System (Shin et al. 2013).

During earthquake No.75, seismic station TTN051 is 19.4 km from the epicenter with the fourth degree intensity scale. The peak amplitude is 18.00 gal in X direction, 18.16 gal in Y direction, and 18.70 in Z direction, as listed and shown in Table 1 and Figure 5. The Fourier spectrum in three directions display peaks at 4.8 Hz with amplitude 1.43 gal in X

direction; 4.7 Hz and 7.4 Hz with amplitude 1.55 gal and 0.81 gal in Y direction; 5.0, 6.6 and 7.8 Hz with amplitude 0.94, 0.89 and 0.46 gal in Z direction (Fig. 6).

From the recordings of accelerator A1 (Fig. 7), the peak acceleration along X direction is 34.87 gal at the 4.98 second, with DFFT iteration root mean square (RMS) 2.25 gal; the peak acceleration in Y direction is 12.16 gal at the 4.88 second, with iteration RMS 2.25 gal; and the peak acceleration along Z direction is 19.05 gal at the 5.24 second, with iteration RMS 2.61 gal. DFFT returns spectrum with peaks on 5.0 Hz, 2.48 gal in X direction; 1.0, 5.0 and 6.4 Hz in correspondence with 0.43, 0.85 and 0.54 gal in Y direction; 4.8, 6.9 and 8.6 Hz with 0.98, 0.60 and 0.63 gal in Z direction, accordingly.

Table 1 contains the analysis results of all monitored data during earthquake No.75. The peak X-acceleration of accelerator A1 and A2, installed at creek side sidewall and vault, occurred at about the same time, but their peak Y- and Z-acceleration do not. Accelerator A3 and A4, mounted on hill side sidewall and vault, reach peak acceleration in three dimension simultaneously.

Table 1. Analysis results of in-situ monitored acceleration.

| No. | Direction | Peak acceleration (gal) | Time (s) | RMS (gal) | Peak amplitude (gal) | Predominant frequency (Hz) | Second peak (gal) | *f* (Hz) |
|---|---|---|---|---|---|---|---|---|
| | X | 196.22 | – | – | 6.84 | 11.5 | 6.53 | 5.3 |
| 41 | Y | 203.62 | – | – | 9.37 | 4.4 | 9.07 | 5.5 |
| | Z | 134.22 | – | – | 9.24 | 5.0 | 3.73 | 10.4 |
| | X | 18.00 | – | – | 1.43 | 4.8 | – | – |
| 51 | Y | 18.16 | – | – | 1.55 | 4.7 | 0.81 | 7.4 |
| | Z | 18.70 | – | – | 0.94 | 5.0 | 0.89 | 6.6 |
| | X | 34.87 | 4.98 | 5.54 | 2.48 | 5.0 | – | – |
| A1 | Y | 12.16 | 4.88 | 2.25 | 0.85 | 5.0 | 0.54 | 6.4 |
| | Z | 19.05 | 5.24 | 2.61 | 0.98 | 4.8 | 0.63 | 8.6 |
| | X | 37.38 | 4.99 | 6.18 | 2.82 | 5.0 | – | – |
| A2 | Y | 22.22 | 5.25 | 2.53 | 0.85 | 6.0 | 0.63 | 8.8 |
| | Z | 14.23 | 5.07 | 2.42 | 1.05 | 4.8 | 0.56 | 6.4 |
| | X | 34.50 | 4.90 | 5.10 | 2.50 | 5.0 | – | – |
| A3 | Y | 18.42 | 5.26 | 2.31 | 0.79 | 5.7 | 0.47 | 8.9 |
| | Z | 18.00 | 5.23 | 2.88 | 1.31 | 4.8 | 0.56 | 11.4 |
| | X | 31.08 | 4.89 | 4.58 | 2.07 | 5.0 | – | – |
| A4 | Y | 14.50 | 5.25 | 1.89 | 0.61 | 5.9 | 0.46 | 13.18 |
| | Z | 18.00 | 5.24 | 2.61 | 1.23 | 4.8 | 0.44 | 11.7 |
| A5 | Y | 10.80 | 4.82 | 1.93 | 0.54 | 5.9 | 0.53 | 3.9 |
| | Z | 18.28 | 5.18 | 2.37 | 1.05 | 4.8 | 0.48 | 9.18 |

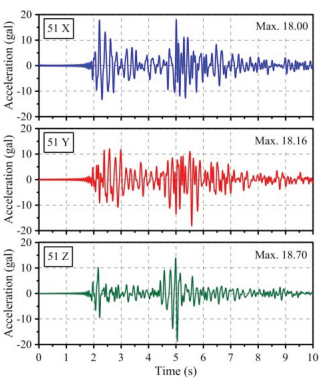


Figure 5. Acceleration of seismic station TTN051.

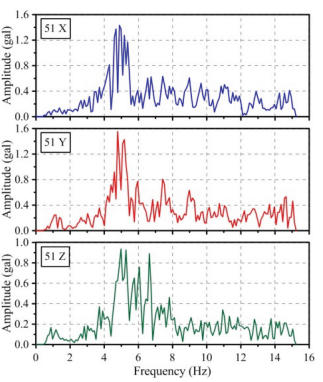


Figure 6. Fourier spectrum in three directions of seismic station TTN051.

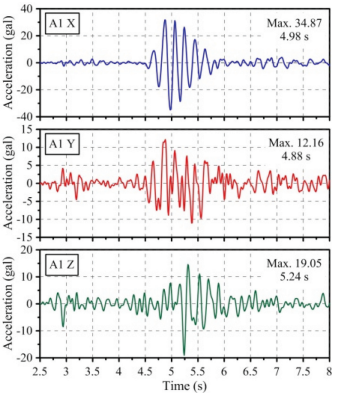


Figure 7. Acceleration of accelerator A1.

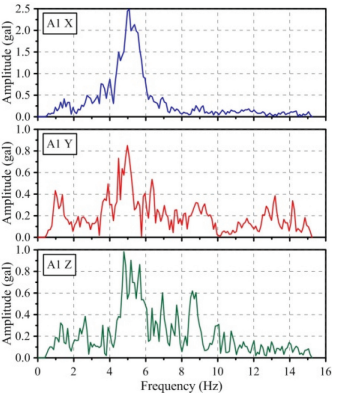


Figure 8. Fourier spectrum in three directions of accelerator A1.

The peak in Y- and Z-Fourier spectrum for seismic station TTN041 (No.41 in Table 1), all three directional Fourier spectrum for seismic station TTN051 (No.51 in Table 1) and accelerator A1-A5 fall on about 5 Hz (Fig. 8). The second peak in Z-direction of A1 and A5, Y-direction of A2 and A3, Z-direction of A3 and A4 are also close with each other.

## 4 DISCUSSIONS

From Table 1, accelerator A1 and A2 has concurrent X-peak acceleration but nonconcurrent Y- and Z-peak acceleration. However, the peaks in three directions of accelerator A3 and A4 arrive just about the same time, suggesting divergent seismic response in hill side and creek side of the tunnel.

The overburden of the monitoring section is not symmetric in hill side and creek side (Fig. 2b). Smaller overburden in creek side act lower pressure on tunnel structure, allowing relatively free vibration during an earthquake. Therefore, the acceleration at different location do not match, peak occurred at different time. Larger overburden in hill side produce higher constraint, giving less freedom in vibrating, thus the peak acceleration arrive closely even at different location.

The predominant frequency of seismic station TTN051 (No.51) in X- Y- and Z-direction lie within 4.7–5.0 Hz, and the predominant frequency of seismic station TTN041 (No.41) in Y- and Z-direction fall in 4.4–5.0 Hz. Although the X-direction peak of TTN041 equals to 11.5 Hz, the second peak is 5.3 Hz, quite similar with the outcome of the others. The data of this research indicate that predominant frequencies of the tunnel in X-, Y- and Z-direction fall within the range 4.8–6.0 Hz, proving that the predominate frequency of a site determines the main properties of tunnel seismic response.

The accelerators in hill side, A3 and A4, display Z-directional second peak of predominant frequencies at 11.4 and 11.7 Hz, higher than the accelerators mounted in creek side, A1 and A2, which show their Z-directional second peak of predominant frequencies at 8.6 and 6.4 Hz. The second peak of predominant frequency in Z-direction for the other accelerator in hill side, A5, equals 9.18 Hz, is close to those of A3 and A4. Besides, when the third peak of Z-acceleration in creek side, A1 and A2, can be identified as 3.9 and 8.5 Hz, the accelerators in hill side, A3 and A4, are both hard to recognize. The differences between accelerators in hill side and creek side demonstrate that besides site characteristics, the predominant frequencies are likely to be influenced by overburden and corresponding structural properties. In creek side where confining constraint is less, inertia effect brings about hysteresis, the motion period of lining during earthquake becomes longer, and thus the second peak of frequency spectrum is smaller. This can also be proved by the time differences between peak acceleration at different locations.

## 5 CONCLUSION

As the proportion of middle and elder tunnels in existing operational tunnels grow higher, the seismic response of tunnels due to earthquake is becoming crucial in tunnel maintenance. This research monitored the acceleration in different locations at a highway tunnel in southeast Taiwan, transform signals to obtain the predominant frequencies, and investigate the influence of site characteristics and tunnel structural properties on tunnel seismic response. The data processing procedure can effectively quantify the coseismic response of the case tunnel, and output the predominant frequencies at different locations in the tunnel.

The peak acceleration of the tunnel during earthquake No.75 is 37.38 gal, the predominant frequencies are within 4–6 Hz. The second peak of Fourier spectra for accelerators in hill side is higher than that of accelerators in creek side, representing a notable effect of topography on tunnel seismic response.

## ACKNOWLEDGMENTS

The authors would like to address special thanks to the Ministry of Science and Technology, Taiwan for partially support the in-situ monitoring under project No. 102-2221-E-027-071-MY3.

## REFERENCES

Asakura, T., Shiba Y., Matsuoka S., Oya T., Yashiro K. 2008. Damage to Mountain Tunnels by Earthquake and its Mechanism. *Taiwan Rock Engineering Symposium 2008*. October, 30–31. Taipei, Taiwan: 20–36.

Baziar, M.H., Moghadam, M.R., Kim, D.S., Choo, Y.W. 2014. Effect of underground tunnel on the ground surface acceleration. *Tunnelling and Underground Space Technology* 44: 10–22.

Chen, C.H. 2011. *Study on the seismic behavior of rock tunnels and failure mechanism of linings*. Doctoral thesis. Department of Civil Engineering. Taipei: National Taiwan University.

Chen, C.H., Wang, T.T., Jeng, F.S. Huang, T.H. 2012. Mechanisms causing seismic damage of tunnels at different depths. *Tunnelling and Underground Space Technology* 28: 31–40.

Chiu, Y.C., Kung, C.L., Liou, J.C., Cheng, D.S., Wang, T.T. 2015. Seismic response of a rock tunnel and associated crack variation. *East Asia Forum on Radwaste Management*. October 25–28. Taichung, Taiwan.

Dowding, C.H. & Rozen, A. 1978. Damage to rock tunnel from earthquake shaking. *Journal of the Geotechnical Engineering Division* 2: 175–19.

Kung, C.L. 2015. A rock tunnel under earthquake impact: in-situ monitoring and numerical simulation on harmonic incident wave excitation. Master thesis. Department of Civil Engineering. Taipei: National Taiwan University.

Lo, B.C. 2013. *Evolution of a deep-seated creeping slope and associated characteristics: A case study*. Master thesis. Institute of Mineral Resources Engineering. Taipei: National Taipei University of Technology.

Sharma, S. & Judd W.R. 1991. Underground opening damage from earthquakes. *Engineering Geology*. 30: 263–276.

Shen, Y.S., Gao, B., Yang, X.M., Tao, S.J. 2014. Seismic damage mechanism and dynamic deformation characteristic analysis of mountain tunnel after Wenchuan earthquake. *Engineering Geology* 180(2014): 85–98.

Shin, T.C., Chang, C.H., Pu, H.C., Lin, H.W., Leu, P.L. 2013. The Geophysical Database Management System in Taiwan. *Terrestrial, Atmospheric and Oceanic Sciences* 24: 11–18.

Sun, T.C., Yue, Z.R., Gao, B., Li, Q., Zhang, Y.A. 2011. Model test study on the dynamic response of the portal section of two parallel tunnels in a seismically active area. *Tunnelling Underground Space Technology* 26(2): 391–397.

Wang, W.L., Wang, T.T., Su, J.J., Lin, C.H., Seng, C.R., Huang, T.H. 2001. Assessment of damages in mountain tunnels due to the Taiwan Chi-Chi Earthquake. *Tunnelling and underground Space Technology* 16: 133–150.

Wang, Z.Z., Gao, B., Jiang, Y.J., Song, Y. 2009. Investigation and assessment on mountain tunnels and geotechnical damage after the Wenchuan earthquake. *Science in China Series E: Technological Sciences* 52(2): 546–558.

Wang, T.T. 2010. Characterizing crack patterns on tunnel linings associated with shear deformation induced by instability of neighboring slopes. *Engineering Geology* 115(1–2): 80–95.

Wang, S.H., Ni, P.P., Guo, M.D. 2014. Response of a tunnel in double-layer rocks subjected to harmonic P—and S-waves. *International Journal of Rock Mechanics and Mining Sciences* 70: 435–443.

*Rock Dynamics: From Research to Engineering – Li et al. (Eds)*
*© 2016 Taylor & Francis Group, London, ISBN 978-1-138-02953-8*

# Numerical simulation of blasting excavation in reconstruction and expansion tunnel

D. Liu
*College of Architecture and Civil Engineering, Beijing University of Technology, Beijing, China*
*Beijing Road Engineering Quality Supervision Station, Beijing, China*

W.X. Gao
*College of Architecture and Civil Engineering, Beijing University of Technology, Beijing, China*

B.P. Sun
*Capital University of Economics and Business, Beijing, China*

D.H. Liu
*Beijing Road Engineering Cost and Quota Management Station, Beijing, China*

ABSTRACT: With the rapid development of economy and tourism, Dong Changyu tunnel which have single lane has been unable to meet the increasing traffic. Due to the terrain and geological conditions, it is unable to build a new one, there is only way to expand the existing tunnel. Based on blasting excavation of collapse cavity section, this paper analyzes rock fragmentation and blasting vibration of multi free surface. Using numerical calculation method with Lagrangian algorithm and full restart, it simulates the effect of blasting vibration on the reinforcement area of collapse cavity and the surrounding rock, and obtains vibration velocities and its law of characteristic points. Compared to the field experiments, the vibration velocities of numerical simulation are close to them. The results indicate that the numerical calculation method can descripts rock fragmentation and blasting vibration in the millisecond delay blasting. The research has reference and guidance for similar engineering.

## 1 INTRODUCTION

With the rapid economic development and the increasing traffic, some old tunnels have been unable to meet the traffic demand due to low design standard and inadequate clearance. There is a development trend to rebuild and expand old tunnels. To rebuild and expand existing tunnel is more difficult than to build a new one. It should expand tunnel section, and remove the original supporting structure. The construction process is very complex, and the risk is increasing. The demolition and expansion repeatedly disturb the surrounding rock, its whole stability and the self-bearing capacity will be further reduced. If it has collapse cavity or big hole in existing tunnel, the difficulty will be even greater; more uncontrolled factors will cause greater risk of blasting construction. Therefore, the safety and stability of existing tunnel reconstruction is one of the leading research topics in geotechnical engineering.

Up to now, the blasting vibration test and numerical simulation on tunnel surface or excavated area have been studied extensively by domestic and foreign scholars. However, the research of blasting vibration and rock fragmentation which have multi free surface on unexcavated area of expansion tunnel is rare. Dong Changyu tunnel which has large collapse cavity in the vault is scarcer, and the relative position is changing between existing tunnel and expansion tunnel. In this paper, by using numerical calculation method with

Lagrangian algorithm and full restart, we study on rock fragmentation and blasting vibration under multi free surface, and simulate the effect of blasting load on reinforcement area and surrounding rock. Compared the simulation results with the monitoring tests; we analyze the effect of rock fragmentation and the rule of blasting vibration in the millisecond delay blasting.

## 2 PROJECT OVERVIEW

The original Dong Changyu tunnel is located in the northern mountainous area of Beijing. It is the only way of nearby villages; it was built in 1980, and its length was 420 meters. Because of the limitation of objective conditions, the tunnel had a single lane, even the narrowest place is about 4 meters. The tunnel section is straight wall arch. In order to meet the increasing traffic; improve the safety capacity; make the tunnel more smooth with existing road. The original tunnel needs to be widened and heightened, while adjust the road alignment. Dong Changyu tunnel is expanded to double lane which clear width is 10 meters and clear height is 5 meters. The total length is 468 meters, including the extension section of 345 meters.

The surrounding rock of the tunnel is mainly quartz sandstone and a thin layer of shale with slightly weathering; Local fracture zone is soft rock. Fracture development is general to more development. There have Vault collapse in K3 + 557 ~ K3 + 586. The surrounding rock is broken, Class-V; the strength coefficient of rocks is about 6. There is a collapse cavity in vault which length is 29 meters, width is 2.5~6.0 meters, height is 2.7~5.5 meters, embedded depth is deeper than 20 meters. Through the investigation, it is found that the top of cavity has exceeded the excavation outline, and the lining of tunnel roof is only 50 cm. Integrated local conditions and schedule requirements, we put forward the measure including existing tunnel reinforcement, collapse cavity treatment and backfill, temporary support demolition and excavation. The process is shown in Figure 1.

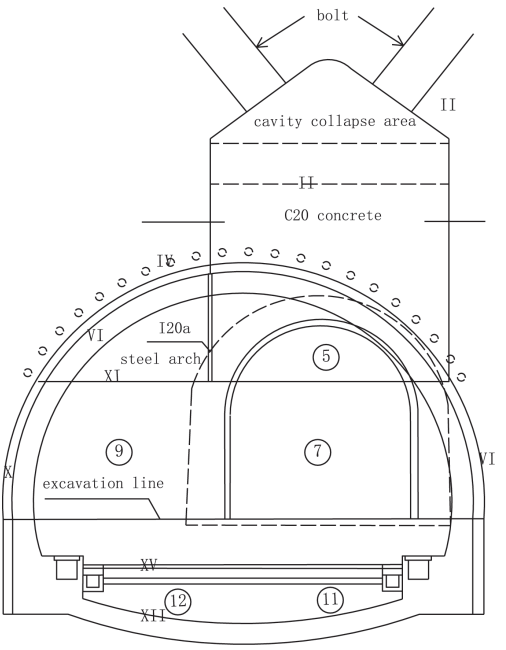


Figure 1. Construction process of collapse cavity expansion.

## 3 TUNNEL BLASTING DESIGN AND VIBRATION MONITORING

### 3.1 *Blasting design*

Different from blasting design of new tunnel need to set the cut hole, expansion of existing tunnel is no longer set it, directly to the existing tunnel as free surface.

There is a small intersecting angle of tunnel axis between the existing and new tunnel, and then its relative position is changing, so blasting design need to be constant adjusted. We select a typical section at K3 + 572, using benching tunneling method. The blasting is row by row initiation by 2, 4, 6, 8, 10, 12 MS delay electric detonators, the perimeter holes use 14MS in series with detonating cord. The depth of holes is 1.5 meters; the maximum explosive quantity of a single hole is 0.6 kg. Layout of blast hole and detonating sequence are shown in Figure 2.

### 3.2 *Blasting vibration monitoring scheme*

The monitoring is to research the effect of blasting vibration on surrounding rock of unexcavated area and collapse cavity, and analyze the blasting vibration and rock fragmentation with multi free surface, so as to optimize the blasting parameters and supporting design. As shown in Figure 3, six measuring points were arranged along the longitudinal axis of the tunnel to unexcavated direction, sensors were planted on the ground of left side, and its spacing is 1 meter and 1.5 meters.

### 3.3 *Monitoring result*

Fourteen times of blasting vibration monitoring were carried out in the construction of collapse section, and the monitoring results of K3 + 572 are shown in Table 1.

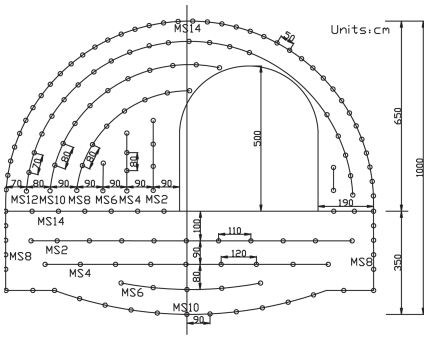


Figure 2. Layout of blast hole and detonating sequence (units: cm).

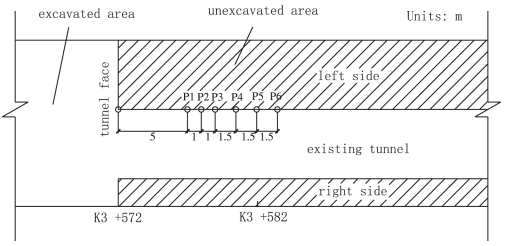


Figure 3. The layout of monitoring points (units: m).

Table 1. The data of vibration monitoring.

| Monitoring points | Distance from the tunnel face/m | Vibration velocity/cm/s | Frequency/Hz |
|---|---|---|---|
| 1 | 5.0 | 22.444 | 41.025 |
| 2 | 6.0 | 19.976 | 210.526 |
| 3 | 7.0 | 18.500 | 210.536 |
| 4 | 8.5 | 12.346 | 61.776 |
| 5 | 10.0 | 9.924 | 57.554 |
| 6 | 11.5 | 14.947 | 61.776 |

## 4 NUMERICAL SIMULATION METHOD

In the process of numerical calculation, the deformation of grid cells after explosion is too large. In general, we use Lagrangian erosion algorithm to calculate the large deformation and fracture of materials, the blasting calculation of rock and soil materials also can be handled by this method. Due to model itself, explosive materials cannot be erosion deletion. In the calculation, oversize grids may lead to negative volume, and then the numerical calculation is terminated. Lagrangian erosion algorithm can be used for numerical calculation of the single hole blasting with the asymmetric structure, which is not suitable for the multi-hole blasting. If using the fluid-solid coupling algorithm, Euler algorithm for explosive material, Lagrangian algorithm for the rock, then the boundary of fracture rock is indistinct. Therefore, the above methods cannot effectively simulate the process of multi-hole blasting. In this paper, by using numerical calculation method with Lagrangian algorithm and full restart, we study rock fragmentation and blasting vibration in multi-hole blasting.

### 4.1 *Numerical calculation method with Lagrangian algorithm and full restart*

Numerical calculation method with Lagrangian algorithm and full restart is to refer to the rock and the charge using Lagrangian algorithm, when the charge deformed too large, we use full restart method to remove the charge which oversize deformation, until all the charge be initiated and deleted. Full restart method of LS-DYNA is an analysis which modify K document of calculation model, such as add a new PART, delete PART, etc. In fact, full restart method is new analysis of using the previous numerical simulation results, it uses the deformation and stress of related part analysis as initial conditions, then continues new analysis which starting time follow the end time of previous simulation. The transmission of stress and deformation is achieved through the keyword *STRESS_INITIALIZATION, we can initialize all or part of the PART in original K files. Using the keyword *DELETE_PART, the method can remove explosive cylinders which oversize deformation and explosion energy consumption completely. It solves simulation termination because of negative volumes, and completely describes rock fragmentation and blasting vibration of multi-hole blasting with delay time in tunnel expansion.

It should be pointed out that each charge segment must be set as an independent part; there is no inevitable connection with them in calculation. If all the charge is set to the same PART, the adjacent charge will be initiated at the same time of the first charge blasting. Owing to charge model itself, different stages of the charge is self-initiation without delay, the purpose of delay initiation is failed. So, each charge segment must be set as an independent part in the numerical calculation method.

### 4.2 *Calculation model*

As shown in Figure 4, the grid of charge is 4 mm; the grid of surrounding rock is gradual change from 1~4 cm to 6~10 cm, they are dense near the charge. The total grid about 120 million calculated by g-cm-ms unit system. Calculation model of blasting holes is shown in Figure 5.

### 4.3 *Material model and parameters*

The surrounding rock of the tunnel is quartz sandstone with shale; we use the bilinear elastic-plastic model to describe the properties and mechanical behavior of the rock. The cavity collapse is reinforced by I14 steel arch and Φ20 steel mesh, C25 concrete pouring, we use the same model to describe this materials, the steel arch and steel mesh are convert into the concrete by stiffness contribution method. The material parameters are shown in Table 2, $E$ is elastic modulus, $v$ is poisson ratio, $\sigma_0$ is yield strength.

The material model of 2# emulsion explosive use high energy explosive model and JWL equation of state of detonation products, the material parameters are shown in Table 3, $D$ is explosion velocity; $A$, $B$, $R_1$, $R_2$ and ω are constant; $E_0$ is internal energy per unit volume.

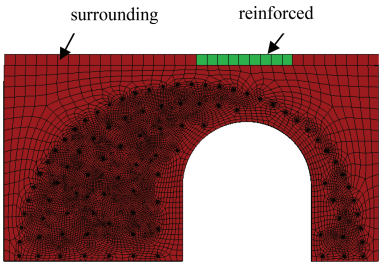


Figure 4. Calculation grid.

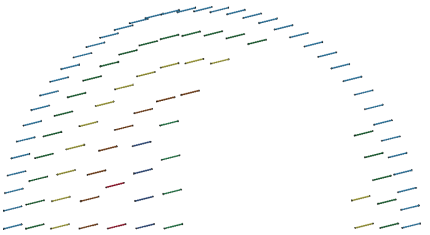

Figure 5. Calculation model of blasting holes.

Table 2. Material parameters.

| Material | ρ/(g cm$^{-3}$) | $E$/GPa | $\nu$ | $\sigma_0$/GPa |
|---|---|---|---|---|
| Surrounding rock | 2.83 | 64.8 | 0.29 | 0.14 |
| Reinforced area | 2.44 | 30 | 0.18 | 0.30 |

Table 3. Parameters of explosive.

| $\rho$/(g cm-3) | $D$/ms$^{-1}$ | $A$/GPa | $B$/GPa | $R_1$ | $R_2$ | $\omega$ | $E_0$/GPa |
|---|---|---|---|---|---|---|---|
| 1.31 | 5500 | 214.4 | 0.182 | 4.2 | 0.9 | 0.15 | 4.192 |

## 5 RESULT ANALYSIS

### 5.1 *Comparative analysis of vibration velocity*

The numerical calculation shows that the velocities of blasting vibration are 21.0 cm/s, 16.7 cm/s, 14.1 cm/s, 10.4 cm/s, 7.8 cm/s and 5.5 cm/s, the distance in front of the tunnel face are 5 meters, 6 meters, 7 meters, 8.5 meters, 10 meters and 11.5 meters correspond to monitoring points of No. 1 to No. 6. As shown in Figure 6, the monitoring data and numerical results are basically the same; the attenuation trends of vibration velocities are consistent with five monitoring points. There is a difference of No.6 point, vibration velocity at No.6 point rise again in many times of monitoring. We propose that there is wave superposition at this place with the blasting seismic wave propagation, so its vibration velocity has increased. It may be related to support structure of the existing tunnel, section shape and measuring point layout and so on.

In the process of blasting excavation, the surrounding rock will be damaged or even destroyed, which leads to the decrease of the carrying capacity of surrounding rock. Monitoring velocity which five meters in front of the tunnel face is 26.914 cm/s; the blasting vibration will produce a slight crack of tensile layer of the surrounding rock. The profile of right side is only 1.9 meters, which should be focused on the damage of surrounding rock; we can modify the blasting parameters to ensure the stability of surrounding rock, such as the maximum explosive quantity of single shot.

Comparison of monitoring date and simulation result of No.1 point in Figure 7, vibration velocities of part charge segment are not very consistent, but the peak value and attenuation rule are basically the same; it generally reflect the propagation law of blasting vibration in front of tunnel face.

### 5.2 *Blasting effect analysis*

Figure 8 is the diagram of blasting pressure and rock fragmentation effect after the MS8 segment blasting (t = 230 MS), Figure 9 is the diagram of blasting pressure and rock fragmentation effect after all charge blasting (t = 850 MS). The previous blasting provides free surface for the subsequent blasting, achieving the purpose of effective rock breaking; blasting effect of numerical calculation is consistent with engineering practice.

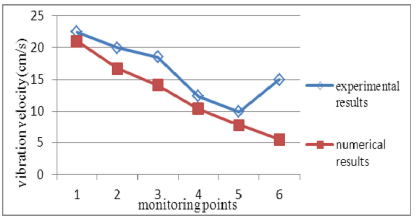


Figure 6. The maximum velocity of two test variation curve.

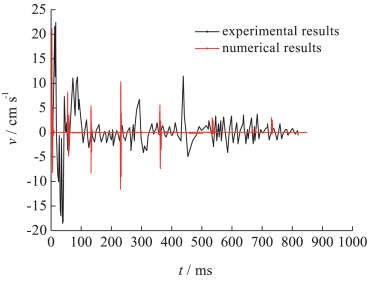


Figure 7. Comparison of vibration velocity between field monitoring and numerical result.

Figure 8. Pressure evolutions and rock fragmentation at 230 ms.

Figure 9. Pressure evolutions and rock fragmentation at 850 ms.

## 6 CONCLUSION

1. Numerical results show a good agreement with monitoring data; both attenuation trends of vibration velocities are consistent. We verify that the method can simulate large deformation of rock blasting, and completely describe rock fragmentation and blasting vibration of multi-hole blasting with delay time in expansion tunnel.
2. Both velocities which five meters in front of the tunnel face are greater than 20 cm/s; the blasting vibration will produce a slight crack of tensile layer of the surrounding rock. We can modify the blasting parameters to ensure stability of surrounding rock.
3. The previous blasting provides free surface for the subsequent blasting, achieving the purpose of effective rock breaking; blasting effect of numerical calculation is consistent with engineering practice.

## REFERENCES

Gao, W. & Deng, H. 2013. *Theory and Technology of Highway Engineering Blasting.* Beijing: Science Press.

Li, Y., Shi, D., Zhao, Y. 2008. *Basic Theory and Engineering Practice of ANSYS 11.0/LS-DYNA*. Beijing: China Water Resources and Hydropower Publishing House.

Yang, W. 2002. *Handbook of Commonly Used Data for Engineering Blasting*. Beijing: China Communication Press.

Chen, Q. 2011. Case study on widening options of jinjishan tunnel. *Tunnel Construction* 31(5):577–582.

Liu, D., Sun, B., Shi, L., Gao, W. 2014. Numerical simulation of multi-hole blasting vibration of road cutting slope excavation. *ACTA ARMAMTRAII* 35(S2): 92–95.

Qian, Q. & Rong, X. 2008. State issues and relevant recommendations for security risk management of China's underground engineering. *Chinese Journal of Rock Mechanics & Engineering* 27(4): 649–655.

Tang, J.S., Liu, S.Y., Tong, L.Y., & Jun, Y.U. 2007. Comparative study on tunneling scheme of shallow overburden and large-span highway tunnel in cracked rock mass. *Rock & Soil Mechanics* 28(S): 469–473.

Yan, Q.X., Chuan, H.E., Yao, Y., & Deng, G. 2004. Numerical simulation analysis of little tremie grouting effect while construction of going into portal at small-distance tunnel. *Rock & Soil Mechanics* 25(S2): 239–242.

Yao, S., Chen, K., Liu, D. 2014. The reconstruction and extension project of tunnel excavation and blasting vibration monitoring and analysis. *Engineering Blasting* 20: 37–40.

*Rock Dynamics: From Research to Engineering – Li et al. (Eds)*
*© 2016 Taylor & Francis Group, London, ISBN 978-1-138-02953-8*

# Rockburst prevention schemes of coal mines in China

Z.H. Ouyang, S.K. Zhao & Q.X. Qi
*China Coal Research Institute, Beijing, China*
*State Key Laboratory of Coal Mining and Clean Utilization, Beijing, China*

ABSTRACT: With the increase of mining depth and the expansion of mining scale, rockburst has become one of the major dynamic disasters in mining since it causes numerous casualties and accidents in China. Two special research in 2012 and 2014, discovered that the quantity of rockburst coal mines increased from 32 in 1988 to 142 in 2012, and that thousands of accidents and casualties were associated with rockbursts and their secondary disasters in the past 10 years. The distribution of rockburst coal mines was studied, and the results showed that China's rockburst coal mines are primarily distributed in four geographic bands near north latitudes 26°, 34°, 39° and 46°, and that about half of the rockburst prone coal mines is located in the Bohai gulf region. Both the current situation and main problems of rockburst prevention technology were analyzed. In order to improve the prevention and control efficiency of rockburst and its secondary disasters, coal mines were divided into three kinds as developing coal mine, general coal mine and rockburst coal mine. Risk assessment, monitoring and forecasting, prevention technology and efficiency testing, rockbursts prevention schemes of each kind of coal mine was provided.

## 1 INTRODUCTION

China is the largest country in coal production and consumption in the world. According to the BP statistical review of world energy, in 2014, China had accounted for 46.0% of coal production and 50.6% of consumption of the world. In recent decades, the coal production of China increased year by year and the death rate per million ton declined rapidly, China's coal mine safety situation improved markedly. Even though, coal rockbursts occasionally happened. For example, on 5 June 2008, 3 November 2011, and 27 March 2014, three serious rockbursts accidents happened in Qianqiu coal mine of Yima Coal Industry Group, killing a total of 29 people and injuring more than 80 people. Also, on 12 January 2013, a rockburst accident happened in Wulong coal mine in Fuxin, Liaoning province, which caused 8 deaths. Furthermore, with the increase of coal mining depth and mining scale, the number of the rockburst coal mines has increased significantly. In 2014, there were 142 rockburst coal mines in China, which is 4.5 times of that in 1985. Rockburst has become one of the major dynamic disasters of Chinese coal mine.

Over years, rockburst has become one of the hottest issues in mining engineering and rock mechanics. Many studies have paid their attention to study the occurrence mechanism, risk assessment, monitoring and forecasting, and disaster prevention of rockburst (Dou et al. 2014). To effectively predict rockburst, various methods and/or models have been established, including fuzzy comprehensive evaluation method (Wang et al. 1998, Yang et al. 2010), Bayes' discriminant analysis (Gong et al. 2010), unascertained measurement approach (Shi et al. 2010), Lyapunov index method (Li et al. 2006), rough set combined with genetic algorithm (Yu et al. 2009), judgment index classification (Chen et al. 2009), stress state determination, rough set theory (Yang et al. 2010), mining and seismological monitoring methods (Li et al. 2011, 2012, Dou et al. 2004, Zhao et al. 2005, Zhao et al. 2011), and optimal relative membership degree (Zeng et al. 2011). In the area of rockbursts danger prediction, many methods such as hydraulic fracturing (Ouyang 2013, Hu et al. 2012), de-stress blasting, rock blasting, de-stress drilling (Li et al. 2009; Zhu et al. 2015), and deep hole pre-cracking blasting (Qi et al. 2007, Ouyang et al. 2015), have been developed and applied for disaster prevention.

## 2 DISTRIBUTION OF ROCKBURST COAL MINES IN CHINA

To assess the seriousness of coal mine rockbursts, the Chinese State Administration of Coal Mine Safety (SAWS) in association with China Coal Research Institute and University of Science & Technology Beijing conducted a special nationwide investigation on rockburst coal mines in 2012. Investigation result revealed that more than 3,000 coal rockbursts have occurred in 142 coal mines in China since the first rockburst occurred at Shengli Coal Mine, Fushun, Liaoning in 1933. And more than 300 people were killed and thousands of people were injured by the coal rockbursts and their secondary disasters in the past ten years.

Figure 1 shows the geographical locations of the 142 rockbursts coal mines. It indicates that the rockburst coal mines were primarily distributed in four geographic bands near north latitudes 26°, 34°, 39° and 46°. About half rockburst prone coal mines were located in the Bohai gulf region. Shandong province alone has the most rockburst coal mines in China.

## 3 PREVENTION SCHEMES OF ROCKBURSTS

Coal rockbursts are affected by many uncertain factors such as bursting proneness of coal and rock stratum, geological conditions, and mining technology. According to their current situations coal mines can be divided into three kinds:

1. Developing coal mines. Developing coal mines refers to the coal mine under construction before meeting production conditions.
2. General coal mine. General coal mine is the producing coal mine that rockburst have never happened before.
3. Rockburst coal mine. Rockburst coal mine is the producing coal mine that has at least one rockburst already.

Different kind of coal mines should adopt different rockbursts prevention schemes.

### 3.1 *Rockburst prevention scheme for developing coal mines*

The whole construction and production process of developing coal mines can be divided into five stages as feasibility study, preliminary design, development, preparation and production. And these coal mines should consider rockbursts prevention in the whole process of mine construction and production, and this kind of coal mine should take the following rockburst prevention schemes as shown in Figure 2.

#### 3.1.1 *Rockburst hazard pre-estimate in feasibility study stage*

In feasibility study stage, developing coal mines especially the mining depth over 600 m ones and the rockburst coal mines neighbouring ones must evaluate the rockburst dangerousness

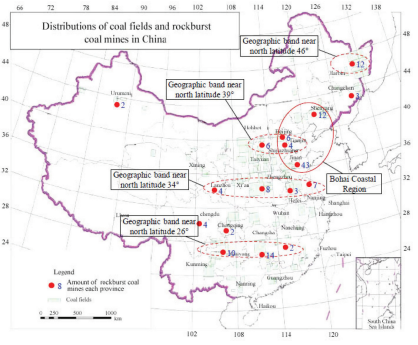


Figure 1. Distribution of rockburst coal mines in China.

in the feasibility study stage. And the evaluation results are the reference and basis of rockburst prevention in preliminary design and development stages.

### 3.1.2 *Specialized design of rockburst prevention in the preliminary design stage*

According to the results of rockburst hazard pre-estimate, the developing coal mine can be divided into two kinds, rockburst risk ones and no rockburst risk ones. The rockburst risk coal mines should compile a specialized prevention design in the preliminary design stage. And the contents of specialized prevention design generally consists of development ways, choice of protective layer, layout of mining area roadway, sequence of mining work face, method of coal mining, production capacity, support form, prediction technique of rockburst risk, rockburst monitoring and early warning method, efficiency testing method of prevention, safeguard procedures, and so on. However, the specialized design is not needed for the no rockburst risk developing coal mines.

### 3.1.3 *In-situ stress measurement and bursting liability testing in the development stage*

The rockburst risk developing coal mine should measure the in-situ stress of and test the bursting liability of coal and roof strata as soon as possible in the development stage. The widely applied in-situ stress measurement methods include hydraulic fracturing and stress relief.

The bursting proneness measurements of roof strata should be conducted by following the Chinese national recommended standard GB/T25217.1-2010, which is named "Methods of test, monitoring and prevention of rockburst—part 1: Classification and laboratory test method on bursting liability of roof strata". In this standard, bending energy index was express appointed to determine and evaluate the bursting proneness of roof strata, just as listed in Table 1.

The bursting proneness measurements of coal and "roof-coal" combinations should be conducted by following the Chinese national recommended standard GB/T25217.2–2010, which is named "Methods of test, monitoring and prevention of rockburst—part 2: Classification and laboratory test method on bursting liability of coal". To determine and evaluate the bursting proneness of coal, four indexes, including duration of Dynamic Fracture (DT), elastic strain energy ($W_{ET}$), bursting energy ($K_E$), and uniaxial compressive strength ($Rc$), are utilized in the testing and analysis. The classification of bursting proneness of coal is listed in Table 2.

### 3.1.4 *Impact risk assessment in the preparation stage*

Based on the results of in-situ stress measurement and the coal and roof strata bursting liability testing, the assessment methods such as multi-index comprehensive, quantitative theoretical, fuzzy matter-element, possibility index, simulation and similar simulation and so on, should be adopted to assess the impact risk of the developing coal mines in the preparation

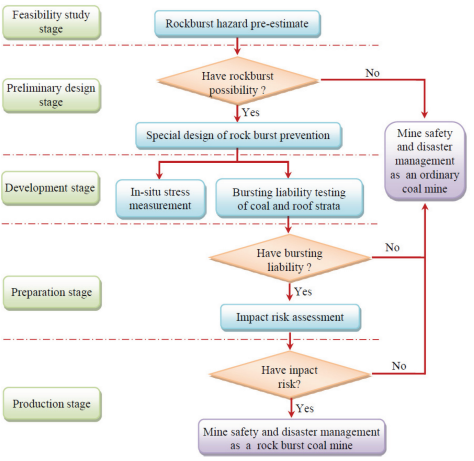


Figure 2. Rockbursts prevention schemes for developing coal mines.

stage. In order to avoid deviation, at least two kinds of methods should be used to evaluate the impact risk. And according to the results of impact risk assessment, coal mines can be divided into four categories as no, weak, medium and strong rockburst coal mines.

3.1.5 *Rockbursts prevention and control in the production stage*
In production stage, for the no rockburst coal mines, ignoring rockburst disaster prevention is admissive approbatory. However, for the weak, medium and strong rockburst coal mines, scheme of disaster prevention should be adopted as is elaborated in 3.3.

3.2 *Rockburst prevention scheme for general coal mines*

The general coal mines should take the following rockburst prevention schemes showed in Figure 3.

3.2.1 *Investigation of rockburst induced factors*
Along with the enhancing of mining strength and the increase of mining depth, more and more general coal mines are tend to induce rockburst. However, few engineer and manager realized this alteration. Currently, the principal main work for these coal mines is seeking induced factors of rockburst especially for the following coal mines.

1. The coal mines with the mining depth over 600 m.
2. The coal mines with the phenomena of coal-gun, roof vibration, coal bumps or rock ejection during excavating and mining.
3. The coal mines closed to the rockburst ones.
4. The coal mines with the thickness of single hard roof rock stratum over10 m and the depth of mining coal over 200 m.
5. The coal mines with special geological conditions such as sharp inclined coal seam, undulates terribly landform, anomalous structure, and so on.

3.2.2 *In-situ stress measurement and bursting liability testing*
The above five kinds of general coal mines and the ones with rockburst induced factors should carry out in-situ stress measurement and bursting liability testing follow the principles and demand as 3.1 mentioned in this article.

3.2.3 *Rockburst dangerousness assessment*
According to the bursting liability testing results of rock stratum and coal, the general coal mines which mined bursting liability coal stratums should adopt comprehensive index method, quantitative theoretical method, fuzzy matter-element method, possibility index

Table 1. Classification of bursting proneness of roof stratum.

| Classification | Type I | Type II | Type III |
|---|---|---|---|
| Bursting proneness | None | Weak | Strong |
| Bending energy index ($U_{WQS}$)/kJ | $U_{WQS} \leq 15$ | $15 < U_{WQS} \leq 120$ | $U_{WQS} > 120$ |

Table 2. Classification of bursting proneness of coal.

| Classification | Type I | Type II | Type III |
|---|---|---|---|
| Bursting proneness | None | Weak | Strong |
| Duration of dynamic fracture ($DT$)/ms | $DT > 500$ | $50 < DT \leq 500$ | $DT \leq 50$ |
| Elastic strain energy index ($W_{ET}$) | $W_{ET} < 2$ | $2 \leq W_{ET} < 5$ | $W_{ET} \geq 5$ |
| Bursting energy index ($K_E$) | $K_E < 1.5$ | $1.5 \leq K_E < 5$ | $K_E \geq 5$ |
| Uniaxial compressive strength ($Rc$)/MPa | $Rc < 7$ | $7 \leq Rc < 14$ | $Rc \geq 14$ |

method, numerical simulation or other evaluation methods to assess the rockburst dangerousness. The rockburst dangerousness general coal mines divided into rockburst coal mines and abide by the prevention scheme as 3.3 mentioned in this article.

### 3.3 *Rockburst prevention scheme for rockburst coal mines*

For rockburst coal mines, series of rockburst preventions should be applied before mining, during mining and after mining. And the prevention scheme of this kind of coal mines is showed in Figure 4.

#### 3.3.1 *Rockburst preventions before mining*

1. Basic information collection

Before the design and excavation of new mining area and coal faces in rockburst mines, the basic information such as the results of in-suit stress measurement and bursting liability testing, the distribution diagrams of coal thickness, bore hole columnar section, the relative position of coal seam group, the distribution of geological structure and mined out section, the physical and mechanical properties of coal and its roof rock stratum, should be collected.

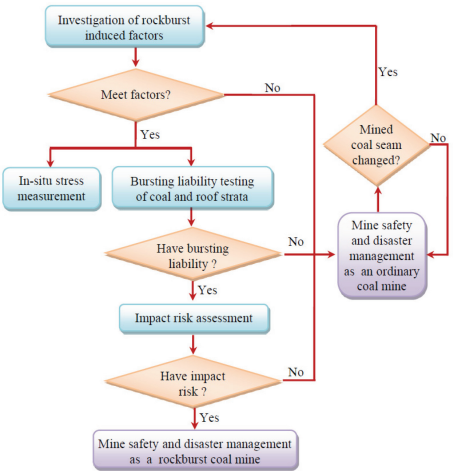


Figure 3. Rockbursts prevention schemes for general coal mines.

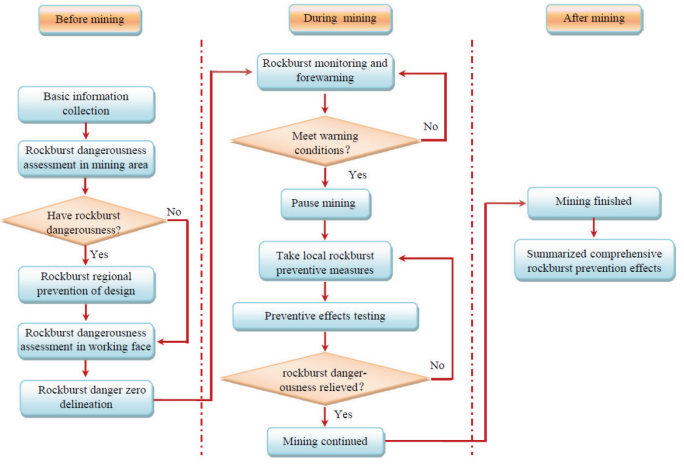


Figure 4. Rockbursts prevention schemes for rockburst coal mines.

2. Rockburst dangerousness prediction

Based on the analyses of mentioned basic information, geological dynamical division, numerical simulation or other evaluation methods should be adopted to predict the rockburst dangerousness of the soon mining area and coal faces.

3. Regional prevention design

According to the results of rockburst prediction, regional measures should be designed to avoid high stress concentration in the potentially dangerous area. And the regional measures including rational mining method, protective layer mining, mining layout optimization, and so on.

4. Rockburst danger zero delineation

In the regional prevention designed mining area, detailed specific rockburst dangerous should be evaluated in every coal faces, especially in the area closed to coal pillar, large geological tectonic belt, mined out area, and other possible stress concentration zones. The rockburst danger range and degree should be delineated in everywhere of the coal faces. And the degree of danger including four levels as no, weak, medium or strong rockburst.

### 3.3.2 *Rockburst preventions during mining*

1. Rockburst monitoring and forewarning

For rockburst coal mines, monitoring and forewarning system is very necessary in every work face. Furthermore, in the delineated zero by specific rockburst dangerous evaluation, multi methods should be adopted to monitor the dangerousness of rockburst. In China, there are five most frequently-used rockburst monitoring and forewarning methods, including ground pressure monitoring, cutting weight monitoring, microseisms monitoring, underground sound monitoring, and electromagnetic radiation monitoring.

In fact, multi-parameter monitoring system was established in most Chinese rockburst coal mines. For example, based on the range of monitored area, three-stage rockburst monitoring systems were established in Jisan Mine of Yankuang Group Co., Ltd, as shown in schematic drawing in Figure 5. SOS micro-seismic monitoring system was used to monitor the rockburst danger of the whole coal mine. KJ550 mining pressure online observation system was used to monitor the rockburst danger of coal face. And KBD5 electromagnetic radiation instrument and cutting weight monitoring were used to monitor the rockburst danger at local mining zones. Particularly, it is worth to mention that a series of new-style customized monitoring devices had been developed in recent years, such as KJ768 micro-seismic monitoring system by China Coal Research Institute and charge detector by Liaoning Technical University.

Except establishing multi-parameter monitoring system, another important work is to build warning index system and forewarn the rockburst dangerousness timely.

2. Local prevention of rockburst

There are two ultimate aims of monitoring and forewarning. One is to mark out the range of rockburst dangerousness area. The other is to pause coal mining and take local prevention measures to avoid the occurrence of rockburst in the dangerous area.

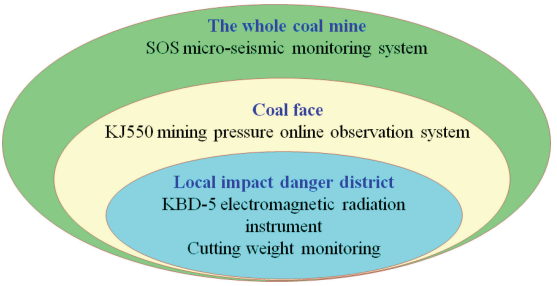


Figure 5. The three-stage rockburst monitoring system of Jisan coal mine.

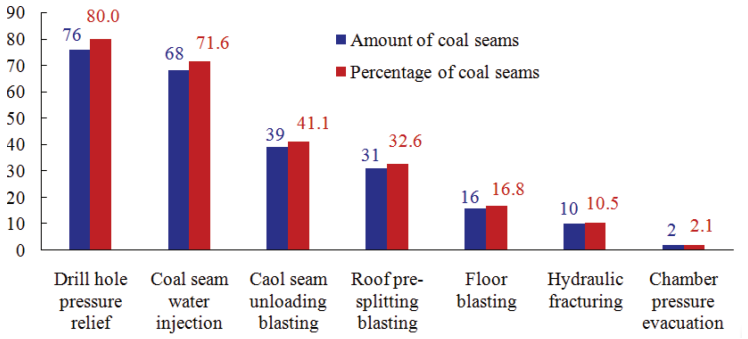


Figure 6. Different rockburst prevention methods of the surveyed coal seams.

In July and August 2014, a special research named Capacity Survey on Rockburst Coal Mines was conducted by State Administration of Coal Mine Safety and China Coal Research Institute. In this special research, 62 rockburst coal mines from Shandong, Heilongjiang, Jilin Liaoning, Henan, Shanxi, Gansu, Jiangsu and Xinjiang provinces were investigated. There are 95 mined coal seams on the 62 rockburst coal mines in the last 5 years. Among the 95 coal seams, the main 7 kinds of local prevention measures successively were drill hole pressure relief, coal seam water injection, coal seam unloading bursting, roof pre-splitting blasting, floor blasting, hydraulic fracturing and chamber pressure evacuation, as shown in Figure 6.

3. Preventive effects testing

In order to check the effect of local rockburst prevention, the established multi-parameter monitoring system should be used again to test the preventive effects. If the rockburst dangerousness can be ensured relieved, coal mining will be continued. Otherwise, another local rockburst prevention should be taken.

3.3.3 *Rockburst preventions after mining*

When the mining work finished, contrasting to the actual generation, the effect of rockburst prevention should be appraised. All of the appraised results are important references and guidance of rockburst prevention for next mining area and coal faces.

## 4 CONCLUSION

1. The frequency and intensity of rockburst have markedly increased. Rockburst has become one of the main dynamic disasters to threaten the safety of deep coal mining. The rockburst coal mines are primarily distributed in four geographic bands near north latitudes 26°, 34°, 39° and 42°, and about half rockburst prone coal mines were located in the Bohai gulf region in China.
2. Coal mines are divided into three kinds as developing, general and rockburst coal mines. And different rockburst prevention schemes are established for different coal mines.
3. As to the developing coal mines, the main work of rockburst prevention includes risk assessment and testing of the bursting liability of coal and rock stratum, and these work should be done in the stages of feasibility study, preliminary design, mine development, preparation and production.
4. As to the general coal mines, the work is to investigate the rockburst induced factors, and then, based on the investigation, in-situ stress measurement, bursting liability of coal and rock stratum testing and rock burst risk assessment should be done.
5. As to the rockburst coal mines, a closed technical scheme which including before mining, during mining and after mining should be formed, and comprehensive treatments should be applied to every stages from design, preparation to production.

## ACKNOWLEDGEMENTS

This work was financially supported by the National Natural Science Foundation of China (Grants No.51574150) and the Major Program of the Innovation Fund of China Coal Technology & Engineering Group Corporation (2013ZD002-04).

## REFERENCES

Chen, X., Sun, J.Z., Zhang, J.K., Chen, Q.S. 2009. Judgment indexes and classification criteria of rock burst with the extension judgment method. *China Civ. Eng. J*. 42(9): 82–88.

Dou, L.M., He, X.Q., Wang, E.Y. 2004. Electromagnetic emission technique of monitoring rock burst and its application. *Journal of China Coal Society* 29(4):396–399. (in Chinese).

Gong, F.-Q., Li, X.B., Zhang, W. 2010. Rockburst prediction of underground engineering based on Bayes discriminant analysis method. *Rock Soil Mech.* 31:370–377.

He, H., Dou, L.M., Fan, J., Du, T.T., Sun, X.L. 2012. Deep-hole directional fracturing of thick hard roof for rockburst prevention. *Tunneling and Underground Space Technology* 32: 34–43.

Li, H., Dai, R.Z., Jiang, J.-Q. 2006. Predicting Model of rock burst based on Lyapunov index. *J. Min. Saf. Eng*. 23: 215–219.

Li, T.,Sun, X.H., Lu, Y.G. et al. 2011. Prediction for the risk of strong mining-induced seismicity based on the rock loading/unloading response theory. *Journal of University of Science and Technology Beijing* 33(11): 1307–1311. (in Chinese).

LI, T., Wang, W., Xie, J.W. et al.2012. Rockbursts prediction based on rock damage of roof and floor induced by mining. *Chinese Journal of Rock Mechanics and Engineering* 31(12):2438–2444. (in Chinese).

Dou, L.M., Mu, Z.L., Li, Z.L. et al. 2014. Research progress of monitoring, forecasting, and prevention of rockburst in underground coal mining in China. *Int J Coal Sci Technol* 1(3): 278–288.

Li, J.K., Xiong, Z.H., Liu, D.S. et al. 2009. Numeric simulation of borehole pressure reliefpreventing roadway rockburst of a mine. *Journal of Xi'an University of Science and Technology* 29(4): 424–426. (in Chinese).

Qi, Q.X., Lei, Y., Li, H.Y. et al. 2007. Theory and application of prevention of rock burst by break-tip blast in deep hole[J]. *Chinese Journal of Rock Mechanics and Engineering* 26(Supp.1): 3522–3527. (in Chinese).

Shi, X.Z., Zhou, J., Dong, L., Hu, H.Y., Wang, H.Y., Chen, S.R. 2010. Application of unascertained measurement model to prediction of classification of rockburst intensity. *Chin. J. Rock Mech. Eng*. 29: 2720–2727.

Srinivasan, C., Arora, S.K., Yaji, R.K. 1997. Use of mining and seismological parameters as premonitors of rockbursts. *International Journal of Rock Mechanics and Mining Sciences* 34 (6): 1001–1008.

Wang, Y., Li, W., Li, Q. 1998 Method of fuzzy comprehensive evaluations for rockburst prediction. *Chin J. Rock Mech. Eng*. 17: 493–501.

Yu, H.-C., Liu, H.-N., Lu, X.-S., Liu, H.-D. 2009. Prediction method of rock burst proneness based on rough set and genetic algorithm. *J Coal Sci Eng (China)* 15: 367–73.

Yang, J.L., Li, X.B., Zhou, Z.L., Lin, H. 2010. A fuzzy assessment method of rockburst prediction based on rough set theory. *Metal. Min*. 408: 26–29.

Zeng, J., Zhang, Y.X., Jin, X.G. 2011. Prediction of rock burst using the method of optimal relative membership degree based on the maximum entropy principle. *J. Civ. Archit. Environ. Eng*. 33: 93–97.

Zhao S.K., Li, H.Y., Liu, J. et al. 2011. The research of deep rock burst dangerous mine prediction with multiparameter and danger rescission technology. *Journal of China Coal Society* 36 (Supp 2): 339–345. (in Chinese).

Zhao, X.D., Tang, C.A., Li, Y.H. et al. 2005. Prediction method of rock burst based on microseismic monitoring and stress field analysis. *Chinese Journal of Rock Mechanics and Engineering* 24 (Supp.1): 4745–4749. (in Chinese).

Ouyang, Z.H. 2013. Mechanism and experiment of hydraulic fracturing in rockburst prevention. In: Zhao & Li (eds), *Rock Dynamics and Applications-State of the Art: Proceeding of the 1st international conference on rock dynamics and applications: 6–8 June 2013*, Lausanine: Switzerland.

Ouyang, Z.H., Qi, Q.X., Zhao, S.K. et al. 2015. The mechanism and application of deep-hole precracking blasting on rockburst prevention. *Shock and Vibration* 2015, Article ID 625691, 7 pages, doi:10.1155/2015/625691.

Zhu, S.T., Jiang, F.X., Shi, X.F. et al. 2015. Energy dissipation index method for determining rockburst prevention drilling parameters. *Rock and Soil Mechanics* 36(8): 2270–2276. (in Chinese).

*Rock Dynamics: From Research to Engineering – Li et al. (Eds)*
*© 2016 Taylor & Francis Group, London, ISBN 978-1-138-02953-8*

# Application of microseismic monitoring technology in deep mining

Z.Y. Song & H.G. Ji
*School of Civil and Environmental Engineering, University of Science and Technology Beijing, Beijing, China*

ABSTRACT: Micro-seismic monitoring technology is based on the theories of acoustic emission and seismology, by monitoring the dynamic destabilization process of rock failure including germination, expansion etc. Micro-seismic monitoring technique can evaluate and predict the location of epicentre, energy, high stress zone and fracture degree, which is a kind of effective geophysical information monitoring technology. An overview of the Micro-seismic monitoring technology, which is widely used in deep mining, and control of mine dynamic disaster presented in this paper. Finally, an example shows the successful application of Micro-seismic monitoring technology in HUATING coalmine. Micro-seismic incident is relatively more powerful near the coal working face mainly with a large energy release. It accounts for 76.84% of total mine earthquake whose average energy is 3.70E+05J. Vibration energy is mainly concentrated in between 10E4J to 10E6J. We can conclude from the space distribution, time order and relatively concentrated districts delineated of Micro-seismic events that relatively concentrated districts of ground pressure correspond to the location of deep mining areas and the concentrated districts are relatively independent.Top and bottom of the surrounding rock is the main danger zone. Establishing the relationship between Micro-seismic events' b value variation and the risk of damage of the surrounding rock can provide a reference for Micro-seismic monitoring based on deep mine disaster forecasting technology.

## 1 INTRODUCTION

With the gradual depletion of shallow resources, deep mining will become an inevitable trend of sustainable development. The increase of mining depth and mining scale will inevitably bring more frequent underground disasters and result in an increasingly complex trend (Yang et al. 2007). Dynamic disasters induced by deep mining have suddenness and enormous energy imposing a serious threat to the safety of the mine production and causing huge economic losses and casualties. Therefore, how to monitor the stability of deep mines and how to warn effectively in case of an expected dynamic disaster become the key for mine production safety.

Micro-seismic refers to the micro vibration issued by a solid material under the influence of an external force, temperature and other factors. The vibration is accompanied by a slight vibration sound, with the stress wave spreading through the surrounding medium. Micro-seismic monitoring equipment can be used to collect, record and analyze Micro-seismic signals and thus to infer and analyze the source characteristics. This technique is called Micro-seismic monitoring technology (Li et al. 2014). There are many important issues needed to be researched in the study of Micro-seismic monitoring technology including establishing Micro-seismic monitoring data acquisition system, arranging Micro-seismic monitoring methods, studying Micro-seismic waveform and mechanism, optimal arranging Micro-seismic monitoring network (Gong et al. 2012), the precise temporal and spatial localization for the source position and so on.

Micro-seismic monitoring technology can evaluate and predict the location of the source, energy, high-stress areas and the extent of rock fracture. It is an effective monitoring technology for geophysical information and there are good value and prospects in safe deep mine exploitation. This article outlines the Micro-seismic monitoring technology widely used in deep mine safety, the prevention of mine dynamic disasters and other areas. In the mining and geological conditions of HUATING based on Micro-seismic monitoring system, we studied the spatial and temporal distribution of Micro-seismic events.

## 2 APPLICATIONS OF MICRO-SEISMIC MONITORING TECHNOLOGY IN DEEP MINING

### 2.1 *Monitoring mine earthquakes and rock-burst*

Mining with large scale and great depth will induce mine earthquake. Mine earthquake monitoring is the earliest application in Micro-seismic monitoring technology. Compared with mine earthquake, rock-burst is a serious dynamic failure in the coal mining process, which usually causes strong sudden and big destruction. Researches show that the application prospect of Micro-seismic monitoring technology in monitoring rock-burst is the widest. Different deep wells of collieries have different mining environment. Due to various occurring types and influencing factors, making full use of Micro-seismic monitoring signal characteristics and distribution characteristics would be helpful for understanding the mechanism of rock burst. As for this, both China and foreign scholars have done deep research. In order to establish a more reasonable and accurate warning system of instable disaster, accuracy in judging the risk of high-energy Micro-seismic events could be improved by comprehensively analyzing the precursory frequency features of Micro-seismic events before the rock-burst, b value of Micro-seismic signal, daily cumulative energy value, spectral characteristics and so on. Zhang et al. (2012) used Qianqiu coal mine Micro-seismic monitoring technology to gain roof recurring event features, dangerous impact areas, impact energy sources and factors of rock-burst pressure, which have provided references for rock-burst prevention.

### 2.2 *Monitoring in high stress areas and stress redistribution*

Micro-seismic events and the existence of high stress are inseparable. High stress areas might appear in the exploitation of forming fixed supporting. Stress might also emerge in the moving abutment pressure formed by current mining. It is also likely to arise from the special geological structure caused by abnormal stress, or be the result of a combination of multiple factors. Micro-seismic monitoring technology that we use not only monitors timely evolutionary process of the rock damages from deep mining but also combines with the position of rock mass for a comparative analysis. Every occurrence of Micro-seismic events is the sudden damage of the coal-rock mass caused by over limit stress concentration. Therefore, the spatial and temporal distribution of Micro-seismic events reflects the concentration of stress in a certain area, as well as the evolution of dynamic process of rock damage. Cai et al. (2007) used Micro-seismic monitoring data to evaluate the damage state of underground surrounding rock. Yang & Xia (2009) have used Micro-seismic monitoring to reveal the distribution characteristic of high stress areas, advanced stresses and lateral supporting pressures.

### 2.3 *Monitoring in tectonic fault activation*

Ground pressure, rock burst and water inrush induced by fault activation of deep well mining can cause serious mine accidents. It is a serious failure phenomenon. Fault shocking mine earthquake has randomness, suddenness and diversity of the destruction forms, which makes the usage of the traditional observation method unable to reveal the mechanism of fault rock-burst from the bottom of the earth. Micro-seismic monitoring technology is a technical method using seismic waves launched by rock itself after deformation and failure. This technology provides a new way for researching fault rock-burst disaster. We can layout Micro-seismic

sensor around the fault area of the mining production area to collect Micro-seismic data in real time. Through Micro-seismic data processing, we can gain the time of Micro-seismic events occurrence and the spatial distribution. Combining with the fault occurrence, spatial distribution, fault stress state, underground production activities and other factors, we can learn the spatial location of faulting, time rules and the relationships among these factor inducing faulting and mining activities. Besides, in order to research the degree of activation and development trend of faults affected by mining activities, we can use the parameter related to Micro-seismic events combining with the research relevant to Quantitative Seismology such as Gutenberg Kerrey characteristic curve. Li et al. (2010), made an analysis of a similar Micro-seismic signal spectrum for faulting shock based on Jisan coal mine geological condition. Zhang Da layout the Micro-seismic monitoring system on the Shouwangfen No.6 large empty area near the fault zone learned and gained the place and time of faulting activities in time (Zhang 2014) and got initial degree and rule of activation of empty area near the fault zone.

### 2.4 *Safety assistance*

Micro-seismic monitoring technology has an advanced positioning function on the epicenter. Therefore, when serious falling, landslides or rock-burst occur during large-scale underground engineering and explorations of underground minerals resources, using Micro-seismic monitoring technology to target underground siege staff can shorten the rescue time and greatly improve the chances of survival of trapped underground. In the 1970s, U.S. Bureau of Mines began to research the Micro-seismic positioning technology aiming at staff trapped mine disasters. In recent years, applying Micro-seismic monitoring technology as the main positioning assistance system has achieved to significant progress. Among all rescue cases, there are many successfully ones in which underground people using metal pipes for help such as QiTaihe coal mine flooding accident (Heilongjiang Province 2011), Tongling mine flooding accident (Anhui Province 2011), Wangjialing coal mine flooding accident (Shanxi Province 2010), Kuqiao coal mine flooding accident (Sichuan Province 2007), Pengshui mine roof collapse accident (Chongqing 2007) and so on (Chen et al. 2014). All of these cases have one thing in common: underground people thrash metal pipes to let rescuers get the information, which makes rescue work go well during the process of assistance.

## 3 APPLIED LIVING EXAMPLE OF MICRO-SEISMIC MONITORING

This study focuses on analysis of the relationship between Micro-seismic events roadway project. To understand preferably the relationship, we choose Huating working face as the main target of monitoring (see Figs. 1 and 2).

### 3.1 *B value of microseismic events' property*

The seismicity of Micro-seismic events is inversely proportional to the probability of occurrence, which means the smaller the seismicity, the higher the probability of occurrence. Researches show

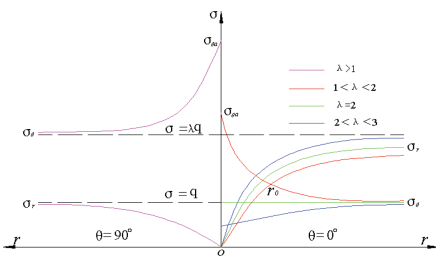


Figure 1. The stress distribution figures roof, floor and the two roadway walls (CUMT).

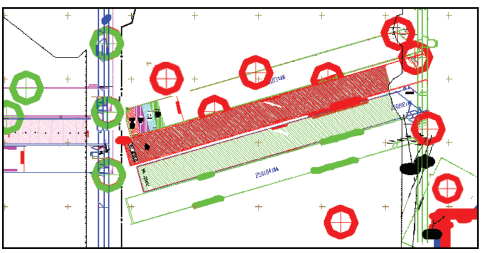

Figure 2. The optimum distribution of the Micro-seismic network.

that mine earthquake induced from mining extraction and natural earthquake follow the same rules. Both of them obey Gutenberg—Richter frequency—magnitude relationship, that is

$$LgN = a - bM \tag{1}$$

The changes of b value reflect adjustment of the internal structure of Micro-seismic events group, showing the number of small earthquakes and indicating how the earthquake proportional relationship changes. For this reason, aiming at the three-month Micro-seismic events monitored by the working face, Micro-seismic events in a month as a unit, the series of events in the interval 0.1 to statistics for the frequency-magnitude charts, in which 2012/4-6 month the frequency of Micro-seismic events-magnitude statistics shown in Figure 3. According to the above relationship, the b value statistical results of 4, 5, 6 month were 1.51, 1.42, 1.23.

### 3.2 *Timeliness of Micro-seismic events*

By collecting and analyzing a large number of Micro-seismic events and key parameters such as seismicity, place and time in the extracting process of Huating coal working face (see Fig. 4), we drew an initial conclusion as follows: Micro-seismic incident is relatively more powerful near the coal working face mainly with a large energy release. It accounts for 76.84% of total mine earthquake whose average energy is 3.70E+05J. Vibration energy is mainly concentrated in between 10E4 to 10E6J. Through analyzing the total energy and the shaking rate of daily Micro-seismic in Huating coal working face, we concluded the following law as the precursory rule when strong mine earthquake and strong shake occur: (1) Before strong mine pressure occurrence happen, mine earthquake's frequency and energy increase rapidly and maintain at a relatively high level. Until a big strong mine pressure occurrence happen, its frequency and energy will decrease obviously. (2) Micro-seismic signal frequency firstly shows a trend of increasing and then falls sharply. When seismic signal frequency increase again, strong mine pressure is coming. (3) Compared with the curve deviation degree before, when the vibration energy curve and vibration frequency curve on the longitudinal appeared obvious deviation, the higher vibration frequency, the smaller vibration energy, the greater the possibilities of strong mine earthquake occur. The increasing number of small shakes suggested that stronger damage of coal rock but the energy dissipation rate was low, which showed that energy was in an accumulating state. The breaking of energy balance led to a system instability and a sudden release of energy.

### 3.3 *The space characteristics of microseismic events*

The advanced stress concentration district of working face hassles shakes at the beginning of extraction. However, with the mining areas' expanding, more shakes appear in the front, along

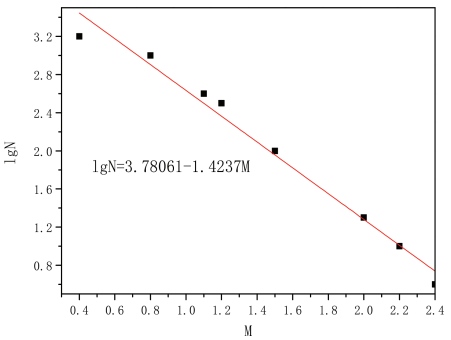


Figure 3. G-R relationship of Micro-seismic events.

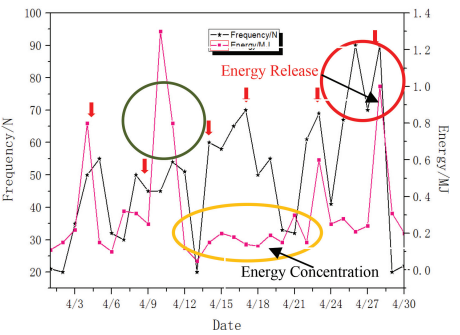


Figure 4. Energy and frequency of at working face. Micro-seismic events at working face.

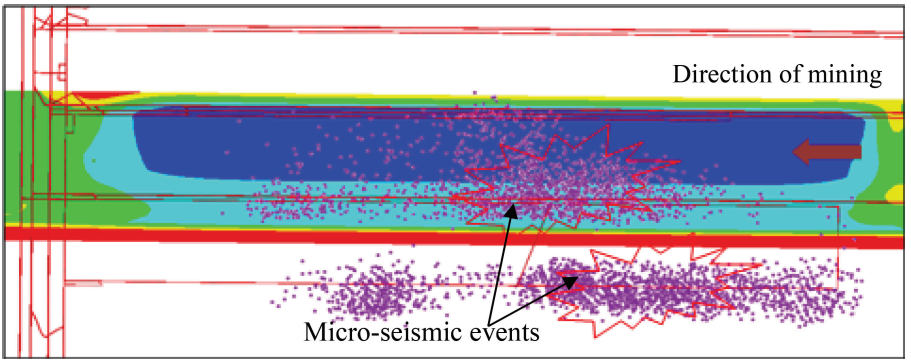


Figure 5. Drawing of horizontal distribution of Micro-seismic events.

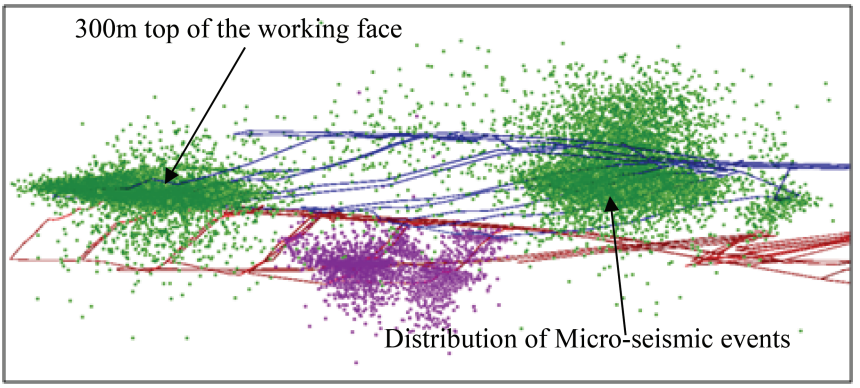


Figure 6. Drawing of vertical distribution of microseismic events.

with several strong mine earthquake events with higher energy. This shows that under advanced supporting pressure, coal rock has appeared a large scope of fracture or destruction.

On the plane space, mine earthquake occurs mainly in the working face and gob side. At the same time, it influences the working face of 240~360 m ahead and 90~180 m tilt up and down which fully embodies the different degree of influence on both advanced supporting pressure and lateral supporting pressure. The shock resulted from mining process of the working face mostly concentrated in the return airways trough of the working face because of increasing pressure close to the gob. Another reason is that the stress concentration resulted from the section of small coal pillar so that the overlying strata are relatively active and the vibration frequency is very high (see Fig. 5).

On the deep space, Micro-seismic event occurs in a scope of 300 m top of the working face and mainly in the elevation 1200 m below. From this we can infer that extraction of the working face affect about 250 m above the rock face in cracking or movement (see Fig. 6).

## 4 CONCLUSIONS

1. The space and time distribution rule of Micro-seismic events monitoring data can well reflect the dynamic process of rock damage evolution, which means we are able to apply Micro-seismic monitoring system in evaluating surrounding rock instability, high stress distribution, rock burst, water inrush and some deep dynamic disasters to provide a powerful tool.
2. We can conclude from the space distribution, time order and relatively concentrated districts delineated of Micro-seismic events that relatively concentrated districts of ground

pressure correspond to the location of deep mining areas and the concentrated districts are relatively independent. Top and bottom of the surrounding rock is the main danger zone.

3. Establishing the relationship between Micro-seismic events' b value variation and the risk of damage of the surrounding rock can provide a reference for Micro-seismic monitoring based on deep mine disaster forecasting technology.

## REFERENCES


Cai, M. et al. 2007. FLAC/PFC coupled numerical simulation of AE in large-scale underground excavations. *Int. J. Rock Mech. Min.* 44:550–564.

Chen, D. 2014. Micro-seismic Monitoring Technology and Its Application in Mine Rescue. *Mining Safety & Environmental Protection* 41 (1):106–112.

Gong, S.Y. et al. 2012. Optimization algorithm of network conjuration for improving location accuracy of microseism in coal mine. *Chinese Journal of Rock Mechanics and Engineering* 31(1): 8.

Li, J. et al. 2014. Review of slope Micro-seismic monitoring in open-pit mine.. *Chinese Journal of Rock Mechanics and Engineering* 22(Suppl2): 3998–4012.

Li, S.L. et al. 2005. Research of multi-channel Micro-seismic monitoring system and its application to Fankou lead-zinc mine. *Chinese Journal of Rock Mechanics and Engineering* 24 (12):2048–2053.

Li, S.L., Yin, X.G. & Li, A.B. 2004. Application for monitoring large blast aftershock by multi-channel Micro-seismic monitoring technology. *Chinese Journal of Rock Mechanics and Engineering* 24(Supp1):4711–4714.

Li, Z.H. et al. 2010. Frequency Spectrum Analysis on Micro-seismic Signal of Similar Simulation Test of Fault Rock Burst. *Journal of Shandong University of Science and Technology* 29(4):51–56.

Tang, L.Z. et al. 2002. Analysis and predication of rock burst dangerous areas in Dongguashan Copper Mine under deep well mining. *Journal of Central South University of Technology (Natural Science)* 33(4):335–338.

Tang, L.Z., Yang, C.X. & Pan, C.L. 2006. Optimization of Micro-seismic monitoring network for large-scale deep well mining. *Chinese Journal of Rock Mechanics and Engineering* 25 (10):2036–2042.

Xia, Y.X. et al. 2011. Study of rule of surrounding rock failure and stress distribution based on high-precision Micro-seismic monitoring. *Journal of China Coal Society* 36(2):239–243.

Yang, T.H. et al. 2007. State of the art of inrush models in rock mass failure and developing trend for prediction and forecast of groundwater inrush. *Chinese Journal of Rock Mechanics and Engineering 26* (2):268–277.

Yang, Z.G. et al. 2009. Mining engineering rock burst high-stress area Micro-seismic monitoring time-spatial distribution. *Chinese Journal of Rock Mechanics and Engineering* 28(2):3632–3637.

Zhang, D. et al. 2014. Study on Fault Activity in Mining area Based on Micro-seismic monitoring Technology. *Nonferrous Metals (Mining Section)* 66(5):1–5.

Zhang, S.J., Yao, J.G. & Ju, W.J. 2012. Relationship of rock burst and Micro-seismic activity in Qianqiu Coal Mine. *Journal of China Coal Society* 37(suppl1):7–12.

*Rock Dynamics: From Research to Engineering – Li et al. (Eds)*
*© 2016 Taylor & Francis Group, London, ISBN 978-1-138-02953-8*

# New brittleness indices to describe rock failure under compressive load

A. Taheri & H. Munoz
*The University of Adelaide, Adelaide, Australia*

ABSTRACT: Brittleness is an important mechanical property of rock. There are several brittleness criteria exist to characterize rock failure based on rock mechanical properties. However, there is not a unique criterion available able to describe quantitative rock brittleness. In this study different rocks with uniaxial compressive strength values ranging between 7-215 MPa were tested to measure pre-peak and post-peak stress-strain relations. A stiff servo-controlled machine was used to undertake lateral displacement controlled tests. Post-peak stress-strain relations were obtained accurately using three-dimensional digital image correlation technique. Several brittleness indices were proposed based on pre-peak energy, elastic energy and post-peak energy. Analysing of the results demonstrated that a pre-peak stress-strain brittleness index proposed solely based on pre-peak stress-strain behaviour doesn't show any correlation with rock peak strength. On the other hand, the proposed brittleness indices based on pre-peak and post-peak stress-strain relations were found to competently describe an unambiguous brittleness scale against rock strength.

## 1 INTRODUCTION

The ability to predict rock failure behaviour is very important for civil engineering and mining development projects. With the ability to predict rock failure, engineers could investigate the effect of rock behaviour on drilling and excavation performance and rock burst occurrence in deep mining. Brittleness refers to deformation that involves hard, strong material that fractures and splits rather than staying whole while pliably deforming. It is important to quantify the brittleness of a rock, so engineers can numerically assess and predict the deformational characteristics of rock masses. The study of brittleness in rock mechanics is relatively popular, and spans back to the 1950's. Many researchers since then have developed different numerical models to assess rock behaviour. Most mathematical models attempting to quantify rock brittleness (brittleness indices) are based on different intrinsic rock properties or on measured deformation of an intact rock specimen. The stress-strain curve is used to measure the deformation process of a rock specimen under compression. The stress-strain curve can be related the ductility-brittleness scale as well (Tarasov & Potvin 2012).

A literature survey shows that many brittleness indices were developed using rock strength values such as the Uniaxial Compressive Strength (UCS) and the tensile strength (Hucka & Das 1974, Coates 1966, Altindag 2003, Yarali & Soyer 2011). Brittleness index, however, is about rock failure behavior which cannot be predicted accurately by rock strength. Brittleness indices based on the stress and strain parameters were also found to be insufficient to describe rock failure characteristics (Tarasov & Potvin 2012). Several brittleness indices based on the energy of the rock under loading have been proposed (Baron et al. 1962), however, these indices are only based on pre-peak rock behaviour. More recent brittleness indices based on fracture energy have been proposed with the use of both pre-peak and post-peak data (Tarasov & Potvin 2012). In this case, two brittleness indices were combined to be used as a scale to describe the ductility-brittleness spectrum; a brittleness index for class II post-peak behaviour for very brittle rocks and another for Class I for softer and more ductile

rocks (Tarasov & Potvin 2012). In this study, both axial and lateral displacement controlled loading methods were used to study different rock stress-strain relations. However, rocks deformed using lateral displacement control generally show both Class I and Class II post-peak behaviour (Hudson et al. 1970). Therefore, a brittleness index based on energy applied to rock stress-strain behaviour regardless of class type would be more efficient and accurate. However, so far, no brittleness index based on energy have been developed which takes into account the entire stress-strain behaviour which can be applied on all types of rock, regardless of post-peak stress-strain behaviour. This is mainly because it is extremely difficult to capture the entire stress-strain behaviour using conventional load controlled or axial displacement controlled testing methods.

In this study several brittleness indices are proposed and investigated based on rock fracture energy obtained from rock pre-peak and post-peak stress strain behavior. Uniaxial compressive strength tests on 8 different rocks using lateral displacement controlled test method were performed to capture accurately pre-peak and post-peak stress strain behavior. Extensometers and strain gauges are very common tools to measure deformation of rock in uniaxial compressive tests. These local measurement tools, however, cannot entirely measure the strains after failure. In this case, extensometer misalignment and strain gauge damage are the main issues. To cope with this problem, three-dimensional Digital Image Correlation (3D DIC) technique was implemented to accurately measure rock deformation in pre-peak and post-peak regimes.

## 2 FRACTURE ENERGY UNDER COMPRESSION

In order to investigate the fracture energies under compression, the stress-strain diagram was used and divided into three areas including pre-peak energy, elastic energy and post-peak energy as shown in Figure 1. The pre-peak energy per unit specimen ($G_{pre}$) indicates the released energy by loading of the specimen up to the peak stress and then the curve is split with the maximum Young's modulus applied at the peak (Baron et al. 1962, Coates 1966, Hucka & Das 1974, Aubertin et al. 1994). The elastic energy per unit specimen ($G_{elastic}$) at peak stress corresponds to the energy after the pre-peak energy and defined by the peak stress and is illustrated in Figure 1b (Baron 1962, Hucka & Das 1974, Aubertin et al. 1994, Jansen & Shah 1997, Tarasov & Potvin 2012). The post-peak energy ($G_{post}$) is defined by the area under the post-peak curve, to the right of the Young's modulus line as shown in Fig 1a (Baron et al. 1962, Hucka and Das 1974, Jansen and Shah 1997, Tarasov & Potvin 2012). In order to calculate $G_{post}$ accurately, Young's modulus is applied to 1/3 of the UCS, as some experiments may end at different times than others (Jansen and Shah 1997, Tung & Tue 2015). This method standardises the end points of all the experiments.

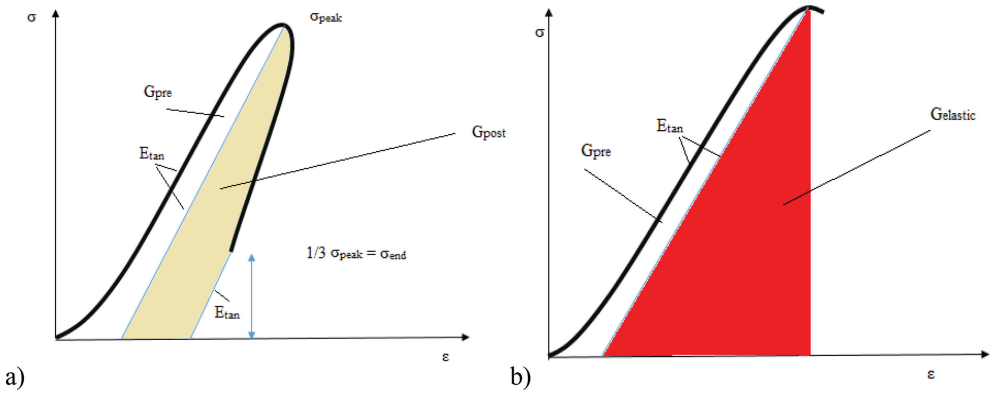


Figure 1. Definition of fracture energy: a) Pre-peak and elastic energy (total energy, $G_{total} = G_{pre} + G_{post}$); b) Pre-peak and post-peak energy (peak energy, $G_{peak} = G_{pre} + G_{elastic}$).

## 3 THE PROPOSED BRITTLENESS INDICES

Several brittleness indices are proposed in this study based on the pre-peak, the elastic and the post-peak energies as previously introduced in section 1. Other brittleness indices based on stress and strain values alone were investigated; however, we were not able to correlate them with rock basic mechanical properties. Energy based brittleness indices, however, are determined to have more accurate results in terms of data correlations, which will be discussed in section 5.

Brittleness Index 1 is calculated as the ratio of the elastic energy to the peak energy. The peak energy is the sum of pre-peak and elastic energy. This definition was developed by Barton et al. (1962). $BI_1$ is can be calculated using the following equation:

$$BI_1 = \frac{G_{elastic}}{G_{peak}} \tag{1}$$

Beside this BI which is developed based on pre-peak stress-strain relations, the following four brittleness indices are proposed in this study using pre-peak and post-peak stress-strain relations as follows:

Brittleness Index 2 ($BI_2$) is calculated as the ratio of the elastic energy to the total energy as follows:

$$BI_2 = \frac{G_{elastic}}{G_{total}} \tag{2}$$

Brittleness Index 3 ($BI_3$) can be obtained as the ratio of the elastic energy to the post energy using the following equation:

$$BI_3 = \frac{G_{elastic}}{G_{post}} \tag{3}$$

Brittleness Index 4 ($BI_4$) is determined as the ratio of the peak energy to the total energy as follows.

$$BI_4 = \frac{G_{peak}}{G_{total}} \tag{4}$$

Brittleness Index 5 ($BI_5$) is calculated as the ratio of the peak energy to the post energy using the following equation:

$$BI_5 = \frac{G_{peak}}{G_{post}} \tag{5}$$

## 4 EXPERIMENTAL STUDY

### 4.1 *Rock samples and apparatus*

Eight rock types involved in this study were chosen with the intention to have a sufficiently diverse uniaxial compressive strengths and material differences appropriate for this study. The eight rock types and their approximate strengths are shown in Table 1. The rocks specimens were cored from a single block to reduce the chances of variation and increase the chances of homogeneity between samples. The rock samples were cored from the block to a cylindrical shape. The rock samples were cored to have a diameter of 42 mm, with a length of 100 mm, resulting in a constant aspect ratios (length: diameter) at 2.4. They were then ground smooth on all surfaces to ensure even contact with the platen of the machine compression arm with reduced chances for bedding error (Taheri and Tani 2008).

A closed-loop servo-controlled testing machine with a loading capacity of 1000 kN and a loading rate capability in the range 0.001–10 mm/s were used. The loading system is equipped with a Linear Variable Differential Transformer (LVDT) to measure axial displacement externally. The load and strain data are acquired automatically by a data acquisition system.

### 4.2 *Testing procedure and results*

The lateral displacement controlled tests were performed in order to capture the entire stress-strain behaviour. Circumferential or lateral strain controlled test is suggested by ISRM suggested testing method (Fairhurst and Hudson 1999). This is mainly because this measurement always monotonically increases even if the axial displacement does not (Tarasov & Potvin 2012). As a result, all the tests were performed using lateral displacement controlled loading method. The lateral displacement was measured by a lateral extensometer which was fed back into the computer. The computer program then adjusts the load on the specimen in order to keep the lateral

Table 1. Rock types used in this study.

| Rock name | Rock type | UCS (MPa) |
|---|---|---|
| Tuffeau | Limestone | 7.0 |
| Savonniere | Limestone | 24.4 |
| Hawksebury | Sandstone | 34.9 |
| Massangis | Sandstone | 84.3 |
| Chassagne | Limestone | 122.8 |
| Harcourt | Granite | 142.6 |
| Alvand | Granite | 182.4 |
| Rocheron | Limestone | 215.3 |

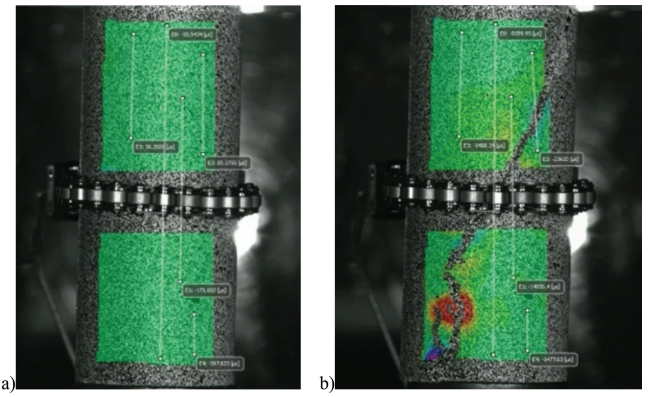


Figure 2. DIC technique measurement results: a) before loading; b) at the end of experiment in post-peak state.

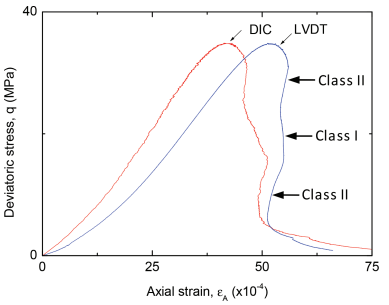


Figure 3. Stress-strain relations by external LVDT and DIC technique in Hawkesbury sandstone.

displacement at a constant rate of 0.16 mm/min. DIC technique and two LVDTs were used to measure axial strain. DIC technique includes setting up two digital cameras pointing at the specimen from two different angles and capturing a series of grey-scale images of the specimen surface pattern to create three-dimensional measurement of displacements (Sutton et al. 2009).

Figure 2, shows results of DIC measurement on Hawkesbury sandstone in the beginning and at the end of the test. Measurements undertaken by the external LVDTs include bedding errors (Taheri and Tani 2008). Results of DIC method, however, are free from bedding errors, and therefore were used directly to define brittleness index values. Figure 3, which show the stress-strain relation for Hawkesbury sandstone, support this argument. As can be seen in this figure, rock post-peak behavior is a combination of class I and class II behavior and therefore, it is very difficult to obtain a single value for post-peak stiffness. Therefore, use of brittleness indices proposed by Tarasov and Potvin (2012) is not possible.

## 5 PERFORMANCE OF PROPOSED BRITTLENESS INDICES

Figure 4 show the plot relation of brittleness indices with the unconfined compressive strength of the rocks. Figure 4a demonstrates that $BI_1$ was not able to represent an unambiguous brittle-to-ductile scale for most of the rocks and it seems to collapse to a single value,

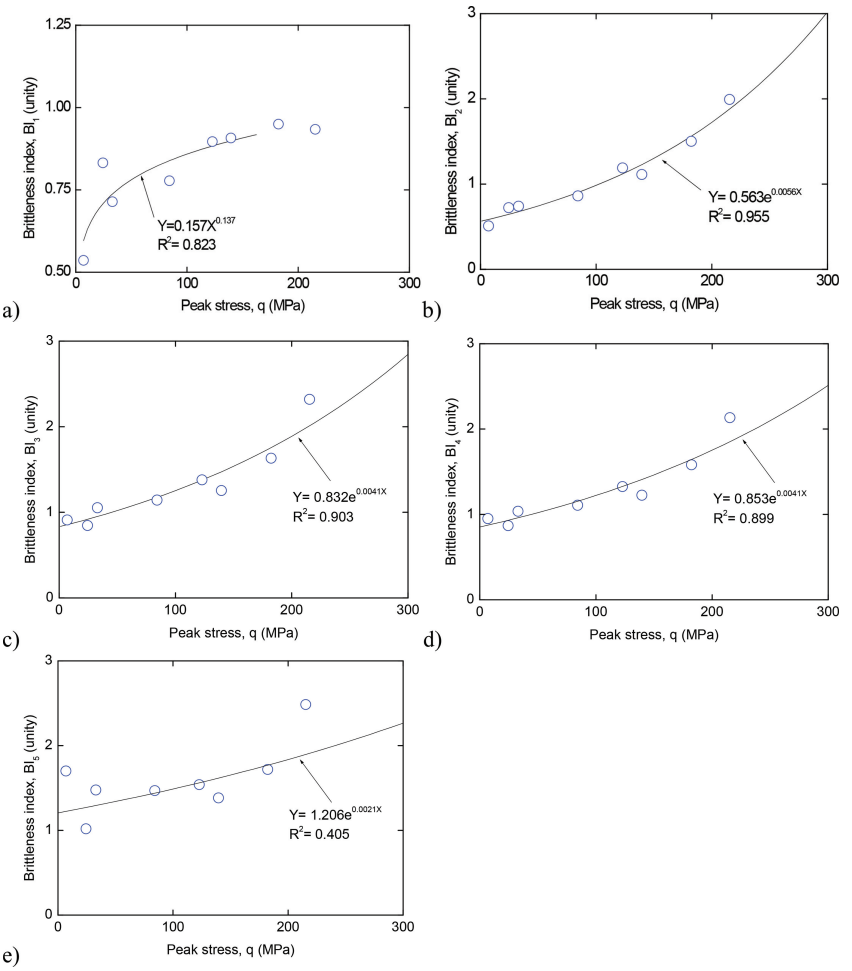


Figure 4. Brittleness indices against rock strength.

about 0.8, as rock strength increases. Among the brittleness indexes which are considered in this study, $BI_1$ is the only one that considers only pre-peak fracture energy values. The rest of brittleness indices developed from pre and post-peak stress-strain curve characteristics show a clear trend of brittleness scale as rock strength increases, i.e. the higher the brittleness index is the more brittle the rock. Coefficient of correlations for $BI_2$, $BI_3$, $BI_4$, and $BI_5$ against rock uniaxial compressive strength indicates that $BI_2$, and $BI_3$ have the highest correlations, therefore, $BI_2$, and $BI_3$ are deemed the most relevant brittleness indices proposed in this study.

## 6 CONCLUSIONS

In this study a couple of brittleness indices were developed based on pre-peak and post-peak stress-strain characteristics. Complete stress-strain relations of different soft, medium-strong and strong rocks (UCS is ranging from 7 to 215 MPa) were measures by implementing successfully lateral-strain controlled loading method on uniaxial compressive loading. Post-peak deformation characteristics of rocks were examined by three dimensional digital image correlation (3D DIC) technique. Analyses of the experimental results demonstrated that a pre-peak stress-strain brittleness index proposed solely based on pre-peak stress-strain behaviour doesn't show any strong correlation with rock peak strength. On the other hand, the proposed brittleness indices based on pre-peak and post-peak stress-strain relations were successfully correlated with rock peak strength. This outcome is relevant to suggest that rock uniaxial compressive strength as potential criteria for assessing and predicting rock brittleness.

## REFERENCES


Aubertin, M., Gill. D. & Simon, R. 1994. On the Use of the Brittleness Index Modified (BIM) to Estimate the Post-Peak Behaviour of Rocks. *1st North American Rock Mechanics Symposium*, 1–3 June, Austin, Texas, 945–952.

Altindag, R. 2003. Correlation of specific energy with rock brittleness concepts on rock cutting. *The Journal of the South African Institute of Mining and Metallurgy* 103: 163–172.

Barton, L.I., Loguntsov, B.M., & Posin, E.Z. 1962. Determination of properties of rocks (in Russian), *NTILGD*, 232, Gozgotekhizdat, Moscow.

Coates, D. 1966. Experimental criteria for classification of rock substances. *International Journal of Rock Mechanics and Mining Sciences* 3: 181–189.

Fairhurst, C.E. & Hudson, J.A. 1999. Draf ISRM suggested method for the complete stress-strain curve for intact rock in uniaxial compression. *International Journal of Rock Mechanics and Mining Sciences* 36: 279–89.

Hucka, V. & Das, B. 1974. Brittleness determination of rocks by different methods. *International Journal of Rock Mechanics and Mining Sciences* 11: 389–92.

Hudson, J., Brown, E. & Fairhurst, C. 1970. Optimizing the Control of Rock Failure in Servo-Controlled Laboratory Tests. *Rock Mechanics* 3: 217–224.

Jansen, D. & Shah, S. 1997. Effect of Length on Compressive Strain Softening of Concrete. *Journal of Engineering Mechanics* 123(1): 25–35.

Sutton, M.A., Orteu. J.J. & Schreier, H. 2009. *Image Correlation for Shape, Motion and Deformation Measurements*. US: Springer.

Taheri, A. & Tani, K. 2008. Use of down-hole triaxial apparatus to estimate the mechanical properties of heterogeneous mudstone. *International Journal of Rock Mechanics and Mining Sciences* 45: 1390–402.

Tarasov, B. & Potvin, Y. 2012. Universal criteria for rock brittleness estimation under triaxial compression. *International Journal of Rock Mechanics & Mining Sciences* 59: 57–69.

Tung, N. & Tue, N. 2015. Post-peak behaviour of concrete specimens undergoing deformation localization in uniaxial compression. *Construction and Building Materials* 99: 109–117.

Yarali, O. & Soyer, E. 2011. The effect of mechanical rock properties and brittleness on drillability. *Scientific Research and Essays* 6(5): 1077–1088.

*Rock Dynamics: From Research to Engineering – Li et al. (Eds)*
*© 2016 Taylor & Francis Group, London, ISBN 978-1-138-02953-8*

# The effect of pre-stress on wave velocity and waveform

M. Tao
*Western Mining Group Co. Ltd., Xining, Qinghai, China*
*School of Resources and Safety Engineering, Central South University, Changsha, Hunan, China*

H.T. Zhao, K. Du, T.B. Yin & X.B. Li
*School of Resources and Safety Engineering, Central South University, Changsha, Hunan, China*

ABSTRACT: By taking influence of pre-stress into account, the governing equation of wave propagation in elastic continuum material is derived. The results indicated that the non-homogeneous pre-stress changed the governing equation of wave propagation. The definite problem of wave propagation in material with non-homogeneous pre-stress was verified by using mathematical physics method. The displacement-time relationship of wave propagation was explored, which indicated that the non-homogeneous pre-stress changed waveform and relationship of displacement-time histories.

## 1 INTRODUCTION

The propagation process of elastic wave propagation in a material and its related seismic exploration has been widely studied. In civil and mining engineering, the problems involve tectonics and earth masses that are initially under stress state. The theory of elastic wave propagation in pre-stressed solids has a long history (Tolstoy 1982). A definite theory explaining the wave propagation of a material under initial stress was developed by Biot & Drucker (1965), which clearly showed that the effect of initial stress on wave propagation cannot be represented by a change in elastic coefficients.

A large number of laboratory measurements of P-wave and S-wave velocities and their characteristics of anisotropy, hysteresis, and splitting have been conducted on various types of rocks by many researchers, such as Birch (1960, 1961), Christensen & Ramananantoandro (1971), Christensen (1974, 1979), Manghnani et al. (1974), and others (Li & Tao 2015). The results indicated that velocity of seismic waves and elastic coefficients are much influenced by initial stress, and thus it is imperative to deal with the problem of wave propagation in a material with initial stress.

Additionally, due to the gravity variation and external force inhomogeneous, and the initial stress may not be homogeneous and initial stress gradient exists. The initial stress gradient also influences the wave propagation. An early study examined the gravity on surface wave by Bromwich (1898). Dowaikh, Ogden and Sotiropoulos derived the equation of plane wave propagation for an incompressible solid under pre-stressed state (Dowaikh & Ogden 1990, Ogden & Sotiropoulos 1997). Sharma derived the wave propagation in a general anisotropic medium under initial stress. Sharma & Garg (2006), Vinh & Seriani (2010), Sethi et al. (2014) and other scholars investigated the influence of gravity on surface waves. Ji et al. (2002) presented part of available data on seismic velocities and anisotropy in minerals and rocks. Some results indicated that rocks may be elastically nonlinear, hysteretic and splitting (Ji et al. 2007, Sun et al. 2012, Asef & Najibi 2013). These results have considerably increased our understanding of wave propagation in materials with initial stress, indicating the overburden pressure may significantly affect propagation velocities.

The present paper investigated the pre-stress affects wave velocity and waveform. The governing equation with pre-stress of wave propagation in one dimension of elastic continuum

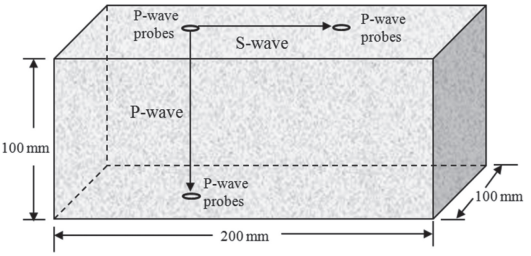


Figure 1. Determination of the velocities of P-waves and S-waves using P-wave probes (pre-stress applied in the horizontal direction).

Table 1. Material properties of rock.

| No. | Poisson's ratio | Density/(Kg·m$^{-3}$) | Uniaxial compression strength / MPa |
|---|---|---|---|
| T1 | 0.19 | 2685 | 152.7 |
| T2 | 0.18 | 2669 | 151.1 |
| T3 | 0.21 | 2608 | 148.7 |
| T4 | 0.20 | 2589 | 147.3 |

materials is derived. Alternatively, by using mathematical software, displacement-time relationships of wave propagation in a material under different initial stress gradient conditions are illustrated. The results indicated that the non-homogenous pre-stress may significantly influence wave propagation and spalling failure.

## 2 VELOCITIES WITH PRE-STRESS

The two probes for a P-wave are coupled in parallel over a distance on the same plane of the rock block via grease. The transmitting probe produces a pulse that causes a P-wave in the normal direction of the plane and simultaneously an S-wave in its shear direction. Therefore, both P-wave and S-wave can be measured with the probes for a P-wave in a rock block with a large plane. Figure 1 shows the experimental set-up, where the size of the specimen is $200 \times 100 \times 100$ mm.

The experiments are conducted using an Instron 1346 hydraulic servo-controlled machine. The experimental system is controlled by a computer, and the load-deformation data are acquired automatically. The several groups of uniaxial pre-stressed specimens are examined using the Instron 1346 machine, which has a load capacity of 2 000 kN.

Uniaxial compression test is first conducted to obtain the basic mechanical properties of granite in the un-stressed state, which provided some rock properties, as presented in Table 1.

The pre-stresses of 5 MPa, 10 MPa, 15 MPa, 20 MPa, 25 MPa and 30 MP are set to measure the relationship of the velocities of P-waves and S-waves; the results are presented in Figure 2.

The results indicate that the velocities of P-waves and S-waves rapidly increase with the initial stress; thus, the experimental work indicated that the initial stress affects the material properties of rock.

## 3 THEORETICAL FORMULATIONS OF ELASTIC WAVE GOVERNING EQUATIONS

The stress-strain relationship of elastic wave propagation in a one dimension material was descripted as

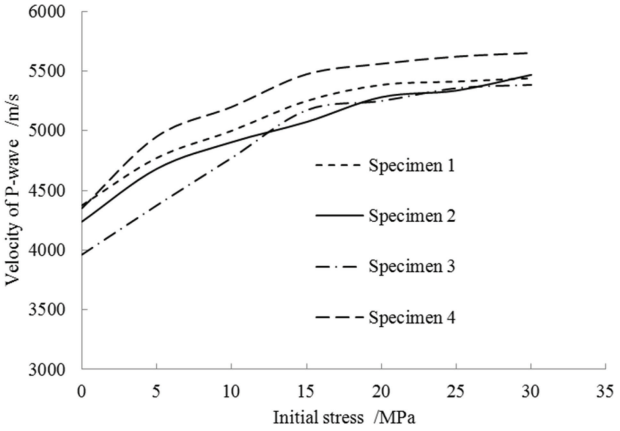


(a) P-wave variation with initial stress

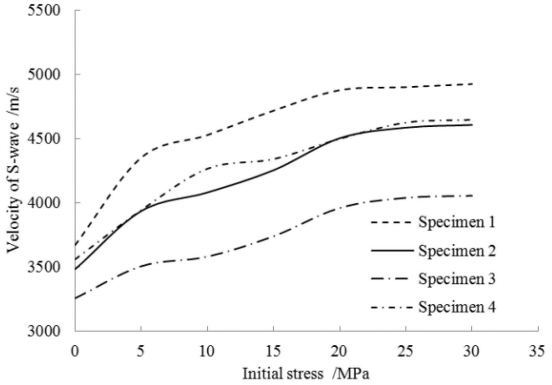


(b) S-wave variation with initial stress

Figure 2. The relationship between pre-stresses and the stress wave velocity.

$$\sigma_x = E\frac{\partial u}{\partial x} \tag{1}$$

where $x$ is the space coordinate measured along the rod, $\sigma x$ is the stress, u is the displacement, and E is Young's modulus. The classical governing equation of dynamics is

$$\frac{\partial}{\partial x}\left(E\frac{\partial u}{\partial x}\right) = \rho\frac{\partial^2 u}{\partial t^2} \tag{2}$$

And then Formula (2) can be written as

$$\frac{\partial \sigma_s(x)}{\partial x} + E\frac{\partial u^2}{\partial x^2} = \rho\frac{\partial u^2}{\partial t^2} \tag{3}$$

Therefore, if the pre-stress is homogenous, Formula (3) same to the traditional wave equation, and if the pre-stress in non-homogenous, Formula (3) is different to the traditional wave equation, and it is related to pre-stress.

To investigate how the pre-stress influence on the wave velocity and dynamic elastic coefficients. Two simple rod models are used, shown in Fig. 3, the right end of the rod is fixed and the left end is conducted a dynamic loading $f(t)$.

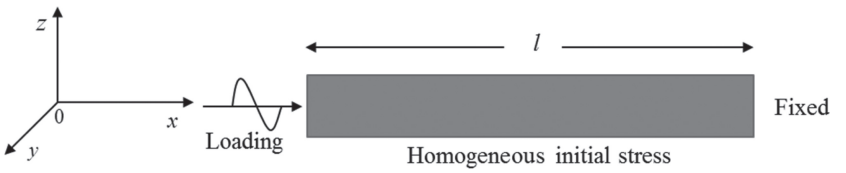


Figure 3(a). Homogenous stress.

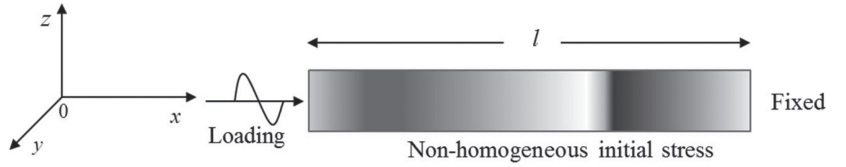


Figure 3(b). Non-homogenous stress.

In this condition, the boundary conditions are

$$\begin{cases} \left.\dfrac{\partial u}{\partial x}\right|_{x=0} = \dfrac{f(t)}{E} \\ u|_{x=l} = 0 \end{cases} \tag{4}$$

And the initial conditions are

$$\begin{cases} u|_{t=0} = 0 \\ \left.\dfrac{\partial u}{\partial t}\right|_{t=0} = 0 \end{cases} \tag{5}$$

The propagation of stress wave can be calculated by mathematical physics method. The physic process of stress wave propagation in the rod is in turn as the follow mathematical equations

$$\begin{cases} \dfrac{\partial \sigma_s(x)}{\partial x} + \dfrac{E\partial u^2}{\partial x^2} = \rho \dfrac{\partial^2 u}{\partial t^2} \\ \left.\dfrac{\partial u}{\partial x}\right|_{x=0} = \dfrac{f(t)}{E}, u|_{x=l} = 0 \\ u|_{t=0} = 0, \left.\dfrac{\partial u}{\partial t}\right|_{t=0} = 0 \end{cases} \tag{6}$$

This is a mathematic physic equation, and the analytical solution can be solved by the principle of separation and other methods when the initial stress function is verified, but it is not straightforward. Meanwhile, the result of equation (6) can be illustrated by mathematical software, such as MATLAB. Thus, the mathematical software is used to illustrate the displacement-time relationships of wave propagation process in the follow sections.

## 4 EXAMPLES OF WAVE PROPAGATION IN ELASTIC MATERIALS

When the initial stress function is verified, the result of displacement-time relationship of wave propagation can be investigated. For example, to consider two typical examples, one is

the initial stress is linear change with the location, the other is non-linear change. Thus, when the relationship of initial stress with location is descripted as follows:

$$\sigma_s(x) = kx \tag{7}$$

where $k$ is a constant coefficient, i.e., the initial stress is linear relationship with the location, the equation (8) can be written as

$$\begin{cases} k + \dfrac{E\partial u^2}{\partial x^2} = \rho \dfrac{\partial^2 u}{\partial t^2} \\ \left.\dfrac{\partial u}{\partial x}\right|_{x=0} = \dfrac{f(t)}{E}, u|_{x=l} = 0 \\ u|_{t=0} = 0, \left.\dfrac{\partial u}{\partial t}\right|_{t=0} = 0 \end{cases} \tag{8}$$

Table 2. Comparison of displacement-time curves under different initial stress states ($x = 4$).

| $\sigma_s(x)$ / $k$ values | $\sigma_s(x)=kx$ | $\sigma_s(x)=kx^2$ |
|---|---|---|
| $k$=0 | 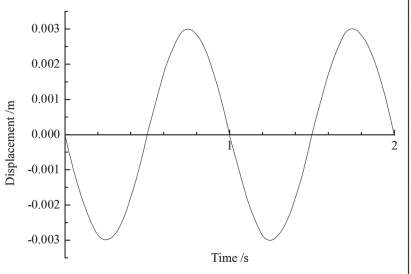 | 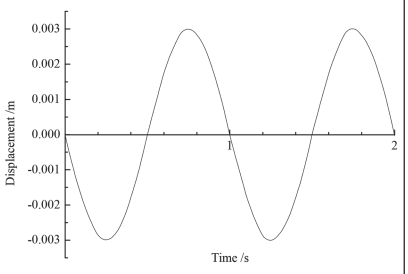 |
| $k$=1×10⁶ | 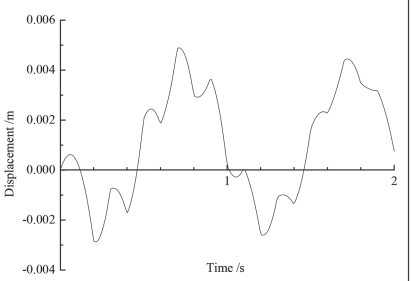 | 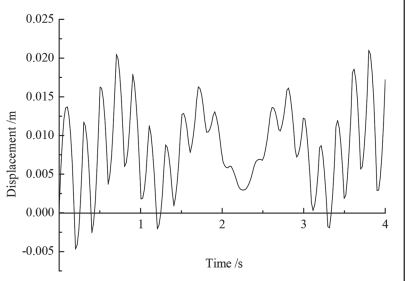 |
| $k$=2×10⁶ | 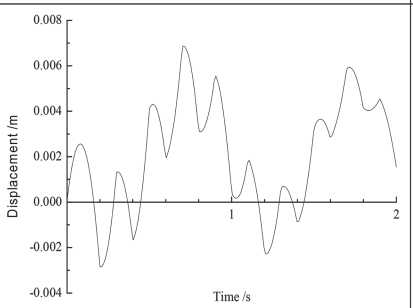 | 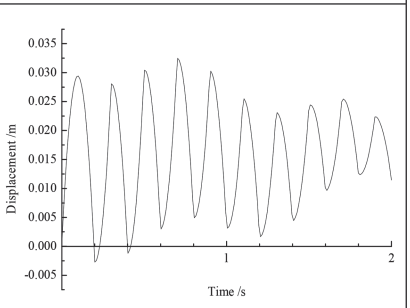 |

And, if the initial stress is non-linear change with the location as follows:

$$\sigma_s(x) = kx^2 \tag{9}$$

The definite problem equation (8) can be written as:

$$\begin{cases} 2kx + \dfrac{E\partial u^2}{\partial x^2} = \rho \dfrac{\partial^2 u}{\partial t^2} \\ \left.\dfrac{\partial u}{\partial x}\right|_{x=0} = \dfrac{f(t)}{E}, u|_{x=l} = 0 \\ u|_{t=0} = 0, \left.\dfrac{\partial u}{\partial t}\right|_{t=0} = 0 \end{cases} \tag{10}$$

When $k$ is equal to zero corresponding with the material is un-stressed. Thus, for a certain known dynamic loading, $f(t)$, when $k$ is known, the displacement-time curve can be illustrated by mathematical software. Additionally, the physical properties of rock are used for numerical simulation as: $E = 40$ GPa, $\rho = 2700$ kg/m$^3$, the rod length $l = 10$ m. The loading wave function is described as

$$f(t) = 2 \times 10^7 \sin\left(\frac{\pi}{0.5} t\right) \tag{11}$$

When $k$ is defined different value, the results of displacement-time curve at $x = 4$ can be illustrated in Table 2.

The results indicated that when the material is un-stressed, i.e., k is equal to zero, i.e., no pre-stress, the form of displacement-time relationship is the same as the original loading wave. However, when stress gradient is not equal to zero, the waveform changes with the initial stress gradient. The higher initial stress gradient leads to the waveform of the wave propagation in the material more different from the original loading wave, and the period and the value of the displacement are also significantly changed. Thus, the initial stress gradient changed the wave propagation, causing different response. The following section further investigates the initial stress gradient on wave propagation.

## 5 CONCLUSIONS

The experimental results demonstrated that *Vp* and *Vs* increase rapidly with the increase of the pre-stress. By using a sample model, the definite problem of wave propagating in a rod with initial stress gradient is investigated, the calculation examples demonstrated that the non-homogeneous pre-stress affects the wave propagation, and it will change the waveform and period. The results derived in this work may be used to compute the exact effect of initial stress and initial stress gradient on wave propagation. For example, when a real data is known, the mathematical model can be used for a variety of geophysical problems, such as earthquake wave propagation, deep underground mining et al.

## ACKNOWLEDGMENTS

The research presented in this paper was jointly supported by the National Natural Science Foundation of China (Grant No. 51404303, 41272304 and 51504287). And Project Funded by China Postdoctoral Science Foundation (grant No. 2015M580701).

## REFERENCES


Asef, M.R. & Najibi, A.R. 2013. The effect of confining pressure on elastic wave velocities and dynamic to static Young's modulus ratio. *Geophysics* 78: D135-D42.

Biot, M.A. & Drucker, D. 1965. Mechanics of incremental deformation. *Journal of Applied Mechanics* 32: 957.

Birch, F. 1960. The velocity of compressional waves in rocks to 10 kilobars, part 1. *Journal of Geophysical Research* 65: 1083–102.

Birch, F. 1961. The velocity of compressional waves in rocks to 10 kilobars: 2. *Journal of Geophysical Research* 66: 2199–224.

Bromwich, T.I.A. 1898. On the influence of gravity on elastic waves, and, in particular on the vibrations of an elastic globe. *Proceedings of the London Mathematical Society* 1: 98–120.

Christensen, N.I. & Ramananantoandro. R. 1971. Elastic moduli and anisotropy of dunite to 10 kilobars. *Journal of Geophysical Research* 76: 4003–10.

Christensen, N.I. 1974. Compressional wave velocities in possible mantle rocks to pressures of 30 kilobars. *Journal of Geophysical Research*79: 407–12.

Christensen, N.I. 1979. Compressional wave velocities in rocks at high temperatures and pressures, critical thermal gradients, and crustal low-velocity zones. *Journal of Geophysical Research: Solid Earth* (1978–2012) 84: 6849–57.

Dowaikh, M. & Ogden, R. 1990. On surface waves and deformations in a pre-stressed incompressible elastic solid. *IMA Journal of Applied Mathematics* 44: 261–84.

Ji, S., Wang, Q., Marcotte, D., Salisbury, M.H., Xu, Z. 2007. P wave velocities, anisotropy and hysteresis in ultrahigh-pressure metamorphic rocks as a function of confining pressure. *Journal of Geophysical Research: Solid Earth* (1978–2012). 112.

Ji, S., Wang, Q., Xia, B. 2002. *Handbook of Seismic Properties of Minerals, Rocks and Ores*. Polytechnique International Press.

Li, X. & Tao, M. 2015. The influence of initial stress on wave propagation and dynamic elastic coefficients. *Geomechanics and Engineering* 8: 377–90.

Manghnani, M.H., Ramananantoandro, R., Clark, S.P. 1974. Compressional and shear wave velocities in granulite facies rocks and eclogites to 10 kbar. *Journal of Geophysical Research* 79: 5427–46.

Ogden, R. & Sotiropoulos, D. 1997. The effect of pre-stress on the propagation and reflection of plane waves in incompressible elastic solids. *IMA Journal of Applied Mathematics* 59: 95–121.

Sethi, M., Bhardwaj, R.,.Sharma, A.K. 2014. Surface waves in homogeneous visco-elastic media of higher order under the influence of gravity and surface stresses. *Advances in Physics Theories and Applications* 30: 65–77.

Sharma, M. & Garg, N. 2006. Wave velocities in a pre-stressed anisotropic elastic medium. *Journal of Earth System Science* 115: 257–65.

Sun, S., Ji, S., Wang, Q., Xu, Z., Salisbury, M., Long, C. 2012. Seismic velocities and anisotropy of core samples from the Chinese Continental Scientific Drilling borehole in the Sulu UHP terrane, eastern China. *Journal of Geophysical Research: Solid Eart*h (1978–2012) 117.

Tolstoy, I. 1982. On elastic waves in prestressed solids. *Journal of Geophysical Research: Solid Earth* (1978–2012) 87: 6823–7.

Vinh, P.C. & Seriani, G. 2010. Explicit secular equations of Stoneley waves in a non-homogeneous orthotropic elastic medium under the influence of gravity. *Applied Mathematics and Computation* 215: 3515–25.

This page intentionally left blank

*Rock Dynamics: From Research to Engineering – Li et al. (Eds)*
*© 2016 Taylor & Francis Group, London, ISBN 978-1-138-02953-8*

# Low transient strength of hard rocks at spontaneous failure

B.G. Tarasov
*The University of Western Australia, Australia*

ABSTRACT: Post-peak properties of intact hard rocks (UCS > 250 MPa) at highly confined compression corresponding to seismogenic depths and shear rupture mechanism operating at these conditions are still experimentally unexplored due to spontaneous failure of extreme dynamics and violence. Recently conducted comprehensive analysis of different side effects accompanying the spontaneous failure resulted in the identification of a unique shear rupture mechanism according to which shear rupture propagation is governed by the fan-shaped fracture head characterized by very low shear resistance (less than frictional strength). Such low shear resistance of the fan-head determines the transient strength of intact rocks during the failure process. The paper discusses briefly main principles of the fan-mechanism and proposes an improved model of strength profiles for hard rocks involving the fan transient strength profile.

## 1 FAN-MECHANISM IN HARD ROCKS

Analysis of available experimental data (e.g. Wawersik & Brace 1971, Shimada 2000, Mogi 2007, Lei et al. 2009) and additional experimental studies (Tarasov 2010, Tarasov & Randolph 2011) show that post-peak properties of hard rocks characterized by uniaxial compressive strength above 250 MPa are still experimentally unexplored at highly confined compression corresponding to seismogenic depths. The reason for that is the impossibility of post-peak control even on ultra-stiff servo-controlled testing machines. Stress-strain curves in Figure 1a obtained on dolerite specimens (UCS = 300 MPa) illustrate typical behavior of hard rocks in the post-peak region tested at conditions $\sigma_1 > \sigma_2 = \sigma_3$ under different levels of confining pressure $\sigma_3$. The testing was conducted on an ultra-stiff, servo-controlled testing machine based upon the loading principles described in Stavrogin & Tarasov (2001). The loading stiffness of the machine was 4 MN/mm, the loop-closure rate of control system was 10 kHz.

Curves in Figure 1a show that increasing confining pressure changes post-peak rock behaviour from Class I to extreme Class II. At $\sigma_3 < 60$ MPa the total post-peak control was provided for both types of rock response: Class I and Class II. At $\sigma_3 \geq 60$ MPa control was only possible at the start of the post-peak stage. After points A on the graphs the unstable failure took place characterized by abnormally high dynamics and violence. The post-peak dynamic failure in all cases associated with propagation of a thin shear fracture (thickness less than 0.1 mm). The reason for loss of control after points A can be explained on the basis of analysis of enlarged fragments of the stress-strain curves for $\sigma_3 = 75$ and 60 MPa involving the post-peak parts at stress degradation from $\sigma_u$ till $\sigma_A$ presented in Figures 1b. The fragments are replicated four times and divided into four steps (from 1 to 4) with equal intervals of differential stress. Each post-peak step is characterized by elastic modulus E (solid lines) and post-peak modulus M (dotted lines). To determine elastic modulus the specimen tested at $\sigma_3 = 75$ MPa was slightly unloaded just before the peak stress. The same value of elastic modulus was used for $\sigma_3 = 60$ MPa. Areas located between the E and M lines at each post-peak step indicate the current post-peak rupture energy $W_r$ associated with shear rupture development. We can see that $W_r$ decreases dramatically with the rupture development from step 1 to step 4. It should be noted that within the whole stress region between $\sigma_u$ and $\sigma_A$

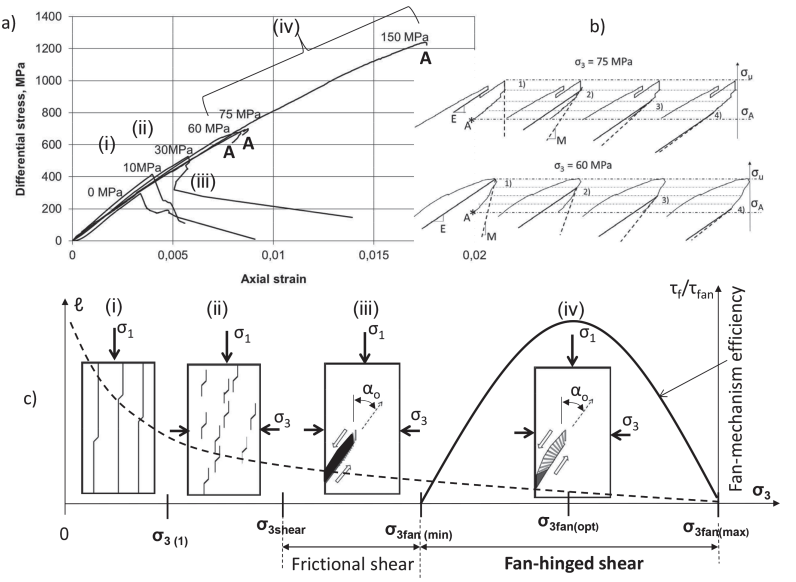


Figure 1. a) Stress-strain curves for dolerite specimens tested at different levels of confining pressure. b) Enlarged fragments of post-peak curves before the instability start at points A for $\sigma_3 = 75$ and 60 MPa. c) The evolution of failure mechanisms in hard rocks with rising confining pressure $\sigma_3$.

the servo-control system provided reliable control of the static fracture growth. However, after points A where the fracture energy became extremely small (post-peak modulus M and elastic modulus E practically coincide) the instable fracture propagation started. Despite very high values of the loading stiffness and the loop-closure rate of control system the machine could not provide sufficiently high unloading velocity to prevent the spontaneous shear rupture propagation beyond points A.

Real post-peak properties of hard rocks and shear rupture mechanism for such stress conditions were virtually unknown until recently. Comprehensive analysis of different side effects accompanying the process of spontaneous failure conducted in Tarasov (2014) resulted in the identification of a unique shear rupture mechanism generated at these conditions and in an improved understanding of real post-peak rock properties. The underlying mechanics of hard rock failure under high $\sigma_3$ can be explained by analysis of the evolution of failure mechanisms in rock specimens (I–IV) with rising confining stress $\sigma_3$ as represented schematically in Figure 1c. Confining pressure $\sigma_3$ increases along the horizontal axis from left to right. At the origin of the horizontal axis $\sigma_3 = 0$. It is known that failure of brittle rocks is accompanied by formation of tensile cracks at any level of $\sigma_3$. However, the ultimate length $\ell$ of tensile cracks which can be developed at failure depends on the level of $\sigma_3$. A dotted line in Figure 1c shows symbolically the typical variation of ultimate length $\ell$ of tensile cracks as a function of $\sigma_3$: the higher $\sigma_3$ the shorter $\ell$. The length $\ell$ of tensile cracks in turn determines the macroscopic failure mechanism and the failure pattern shown schematically in rock specimens (i) to (iv).

At confining pressures $0 \le \sigma_3 < \sigma_{3shear}$ shear rupture cannot propagate in its own plane due to creation at the rupture tip of relatively long tensile cracks that prevent the shear rupture propagation. Two failure mechanisms may be distinguished at these stress conditions:

1. *Splitting by long tensile (extension) cracks*—specimen (i) in Figure 1c, and
2. *Distributed micro-cracking followed by coalescence of microcracks*—specimen (ii) in Figure 1c.

   At $\sigma_3 \ge \sigma_{3shear}$ the failure mode is localised shear. Here high confining pressure suppresses the formation of long tensile cracks and tensile cracks generated in the rupture tip become sufficiently short to assist shear rupture to propagate in its own plane. According to Reches and Lockner (1994) the fracture front moves through the rock due to creation of

an echelon of micro tensile cracks in the fracture tip. Here dilation of one micro-crack induces dilation of closely spaced neighbouring cracks. This micro-cracking process creates inclined intercrack blocks (known as domino-blocks) which are subjected to rotation at shear displacement of the rupture interfaces (Peng & Johnson 1972, King & Sammis 1992, Reches & Lockner 1994). However, the decrease in length of tensile cracks and domino-blocks with rising $\sigma_3$ causes fundamentally different behaviour of rotating domino-blocks within different ranges of $\sigma_3$. Two specific shear rupture mechanisms have been distinguished here:

3. *Frictional shear*—specimen (iii) in Figure 1c. This mechanism operates within the pressure range $\sigma_{3shear} \leq \sigma_3 \leq \sigma_{3fan(min)}$ and represents the frictional shear rupture mechanism characterized by collapse of relatively long domino-blocks during rotation and creation of friction in the fracture head.
4. *Fan-hinged shear*—specimen (iv) in Figure 1c. Within the pressure range $\sigma_{3fan(min)} < \sigma_3 < \sigma_{3fan(max)}$ specifically short domino-blocks formed from very strong material (UCS ≥ 250 MPa) can withstand the rotation caused by shear displacement of the rupture faces without collapse. In this case the domino-blocks behave as hinges, decreasing dramatically friction between the rupture faces. Due to consecutive generation and rotation of the domino-blocks they create a fan-structure representing the shear rupture head. Analysis of the fan structure (Tarasov, 2014) conducted for idealized physical and theoretical models showed that the fan-head can have very low shear resistance $\tau_{fan}$ (by the factor of ten less than the frictional strength $\tau_f$). In real rocks the efficiency of the fan-mechanism is determined by how perfect and uniform the fan structure is. At the low end of the fan-hinged shear in Figure 1c (at $\sigma_{3fan(min)}$), when the length (length/thickness) of the domino-blocks is still relatively large, the blocks are subjected to partial destruction as they rotate. In this case the fan-mechanism efficiency (determined as $\tau_f/\tau_{fan}$) is slightly above the unity. At higher $\sigma_3$, with shorter blocks, this imperfection decreases, rendering the fan-mechanism more efficient. The optimal efficiency takes place at $\sigma_{3fan(opt)}$ when the blocks rotate with minimum destruction. At greater $\sigma_3$ the efficiency reduces because shorter blocks gradually lose any potential for operation as hinges. Finally very short blocks lose this capability completely and the rock behaviour returns to the conventional frictional mode. This happens at $\sigma_{3fan(max)}$. The bold curve in Figure 1c illustrates graphically a possible variation of the fan-mechanism efficiency $\tau_f/\tau_{fan}$.

## 2 LOW TRANSIENT STRENGTH AND IMPROVED STRENGTH PROFILES FOR HARD ROCKS

### 2.1 *Low transient strength caused by the fan-mechanism*

Because of the impossibility of direct studies of the fan-mechanism on real materials due to spontaneous failure characterized by extreme dynamics and violence unique properties of the fan-structure have been studied using physical and mathematical models of the fan-mechanism (Tarasov 2014). One of the important results obtained on the models concerns the loss of stability caused by the fan-structure. The completed fan-structure can be created in stable regime by application of a local shear stress. The formation of the first half of the fan is accompanied by increasing shear resistance of the fan-structure up to the material strength while the formation of the second half is accompanied by dramatic decrease in shear resistance of the fan-structure. However, at the presence of distributed shear stress applied to the whole material the second half of the fan is inevitably created in unstable regime. The impossibility of post-peak control at testing of hard rocks under highly confined compression is explained by the fact that when the first hard of the fan has completed the level of distributed shear stress is equal to the material strength. Due to this further formation of the fan-head and its propagation through material is extremely unstable. This situation is explained in more detail below.

Figure 2a shows five stages of the fan-head formation and propagation in a rock specimen along the dotted line ON. The fan-head here is shown as an open ellipse. Axial loading $\sigma_1$

induces distributed shear stress τ along the line ON. Acoustic emission studies (e.g. Reches & Lockner 1994, Lei at al. 2000) show that in hard rocks under high confining stresses the localised shear fracture nucleates at the pre-peak stage close to peak stress. Curve in Figure 2b illustrates the variation in shear resistance of the fan-head during the fan-structure formation and propagation through the specimen between points O and N. Points on the curve indicate identical stages of shear rupture propagation shown in Figure 2a. Point S corresponds to the level of distributed shear stress at which the fan-head starts developing. Further its development is caused by further increasing axial load and, consequently, distributed shear stress. Between points S and 1 the stable formation of the first half of the fan takes place. At point 1, when the first half of the fan has completed, the level of distributed shear stress applied along the dotted line ON is equal to the maximum shear resistance of the half fan. Point 1 therefore represents the onset of instability in the developing fan-structure. Further development of the fan-head and its propagation through the specimen occurs in the dynamic regime because shear resistance of the fan-structure at this stage is less than the level of distributed shear stress applied. The stage between points 1 and 2 reflects shear resistance of the fan-structure during dynamic formation of the second half of the fan. Experiments conducted on hard rocks show that at the start of uncontrollable failure (points A in Fig. 1) the post-peak modulus M and elastic modulus E are practically coincide, indicating vanishingly small post-peak rupture energy. At point 2 shear resistance of the fan-head equal to $\tau_{fan}$ is determined by the completed fan structure.

It should be emphasised that, after completion of the fan-head, the spontaneous propagation of shear rupture through the intact material between stages 2 and 4 can proceed at any level of stress exceeding $\tau_{fan}$. This means that during such failure process *the transient strength* of intact rock is equal to $\tau_{fan}$ which is significantly less than the frictional strength $\tau_f$. To prevent spontaneous failure the stress applied to the specimen at point 1 should be dropped below $\tau_{fan}$ before the head has crossed the specimen. Due to the fact that shear rupture can propagate with intersonic speeds (Archuleta 1984, Rosakis 2002) modern servo-controlled testing machines cannot provide sufficiently high speed of unloading to interrupt the failure process. As a result the failure occurs with extreme dynamic. When the fan-head has crossed the specimen (stage 5), the specimen strength becomes equal to $\tau_f$.

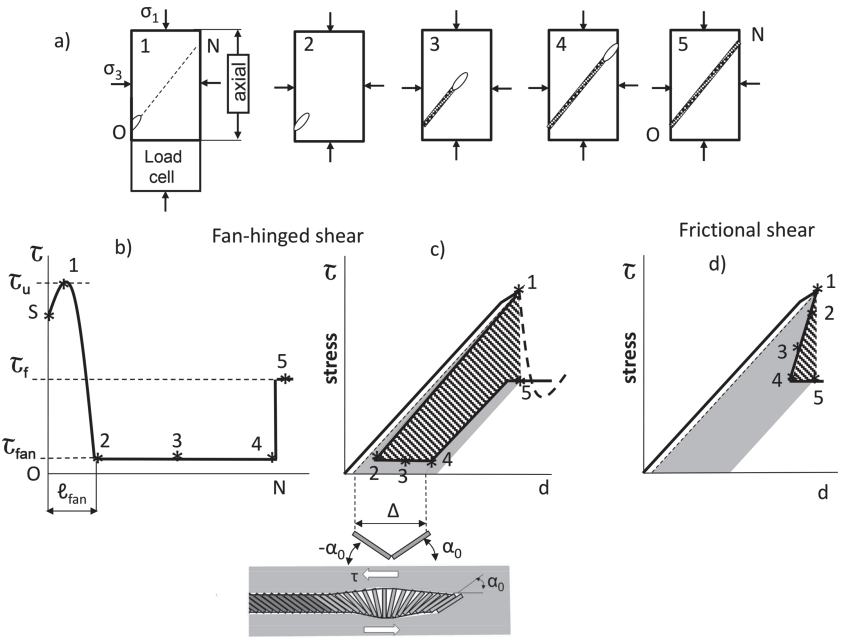


Figure 2. Features of the failure process governed by the fan-mechanism in specimens of hard rocks tested at high confining stresses.

It is important to note that during the failure process shear resistance and displacement along the developing fault ON is very irregular. Three specific zones can be distinguished: 1) the fan-head zone with shear resistance $\tau_{fan}$ where the failure process and domino-block rotation is in progress; 2) the frictional zone with shear resistance $\tau_f$, which is located behind the fan-head where the blocks have completed their rotation and full friction is mobilised; and 3) the intact zone in front of the fan-head with shear resistance $\tau_u$. A load cell and an axial gauge in Figure 2a(1) mounted on the specimen, as is commonly used in experiments, can only measure the average load-bearing capacity and displacement of the specimen during the failure process. Results obtained on the basis of these gauges do not allow estimation of the real material properties during the failure process. The dotted curve in Figure 2c illustrates post-peak part of the stress-displacement graph typically measured at spontaneous failure. This curve does not reflect the real rock properties during the post-peak failure process determined by the fan-mechanism–$\tau_{fan}$.

The new knowledge about the fan-mechanism gives us a chance to derive the inaccessible information about real post-peak properties of hard rocks at high confining stresses as illustrated in Figure 2c by bold lines. The horizontal line here represents the transient strength $\tau_{fan}$ of the intact material during the failure process. We will refer to this strength as the fan-strength $\tau_{fan}$. The displacement $\Delta$ with very small shear resistance $\tau_{fan}$ is provided by rotating domino-blocks of the fan-mechanism which is illustrated by images under the graphs representing the fan-head. The post-peak properties determined by the fan-mechanism differ remarkably from the generally accepted properties of hard rocks illustrated in Figure 2d. Grey areas in Figures 2c and 2d represent post-peak rupture energy up to stage 5. The fan-mechanism is the most energy efficient shear rupture mechanism. Hatched areas correspond to elastic energy released from the specimens during post-peak failure. Abnormally high released energy caused by the fan-mechanism is the source of extreme dynamics and violence.

### 2.2 *Strength profiles for hard rocks*

Variable efficiency of the fan-mechanism at different levels of confining stresses $\sigma_3$ determines corresponding variation in the transient strength of hard rocks. Figure 3a shows schematically an improved model of strength profiles involving the transient fan strength $\tau_{fan}$ profile (dotted curve) along with conventional fracture $\tau_u$ and frictional $\tau_f$ strength profiles. Stress-displacement curves in Figures 3b and 3c reflecting real post-peak rock properties (similar to discussed in Figure 2c) explain the meaning of the fan strength and its variation versus $\sigma_3$. Figure 3b illustrates the situation at $\sigma_3 = \sigma_{3fan(opt)}$ where the fan-mechanism exhibits the maximum efficiency. At peak stress the material strength is $\tau_u$. During spontaneous failure the completed fan-head determines the transient material strength $\tau_{fan}$. This means that the shear fracture governed by the fan-mechanism can propagate through the material at any level of shear stress above $\tau_{fan}$. After completion of the failure process the material strength is determined by the frictional strength $\tau_f$ of the new fault.

For confining pressures $\sigma_3 < \sigma_{3fan(opt)}$ or $\sigma_3 > \sigma_{3fan(opt)}$ the fan-mechanism efficiency is lower. The graph in Figure 3c indicates the relative values of $\tau_u$, $\tau_f$ and $\tau_{fan}$ and their positions on the envelops for the situation where $\sigma_3 < \sigma_{3fan(opt)}$. It should be noted that improper operation of domino-blocks at low efficiency of the fan-mechanism increases the level of $\tau_{fan}$ and also provides the possibility for restricted post-peak control up to point A (see experimental curves in Figure 1) before the start of instability. Stress-strain curves in Figure 1a show that the controllable post-peak part (between $\sigma_u$ and $\sigma_A$) decreases with rising confining pressure indicating the improvement of the fan-mechanism operation. At $\sigma_3 = 200$ MPa the instability started right at the peak stress due to optimal efficiency of the fan-mechanism for this testing condition.

Tarasov (2010) showed that the pressure range of the fan-mechanism activity $\sigma_{3fan(min)} < \sigma_3 < \sigma_{3fan(max)}$ and the level of optimal efficiency of this mechanism depends on the rock hardness (strength): the harder the rock the greater the pressure range and the higher the fan-mechanism efficiency. It was supposed also that the maximum pressure $\sigma_{3fan(max)}$ of the range corresponds to conditions at which the fracture and frictional strength profiles in Figure 3a intersect. This question, however, requires special studies.

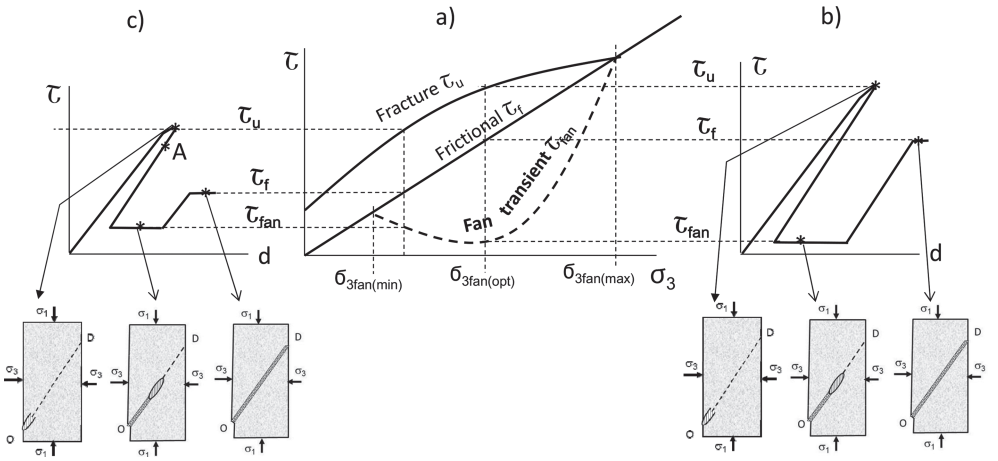


Figure 3. a) Strength profiles of the fracture $\tau_u$, frictional $\tau_f$ and fan transient $\tau_{fan}$ strength for hard rocks. b) and c) Illustration of material strength at different stages of the failure process governed by the fan-mechanism.

## REFERENCES


Archuleta, R. 1984. A faulting model for the 1979 Imperial Valley earthquake. *J. Geophys. Res*. 89: 4559–4585, doi:10.1029/JB089iB06p04559.

King, G.C.P. & Sammis, C.G. 1992. The mechanisms of finite brittle strain. *PAGEOPH* 138(4): 611–640.

Lei, X., Kusunose, K., Rao, M.V.M.S., Nishizawa, O., Saton, T. 2000. Quasi-static fault growth and cracking in homogeneous brittle rock under triaxial compression using acoustic emission monitoring. *J. Geophys. Res.* 105(B3): 6127–6139.

Megahid, A.R., Soghair, H., Hageed, M.A.A., Hafer, A.M.A.A. 1993. Strength and deformation capacity of slender RC beams. In *Proceedings of Fracture and Damage of Concrete and Rock—FDCR-2*, Rossmanith H.P. (ed).

Mogi, K. 2007. *Experimental Rock Mechanics*. New York: Taylor & Francis.

Peng, S. & Johnson, A.M. 1972. Crack growth and faulting in cylindrical specimens of Chelmsford granite. *International Journal of Rock Mechanics and Mining Science* 9: 37–86.

Reches, Z. & Lockner, D.A. 1994. Nucleation and growth of faults in brittle rocks. *Journal of Geophysical Research* 99(B9): 18159–18173.

Rosakis A.J. 2002. Intersonic shear cracks and fault ruptures. *Adv. Phys*. 51: 1189-12-1257.

Shimada, M. 2000. Mechanical Behaviour of Rocks under High Pressure Conditions. Rotterdam: Balkema.

Stavrogin, A.N & Tarasov B.G. 2001. *Experimental Physics and Rock Mechanics*. Balkema.

Tarasov, B.G. 2008. Intersonic shear rupture mechanism. *International Journal of Rock Mechanics and Mining Science* 45(6): 914–928.

Tarasov, B.G. 2010. Superbrittleness of rocks at high confining pressure. *Fifth International Seminar on Deep and High Stress Mining*, Santiago, Chile, 119–133.

Tarasov, B.G. 2014. Hitherto unknown shear rupture mechanism as a source of instability in intact hard rocks at highly confined compression. *Tectonophysics* 621: 69–84.

Tarasov B.G. & Guzev M.A. 2013. New insight into the nature of size dependence and the lower limit of rock strength. *8th International symposium on Rockbursts and Seismicity in Mines*, Saint Petersburg-Moscow, 31–40.

Tarasov, B.G. & Randolph, M.F. 2011. Superbrittleness of rocks and earthquake activity. *International Journal of Rock Mechanics and Mining Science* 48: 888–898.

Wawersik, W.R. & Brace, W.F. 1971. Post-failure behavior of a granite and diabase. *Rock Mechanics* 3: 61–85.

*Rock Dynamics: From Research to Engineering – Li et al. (Eds)*
*© 2016 Taylor & Francis Group, London, ISBN 978-1-138-02953-8*

# Numerical simulation and analysis of rock heap formation under seismic motion

J.X. Wang
*College of Civil Engineering, Tongji University, Shanghai, China*
*Key Laboratory of Geotechnical and Underground Engineering of Ministry of Education, Tongji University, Shanghai, China*

Y. Yin
*Department of Geotechnical Engineering, Tongji University, Shanghai, China*

ABSTRACT: Sometimes, rock heaps are developed in some areas where railways, highways and other transportation projects are constructed. The physical and mechanical characteristics of the rock heaps are determined by the structures formed in different conditions. Numerical simulation and analysis of rock heap formation were performed to understand the rock structure formed under seismic motion. Discrete element method was adopted in simulating the formation process of rock heap. The cataclastic texture rock slopes were selected as the potential material supplying sources forming rock heap under seismic motion. The formation mechanism and development process are studied in different terrain conditions. The results show that the responses of slope surface increased from down to top, the blocks on the top surface were more likely to be thrown; the bottom shear failure in cataclastic texture slope was the main reason for the collapse of slope and formation of rock heaps. In addition, the inner structure of rock heap is analyzed using sectional slicing and three-dimensional sampling method.

## 1 INTRODUCTION

Rock heap is formed from an accumulation composed of rock fragments due to physical weathering, the movement of rock fragments from top to bottom is mainly rely on gravity. It is mainly distributed in the steep slopes and foothills of mountainous areas (Dong & Ding 2001). Its formation process can be divided into three stages: (1) Parent rock disintegration; (2) Relocation of weathering products; (3) Accumulation of weathering products. Three regions can be divided corresponding to the three stages (Fig. 1).

Rock heap is often encountered in highways and railways construction projects. Its structure is important in determining its physical and mechanical characteristics. Complex rock heap formations form special physical and mechanical characteristics. Yan et al. (2011) analyzed the influence of ground motion parameters on the seismic responses of a bedding rock slope

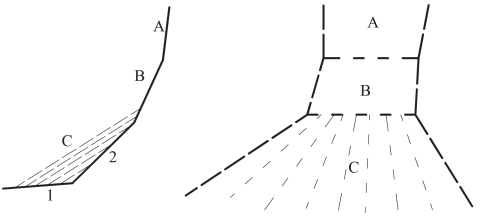


A: Supply area; B: Relocation area; C: Accumulation area;
1: Datum level of rock heap; 2: Leaning Area

Figure 1. Sketch map of rock heap formation and accumulation process.

using FLAC$^{2D}$. Lin et al. (2012) studied a jointed rock slope in the mileage K0526 + 300 of Lan-Cheng-Yu product oil pipeline and indicated that the effects of earthquake declined the contact force between rocks, damaged the rock, ultimately resulted in slope collapse. Moore et al. (2012) showed that ground motions may be amplified up to eight at certain frequencies, meaning that the potential for earthquake-triggered failure would be underestimated if this potentially important effect were ignored in seismic slope stability models. Sun & Yin (2012) analyzed the effect of vertical earthquake force on the failure mechanism of a large rock avalanche and proved the large vertical component of acceleration was the main reason why rock and soil masses were thrown during the earthquake. Song & Gao (2013) used Newmark decoupled model considering the nonlinear properties of soils to calculate the seismic displacement of slopes, indicating the existing empirical models for seismic displacement of slopes significantly underestimated the displacement induced by near-fault pulse-like ground motions. Long (2014) simulated the collapse process of Luo Quan Wan slope under Wenchuan earthquake, indicating that the firstly moving parts of discontinuities were in bedrock.

In recent years, the corresponding researches were mainly concerning engineering construction technology (Jiang 2015, Lin et al. 2012, Moore 2012, Yan et al. 2011) and comprehensive control measures (Long 2014, Song & Gao 2013, Sun et al. 2012) for rock heap slopes. Few attentions focused on rock heap structure and formation history under seismic motion. This paper studied the formation of rock heap formed under seismic motion and its structure characteristics.

## 2 NUMERICAL EXPERIMENT OF ROCK HEAP FORMED UNDER SEISMIC MOTION

### 2.1 *Calculation model of slope with cataclastic texture*

A conceptual model of cataclastic texture slope near a highway was established (Fig. 2). It was treated as the material supplying source for the potential rock heap formed under seismic motion. In order to reduce the influence of boundary reflection wave, the slope bottom was treated as viscous boundary, and the others were free boundary, and the boundary condition of velocity was zero velocity boundaries.

### 2.2 *Rock mass parameters*

The earthquake waves were input at the bottom of the slope (Fig. 2). The perpendicular shear stress waves were applied to simulate ground vibration. Strong vibration with high frequency and large stress was used as input to reduce calculating time and speed up structural damage, the shear stress wave equation is:

$$\sigma_s = 5 \times \left(1.0 - \cos(2 \times freq \times \Delta t)\right) \times 10^6 \tag{1}$$

where *freq* is ground motion frequency (50 HZ); $\Delta t$is loaded time (unit/second) of ground motion.

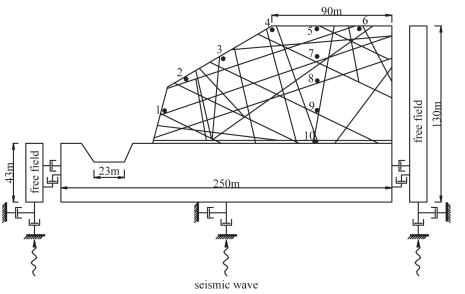


Figure 2. Geometric model of rock slope.

Rock response was simulated with Mohr-Coulomb constitutive model. Specific parameters are shown in Tables 1 and 2.

2.2.1 *Generalized stress and strain components*
The three principal stresses:

$$\sigma_1 \le \sigma_2 \le \sigma_3 \tag{2}$$

This criterion may be represented in the plane ($\sigma_1$, $\sigma_3$), as illustrated in Figure 3. The failure envelope f ($\sigma_1$, $\sigma_3$) = 0 is defined from point A to B by the Mohr-Coulomb failure criterion $f^s = 0$ with

$$f^s = \sigma_1 - \sigma_3 N_\phi + 2c\sqrt{N_\phi} \tag{3}$$

and from B to C by a tension failure criterion of the form $f^t = 0$ with

$$f^t = \sigma_3 - \sigma^t \tag{4}$$

where $\phi$ is the friction angle, $c$ is the cohesion, $\sigma^t$ is the tensile strength, and

$$N_\phi = \frac{1+\sin(\phi)}{1-\sin(\phi)} \tag{5}$$

Note that the tensile strength of the material cannot exceed the value of $\sigma_3$ corresponding to the intersection point of the straight lines $f^s = 0$ and $\sigma_1 = \sigma_3$ in the f($\sigma_1 = \sigma_3$) plane. This maximum value is given by

Table 1. Mechanical parameters of rock.

| Rock type | Density/ (kg · m$^{-3}$) | Bulk modulus/ GPa | Shear modulus/ GPa | Cohesion/ MPa | Friction angle/ (°) | Dilation angle/ (°) | Tensile strength/ MPa |
|---|---|---|---|---|---|---|---|
| Dolomite | 2620 | 56.4 | 25.6 | 2.2 | 36 | 10 | 5.67 |

Table 2. Mechanical parameters of joints.

| Joint plane | Normal stiffness/ (GPa · m$^{-1}$) | Shear rigidity/ (GPa · m$^{-1}$) | Friction angle/ (°) | Dilation angle/ (°) | Cohesion/ MPa | Tensile strength/ MPa |
|---|---|---|---|---|---|---|
| F | 0.44 | 0.62 | 10 | 10 | 0.2 | 0.2 |

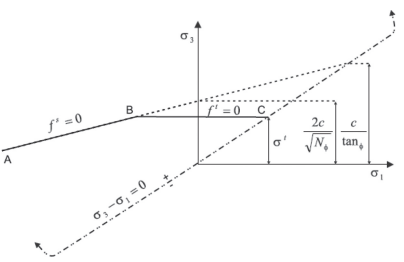


Figure 3. Mohr-Coulomb failure criterion.

$$\sigma'_{\max} = \frac{c}{\tan\phi} \tag{6}$$

2.2.2 *Coulomb-slip joint model (Itasca 2013)*

The basic joint constitutive model incorporated is the generalization of the Coulomb friction law. This law works in a similar fashion both for sub-contacts between rigid blocks and for sub-contacts between deformable blocks. Both shear and tensile failure are considered, and joint dilation is included.

For an intact joint (i.e., without previous slip or separation), the tensile normal force is limited to

$$T_{\max} = -TA_c \tag{7}$$

where $T$ is the joint tensile strength.

The maximum shear force allowed is given by

$$F^s_{\max} = cA_c + F^n \tan\phi \tag{8}$$

where $c$ and $\phi$ are the joint cohesion stress and friction angle.

Once the onset of failure is identified at the sub-contact, in either tension or shear, the tensile strength and cohesion are taken as zero:

$$T_{\max} = 0 \tag{9}$$

$$F^s_{\max} = F^n \tan\phi \tag{10}$$

This instantaneous loss of strength approximates the "displacement-weakening" behavior of a joint. The new contact forces are corrected in the following manner (normal compressive force is positive):
for tensile failure

$$\text{If } F^n < T_{\max}, \text{ then } F^n = 0 \text{ and } F^s_i = 0 \tag{11}$$

for shear failure

$$\text{If } F^s < F^s_{\max}, \text{ then } F^s_i := F^s_i \frac{F^s_{\max}}{F^s} \tag{12}$$

where the shear force magnitude $F^s$ is given by

$$F^s = (F^s_i F^s_i)^{1/2} \tag{13}$$

Dilation takes place only when the joint is at slip. The shear increment magnitude $\Delta U^s$ is given by

$$\Delta U^s = (\Delta U^s_i \Delta U^s_i)^{1/2} \tag{14}$$

This displacement leads to a dilation of

$$\Delta U^n(dil) = \Delta U^s \tan\psi \tag{15}$$

where $\psi$ is the dilation angle.

## 2.3 *Dynamic response of rock slope under ground motion*

The three-dimensional (3D) numerical model of the cataclastic texture slope nearby a highway is shown in Figure 4. Before seismic analysis, static calculation under the self-weight

stress was performed to reach approximate static equilibrium state. The maximum unbalance force should be less than 0.01% of the initial unbalance force. The maximum unbalanced force was close to 0 in the 4000th calculation step, as shown in Figure 5.

When the static equilibrium was reached, the seismic shear stress waves were exerted at slope bottom, the duration of which was 1.32 s. The seismic particle acceleration of Points 1–6 and the maximum shear stress of Points 6, 7–10 were monitored (Fig. 2).

During the seismic course, the slope surface, especially the trailing edge of slope, cracked firstly along the joints, small rock blocks were thrown out (Fig. 6). The longitudinal joints cracked earlier and the top edges generated wide fissures along joints (Figs. 7 and 8).

Figures 9–12 shows the particle vibration acceleration time history curve of Point 1~6 compared with Point 2, respectively. Due to the input seismic waves consisted of high frequency and large stresses, the accelerations were much larger than general seismic accelerations but would not affect vibration dynamic response process. Point 1 firstly reached the peak of particle vibration acceleration, but its peak value was less than that of Points 2, 3. The acceleration values of Points 2, 3 were consistent and less than that of Point 6. Point 6 is located in the trailing edge of slope top, so little rocks were thrown firstly in the trailing edge of slope top with the maximum throwing amplitude (Fig. 6). The particle vibration acceleration values of Point 4, 5 were nearly the same but smaller than above. It is because the leading edge of slope top forward squeezed and sank along main joints during the process of earthquake and the stress couldn't be released timely (Fig. 7). At the same time, it also accelerated the generation of the middle ground fissures, the release of internal structural stress and the throwing of rock blocks.

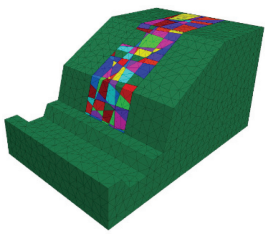

Figure 4. 3DEC slope model.

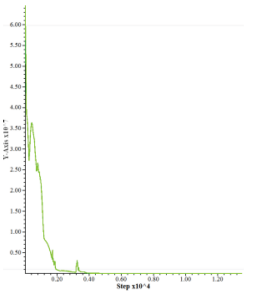

Figure 5. History curve of unbalance force.

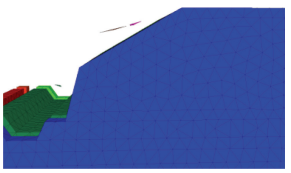

Figure 6. Throwing of small rock blocks.

Figure 7. Profile of slope.

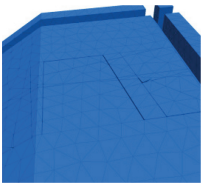

Figure 8. Seismic response of slope top.

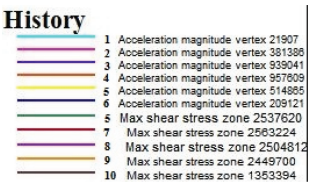


Figure 9. Representative curve of each monitoring point.

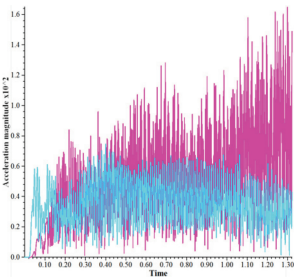

Figure 10. Acceleration time history curve of Points 1, 2.

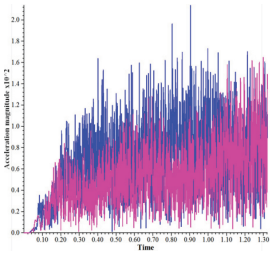

Figure 11. Acceleration time history curve of Points 2~5.

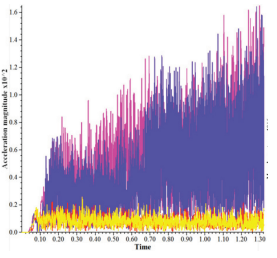

Figure 12. Acceleration time history curve of Points 2, 6.

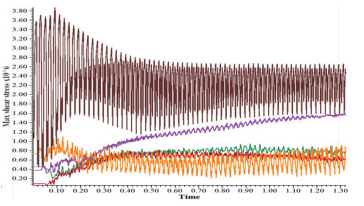

Figure 13. Max shear stress time history curve of Points 5, 7~10.

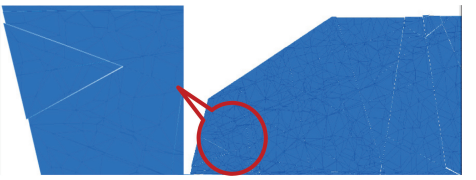

Figure 14. Sectional view of Static calculation results.

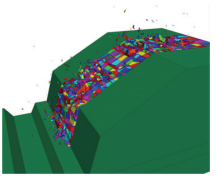

Figure 15. 3D dynamic calculation model of improved cataclastic texture slope.

Figure 16. Dynamic calculation section of improved model.

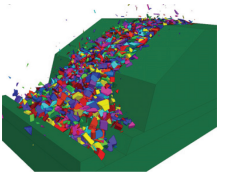

Figure 17. 3D rock heap of improved model.

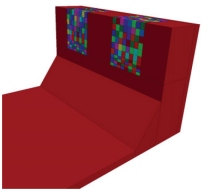

Figure 18. Idealized cataclastic texture model.

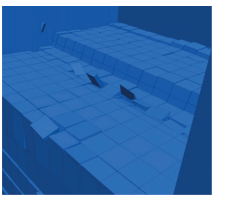

Figure 19. Blocks throwing from slope surface.

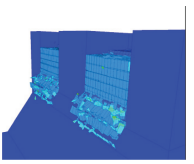

Figure 20. Shear failure at the bottom.

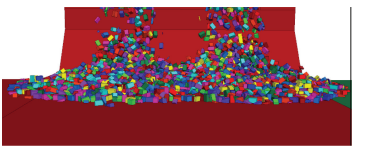

Figure 21. Rock heap formation.

Figure 13 shows the maximum shear stress history contrast diagram of the block region where Point 6~10 is located. The initial shear stresses of each position under static stability conditions were not the same with each other. Stress waves transferred from slope bottom to top once the earthquake waves were input. The shear stress waves decayed with time and tended to stable from bottom to top by each point, but the shear stress nearby the top had amplification in a certain extent, the stress value of Point 5 was larger than that of Point 7. The stress value of Point 8 was special whose shear stress increased constantly and tended to

the value of the bottom. Point 8 was located in the joint communicating with slope bottom, the reflection and filtering effects were not obvious.

Static calculation was performed again when the seismic wave input was finished. During the static calculation, crack continued to expand obviously, the toe joints cracking became more and more obvious and the rock in the area tended to collapse (Fig. 14). The serious damage at the slope foot may be the main reason to cause the entire collapse of slope during seismic process.

### 2.4 *Improved cataclastic texture model*

Stochastic fracture network model on the basis of the original model was adopted to observe the damage position of slope more directly. The same seismic waves were input, small rock blocks generated the phenomena of throwing and cataclastic structure slope had forward collapse tendency under the seismic motion (Fig. 15). The collapse tendency was gradually formed and the first failure surface located near the foot of slope (Fig. 16), which was consistent with the previous models.

In accordance with the aforementioned method, static calculation was carried out when the seismic motion was finished. After the seismic motion, cataclastic texture rock mass continued to lose stability, slide and formed a new rock heap on the highway (Fig. 17).

### 2.5 *Idealized cataclastic texture model*

In order to verify initial failure location of cataclastic texture rock under seismic motion, an idealized cataclastic texture model was established for different terrain conditions and cataclastic texture regularity (Fig. 18). The cataclastic texture was mainly dominated by regular square and wedge blocks, and the seismic shear stress waves were input after static stability calculation. In the same seismic conditions, the slope failure process and the formation mechanism of rock heap were compared with the aforementioned models. In the collapsing process (Figs. 19–21), small blocks of the slope top were thrown firstly, the bottom of cataclastic texture was the first collapsing place. Throwing phenomenon was observed firstly in the propagating process of shear stress. The shear damage at the bottom of the fracture structure was the source of the formation of rock heaps.

## 3 ROCK HEAP STRUCTURE ANALYSIS

The inner rock heap structure can be obtained using the sectional slicing, three-dimensional sampling method for the rock heap formed under seismic motion.

Take the rock heap in Models 2 and 3 as examples, the distribution of rock blocks on different sections is shown in Figure 22. The 3D sampling within the region of 10 m in length for the rock heap on highway is shown in Figure 23. The rock heap slices and three-dimensional

Figure 22. Cross-sections of rock heap.

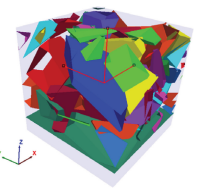

Figure 23. 3D sampling of rock heap.

Figure 24. Rock heap cross-sections.

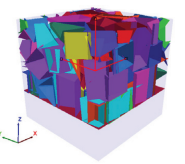

Figure 25. 3D rock heap sampling.

sampling plans of Model 3 are shown in Figures 24–25. The structure of rock heap was relatively stable, internal rock blocks were compacted and uniform distribution.

## 4 CONCLUSION

1. A seismic response conceptual model of cataclastic texture rock mass was established to simulate the rock heap formation under seismic motion.
2. According to particle vibration acceleration and rock blocks throwing phenomena, the responses of slope surface increased from down to top, the blocks on the top surface were more likely to be thrown.
3. Due to the complex distribution of joints and cracks, the stress propagation process does not continuous decay from the bottom to the upper, amplification effect was observed close to the slope surface;
4. The bottom shear failure in cataclastic texture slope was the main reason for the collapse of slope and formation of rock heaps.
5. Sectional slicing and three-dimensional sampling method were proposed to distinguish the structure of rock heap formed under seismic motion.

## ACKNOWLEDGMENTS

This work is supported by the research grant (2014CB046900) from National Key Basic Research Program of China, GDUE Open Funding (SKLGDUEK1417) and the Foundation of China Railway No. 2 Engineering Group Co. Ltd. (No. 201218).

## REFERENCES

Dong, X.P. & Ding, R. 2001. Construction technique in unstable tunnel accumulated with porous surrounding rock. *Journal of Railway Engineering Society* 2001(2): 47–50.

Itasca 2013. Three Dimensional Distinct Element Code: Theory and Background. Minneapolis: Itasca Consulting Group Inc.

Jiang, X.Y. 2015. Characteristics of rock heaps and its influence on tunnel engineering. *Sichuan Building Materials* 41(2): 171–172.

Lin, Y., Zhu, D., Deng, Q. et al. 2012. Collapse analysis of jointed rock slope based on UDEC software and practical seismic load. *Procedia Engineering* 31: 441–446.

Liu, S.X. 2008. Construction techniques for dayandong tunnel of loose rock pile. *Journal of Shijiazhuang Institute of Railway Technology* 04: 26–29.

Long, H. 2014. Under Conditions of High Earthquake Steep Rock Slope Collapses and Dynamic Response Characteristics of Rock Pile Toe. Chengdu University of Technology.

Moore, J.R., Gischig, V., Burjanek, J. et al. 2012. Earthquake-triggered rock slope failures: Damage and site effects. *Proceedings of 11th International & 2nd North American Symposium on Landslides*.

Shen, S.R., Zeng, F.C., Xie, Q.M. et al. 2013. Study on the optimization of treatment schemes of talus in mountain area road. *Journal of Wuhan University of Technology* 01: 108–112.

Shi, H.Z. 2006. The characteristics of highway transportation station piled on both sides of the Jinsha River rock of Xiluodu hydropower. *Gansu Science and Technology* 22(3): 102–104.

Song, J. & Gao, G.Y. 2013. Empirical predictive model for seismic displacement of slopes under velocity pulse-like ground motions. *Chinese Journal of Geotechnical Engineering* 35(11): 2009–2017.

Sun, P., Yin, Y., Wu, S. et al. 2012. Does vertical seismic force play an important role for the failure mechanism of rock avalanches? A case study of rock avalanches triggered by the Wenchuan earthquake of May 12, 2008, Sichuan, China. *Environmental Earth Sciences* 66(5): 1285–1293.

Wang, G.B., Xie, Q.M., Fu, J. 2012. Study on optimization of treatment scheme for Sanlihua rock heap along Yingchang-Badong highway. *Subgrade Engineering* 05: 23–26.

Wei, Y.X. 2004. Engineering technique for subgrade through rocky heaps in Neijiang-Kunming railroad. *Railway Survey* 2: 27–30.

Wu, F.Z. Construction technologies for Yingzuiyan Tunnel rock-heap formation. *Highway* 12: 230–233.

Yan, Z.X., Zhang, S., Zhang, X.D. et al. 2011. Study of dynamic response of bedding rock slope under earthquake and influence of ground motion parameters. *Chinese Journal of Rock Mechanics and Engineering* 30(S2): 3522–3528.

*Rock Dynamics: From Research to Engineering – Li et al. (Eds)*
*© 2016 Taylor & Francis Group, London, ISBN 978-1-138-02953-8*

# Nondestructive detection and intelligent diagnosis technology of anchorage system

M. Xu & X.S. Liu
*School of Civil Engineering, Chongqing University, Chongqing, China*

Z.X. Yan
*School of Civil Engineering and Mechanics, Lanzhou University, Lanzhou, China*

ABSTRACT: Sonoprobe method has been applied in non-destructive inspection of anchorage project. The fundament is that dynamic transient excitation causes the elastic vibration of an anchor bar, and flaws can be estimated or deduced by determining transient response of the anchor bar. FEA numerical solution of hyperbolic equation indicates that deductions must comply with acoustic parameters such as velocity of sound, vibration range, wave shape etc. when inspecting interior flaws in the grout of an anchor bar. Based on wavelet packet analysis, the energy eigenvector is a flaw vector, which could be regarded as the basis in the non-destructive inspection of anchors. As a non-linear dynamical system, artificial neural networks dealing with quality inspection of grey system have been proved efficient.

## 1 INTRODUCTION

Anchor rope is a component under great ground pressure. The failure in predicting stability of the anchorage system will bring projects inestimable loss, so it is necessary to check if the anchor bars play the roles according previous design. The low strain dynamic detection has been applied in quality test of anchor bar. On the mechanics field this method means that information of disturbance resource, boundary conditions and initial conditions have been given, and the dominant equation describing medium motion has been established. Thereby the dynamic response could be solved. In fact it is dealing with the variable field question that is come down to the question of initial value or initial-boundary value of hyperbolic type or hyperbolic-diffusibility type.

In hyperbolic equations, neither the effect of the dispersion in actual situation nor the effect on the wave propagation owing to objects' irregularity of geometry shape or medium's heterogeneity have usually been taken into consideration. It is extremely difficult to get accurate solution of the transient wave in flexible wave-guide that is more applicable practically. So the main approach managing this sort of dynamic issue is different numerical method and approximate method.

## 2 HYPERBOLIC EQUATION

There are some hypothetical conditions or applicative premises in dynamic test. Here are some necessary basic hypotheses on anchor bar as the follows (Zhang & Xu 2002, Sun et al. 2015):

1. The excitation vibration of anchor bar is within elastic limitation.
2. The material of anchor bar is uniform or sectionally uniform and isotropy in addition.
3. When anchor bar vibrates under excitation, its section keeps plane.

According to the hypothetical conditions the control equation of longitudinal wave is given by:

$$\frac{E}{\rho}\frac{\partial^2 u}{\partial x^2} - \frac{R}{\rho A} = \frac{\partial^2 u}{\partial t^2} \tag{1}$$

where the mass force is not considered; u is longitudinal displacement of particle; t is time counted from the point of impact; x is position of anchor section; E is modulus of elasticity; ρ is mass density; R is cohesive friction resistance in a unit of length along interface of medium and anchor bolt; A is area of cross section.

The friction resistance R is related to factors such as medium characteristic, compaction rate, roughness of segment profile, and execution method of anchor bar. It is very difficult to define these factors accurately, so ideal elastic model is used in describing them

$$\frac{R}{\rho A} = \mathrm{a} * u$$

where a is a constant.

Put the above equation into Equation (1), and then get

$$u'' - \mathrm{div}(\mathrm{c} * \mathrm{grad}(u)) + \mathrm{a} * u = 0 \tag{2}$$

where c = E/ρ.

To acquire displacement function u(x,t) solely in the light of the wave equation, the initial vibration condition of the anchor bar and propagation boundary condition of stress wave should be given.

Initial condition is the disturbing statement at initial point t = 0, i.e. initial displacement and velocity of the anchor bar. Usually there are

$$u(x,t)\big|_{t=0} = u(x,0) = 0 \tag{3}$$

$$\frac{\partial u(x,t)}{\partial t}\Big|_{t=0} = u_t(x,0) = 0 \tag{4}$$

Boundary condition is the statement of the stress wave in anchor bar's boundary section (i.e. anchor cone top and anchorage body bottom) in any time of t > 0.

The bottom of anchor bar used in rock can be treated as fixed end due to low input energy of low strain method and relatively hard bedrock. According to the 'Dirichlet' boundary condition, the displacement at the bottom equals zero:

$$u = 0 \tag{5}$$

As anchor cone is free, 'Neumann' boundary condition can be used here. Based on the collision theory of rigid body and rod (Kates, et al. 2001, Zeng et al. 2004), momentum increment of rigid body equals force impulse between the interface of striking body and rod. So the displacement of head face can be solved. The strain of anchor cone is expressed as follow:

$$\vec{n} \bullet (\mathrm{grad}(u)) = \mathrm{g} * \exp(-t) \tag{6}$$

where g is a constant.

## 3 NUMERICAL SOLUTION

To figure out the finite solution, x direction is defined as anchor bar's length direction while y direction is defined as diameter direction. Within the domain gridding is built and refined. z direction (vertical direction) denotes displacement of particle.

At the center of solution domain, a circular region and a square region are cut open respectively to represent flaws in the anchor bar. The model with complete solution domain and the model with center hole are numerically solved respectively. The distortion gridding of output solution at some given moment is showed as follow (Fig. 1):

The displacement curves of anchor cone are shown in Figure 2, where 'flat' means the solution of model with complete domain; 'circular' means the solution of model with a round hole; 'square' means that with a quadrate hole. It is observed that the first solution curve is smooth, and displacement amplitude is relatively great. The second and the third curve have some deformation, the phase is hysteretic too. This phenomenon reflects that the velocity of pressure wave is decreasing. Thus it can be seen that arrival time of stress wave and wave shape's changement are greatly important in identifying flaw.

Figure 3 shows density curves of power spectrum of anchor cone acceleration, which appear in singlet. The flaws not only cause peak value of power spectrum curves to sink, but dominant frequency to drift. At the same time, total area of power spectrum that is total energy of respective frequency component decreases either. Scattered by microfissuring interface when impulse wave gets across flaw zone, stress wave's energy is attenuated, and frequency spectrum curves appear distortion. The variation of spectrum eigenvalue is much greater than that of travel time, especially the transformation of amplitude is sensitive.

The variation of amplitude spectrum and frequency caused by rock matrix's absorbency toward sound wave primarily reflects its structural composition and other physical mechanic

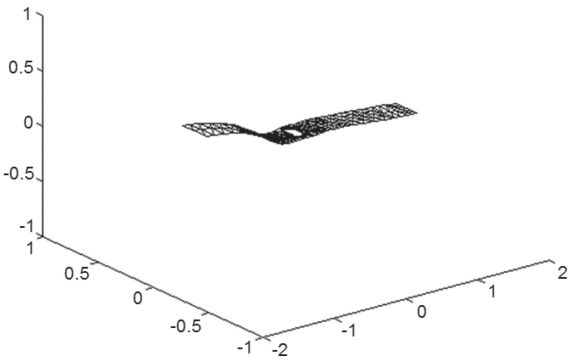


Figure 1. Transformative gridding of district with a centric hole.

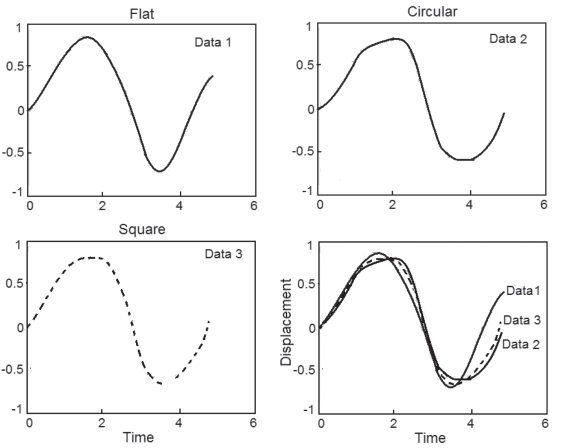


Figure 2. Displacement curves of top face of anchor bar.

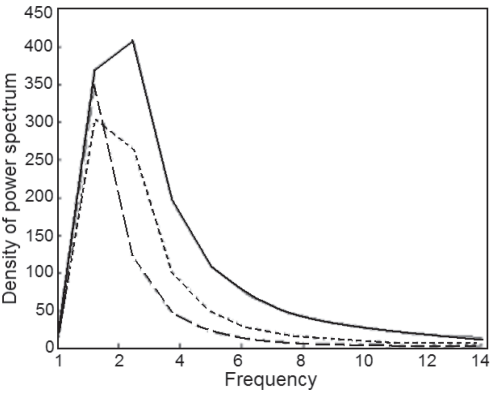


Figure 3. Power spectrum density of acceleration.

property. Therefore if we analyze frequency spectrum of elastic wave including amplitude spectrum, phase spectrum, energy spectrum, etc. We could gain more effectual information than simply using elastic wave velocity representing structural state of rock mass. The vital theoretical basis of acoustic soundex lies in this viewpoint too.

## 4 WAVELET ANALYSIS

When one system is disturbed by an input signal containing abundant frequency band, the flaws in the system restrain and enhance particular frequency band. Some frequency component is choked back, while the other is boosted up. So the output of the system has relatively difference comparing with healthy system. Signal energy minishes in some frequency band, and augments in the other band (Beard & Lowe 2003, Huang et al. 2005, Sih 2008).

Thus each frequency band's energy in the signal contains plenty information of flaws. Certain change in frequency band's energy represents a sort of flaw circumstance.

Wavelet analysis belonging to a kind of time-frequency analysis is outcome of harmonic analysis in mathematics field since semi-centenary. Wavelet transform is a type of time-frequency analytical procedure, which possesses characteristic of multi-resolution analysis, and moreover, competence displaying signals' local feature in time-frequency two fields. Wavelet transform has self-adaptivity to the signal. Its characteristic is adept to detect transient abnormal phenomenon carried in natural signal and reveal its components. There is nicer effect if continuous wavelet transform is made use on fault detection and diagnosis in dynamic system (Zou et al. 2007).

Through wavelet packet analysis on the displacement curves of anchor cone under conditions of 'haar' wavelet packet function, '3' decomposition layer, and 'shannon' entropy standard, signal features of 8 frequency ingredient in the third layer from low frequency (crunode (3,0)) to high frequency (crunode (3,7))are collected.

After wavelet packet transform, decomposition coefficients of wavelet packet are reconstructed and signals of different frequency bands are extracted. Figure 4 shows the third layer coefficient reconstruction of anchor bar without flaw. Figure 5 shows the third layer coefficient reconstruction of anchor bar with circular aperture. It is obvious that each frequency range of dynamic test signals has fair sized changement all when anchor bolt has flaws.

When the system has flaws, signals' energy in each frequency band is affected greatly. Regarding energy $((\sum V_i^2)^{\frac{1}{2}}$, $V_i$ presents amplitude value of discrete spots of reconstruction signals) as element, a characteristic vector can be gained. According to eigenvectors classification and decision-making can be ascertained if there are flaws. The eigenvectors of each reconstruction coefficient are $\sigma_{flat}$ = [16.3045 0.2436 0.1218 0.0022 0.0609 0.0011 0.0006

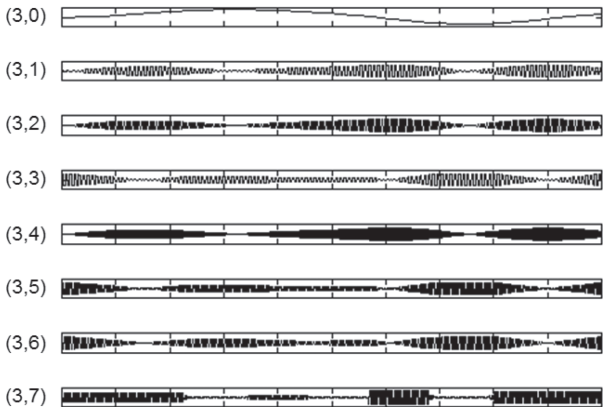


Figure 4. Reconstruction of wavelet packet crunode (anchor bar without a flaw).

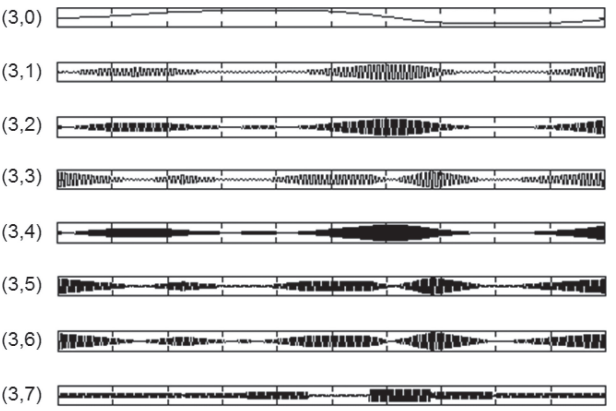


Figure 5. Reconstruction of wavelet packet crunode (anchor bar with a circular aperture).

0.0000]; $\sigma_{circular}$ = [16.7902 0.2147 0.1074 0.0024 0.0537 0.0012 0.0006 0.0000]; $\sigma_{square}$ = [16.6878 0.2205 0.1102 0.0023 0.0551 0.0011 0.0006 0.0000].

## 5 PREDICTION BASED ON ARTIFICIAL NEURAL NETWORK

A BP (Back Propagation) network must be built firstly, regarding eigenvectors of reconstruction coefficient as 8 input data in net input layer, integrity factor of anchor bar (interval (0,1)) as desired output of net output layer. Then integrity test on anchorage system can be operated. This inspective method can avoid contrived subjectivity on analyzing time-frequency characteristic and advance flaws' recognizable precision. Nerve cells in concealed layer utilize 'sigmoid' transmit functions. Nerve cells in output layer employ linearity transmit functions. The network is trained through in-out sample set. Trained BP net possesses association ability. Therefore it can also give appropriate output for input beyond sample set and can predict anchor bars' integrity on site.

Predicting capability of artificial neural networks is closely related to choice of training sample set. More comprehensive sample set is and more widely parameters' range covers, more satisfying predicting effect is (Yu et al. 2013).

## 6 CONCLUSIONS

1. Detecting inner flaws of anchorage grouting such as pore space, cranny, honeycomb, we can regard a series of sound parameters such as propagation time, wave amplitude, wave profile etc. as judgement basis. If frequency spectrum aberrance parameters on flaw location can be considered, the judgement will be more reliable.
2. The energy characteristic vector gained from reconstruction of wavelet packet crunode can act as the vector of flaw characteristic in conducting nondestructive detection. This flaw diagnostic way can collect and diagnose flaws rapidly without establishing mathematics model of diagnosed system.
3. An artificial neural network is utilized to predict integrity of anchor bar. This way has several advantages: high precision, satisfactory predicting result, well error tolerance, reliable and applicable.

Low strain dynamic test on detecting quality system of anchor bar is on groping stage. Its testing profundity is limited. The limitation can be overcome and enhanced through advancing technology and complementing more relative information such as engineering geology document, initial construction record, construction method, field condition, type of anchor bar etc. in pattern recognition.

## ACKNOWLEDGEMENTS

Project supported by the National Basic Research Program of China (No. 2014CB046903), the National Natural Science Foundation of China (No. 51478065), the Fundamental Research Funds for the Central Universities (No. 106112014CDJZR200015 and No.106112014CDJZR200014).

## REFERENCES

Beard, M.D. & Lowe, M.J.S. 2003. Non-destructive testing of rock bolt using guided ultrasonic waves. *International Journal of Rock Mechanics & Mining Sciences* 40(4): 527–536.

Huang, H., Zhu, Z., Yang, T. et al. 2005. A discussion on the nondestructive detection technique for qualities of roof bolts and anchors in tunnels. *Geophysical & Geochemical Exploration* 29(6): 551–553.

Kates, R., Clark, W., Corell, R., Hall, J. et al. 2001. Environment and development: sustainability science. *Science* 292(5517): 641–642.

Sih, G.C. 2008. Disproportionate available to dissipated energy density model related to emission of $CO_2$ and evaluation of structural energy efficiency. *Theoretical and Applied Fracture Mechanics* 50(1): 1–8.

Sun, B., Zeng, S., Guo, S., Yang, C. 2015. Variation characteristics of stress wave speed for anchorage system under instantaneous excitation. *Geotechnical & Geological Engineering* 33: 1–7.

Yu, J.D., Bae, M.H., Lee, I.M., Lee, J.S. 2013. Nongrouted ratio evaluation of rock bolts by reflection of guided ultrasonic waves. *Journal of Geotechnical & Geoenvironmental Engineering* 139(2): 298–307.

Zeng, X.Y., Tang, S.M., Deng, A.F. 2004. Laboratory similar model test investigation of prestressed anchor rope strengthened slope fractured rock mass. *Journal of Chongqing University* 27(8): 128–131. (in Chinese).

Zhang, Y.X. & Xu, M. 2002. Theory and application of Intelligent Diagnosis Technology of Anchorage System Quality. Beijing: China Building Industry Press. (in Chinese).

Zou, D.H., Cui, Y., Madenga, V., Zhang, C. 2007. Effects of frequency and grouted length on the behavior of guided ultrasonic waves in rock bolts. *International Journal of Rock Mechanics & Mining Sciences* 44(6): 813–819.

*Rock Dynamics: From Research to Engineering – Li et al. (Eds)*
*© 2016 Taylor & Francis Group, London, ISBN 978-1-138-02953-8*

# Multi-scale characteristics of rockburst under the multi-level stress control

S.K. Zhao
*School of Mechanics and Civil Engineering, China University of Mining and Technology (Beijing), Beijing, China*
*Safety Technology Branch of CCRI, Beijing, China*

Q.X. Qi, Z.H. Ouyang & Z.G. Deng
*Safety Technology Branch of CCRI, Beijing, China*

ABSTRACT: As a kind of dynamic damage in coal mine, rockburst is the result of deformation and failure under different scale stress. Under the action of tectonic stress, in-situ stress and mining stress, both of the macro occurrence form of coal-rock mass and its surface and internal microstructure were changed. The superposition of in-situ stress and mining stress is the foundation of rockburst, the higher stress increment is the root cause of rockburst induced. Based on the effective monitoring and accurate evaluation on stress in different scales, According to the multi-scale mechanical impact characteristics on coal mine dynamic disaster, from regional stress compatible to local stress control, the space-time monitoring and evaluation system of multilevel different-sources was established. The cut transfixion of island working face with strong probability of rock burst were solved under the direction of this technology.

## 1 INTRODUCTION

Whether the collision, blast and combination of stars in the universe and the galaxy or sun alternate and continental drift on earth, whether earthquake, tsunami and volcanic eruption of local extent or the instability of physical structures and fracture development, all of these phenomenon occurrence are related to force and the differences among them is the magnitude and the scale range of force. The force in the universe can be divided into Gravitation, electromagnetic force, strong nuclear force and weak nuclear force on the basis of force sources and the scale of force (Sun 2008). The force on the earth can be divided into internal force and external force on the basis of force source mechanism. The lithosphere geological force and the displacement movement caused by the internal force of the earth was called tectonic movements. The movement can be divided into extruded, extrusion destructive, shear, tension-type and Wilson cycle (Wu 2006). However, even the same type of tectonic movements, the different size and scale of the force make rock deformation mechanism and mode of failure has a clear distinction in different scales. Different levels of force control the stability of rock mass structural and the characteristics of deformation failure in different ranges. In the practical geotechnical engineering, the force effect on body of engineering should be analyzed and controlled in multi-scale. For the occurrence of rockburst in coal mine, which is mainly caused by the movement and fracture of overlying strata in the mining areas. Although the location and energy different, the root are mainly the impact of the regional stress and the mining-induced stress. Reasonably coordinate crustal stress and effectively control mining-induced stress, the rockburst can be prevented.

## 2 STRESS ANALYSIS AND FAILURE CHARACTERISTICS OF COAL AND ROCK MASS IN DIFFERENT SCALES

### 2.1 *Characteristics modern tectonic stress field in our country and regional stress characteristics of the main coalfield in its impact*

The occurrence characteristics of coal seam are easily deformed because it's composed by some small block and poor stability in China. The synthesis of microcontinent was not only low intensity and poor stability, but also the sedimentary cover easily deformation for tectonics movement. China's coal deposits can be divided into the north china, northeast, south china, northwest, Yunnan-Tibet and other coal regions on the basis of the spatial and temporal distribution of the coal-bearing stratum and tectonic characteristics of the earth (Dai 2006, Xie 2007). Meanwhile, China's present-day crustal movement is mainly affected by the Himalayan crustal movement system and the Pacific crustal movement system. Pacific plate subduction caused the back arc area expansion and the NW-SE tension of continental back-arc side, which lead to the northeast, east of North China and southeast coast in the high-stress and high heat flux station. The wedge northward of the Indian plate results in a higher stress of the western region (Rummel 1986, Zhao 2013). Under these factors influences, the distribution of tectonic stress in China main coal filed was as follows: The Eastern distortion zone: Compressive stress was dominated in south of Qinling-Dabie mountain and stretch stress was obvious in northeast and north China. The basic structure of coal series deformation was NE-NNE trending, a parallel arrangement of streak structure combination, with deformation amplitude and intensity decreasing from east to west. The Central distortion zone: Crustal structure was stable and the evolution of coal basin was characterized by the succession; the coal series deformation division in Ordos Basin and Sichuan basin was characterized by the typical "platform type" concentric ring band structure. The Western distortion zone: The feature on structural pattern was a compressive stress system. Tectonic line was in arc distribution and the direction was NW-NWW-NNW, the deformation strength decreases from south to north. The parallel streak structure in Yunnan-tibetan region change into multicenter band structure in northwest China.

### 2.2 *Analysis of the stress distribution characteristics in Mining area and the coal seam stress characteristics*

Tectonic stress mainly affected the coal seam occurrence characteristics and the size and direction of in-situ stress, which was the main reason for the deformation and failure of roadway in stope. The stress distribution characteristics of working face and bearing pressure in roadway was mainly affected by the mining-induced stress. In rockburst mine, the mining-induced stress and tectonic stress were the main stress for coal and rock instability and the higher stress increment caused by the outside dynamic load often result in rockburst. In order to clarify the stress evolutionary process of mining working face and surrounding rock of roadway under the influence of mining, KSE-II-1 type borehole was installed in different depths to monitor the stress changes, which successfully record a small-scale rockburst. The monitoring curve showed in Figure 1.

With the working face advancing, it was clear that the development of rockburst went through four states: relative stability, unsteady equilibrium, impact dynamics and relative stability. The adjacent stage was in a dynamic and unsteady equilibrium station. The change of stress was immediate reason for the stage transformation. The superposition of in-situ stress and mining stress is the foundation of rockburst, the higher stress increment is the root cause of rockburst induced.

### 2.3 *Analysis of load and deformation and failure characteristics for loaded simple of coal and rock*

Under the influence of multi-level stress, microscopic structural properties and mechanical properties of coal and rock mass were changed and the tensional, shearing and compres-

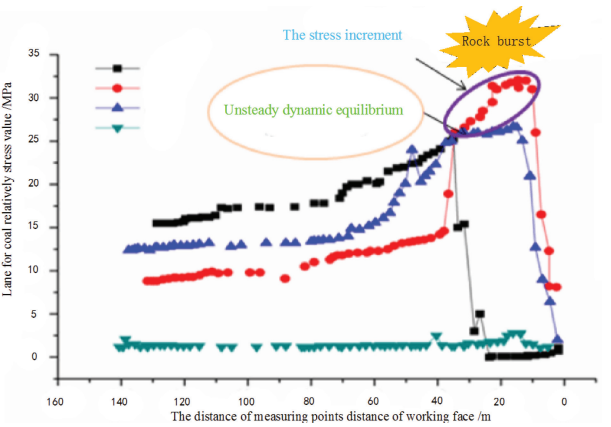


Figure1. Stress curve of "3.1" rockburst in Yuejin coal.

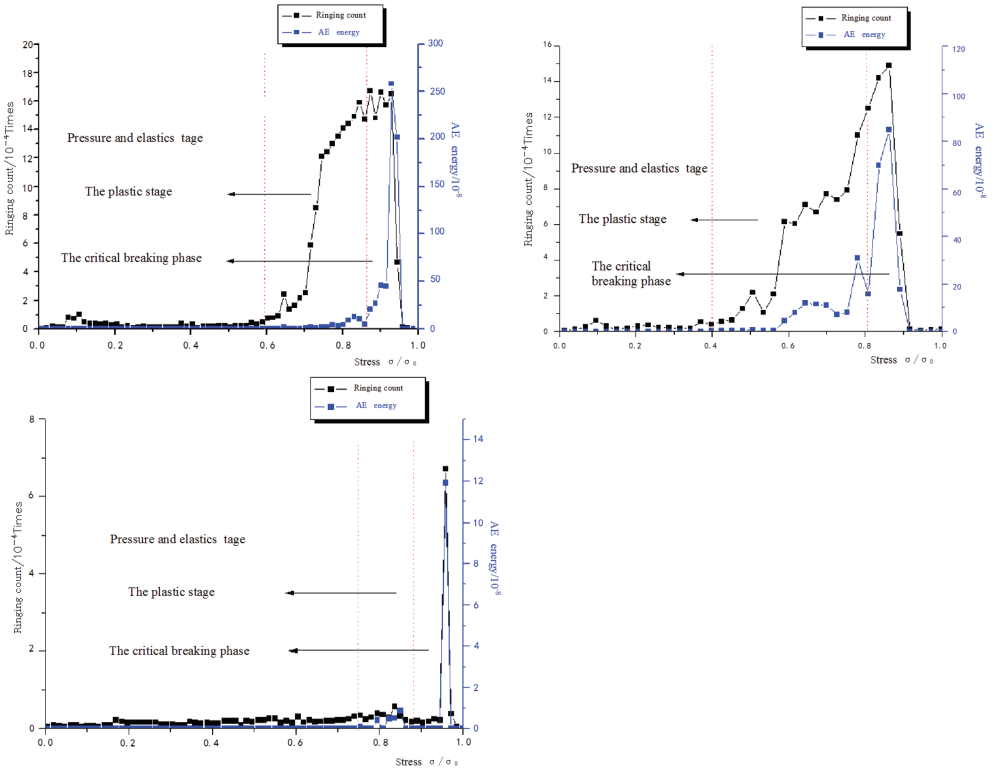


Figure 2. Counts and AE energy of non, weak and strong—impact coal.

sional fissures caused by tectonic movements were increased. Rockburst tendency as a testing index of the possibility of dynamic failure, which have strong, weak, no three different burst tendency and they have obvious differences under the action of compressive stress, such as deformation and the acoustic emission laws. First, pore fracture in no burst tendency coal mass was developed and the carrying capacity was poor, so the form of ultimate failure mostly crushed. The initial fissure of burst coal mass was undeveloped and carrying capacity bearing. With the development of the burst tendency, coal bearing was more similar to rock mass and pore fracture was located in around the main crack and some secondary crack, ulti-

mate destruction was mostly shearing failure of several cut-through crack. Acoustic emission ring count and AE energy peak appear at this stage. The burst tendency of coal sample was stronger, the amplification relative to the previous peak levels was greater. The strong burst tendency coal also exhibited low ring count and "quiet period" of AE energy level before breaking. Meanwhile, when the burst tendency of coal samples was greater, the amplification of acoustic emission intensity was more frequent and focused on high frequency. Second, the elastic stage lasted short and entered the stage of local failure fast, less elastic energy was saved during the no burst coal mass compression, while the elastic stage of burst tendency coal mass that lasted a long time and accumulated great elastic energy during the stronger tendency of coal mass compression. From the acoustic emission parameters, during the preceding loading (compaction and elastic stage), ring count and AE energy was less and acoustic emission intensity increased, the acoustic emission frequency changed and the acoustic emission b value was approximately level fluctuation, as shown in Figure 2.

## 3 THEORY AND SYSTEM OF MULTI-LEVEL STRESS CONTROL ON ROCK BURST

Coal rock structure mass as a small structural body in the coal measure strata, the stress had a general characteristics under the influence of regional tectonic stress field characteristics, also has the small-scale characteristics under the influence of mine in-situ stress state and mining-induced stress. The loading process from the overall impactive instability of cover rock structure within mining area to the change of burst tendency of coal and rock mass

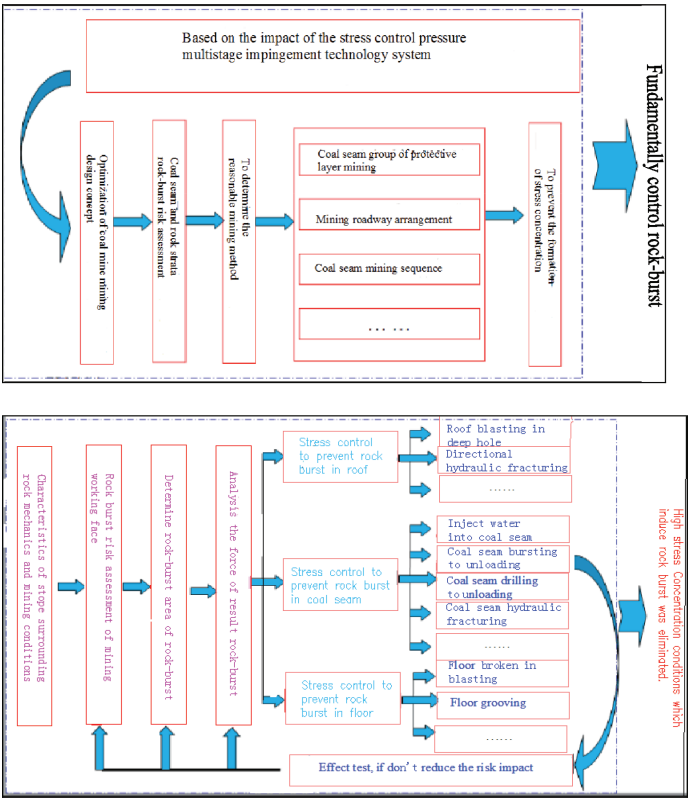


Figure 3. Multistage rockburst prevention technology system based on stress control.

microstructure, which is caused by the stress at different levels and different scales. As far as mine dynamic appearance was concerned, shock bump often caused by the tectonic movement and overlying strata roof broken in mine scale, the influence scope was quite large and strongly felt; the dynamic appearance in mining working face and roadways was rock burst, which have low magnitude and the influence range relative small. Therefore, the monitoring and control of rock burst should be based on the characteristics of stress in different scales and the influence extent on instability of coal and rock mass. On the basis of effective monitoring and evaluation of coal body stress indifferent scales, the corresponding stress prediction and control scheme should be established on the basis of stress, which aimed at the influence of stress in different scales. Ming scale: the reasonable layout of the roadway location and direction was determined on the basis of regional geological dynamic zoning and in-situ stress measurement. Mining area scale: the mining-induced stress regularities of distribution and characteristics of coal rock mass were determined on the basis of the district 3D inversion of in-situ stress and microseismic monitoring results. According to choosing reasonable mining method and mining protection layer, the formation of high stress can be avoided. Working face scale: according to the detecting system of mining-induced stress and drill cuttings method of monitoring, the usage of break-tip blast, large bore unloading pressure can transfer the surrounding lateral high stress of mining roadway. Coal mass micro scale: according to the laboratory multi parameter monitoring system, with water injection in coal seam to change coal mass microstructure, the effective prevention from rock burst at different scales can be achieved, as shown in Figure 3.

## 4 PRACTICE OF PREVENT ROCK BURST UNDER THE MULTI-LEVEL STRESS CONTROL

In order to achieve smoothly cut-through of 23070 working face open-off cut, Based on the Yuejin coal mine existing monitoring equipment and site construction conditions, rockburst multi parameter monitoring system was extablished. It inclued of electromagnetic radiation monitoring, drilling cuttings weight monitoring, stress monitoring, roadway deformation monitoring, borehole stress monitoring and microseismic monitoring. In view of the different stages of the open-off cut period, different prevention and unloading pressure mathods was used based on main stress changed. During open-off cut driving in opposite direction, the stress control mode of "head water infection + head unloading pressure and burst + blasting floor off" in working face scale was used and the technique of large bore pressure release was used to control high stress in local area.

With the increase of cut-hole driving, especially after entered the solid coal, parallel intake entry driving head pressure was significantly increased, drilling hard with incentive appearing, surrounding rock near the head of drill deformation being accelerated, coal burst incidents occurred continually. It means that multi-parameter monitoring and stress control

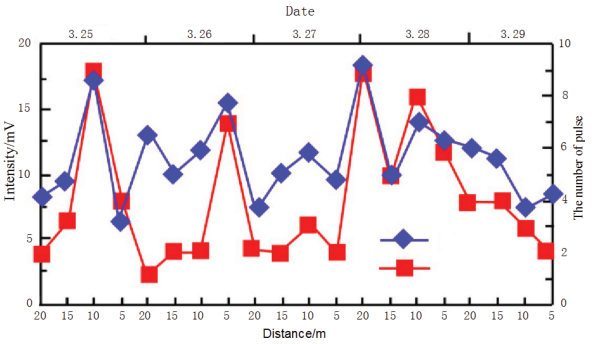


Figure 4. Change curve of electromagnetic radiation in the range of 30 m around driving place.

prevent burst measures at this time was unable to meet demand and it had to adjust the parameters immediately. In the aspect of multi-parameter dynamic monitoring and early warning, the amount of electromagnetic radiation and cuttings monitor was encrypted and increased roadway deformation monitoring. In the aspects of multi-level stress control, as the mining stress superimposed in front of driving head, the head coal and rock mass stress and rockburst was increased. According to the different of stress in upper and lower cut-hole driving head, advanced water injection coefficient and large relief drilling parameters were adjusted and increased the large diameter drill hole relief at high stress areas. The stress of the coal and rock mass surround the upper and lower cut-hole driving head has been effectively controlled by adjusting the multi-level stress control technology, the deformation of roadway have been eased. The electromagnetic radiation intensity and pulse of the lower cut-hole driving head was decreased obviously, as shown in Figure 4.

## 5 CONCLUSION

1. The mechanical action marks at different scales in coal layer structure, which affects the characteristics of the occurrence and change the mechanical properties of coal and rock mass in macro and micro. Multi-level stress will result in the deformation and failure of coal and rock mass in different scales. Rockburst was caused by multi-level stress and it's a sudden release of elastic energy of coal and rock mass in nature.
2. Stress was the root cause of rockburst. The research on mechanism of rockburst should be based on the stress evolution process in multi-level. According to feedback of rockburst monitoring, the stress control subjects should be real-time dynamically adjusted and the compound modes and parameters of monitoring and stress control technology should be constantly adjusted. Only in this way can working face open-off cut with strong burst risk be smoothly holed.

## REFERENCES


Dai, J.S. 2006. *Structural Geology and Tectonics*. Beijing: Peking University Press.

Rummel, F., 1986. Stresses and tectonics of the upper continental crust—a review. *Proceeding of the International Symposium on Rock Stress and Rock Stress Measurements*.

Sun, Y.S. 2008. *Introduction to Modern Celestial Mechanics.* Beijing: Higher Education Press.

Wu, J.M. 2006. *Engineering Geology.* Beijing: Higher Education Press.

Xie, W.H. 2001. Mechanism analysis on flexible and folded floor lift and study of its control counter measure. *Chinese Journal of Rock Mechanics and Engineering* 20(1): 57–60.

Zhao, S.K. 2013.Theory and application of prevention of rock burs by advanced deep hole roof blasting. *Chinese Journal of Rock Mechanics and Engineering* 32(Supp.2): 3468–3776.

*Rock Dynamics: From Research to Engineering – Li et al. (Eds)*
*© 2016 Taylor & Francis Group, London,* *ISBN 978-1-138-02953-8*

# Time history analysis method for dynamic fuzzy reliability of bedding rock slope

X.H. Zhong, W.H. Gong, X.L. Chen, J.W. Qiu & Y. Li
*School of Civil Engineering and Mechanics, Huazhong University of Science and Technology, Wuhan, China*

ABSTRACT: Because pseudo static method ignores the dynamic characteristics of rock and effect of seismic characteristics, time history method is used to analyze the dynamic response of the bedding rock slope under seismic action. Using the finite difference software FLAC3D, a model of the bedding rock slope with weak intercalated layer is established. The probability density function is determined by the maximum entropy principle which makes full use of high order moment information of random variables. The failure probability time history curve and the reliability index time history curve are calculated considering the fuzziness of the slope stability and the average maximum failure probability is presented as the evaluating index. The results show that the time history analysis method reasonably considering the effects of main factors can show the dynamic response of slope accurately which is more secure and reliable compared to the traditional methods.

## 1 INTRODUCTION

The problem of slope stability caused by the earthquake has been highly concerned by the field of geotechnical engineering and geological disaster prevention. Pseudo-static method, slider displacement analysis, time history analysis method are the mainly three calculation methods of slope seismic stability. Pseudo-static method recommended by specification to analyze slope seismic stability needs less parameters and easy to implement, but it ignores characteristics of earthquake and dynamic properties of slope material so that cannot reflect the seismic response characteristics of slope accurately. Based on the rigid body limit equilibrium method, the sliding block displacement analysis method firstly proposed by Newmark (Liu et al. 2001) calculates the permanent deformation may occur after the earthquake, but it is unable to put forward reasonable stability criteria due to lack of practical engineering experience. The time history analysis method is difficult in calculation and complex in data processing, but it can directly reflect the dynamic response of slope under seismic action, including speed, displacement, stress, and so on. Yan et al. (2011) and Li et al. (2007) studied the seismic dynamic response of bedding rock slope by numerical simulation to obtain the time history curve of the relevant parameters. Because the slope stability is a dynamic process under seismic action, it is very important to select a reasonable safety factor to evaluate the seismic stability of the slope. Zhang et al. (1999, 2000) evaluated the slope seismic stability by the minimum dynamic safety factor in dynamic safety factor time history of slope. Zhao et al. (2002) put forward the dynamic equivalent method to average the seismic safety. Liu et al. (2003) proposed minimum average safety factor as the index to evaluate the slope seismic stability. The minimum average safety factor is the most reasonable, but it is still based on the deterministic theory framework, so the evaluation result is lack of the consideration of risk, which leads to the dynamic reliability analysis of the slope.

There are a lot of uncertainties in slope engineering, including randomness and fuzziness, in which fuzziness is more profound and general. At present, the dynamic reliability analysis method based on pseudo static method is in the mainstream. Al-Homoud & Tahtamoni

(2001), Shinoda et al. (2006), Fan et al. (2008) studied the seismic reliability of the structure considering the uncertainty of the parameters and the impact of the earthquake based on the pseudo static method. A new method of dynamic reliability analysis of rock slope based on time history analysis is presented to overcome the defects of the pseudo static method, which cannot truly reflect the dynamic response of slope. The dynamic stress field obtained by numerical simulation adds to the initial stress field, and then the optimal probability density function is determined by maximum entropy method. The fuzzy reliability of the bedding rock slope under seismic action is analyzed by the average failure probability as the evaluation index of the slope stability considering the fuzziness of limit state.

## 2 DYNAMIC LIMIT STATE EQUATION OF BEDDING ROCK SLOPE

### 2.1 *Dynamic response analysis method*

The time history analysis method is to import a number of seismic acceleration records or artificial acceleration time history curve to the basic motion equation of the structure and obtain the internal force and deformation of the structure during the earthquake through the integral operation.

Two assumptions are made when the dynamic limit state equations are established in the paper. First, the deformation failure mode of the bedding rock slope is bedding-slip failure, and the slip surface is paralleled to surface of the rock mass of the sliding bed located in the middle of the weak interlayers in this paper (Liu 2006). Second, the limit equilibrium state is reached and the yield criterion of Mohr-Coulomb is satisfied on the slip surface.

Regarding the rock as a viscoelastic body in the seismic response analysis of bedding rock slope, the basic equation of static and dynamic is:

$$[K]\{\delta\} = \{F\} \tag{1}$$

$$[M]\{\ddot{\delta}\} + [C]\{\dot{\delta}\} + [K]\{\delta\} = -[M]\{\ddot{\delta}_g\} \tag{2}$$

where $[K]$ is the integral stiffness matrix; $\{\delta\}$ is the displacement matrix of the element node; $\{F\}$ is the external load matrix; $[M]$ is the integral mass matrix; $[C]$ is the integral damping matrix; $\{\ddot{\delta}\}$,$\{\dot{\delta}\}$ are the acceleration matrix and velocity matrix, respectively; and $\{\ddot{\delta}_g\}$is the seismic acceleration matrix.

The integral damping matrix $[C]$ is composed of damping matrix of elements and the element damping matrix $[c]$ can be regarded as the linear combination of mass matrix and stiffness matrix, that is:

$$[c] = \alpha[m] + \beta[k] \tag{3}$$

where $\alpha_i = \lambda_i\omega_1$, $\beta_i = \lambda_i/\omega_1$; $\lambda_i$ is damping ratio of the element; and $\omega_1$ is the vibration frequency of soil.

### 2.2 *The establishment of the dynamic limit state equation*

The model of the bedding rock slope under seismic action is established by FLAC$^{3D}$ to calculate the stress field of the slope then the stress components in the X and Y direction and shear stress of the slip surface can be easily obtained. The normal stress and shear stress of a point of slip surface can be obtained by its stress value of the finite element analysis according to the force balance equation (Gong, 2013). As the Figure 1 shows, the pressure is positive, $\alpha$ is the angle between slip surface and the positive direction of $\times$ axis and counterclockwise rotation is positive.

The equations of normal stress and shear stress are represented as follows:

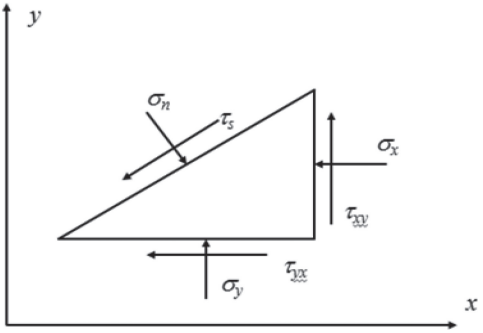


Figure 1. Stress state of a point on the slip surface of slope.

$$\sigma_n = \frac{1}{2}(\sigma_x + \sigma_y) - \frac{1}{2}(\sigma_x - \sigma_y)\cos 2\alpha + \tau_{xy}\sin 2\alpha \tag{4}$$

$$\tau_s = -\frac{1}{2}(\sigma_x - \sigma_y)\sin 2\alpha - \tau_{xy}\cos 2\alpha \tag{5}$$

The slope stability safety factor $F_S$ is defined as the ratio of anti-slide force to the sliding force according to the limit equilibrium theory. According to the actual engineering characteristics and the importance of the slope, $F_S$ is required to be more than 1.2 generally. This paper takes $F_S = 1.2$ as the critical state. The slope is in stable state when $F_S > 1.2$ and unstable when $F_S \leq 1.2$.

The equation of the safety factor of the slope stability is represented as follows:

$$F_s = \frac{T'}{T} = \frac{cL + N\tan\varphi}{T} \tag{6}$$

where $T'$ and T are anti-sliding force and sliding force, respectively; c and $\varphi$ are cohesion and friction angel, respectively; L is the length of the sliding surface; and N is normal supporting force.

The calculation of seismic safety factor time history of the slope is carried out on the basis of static and dynamic finite element analysis. Static normal stress $\sigma_{ns}$, static shear stress $\tau_{ss}$, dynamic normal stress $\sigma_{nd}$ and dynamic shear stress $\tau_{sd}$ are calculated respectively on the basis of the initial stress field of static calculation and each moment of additional dynamic stress field. The safety factors of the t moment under the earthquake action can be obtained as follows according to Eq. (6):

$$F_s(t) = \frac{\int_\Gamma (c_i + [\sigma_{nsi} + \sigma_{ndi}(t)\tan\varphi_i)d\Gamma}{\int_\Gamma (\tau_{ssi} + \tau_{sdi})d\Gamma} \tag{7}$$

where $\sigma_{nsi}$ and $\tau_{ssi}$ are the static normal stress and shear stress of $i$ element of slip surface, $\sigma_{ndi}$ and $\tau_{sdi}$ are the dynamic normal stress and shear stress of $i$ element of slip surface, $\Gamma$ is slip surface. $c_i$ is the internal cohesion and $\varphi_i$ is the friction angle of $i$ element of slip surface. The dynamic limit state equation under seismic action is represented as follows:

$$\frac{\int_\Gamma (c_i + [\sigma_{nsi} + \sigma_{ndi}(t)\tan\varphi_i)d\Gamma}{\int_\Gamma (\tau_{ssi} + \tau_{sdi})d\Gamma} - 1.2 = 0 \tag{8}$$

## 3 THE MAXIMUM ENTROPY METHOD TO DETERMINE THE PROBABILITY DENSITY FUNCTION

In 1948, Shannon introduced the concept of thermodynamic entropy into the information theory. He firstly proposed the concept of information entropy as a measure of the uncertainty of a random event or the amount of information (Pandey 2000; Sobczyk & Trebicki 1999).

The information entropy is only one for a particular information source. The information entropy is different for different information sources. Shannon defined the mathematical expectation of information as the information entropy, that is, the average information of the information source. Shannon introduced the following functions:

$$H(X) = E[\ln P(X_i)] = -\sum_{i=1}^{n} P(X_i) \ln P(X_i) \tag{9}$$

If the random event obeys to the continuous distribution of which the probability density is $f_X(x)$, the Shannon entropy is:

$$H(X) = -\int_{-\infty}^{+\infty} f_X(x) \ln f_X(x) dx \tag{10}$$

The probability distribution obtained is the least bias when the information entropy is the maximum by given additional constraint conditions, which can obtain a way to construct the optimal probability distribution. The meaning of the maximum entropy principle is that in all feasible solutions the largest entropy should be chosen to meet certain constraints when the data or conditions are not enough. Because entropy can indicate the degree of uncertainty of a system, it is the most objective for the solution containing the least subjective elements (Zhang 2009).

The m order origin moments of the random variable $v_{X_i} (i = 0,1,\ldots,m)$ used as the constraint conditions are as follows to make Eq. (20) to the maximum:

$$\nu_{X_i} = E(X^i) = \int_{-\infty}^{+\infty} x^i f_X(x) dx \quad i = 0,1,\ldots,m \tag{11}$$

The central moment of random variable $X$ is:

$$\mu_{X_i} = E[(X - \mu_X)^i] = \int_{-\infty}^{+\infty} (x - \mu_X)^i f_X(x) dx \quad i = 0,1,\ldots,m \tag{12}$$

where $\mu_x$ is the mean value of $X$, that is $v_{X_1}$

The establishment of the Lagrange functions is as follows using Lagrange multiplier method:

$$L = H + \sum_{i=0}^{m} \lambda_i [\int_{-\infty}^{+\infty} x^i f_X(x) dx - v_{X_i}] \tag{13}$$

where $\lambda_0, \lambda_1, \ldots, \lambda_m$ are undetermined constants. In the stable point $\dfrac{\partial L}{\partial f_X(x)} = 0$.

The maximum entropy probability density function is:

$$f(x) = \exp(\lambda_0 + \sum_{i=1}^{n} \lambda_i x^i) \tag{14}$$

The expression of $\lambda_0, \lambda_1, \ldots, \lambda_m$ can be obtained as follows by the constraints:

$$m_i = \frac{\int_R x^i \exp\left(\sum_{i=1}^{n} \lambda_i x^i\right) dx}{\int_R \exp\left(\sum_{i=1}^{n} \lambda_i x^i\right) dx} \tag{15}$$

Eq. (15) can be rewritten as follows to facilitate the numerical solution:

$$1 - \frac{\int_R x^i \exp\left(\sum_{i=1}^{n} \lambda_i x^i\right) dx}{m_i \int_R \exp\left(\sum_{i=1}^{n} \lambda_i x^i\right) dx} = r_i \tag{16}$$

In order to establish optimization function expression, define:

$$R = \sum_{i=1}^{m} r_i^2 = \min \tag{17}$$

where $r_i$ is the residuals. The method of numerical calculation can be used to reduce Eq. (16) to zero. The minimum value of $R$ can be obtained by nonlinear programming. We consider Eq. (17) convergent when $R < \varepsilon$ or $|r_i| < \varepsilon$ and then $\lambda_0, \lambda_1, \ldots, \lambda_m$ can be solved.

Maximum entropy method is better fitting the probability density function and more in line with the practice engineering, as it makes full use of each moment, skew coefficient, kurtosis coefficient of the parameters to directly reflect the true information.

## 4 DYNAMIC FUZZY RELIABILITY ANALYSIS UNDER SEISMIC ACTION

### 4.1 *The establishment of dynamic fuzzy limit state equation*

The seismic action is complex and special in the reliability analysis of the bedding rock slope under seismic action, and its influence is usually determined by experience, so it has very strong fuzziness. Fuzzy random event of slope instability of can be represented as follows due to the fuzziness of slope instability:

$$\tilde{E} = \left\{(z, \mu_{\tilde{E}}(z)) \middle| z \in \tilde{\Omega}\right\} \tag{18}$$

where $z$ is the state random variable of fuzzy random event $\tilde{\Omega}$.

It is unreasonable to define the performance function equal to zero to indicate limit state of slope stability due to the fuzziness of slope instability. The membership function $\mu_{\tilde{E}}(z)$ is introduced to characterize the stability of the slope when the slope is in the middle of the transition from "total instability" to "complete stability". Meanwhile fuzzy limit interval is introduced to replace the traditional limit state which is near zero, as shown in Figure 2. Fuzzy limit interval is expressed by [$a$,$b$] where $a$ and $b$ are the undetermined constants (Li et al. 2006). The comparison is shown as follows:

Fuzzy random event of slope instability can be represented as:

$$\tilde{E} = \left\{(z, \mu_{\tilde{E}}(z)) \middle| z \in \tilde{\Omega}\right\} \tag{19}$$

The probability of slope instability event $\tilde{E}$ is:

$$\tilde{p}_f = \int_{-\infty}^{+\infty} \mu_{\tilde{E}}(z) f_Z(z) dz \tag{20}$$

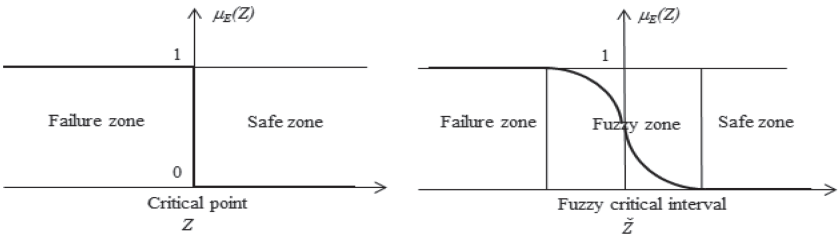


Figure 2. Comparison of fuzzy critical interval and conventional critical point.

If the probability density function of the random variable affecting slope failure events $X(X1,X2,\ldots\ldots)$ is expressed as $f_X(x)$, the probability of the failure of the slope is represented as follows:

$$\tilde{p}_f = \int_{-\infty}^{+\infty} \mu_{\tilde{E}}(z)[g_X(x)]f_X(x)dx \tag{21}$$

The membership function $\mu_{\tilde{E}}(z)$ of slope stability coefficient is decreasing function and, so $1-\mu_{\tilde{E}}(z)$ can be regarded as a random variable, like the cumulative distribution function $F_{X_{n+1}}(x_{n+1})$ of $X_{n+1.}$ Hence, Eq. (21) can be turned into as follows:

$$\tilde{p}_f = \int_{-\infty}^{+\infty} \{1 - F_{X_{n+1}}[g_X(x)]\} f_X(x)dx = \int_{-\infty}^{+\infty}\int_{g_X(x)}^{+\infty} f_{X_{n+1}}(x_{n+1})f_X(x)dxdx_{n+1} \tag{22}$$

The cumulative distribution function and probability density function of the new random variable $X_{n+1}$ are represented as follows:

$$F_{X_{n+1}}(x_{n+1}) = 1 - \mu_{\tilde{E}}(x_{n+1}) \tag{23}$$

$$f_{X_{n+1}}(x_{n+1}) = -\frac{\partial \mu_{\tilde{E}}(x_{n+1})}{\partial x_{n+1}} \tag{24}$$

The failure domain of the fuzzy reliability of slope is $\{x \mid g_X(x) \le x_{n+1}\}$ according to Eq. (22), therefore the corresponding equivalent performance function is:

$$\tilde{Z} = g_X(X) - X_{n+1} \tag{25}$$

$[a,b]$can be approximated by the "zero" point to the interval of the symmetry, that is, $a=-b$. The membership function is taken as the descending half trapezoid distribution, that is:

$$\mu_{\tilde{E}}(z) = \begin{cases} 1 & z \le a \\ \dfrac{b-z}{b-a} & a < z \le b \\ 0 & z > b \end{cases} \tag{26}$$

The dynamic fuzzy performance function of bedding rock slope under seismic action can be obtained as follows according to the dynamic limit state equations of slope (8):

$$\tilde{Z} = \frac{\int_{\Gamma}(c_i + [\sigma_{nsi} + \sigma_{ndi}(t)\tan\varphi_i)d\Gamma}{\int_{\Gamma}(\tau_{ssi} + \tau_{sdi})d\Gamma} - 1.2 - X_3 \tag{27}$$

where the internal cohesion $c$ and the friction angle $\varphi$ are the random variable and $X_3$ is the new random variable. $X_3$ obeys uniform distribution on the interval (a, b), of which the cumulative distribution function and probability density function are as follows:

$$f_U(x_3) = \frac{1}{b-a}, \ a \le x_3 < b \tag{28}$$

$$F_U(x_3) = \begin{cases} 0 & x_3 \le a \\ \dfrac{x_3 - a}{b-a} & a < x_3 \le b \\ 1 & x_3 > b \end{cases} \tag{29}$$

where the mean value of $X_3$ is $\mu_{X_3} = \frac{a+b}{2}$ and the standard deviation is $\sigma_{X_5} = \frac{b-a}{2\sqrt{3}}$.

Hence, the dynamic fuzzy limit state equation of bedding rock slope under seismic action is:

$$\frac{\int_\Gamma (c_i + [\sigma_{nsi} + \sigma_{ndi}(t)\tan\varphi_i)d\Gamma}{\int_\Gamma (\tau_{ssi} + \tau_{sdi})d\Gamma} - 1.2 - X_3 = 0 \tag{30}$$

### 4.2 *The method of calculating the dynamic fuzzy reliability*

The equivalent performance function can be obtained according to the expression (27). If the mean value and former $N$ order central moments of random variable $\tilde{Z}$ are the constraint conditions of performance function $\tilde{Z}$, the optimization problem can be obtained as follows:

$$\max H = -\int_R f(\tilde{Z}) \ln f(\tilde{Z}) d\tilde{Z} \tag{31}$$

The constraint conditions are represented as follows:

$$\int_R f(\tilde{Z}) d\tilde{Z} = 1 \tag{32}$$

$$\int_R \tilde{Z} f(\tilde{Z}) d\tilde{Z} = m_{\tilde{Z}} \tag{33}$$

$$\int_R (\tilde{Z} - m_{\tilde{Z}})^i f(\tilde{Z}) d\tilde{Z} = \mu_{\tilde{Z}}^{(r)} \tag{34}$$

where $m_{\tilde{Z}}$ is the mathematical expectation of random variable $\tilde{Z}$, $\mu_{\tilde{Z}}^{(r)}$ is the r order central moment of random variable $\tilde{Z}$.

The mathematical expectation $m_{\tilde{Z}}$ and each order central moment $\mu_{\tilde{Z}}^{(r)}$ of equivalent performance function can be calculated approximately by the mathematical expectation $m_{x_i}$ and each order central moment $\mu_{x_i}^{(r)}$ of basic random variable $x_i$.

The analytic form of maximum entropy probability density function of the equivalent [performance function $\tilde{Z}$ can be obtained as follows through Lagrangian multiplier method:

$$f(\tilde{Z}) = \exp(\lambda_0 + \sum_{i=1}^{n} \lambda_i (\tilde{Z} - m_{\tilde{Z}})^i) \tag{35}$$

Hence the fuzzy failure reliability of the slope instability is:

$$\tilde{p}_{\mathrm{f}} = P_r(\tilde{Z} \le 0) = \int_{-\infty}^{0} f(\tilde{Z})d\tilde{Z} = \int_{-\infty}^{0} \exp(\lambda_0 + \sum_{i=1}^{n} \lambda_i (\tilde{Z} - m_{\tilde{Z}})^i)d\tilde{Z} \tag{36}$$

Therefore, the fuzzy failure reliability can be solved on condition that the Lagrangian multiplier $\lambda_0, \lambda_1, \ldots, \lambda_m$ are solved by related mathematical program implementation.

### 4.3 *Dynamic fuzzy reliability evaluation method for slope stability*

The failure probability of the slope becomes a random variable with the time variation under seismic load. Therefore, how to give a single value evaluation criterion which is similar to static conditions becomes a problem.

In the whole process of earthquake, the failure probability of slope is likely to be instantaneous, and the failure probability can be rapidly changed due to the change of seismic acceleration direction, which may cause a certain shear failure or excessive deformation. The failure probability of slope is likely to be very large but decrease rapidly next moment for the change of the directions of the seismic acceleration in the whole process of earthquake. In that case there may be a certain shear failure or excessive deformation of the rock and soil but the slope isn't necessarily unstable. Hence it is conservative to evaluate the stability of the slope by the maximum failure probability; moreover the average failure probability may overestimate the dynamic stability of the slope.

Therefore, the average maximum failure probability is presented in this paper as the evaluation index. If the failure probability of the slope under static action is $p_{\mathrm{fo}}$, the failure probability will be larger than $p_{\mathrm{fo}}$ due to the seismic action and the failure probability will be fluctuated with time. The failure probability which are smaller than $p_{\mathrm{fo}}$ are ignored to not overestimate the slope stability. The average maximum failure probability is defined as follows:

$$\bar{p}_{\mathrm{ff}} = \frac{\sum_{i=0}^{n} \int_{2i}^{2i+1} p_{\mathrm{f}}(t)}{\sum_{i=0}^{n} (t_{2i+1} - t_{2i})} \tag{37}$$

where $\bar{p}_{\mathrm{ff}}$ is the average maximum probability, $p_{\mathrm{f}}(t)$ is the failure probability time history, $\sum_{i=0}^{n} \int_{2i}^{2i+1} p_{\mathrm{f}}(t)$ is represented for the integration of failure probability of each period of time when the failure probability is greater than $p_{\mathrm{fo}}$ to each period of time, that is the area of shadow. $\sum_{i=0}^{n} (t_{2i+1} - t_{2i})$ is represented for the sum of the time when the failure probability is larger than $p_{\mathrm{fo}}$. The calculation diagram is shown in Figure 3.

The expression of the average maximum failure probability is simplified as follows:

$$\bar{p}_{\mathrm{ff}} = \frac{\sum p_{\mathrm{ff}}}{n} \tag{38}$$

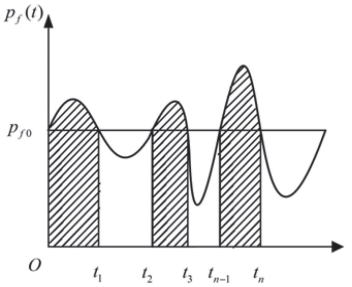


Figure 3. Calculation diagrammatic sketch of the average big failure probability.

where $\overline{p}_{ff}$ is the average maximum probability, $p_{ff}$ is the probability of each period of time which are greater than $p_{f0}$ that is the maximum failure probability, n is the total number of points of maximum failure probability of time history curve.

## 5 ILLUSTRATIVE EXAMPLE

The bedding rock slope with two weak interlayers is chosen as the calculation model. The slope height H = 30 m, the slope angle is 60 degrees and the angle of the weak interlayers is 20 degrees. The geometrical dimension of the slope is shown in Figure 4.

### 5.1 *Numerical simulations*

The numerical simulation of the bedding rock slope is conducted by the dynamic analysis module of finite difference software FLAC$^{3D}$. Because FLAC$^{3D}$ is weak in before processing, the finite element software ANSYS with powerful modeling function is taken advantaged of to establish a three-dimensional model of the rock slope, and then import the model into FLAC$^{3D}$ by use ANSYS TO FLAC$^{3D}$ interface program for static and dynamic analysis. The calculation model and the grid are shown in Figure 5. The rock mass and the soft interlayer material are the elastic plastic material in the model, and the Mohr—Coulomb yield criterion is used. The physical mechanical parameters of rock mass are shown in Table 1. The slip surface is parallel to surface of the rock mass of the sliding bed located in the middle of the weak interlayers in this paper.

Rayleigh damping, local damping and viscous damping are provided in FLAC$^{3D}$ dynamic analysis module. The damping coefficient is adopted In this paper that is 0.156. Local damping can achieve convergence by increasing or decreasing the quality of the node or the structure unit in the vibration cycle. The static boundary (viscous boundary) and the free field boundary in the dynamic analysis are provided in FLAC$^{3D}$, which is a good solution to the boundary problem in dynamic analysis. The research object is the rock slope in this paper. Because the bedrock modulus is large, it can be considered as a rigid foundation, therefore the model base don't have to set the static boundary conditions, but to set free field boundary surrounding the model. Boundary is set as shown in Figure 6.

The Kobe is selected as the seismic wave and imported after filtering and baseline correction. The peak acceleration of seismic wave is 0.3447 g and the duration of it is 20s. The acceleration time history curve of seismic wave is shown in Figure 7.

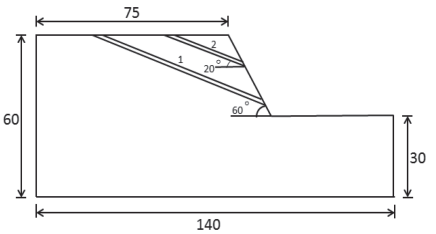


Figure 4. Geometric dimension of slope model.

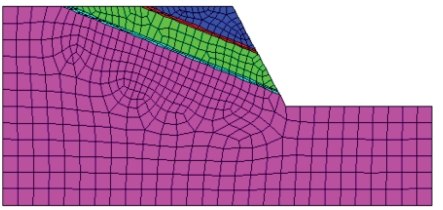

Figure 5. Computational model and grid partition.

The fuzzy critical interval [a, b] (which is with "zero" point for the symmetric interval), the absolute value of a and b are taken as a time of the fuzzy limit state variable. The time history curve of fuzzy failure probability and reliability index can be solved according to the fuzzy limit state equation of slope.

### 5.2 *The calculation results and comparison analysis*

The initial static stress field calculated by FLAC$^{3D}$ is shown in Figures 8–10. It can be seen that $\sigma_x$,$\sigma_y$ and $\tau_{xy}$ of slope are in line with the law of stress distribution and the shear stress is concentrated at the foot of slope.

The normal stress and shear stress of slip surface can be calculated by Eqs. (4) and (5) after the initial static stress field and dynamic stress field are plugged into. Then the fuzzy limit state equation can be obtained by Eq. (29). The fuzzy failure probability of the two slip surfaces can be obtained as shown in Figure 11, and the reliability index is shown in Figure 12.

The fuzzy failure probability of the bedding rock slope under static action is 20.22%. The average maximum fuzzy probability of slip surface 1 is 36.28% and the reliability index is 0.3509. The average maximum fuzzy probability of slip surface 2 is 25.02% and the reliability index is 0.6738. The calculation results of pseudo static method are shown in Table 2 to compare easily.

Table 1. Materials of soil mechanical parameters.

| Rock stratum | Density $\rho$/kg/m$^3$ | Shear modulus G/GPa | Bulk modulus K/GPa | Extension strength $\sigma_t$/MPa | Cohesion $c$/MPa | | Internal friction Angle $\varphi$/(°) | |
|---|---|---|---|---|---|---|---|---|
| | | | | | Mean value | Standard deviation | Mean value | Standard deviation |
| Weak interlayers | 2300 | 1.65 | 3.05 | 0.01 | 0.03 | 2.77 | 32 | 4.58 |
| Rock mass | 2600 | 10.22 | 14.65 | 1.60 | 1.00 | 2.77 | 47 | 4.58 |

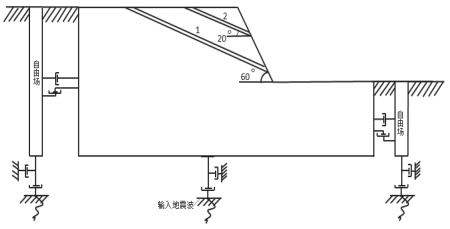


Figure 6. Sketch map of slope boundary condition.

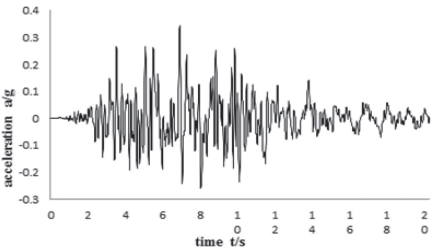


Figure 7. Seismic acceleration time history curve.

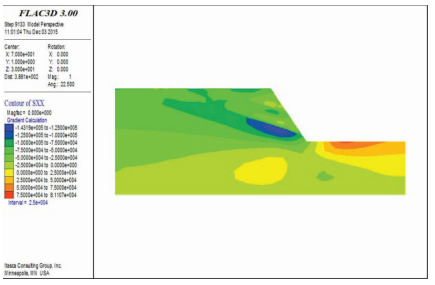


Figure 8. Static stress $\sigma_x$ contour image of slope.

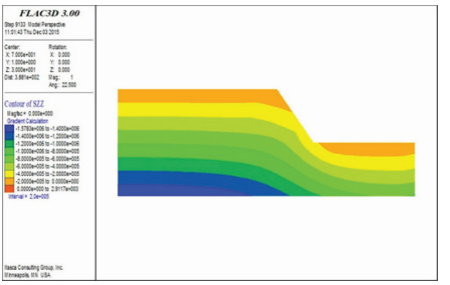


Figure 9. Static stress $\sigma_y$ contour image of slope.

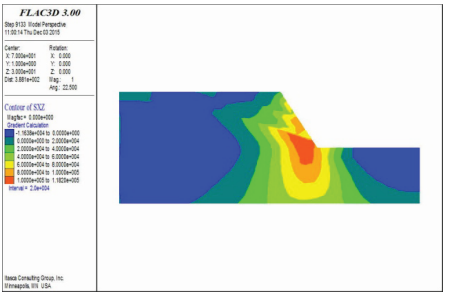


Figure 10. Static stress $\tau_{xy}$ contour image of slope.

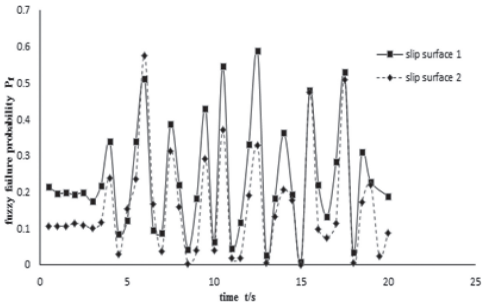


Figure 11. Failure probability time history curve.

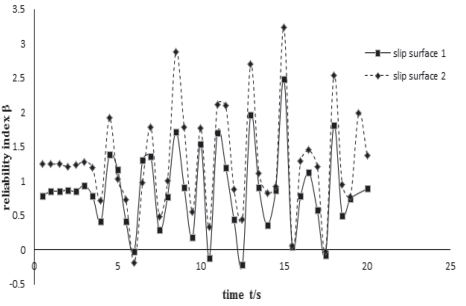


Figure 12. Reliability index time history curve.

Table 2. Computation results of fuzzy failure probability.

| Methods | Slip surface 1 | | Slip surface 2 | |
|---|---|---|---|---|
| | Fuzzy failure probability | Reliability index | Fuzzy failure probability | Reliability index |
| Method of the paper | 36.28% | 0.3509 | 25.02% | 0.6738 |
| Pseudo static method | 32.55% | 0.4522 | 23.28% | 0.7296 |

The results can be seen from the table that the fuzzy failure probability of the pseudo static method is smaller than the method of the paper. The pseudo static method ignores the seismic characteristics and the dynamic properties of rock and soil so that it may give the dangerous results. As a result, the method used in the paper is more reliable which can reflects the dynamic characteristics of the slope factually and it can not only give the fluctuation curve of fuzzy failure probability in the whole duration of the seismic action but also evaluate stability of the slope more safely by the average maximum failure probability index.

## 6 CONCLUSIONS

In this paper, the time history analysis method is used to analyze the dynamic response of slope under seismic action. The maximum entropy method is used to determine the probability density function and the dynamic fuzzy reliability is calculated considering the fuzziness of the limit state. The conclusions can be drawn as follows:

1. Time history analysis method can give accurate results as it considers various factors. The dynamic response rule can be reflected factually by the internal force and deformation of each period of time during the earthquake process.

2. The maximum entropy method used in the paper to determine the probability density function break through the restrictions that the probability distribution of random variable is known. The reliability of geotechnical engineering can be solved more accurately while each order moments, skew coefficient and kurtosis coefficient of sample parameters are fully made use of.
3. The failure mechanism and stability evaluation of slope under dynamic action is a very complex problem. The maximum failure probability is too conservative, and the average failure probability may overestimate the dynamic stability of slope as the evaluation index. In this paper, the average failure probability is proposed as the evaluation index, and the corresponding calculation method is given. This method has a good reference value for bedding rock slope engineering, but it should be pointed out that the standard value of slope stability under the seismic action should be tested and corrected by a large number of earthquake examples to be used for engineering practice.

## REFERENCES


Al-homoud, A.S. & Tahtamoni, W.W. 2001. A reliability based expert system for assessment and mitigation of landslides hazard under seismic loading. *Natural Hazards* 24(1): 13–51.

Fan, S.L. et al 2008. Reliability analysis of roller compacted concrete. *Chinese Journal of Rock Mechanics and Engineering* 27(3): 564–571.

Gong, W.H. 2013. *Soil Mechanics*. Wuhan: Huazhong University of Science and Technology Press.

Li, H.B. et al 2007. Factor of safety analysis of bedding rock slope under seismic load. *Chinese Journal of Rock Mechanics and Engineering* 12: 2385–2394.

Li, H.S. et al 2006. Calculation of random-fuzzy reliability of steep slopes. *Chinese Journal of Geotechnical* 08: 1019–1022.

Liu, H.S. 2006. *Study on Analysis Method of Rock Slope Seismic Stability*. Institute of Engineering Mechanics, China Earthquake Administration.

Liu, H.L. et al 2003. Time history analysis method of slope seismic stability. *Rock and soil mechanics* 04: 553–556+560.

Liu, L.P. et al 2001. The evaluation of seismic slope stability analysis methods. *Journal of Chongqing Jiaotong University* 03: 83–88.

Pandey, M.D. 2000. Direct estimation of quantile functions using the maximum entropy principle. *Structural Safety* 22(1): 61–79.

Shinoda, M. et al 2006. Reliability-based seismic deformation analysis of reinforced soil slopes. *Soils and Foundations* 46(4): 477–490.

Sobczyk, K. & Trebicki, J. 1999. Approximate probability distributions for stochastic systems: maximum entropy method. *Computer Methods in Applied Mechanics and Engineering* 168(1): 91–111.

Wang, Y.J. et al 2014. Research and Application of the Theory of Non-determination of Geotechnical Engineering. Beijing: Science Press.

Yan, Z.X. et al 2011. Dynamic response and deformation mechanism of a bedding rock slope under earthquakes. *Chinese Journal of Geotechnical Engineering* S1:61–65.

Zhao, J.M. et al 2002. Analysis of earth rock fill dam slope stability under seismic action. In Li, Y.S. & Gao G.Y. (eds.), *Environmental geotechnical engineering theory and practice*. Tongji University Press, Shanghai, 239–243.

Zhang, B,Y. et al 2000. Arch dam abutment aseismic stability analysis. *Journal of Hydraulic Engineering* 11: 55–59.

Zhang, J.H. et al 1999. Dynamic safety evaluation of slopes or dam foundation using rigid body-spring element method. *Chinese Journal of Rock Mechanics and Engineering* 4:19–23.

Zhang, M. 2009. *Methods and procedures of structural reliability analysis*. Beijing: Science Press.

*Rock Dynamics: From Research to Engineering – Li et al. (Eds)*
*© 2016 Taylor & Francis Group, London, ISBN 978-1-138-02953-8*

# Pseudo-dynamic analysis of stability of layered rock slope subjected to seismic loads

W. Zhou, H.B. Li, Y.Q. Liu & S.B. Chai
*State Key Laboratory of Geomechanics and Geotechnical Engineering, Institute of Rock and Soil Mechanics, Chinese Academy of Sciences, Wuhan, China*

ABSTRACT: This paper presents a study on the stability of slope in considering of dynamic characteristics of seismic loads. A new formula is proposed to calculate the safe factor of layered rock slope under seismic loads, based on the combination of the limit equilibrium analysis and the pseudo-dynamic method. Then, by comparing with the safe factor calculated by pseudo-static method, the deduced formula is proved to be available to calculate the safe factor of layered rock slope. Finally, parametric studies are carried out to investigate the influence of the joint friction angle, the seismic acceleration coefficients, the dip angle of the joint surface and the slope angle on seismic stability of layered rock slopes.

## 1 INTRODUCTION

Stability analysis of rock slopes is crucial for safe design in geotechnical engineering. The analytical study of stability of slopes under static condition has been carried out extensively by using the limit equilibrium method (e.g. Srbulov 2001), the upper bound limit analysis (e.g. Porbaha 2000), the lower bound limit analysis (e.g. Singh 1993, Michalowski 1995), and the slop line method (e.g. Zhao 1996). Under seismic loading, Ling et al. (1997) used the pseudo-static approach in conjunction with the limit equilibrium method to assess the stability and permanent displacement of geosynthetic reinforced soil structures subjected to horizontal earthquake acceleration.

In the pseudo-static method, the inertia forces are simply obtained by the product of seismic coefficients and the weight of the failure wedge. However, the dynamic nature of seismic loading is not considered in this method. In order to overcome the shortcoming of pseudo-static method, Steedman & Zeng (1990) presented a time-dependent approach called "pseudo-dynamic method" to compute seismic active earth pressure on vertical retaining walls. The influences of the phase and amplitude variations of horizontal and vertical earthquake accelerations, velocity of primary and shear waves, and the period of lateral shaking can be taken into account by the pseudo-dynamic approach. Ebeling & Morrison (1993) studied the soil mechanics aspects of the design of waterfront retaining structures built to withstand the effects of earthquake loadings by the pseudo-dynamic approach. Choudhury et al. (2007) applied the pseudo-dynamic approach with the help of upper bound limit analysis to evaluate the seismic stability of reinforced soil walls with cohesionless backfills. Basha & Babu (2009) presented the use of the pseudo-dynamic method to compute the rotational displacements of gravity retaining walls under the passive condition when subjected to seismic loads. Shafiee et al. (2010) used the pseudo-dynamic approach to estimate seismic passive earth thrust on retaining walls with cohesive-frictional backfills. Ghosh & Kolathayar (2011) studied the seismic passive earth pressure behind a non-vertical cantilever retaining wall by the pseudo-dynamic method.

The aim of present study is to evaluate the stability of the layered rock slope under seismic action. The pseudo-dynamic method is used to simulate the input of acceleration-time history, the mathematical expression of the safe factor of slope are then obtained by the limit equilibrium method. Then, compared with the pseudo-static method, the deduced expression

is proved to be feasible to evaluate the stability of layered rock slope subjected to seismic loads. At last, the parametric studies show that the stability of layered rock slope is influenced to some extents by joint friction angle, seismic acceleration coefficients, the dip angle of the joint surface and slope angle. Besides, the effects of each of these mentioned parameters are also investigated.

## 2 ANALYSIS METHOD

### 2.1 *Pseudo-dynamic approach*

In the pseudo-dynamic approach, the earthquake acceleration is simulated by sinusoidal motions. The rationality of choosing sinusoidal wave is verified by Basha & Babu (2010). The earthquake acceleration is considered as a uniform sinusoidal function of time ($t$) and depth ($z$) with the period of seismic shaking ($T$) as follows:

$$\alpha_h(z,t) = k_h g \sin 2\pi\left(\frac{t}{T} - \frac{H-z}{v_s}\right) \tag{1}$$

$$\alpha_v(z,t) = k_v g \sin 2\pi\left(\frac{t}{T} - \frac{H-z}{v_p}\right) \tag{2}$$

where $\alpha_h(z,t)$ and $\alpha_v(z,t)$ are horizontal and vertical seismic accelerations with amplitudes of $k_h g$ and $k_v g$ at the base of slope, $H$ is the height of slope, and $T$ is the period of earthquake shaking equal to $2\pi/\omega$.

The parameters $v_s$ and $v_p$ are transverse and longitudinal seismic wave propagation velocity in rock mass, which are calculated as:

$$v_s = \sqrt{G/\rho} \tag{3}$$

$$v_p = \sqrt{\frac{G(2-2\mu)}{\rho(1-2\mu)}} \tag{4}$$

where $\rho$ is density and $\mu$ is Poisson's ratio, $G$ is the rock mass shear modulus and is calculated by the following equation:

$$G = \frac{E}{2(1+\mu)} \tag{5}$$

where $E$ is the rock mass elastic modulus.

### 2.2 *Problem definition and solution*

As shown in Figure 1, the slope and the translational failure surface make angles $\beta$ and $\alpha$, respectively with the horizontal plane.

According to the geometrical relationship shown in Figure 1, the weight of the failure wedge $ABC$ can be expressed as follows:

$$W = 0.5\gamma H^2(\cot\alpha - \cot\beta) \tag{6}$$

where $\gamma$ is rock unit weight.

The mass of shaded element of thickness ($dz$) in Figure 1 can be expressed by

$$m(z) = \frac{\gamma(H-z)[\cot(\delta-\theta) - \cot\delta]dz}{g} \tag{7}$$

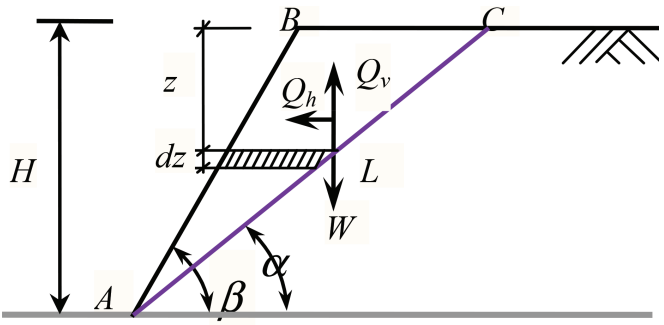


Figure 1. Model slope and failure mechanism.

The horizontal inertia force on the shaded element is equal to $m(z) \cdot \alpha_h(z,t)$. Thus, the total horizontal inertia force $Q_h$ within the failure wedge $ABC$ can be expressed by

$$Q_h = \int_0^H m_{(z)}\alpha_h(z,t) = \frac{\lambda k_h \gamma(\cot\alpha - \cot\beta)}{4\pi^2}\left\{2\pi H\cos 2\pi\left(\frac{t}{T}-\frac{H}{\lambda}\right)+\lambda\left[\sin 2\pi\left(\frac{t}{T}-\frac{H}{\lambda}\right)-\sin 2\pi\left(\frac{t}{T}\right)\right]\right\} \quad (8)$$

where $\lambda$ is the wave length of shear waves equal to $T \cdot v_s$.

In the similar manner, the total vertical inertia force $Q_v$ within the failure wedge $ABC$ is given by

$$Q_v = \int_0^H m_{(z)}\alpha_v(z,t) = \frac{\eta k_v \gamma(\cot\alpha - \cot\beta)}{4\pi^2}\left\{2\pi H\cos 2\pi\left(\frac{t}{T}-\frac{H}{\eta}\right)+\eta\left[\sin 2\pi\left(\frac{t}{T}-\frac{H}{\eta}\right)-\sin 2\pi\left(\frac{t}{T}\right)\right]\right\} \quad (9)$$

where $\eta$ is the wave length of primary waves equal to $T \cdot v_p$.

According to Figure 1, tangential force $S$ and normal force $N$ of sliding surface $AC$ can be expressed by

$$S = (W - Q_v)\sin\alpha + Q_h\cos\alpha \quad (10)$$

$$N = (W - Q_v)\cos\alpha - Q_h\sin\alpha \quad (11)$$

Based on the limit equilibrium method, the safe factor $K$ can be defined combined with Figure 1, and the expression is:

$$K = \frac{cl + N\tan\varphi}{S} \quad (12)$$

where $l$ is the length of sliding surface $AC$, as equals to $H/\sin\alpha$. $c$ is joint cohesion, and $\varphi$ is the joint friction angle.

Having substituted Eqs. (6), (8), (9), (10) and (11) into Eq. (12), $K$ can be expressed by

$$K = \frac{\dfrac{4\pi^2 cH}{\gamma(\cot\alpha - \cot\beta)\sin\alpha} + [(2\pi^2H^2 - \eta k_v x)\cos\alpha - \lambda k_h y\sin\alpha]\tan\varphi}{(2\pi^2H^2 - \eta k_v x)\sin\alpha + \lambda k_h y\cos\alpha} \quad (13)$$

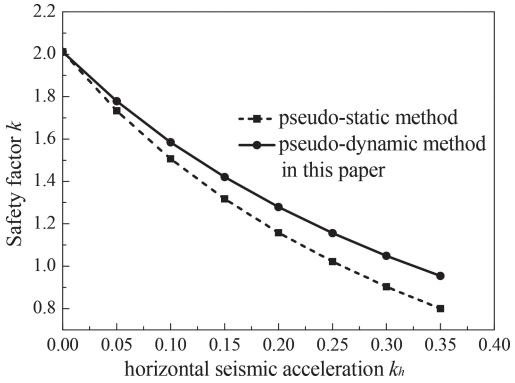


Figure 2. Comparison of safe factors by different methods.

where,

$$x = 2\pi H \cos 2\pi\left(\frac{t}{T} - \frac{H}{\eta}\right) + \eta\left[\sin 2\pi\left(\frac{t}{T} - \frac{H}{\eta}\right) - \sin 2\pi\left(\frac{t}{T}\right)\right] \tag{14}$$

$$y = 2\pi H \cos 2\pi\left(\frac{t}{T} - \frac{H}{\lambda}\right) + \lambda\left[\sin 2\pi\left(\frac{t}{T} - \frac{H}{\lambda}\right) - \sin 2\pi\left(\frac{t}{T}\right)\right] \tag{15}$$

Thus, for a certain layered rock slope with the basic parameters shown in Figure 1, the stability of the slope under seismic action can be evaluated by Eq. (13).

### 2.3 *Verification*

In this section, a case is carried out to validate the feasibility of pseudo-dynamic approach to calculate the stability of slope under seismic action. Figure 2 shows the variation of safe factor $K$ with the horizontal seismic acceleration coefficient $k_h$ calculated by pseudo-static approach and pseudo-dynamic approach respectively for $H$ = 100 $m$, $k_v$ = 0.5 $k_h$, $\alpha$ = 20°, $\beta$ = 60°, $c$ = 30 kPa, $\varphi$ = 35°, $\gamma$ = 27000 $N/m^3$ and $T$ = 0.2$s$. It can be seen from the figure that the variation tendency of $K$ with $k_h$ calculated by pseudo-dynamic method is basically consistent to which is calculated by pseudo-static method. However, $K$ calculated by pseudo-dynamic method is greater than that calculated by pseudo-static method. The mainly reason is that phase change in seismic wave propagation and time factor are taken into account in pseudo-dynamic method. By pseudo-dynamic method, the seismic inertia force is not entirely calculated according to the peak value of seismic acceleration, but is calculated according to the peak value of seismic acceleration by pseudo-static method. Hence, the seismic inertia force calculated by pseudo-static method is greater than which is calculated by pseudo-dynamic method, and $K$ in pseudo-dynamic method is greater than that in pseudo-static method.

## 3 PARAMETRIC STUDY

From Eq. (13), the stability of the slope is influenced by slope parameters $\alpha$ and $\beta$, joint cohesion $c$, joint friction angle $\varphi$, and the seismic parameters $k_h$ $k_v$. Therefore, it is necessary to carry out parametrical study to analyze impacts of these factors on the safe factor. In this section, it's assumed that $H$ = 50 $m$, $\gamma$ = 27000 $N/m^3$, $\mu$ = 0.25, $G$ = 10 $GPa$, $T$ = 0.2 $s$.

### 3.1 *Effect of seismic acceleration coefficients on safe factor*

Figure 3(a) shows the variation of safe factor $K$ with the horizontal seismic acceleration coefficient $k_h$ and joint friction angle $\varphi$ for $c$ = 30 kPa, $k_v$ = 0.5 $k_h$, $\alpha$ = 20° and $\beta$ = 60°. It can

be seen from the figure that $\varphi$ has an increasing effect while $k_h$ has a decreasing effect on the safe factor $K$. That is because a greater horizontal seismic acceleration coefficient means a greater sliding force, and a lower friction angle implies a smaller joint friction factor, both of which threaten the stability of slope. Figure 3(a) also depicts that with the increasing $\varphi$, the distance between the three curves is increasing. This phenomenon shows that with the increase of $\varphi$, $k_h$ has a greater effect on $K$.

The influence of vertical seismic coefficient $k_v$ on $K$ for $c$ = 30 kPa, $k_h$ = 0.2, $\alpha$ = 20° and $\beta$ = 60°is shown in Figure 3(b). It can be observed that the safe factor $K$ monotonously increases with the increasing joint friction angle $\varphi$. Moreover, the different $k_v$ curves are almost coincident. This kind of behavior means the variation of $k_v$ has little influence on $K$.

### 3.2 *Effect of the dip angle of joint surface and slope angle on safe factor*

The influence of dip angle of joint surface $\alpha$ and slope angle $\beta$ on safe factor is shown in Figures 4(a) and 4(b) for $c = 30\ kPa$, $k_h = 0.2$, $k_v = 0.5\ k_h$.

It can be seen from the Figure 4(a) that $\alpha$ has a decreasing effect on the safe factor $K$. The reason is that with the larger value of $\alpha$, the volume of sliding mass is larger, which means a greater sliding force in earthquake. And it can also be seen from the figure that with the increase of $\alpha$, the distance between the three curves is increasing, which means with the increase of joint friction angle $\alpha$ has a greater effect on $K$.

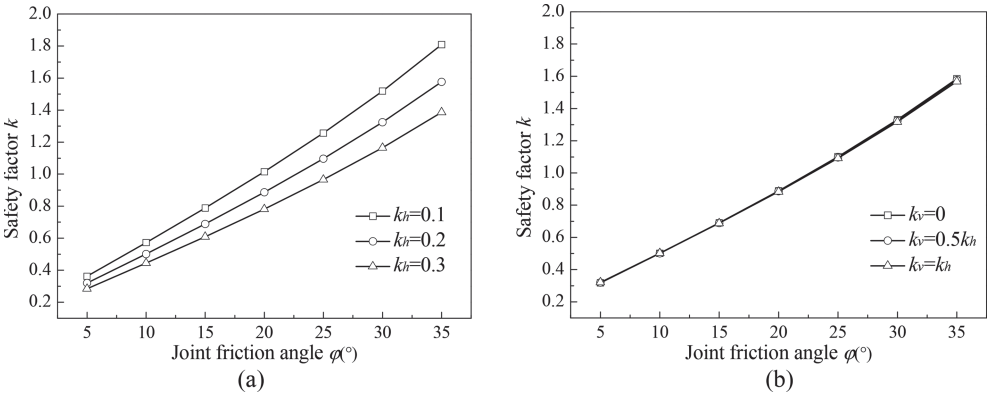


Figure 3. Effect of seismic acceleration coefficients on safe factor: (a) Effect of horizontal seismic acceleration coefficient, (b) Effect of vertical seismic acceleration coefficient.

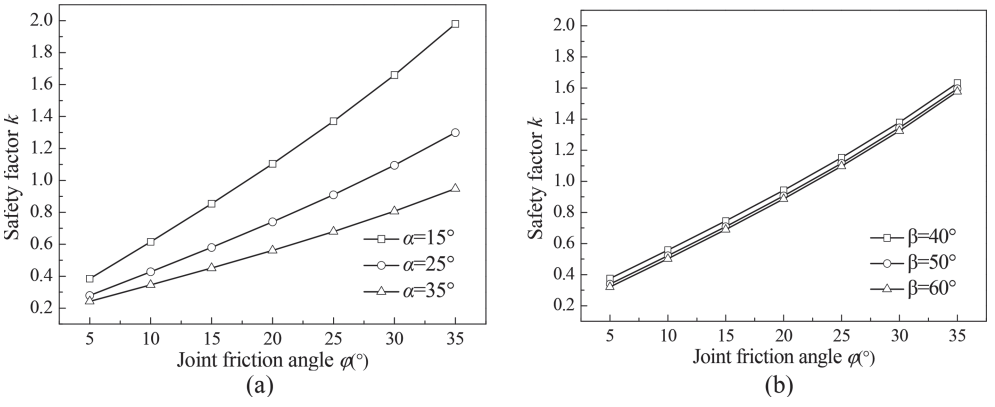


Figure 4. Effect of slope parameters on safe factor: (a) Effect of the dip angle of joint surface, (b) Effect of slope angle.

As shown in Figure 4(b), it can be observed that the value of $K$ decreases with the increase of $\beta$. It is because as the value of dip angle of joint surface is certain, the volume of sliding mass is larger when slope angle increases, which threatens the stability of slope. Figure 4(b) also depicts that when the value of $\varphi$ is certain, the distance between $\beta = 40°$ and $\beta = 50°$ is smaller than the distance between $\beta = 50°$ and $\beta = 60°$. This phenomenon indicates that when the value of $\varphi$ is certain, the smaller value of $\beta$ has a greater effect on $K$.

## 4 CONCLUSIONS

The approach of limit equilibrium analysis in conjunction with pseudo-dynamic method is used to deduce the mathematical expression of the seismic stability of layered rock slope. By verification, this approach is feasible to calculate the safe factor of slope. Moreover, by considering the dynamic characteristics of seismic loads, the safe factor calculated by pseudo-dynamic method is greater than the value calculated by pseudo-static method, which is more consistent with real situation. The parametric studies indicate that the dip angle of joint surface, slope angle and the horizontal seismic acceleration coefficient have a decreasing effect on the safe factor, while joint friction angle has an increasing effect on the safe factor. In addition, with the increase of joint friction angle, the horizontal seismic acceleration coefficient and the dip angle of joint surface have a greater influence on the safe factor of slope.

## ACKNOWLEDGEMENTS

The study is supported by the National Science Foundation of China (No. 51174190).

## REFERENCES

Basha, B.M. & Babu, G.L.S. 2009. Seismic rotational displacements of gravity walls by pseudodynamic method with curved rupture surface. *International Journal of Geomechanics* 10(3): 93–105.

Basha, B.M. & Babu, G.L.S. 2010. Reliability assessment of internal stability of reinforced soil structures: A pseudo-dynamic approach. *Soil Dynamics and Earthquake Engineering* 30(5): 336–353.

Choudhury, D., Nimbalkar, S.S. & Mandal J.N. 2007. External stability of reinforced soil walls under seismic conditions. *Geosynthetics International* 14(4): 211–218.

Ebeling, R.M. & Morrison, Jr. E.E. 1993. *The Seismic Sesign of Waterfront Retaining Structures (No. WES/TR/ITL-92-11)*. Army Engineer Waterways Experiment Station Vicksburg Ms Information Technology Lab.

Ghosh, P. & Kolathayar, S. 2011. Seismic passive earth pressure behind non vertical wall with composite failure mechanism: Pseudo-dynamic approach. *Geotechnical and Geological Engineering* 29(3): 363–373.

Ling, H.I., Leshchinsky, D. & Perry, E.B. 1997. Seismic design and performance of geosynthetic-reinforced soil structures. *Geotechnique* 47(5): 933–952.

Michalowski, R.L. & Zhao, A. 1995. Continuum versus structural approach to stability of reinforced soil. *Journal of Geotechnical Engineering* 121(2): 152–162.

Srbulov, M. 2001. Analyses of stability of geogrid reinforced steep slopes and retaining walls. *Computers and Geotechnics* 28(4): 255–268.

Porbaha, A., Zhao, A., Kobayashi, M. & Kishida, T. 2000. Upper bound estimate of scaled reinforced soil retaining walls. *Geotextiles and geomembranes* 18(6): 403–413.

Shafiee, A.H., Eskandarinejad, A. & Jahanandish, M. 2010. Seismic passive earth thrust on retaining walls with cohesive backfills using pseudo-dynamic approach. *Geotechnical and Geological Engineering* 28(4): 525–531.

Singh, D.N. & Basudhar, P.K. 1993. Determination of the optimal lower-bound-bearing capacity of reinforced soil-retaining walls by using finite elements and non-linear programming. *Geotextiles and Geomembranes* 12(7), 665–686.

Steedman, R.S. & Zeng, X. 1990. The influence of phase on the calculation of pseudo-static earth pressure on a retaining wall. *Geotechnique* 40(1): 103–112.

Zhao, A., Montanelli, F. & Rimoldi, P. 1996. Design of reinforced foundations by the slip-line method. *Proceedings of the Earth Reinforcement*. Ochiai Japan, 709–714.

*Rock Dynamics: From Research to Engineering – Li et al. (Eds)*
*© 2016 Taylor & Francis Group, London, ISBN 978-1-138-02953-8*

# Microseismic energy evolution of high rock slop during excavation and after reinforcement

D.Y. Zhuang, Z.Z. Liang & C.A. Tang
*Institute of Rock Instability and Seismicity Research, Dalian University of Technology, China*

K. Ma
*Institute of Mechanics, Chinese Academy of Sciences, China*

ABSTRACT: Rock mass is known to exchange energy with the external environment when it is under load until it fails, a destabilization phenomenon driven by energy. In order to investigate the energy evolution of high rock slope and its relation with rock mass failure of the slope during slope excavation and after reinforcement, a parameter called microseismic energy density was proposed and the relationship between microseismic energy density and the stress and strain of rock mass was discussed. Taking right bank slope of the Dagangshan Hydropower station as an example, the microseismic energy release and energy transference of rock mass during slope excavation and after reinforcement were revealed. These lead to conclusions: Firstly, not only the distribution and intensity of microseismicity but also the potential dangerous area of the slope can be determined synthetically by microseismic energy density. Secondly, the distribution of high energy release zones is closely related to the locations of the deep unloading fracture zones $XL_{316-1}$ and the fault $f_{231}$ moderately dipping out of the slope. Finally, the microseismic event rate and energy density decreased significantly after reinforcing, and the relative high energy release zones transferred to the edge of anti-shear tunnels and low-threat faults, dikes in the deeper area of the slope, so its mechanical behavior was obviously improved. Conclusions can provide references for developing energy criterion and the prediction method of high rock slope failure.

## 1 INTRODUCTION

Rock mass is under external loading, it either absorbs external energy (e.g., mechanical energy and thermal energy) or converts it to its own internal energy or releases its internal strain energy in a certain form until it fails. This is an energy-driven destabilization phenomenon (Xie et al. 2008). Energy evolution during rock deformation and failure can be mainly divided into four processes: energy input, energy accumulation, energy dissipation and energy release (Zhang et al. 2015). Many studies concentrated on energy evolution patterns of rock through theoretical and experimental studies. Zhang & Gao (2015) studied the confining pressure effects on variation and allocation pattern of elastic energy and dissipated energy by conducting axial loading and unloading tests under six different confining pressures for sandstone samples. In order to determine the relationship between energy transformation and coal failure, Peng et al. (2015) investigated the mechanical behaviors of coal specimens taken from a 600-m deep mine conventional triaxial compression tests using five different confining pressures. In engineering practice, Murphy et al. (2012) investigated the relative radiated seismic energy of the explosion by collecting seismic signatures from underground explosions. Zhang et al. (2013) offered a method for hazard assessment in mines, which is based on seismic energy release distribution. Thus, energy release, also seismic radiated energy provides a practical index for evaluating the stability of rock mass structures, including high rock slope. However, little research focused on the relationship between monitoring energy release and stress and strain of rock, an important mechanical concept for assessing the slope stability,

which hinders the stability evaluation of engineering rock masses using microseismic monitoring technique. Meanwhile, with high rock slope widely used, it is necessary to develop stability evaluation and failure prediction methods based on energy monitored which is more available and authentic than theoretical analysis.

In this study, a parameter called microseismic energy density comprehensively reflecting the location and intensity of micro-cracking in rock mass was proposed and the relationship between microseismic energy density and the stress and strain of rock mass was discussed. Using microseismic monitoring data of right bank slope of the Dagangshan Hydropower station, the microseismic energy release and energy transference patterns of rock mass in high rock slope during slope excavation and after reinforcement were revealed.

## 2 MICROSEISMIC ENERGY DENSITY

The elastic energy in rock mass is transformed into inelastic strain energy during fracturing and sliding. Other than the energy dissipated by fracturing and seismic wave propagation, the remaining energy is the microseismic radiation energy received by the sensors. As a measurement for the intensity of microseismic events, the microseismic radiation energy is widely used in studies on microseismic activity for mines (Snelling et al. 2013). According to the studies by Boatwright & Fletcher (1984), the microseismic energy of the seismic source can be calculated from the monitored body wave (P-wave and S-wave):

$$E = 4\pi\rho c R^2 \frac{J_c}{F_c^2} \tag{1}$$

where $E$ is the microseismic energy, $\rho$ is the rock mass density, $c$ is the body wave velocity of the seismic source, $R$ is the distance between the seismic source and sensor, $J_c$ is the energy flux, which can be obtained by integration of particle velocity spectra in the frequency domain, and $F_c$ is the empirical coefficient for the type of seismic wave radiation, which is 0.52 and 0.63 for P-wave and S-wave, respectively (Aki & Richards, 1980). The total energy of the two body waves is the microseismic energy.

For a particular micro-crack, called microseismic event in rock engineering, Source volume, the volume of coseismic inelastic deformation that radiated the recorded seismic waves can be estimated from

$$V = M / \Delta\sigma \tag{2}$$

where $M$ is the seismic moment of microseismic events and $\Delta\sigma$ is the stress drop of the microseismic source before and after micro-cracking.

Since apparent stress $\sigma_A$ scales with stress drop and there is less model dependence in determining the apparent stress than there is in determining corner frequency cubed dependent static stress drop, the apparent volume $V_A$ can be defined as follows (Mendecki 1997):

$$V_A = \frac{M}{2\sigma_A} = \frac{M}{2\mu E} \tag{3}$$

where $\mu$ is the stiffness of rock mass. The apparent volume for a given microseismic event measures the volume of rock with coseismic inelastic strain with accuracy in the order of magnitude of apparent stress divided by rigidity.

The microseismic energy density can be defined as follows:

$$E_d = E / V_A \tag{4}$$

Substituting Eq. 3 into Eq. 4, and assuming that the apparent strain of seismic source is equal to the strain change, we have:

$$E_d = 2\sigma_A \cdot \varepsilon_A \approx \Delta\sigma \cdot \Delta\varepsilon \tag{5}$$

As the energy release during micro-cracking in unit volume of rock mass, the microseismic energy density can not only comprehensively reflect the location and intensity of micro-cracking in rock mass, but also represent the strain energy storage and release process of rock masses in the microseismic source zone. Meanwhile, it can be used to investigate the state of engineering rock mass under external disturbances. The high energy density zone in the slope corresponds to the high energy release zone, and also the micro-cracking concentration and rock damage zone after the rock mass strength is reached.

## 3 MICROSEISMIC ENERGY EVOLUTION OF HIGH ROCK SLOPE

### 3.1 *Project overview*

This case study is the right bank slope of Dagangshan Hydropower Station, which is located at Dadu River in Wajiao Township, Shimian County, Sichuan Province, southwest China. As a typical deep "Ω"-shaped valley, the slopes have experienced long-term epigenetic reformation. As a result, a great amount of diabase and granite aplite dikes are developed in the slope, which are fractured and have poor mechanical properties. The existence of structural planes (such as $XL_{316-1}$, $XL_{9-15}$ and $f_{231}$) dipping out of slope lead to reduced rock mass strength and integrity, and results in anisotropy of rock masses. The slope is featured by large slope angles, complex geological conditions and outstanding stability problems (Fig. 1).

Obvious local deformation and failure was observed on the slope surface during excavation due to complex rock mass structures, and the slope excavation is forced to stop at elevation 1070 m because of instable large rock blocks (Ma 2014). For an extremely large-scale controlling structure with specific boundaries and prone to failure, anti-shear tunnels were adopted to replace weak structures with micro-expansion concrete so as to control the continuing slope deformation. After completing excavation and backfill of the lower 3 anti-shear tunnels in June 2010, slope excavation was restored and the elevation of slope excavation extended to 917 m in June 2011. The excavation of anti-shear tunnels and slope were finished before 30 September 2011, and reinforcement by anti-shear tunnels was fully done until November 2011.

### 3.2 *Distribution of microseismic energy release during excavation*

Figure 2 shows the temporal distribution of elevation of excavation and accumulative microseismic energy from 4 May 2010 to 31 May 2012. Without regard to the failure of monitoring

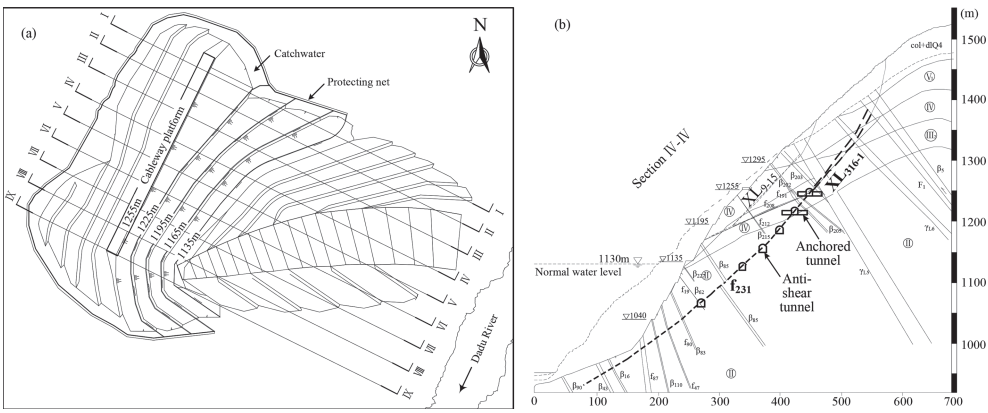


Figure 1. Schematic diagram of Dagangshan right bank slope: (a) excavation outline and (b) geological map of IV-IV section profile.

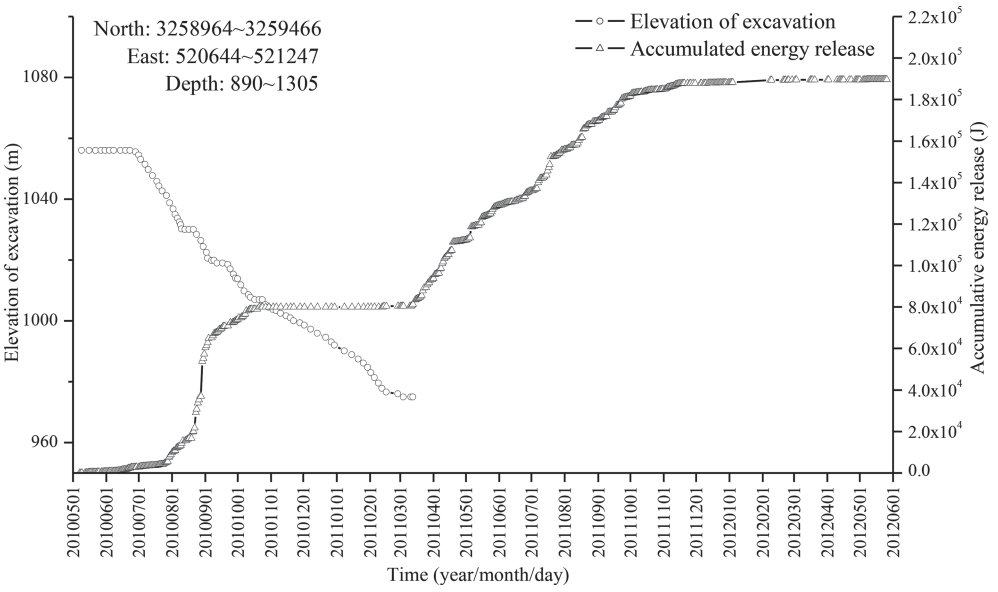


Figure 2. Chart of elevation of slope excavation and accumulative energy release.

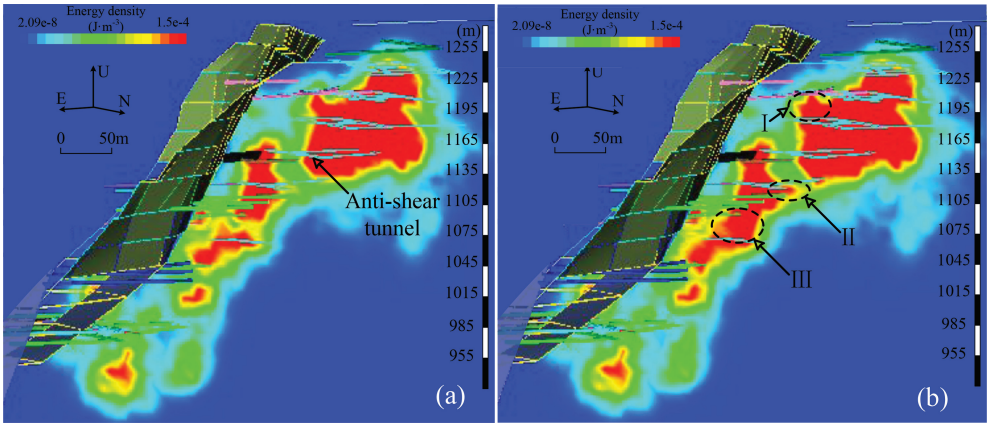


Figure 3. Spatial distribution of microseismic energy density: (a) during excavation and (b) after reinforcement.

system from October 2010 to February 2011, the amount of accumulative energy release increased rapidly prior to November 2011. But the gradient of accumulative energy release curve in August 2010 increased more significantly than that of 2011, which indicates that large-scale slope excavation triggered more high-energy events in this area when excavation restored. According to Figure 3(a), the distribution pattern of high energy release zones is basically consistent with the deep unloading fracture zone $XL_{316-1}$ and the fault $f_{231}$. The high energy zone was extended to the shear exit of the fault $f_{231}$ at elevation 1060 m (The red area in Fig. 3(a)).

The locations of anti-shear tunnels, major structural planes and geodetic coordinates are projected on the energy density map at the corresponding elevation. As seen from Figure 4(a), during slope excavation, the microseismic energy density was high at elevation 1240 m between two anchored tunnels at the south side of the anti-shear tunnel. The rock mass surrounding the anti-shear tunnel and construction tunnel at elevation 1150 m are the locations for

concentrated microseismic energy release, which is about 60 m from the slope surface (Fig. 4(b)). The high energy density zone at the north side and south-west end of the anti-shear tunnel at elevation 1060 m extends about 40 m and generally along the direction of the anti-shear tunnel (Fig. 4(c)). By comparing Figures 4(a)~4(c), it is found that the distribution of high energy release zones is closely related to the locations of the deep unloading fracture zones $XL_{316-1}$ and the fault $f_{231}$.

### 3.3 *Microseismic energy evolution after reinforcement*

After reinforcement by anti-shear tunnels, the accumulative microseismic energy increased slowly (Fig. 5), the high-energy release zones extended by about 10 m into the region at the south side of anti-shear tunnels at elevations 1210 m and 1180 m (I in Fig. 3(b)), the north side of anti-shear tunnel at elevation 1120 m (II in Fig. 3(b)), and the region above elevation 1060 m (III in Fig. 3(b)). These regions were distributed at the edge of anti-shear tunnels and small in area compared to the distribution range of high-energy release zones during excavation, indicating that the stresses in the slope transferred toward the edge of anti-shear tunnels after reinforcement and a small amount of low-energy events were triggered.

Besides, the microseismic energy density at the elevation 1240, 1150 and 1060 m decreased significantly after reinforcement, and the relative high energy release transferred to the edge of anti-shear tunnels and low-threat faults, dikes in the deeper area of the slope. In details, there is no high energy release zone at elevation 1240 m, while relative high energy release transferred to diabase dike ($\beta_{202}$) and intersection of anti-shear tunnel and construction tunnel at elevation 1150 m and to diabase dike ($\beta_{202}$) and fault $f_{167}$ in the deeper area 200 m away from slope surface at elevation 1060 m, so its mechanical behavior was obviously improved.

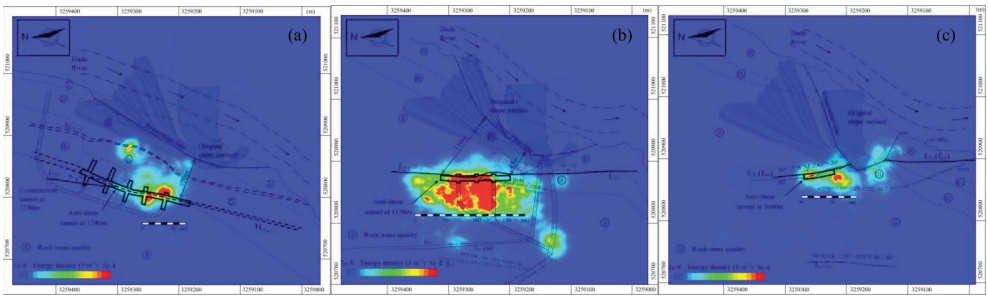


Figure 4. Distribution of microseismic energy density at various elevation levels during excavation: (a) 1240 m; (b) 1150 m; and (c) 1060 m.

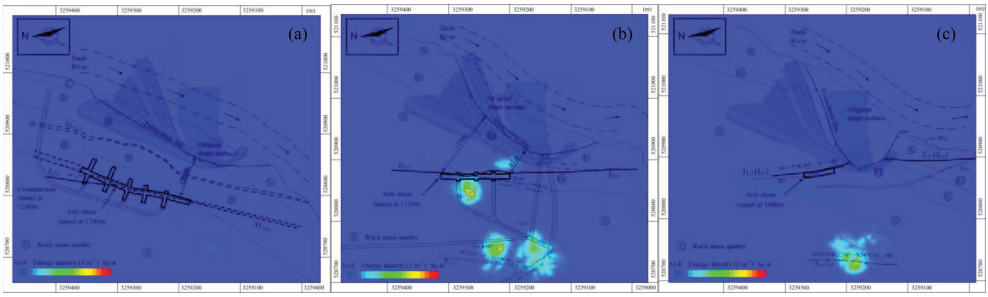


Figure 5. Distribution of microseismic energy density at various elevation levels after reinforcement: (a) 1240 m; (b) 1150 m; and (c) 1060 m.

## 4 CONCLUSIONS

This study shows that microseismic energy density is a practical index for comprehensively reflecting the location and intensity of micro-cracking in rock mass and analyzing the strain energy storage and release process of rock masses in the microseismic source zone. Potential dangerous area of the slope during exaction and after reinforcement can be determined using microseismic energy density. Due to the disturbance of the unloading fissures $XL_{316-1}$ under slope excavating, high energy density area was induced between two anchored tunnels both south of anti-shear tunnels at elevation 1240 m, while the disturbance of fault $f_{231}$ dipping out of the slope resulted in development of high energy release area along with fault strike at the 1150 and 1060 m elevation, which led to the formation of excavation damage zone extending to about 150 m inside the slope. Microseismic energy density at different elevation decreased significantly after reinforcement, and the relative high energy release transferred to the edge of anti-shear tunnels and low-threat faults, dikes in the deeper area of the slope, which indicates that the anti-shear tunnels played an active role in reinforcement and stress transference, and enhanced the mechanical performance of structural planes. Conclusions can provide references for developing energy criterion and prediction method of high rock slope failure.

## REFERENCES


Aki, K. & Richards, P.G. 1980. *Quantitative Seismology: Theory and Methods ( Vol I and II)*. San Francisco: W.H. Freeman and Co.

Boatwright, J., & Fletcher, J.B. 1984. The partition of radiated energy between P and S waves. *Bulletin of the Seismological Society of America* 74: 361–376.

Ma, K. 2014. *Study on the Potential Failure Mechanism, Monitoring and Controlling Methods of Rock Slope under Excavation*. PhD Thesis, Dalian University of Technology. (in Chinese).

Mendecki, A.J. 1996. *Seismic Monitoring in Mines*. London: Chapman & Hall: 181–186.

Murphy, M.M., Westman, E.C., Iannacchione, A.T. et al. 2012. Relationship between radiated seismic energy and explosive pressure for controlled methane and coal dust explosions in an underground mine. *Tunnelling and Underground Space Technology* 28: 278–286.

Peng, R.D., Ju, Y., Wang, J.G. et al. 2015. Energy dissipation and release during coall failure under conventional triaxial compression. *Rock Mechanics and Rock Engineering* 48: 509–526.

Snelling, P.E., Laurent, G. & Mckinnon, S.D. 2013. The role of geologic structure and stress in triggering remote seismicity in Creighton Mine, Sudbury. *International Journal of Rock Mechanics and Mining Sciences* 58: 167–179.

Xie, H.P., Ju, Y., Li, L.Y. et al, 2008. Energy mechanism of deformation and failure of rock masses. *Journal of Rock Mechanics and Geotechnical Engineering* 27(9): 1729–1740.

Zhang, Z.Z. & Gao, F. 2015. Confining pressure effect on rock energy. *Chinese Journal of Rock Mechanics and Engineering* 34(1): 1–10. (in Chinese).

Zhang, Z.Z. & Gao, F. 2015. Experimental investigation on the energy evolution of dry and water-saturated red sandstones. *International Journal of Mining Science and Technology* 25(3): 383–388.

Zhang, M.W., Shimada, H., Sasaoka, T. et al. 2013. Seismic energy distribution and hazard assessment in underground coal mines using statistical energy analysis. *International Journal of Rock Mechanics and Mining Sciences* 64: 192–200.

**Rock Dynamics: From Research to Engineering** is a collection of the scientific and technical papers presented at the Second International Conference on Rock Dynamics and Applications (RocDyn-2, Suzhou, China, 18-19 May 2016).

The book has four sections. The first section contains 8 keynote papers, covering a wide range of dynamic issues related to rock mechanics and rock engineering, from rock failure mechanism and stress wave propagation to seismic behaviour and impact. Section 2 includes papers on rock dynamic theory and numerical modelling, focussing on theoretical aspects of rock fracture dynamics, wave propagation, numerical methods and numerical modelling works. Papers on laboratory testing and experimental techniques are collected in Section 3, including new testing facilities, data monitoring and data analysis. Section 4 deals with case studies and engineering applications, and presents state-of-the-art papers on rock engineering related to dynamic conditions such as earthquake and blasting.

**Rock Dynamics: From Research to Engineering** will serve as a must-have reference, presenting the results of recent developments in rock dynamics scientific research and rock dynamics engineering applications.

ISBN 978-1-138-02953-8

9 781138 029538

an **informa** business

CRC Press
Taylor & Francis Group
an **informa** business
www.crcpress.com

6000 Broken Sound Parkway, NW
Suite 300, Boca Raton, FL 33487
Schipholweg 107C
2316 XC Leiden, NL
2 Park Square, Milton Park
Abingdon, Oxon OX14 4RN, UK